Graduate School of the Southampton Oceanography Centre

University of Southampton

This PhD thesis by

Nicola Grace Holland

has been produced under the supervision of the following persons

Supervisors:	**Dr. Steven Roberts** University of Southampton
	Dr. Richard Herrington The Natural History Museum, London
Chair of Advisory Panel:	**Prof. Chris German** University of Southampton
Member of Advisory Panel:	**Prof. Martin Palmer** University of Southampton

UNIVERSITY OF SOUTHAMPTON

ABSTRACT

FACULTY OF SCIENCE
SCHOOL OF OCEAN AND EARTH SCIENCE

Doctor of Philosophy

THE FORMATION OF AN ANCIENT, GOLD-RICH VOLCANOGENIC MASSIVE SULPHIDE DEPOSIT: A STUDY OF THE BALTA TAU DEPOSIT IN THE SOUTHERN URALS OF RUSSIA

Balta Tau is a high grade, gold-rich VMS deposit located in well preserved Palaeozoic island arc volcanics of the Southern Urals in Russia. Host sequences are andesitic island arc tholeiites of the Irendyk Formation, deposited in a fore-arc to mainstage island arc setting in shallow waters. Regional prehnite/actinolite-pumpellyite grade metamorphism is characteristic of seawater interaction with volcanic rocks. Massive sulphide mineralization comprises pyrite-chalcopyrite and pyrite-sphalerite-rich ores and upper sphalerite-rich and barite-rich facies, overlain by a barite-dominated horizon which contains an unusual tennantite-chalcopyrite(-galena) assemblage with abundant coarse electrum. Ore textures are consistent with sulphide-barite deposition at the seafloor, and indicate a primary hydrothermal origin for electrum. Compositionally layered sulphides are found at the margins of the massive sulphide lens, and represent fine grained clastic sulphides that recrystallized during late stages of ore formation. Beneath the sulphide lens, footwall volcanics contain extensive vein-hosted and disseminated sulphides, with chalcopyrite-pyrite rich horizons in the central zones and sphalerite-rich sulphides dominating the marginal zones.

Palaeofluid, stable and radiogenic isotope analyses indicate that ore forming fluids were derived from the interaction of Devonian seawater and volcanic arc rocks, with estimated fluid $\delta^{18}O$ of –2.5 to +1‰, $^{87}Sr/^{86}Sr$ of 0.7045 and salinities of 2.4 to 6.4 wt% NaCl eqiv., the latter suggestive of sub-seafloor phase separation. The sphalerite and barite rich ore facies appear to have formed at low temperatures of 130 to 170°C, while solubility constraints suggest chalcopyrite-rich ores to have formed at 250 to 300°C. Observed mineral assemblages suggest oxidation conditions were buffered in the pyrite field, below the stability of bornite, and at low to moderate sulphidation. Barite $^{87}Sr/^{86}Sr$ (0.7050 to 0.7069) and $\delta^{18}O$ (+8.3 to +13.7‰) indicate significant conductive cooling of hydrothermal fluids and 5 to 50% seawater mixing during ore formation, most likely facilitated by the high porosity of footwall volcanics. Sulphides (with $\delta^{34}S$ of –3.3 to +2.4‰) precipitated from hydrothermal H_2S derived from underlying volcanic rocks, while the sulphate in barite (with $\delta^{34}S$ of +17.6 to +21.6‰) was supplied by seawater during fluid mixing. Sulphur isotopic equilibrium was not attained between aqueous H_2S and SO_4^{2-}, however barite $\delta^{18}O$ suggests there was an approach to oxygen isotopic equilibrium between aqueous SO_4^{2-} and fluid H_2O. Footwall quartz-Mg-chlorite alteration formed at 100 to 150°C during waning stages of hydrothermal activity. Sericitization of the hanging-wall unit is also likely to have occurred at this time, indicating that deposition of the immediate hanging-wall volcanic unit occurred prior to or during these late stages of hydrothermal activity.

The Au-Ag-Pb-Ba enrichment and moderately high oxidation of Balta Tau ores may be attributed to source rock composition. However, deposit scale factors were important in determining the composition, mineralogy and gold enrichment of specific ore facies. The compositional zoning in footwall and massive sulphides reflects differences in the saturation temperatures of base metals transported as chloride complexes, with Cu-rich ores in central, higher temperature zones giving way to Zn(Pb-As-Sb) rich sulphides in cooler marginal zones. The gold-barite rich ores most likely formed in a barite structure that trapped hydrothermal fluids emerging from the sulphide mound and limited the extent of seawater mixing. Precipitation of Au and other trace metals was facilitated by the long residence time of fluids in the barite structure, low pH (due to extensive sulphide precipitation in the mound) and low temperatures of around 150°C. The high barite/base metal and precious/base metal ratios of these ores reflects the base metal depletion of fluids following sulphide deposition in the mound.

ACKNOWLEDGMENTS

Financial support for this project was provided by both Anglo American plc and BHP Billiton plc.

Many thanks to Richard Herrington and Steve Roberts for their support, supervision and patience throughout this study. Thanks also to the numerous people who have assisted with this work, in particular Valeriy Maslennikov, Igor Servakin, Victor Puchkov and many other Russian colleagues for providing superb fieldwork support, logistics and a wealth of information; Tina Hayes and Matt Cooper for their dedication and perseverance with whole rock dissolutions and Sr isotope analyses; Andy Milton and Ian Croudace for much help with ICP-MS and XRF respectively; Adrian Boyce and Tony Fallick for invaluable discussions and assistance with stable isotope work; John Spratt for assisting with microprobe analyses; Damon Teagle and Rex Taylor for general discussions and advice; Barry Marsh for providing excellent photos of so many samples; Berndt Buschmann and Peter Jonas for their support and lengthy discussions during fieldwork, and Jamie Wilkinson for assistance with fluid inclusion studies.

My huge thanks to Mum and Dad for their unwavering support, encouragement and confidence in my abilities and to Phil for such understanding, dedication and endurance of day-to-day stresses particularly during writing up; I could not have achieved this without such support. Also huge thanks to Nana for relentless cups of tea and showing such an interest in my work, I wish you could have been here to see the final result. Finally, many thanks to Richard Barnes for continued friendship and considerable help with getting started, and to Robin Armstrong, Tina Hayes, Iain Pitcairn, Ross McGowan and Claire Chamberlain for their valued friendship throughout.

CONTENTS

1 INTRODUCTION

1.1 VOLCANOGENIC MASSIVE SULPHIDE DEPOSITS

Volcanogenic massive sulphide deposits (VMS) are a major source of Cu and Zn and may also contain economically recoverable Pb, Ag and Au. VMS deposits consist of sulphide dominated ores hosted in volcanic sequences, and have formed throughout much of the Earth's history from the Archean to the present day. In recent decades, actively forming sulphide deposits on the seafloor have been recognised as modern analogues of VMS deposits, and studies of these systems have advanced our understanding of ore forming processes responsible for ancient VMS deposits.

Numerous publications dedicated to VMS deposits summarise their features and address formational processes, including Hutchinson, 1973; Large 1977; Franklin et al., 1981; Eldridge et al., 1983; Ohmoto et al., 1983 and Lydon et al., 1984. In brief, definitive characteristics and fundamental aspects of their formation include:

- Host rocks are oceanic volcanic sequences which are broadly cogenetic with sulphide ores.
- Mineralization typically comprises a conformable horizon of massive sulphides which precipitated at or close to the seafloor, underlain by vein and disseminated sulphides replacing host volcanics rocks in the footwall.
- Sulphides are dominated by pyrite-pyrrhotite-chalcopyrite-sphalerite, often with significant galena and sulphosalts and a wide range of rare minerals. In addition to the major metals Cu, Fe, Zn and Pb, ores may be considerably enriched in Au, Ag, As, Sb, Hg, Cd, Te, Se, Ge, Hg, Co and Mo.
- Footwall volcanic rocks are extensively altered, with typical assemblages dominated by quartz, chlorite, sericite and clay minerals such as illite and smectite. The alteration zone may be stratigraphically controlled or discordant and pipe-like.
- Ore forming fluids are derived form the high temperature interaction of seawater with volcanic rocks of the ocean crust. Fluid-rock interaction results in a hydrothermal fluid that is rich in metals leached from the volcanic rocks, and sulphur derived from the volcanic rocks and reduction of seawater sulphate.
- Intrusive rocks at depth in the ocean crust supply heat to drive hydrothermal convection, and in some cases may directly contribute metal and sulphur rich volatiles to the hydrothermal fluids.
- Precipitation of sulphides at or just below the seafloor results primarily from conductive cooling of hydrothermal fluids and mixing with seawater. Additional processes such as fluid boiling have been demonstrated to be important in some deposits.

1.2 COMPOSITIONAL VARIATION AND GOLD ENRICHMENT OF VMS ORES

VMS deposits display a high degree of compositional diversity both between and within orebodies, with variable base metals ratios and selective precious metal enrichment. Similar compositional variations documented from actively forming systems suggest that in many cases these are a primary feature of massive sulphide deposits. Factors that may influence or the composition of ores include:

- Variations in source rock composition (e.g. Barrie and Hannington, 1989).
- Additional sources of fluids and/or metals, such as a direct input of magmatic volatiles (e.g. Herzig et al., 1998).
- Hydrothermal fluid properties and evolution; temperature, pH, salinity and oxidation may all affect the ability of fluids to transport and deposit metals (e.g. Huston and Large, 1989, Hannington and Scott, 1989; Large, 1992).
- Fluid boiling segregating metals and increasing efficiency of metal deposition, in particular gold (e.g. Sherlock et al., 1999).
- Syn-formational reworking and segregation of sulphides during zone refining (e.g. Hannington et al., 1995).
- Remobilisation and concentration of selected metals into particular ore horizons or late veins during metamorphism (e.g. Larocque and Hodgson, 1995; Marignac et al., 2003).
- Introduction of metals during a later stage of mineralization that is genetically unrelated to the formation of VMS ores (e.g. Marquis et al., 1990).

Determining which of these processes are the most influential over the composition of ancient VMS deposits is often impaired by metamorphism and deformation overprinting primary features. Studies of modern systems have aided understanding of formational processes but focus on sulphide deposits forming at mid ocean ridges, which may not be directly comparable to the majority of ancient deposits that formed in subduction-related environments.

A particular aspect of VMS deposits that has attracted considerable attention is the selective gold enrichment of ores (Hannington et al., 1999; Huston, 2000), which can transform an otherwise sub-economical deposit into a viable mining project. The occurrence of coarse, visible gold is commonly reported from ancient deposits, but is scarce to absent in active systems. This discrepancy is not yet fully understood, and may indicate that modern systems analogous to ancient gold-rich deposits have yet to be discovered, or that the coarse gold in ancient deposits is entirely the result of post-formational modification of VMS ores.

1.3 THE SOUTHERN URALS VMS DISTRICT

The Ural Mountains of Russia form a narrow, north-south trending belt located approximately 1700km East of Moscow, extending from polar regions in the North to the border with Kazakhstan in the South (Figure 1.1a). Geographically, the Urals are an important region as they form the divide between Europe and Asia. Geologically, the Urals comprise a diverse range of geodynamic zones that record the closure of a Palaeozoic ocean, which are now preserved between the East European and Kazakhstan Continental platforms. In addition, the Urals host a vast mineral wealth, including industrial minerals, base metals, precious metals, platinum group elements and gemstones.

The southern Urals host at least 80 VMS deposits (Herrington et al., 2002) and are one of the world's largest VMS districts. A significant proportion of these VMS deposits are located in well preserved Palaeozoic island arc sequences of the Magnitogorsk Zone, and formed in a range of formational settings with variable host rocks, tonnage, and metal content (Figure 1.1b). The diverse characteristics of these deposits coupled with a low degree of metamorphic and deformational overprinting present an excellent opportunity for studying the development of ancient arc-related VMS systems, from large scale influences of tectonic setting and host rock composition to deposit scale controls of ore forming processes.

The classification of Uralian VMS deposits as defined by Russian workers broadly links deposit style, composition and host rocks as follows (Prokin and Buslaev, 1999; Maslennikov et al., 2000; Herrington et al., 2002):

- Cyprus type deposits; Cu-rich and hosted in MORB-like units.
- Urals type deposits; large Cu-Zn deposits hosted in bimodal volcanic sequences.
- Baimak type deposits; small, polymetallic and gold-rich deposits hosted in felsic volcanic and intrusive complexes.

There is poor agreement in Russian literature concerning the relationship of these deposit types with tectonic development of the island arc, particularly with regard to the Urals and Baimak type deposits. In addition, there is no consensus as to the cause of high precious metal content of Baimak type deposits, with suggestions including a continental contribution to metal budgets (Prokin et al., 1999), differing host rock chemistry (Herrington et al., 2000), a genetic link with felsic intrusives (Buschmann et al., 2000), enrichment during seafloor interaction of sulphides with seawater (Maslennikov et al., 2000), and a progression to more epithermal characteristics reflecting shallow water depths (Herrington et al., 2002). Further studies of these deposits are required to better understand the causes of compositional variation and gold enrichment, and the relationship between deposit formation and island arc development.

a. Location map of the Ural Mountains in Russia.

b. Location of the Balta Tau deposit in relation to the Magnitogorsk Zone, other VMS deposits and major towns in the southern Urals. The area of this map is represented by the red box in Figure (a).

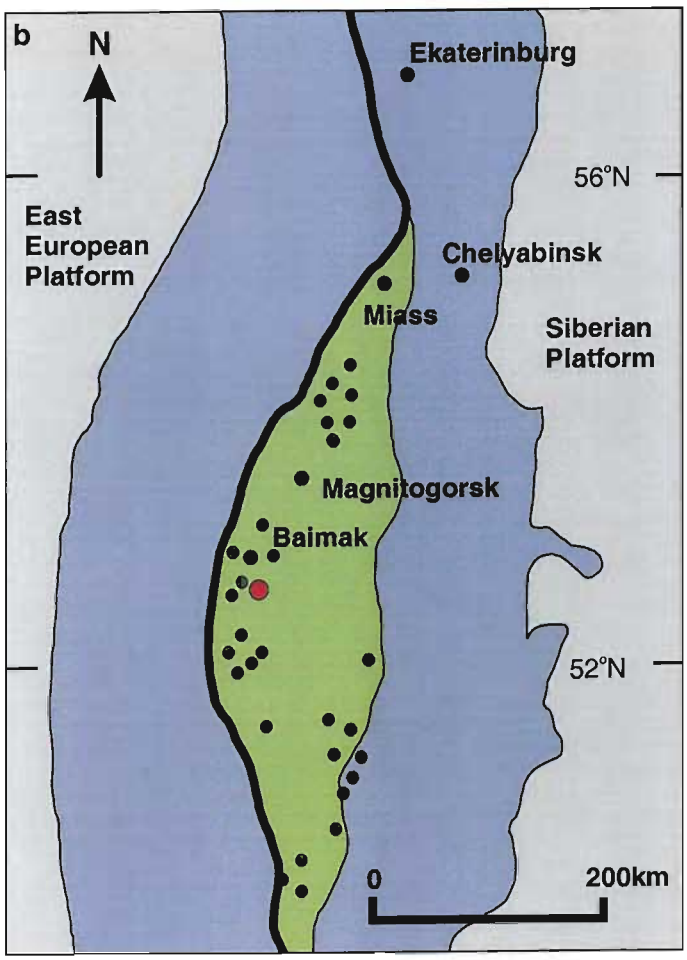

Figure 1.1. Location of the southern Urals Magnitogorsk Zone and the Balta Tau deposit.

1.4 THE BALTA TAU DEPOSIT AND PROJECT RATIONALE

Balta Tau is a small, polymetallic and precious metal rich VMS deposit in the southern Urals exploited by open pit (Figure 1.2). In addition to high Cu and Zn contents, Balta Tau is unusually Au-rich and is estimated to comprise 3.5 millions tonnes grading 3% Cu, 5% Zn and 5g/t Au (Maslennikov, pers. comm.) as well as significant enrichment in Pb, As, Sb and Ag. The Au enrichment is confined to a barite-rich horizon which is mineralogically distinct from the massive sulphides. In spite of the high precious and base metal contents and unusual mineralogy, published studies of the Balta Tau deposit are restricted to Russian monographs and the deposit has received little more than a mention in western literature. Balta Tau is classified as a Baimak Type deposit by Russian workers (e.g. Prokin and Buslaev, 1999), however the host units are not typical of this deposit type and there is some debate as to which volcanic formation they belong to.

This study aims to improve understanding of the formation of Uralian VMS deposits and in particular investigate processes of gold enrichment. The Balta Tau deposit has been selected as a focus for this work on the basis of:

- Good preservation of sulphide ores and their host rocks.
- High grade and polymetallic nature of ores with an unusual mineralogy and gold enrichment.
- Lack of comprehensive studies of ore formation prior to this project.
- Good preservation of volcanic units on a regional scale, enabling the Balta Tau deposit to be considered within a well defined tectonic framework.

Figure 1.2. General view of the Balta Tau open pit.

1.5 PROJECT AIMS

The overall aims of this project are:

(i) To understand the formational processes responsible for the various ore facies of the Balta Tau deposit, in particular gold-rich horizons.

(ii) To ascertain the relative importance of regional factors relating to tectonic setting and island arc evolution compared to ore forming processes at the scale of individual ore horizons on the formation and composition of ores.

(iii) To provide a link between ore facies in ancient metamorphosed VMS systems and those of modern, actively forming systems, in particular with regard to gold enrichment in ores.

These will be addressed by the following specific objectives:

- Identify the volcanic formation hosting Balta Tau and interpret the depositional environment of ore formation and temporal relationship to island arc evolution.
- Establish the genetic and temporal relationship between gold and sulphide ores and in particular determine if gold precipitation is cogenetic with massive sulphide formation.
- Interpret processes of ore formation responsible for the diverse styles of mineralization, including sources of metals and fluids, conditions of ore formation and precipitation mechanisms.
- Draw comparisons between the ore facies of Balta Tau and those of actively forming modern systems.
- Evaluate and discriminate between the effects of post-ore forming processes including late stage hydrothermal activity, diagenesis, metamorphism and deformation.

1.6 METHODOLOGY AND THESIS OUTLINE

A total of eleven weeks were dedicated to fieldwork in the southern Urals. Fieldwork commenced with attending the MinUrals geodynamic expedition, 2001 (lead by V. Puchkov), a three week excursion to key sites in the southern and middle Urals to understand the regional development of the southern Urals belt. This is summarised in Chapter 2.

The remaining fieldwork was focussed on the Balta Tau Mine and surrounding area. Access to the Balta Tau open pit enabled detailed mapping and collection of a comprehensive sample suite in 2001, and a further opportunity to map and sample during a brief return visit in 2002. Additional samples of mineralization from Balta Tau were provided by R. Herrington and V. Maslennikov, which had been collected during previous visits in 1995, 1999 and 2000. Volcanic units exposed

in the area surrounding the Balta Tau deposit were also mapped and sampled, and where possible neighbouring VMS deposits were visited.

Sample suites, field observations and mapping have been utilised as follows:

- A petrological and geochemical investigation of mine sequences and local volcanic units which combines petrographical descriptions with whole rock analyses of major and trace elements using XRF and ICP-MS, presented in Chapter 3.
- Interpretation of ore paragenesis based on detailed studies of mineralogy and textures of Balta Tau mineralization in hand specimen and polished thin section, described in Chapter 4.
- Determination of major and trace element chemistry of sulphide and alteration phases using an electron microprobe and their implications for ore forming conditions and processes, presented and discussed in Chapter 5.
- A study of palaeofluids, S, O and Sr isotope systematics to provide further insights into ore forming processes, presented in Chapter 6.

A discussion of ore formation in Chapter 7 brings these studies together in conjunction with chemical aspects of ore precipitation, and a model of ore formation including a hypothesis for the formation of the gold-rich barite mineralization is presented. Finally, conclusions and implications for the understanding of VMS ore formation in other ancient and modern deposits are given in Chapter 8.

2 GEOLOGICAL FRAMEWORK AND METALLOGENY OF THE SOUTHERN URALS

2.1 GEODYNAMIC UNITS AND TECTONIC EVOLUTION OF THE SOUTHERN URALS

2.1.1 Introduction

The Ural Mountains are a North-South trending belt extending for almost 2000km along the boundary between the East European and West Siberian platforms. The Southern Urals comprise a series of well preserved terranes which record the opening and closure of a palaeo-ocean during the Lower to Middle Palaeozoic, and provide an excellent opportunity to study processes of intra-oceanic subduction and island-arc formation, arc-continent collision, accretion and continental collision during the Palaeozoic (e.g. Puchkov, 1997; Brown et al., 1997). The region is also of significant economic interest, hosting extensive mineral resources including gold, platinum group elements, base metals, chromite and magnetite.

The Urals are a Late Palaeozoic orogenic belt bounded by the East European Craton to the West, and extensive Mesozoic and Cenozoic sedimentary basins to the South and West (Figure 1). These recent sedimentary basins obscure the relationship between the Urals and Palaeozoic orogenic belts of the Altaid Collage (or Central Asian Foldbelt), leading to conflicting interpretations of the Urals as either an isolated fold belt or part of the Altaids (Herrington et al. 2002, and references therein). Recent studies of regional aeromagnetic data reveal structures beneath these basins that suggest the Urals to be a continuous extension of the Altaid belt. Magmatic arcs start to the south of the Urals under the Ust-Yurt plateau, extend northwards along exposed sections of the Urals, and continue from the Polar Urals in a southeasterly direction under Mesozoic-Cenozoic sediments of the West Siberian basin to link up with synchronous arcs of Rudny Altai in West Siberia (Figure 2.1) (Yakubchuk, 2001; Herrington et al., 2002).

Early tectonic interpretations of the Urals varied considerably and stemmed mainly from Soviet theories of geosynclinal development. With development of the plate tectonic theory, which was first applied to the Urals belt by Zoneneshain et al. (1984), and imaging of deep crustal structures from seismic reflection profiles, gravity and magnetic data (e.g. Puchkov, 1997), the Urals was increasingly recognised as remnants of a closed Palaeozoic ocean. Detailed interpretation of the southern Urals was enhanced by the Uralides Project launched by EUROPROBE in 1995, which employed a variety of geological, geochemical and geophysical techniques to investigate the nature and evolution of the Uralide Orogen.

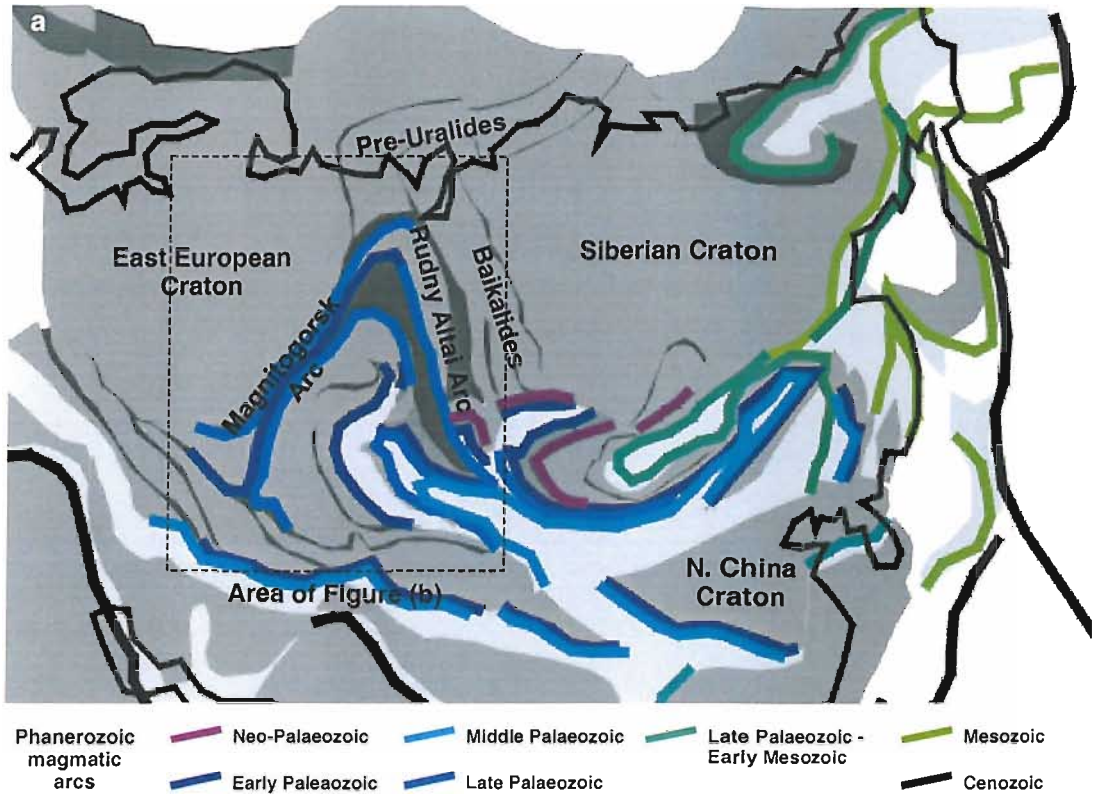

Major cratonic blocks and Phanerozoic magmatic arcs of Eurasia based on interpretation of regional aeromagnetic data, showing the relationship between the Magnitigorsk Arc of the Urals and those of the Altaid belt (Yakubchuk and Schissel, 2002).

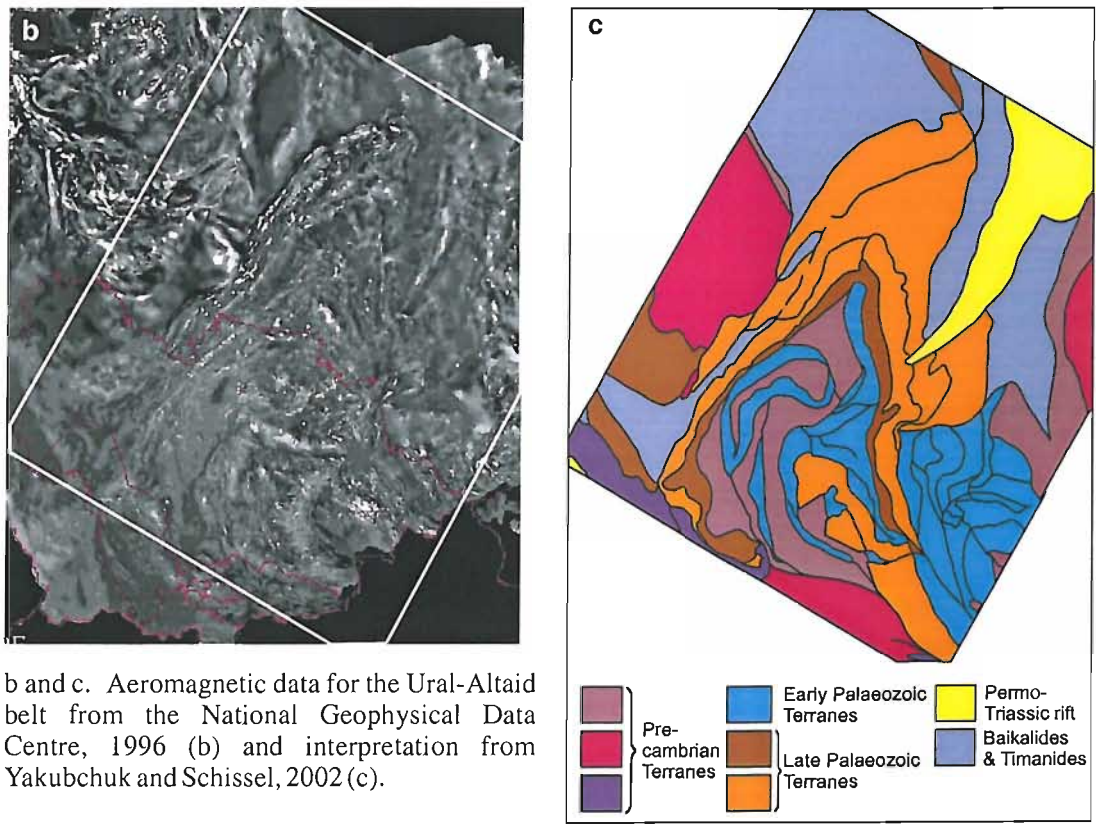

b and c. Aeromagnetic data for the Ural-Altaid belt from the National Geophysical Data Centre, 1996 (b) and interpretation from Yakubchuk and Schissel, 2002 (c).

Figure 2.1. Relationship between the Urals orogenic belt and the Altaides based on interpretation of regional aeromagnetic data.

The principal geodynamic units of the southern Urals are shown in Figure 2.2. The most dominant feature is the Main Uralian Fault Zone (MUFZ), an extensive melange zone continuous over the entire length of the Urals. Immediately West of this fault are a number of allochthonous units interpreted as an accretionary wedge (Brown et al., 1998) including obducted oceanic crust and an exhumed high pressure metamorphic facies. Further west of the accretionary complex are platform and passive margin sediments overlying the East European Craton exposed in a foreland thrust and fold belt and foreland basin. To the East of the MUFZ are autochthonous Devonian island arc volcanics and associated sediments of the Magnitogorsk Zone (e.g. Puchkov, 1997; Brown et al., 1998).

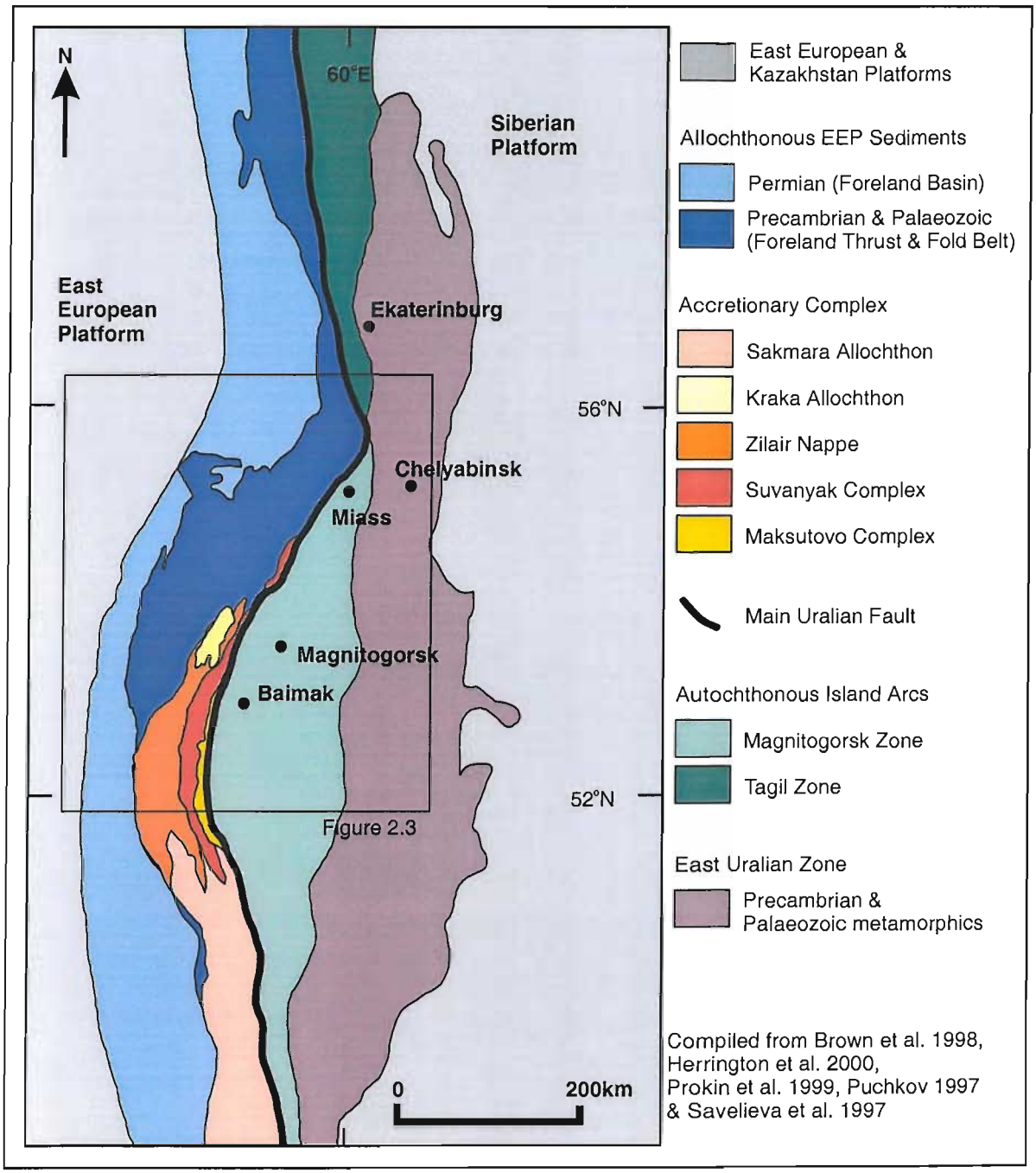

Figure 2.2. Principal geodynamic zones of the Urals.

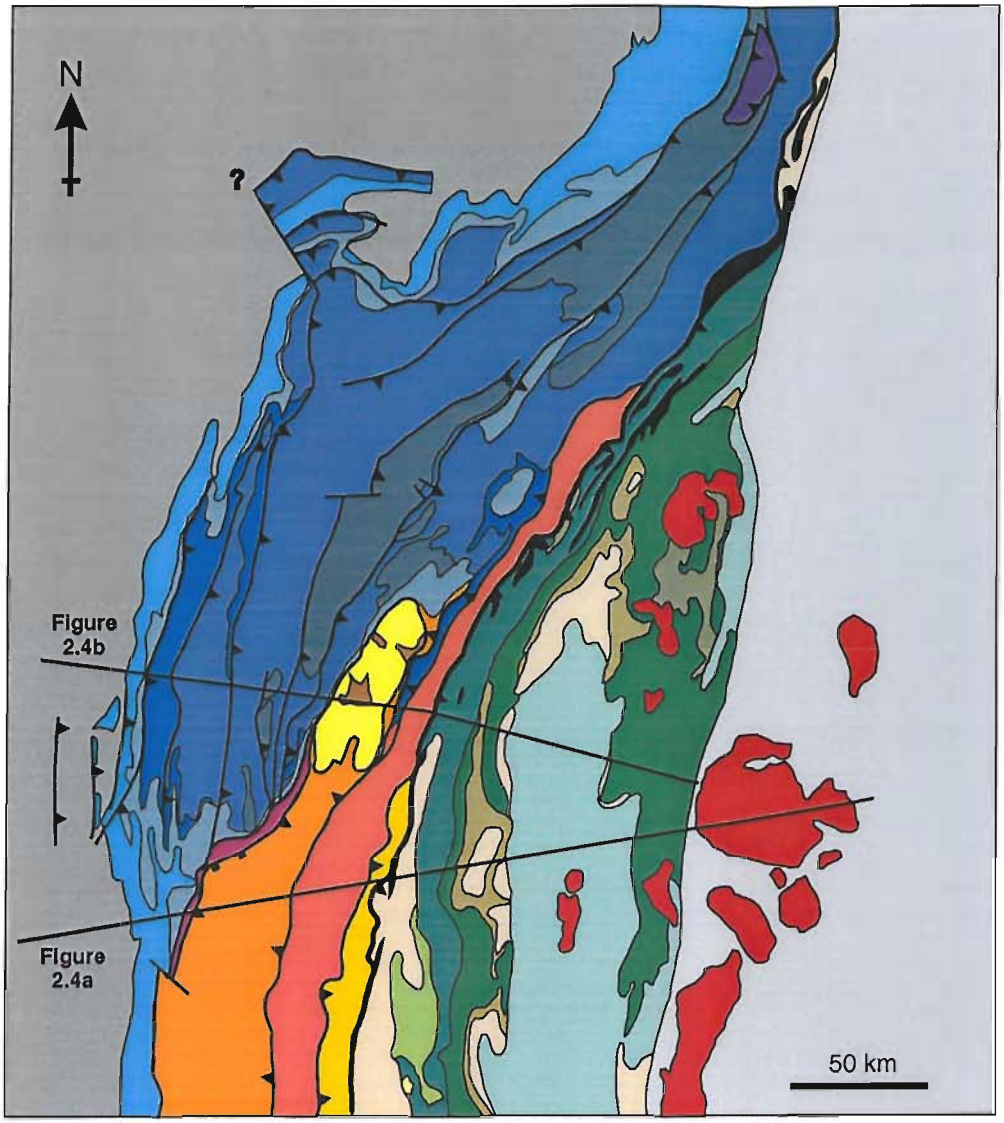

Foreland thrust and fold belt
- Permian
- Carboniferous
- Ordovician, Silurian and Devonian
- Vendian
- Middle and Upper Riphean
- Lower Riphean
- Taratash Metamorphic Complex

Accretionary Complex
- Timorovo Thrust System
- Suvanyak Complex
- Zilair Nappe
- Uzayan Nappe
- Kraka Allochthon
- Maksutovo Complex

Magnitogorsk Zone
- Carboniferous
- Upper Devonian - Carboniferous (Upper Zilair Fm)
- Upper Devonian (Lower Zilair Fm)
- Middle Devonian (Karamalytash & Ulutau Fm)
- Lower Devonian (Irendyk Fm)
- Lower Devonian (Baimak-Buribai Fm)
- Silurian - Devonian undifferentiated
- Granitoids

Main Uralian Fault Zone
- Main Uralian Fault
- Devonian blocks in melange

East Uralian Zone
- Precambrian & Palaeozoic metamorphics
- Granitoids

(After Brown et al., 1998)

Figure 2.3. Geotectonic units of the Southern Urals.

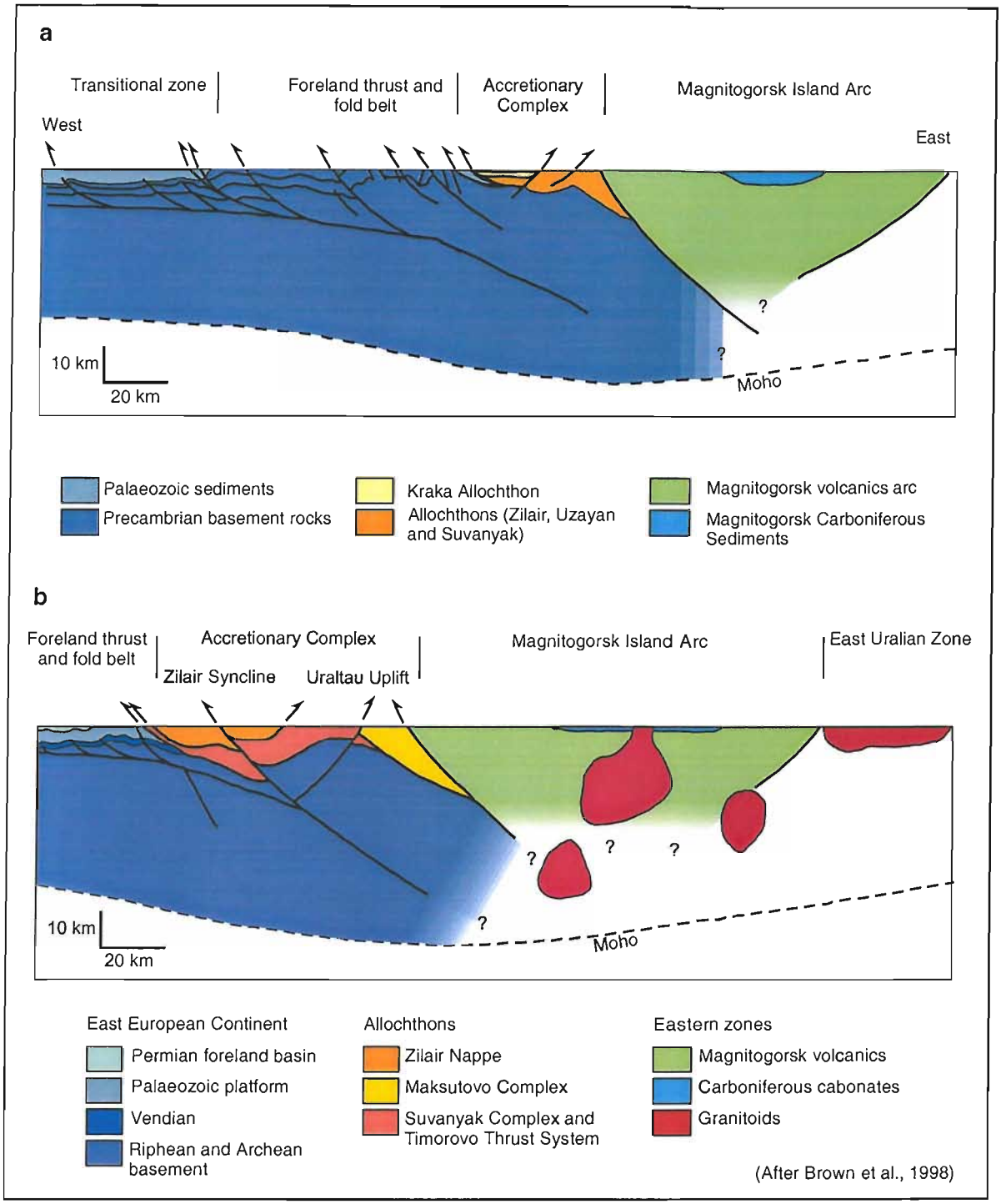

Figure 2.4. Cross-sections of the southern Urals based on interpretation of seismic sections.

2.1.2 Foreland Fold and Thrust Belt of the East European Continental Margin

The western region of the southern Urals is dominated by Proterozoic and Palaeozoic sediments and carbonates of the East European Platform (Figures 2.2 and 2.3). These sequences are disrupted by the development of a foreland basin and a foreland thrust and fold belt (Figure 2.4) associated with continental collision of the East European and Kazakhstan Continents during Late Carboniferous to Early Permian (Brown et al. 1997).

Precambrian Sequences

The oldest rocks exposed in the southern Urals are the late Archean Taratash Metamorphic Complex (Figure 2.3), which are suggested to represent the European Craton crystalline basement assumed to underlie all Proterozoic sequences (Puchkov, 1997). The Proterozoic consists of Riphean (~1700-800Ma) platform carbonates and siliciclastics totalling 12km in thickness that host extensive economic siderite and magnesite deposits. Basaltic volcanics in the Lower and Middle Riphean may reflect episodes of continental rifting (Puchkov, 1997). The Riphean is unconformably overlain by Vendian (~610-543Ma) polymict conglomerates, sandstones and shales, with Upper Vendian sequences suggested to be the molasse of a pre-Uralide orogenic event (Brown et al, 1997; Puchkov 1997). The Proterozoic successions are variably metamorphosed and deformed. In the West, Riphean carbonates are remarkably unmetamorphosed and in overlying sequences the contact between Vendian and Ordovician sediments is a stratigraphic unconformity (Figure 2.5a) with no evidence of a Precambrian deformational event (Puchkov, pers. comm.). By contrast, further East the Riphean is metamorphosed to amphibolite facies, with a sharp angular unconformity between Riphean schists and overlying unmetamorphosed basal conglomerate of the Ordovician (Figure 2.5b). This metamorphism of the Riphean is dated as Vendian and provides further evidence for a Pre-Uralide orogenic event (Puchkov 1997).

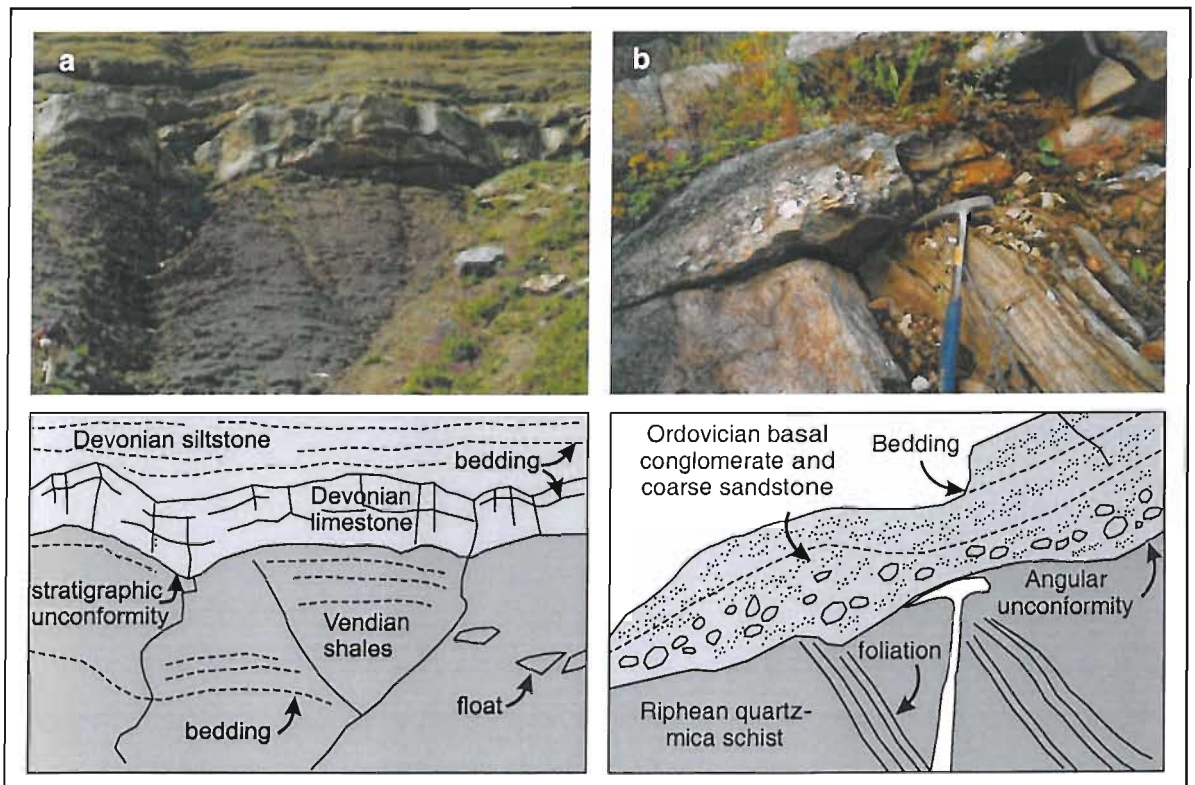

a. Stratigraphic unconformity between Vendian shales and overlying Devonian quartzites (the lower Palaeozoic is absent). In this exposure the only deformation to have affected sequences is a weak Palaeozoic event.

b. Angular unconformity between metamorphosed Riphean sediments and overlying Ordovician conglomerate grading upwards into sandstone provides evidence of a Precambrian deformational event.

Figure 2.5. Relationship between the Precambrian and overlying Palaeozoic sequences exposed in the foreland thrust and fold belt of the South-West Urals.

Palaeozoic Sequences

Early to Middle Palaeozoic sediments unconformably overly the Proterozoic and record a shallow to deep water shelf environment on the passive margin of the East European Continent during continental rifting and opening of the Uralian ocean (Zonenshain et al., 1984; Brown et al., 1997). The lower Palaeozoic is represented by a transgressive sequence of basal conglomerate fining upwards to sandstones, shales and carbonates which pinch out to the West. These are overlain by Devonian interbedded siliciclastics and limestones and Carboniferous shallow marine carbonates. The first appearance of siliciclastic turbidite sequences in the Late Carboniferous to Early Permian marks the onset of foreland basin development associated with continental collision, with the foreland basin comprising up to 3km of Upper Carboniferous to Permian syn-orogenic sediments, marls, limestones and evaporites (Puchkov 1997; Brown et al, 1997).

Structural Development

The foreland thrust and fold belt is characterized by a west vergent thrust stack incorporating Proterozoic, Palaeozoic shelf and Permian syn-orogenic sequences. Numerous east dipping thrusts in the foreland thrust and fold belt and transitional zone (Figure 2.4a) developed during continental collision in the early Permian to early Triassic (Brown et al., 1997). At their eastern margin, the Timorovo Thrust (Figure 2.3) coincides with the north-west boundary of the Zilair Nappe (Section 2.1.3), marking the transition from the foreland fold and thrust belt to accreted allochthonous units further East (Brown et al., 1997). Formation of the Timorovo Thrust is considered to pre-date continental collision, coinciding with movement of the Zilair Thrust during emplacement of allochthonous units (Brown et al., 1997).

2.1.3 Allochthonous units of the Accretionary Complex

A number of allochthonous units have been thrust over the East European continental margin and lie immediately west of the MUFZ, which are interpreted as an accretionary complex comparable to those found in modern subduction systems (Puchkov 1997; Brown et al. 1998). These allochthons include ultramafics massifs of the Kraka and Sakmara Zones, the high-pressure metamorphic Maksutovo Complex, and sediments of the Suvanyak Complex and Zilair Nappe (Figure 2.3). Emplacement is dated as Late Devonian to Early Carboniferous, coincident with collision between the East European Continent and the Magnitogorsk island arc which marked the end of subduction. Subsequent to emplacement, the Zilair Nappe and Kraka Allochthon have been gently folded into a synclinal structure commonly referred to as the Zilair syncline, while the Maksutovo and Suvanyak Complexes are structurally separate and form the Uraltau Uplift (Figure 2.4b) (e.g. Zonenshain et al., 1984; Chemenda et al., 1997).

Zilair Nappe

The Zilair Nappe (Figure 2.3, 2.4a) is composed of upper Devonian to lower Carboniferous flysch of the Zilair Formation. The Zilair Formation comprises polymictic turbidites with a thickness of 6km which are laterally extensive, occurring both in the Zilair Nappe and further east in the Magnitogorsk Zone (Section 2.5) (Zonenshain et al., 1984; Bastida et al., 1997; Brown et al., 1998). The Nappe has complex internal folding and thrusting, with low grade metamorphism varying from lower to sub- greenschist facies (Bastida et al., 1997; Brown et al., 1998).

The questionably allochthonous nature of the Zilair Nappe is a matter of ongoing debate due to conflicting evidence from field observations and seismic sections (e.g. Bastida et al., 1997). The northwest basal contact is the Zilair Thrust which appears from seismic profiles to be laterally continuous (Figure 2.6a), while contacts in the south and east appear faulted in some exposures and stratigraphic in others (Bastida et al., 1997). Interpretations of the Nappe include autochthonous sediments deposited in a basin linked to the East European Continental margin (e.g. Zonenshain et al. 1984; Puchkov 1997), and allochthonous sediments deposited in the fore-arc/collision zone with subsequent tectonic emplacement over the East European Continental margin during arc-continent collision (e.g. Brown et al. 1996, 1997, 1998; Alvarez-Marron; 2000). Either way, it is evident that sediments of the Zilair Formation were deposited over an extensive area stretching from the fore-arc region (in the Magnitogorsk Zone) across the collision zone to the East European Continental margin.

The abundance of immature volcanic-derived material reflects a proximal volcanic source which is most likely to be the Magnitogorsk island arc (Section 2.1.5), and less abundant metamorphic fragments point to an additional source suggested to be the Maksutovo Complex (described below) (Zonenshain et al., 1984, Bastida et al., 1997). This implies that both the Magnitogorsk Arc and Maksutovo Complex were exposed during the upper Devonian to lower Carboniferous. These flysch deposits are therefore important in constraining the tectonic evolution of the Urals since their deposition marks the onset of collision between the Magnitogorsk Island Arc and the East European Continental Crust, which triggered exhumation of the Maksutovo Complex and uplift of the Magnitogorsk Arc.

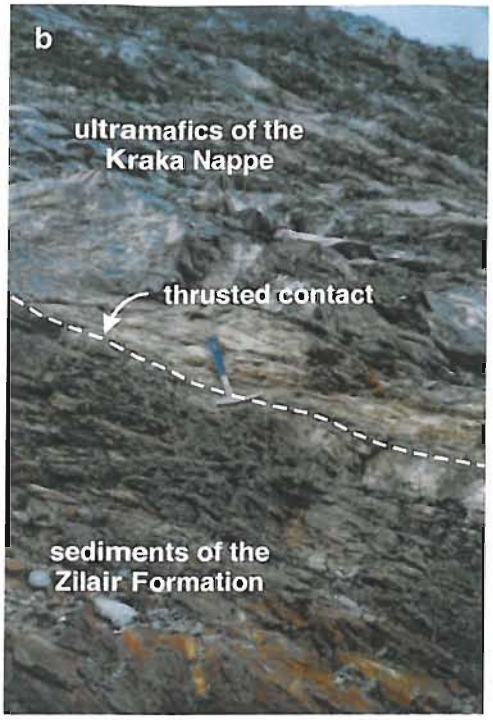

(a). Sheared sediments of the Zilair Formation close to a tectonic contact with underlying continental shelf deposits.

(b). Thrusted contact between the Zilair Formation and overlying ultramafics of the Kraka Nappe.

Figure 2.6. Upper and Lower contacts of the Zilair Nappe.

Kraka Allochthon

The ultramafic Kraka allochthon is structurally the highest unit of the accretionary complex (Figures 2.3, 2.4a). The basal contact with the underlying Zilair Nappe and locally the Uzayan Nappe (comprising lower Palaeozoic sediments and mafic volcanics) is a major thrust (Figure 2.6b), with local development of extensive melange (Zonenshain et al., 1984; Brown et al., 1996, 1998). K/Ar and Ar/Ar dating of footwall rocks indicate greenschist metamorphism relating to emplacement during arc-continent collision in the Carboniferous (Puchkov, pers. comm.). Kraka is dominated by lherzolites and comparable with the Nurali and Mindyak massifs in the Main Uralian Fault zone (Section 2.4) (Savelieva et al., 1997; Fershtater et al., 1997). Typical ophiolitic sequences of gabbros, sheeted dyke and pillow lavas are absent, and these lherzolite massifs are suggested to be either lithospheric mantle derived from the East European passive continental margin (Fershtater et al.,1997) or upper mantle tectonically denuded during early rifting prior to mid-ocean ridge spreading (Savelieva et al., 1997).

Maksutovo and Suvanyak Complexes

The Maksutovo and Suvanyak Complexes form the east and west portions of a dome-like structure known as the Uraltau Uplift, (Figure 2.4b), with the Maksutovo Complex located immediately adjacent to the MUFZ (Figure 2.3). The Maksutovo Complex is characterized by high-pressure/low-temperature (HP-LT) blueschist, eclogite and greenschist facies, which are thought to

be mainly Riphean to Palaeozoic in age, the latter confirmed by conodonts from marbles (Puchkov, 1997). Peak metamorphic conditions are estimated at 550 to 600°C and 17 to 25kbar (Lennykh et al. 1995), and a metamorphic cooling age of 365 to 380 Ma has been determined from $^{39}Ar/^{40}Ar$ dating of phengites (Matte et al., 1993; Lennykh et al., 1995).

By comparison with modern subduction settings, Chemenda et al. (1997) interpret the Maksutovo Complex as a slab of partially subducted continental crust which was exhumed and emplaced between the accretionary complex and the Magnitogorsk Island Arc to form the Uraltau Uplift. Alternatively Puchkov (1997) suggests partial subduction of the accretionary complex and subsequent exhumation, with antiformal folding and tectonic emplacement taking place during late Palaeozoic continental collision. Either way, the HP-LT facies are interpreted to reflect the entrance of continental crust to the subduction zone, and the metamorphic age of this unit therefore provides important constraints on the timing of arc-continent collision.

The Suvanyak Complex comprises deformed sediments metamorphosed to greenschist facies with fauna indicating an Ordovician to Middle-Devonian age (Puchkov, 1997). The contact with the Maksutovo Complex to the east is a thrust, while the western boundary with the Zilair Formation is more difficult to interpret, with conflicting field evidence suggesting faulted and stratigraphic contacts (see discussion in Section 2.3.2). Puchkov (1997) interprets this unit as autochthonous deep water sediments of the East European margin, while others (e.g. Chemenda et al., 1997; Brown et al., 1998; Alvarez-Marron, 2000) propose an allochthonous origin, derived from sediments that were scraped from the subducting continental crust at shallow levels and subsequently exhumed together with the Maksutovo Complex.

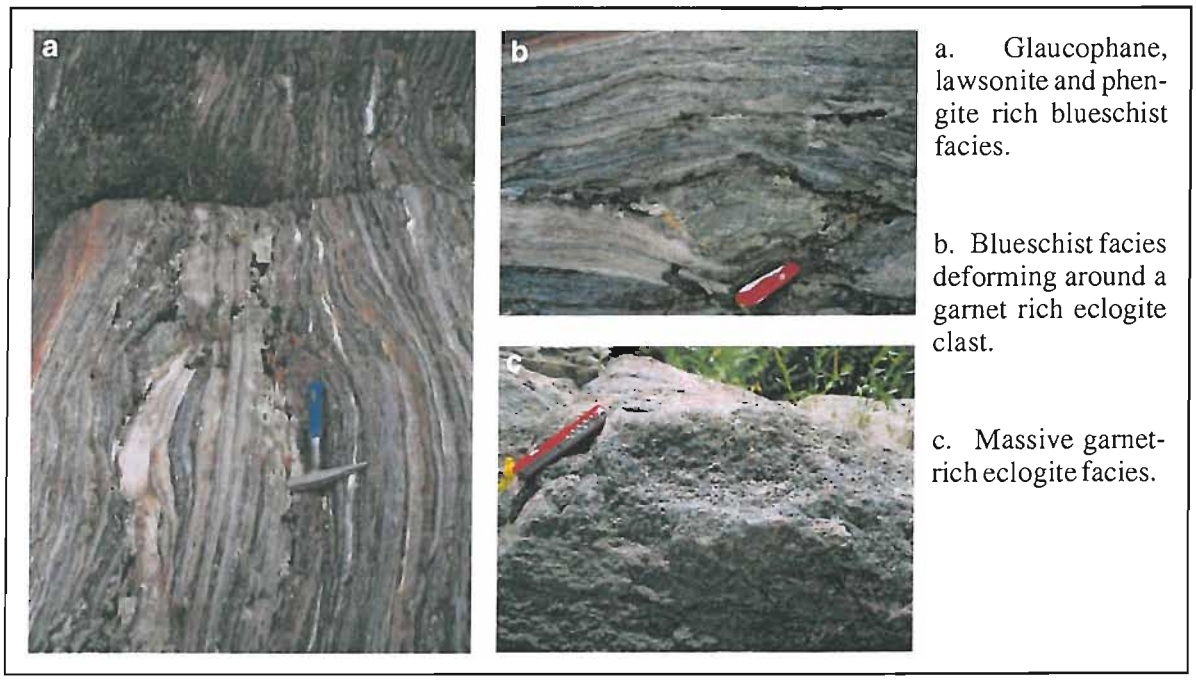

a. Glaucophane, lawsonite and phengite rich blueschist facies.

b. Blueschist facies deforming around a garnet rich eclogite clast.

c. Massive garnet-rich eclogite facies.

Figure 2.7. High pressure-low temperature blueschist-eclogite facies of the Maksutovo Complex.

Sakmara Zone

The Sakmara allochthon is located between the foreland thrust and fold belt to the west and the MUFZ to the east (Figure 2.2) and lies to the south of the majority of allochthonous units, occupying the highest structural position in the accretionary complex equivalent to that of Kraka (Brown et al., 2000). The Sakmara Zone comprises Ordovician to Silurian sedimentary, volcanic and ultramafic units, with stratigraphic correlation complicated by the development of extensive internal melange (Buschmann et al., 2001b). Volcanic units are characteristically bimodal, which are interpreted as island arc sequences formed in an immature arc or fore-arc setting (Herrington et al., 2002; Puchkov & Seravkin, 2001) and host the economically important VMS deposits of the Mednogorsk Ore District. Ultramafic units include the harzburgite dominated Kharbarny and Kempirsai allochthons which are typical of ophiolitic sequences and inferred to represent the tectonic evolution from rifting to mainstage spreading and ocean crust formation (Savelieva et al., 1997; Fershtater et al., 1997). These massifs are distinct from the lherzolite dominated Kraka, Nurali and Mindyak ultramafics further north. The Kempirsai Massif is economically very important, hosting world-class chromite deposits.

The Sakmara Zone therefore provides evidence of rifting and ocean crust formation, intra-oceanic subduction and island arc development during the early Palaeozoic, either prior to (Zonenshain et al., 1984), or in the early stages of (Zaykov et al., 2000) opening of the Uralian ocean.

2.1.4 Main Uralian Fault Zone

The Main Uralian Fault Zone (MUFZ) is a 2 to 5 km wide, east-dipping structure continuous for more than 2000km along the Urals belt, and developed in a supra-subduction zone during Devonian subduction, later forming the suture between the East European Craton and Magnitogorsk Arc in the collision that followed (e.g. Zonenshain et al., 1984; Puchkov, 1997; Chemenda et al., 1997; Brown et al., 1998). In the southern Urals, the fault zone is a serpentinitic melange containing ultramafic allochthons such as the Mindyak and Nurali massifs, and volcanics derived from the Magnitogorsk Island Arc (Puchov, 1997; Brown et al., 1998). The MUFZ hosts a variety of mineral deposits including ultramafic hosted VMS and sub-economic PGE-chromite mineralization (e.g. at Nurali), as well as orogenic gold deposits such as those exploited at Mindyak.

There is strong evidence to suggest that the MUFZ has a complex history with movement in both compressional and extensional regimes (Matte et al., 1993; Chemenda et al., 1997). The end of fault activity is constrained by the youngest rocks incorporated in the fault being Early Carboniferous in age, and undeformed Jurassic sediments overlying the fault zone in the south, implying movement ceased in early Carboniferous to Jurassic times (Brown et al., 1996). This is

supported by an age of 327 (±2) Ma determined by Montero et al. (2000) for an undeformed granite intruding the southern MUFZ.

The MUFZ hosts a number of ultramafic allochthons including Mindyak and Nurali massifs. These are lherzolitic massifs geologically and geochemically similar to the Kraka allochthon (Section 2.3.4) and have been suggested to represent upper mantle of the East European Craton (Fershtater et al., 1997) with a supra-subduction signature inferred by Scarrow et al. (1999). Within upper mantle sequences of Mindyak a tectonic breccia hosts metamorphosed gabbros which originally crystallized at low pressures. High pressure metamorphic facies are interpreted to reflect subduction and metamorphism at upper mantle conditions (800°C, 10kbar) dated at 415 to 410Ma (U-Pb and Pb-Pb from zircon; Sm-Nd mineral isochron), suggesting that subduction had commenced by Lochkovian to Pragian times (Brown et al., 2000). Since the oldest volcanic arc rocks of the Magnitogorsk Zone are Emsian, this suggests the subducting slab did not reach sufficient depths to induce melting until the Emsian, and Mindyak records an early non-volcanic stage of subduction (Brown et al., 2000).

2.1.5 Magnitogorsk Zone

The Magnitogorsk Zone lies immediately East of the MUFZ, bounded to the west by the MUFZ and to the East by the East Uralian Zone (Figures 2.2, 2.3), and comprises Middle Palaeozoic volcanic rocks and associated sediments. There is widespread agreement that this zone is an autochthonous island arc system formed by intra-oceanic subduction within the Uralian Ocean during the Devonian (e.g. Zonenshain et al., 1984; Puchkov, 1997; Brown et al., 1998). To the north the Magnitogorsk Zone pinches out against the MUF, while to the south the arc system continues into the West Mugodzhary Zone of Kazakhstan (Zaykov et al., 2000). The Magnitogorsk Zone is of considerable economic importance, with numerous VMS deposits providing an extensive source of base metals and in many cases significant recoverable precious metals.

Volcanic sequences record stages of fore-arc, mainstage island arc and back-arc development, spanning late Emsian to Givetian times (Brown and Spadea, 1999, Herrington et al., 2002). Subsequent deposition of the Zilair Formation (Section 2.1.3) containing extensive immature volcanic derived material took place from the late Frasnian through to the Tournasian, reflecting uplift and erosion of the arc coincident with a cease in volcanic activity and the onset of arc-continent collision (Bastida et al., 1997; Brown et al., 2001). During the Lower Carboniferous, limestones deposited unconformably over the Zilair Formation are interpreted to mark the syn-collisional collapse of the arc (Brown et al., 1998, 2001). Extensive granitoids intruding central and eastern regions (Figure 2.3) reflect continental collision during the late Carboniferous to early

Triassic (Brown et al., 1998). The geology and evolution of the Magnitogorsk Zone is discussed further in Section 2.2.

2.1.6 East Uralian Zone

The East Uralian Zone lies immediately East of the Magnitogorsk Zone (Figure 2.2), with a series of faults forming the contact between the two (e.g. Brown et al., 1998). This zone contains Precambrian metamorphic continental crustal blocks such as the East Mugodzhar Zone, together with Palaeozoic magmatic arc and ophiolitic sequences, all of which have been strongly metamorphosed during the intrusion of granitoids (shown in Figures 2.3 and 2.4a). The intrusive event is thought to have occurred during continental collision between Kazakhstan and East European plates, with granitoids dated using Rb-Sr and $^{207}Pb/^{206}Pb$ at 291(±4)Ma and 254(±5)Ma respectively (Montero et al., 2000).

The East Mugodzhar Zone has been interpreted in a number of ways, including a floating fragment of continental crust (the East Mugodzhar Microcontinent) which collided with Kazakhstan Continent prior to closure of the Uralian ocean (Zonenshain et al., 1984; Puchkov 1997), or a strike-slip intruded fragment of continental crust (Herrington et al., 2003). Interpretations of the Palaeozoic arc are also varied, and include formation during subduction prior to collision between the East Mugodzhar Microcontinent and Kazakhstan margin (e.g. Puchlov, 1997), or a fragment of the Magnitogorsk Zone offset by regional sinistral strike slip faults (Herrington et al. 2003). The most economically significant mineral resources of the East Uralian Zone are orogenic gold including the extensive Berezovskoe deposit, and skarn magnetite (Koroteev et al., 1997).

2.1.7 Tectonic Evolution of the Southern Urals

The tectonic evolution of the Urals has been reconstructed based on interpretation of the geological units discussed in preceding sections (summarised in Table 2.1). Prior to the opening of the Uralian ocean during the Palaeozoic, rocks of the East European continent show evidence of continental rifting during the Riphean to early Vendian, followed by an orogenic event during the late Vendian which may correlate with the Cadomian Orogeny in northern Europe (Puchkov, 1997). The Palaeozoic history of the Urals is dominated by the opening and closure of the Uralian Ocean. Figure 2.8 outlines the probable Palaeozoic evolution of the Urals compiled from interpretations of Zonenshain et al., 1984; Puchkov, 1997; Brown et al., 1998, 2000; and Herrington et al., 2002.

	Formation/Unit	Age	Comments
East European continental margin	Taratash Metamorphic Complex	Archean	representative of EEC basement?
	Precambrian carbonates and sediments	Riphean-Vendian	provide evidence of pre-Uralide orogenic event
	Palaeozoic sediments and carbonates	Ordovician to Carboniferous	record development of the passive EEC margin during continental rifting and opening of the Uralian ocean
	Late Palaeozoic turbidites	upper Carboniferous to Permian	syn-orogenic sediments marking the collision of the EEC and KC
Allochthons of the Accretionary Complex	Kraka Allochthon	Metamorphic age: Carboniferous	lherzolite dominated; lithospheric mantle? emplaced during late stages of EEC-MZ collision
	Sakmara Zone	Ordovician to Silurian	includes harzburgite dominated ophiolites and island arc volcanics indicating ocean spreading and subduction during the Early Palaeozoic
	Zilair Nappe	upper Devonian to lower Carboniferous	allochthonous or autochthonous? sediments from Magnitogorsk arc and Maksutovo complex indicate EEC-MZ collision with uplift of MZ and exhumation of Maksutovo Complex
	Maksutovo Complex	Riphean to Palaeozoic metamorphic cooling age: 365-380Ma	high pressure-low temperature facies representative of continental crust that was partially subducted then exhumed; indicates EEC crust was being subducted by Middle Devonian
	Suvanyak Complex	Ordovician to Middle Devonian	allochthonous or autochthonous? metamorphosed greenschist EEC margin sediments, possibly partially subducted at shallow levels and exhumed
Autochthonous island arc	Magnitogorsk Zone	Devonian to Carboniferous	volcanic units recording intra-oceanic subduction

Table 2.1. Summary of the geological units of the southern Urals.
(EEC – East European Continent; KC – Kazakhstan Continent; MZ – Magnitogorsk Zone).

Continental rifting of the East European Continent commenced in the Early Palaeozoic, with sediments and carbonates of the East European platform recording the existence of a passive margin from the Ordovician through to the Devonian (Figure 2.8a to d). The Cambrian is largely absent in the southern Urals, however minor occurrences elsewhere in the Urals suggest that continental rifting may have commenced in the Cambrian (Puchkov, 1997). Relicts of Ordovician to Silurian ophiolites located in the Sakmara allochthon confirm that oceanic crust was forming by this time, with the development of an island arc system reflecting a period of eastward intra-oceanic subduction during the Silurian (Figure 2.8b).

During the Middle Devonian, eastward intra-oceanic subduction lead to the formation of the Magnitogorsk Island Arc, possibly a continuation of the activity that formed the Sakmara Zone or

due to a renewed period of subduction. Dating of volcanic suites suggest that volcanism commenced during the Emsian (Figure 2.13d), although dating of high pressure-high temperature metamorphic facies from the Mindyak allochthon (located in the MUFZ, Section 2.4) suggests that subduction had commenced by Lochkovian to Pragian times (Figure 2.13c). The volcanics of the Magnitogorsk Zone record the formation of Emsian fore-arc boninites during early stages of subduction followed by the development of an accretionary arc system as volcanism progressed through late Emsian to Givetian (Figure 2.8d; Table 2.2).

The high pressure metamorphic facies of the Maksutovo Complex mark the subduction of continental crust (Figure 2.8e) at the onset of collision between the East European Continent and Magnitogorsk Island Arc. The collisional event is recorded by exhumation of the Maksutovo Complex, together with uplift and erosion of the arc and deposition of the Zilair flysch which began to accumulate in late Frasnian times (Figures 2.8f and g).

The final stage in the development of the Urals belt involved continental collision between the East European Continent (and accreted Magnitogorsk Arc) and the Kazakhstan Continent, as the palaeo-ocean East of the Magnitogorsk arc closed (Figure 2.8g and h). Collision during the Late Carboniferous to Early Triassic is signified by thrusting of the accretionary complex over the East European Margin, followed by the development of a foreland fold and thrust belt and foreland basin during the Early Permian to Early Triassic. Continental collision is also marked by granitoid intrusives in the Magnitogorsk Zone, and regional orogenic gold mineralization. Movement of the Main Uralian Fault ceased around 330Ma, with no significant tectonic activity recorded in the Urals after the Early Triassic.

The origin and development of the East Uralian Zone is not clear; the model presented in Figure 2.8 assumes the Precambrian crust of this zone to have been a microcontinent that accreted to the Kazakhstan Continent during the Devonian, prior to continental collision with the East European Continent. Other explanations imply that the this Precambrian crust would not be emplaced/exposed until continental collision between the East European and Kazakhstan continents in the Late Carboniferous to Triassic.

Formation	Age	Comments
Baimak-Buribai	Emsian, Devonian	fore-arc sequences including boninite-like rocks and bimodal volcanics
Irendyk	Emsian-Eifelian, Devonian	andesite dominated, mainstage island arc
Karamalytash	Eifelian, Devonian	bimodal sequences reflecting intra-arc/back arc spreading
Ulutau	Givetian, Devonian	abundant volcaniclastics reflect shallow volcanism and/or emergence and erosion of arc

Table 2.2. Volcanic Formations of the Magnitogorsk Zone.

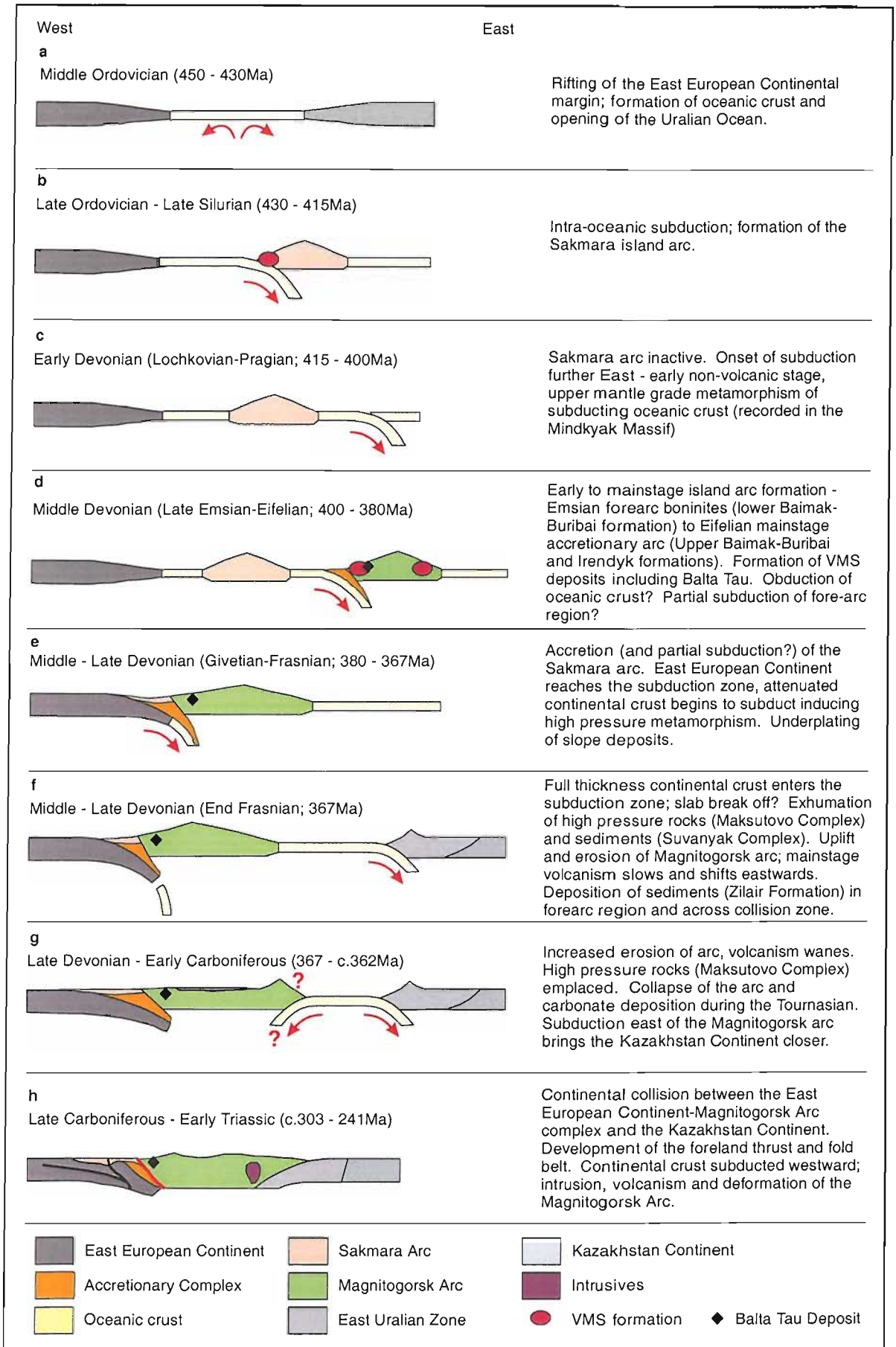

Figure 2.8. Tectonic evolution of the southern Urals during the Palaeozoic.

2.2 GEOLOGY OF THE MAGNITOGORSK ZONE

2.2.1 Introduction

Volcanics units of the Magnitogorsk Zone form in two approximately North-South trending outcrops which are separated by a basin infilled with Carboniferous limestone (Figures 2.3, 2.9a). These are commonly referred to as the Eastern and Western arcs (Figure 2.9a), although the tectonic relationship between these two belts remains a matter of considerable debate and there is no consensus that they do in fact represent two volcanic arcs, but may instead be a single segmented arc (discussed further in Section 2.2.3). To avoid genetic implications, these are referred to as the eastern and western volcanic belts in the following sections.

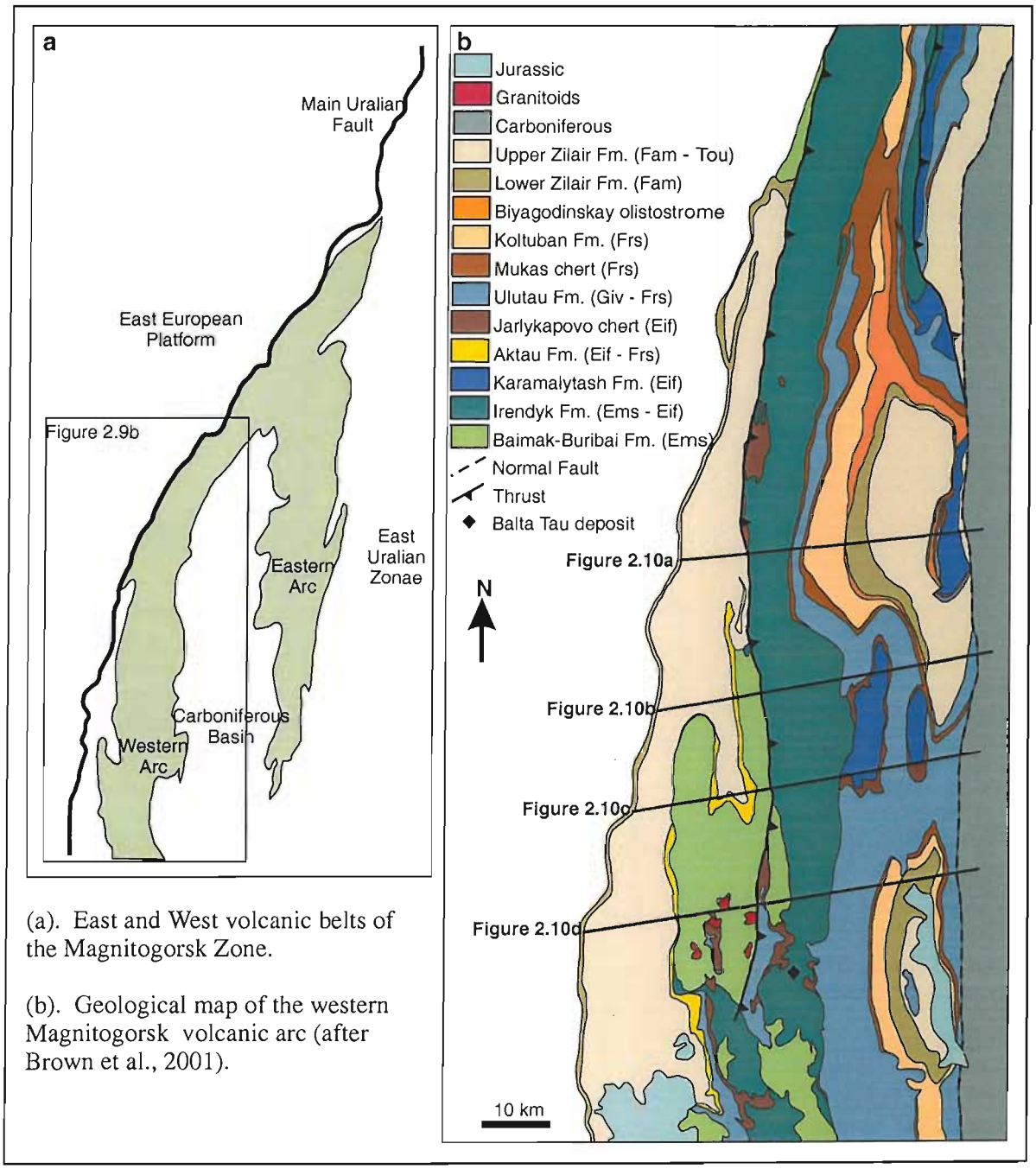

(a). East and West volcanic belts of the Magnitogorsk Zone.

(b). Geological map of the western Magnitogorsk volcanic arc (after Brown et al., 2001).

Figure 2.9. Geology of the Magnitogorsk Island Arc.

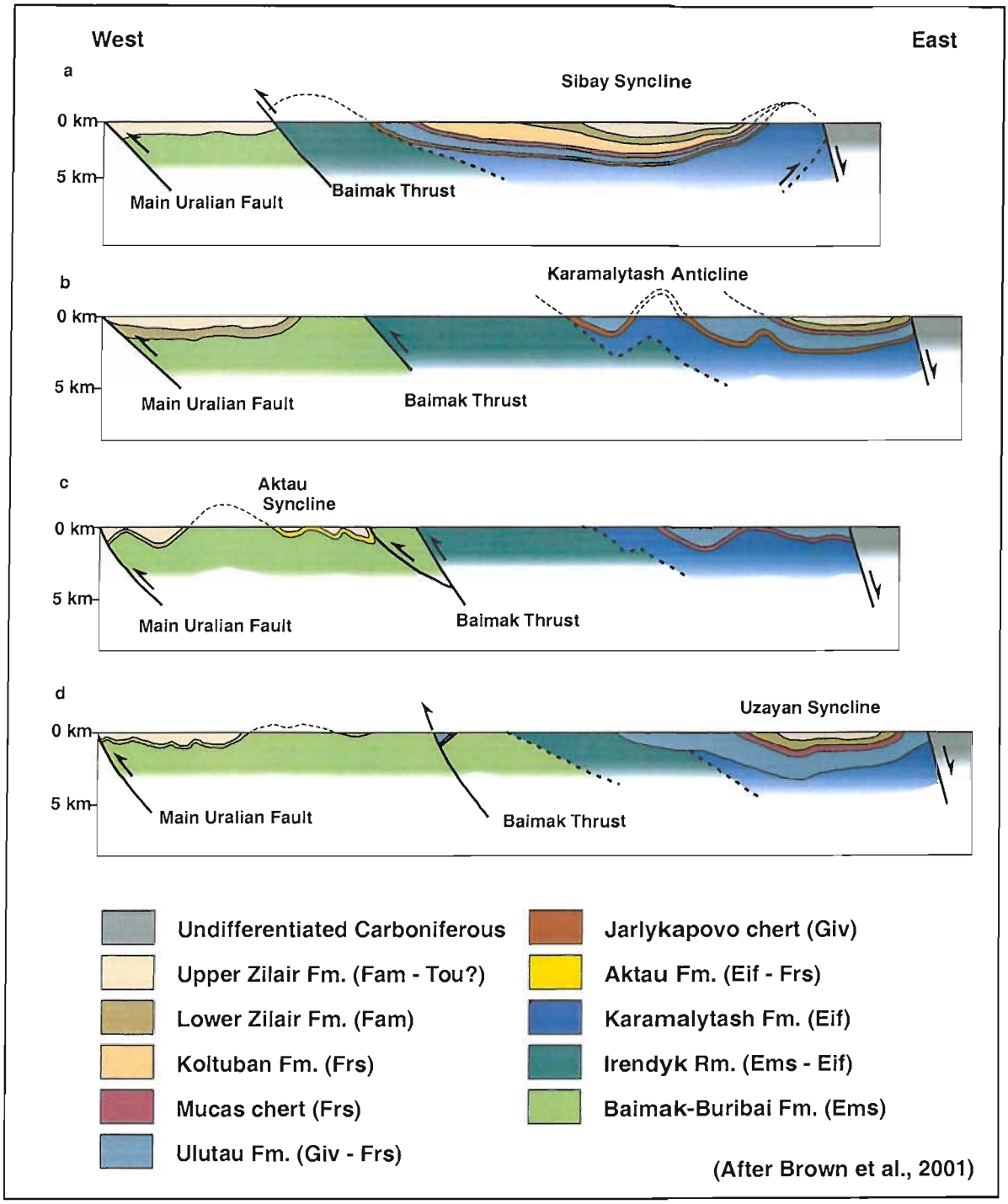

Figure 2.10. Cross-sections through the southern Magnitogorsk Island Arc.

2.2.2 Stratigraphy

Formations of the Magnitogorsk Zone generally young to the east, with ages of sedimentary sequences well constrained by dating of conodonts in chert horizons. The volcanic units are more problematic, since conodont bearing cherts occur only sparsely and correlation of sequences is difficult. Very few radiometric dates of volcanic units have been obtained, with the only available data restricted to several K/Ar ages obtained from sericitic alteration associated with VMS

deposits. One of these ages agrees well with corresponding conodont dating (390±2Ma from the Molodyeznhoe deposit, Karamalytash Formation, Herrington et al., 2001a), and a further two give ages that are younger but do not contradict conodont dating when the large errors are considered (376±13Ma from Gai, Prokin and Buslaev 1999, and 360±29Ma from Podolskoye, Herrington et al., 2000c). The reminder indicate ages that are unrealistically young (in the range 328 to 347Ma, Herrington et al., 2000c) and were probably reset during later collisional events.

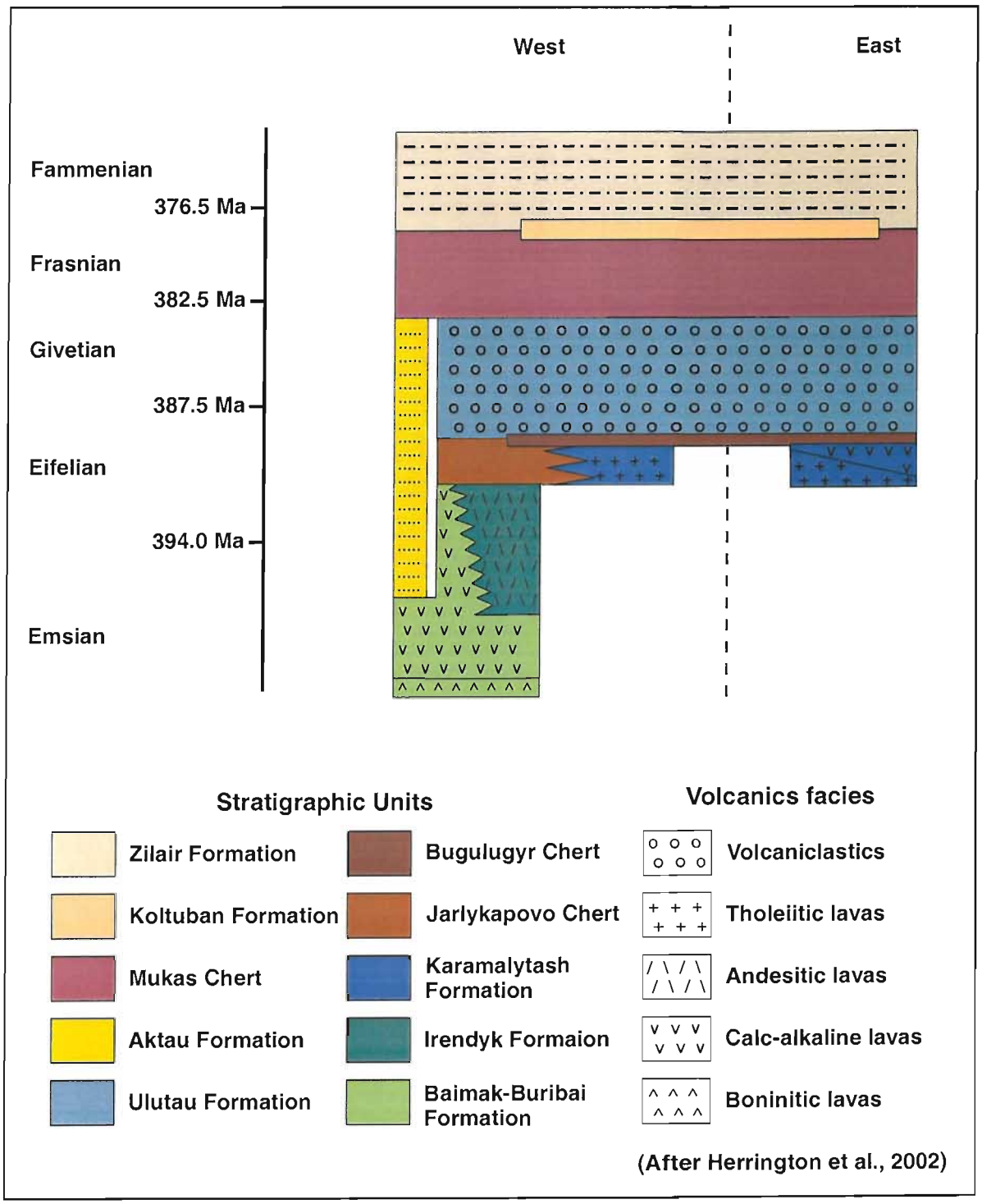

Figure 2.11. Stratigraphic column of Magnitogorsk Island Arc volcanics and associated sediments.

The stratigraphy of the Magnitogorsk Zone is presented in Figure 2.11. The oldest exposed sequences are volcanics of the Baimak-Buribai Formation that outcrop in a 150 km long belt along the western side of the western volcanic belt. Conodont dating indicates an Upper Emsian age of 400-395Ma (serotinus and patulus zones; Maslov et al., 1993). At the base of this unit basaltic dykes and pillow lavas are exposed (Figure 2.12), which grade up-stratigraphy to bimodal sequences followed by dominantly felsic volcanics in the upper units (Spadea et al., 1997; Herington et al., 2002). The upper sequences of the Baimak-Buribai Formation are further discussed and illustrated in Section 3.2.1. Locally, small felsic intrusives are found in the Baimak-Buribai volcanics which have yet to be dated.

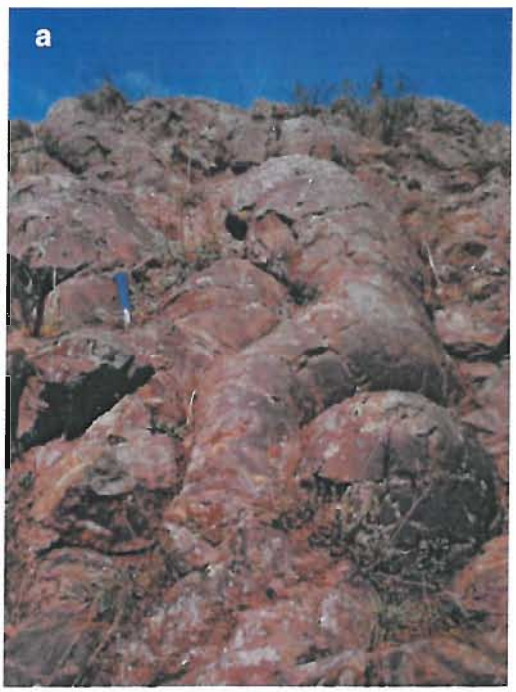

Typical facies of the lower Baimak-Buribai Formation:

(a). Basaltic lava tubes with boninite-like geochemistry.

(b) and (c). Pillow basalts with highly amygdoidal cores of pillows grading to glassy margins, and variable alteration from core to margins.

(d). Felsic and mafic parallel dykes cutting basalts.

Figure 2.12. Typical exposures of the lower Baimak-Buribai volcanics.

The Baimak-Buribai volcanics are overlain by the Irendyk Complex, with a probable temporal overlap between the two. The Irendyk is an uppermost Emsian to Lower Eifelian volcanic chain extending 400 km North-South and forms the bulk of the western volcanic belt and represents a main stage of island arc formation, composed of basalts and andesites with abundant hyaloclastic breccias and intercalated epiclastics (Brown and Spadea, 1999; Herrington et al., 2002). The Irendyk is overlain by the Jarlykapovo Chert, and locally the Karamalytash and Bugulygyr formations which are temporal equivalents to the Jarlykapovo chert (Figure 2.10), (Puchkov pers. comm.; Brown et al., 2001; Herrington et al., 2002). The Jarlykapovo, Karamatalash and Bugulygyr formations are best exposed in the Karamalytash anticline (Figures 2.9b, 2.10b; note in these figures the Bugulygyr Chert is not distinguished from the Jarlykapovo Chert). The Jarlykapovo chert reaches 200m in thickness (Brown et al., 2001), comprising chert and red jasper (Figure 3.10) with conodonts of australis and kockelianus zones indicating an Upper Eifelian age (Maslov et al. 1993). The contemporaneous Karamalytash Formation comprises Lower to Upper Eifelian bimodal basalt-rhyodacite sequences (Herrington et al., 2002) including columnar and pillow basalts interlayered with chert horizons (Figure 2.13a, b), constrained by conodonts zones costatus, australis and kockelianus (Maslov et al. 1993). The Bugulygyr chert horizon is dominated by red jaspers, overlies the Karamalytash Formation and temporally correlates with the upper Jarlykapovo chert (Brown et al., 2001; Herrington et al., 2002).

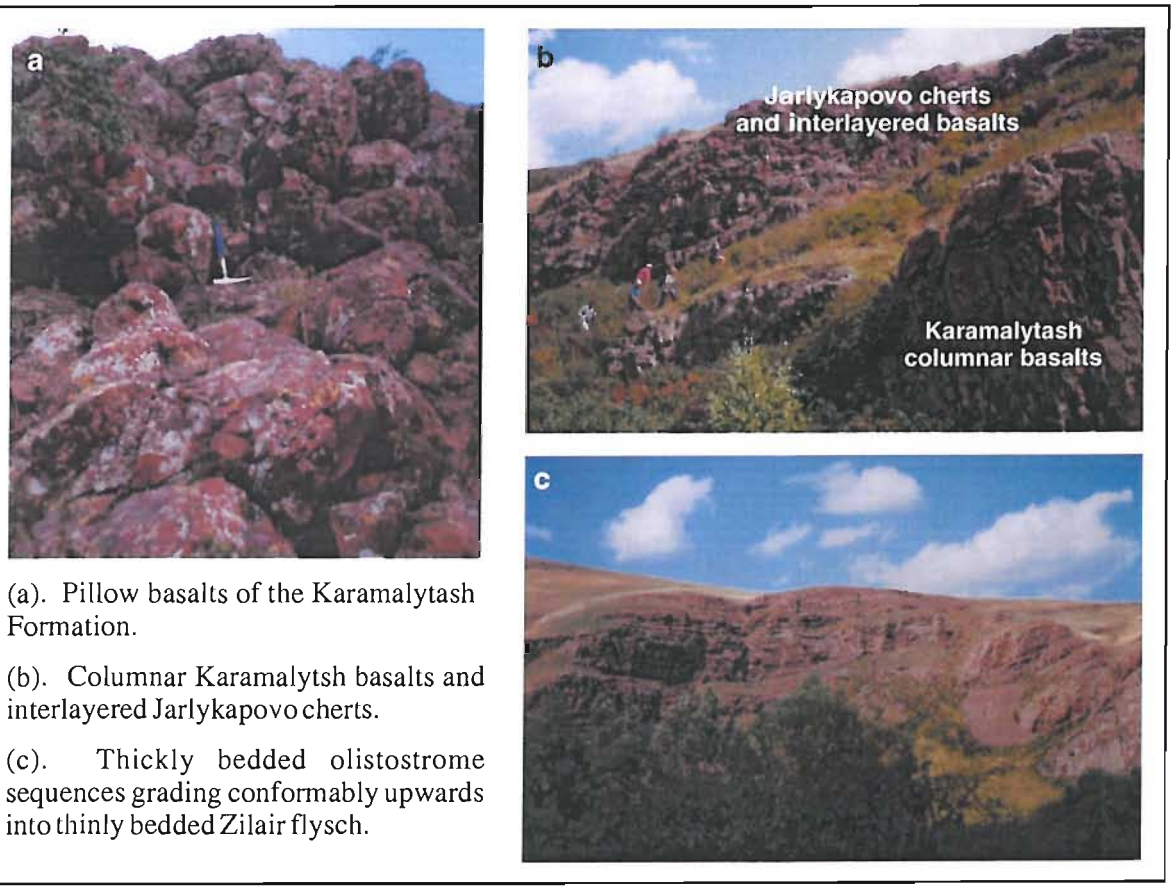

(a). Pillow basalts of the Karamalytash Formation.

(b). Columnar Karamalytsh basalts and interlayered Jarlykapovo cherts.

(c). Thickly bedded olistostrome sequences grading conformably upwards into thinly bedded Zilair flysch.

Figure 2.13. Examples of the Karamalytash Formation and sediments of the Koltubanian and Zilair Formations overlying island arc volcanics.

The Ulutau Formation directly overlies the Jarlykapovo chert, comprising several hundred to 2000m westward thickening Givetian to lowermost Frasnian sequences in both the eastern and western volcanic belts. The Ulutau of the western belt is characterized by bedded volcanic sandstone with thinly interbedded tuffaceous chert and siliceous shales, while the eastern belt Ulutau consists of andesitic to dacitic lavas, near-vent breccias, and sills intruding volcaniclastic sequences (Brown et al., 2001). Lower sequences of the Ulutau in the western belt are illustrated and discussed further in Section 3.2.3.

The Ulutau Formation is overlain by the Frasnian aged Mukas chert (Brown et al 2001; Herrington et al., 2002). This comprises 10 to 100m thickness of tuffaceous chert with a diachronous upper boundary grading laterally into and coeval with the Koltuban Formation (Brown et al., 2001). The Koltuban Formation consists of up to 1500m of thinly bedded volcanic sandstone and interbedded tuffaceous chert, grading into upper unit of siliceous siltstones. Widespread syn-sedimentary deformation and olistostrome formation is also characteristic of upper sequences (Figure 2.13c), and suggestive of significant tectonic activity during deposition (Brown et al., 2001).

The Koltuban Formation is conformably overlain by extensive Fammenian to Lower Tournasian flysch deposits of the Zilair Formation (Figure 2.13c). These consist of up to 2000m of westward thickening sequences dominated by volcanic clasts with minor metamorphic components including garnet, mica, and scarce glaucophane (Brown et al. 2001). The majority of sediments are believed to have been derived from the Magnitogorsk Arc, implying uplift and erosion of the arc at this time resulting from partial subduction of East European Continental crust. This is consistent with the timing of continent-arc collision, with continental crust entering the subduction zone (indicated by metamorphic ages of the exhumed high pressure Maksutovo Complex, Section 2.1.3) coinciding with deposition of the earliest Zilair successions. The Zilair formation is inferred to have been deposited right across the fore-arc region and collision zone, and is found in the questionably allochthonous Zilair Nappe to the West of the MUFZ (Section 2.1.3).

Lower Carboniferous limestones unconformably overlie the Zilair Formation (Brown et al., 2001), infilling a basin in the central Magnitogorsk Zone which divides island arc volcanics into East and West belts (Figure 2.9a). These are interpreted to mark the syn-collisional collapse of the arc (Brown et al., 1998), together with minor sub-alkaline volcanism which ceased in the late Carboniferous (Brown et al., 1998). The youngest sediments of the Magnitogorsk Zone are Jurassic in age, unconformably overlying Zilair Formation sediments and Carboniferous carbonates (Figure 2.9b) (Brown et al., 2001).

In the western area of the Magnitogorsk Zone the Aktau Formation overlies Baimak-Buribai volcanics, outcropping narrowly along the western margin and more extensively in a small

synformal structure (Figures 2.9b, 2.10c). In this synform up to 150m of Eifelian to Lower Frasnian tuffaceous sandstones, cherts, red jaspers and minor conglomerates are exposed, which are temporally equivalent to the Irendyk, Karamalytash, Jarlykapovo, Bugulygyr and Ulutau formations (Figure 2.11) (Brown et al., 2001), and are conformably overlain by the Mukas chert and Zilair Formation. The Aktau formation is a condensed sequence deposited in the fore-arc region, which is most likely to have been sheltered from significant sedimentation by the extensive ridge of Baimak-Buribai and Irendyk arc volcanics that would have been established at this time (Herrington et al., 2002).

2.2.3 Structures and Deformation

Subsurface structures of the Magnitogorsk Zone are more difficult to interpret than those in units West of the MUF due to the lack of continuous marker horizons within volcanic suites. In particular, structures of the Baimak-Buribai and Irendyk formations are poorly constrained, and these are therefore shown as internally homogeneous units of unknown vertical extent in the cross sections of Figure 2.10 (Brown et al., 2001). Within the western arc system, the most prominent structure that is visible both in surface exposures and seismic profiles is the Baimak Thrust (Figures 2.10a to d), a melange zone with a throw of several hundred metres. In central and northern areas this thrusts the Irendyk in its hanging-wall over the Baimak-Buribai Formation, while further South the Baimak Thrust is contained entirely within the Baimak-Buribai Formation (Figure 2.10d). To the East of the Baimak Thrust volcanic and sedimentary successions have been deformed in a series of open folds, forming from South to North the Uzayan Syncline, Karamalytash Anticline and Sibay Syncline (Figures 2.9b and 2.10), with a further syncline in the northeast Verkneuralsk region.

2.2.4 Tectonic and geochemical evolution of the Magnitogorsk Arc

Western volcanic belt

A west to east progression from fore-arc to mainstage accretionary arc and finally inter-arc/back-arc spreading environments has been identified in the Western volcanic belt (Figure 2.14). The oldest volcanics exposed are those of the Lower Baimak-Buribai Formation, which include basaltic dykes and pillow lavas (Figure 2.12) with a tholeiitic to boninitic geochemical signature highlighted by elevated Mg and low Ti, and flat to saucer-like chondrite-normalized REE signatures (Spadea et al., 1998; Herrington et al., 2002). By comparison with volcanics found in the modern subduction system of the Izu-Bonin area, these are interpreted to have erupted in a fore-arc setting during early stages of subduction (Figure 2.14), with the absence of intercalated sediments suggesting the arc was non-accretionary at this time (Spadea et al., 1998). There is a

progressive geochemical change within the Baimak-Buribai Formation up-stratigraphy from boninitic/ tholeiitic volcanics at the base to tholeiitic-bimodal and finally calc-alkaline volcanics at the top, interpreted to reflect the evolution from fore-arc to mainstage accretionary arc environments (Spadea et al., 1998; Herrington et al., 2002).

The Irendyk Formation is interpreted to be the main stage of accretionary arc formation (Figure 2.14) (Herrington et al., 2002). The limited geochemical data available for the Irendyk Formation include REE analyses of pyroxene-phyric lavas which show flat chondrite-normalized patterns (Herrington et al., 2002) and Th/Yb-Ta/Yb indicating intra-oceanic island arc affinities (Brown et al., 2001). The abundance of clastic material and occurrence of possible epithermal-style baryte-gold mineralization may reflect a shallowing and possibly emergent arc system at this time (Herrington et al., 2002).

The bimodal Karamalytash Formation locally overlies the Irendyk. Basalts are geochemically distinct from the Baimak-Buribai and Irendyk Formations, with MORB-like and LREE depleted REE signatures characteristic of an extensional environment. In upper felsic sequences negative Eu anomalies are indicative of a high degree of fractionation (Herrington et al., 2002). Based on these geochemical characteristics, the Karamalytash is inferred to represent a zone of inter-arc or back-arc spreading (Figure 2.14). The Ulutau Formation overlies both the Irendyk and Karamalytash and comprises predominately volcaniclastic material of calc-alkaline affinity (Buschmann et al., 2001a). This has been interpreted to reflect shallow water explosive volcanism (Buschmann et al., 2001a), or alternatively reworking of volcanic material during uplift, emergence and erosion of the pre-existing arc implying the volcanics are epiclastic (Brown and Spadea, 1999).

Eastern volcanic belt

The Eastern belt is composed mainly of the Karamalytash and Ulutau Formations. The Karamalytash here is similar to the Western belt with bimodal and tholeiitic volcanics indicative of a spreading environment, but in uppermost sequences (where it hosts the Alexandrinka deposit) there is a progression to more calc-alkaline characteristics suggesting a return to an arc-like eruptive setting. The Ulutau in the Eastern belt comprises lava flows and near-vent facies as well as volcaniclastics, with a calc-alkaline, arc-like geochemical signature (Brown et al., 2001).

Evolution of the East and West belts

The relationship between the western and eastern volcanic belts is ambiguous and several suggestions have been proposed. The most probable explanations for the existence of two volcanic belts are either segmentation or migration of a single volcanic arc produced by an East dipping subduction zone. Buschmann et al. (2001a) and Herrington et al. (2002) suggest the East

and West belts to reflect the migration and geochemical evolution of a single volcanic arc in response to variations in subduction angle. During early stages of subduction hot oceanic crust subducted with a shallow dip producing the calc-alkaline arc suites of the Baimak-Buribai and Irendyk Formations. Subsequent subduction of cold oceanic crust resulted in steepening of the subduction angle producing tholeiitic back-arc volcanics of the Karamalytash Formation. Finally, entrance of buoyant continental crust to the subduction zone resulted in a return to calc-alkaline volcanism in the eastern part of the upper Karamalytash and subsequent Ulutau volcanics. Thicker continental crust terminated subduction and arc volcanism. Brown et al. (2001) also suggest arc migration, with the western belt (that they term the Irendyk volcanic front) active during intra-oceanic subduction in the Emsian-Eifelian, which then ceased in the Givetian when activity shifted eastwards to form the eastern arc comprising calc-alkaline Ulutau volcanism from the Givetian to Frasnian. This eastward migration of activity coincided with arrival of continental crust in the subduction zone, with volcanism relating to arc-continent collision.

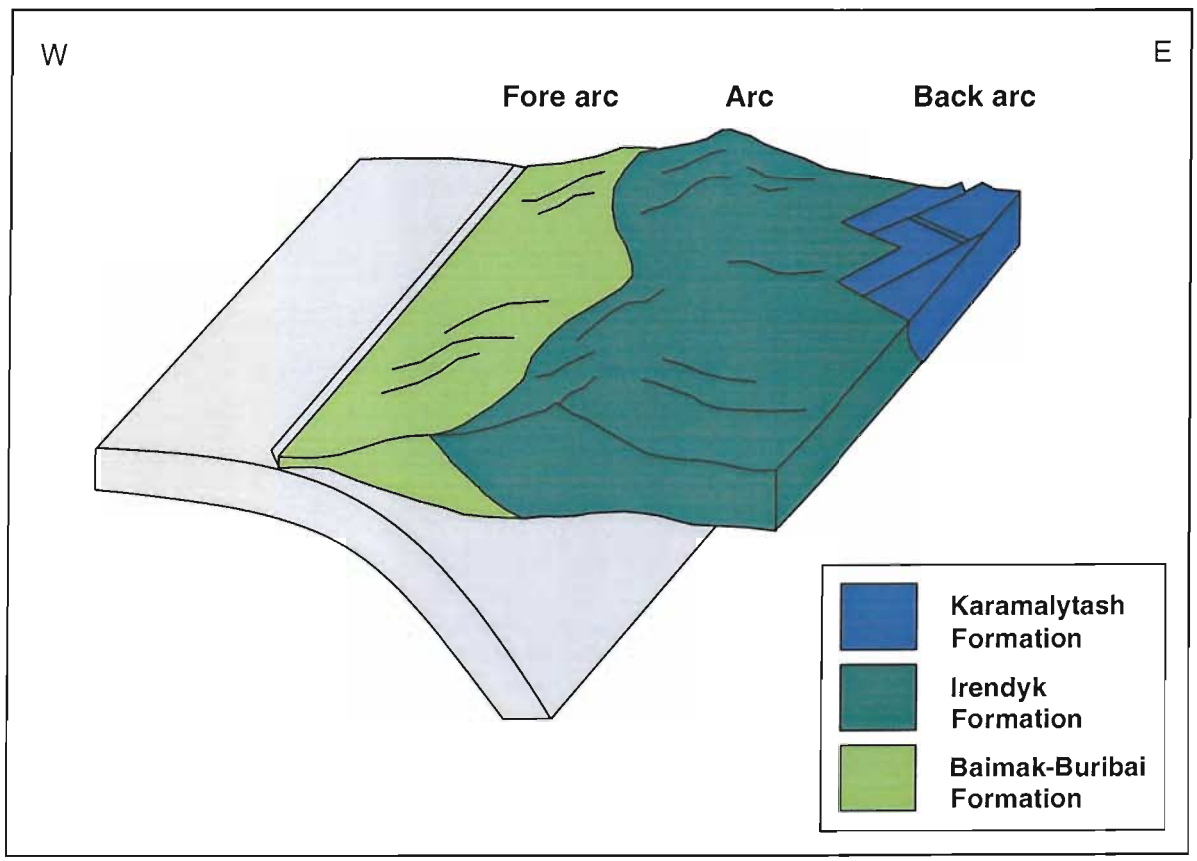

Figure 2.14. Tectonic development of the Magnitogorsk Island Arc (western volcanic belt) in the Middle Devonian (Eifelian), after Herrington et al., 2002.

The most likely alternative to arc migration is if the two belts originally formed part of the same, coeval arc which has been segmented during later tectonic activity, supported by the .identification of large regional scale sinistral strike-slip faults (e.g. Herrington et al., 2003). Other suggestions include the development of a double arc by opposing subduction zones resulting in the East and

West volcanic belts separated by an inter-arc basin, which is consistent with the observation that this basin is a continuation of the well defined inter-arc basin of the West Mugodzhar Zone further South in Kazakhstan. In this scenario the western arc formed from an East dipping subduction zone, which subsequently became inactive and westward dipping subduction began further East to produce the Eastern arc, with an inter-arc spreading zone separating the two (Prokin et al., 1999; Gusav et al., 2000).

2.2.5 VMS deposits of the Magnitogorsk Zone

Volcanic sequences of the Magnitogorsk Zone host numerous VMS deposits (Figure 2.15) which vary considerably in grade and tonnage, from giants such Gai where over 300Mt grade at 1.6% Cu and 0.8% Zn, to small but high grade deposits such as Bakr Tau with 1.3Mt at 2.6% Cu, 4.7% Zn and 1.5g/t Au (Herrington et al., 2000a). Examples of economically important deposits are listed in Table 2.3.

The composition, grade and tonnage of Uralian VMS have been found to vary systematically with host rock lithology and tectonic setting (e.g. Prokin and Buslaev, 1999; Herrington et al., 2002), with trends comparable to those observed in a number of other VMS districts worldwide (e.g. Sawkins, 1990). The good preservation of the Magnitogorsk arc enables the distinction of fore-arc, accretionary arc and back-arc environments and makes this region highly suitable for studying the relationship between VMS deposit styles and formational tectonic settings and host rocks.

The Uralian VMS deposits are broadly classified into three groups by Russian workers, summarised by Herrington et al. (2002) as follows:

- Cyprus Type; Cu-rich ores dominated by pyrite and chalcopyrite with minor sphalerite and containing relatively high levels of Co, with low Au. Host units are tholeiitic basalts which in the Magnitogorsk Zone are found in the lowermost Baimak-Buribai sequences and are interpreted to have formed in a supra-subduction setting.
- Urals Type; large Cu-Zn deposits hosted in bimodal basalt-rhyolite volcanics reflecting formation in a back arc environment. Orebodies are complex and zoned and dominated by pyrite, chalcopyrite and sphalerite, but also contain significant pyrrhotite at the base and sulphosalts toward the top, with significant enrichment in Ag, Cd, Ge and elevated contents of Au. The majority of large, active mines in the Magnitogorsk Zone are exploiting Urals type deposits.
- Baimak Type; smaller polymetallic deposits with more variable characteristics, but generally hosted in felsic dominated bimodal basalt-rhyolite sequences with associated felsic intrusives. Ore bodies have a high proportion of stockwork and disseminated ore relative to massive

sulphides, and contain a wide range of minerals with high concentrations of Ba, Pb, As, Sb Ag, Cd and in particular Au.

There is considerable controversy regarding the formational settings and relative ages of Urals and Baimak type deposits. For example, Prokin and Buslaev (1999) interpret the Urals type to have formed during early stages of island arc development and the Baimak type to be younger, having formed in a mature island arc setting, whereas Koroteev et al. (1997) proposed the Urals type to have formed within island arc sequences, with Baimak type in basins associated with these arcs. More recent studies indicate that Urals type deposits formed in back arc basins, while Baimak type are older and associated with early to mainstage island arc sequences (Herrington et al., 2002).

There are also ambiguities regarding the distinction of Baimak and Urals type mineralization and it has become increasingly apparent that some deposits show features typical of both Urals and Baimak type ores. For example, large Urals type deposits such as Uzelga have vertically zoned, stacked lenses and the uppermost ores are gold-rich and polymetallic, comparable with the Baimak type deposits (Herrington et al., 2000b). Other examples include the Alexandrinka deposit which was initially considered to be Urals type (e.g. Prokin and Buslaev, 1999) but has since been reclassified as Baimak type (e.g. Herrington et al., 2002). Balta Tau is another deposit that does not fall neatly into the above classification. The polymetallic and Au-rich nature of ores is consistent with the current definition as a Baimak Type deposit (Prokin and Buslaev, 1999; Herrington et al., 2002). However, the host sequences are dominated by andesites, and intrusive units have not been identified in the immediate vicinity (discussed in Chapter 3). In general, these inconsistencies highlight the need for further studies of Uralian VMS deposits and a re-examination of the Urals and Baimak type classification.

Deposit	Orebody	Type	tonnage	Cu %	Zn %	Pb %	Au g/t	Ag g/t
Buribai	all deposits	Cyprus	~200	1.9	1.2	0.1	nd	nd
Sibay	main deposit	Urals	115	1.0	nd	nd	0.6	nd
Sibay	Bakr Uzyak	Urals	1	1.5	1.6	0.04	1-1.5	16
Uchaly	open pit	Urals	113	1.1	3.7	0.1	1.3	nd
Uzelga	Cu-rich	Urals	27	2.1	0.2	0.1	0.8	12.6
Uzelga	Zn-rich	Urals	42	0.9	4.6	nd	nd	nd
Podolskoye	whole deposit	Urals	81	1.7	1.8	0.13	nd	nd
Gai	all ore lenses	Urals	>300	1.6	0.8	0.06	nd	nd
Alexandrinka	open pit	Baimak	9.8	4.4	5.5	nd	1.1	37
Bakr Tau	whole deposit	Baimak	1.3	2.6	4.7	0.67	1.5	nd

Table 2.3. Grade and tonnage data for selected VMS deposits in the Magnitogorsk Island Arc. Data from Herrington et al. (2000a). nd = no data.

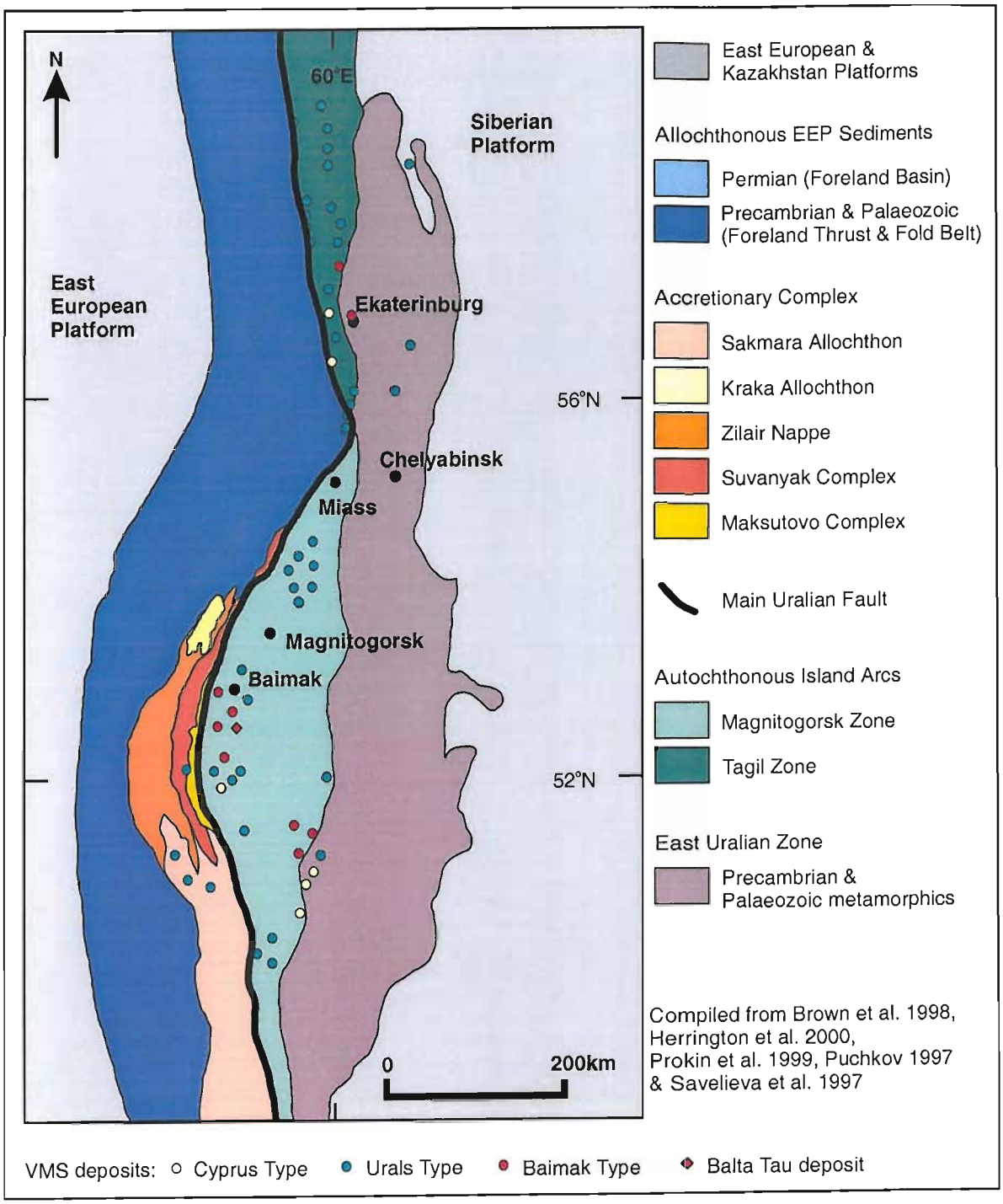

Figure 2.15. Location and classification of VMS deposits in the Magnitogorsk Zone.

3 GEOLOGY OF THE BALTA TAU MINE AND SURROUNDING AREA

3.1 INTRODUCTION

The region surrounding Balta Tau comprises sequences of the upper Baimak-Buribai, Irendyk, Jarlykapovo and Ulutau formations, with the Balta Tau deposit located close to the upper Baimak-Buribai - Irendyk contact (Figure 3.1). The contact between Baimak-Buribai and Irendyk volcanics is difficult to identify in the field due to limited exposure and alteration overprinting the primary mineralogy. It is therefore difficult to establish with certainty whether the Balta Tau deposit is hosted by Irendyk or Baimak-Buribai suites. Suggestions that Balta Tau is hosted in the Upper Baimak-Buribai are based principally on comparison with similar, small, gold-rich VMS deposits further West (e.g. Tash Tau and Bakr Tau, Figure 3.1) which are located in upper Baimak-Buribai successions (e.g. Herrington et al., 2000a). However, Russian geological survey mapping indicates that Balta Tau is hosted entirely within Irendyk volcanics, and others suggest the deposit to lie at the contact with Baimak-Buribai volcanics in the footwall and Irendyk in the hanging-wall (Seravkin, pers. comm.).

While the Lower Baimak-Buribai Formation has been studied in detail following the discovery of boninitic-like lavas in this unit (Spadea et al. 1998), the Upper Baimak-Buribai, Irendyk and Ulutau formations have received little attention. Limited petrographical descriptions and whole rock analyses of upper Baimak-Buribai, Irendyk and basal Ulutau volcanics have been published by Zonenshain et al. (1984) and Herrington et al. (2002). However these data are insufficient to confidently characterize the host rocks of the Balta Tau deposit.

This study of the volcanic units in the vicinity of Balta Tau aims to:

- Describe field relationships and lithologies.
- Define petrological distinctions between volcanics of the upper Baimak-Buribai, Irendyk and Ulutau Formations.
- Identify unit(s) hosting Balta Tau mineralization.
- Obtain and interpret whole rock geochemical data to (i) investigate element mobility during regional and VMS-related hydrothermal alteration; (ii) use immobile elements to identify rock types compositionally and interpret the tectonic setting during formation.

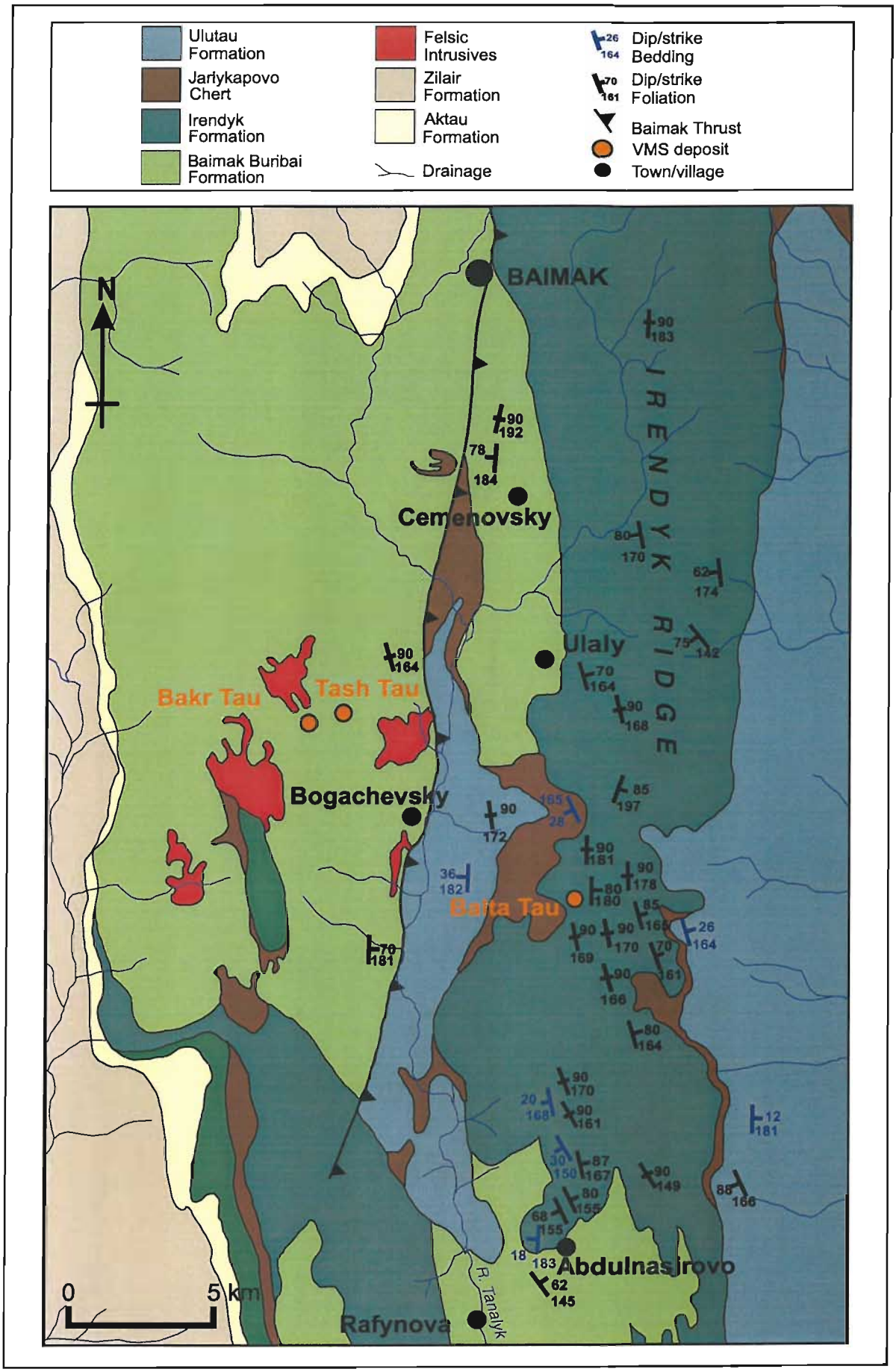

Figure 3.1. Geological map of the area surrounding the Balta Tau mine, modified from the Russian 1:200,000 series. Structural data shown was obtained in this study.

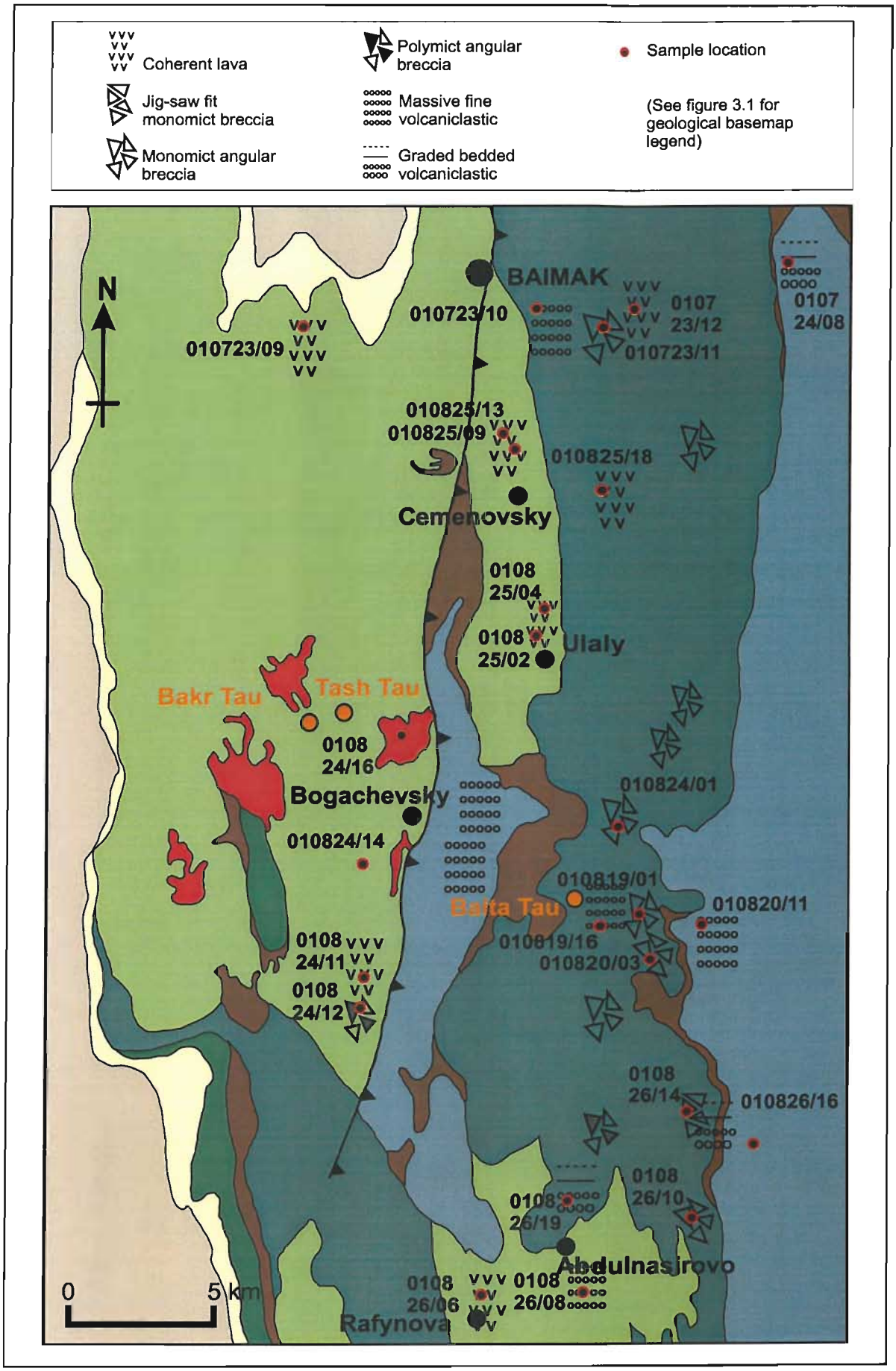

Figure 3.2. Geological map as shown in Figure 3.1, with regional sample locations and lithofacies.

3.2 LOCAL GEOLOGY AND PETROLOGY

3.2.1 Introduction

The mapping and sampling of this study focussed on the Baimak-Buribai and Irendyk sequences in the vicinity of Balta Tau. To the East of Balta Tau, a topographically high ridge comprising the Irendyk stretches North-South, referred to as the "Irendyk Ridge". The contact between the Irendyk volcanics and the Baimak-Buribai Formation also trends North-South and on Russian geological survey maps passes just to the West of Balta Tau (Figure 3.1), following a valley that runs parallel to and West of the main Irendyk ridge. In the vicinity of Balta Tau and to the South, the contact is concealed beneath sequences of Jarlykapovo chert and Ulutau volcaniclastics which are exposed in a synformal structure and conformably overlie both the Baimak-Buribai and Irendyk suites. The occurrence of Jarlykapovo chert directly overlying Baimak-Buribai volcanics is unusual and only occurs in a few isolated areas according to Russian 1:200,000 geological maps. Further South, the Baimak-Buribai volcanics are again exposed, and terminate the Irendyk Ridge with an irregular East-West contact (Figure 3.1).

Using the Russian 1:200,000 series as a base geological map, Figure 3.1 gives structural data obtained in this study and Figure 3.2 provides sample locations and a summary of the volcanic lithofacies mapped at sampling sites and additional exposures. The Russian 1:200,000 map has been modified according to results of this study. In particular, a number of small (100's m to km scale) outcrops of volcaniclastic material depicted on the Russian map as islands of Ulutau enclosed in the Irendyk are more likely to be part of the Irendyk unit (described further in Section 3.2.3) and are therefore shown as Irendyk not Ulutau on Figures 3.1 and 3.2. The following sections give an overview of lithologies encountered in each of the formations; descriptions of relevant samples are given in Appendix A1.

3.2.2 Baimak-Buribai Formation

The Upper Baimak-Buribai Formation is characterized by felsic lavas, breccias and finer volcaniclastic horizons. Mapping and sampling of this unit focussed on exposures close to the contact with the Irendyk Formation.

Coherent lavas

Between Balta Tau and the town of Baimak, and South of Balta Tau in the vicinity of Rafynova village (sample location 010826/06), the Baimak-Buribai exposures are predominately coherent lavas with some development of columnar jointing (Figure 3.3a). These are typically massive, grey-green, dark green or dark purple and weakly to moderately porphyritic (e.g. Figure 3.3b).

a. Small scale columnar jointing in a massive, weaky porphyritic felsic lava. Exposure close to location of sample 010825/09.

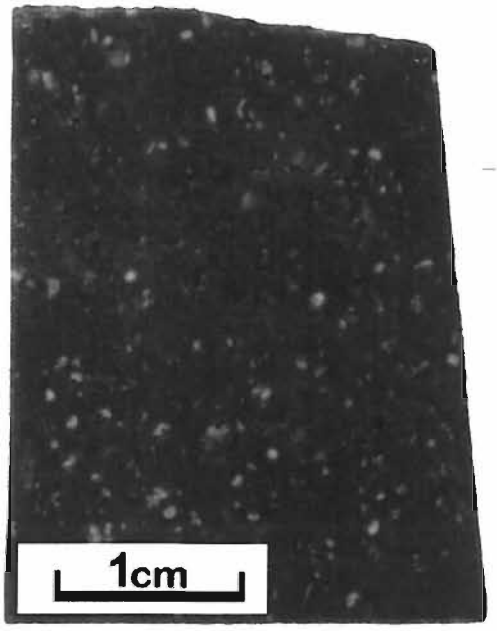

b. Typical massive lava with small feldspar phenocrysts in low abundance. Sample 010825/02.

c. Amygdaloidal, weakly porphyritic massive lava. Amygdales are mostly unstretched and spherical comprising epidote, zeolite, chlorite, quartz, actinolite and rarely pyrite-chalcopyrite.

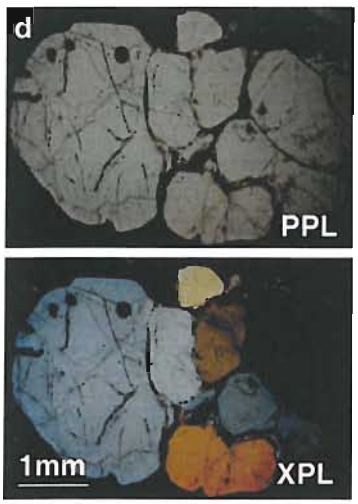

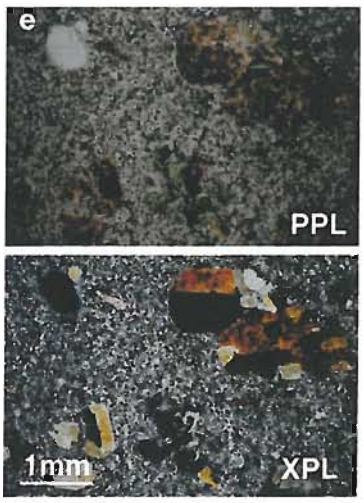

d. Glomeroporphyritic, slightly rounded quartz phenocrysts. Sample 010825/04.

e. Typical feldspar phenocrysts with simple twinning. The matrix is a very fine grained, equigranular mosaic of felsic minerals (feldspar/ quartz). One small, rounded quartz phenocryst (top left) has margins that grade into the enclosing matrix. Sample 010826/06.

Figure 3.3. Coherent lavas of the Baimak-Buribai Formation.

Feldspar phenocrysts are ubiquitous with an abundance of <1% to around 10%, and form stubby euhedral crystals <0.5mm to 2mm which commonly exhibit a glomeroporphyritic texture (Figure 3.3e). Twinning is often absent, and where present tends to be simple twinning or more rarely lamellae twinning. The morphology and twinning are typical of alkali feldspars, and suggests a high proportion of alkali feldspar relative to plagioclase. Quartz phenocrysts are sometimes present in low abundance (<3%), varying in size from 0.2 to 3mm within the same sample, and are sometimes glomeroporphyritic (Figure 3.3d), fractured and embayed (Figure 3.3d). In some samples two populations of quartz phenocrysts can be distinguished. The first are small, rounded and spherical with embayed and/or corroded margins that often grade into the enclosing groundmass (Figure 3.3e). The second generation are larger, euhedral, and rarely embayed and only slightly to moderately rounded (Figure 3.3d). In addition to quartz and feldspar, completely altered phenocrysts which may originally have been mafic phases are occasionally present in low abundance (<5%), although no relict primary mafic minerals have been found. The groundmass usually comprises very fine grained, equigranular felsic minerals (e.g. Figure 3.3e), or more rarely fine feldspar laths which may define a weak trachytic texture. Amygdaloidal lavas are abundant (Figure 3.3c) and contain mostly spherical and unstretched amygdales composed of zeolite, chlorite and quartz.

The phenocryst proportions suggest that the Baimak-Buribai lavas are felsic with a dacitic to rhyodacitic composition. Rounding and embayments of quartz phenocrysts probably reflect partial resorbtion of quartz in to the melt after crystallization, and where two populations can be distinguished textures suggest that two phases of quartz crystallization occurred, with crystals from the earliest phase experiencing a greater degree of resorbtion than the second.

Volcaniclastics

Volcaniclastics of the Baimak-Buribai Formation are exposed immediately West of the Tanalyk River, just South of Bogachevsky village. These are felsic, polymict breccias with angular cm sized clasts containing variable proportions of feldspar phenocrysts, and some are silicified with banding that may be relict flow banding (Figure 3.4). The polymict nature of these breccias together with absence of textures indicative of hot emplacement (as defined in McPhie et al., 1993) suggests that they are sedimentary reworked deposits rather than of primary hyaloclastic or pyroclastic origin. The poor sorting and angularity of clasts suggests minimal transportation, and these sequences may be the result of localized slumping.

Alteration of the Upper Baimak-Buribai volcanics is typically weak to moderate but may be intense. Feldspar phenocrysts are frequently partially altered to sericite, and sometimes replaced by quartz, quartz-carbonate, or sericite-actinolite. Completely altered phenocrysts which may originally have been mafic phases are altered to chlorite, chlorite-actinolite(±titanite±Fe oxides)

and rarely epidote(-Fe oxides-rutile). The groundmass is commonly partially altered to patchy sericite-chlorite(-titanite-rarely epidote) or pervasive sericite-hematite.

Poorly sorted, polymict, angular breccia with clasts showing variable phenocrysts, groundmass, textures and alteration. Some clasts are distinctly banded, which may be primary flow banding. Sample 010824/12.

Figure 3.4. Volcanic breccia of the Baimak-Buribai Formation.

A granitic intrusive body lies just North of Bogachevsky village (Figure 3.1). The granite is inequigranular but non-porphyritic, comprising predominately quartz and feldspar with a high abundance of plagioclase relative to alkali feldspar. A minor mafic phase which may have been biotite is completely altered to chlorite with minor epidote and traces of titanite. The Bogachevsky plagiogranite has not been dated, and may either be syn-volcanic or post-volcanic, in the latter case intruding during collisional events of the Carboniferous.

The contact between Baimak-Buribai and Irendyk Formations was not observed in the field, although lithological variations at sampling sites correspond well with the location of the contact as shown on Figure 3.1.

3.2.3 Irendyk Formation

The Irendyk Formation is dominated by intermediate to mafic lavas and breccias with pockets of graded bedded volcaniclastics. Sampling focussed on the western slope of the Irendyk Ridge and in the adjacent valley up to the contact with the Baimak-Buribai Formation, from the Town of Baimak North of Balta Tau to the area of Abdulnasirovo village South of Balta Tau.

Lavas and autobreccias

Coarse volcanic breccias and coherent lavas dominate the West slope of the Irendyk Ridge and continue to the contact with Baimak-Buribai and Ulutau Formations (Figure 3.2). Coherent lavas are massive with an absence of columnar jointing or pillow structures. The breccias exhibit a variety of lithofacies reflecting different formational mechanisms, but the majority contain angular cm to 10's cm sized monomict clasts suggestive of autobrecciation. An exposure at the southern extreme of the Irendyk Ridge (near to sample 010826/14 location) consisted of a fractured coherent lava grading into an angular, jigsaw-fit, monomict breccia (Figure 3.5a). The breccia is typical of a hyaloclastite (based on criteria in McPhie et al., 1993) formed by quench fragmentation due to the interaction of hot lavas with cold water (Fisher & Schmincke, 1984). On a smaller scale a number of hand specimens are also indicative of a hyaloclastic origin, with characteristics including angular cm clasts enclosed in a matrix containing smaller mm sized clasts of the same material, jigsaw fit textures, and clast margins grading into the matrix (Figure 3.6b). Other Irendyk lithofacies are more ambiguous, comprising monomict angular autobreccias without a jigsaw-fit texture which may be reworked rather than in situ hyaloclastites (e.g. Figures 3.5b and c). In general, the large volume of autobreccias occurring along the Irendyk Ridge is consistent with a hyaloclastic origin since quench fragmentation is particularly capable of producing huge volumes of angular, juvenile material (Cas, 1992). The occurrence of hyaloclastites is highly suggestive of a submarine eruptive setting for these sequences, although hyaloclastites may also form when subaerially erupted lavas flow into cold water (Cas, 1992).

Lavas and breccia clasts of the Irendyk are plagioclase-pyroxene±quartz-phyric and sometimes amygdaloidal. Plagioclase phenocrysts vary in abundance from 5 to 30% with the majority of samples containing 15 to 25%, and form elongate crystals 0.2 to 2mm with lamellae twinning (Figure 3.7c). Pyroxene phenocrysts typically have an abundance of 3 to 5%, although lavas to the South of Balta Tau locally contain up to 25%. Crystals are euhedral and usually 0.5 to 3mm in size, increasing to over 1cm in size in the pyroxene-rich samples, and exhibit optical properties characteristic of clinopyroxene (Figures 3.7a and b). South of Baimak towards the contact with the Baimak-Buribai Formation, the Irendyk contains 1 to 2% quartz phenocrysts which coexist with pyroxene as well as plagioclase phenocrysts (e.g. sample 010723/11), forming 0.2 to 2mm equant crystals that are rounded, fractured and embayed (Figure 3.7e). The groundmass, where unaltered, is commonly semi-opaque and glassy (e.g. Figure 3.7b) and sometimes contains feldspar laths occasionally defining a weak trachytic texture. Amygdales are sometimes present in 5 to 10% abundance and are spherical to weakly stretched, comprising quartz-pumpellyite or quartz-epidote-zeolite (e.g. Figure 3.7a).

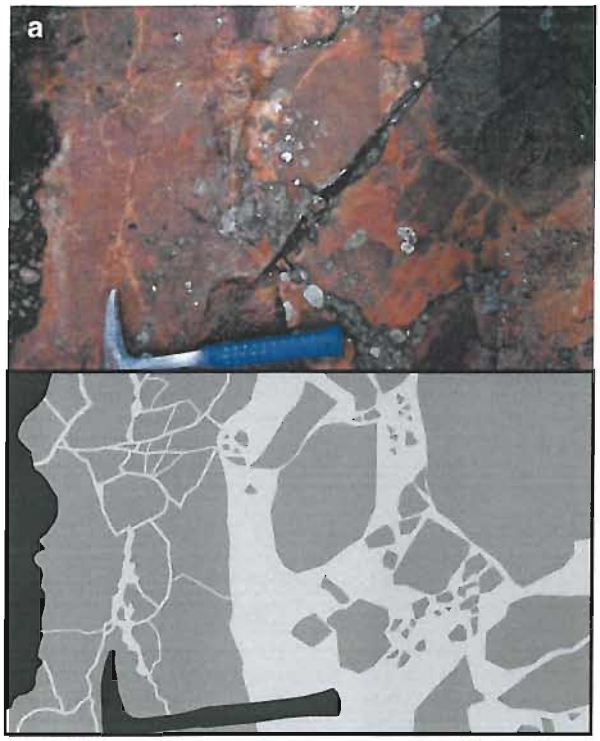

a. Exposure of in situ brecciated lava, showing the contact between the top of a fractured flow (left) and an hyaloclastic jig-saw fit breccia (right). Exposed approximately 1km West of sample location 010826/14.

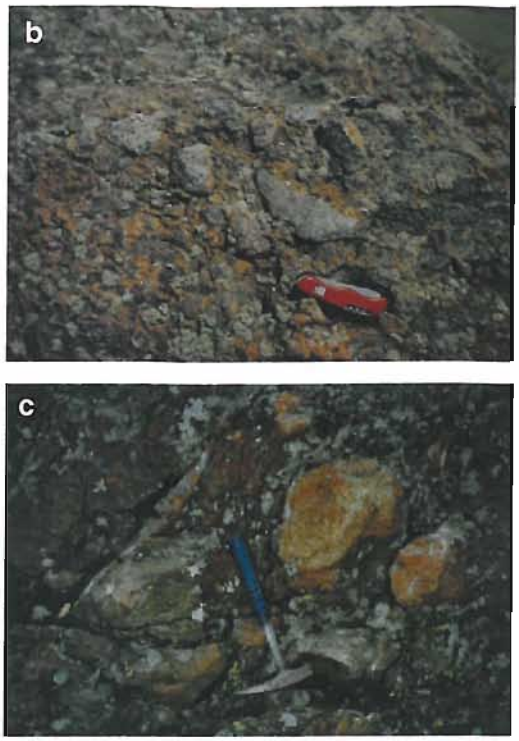

b and c. Typical volcanic breccias of the Irendyk ridge. Clasts appear rounded due to weathering and colour relates to the mineralogy of alteration, with purple clasts in (b) hematite-rich, and greenish clasts in (c) altered to chlorite-epidote.

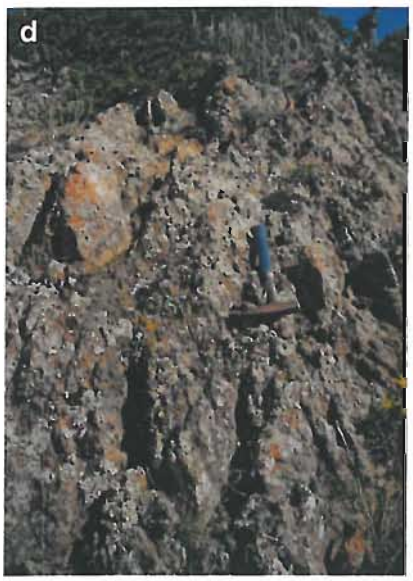

(d). Volcanic breccia on the Irendyk Ridge with typical weak North-South trending foliation developed in the matrix that folds around clasts.

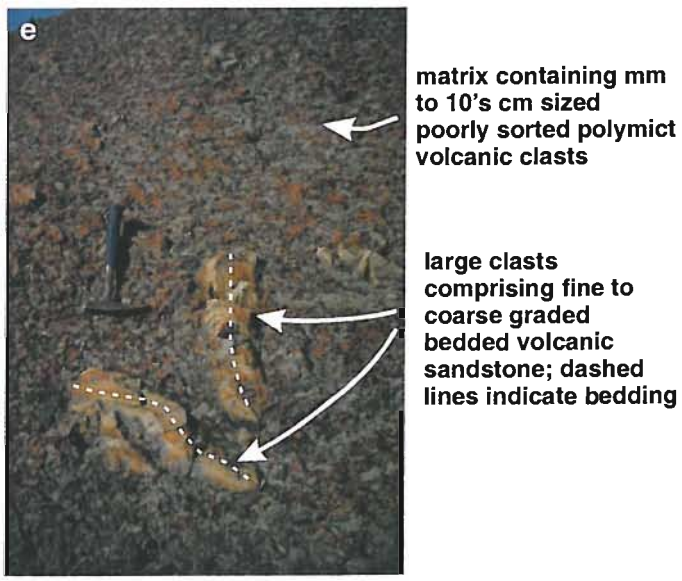

(e). Reworked volcanic breccia. Polymict and highly unsorted, this breccia contains clasts of porphyritic lava in the matrix, which encloses large blocks of fine volcaniclastic material with graded bedding (similar to that of Figure 3.9). Exposed approximately 2km Northeast of sample location 010826/19.

Figure 3.5. Volcanic breccias of the Irendyk Formation.

The phenocryst abundances of Irendyk lavas indicate a basaltic to andesitic composition and samples with high abundances of plagioclase or pyroxene probably reflect stages of phenocryst accumulation. The presence of co-existing quartz and pyroxene phenocrysts is unusual, since the presence of quartz indicates melt saturation with respect to silica while pyroxenes crystallize from silica undersaturated melts. This together with the rounded and embayed nature of quartz indicative of partial resorbtion suggests that the melt composition changed dramatically during crystallization.

Alteration is usually moderate to intense, with plagioclase partially or completely altered to sericite, sericite-actinolite, sericite-chlorite or rarely chlorite-epidote-actinolite, and pyroxene frequently replaced by quartz-epidote-chlorite (Figure 3.7c) or epidote-carbonate(-chlorite). Alteration of the groundmass is highly variable and includes sericite-chlorite, actinolite-epidote, zeolite-pumpellyite-chlorite-sericite and hematite rich assemblages.

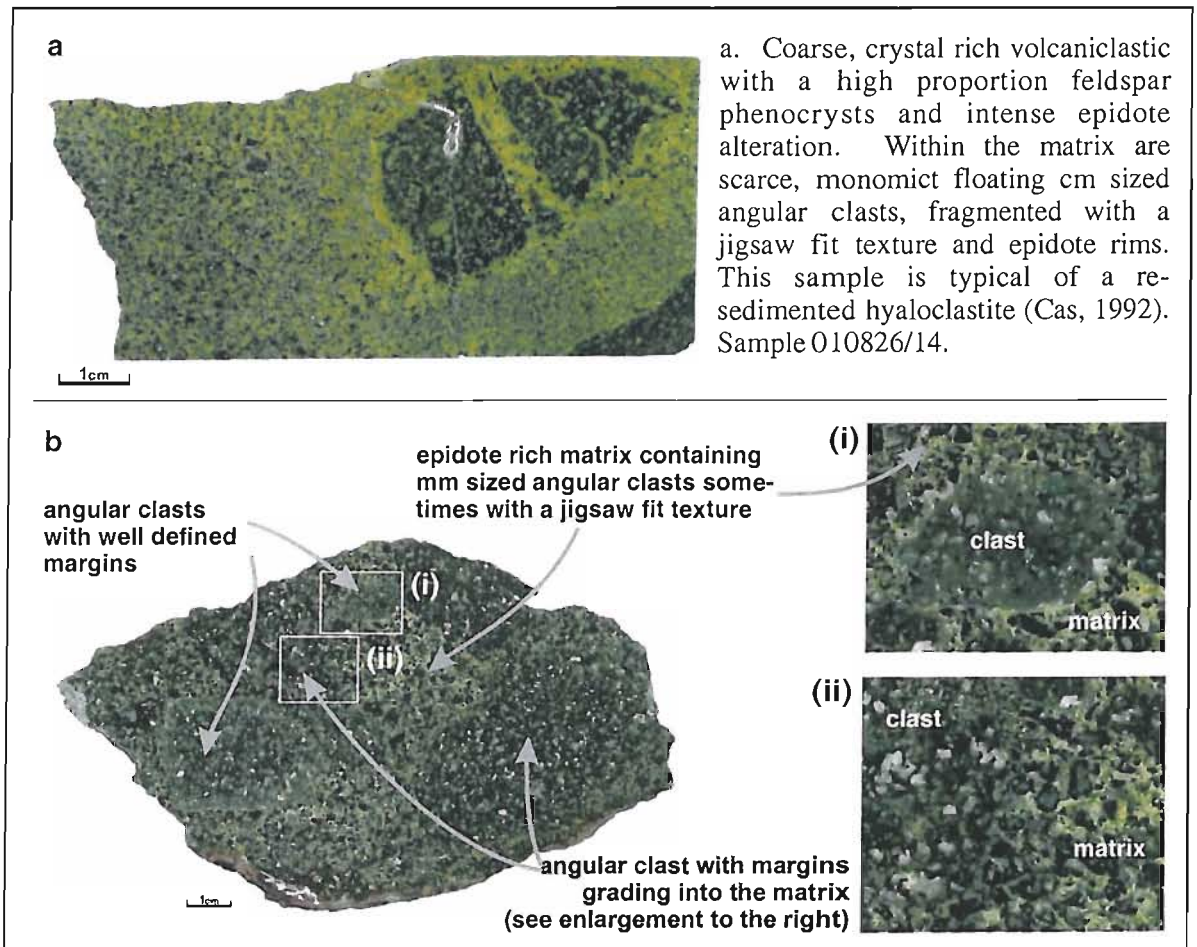

a. Coarse, crystal rich volcaniclastic with a high proportion feldspar phenocrysts and intense epidote alteration. Within the matrix are scarce, monomict floating cm sized angular clasts, fragmented with a jigsaw fit texture and epidote rims. This sample is typical of a re-sedimented hyaloclastite (Cas, 1992). Sample 010826/14.

b. Hyaloclastic volcanic breccia. Angular monomict clasts share the same proportion and size of feldspar and minor mafic phenocrysts, but display variable alteration. Clast margins vary fromangular and well defined (e.g. inset (i)) to irregular and grading into the matrix (e.g. inset (ii)). The matrix comprises small angular mm sized fragments of the same material sometimes with a jigsaw fit texture enclosed in a pale green epidote rich matrix. Sample 010824/07.

Figure 3.6. Hyaloclastic breccias of the Irendyk Formation.

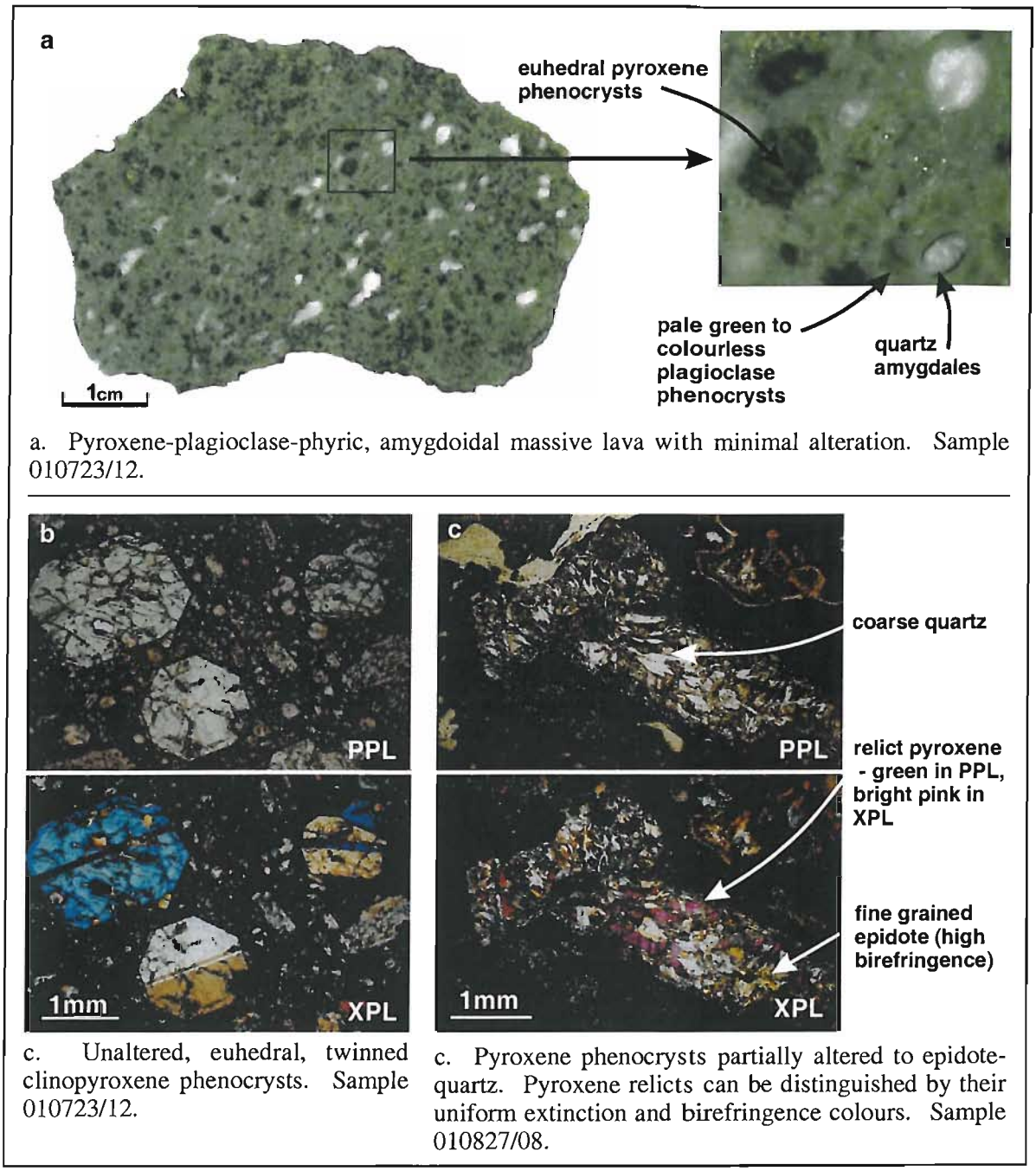

a. Pyroxene-plagioclase-phyric, amygdoidal massive lava with minimal alteration. Sample 010723/12.

c. Unaltered, euhedral, twinned clinopyroxene phenocrysts. Sample 010723/12.

c. Pyroxene phenocrysts partially altered to epidote-quartz. Pyroxene relicts can be distinguished by their uniform extinction and birefringence colours. Sample 010827/08.

Figure 3.7. Coherent lavas of the Irendyk Formation.

Polymict breccias

Although the Irendyk is dominated by monomict breccias (described above), polymict breccias are also present with angular to sub-rounded clasts ranging from cm to several 10's cm in size. Exposures to the South of Balta Tau contain clasts of porphyritic lavas and graded-bedded volcaniclastics (Figure 3.5d). The large size, poor sorting and angularity of clasts suggests they have not been transported far and may be the result of mass slumping, and the graded volcaniclastic clasts contain fine laminations which are undeformed, suggesting the volcaniclastic material had consolidated prior to reworking. The breccias are located approximately 2 km North of extensive volcaniclastic sequences (discussed below) which are a likely source of the volcaniclastic clasts.

Fine grained volcaniclastic sequences

Exposures of fine volcaniclastic material within the Irendyk include massive and finely bedded sequences, the latter with mm to cm scale graded bedding and thinly interlayered ashy/chert horizons (Figure 3.8a, b). These volcaniclastics are mainly exposed in 100's m to few km scale outcrops to the South of Balta Tau, close to the irregular East-West contact with the Baimak-Buribai Formation. Bedding dips gently to the East, consistent with the regional dip observed in the overlying Jarlykapovo and Ulutau Formations. An additional exposure caps a small hill a few hundred metres East of Balta Tau, and probably correlates with hanging-wall volcaniclastics exposed in the open pit (Section 3.3.5).

The coarser horizons of these volcaniclastics are dark green and contain whole and fragmented feldspar and pyroxene phenocrysts. Pyroxenes are sometimes unaltered (Figure 3.8c) but more frequently replaced by chlorite and/or epidote, and feldspar is commonly partially to completely altered to sericite. Angular to irregular feldspar-phyric lithic clasts generally less than 5mm in size are also present, which are variably altered but may be monomict based on their similar phenocryst proportions. Finer material is pale green and has a cherty appearance (Figure 3.8b), comprising extremely fine grained sericite/illite, quartz and minor chlorite. These exposures of volcaniclastic material are represented as pockets of the Ulutau Formation on the Russian 1:200,000 geological maps. However, there are fundamental lithological differences between the Ulutau and these sequences. Most notably, the volcaniclastics described here contain pyroxene phenocrysts (Figure 3.9c) and mafic/intermediate lithic clasts with a notable absence of quartz, whereas the Ulutau contains abundant quartz and feldspar crystal fragments (Section 3.2.4). These sequences are therefore interpreted as part of the Irendyk Formation and mapped as such on Figures 3.1 and 3.2.

Interpretation of the Irendyk volcaniclastics is hindered by alteration that overprints primary features, but textures can be used to constrain likely formational processes and depositional mechanisms (based on criteria in Cas, 1992 and McPhie et al., 1993). The parallel planar, massive and graded bedding and absence of cross-laminations suggest deposition by mass flow below the wave base. The textural immaturity of lithic and crystal fragments and probable monomict nature of lithic clasts suggest that they have not been transported far and are probably resedimented hyaloclasts and/or pyroclasts rather than epiclasts. The absence of vesicles in lithic fragments points to a hyaloclastic origin, although pyroclasts may not be vesiculated if formed during a phreatomagmatic explosion prior to exsolution and vesiculation of magmatic volatile phase (Cas, 1992). In finer horizons the abundance of fine, ash grade material cementing sparse, coarser clasts is more suggestive of a pyroclastic origin.

These observations suggest that the volcaniclastic sequences are a mixture of hyaloclastic and pyroclastic material that was resedimented soon after primary deposition without being transported

a significant distance ("syn-eruptive resedimented" according to the classification by McPhie et al., 1993).

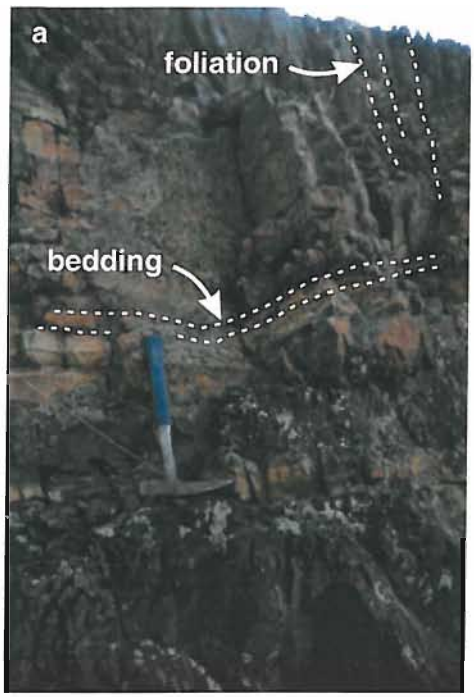

a. Graded bedded volcaniclastics exposed at sample location 010826/19.

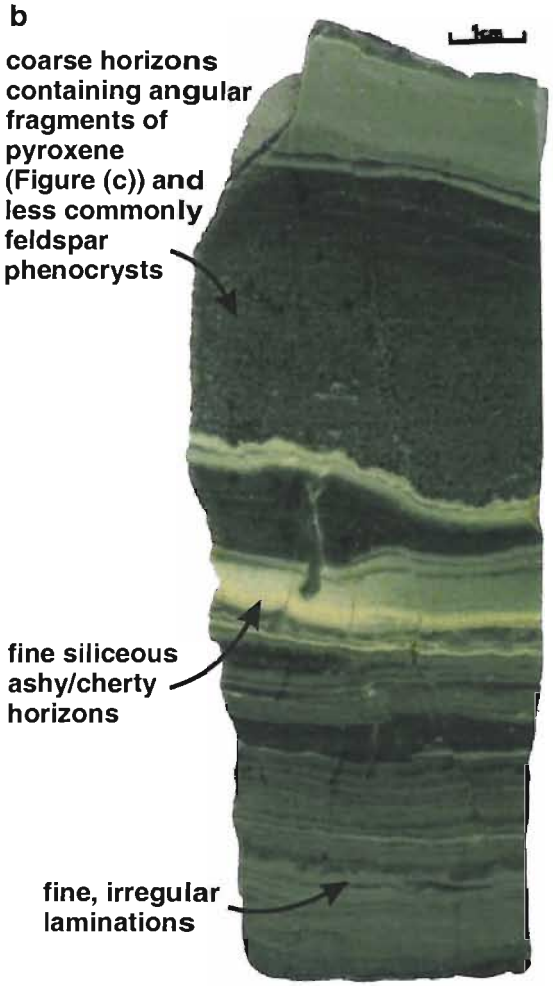

b. Volcaniclastics display fine mm to cm scale graded bedding and contain interlayered cherty material. Coarser layers contain angular fragments of pyroxene phenocrysts, lithic clasts and scarce white angular feldspar fragments. No quartz is visible. Sample 010826/19.

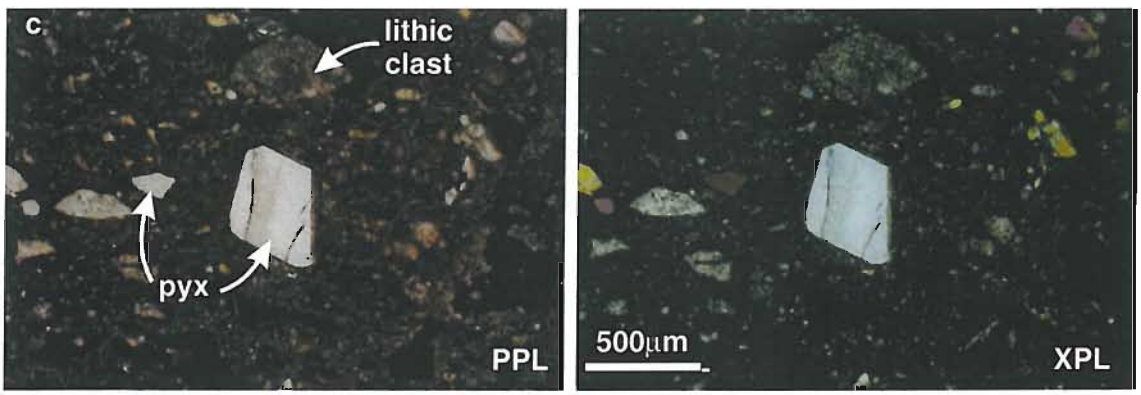

c. Coarse unaltered fragment of a euhedral pyroxene phenocryst (centre) in fine grained ashy matrix containing numerous small angular fragments of pyroxene and rarely feldspar phenocrysts, and small lithic fragments. Sample 010826/20.

Figure 3.8. Graded volcaniclastics of the Irendyk Formation.

3.2.4 Jarlykapovo Chert and Ulutau Formation

The Jarlykapovo Chert is a distinctive marker horizon occurring sporadically at the contact between the Irendyk and Ulutau Formations and dips gently to the East. In the Balta Tau area, the Jarlykapovo Chert is exposed along North-South trending ridges to the East and West of the mine. To the East, the chert occupies its normal stratigraphic position, resting conformably between the Irendyk below and Ulutau above. To the West, the Jarlykapovo (and overlying Ulutau) is exposed in a synformal structure (Figure 3.2), and here appears to directly overlie both Irendyk and Baimak-Buribai volcanics. This relationship suggests the Upper Baimak-Buribai and Lower Irendyk suites to have formed contemporaneously. The Jarlykapovo chert comprises finely layered red jaspers and grey/brown cherts (Figure 3.9b).

The Ulutau Formation outcrops over a wide area adjacent to and East of the Irendyk Ridge, as well as occupying the central portion of the small synform West of Balta Tau. The Ulutau is dominated by thick volcaniclastics dipping gently East, which gives the landscape a distinctive smooth lineation (Figure 3.10a) in contrast to the rough irregular terrane of the Irendyk Ridge. The base of the Ulutau is characterised by a thin (few meter thick) basal polymict breccia, which is exposed in sequences overlying the Irendyk (in the Karamalytash anticline to the North of Balta Tau) and overlying Jarlykapovo chert immediately East of Balta Tau. This grades upwards into characteristic graded bedded to massive volcanic sandstones (Figure 3.10b), which contain abundant, angular, whole and fragmented feldspar and quartz phenocryst 0.2 to 0.5mm (Figure 3.10c).

a. Gently dipping beds of grey and brown cherts, looking South along a Jarlykapovo ridge southeast of Balta Tau.

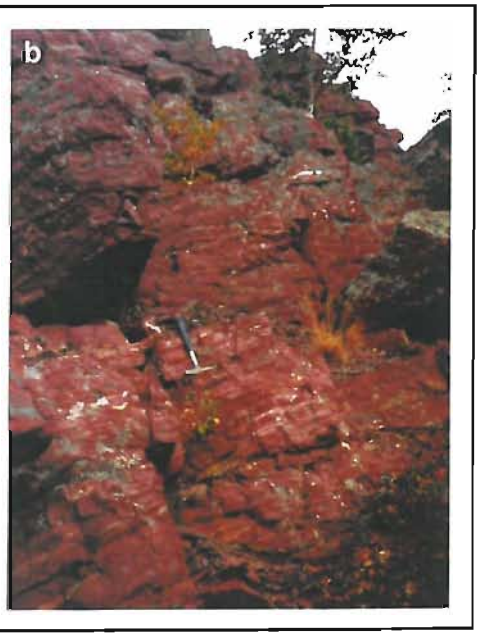

b. Red, banded chert/jasper exposed on the hill immediately west of Balta Tau.

Figure 3.9. Exposures of the Jarlykapovo Chert.

Lithic and crystal fragments are generally polymict, well sorted and angular to slightly rounded, and lithic clasts do not exhibit feathery or irregular margins. These features are more characteristic of immature epiclastic deposits than reworked hyaloclastic or pyroclastic sequences. This is supported by the fact that a single eruptive source is unlikely given the polymict nature of lithic clasts and widespread occurrence of thick sequences. Such voluminous deposits are more likely to result from the sedimentation of epiclastic volcanic material derived from subaerial erosion, which is deposited as megaturbidites (Cas, 1992).

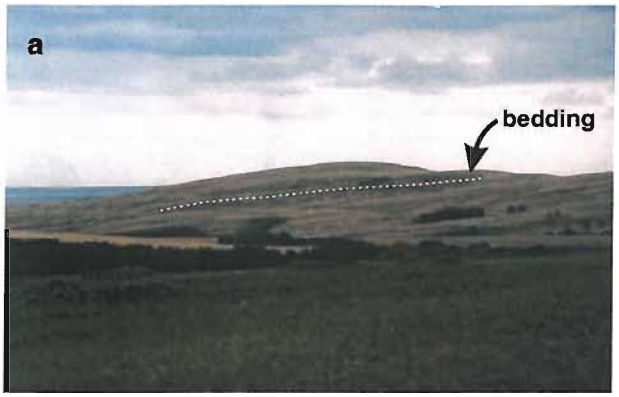

a. View looking southeast towards hills of the Ulutau Formation from sample location 010826/14. Layering reflects thickly bedded volcanic sandstones dipping gently East.

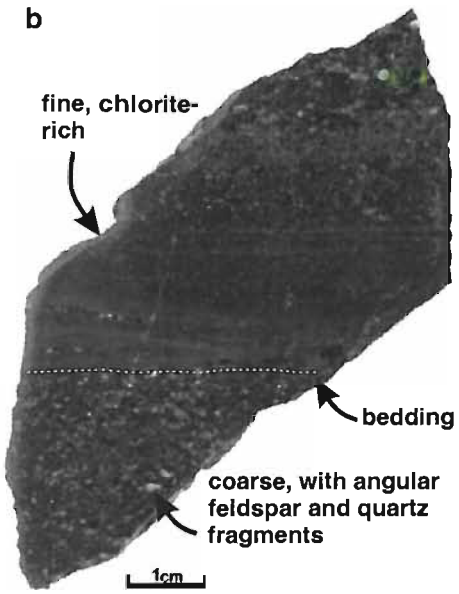

b. Graded bedded volcanic sandstone with coarse feldspar and quartz fragments. Sample 010724/04.

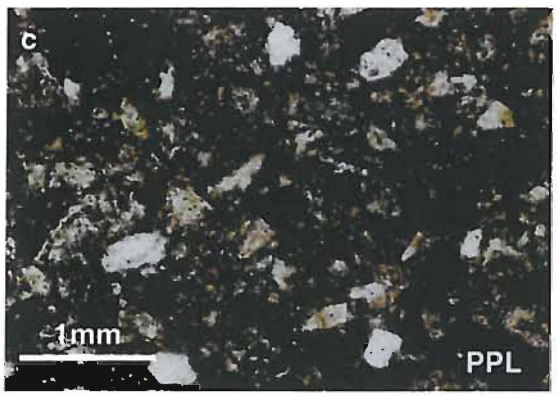

c. Fine grained volcanic sandstone rich in angular to sub-angular quartz and feldspar crystal fragments (colourless) enclosed in a very fine grained, semi-opaque matrix. Sample 010820/11.

Figure 3.10. Volcanic sandstones of the Ulutau Formation.

3.2.5 Structures, deformation and metamorphism

Volcanic units in the Balta Tau region are mostly massive and the scarcity of traceable lithological horizons makes structures difficult to define. The Baimak Thrust (Chapter 2, Section 2.5.2) is sometimes to the West of the Irendyk-Baimak-Buribai contact, in places within Baimak-Buribai volcanics and elsewhere forms the contact between Baimak-Buribai volcanics and the synformal Jarlykapovo-Ulutau sequences, where the thrust terminates the western limb of this synform (Figure 3.1). The interpretation of this fault as a thrust is based predominately on evidence from seismic sections (Brown et al., 1998), however, there is no stratigraphic justification since the hanging-wall units (Baimak-Buribai and Jarlykapovo-Ulutau in this area; Irendyk on a more regional scale; Figure 2.10) are contemporaneous or younger than units in the footwall (the Baimak-Buribai Formation).

Bedding in the Jarlykapovo chert, the Aktau Section and volcaniclastic horizons of the Irendyk and Ulutau (Figure 3.1) generally dips gently to the East which is typical of the regional bedding in the southern Magnitogorsk Zone. However, to the West of Balta Tau the Jarlykapovo chert and volcaniclastics of the Irendyk and Ulutau dip West providing evidence of the synformal structure which exposes the Jarlykapovo chert and Ulutau Formation. There is weak to moderate development of a regional foliation S_1 (Figure 3.1) which in general is near vertical and strikes NNW-SSE, but deviates locally to dips as shallow as 70° East and West and to N-S and NNE-SSW strikes.

Major alteration minerals are chlorite, epidote, actinolite, quartz, sericite and pumpellyite, with minor zeolite, prehnite and hematite, and scarce carbonate and titanite. These are consistent with predominately low grade prehnite-pumpellyite and pumpellyite-actinolite metamorphism, indicating temperatures of 180 to 300°C with pressures of 1 to 3kbar for prehnite-pumpellyite facies and 2 to 8kbars for pumpellyite-actinolite facies (Robinson & Bevins, 1999). The common occurrence of zeolites, although not a dominant phase, suggests temperatures were generally at the lower end of this range, and for discussions in the following chapters are taken as 180 to 250°C. The alteration intensity is highly variable with well preserved primary volcanic textures and random alignment of alteration minerals. These alteration characteristics are more typical of seawater interaction with volcanics than low grade metamorphism associated with burial or regional tectonic activity.

3.2.6 Mineralization

The Balta Tau deposit is one of a number of economic and sub-economic massive sulphide deposits in this area (Figure 3.2). Also hosted in the Irendyk are the Tubakayene massive sulphide deposit located immediately West of Balta Tau, which is now completely mined out with the open

pit backfilled, and deposits at Ulaly to the North of Balta Tau, where massive sulphides and barite-gold mineralization were exploited by a series of small open pits. Further South of Balta Tau is the Podolskoe deposit, a Cu-Zn rich massive sulphide deposit currently exploited by open pit (see Table 2.1) which is thought to be hosted in the same stratigraphic sequences as Balta Tau (Seravkin, pers. comm.). Approximately 10km West of Balta Tau are the gold-rich massive sulphide deposits of Tash Tau and Bakr Tau, which are hosted within Upper Baimak-Buribai sequences and currently mined by open pit.

3.2.7 Discussion

Petrographical distinction between formations

Volcanic lithologies of the Upper Baimak-Buribai, Irendyk and Ulutau Formations in the vicinity of Balta Tau can generally be distinguished based on phenocryst abundance, volcanic textures and dominant alteration assemblages. The Upper Baimak-Buribai Formation is dominated by felsic coherent lavas and minor polymict angular breccias, which are weak to moderately feldspar±quartz phyric (<1 to 15%). Alteration is dominated by sericite and quartz with variable chlorite, hematite and carbonate, and scarce epidote, actinolite and pumpellyite. By contrast, the Irendyk comprises intermediate to mafic coherent lavas, abundant monomict breccias and graded volcaniclastics, which are typically moderately to highly plagioclase-pyroxene(±quartz)-phyric (20 to 35%). Alteration assemblages in the Irendyk are distinct from those of the Baimak-Buribai lavas, being dominated by epidote, actinolite, chlorite and pumpellyite in addition to sericite and quartz. The quartz-phyric Irendyk lavas are commonly located close to the contact with Baimak-Buribai volcanics and are suggested to be a "hybrid" magma transitional between the Baimak-Buribai and Irendyk Formations (Seravkin, pers comm.).

The Lower Ulutau comprises thick volcaniclastic sequences that have a similar petrography over a wide area, including exposures North-East of Baimak, South East of Balta Tau and in the synformal structure West of Balta Tau. They are rich in quartz and feldspar fragments and which show a small degree of rounding and may be epiclastic in origin. Volcaniclastic horizons within the Irendyk lavas have previously been mapped as pockets of the Ulutau Formation (Russian 1:200,000 geological maps), however their mafic composition, absence of quartz phenocrysts and textures typical of immature, resedimented hyaloclastic/pyroclastic material distinguishes them from the Ulutau material and suggests they are volcaniclastic horizons within the Irendyk Formation.

Interpretation of eruptive settings and depositional mechanisms

The Irendyk Formation is dominated by intermediate to basic angular breccias, which in many cases are characteristic of hyaloclastites. These confirm a submarine eruptive environment and are typical facies of mainstage island arc volcanics.

Finer grained volcaniclastic sequences of the Irendyk have characteristics indicative of resedimented hyaloclastic and pyroclastic material which has not been transported far from the site of initial formation. These sequences are defined as "syn-eruptive resedimented" according to the classification of McPhie et al. (1993), which implies that resedimentation occurred during the same period of volcanic activity that formed the primary deposits. The presence of pyroclastic material is indicative of shallow water conditions of probably less than 1000m (Cas, 1992) in the area of explosive volcanism that formed the pyroclasts. This does not provide a direct indication of the water depth at the site where material has been redeposited, but does imply that shallow waters were present in the Irendyk arc.

The Ulutau volcaniclastics are texturally distinct from the Irendyk, and more typical of epiclastic deposits. The age of the Ulutau Formation corresponds to the estimated time of collision between the Magnitogorsk Arc and the encroaching East European Continent (Chapter 2, Section 2.2.3), which resulted in uplift of the arc. The interpretation of these Ulutau sequences is consistent with uplift resulting in subaerial exposure of the arc, followed by erosion and accumulation of voluminous and regionally extensive epiclastic sequences (as proposed by Brown and Spadea, 1999).

3.3 MINE GEOLOGY

3.3.1 Introduction

The Balta Tau deposit is hosted in volcanic sequences that lie stratigraphically beneath the Jarlykapovo Chert, observed capping hillsides to the northeast and west of the mine. A geological plan of the open pit produced in 2001 and corresponding cross-section are shown in Figures 3.11, and 3.12 respectively. Stratigraphically, the lowest rocks exposed in the pit are intensely altered volcanics, which pass conformably up into massive sulphide mineralization. Overlying the massive sulphides is a thin horizon of brecciated lava, passing conformably into thick sequences of fine volcaniclastic material. In the East of the pit a major fault (in this study named the "Eastern Fault") terminates ore bearing sequences, juxtaposing coherent and brecciated lavas (the "Eastern Volcanics") against footwall to hanging-wall sequences. These units are described in the following sections.

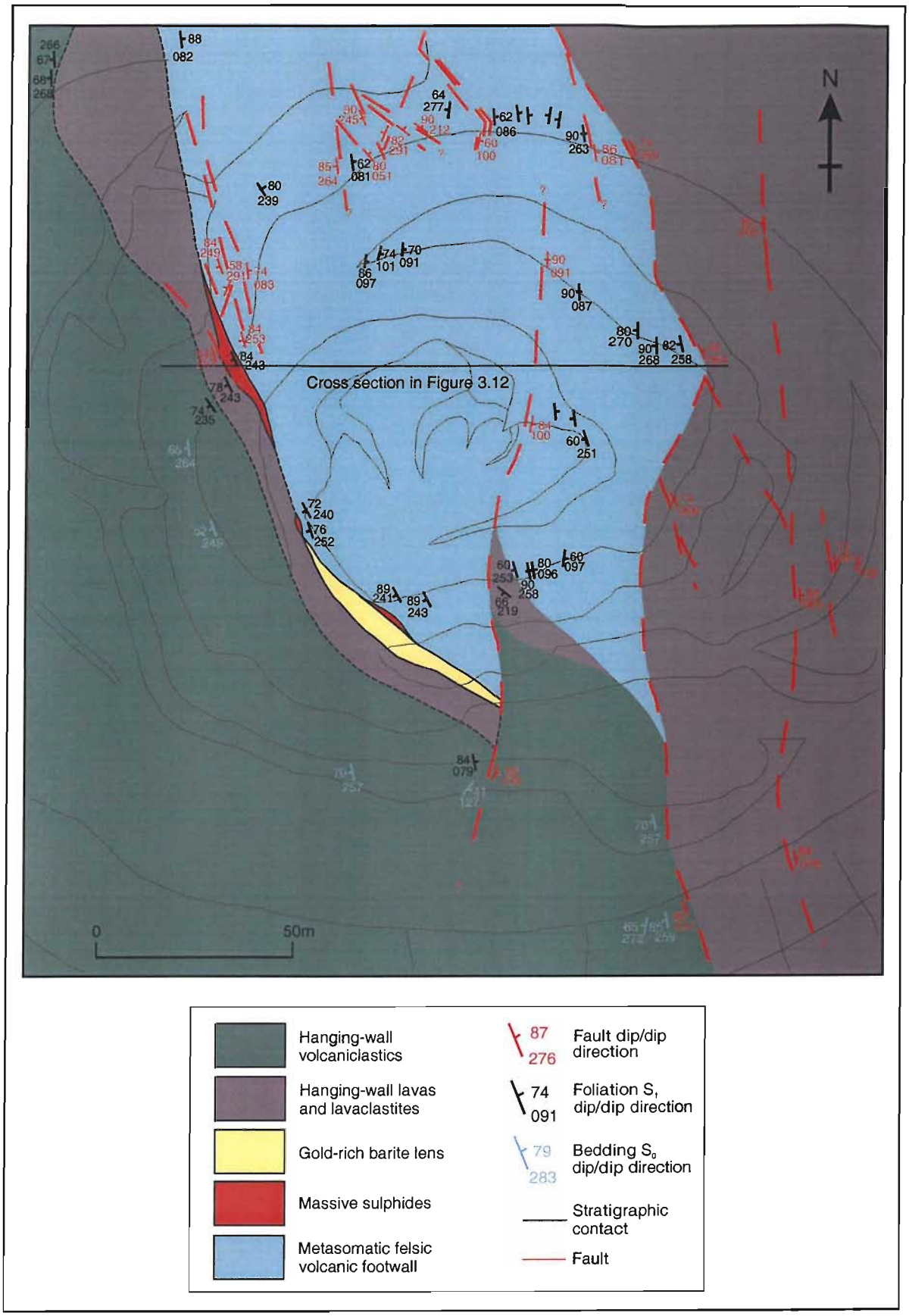

Figure 3.11. Geological plan of the Balta Tau open pit mine.

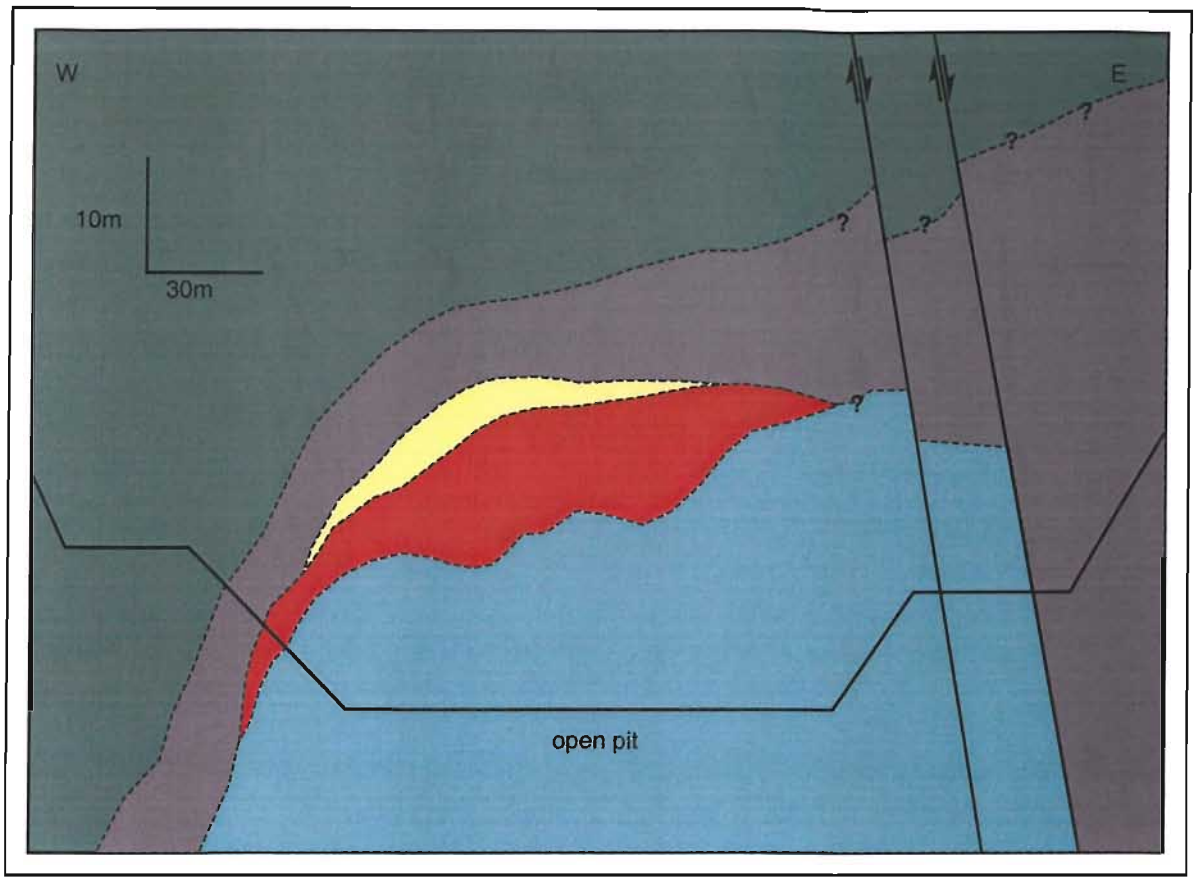

Figure 3.12. Cross section of the Balta Tau deposit. (for legend see Figure 3.11).

3.3.2 Footwall Volcanics

Volcanic rocks beneath the massive sulphides are intensely altered to quartz-chlorite-(pyrite-sericite) and quartz phenocrysts are the only remaining primary volcanic phase (e.g. Figure 3.13b). These altered volcanics are typically pale to dark green resulting from variable proportions of quartz and chlorite and locally a pale grey in sericite-rich areas. Quartz phenocrysts are ubiquitous with <1% to 5% abundance, forming crystals <1mm to 8mm which are commonly rounded and fractured with matrix filled embayments, and sometimes angular and fragmented. Euhedral morphologies of altered feldspar and possibly mafic phenocrysts are preserved by alteration assemblages such as coarse quartz (Figures 3.13d, e), fine grained chlorite(-pyrite) (Figure 3.13g), or more rarely sericite-quartz (Figure 3.13f). These phenocrysts are typically 0.5 to 3mm in size, with an average abundance of 10%. Fine grained euhedral rutile and pyrite replace a cubic mineral which was most likely primary magnetite. Primary clastic textures are preserved by variations in the grain size of alteration minerals (Figure 3.13c). Abundant breccia-like textures are defined by irregular areas of chlorite enclosed in a more siliceous matrix (Figure 3.13a), which probably represent primary volcanic breccias but may also have developed due to variable fracture controlled alteration of coherent volcanics. The footwall unit hosts extensive disseminated and vein hosted sulphide mineralization which replaces the volcanic rocks (Chapter 4, Section 4.2.2).

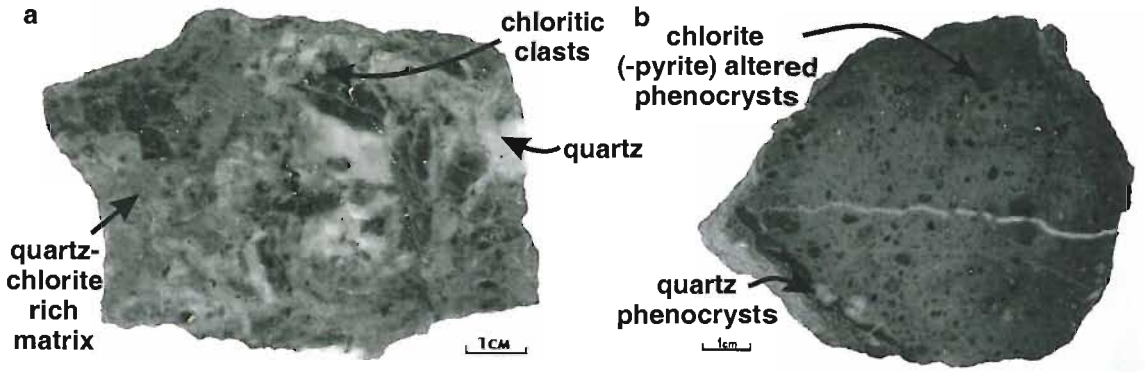

a. Variable alteration with dark green chlorite(-pyrite) areas enclosed in paler green fine grained quartz -chlorite and white quartz-rich zones. This may reflect variable alteration of clasts and matrix in a volcanic breccia, or be the result of brecciation during alteration. Sample 00BT01.

b. Large, uniformly altered volcanic breccia clast with quartz phenocrysts preserved and feldspar (and mafic?) phenocrysts completely altered to chlorite(-pyrite). The enclosing matrix is completely altered to very fine grained quartz-chlorite. Sample 02BT09.

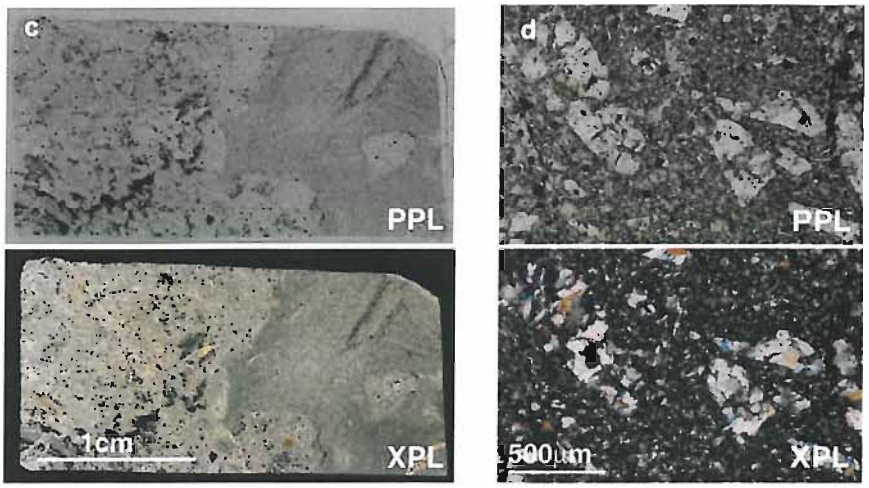

c. Volcani-clastic texture defined by coarse (left) and fine (right) areas of quartz and chlorite. Sample 00BT02.

d. Quartz replacing ?feldspar phenocrysts enclosed in a fine quartz-chlorite matrix. Sample 00BT12.

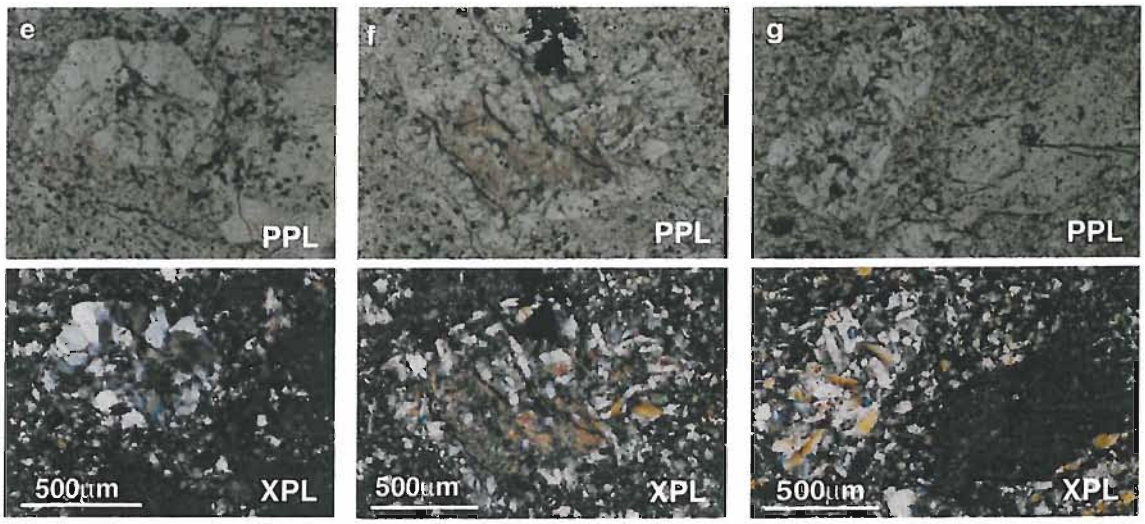

e, f and g. Euhedral morphologies of ?feldspar phenocrysts replaced by (e) quartz, (f) quartz-sericite-pyrite, and (g) quartz and chlorite-pyrite. Sample 00BT14.

Figure 3.13. Footwall volcanics of the Balta Tau deposit.

The primary composition of the footwall volcanics is difficult to estimate given the extent of alteration, however the abundance of quartz phenocrysts suggests a felsic lithology. Relict clastic textures and fragmented phenocrysts suggest this unit to have comprised or contained coarse volcaniclastic horizons.

3.3.3 Massive sulphides

The massive sulphide orebody forms a conformable lens. During visits in this study the majority of massive sulphide ore had been mined out leaving a 2m thick marginal zone of the orebody exposed. These marginal massive sulphides form a narrow, steeply dipping zone at the western end of the orebody. The footwall contact is gradational (Figure 3.14a), with the proportion of sulphide minerals in the footwall increasing dramatically within a few metres of massive ores, reaching over 50%. By contrast, the hanging-wall contact is sharp and deformed, with intense shearing of the immediate hanging-wall unit (Figure 3.14b).

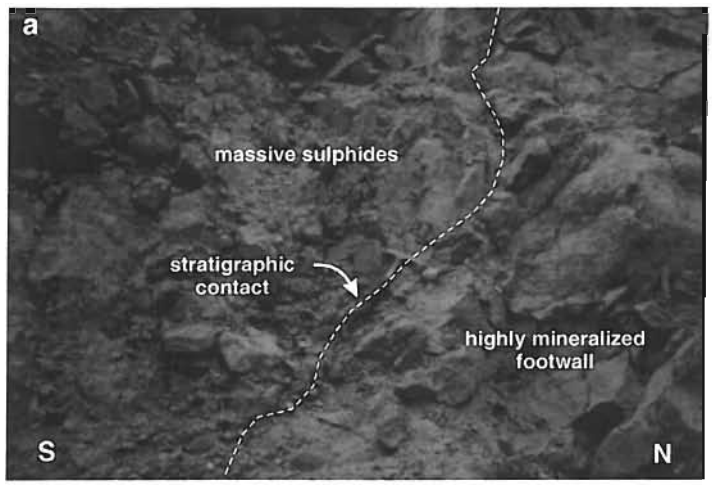

a. Stratigraphic contact between the footwall and the massive sulphide lens. The proportion of sulphides in the footwall gradually increases towards the massive ores and reaches over 50% sulphides, making the actual contact hard to define.

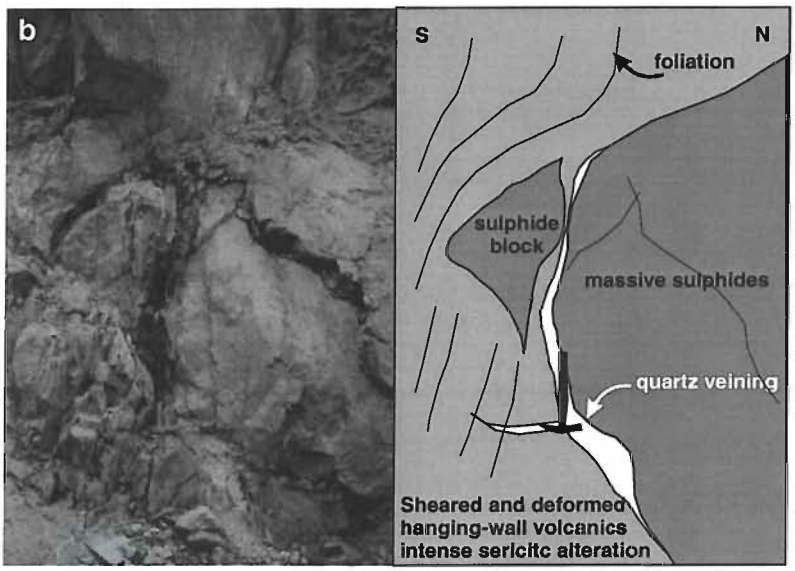

b. Hanging-wall contact of the massive sulphides. The contact is deformed and undulating and the hanging-wall volcanics are foliated with intense alteration to sericite.

Figure 3.14. Footwall and hanging-wall contacts of the massive sulphide orebody at Balta Tau.

Earlier mapping and core logging by Seravkin et al. and Sitnov et al. (unpublished) depict an approximately flat lying lens-like body with smooth hanging-wall and irregular footwall contacts, measuring approximately 100m East-West, 50m North-South and averaging 40m in thickness (Seravkin, pers. comm.). These dimensions define a massive sulphide orebody of about 1.1 million tons (using an average density of 4.5g/cm^3), approximately one third of the economical ore at Balta Tau. This is consistent with the high proportion of economic sulphides being hosted in the footwall (Maslennikov, pers comm.).

3.3.4 Immediate Hanging-wall

The immediate hanging-wall comprises quartz-phyric volcanics with a thickness of less than 10m thick in the South of the pit increasing to over 30m thick in the North (Figure 3.11). Intense sericitic alteration immediately above massive sulphide ores decreases in intensity with increasing lateral and vertical distance from the massive sulphide horizon.

The least altered samples contain euhedral morphologies of chloritized ?mafic phenocrysts and pale yellowish green sericitized feldspar phenocrysts (Figure 3.15b) as well as quartz phenocrysts (Figure 3.15a). The groundmass is variably altered to fine sericite-chlorite giving a greenish grey colour, and hematite giving a deep purple colour (Figure 3.15a). Primary textures are well preserved and dominated by coarse angular monomict breccias (Figure 3.15b) with clasts showing zoning in alteration from the cores to margins, which are characteristic features of hyaloclastites or reworked hyaloclastites and indicate a probable submarine eruptive environment (McPhie et al., 1993). Phenocryst proportions in the least altered hanging-wall are consistent with a dacitic composition. Comparison of lithological characteristics such as clastic textures and relict phenocrysts suggests that the immediate hanging-wall may be the same volcanic unit as the footwall sequences, although this can not be established with certainty due to the intense alteration of the footwall. The hanging-wall is also very similar to the Eastern volcanic unit (Section 3.3.6), suggesting that these may also be the same unit and correlate stratigraphically.

Clastic and porphyritic textures become increasingly stretched, deformed and finally obliterated with increasing alteration and shearing towards the massive sulphide orebody (Figure 3.16 a to c). The most intensely altered samples from immediately above massive sulphide ores comprise almost entirely sericite (Figure 3.16c, d) with spotty titanite (Figure 3.17e), bright green Cr-mica (fuchsite, Figure 3.16b) and traces of zeolite (Figure 3.16d). Quartz phenocrysts, the only remaining primary volcanic feature, are commonly fractured and fragmented (Figure 3.16e) with some fragments isolated and others in jig-saw fit clusters. Fracturing probably occurred during deformation rather than primary volcanic processes, since the fragmented quartz is mainly

restricted to sericitized and sheared zones. The intense sericitization of the immediate hanging-wall is spatially related to massive sulphide mineralization (Chapter 4, Section 4.7).

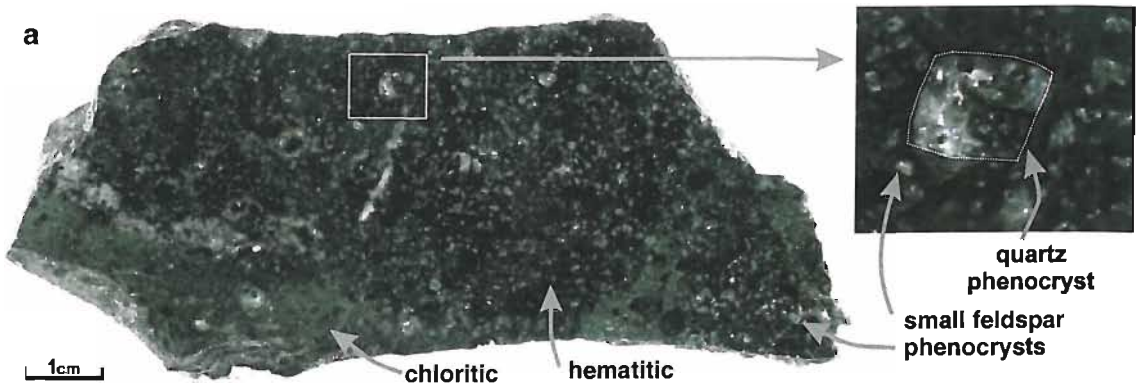

a. Feldspar- quartz- phyric lava with variable chloritic (green) and hematitic (red) alteration. Sample 02BT13.

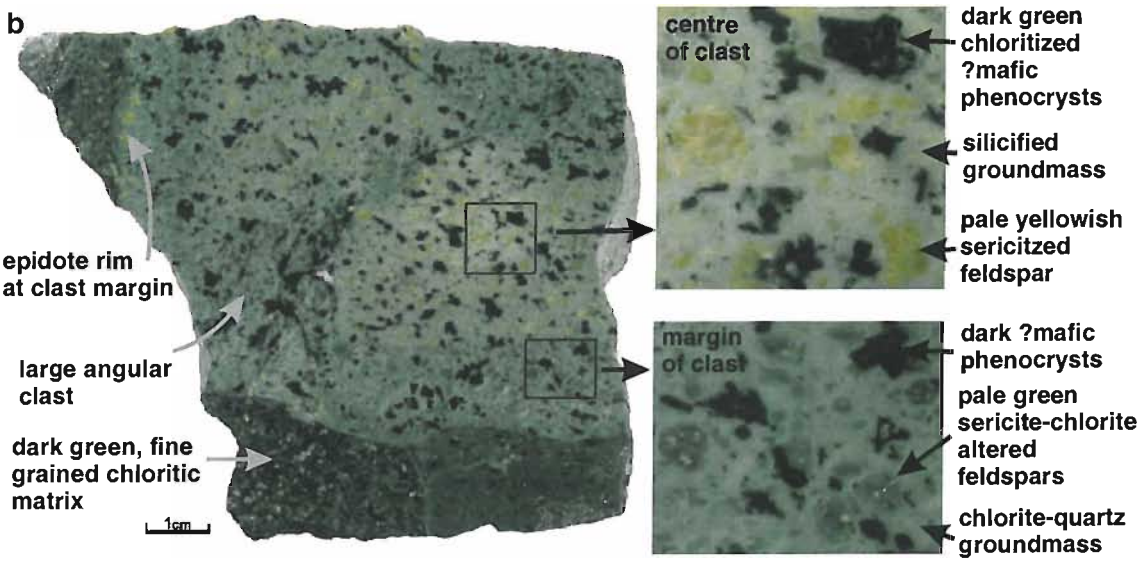

b. Large angular clast from a coarse volcanic breccia. Clast contains numerous, dark green, chloritized ?mafic phenocrysts together with pale altered feldspar phenocrysts. Alteration within the clast is zoned, with yellowish sericitized feldspar and silicified groundmass in the centre grading to more chlorite-rich feldspars and groundmass at the margins; alteration of ?mafic phases is the same throughout the clast. The matrix is dark green, fine grained and chloritic, and contains smaller phenocrysts in low abundance. Sample 02BT02.

Figure 3.15. Volcanic facies of the immediate hanging-wall at Balta Tau.

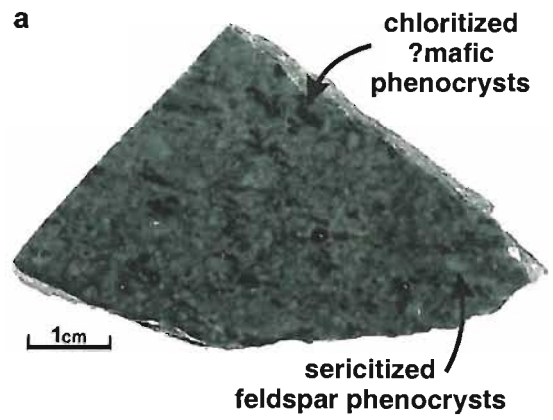

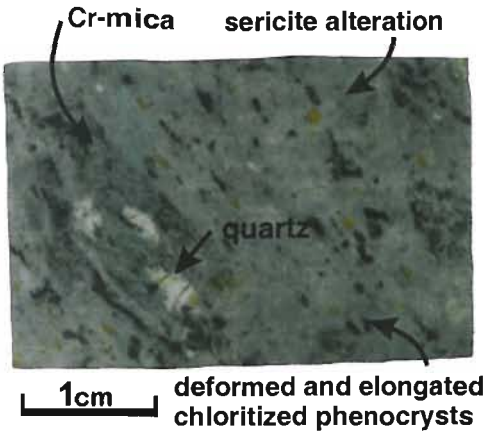

a, b & c. Progressive sericitic alteration of felsic hanging-wall volcanics: (a) hanging-wall lateral to the orebody with weak sericitization and good preservation of phenocryst morphologies (sample 01BT022). (b) above the main sulphide lens, intense sericitic alteration with abundant Cr-mica, well developed foliation and phenocryst morphologies weakly preserved (sample 01BT019). (c) from immediately above the orebody, very intense sericitic alteration with no primary features preserved except fractured quartz phenocrysts (sample 908).

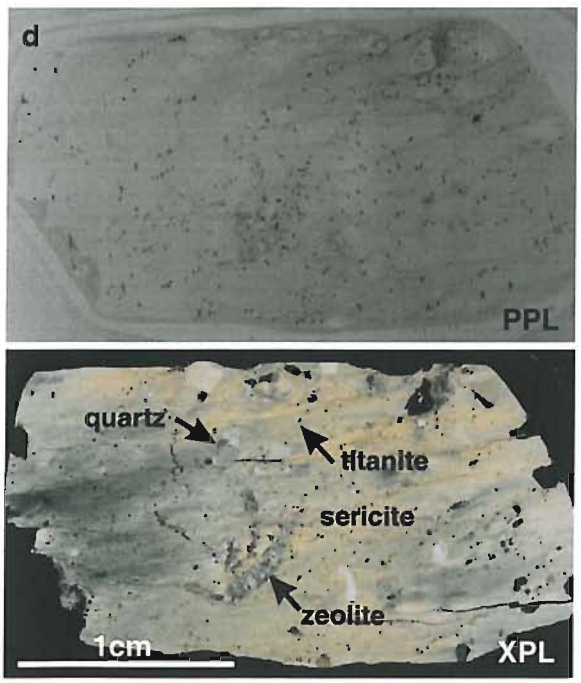

d. Sample 908 (shown in (c)). Complete alteration to fine grained, foliated sericite, with whole and fragmented quartz phenocrysts, coarse zeolite crystals and spotty titanite.

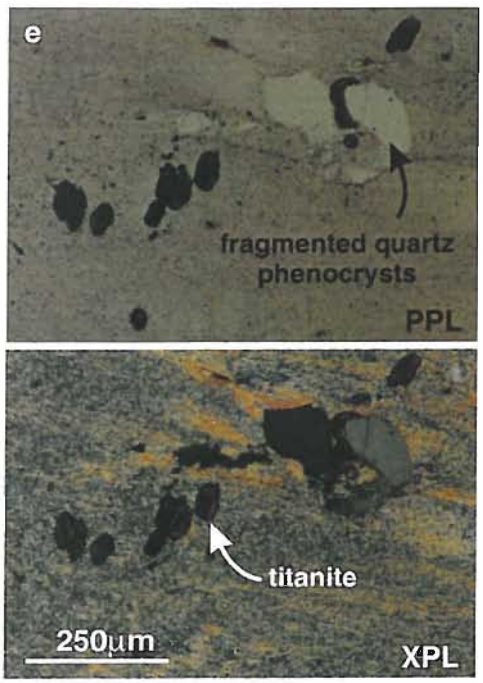

e. Fragments of quartz phenocrysts and subhedral titanite enclosed in fine grained sericite. The titanite appears to be elongated at approximately right-angles to foliation. Sample 908.

Figure 3.16. Intense sericitic alteration of the immediate hanging-wall volcanics at Balta Tau.

3.3.5 Hanging-wall volcaniclastics

The immediate hanging-wall unit passes conformably into thick sequences of volcaniclastic material which vary on a meter scale from massive to mm/cm scale graded bedding (Figure 3.17a and b). Graded bedding is often non-linear and disturbed (Figure 3.18b), but cross-bedding and cross-laminations have not been observed. Fine grained horizons are dark green and consist of a very fine grained chlorite-sericite matrix containing scarce angular fragments of feldspar phenocrysts and lithic clasts (Figure 3.17c). Coarser sequences in graded and massive beds are mostly dark green and vary considerably in composition. Some sequences are dominated by abundant feldspar crystal fragments and feldspar-(?mafic-)phyric lithic fragments 1-10mm which are poorly sorted and have irregular to feathery margins (Figure 3.17c); these are typical of resedimented hyaloclasts and possibly pyroclasts with minimal transportation. Other horizons contain a greater proportion of fine grained ashy material enclosing irregular areas of chlorite 0.1 to 0.5mm which are typical of altered platey glass shards (Figure 3.18e), and are probably pyroclastic in origin. The textures of clasts suggest resedimentation of hyaloclastic and pyroclastic deposits with minimal transportation (e.g. McPhie et al., 1993).

Alteration is moderate to intense, with sericite-chlorite-actinolite replacing feldspars, chlorite-epidote replacing ?mafic phenocrysts, chlorite replacing glass shards and patchy actinolite-chlorite-titanite alteration of lithic clasts and interstitial matrix. Coarser beds in graded sequences sometimes have intense spotty epidote alteration resulting in distinctive bright green horizons (Figure 3.17b). Fine grained horizons are dark green reflecting intense chloritic alteration, and sometimes contain thin beds that are dark purple due to fine grained pervasive hematite alteration (Figure 3.17a, d).

a. Massive and graded volcaniclastic sequences. Most are dark green with chloritic alteration; some beds are defined by a purple colour due to local hematitic alteration. Bench is approximately 4m high.

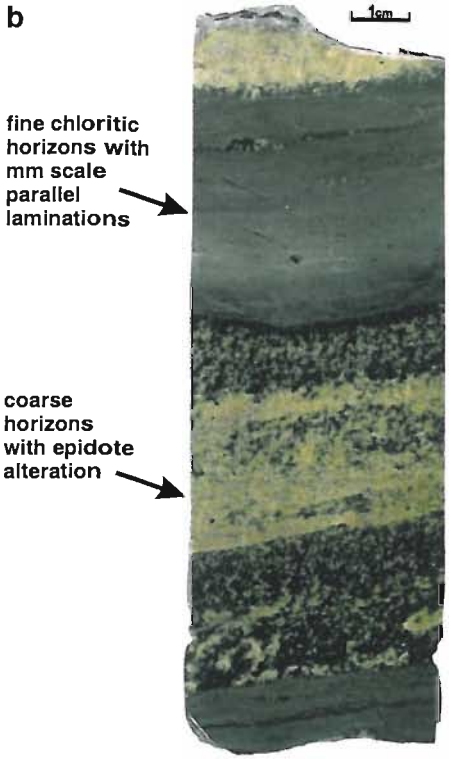

b. Graded sequences containing fine, dark green chloritic horizons and coarser, pale green horizons with spotty epidote alteration. Sample 01BT039.

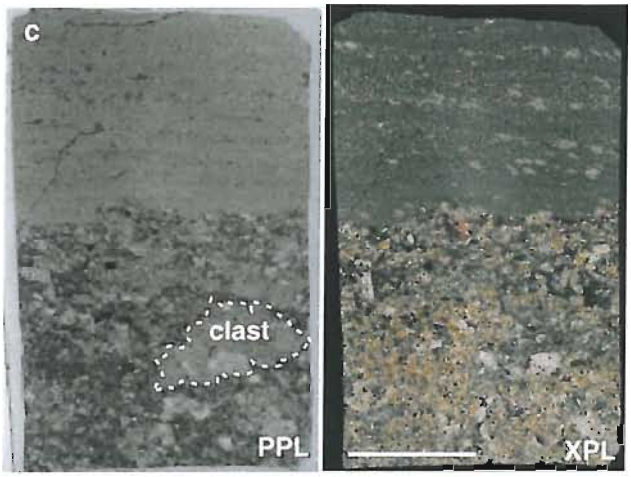

c. Sharp contact between fine chloritic material and a coarse, crystal-rich horizon containing porphyritic lithic clasts and intense epidote alteration Sample 00BT10.

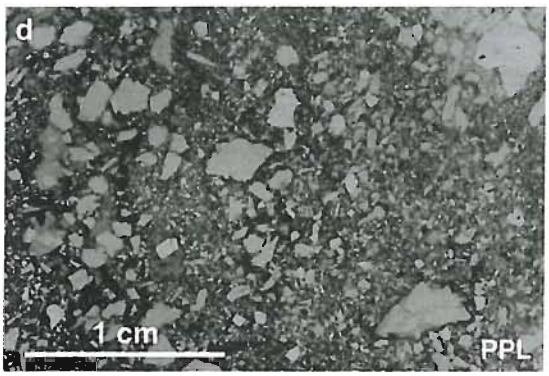

d. Coarse horizon with abundant, poorly sorted angular to irregular crystal fragments and less abundant irregular porphyritic lithic clasts. The texture is enhanced by a fine grained, pervasive hematite alteration in the matrix between clasts. Sample 00BT21.

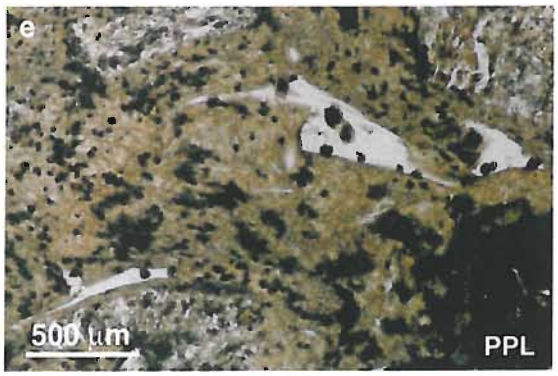

e. Zones of chlorite (colourless) replacing platey glass shards that wrap around altered feldspar phenocrysts, all enclosed in a fine grained, altered matrix. Sample 00BT10.

Figure 3.17. Hanging-wall volcaniclastic sequences.

3.3.6 Eastern volcanic unit

To the East of the Eastern Fault are undeformed lavas and breccias. Coherent lavas are massive and devoid of internal structures such as pillows or columnar jointing. Breccias are angular, poorly sorted and monomict, with jigsaw fit textures visible on a large and small scale suggesting a hyaloclastic origin (Figure 3.18a and b).

All sequences are feldspar±quartz phyric, containing 10 to 20% feldspar phenocrysts 0.5 to 2mm in size, with lamellae twinning and concentric zoning preserved in the least altered crystals (Figure 3.19b). Where altered, feldspar is partially to completely replaced by sericite±carbonate±hematite, and more rarely chlorite±carbonate±hematite or epidote±carbonate ±hematite (Figure 3.19c, d). Quartz phenocrysts are present in most samples in low abundance (<1 to 3%) and vary in size from 0.2 to 1.5mm. Smaller crystals are highly rounded with corroded margins, whereas larger crystals are more euhedral and some are fractured and/or embayed (Figure 3.19a). Some samples contain phenocrysts that are completely replaced by chlorite-epidote-titanite which may have been a mafic phase. None of the exposed volcanics are amygdaloidal.

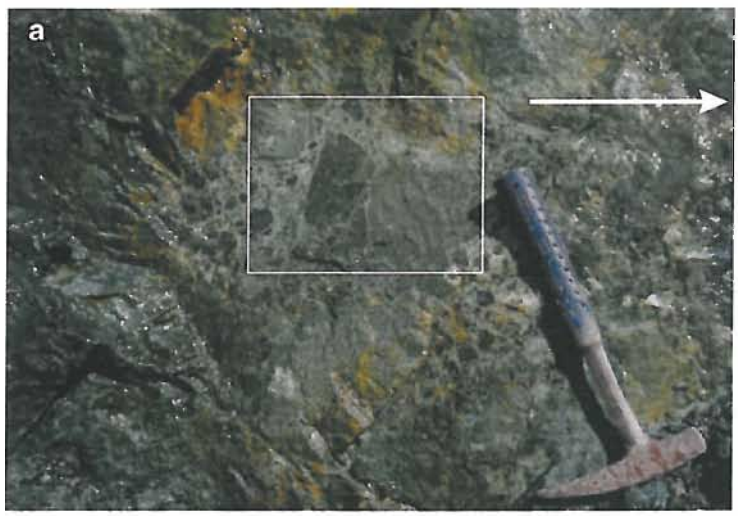

a. Monomict breccia with clasts showing a jigsaw fit texture enclosed in a matrix containing small clasts of the same material.

b. Hyaloclastic breccia. Jigsaw fit texture with monomict, porphyritic, angular to curvi-planar clasts with chloritic alteration. The enclosing matrix is bright green and epidote rich, and contains mm sized clasts of the same material. Sample 01BT210..

Figure 3.18. Hyaloclastic textures in the Eastern volcanic hanging-wall unit at Balta Tau.

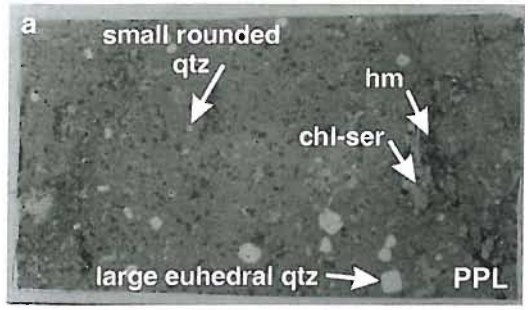

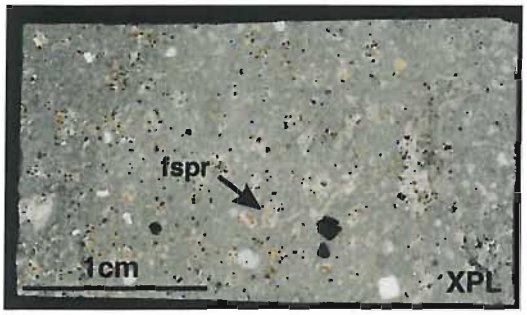

a. Euhedral to rounded quartz phenocrysts and sericitized feldspar phenocrysts enclosed in a fine grained matrix with patchy hematite and chlorite-sericite alteration. Sample 00BT19.

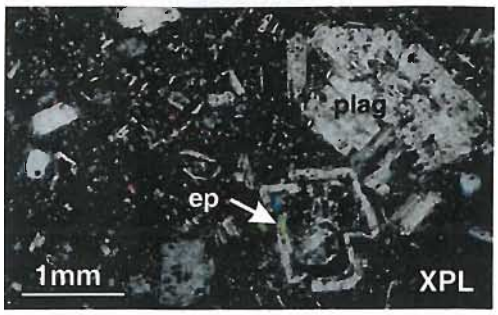

b. Concentrically zoned plagioclase phenocrysts, with epidote replacing selected zones. Groundmass comprises fine plagioclase (also zoned) enclosed in opaque glass. Sample 01BT183.

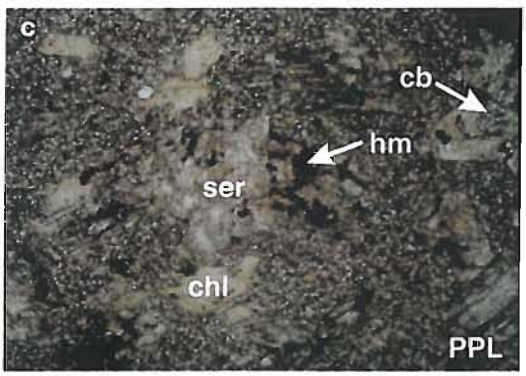

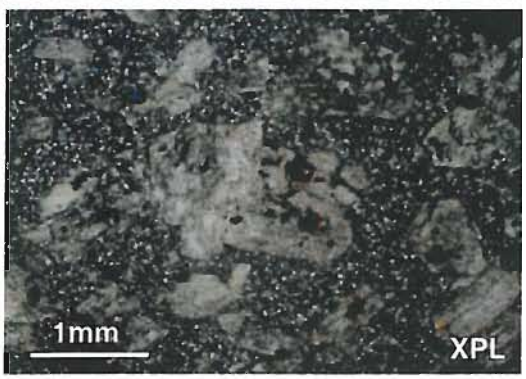

c. Feldspar phenocrysts altered to sericite(-hematite) and chlorite(-carbonate), enclosed in a fine grained felsic groundmass with fine sericite-chlorite- hematite alteration. Sample 01BT188.

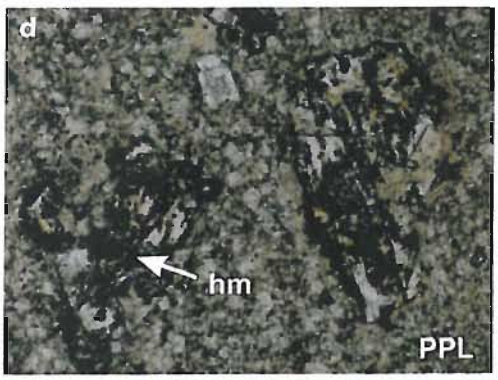

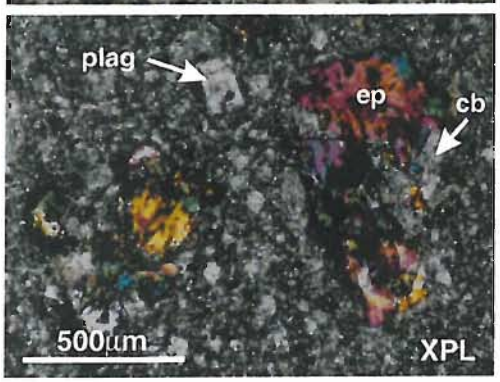

d. Epidote(-carbonate-hematite) replacing feldspar phenocrysts, with a fine felsic groundmass containing small euhedral sericitized feldspars. Sample 00BT19.

Figure 3.19. Lithologies of the Eastern volcanic hanging-wall at Balta Tau.

The groundmass generally comprises a fine grained, equigranular felsic mosaic of quartz and/or feldspar (Figure 3.19d), or more rarely randomly orientated feldspar laths enclosed in an altered glassy matrix (e.g. Figure 3.19b). Alteration is moderate to intense with development of fine grained chlorite-sericite and/or hematite (Figure 3.19c), and primary textures such as feldspar laths are seldom well preserved. Variations in alteration assemblages are reflected in the colour of volcanics, which alternates between dark green (chlorite rich), paler green (weakly altered and sericitic), and dark purple (hematitic) on a 10's of meters scale (Figure 3.20a) to a mm to cm scale (Figure 3.19a). Where volcanics are brecciated, the matrix between clasts comprises fragmented quartz phenocrysts and irregular patches of fine material that is similar to the clast groundmass, cemented by coarse felty chlorite, sericite, hematite and epidote.

Phenocryst abundances are consistent with a dacitic composition, and this unit is petrographically very similar to the immediate hanging-wall volcanics (Section 3.3.4). The two distinct populations of quartz phenocrysts represent two separate phases of quartz crystallization. The smaller, rounded phenocrysts are probably an earlier phase that suffered an episode of resorbtion before the second, larger euhedral population crystallized. These textures indicate fluctuations in melt composition during crystallization, supported by oscillatory zoning in well preserved plagioclase crystals. The well preserved hyaloclastites confirm a likely seafloor eruptive setting and alteration is consistent with interaction of volcanics with seawater, with abundant hematite indicating locally oxidizing conditions.

3.3.7 Structures and deformation

Bedding in mine sequences is only present in the hanging-wall volcaniclastics where it generally dips moderately to steeply West or Southwest (Figure 3.17a). This dip is similar in direction but steeper than bedding in the Jarlykapovo and Ulutau Formations in the East limb of the synform to the West of Balta Tau (Section 3.2.5, Figure 3.1). A weak to moderate pervasive foliation penetrates both footwall and hanging-wall sequences but is not apparent in the Eastern volcanics, and is approximately bedding-parallel with a general North-South strike and steep to vertical dip fluctuating between East and West. This foliation is consistent with the dip and direction of regional foliation in the Irendyk Ridge (Figure 3.1). In the vicinity of the ore horizon, the footwall and in particular hanging-wall rocks are foliated in a shear zone that is approximately parallel to bedding.

The mine sequences are cut by numerous faults which are particularly evident in the footwall (Figure 3.11). The most dominant structure is a major, near-vertical fault (the "Eastern Fault") trending North-South across the eastern side of the pit (Figures 3.20, 3.21). This fault has a 10 to 20cm wide clayey melange zone, and juxtaposes lavas to the East of the fault ("Eastern

volcanics") against footwall to hanging-wall ore bearing sequences West of the fault. In the adjacent footwall rocks a wide zone of deformation associated with the Eastern Fault contains cm to m sized rounded blocks of competent, siliceous footwall enclosed in a deformed and foliated chloritic/sericitic matrix. This deformational zone continues into the immediate hanging-wall in the South of the pit, where cm-m sized blocks of both footwall and massive sulphide are enclosed in highly sericitized and chloritized, foliated hanging-wall (Figure 3.20b, c). A second, near-vertical normal fault approximately parallel to and West of the Eastern Fault displaces ore bearing sequences by approximately 40m (Figure 3.11).

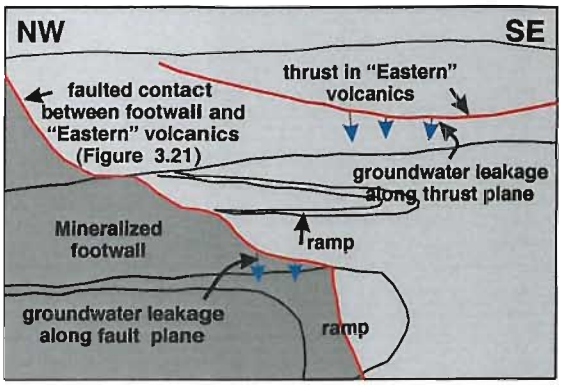

a. General view of the open pit showing the position of the "Eastern Fault" and thrust in the Eastern volcainc unit.

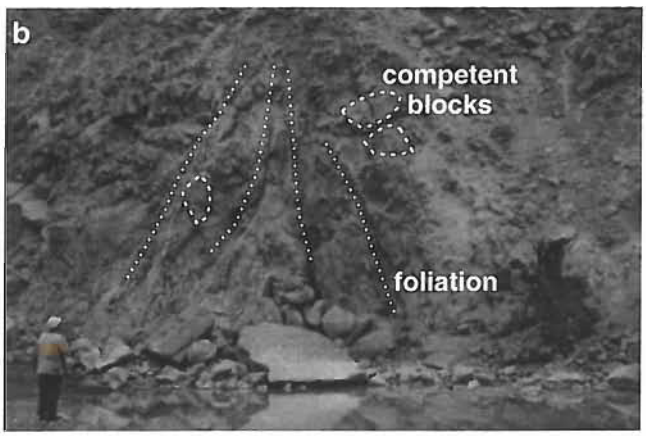

b. General view of the shear zone adjacent to the Eastern fault, with altered and foliated hanging-wall rocks containing rounded blocks of competent siliceous footwall and massive sulphides.

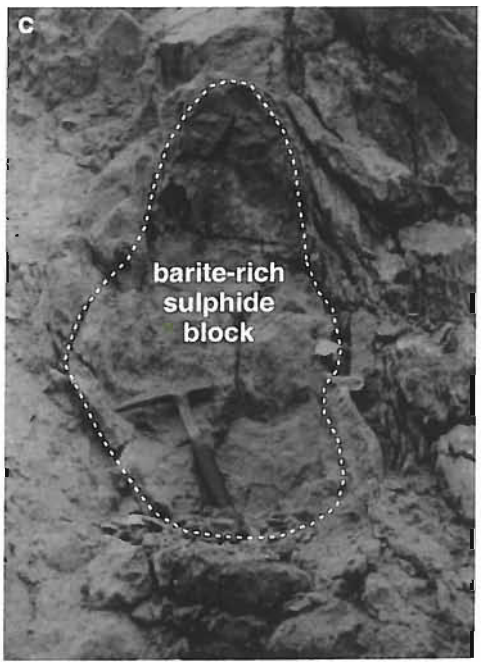

c. Large barite-sulphide block enclosed in sheared hanging-wall rocks.

Figure 3.20. General view of the Eastern Fault and sulphide blocks incorporated in the adjacent melange zone.

Comparison of lithological characteristics suggests the Eastern volcanics may correlate with the those of the immediate hanging-wall. A much greater thickness of this unit is exposed to the East of the fault than in the immediate hanging-wall, which may be partly due to a thrust cutting the Eastern volcanics and carrying the same unit in its hanging-wall. Access to the exposed thrust was not possible precluding structural measurements, however the position of the fault plane was clearly defined by groundwater leakage (Figure 3.20a).

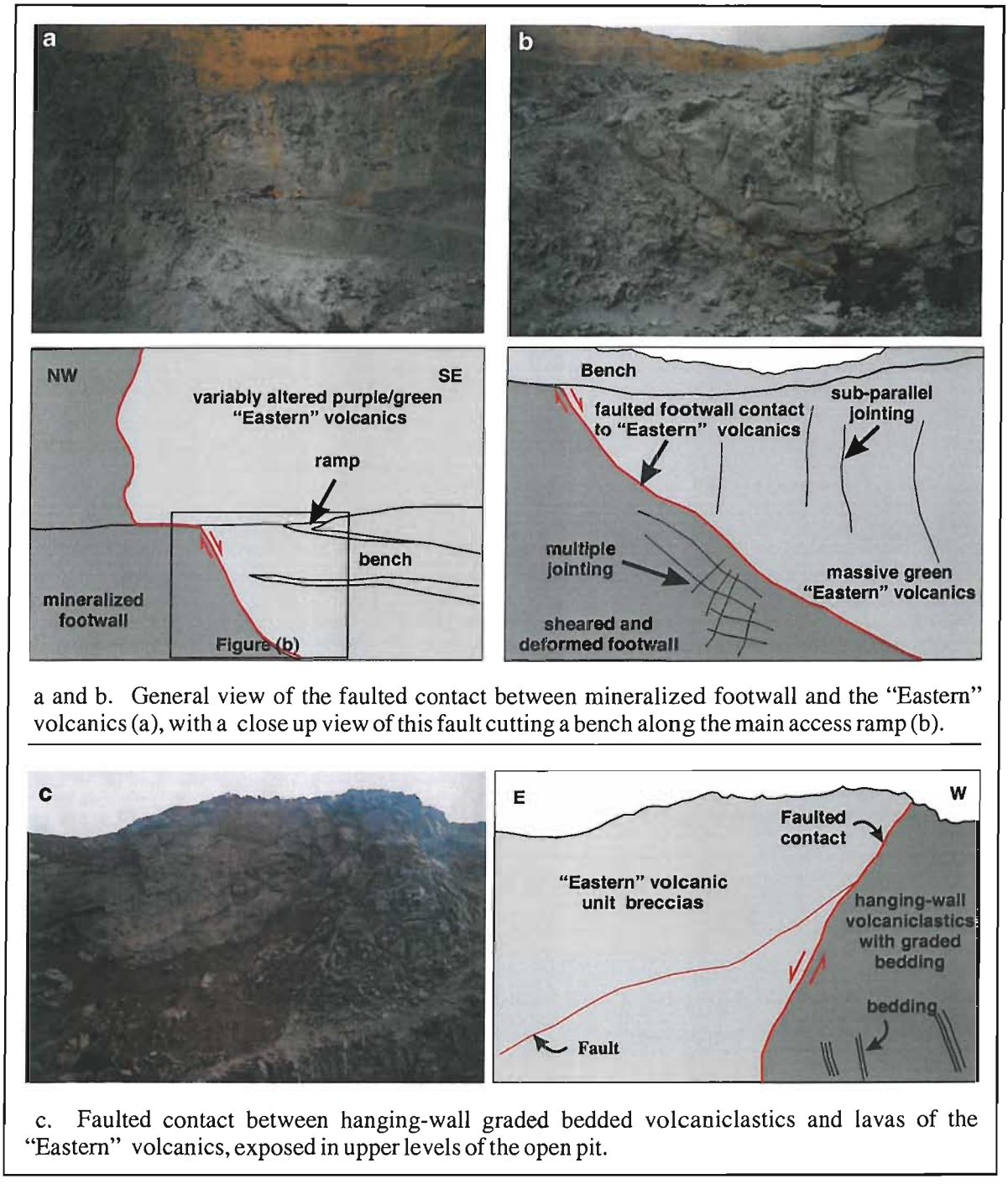

a and b. General view of the faulted contact between mineralized footwall and the "Eastern" volcanics (a), with a close up view of this fault cutting a bench along the main access ramp (b).

c. Faulted contact between hanging-wall graded bedded volcaniclastics and lavas of the "Eastern" volcanics, exposed in upper levels of the open pit.

Figure 3.21. Contacts between the Eastern Fault and footwall to hanging-wall ore sequences.

3.3.8 Discussion

Comparison of Balta Tau mine sequences with regional formations

In spite of the intense alteration in the footwall and hanging-wall at Balta Tau, relict primary volcanic features can be used to compare these sequences with regional facies. The footwall and immediate hanging-wall units appear to have similar lithologies to the less altered Eastern volcanics, including quartz and feldspar phenocryst abundance and clastic textures which can often be identified as hyaloclastic. This suggests that the footwall, immediate hanging-wall and Eastern volcanics may form part of the same lithological unit.

Feldspar-quartz-phyric volcanics comparable to the mine sequences can be found locally in both the Irendyk Formation (e.g. samples 010823/10 and 010823/11) and the Baimak-Buribai Formation (e.g. 010826/06). The possible presence of mafic phenocrysts in the Balta Tau sequences, suggested by Cr-mica and highly chloritized phenocrysts in the hanging-wall unit, is more comparable with the Irendyk where quartz and pyroxene phenocrysts coexist; mafic phenocrysts are generally absent from the Baimak-Buribai Formation. The abundant coarse volcanic breccias and hyaloclastites are also typical of the Irendyk Formation.

The hanging-wall graded volcaniclastic sequences probably correlate stratigraphically with similar material exposed on a small hillside to the East of the mine, which, although originally mapped as the Ulutau Formation by the Russian Geological Survey, are interpreted to be part of the Irendyk Formation based on observations from this study (Section 3.4.9).

Therefore lithological characteristics of the immediate footwall, immediate hanging-wall, hanging-wall volcaniclastic sequences and the Eastern volcanics are all comparable with those of the Irendyk Formation, suggesting that the Balta Tau deposit is hosted entirely within Irendyk volcanic sequences.

3.4 GEOCHEMISTRY OF VOLCANIC SUITES

3.4.1 Introduction and methodology

Geochemical data has been obtained from representative samples of regional and mine sequences with the following aims:

- Establish the mobility of major and trace elements during alteration.
- Identify lithologies geochemically.
- Use immobile elements to discriminate between volcanic suites, and interpret tectonic settings and magmatic sources.
- Identify host rocks to Balta Tau based on geochemical comparison with locally exposed formations.

Whole rock analyses of major and trace elements were carried out on 21 samples from volcanics exposed locally in the Balta Tau area and 9 samples from the footwall and hanging-wall sequences in the open pit. As far as possible, homogeneous samples were selected from a variety of lithologies within each formation with variable degrees of alteration and broad spatial diversity. Petrographical descriptions of samples analysed are given in Appendix A2.

Samples were analysed for major elements by XRF (beads), and trace elements using a combination of XRF (pellets) and ICP-MS. Details of sample preparation and analytical procedures are given in Appendix A3, together with a complete data listing.

3.4.2 Alteration and element mobility

Volcanic suites of the Balta Tau region have been subject to low grade seafloor hydrothermal alteration, and sequences immediately above and below the Balta Tau ore horizon have undergone intense hydrothermal alteration. Under these conditions most major elements are highly mobile and can provide information regarding hydrothermal fluid chemistry and fluid-rock interaction, but are unreliable for the identification of igneous rock types and petrogenetic trends. To investigate these primary characteristics it is more suitable to use elements that can be established as immobile during alteration, which commonly include Al, Ti, Zr, Y, Nb (Cann, 1970; Maclean & Kanidiotis, 1987), and HREE, Ta, Hf, Cr, Th, and Ga during low grade metamorphism (Pearce, 1996). However, element mobility is influenced by a number of factors including hydrothermal fluid chemistry, fluid-rock ratios and rock composition, and in some cases elements that are normally considered to be immobile may be significantly leached or enriched (e.g. Finlow-Bates & Sumpfl, 1981; Rubin et al., 1993). It is therefore important to identify elements that were immobile in the specific rock types and alteration of the Balta Tau area in order to reliably discriminate rock types and tectonic settings.

Isocon diagrams

The isocon method of Grant (1986) provides a means of investigating the effects of alteration on element concentrations and has been widely applied to the study of altered volcanic rocks. The isocon diagram is designed to distinguish between and quantify (i) the dilution or concentration of elements due to alteration related volume changes, and (ii) actual loss or gain of elements due to mobile behaviour, using sample pairs that share the same petrochemistry but have different degrees of alteration. Isocon diagrams have been constructed for the regional volcanic rocks and Balta Tau mine sequences (see Appendix A4 for details of method, sample selection and isocon diagrams).

For the mine sequences, the major element changes indicated by the isocon plots are consistent with the observed alteration assemblages, with for example large increases in Mg and Si in the footwall and large increases in K in the hanging-wall (Appendix A4). For trace elements, however, results are generally not plausible. For example, in the footwall samples HREE's are suggested to show both a significant gain (e.g. Yb) and a significant loss (e.g. Lu), which is unrealistic since this group of elements would be expected to behave in a similar way during alteration. Similarly, results are generally unrealistic for the regional volcanic samples.

Estimates of volume changes during alteration are based on the assumptions that Zr is immobile and had the same initial concentration in the samples of each sample pair, and indicate a large volume increase of around two thirds during footwall alteration, which is consistent with extensive quartz veining observed throughout footwall samples, and a volume reduction of around 10% during intense sericitic alteration of the immediate hanging-wall. Regional samples show variable changes of a 1% decrease in the Baimak-Buribai samples and 8% increase in the Irendyk samples.

The generally implausible results of isocon diagrams in particular in relation to trace element mobility is probably due to primary petrogenetic differences between the sample pairs, since although the samples selected are from the same formation and have similar petrography, they are from different locations (since no single exposure contained the required variation in alteration) and may not have had the same trace element chemistry. This highlights the importance and difficulty of obtaining samples pairs with the same primary geochemistry but a significantly different degree of alteration, which in this case limits the usefulness of the isocon method.

3.4.3 Alteration and petrogenetic trends using Covariation diagrams

Covariation diagrams use the correlation between two elements to investigate and distinguish primary igneous trends and alteration trends, and enable element mobility to be evaluated in a co-magmatic suite of samples without the isocon method prerequisite of using samples with the same

initial trace element concentrations. The least altered samples can be used to define a primary igneous fractionation trend, which for two similarly incompatible elements forms a line with positive gradient passing through the origin, and for a compatible-incompatible element pair forms a line or curve with negative gradient (Figure 3.22). Deviation from the igneous trend due to alteration can result from two processes, (i) dilution/concentration due to a volume change, which results in a linear trend with a positive slope that passes though the origin, and (ii) actual loss/gain of that element which results in a scattering of data parallel to that element axis (Finlow-Bates & Stumpfl, 1981; Maclean & Kranditois, 1987; Maclean, 1990). These trends are summarised in Figure 3.22.

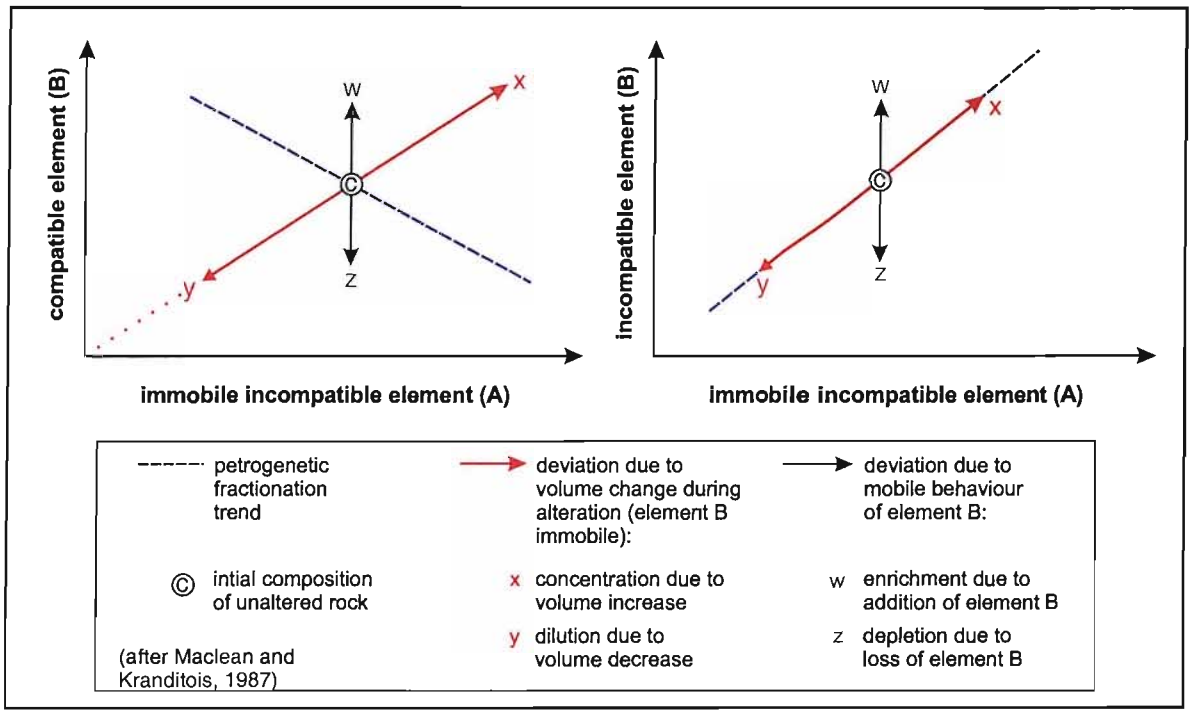

Figure 3.22. Characteristic petrogenetic and alteration trends on covariation diagrams.

The compatible-incompatible element pairs and similarly incompatible element pairs that are investigated in the following sections have been selected based on the degree of compatibility and usefulness of elements for geochemical interpretation as outlined in Pearce et al. (1983) and Pearce (1986).

Covariation diagrams for compatible-incompatible element pairs

Zr has been chosen as the fractionation indicator for these plots, since it is immobile under most conditions (e.g. Maclean & Kranditois, 1987) and highly incompatible (therefore providing well defined fractionation trends). The compatible elements selected are Ti, Al, Ti, Sc and V, all of which are useful for interpreting primary petrogenetic characteristics (Figure 3.23).

For Ti, Al, Sc and V, the less altered samples define clear fractionation trends. The variable slopes of these trends can be explained by differences in the behaviour of each element with respect to Zr. Ti and Zr are similarly incompatible during crystallization of mafic phases, but with increased fractionation Ti becomes highly compatible as magnetite begins to crystallize while Zr remains incompatible, producing a curved fractionation trend. By contrast, Al is highly compatible as soon as feldspars begin to crystallize giving a linear, almost horizontal trend. Sc and V, although moderately incompatible, are significantly more compatible than Zr and therefore give a linear fractionation trend with a negative slope.

For Al, V and Sc, regional samples show relatively minor scattering indicating that these elements were generally immobile during regional alteration. For Ti most data lie close to the fractionation trend, although minor scattering of a few data points suggests that Ti may have been weakly mobile in some samples. All four of these elements distinguish the Irendyk and Ulutau from the Baimak-Buribai Formation, with Baimak-Buribai samples more fractionated. They also divide the Irendyk into two groups, one containing the majority of data with a relatively small degree of fractionation, and three anomalous points (samples 010820/03, 010819/16 and 010826/10) that do not fit the trends very well due to high trace element concentrations, and appear more fractionated on the Al-Zr covariation plot.

The least altered Balta Tau mine sequences are close to the fractionation trends of the "normal" Irendyk samples. The intensely altered Balta Tau footwall and hanging-wall sequences do not fall on the fractionation trend but define an alteration line, indicating that the element concentrations deviate largely due to a volume change during alteration rather than element mobility. The alteration line bisects the fractionation trend close to the position of least altered Balta Tau samples, suggesting the altered hanging-wall and footwall samples originally had a similar composition to the least altered Balta Tau sequences, which are also similar to the Irendyk Formation. Footwall samples have depleted concentrations suggesting dilution from a volume increase, while hanging-wall samples have increased concentrations suggesting concentration from a volume decrease; these are consistent with the volume changes indicated by isocon diagrams (Section 3.4.2).

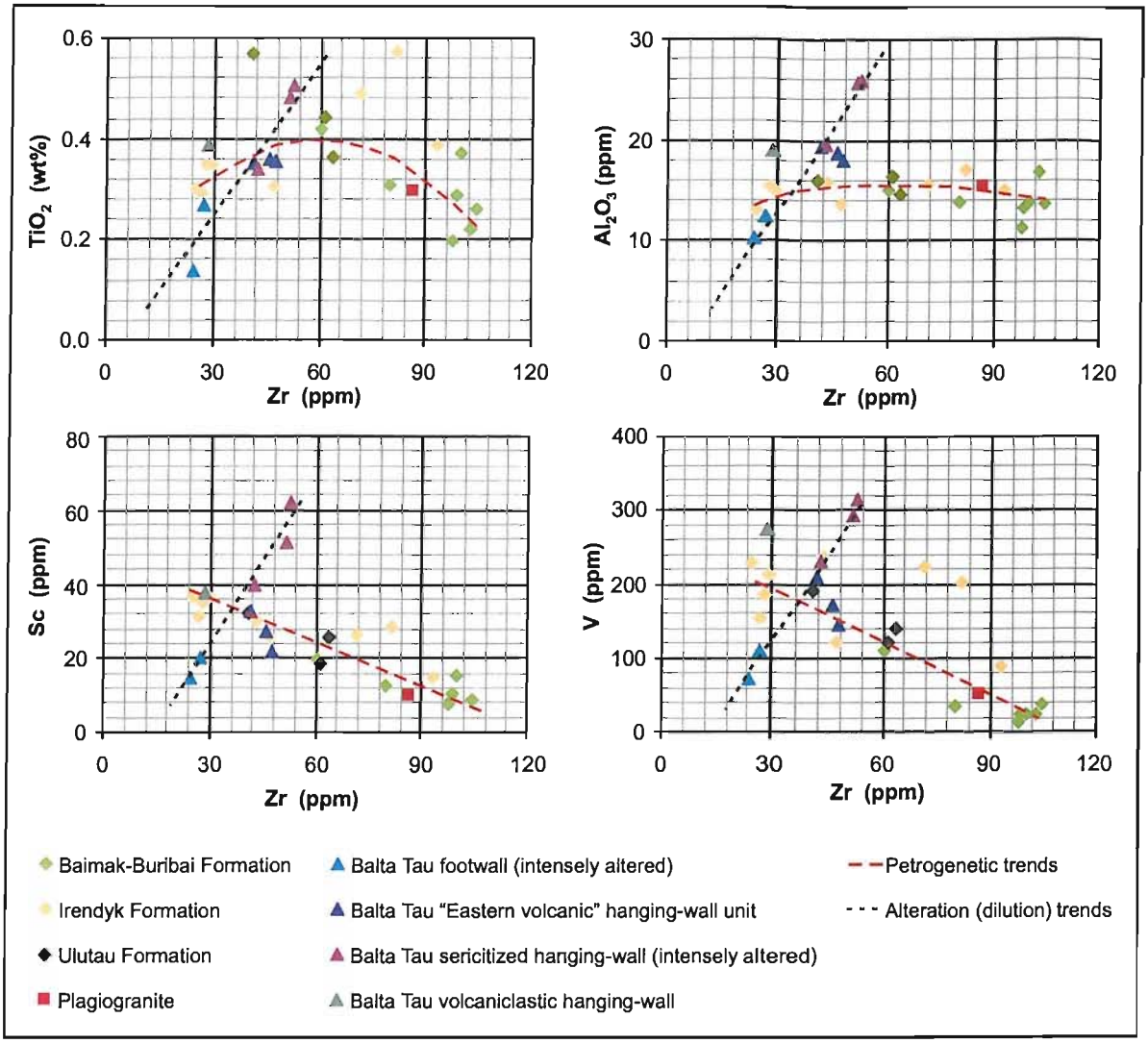

Figure 3.23. Covariation diagrams for compatible-incompatible element pairs.

Covariation diagrams for similarly incompatible element pairs

Covariation plots of two similarly incompatible elements do not easily distinguish between petrogenetic trends and those resulting from volume changes during alteration, since both produce a linear trend with positive gradient that passes through the origin (Figure 3.22). However, they still provide an indication of element mobility since mobile behaviour would cause a deviation from these trends unless both elements were enriched or depleted to the same degree. The imcompatible elements pairs that have been selected are Nb-Ta, Nb-La, Th-Ce, Y-Yb and Sr-La all of which produce positive linear correlations passing through the origin except for Sr-La (Figure 3.24).

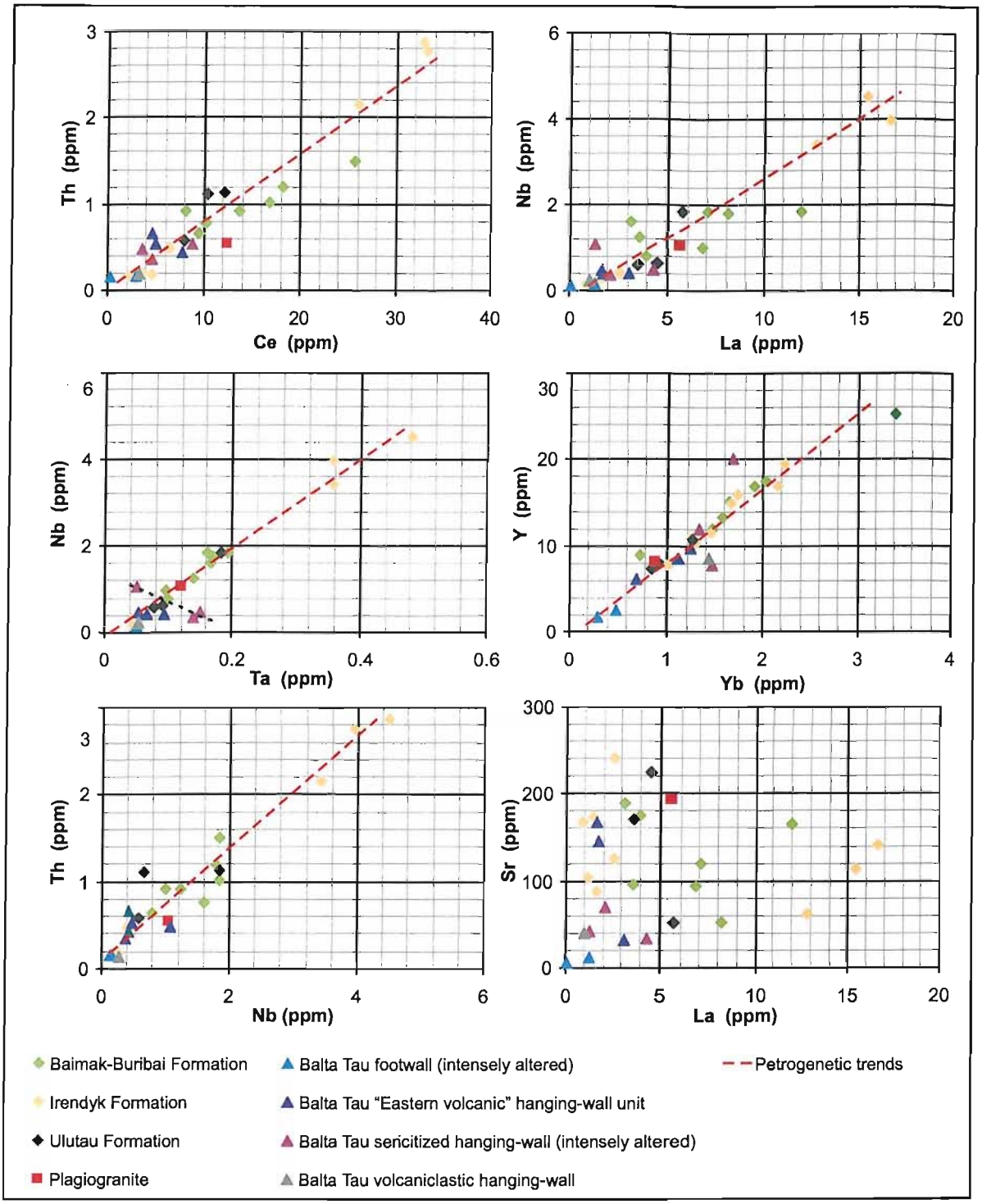

Figure 3.24. Covariation diagrams for pairs of elements with similar incompatibilities.

For regional samples, the covariation plots do not indicate significant mobility for any of the elements selected except for Sr. They provide a similar distinction between formations as the compatible-incompatible plots, and within the Irendyk three anomalous samples contain significantly higher trace element concentrations than any other samples. In the mine sequences, the footwall samples are very close to the origin reflecting the significant trace element dilution from volume increase during alteration. This makes deviations from the fractionation trends difficult to identify, but the data do suggest a possible depletion in Ce, Y and possibly Nb due to

element mobility in addition to the effects of dilution. The hanging-wall samples generally fall on the fractionation trends close to the bulk of the Irendyk samples, although there is some scatter for Nb, Ta and Y in the sericitized hanging-wall suggesting a degree of mobility of these elements during the sericitic alteration.

Sr data are extremely scattered with no definable fractionation trend, reflecting extreme mobility of Sr during both regional and ore-related alteration (since La is demonstrated to be nearly immobile in the La-Nb plot). This is consistent with the generally mobile nature of Sr (e.g. Pearce, 1986), and precludes the use of this element for petrogenetic interpretation.

3.4.4 Multielement Diagrams

Multielement diagrams enable eruptive settings of volcanic rocks to be compared using elements that were immobile during alteration. For the purposes of investigating subduction-related volcanics, it is useful to normalise data to N-MORB, as this represents the likely parental magma derived from decompressional melting of an uncontaminated, depleted upper mantle source. Deviations from this melt which are commonly encountered in arc environments, such as addition of a subduction component, are therefore easily identified (Pearce, 1982). Data have been plotted using a simplified multielement diagram devised by Pearce (1996) that utilises Th-Nb-Ce-Zr-Ti-Y to discriminate between eruptive settings, magma sources and melting and crystallization histories (Figure 3.25).

On these diagrams, a negative Nb anomaly indicates the addition of a subduction component to source magmas and is therefore characteristic of volcanic arc rocks. Tholeiitic arc volcanics are characterised by an absolute depletion of Nb, Zr, Y and Ti relative to MORB, whereas calc-alkaline arc rocks tend to have higher concentrations of Nb and Zr relative to MORB but lower Ti and Y. A negative Ti anomaly is indicative of fractionation to intermediate/felsic compositions (Pearce, 1996).

Based on these criteria, all of the regional samples and mine sequences analysed have an arc signature indicated by a negative Nb anomaly. The Baimak-Buribai samples (Figure 3.25a) are highly fractionated with borderline tholeiitic to calc-alkaline characteristics. By contrast the majority of the Irendyk Formation (Figure 3.25b) are tholeiitic with a very small degree of fractionation, although three samples (010819/16, 010820/03 and 010826/10, the three "anomalous" samples on covariation plots) are distinctly calc-alkaline and slightly more fractionated. The Ulutau Formation (Figure 3.25c) are very weakly fractionated and have tholeiitic to slightly calc-alkaline characteristics.

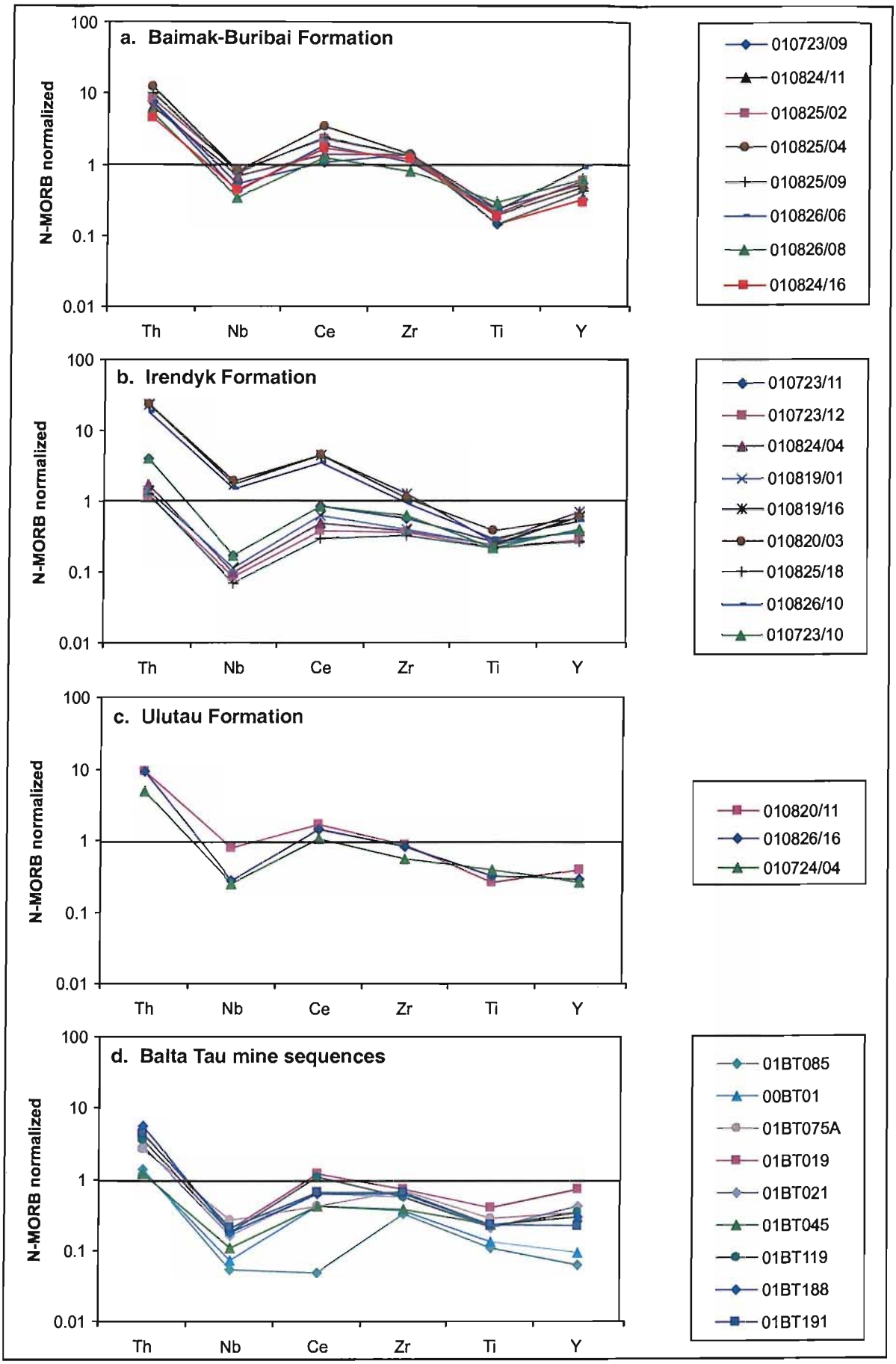

Figure 3.25. Multielement diagrams for regional volcanics and Balta Tau mine sequences.

In the Balta Tau mine sequences (Figure 3.25d), both weakly altered and intensely sericitized hanging-wall sequences share similar patterns with a tholeiitic, weakly fractionated signature comparable to the tholeiitic type Irendyk samples. The footwall patterns are more erratic, with overall low concentrations probably reflecting dilution during alteration, and anomalously low Ce in one sample and Y in both probably reflecting element mobility. In spite of these irregularities, it can however be seen that the footwall samples were only weakly fractionated (based on the value of Ti relative to Zr) and excluding Ce and Y have similar tholeiitic patterns to the hanging-wall samples.

3.4.5 Rare Earth Element Plots

REE patterns are also useful for the characterization of volcanic rocks, with concentrations typically normalised to chondrite values to enable trends to be clearly recognised and compared with published data. Figures 3.27 and 3.28 present REE plots for chondrite-normalised regional samples and mine sequences (normalizing values are given in Appendix A5). With the exception of the Balta Tau footwall samples (00BT01 and 01BT085) and one Baimak-Buribai sample (010824/11), the patterns are generally smooth suggesting minimal REE mobility during alteration.

Baimak-Buribai samples contain approximately ten times chondritic REE concentrations and show moderate LREE enrichment, which are characteristic of fractionated island arc volcanics with a moderately calc-alkaline signature. The anomalous patterns of sample 010824/11, in particular La depletion, may be due to LREE mobility during alteration, and the large positive Eu anomaly is probably an analytical artefact resulting from unusually high Ba in this sample (Appendix A3). The plagiogranite which intrudes this formation (sample 010824/16) has a very similar LREE enriched pattern to the host Baimak-Buribai volcanics. Data published for similar Upper Baimak-Buribai sequences in Herrington et al. (2002) show REE patterns comparable to these samples.

The majority of Irendyk samples have flat REE patterns at five to ten times the chondritic values, which are typical of weakly fractionated and tholeiitic arc volcanics. The presence of small, negative Eu anomalies indicate that feldspar fractionation has taken place (e.g. Rollinson, 1993). Three anomalous samples (which are the same as the anomalous samples in covariation and multielement diagrams) have significant LREE enrichment and overall higher REE concentrations at greater than ten times chondritic values. These patterns are suggestive of calc-alkaline and slightly more fractionated characteristics, with small negative Eu anomalies again indicating feldspar fractionation in the melt's history.

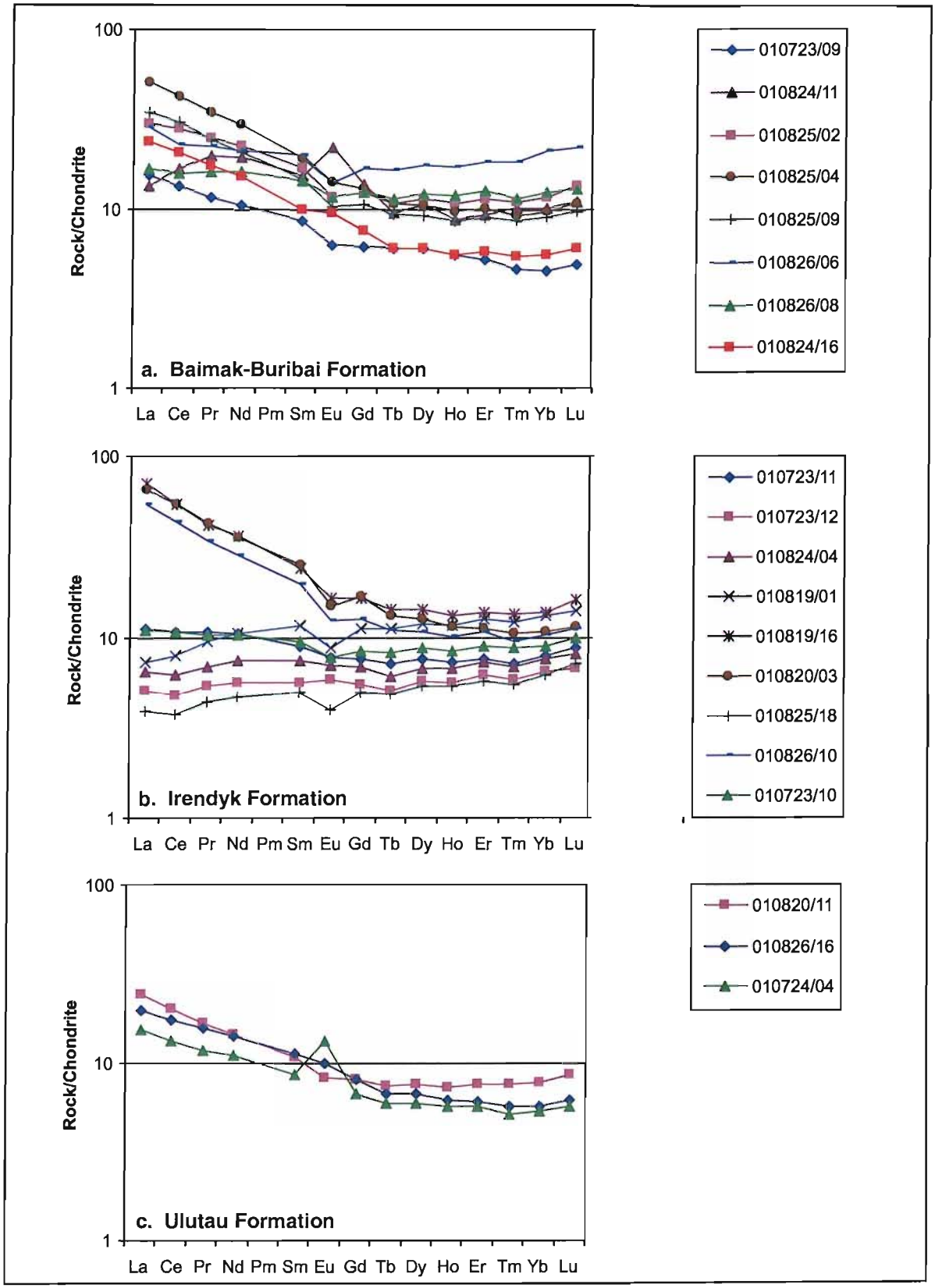

Figure 3.26. REE plots for regional volcanic samples.

The Ulutau samples have REE concentrations of around ten times chondritic values and show moderate LREE enrichment, suggesting a small degree of fractionation and a weak to moderate calc-alkaline character. The large positive Eu anomaly in sample 010724/04 probably reflects significant accumulation of plagioclase in the sample.

The immediate hanging-wall, Eastern volcanic unit and hanging-wall volcaniclastic sequences at Balta Tau have approximately flat patterns at around five to ten times chondritic values. These patterns are suggestive of weakly fractionated, tholeiitic volcanics comparable to those of the Irendyk Formation. The intense sericitic alteration of the immediate hanging-wall does not appear to have influenced the REE patterns, except for a large positive Eu anomaly that is probably an analytical artefact due to high Ba in these samples (Appendix A3). The sericitized samples also have slightly higher REE concentrations compared to less altered hanging-wall units, which may be due to the effect of volume reduction during alteration (as indicated by isocon and covariation diagrams).

The two footwall samples have generally low REE concentrations which probably reflect significant dilution during alteration (as noted from isocon plots and covariation diagrams). The patterns are very different for the two footwall samples, in particular in relation to LREE which are enriched relative to HREE in one sample and depleted relative to HREE in the other. This extreme variability is likely to be the result of element mobility during alteration, and precludes the use of REE signatures for geochemical interpretation of the footwall and comparison with hanging-wall and regional sequences. The negative Eu anomalies may also be the result of alteration, since Eu is the only REE capable of forming divalent ions and may therefore be more mobile than adjacent REE's during alteration.

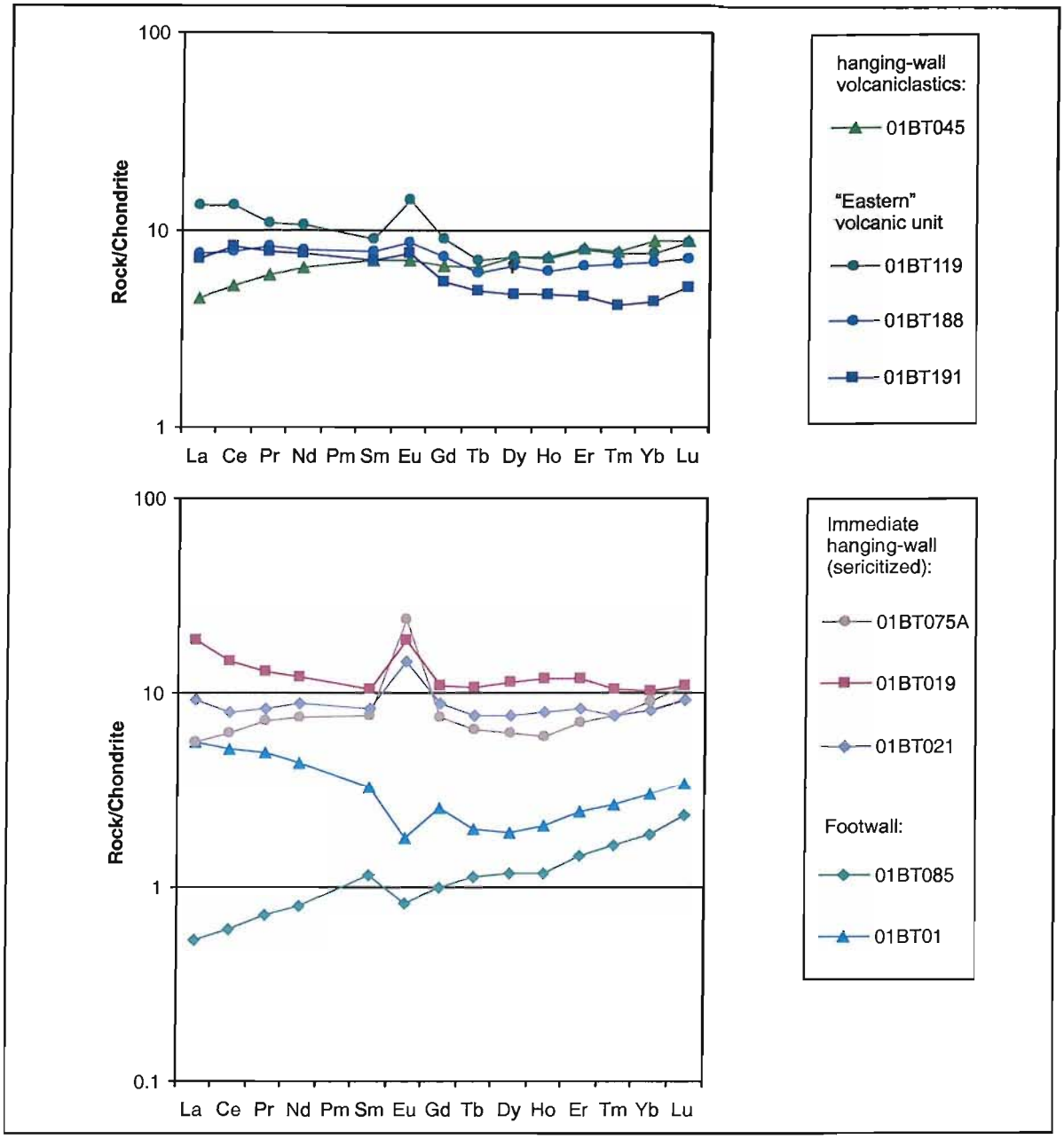

Figure 3.27. REE plots for Balta Tau mine sequences.

3.4.6 Discrimination plots for lithologies and tectonic environments

Discrimination diagrams use the covariation of two or more elements or element ratios and discriminate between specific lithologies and/or eruptive settings, with specific boundaries for rock types obtained by plotting a large volume of geochemical data from modern unaltered rocks of known petrography and tectonic setting. Two discrimination diagrams have been selected for the Balta Tau mine sequences and regional samples; (i) Zr/TiO_2 vs Nb/Y to define lithologies and (ii) Th/Yb vs Nb/Yb to investigate island arc characteristics. Both of these diagrams use element ratios rather than absolute values which remove the effect of volume changes during alteration, and use elements that were immobile in the majority of samples analysed.

Zr/TiO_2 vs Nb/Y

The Zr/TiO_2 vs Nb/Y diagram of Winchester & Floyd (1977) discriminates between rock types using Zr/TiO_2 as an indicator of fractionation and Nb/Y to indicate alkalinity, and may be used for both mafic and felsic rocks. In Figure 3.26a, data has been plotted using the modification of Pearce et al. (1996), who redefined the lithological boundaries based on a larger and improved dataset. Regional and mine sequences plot predominately in the sub-alkaline andesite field for the Irendyk, Ulutau and Balta Tau sequences, and the majority of Baimak-Buribai units are in the dacite/rhyodacite field (Figure 3.28). The plot supports the more calc-alkaline nature of the three anomalous Irendyk, the Ulutau and felsic Baimak-Buribai samples, which lie to the right of the diagram (i.e. have higher Nb/Y ratios) relative to the rest of the Irendyk and Balta Tau samples.

Th/Yb vs Nb/Yb

The Th/Yb – Nb/Yb diagram has been modified from Pearce (1982) and is designed specifically for the characterization of arc volcanic rocks. Th is used to indicate subduction zone enrichment due to its non-conservative behaviour (i.e. readily transferred from the subducting plate to the mantle wedge) and incompatibility, while Nb is selected to indicate non-subduction variations, being highly conservative and incompatible, and both elements are normalised to Yb. This diagram is designed for use with basaltic to andesitic rocks, but can also be used for felsic rocks providing a potential small increase in Nb/Yb due to fractionation is taken into consideration (e.g. Reid et al., 1987).

It can be seen from Figure 3.26b that all regional and mine samples show considerable subduction zone enrichment as indicated by the high Th/Yb ratios relative to N-MORB. The majority of samples reflect a strongly to weakly depleted mantle source, with the exception of the three anomalous Irendyk samples that are suggestive of a slightly enriched mantle source. Such heterogeneity is typical of the mantle wedge overlying subducting crust as determined from studies of active subduction zones (e.g. Gamble et al., 1995). Using the boundaries of Pearce (1982) for the division of tholeiitic and calc-alkaline arc suites indicates that the majority of Irendyk and Balta Tau sequences are tholeiitic, while the majority of Baimak-Buribai, Ulutau and three anomalous Irendyk samples are calc-alkaline. This is consistent with the interpretation of multielement diagrams (Section 3.4.4) and REE trends (Section 3.4.5).

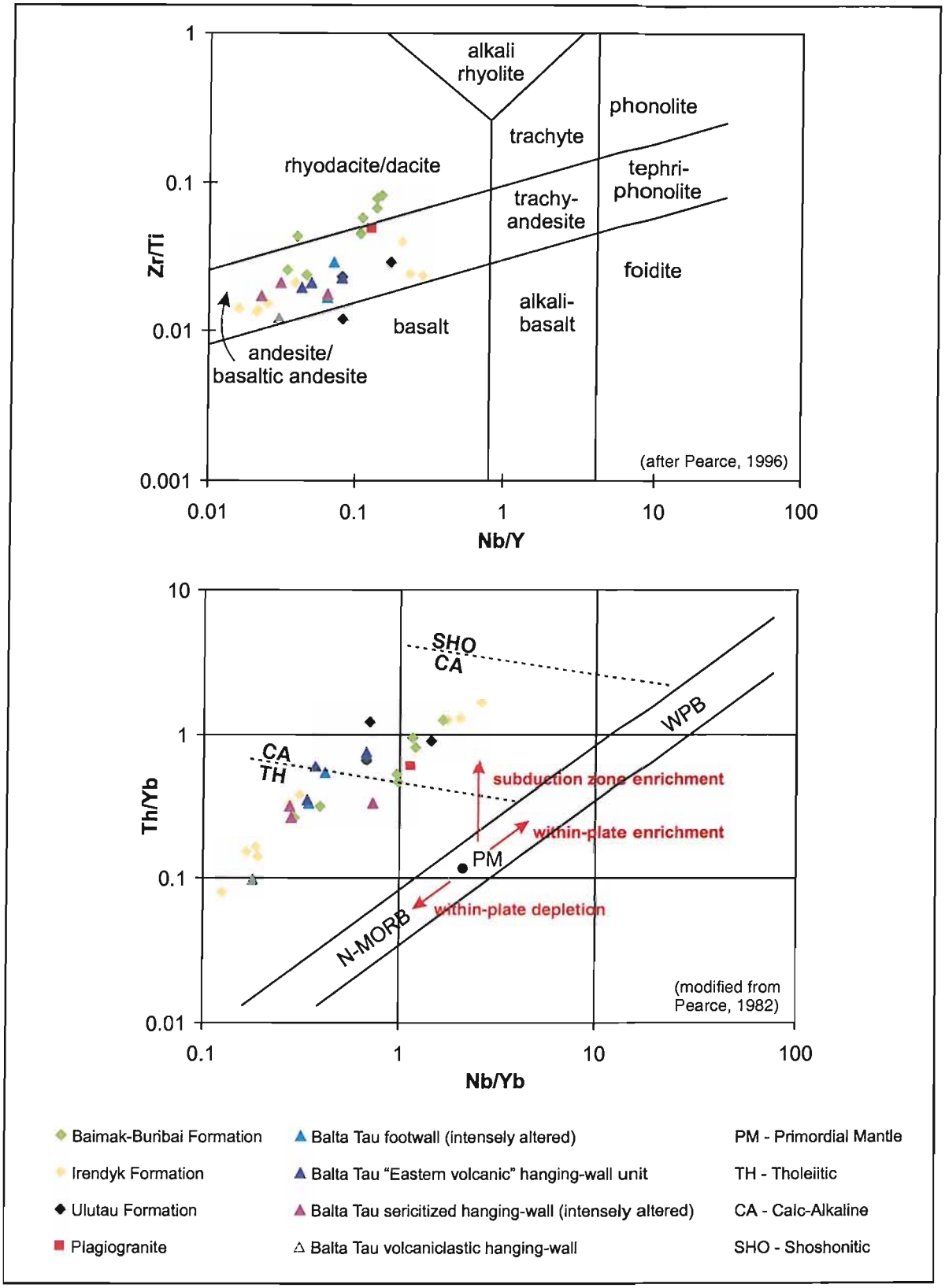

Figure 3.28. Discrimination diagrams for regional volcanics and Balta Tau mine sequences.

3.4.7 Discussion

Element mobility and alteration

The mobility of elements in Balta Tau mine sequences and regional volcanic samples is best investigated using covariation diagrams, and the mobility of selected elements that are useful petrogenetic indicators is summarised in Table 3.1. In footwall and hanging-wall samples, element concentrations have been significantly affected by volume changes associated with alteration, with low concentrations in the footwall reflecting dilution and elevated concentrations in the sericitized hanging-wall reflecting a decrease in volume.

Alteration	Elements immobile	Elements weakly mobile	elements strongly mobile
regional (including distal hanging-wall)	Al, Ti, Zr, Nb, Ta, REE, Th, Y, Sc, V	Rb	Sr
footwall mine	Al, Ti, Zr, Ta, Th, Sc, V	Nb, HREE	Sr, Rb, LREE, Y
immediate sericitized hanging-wall	Al, Ti, Zr, REE*, Th, Sc, V	Ta, Nb, Y	Sr, Rb, Eu

Table 3.1. Element mobility in Balta Tau mine sequences and regional volcanic rocks. *REE excludes Eu.

Geochemistry of volcanic suites

All of the regional volcanic and mine sequences have geochemical signatures indicative of island arc volcanic rocks, with enrichment of non-conservative elements (e.g. Th and Ce) confirming a subduction-related component to generally depleted mantle parental magmas. The geochemical characteristics of Balta Tau and surrounding formations may be summarised as follows:

- The Baimak Buribai Formation comprises highly fractionated sequences that are predominately dacites with minor andesites and have weakly calc-alkaline characteristics.
- The Irendyk Formation in the vicinity of Balta Tau is dominated by andesites that can be divided geochemically into two groups. The first group, which encompasses the majority of samples, have a tholeiitic signature, while the second (samples 010820/03, 010819/16 and 010826/10) are slightly more fractionated with a strong calc-alkaline signature. These differences do not appear to be reflected in the petrography, with both samples including examples of feldspar-pyroxene phyric rocks, and also the unusual quartz-phyric samples.
- The Ulutau samples are also andesitic in composition and have a moderate calc-alkaline signature. One sample (010724/04) is slightly less fractionated than the others and may classify as a basalt rather than an andesite.
- Data from a single sample of the plagiogranite intrusion was included on all of the geochemical plots to compare the trace element chemistry with the enclosing Baimak-Buribai

volcanics. The classification on discrimination diagrams can not be applied to intrusive rocks, however Figures 3.23 through to 3.28 do indicate that the plagiogranite has a very similar trace element signature to the Baimak-Buribai suite and it is therefore likely to be comagmatic with these volcanic rocks.

- Balta Tau mine sequences are andesitic in composition and generally have tholeiitic signatures. The footwall samples are difficult to characterize due to the large dilution and element mobility during alteration. However, in multielement and discrimination diagrams that appear the least affected by alteration, the footwall rocks also appear to have been tholeiitic andesites and may well be part of the same unit as the overlying hanging-wall rocks. The Balta Tau sequences are geochemically most comparable with the tholeiitic volcanics of the Irendyk Formation.

3.5 SUMMARY

The Baimak-Buribai and Irendyk Formations in the vicinity of Balta Tau comprise andesites and dacites and include coherent lavas, hyaloclastites, polymict breccias and syn-eruptive resedimented hyaloclastic and pyroclastic material. These lithofacies confirm a submarine eruptive setting, with the presence of pyroclastic material indicative of shallow water conditions. The Ulutau Formation is dominated by epiclastic volcanic sandstones, and may reflect a period of subaerial exposure and erosion of the arc.

Geochemically these sequences are characteristic of island arc systems, with a distinct subduction zone signature and variable tholeiitic to calc-alkaline affinity. The dominance of andesites in the Irendyk Formation is characteristic of mainstage accretionary island arc formation, although the tholeiitic (as opposed to calc-alkaline) signatures in units surrounding Balta Tau might suggest that these formed during early stages of island arc formation. The plagiogranite to the West of Balta Tau has a very similar geochemical signature to the host Baimak-Buribai Formation, which strongly suggests that the plagiogranite is syn-volcanic and comagmatic with these volcanic suites.

Primary lithological and geochemical characteristics that are preserved in the immediate footwall and hanging-wall units to the Balta Tau deposit suggest that these sequences are andesitic and contain hyaloclastic breccias and resedimented hyaloclastic/ pyroclastic material, with a tholeiitic island arc signature. These characteristics are comparable with those of the Irendyk Formation suggesting that the Balta Tau deposit is hosted within the tholeiitic andesites of the Irendyk Formation.

4 MINERALIZATION AND ALTERATION

4.1 INTRODUCTION

Balta Tau is a small, high grade deposit estimated at 3.5Mt averaging 5% Zn, 3% Cu and 5g/t Au, together with significant Ag, Sb and As (Maslennikov, pers. comm.). The base and precious metal mineralization at Balta Tau has many features characteristic of VMS deposits, including a conformable lens-like body of massive sulphides hosted in sea-floor volcanic rocks, with an extensive zone of alteration and disseminated and vein-hosted sulphide mineralization in the volcanic rocks immediately beneath the massive sulphide body. In spite of being Devonian in age, these ore facies are well preserved with minimal metamorphic overprinting compared to many of the Palaeozoic VMS deposits (such as Carboniferous deposits of the Iberian Pyrite Belt and Cambrian deposits hosted in the Mt. Read volcanics, Tasmania). The high base and precious metal contents coupled with good preservation of ores at Balta Tau provide an ideal opportunity to study ore forming processes and precious metal enrichment in an ancient VMS system.

In this study the mineralization at Balta Tau has been subdivided into footwall sulphides, massive sulphides (including chalcopyrite-pyrite, pyrite-sphalerite and sphalerite rich zones), layered sulphides, gold-barite rich sulphides and a gold-rich barite lens based on ore composition, textures and stratigraphic position, shown schematically in Figure 4.1. The following sections describe these five ore facies, interpret ore paragenesis and compare mineralization at Balta Tau with other ancient and modern VMS systems.

Sampling

The majority of samples were collected from the Balta Tau open pit during 2001. At this time there were good exposures of central and marginal footwall zones, a complete section from the footwall across marginal massive sulphides to hanging-wall volcanics, and the barite lens (as shown in Figure 3.12, the pit map produced at the same time as sample collection). In addition, a number of samples collected in previous visits to Balta Tau were studies, which include sulphides from the central portion of the massive sulphide lens (which had been completely mined out by 2001) and the overlying barite lens. A complete sample listing is given in Appendix A1.

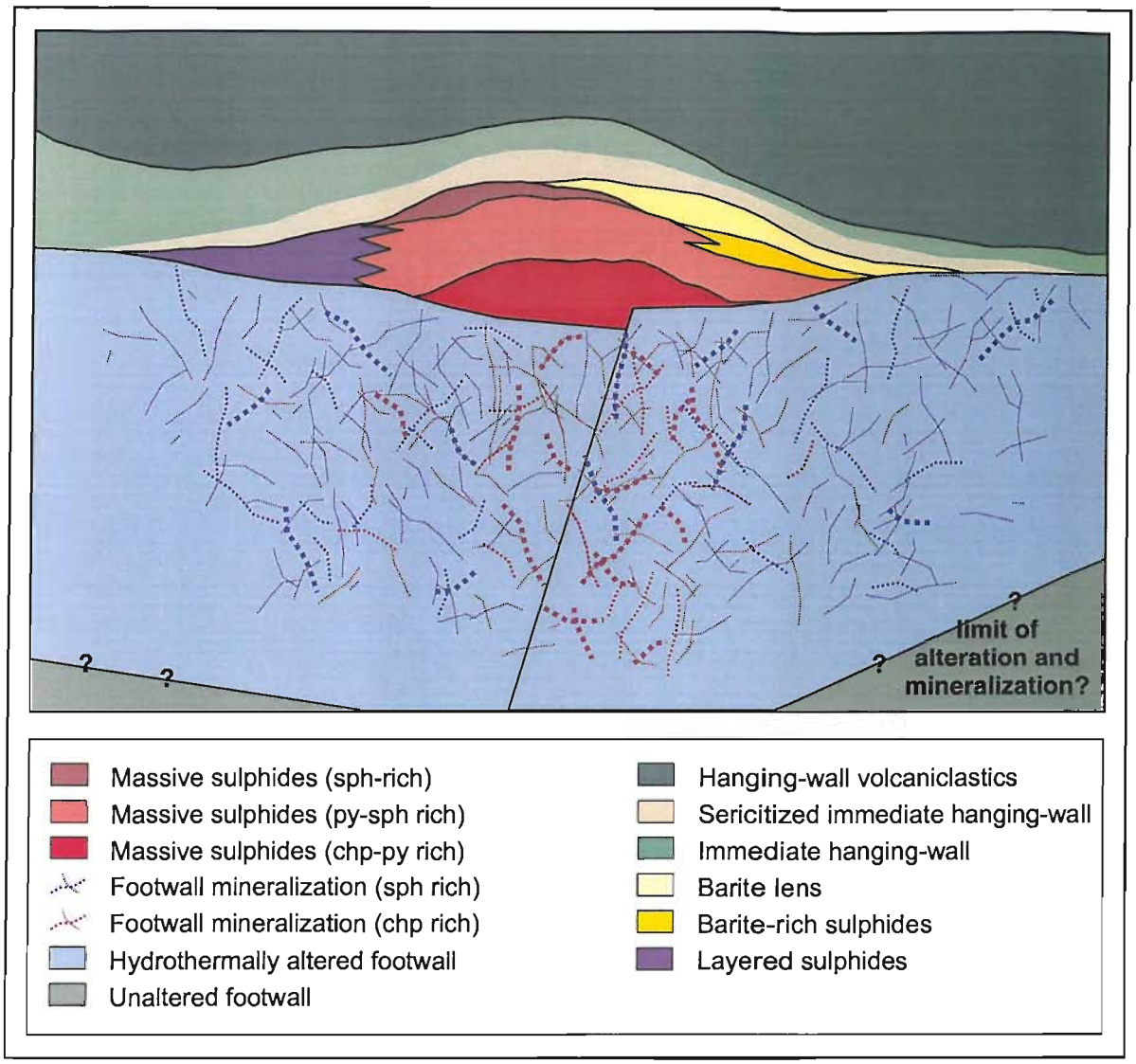

Figure 4.1. Schematic diagram of ore facies at Balta Tau.

4.2 FOOTWALL MINERALIZATION AND ALTERATION

4.2.1 Introduction

The volcanic rocks stratigraphically beneath the massive sulphide lens are intensely altered and host extensive sulphide mineralization which accounts for a significant proportion of the economic ore at Balta Tau. Alteration is dominated by a chlorite-quartz assemblage, and the main stage of footwall sulphide mineralization comprises sphalerite-chalcopyrite-pyrite(-tennantite-galena), which is overprinted by sparse quartz-tennantite veins. Although generally well preserved, the footwall is deformed locally by a shear zone that runs approximately parallel to the massive sulphide footwall contact, and also in a deformational zone adjacent to the Eastern Fault (Figure 3.12).

4.2.2 Mineralogy and textures of mainstage sulphide mineralization

The mainstage footwall mineralization comprises disseminated and vein-hosted sphalerite, chalcopyrite, pyrite and minor to trace tennantite and galena, with sulphide abundance varying on a metre scale from on average 1 to 30%, and increasing to over 50% close to the contact with massive sulphides. The disseminated sulphides are more abundant than veins. There is a broad mineralogical zonation across the footwall, with chalcopyrite-pyrite dominating the central zone (which lies beneath the mined out central portion of the massive sulphide lens), grading to sphalerite-chalcopyrite-pyrite and sphalerite-chalcopyrite-pyrite-galena-tennantite in the outer, marginal footwall zones (Figure 4.2).

Chalcopyrite and pyrite

Chalcopyrite and pyrite dominate the central footwall zone where they form veins up to 20cm wide (Figure 4.3a) and irregular disseminations (Figures 4.3c, d). Chalcopyrite characteristically forms cm sized aggregates of coarse, anhedral crystals up to 5mm, whereas pyrite occurs as euhedral to subhedral crystals <0.5mm with no evidence of crystal zoning, which are frequently enclosed in coarse chalcopyrite (Figure 4.3b). Disseminations and veins comprising almost entirely pyrite are also common (Figures 4.3d, e), with other sulphides (chalcopyrite, sphalerite and tennantite) present in minor to trace amounts as associated grains and inclusions. Areas of intense pyrite-chalcopyrite-quartz mineralization commonly enclose angular fragments of altered, unmineralized volcanics (Figure 4.3e). These may have formed by the selective mineralization and alteration of matrix in a volcanic breccia, and/or reflect brecciation during mineralization of a previously coherent lava. Given the identification of clastic textures in less mineralized footwall samples (Chapter 3, Section 3.3.2), is it probable that at least some of these facies represent primary volcanic breccias.

Pyrite and chalcopyrite are also abundant as minor constituents of sphalerite-rich veins and disseminations in marginal footwall zones. Here, chalcopyrite occurs as anhedral grains up to 1mm and is sometimes found associated with tennantite forming rims around coarse sphalerite. Pyrite forms subhedral crystals <0.5mm, closely associated with, and sometimes as inclusions in, coarse sphalerite crystals.

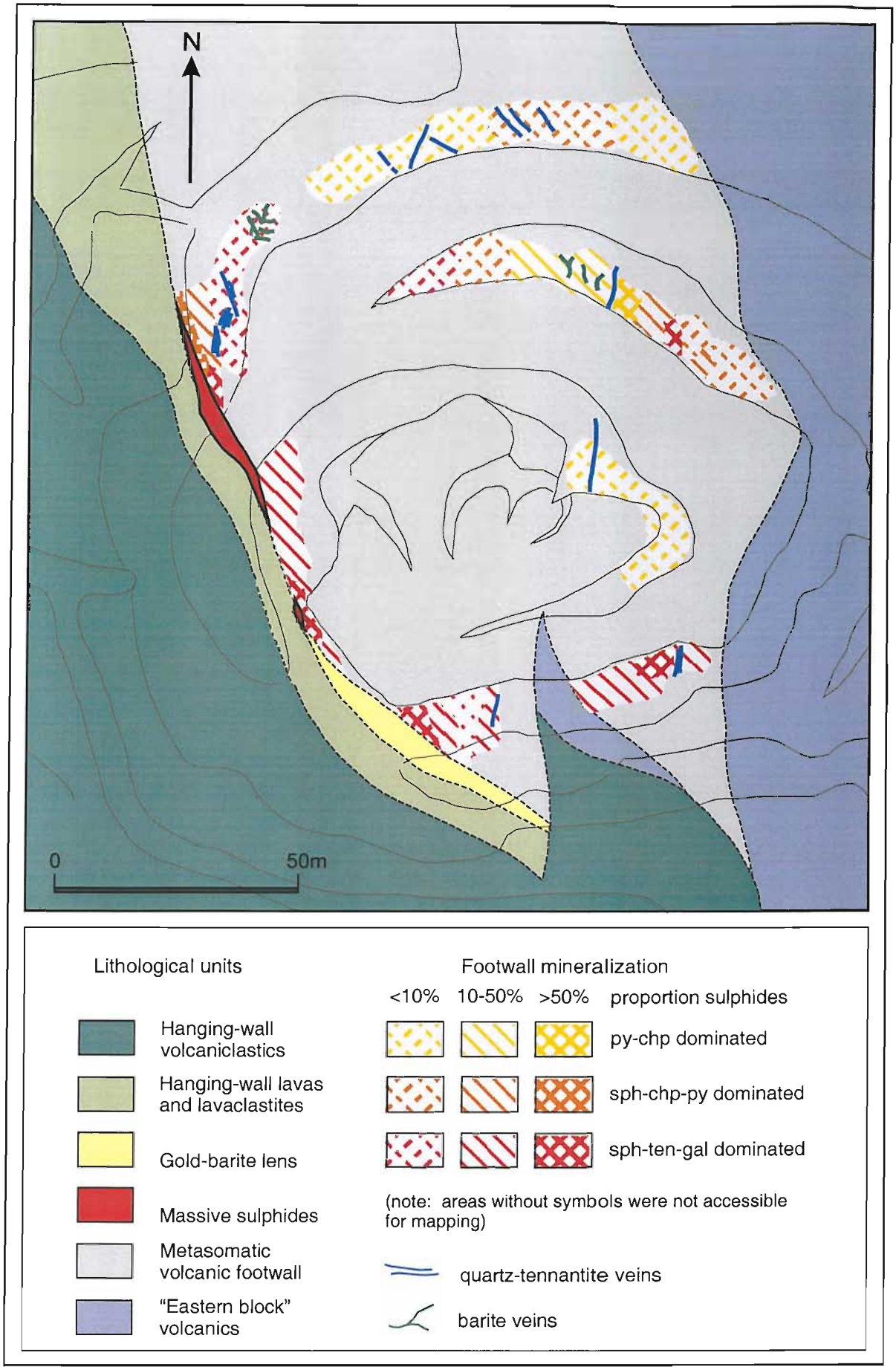

Figure 4.2. Sulphide zonation across the footwall exposed in Balta Tau open pit.

a. Large boulder with a thick (>20cm) chalcopyrite-pyrite vein, typical of the central footwall zone.

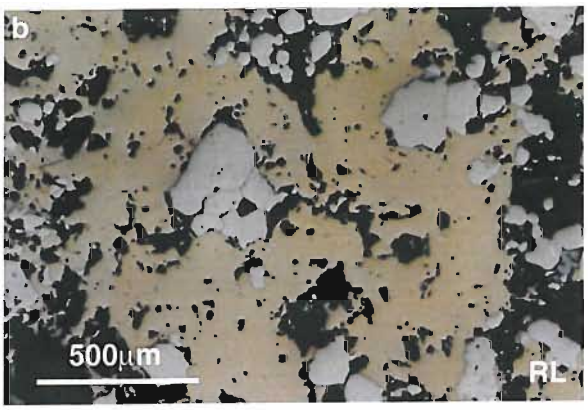

b. Typical vein textures with coarse anhedral chalcopyrite enclosing finer euhedral pyrite. Sample 01BT110.

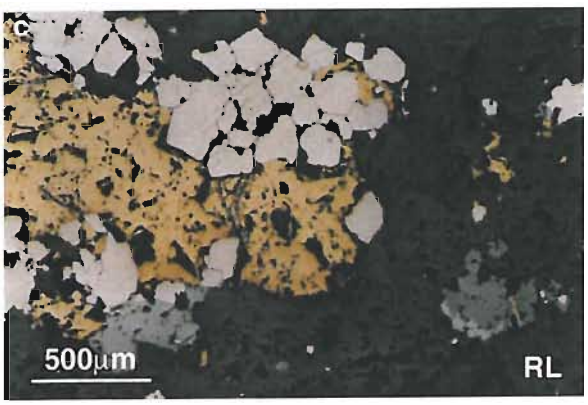

c. Disseminated chalcopyrite-pyrite with minor tennantite and sphalerite. Sample 00BT13.

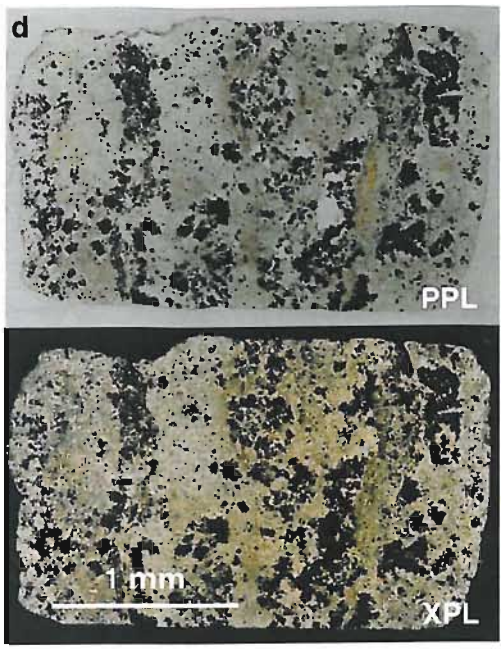

d. Typical textures in disseminated pyrite-chalcopyrite dominated sulphides. Sample 00BT13.

e. Pyrite (chalcopyrite-sphalerite)-quartz enclosing chlorite-altered volcanic clasts. The clastic texture may be a primary volcanic feature or be the result of brecciation during mineralization. Sample 01BT090.

Figure 4.3. Pyrite-chalcopyrite rich vein and disseminated footwall ore facies.

Sphalerite

Sphalerite is widespread in the marginal footwall zones as disseminations and veins up to 5cm wide (Figure 4.4a). Crystals are typically coarse and euhedral to subhedral, ranging from 0.5-5mm

in disseminations to 1-10mm in veins (Figure 4.4b). In transmitted light, sphalerite is transparent with multiple and complex zoning alternating between dark grey-blue, yellow, orange, brown and pale beige (Figures 4.4c, d). The dark blue-grey zones are caused by very fine (<5μm), dense chalcopyrite disease, which also occurs sparsely in yellow zones, but is scarce to absent in orange, brown and pale beige zones. Sphalerite crystals also contain anhedral 20-100μm inclusions of chalcopyrite, pyrite, tennantite and more rarely galena.

Sphalerite is less abundant in the central footwall, but is still present in most samples as dark zoned crystals 0.5-1mm in size, and anhedral inclusions in chalcopyrite and less commonly pyrite.

Tennantite and galena

Tennantite and galena are minor phases by comparison with the chalcopyrite-pyrite-sphalerite assemblage, but are nonetheless significant constituents of footwall ores. Tennantite occurs in minor to trace amounts in the majority of samples and displays a strong association with both chalcopyrite and sphalerite. It is most abundant (up to 5%) in the sphalerite-rich marginal zones, forming small anhedral grains <20 to 500μm either enclosed in or adjacent to sphalerite, and in some vein samples also forms distinct partial rims around sphalerite crystals. In the central footwall it is still common but in low abundance (<1%), occurring mainly as small 20 to 200μm inclusions in chalcopyrite.

The occurrence of galena is mostly restricted to marginal sphalerite-rich footwall, forming anhedral to subhedral crystals up to 2mm in polymineralic aggregates with sphalerite, pyrite, tennantite and chalcopyrite, and sometimes forming partial rims around sphalerite. In the central footwall, galena occurs only in trace amounts, as small (<100μm) anhedral inclusions in chalcopyrite, sphalerite and pyrite. Both galena and tennantite are notably abundant just below the contact with the marginal massive sulphide lens, which coincides with a footwall shear zone, discussed further in Section 4.2.7.

Ore textures

Both vein-hosted and disseminated sulphides occur predominately as polymineralic aggregates of interlocking grains with little evidence of successive crystallization or replacement, suggesting co-precipitation of pyrite, chalcopyrite, sphalerite, tennantite and galena. Exceptions are the occurrence of tennantite-chalcopyrite-galena rims around coarse sphalerite crystals indicating precipitation of chalcopyrite, tennantite and galena after sphalerite. However, the common occurrence of tennantite and chalcopyrite inclusions in sphalerite and vice versa indicates that there was also significant overlap in the precipitation of these phases. The rim textures may either reflect continued precipitation of chalcopyrite-tennantite-galena after sphalerite formation, or localized remobilisation of chalcopyrite-tennantite-galena after sphalerite formation.

a. Sulphide vein dominated by coarse sphalerite with minor chalcopyrite-pyrite and lesser tennantite-galena and quartz. The vein is over 4cm wide, and cuts quartz-chlorite altered footwall volcanics. Sample 01BT127.

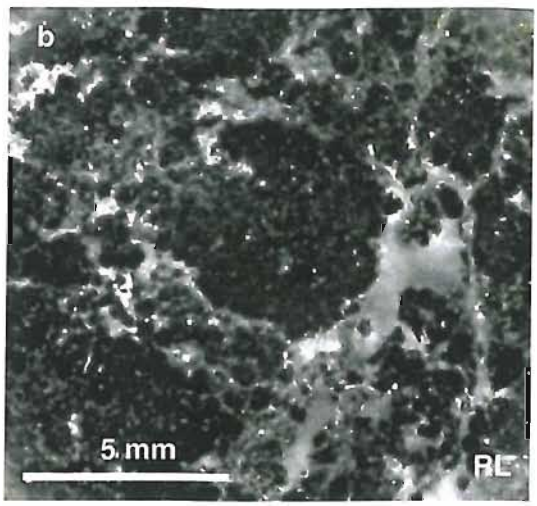

b. Coarse euhedral sphalerite crystals from the central portion of a sphalerite vein with minor chalcopyrite and tennantite. The white gangue phase is fine grained, transparent quartz. Sample 01BT157.

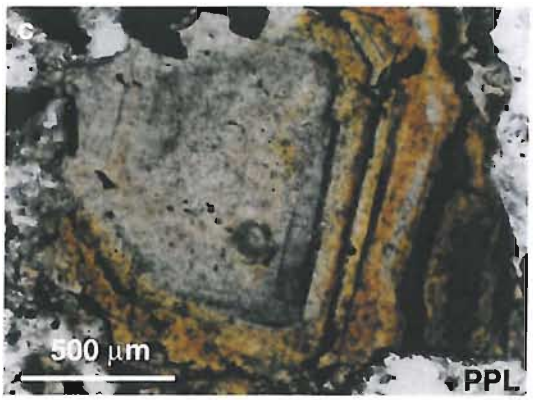

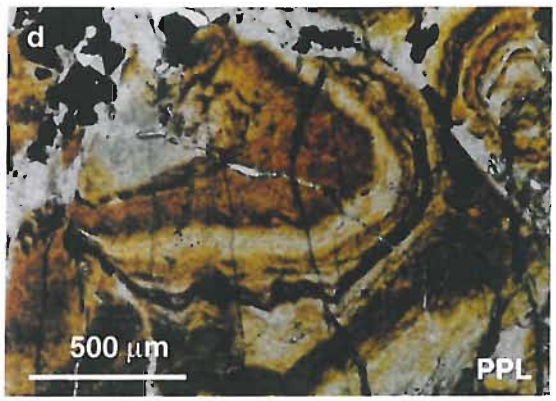

c and d. Complex zoning in sphalerite crystals views in transmitted light. Overall high degree of transparency suggests these sphalerites are Fe-poor. Sample 01BT067.

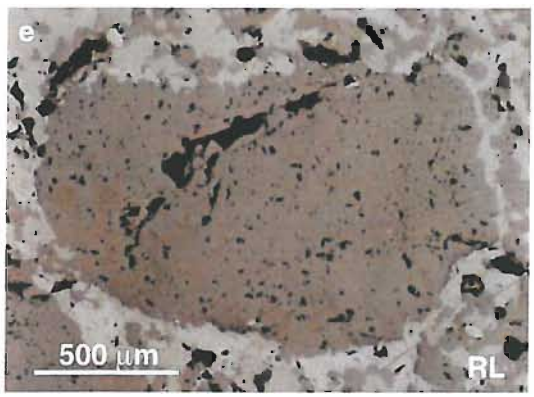

e. Large subhedral sphalerite with rims of finer grained tennantite-galena and sphalerite. Sample 01BT073.

Figure 4.4. Sphalerite-rich vein and disseminated footwall ore facies.

Gangue phases

The main gangue phases associated with both vein and disseminated sulphides are quartz and chlorite. Quartz typically forms aggregates of anhedral, transparent and colourless crystals 100μm-1mm which are relatively inclusion-free (Figures 4.5b, c). In a few samples, quartz has euhedral, blocky morphologies which are not typical of vein quartz and may be pseudomorphs of an earlier phase (Figure 4.5c). Chlorite forms coarse fanning aggregates of platey crystals up to 1mm which are closely associated with quartz and sulphides (Figure 4.5a, b). The optical properties of this chlorite (colourless to slightly beige in plane polarised light with low first order grey-yellow-orange birefringence in crossed polarized light) suggest a low Fe, high Mg content (Figure 4.5b). In many cases chlorite forms rims around chalcopyrite and sphalerite, and appears to penetrate the margins of sulphide crystals (e.g. Figure 4.5b), suggesting it post-dates sulphide formation. Sericite and muscovite are also widespread in low abundance, with scarce fine grained sericite intergrown with chlorite, and coarse muscovite more common in the sheared sections of footwall, discussed further in Section 4.3.2.

Carbonates are extremely rare in the footwall and have only been identified in one sample (01BT073) associated with a sphalerite-tennantite-galena vein. Here the carbonate forms pale beige, subhedral crystals averaging 100μm infilling vugs in the sulphides (Figure 4.6a). In crossed polars crystals do not show twinning, but concentric rhombic zones are visible, some of which are defined by tiny inclusions (<10μm) of sphalerite (Figure 4.6b). Although the carbonate is infilling vugs, the nature of sphalerite inclusions suggest that both carbonate and sulphides precipitated during the same mineralising event.

4.2.3 Barite-quartz veins

Barite occurs in the footwall as very thin (<5mm wide) barite±quartz veins which are not closely associated with sulphide mineralization. Barite forms coarse, tabular, subhedral to euhedral crystals 0.5-3mm in length which are transparent and colourless (Figure 4.6c, d). Only a few examples of these veins were found, however they are difficult to identify in the field due to the thin, transparent and colourless nature of the barite, and may be more common than mapping (Figure 4.2) would indicate. The general absence of associated sulphides suggests the barite formed separately to sulphides, although the relative timing is difficult to determine. However, in one sample (01BT151) thin irregular barite veins appear to branch off from a thick sphalerite(-chalcopyrite-pyrite-tennantite-galena)-quartz vein (Figure 4.6c) which itself contains traces of barite, suggesting the barite is contemporaneous with mainstage sulphide mineralization.

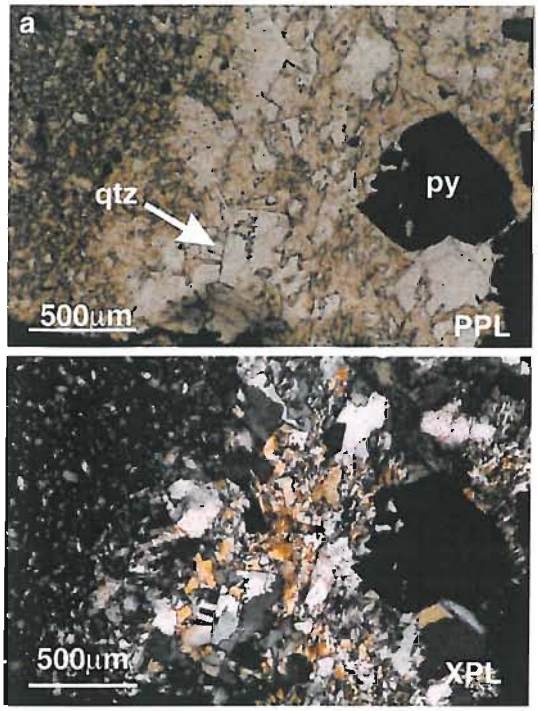

a. Quartz-chlorite in a pyrite-chalcopyrite rich footwall vein. Quartz has an unusual blocky morphology and may be replacing an earlier phase, possibly anhydrite? Sample 00BT12.

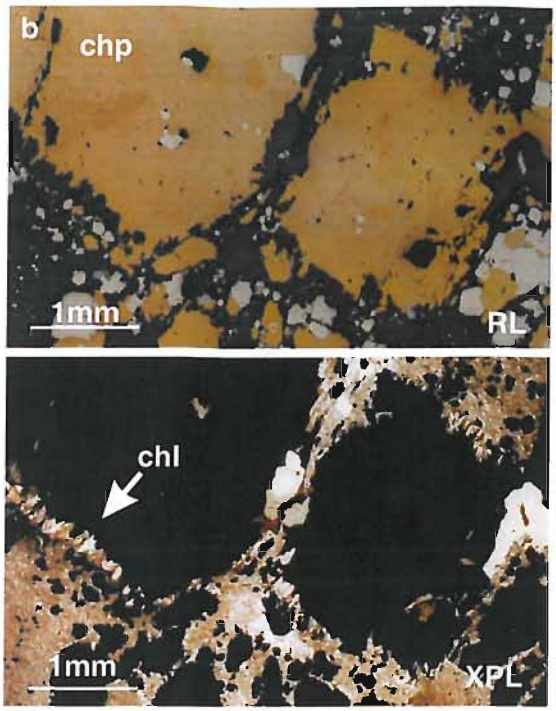

b. Typical chlorite rims around coarse chalcopyrite in a footwall vein. Chlorite replaces chalcopyrite at the margins suggesting it formed after the chalcopyrite. Sample 01BT001b.

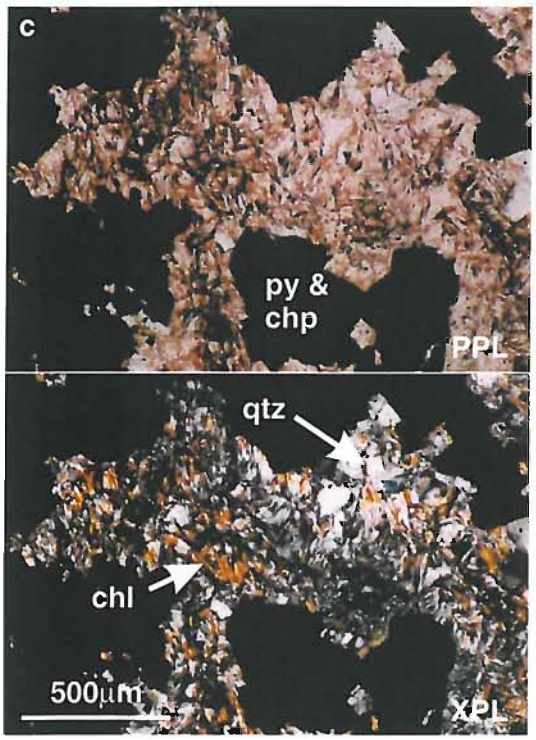

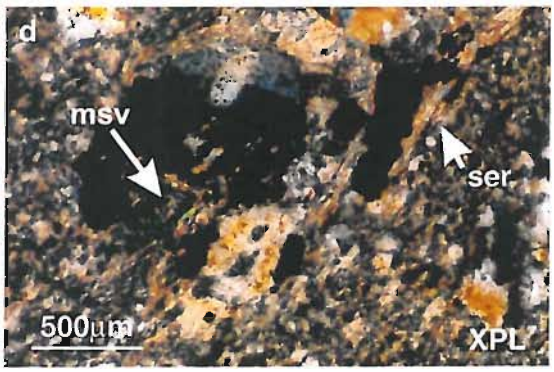

c. Typical chlorite associated with footwall vein and disseminated sulphides, here pyrite-dominated. Optical properties (virtually colourless in PPL and anomalous yellow-bluish in XPL) are indicative of an Mg-rich, Fe-poor composition.

d. Sericite forming a foliation-parallel band in altered volcanics with disseminated sulphide mineralization, and coarse muscovite replacing pyrite. Sample 01BT004.

Figure 4.5. Gangue phases associated with footwall sulphide mineralization.

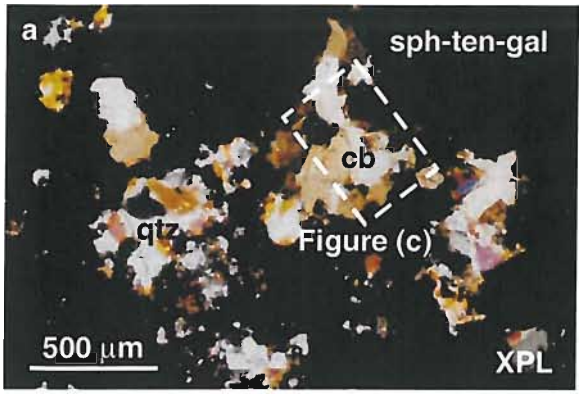

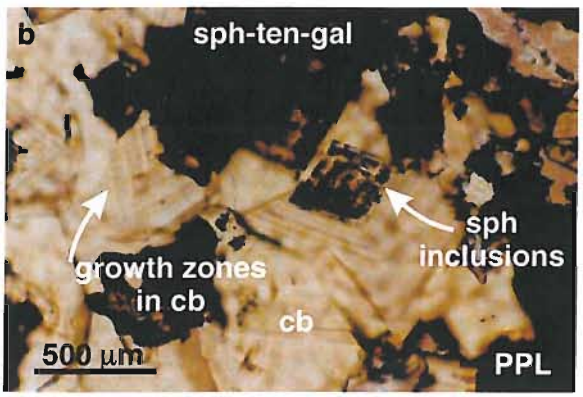

a and b. Carbonate crystals infilling a vug in a sphalerite-tennantite-galena vein. The carbonate is a pale beige and weakly zoned, and contains zones of timy sphalerite inclusions that follow growth zones as shown in the enlargement in (c). Sample 01BT073.

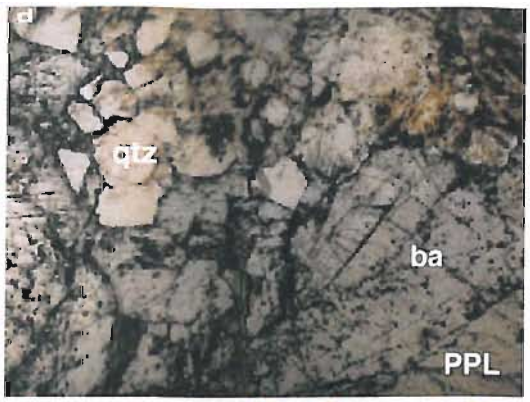

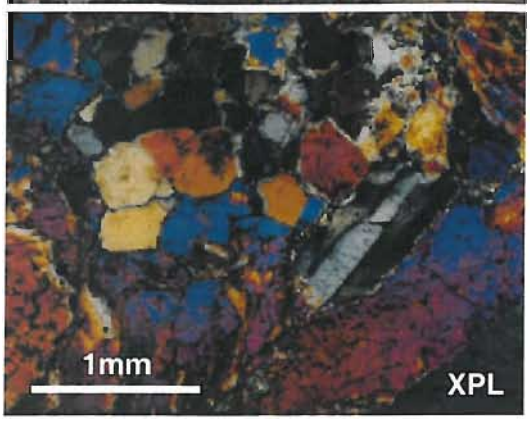

d. Barite-quartz vein comprising coarse, tabular barite crystals with equant subhedral quartz at the vein margins. There are no sulphide phases associated with the barite. Sample 01BT145 (note thin section is thicker than 30µm resulting in high birefringence colours).

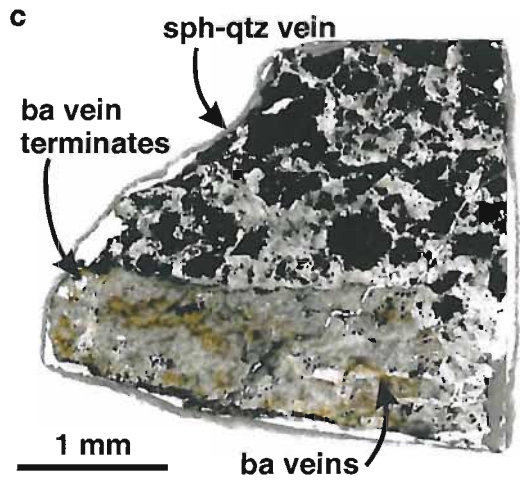

c. Thin barite veins in chlorite(-sericite)-quartz altered volcanics terminated by the thick sphalerite-quartz dominated sulphide vein. Sample 01BT151.

Figure 4.6. Footwall barite and carbonate mineralization.

4.2.4 Late stage quartz-tennantite veins

In addition to mainstage mineralization, the footwall is host to a number of milky quartz veins 1 to 5cm wide, containing abundant coarse, subhedral to anhedral tennantite crystals up to 10mm in

size (Figure 4.7). These veins overprint vein and disseminated sulphides indicating they post-date the mainstage footwall sulphide mineralization.

a. Typical quartz-tennantite vein exposed in the footwall.

b. Coarse tennantite crystals enclosed in milky quartz from a vein similar to that shown in (a). The tennatite is very clean with no inclusions of other sulphides. Sample 01BT158.

Figure 4.7. Footwall late stage quartz-tennantite veins.

4.2.5 Secondary sulphides

Mainstage sulphides are locally altered to covellite and digenite along fractures and at crystal margins (Figures 4.8a, b). These secondary sulphides are unlikely to be supergene in origin since these samples were collected from recently exposed footwall below the level of supergene influence, and therefore more probably formed during oxidation by late stage ore forming, diagenetic or metamorphic fluids.

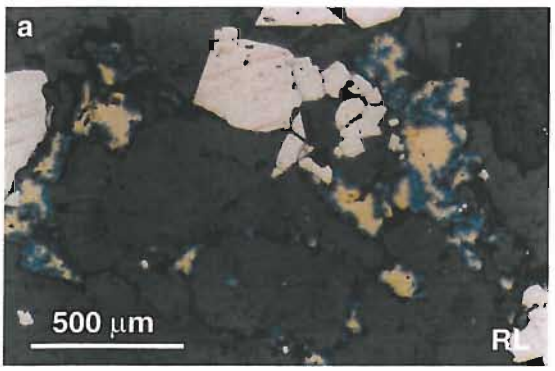

a. Covellite rimming chalcopyrite in footwall disseminated sulphides. Sample 00BT13.

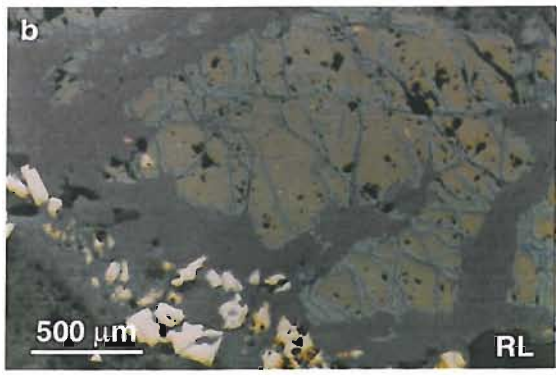

b. Digenite-covellite replacing sphalerite with pyrite in a footwall vein. Sample 00BT15.

Figure 4.8. Secondary sulphides in disseminated and vein-hosted footwall ores.

4.2.6 Footwall alteration

Footwall volcanic rocks exposed in the open pit are uniformly intensely altered to quartz-chlorite(-sericite-pyrite). The absence of unaltered footwall exposures distal to the deposit precludes interpretation of the extent and morphology of the alteration zone, which may be discordant or stratigraphically controlled. There is no apparent zonation in mineralogy, with approximately equal proportions of quartz and Mg-chlorite with minor pyrite dominating the footwall to both central and marginal zones of the massive sulphide lens. Muscovite and sericite are present in minor to trace amounts, mostly as fine grained sericite sometimes intergrown with quartz-chlorite, with coarse muscovite more abundant in zones of deformation. The alteration minerals replace all primary volcanic phases except for quartz phenocrysts and preserve volcanic textures (discussed and illustrated in Chapter 3, Section 3.3.2). Quartz is typically fine grained and granular, and chlorite is extremely fine grained forming felty masses as well as fine intergrowths with quartz (Figure 3.14, Section 3.3.2). The texture of chlorite in altered volcanics is very different to the coarse crystals intimately associated with vein and disseminated sulphides (Section 4.2.2). However, there is a gradual transition from the coarse chlorite associated with sulphides to the surrounding fine-grained chlorite and they share a similar Mg-rich composition (inferred from optical properties in thin section), suggesting that in spite of textural variations they are the same generation of chlorite. Pyrite occurs throughout the footwall as an alteration product, forming fine (10-50μm) euhedral crystals intergrown with chlorite and sericite.

4.2.7 Metamorphism and deformation

Sulphides and associated gangue minerals are deformed in the shear zone passing through the footwall close to and parallel with the contact with the exposed marginal massive sulphide lens (Section 3.3.7). The shearing post-dates VMS-related mineralization, illustrated on a macro-scale by deformation of quartz-sulphide vein networks (Figure 4.9b). On a micro-scale, disseminated sulphide grains are elongated, fragmented and define a distinct foliation. Muscovite and to a lesser degree sericite are closely associated with this zone, forming foliation-parallel lenses and bands in both mineralized and unmineralized sheared zones. Where these bands encounter disseminated sulphides, coarse muscovite partially replaces the sulphide grains (Figure 4.5d). These observations suggest that the muscovite and sericite post-date sulphide formation and either formed or recrystallized during deformation. Galena and to a lesser extent tennantite are more abundant in the deformed and foliated ores of the footwall shear zone, suggesting they may have been remobilised and concentrated in the shear zone during deformation.

The footwall also contains sparse zones of coarse zeolite (identified by microprobe in Chapter 5, Section 5.4.6) replacing the quartz-chlorite matrix and enclosing sulphide grains. This post-dates ore formation and is likely to have formed during diagenesis and/or low grade metamorphism.

a. Quartz-sulphide veins in undeformed footwall.

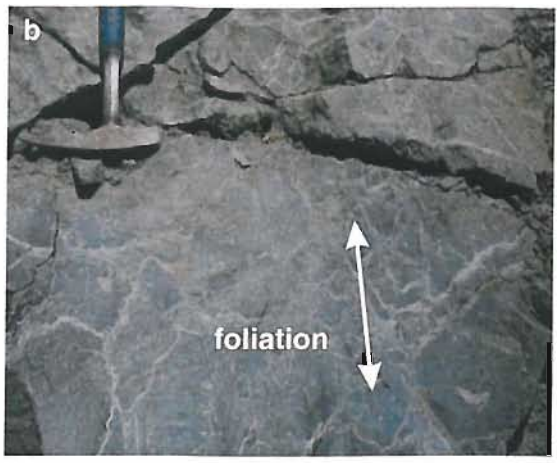

b. Quartz-sulphide veins in sheared footwall, showing deformation of the veining parallel to foliation, indicating deformation post-dates the footwall vein mineralization.

Figure 4.9. Deformation of footwall quartz-sulphide veins.

4.2.8 Footwall ore formation, alteration and paragenesis

Paragenesis

Figure 4.10 summarises the paragenesis of footwall sulphides and alteration minerals. Textures in mainstage sulphides are generally indicative of co-precipitation of the mainstage pyrite, chalcopyrite, sphalerite, tennantite and galena.

One or more later stages of sulphide precipitation and/or remobilisation are suggested by the following:

- Tennantite-chalcopyrite-galena rims around sphalerite in veins, which may reflect either continued precipitation of these phases after sphalerite formation during later stages of ore formation, or remobilisation of these sulphides during late stages of ore formation, diagenesis or metamorphism.
- Galena and to a lesser extent tennantite enrichment coincident with deformation and shearing in the marginal footwall. This may be attributed either to primary footwall zonation or remobilisation during deformation, or a combination of the two.
- Tennantite is abundant in late stage quartz-tennantite veins which post date mainstage footwall sulphides. The confinement of these veins to the mineralized footwall zone suggests they may have formed prior to deposition of the hanging-wall sequences during late stage hydrothermal activity rather than during metamorphism and deformation, and that the tennantite was derived from the remobilisation of footwall sulphides rather than introduced during a separate mineralising event.

Since the timing of these "late stages" is rather ambiguous, they are represented on Figure 4.10 as possible precipitation of chalcopyrite-tennantite-galena and formation of quartz-tennantite veins during late stages of ore formation, and possible remobilisation of chalcopyrite-tennantite-galena during late stages of ore formation, and remobilisation of tennantite and galena during deformation (as indicated by their abundance in shear zones). The timing of minor covellite and digenite formation is equally ambiguous, and may have occurred during one or more of late stage ore formation, diagenesis or metamorphism.

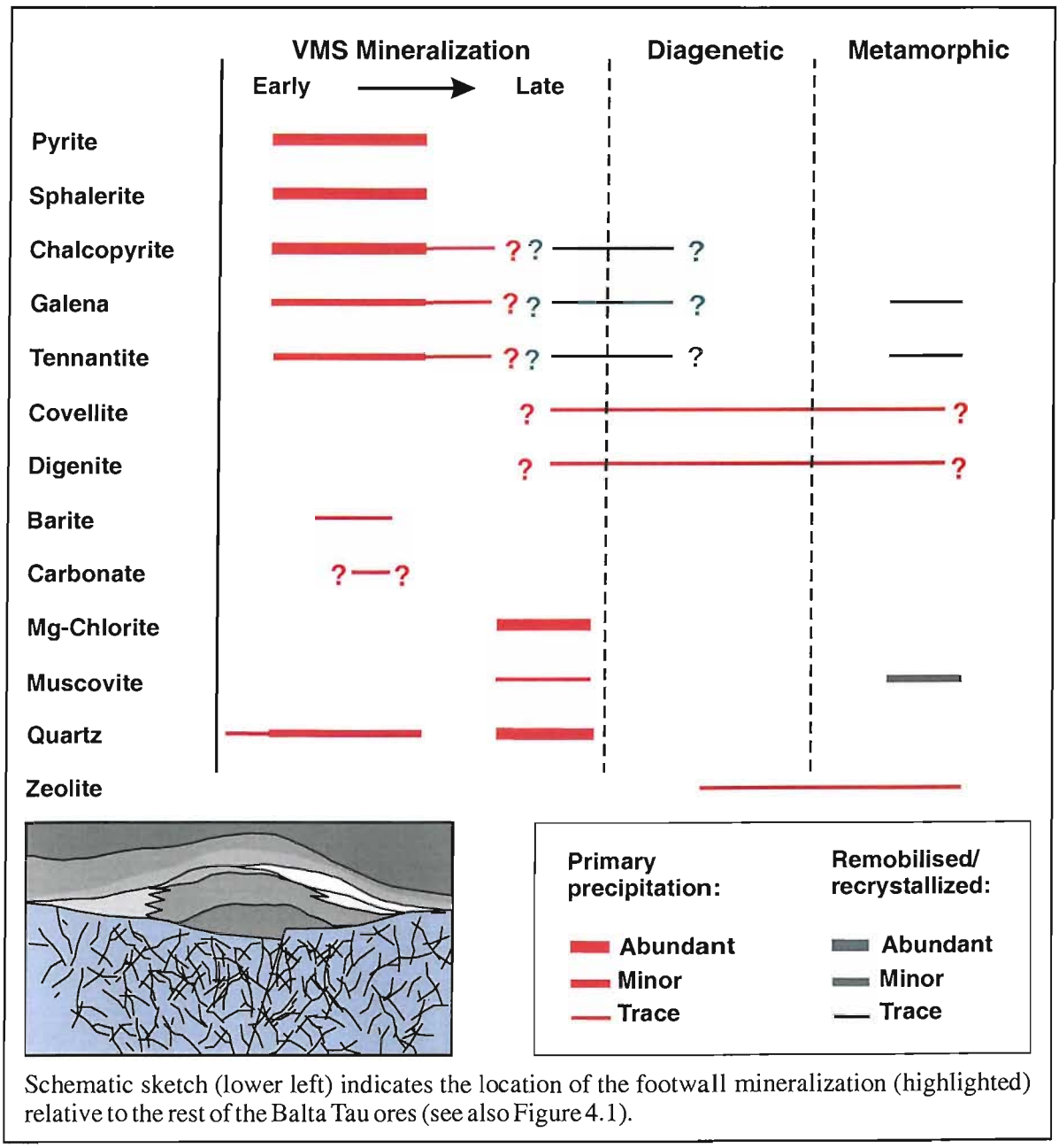

Schematic sketch (lower left) indicates the location of the footwall mineralization (highlighted) relative to the rest of the Balta Tau ores (see also Figure 4.1).

Figure 4.10. Footwall paragenesis.

Textures in gangue phases suggest co-precipitation of quartz with sulphides, while chlorite and muscovite clearly post-date sulphide phases. The close association of chlorite with sulphides,

random orientation of crystals and ubiquitous occurrence through both deformed and undeformed footwall suggest this chlorite formed during late stages of the ore-forming hydrothermal system rather than during later diagenesis or metamorphism. By contrast, the abundance of muscovite and sericite in zones of deformation and the foliation-parallel orientation of grains and bands point to formation during regional metamorphism and deformation.

The footwall barite-quartz veins are seldom closely associated with sulphides, however one sample suggests that they are contemporaneous with the main sulphide event (Figure 4.6c). The carbonate found in just one sample appears to have formed at the same time as the associated sphalerite-tennantite-galena vein assemblage, whereas patchy zeolite replaces alteration assemblages and probably formed during diagenesis and/or metamorphism.

Ore formation and alteration

The disseminated and vein-hosted nature of mineralization in the footwall indicate that the sulphides precipitated by fracture-filling and replacement of the host volcanic rocks. The broad zonation of pyrite-chalcopyrite rich ores in central footwall to sphalerite-rich in marginal zones is common in VMS deposits (e.g. Eldridge et al., 1983, referring to Kuroko deposits; Franklin et al., 1981 for some Precambrian deposits; Large 1992 referring to "classic mound" style Australian VMS). Spatially the zonation in footwall sulphides at Balta Tau is centred under the massive sulphide lens as observed in other deposits (see references above) suggesting that in spite of the shearing observed in the footwall close to the contact of marginal massive sulphides, the lateral displacement between the sulphide lens and footwall is minimal. The zoning is generally considered to reflect lateral and vertical gradients in the physical and chemical properties of mineralising fluids in the sub-seafloor environment. These gradients may be attributed to various processes including conductive cooling, interaction of fluids with volcanic rocks, mixing of ore-forming fluids with seawater and mineral precipitation, (discussed further in Section 4.8 and Chapter 7, Section 7.4.5).

The zonation of sulphide mineralization is usually mirrored by the associated alteration phases of VMS footwall zones, which typically exhibit zoning of the common alteration minerals sericite, chlorite and quartz, as well as systematic variations in the Fe/Mg ratio of chlorites. Ancient deposits such primary zoning is preserved include the eastern Black Sea and Küre deposits of Turkey (Çagatay, 1993), Kuroko deposits (summarised in Franklin et al., 1981), the Millenbach deposit, Noranda, Quebec (Riverin & Hodgson, 1980), and Hellyer and Mt. Lyell in Tasmania (Large, 1992, Gemmel and Fulton, 2001). Similar alteration zones have also been interpreted from drill core recovered from the footwall of the actively forming TAG system, Mid Atlantic Ridge (Teagle et al., 1998). At Balta Tau, the alteration assemblage of Mg-chlorite-quartz(-pyrite) is comparable in mineralogy to many other VMS footwalls, but does not have the typical zoning and

is uniform both laterally and vertically beneath massive ores. This suggests there was little variation in fluid properties in the footwall at the time that the observed alteration was formed, and textures indicate this episode of alteration post-dates sulphide precipitation.

Balta Tau has a high proportion of disseminated sulphides relative to vein-hosted ores, suggesting the footwall rocks were porous resulting in pervasive mineralization rather than confinement to fracture networks. This is consistent with relict clastic textures in footwall volcanic rocks (Chapter 3, Section 3.3.2) suggesting they were at least partly volcanic breccias/volcaniclastic sequences rather than coherent lava flows. The footwall zones of deposits hosted by porous volcaniclastics are typically more strata-bound and laterally extensive than the "classic" discordant pipe that forms in coherent rocks, and have less of a tendency to show zonation (e.g. Large, 1992). High porosity in the footwall could therefore explain the uniformity of footwall alteration by the relatively unrestricted flow of late stage fluids penetrating the entire footwall and overprinting earlier alteration minerals, rather than being focussed on fracture-controlled zones. By the same reasoning, a high porosity may also explain the fact that a large vein network acting as the main feeder system (i.e. where the upwelling of mineralising fluids was focussed) is not observed.

Sub-seafloor drilling of actively forming seafloor systems has revealed abundant anhydrite in footwall zones, occurring particularly in veins associated with sulphides (e.g. Teagle et al., 1998; Roberts et al., 2003). Due to the retrograde solubility of anhydrite (Blout & Dickson, 1969), it is likely to dissolve as a hydrothermal system cools down (supported by observations from modern inactive sulphide chimneys, Hannington et al., 1995) and is therefore rarer in ancient VMS deposits compared to modern active systems. However, anhydrite has been reported to occur extensively in the mineralized footwall zones of the Snow Lake deposits (in the Precambrian Churchill Province of N. America; Franklin et al., 1981) and is abundant in the Kuroko deposits (Shikazono et al., 1983) confirming that it did form in ancient deposits. No anhydrite has been identified from Balta Tau. However, atypical textures in vein quartz associated with sulphides may be the result of replacement of anhydrite by quartz. In contrast to anhydrite, barite is generally insoluble in the hydrothermal environment (Blout, 1977), and is therefore more likely to be preserved in ancient deposits. At Balta Tau barite is found in the footwall but is not associated with sulphides, instead appearing to pre-date them. This suggests that conditions favourable for barite precipitation occurred prior to mainstage sulphide precipitation in the footwall, and it is possible that during sulphide precipitation anhydrite was the main sulphate phase to form, which was later replaced by quartz.

4.3 MASSIVE SULPHIDES

4.3.1 Introduction

Samples from the massive sulphide lens are dominated by pyrite-sphalerite-chalcopyrite and contain well preserved primary hydrothermal textures. There is a broad zonation from pyrite-chalcopyrite-sphalerite rich ores in the central lens to sphalerite(-pyrite-galena-tennantite) dominated ores in upper and marginal zones. There are insufficient samples available from the lower and central lens, mined out before the time of this study, to allow a detailed investigation of vertical or lateral zoning.

4.3.2 Mainstage sulphide ores

Collomorphic ores

A number of samples from central parts of the massive sulphide lens contain well preserved collomorphic textures in pyrite(-chalcopyrite) and pyrite-sphalerite. Pyrite(-chalcopyrite) ores comprise on average 70% pyrite with collomorphic zoning defined by concentric and radial inclusions of chalcopyrite, tennantite and galena which co-precipitated with the pyrite (Figure 4.11a to d). Chalcopyrite is much less abundant accounting for no more than 5% and forms thin, parallel, collomorphic bands as well as inclusions in pyrite.

In pyrite-sphalerite dominated ores the composition varies between 30 and 75% pyrite and 10 and 45% sphalerite, with minor to trace chalcopyrite (no more than 5%) and trace galena and tennantite. Pyrite is mostly inclusion-free and forms concentric and crustiform bands of fine euhedral cubic crystals 10-50μm intergrown with sphalerite (Figure 4.12a-e). Sphalerite is fine grained and contains dense, fine chalcopyrite disease as well as numerous inclusions of euhedral pyrite (Figure 4.13b). In transmitted light the majority of sphalerite is dark brown and semi-opaque due to chalcopyrite and pyrite inclusions, with thin, transparent pale beige margins which are mostly free of chalcopyrite and pyrite (Figure 4.13a). The transparency indicates a low Fe content of the sphalerite rims; the composition of cores are difficult to estimate since optical properties are masked by the chalcopyrite disease. The pyrite-sphalerite textures are complex and variable, with some samples showing finely alternating concentric zones while others have sphalerite cores rimmed with pyrite, and vice versa. One sample has patchy dentritic-like pyrite-sphalerite intergrowths (Figure 4.12e) interspersed with collomorphic textures, which appear to be the result of pyrite replacing sphalerite.

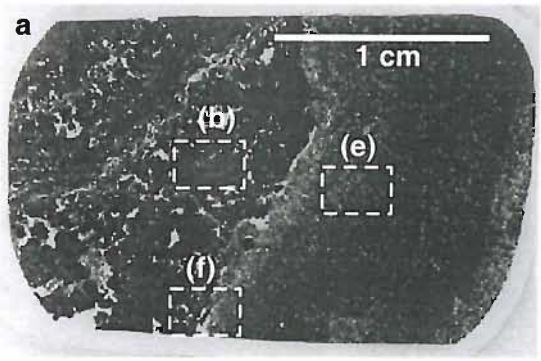

a. A sharp irregular contact between fine grained granular sulphides (right; see also figure (e)) and collomorphic sulphides (left; see also figure (b)). Sample 902.

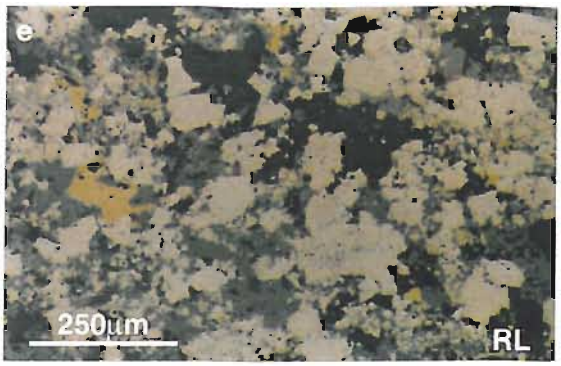

e. Granular sulphides comprising euhedral clusters of fine pyrite enclosed in a matrix of anhedral chalcopyrite-sphalerite-carbonate. Sample 902.

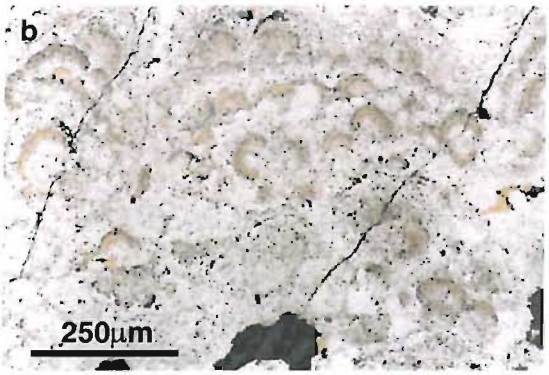

b. Pyrite dominated collomorphic ores with spherical/radial textures defined by intergrown chalcopyrite, tennantite and galena. Sample 902.

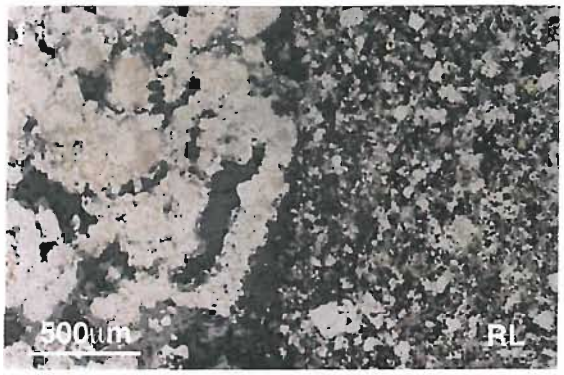

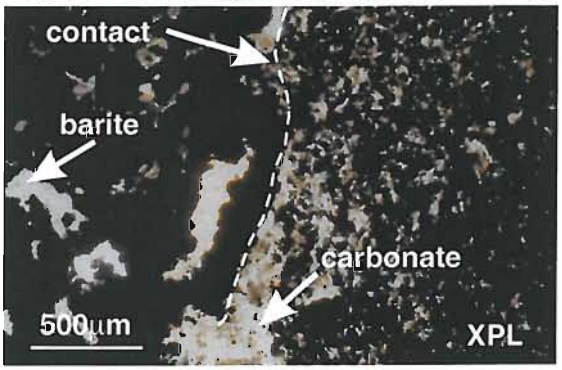

f. Close up view of the contact shown in (a). To the right in granular sulphides the gangue is mainly fine grained carbonate, whereas to the left barite infills cavities in the collomorphic ores. Sample 902.

c and d. Concentric chalcopyrite-tennantite (c) and radial galena (d) inclusions in the collomorphic pyrite shown in (b). Sample 902.

Figure 4.11. Primary hydrothermal collomorphic and granular textures in pyrite-dominated massive sulphides.

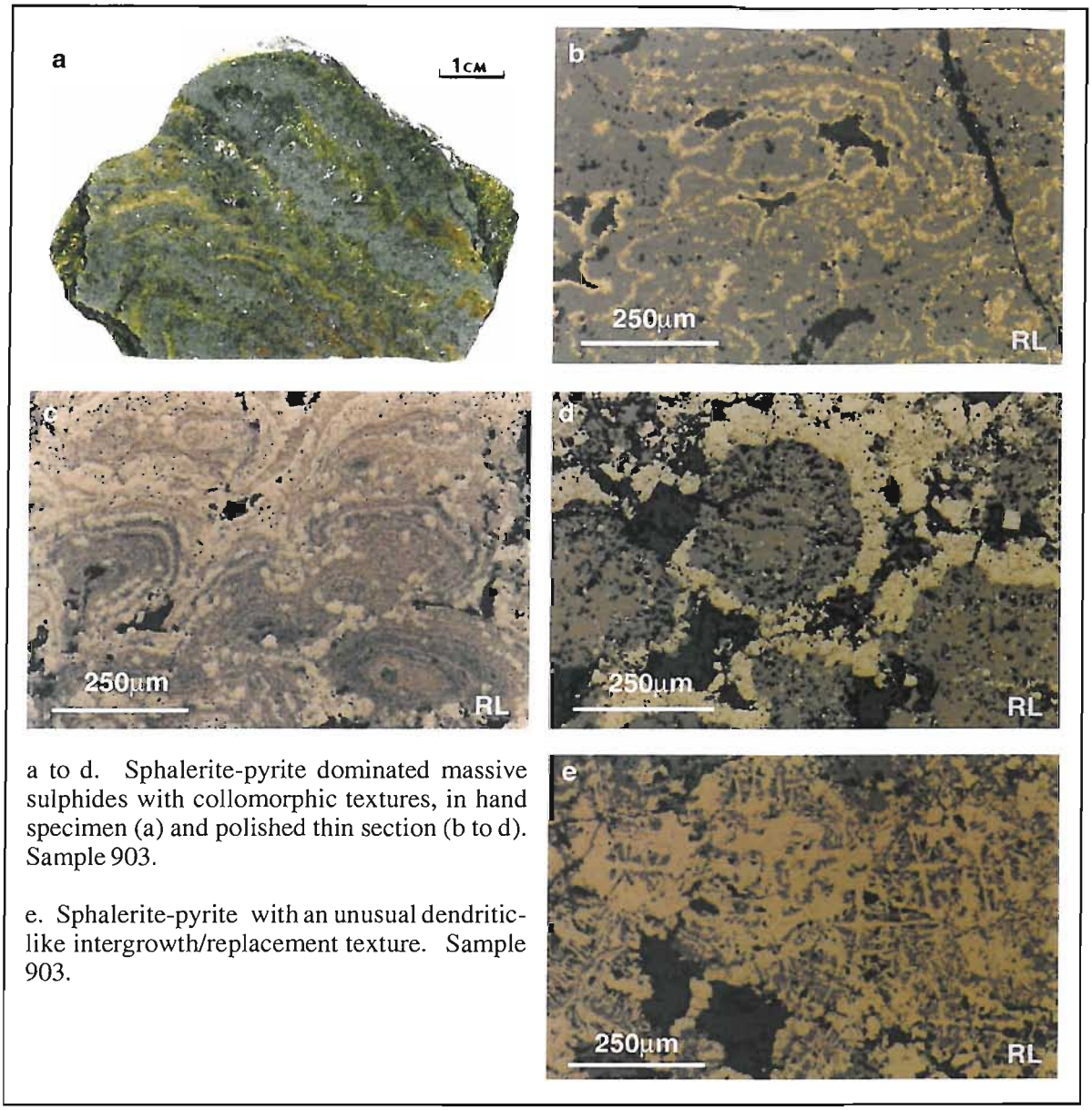

a to d. Sphalerite-pyrite dominated massive sulphides with collomorphic textures, in hand specimen (a) and polished thin section (b to d). Sample 903.

e. Sphalerite-pyrite with an unusual dendritic-like intergrowth/replacement texture. Sample 903.

Figure 4.12. Primary hydrothermal textures in collomorphic pyrite-sphalerite massive sulphides.

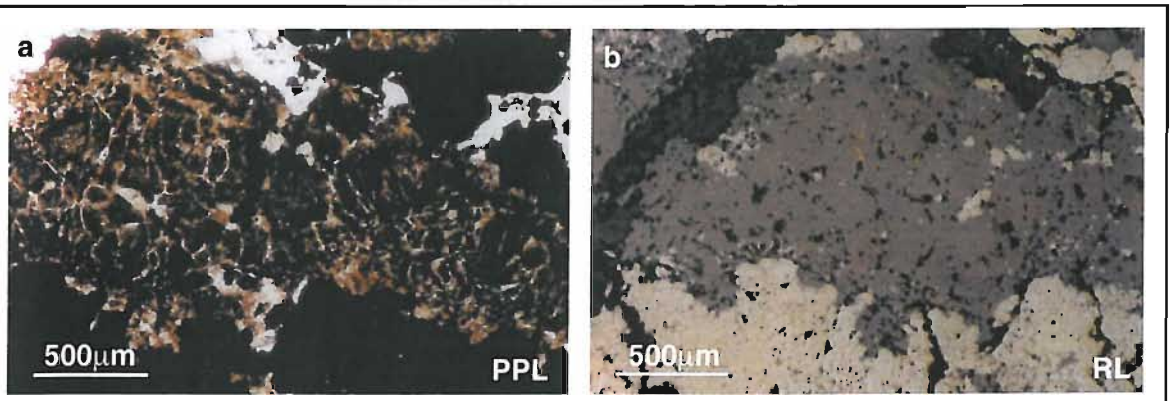

a and b. Typical sphalerite in collomorphic massive sulphides with extensive, dense chalcopyrite disease in crystal cores. In thin section, this can be seen both in transmitted light (a) as opaque cores with transparent beige crystal margins, and in reflected light (b) as yellowish patches in the centre of the sphalerite aggregate. Sample 903.

Figure 4.13. Chalcopyrite disease in sphalerite from collomorphic massive sulphides.

Gangue phases have abundances of 5 to 10% in collomorphic ores and consist of barite with minor quartz. In some samples coarse, tabular barite crystals up to 2mm in length form part of the collomorphic texture with no evidence of barite replacing sulphides or vice versa, suggesting co-precipitation of barite with sulphides (Figure 4.14a, b). In other samples single barite crystals infill irregular vugs in sulphides, suggesting that barite post-dates sulphide formation (Figure 4.14c). Generally barite-sulphide co-precipitation textures are more common in sphalerite-pyrite ores, while the barite appears later in pyrite(-chalcopyrite) ores. Quartz forms anhedral grains interstitial to sulphides which often enclose bleb-like sulphide inclusions, in particular sphalerite, which indicate that although quartz is later than the sulphides as indicated by the interstitial textures, it precipitated soon afterwards during the same mineralising event.

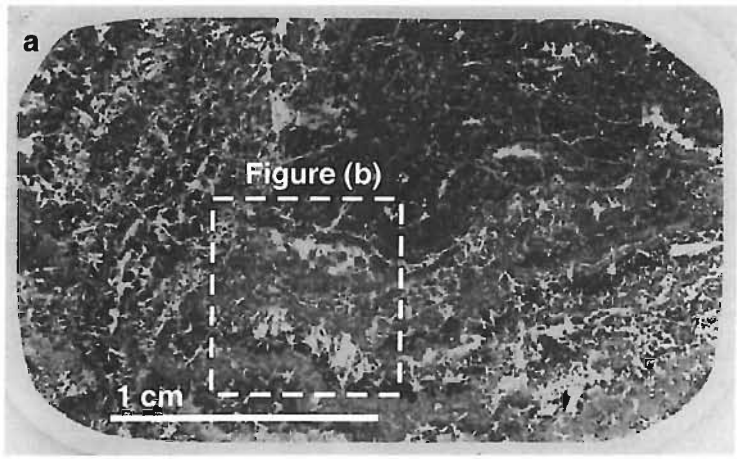

a and b. Collomorphic sphalerite-pyrite dominated sulphides with significant barite. The barite forms bands within sulphides and in coarser zones barite forms tabular euhedral crystals orientated approximately 90° to colloform bands (enlargment and sketch, b), suggesting overall co-precipitation with sulphides rather than later precipitation infilling vugs. Sample 903.

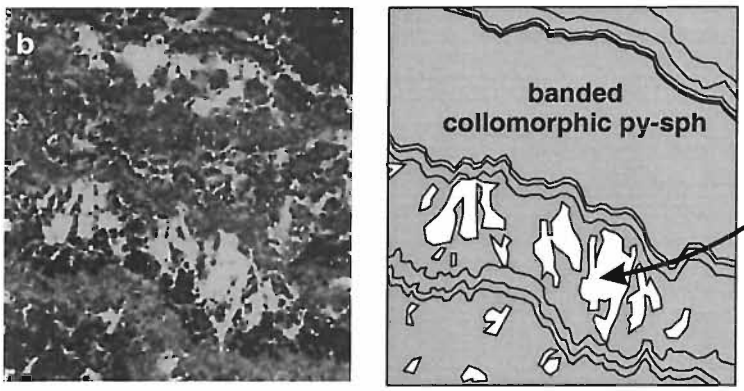

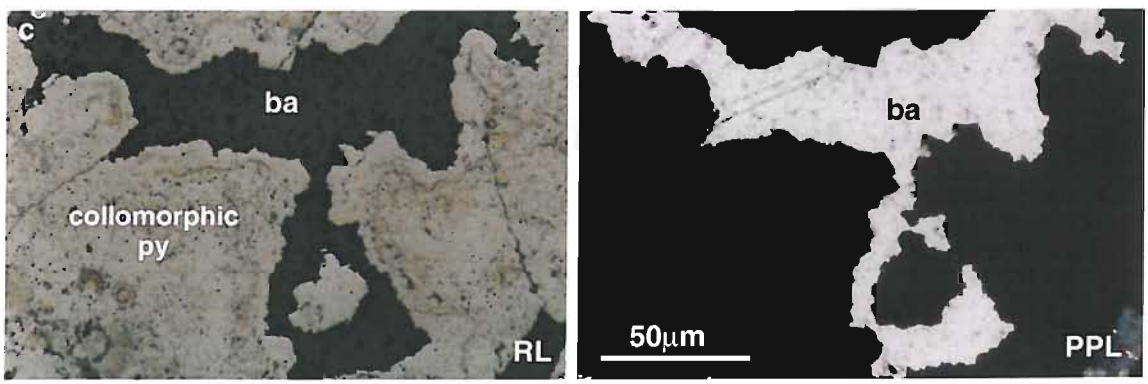

c. Exampe of a single barite crystal infilling a vug in collomorphic pyrite. Sample 902.

Figure 4.14. Textural relationship of barite and sulphides in massive sulphide ores.

Granular sulphides

Some samples of fine grained pyrite-chalcopyrite(-sphalerite) from the central massive sulphide lens are more granular without collomorphic textures. Pyrite-chalcopyrite rich granular sulphides contain on average 80% pyrite, 15% chalcopyrite and <5% sphalerite with trace amounts of tennantite (Figure 4.15a, b). Pyrite forms both coarse mm-cm aggregates of subhedral crystals (up to 0.5mm) which show no evidence of crystal zoning, and abundant finer euhedral crystals (20 to 100μm). The pyrite is enclosed in a matrix of anhedral to subhedral fine to medium grained chalcopyrite with minor sphalerite and traces of tennantite, the latter forming inclusions in chalcopyrite (Figure 4.15b). Fractures in the coarse pyrite aggregates are filled with chalcopyrite. Arsenopyrite is a rare phase in these samples, forming coarse euhedral crystals 50-200μm which are also fractured and enclosed in chalcopyrite with sphalerite (Figure 4.15c). Gangue phases account for less than 2% and consist of anhedral, transparent, colourless quartz together with pockets of chlorite intergrown with and infilling vugs in sulphides. The chlorite is bright green and pleochroic in plane polarised light, and shows anomalous blue-yellow birefringence in crossed polars (Figure 4.15d) suggesting a moderate to high Fe content (in contrast to footwall chlorites; sections 4.2.2 and 4.2.6). The finely intergrown nature of quartz and chlorite with sulphides and the lack of replacement or fracture-related textures suggest the quartz, chlorite and sulphides co-precipitated.

A more sphalerite-rich sample (sample 902) with similar granular textures to the pyrite-chalcopyrite ores comprises fine granular pyrite (55%) enclosed in a matrix of sphalerite (25%), chalcopyrite (5%) with a significant proportion of gangue (barite and carbonate, 15%) (Figure 4.11e). All of these phases are intergrown and fairly equigranular, averaging 50 to 200μm. There is a sharp irregular contact between these granular sulphides and pyrite-dominated collomorphic sulphides (Figure 4.11f), marked by abundant carbonate which penetrates the granular sulphides with abundance decreasing away from the contact as carbonate gives way to barite, but does not penetrate the collomorphic ores which contain only barite. This suggests the carbonate precipitated later than the sulphides and barite, during either late stages of hydrothermal activity or diagenesis, infilling porosity along the contact of the two facies and penetrating the potentially more porous granular sulphides close to the contact. The sharp, irregular nature of this contact and the significant textural differences of the sulphides either side suggests sulphides formed in different parts of the system were brecciated and re-consolidated, and the lack of deformation or tectonic fabric in this sample points to this being a syn-formational process rather than post-formational tectonic reworking of ores.

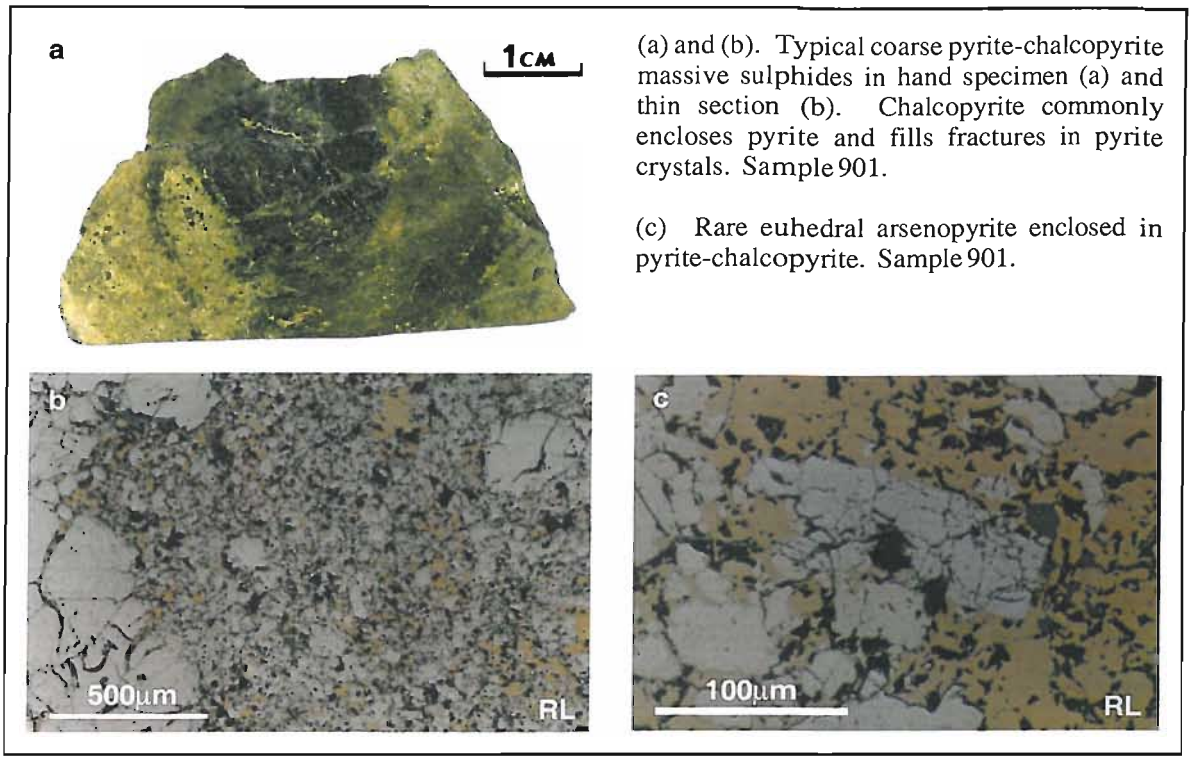

(a) and (b). Typical coarse pyrite-chalcopyrite massive sulphides in hand specimen (a) and thin section (b). Chalcopyrite commonly encloses pyrite and fills fractures in pyrite crystals. Sample 901.

(c) Rare euhedral arsenopyrite enclosed in pyrite-chalcopyrite. Sample 901.

Figure 4.15. Primary hydrothermal textures in pyrite-chalcopyrite dominated granular massive sulphides.

4.3.3 Late stage sulphides

Thin fractures and vugs in collomorphic and granular sulphides are commonly filled with a coarser grained assemblage of subhedral chalcopyrite-tennantite-sphalerite-galena (Figure 4.16a, b), together with euhedral rhombic crystals of arsenopyrite 50 to 100µm in size which are morphologically distinct from the coarse, blocky arsenopyrite found with mainstage pyrite in granular ores. The fracture filling nature of this assemblage suggests that it post-dates formation of the collomorphic ores.

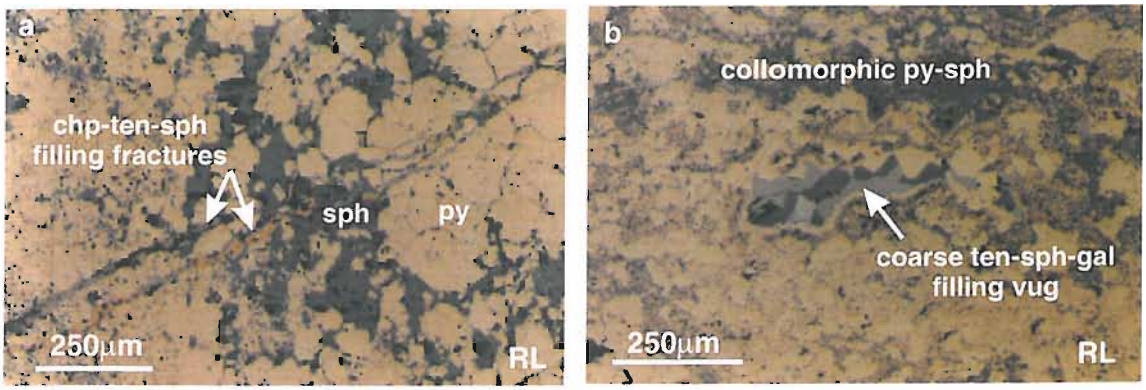

a. Fracture in granular pyrite-sphalerite infilled with later chalcopyrite-tennantite-sphalerite. Sample 910.

b. Vug in finely intergrown and collomorphic pyrite-sphalerite infilled with later, coarse sphalerite-tennantite-galena. Sample 910.

Figure 4.16. Late stage sulphide assemblage filling vugs and fractures in granular and collomorphic massive sulphides.

4.3.4 Sphalerite-rich partially recrystallized sulphides

Sphalerite-rich ores from upper, marginal zones of the massive sulphide lens have textures suggestive of partial recrystallization. These ores comprise on average 50% sphalerite, 10% pyrite, 10% galena, 10% tennantite, and traces of chalcopyrite (Figure 4.17a).

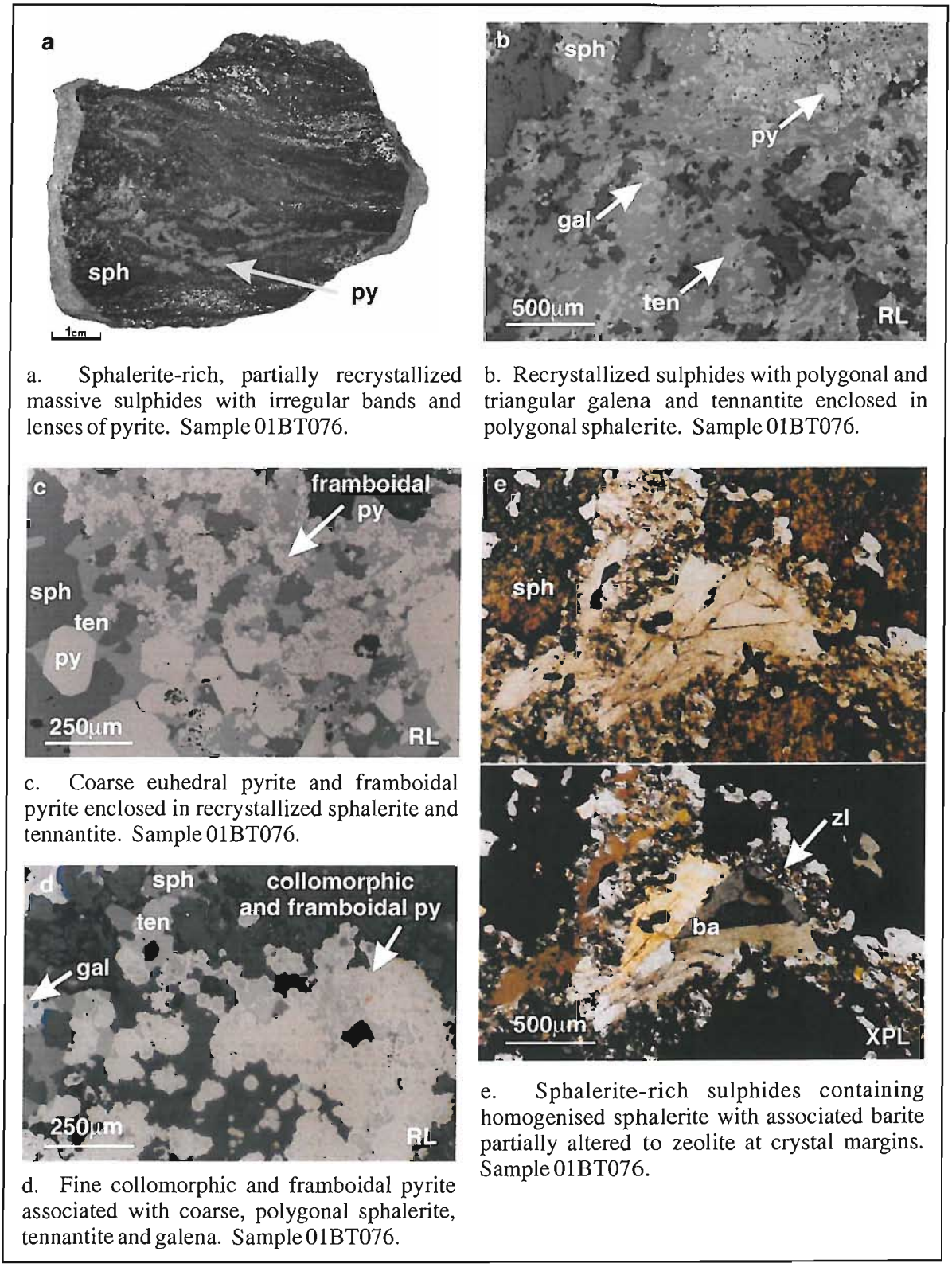

a. Sphalerite-rich, partially recrystallized massive sulphides with irregular bands and lenses of pyrite. Sample 01BT076.

b. Recrystallized sulphides with polygonal and triangular galena and tennantite enclosed in polygonal sphalerite. Sample 01BT076.

c. Coarse euhedral pyrite and framboidal pyrite enclosed in recrystallized sphalerite and tennantite. Sample 01BT076.

d. Fine collomorphic and framboidal pyrite associated with coarse, polygonal sphalerite, tennantite and galena. Sample 01BT076.

e. Sphalerite-rich sulphides containing homogenised sphalerite with associated barite partially altered to zeolite at crystal margins. Sample 01BT076.

Figure 4.17. Primary and recrystallized textures in sphalerite dominated massive sulphides.

Zones of equigranular and polygonal textures in all sulphides except for pyrite are suggestive of localised recrystallization and annealing (Figure 4.17b), and there is development of a patchy, weak foliation. Pyrite occurs as both euhedral equant crystals of similar grain size to the recrystallized sulphides, and as very fine grained collomorphic and framboidal masses forming mm scale irregular bands and lenses (Figure 4.17c, d). The framboidal and collomorphic pyrite are typical of primary hydrothermal textures, suggesting that in places the sphalerite-tennantite-galena has recrystallized without modification of the co-existing pyrite. The coarser euhedral pyrite is more typical of recrystallization and may have formed from the recrystallization and coarsening of framboidal and collomorphic pyrite. The gangue in these sulphides is mainly barite (10% abundance), forming coarse euhedral to subhedral tabular crystals up to 5mm generally interstitial to sulphides, with minor quartz (5%) forming anhedral interlocking grains (50-200μm). The sulphides and barite are in places replaced by minor pumpellyite (identified by microprobe; Chapter 5, Section 5.4.6) which forms spherical radiating aggregates with no preferred orientation (similar to textures in Figure 4.28 from the gold-barite-rich massive sulphides). Barite is also replaced at crystal margins by granular to coarse zeolite (scolecite, identified by microprobe, Chapter 5, Section 5.4.6) (Figure 4.17e). The muscovite and zeolite clearly post-date ore formation and formed during diagenesis or metamorphism.

4.3.5 Massive sulphide ore formation and paragenesis

Paragenesis

The suggested paragenetic sequence for massive sulphides is shown in Figure 4.18. An early pyrite(-arsenopyrite) stage reflects the large pyrite aggregates found in the pyrite-chalcopyrite rich granular ores which pre-date the enclosing chalcopyrite(-sphalerite-tennantite-chlorite-quartz) matrix. In collomorphic ores, textures on a micro-scale suggest multiple cycles of pyrite and sphalerite precipitation with variable minor to trace chalcopyrite, galena and tennantite, but on a larger scale these textures can be generalised as co-precipitation of these phases. A chalcopyrite-sphalerite-tennantite-galena-arsenopyrite assemblage filling vugs and fractures in the massive sulphides relates to a late stage of mineralization.

Barite is the most abundant gangue phase in collomorphic ores where it appears to have precipitated after the pyrite-dominated sulphides but co-precipitated with sphalerite-pyrite ores. Quartz and Fe-chlorite are both intergrown with and fill vugs in sulphides, suggesting they co-precipitated with sulphides. In the one sample containing carbonate, textures indicate the carbonate may be of late stage hydrothermal or diagenetic origin.

There is no evidence of metamorphic overprinting in the collomorphic and granular ores from the central massive sulphide orebody. However, sphalerite-rich samples from the uppermost horizons exhibit typical annealing textures in sphalerite-tennantite-galena-chalcopyrite reflecting recrystallization of these phases, which probably occurred during regional metamorphism and deformation (discussed below). The recrystallized nature of the sphalerite-galena-tennantite(-chalcopyrite) masks the primary hydrothermal paragenesis of this assemblage. The development of minor zeolite and pumpellyite replacing sulphides and barite probably formed either during diagenesis or metamorphism.

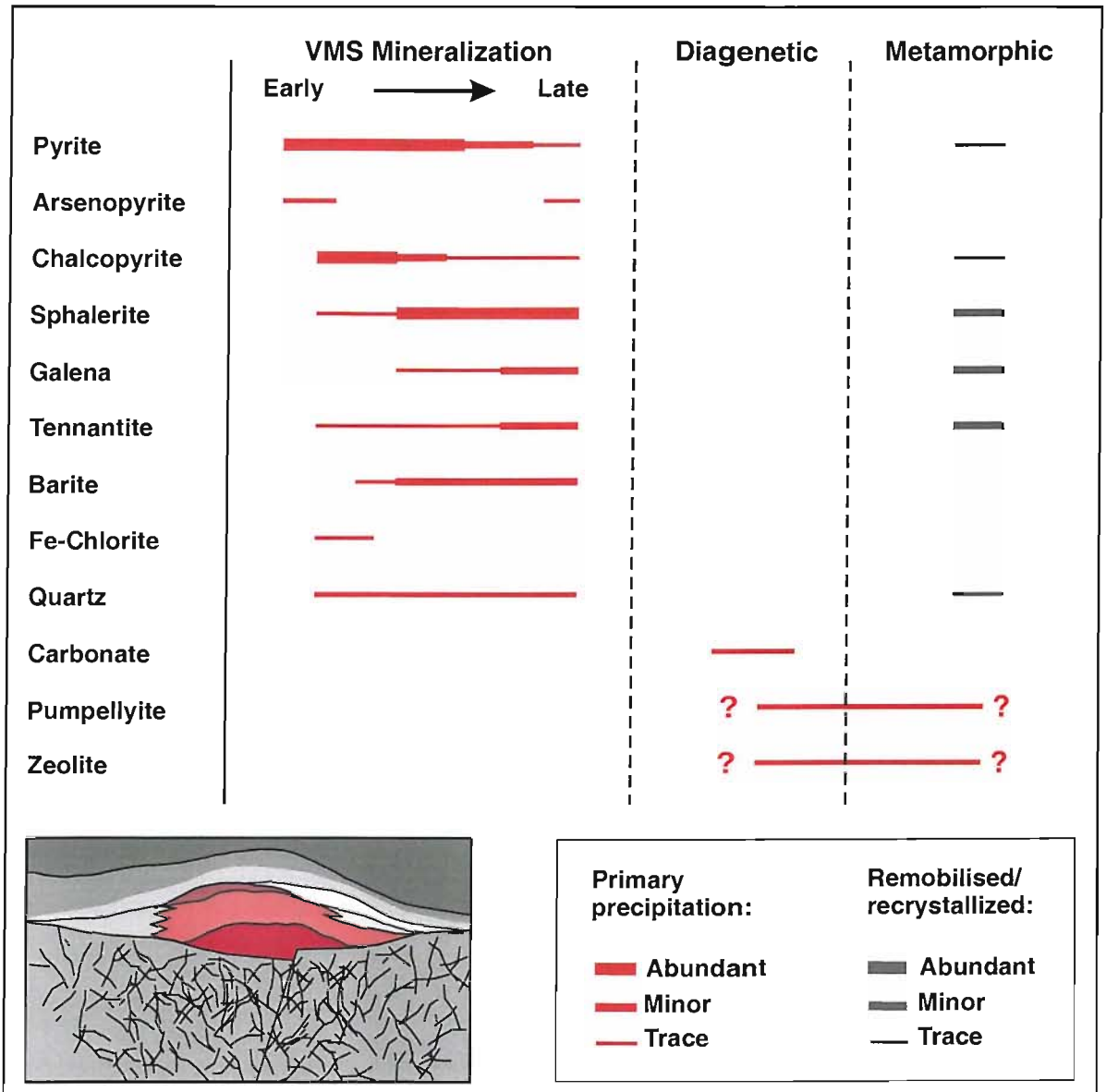

Schematic sketch (lower left) indicates the location of massive sulphide horizons (highlighted) relative to the rest of the Balta Tau mineralization (see also Figure 4.1).

Figure 4.18. Paragenesis of massive sulphides.

Ore formation and zoning

Textures in both collomorphic and granular sulphides are comparable with samples recovered from active chimneys and mounds of modern sea floor systems (e.g. the granular pyrite-chalcopyrite is similar to samples from the active TAG mound in Hannington et al. 1995, page 132, Figure 15c; framboidal pyrite associated with galena-tennantite-sphalerite comparable with the primary pyrite textures in recrystallized sphalerite ores from the Central Okinawa Trough, Japan, Halbach et al., 1993, pg 2217, Figure 6P). These textures, together with the conformable nature of massive ores, support a sea-floor depositional environment for the massive sulphides at Balta Tau. The broad zonation from pyrite-chalcopyrite ores in the lower/central orebody to sphalerite-rich ores at upper and marginal zones is typical of the zonation seen in a number of other Uralian VMS deposits (e.g. Prokin and Busleav, 1999; Herrington et al., 2002) as well as ancient deposits in other mining districts (e.g. Stanton, 1955; Braithwaite 1974; Franklin et al., 1981; Large, 1992) and has also been observed at modern actively forming seafloor systems (e.g. Fouquet et al., 1993; Halbach et al., 1993; Hannington et al., 1995). Formation of this zoning is discussed in Chapter 7, Section 7.4.5.

Partially recrystallized sphalerite-rich ores retain some primary framboidal and collomorphic pyrite textures. Recrystallization of sulphides can occur at the seafloor during late stages of ore formation and zone refining (e.g. Hannington et al., 1995; Halbach et al., 1993). However, the localised development of a weak foliation and the location of these sulphides close to the contact with highly deformed and sheared hanging-wall volcanics suggest that recrystallization probably occurred during regional metamorphism and deformation. The preservation of pyrite textures such as framboids reflects the ability of pyrite to resist recrystallization at low, sub-greenschist temperatures where other sulphides will more readily recrystallize, as noted by Craig and Vokes (1993), and primary pyrite textures in otherwise recrystallized ores have been noted from other ancient VMS deposits (e.g. Natale, 1966; Sinclair et al., 2000). Textures in the enclosing sphalerite-galena-tennantite are typical of annealing in recrystallized sulphides, and similar textures are described by Stanton (1964) where galena as the minor phase forms small lenses and triangular grains in sphalerite, the dominant phase.

Fe-rich chlorite occurs in minor to trace amounts in granular pyrite-chalcopyrite ores with textures indicating co-precipitation of this chlorite and sulphides. This suggests that the Fe-chlorite precipitated from the ore forming hydrothermal fluid together with the mainstage sulphides, unlike the Mg-rich chlorite in the footwall (Sections 4.2.2, 4.2.6) which post-dates sulphide formation.

4.4 LAYERED SULPHIDES

4.4.1 Introduction

The thin marginal portion of the massive sulphide lens (exposed in the pit at the time of mapping) comprises compositionally layered sulphides. Although these form part of the massive sulphide orebody, they are described separately as "layered sulphides" since they are texturally very distinct from the other massive sulphide ores.

4.4.2 Mineralogy and textures

The compositional layering is defined on a mm to cm scale by alternating sphalerite, chalcopyrite, and to a lesser extent pyrite, galena and tennantite-rich bands that are approximately parallel to footwall and hanging-wall contacts. Some bands are traceable for over 1m across exposures (Figure 4.19a), while others are irregular or lens-like and discontinuous (Figure 4.19b).

a. Layered sulphides dominated by sphalerite-chalcopyrite-pyrite exposed in the open pit. Compositional layering is on a mm to cm scale with some layers traceable for metres.

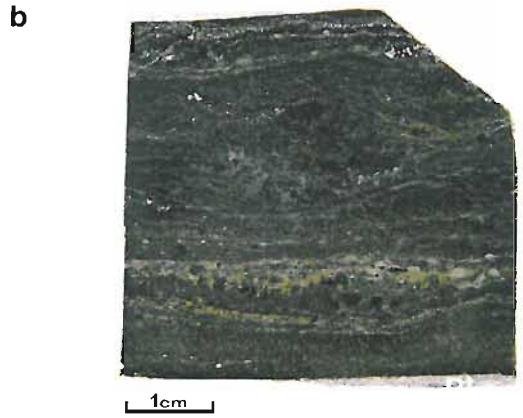

b. Layered sulphides in hand specimen, with layers of fine brown sphalerite, chalcopyrite, chalcopyrite-pyrite and coarse, dark sphalerite crystals. Sample 01BT033.

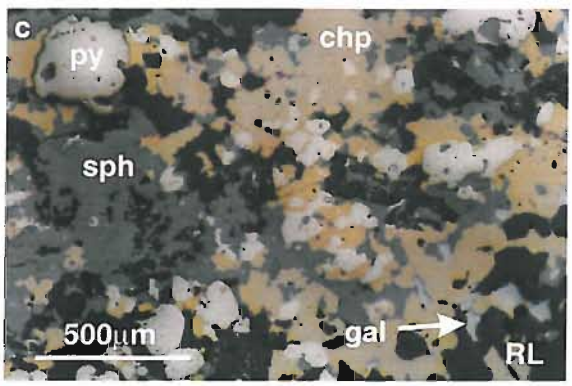

c. Chalcopyrite-pyrite rich layer, with a coarse pyrite(I) crystal (top left) displaying characteristic embayments, coroded crystal margins and high relief. Sample BL10-19B.

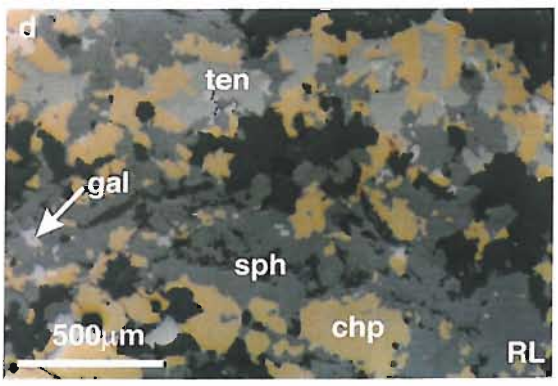

d. Layered sulphides with tennantite-chalcopyrite(-galena) at the top passing into sphalerite and then chalcopyrite at the bottom. Gangue is mainly quartz. Sample BL10-19B.

Figure 4.19. Textures and mineralogy of compositional layering in layered sulphide ores.

The majority of layered ores comprise greater than 90% sulphide minerals, with less typical samples containing as low as 75% sulphides. Sphalerite is by far the most abundant mineral, generally accounting for 40 to 70%, followed by chalcopyrite (10 to 35%), pyrite (mostly 2 to 5%, but varies between <1 to 25%), tennantite (commonly <1%, but in some samples up to 10%) and galena (mostly <1 to 5%, rarely as high as 15%).

Sphalerite

Sphalerite forms two habits. The first are large (0.5-5mm) euhedral crystals with complex dark brown/yellow/orange/beige zoning and contain minor chalcopyrite disease mainly in yellow zones. These crystals form indistinct layers within finer grained sphalerite and also occur as isolated crystals interrupting layers of other sulphides (Figures 4.20a, b, c; 4.21c) and are referred to as first generation sphalerite (sphalerite(I)). The surrounding sulphide, quartz and muscovite matrix encloses and wraps around these large sphalerite crystals, sometimes partially replacing the sphalerite at the margins (Figure 4.20b). The second generation of sphalerite (sphalerite(II)) is finer grained (50-200μm), granular, subhedral and very transparent. This sphalerite shows less zoning and varies from almost colourless to beige and pale orange, rarely with darker red/orange cores, and is free of chalcopyrite disease except for small isolated patches and coarse chalcopyrite disease at crystal margins and along fractures. The sphalerite(II) crystals are the major constituent of the sphalerite layers, and often enclose larger first generation sphalerite crystals (Figures 4.20d).

Chalcopyrite, pyrite, galena, tennantite and rare phases

Chalcopyrite forms irregular anhedral masses up to 3mm in size, often intergrown and interlocking with sphalerite, with the grains commonly elongated parallel to the compositional layering. Chalcopyrite is the most abundant sulphide after sphalerite, with most samples containing numerous thin chalcopyrite-rich layers (Figures 4.19c, 4.20b). Galena occurs as coarse (up to 1mm), anhedral grains often intergrown with sphalerite, chalcopyrite and tennantite. Galena-rich layers often have either equigranular, polygonal textures or grains elongated oblique to compositional layering. Both of these textures are suggestive of remobilisation and recrystallization of galena, which is discussed further in Section 4.4.3. Tennantite is present as small anhedral grains commonly associated with chalcopyrite, which are generally scarce and isolated but sometimes form tennantite-rich bands (Figure 4.19d). Pyrite occurs in two distinct habits. The first are coarse crystals up to 1mm which are often concentrated in chalcopyrite-rich bands and have well developed embayments and corroded, irregular margins (Figure 4.19c) which results in a skeletal texture in extreme cases; these are referred to as pyrite(I). Pyrite also occurs as finer euhedral crystals (<100um) without significant embayments, which form discrete and often discontinuous bands in sphalerite, referred to as pyrite(II). Hessite (AgTe) is a very rare phase (identified by microprobe, Chapter 5, Section 5.2.9) occurring in 50-200μm grains associated with galena enclosed in sphalerite.

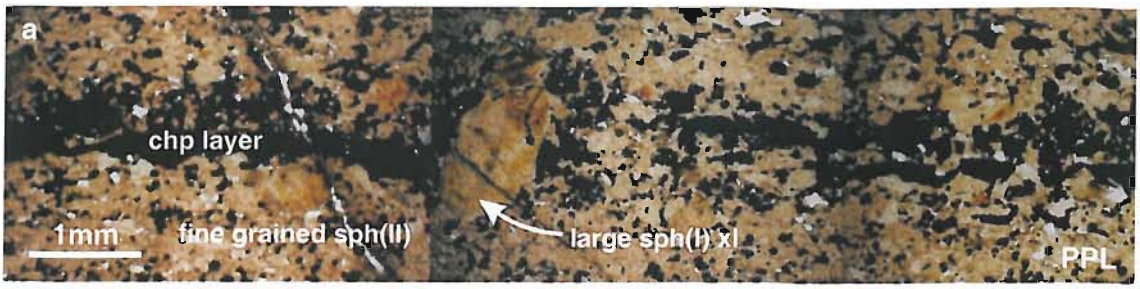

a. Thin continuous chalcopyrite layer interrupted by a large, zoned sphalerite(I) crystal. Sample 01BT033b.

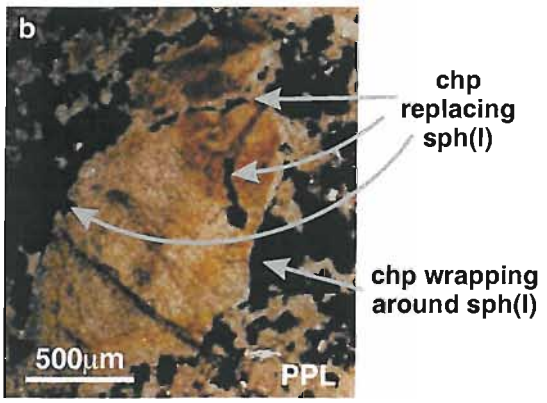

b. Enlargement of the coarse sphalerite(I) crystal shown in (a). The enclosing chalcopyrite replaces the sphalerite(I) at the margins, in one area towards the center, and along a fracture. Sample 01BT033b.

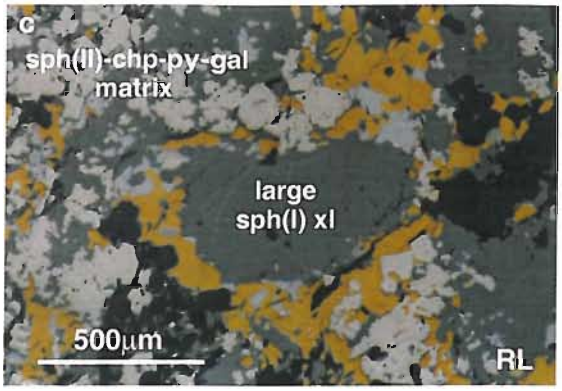

c. Coarse sphalerite(I) crystal enclosed in a finer grained sphalerite(II)-chalcopyrite-pyrite(-galena) matrix which replace the sphalerite(I) at crystal margins giving an irregular boundary. Sample BL10-18A.

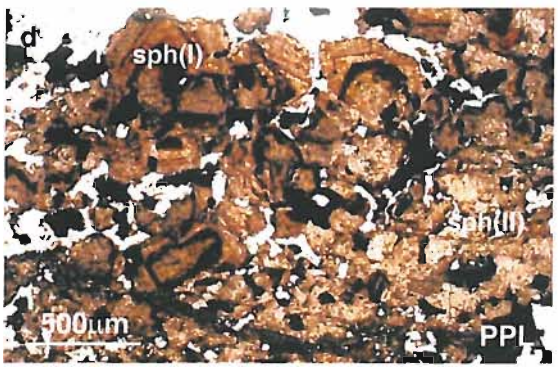

d. Sphalerite layer containing both coarse, euhedral, zoned sphalerite(I) crystals, and finer pale beige homogeneous subhedral to anhedral sphalerite(II). Both are transparent with little to no chalcopyrite disease. Sample 01BT012.

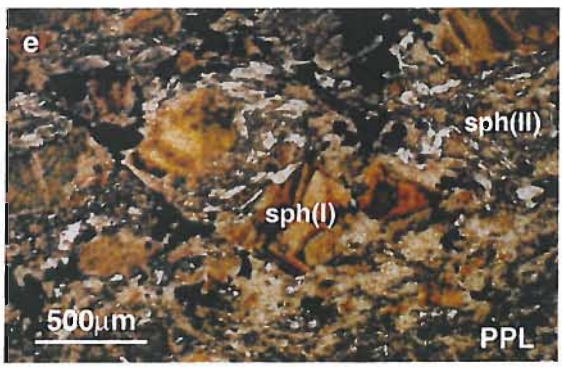

e. Sphalerite-rich layer containing fragmented coarse, zoned sphaleite(I) crystals enclosed in a matrix of finer, anhedral, transparent, beige sphalerite(II) with muscovite. Sample 01BT032.

Figure 4.20. Sphalerite textures in layered sulphides.

Gangue phases

Gangue phases account for between 5 and 25% of the layered ores, and consist of variable proportions of quartz and muscovite. Quartz forms anhedral grains <500μm with sutured grain boundaries which are mostly interstitial to sulphides and most abundant in chalcopyrite-rich layers.

Quartz is very transparent and colourless, and sometimes contains inclusions of fine grained, pale beige sphalerite. Muscovite is abundant in both sphalerite-rich and galena-rich layers, but scarce in chalcopyrite dominated layers. Fine platey crystals are usually aligned approximately parallel to compositional layering (Figure 4.21a), and commonly replace sulphides (Figure 4.21a, b). In sphalerite-rich layers muscovite tends to be intergrown with fine grained sphalerite, forming a matrix that wraps around large first generation sphalerite crystals (Figures 4.20e, 4.22c).

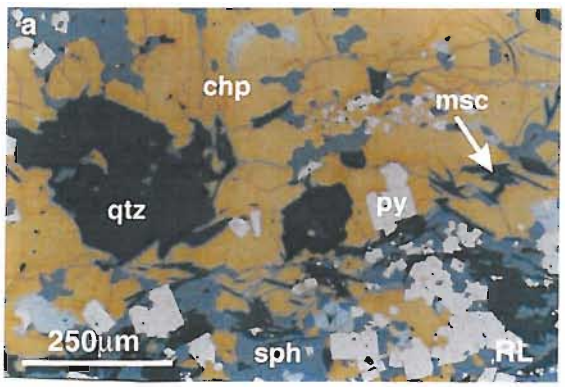

a. Muscovite replacing chalcopyrite and sphalerite; coarse gangue mineral is quartz. The muscovite is aligned approximately parallel to compositional layering, and there are well developed covellite rims where the muscovite is in contact with sulphides. Sample BL10.18A.

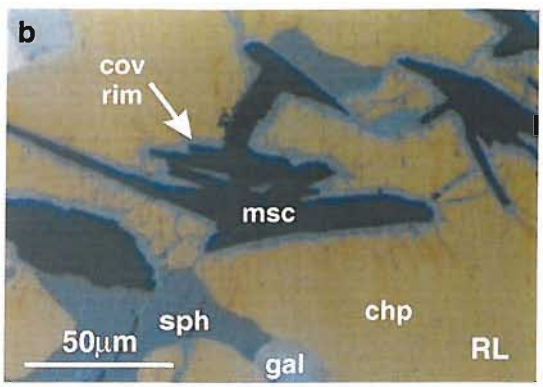

b. Close-up view of covellite rimming chalcopyrite and sphalerite where they come into contact with muscovite. Sample BL10.18A.

Figure 4.21. Textural relationships between sulphides and muscovite in layered ores.

4.4.3 Textural overprinting of compositional layering

In some galena-rich layers, a second fabric can be identified which is oblique to the compositional layering, defined by approximately parallel elongate grains and aggregates of anhedral galena and chalcopyrite, and sometimes tennantite (Figure 4.22a, b). This is suggestive of remobilisation of galena-chalcopyrite-tennantite and recrystallization during metamorphism and deformation. Other galena-rich layers have a polygonal, equigranular annealing texture in galena, sphalerite, tennantite and quartz with abundant triple junctions (Figure 4.22d), indicative of localised recrystallization during diagenesis or metamorphism without significant deformational stress. The confinement of these late stage fabrics to galena-rich layers suggests that galena and to a lesser extent chalcopyrite and tennantite are more easily remobilised than the sphalerite and pyrite.

Muscovite occurs in minor to trace amounts throughout the ores replacing sulphides and tends to be concentrated in sphalerite rich layers. Crystals are aligned parallel to compositional layering, however they clearly replace sulphides and where in contact with chalcopyrite and galena

secondary covellite-digenite rims border these sulphides (Figure 4.21b, c). The aligned muscovite wrap around coarse generation 1 sphalerite, and where a second fabric is defined by galena(-chalcopyrite-tennantite) the muscovite orientation is modified and shows weak development of a crenulation cleavage (Figure 4.22c). Therefore although the muscovite clearly replaces layered sulphides, the association with specific (sphalerite-rich) layers, orientation of grains parallel to compositional layering and modification of grain orientation during metamorphic overprinting suggest the muscovite formed during later stages of the same process that formed the compositional layering rather than during regional metamorphism and deformation.

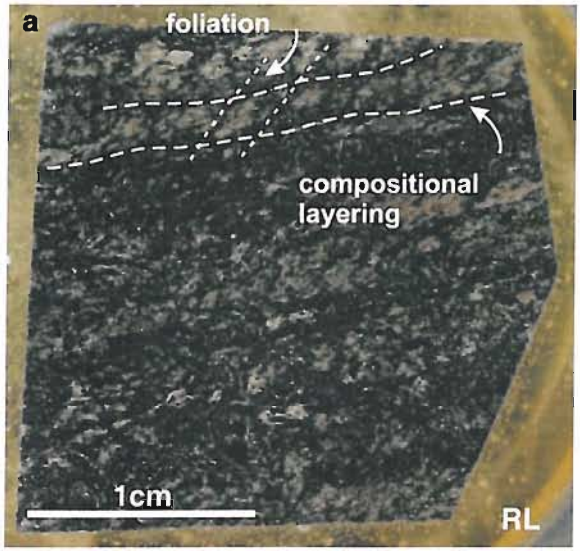

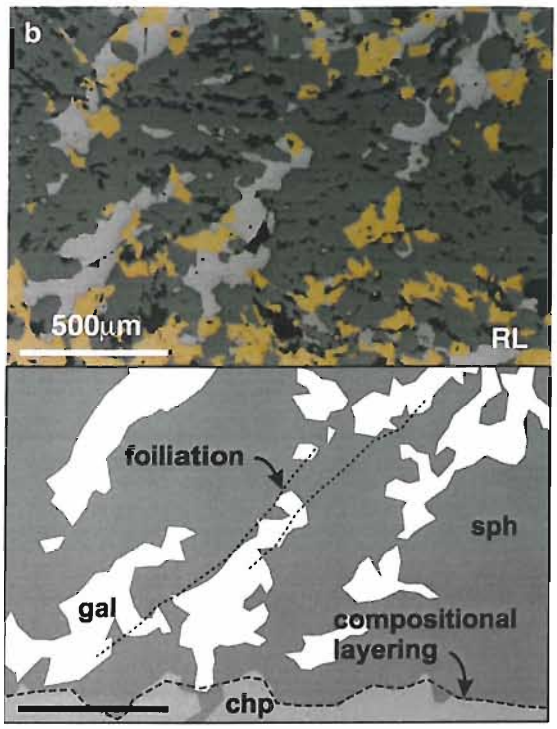

a and b. Relationship between compositional layering and second overprinting fabric, the latter defined by parallel segregations of galena and chalcopyrite oblique to the compositional layering. Sample 711A.

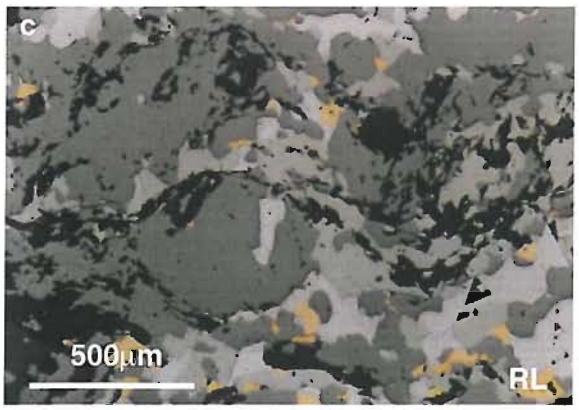

c. Coarse rounded sphalerite crystal enclosed in a finer matrix of anhedral sphalerite, tennantite, chalcopyrite and galena with muscovite. The muscovite defines a foliation which wraps around the coarse sphalerite. Sample 711A.

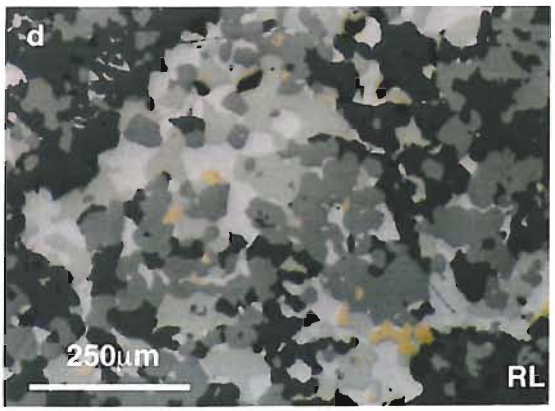

d. Equigranular sphalerite-tennantite-galena with minor chalcopyrite, showing unfoliated, polygonal textures typical of annealing and recrystallization. The gangue phase is mainly quartz. Sample BL10.19B.

Figure 4.22. Textures overprinting compositional layering in layered sulphide ores.

4.4.4 Layered sulphide paragenesis and ore formation

Paragenesis

The inferred paragenesis for layered ores is shown in Figure 4.23. Textures suggest the coarse sphalerite(I) and embayed pyrite(I) crystals formed at an earlier stage than the rest of the sulphides. The interlocking, equigranular nature of the layered sphalerite(II), chalcopyrite, tennantite, galena, pyrite(II), quartz and traces of hessite do not show evidence of a systematic paragenetic sequence and probably formed at the same time. The formation of these compositional layers is most likely to have occurred during late stages of ore formation or during diagenesis, as discussed in the following section.

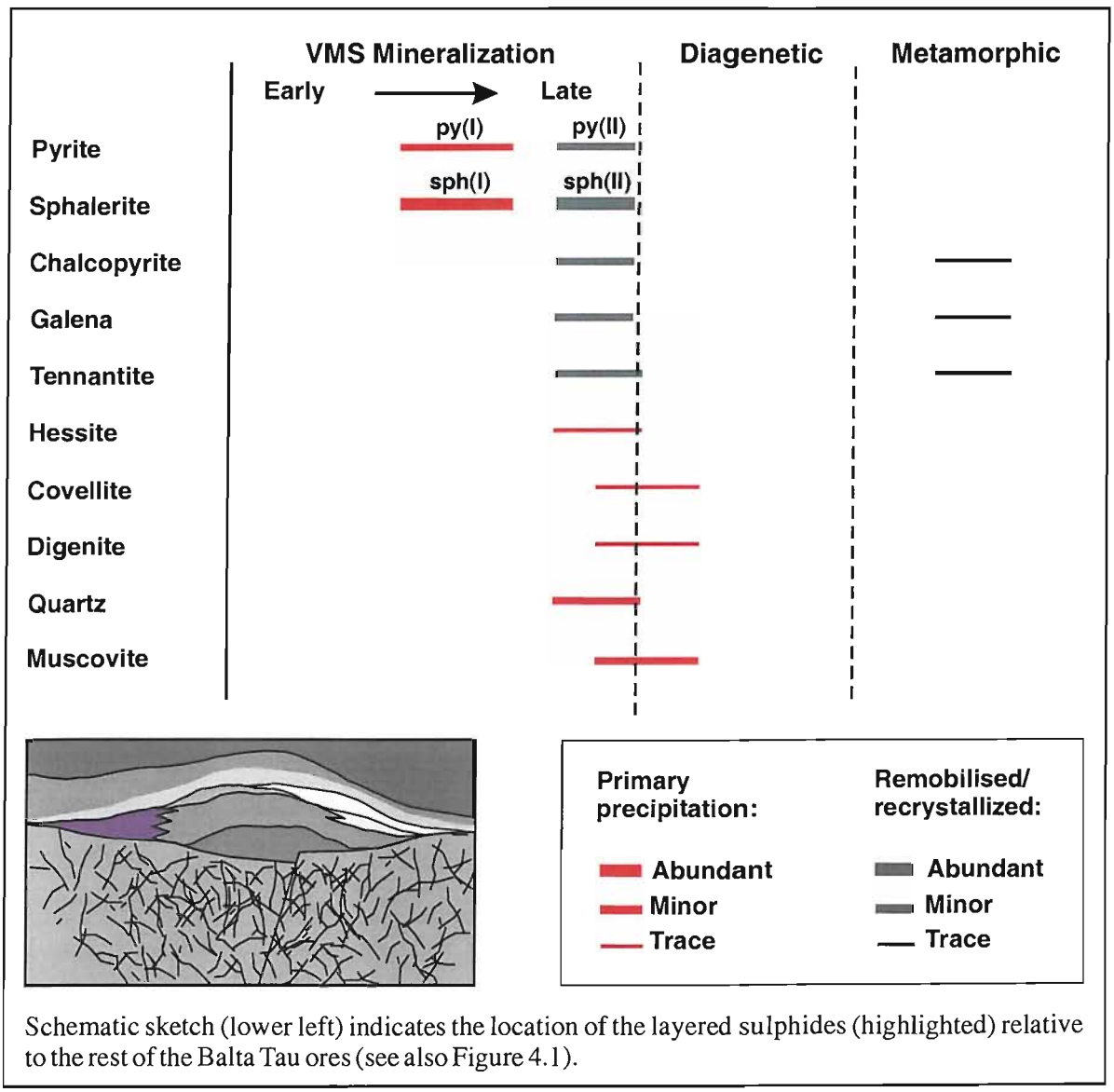

Schematic sketch (lower left) indicates the location of the layered sulphides (highlighted) relative to the rest of the Balta Tau ores (see also Figure 4.1).

Figure 4.23. Paragenesis of layered ores.

The muscovite and secondary covellite-digenite post-date the formation of layered sulphides, and probably formed during late stages of the same process that was responsible for the compositional

layering. Metamorphic overprinting occurred subsequent to the formation of layering and resulted in local remobilisation of galena, chalcopyrite and tennantite forming an oblique foliation, and recrystallization and annealing of galena-sphalerite-tennantite-quartz.

Formation of compositional layering

Compositionally layered or banded ores are common in ancient VMS deposits, and their origin has long been a source of debate and controversy (e.g. Vokes, 1969, Green et al., 1981; Large, 1992). Compositionally layered and segregated sulphides similar to the material from Balta Tau have been described from a number of deposits including the Archean deposits of Canada, particularly in upper and marginal ores, (Franklin et al., 1981); deposits of the Bathurst Area, New South Wales (Stanton, 1955; in particular textures in Figure 11, page 696), the Hercules and Rosebery deposits, Tasmania (Braithwaite, 1974; Green et al., 1981; Aerden, 1993; 1994); Stekerjokle Deposit of Sweden (Franklin et al., 1981), and the Ashele Deposit in Xinjiang, NW China (Denghong et al. 1998).

A variety of mechanisms have been proposed for the formation of these textures, including a metamorphic origin (e.g. Vokes, 1969 and references therein), a clastic sedimentary origin (e.g. Large & Both, 1980; Eldridge et al., 1983) and selective replacement of host rocks controlled by parallel fractures or cleavage (e.g. Watson, 1959; Aerden 1993; 1994).

The compositionally layered sulphides at Balta Tau are mostly recrystallized, as indicated by the absence of primary hydrothermal textures, equigranular nature with mutual, interlocking boundaries and lack of paragenetic indicators suggesting sulphides all crystallized at the same time. However, the sulphide grains do not show signs of metamorphic fabrics such as preferred orientation or elongation of grains, and composition layering is bedding-parallel suggesting that it may relate to the seafloor deposition of sulphides.

Sphalerite(I) and pyrite(I) crystals are texturally distinct from the enclosing layered and recrystallized matrix. The following observations suggest that these are a relict primary, sedimentary feature, representing sulphide clasts that were probably derived from the mechanical degredation of seafloor sulphides:

- Crystals are often fragmented and/or have corroded grain boundaries, and are sometimes concentrated in bedding-parallel layers as well occurring as isolated crystals.
- The sphalerite(I) crystals are zoned and similar in appearance to the coarse, primary hydrothermal sphalerite in other ore facies but distinct from the more homogeneous, zone-free sphalerite(2) in the enclosing matrix.
- Both sphalerite(I) and pyrite(I) predate the enclosing sulphides (e.g. chalcopyrite forming rims around the sphalerite and filling fractures; matrix filling embayments in pyrite).

The sphalerite(I) and pyrite(I) crystals therefore provide evidence for a sedimentary origin for the layered sulphides. The enclosing recrystallized sulphides are likely to have originated as a fine grained sulphide mud and sand which was also derived from the degradation of seafloor sulphide mound/chimney structures and possibly from fine particles settling out of hydrothermal fluids emitted from nearby vents. Such fine grained sulphide material would have been more susceptible to recrystallization, whereas larger clasts were coarse enough to resist recrystallization.

Sedimentary sulphides have been identified in well preserved ancient deposits, such as other deposits in the Urals (e.g. Yaman Kasy, Herrington et al., 1998; Alexandrinka, Tessalina et al., 2003) and in Kuroko deposits (e.g. Eldridge et al., 1983; Yui, 1983). These sulphides display sedimentary features such as graded bedding, cross bedding and soft sediment deposition, and also contain large clasts of whole and fragmented sulphide crystals comparable to the sphalerite(I) and pyrite(I) from Balta Tau. Sedimentary features such as graded bedding are not preserved in the recrystallized sulphides from Balta Tau, however the compositional layering that is bedding parallel is probably a relict of sedimentary layering. Such distinct compositional segregation is not observed in normal clastic sulphides in ancient or modern deposits, but may reflect weak compositional variations in the fine sulphide sediments that are exaggerated due to recrystallization and coarsening, with the most abundant sulphides in the mud recrystallizing to form coarse grains at the expense of other sulphides present.

The recrystallization can be constrained as occurring before metamorphism, as indicated by textural overprinting with an oblique fabric and annealing during metamorphism, and is therefore likely to have occurred during ore formation or diagenesis. The absence of directly comparable layered ores in modern systems supports the inference that they form during late stage ore formation or diagenesis. However, metalliferous sediments have been found which may be representative of the precursor sulphide mud (e.g. Hannington et al. 1986; Zierenberg et al. 1993; Fouquet et al. 1993). Furthermore, some smaller scale layering in a variety of ores have been identified from modern systems which could represent early stages of recrystallization and the development of compositional layering, e.g. at Snake Pit (Mid Atlantic Ridge), slabs of Zn-rich material covering talus at the top of a mound exhibit weak mineralogical layering as alternating sphalerite-rich and sphalerite-poor zones (Fouquet et al., 1993), and coarse recrystallized sulphides from seafloor sulphide mounds may also show compositional layering (e.g. Figure 9e in Hannington et al., 1995). These examples highlight the potential for forming layered ores in a seafloor environment, and the latter case may represent the early stages of formation of layered ores during seafloor modification of sulphides.

Overprinting of compositional layering

The compositional layering is overprinted by two textures indicative of remobilisation and recrystallization, which are likely to be metamorphic in origin:

- Remobilisation of galena-chalcopyrite-tennantite to form elongated grains and aggregates which are aligned oblique to and overprint the compositional layering. This is the same as the assemblage inferred to have been remobilised in the footwall (Section 4.2.8) and the selective mobilisation of Pb, As and Sb during metamorphism has been observed from deposits in central Europe, Norway, Urals, Bavaria and Australia (Vokes, 1969 and references therein).
- Recrystallization of sphalerite-galena-tennantite-quartz forming a mosaic of polygonal, equant and equigranular grains with well developed 120° triple-junctions. This texture is typical of recrystallization of sulphides without the influence of deformational stresses (e.g. Stanton, 1964; Vokes, 1969).

The existence of both of these textures might suggest that they formed at different stages of metamorphism and deformation, for example the oblique fabric developing during peak metamorphism-deformation, and the polygonal texture during waning stages of metamorphism where temperatures are still elevated but deformational stress has ceased (Vokes, 1969). Alternatively they may indicate that the strain within the sulphide body was heterogeneous and taken up more in some layers than others, simultaneously forming different recrystallization textures.

4.5 BARITE RICH SULPHIDES

4.5.1 Introduction

A suite of barite-rich (>10% barite), gold bearing sulphides which are texturally distinct from other massive ores were collected from large (1 to 3m) tectonically emplaced blocks of sulphides in the shear zone associated with the Eastern Fault (Chapter 3, Figure 3.21). None of these samples were collected in situ since have all been tectonically detached from the massive sulphide lens, therefore the stratigraphic and spatial relationship of this ore facies to other styles of mineralization can not be established with certainty. However, mineralogical and textural characteristics are intermediate between mainstage pyrite-rich massive sulphides (Section 4.3) and the barite lens (Section 4.6), suggesting that these gold-barite rich sulphides originated from the upper horizons of the massive sulphide lens, stratigraphically between the massive sulphides and overlying gold-barite lens.

4.5.2 Mineralogy and textures

Pyrite clasts

Barite-rich sulphides are characterized by mm to cm sized pyrite clasts enclosed in a barite-chalcopyrite-sphalerite-tennantite-galena assemblage. The pyrite clasts comprise aggregates of coarse crystals 1 to 10mm, and some appear homogeneous and inclusion free (Figure 4.24a to c), while others display growth zones defined by concentrically arranged tennantite, sphalerite and galena inclusions (Figure 4.25a to c). Clast margins vary from abrupt and well defined to gradational where fine, euhedral pyrite at clast margins grades into fine pyrite of the surrounding matrix. Clasts are poorly sorted, unevenly distributed, and account for on average 30% of the ores.

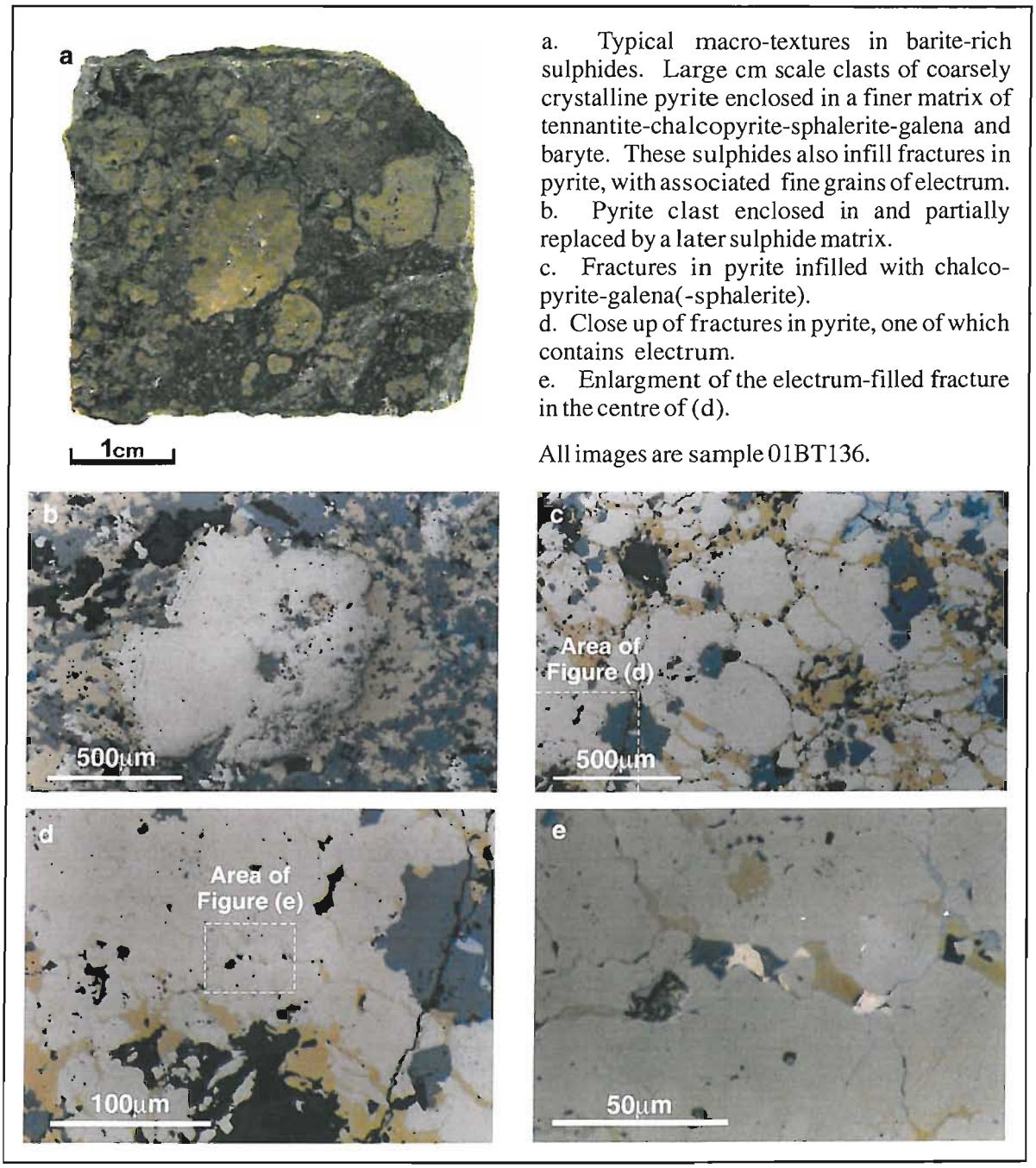

a. Typical macro-textures in barite-rich sulphides. Large cm scale clasts of coarsely crystalline pyrite enclosed in a finer matrix of tennantite-chalcopyrite-sphalerite-galena and baryte. These sulphides also infill fractures in pyrite, with associated fine grains of electrum.
b. Pyrite clast enclosed in and partially replaced by a later sulphide matrix.
c. Fractures in pyrite infilled with chalcopyrite-galena(-sphalerite).
d. Close up of fractures in pyrite, one of which contains electrum.
e. Enlargment of the electrum-filled fracture in the centre of (d).

All images are sample 01BT136.

Figure 4.24. Pyrite clasts and fracture-related electrum in barite-rich sulphide ores.

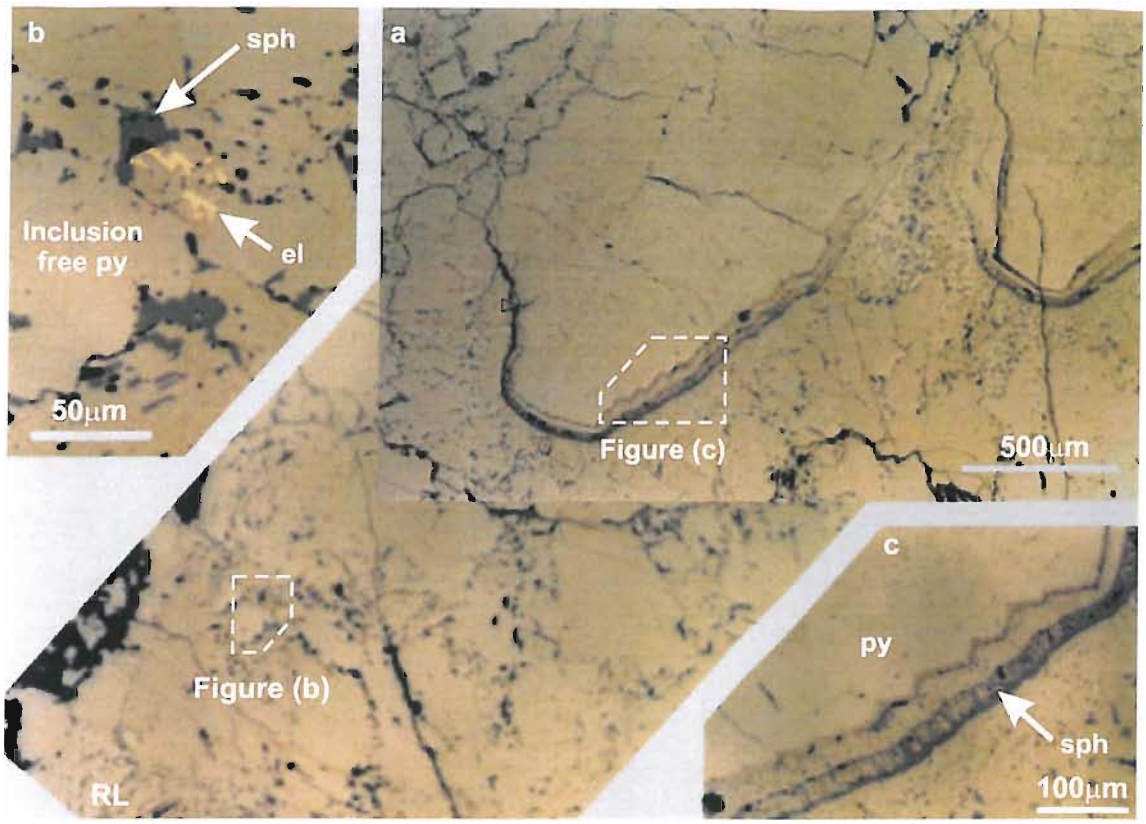

a. Large pyrite clast with several generations of pyrite defined by growth zones, rims and inclusions of sphalerite with minor tennantite.
b. Inclusion-free pyrite core enclosed in spongy pyrite with numerous inclusions of sphalerite and irregular electrum infilling porosity/replacing pyrite.
c. Growth zone to show fine texture of sphalerite and minor tennantite.

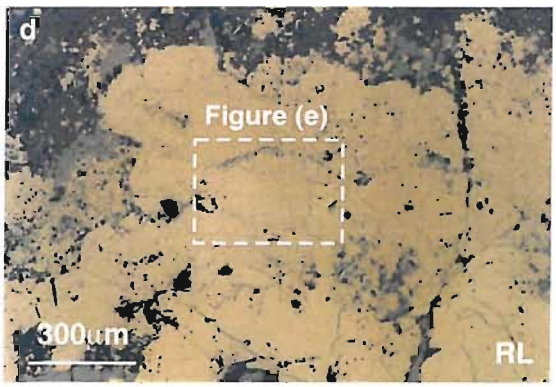

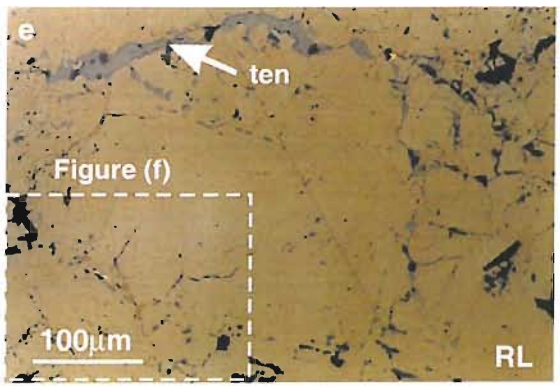

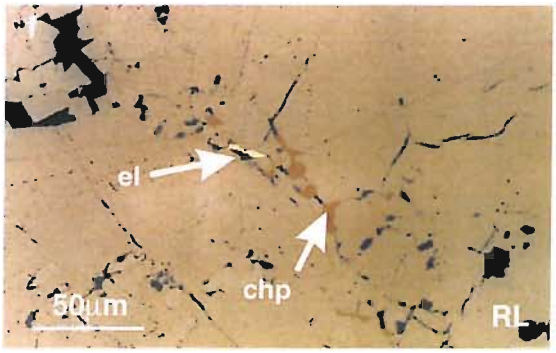

d, e and f. Example of electrum with tennantite and chalcopyrite filling fractures in coarse clastic pyrite, where fractures appear to have exploited growth zones in pyrite The matrix around the pyrite clast (shown in (d)) comprises barite-tennantite-sphalerite(-pyrite-chalcopyrite-galena). Sample 01BT136.

Figure 4.25. Growth zoned pyrite clasts containing small grains of electrum replacing pyrite in barite-rich sulphide ores.

Sulphide-barite matrix

The matrix surrounding pyrite clasts contains on average 40 to 60% sulphides comprising finely intergrown sphalerite-pyrite with up to 5% each of chalcopyrite, galena, and tennantite (Figure 4.26a). Sphalerite is fine and equigranular (50 to 100μm), transparent and pale beige with weak orange-brown zoning and very little chalcopyrite disease, while pyrite forms fine euhedral cubes 10 to 100μm intergrown with, and enclosed in, sphalerite (Figure 4.26a). Sphalerite also occurs as coarse aggregates of more euhedral, zoned crystals associated with chalcopyrite-tennantite-galena rather than pyrite (Figure 4.26b). There are no systematic replacement textures within the matrix, and the finely intergrown nature of sulphides suggests co-precipitation of this assemblage.

The pyrite clasts contain numerous fractures filled with a tennantite-galena-sphalerite-chalcopyrite-electrum assemblage which also partially replaces the pyrite, and precipitated after pyrite clast formation. The fact that fractures do not penetrate the enclosing sulphide-barite matrix, together with the similar mineralogy of fracture-fills and the matrix, suggest the fracture filling assemblage and sulphide-barite matrix are the same stage of mineralization and precipitated at the same time.

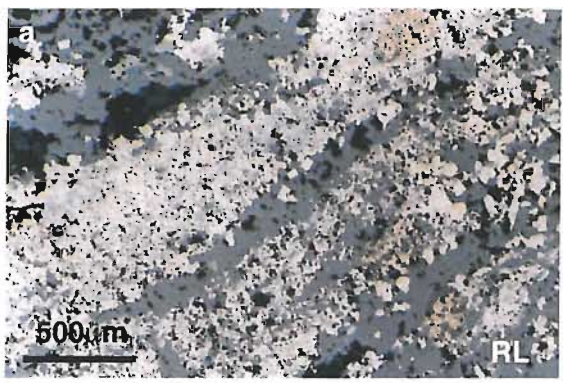

a. Coarse, subhedral zoned sphalerite with interstitial galena and tennantite. Sample 01BT082.

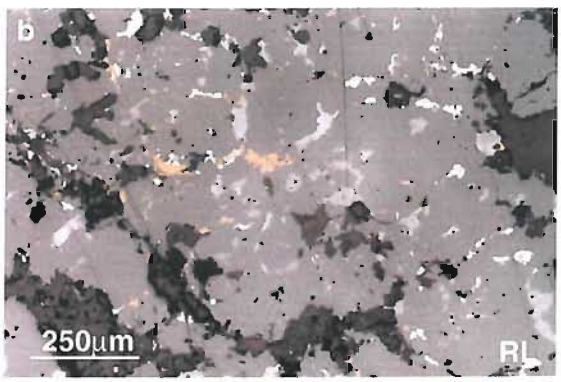

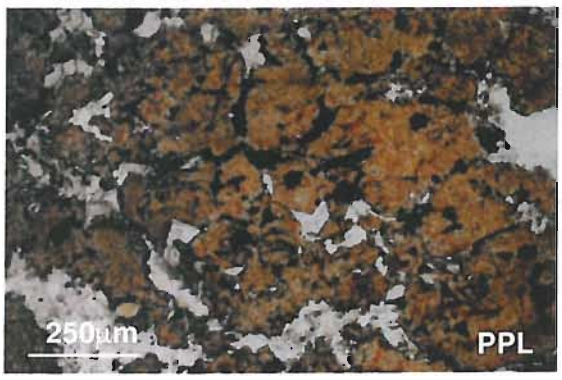

b. Typical sulphide-rich matrix comprising fine euhedral pyrite with fine sphalerite and galena. Other areas of this matrix have similar textures but are rich in tennantite. Sample 01BT135.

Figure 4.26. Typical textures of fine grained sulphide matrix enclosing pyrite clasts in electrum-barite-rich massive sulphides.

Barite varies in abundance from 10 to 45% and forms coarse, euhedral tabular crystals often arranged in fanning and radial aggregates (Figure 4.27b). The relationship between barite and sulphides is complex, with sulphides occurring interstitial to coarse barite (e.g. Figure 4.27b), enclosed in barite crystals, and replaced by barite (Figure 4.27a) in the same sample. These textures suggest that locally on a mm to cm scale, barite precipitated both before, during and after the sulphides, and on a broader scale the barite and sulphides co-precipitated.

Gangue phases other than barite

Quartz occurs in minor amounts (2 to 5%) and forms anhedral interlocking grains varying from 50um to 1mm in size and often interstitial to sulphides and barite. Quartz is colourless and transparent except for numerous blebs and inclusions of sulphides, in particular sphalerite and pyrite. The interstitial textures and abundance of sulphide inclusions suggests quartz precipitated during to slightly later than sulphide-barite formation.

One sample contains around 2% carbonate associated with barite, forming coarse anhedral to subhedral grains (0.2 to 1mm) with multiple twinning, which may either have co-precipitated with the barite-sulphides or formed afterwards infilling porosity. Fine grained sericite/muscovite are also present occurring mostly along barite grain boundaries suggesting they post-date barite-sulphide formation and may relate to late stage ore formation or diagenesis.

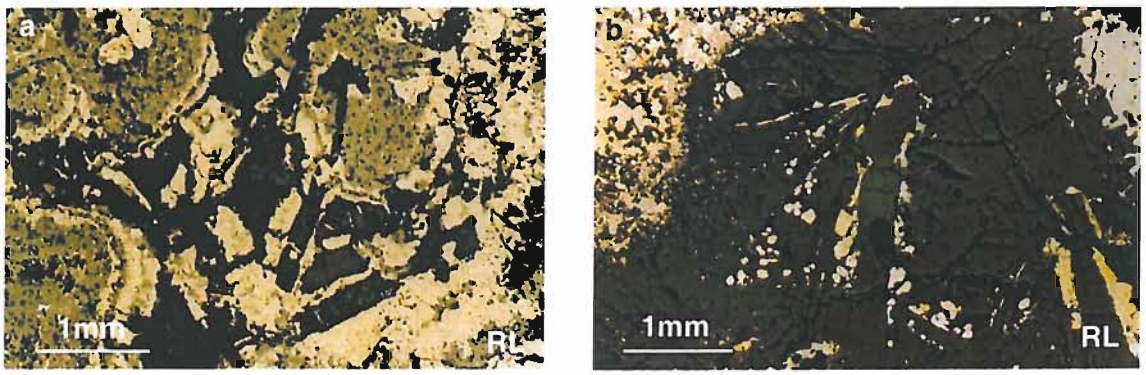

a and b. Contrasting textures in barite-sulphide ores. (a) shows euhedral tabular barite replacing finely intergrown and collomorphic pyrite-sphalerite. In (b), pyrite dominated sulphides occur interstitially along the grain boundaries within a fanning aggregate of coarse euhedral barite. Both examples are from the same sample, 01BT136.

Figure 4.27. Textural relationship between barite and sulphides in barite rich sulphide ores.

Electrum

Numerous grains of electrum have been found in these samples which are generally less than 50μm in size and associated with one or more of chalcopyrite, tennantite, galena and sphalerite. The classification of these grains as electrum rather than native gold has been confirmed by microprobe analyses, discussed in Chapter 5, Section 5.2.8. They occur mainly along fractures in pyrite clasts (Figures 4.24e and 4.25f) and as irregular areas replacing pyrite (Figure 4.25b). Rarely, electrum occurs as very fine grains in the pyrite-sphalerite matrix, where it forms small spherical blebs less than 20μm, and scarce coarser grains up to 300μm, mostly enclosed in or adjacent to sphalerite-galena-tennantite (textures are very similar to those in Figure 4.36 from the barite lens) and sometimes enclosed in barite(-quartz). The majority of electrum is closely associated with the fracture-filling and matrix assemblage of sphalerite-tennantite-chalcopyrite-galena, and textures indicate co-precipitation of electrum with these sulphides.

Although the majority of electrum is fracture-related, these fractures only occur in pyrite clasts and do not penetrate the enclosing matrix, precluding the late stage (post-VMS) introduction of electrum into these samples and confirming that it is co-genetic with sulphides. The relative abundance of electrum in fractures in pyrite compared with the scarcity of electrum in the enclosing matrix suggests that pyrite was an important factor in the precipitation of electrum, either providing a site for precipitation or as a source of "invisible" gold that may have been leached from the pyrite and concentrated into fractures (discussed further in Chapter 5, Section 5.3.1).

4.5.3 Textural overprinting

Pumpellyite and the zeolite scolecite (identified by microprobe, Chapter 5 Section 5.4.6) occur sporadically in a number of samples, and probably formed during diagenesis and/or low grade regional metamorphism. Scolecite occurs as coarse crystals replacing barite, and pumpellyite forms isolated and radial aggregates of euhedral platey crystals replacing sulphides (Figure 4.28).

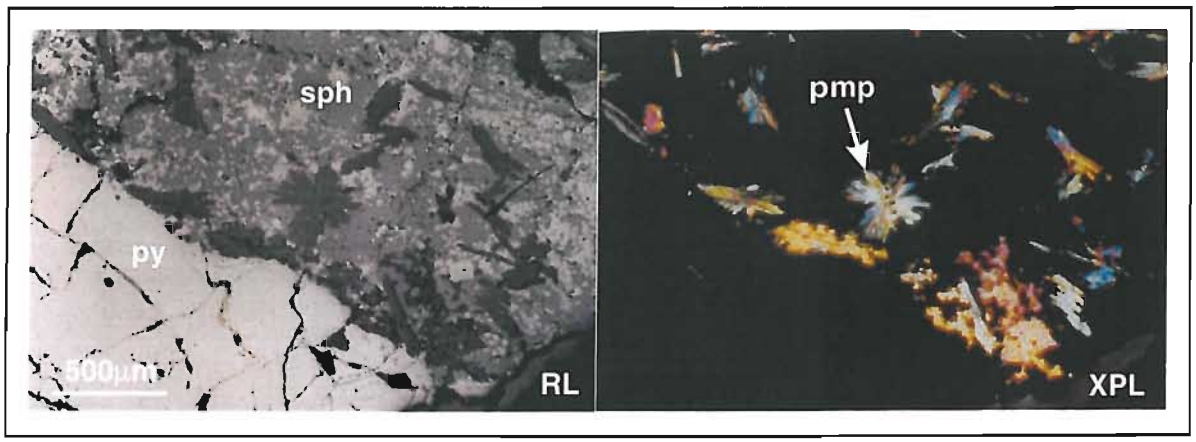

Figure 4.28. Pumpellyite replacing sulphides in gold-barite rich sulphide ores.

4.5.4 Ore Formation and Paragenesis

Paragenesis

The paragenesis of barite-rich sulphides is summarised in Figure 4.29. Pyrite clasts are the earliest phase and the enclosing matrix and fracture-filling assemblage precipitated at a later stage. Within the matrix, textures are consistent with the co-precipitation of sphalerite-pyrite-chalcopyrite-tennantite-galena-electrum, and generally co-precipitation of these sulphides with barite. Quartz and carbonate may have precipitated during and/or subsequent to main ore formation, while muscovite clearly post dates mainstage barite and probably formed during late stages of hydrothermal activity or diagenesis. Pumpellyite and zeolite replace barite and sulphides, and probably formed during diagenesis or metamorphism.

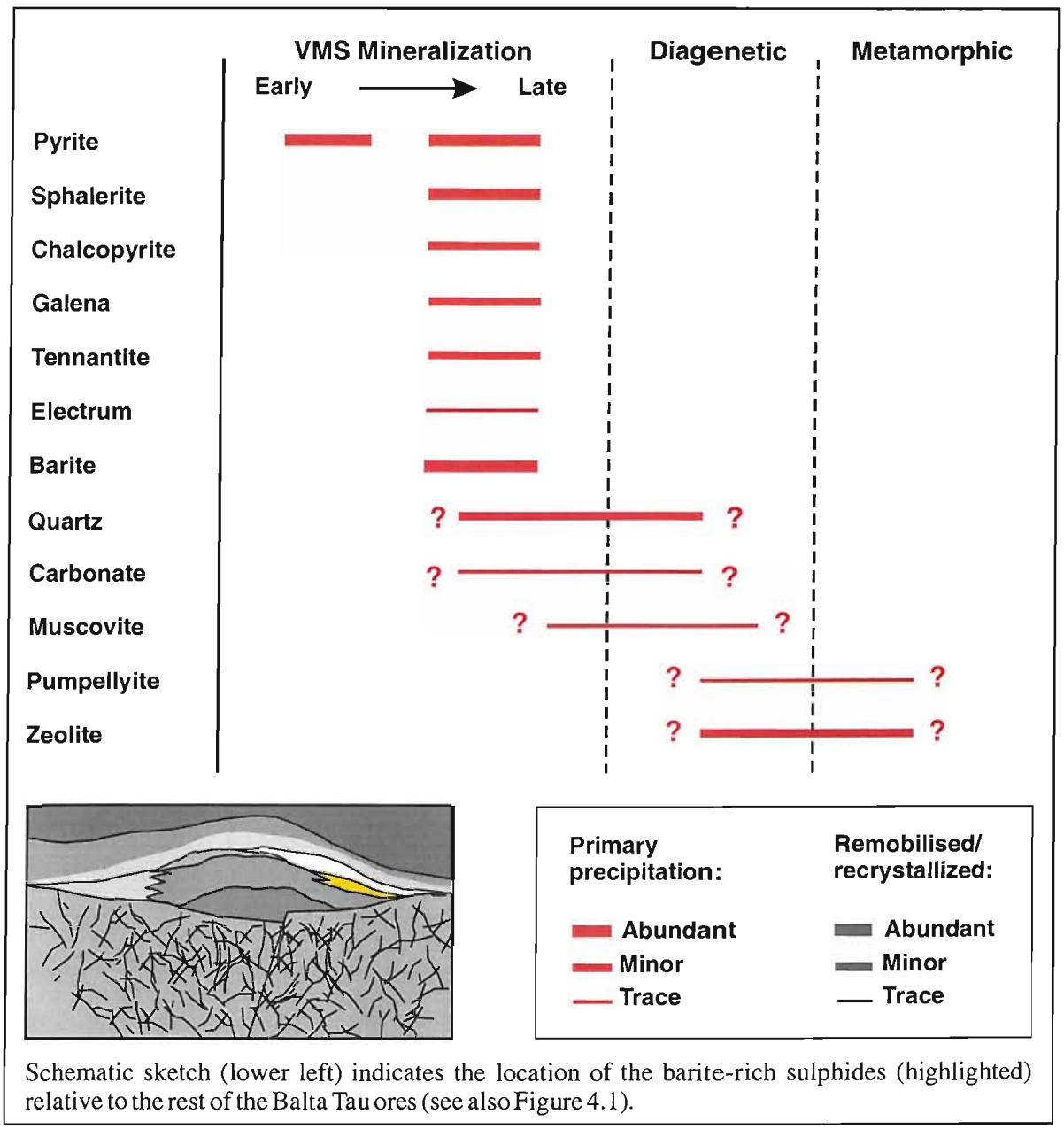

Schematic sketch (lower left) indicates the location of the barite-rich sulphides (highlighted) relative to the rest of the Balta Tau ores (see also Figure 4.1).

Figure 4.29. Paragenesis of gold-barite-rich massive sulphides.

4.6 GOLD-RICH BARITE LENS

4.6.1 Introduction

The gold-rich barite lens is located stratigraphically at the contact between massive sulphides and the hanging-wall volcanics. Although not laterally continuous along this contact, the barite lens is an extensive zone of mineralization extending from immediately overlying central portions of the massive sulphide lens (Figure 4.30) to overlying and onlapping thin marginal zones of massive sulphides (as exposed in 2001, Figure 3.12), and was exposed in the open pit over a period of at least seven years (observed and sampled during visits from 1995 to 2002, Herrington pers. com.). The lower contact between massive sulphides and the barite lens appears normal and stratigraphic (Figure 4.30); interpretation of the hanging-wall contact is obscured by extensive shearing of the immediate hanging-wall unit.

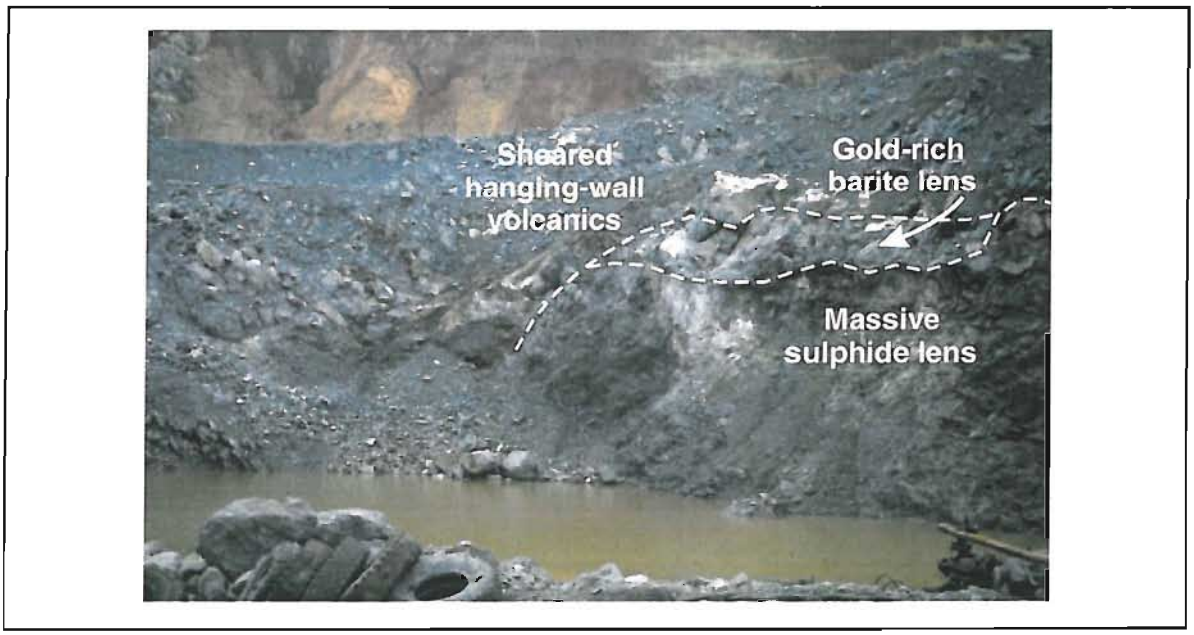

Figure 4.30. Exposure of the barite lens conformably overlying massive sulphides (photograph taken by Herrington, 2000).

4.6.2 Mineralogy and textures

Sulphides and barite

The sulphide assemblage in the barite lens is different to the other mineralised horizons at Balta Tau. Sulphides are dominated by fine intergrowths of tennantite-chalcopyrite forming irregular mm to cm sized masses enclosed in a barite-sulphide matrix. The intergrowths are commonly irregular and patchy (Figure 4.31a, b) and may contain significant galena (Figure 4.31c), or more rarely form collomorphic textures (Figure 4.31e, f). The margins are irregular and do not appear clastic, but grade into disseminated sulphides of the enclosing matrix (Figure 4.31d).

Sulphides in the barite-sulphide matrix form coarse and fine polymineralic tennantite-chalcopyrite-galena-sphalerite aggregates and disseminations (Figure 4.32a, b). Sulphides are anhedral and irregular with mutual, sometimes interlocking grain boundaries. Sphalerite associated with these disseminations is mostly pale beige, completely transparent and devoid of chalcopyrite disease. More rarely, sphalerite occurs as equant, subhedral to euhedral crystals with brown to orange-red zoning (Figure 4.33b) and little to no chalcopyrite disease. These coarser sphalerite crystals are commonly enclosed in the polymineralic disseminated sulphides (Figure 4.34c), and are replaced by coarse barite crystals at their margins (Figure 4.33b) or by tennantite-chalcopyrite (Figure 4.31e), suggesting they formed earlier than both the sulphides and the barite.

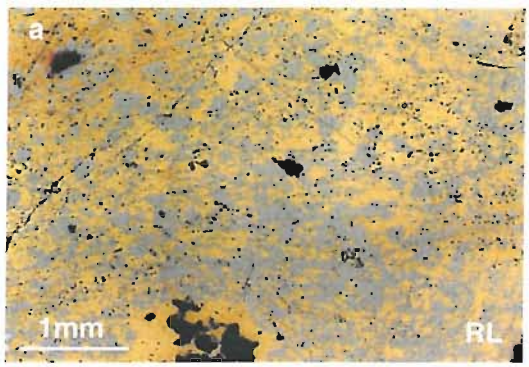

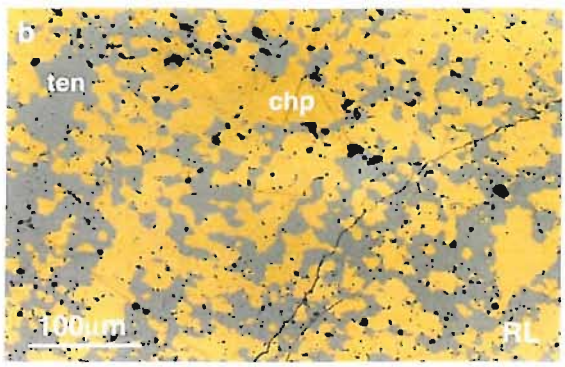

a and b. Typical coarse aggregates of intergrown chalcopyrite and tennantite. Sample BTB01(D).

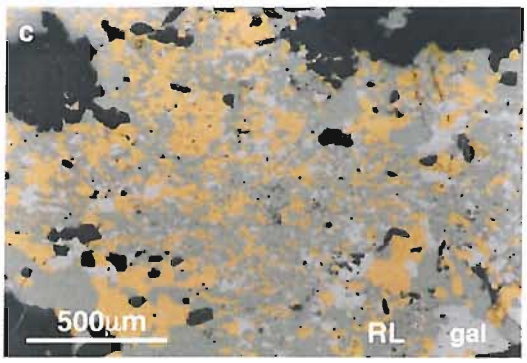

c. Rare chalcopyrite-tennantite intergrowth containing significant galena. Sample BL1a.

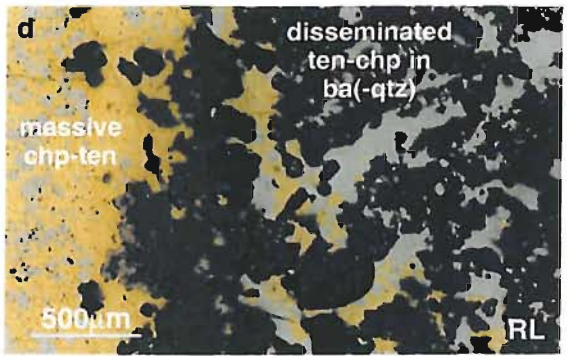

d. Gradation from the margin of a tennantite-chalcopyrite intergrowth to disseminated tennantite-chalcopyrite. Sample BTB01(D).

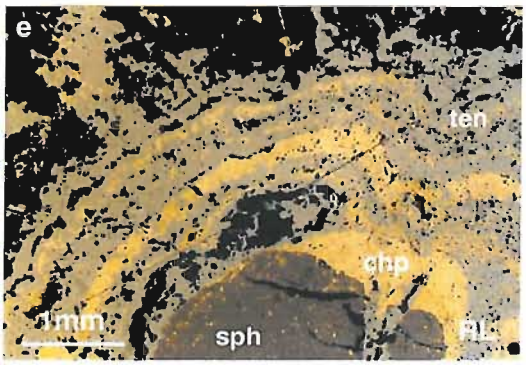

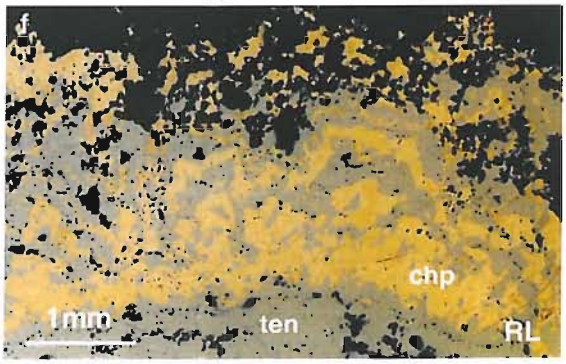

e and f. Rare collomorphic textures in chalcopyrite-tennantite enclosing earlier coarse sphalerite. The chalcopyrite-tennantite also forms tiny, irregular inclusions in sphalerite (seen in (e)) which are suggestive of minor replacement of sphalerite by chalcopyrite-tennantite. Sample BTB01(D).

Figure 4.31. Chalcopyrite-tennantite intergrowths in the barite lens.

Pyrite is also present in the sulphide-barite matrix although usually rarer than the other sulphides, occurring as fine (20 to 50μm) euhedral crystals and fine framboidal masses (Figure 4.32c) disseminated in barite. Pyrite is not generally associated with other sulphides, except for the occurrence of framboids enclosed in, or at the margins of, tennantite.

Barite forms coarse, euhedral, tabular crystals reaching 5mm in length, arranged in fanning and radial aggregates (Figure 4.33a, c). Quartz tends to be interstitial to both barite and sulphides, forming anhedral, transparent grains 50 to 300μm which are generally inclusion free, and fine grained (20 to 50μm) platey muscovite is widespread in low abundance along barite crystal boundaries.

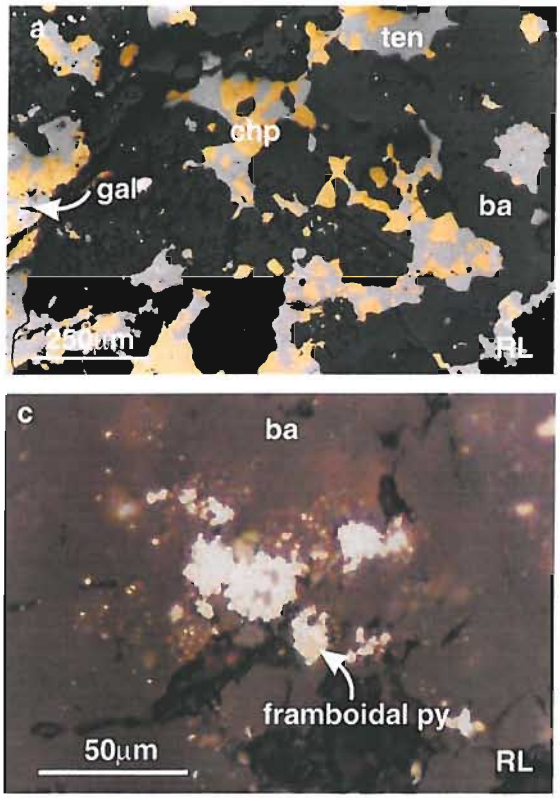

a and b. Typical coarse, disseminated polymineralic sulphides in coarse barite with quartz. In (a) sulphides are tennantite-chalcopyrite with traces of galena, and in (b) are sphalerite-tennantite-chalcopyrite-galena. Sample BL2.

c. Fine grained framboidal pyrite enclosed in coarse barite crystals. Sample 01BT226a.

Figure 4.32. Disseminated sulphides in the sulphide-barite(-quartz) matrix of the barite lens.

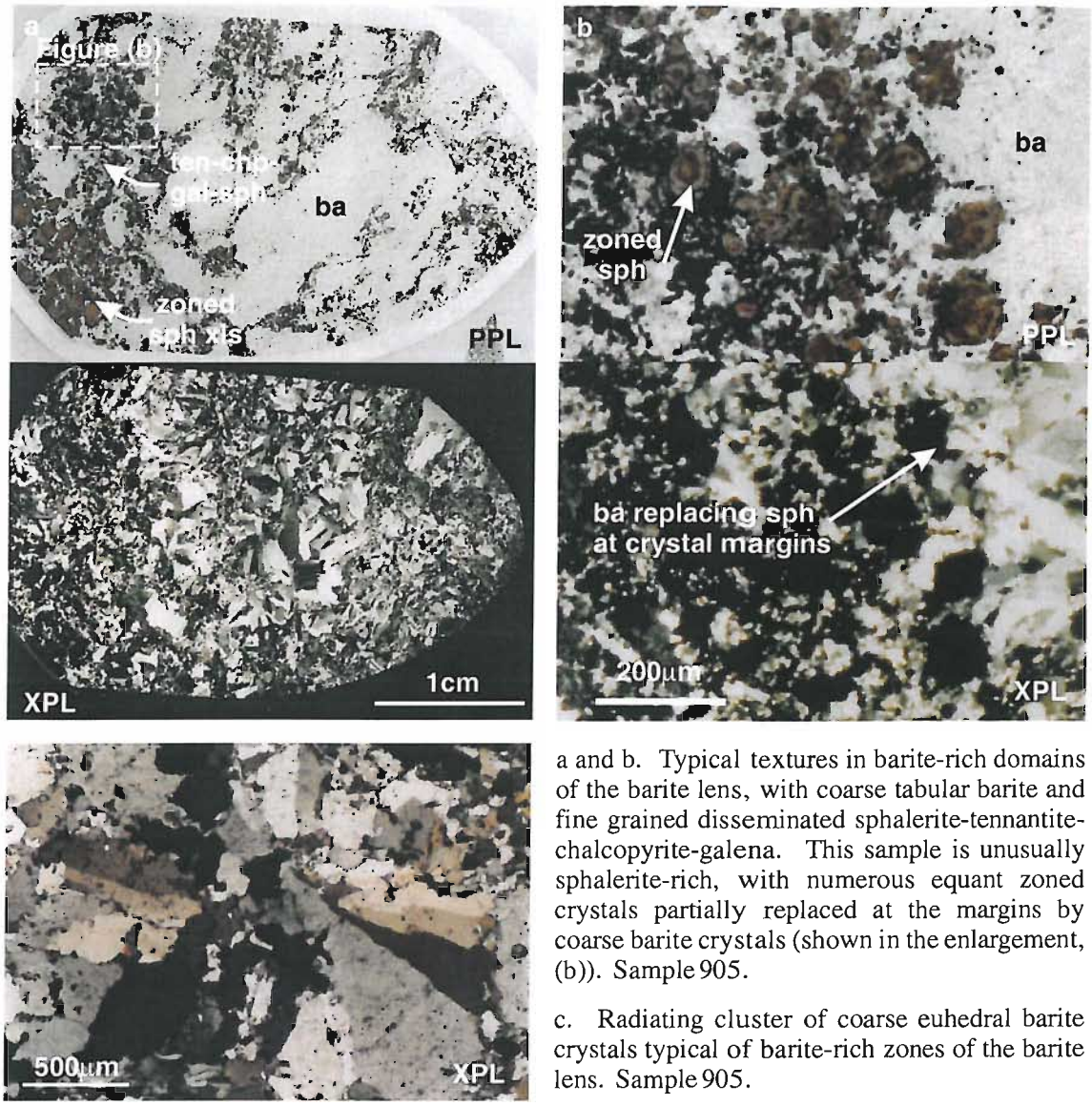

a and b. Typical textures in barite-rich domains of the barite lens, with coarse tabular barite and fine grained disseminated sphalerite-tennantite-chalcopyrite-galena. This sample is unusually sphalerite-rich, with numerous equant zoned crystals partially replaced at the margins by coarse barite crystals (shown in the enlargement, (b)). Sample 905.

c. Radiating cluster of coarse euhedral barite crystals typical of barite-rich zones of the barite lens. Sample 905.

Figure 4.33. Barite and early stage sphalerite textures in the barite lens.

Electrum

Numerous grains of electrum have been identified with various modes of occurrence, and their classification as electrum rather than native gold is confirmed by microprobe analyses, (Chapter 5, Section 5.2.8). The majority of electrum occurs as coarse polygonal grains and clusters of grains associated with disseminated polymineralic tennantite-chalcopyrite-galena-sphalerite aggregates (Figure 4.34a-d). These coarse grains vary from 50µm to 0.8mm in size and are most commonly located at the contact between sulphides and barite, although they do also occur completely enclosed in sulphides. Electrum also forms very small (2 to 20µm) rounded blebs enclosed in fine disseminated tennantite-chalcopyrite-galena-sphalerite, and sometimes in barite crystals (Figure 4.36d, e). In one sample electrum also occurs as small (5 to 50µm) fracture-related inclusions in a coarse "early" sphalerite crystal associated with galena, chalcopyrite and barite. The sphalerite is altered to digenite along the fractures hosting these inclusions (Figure 4.34e, f).

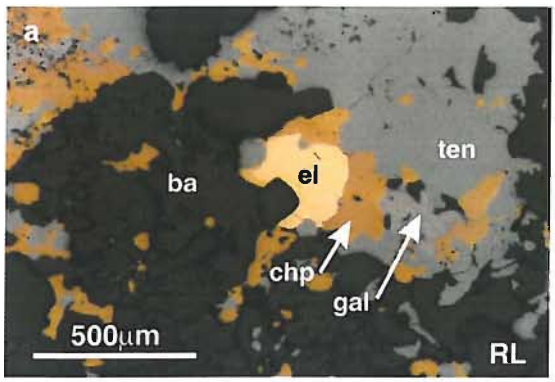

a Large grain of electrum at the contact between barite and tennantite-chalcopyrite-galena. Sample BTB01(B).

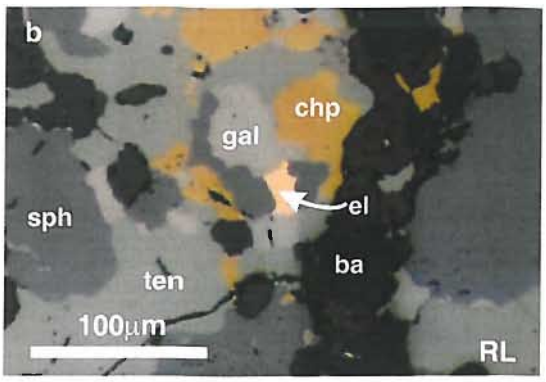

b. Small electrum grain completely enclosed in a sulphide assemblage dominated by sphalerite-tennantite with chalcopyrite and galena. Sample BTB01(B).

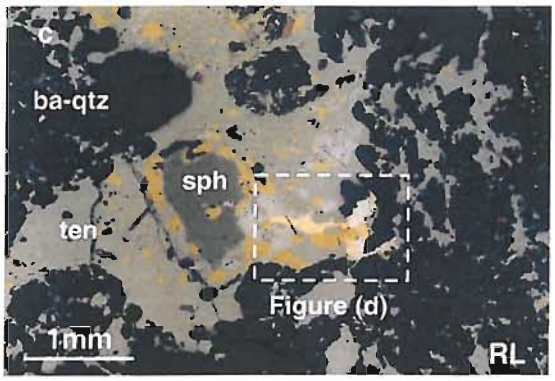

c. Coarse sphalerite enclosed in a polymineralic aggregate of anhedral tennantite-chalcopyrite-galena-electrum. Sample BTB01(D).

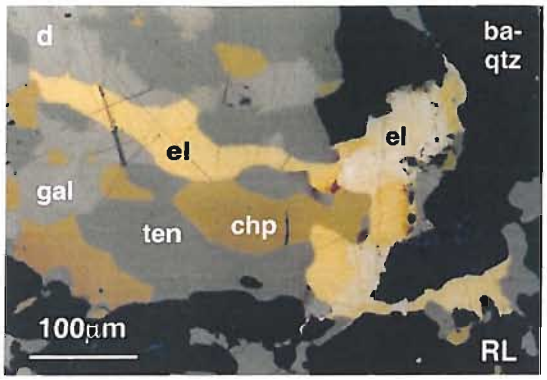

d. Enlargment of the electrum grains shown in (c); the largest is 0.8mm in length and largest electrum grain found at Balta Tau in this study. Sample BTB01(D).

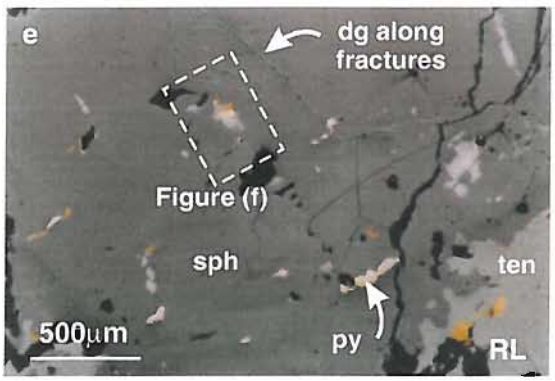

e. Coarse, twinned sphalerite containing numerous polymineralic inclusions of tennantite-chalcopyrite-galena(-electrum), and isolated pyrite inclusions. Fractures associated with these inclusions show fine hairline alteration to digenite. Sample BTB01(C).

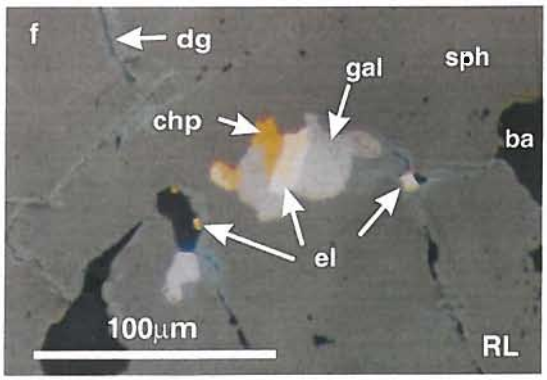

f. Enlargement of the polymineralic, electrum-bearing inclusion in sphalerite shown in (e). Electrum grains are associated with galena-chalcopyrite, and smaller grains with barite. Sample BTB01(C).

Figure 4.34. Electrum and associated sulphides in the gold-rich barite lens.

Textural relationships of disseminated sulphides, electrum and barite

Excluding the "early" sphalerite crystals that pre-date the barite-sulphides, textural relationships between the barite and disseminated tennantite-chalcopyrite-galena-sphalerite-electrum are variable and can be divided into three categories:

- Polymineralic aggregates of coarse (100 to 200μm) anhedral tennantite-chalcopyrite-galena-sphalerite and electrum appear to have co-precipitated with barite, forming interlocking masses with no evidence of replacement (e.g. Figures 4.32a, b and 4.34a, b).
- Fine to medium grained (20 to 100μm) polymineralic tennantite-chalcopyrite-galena-sphalerite and electrum occur interstitial to barite, forming linear trends that define barite crystal margins (Figure 4.35a, b). These suggest precipitation of some sulphides post-dates barite formation.
- Zones of very fine rounded and rod-like monomineralic and rarely polymineralic inclusions of tennantite, chalcopyrite, galena, sphalerite and electrum (5-20μm) follow growth zones in coarse barite crystals, giving an effect that resembles chalcopyrite disease in sphalerite (Figure 4.36a-d). These inclusions are not fracture or cleavage related, and point to the co-precipitation of sulphides, electrum and barite.

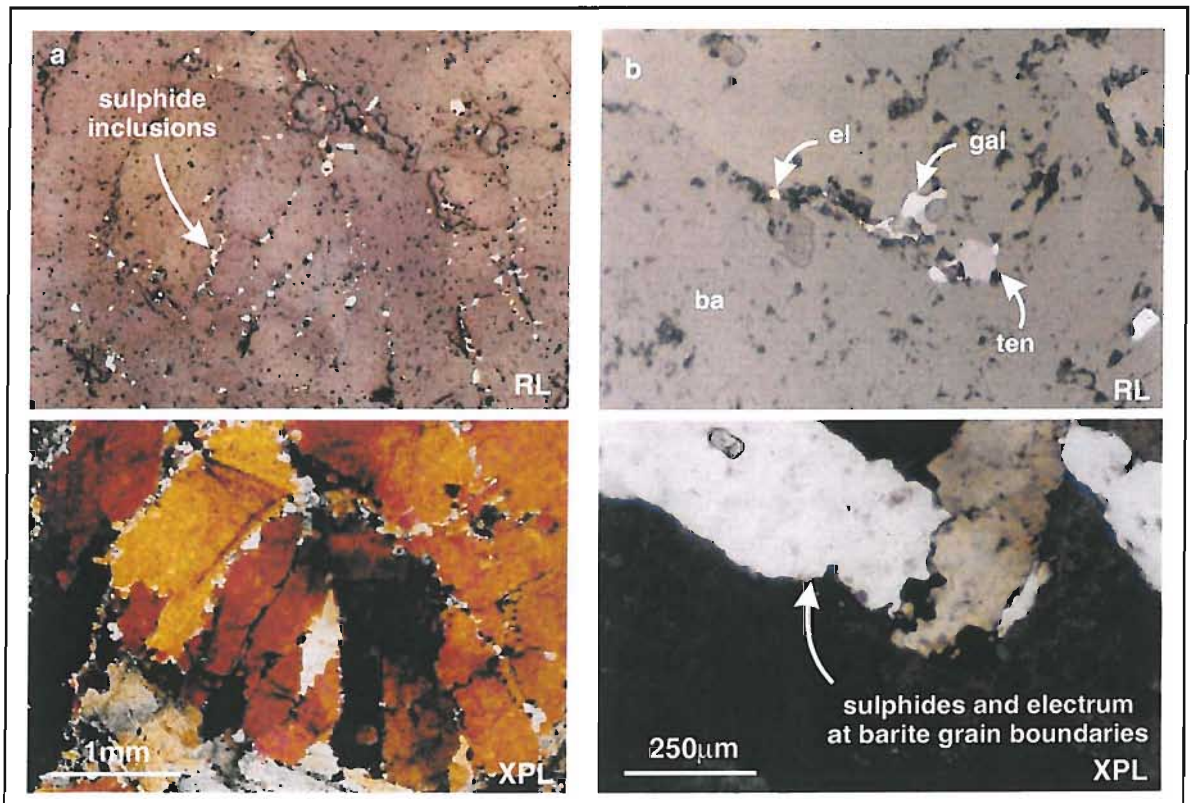

a. Small grains of tennantite, chalcopyrite, galena and sphalerite interstitial to coarse tabular barite crystals. Sample 01BT226d.

b. Small grain of electrum and polymineralic galena-tennantite-sphalerite interstitial to coarse barite grains. Sample 01BT226d.

Figure 4.35. Fine grained sulphides and electrum interstitial to barite in the barite lens.

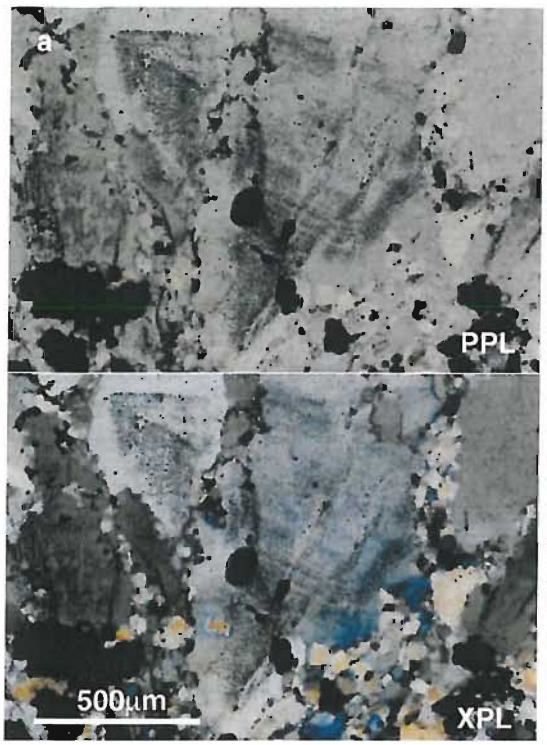

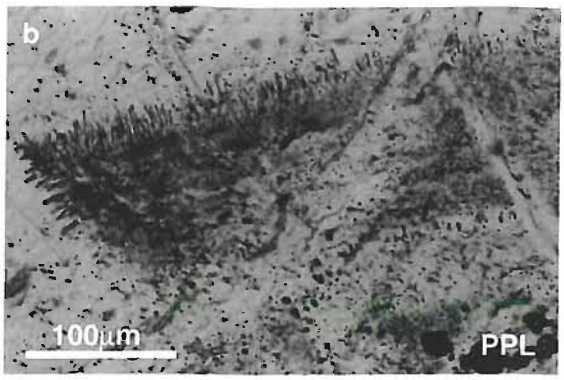

a. Large subhedral barite crystals with dark cloudy zones of micro-inclusions of sulphides. The lower image is in XPL to show crystal boundaries; the zones of inclusions are contained within single, large crystals rather than along grain boundaries. Sample 01BT226b.

b. Close up view of a single barite crystal containing zones of micro-inclusions of sulphides. Sample 01BT226b.

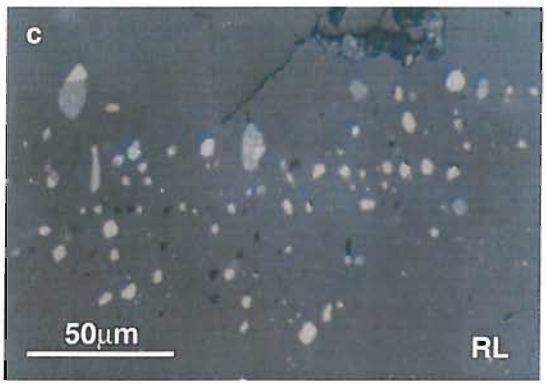

c. Zone of chalcopyrite, galena, tennantite and sphalerite micro-inclusions within a single barite crystal. This sulphide assemblage mirrors the sulphides found in sulphide rich zones. Sample 01BT226b.

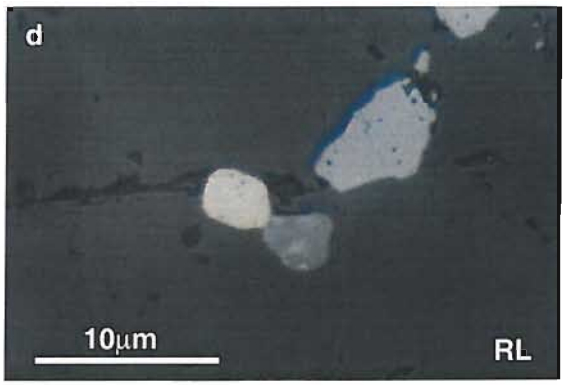

d. Micro-inclusions in barite, with one electrum inclusion (left), adjacent sphalerite showing internal reflections (lower centre) and a tennantite inclusion (upper right). Sample 01BT226b.

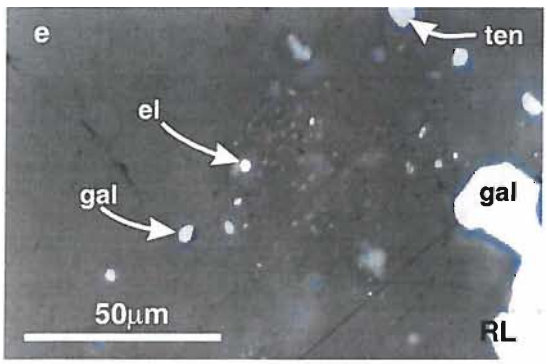

e. Small electrum inclusion together with numerous small and larger galena and tennantite inclusions in a single barite crystal. Sample 01BT226a.

Figure 4.36. Zones of sulphide-electrum micro-inclusions in barite from the barite lens.

In all three of these categories, electrum is closely related to, and co-precipitated with, the sulphide assemblages. All three textures described are found in single samples, suggesting that on a mm-

cm scale sulphide-electrum assemblages formed before, during and after barite precipitation. On a larger scale, no single texture is prevalent, and it is therefore reasonable to regard the formation of these facies as co-precipitation of sulphides, electrum and barite with small scale variations.

The aggregates of intergrown tennantite-chalcopyrite are texturally distinct from the disseminated sulphides considered above. However, the gradation from tennantite-chalcopyrite masses to surrounding disseminated sulphides suggests they formed at the same time as the disseminations, supported by the lack of replacement of these masses by any other sulphides. This is also consistent with the lack of replacement textures with barite, which generally co-precipitated with disseminated sulphides.

Rare phases

Scarce anhedral grains of pearcite (a member of the pearcite-polybasite series, with the general formula $(Ag,Cu)_{16}(Sb,As)_2S_{11}$) have been identified by microprobe (Chapter 5, Section 5.2.9) from two samples of the barite lens, forming grains up to 300μm in size enclosed in barite with galena-rich disseminated sulphides. Pearcite is an extremely rare mineral and seldom found in VMS deposits, but has been reported from the Kuroko deposit of Uwamuki (Matsukuma et al., 1974) and both pearcite and polybasite are listed by Shimazaki (1974) as rare phases in Kuroko deposits. Native silver has also been identified in one sample, where it forms small (<5um) grains with a wirey habit which are interstitial to coarse barite crystals and in places bend and wrap around very fine grained disseminated sulphides. Native silver has also been identified from the Sulitjelma deposit in Norway, where it contains 1 to 4 at% Au and is considered to have formed from the breakdown of Ag minerals such as pyrargyrite or freibergite (Cook, 1996), and from the actively forming Jade deposit, Okinawa Trough, where it forms fine dendritic aggregates in the pore spaces between barite crystals (Halbach et al. 1993). The occurrence at Balta Tau has many similarities with that from Jade suggesting formation at the seafloor.

4.6.3 Oxidation of sulphides and remobilisation of electrum

A few samples contain traces of secondary sulphides, mainly covellite and rare digenite, which form rims around sulphide grains and are interstitial to coarse barite, and in the latter case are associated with very fine (<20μm) irregular grains of electrum. One sample (BL1) has extensive oxidation of sulphide grain boundaries with covellite and other unidentified secondary minerals forming bright blue/green rims around chalcopyrite, galena and sphalerite, and brownish rims around tennantite (Figure 4.37a, b). Coarse, irregular areas of electrum enclose and rim these sulphides outside the oxidation layer suggesting the electrum has precipitated after sulphide oxidation. The electrum has very bright iridescent colours in polished section which are indicative of significant impurities, and the formation of thin rims around sulphide grains suggest that it has

been remobilised. The lack of deformation or metamorphic overprinting in this sample, and the fact that none of the highly deformed samples contain remobilised electrum, suggests remobilisation occurred during late stages of ore-related hydrothermal activity or diagenesis rather than during metamorphism.

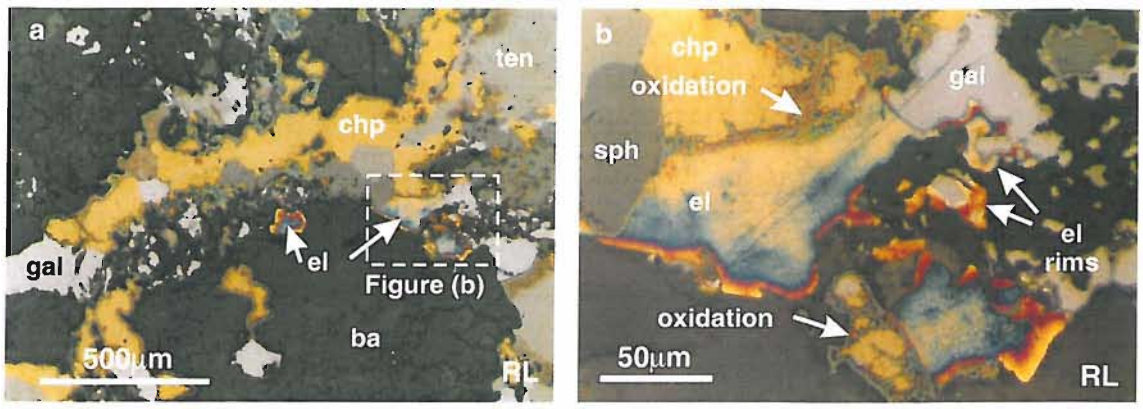

a. Remobilized electrum forming irregular grains and rims enclosing partially oxidized disseminated tennantite-chalcopyrite-galena-sphalerite. The strong irridescent colours of the electrum suggest impurities. Sample BL1.

b. Electrum forming rims around sulphides which have been oxidized at grain margins prior to or comtemporaneously with the remobilisation of electrum. Sample BL1.

Figure 4.37. Remobilised electrum and oxidized sulphides from the gold-rich barite lens.

4.6.4 Deformation and overprinting

The barite lens is adjacent to hanging-wall rocks that are highly sericitized, deformed and sheared. Locally the barite lens itself is also deformed, with development of a foliation in sulphides coincident with coarse muscovite replacing the sulphide/barite assemblage (Figure 4.38). Minor fine grained euhedral pyrite is associated with the muscovite. Where muscovite replaces chalcopyrite, there is minor oxidation to covellite (Figure 4.38c) at the contact with the invading muscovite. Although no triple-junction or annealing textures were observed in the sulphide assemblage, sphalerite is deformed, elongated parallel to foliation and appears very homogeneous in transmitted light (Figure 4.38b) suggesting recrystallization has occurred.

As with the barite-rich massive sulphides, coarse crystals of zeolite replace barite in irregular patches in both sheared and undeformed ores, with little or no modification of the enclosed and adjacent sulphides. This may be related either to diagenesis or metamorphism, since unlike the muscovite(-pyrite) formation, there is no evidence of a direct link between metamorphism and zeolite formation.

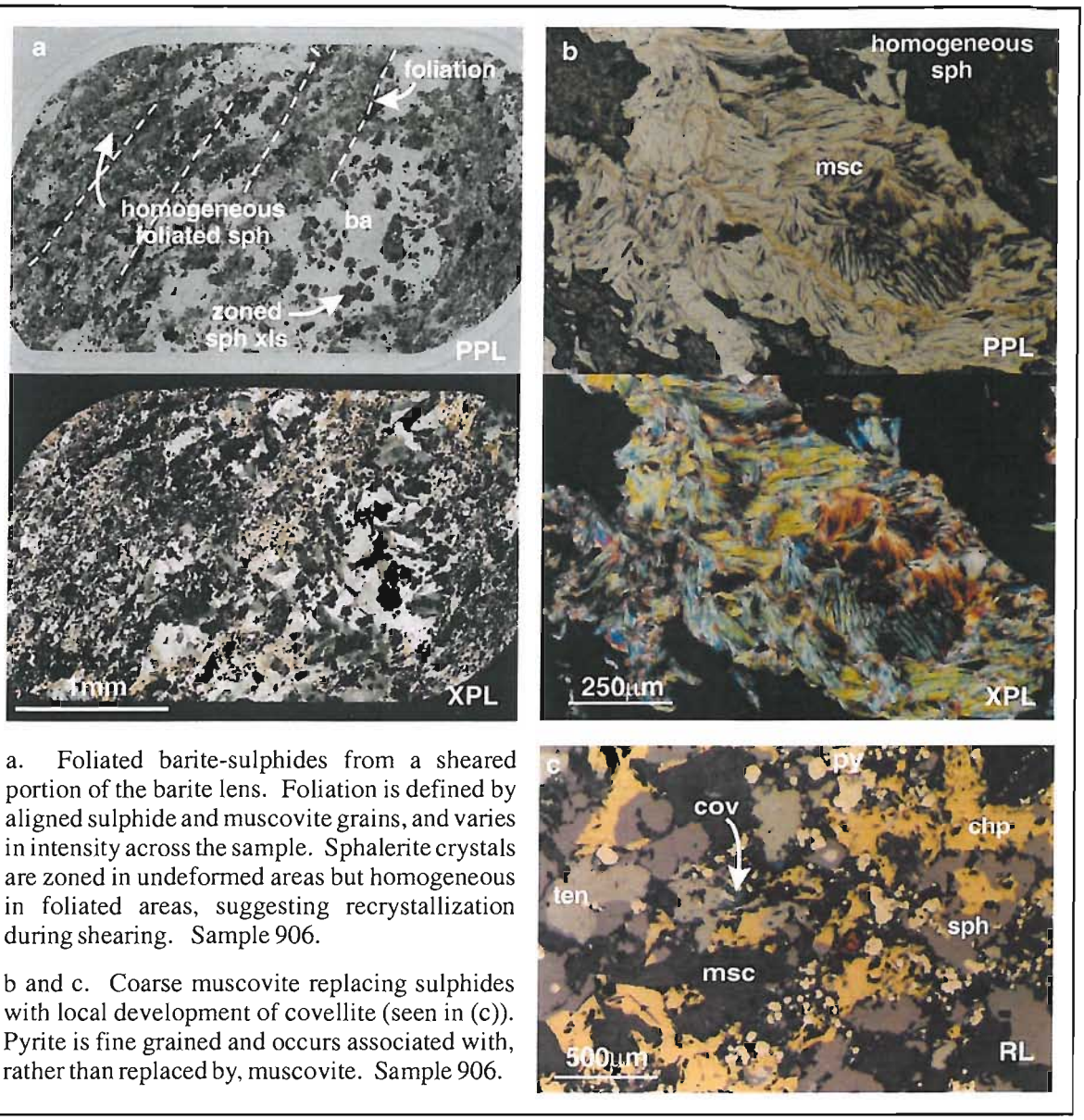

a. Foliated barite-sulphides from a sheared portion of the barite lens. Foliation is defined by aligned sulphide and muscovite grains, and varies in intensity across the sample. Sphalerite crystals are zoned in undeformed areas but homogeneous in foliated areas, suggesting recrystallization during shearing. Sample 906.

b and c. Coarse muscovite replacing sulphides with local development of covellite (seen in (c)). Pyrite is fine grained and occurs associated with, rather than replaced by, muscovite. Sample 906.

Figure 4.38. Foliation and muscovite overprinting in the barite lens.

4.6.5 Gold-rich barite lens paragenesis and ore formation

Paragenesis

Figure 4.39 summarises the paragenetic sequence interpreted for the barite lens. The earliest phase to have formed is coarse, zoned sphalerite, followed by the co-precipitation of mainstage sulphides-electrum-barite, including tennantite-chalcopyrite intergrowths, disseminated chalcopyrite-tennantite-galena-sphalerite-electrum, pyrite and barite. Quartz may have precipitated during and/or after barite-sulphide ore formation, and muscovite probably post-dates ore formation.

There is evidence of late stage sulphide oxidation and electrum remobilisation which probably pre-dates metamorphism, occurring during late stages of the ore-formation or during diagenesis. Later metamorphism and deformation caused localized shearing of the barite lens, accompanied by the development of coarse muscovite and minor pyrite replacing mainstage sulphides and barite. The replacement of barite by zeolite may have occurred either during diagenesis or metamorphism.

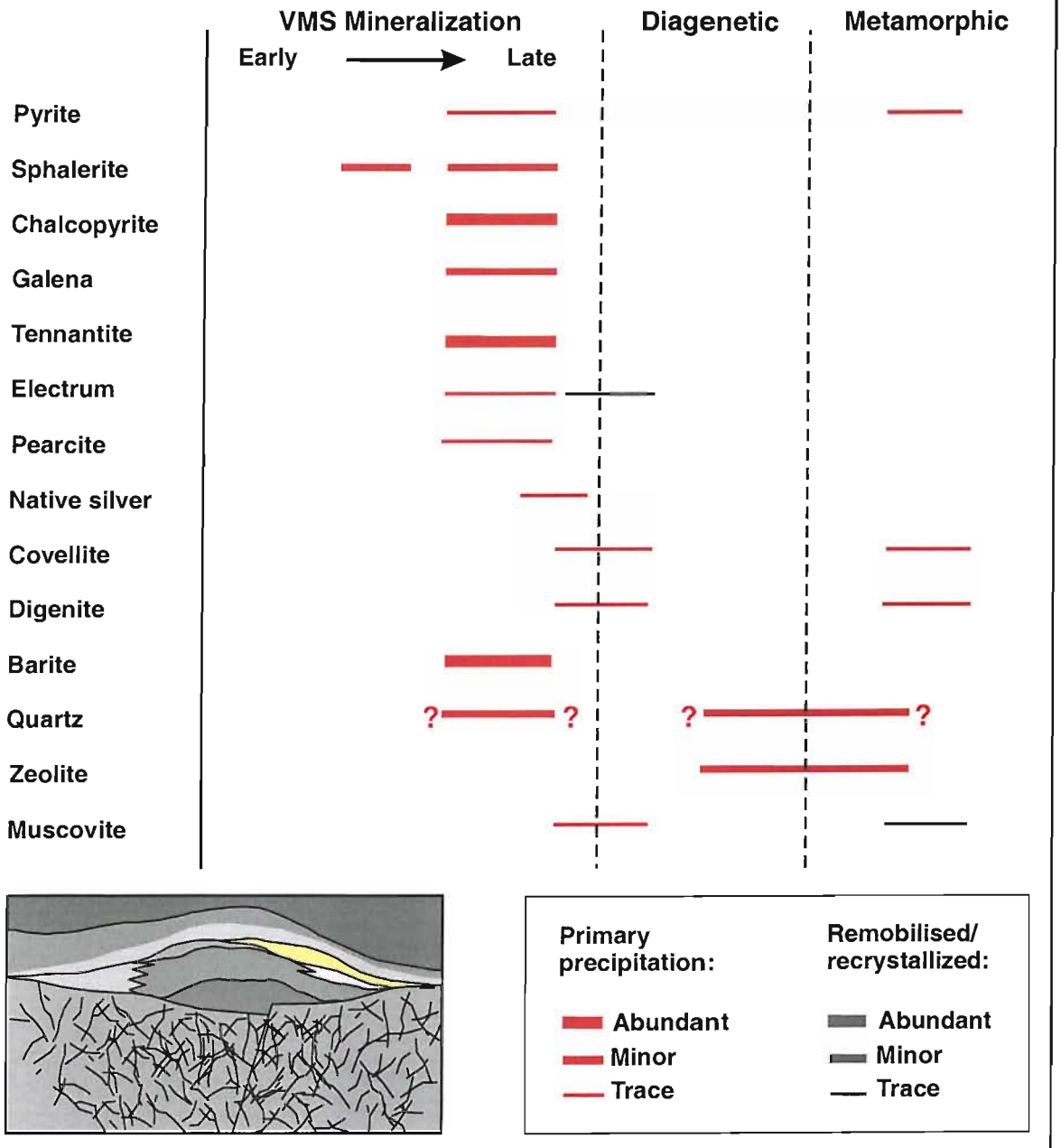

Schematic sketch (lower left) indicates the location of the barite lens (highlighted) relative to the rest of the Balta Tau ores (see also Figure 4.1).

Figure 4.39. Barite lens paragenesis.

Ore formation

The barite lens is conformable and appears to have formed as part of the VMS system, co-genetic with massive sulphides. The stratigraphic position suggests formation after the massive sulphide ores, during later stages of the hydrothermal ore-forming system.

Baritic caps to massive sulphide ores are reported from a number of ancient VMS deposits. Examples comparable to Balta Tau include gold-rich VMS deposits of Tasmania such as the Hellyer deposit, where up to 15m of massive barite with pyrite-sphalerite-galena and pyrite-silica overlie massive sulphides (Solomon & Zaw, 1997), and the Hercules and Rosebery deposits where baritic ores contain minor to trace sphalerite-galena-tetrahedrite-electrum (Zaw & Large, 1992). The Kuroko deposits of Japan commonly have a baritic cap although the barite is not reported to be enriched in gold (e.g. Shimakazi, 1974). At Wetar Island massive sulphides are flanked by unconsolidated Au-Ag-rich barite sands (Scotney et al., 2002). Deposits in China include the Gacun deposit (Yidun Fold Belt) where barite ores are Ag-rich and contain pyrite-galena-sphalerite-tetrahedrite, and the Xiaotieshan deposit (Baiyenchang District) where barite contains chalcopyrite-tennantite-tetrahedrite (Haitian, 1992), the latter being particularly comparable to the barite lens at Balta Tau.

In modern systems, actively venting barite-rich chimneys and diffusers ("white smokers") are a probable analogue to the barite lens at Balta Tau. These are commonly found on the flanks and tops of sulphide mounds, and may co-exist with sulphide-dominated "black smoker" structures. Examples are numerous, with some of the best documented being Axial Seamount (Hannington et al., 1986;, Southern Explorer Ridge (Hannington et al., 1986); PACMANUS (Scott & Binns, 1995); Jade, Central Okinawa Trough (Halbach et al., 1993) and several systems of the Lau Back Arc Basin (Herzig et al., 1990; Herzig et al., 1993; Fouquet et al., 1993). These are typically porous structures dominated by barite, amorphous silica and collomorphic low-Fe sphalerite and/or wurtzite with minor galena, sulphosalts (most commonly tennantite-tetrahedrite) and sometimes marcasite and chalcopyrite. Tennantite-tetrahedrite, galena and chalcopyrite are often associated with the latest stage of precipitation, and barite commonly appears to pre-date the majority of sulphides. In all of the examples listed, baritic ores are enriched in gold and silver relative to the massive sulphide mounds and chimneys. The mineralogy, relationship with mainstage sulphide ores and direct measurements of vent fluids suggest these form from late stage, low temperature and more oxidizing fluids (e.g. Hannington et al., 1986).

Small scale textures observed in barite-sulphides from active systems are also comparable with those from the barite lens at Balta Tau. These include intimate intergrowths of sulphides and aggregates of euhedral barite from the Lau Back-Arc basin (Herzig et al. 1990), fine grained sulphides interstitial to the barite and extremely fine grained sulphide minerals enclosed in large

barite crystals from the Jade deposit (Halbach et al., 1993). The latter texture is particularly analogous with observations from Balta Tau, and suggests that minute amounts of sulphide minerals grew on barite crystal faces during pauses in barite crystal growth. The occurrence of native silver interstitial to barite has been noted in association with biogenic activity (also at Jade, Halbach et al., 1993). The interstitial quartz found in the barite lens may well have originated as amorphous silica which is abundant in baritic chimneys of modern systems (see examples of "white smokers" above) which has been transformed to crystalline quartz during post-formational diagenesis and/or metamorphism.

Although there are many similarities between barite facies in modern systems and those of Balta Tau, there are also some fundamental differences mineralogy. The most striking of these is the abundance and coarseness of visible electrum at Balta Tau, which is not reported from active systems in spite of their elevated gold contents. Rare occurrences of primary visible gold/electrum that have been documented include fine grained (<20μm) electrum from Vai Lili, Lau Back Arc Basin associated with sphalerite-tennantite-chalcopyrite (Herzig et al., 1990; Figure 4a and d, page 2188, Herzig et al. 1993), and minute (few μm) grains interstitial to barite from the Jade deposit (Halbach et al., 1993). Gold in seafloor systems is more commonly encountered in secondary assemblages of sea-floor altered ores, observed at the Southern Explorer Ridge (Hannington et al. 1986) and Snake Pit (Fouquet et al., 1993) deposits. The dominant chalcopyrite-tennantite assemblage associated with barite at Balta Tau is also unusual, and has not been described from modern systems which tend to have sphalerite as the dominant sulphide in barite rich ores.

4.7 HANGING-WALL ALTERATION

The immediate hanging-wall volcanic unit is intensely altered to sericite(-fuchsite-titanite), described in Chapter 3, Section 3.3.4. This unit does not contain ore mineralization; the only sulphide present is pyrite which occurs with sericite as part of the alteration assemblage. The alteration reduces significantly in intensity with increasing lateral and vertical distance from the massive sulphides suggesting it is related to the hydrothermal system.

Figure 4.40. Quartz-epidote vein cutting hanging-wall volcaniclastic sequences.

The volcaniclastic sequences further above the massive sulphides are cut by numerous quartz-epidote, carbonate-epidote and quartz-carbonate-epidote veins ranging in thickness from a few mm to 10's cm wide (Figure 4.40). Although similar veins do occur sparsely in regional volcanics distal from the deposit, the density of these veins is far greater in the hanging-wall mine sequences, again suggesting increased hydrothermal activity post-ore formation in the hanging-wall unit above the VMS ores. This is also suggested by the pervasive epidote alteration of these sequences (Chapter 3, Section 3.3.5).

4.8 SUMMARY

The mineralogy and textures of each ore facies described are summarised in Table 4.1, and the overall paragenesis paragenetic sequence for the whole deposit is shown in Figure 4.41. The paragenesis is based on the individual paragenetic sequences for each ore facies (Figures 4.10, 4.18, 4.23, 4.29 and 4.39) combined with the observed and inferred stratigraphic relationships between ore facies illustrated schematically in Figure 4.1.

The massive sulphides and barite-rich ores at Balta Tau are conformable horizons with ore mineralogy and textures indicative of sea floor precipitation as mound and possibly chimney structures. The extensive electrum in barite-rich ores appears texturally to be cogenetic with massive sulphides and barite. The layered sulphides are also a conformable horizon, and are interpreted as clastic sulphide material that accumulated at the margins of the sulphide mound and recrystallized during late stage hydrothermal activity.

In the footwall, sulphide veins and disseminations replace the host volcanic rocks and are typical of sub-seafloor mineralization in ancient and modern VMS systems. The high proportion of disseminated ore suggests that mineralising fluids permeated through the volcanic rocks rather than being focussed along specific pathways, suggesting that the footwall lithology had a high porosity. This is consistent with clastic textures identified in the footwall (Chapter 3, Section 3.3.2). The footwall volcanics are also extensively altered to an Mg-chlorite which post-dates sulphide ore formation and probably overprint alteration minerals that were cogenetic with sulphides. Late stage footwall quartz-tennantite veins also post-date mainstage mineralization. Zoning and compositional variations within the footwall and massive sulphide horizons are typical of ancient massive sulphide deposits (e.g. Large, 1977; Franklin et al., 1981) and have also been recognised in actively forming systems suggesting that they are a primary feature of VMS deposits (e.g. Fouquet et al., 1993). The formation of compositional variations and zoning is investigated in Chapter 7, Section 7.4.5.

There is little evidence of sea floor oxidation of sulphide ores such the extensive development of secondary Cu sulphides and Fe oxides which have been described from other ancient deposits (e.g. Constantinou and Govett, 1973; Corbett, 2000) and from modern sea-floor systems (e.g. TAG, MAR, Hannington et al. 1988). Minor development of digenite-covellite in the barite lens may reflect a small degree of sea-floor alteration of sulphides, however the lack of extensive alteration suggests that the sulphides at Balta Tau were buried soon after deposition and were not significantly altered by sea floor supergene processes. The extensive sericitic alteration in the immediate hanging-wall locally above massive sulphide ores suggests that hydrothermal activity continued after deposition of the hanging-wall sequences.

During diagenesis/low grade metamorphism, there was minor precipitation of carbonate, zeolite and pumpellyite in ore horizons. Sulphide remobilisation/recrystallization during metamorphism and deformation was minimal and the only evidence found is minor remobilisation of chalcopyrite-tennantite-galena in the footwall and layered sulphides, and recrystallization of ores and muscovite in sheared footwall/barite lens.

The tennantite-chalcopyrite dominated sulphide mineralogy of the barite lens is not typical of upper horizons of VMS deposits and it is unusual for such high proportions of chalcopyrite to be present in baritic ores, as these are generally interpreted to have formed at low temperatures whereas chalcopyrite is generally associated with high temperature ore facies. The formation of this ore horizon is of particular interest due to the significant precious metal enrichment, and is a main focus in the following chapters.

Ore facies		Subdivisions of ore facies
I	Footwall	**Ia** Mainstage (vein and disseminated py-chp-sph-ten-gal) **Ib** Late stage (ten-qtz veins)
II	Massive sulphides	**IIa** Py-rich: **IIa(i)** Py-chp rich (granular, collomorphic); **IIa(ii)** Py-sph rich (collomorphic) **IIb** Sph-rich (partially recrystallized) **IIc** Late stage vug and fracture filling assemblage (chp-ten-sph-gal-asp)
III	Layered sulphides	Sph-chp-py-ten-gal-tet with trace hessite
IV	Barite-rich sulphides	**IVa** Py clasts **IVb** Sph-py-chp-ten-gal-elec matrix and fracture fill
V	Barite lens	Massive barite with ten-chp-sph-gal-py-electrum

Table 4.1. Classification of mineralization at Balta Tau.

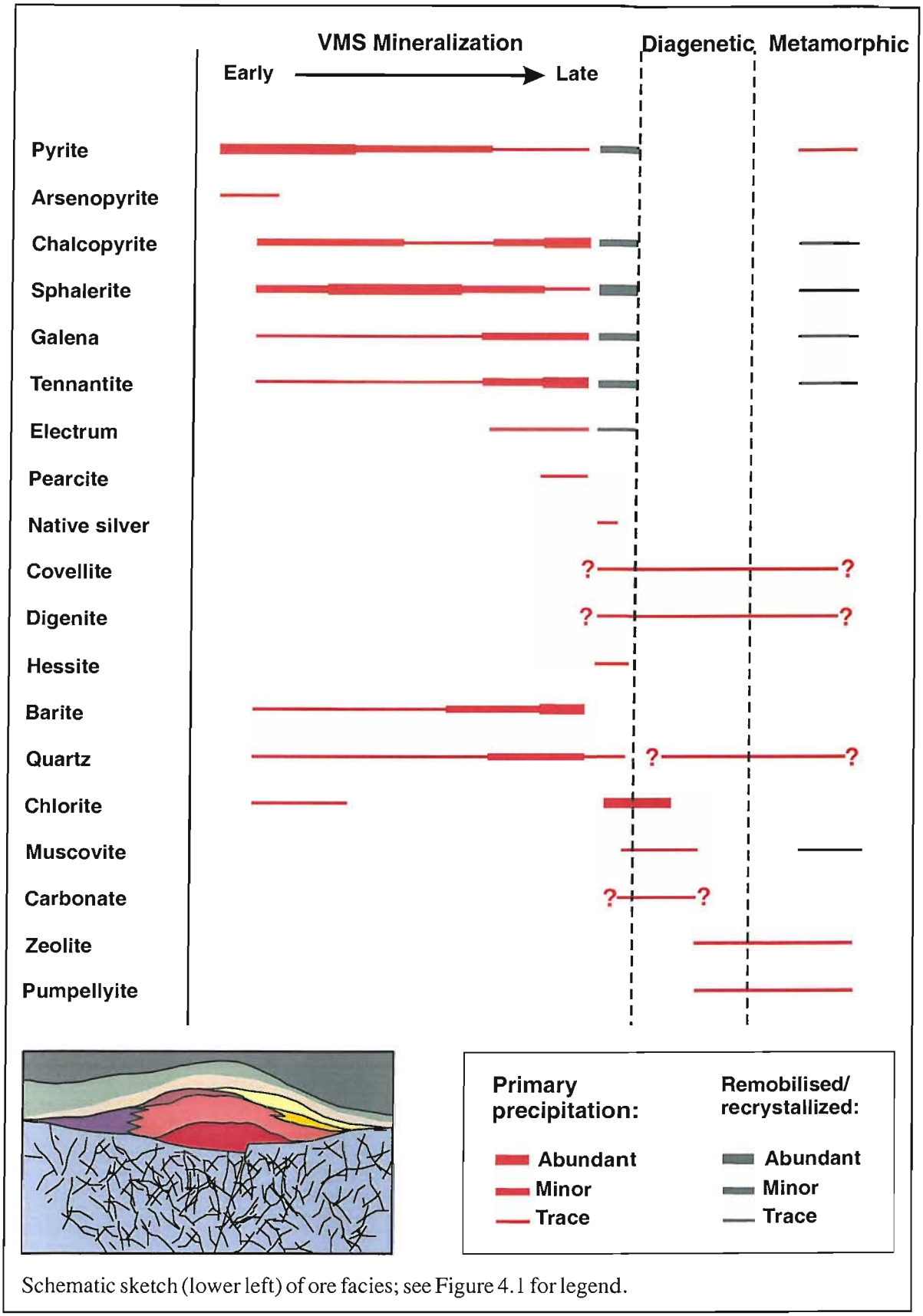

Schematic sketch (lower left) of ore facies; see Figure 4.1 for legend.

Figure 4.41. Paragenesis of the Balta Tau deposit.

5 CHEMISTRY OF ORE AND ALTERATION PHASES

5.1 INTRODUCTION

Microprobe data was obtained from both ore and alteration phases to provide information on formational conditions and investigate compositional variations between ore facies. In particular, the concentration of trace elements in specific sulphide phases and zoning in trace elements across the deposit, and the composition and zoning of electrum grains in various modes of occurrence were determined. In addition, close attention was given to the composition of alteration minerals and variations between footwall, hanging-wall and regional facies and zoning within the footwall.

All analyses were carried out using a Cameca SX-50 electron microprobe at the Natural History Museum, London with element concentrations calculated from relative peak intensities using the PAP method (Pouchou and Pichoir, 1984).

5.2 ORE CHEMISTRY

5.2.1 Introduction and methodology

Sulphide phases were analysed for S, Fe, Cu, Zn, Pb, Sb, As, Ag, Au, Te, Se, Cd, Hg, Bi, and in some cases Ge, Ga, Cr, In and Co. Counting times were 10 to 30 seconds for each element with a beam current of 20nA and an accelerating voltage of 20kV, giving detection limits in the range 0.04 to 0.10wt% for most elements. Analytical details for each element (count time, standard used for calibration, detection limit, corrections for spectral overlaps) and a full data listing are given in Appendix B1.

The following sections present data for each mineral phase and investigate trends in major and trace element composition within single grains, and on a large scale within and between ore horizons. For each mineral, analyses are grouped according to the mineralised horizons defined and discussed in Chapter 4 (Table 4.1). Microprobe data is presented as atomic percent (at%) in all discussions and graphs.

5.2.2 Pyrite

Pyrite analysed from all mineralized horizons at Balta Tau is close to the ideal stoichiometry FeS_2 and the trace elements detected are As, Zn, Cu and Sb (Table 5.1). None of the pyrite analysed contains Au above detection (0.02 at%).

a. Pyrite (weight %)	n	S	Cu	Fe	As	Sb	Zn	Total
footwall mainstage	28	53.07	0.07	47.92	0.27	0.04	bd	101.41
py-chp granular massive sulphides	19	52.50	0.23	47.25	0.39	bd	0.12	100.62
py-(sph) colloform massive sulphides	17	52.41	0.28	47.16	0.12	bd	bd	100.15
sph-rich massive sulphides	19	53.13	bd	46.87	0.81	0.12	0.26	101.23
layered sulphides	3	52.45	0.08	47.67	0.08	bd	0.40	100.69
barite-rich sulphides	28	52.68	0.15	46.74	1.45	0.14	bd	101.21
gold-rich barite lens	4	52.44	0.28	47.12	0.47	0.34	bd	100.70

b. Pyrite (atomic %)	n	S	Cu	Fe	As	Sb	Zn	Total
footwall mainstage	28	65.64	0.05	34.04	0.14	0.01	bd	99.90
py-chp granular massive sulphides	19	65.58	0.15	33.89	0.21	bd	0.07	99.90
py-(sph) colloform massive sulphides	17	65.69	0.19	33.94	0.06	bd	bd	99.93
sph-rich massive sulphides	7	65.88	bd	33.37	0.43	0.04	0.16	99.91
layered sulphides	3	65.42	0.05	34.13	0.04	bd	0.25	99.89
barite-rich sulphides	28	65.57	0.10	33.41	0.78	0.04	bd	99.92
gold-rich barite lens	4	65.50	0.18	33.79	0.26	0.11	bd	99.87

Table 5.1. Summary of microprobe data for pyrite, presented as (a) weight % and (b) atomic %. (Data are the mean of "n" number of analyses; bd = below detection).

Pyrite from all mineralized horizons contains detectable As (>0.03at%), reaching 2.2at% in pyrite clasts of the barite-rich sulphides (Figure 5.1a). Pyrite from the barite-rich sulphides (Figure 5.2) and more rarely the footwall (Figure 5.3a, b) exhibits highly variable As contents within single crystals, while collomorphic pyrite from massive sulphides shows a slight variability in As (Figure 5.3d) and pyrite from coarse granular massive sulphides, layered sulphides and the barite lens has homogeneously low As (e.g. Figure 5.3c). The variation in As from pyrite in the footwall and barite-rich sulphides correlates with oscillatory zoning observed on backscatter electron images, where intensity reflects the molecular mass (e.g. Figures 5.2a, b and 5.3 a, b). This zoning is not observed in uniformly As-poor pyrite (e.g. Figure 5.3c).

Sb enrichment of pyrite is less extensive and at lower concentrations than As. Pyrite in sphalerite-rich sulphides, barite-rich sulphides and the barite lens contains Sb above detection (0.01at%) with concentrations reaching 0.44at%. Some analyses contain elevated As and Sb (Figure 5.1b), however the lack of correlation between either As and Cu (Figure 5.1c) or Sb and Cu indicate that enrichment in As and Sb is not due to the incorporation of tennantite-tetrahedrite inclusions.

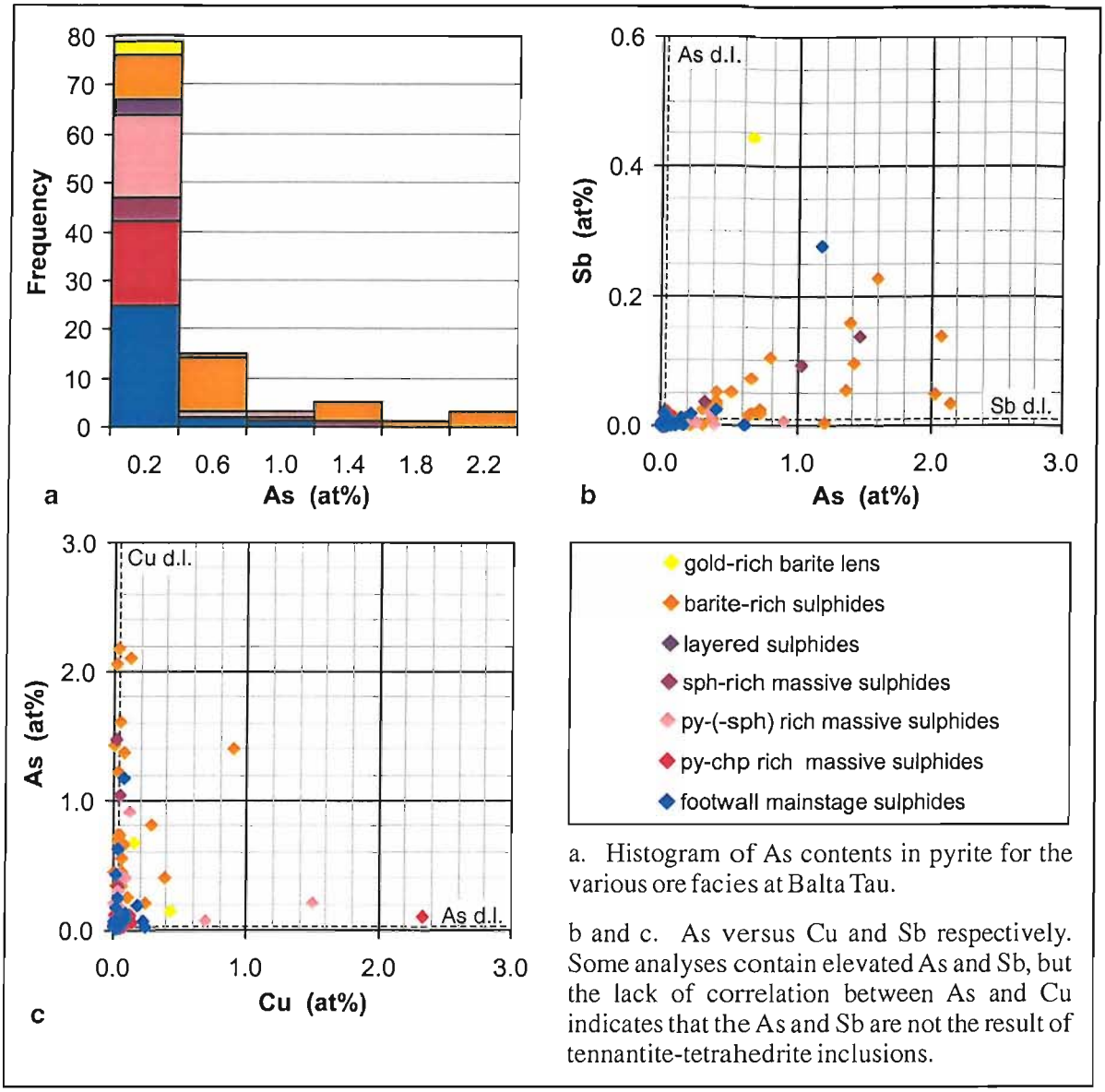

a. Histogram of As contents in pyrite for the various ore facies at Balta Tau.

b and c. As versus Cu and Sb respectively. Some analyses contain elevated As and Sb, but the lack of correlation between As and Cu indicates that the As and Sb are not the result of tennantite-tetrahedrite inclusions.

Figure 5.1. Trace element concentrations in pyrite from Balta Tau.

A zoned pyrite aggregate from the barite-rich sulphides was selected for x-ray mapping of As, Sb and Cu content (Figures 5.4a, b, c). The most prominent feature is the complex oscillatory zoning of As defining euhedral pyrite crystal cores with multiple stages of overgrowths. The As-rich zones are not associated with elevated Cu confirming that they are not sub-microscopic tennantite-tetrahedrite inclusions but may reflect As substitution in the pyrite lattice. Clark et al. (1960) demonstrated that a maximum of 0.53wt% As can be dissolved in pyrite as solid solution, which is much lower than the As levels recorded here. However, Fleet et al. (1989) suggest that high As (up to 8.4wt%) in zoned pyrite from stratabound gold deposits occurs as a metastable $Fe(As,S)_2$ solid solution, which may account for the high As in pyrite from Balta Tau. Sb mimics the As zoning but at much lower concentrations (Figure 5.4b) which is consistent with the coupled enrichment of As and Sb in a number of point analyses (Figure 5.1b), and the association of these two elements as substitutions is reasonable given the similarities in their chemical behaviour.

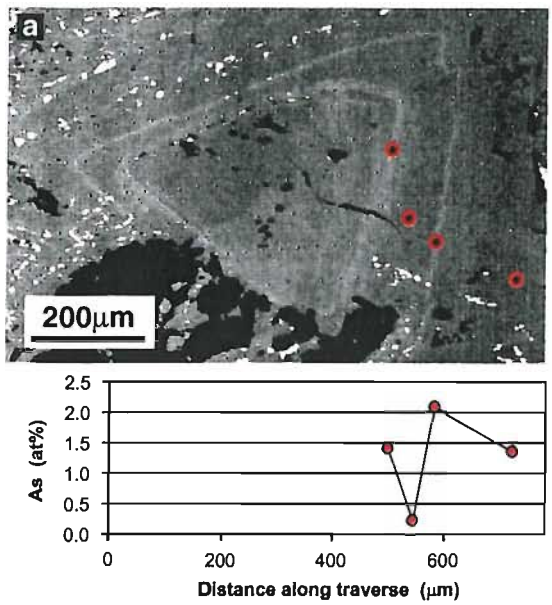

a. Backscatter electron image of pyrite from a large clastic pyrite mass with distinct zoning, where bright zones contain up to 2at% As and dark zones are As poor. Bright inclusions in the pyrite are tennantite and galena, and the black phases are quartz and muscovite.

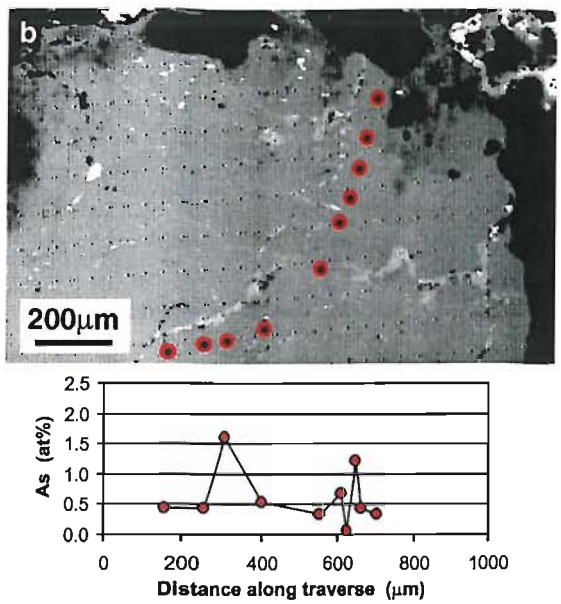

b. Backscatter electron image of coarse pyrite crystal with highly elevated and zoned As contents. The zoning is not visible on the backsattered image at this large scale, but As values vary from below detection to over 1.5at%. Inclusions are chalcopyrite (dull) and galena (bright). Sample 01BT082.

Figure 5.2. Variation of As content within single pyrite grains from the barite-rich sulphides.

The x-ray mapping also highlights numerous small (<20μm) tennantite-tetrahedrite inclusions which appear as irregular areas of high As, Sb and Cu (Figures 5.4a, b and c) and commonly define growth zones in the pyrite. These inclusions were also observed in polished thin section (Chapter 4, Section 4.5.2, Figure 4.25) and in backscatter images on the microprobe (and were avoided for point analyses and traverses).

Numerous analyses contain Zn and Cu above detection, and since no mechanism has been established for substitution of these elements into the pyrite lattice they probably result from the incorporation of unseen (either sub-microscopic or sub-surface) sphalerite and chalcopyrite inclusions (e.g. Goodfellow & Franklin, 1993; Huston et al., 1995).

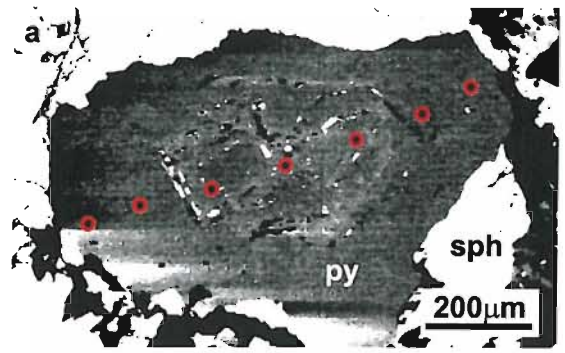

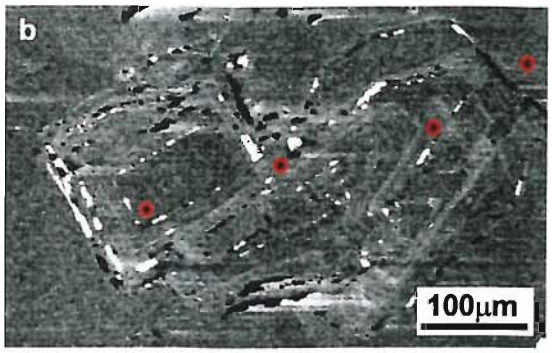

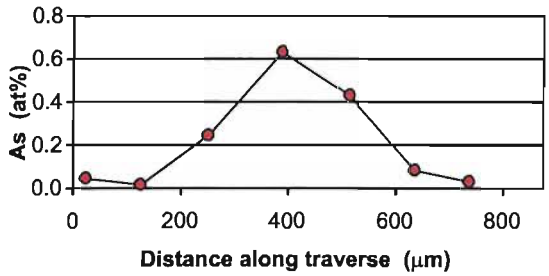

a. Backscatter electron image of a zoned pyrite crystal from a sphalerite-rich footwall vein. In the crystal core, brighter zones contain up to 0.6 at% As. Sample 01BT162.

b. Enlargement of the zoned core in (a) showing oscillatory As-rich and As-poor growth zones. Sample 01BT162.

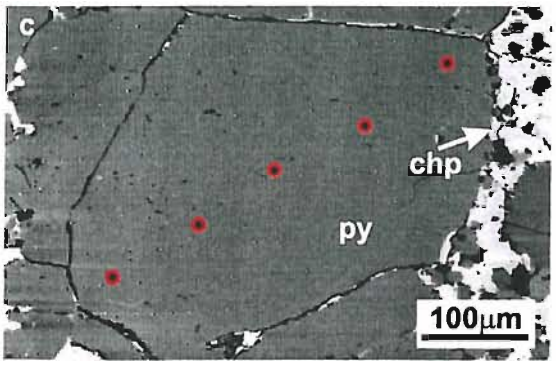

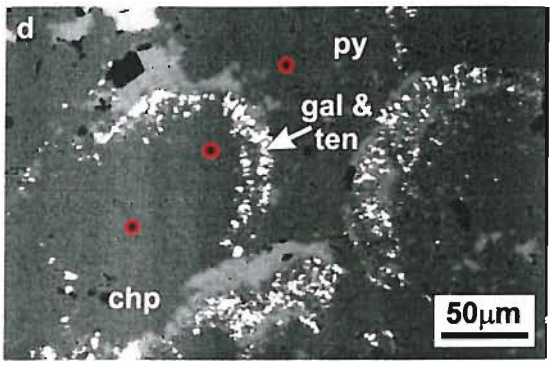

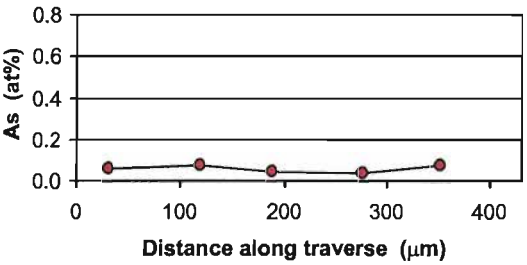

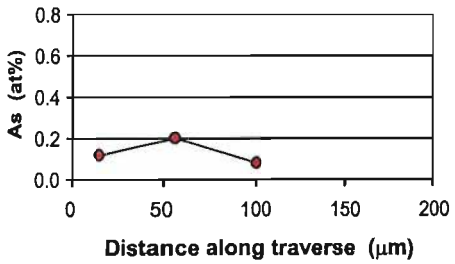

c. Backscatter electron image of a large pyrite crystal from pyrite-chalcopyrite rich massive sulphides enclosed in finer grained pyrite and chalcopyrite. The pyrite is homogeneous with no visible zoning and probe data indicates very low As contents. Sample 901.

d. Backscatter electron image of collomorphic pyrite containing radial inclusions of galena, tennantite and chalcopyrite. This pyrite contains some As but much less than that of the barite-rich

Figure 5.3. Variation of As content within single pyrite grains from the footwall sulphides and massive sulphides.

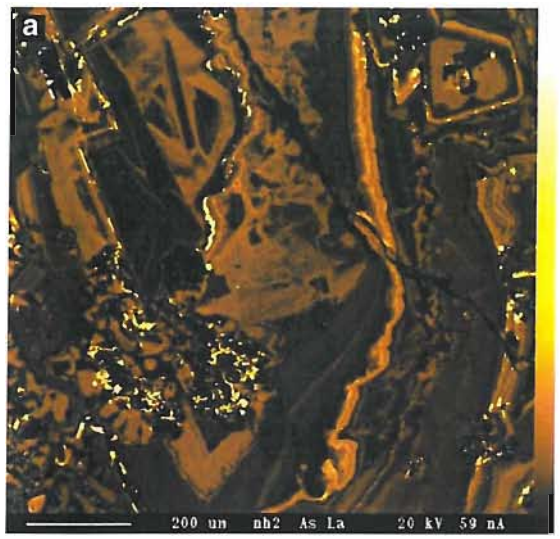

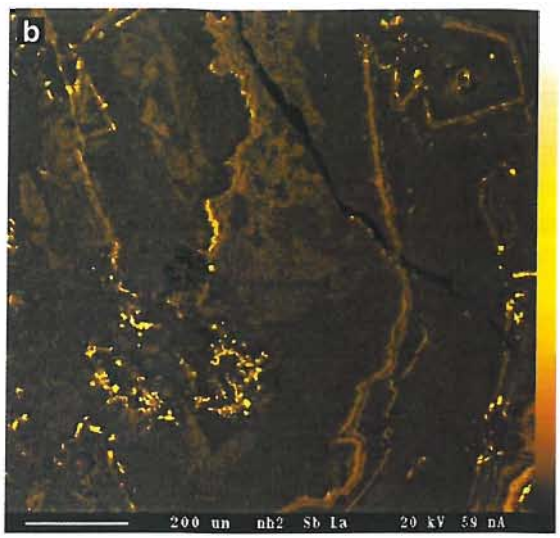

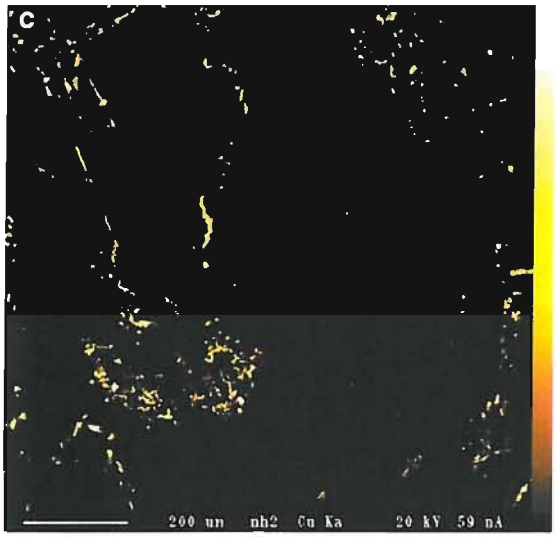

a, b and c. False colour images representing concentrations of As, Sb and Cu respectively produced by x-ray mapping of pyrite. Small (<20μm) bright spots correlate spatially on all three maps and represent fine inclusions of tennantite-tetrahedrite. Large scale zoning in As concentration is evident in (a) and defines multiple stages of pyrite growth including euhedral crystal cores with irregular overgrowths. In (b) Sb mirrors the As pattern but at lower concentrations. Cu contents (c) do not mirror this zoning, indicating that it is not the result of sub-microscopic tennantite-tetrahedrite inclusions. Sample 01BT136.

Figure 5.4. X-ray maps of As, Sb and Cu concentrations in pyrite from the barite-rich sulphides.

5.2.3 Arsenopyrite

Arsenopyrite is rare at Balta Tau and has only been identified in massive sulphides, where it forms coarse, blocky crystals in granular pyrite-chalcopyrite (Figure 5.5a) and small bladed crystals in late stage massive sulphides (Figure 5.5b).

Microprobe data were obtained from one large grain enclosed in pyrite-chalcopyrite rich massive sulphides and two smaller grains from the late stage assemblage (Table 5.2). The Fe content is stoichiometric at 33.3at% while the As/S ratio is variable and lower than the ideal proportions (Figure 5.5c and d), and Au, Se, Te, Zn and Cu were detected in trace amounts. Se and Te reach a maximum of 0.17at% and 0.12at% respectively, and probably substitute stoichiometrically for S. Au is below detection in the calculated means of analyses shown in Table 5.2, however two individual analyses from the late stage arsenopyrite contain 0.04at% Au, which although close to

the detection limit (0.03at%) suggest variable Au enrichment in crystals of this late stage assemblage. The elevated Zn and Cu are probably caused by sub-surface and/or sub-microscopic inclusions of sphalerite and chalcopyrite, since arsenopyrite is not known to accommodate either Zn or Cu by lattice substitutions.

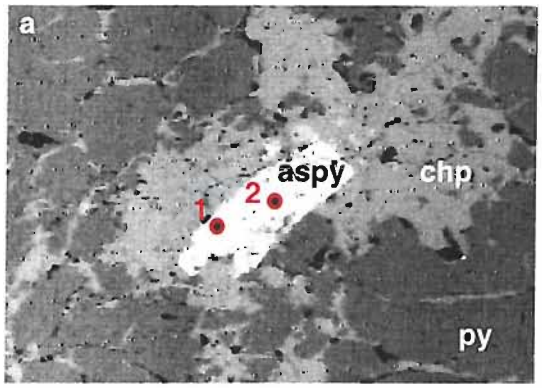

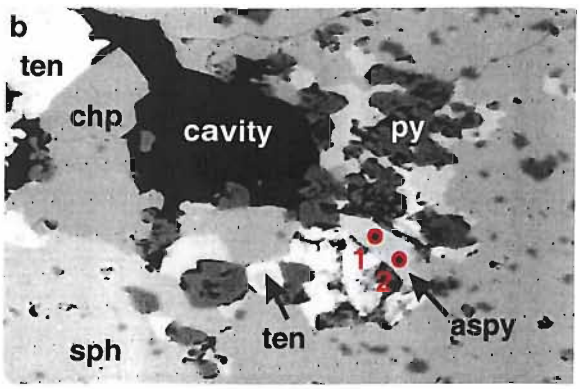

n	S	Au	Fe	As	Se	Zn
#1	33.31	bd	33.89	32.30	0.14	bd
#2	33.64	bd	33.12	32.87	0.14	bd

n	S	Au	Fe	As	Se	Zn
#1	34.93	bd	33.36	31.14	0.08	0.28
#2	33.71	0.04	33.29	32.02	0.10	0.70

a and b. Backscatter electron images and compositions of arsenopyrite from (a) mainstage pyrite-chalcopyrite dominated massive sulphides, and (b) late stage massive sulphides associated with tennantite, chalcopyrite and pyrite filling a cavity in earlier collomorphic sphalerite(-pyrite).

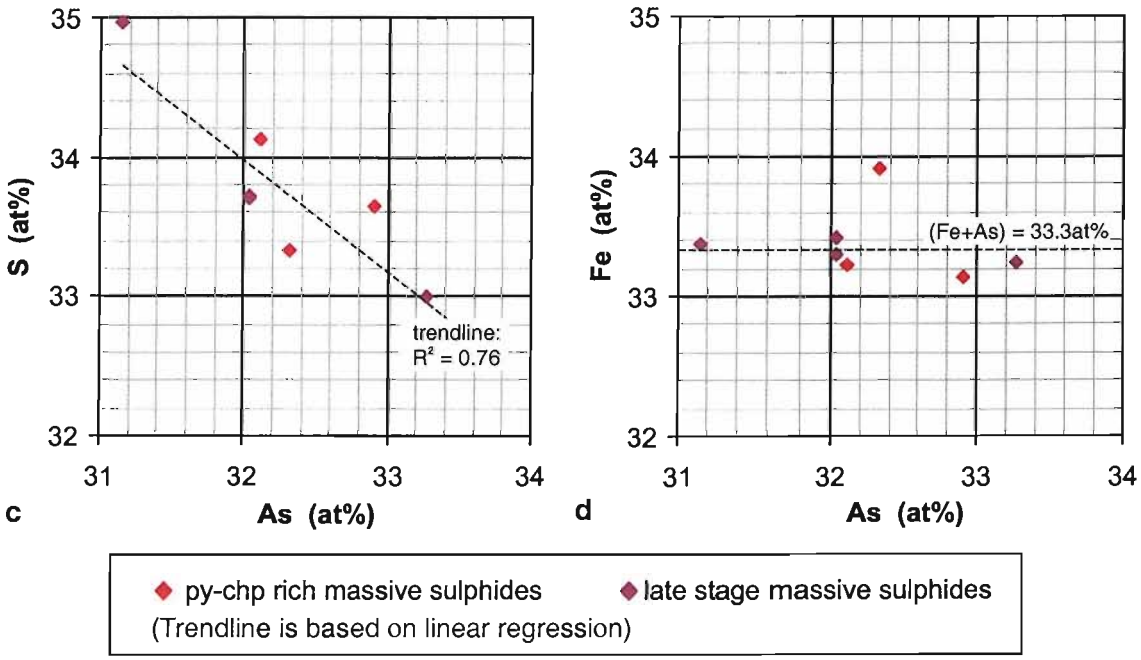

c and d. Scatter plots of S and Fe versus As for arsenopyrite indicate that S correlates negatively with As while Fe remains approximately constant and close to 33.3at%. This is consistent with arsenopyrite lattice accomodating systematic variations in As/S while Fe remains contant at the stoichiometric value.

Figure 5.5. Composition of arsenopyrite in mainstage and late stage massive sulphides.

a. Arsenopyrite (weight %)	n	S	Au	Cu	Fe	As	Sb	Se	Te	Zn	Total
py-chp rich massive sulphides	3	19.57	bd	0.14	33.81	44.02	bd	0.21	0.17	bd	98.00
late stage massive sulphides	4	20.22	bd	0.13	34.68	44.82	bd	0.13	0.05	0.51	100.64

b. Arsenopyrite (atomic %)	n	S	Au	Cu	Fe	As	Sb	Se	Te	Zn	Total
py-chp rich massive sulphides	3	33.69	bd	0.12	33.41	32.42	bd	0.15	0.07	bd	99.89
late stage massive sulphides	4	33.83	bd	0.11	33.32	32.10	bd	0.09	0.02	0.42	99.92

Table 5.2. Summary of microprobe data for arsenopyrite, presented as (a) weight % and (b) atomic %. (Data are the mean of "n" number of analyses; bd = below detection).

5.2.4 Chalcopyrite

Chalcopyrite analyses are close to the ideal stoichiometry $CuFeS_2$ and contain trace amounts of Zn, Ag, As and rarely Sb (Table 5.3).

a. Chalcopyrite (weight %)	n	S	Ag	Cu	Fe	As	Zn	Total
footwall mainstage	8	35.34	bd	35.10	30.14	0.08	0.13	100.80
py-rich massive sulphides	14	35.69	bd	34.20	29.77	0.07	0.13	99.90
layered sulphides	4	35.21	bd	34.89	30.19	0.10	0.27	100.67
barite lens	11	34.83	0.17	34.29	29.57	0.15	0.51	99.53

b. Chalcopyrite (atomic %)	n	S	Ag	Cu	Fe	As	Zn	Total
footwall mainstage	8	50.10	bd	25.11	24.54	0.05	0.09	99.90
py-rich massive sulphides	14	50.51	bd	24.73	24.48	0.04	0.09	99.86
layered sulphides	4	50.01	bd	25.00	24.62	0.06	0.19	99.89
barite lens	11	50.07	0.08	24.88	24.41	0.09	0.36	99.90

Table 5.3. Summary of microprobe data for chalcopyrite, presented as (a) weight % and (b) atomic %. (Data are the mean of "n" number of analyses; bd = below detection).

Ag enrichment above detection (0.04at%) is restricted to chalcopyrite from the barite lens and from pyrite-rich massive sulphides. In the barite lens, chalcopyrite contains up to 0.37at% Ag which correlates positively with As (Figure 5.6), suggesting both may be derived from sub-surface or sub-microscopic inclusions of Ag-rich tennantite which is abundant in this zone. By contrast, chalcopyrite in pyrite-rich massive sulphides contains no more than 0.06at% Ag which is not accompanied by As (Figure 5.6) and may be the result of Ag substituting for Cu in the chalcopyrite lattice (e.g. Huston et al., 1995).

The majority of chalcopyrite analysed from the mainstage footwall sulphides, layered sulphides and the barite lens is enriched in As. In the barite lens, elevated As reaching 0.48at% correlates with Ag and probably reflects Ag-tennantite inclusions (discussed above). The remaining low

level As enrichment (up to 0.07at%) does not correlate with any other trace element and may result from As substituting for Fe in the chalcopyrite lattice. This is has also been observed by Huston et al. (1995), who suggest that up to 0.2wt% (0.12at%) As may substitute for trivalent Fe in the chalcopyrite lattice.

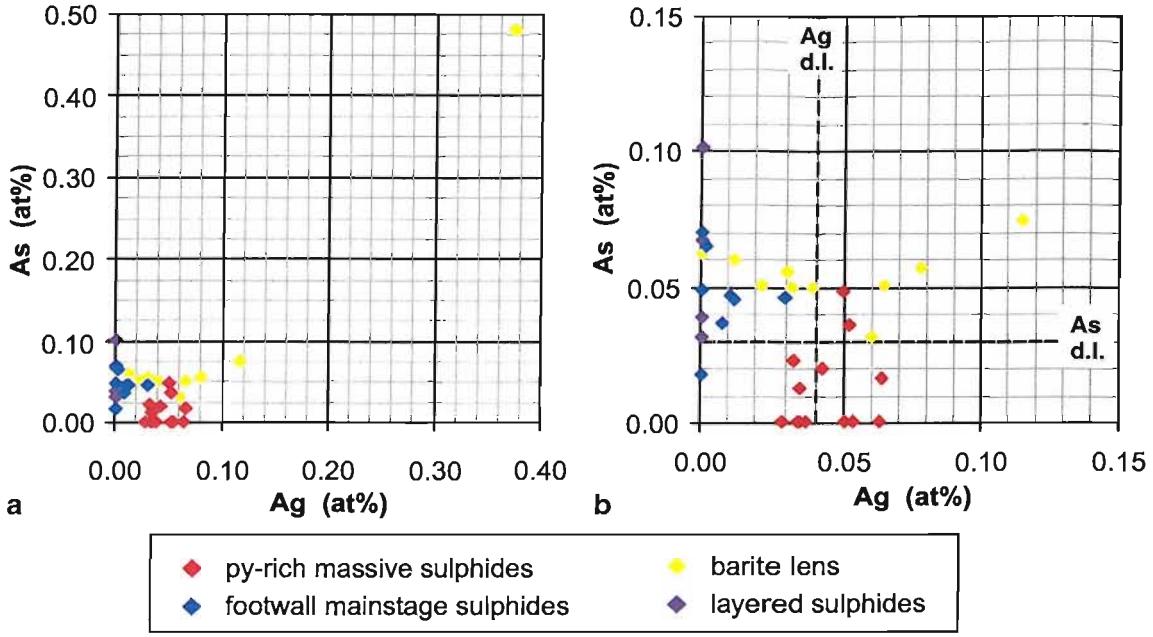

a. Plot of As versus Ag suggests a positive correlation between Ag-As in some chalcopyrite from the barite lens where Ag is above detection. Chalcopyrite from the pyrite-rich massive sulphides is generally enriched in Ag but As-poor, while chalcopyrite from the footwall is As-rich and Ag-poor.

b. The same plot as that shown in (a) but excluding the most As- Ag-rich analysis to show trends in data at low Ag and As concentrations.

Figure 5.6. Trace contents of As and Ag in chalcopyrite.

Detectable Zn (>0.05at%) is present in chalcopyrite from all mineralised horizons. A number of erratic high values in the range 0.5 to 1.0at% Zn are from analyses of small (10-20μm) chalcopyrite inclusions in sphalerite and may be attributed to the enclosing sphalerite being included in the analyses. The more consistent background enrichment of 0.1 to 0.5at% Zn may be attributed to the substitution of Fe by Zn in the chalcopyrite structure, which can account for up to 0.6at% Zn in chalcopyrite at 300°C (Kojima & Sugaki, 1985).

5.2.5 Sphalerite

The composition of sphalerite can be written stoichiometrically as (Fe,Zn)S and varies between an FeS rich end member and a pure ZnS end member, with metals such as Cd, Mn, Cu commonly substituting for Zn-Fe in trace amounts (e.g. Urabe, 1974; Huston et al., 1995). Sphalerite from the footwall, pyrite-rich massive sulphides, layered sulphides and the barite lens at Balta Tau is consistently Zn-rich and Fe-poor with variable enrichment in Cu and Cd (Table 5.4).

a. Sphalerite (weight %)	n	S	Cu	Fe	Zn	Cd	Total
footwall mainstage	4	33.57	0.41	0.10	67.04	0.38	101.49
py-chp rich massive sulphides	3	32.67	0.34	2.06	65.10	0.15	100.32
py-sph rich massive sulphides	10	33.49	0.12	1.25	66.00	0.21	101.08
late stage massive sulphides	4	33.38	0.21	1.03	66.60	0.17	101.39
layered sulphides	6	33.44	0.26	0.39	66.62	0.34	101.00
barite-rich sulphides	4	32.61	0.42	0.70	65.55	0.36	99.64
gold-rich barite lens	5	32.56	0.27	0.22	65.55	NA	98.61

b. Sphalerite (atomic %)	n	S	Cu	Fe	Zn	Cd	Total
footwall mainstage	4	50.17	0.31	0.08	49.14	0.16	99.86
py-chp rich massive sulphides	3	49.46	0.26	1.79	48.33	0.06	99.91
py-sph rich massive sulphides	10	50.16	0.09	1.07	48.47	0.09	99.89
late stage massive sulphides	4	49.93	0.16	0.89	48.86	0.07	99.90
layered sulphides	6	50.20	0.20	0.34	49.05	0.15	99.93
barite-rich sulphides	4	49.77	0.32	0.61	49.06	0.16	99.93
gold-rich barite lens	5	50.06	0.21	0.19	49.42	na	99.87

Table 5.4. Summary of microprobe data for chalcopyrite, presented as (a) weight % and (b) atomic %. (Data are the mean of "n" number of analyses; na= not analysed).

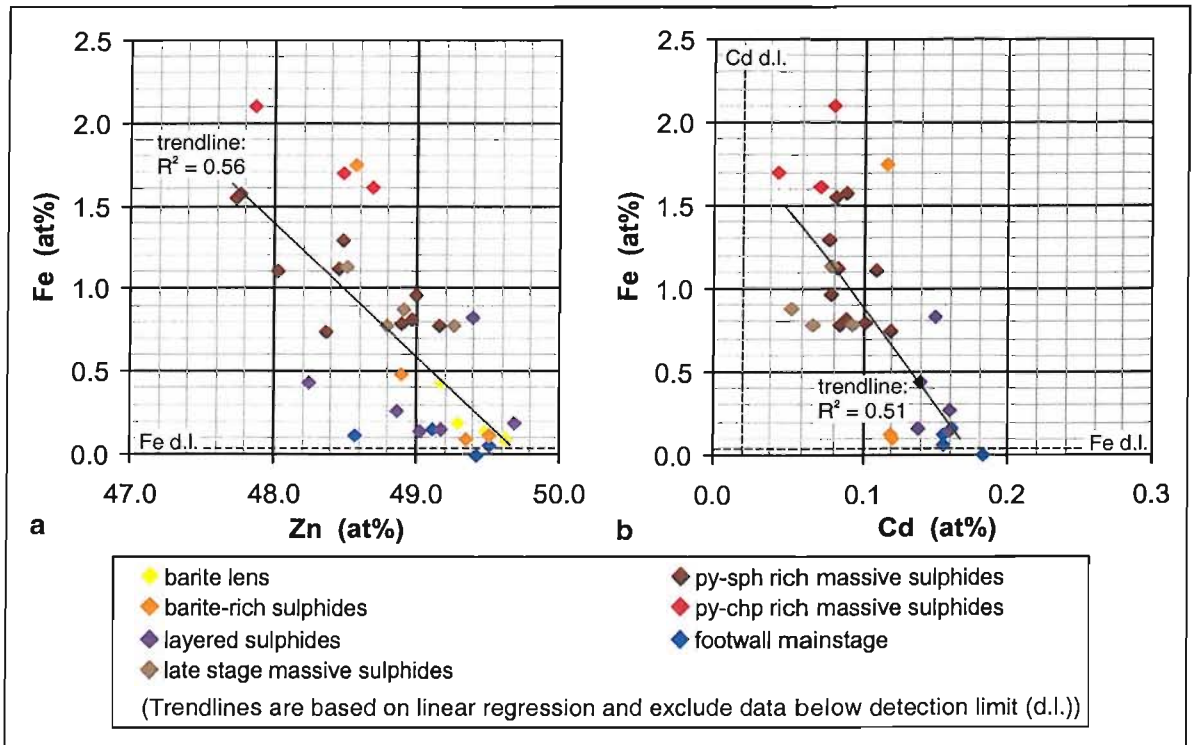

a. Scatter plot of Fe versus Zn. There is a negative correlation consistent with Fe-Zn substitution in sphalerite and the Fe content is notably higher in massive sulphides compared to footwall, layered and barite-rich sulphides and the barite lens.

b. Scatter plot of Fe versus Cd. There is a weak negative correlation with Cd more enriched in footwall, layered and barite-rich sulphides than in massive sulphides. There is no data for the barite lens because Cd was not analysed in sphalerite from this horizon.

Figure 5.7. Major and trace elements in sphalerite from microprobe analyses.

The Cu content ranges from below detection (0.04at%) to 0.52at% with the majority of data between 0.1 and 0.5at%. Elevated Cu in sphalerite is often attributed to chalcopyrite disease (e.g. Huston et al., 1995; Herzig et al., 1990; Goodfellow & Franklin, 1993), particularly where values are erratic and higher than the maximum Cu that may dissolve in sphalerite (0.5wt% or 0.38at%; as determined by Wiggins and Craig, 1980). However, the consistent low level Cu enrichment in sphalerite from Balta Tau is mostly within the limits of Wiggins and Craig (1980) suggesting that Cu may be dissolved in the sphalerite by lattice substitution for Zn-Fe. Furthermore, since the sphalerite at Balta Tau is Fe-poor, a number of analyses contain more Cu than Fe indicating that, in these analyses at least, the Cu can not be derived from chalcopyrite.

The Fe/Zn ratio is consistently low with Fe ranging from below detection (0.02at%) to 2.1at%, and the negative correlation between Fe and Zn (Figure 5.7a) is consistent with these elements occupying the same site in the sphalerite lattice. The mainstage footwall, layered and barite-rich sulphides and the barite lens contain less than 0.5at% Fe, which increases to 0.7 to 1.6at% Fe in sphalerite from pyrite-sphalerite rich and late stage massive sulphides, and to a maximum of 1.6 to 2.1at% Fe in sphalerite from pyrite-chalcopyrite rich massive sulphides. This defines a deposit scale vertical zonation in sphalerite composition, from Fe-poor in the footwall to relatively Fe-rich in lower massive sulphides and returning to Fe-poor in upper sulphides and the barite lens.

Much of the sphalerite from Balta Tau displays multiple zoning with colours in thin section (transmitted light) alternating between dark brown, reddish, beige, yellow and bluish (Chapter 4). It is generally recognised that dark, semi-opaque sphalerite tends to be Fe-rich while paler, transparent sphalerite is close to the Zn-rich end member (e.g. Gribble and Hall, 1985), which is broadly consistent with the Balta Tau sphalerite that is generally very transparent in thin section and has a consistently low Fe content. In order to investigate the relationship between colour and composition on a micro-scale, a large, intensely zoned crystal from the footwall (Figure 5.8a) was selected for x-ray mapping. This reveals a notably uniform Fe content (Figure 5.8b) across the whole crystal, although there is a slight increase in Fe content in the darkest zones. Urabe (1974) also note very little correlation between the colour and Fe content in similar Fe-poor sphalerite from Kuroko ores. This suggests that where the Fe content of sphalerite is overall very low, colour variations may be due to the presence of trace elements rather than the Fe content.

The sphalerite from Balta Tau has a consistent Cd enrichment of 0.04 to 0.18at% except for one erratically high value of 0.28at% (note that no data was obtained for Cd in sphalerite from the barite lens), and there is a negative correlation between Cd and Fe (Figure 5.7b).

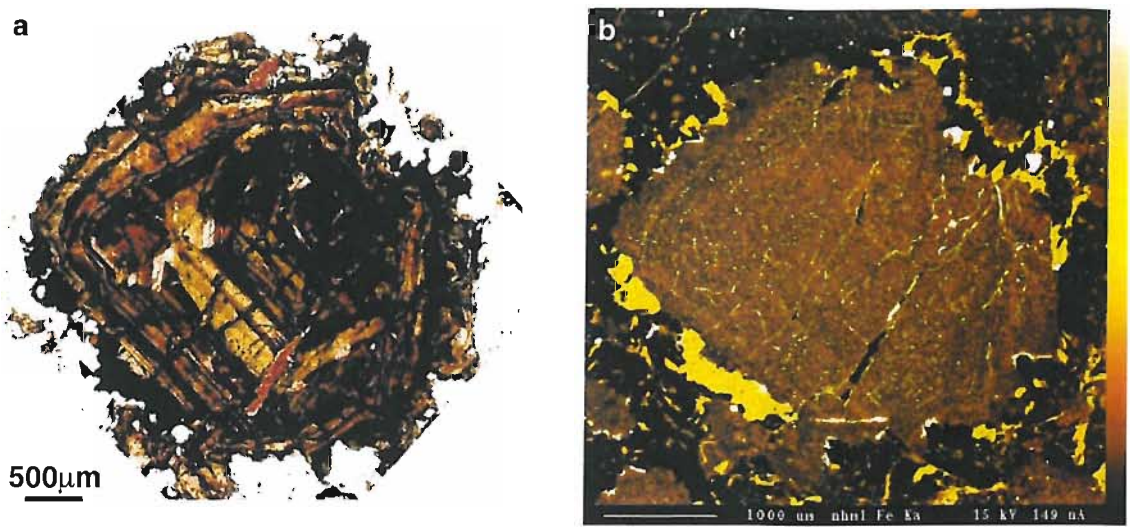

a. Zoned sphalerite crystal with patchy chalcopyrite disease from a footwall vein (Sample 01BT157).

b. X-ray map of Fe content over the same area of the sphalerite crystal as shown in (a). Mapping shows overall low Fe content with little variation in spite of the colour zoning. The darkest brown zones do however contain slightly more Fe than the other zones.

Figure 5.8. X-ray mapping of the Fe concentration in a zoned sphalerite crystal.

5.2.6 Tennantite-tetrahedrite

The tennantite-tetrahedrite solid solution series are part of the Fahlore group of minerals, defined by Ramdohr (1969) as the "Fahlerzgruppe" isomorphous series $M_6^{TRG}M_6^{TET}X_4Y_{13}$, where M is a metal (Ag, Cu, Zn, Fe) in trigonal-planar and tetrahedral sites, X is As or Sb, and Y is S. The tennantite-tetrahedrite group approximate to the ideal stoichiometry:

$(Ag,Cu)_6^{TRG}[(Ag,Cu)_{2/3}(Fe,Zn)_{1/3})]_6^{TET}(As,Sb)_4S_{13}$ (Sack & Loucks, 1985)

The large capacity for stoichiometric exchange in this structure results in a wide range of possible compositions, and tennantite-tetrahedrite may also contain a variety of trace elements including Cd, Hg, Bi, Te and Se (Johnson et al., 1986).

Analyses of fahlore from Balta Tau are generally consistent with the tennantite-tetrahedrite stoichiometry and can be divided compositionally into three groups:

- Those closest to tennantite with As > Sb, which includes the majority of analyses (Table 5.5).
- Those closest to tetrahedrite with Sb > As (Table 5.6).
- Highly argentiferous tennantite with Ag ≈ 10at% (Table 5.7).

a. Tennantite (weight %)	n	S	Ag	Cu	Fe	As	Se	Sb	Te	Zn	Hg	Cd	Total
footwall late stage	9	28.26	bd	43.32	1.78	20.34	0.09	0.75	0.04	6.63	bd	0.07	101.45
footwall mainstage	14	28.21	0.19	42.11	1.51	17.91	0.07	4.13	0.04	7.02	0.07	0.10	101.44
sph-rich ms	3	27.24	0.29	40.95	1.82	16.30	0.05	6.95	bd	6.99	0.32	0.12	101.14
late stage ms	6	28.35	0.52	41.58	4.24	15.65	0.07	8.00	0.04	4.03	bd	0.04	102.59
layered sulphides	4	27.92	1.49	40.65	2.43	13.94	0.09	9.99	0.14	5.93	bd	0.10	102.73
barite-rich ms	17	27.67	0.69	41.80	2.04	17.69	0.07	4.76	bd	6.46	0.08	0.10	101.43
barite lens	29	27.88	0.78	41.58	1.53	17.11	0.07	5.02	bd	6.81	0.10	bd	100.99

b. Tennantite (atomic %)	n	S	Ag	Cu	Fe	As	Se	Sb	Te	Zn	Hg	Cd	Total
footwall late stage	9	44.57	bd	34.47	1.61	13.73	0.06	0.31	0.01	5.12	bd	0.03	99.98
footwall mainstage	14	44.99	0.09	33.90	1.38	12.22	0.05	1.75	0.02	5.50	0.02	0.04	99.97
sph-rich ms	3	44.37	0.14	33.65	1.70	11.36	0.04	2.98	0.00	5.58	0.08	0.06	99.99
late stage ms	6	45.15	0.25	33.41	3.87	10.64	0.04	3.38	0.02	3.16	bd	0.02	99.96
layered sulphides	4	45.09	0.72	33.13	2.26	9.64	0.06	4.25	0.06	4.70	bd	0.05	99.96
barite-rich ms	17	44.47	0.33	33.90	1.88	12.15	0.04	2.03	0.01	5.09	0.02	0.05	99.98
barite lens	29	44.94	0.38	33.82	1.41	11.80	0.05	2.13	0.01	5.38	0.03	bd	99.98

Table 5.5. Summary of microprobe data for tennantite, presented as (a) weight % and (b) atomic %. (Data are the mean of "n" number of analyses; bd = below detection; ms = massive sulphides).

a. Tetrahedrite (weight %)	n	S	Ag	Cu	Fe	As	Se	Sb	Te	Zn	Hg	Total
py-chp ms	6	26.02	bd	39.52	4.97	8.28	0.08	18.92	bd	3.43	bd	101.49
late stage ms	1	26.64	1.78	38.21	1.81	7.82	bd	20.33	0.04	5.95	0.16	102.80
layered sulphides	1	26.67	2.01	38.51	0.85	8.12	0.11	19.09	0.05	7.04	bc	102.69

b. Tetrahedrite (atomic %)	n	S	Ag	Cu	Fe	As	Se	Sb	Te	Zn	Hg	Total
py-chp ms	6	44.00	bd	33.73	4.82	5.99	0.05	8.43	bd	2.85	bd	99.97
late stage ms	1	44.99	0.89	32.55	1.76	5.65	bd	9.04	0.02	4.93	0.04	99.91
layered sulphides	1	44.98	1.01	32.78	0.82	5.86	0.07	8.48	0.02	5.83	bd	99.93

Table 5.6. Summary of microprobe data for tetrahedrite, presented as (a) weight % and (b) atomic %. (Data are the mean of "n" number of analyses; bd = below detection; ms = massive sulphides).

a. Ag-tennantite (weight %)	n	S	Ag	Cu	Fe	As	Se	Sb	Te	Zn	Hg	Cd	Total
barite lens	4	25.12	19.00	33.09	1.53	10.44	0.06	4.47	bd	5.47	0.07	0.06	99.41

b. Ag-tennantite (atomic %)	n	S	Ag	Cu	Fe	As	Se	Sb	Te	Zn	Hg	Cd	Total
barite lens	4	44.26	9.96	29.42	1.55	7.88	0.04	2.07	bd	4.73	0.02	0.03	99.98

Table 5.7. Summary of microprobe data for argentiferous tennantite, presented as (a) weight % and (b) atomic %. (Data are the mean of "n" number of analyses; bd = below detection).

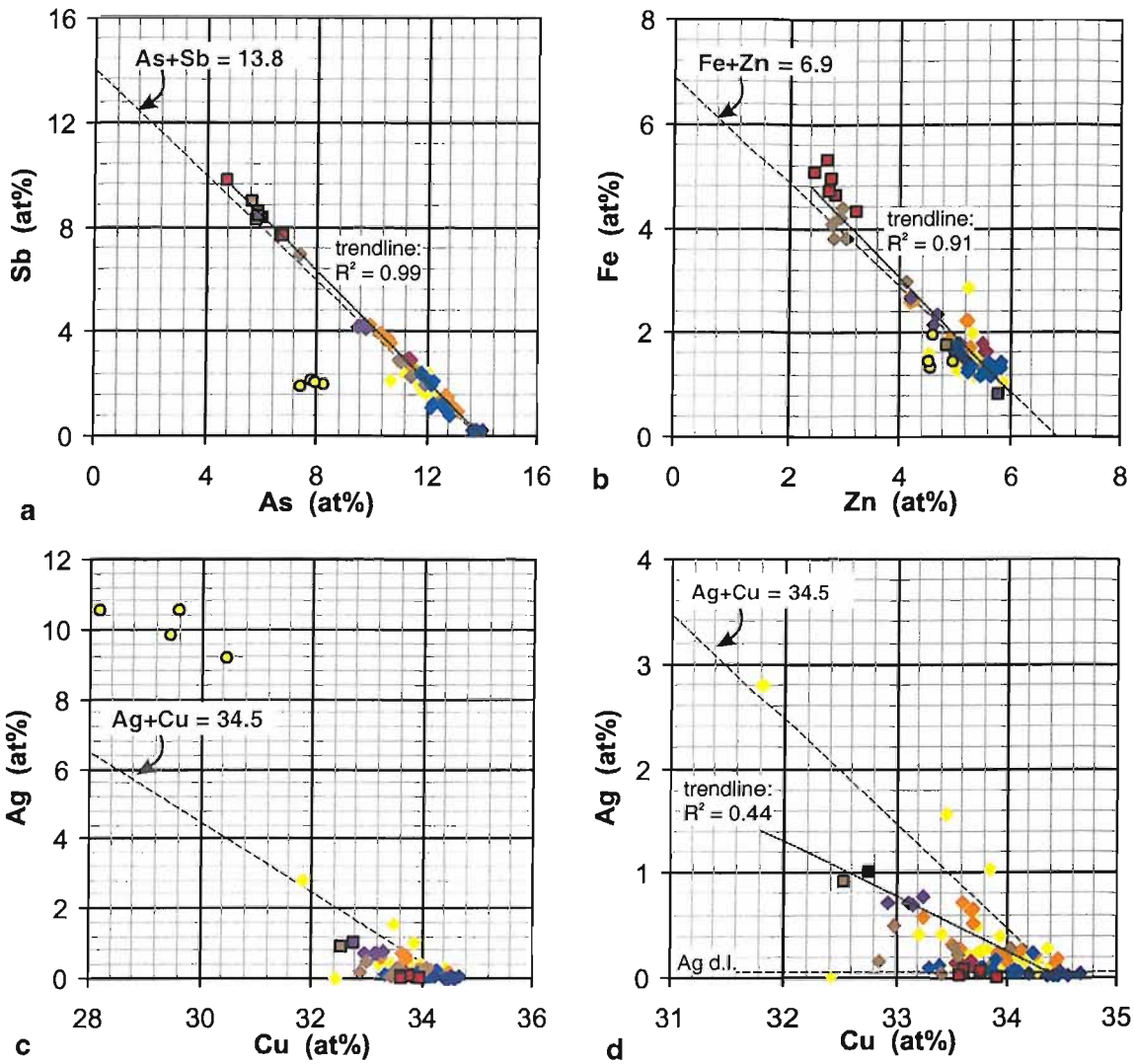

a. Scatter plot of Sb versus As. There is a good negative correlation with total (As+Sb) close to the stoichiometric ideal of 13.8at% with the exception of Ag-rich tennantite from the barite lens.

b. Scatter plot of Fe versus Zn. There is a negative correlation and the total (Fe+Zn) is close to the ideal stoiciometric value of 6.9at%.

c and d. Scatter plots of Ag versus Cu. The total data set is plotted in (c), while in (d) the highest Ag analyses are omitted to emphasise trends at lower concentrations. There is considerable scatter at low Ag concentrations close to and below the Ag detection limit. At higher Ag concentrations there is a poor negative correlation but values of total (Ag+Cu) are not consistent with the stoichiometric ideal of 34.5at%.

Figure 5.9. Major element correlations in tennantite-tetrahedrite.

Element substitutions

Tennantite-tetrahedrite data show negative correlations between elements that are exchangeable in the fahlore structure (Figure 5.9). Excluding the Ag-tennantite, strong negative correlations between As and Sb (Figure 5.9a) and between Fe and Zn (Figure 5.9b) are consistent with As ⇔ Sb and Fe ⇔ Zn substitution respectively in the fahlore lattice. The correlation between Cu and Ag (Figure 5.9c and d) is less well defined because many grains contain Ag below detection (0.05at%). There is however a general negative correlation in analyses where Ag is greater than 0.2at% which is consistent with stoichiometric substitution between Ag and Cu. The average values of (As+Sb), (Fe+Zn) and (Ag+Cu) are 14.06at%, 6.93at% and 34.10at% respectively, which are close to the ideal stoichiometry.

The Ag-tennantite does not conform to the tennantite-tetrahedrite stoichiometry. Analyses indicate a significant depletion in total As+Sb (averaging 9.95at%), a slight depletion in Fe+Zn (averaging 6.28at%) and a significant enrichment in Ag+Cu (averaging 39.38at%). It is possible for Cu to substitute for Zn-Fe in small amounts (Johnson et al., 1986) which may explain the slight decrease in Fe+Zn but can not account for the large excess of Ag+Cu, and since neither Ag or Cu have semi-metal tendancies they are unlikely to substitute for As or Sb. A possible explanation for the Ag-tennantite composition is the presence of sub-microscopic inclusions of an Ag, S and possibly Cu bearing phase such as argentite-acanthite Ag_2S, mackinstryite $(Ag,Cu)_2S$, jalpaite Ag_3CuS_2 or stromeyerite AgCuS. Although not identified from Balta Tau, these minerals are found in trace amount in other VMS deposits (e.g. Uralian deposits, Maslennikov et al., 2000; Kuroko deposits, Shimazaki, 1974). The presence of such inclusions may account for the high Ag+Cu and depleted As+Sb and Fe+Zn, although it does not explain the fact that the decrease in Fe+Zn is proportionally smaller than the decrease in As+Sb. The uniform nature of Ag-enrichment (9.1 to 10.5at%) suggests that if Ag is hosted in a separate phase, this phase must be uniformly distributed throughout the fahlore at a sub-microscopic level.

Compositional zoning within grains

The majority of grains studied from mainstage footwall sulphides, massive sulphides and the barite lens are weakly heterogeneous with up to 0.4at% variation in As-Sb, Ag-Cu, and Fe-Zn, while a few contain more significant variations of 0.5 to 1.0at%. The compositional variations appear random, with no consistent trends from core to margins. Tennantite in late stage footwall veins are the most homogeneous and show little compositional variation.

Compositional zoning between ore facies

The range in major element compositions of fahlore from each ore facies is shown in Table 5.8. Mainstage footwall sulphides, sphalerite-rich massive sulphides, barite-rich sulphides and the barite lens contain Zn-rich tennantite with variable Ag contents that are highest in the barite lens.

The pyrite-chalcopyrite rich massive sulphides contain an Fe-rich, Ag-poor tetrahedrite which is distinct from the rest of the fahlore at Balta Tau (Figure 5.11). Fahlore in late stage massive sulphides and layered sulphides has variable As/Sb and slight Ag enrichment, and Fe/Zn is moderate to high in the late-stage massive sulphides and low in layered ores. The late stage footwall tennantite is homogeneous with notably high As/Sb and Zn/Fe and Ag below detection.

Compositional ranges	mineral	n	Ag	Cu	As	Sb	Fe	Zn
footwall late stage	ten	9	bd	34.21-34.67	13.62-13.80	0.28-0.35	1.50-1.67	5.06-5.26
footwall mainstage	ten	14	bd-0.23	33.32-34.26	11.73-12.81	0.90-2.47	1.16-1.80	4.94-5.90
py-chp rich ms	tet	6	bd-0.08	33.60-33.94	4.74-6.79	7.69-9.81	4.31-5.31	2.52-3.29
late stage ms	ten	6	bd-0.49	32.87-34.05	7.39-11.91	2.08-6.95	2.96-4.40	2.83-4.16
	tet	1	0.89	32.55	5.65	9.04	1.76	4.93
sph-rich ms	ten	3	0.13-0.15	33.59-33.69	11.34-11.38	2.96-3.02	1.63-1.81	5.53-5.63
layered sulphides	ten	4	0.69-0.71	32.95-33.27	9.47-9.72	4.18-4.31	1.81-2.67	4.25-5.14
	tet	1	1.01	32.78	5.86	8.48	0.82	5.83
barite-rich ms	ten	17	0.14-0.70	33.25-34.49	9.90-13.08	1.02-4.28	1.30-2.69	4.25-5.81
barite lens	ten	29	bd-2.79	31.84-34.47	10.65-12.34	1.53-2.89	1.04-2.87	4.59-5.93
	Ag-ten	4	9.11-10.49	28.18-30.45	7.44-8.27	1.99-2.19	1.32-1.98	4.58-5.04

Table 5.8. Variation in major element composition of tennantite-tetrahedrite. All data are atomic%. (Data are the mean of "n" number of analyses; bd = below detection; ms = massive sulphides; ten = tennantite; tet = tetrahedrite).

Trace elements

Hg, Cd, Se and Te are above detection (0.02 to 0.03at%) in fahlore from certain ore horizons. Cd is enriched up to 0.10at% in tennantite from barite-rich sulphides and up to 0.07at% in mainstage footwall and sphalerite-rich massive sulphides. Hg is between 0.06 and 0.11at% in tennantite from sphalerite-rich massive sulphides, and Te is enriched up to 0.07at% in fahlore from layered sulphides. Se enrichment is more ubiquitous with fahlore from all ore facies except for the sphalerite-rich massive sulphides reaching 0.07 to 0.08at%.

5.2.7 Galena

Galena analyses from all ore horizons are generally close to the stoichiometric ideal PbS, with slightly low Pb contents due to the presence of trace metals (Table 5.9). The trace elements detected are Ag, Se, Cu, Fe and Zn, which show systematic variations according to the host ore facies (Figure 5.10).

a. Galena (weight %)	n	S	Ag	Cu	Fe	Se	Zn	Pb	Total
footwall mainstage	9	13.44	bd	0.18	0.05	0.20	0.18	85.70	99.77
py-sph massive sulphides	6	14.17	bd	bd	0.74	0.13	0.30	86.09	101.49
sph-rich massive sulphides	17	13.52	bd	0.06	0.05	bd	0.24	86.25	100.17
layered sulphides	5	13.85	bd	bd	bd	0.13	0.41	86.43	100.88
barite-rich sulphides	33	13.48	bd	0.20	0.06	0.04	0.11	86.22	100.14
gold-rich barite lens	41	13.66	0.30	0.51	0.04	0.08	0.23	85.66	100.49

b. Galena (atomic %)	n	S	Ag	Cu	Fe	Se	Zn	Pb	Total
footwall mainstage	9	49.70	bd	0.34	0.11	0.29	0.33	49.05	99.84
py-sph massive sulphides	6	50.26	bd	bd	1.51	0.18	0.52	47.26	99.80
sph-rich massive sulphides	17	49.92	bd	0.11	0.10	bd	0.42	49.29	99.91
layered sulphides	5	50.26	bd	bd	bd	0.19	0.74	48.56	99.85
barite-rich sulphides	33	49.80	bd	0.37	0.12	0.06	0.20	49.28	99.86
gold-rich barite lens	41	49.72	0.32	0.92	0.09	0.12	0.41	48.27	99.85

Table 5.9. Summary of microprobe data for galena analyses, presented as (a) weight % and (b) atomic %. (Data are the mean of "n" number of analyses; bd = below detection).

a. Galena (weight %)	S	Ag	Cu	Fe	Se	Zn	Pb	Total
footwall #1	13.39	bd	0.25	3.28	1.71	0.07	79.75	98.50
footwall #2	15.18	bd	bd	3.54	0.37	bd	83.51	102.63

b. Galena (atomic %)	S	Ag	Cu	Fe	Se	Zn	Pb	Total
footwall #1	46.95	bd	0.44	6.61	2.43	0.12	43.27	99.86
footwall #2	49.97	bd	bd	6.69	0.49	bd	42.56	99.76

Table 5.10. Two additional galena analyses from the footwall sulphides containing high Fe due to the incorporation of pyrite in the analyses and high Se. Note that these two analyses are not included in the data summary in Table 5.9. (Data are the mean of "n" number of analyses; bd = below detection).

Ag enrichment above detection (>0.11at%) is confined to galena in the barite lens (Figure 5.10a), where Ag reaching 0.84at% may be attributed to Ag substituting for Pb in the galena lattice (which can accommodate up to 0.4mol% Ag_2S, equivalent to 0.8at% Ag; Van Hook, 1960). Anomalously high Ag contents of 1.6 to 1.9at% were recorded from three analyses of a single galena grain in the barite lens. Such elevated Ag in galena is usually attributed to coupled substitution of Ag^+ and either Sb^{3+} or Bi^{3+} (Van Hook, 1960; Sharp & Buseck, 1993), but the Ag-rich grain from Balta Tau does not contain detectable Sb, Bi or any other trace element except for Cu. The Ag may be hosted in sub-microscopic inclusions of a separate Ag-(Cu) bearing phase such as argentite-acanthite, jalpaite, mackinstryite or stromeyerite, as proposed for Ag enrichment in tennantite from the barite lens. The homogeneous nature of the Ag (and Cu) contents in the galena grain suggests that fine inclusions are evenly distributed throughout the grain at a sub-microscopic level. This

texture may result from the Ag-phase co-precipitating with or replacing galena but is unlikely to formed by exsolution given the limited solubility of Ag in PbS even at high temperatures (Van Hook, 1960).

Mainstage footwall galena is consistently enriched in Se containing between 0.10 and 0.46at%, and the pyrite-rich massive sulphides, barite lens and layered sulphides have a more sporadic enrichment of up to 0.3at% Se (Figure 5.10a). This low level enrichment probably reflects the stoichiometric substitution of Se for S (e.g. Huston et al., 1995). Two analyses from a small galena inclusion in footwall pyrite contain 2.35 and 0.49 at% Se (Table 5.10). The erratic high value of 2.35at% suggests that a sub-microscopic inclusion of lead selenide, possibly clausthalite, may be enclosed in the galena or located at the galena-pyrite grain boundary. This mineral is very rare in VMS deposits but a lead selenide, probably clausthalite, was identified in galena from the Sultijelma deposit in Norway (Cook, 1996) and is also recorded as a rare phase from Uralian VMS deposits (Maslennikov et al., 2000).

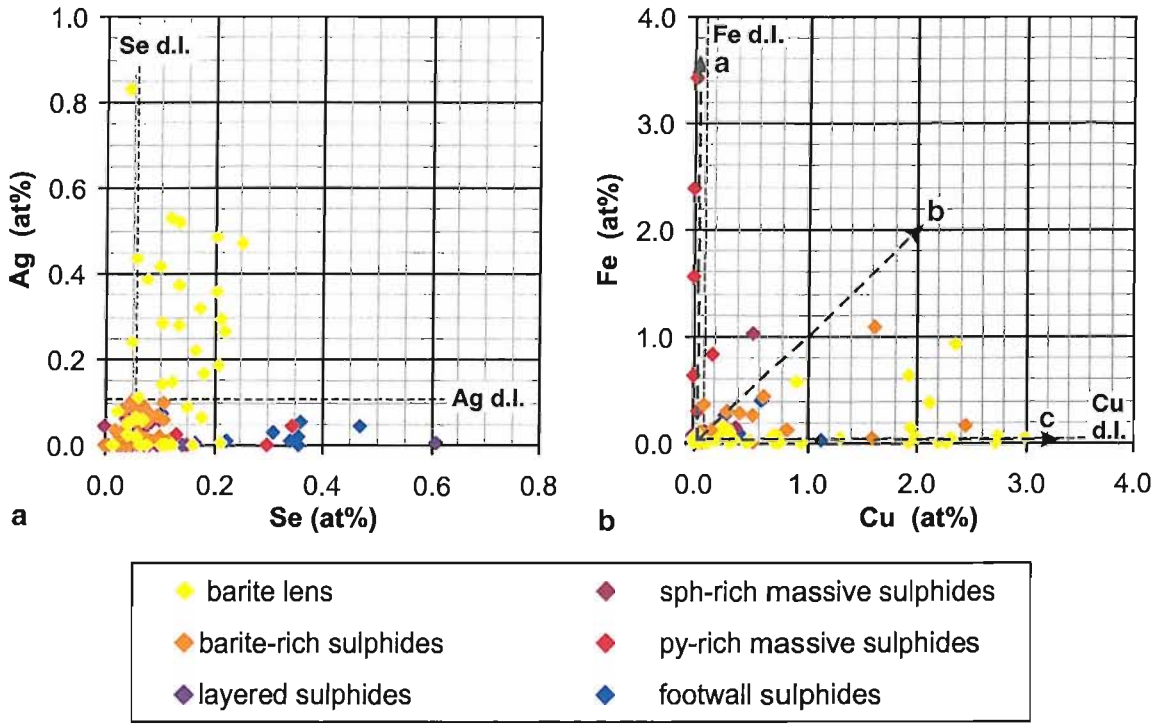

a. Scatter plot of Ag versus Se in galena. In order to show the trends in detail three high silver analyses (>1at%) and one high Se analysis (>0.8at%) have been omitted. Detection limits (d.l.) are indicated by dashed lines. Galena from the footwall have distinct Se enrichment, while galena from barite lens is enriched in Ag.

b. Scatter plot of Fe versus Cu in galena. Elevated Fe contents without corresponding Cu enrichment (arrow (a)) probably correspond to incorporation of pyrite in the analyses, while elevated Fe and Cu (arrow (b)) probably reflect chalcopyrite. The high Cu contents without associated Fe (arrow (c)) are more problematic and possibly reflect covellite or digenite since no other trace elements correlate with Cu.

Figure 5.10. Scatter plots of trace elements in galena from microprobe analyses.

Many galena analyses are enriched in Cu, Fe and Zn with concentrations of each reaching between 2.5 to 3.0at%. Since none of these elements are known to substitute into the galena lattice, the Zn is probably derived from inclusions or adjacent grains of sphalerite and Fe and Cu from pyrite, chalcopyrite and in some cases covellite/digenite alteration rims (Figure 5.10b).

5.2.8 Electrum

Introduction

Analyses of electrum from the barite-rich sulphides and the barite lens are summarised in Table 5.11. The at% data quoted in this section are Au, Ag and Hg contents expressed as a percentage of the total (Au+Ag+Hg) rather than the measured at%. This is to enable compositions of electrum to be compared even where analyses contain significant proportions of other elements from the enclosing minerals (where electrum is very fine grained). These values are summarised together with measured at% in Table 5.11b. Similarly, the weight % data in Table 5.11a includes fineness (where fineness = Au wt% / (Au wt% + Ag wt%)*1000; Harris, 1990) which is useful for comparison with data from other VMS deposits where compositions are quoted as fineness.

a. electrum (weight %)		n	grain size (μm)	Au	Ag	Hg	Total	fineness	Au/Ag
barite-rich sulphides	in barite	10	184	61.69	34.66	3.55	99.90	639.04	1.82
	fractures in py	3	9	38.52	25.70	2.81	67.04	592.78	1.51
barite lens	in coarse ten-chp(-gal)	10	289	75.87	22.25	0.60	98.71	773.33	3.43
	in barite	18	100	63.37	34.55	1.50	99.41	644.51	1.98
	very fine gr. in barite	2	<1	2.64	9.73	0.03	12.40	213.89	0.28
	fractures in sphalerite	7	16	52.21	42.18	5.18	99.57	546.63	1.52
	remobilised	7	84	55.87	34.87	2.26	93.00	605.34	1.74

b. electrum (atomic %)		n	grain size (μm)	at%				at%/(Au+Ag+Hg)*100			Au/Ag
				Au	Ag	Hg	Total	Au	Ag	Hg	
barite-rich sulphides	in barite	10	184	47.70	48.69	2.65	99.03	48.17	49.16	2.67	1.00
	fractures in py	3	9	21.71	27.05	1.45	50.21	43.12	53.59	3.29	0.83
barite lens	in coarse ten-chp(-gal)	10	289	64.14	34.28	0.49	98.91	64.84	34.66	0.50	1.88
	in barite	18	100	49.64	48.39	1.06	99.10	50.09	48.84	1.07	1.08
	very fine gr. in barite	2	<1	2.59	17.29	0.03	19.91	13.09	86.77	0.15	0.15
	fractures in sphalerite	7	15	37.91	52.59	3.34	93.84	40.06	48.05	3.24	0.83
	remobilised	7	84	40.69	45.26	1.55	87.51	45.77	52.43	1.80	0.95

Table 5.11. Summary of electrum microprobe data, presented as (a) weight % and (b) atomic %. (Data are the mean of "n" number of analyses).

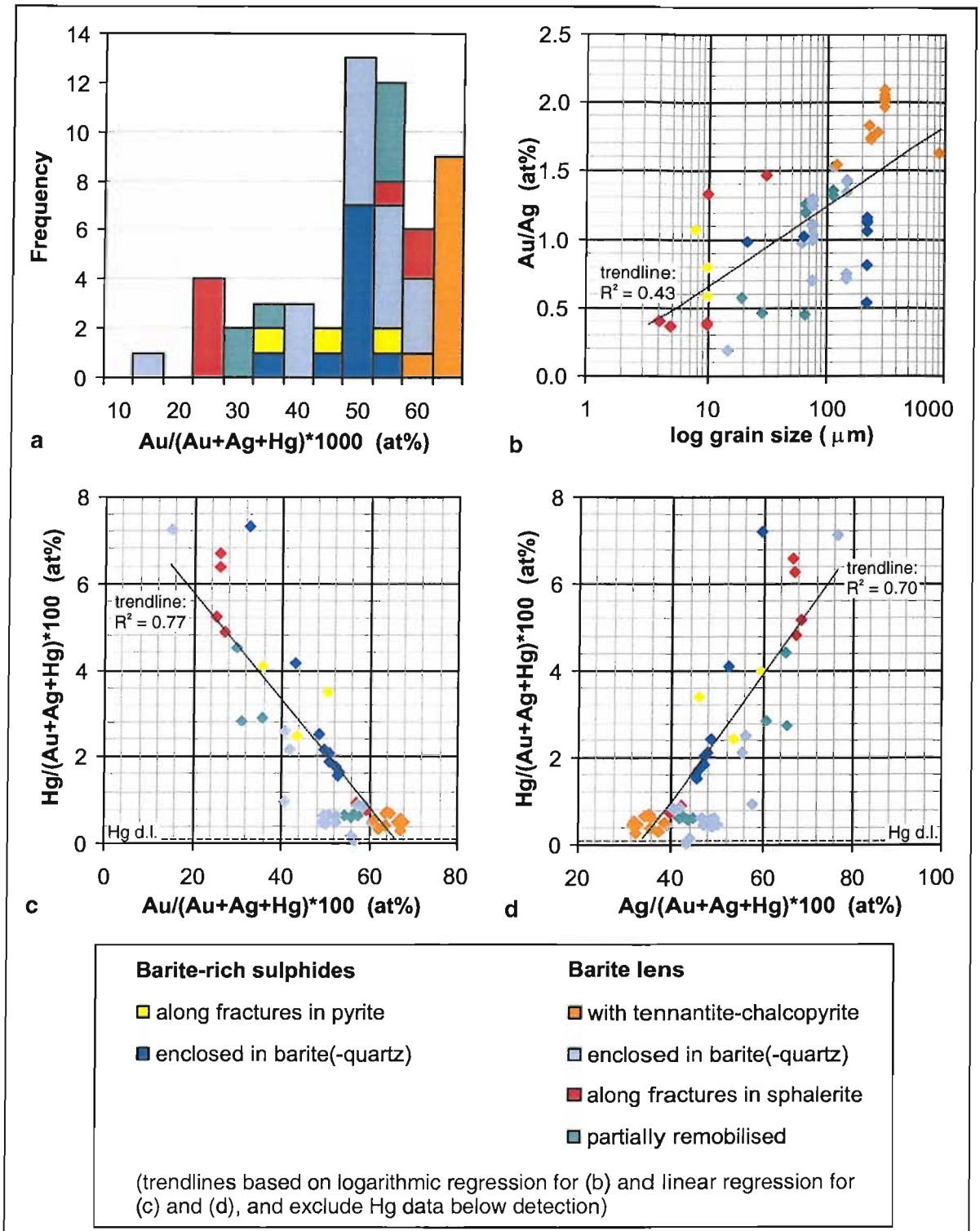

a. Histogram to show the range of gold contents in electrum.

b. Scatter plot of Au/Ag ratio (based on at% data) against grain size plotted on a log scale shows a weak positive correlation.

c and d. Scatter plots to show a positive correlation between Hg and Ag (c) and negative correlation between Hg and Au (d).

(Note: data for very fine grained electrum in barite have been omited from these plots due to the uncertainty in composition, see text for explanation).

Figure 5.11. Major element composition of electrum.

The composition of electrum at Balta Tau varies considerably, with Au ranging from 9 to 67at% with a mode at 55at% and a negatively skewed distribution (Figure 5.11a) and Ag ranging from 32 to 91at%. The majority of grains contain between 20 and 40wt% Ag and are therefore defined as electrum (Harris, 1990). A few grains containing more than 40wt% Ag should strictly be termed auriferous silver (Harris, 1990), however this term is rarely used and for simplicity all grains will be classed as electrum in the following discussions. The majority of analyses also contain Hg above detection (0.04 to 0.05at%) with a maximum of 6.6at%, and there is a negative correlation between Au and Hg (Figure 5.11c) and a corresponding positive correlation between Hg and Ag (Figure 5.11d). There is also a broad correlation between grain size and composition (Figure 5.13b), with Au/Ag increasing with grain size. The electrum analyses are discussed according to six distinct modes of occurrence as follows.

Electrum in chalcopyrite-tennantite(-galena)

Electrum associated with chalcopyrite-tennantite in the barite lens forms coarse grains (Figure 4.34a and b, Chapter 4) that have generally homogeneous compositions both within and between grains, with Au/Ag averaging 1.88 and low Hg contents of 0.28 to 0.70at% (Figure 5.12a). However, a detailed traverse of 42 analyses across a single grain (Figure 5.13; Herrington, 2000 unpublished data) reveals a homogeneous composition in the central portion of the grain with Ag enrichment in a narrow zone at the very margin.

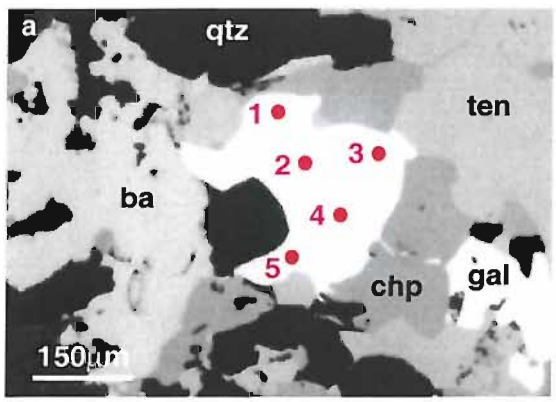

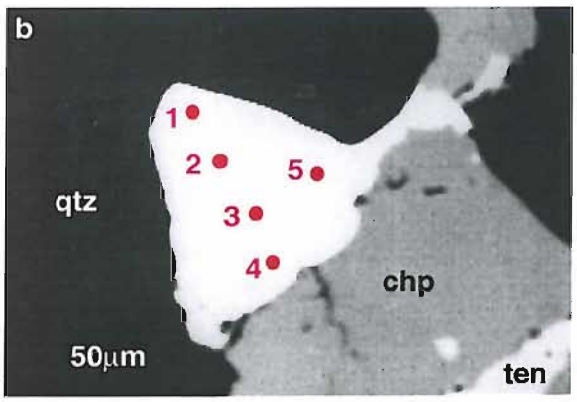

#	Au	Ag	Hg	Au/Ag
1	66.73	32.99	0.29	2.02
2	66.74	32.98	0.28	2.02
3	67.32	32.23	0.45	2.09
4	66.83	32.61	0.56	2.05
5	66.05	33.48	0.47	1.97

#	Au	Ag	Hg	Au/Ag
1	50.57	48.83	0.61	1.04
2	52.13	47.40	0.47	1.10
3	52.24	47.12	0.64	1.11
4	49.71	49.65	0.63	1.00
5	50.07	49.49	0.43	1.01

a and b. Back scatter electron images of electrum with microprobe analyses corresponding to the data listed in the tables below (at%). The electrum in (a) is a typical Au-rich grain associated with tennantite-chalcopyrite (sample BTB01B). The electrum in (b) is typical of more Ag-rich grains enclosed in barite-quartz with disseminated sulphides (sample 01BT226b).

Figure 5.12. Variation in electrum composition within single grains.

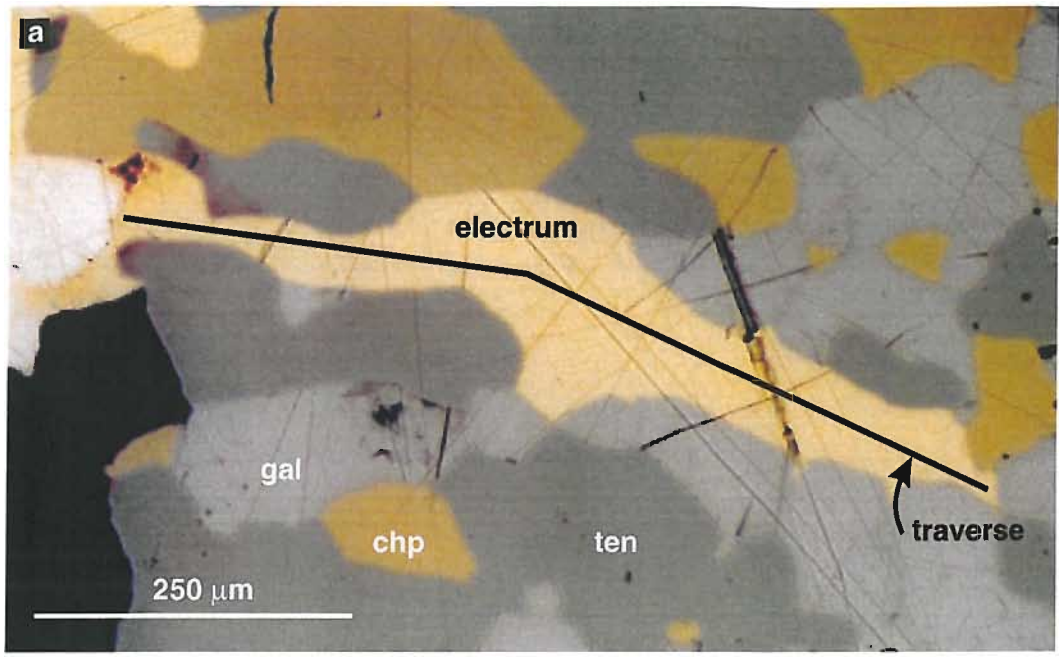

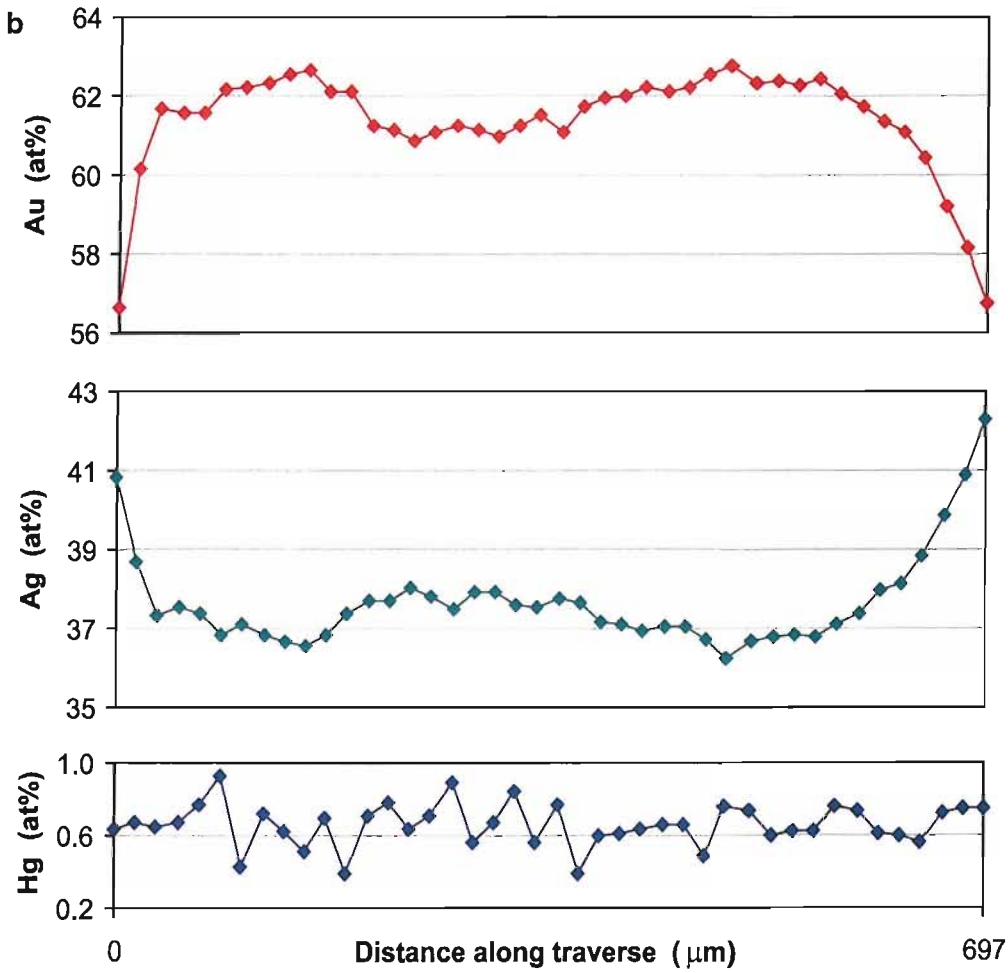

a. Coarse electrum grain enclosed in tennantite-chalcopyrite-galena (sample BTB01(D)), analysed at 42 evenly spaced points along the traverse shown.

b. Au, Ag and Hg contents along the traverse. The composition is generally homogeneous but shows a distinct enrichment in Ag and corresponding decrease in Au at the grain boundary (data acquired by Herrington, 2000).

Figure 5.13. Compositional variation in coarse electrum associated with tennantite-chalcopyrite.

Electrum in barite(-quartz)

Electrum grains enclosed in and interstitial to barite(-quartz) occur in the barite-rich sulphides and the barite lens. They are variable in size (10-240μm) and more Ag-Hg-rich compared to grains associated with chalcopyrite-tennantite, with an average Au/Ag ratio of 1.05 and Hg ranging from below detection to 7.21at%. The compositional variation within individual grains was investigated by microprobe analyses and x-ray mapping (Figures 5.12b and 5.14).

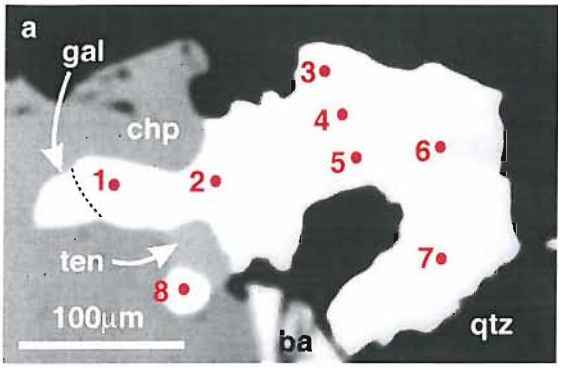

#	Au	Ag	Hg	Au/Ag
1	50.62	47.54	1.84	1.06
2	32.60	60.19	7.21	0.54
3	52.09	46.19	1.73	1.13
4	52.48	46.00	1.53	1.14
5	50.51	47.46	2.03	1.06
6	52.87	45.53	1.60	1.16
7	42.96	52.93	4.10	0.81
8	48.39	49.16	2.45	0.98

a. Backscatter electron image of two electrum grains associated with chalcopyrite-tennantite-galena enclosed in a matrix of barite-quartz-carbonate. The microprobe analyses (data in at%) indicate that both grains are Ag- and Hg-rich and the coarse grain is heterogeneous. Sample 01BT082.

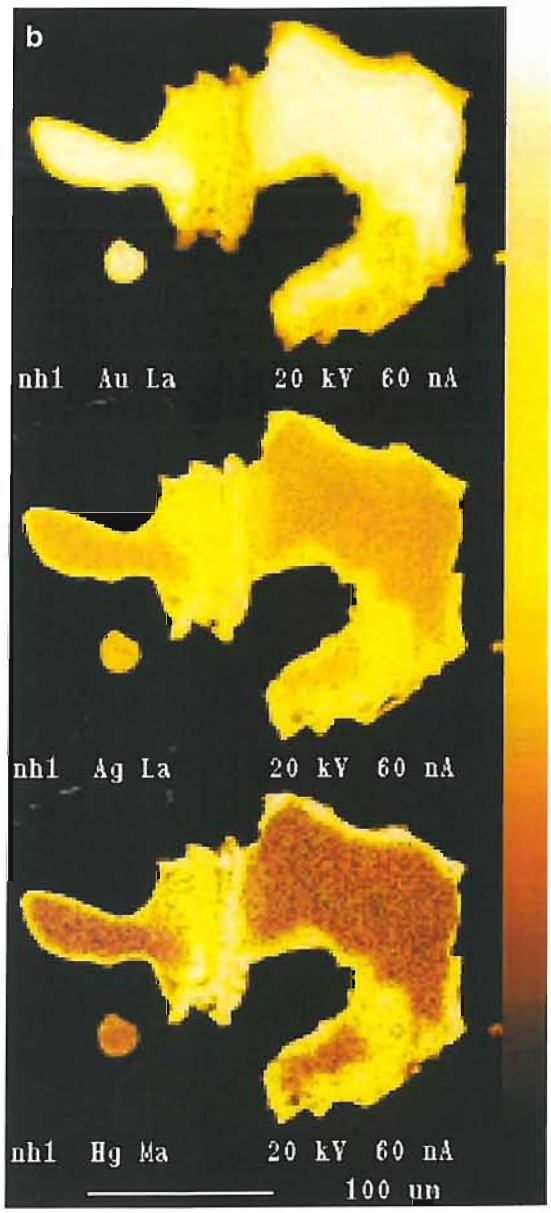

b. False colour images of Au, Ag and Hg concentrations produced by x-ray mapping across the electrum grains shown in (a). The margins of the coarse grain are Ag- and Hg-rich relative to the core. A linear Ag- Hg-rich band crossing the left hand margin appears to be a microfracture within the electrum grain which is enriched in Ag and Hg relative to the rest of the grain. The small grain (lower left) is more homogeneous with the same composition as the core of the coarse grain, with weak enrichment of Ag and Hg at the rim. Sample 01BT082.

Figure 5.14. X-ray mapping of compositional variation in a coarse electrum grain enclosed in barite-quartz.

Five microprobe analyses from a typical grain (Figure 5.12b) reveal a variation in Au and Ag contents of just over 2.0at%, with the most Ag-rich analyses located in the margins of the grain. The Hg content of this grain is generally low, and does not reflect the positive correlation with Ag that is seen in the overall electrum dataset. The coarse electrum grain illustrated in Figure 5.14 displays a much greater compositional variation, a strong positive correlation between Hg and Ag, and a much more pronounced Ag-Hg enrichment at the margins. These characteristics are evident from the microprobe analyses (Figure 5.14a) and are also shown very clearly by x-ray mapping of the grain (Figure 5.14b). The x-ray mapping also reveals an Ag-Hg rich dislocation that bisects the grain, isolating the Au rich core of the left hand lobe from the central core of the grain.

Very fine grained electrum in barite

Barite from the barite lens and more rarely the barite-rich sulphides contains very fine grained (mostly <1μm) rounded and rod-like inclusions of sulphides and electrum which define growth zones in the barite crystals (Chapter 4, Section 4.6.2 and Figure 4.36). Analyses of two electrum grains from these inclusion zones have been obtained, which due to the very small grain size incorporate the enclosing barite and adjacent sulphide inclusions as well as the electrum. In spite of this shortcoming, the data can still provide an approximate value for the Au/Ag ratio of these grains. The measured values for Au and Ag contents give an average Au/Ag of 0.15. However, since other potentially Ag-bearing minerals such as fahlore are included in the analyses, the ratio of Au/Ag in the electrum can only be constrained to the range of 0.15-0.55 (see Appendix B2 for details). In spite of this uncertainty, it can still be inferred that the very fine grained inclusions of electrum in barite are Ag-rich and may be significantly more Ag-rich than electrum in any other mode of occurrence.

Electrum inclusions in pyrite

In the barite-rich sulphides, fine grained electrum associated with one or more of chalcopyrite, sphalerite, tennantite and galena occurs along fractures and as minor replacements in coarse pyrite clasts (illustrated in Figure 4.24, Chapter 4). These electrum grains are thin, irregular and fine grained (<1 to 10μm), resulting in the incorporation of adjacent sulphides (chalcopyrite and pyrite) in the analyses. The data can however be used directly to estimate the Au/Ag ratio which varies from 0.6 to 1.1 with an average of average 0.83, and Hg is consistently enriched from 2.4 to 4.0at%.

Electrum in fractures in sphalerite

Five small electrum inclusions hosted in fractures in coarse sphalerite from the barite lens (Chapter 4, Figure 4.34e and f) are Ag- and Hg- rich with an average Au/Ag of 0.90 and 0.73 to 6.59at% Hg (Figure 5.15). The two larger electrum grains (10 and 35μm) form a polymineralic inclusion with chalcopyrite and galena and have a higher Au/Ag than the three smaller (<5μm) grains which are isolated along fractures.

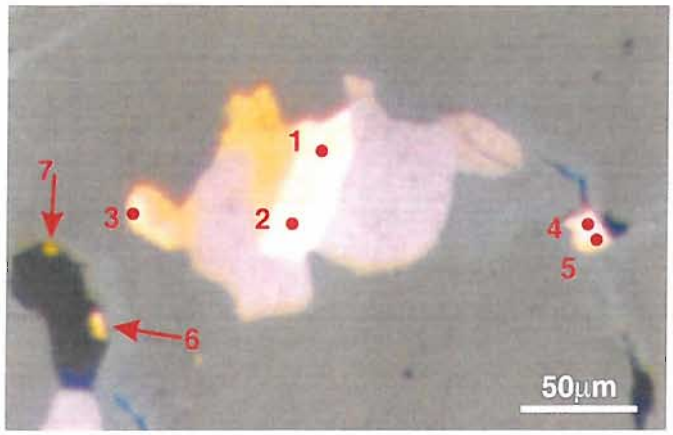

#	Au	Ag	Hg	Au/Ag
1	59.12	40.15	0.73	1.47
2	59.12	40.13	0.74	1.47
3	56.64	42.48	0.89	1.33
4	26.17	67.24	6.59	0.39
5	26.30	67.43	6.27	0.39
6	25.69	69.15	5.16	0.37
7	27.36	67.83	4.81	0.40

(Au, Ag and Hg are expressed as at%)

Figure 5.15. Composition of fine electrum grains hosted in fractures in coarse sphalerite.

Remobilised electrum

Partially remobilised electrum from the barite lens (Chapter 4, Section 4.6.3) shows considerable Ag-Hg- enrichment at grain margins and where the electrum forms thin rims around adjacent sulphides, with Au/Ag as low as 0.46 and Hg reaching 4.44at% (Figure 5.16). Cu and S contents also become significant towards grain margins, suggesting the electrum may be intergrown with secondary Cu sulphides which are observed forming alteration rims around adjacent sulphides (Figure 5.16). The cores of coarse electrum grains have a high Au/Ag ratio of 1.20 to 1.36 and consistent Hg contents averaging 0.63at%. Chalcopyrite, galena and tennantite adjacent to the remobilised electrum contain 0.12 to 0.52at% Ag and an alteration rim around adjacent sphalerite contains 0.66at% Ag, but none of these phases contain Au above detection (Figure 5.16).

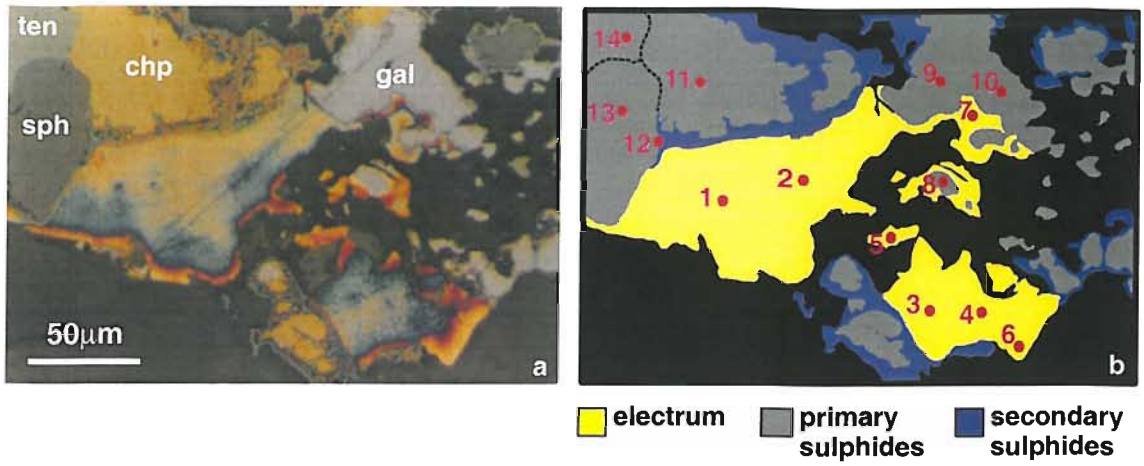

atomic %	#	S	Au	Ag	Cu	Fe	As	Sb	Zn	Pb	Hg	Total
electrum	1	5.94	53.03	39.08	1.18	bd	bd	bd	bd	bd	0.57	99.79
	2	5.15	52.96	40.16	0.74	bd	bd	bd	bd	bd	0.63	99.73
	3	9.24	49.32	39.05	1.57	0.08	0.12	bd	bd	bd	0.53	99.92
	4	7.27	49.59	41.27	0.79	0.15	0.10	0.04	bd	bd	0.59	99.79
	5	2.14	34.78	59.25	0.50	0.22	bd	bd	bd	0.20	2.77	99.89
	6	0.59	29.41	64.55	0.74	0.11	bd	bd	bd	bd	4.36	99.74
	7	26.39	15.77	33.47	21.11	bd	bd	bd	bd	1.67	1.40	99.80
galena	8	49.56	bd	0.52	0.52	bd	bd	bd	bd	49.04	bd	99.64
	9	49.18	bd	0.22	0.73	0.08	bd	bd	0.29	49.29	bd	99.79
	10	49.21	bd	0.29	0.74	bd	bd	bd	0.54	48.91	bd	99.71
chalcopyrite	11	49.88	bd	0.12	24.92	24.77	0.07	bd	0.16	bd	0.03	99.95
sphalerite	12	50.10	bd	0.66	1.52	0.03	bd	bd	47.58	bd	0.03	99.92
	13	50.30	bd	bd	0.19	0.19	0.04	bd	49.27	bd	bd	99.99
tennantite	14	44.32	bd	0.20	34.24	1.31	12.07	1.90	5.88	bd	0.02	99.94

Photograph (a) and sketch (b) of partially remobilised electrum enclosing primary and secondary sulphides. The table lists data in atomic % for the analytical points shown on (b). In the centre of coarse electrum grains (points 1 to 4), the composition is similar to other coarse electrum in the barite lens except for minor amounts of S and Cu. However, at the rims of the electrum and where it forms thin rims around the sulphides, the Ag and Hg contents are significantly higher and considerable S and Cu are present. Adjacent galena (points 8 to 10), chalcopyrite (point 11), tennantite (point 14) and secondary sulphides rimming sphalerite (point 12) all contain trace amounts of Ag; the central sphalerite is the only phase to contain Ag below detection (point 13). By contrast, none of the sulphide phases contain Au above detection. Sample BL1.

Figure 5.16. Compositional variations in coarse, partially remobilised electrum.

5.2.9 Rare phases

Pearcite

Analsyes of two Ag-sulphosalt grains from the barite lens are consistent with the pearcite-antimonpearcite and polybasite-arsenopolybasite solid solution series, $(Ag,Cu)_{16}Sb,As)_2S_{11}$ (Table 5.12). Based on the Ag/Cu and As/Sb ratios, the grains from Balta Tau can be identified as pearcite according to the classification of Hall, 1967 (Figure 5.17a). There are significant compositional variations both within and between the two grains with negitive correlations between As and Sb, and Ag and Cu (Figures 5.17b and c) consistent with the element substitutions in this series.

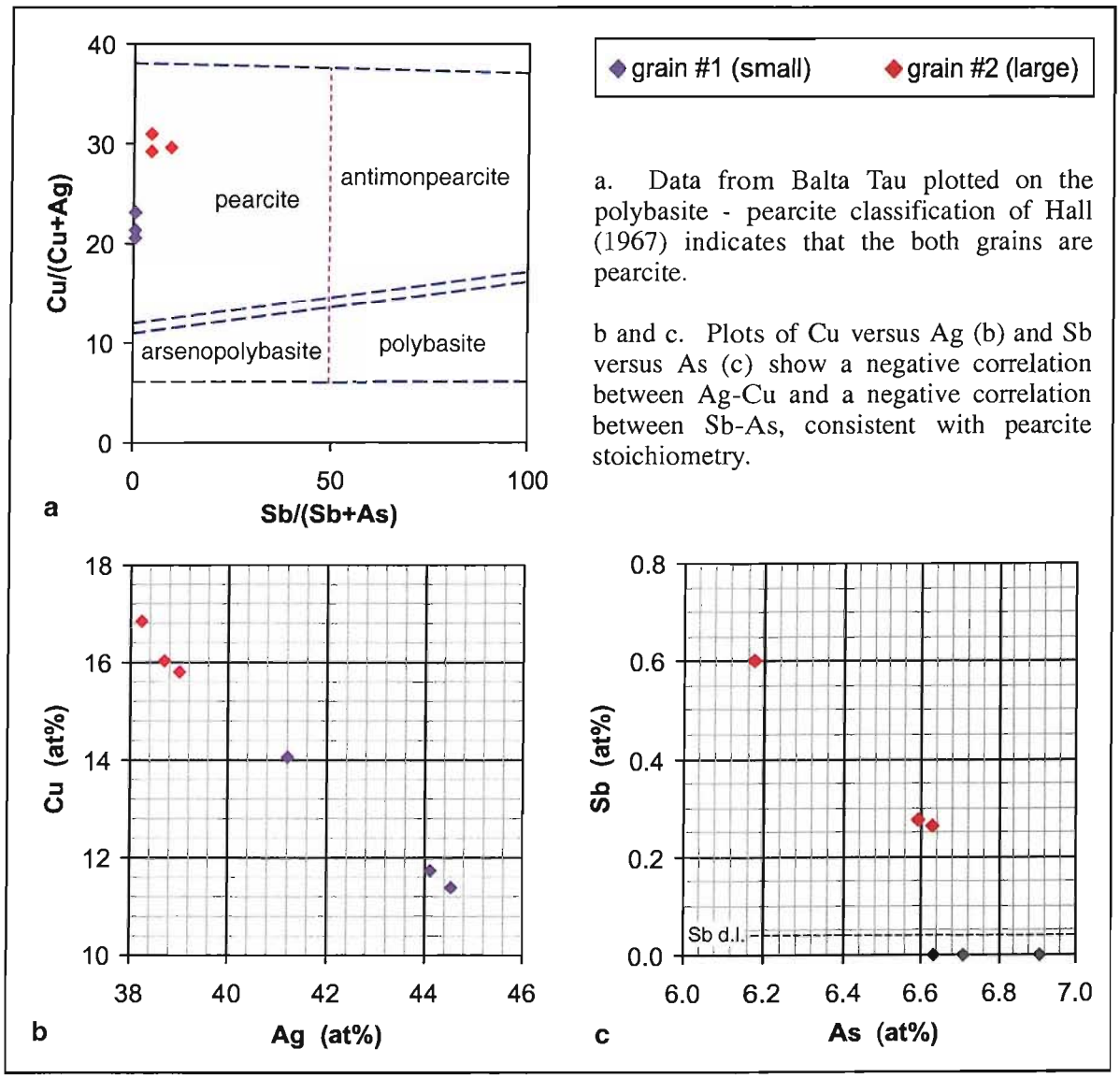

Figure 5.17. Identification and compositional variations of pearcite from the barite lens.

a. Pearcite (weight %)	n	S	Ag	Cu	As	Sb	Total
gold-rich barite lens	6	16.94	62.21	12.59	6.93	0.33	99.01

b. Pearcite (atomic %)	n	S	Ag	Cu	As	Sb	Total
gold-rich barite lens	6	37.69	41.21	14.09	6.61	0.19	99.79

Table 5.12. Microprobe data for pearcite presented as (a) weight % and (b) atomic %. (Data are the mean of "n" number of analyses).

Hessite

A rare phase in layered sulphides has been identified as hessite, a silver telluride with the formula AgTe (Table 5.13). The hessite contains significant Au above detection limit, which may be in solid solution or represent tiny sub-microscopic inclusions of a gold telluride.

a. Hessite (weight %)	n	S	Au	Ag	Sb	Te	Zn	Pb	Total
gold-rich barite lens	2	0.25	0.30	61.55	0.21	36.10	0.90	0.23	99.52

b. Hessite (atomic %)	n	S	Au	Ag	Sb	Te	Zn	Pb	Total
gold-rich barite lens	2	0.88	0.17	64.70	0.20	32.08	1.55	0.12	99.70

Table 5.13. Summary of microprobe data for hessite analyses, presented as (a) weight % and (b) atomic %. (Data are the mean of "n" number of analyses).

Native silver

Native silver has been identified forming very fine grains in the barite lens, with analyses summarised in table 5.14. There was no gold above detection in these grains, and small amounts of Zn and Cu probably relate to the adjacent sulphide grains.

a. Native silver (weight %)	n	Ag	Cu	Zn	Total
gold-rich barite lens	2	95.70	0.22	0.30	96.30

b. Native silver (atomic %)	n	Ag	Cu	Zn	Total
gold-rich barite lens	2	98.58	0.38	0.51	99.51

Table 5.14. Summary of microprobe data for native silver, presented as (a) weight % and (b) atomic %. Note totals are low due to the very small grain size (<5um). (Data are the mean of "n" number of analyses).

5.3 DISCUSSION OF ORE CHEMISTRY

5.3.1 Gold

Primary electrum and compositional variations

One of the most important considerations concerning of the origin of gold at Balta Tau is whether or not the electrum is of a primary hydrothermal origin. In the discussions of this section and the chapters that follow, the term "primary electrum" refers to electrum that precipitated directly from hydrothermal fluids at or close to the seafloor during VMS ore formation. This includes electrum that may have precipitated during the redistribution and possible concentration of gold from early VMS mineralization by later stage VMS hydrothermal fluids (e.g. during "zone refining"), but excludes electrum formed by the remobilisation or concentration of gold subsequent to VMS ore formation, e.g. during seafloor supergene enrichment, diagenesis or metamorphism, or the introduction or remobilisation of gold during a later (post-VMS) mineralizing event.

The following observations suggest that the majority of electrum at Balta Tau is primary in origin:

- Electrum grains are mostly associated with sulphides and/or barite that display primary hydrothermal textures, and texturally appear to have co-precipitated with these assemblages.
- Compositional variations between electrum grains broadly correlate with their mode of occurrence, suggesting the composition reflects formational conditions specific to each ore facies and has not been altered significantly since initial precipitation.
- Remobilised electrum can be identified and distinguished from primary electrum.

The composition of electrum associated with tennantite-chalcopyrite is more homogeneous and Au-rich than electrum from all other associations. Electrum composition may be influenced by a number of factors including the Au/Ag of the mineralising fluid, salinity, pH, total dissolved sulphide, temperature, and depositional mechanism (Gammons & Williams-Jones 1995). However, Au-rich compositions are often considered to reflect higher formational temperatures (e.g. Ebel and Sack, 1989; Huston et al., 1992), suggesting that the tennantite-chalcopyrite-electrum may have formed at a higher temperature than the other electrum bearing assemblages.

The positive correlation between Ag and Hg observed at Balta Tau has been reported from a number of other VMS deposits (e.g. Trout Lake deposit, Manitoba, Heanly and Petruk, 1990; Rosebery, Australia, Huston & Large, 1988; South Hercules deposit, Australia, Zaw & Large, 1992). This correlation, seen at Balta Tau in both primary and remobilised electrum, suggests that

Hg behaves more like Ag than Au during hydrothermal transportation and precipitation and during post-depositional remobilisation.

Formation of Ag-rich rims

Electrum grains with Ag-rich rims similar to those observed at Balta Tau have been reported from Rosebery in Australia (Huston and Large, 1988), Mt. Lyell in Australia (Huston et al., 1992) and Kuroko ores (Shimakazi, 1974). These examples are from well preserved deposits and are therefore unlikely to be the result of metamorphic recrystallization, but may be primary zoning or due to modification of the electrum grains during late stages of ore formation, diagenesis or low grade metamorphism.

Shimakazi (1974) and Huston et al. (1992) suggest the Ag-rims are a primary feature and formed due to a decrease in temperature during late stage of ore formation. However, observations from Balta Tau do not support this mechanism for two reasons:

- Given the sensitivity of electrum composition to formational conditions, electrum grains would be expected to exhibit complex primary zoning reflecting numerous fluctuations in conditions such as temperature, rather than just two stages of precipitation represented by relatively Au-rich homogeneous cores and Ag-rich rims.
- The addition of Ag (and Hg) to electrum during late stages of precipitation should have produced rims of similar thickness around neighbouring electrum grains regardless of grain size. However, the x-ray mapping in Figure 5.16b shows that while the coarse grain has quite distinct rims, the small grain located less than 30um away only has a very slight Ag-Hg-enrichment at the margin which is barely visible.

The Ag rims are also unlikely to have formed by leaching of gold from grain margins because both Ag and Hg are more mobile than Au over a wide range of conditions, illustrated by the high purity native gold found in zones of supergene weathering (Krupp & Weiser, 1992) and in sea-floor supergene zones of VMS ores (e.g. TAG; Hannington et al., 1988; VMS of the Troodos Ophiolite, Herzig et al., 1991).

Observations from Balta Tau suggest that the Ag-rich rims formed during post-depositional modification of electrum where Ag migrates from the cores to the margins of grains by solid state diffusion. This mechanism would destroy primary zoning within the electrum grain and can therefore account for the relative homogeneity of electrum cores. The extent of development of the Ag rims would reflect the amount of Ag originally in the electrum and therefore relate to both the bulk primary composition and the grain size. This can explain the more extensive development of Ag rims around barite-hosted electrum compared to the more Au-rich tennantite-chalcopyrite hosted electrum, and it can also explain the correlation between the thickness of Ag

rims and grain size observed in the x-ray mapping. Calculations of Gammons & William-Jones (1995, Figure 10) suggests that Ag can disperse through Au by solid-state diffusion over distances in the order of 10μm /1000 years at 300°C or 10μm/1 million years at 200°C. It is therefore feasible that Ag could diffuse through electrum during diagenesis and/or low grade regional metamorphism.

Remobilised electrum

The partial remobilisation of electrum has been identified in a number of samples from Balta Tau and is illustrated by the following examples:

- Rims of Ag-Hg rich electrum around sulphide grains, where the remobilised Ag-Hg-Au is derived from adjacent coarse electrum grains (Figure 5.16). The migration of electrum is very localised involving distances of less than 1mm, but these are the most extreme cases of remobilisation that have been identified.
- Ag-Hg enrichment of a micro-scale dislocation within a single electrum grain, revealed by x-ray mapping. This indicates selective migration of Ag and Hg from the electrum grain into a zone of high strain related to micro-scale deformation. The extent of this Ag-Hg enrichment in this case is limited to the vicinity of the electrum grain indicating very localised mobilisation.

This partial remobilisation is probably an advanced stage of the development of Ag-rich rims (discussed above), where partial remobilisation favours migration of Ag-Hg over Au to form Ag-Hg rich zones not only as rims around electrum but around adjacent sulphide grains and infilling micro-fractures. As with the Ag-rims, these may have developed during late stages of ore formation, diagenesis or metamorphism. The most extreme cases of electrum remobilisation coincide with localised alteration of sulphides at grain boundaries and the electrum itself is tarnished, which probably reflects the formation of secondary Ag and possibly Au sulphides (Barton & Toulmin, 1964) supported by the high S content of this electrum (Figure 5.16).

Origin of electrum in pyrite

The occurrence of electrum/native gold along fractures in pyrite is recognised from numerous ancient VMS deposits (e.g. Huston et al 1992) and two mechanisms involving the concentration of "invisible" Au in pyrite have been proposed to explain this association:

- Precipitation of Au triggered by a decrease in the activity of H_2S in the microenvironment around crystallizing pyrite results in sub-microscopic grains of Au enclosed in pyrite crystals. During later recrystallization Au migrates to fractures in the pyrite by solution-reprecipitation (Huston et al. 1989).
- Au enrichment of arsenian pyrite by metastable, coupled substitution of $[AsS]^{3-}$ and Au^{3+} for S^{2-} and Fe^{3+} respectively in the pyrite lattice (Cook and Chryssoulis, 1990), consistent with positive correlations between Au and As observed from a number of deposits (e.g. Simon et

al., 1999; Reich et al., 2003). Au is then expelled during post-formational recrystallization and concentrated in fractures in pyrite (Huston et al., 1992).

The fracture-hosted Au produced by these mechanisms is very similar to that found in the barite-rich sulphides at Balta Tau. However, the following observations suggest that at Balta Tau the electrum did not originate as "invisible" Au in pyrite, but was introduced to fractures during precipitation of the electrum-bearing barite-rich matrix that encloses the pyrite clasts:

- Zoning in As in the pyrite clasts is well preserved (Section 5.2.2) indicating that the pyrite has not recrystallized or been significantly modified since formation. This suggests that any Au present as either micro-inclusions or lattice substitutions is still locked in the pyrite.
- The electrum is associated with one or more of chalcopyrite, tennantite, sphalerite and galena that also occur along fractures in pyrite and appear have been introduced during formation of the enclosing barite-rich matrix.
- The Au/Ag content of fracture-hosted electrum is quite low and comparable to that of electrum in the barite-rich matrix.
- Similar electrum occurs in fractures in sphalerite. Unlike pyrite, sphalerite does not host "invisible" Au and this electrum is most likely to have been introduced during precipitation of the enclosing matrix.

An important consequence of these observations is the possibility of significant "invisible" Au remaining locked in the arsenian pyrite of barite-rich sulphides, held as a metastable, coupled substitution within the pyrite lattice. Although this pyrite does not contain gold above the microprobe detection limit of 1000ppm, lower levels of gold enrichment (e.g. 50-200ppm; Huston et al., 1995) may still account for a high proportion of the total gold contained in VMS ores. Therefore the arsenian pyrite may be an important source of Au in Balta Tau ores in addition to electrum, particularly in the barite-rich sulphides and possibly footwall sulphides, and may increase the overall Au content of the deposit significantly. However, "invisible" Au in pyrite may be less significant from an economic perspective, since the finely dispersed nature makes it difficult to recover effectively during ore processing compared to the free Au contained in coarse electrum.

Incorporation of As in pyrite most commonly occurs during rapid precipitation, since metastable substitutions will only occur under disequilibrium conditions (Huston et al., 1995). Collomorphic pyrite is typically a product of rapid precipitation (Huston et al., 1995), however the collomorphic pyrite in massive sulphides at Balta Tau is generally As poor and devoid of As zoning. This suggests that As may have already been expelled from the pyrite and if this occurred during late stages of ore formation (e.g. zone refining) may have provided a source of Au for the barite-rich

sulphides and the barite lens. However, the collomorphic texture of this pyrite does not show evidence of leaching or recrystallization.

Comparison with gold in other ancient VMS deposits

Numerous ancient VMS deposits contain native gold and/or electrum, which in the majority of cases occurs in metamorphosed ores and the abundance and grain size often increase with the degree of metamorphism, leading to the interpretation that coarse electrum is a product of metamorphic recrystallisation (e.g. VMS of the Notre Dam Bay area, Newfoundland, Santaguida & Hannington, 1996; Mobrun deposit in Noranda, Quebec, Larocque et al., 1993; Rosebery deposit in Australia, Huston & Large, 1988). The electrum at Balta Tau is quite different to these occurrences, forming abundant, coarse grains enclosed in sulphide-barite ores that retain primary textures.

Huston and Large (1989) and Huston et al. (1992) observe that although metamorphism does increase the abundance and grain size of electrum by releasing and concentrating "invisible" gold from sulphide phases, not all electrum in VMS deposits has been derived from this process. They classify occurrences of native gold/electrum in VMS according to mineralogical associations as follows:

- An Au-Cu association where Au-rich electrum with a narrow compositional range is associated with chalcopyrite-rich ores occurring predominately in the footwall and lower massive sulphide ore zones.
- An Au-Zn association where Au is concentrated in the upper horizons of Zn-rich massive sulphides. The Au may take a number of forms, including "invisible" Au in pyrite and/or arsenopyrite, or electrum with a wide range of generally Ag-rich compositions associated with in Zn-Pb-Ag sulphides and in baritic ores.

The characteristics of Au enrichment at Balta Tau are broadly consistent with the Au-Zn association. Within this association Huston et al. (1992) describe Au enrichment of baritic ores characterised by primary electrum of variable fineness without a particular mineral association, which is particularly comparable to the electrum at Balta Tau. There are few ancient VMS deposits which contain coarse primary electrum analogous to that of Balta Tau, but possible examples are the well preserved Kuroko deposits (Shimakazi, 1974), Mt. Chalmers where primary ore textures are preserved and electrum grains commonly reach 2mm in size (Huston et al. 1992), and the barite ores of the Rosebery deposit (Huston et al. 1992).

Comparison with gold in modern VMS systems

There have been numerous discoveries of actively forming gold-rich barite-sulphide deposits (e.g. Herzig et al., 1990; Binns et al., 1997) but only a few occurrences of primary hydrothermal native gold/electrum have been documented, summarised in Table 5.15. These examples do not include a modern analogue of the coarse electrum in baritic ores at Balta Tau, however they do confirm that native gold/electrum can precipitate directly from hydrothermal fluids, and electrum identified at Franklin Seamount and in lower temperature assemblages from Logatchev, MAR have a similar composition and mineralogical association to that of Balta Tau. Samples of sea-floor sulphides are difficult to obtain (for example, ODP cores do not begin at the upper surface of seafloor sulphides and only recover a small volume of material; grab samples only recover a limited selection of ore facies), and only a few examples of coarse primary electrum comparable to Balta Tau have been found in ancient deposits despite the vast number of deposits that have been studied. Therefore, given the scarcity of electrum occurrences comparable to Balta Tau on land and the relatively small volume of material studied from active systems, it is not surprising that a modern analogue for Balta Tau has not yet been identified. A recent shallow drilling program (Herzig et al., 2003) has recovered extensive sulphides from a number of sites including gold-rich samples from the Manus Basin (Petersen et al., 2003); these have yet to be examined in thin section (Herzig, pers. comm.) and may add to the occurrences of primary electrum on the sea-floor.

Hydrothermal site	Electrum grain size	Electrum composition	Associated phases	Reference
Vai Lili, Valu Fa Ridge	<1 to 18μm	av. 5.8wt% Ag	> 200 electrum grains with sph, minor ten, chp, ba	Herzig et al., 1993
Jade, Okinawa Trough	a few μm	low Ag	interstitial to barite	Halbach et al. 1993
Franklin Seamount, Woodlark Basin	3 to 5μm	44-48at%Ag, 52-56 at% Au	fine grained py-silica-(sph-chp-gal) on ba	Binns et al. 1997
Logatchev, Mid Atlantic Ridge	<1 to 5μm	Au/Ag (wt%) < 10	>300 ass with sph-low T assemblage	Murphy & Meyer, 1998
	rare grains	Au/Ag (wt%) ≈ 20	in primary chalcopyrite	
	<0.5 to 15μm	Au/Ag (wt%) 25 to > 100	abundant grains in secondary Cu sulphides e.g. bornite	
Escanaba Trough, NE Pacific	most <1μm	native gold to electrum	Bi phases, sulpharsenides & arsenides	Tormanen & Koski, 2003

Table 5.15. Documented occurrences of primary native gold/electrum in modern sea floor VMS systems.

5.3.2 Major sulphide phases and phase equilibria

Mineral assemblages that co-precipitated in equilibrium may be used to constrain formational conditions such as temperature, pH, oxidation and sulphidation (Holland, 1959). Although precipitation in the dynamic environment of VMS systems is unlikely to occur in complete equilibrium, phase equilibria have been applied to VMS ores with some degree of success (e.g. Hannington and Scott, 1989a; Herzig et al., 1993) suggesting that the mineralogy and chemistry of ore assemblages do reflect formational conditions.

Phases in the Fe-Cu-Zn-S system

Minerals in the Fe-Zn-Cu-S systems that are commonly found in VMS systems are pyrrhotite and pyrite, issocubanite and chalcopyrite with variable Cu/Fe, bornite, and sphalerite with variable Fe/Zn. At Balta Tau this assemblage is restricted to pyrite, stoichiometric chalcopyrite and Fe-poor sphalerite. According to experimental results of Kajima and Sugaki (1985), this assemblage is consistent with equilibrium precipitation and may have formed over a wide temperature range (300-600°C).

Sulphidation and temperature

Figure 5.18 shows the stability of mineral phases and the composition of sphalerite as a function of temperature and sulphur activity. The dominant assemblages at Balta Tau suggest low to moderate formational temperatures in the range <180 to 300°C and low to moderate sulphur activity of 10^{-15} to 10^{-9}atm. Figure 5.18 also shows typical formational conditions of well recognised styles of VMS mineralization. By comparison with "black smokers" which produce pyrrhotite, pyrite, Fe-rich chalcopyrite, isocubanite and Fe-rich sphalerite (e.g. East Pacific Rise, Fouquet et al., 1988; Bent Hill, Middle Valley, Juan de Fuca Ridge, Goodfellow & Franklin, 1993), Balta Tau formed at lower temperatures and similar to slightly higher sulphidation conditions. By comparison with "high sulphidation" VMS (Sillitoe et al., 1996) which typically contain low Fe sphalerite and primary enargite, tennantite, bornite, covellite and sometimes stibnite, cinnabar, realgar and orpiment (e.g. selected ore facies of Kuroko deposits, Sato, 1974; Hine Hina, Valu Fa Ridge, Herzig et al., 1998; Jade, Okinawa Trough, Halbach et al., 1993), Balta Tau formed at lower sulphidation and similar to lower temperatures. The conditions of formation of Balta Tau are most comparable with low temperature, low sulphidation systems, i.e. "white smokers", which contain low-Fe sphalerite, stoichiometric chalcopyrite, pyrite, galena and often tennantite-tetrahedrite (e.g. Axial Seamount, Juan de Fuca Ridge, Hannington et al., 1986; Vai Lili, Valu Fa Ridge, Lau Back-Arc Basin, Herzig et al., 1990; Kita-Bayonnaise Caldera, Izu-Ogasawara Arc, NW Pacific, Iizasa et al., 1997).

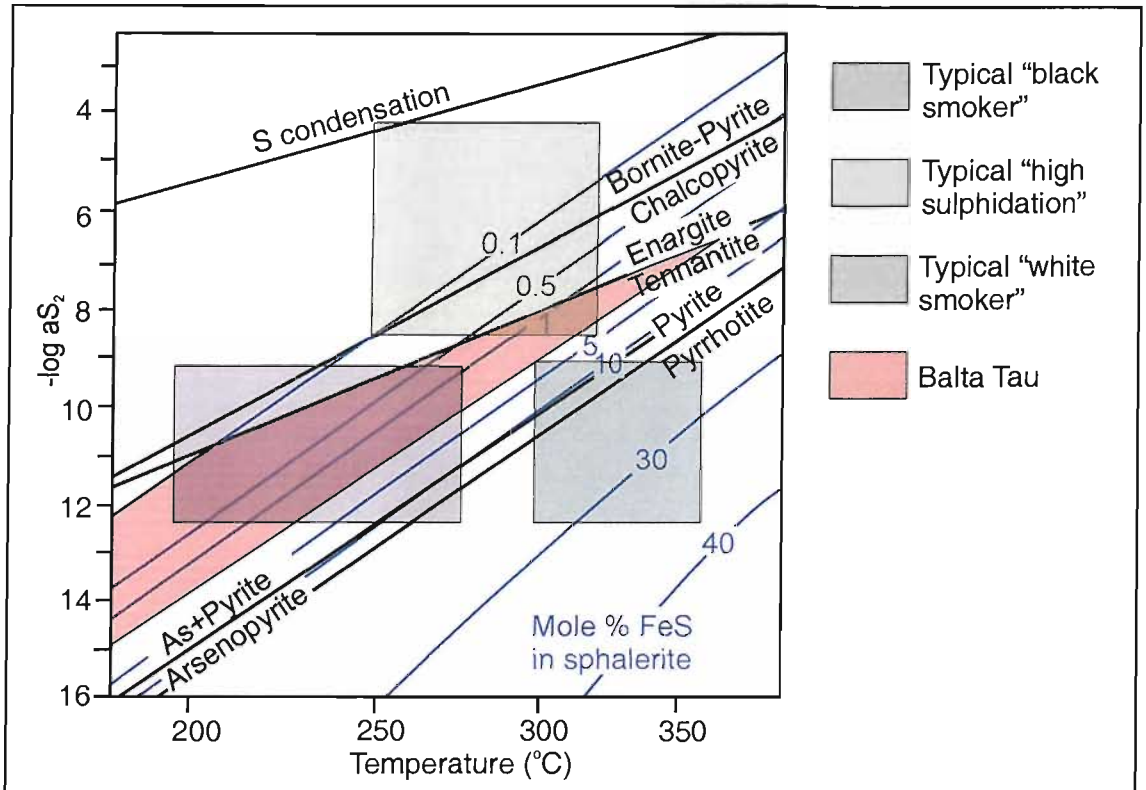

The stability of mineral pairs and the composition of sphalerite coexisting with pyrite and/or pyrrhotite as a function of temperature and sulphur activity (reproduced from Ohmoto and Goldfaber, 1997). The possible range of formational conditions of Balta Tau ores are indicated, together with typical formational conditions of sulphide assemblages from black smoker, high sulphidation and white smoker systems for comparison. The stability field for Balta Tau ores may extend below 200°C, however the thermodynamic data is uncertain at these temperatures and stability curves have not therefore been extended.

Figure 5.18. Temperature-sulphidation diagram comparing formational conditions of Balta Tau assemblages with styles of VMS mineralization.

Investigating the formation of Balta Tau ores in more detail according to specific ore facies (Figure 5.19) suggests a progressive decrease in temperature and/or increase in sulphidation from the stratigraphically lower, central ores (pyrite-chalcopyrite rich massive sulphides) through upper and marginal horizons (sphalerite-rich massive sulphides, layered sulphides and barite-rich massive sulphides) to the uppermost mineralised horizon (the barite lens).

Sphalerite compositions indicate that the footwall contains low temperature and/or high sulphidation assemblages comparable to the barite lens, however pyrite-chalcopyrite veins in the core of the footwall which do not contain significant sphalerite may have formed under conditions more comparable to the pyrite-rich massive sulphides. Zoning in ore assemblages that reflects a decrease in temperature and an increase in sulphidation from lower to higher ore horizons has been observed from other VMS deposits (e.g. sphalerite compositions at Rosebery, Australia, Huston et al., 1995; Uwamuki Kuroko deposit, Japan, Urabe, 1974).

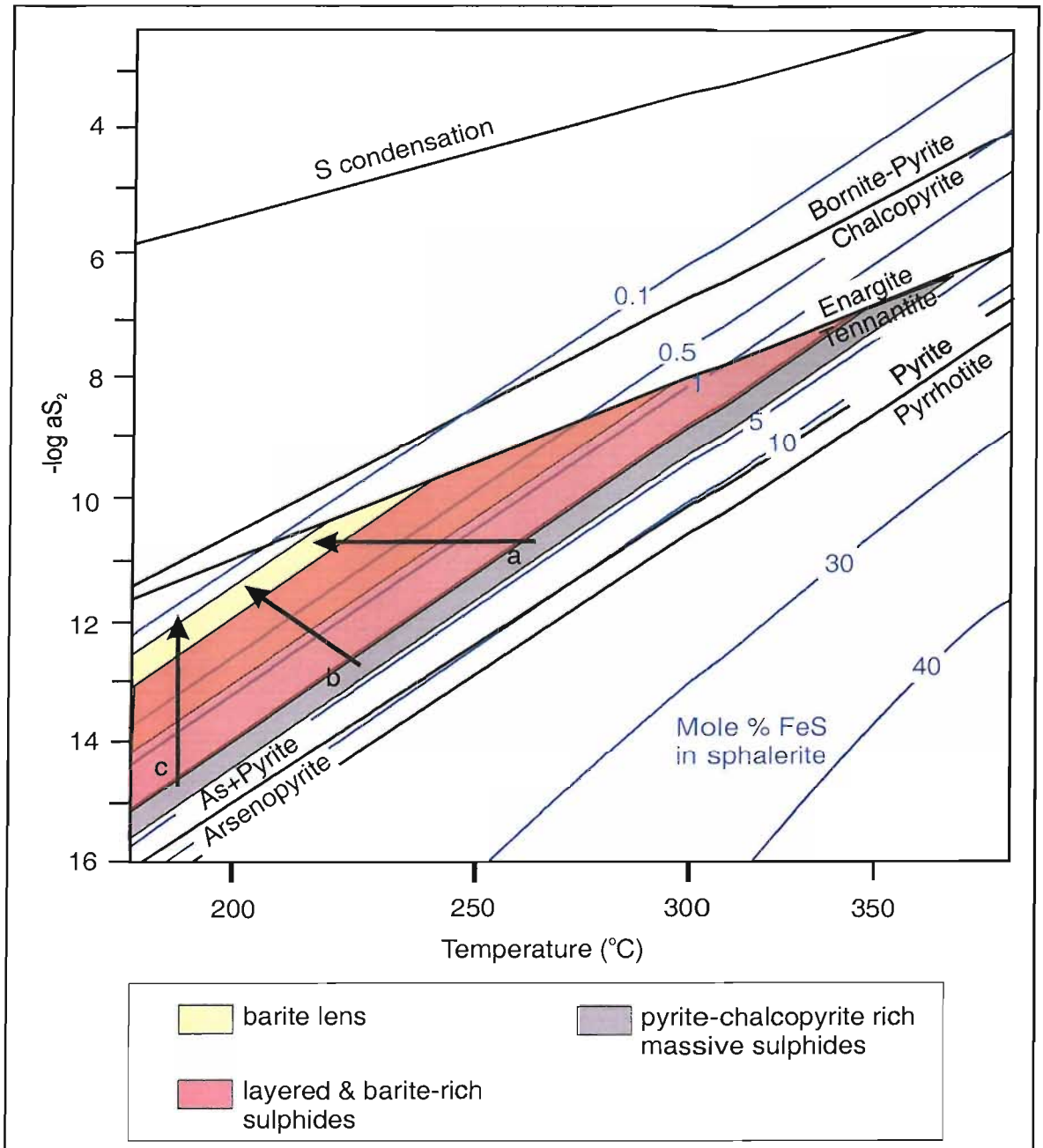

Sulphur activity - temperature diagram showing the formational conditions for selected ore facies at Balta Tau. The change in ore facies from massive sulphides to the barite lens may represent a decrease in temperature (path a), increase in sulphidation (path c) or a combination of the two (path b).

Figure 5.19. Temperature-sulphidation diagram showing the variation in formational conditions across ore facies at Balta Tau.

The pyrite-chalopyrite-rich massive sulphides and late stage massive sulphides contain minor arsenopyrite. The composition of co-existing sphalerite in these ore facies is considerably lower than 10mol% FeS suggesting that the arsenopyrite did not precipitate in equilibrium with the sphalerite (Scott, 1983). For this reason, and for the fact that the arsenopyrite is only a minor phase in these ore facies, the range of formational conditions for these ore facies have not been extended in to the stability field of arsenopyrite in Figures 5.18 and 5.19.

Geothermometry

A geothermometer based on coexisting fahlore-electrum-sphalerite-pyrite-chalcopyrite presents fahlore composition (Ag/Cu and As/Sb) as a function of temperature, electrum composition (Au/Ag) and sphalerite composition (Fe/Zn), enabling the formational temperature to be estimated if the compositions of coexisting fahlore-electrum-sphalerite are known (Ebel and Sack, 1991).

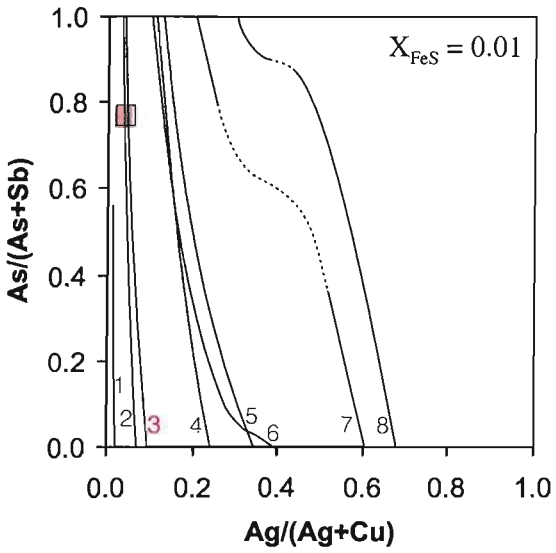

	$X_{Ag}El$	T°C
1	0.20	200
2	0.20	300
3	0.40	200
4	0.42	300
5	0.24	400
6	0.60	200
7	0.80	200
8	1.00	200

Mean values of data from the barite lens:

tennantite:
Ag/(Ag+Cu) = 0.04
As/(As+Sb) = 0.79

sphalerite:
X_{FeS} = 0.004

electrum:
X_{Ag} = 0.45

Reproduction of the geothermometer of Ebel & Sack (1991) based on the composition of fahlore co-exisitng with sphalerite containing 0.01 mol% FeS. Each curve represents the variation in fahlore composition for different temperatures and compositions of co-exisitng electrum (tabulated to the right). The average composition of tennantite in the barite lens (small red box) falls very close to curve numbers 2 and 3. The average composition of electrum in the barite lens is closest to that of curve 3, suggesting a formational temperature of 200°C for this horizon.

Figure 5.20. Application of a fahlore geothermometer to assemblages of the barite lens.

This geothermometer is applicable to the mineral assemblage of the barite lens, although the anomalous nature of Ag enrichment in tennantite (Section 5.2.6) may affect results because the geothermometer relies on Ag exchange between electrum and fahlore. However, average compositions of mineral phases yields a formational temperature of 200°C (Figure 5.20) which is consistent with the temperature range in the sulphidation-temperature diagram of Figure 5.19.

5.3.3 Trace element characteristics

The Balta Tau deposit contains trace amounts of Ag, Au, Hg, Cd, Te, Se as well as the more abundant Pb, As and Sb and the major metals Fe, Cu and Zn. The trace elements show distinct stratigraphic zoning across the Balta Tau deposit, summarised in Figure 5.21.

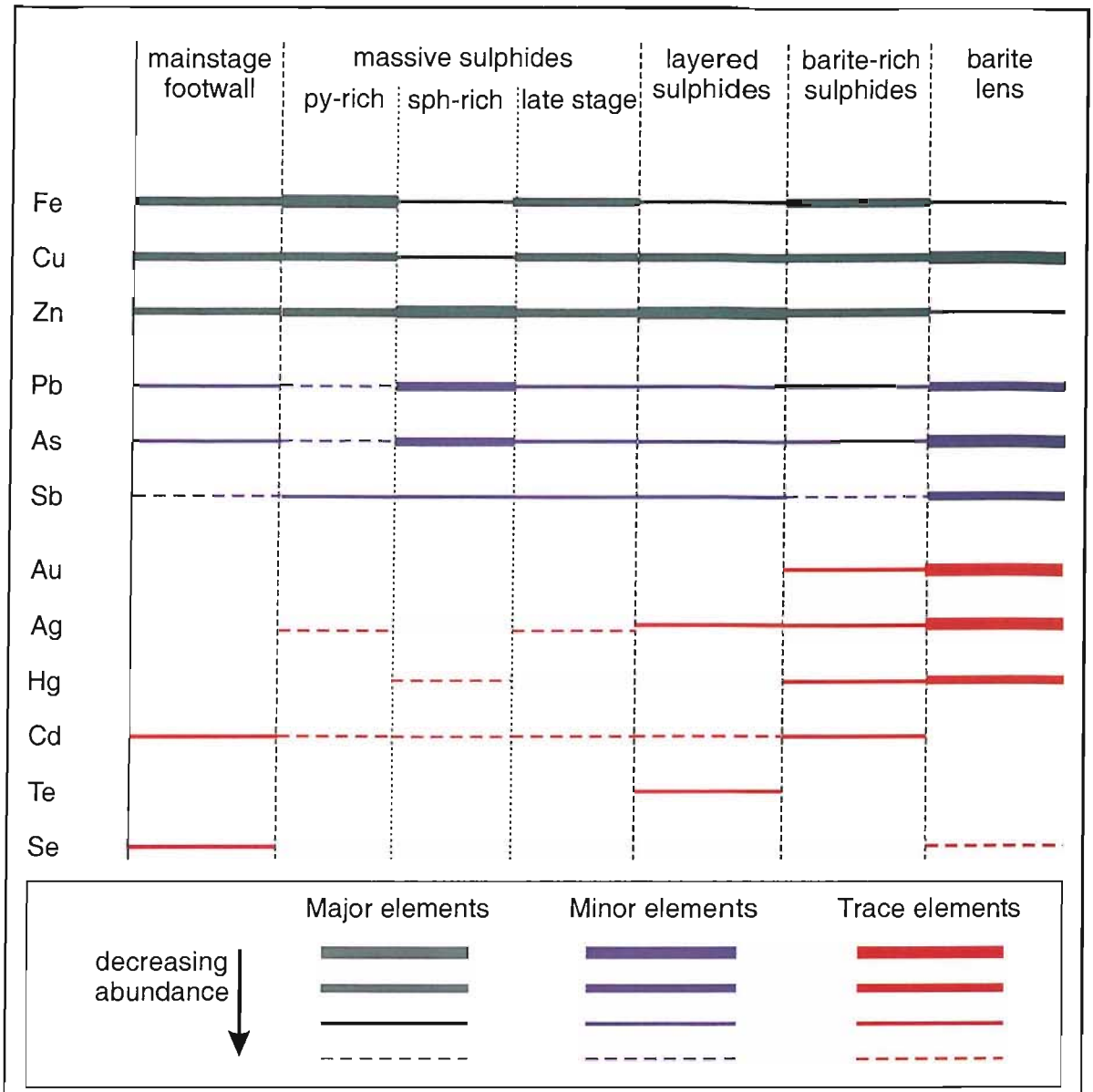

Variations in the minor and trace element distribution between ore facies at Balta Tau. Approximate abundance of the major elements Cu, Fe and Zn are also shown.

Figure 5.21. Minor and trace element zoning between ore facies at Balta Tau.

Silver and gold

Enrichment of the precious metals Au and Ag is mostly confined to the upper baritic ores. Microprobe data indicates that Au is almost exclusively hosted in electrum (except for isolated occurrences of Au enrichment in arsenopyrite in massive sulphides and hessite in layered sulphides) although Au may be present in trace amounts below the microprobe detection limit in pyrite (Section 5.3.1). By comparison, Ag is more abundant and widespread and occurs in a variety of different phases. In the barite lens, Ag is most abundant as electrum but also forms pearcite and native silver, occurs as a major to trace element tennantite and a trace element in galena and chalcopyrite. The exact nature of Ag enrichment in galena and tennantite of the barite lens is questionable, and it may be forming tiny inclusions of an Ag(-Cu?) sulphide. Ag also

occurs as electrum in barite-rich sulphides, as trace amounts in tennantite-tetrahedrite in barite-rich sulphides, massive sulphides and layered sulphides, and as hessite in layered sulphides. The enrichment of precious metals towards the top of VMS deposits has been reported from numerous ancient and modern systems and is often attributed to processes of zone refining (Chapter 7, Section 7.4).

Tellurium

Te enrichment is generally confined to the layered ores where it forms hessite and occurs in trace amounts in tennantite-tetrahedrite, which might indicate that these ore facies have a primary Te enrichment or that enrichment occurred during recrystallization.

Cadmium and mercury

Cd is enriched above detection in sphalerite throughout the Balta Tau ores with the highest concentrations in the footwall and lowest concentrations in the pyrite-rich massive sulphides reflecting the overall negative correlation with Fe in sphalerite. Similar levels of Cd enrichment occur in Fe-poor sphalerite in other deposits (e.g. Valu Fa Ridge, Lau Back Arc Basin, Herzig et al. 1990; Uchinotai-Higashi Kuroko deposit, Urabe, 1974; Rosebery, Australia, Huston et al., 1995), whereas deposits containing Fe-rich sphalerite tends to be Cd poor (e.g. Bent Hill, Middle Valley, Goodfellow & Franklin, 1993), suggesting the negative correlation between Cd and Fe exists on a broader scale between deposits as well as within ore facies at Balta Tau.

Hg is generally confined to electrum and therefore mostly occurs in the upper baritic horizons, with a few exceptions of Hg enrichment in fahlore from the sphalerite-rich massive sulphides. Sphalerite does not contain detectable Hg in spite of the potential for Hg to substitute for Zn in the sphalerite structure.

Selenium

Se occurs in trace amounts in galena and is strongly enriched in the footwall, slightly enriched in the massive and layered sulphides, below detection in upper sulphide horizons (sphalerite-rich massive sulphides and barite-rich sulphides) and variably enriched in the barite lens. Similar trends in Se enrichment of other sulphide phases such as pyrite have been observed in Australian VMS deposits by Huston et al. (1995), who suggest that the Se content of sulphides may provide important information on fluid sources and precipitation mechanisms.

5.3.4 Fahlore chemistry

Fahlore minerals are often the most economically important source of Ag in VMS deposits (e.g. e.g. Shimazaki, 1974) and commonly retain their primary depositional chemistry (Wu and Petersen, 1977; Hackbarth and Petersen, 1984; Seal et al., 1990). However, controls on the composition of fahlore minerals have not been investigated to same extent as other ore phases due to their complex chemistry and the lack of available experimental data. Limited data from other VMS deposits suggests the composition of fahlore is variable both within and between deposits (e.g. Kuroko ores, Shimazaki, 1974; Sulitjelma deposit in Norway, Cook, 1996; Jade, Central Okinawa Trough; Halbach et al., 1993). The abundance of fahlore in a wide range of ore facies at Balta Tau provides an opportunity to investigate influences on the composition of fahlore during ore formation, and variations in As/Sb, Fe/Zn and Au/Cu are considered as follows.

As/Sb

The fahlore at Balta Tau is dominated by As-rich tennantite with most compositions from the mainstage footwall, sphalerite-rich sulphides and the barite lens falling in the range of 11-13at% As and 1-3at% Sb. However, pyrite-chalcopyrite rich and late stage massive sulphides and layered sulphides show large deviations to more Sb rich compositions. The As/Sb does not correlate with formational temperature and sulphidation (inferred from associated sulphides, see section 5.3.2) suggesting these are not important influences, which is also indicated by a wide range of compositions occurring in similar mineral assemblages with Fe-poor sphalerite from other deposits (e.g. Shimazaki, 1974; Halbach et al., 1993; Iizasa et al. 1997).

In a study of fahlore in epithermal systems, Hackbarth and Petersen (1984) suggest that the As/Sb is controlled by fractional crystallization, with early fahlore having a high As/Sb because As is preferentially incorporated into the fahlore structure, becoming progressively more Sb-rich as crystallization proceeds due to an increase in the residual Sb/As of evolving fluids. The abundance of high As/Sb compositions in the majority of ore facies at Balta Tau suggests that either the As/Sb of mineralising fluids was high enough to sustain extensive precipitation of As-rich tennantite, or that the fluids were constantly replenished and did not get a chance to evolve to more Sb rich compositions. Given the rapid and complex nature of fluid flow, fluid mixing and precipitation in modern VMS systems, the latter explanation seems most probable. The Sb-rich compositions in pyrite-chalcopyrite rich and late stage massive sulphides ores may be linked to the presence of arsenopyrite in these two ore facies, with As preferentially incorporated into the arsenopyrite reducing the As/Sb ratio of associated fahlore. The layered sulphides also contain Sb-enriched fahlore, which may indicate a tendency for Sb enrichment to occur during recrystallization.

Fe/Zn

The Fe/Zn ratio of fahlore appears to be influenced by the proportion of pyrite and sphalerite in associated sulphides, with a negative correlation between Fe/Zn and pyrite/sphalerite. For example, pyrite-chalcopyrite rich massive sulphides host the most Fe-rich fahlore, whereas the barite lens, mainstage footwall sulphides and sphalerite-rich massive sulphides contain fahlore with uniformly low Fe/Zn. This association is unlikely to have resulted from Fe-Zn exchange between fahlore and sphalerite (proposed by Leary and Sack, 1987) since there is no difference between fahlore grains immediately adjacent to sphalerite and those with no sphalerite in the immediate vicinity. It may however reflect variations in the degree of metal sulphide saturation of mineralising fluids, with high Fe/Zn during pyrite-rich precipitation and low Fe/Zn during sphalerite-rich precipitation. The presence of chalcopyrite does not seem to influence the Fe/Zn ratio, since fahlore which is intimately associated with chalcopyrite has high Fe/Zn in the pyrite-chalcopyrite rich massive sulphides and low Fe/Zn in the barite lens.

The Fe/Zn can also be investigated in relation to the As/Sb content (Figure 5.22a). A general negative correlation is probably a reflection of the mineral associations discussed above (e.g. in pyrite-chalcopyrite rich sulphides fahlore has a high Fe/Zn due to the abundance of pyrite and low As/Sb due to the presence of arsenopyrite; conversely in sphalerite-rich facies which do not contain arsenopyrite fahlore has a low Fe/Zn and high As/Sb). However, data from individual ore facies which contain a range of fahlore compositions define a series of parallel, positive correlations. These may be explained by element incompatibilities in the fahlore structure. Sack and Loucks (1985) experimentally derived a positive value of 2.59 ±0 .14 kcal/gfw for the molar Gibbs energy of the exchange reaction:

$$Cu_{10}Zn_2Sb_4S_{13} + Cu_{10}Fe_2As_4S_{13} = Cu_{10}Fe_2Sb_4S_{13} + Cu_{10}Zn_2As_4S_{13} \qquad (5.1)$$

indicating an Fe-Sb incompatibility that will result in a positive correlation between Fe/Zn and As/Sb if equilibrium is achieved. Therefore the large scale variations in the Fe/Zn of fahlore correlate with associated pyrite/sphalerite and may reflect the degree of metal saturation in the hydrothermal fluid, while small scale variations within single ore facies may be due to element incompatibilities in the fahlore structure. Variations in the relative importance and effects of these two factors may explain why both negative and positive correlations between As/Sb and Fe/Zn have been reported from epithermal deposits (e.g. Hackbarth & Petersen, 1984, and references therein).

Ag/Cu

The Ag/Cu ratio of fahlore does not show a correlation with the associated mineral assemblages, but does correlate with the corresponding As/Sb ratios (Figure 5.22b). Data from the barite lens define an almost vertical trend indicating little change in As/Sb over a wide range of Ag/Cu. Layered sulphides, barite-rich sulphides and late stage massive sulphides have a negative correlation between As/Sb and Ag/Cu, while data from the pyrite-chalcopyrite rich massive sulphides are clustered with uniformly low Ag/Cu and low As/Sb(Figure 5.22c).

A negative correlation between Ag/Cu and As/Sb in fahlore has been identified from several deposits (e.g. Wu and Petersen, 1977; Hackbarth and Petersen, 1984) and has been attributed to element incompatibilities in the fahlore structure. This has been shown experimentally by Sack and Loucks (1985) who demonstrate that the exchange reaction

$$Ag_6Cu_4Fe_2Sb_4S_{13} + Cu_{10}Fe_2As_4S_{13} = Cu_{10}Fe_2Sb_4S_{13} + Ag_6Cu_4Fe_2As_4S_{13} \quad (5.2)$$

has a large positive value for the molar Gibbs energy of 17±5kcal/gfw, which defines an Ag – As incompatibility and implies a negative correlation between Ag/Cu and As/Sb if equilibrium is reached. This can explain the negative correlation observed in a number of ore horizons at Balta Tau and suggests that Ag-As incompatibility is an important influence over the chemistry of fahlore. However, exceptions such a the Sb-rich, Ag-poor composition of tetrahedrite in the pyrite-chalcopyrite rich massive sulphides indicates that locally other factors such as associated sulphide assemblages and degree of metal saturation in ore forming fluids may be more important.

The anomalous trend in tennantite from the barite lens is probably a consequence of the deviation of Ag-tennantite from stoichiometry. As discussed in Section 5.2.6, this deviation may be caused by the presence of sub-microscopic inclusions of a separate Ag-bearing phase, which would explain the uniform As/Sb ratios of both Ag-rich and Ag-poor tennantite (Figure 5.11a). Tennantite from the barite lens with only a slight Ag-enrichment also falls on the trend defined by the Ag-tennantite (Figure 5.22b), suggesting that even this low level Ag-enrichment is anomalous and may also be the result of inclusions of a separate Ag-bearing phase.

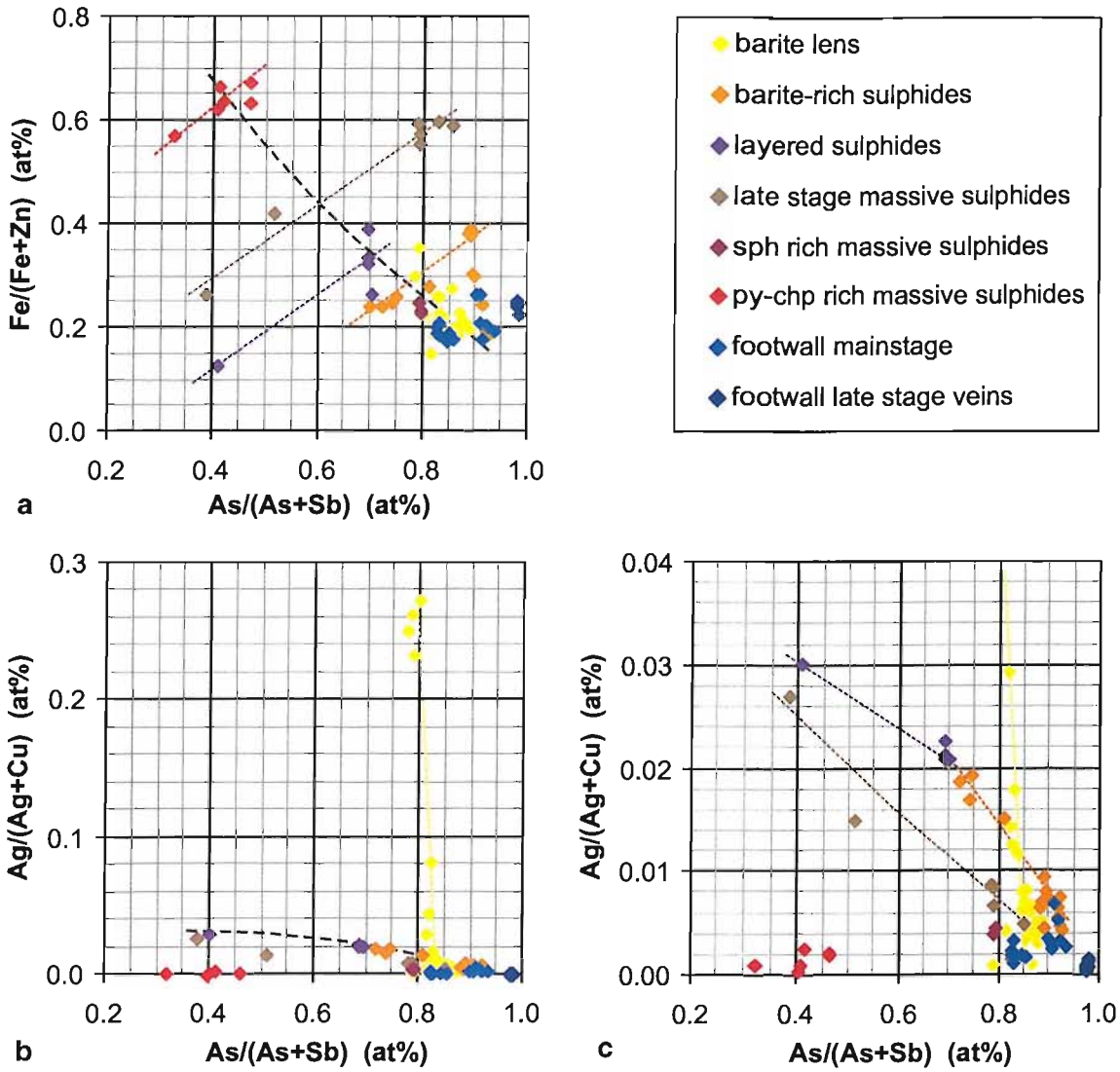

a. Fe/(Fe+Zn) versus As/(As+Sb)suggests an overall negative correlation, but individual ore facies define a series of parallel positive trends.

b. Ag/(Ag+Cu) versus As/(As+Sb) has a near vertical trend in data from the barite lens, while the rest of the data show a weak negative correlation.

c. The same plot as (b) but excluding Ag-rich data of the barite lens. A negative correlation is seen in layered sulphides, late stage massive sulphides and barite-rich sulphides. Data from the pyrite-chalcopyrite-rich sulphides is anomalous with low Ag/(Ag+Cu) and low As/(As+Sb).

(general trends are indicated by black dashed lines; trends for individual ore facies are indicated by dashed lines of the same colour as the corresponding data points).

Figure 5.22. Correlation between element ratios in tennantite-tetrahedrite from microprobe data.

5.4 ALTERATION AND GANGUE MINERAL CHEMISTRY

5.4.1 Introduction

In alteration and gangue assemblages, silicate phases were analysed for Si, Al, Fe, Mg, Na, Ca, K, Ti, Mn, Sr, Cr, P and S; sulphates for Ba, Ca, Sr and S, and carbonates for Ca, Ba, Fe, Mg, Mn and Sr. Counting times were 10-25 seconds for each element with a beam current of 15nA and an accelerating voltage of 15kV, giving a detection limits in the range 0.02-0.04 wt% for all elements analysed. Analytical details for each element (count time, standards for calibration and detection limit) and a full data listing is given in Appendix B1. The following sections present data separately for each mineral phase, with analyses grouped according to the ore facies defined Chapter 4 (Table 4.1).

5.4.2 Chlorite

The composition of chlorite is highly variable due to a number of substitutions that may take place, and can be represented by the general expression of a half cell unit:

$(R^{2+}_u + R^{3+}_y + \square_z)^{VI}(Si_{4-x}\ Al_x)^{IV}O_{10+w}(OH)_{8-w}$ (de Caritat et al., 1993)

Where R^{2+} is usually Mg^{2+} or Fe^{2+}, R^{3+} is usually Fe^{3+} or Al^{3+} and □ represents structural vacancies; $u + y + z = 6$, $z = (y - w - x)/2$, and w is generally close to or equal to zero (de Caritat et al., 1993).

Wt% oxide data for chlorites and corresponding calculated half cell formulae are summarised in Table 5.16. Calculation of formula proportions (based on the method of Deer et al., 1966; Appendix B3) enables the division of Al between tetrahedral and octahedral sites but does not allow distinction between Fe^{2+} and Fe^{3+} (all Fe is assumed to be divalent) and the proportion of OH is assumed to be the ideal value of 8 (i.e. "*w*" is set as zero). The chlorites analysed fall within the "normal" range of compositions according to the compilation of data by Foster (1962), with Si^{IV} in the range 2.34 to 3.45 and octahedral vacancies in the range –0.5 to 0.55.

A number of different classification schemes have been devised for chlorites many of which involve complicated nomenclature (e.g. Hey, 1954; Phillips, 1964), however for the purposes of this study the simple classification of McLeod & Stanton (1984) is used (Figure 5.23a). Chlorite from the footwall and layered sulphides are particularly Mg-rich and close to end member clinochlore, with Mg/(Mg+Fe) ranging from 0.92-0.98; chlorite in massive sulphides is an Mg-Al-

chamosite, and the regional and hanging-wall chlorites are an Fe(-Al)-clinochlore. The chamosite from massive sulphides generally has a smaller proportion of tetrahedral Si compared to the clinochlore (Figure 5.23a), and the chlorite in mineralised horizons contain more Al in octahedral sites than chlorite from the hanging-wall and regional volcanics (Figure 5.23b).

		footwall (coarse)	footwall (fine)	layered sulphides (coarse)	massive sulphides (coarse)	hanging-wall (fine)	Regional (Irendyk) (fine)
Number of analyses		28	15	4	8	3	9
weight percent oxides	SiO_2	29.32	31.77	29.21	23.73	26.76	27.03
	Al_2O_3	24.10	23.80	24.32	20.06	21.13	17.87
	FeO	2.03	2.24	1.77	33.78	18.05	24.11
	MnO	0.17	0.17	0.17	0.74	0.45	0.37
	MgO	29.21	27.19	29.45	7.76	20.05	16.39
	H_2O	12.57	12.71	12.59	10.57	11.68	11.20
	total	97.47	98.02	97.51	96.69	98.16	97.10
formula proportions	Si^{4+}	2.80	3.00	2.78	2.69	2.75	2.89
	Al^{3+} (total)	2.71	2.65	2.73	2.68	2.56	2.26
	Fe^{2+}	0.16	0.18	0.14	3.21	1.55	2.16
	Mn^{2+}	0.01	0.01	0.01	0.07	0.04	0.03
	Mg^{2+}	4.15	3.83	4.18	1.31	3.07	2.62
	total R^{2+} ("u")	4.33	4.02	4.34	4.59	4.66	4.81
	tet. Al^{3+} ("z")	1.20	1.00	1.22	1.31	1.25	1.11
	oct. Al^{3+} ("y")	1.51	1.64	1.51	1.37	1.31	1.15
	total tet.	4.00	4.00	4.00	4.00	4.00	4.00
	total oct.	5.84	5.67	5.85	5.96	5.97	5.96
	oct. vacancy	0.16	0.33	0.15	0.04	0.03	0.04
	total (OH)	8.00	8.00	8.00	8.00	8.00	8.00
Mg number	Mg/(Mg+Fe)	0.96	0.95	0.96	0.29	0.66	0.54

Table 5.16. Composition of chlorites from microprobe data expressed as weight % oxides and atoms per half cell formula unit. (Appendix B3; based on 14 oxygen atoms). *Values "u", "y" and "z" relate to quantities in the half cell unit as defined in the text.

Compositional variations in chlorites can be related to a number of exchange reactions, as defined by Walshe (1986). The Al content, which is particularly high in chlorites associated with mineralization at Balta Tau, results mainly from the substitution $(R^{2+})^{VI}(Si^{4+})^{IV} \Leftrightarrow (Al^{3+})^{VI}(Al^{3+})^{IV}$, which adds Al to tetrahedral and octahedral sites in equal proportions. The Al-rich chlorites from Balta Tau contain more octahedral Al than tetrahedral Al indicating that the substitution $3(Mg,Fe^{2+})^{VI} \Leftrightarrow 2(Al^{3+})^{IV}\square^{VI}$ is also important, which creates an vacant octahedral site to compensate for the charge difference between R^{2+} and Al^{3+}. Fe^{3+} is unlikely to be present in the

end member clinochlore since the bulk Fe content of this chlorite is very low. However, significant Fe^{3+} may be present in massive sulphide chamosite and hanging-wall and regional Fe-Al-clinochlore, either by direct substitution for Al^{VI} or by the exchange $(Fe^{2+})^{VI}\ 2(OH)^- \Leftrightarrow (Fe^{3+})^{VI}\ O^{2-}(OH)^- + H^+$ (Walshe, 1986).

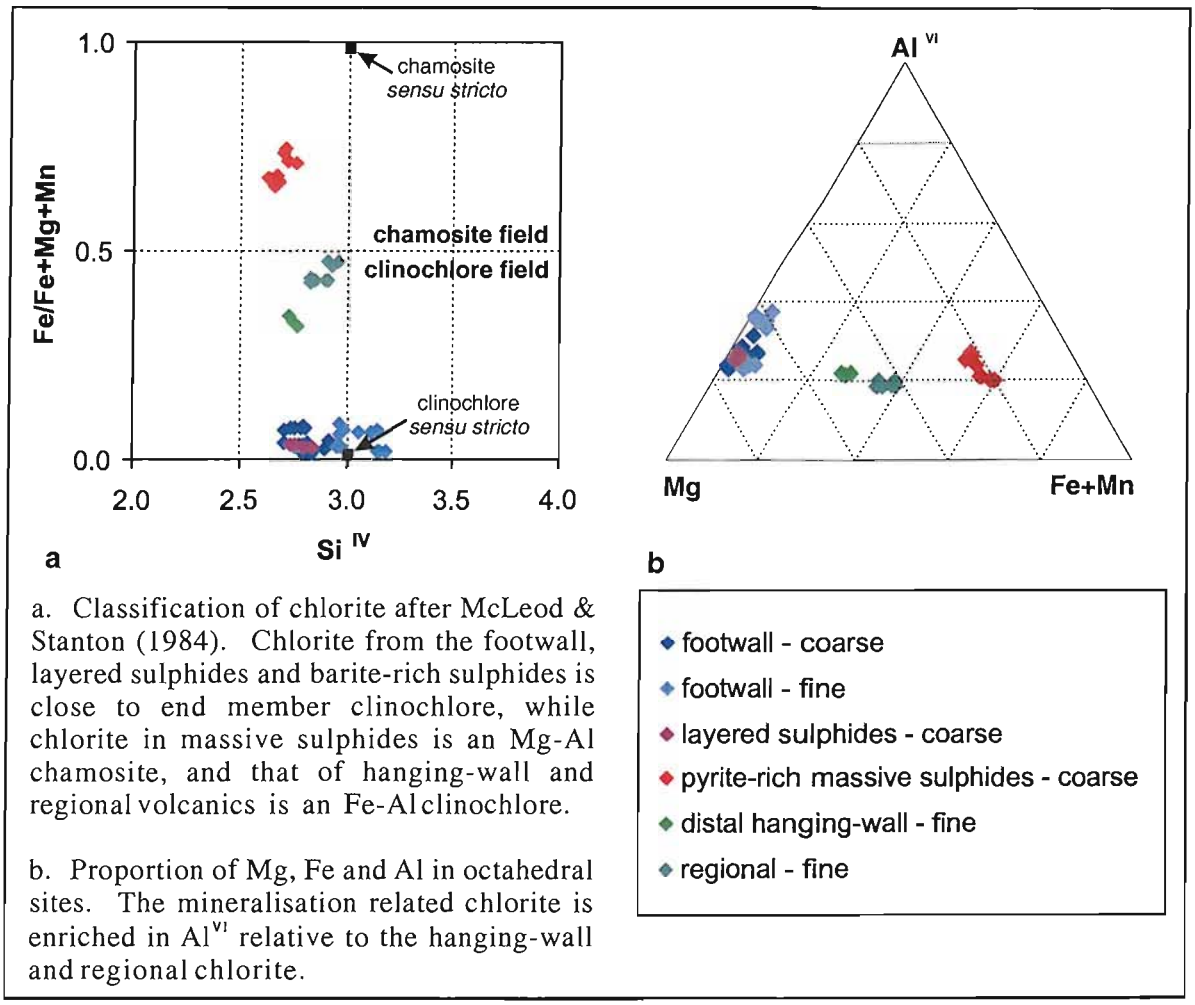

a. Classification of chlorite after McLeod & Stanton (1984). Chlorite from the footwall, layered sulphides and barite-rich sulphides is close to end member clinochlore, while chlorite in massive sulphides is an Mg-Al chamosite, and that of hanging-wall and regional volcanics is an Fe-Al clinochlore.

b. Proportion of Mg, Fe and Al in octahedral sites. The mineralisation related chlorite is enriched in Al^{VI} relative to the hanging-wall and regional chlorite.

Figure 5.23. Composition of chlorite from Balta Tau and surrounding volcanic rocks based on microprobe data.

5.4.3 Muscovite

Muscovite is a member of the mica group of phyllosilicates and ideally has the composition $KAl_2(Si_3Al)O_{10}(OH)_2$. However, muscovite usually deviates from this end member composition due the substitution $Al^{IV}Al^{VI} \Leftrightarrow (Mg,Fe)Si$ which introduces divalent Fe and Mg, increases Si and decreases Al, and the proportion of mica containing Fe and Mg can be described in terms of a celadonite component, $K(Mg,Fe)Si_4O_{10}$. Muscovite compositions may also deviate by the substitution $KAl^{IV} \Leftrightarrow Si$, which introduces a component of pyrophyllite, $Al_2Si_4O_{10}(OH)_2$ (Yoder & Eugster, 1955). Additionally, $K \Leftrightarrow Na$ exchange results in a partial solid solution series between muscovite and the Na end member paragonite, $NaAl_2(Si_3Al)O_{10}(OH)_2$ (Deer et al., 1966).

Analyses of coarse muscovite from all mineralised horizons and fine sericite from the footwall, intensely altered immediate hanging-wall and less altered distal hanging-wall are summarised in Table 5.17. Coarse muscovite in all mineralised horizons and the immediate hanging-wall is close to the ideal muscovite composition, containing no more than 10% celadonite and 5 to 10% pyrophyllite, and the footwall sericite is also close to this end member composition containing just above 10% each of pyrophyllite and celadonite (Figure 5.24a). Sericite from the distal hanging-wall has a much more variable composition containing 10 to 40% celadonite but less than 10% pyrophyllite. There is a significant difference in the Mg/Fe of the celadonite component, with all mineralization-related micas containing a high Mg/Fe while those from the distal hanging-wall are more Fe rich (Figure 5.24b).

		footwall (fine)	footwall (coarse)	layered sulphides (coarse)	barite-rich sulphides (coarse)	barite lens (coarse)	immediate hanging-wall (fine)	Distal hanging-wall (fine)
Number of analyses		3	12	3	3	7	3	6
weight percent oxides	SiO_2	47.56	45.79	45.59	43.49	44.94	45.26	48.70
	Al_2O_3	33.49	34.69	34.82	32.92	34.00	33.01	26.92
	FeO	0.30	0.18	0.17	0.64	0.15	0.20	4.39
	MgO	1.08	0.76	0.78	0.44	0.83	1.29	3.02
	CaO	0.12	0.05	0.02	0.10	0.02	0.26	0.11
	Na_2O	0.85	0.96	1.21	0.78	0.55	0.47	0.33
	K_2O	8.95	9.09	8.78	8.45	9.70	9.39	10.40
	H_2O	4.44	4.39	4.38	4.16	4.31	4.31	4.37
	total	96.77	95.91	95.75	90.99	94.51	94.51	98.31
formula prop-ortions	Si^{4+}	3.21	3.13	3.12	3.13	3.13	3.15	3.34
	Al^{3+} (total)	2.67	2.79	2.81	2.80	2.79	2.71	2.18
	Fe^{2+}	0.02	0.01	0.01	0.04	0.01	0.03	0.25
	Mg^{2+}	0.11	0.08	0.08	0.05	0.09	0.13	0.31
	Ca^{2+}	0.01	0.00	0.00	0.01	0.00	0.02	0.01
	Na^{+}	0.11	0.13	0.16	0.11	0.07	0.06	0.04
	K^{+}	0.77	0.79	0.77	0.78	0.86	0.83	0.91
	tet. Al^{3+}	0.79	0.87	0.88	0.87	0.87	0.85	0.66
	oct. Al^{3+}	1.88	1.92	1.92	1.93	1.91	1.86	1.52
	total tet.	4.00	4.00	4.00	4.00	4.00	4.00	4.00
	total oct.	2.00	2.01	2.01	2.02	2.01	2.03	2.08
	(K,Na,Ca)	0.89	0.92	0.93	0.89	0.94	0.92	0.96
	total (OH)	2.00	2.00	2.00	2.00	2.00	2.00	2.00

Table 5.17. Composition of micas from microprobe data expressed as weight % oxides and atoms per structural formula (Appendix B3; based on 22 oxygen atoms).

All the analyses have a high K/Na and there is no distinction between the muscovite in mineralised sequences and that of the distal hanging-wall. Within the ore horizons there is a systematic variation in K/Na, with footwall and layered and barite-rich sulphides being relatively Na-rich, and hanging-wall sequences (barite lens and hanging-wall) more K-rich (Figure 5.24c).

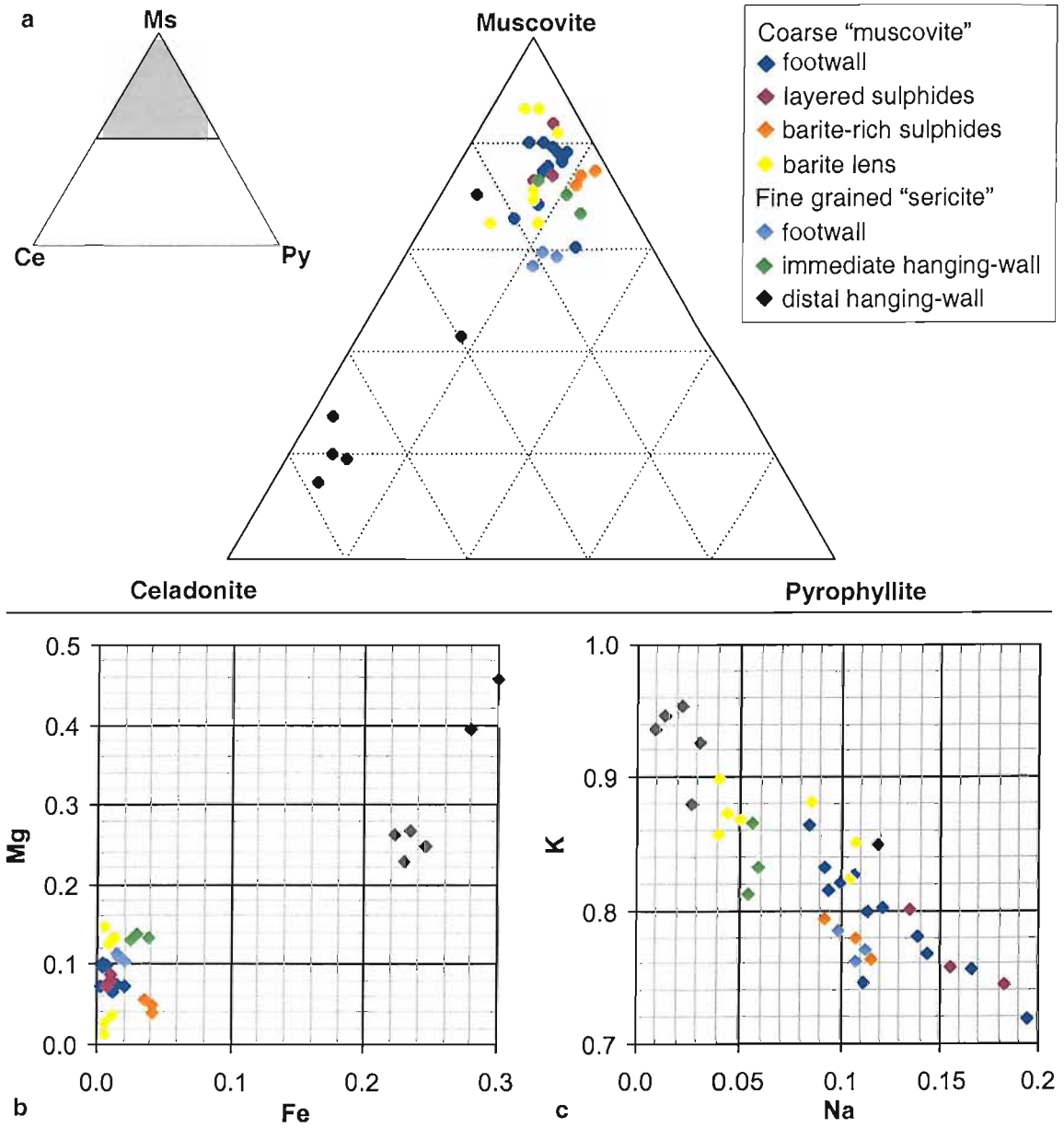

a. Composition of micas expressed as proportions of muscovite, celadonite and pyrophyllite (after Hower & Mowatt, 1966). Mineralization-related micas have a low caledonite and pyrophyllite content and are close to end member muscovite, whereas sericite from the distal hanging-wall contains significant and variable celadonite.

b. Plot of Fe versus Mg. Mineralization-related micas have very low Fe/Mg ratios, whereas the distal hanging-wall has higher Fe/Mg.

c. Plot of K versus Na. All micas are K rich with only minor Na. There is a general trend towards greater enrichment in Na at stratigraphically lower and mainstage ore horizons compared to hanging-wall horizons.

Figure 5.24. Composition of micas from Balta Tau mine sequences based on microprobe analyses.

5.4.4 Barite

Microprobe analyses of barite from massive sulphides, barite-rich sulphides and the barite lens are summarised in Table 5.18. Compositions are close to the ideal stoichiometry of $BaSO_4$, with trace amounts of Sr substituting for Ba. The Sr enrichment is variable with barite from massive sulphides containing 0.48 to 0.52at% Sr, barite from barite-rich sulphides varying from below detection to 0.5at% Sr, and barite from the barite lens 0.1 to 0.23at% Sr.

	n	S	Ba	Sr	O	Total
Pyrite-rich massive sulphides	3	16.16	17.18	0.51	66.16	100.00
Barite-rich sulphides	6	16.31	17.06	0.31	66.32	100.00
Barite lens	4	16.31	17.20	0.17	66.32	100.00

Table 5.18. Microprobe analyses of barite expressed as atomic %.

5.4.5 Carbonate

Carbonate analyses are summarised in Table 5.19. The footwall carbonate which infills vugs in sphalerite is visibly zoned in thin section (Chapter 4, Figure 4.6) and in backscatter images, and has a complex chemistry with compositions intermediate between smithsonite and siderite with a small calcite component, minor Mg and Mn and trace Ba. Carbonate from massive sulphides is a mixture of calcite and intermediate siderite-calcite with significant Mg, both of which are enriched in Sr and Mn, while the barite-rich sulphides and distal hanging-wall contain calcite enriched in Mn and Mg.

	n	$MgCO_3$	$CaCO_3$	$MnCO_3$	$FeCO_3$	$ZnCO_3$	$SrCO_3$	$BaCO_3$	Total
Footwall	1	1.86	3.39	1.06	60.97	32.62	0.06	0.04	100.00
	1	1.46	6.07	1.85	68.89	21.60	0.00	0.11	100.00
	1	1.63	9.16	2.43	71.48	15.23	0.00	0.06	100.00
Pyrite-rich massive sulphides	3	16.18	50.39	2.43	30.51	0.00	0.48	0.01	100.00
	3	0.32	94.02	2.08	3.30	0.04	0.20	0.04	100.00
Barite-rich sulphides	13	0.17	98.85	0.80	0.09	0.03	0.05	0.02	100.00
Distal hanging-wall	4	1.02	95.45	3.34	0.07	0.04	0.04	0.04	100.00

Table 5.19. Microprobe analyses of carbonate phases expressed in mol%.
Note: Three analyses from adjacent grains in a footwall vein are shown separately to illustrate zoning in Zn content; two grains from pyrite-rich massive sulphides are summarised separately as they have very different compositions.

5.4.6 Zeolite and pumpellyite

Analyses of zeolite and pumpellyite were carried out principally to confirm identification of these minerals, since they are important indicators of the grade of regional metamorphism; results are

summarised in Table 5.20. The pumpellyite identified in barite-rich sulphides conforms well to the ideal composition $Ca_2Al_2(Mg,Fe^{2+},Fe^{3+},Al)(SiO_4)(Si_2O_7)(OH)_2(H_2O,OH)$ with analyses indicating proportions close to $(H_2O)_{0.5}(OH)_{0.5}$ in the final bracket.

Zeolite observed in the footwall, sphalerite-rich massive sulphides, barite-rich sulphides, barite lens and the immediate hanging-wall has a composition close to that of scolecite, which is a member of the natrolite group and has the composition $CaAl_2Si_3O_{10}\cdot 3H_2O$. This identification is consistent with extensive multiple twinning observed in thin section which is characteristic of scolecite (Gribble & Hall, 1992). The low wt% totals and deficiency in the formula proportion of Ca suggest that another cation may also be present that was not analysed for, such as Ba or Sr. There is no significant variation in the zeolite chemistry between ore facies, with all analyses close to the mean values quoted in Table 5.20.

scolecite n = 12				pumpellyite n = 6			
weight percent oxides		formula proportions		weight percent oxide		formula proportions	
SiO_2	45.78	Si^{4+}	3.16	SiO_2	37.09	Si^{4+}	3.09
Al_2O_3	23.89	Al^{3+}	1.94	Al_2O_3	25.96	Al^{3+}	2.55
FeO	0.04	Fe^{2+}	0.00	FeO	0.97	Fe^{2+}	0.14
MgO	0.02	Mg^{2+}	0.75	MgO	3.49	Mg^{2+}	0.43
CaO	10.11	Ca^{2+}	0.01	CaO	23.32	Ca^{2+}	2.08
Na_2O	0.11	Na^+	0.00	Na_2O	0.04	Na^+	0.01
K_2O	0.03	K^+	0.76	K_2O	0.02	K^+	0.00
H_2O	13.03	(OH)	0.00	H_2O	6.30	(OH)	2.50
total	93.00	H_2O	3.00	total	97.52	H_2O	0.50

Table 5.20. Microprobe analyses of scolecite and pumpellyite expressed as oxide wt% and atoms per structural formula (Appendix B3; calculations are based on 12.75 and 10 oxygen atoms for pumpellyite and scolecite respectively, and all Fe is assumed to be divalent).

5.4.7 Discussion of alteration and gangue mineral chemistry

Formation of chlorite associated with mineralization

The chlorite associated with mineralization is compositionally distinct from that of the distal hanging-wall and regional volcanics, suggesting that it did not form during diagenesis or regional metamorphism. This is consistent with textural studies (Chapter 4) which also suggest that the chlorite in mineralised sequences did not form during regional metamorphism. Chlorite is one of the most common alteration minerals in VMS deposits and is generally interpreted to be cogenetic with sulphide mineralization, and variations in the composition of footwall chlorite often correlate with the mineralogy of associated sulphides, with Mg-rich chlorite associated with Fe-poor

sphalerite and Fe-rich chlorite with Fe-rich sphalerite and chalcopyrite (McLeod & Stanton 1984). The Fe-rich chlorite in pyrite-chalcopyrite rich massive sulphides at Balta Tau is consistent with this trend, which together with textural observations suggests that this chlorite is cogenetic with the massive sulphides. However, chlorite in the footwall and layered sulphides is Mg-rich whether associated with chalcopyrite-pyrite veins or Fe-poor sphalerite and replaces sulphides at grain boundaries, indicating that the footwall chlorite is not cogenetic with sulphides but formed after the main mineralising event.

The intense and pervasive nature of footwall alteration suggests a high fluid : rock ratio where the chemistry of alteration products is more likely to have been influenced by fluid chemistry than the original rock composition (Saccocia & Gillis, 1995). Hydrothermal fluids tend to be Fe-rich and Mg-poor and typically form chlorites with moderate to high Fe contents such as the chamosite found in massive sulphides at Balta Tau. The formation of Mg-chlorites requires a source of Mg which is generally inferred to be seawater mixing with the hydrothermal fluid (e.g. Zierenberg et al., 1993). The precipitation of Mg-rich chlorite may then occur due to the partitioning of Fe into associated pyrite according to the reaction (Kalogeropoulos & Scott, 1983):

$$\text{Fe chlorite} + S_2 = \text{Mg chlorite} + \text{pyrite} \qquad (5.3)$$

or due to formation from fluids with a high concentration of reduced sulphur and low salinity (Saccocia & Gillis, 1995). However, fluid mixing generally results in variable formational conditions leading to zoning in the mineralogy and chemistry of footwall alteration which is typical of VMS deposits (e.g. Schardt et al., 2001). The ubiquitous occurrence of Mg-rich chlorite with little compositional variation in the footwall at Balta Tau is therefore not suggestive of formation during fluid mixing. A more likely explanation is precipitation from seawater circulating the footwall after ore deposition with little or no input from hydrothermal fluids, which can account for the Mg-rich compositions, absence of zoning and lack of compositional correlation with associated sulphides. A similar process has been documented from the footwall margins of the active TAG system, MAR, where Mg-rich chlorite is interpreted to reflect infiltration of seawater during waning stages of the hydrothermal system (Teagle et al. 1998). The Mg-chlorite probably formed at lower temperatures than the mineralization, and may be overprinting earlier alteration minerals which co-precipitated with sulphides such as Fe-chlorite or sericite.

Chlorite geothermometry

Table 5.21 summarises formational temperatures estimated from four geothermometers utilising the composition of chlorite (methods and calculations are given in Appendix B4). These are an empirical geothermometer based on the proportion of tetrahedral Al from Cathlineau (1988), two

revisions of this method by (Kranidiotis & MacLean 1987) and Jowett (1991) which attempt to take into account variations in Fe/(Fe+Mg), and a geothermometer based on thermodynamic constraints from Walshe (1986). The empirical approach relies on the temperature dependence of Al substituting into the tetrahedral site; however, de Caritat et al. (1993) demonstrate that other factors such as original rock composition and fluid composition also affect the amount of Al^{IV}. Therefore different rock types and formational environments are likely to produce different Al^{IV}-temperature relationships and the empirical geothermometers are only likely to give reliable results for chlorites that precipitated in a similar environment to those used for the calibration.

host ore facies	number of analyses	Temperature estimates (°C)			
		Cathelineau (1988)	Jowett (1991)	Kranidiotis & MacLean (1987)	Walshe (1986)
footwall (fine)	15	261	252	128	103
footwall (coarse)	28	325	316	148	143
massive sulphides (coarse)	8	359	371	209	191[1]
layered sulphides (coarse)	4	330	320	149	148
distal hanging-wall (fine)	3	341	341	175	218
regional (fine)	9	294	298	169	153[2]

Table 5.21. Temperature estimates based on chlorite compositions from microprobe data. Notes: [1] number of analyses = 5; [2] n=6 (Appendix B4). Estimates based on Kranidiotis and Maclean (1987) and Walshe (1986) are considered the most reliable (see text).

The temperatures estimated using the Cathelineau (1988) and Jowett (1991) geothermometers are similar because the modification of Jowett is only minor, and these temperatures are probably too high since footwall chlorite precipitating from seawater (see above discussion) would probably form at temperatures far lower than 320°C, and the formation of massive sulphides is likely to be <300°C according to sulphide equilibria (Section 5.3.2). Similar findings are reported by de Caritat et al. (1993) who demonstrate that these two geothermometers overestimate temperatures by up to 200°C, particularly for Al-rich chlorites. The modification of Kranidiotis & MacLean (1987) produces considerably lower temperatures which are generally more consistent with expected values. This geothermometer is designed for chlorites that precipitated in Al-saturated environments, which may be more applicable to the chlorites from mineralised sequences since they are Al-rich. The distal hanging-wall and regional chlorites are less aluminous and the temperature estimates for these are probably too low given the prehnite-pumpellyite grade of regional metamorphism which suggests formational temperatures of at least 180°C (Robinson & Bevins, 1999). The geothermometer based on thermodynamic constraints from Walshe (1986) does not assume that temperature is the only influence on chlorite composition, thereby eliminating the principle limitation of empirical methods. However, the assumption made in formula calculations that all Fe is divalent is a limitation for this method, since this

geothermometer uses the proportion of octahedral vacancies which increases with the presence of Fe^{3+}. Therefore if Fe^{3+} is present the temperature estimates will be too low. Temperatures estimated by this method are likely to be accurate for the mineralization-related clinochlore which contains very little Fe but may be too low for the massive sulphide chamosite and hanging-wall and regional Fe-clinochlore.

There is a negative correlation between the tetrahedral Si and temperatures calculated from thermodynamic constraints of Walshe, 1986 (Figure 5.25) illustrating the temperature dependence of Si^{IV} (and therefore Al^{IV}) that forms the basis of the empirical geothermometers. The clinochlore and chamosite from mineralised horizons form trend lines that are distinct from those of regional and hanging-wall Fe-Al-clinochlore. This supports the inference of de Caritat et al. (1993) that Si^{IV}/Al^{IV} is affected by other factors as well as temperature and that empirical geothermometers should only be applied to chlorites similar to those used for calibration. The trends also support the inference that chlorite in mineralized sequences formed in a different environment to those of distal hanging-wall and regional volcanics.

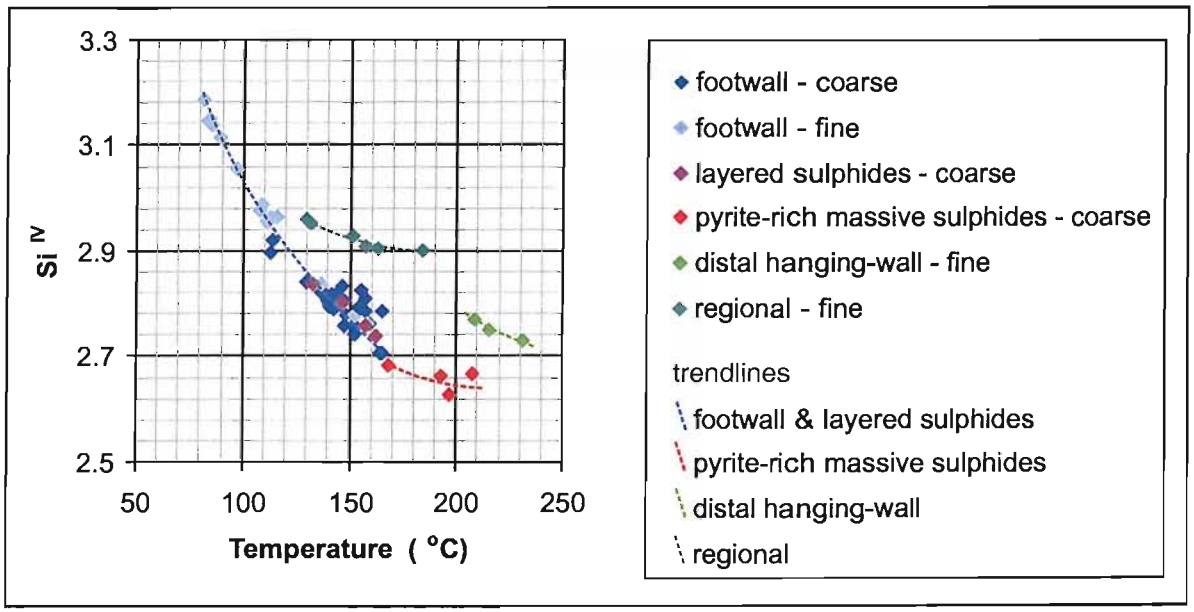

Figure 5.25. Relationship between Si^{VI} in chlorite and formational temperatures estimated using thermodynamic constraints.

Formation of micas associated with mineralization

Replacement textures observed in thin section indicate that coarse mica in mineralized horizons post-dates sulphide phases, and mica is often foliated in zones of deformation (e.g. Chapter 4, Figures 4.5 and 4.38). However, compositional differences between mica associated with mineralization and that of the distal hanging-wall, together with the footwall to hanging-wall zoning in Na/K of mica in ore horizons, suggests that the mica in ore horizons initially formed

during mineralization-related events rather than during metamorphism. Backscatter images from footwall samples indicate an intimate relationship between fine plates of mica (which were not observed in thin section) and coarse Mg-chlorite, indicative of co-precipitation of these phases as well as the replacement of chlorite and sulphides by mica which is evident in thin sections. The high Mg/Fe ratios of both the mica and associated chlorite also suggests that they may be genetically related (McLeod & Stanton 1984). The formation of this mica and its relationship with Mg-chlorite is discussed further in Chapter 7, Section 7.53.

Metamorphism

The presence of pumpellyite and scolecite in mineralized horizons indicate very low grade metamorphism of the Balta Tau deposit, probably near to the border between zeolite facies and prehnite-pumpellyite facies corresponding to low temperatures of around 180 to 250°C (Robinson & Bevins, 1999). This is consistent with the occurrence of scolecite which is one of the least hydrated of the zeolite group and typically associated with the higher grade portion of the zeolite facies. These alteration minerals are broadly consistent with those found in the volcanics surrounding Balta Tau, with the regional metamorphism varying between prehnite-pumpellyite and pumpellyite-actinolite facies (Chapter 3, Section 3.2.7).

5.5 SUMMARY

The Balta Tau deposit is enriched in a variety of elements in addition to the major metals Fe, Cu, and Zn including minor As, Sb and Pb and trace Au, Ag, Hg, Cd, Te and Se. Sulphide assemblages suggest low to moderate formational temperatures of <180 to 300°C, and low to moderate sulphidation of 10^{-15} to 10^{-9}atm. These assemblages and formational conditions are comparable with modern low temperature, low sulphidation systems commonly referred to as "white smokers", which also typically exhibit high precious metal contents associated with Zn-Pb-Ba-Sb-As. Mineralogical zoning across ore facies is accompanied by zoning in the major and trace element chemistry of sulphide phases and variations in the abundance of rare minerals such as electrum.

The main host for Au and Ag is the abundant electrum in baritic ores. Significant Au has not been detected in other phases, although there may be considerable low level Au enrichment in pyrite, particularly the arsenian pyrite from barite-rich sulphides. By contrast, Ag occurs in a number of phases other than electrum and the most important of these is the widespread Ag enrichment of fahlore. The variable compositions of fahlore including Ag content appear to be influenced by the associated mineral phases and thermodynamic effects of element incompatibilities. The majority

of electrum in barite ores is interpreted to be of primary hydrothermal origin. The occurrence of abundant coarse, primary electrum in VMS is rare with only a few comparable examples in ancient deposits. Primary hydrothermal electrum of similar composition and mineralogical association has been identified from actively forming VMS systems but grains are much finer and in lower abundance. Partial remobilisation of electrum at Balta Tau results in Ag-rich electrum forming rims around primary electrum grains and adjacent sulphides.

Chlorite in massive sulphides is an Mg-chamosite and probably co-precipitated with sulphide minerals. By contrast, chlorite in the footwall and layered ores is almost end-member clinochlore and probably a product of late stage seawater circulation, and may well be replacing alteration minerals that were cogenetic with sulphide mineralization such as Fe-chlorite and sericite. Muscovite and sericite from ore horizons may also have formed during this late stage seawater circulation, and the increase in abundance and K/Na of the mica towards the hanging-wall may reflect the modification of seawater to more K-rich, Mg-poor compositions through interactions in the footwall. Chlorite geothermometry has a number of limitations, but the geothermometers considered to be the most reliable (Kranidiotis and Maclean, 1987 and Walshe, 1986) suggest formational temperatures of 100 to 150°C for clinochlore in footwall and layered sulphides and at least 190°C for chamosite in massive sulphides. Metamorphism of the deposit was low grade bordering zeolite/prehnite-pumpellyite facies as indicated by the occurrence of scolecite and pumpellyite in ore horizons, with chlorite geothermometry indicating temperatures in the range of 150 to 300°C.

6 PALAEOFLUID, STABLE AND RADIOGENIC ISOTOPE ANALYSES

6.1 INTRODUCTION

Fluid inclusion microthermometry and stable and radiogenic isotope analyses (S, O and Sr) of whole rock and mineral separates were undertaken to allow better understanding of ore formation at Balta Tau. In particular to:

- Establish the properties of ore forming fluids, temperature, salinity, oxygen isotopic composition, and to constrain fluid sources.
- Identify sources of sulphur and infer sources of metals.
- Investigate precipitation mechanisms.
- Investigate possible mechanisms for the formation of the barite lens and factors responsible for the unusual mineralogy and gold enrichment of this ore facies.

6.2 FLUID INCLUSION STUDY

6.2.1 Introduction and methodology

The petrography of fluid inclusions in quartz, sphalerite and barite were studied and described using standard polished thin sections, and from these representative samples of each ore facies containing suitable inclusions for microthermometry (two phase liquid-vapour inclusions at least 4μm in size) were selected. Analyses were performed on doubly polished wafers 80 to 150μm thick using a Linkam THMS600 heating-freezing stage which is routinely calibrated at -56.6, 0.0, 10.0, 30.8 and 294°C using H_2O-CO_2 synthetic fluid inclusion standards. These standards indicate accuracies of ±0.2°C for the temperatures range -100 to +30°C, and ±0.5°C for temperatures greater than 30°C. Since inclusions in barite and sphalerite can be problematic during heating due to stretching or leakage (Shepherd et al., 1985), images were taken at room temperature before and after heating and homogenisation temperatures only reported from inclusions where the degree of fill was not visibly altered by heating.

6.2.2 Petrography

Fluid inclusions in quartz, barite and sphalerite were classified following Shepherd et al. (1985), as summarised in Table 6.1. In general, primary (P) and pseudosecondary (PS) inclusions vary from 1 to 40μm in size and are predominately two phase liquid + vapour (L+V), with the degree of fill

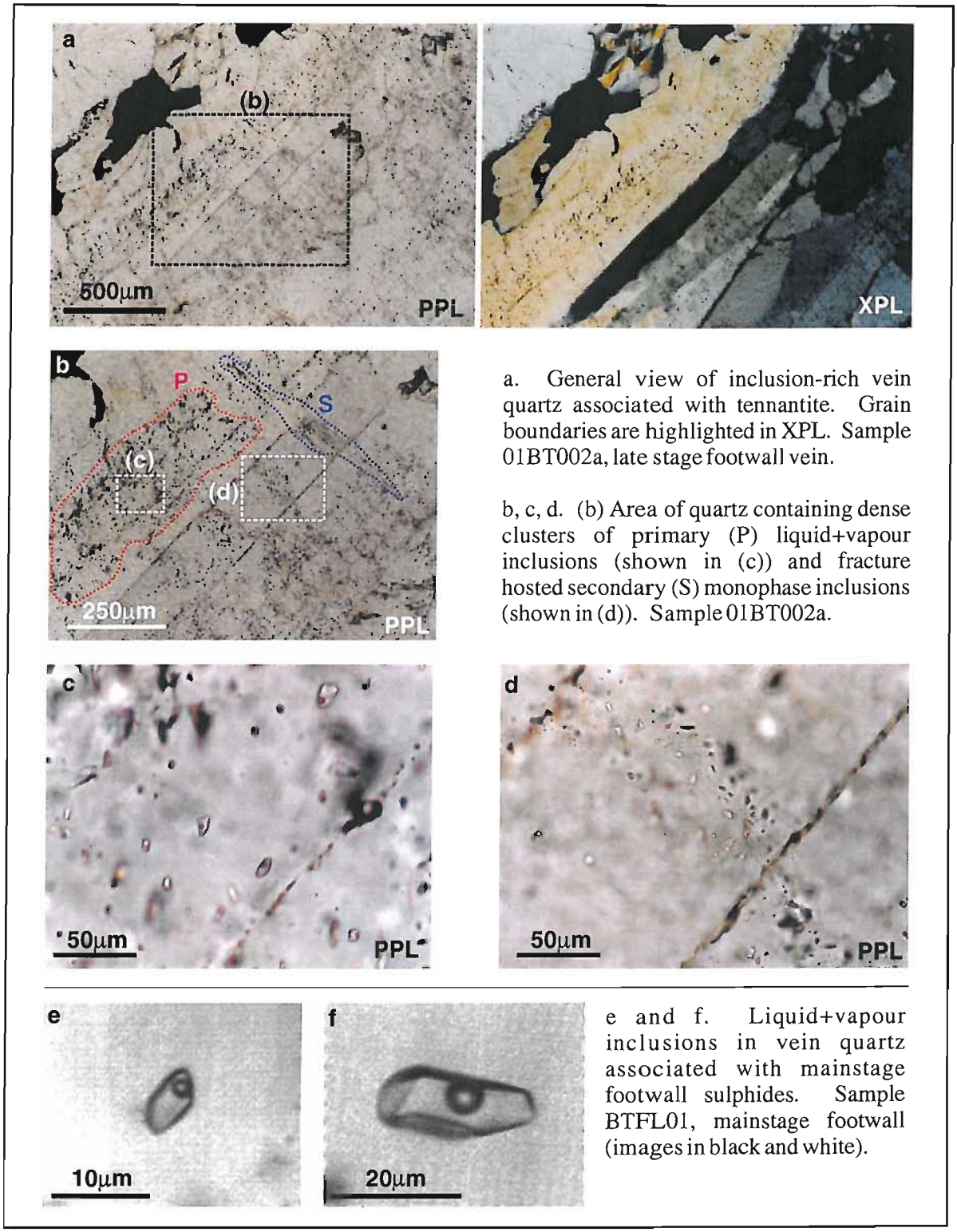

a. General view of inclusion-rich vein quartz associated with tennantite. Grain boundaries are highlighted in XPL. Sample 01BT002a, late stage footwall vein.

b, c, d. (b) Area of quartz containing dense clusters of primary (P) liquid+vapour inclusions (shown in (c)) and fracture hosted secondary (S) monophase inclusions (shown in (d)). Sample 01BT002a.

e and f. Liquid+vapour inclusions in vein quartz associated with mainstage footwall sulphides. Sample BTFL01, mainstage footwall (images in black and white).

Figure 6.1. Fluid inclusions in quartz from Balta Tau.

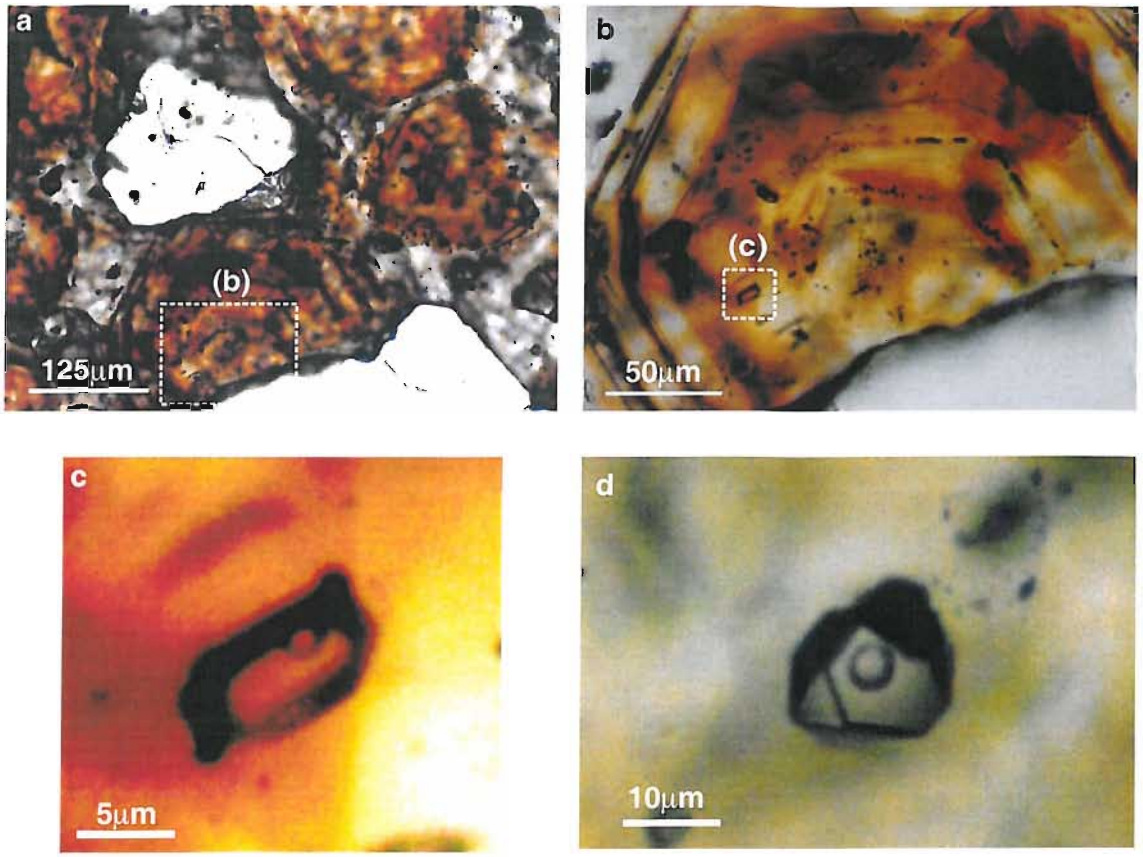

a, b, c. Zoned sphalerite (a) with primary L+V inclusions up to 15μm in crystal cores (b) with a degree of fill in the range 0.9 to 0.95 (c). Sample 01BT226, barite lens.

d. Primary L+V inclusion in sphalerite from the main-stage footwall. Sample 01BT067.

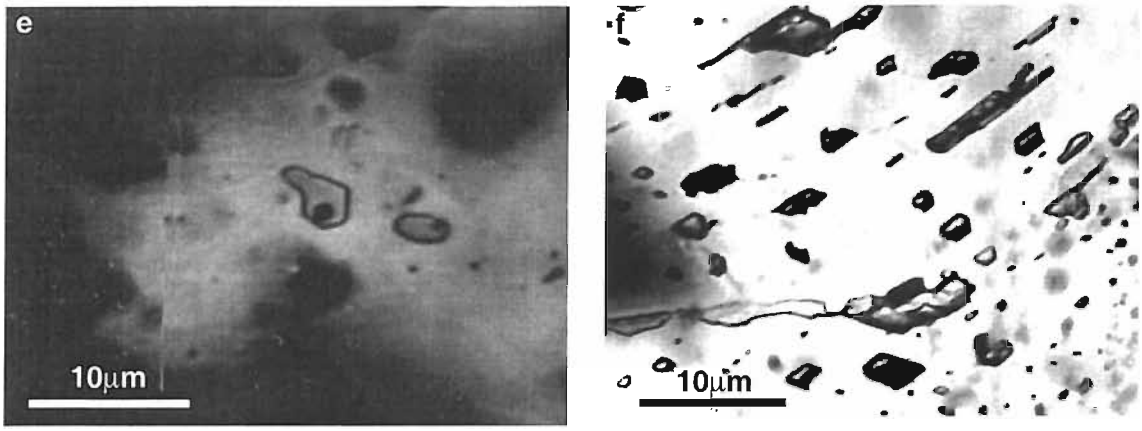

e. Rare primary L+V inclusions in transparent areas of sphalerite finely intergrown with pyrite and chalcopyrite from massive sulphides. Sample 902 (black & white image).

f. Fracture hosted secondary L+V and monophase inclusions in sphalerite, some of which contain an opaque solid phase. Sample 01BT003, footwall sulphides (black & white image).

Figure 6.2. Fluid inclusions in sphalerite from Balta Tau.

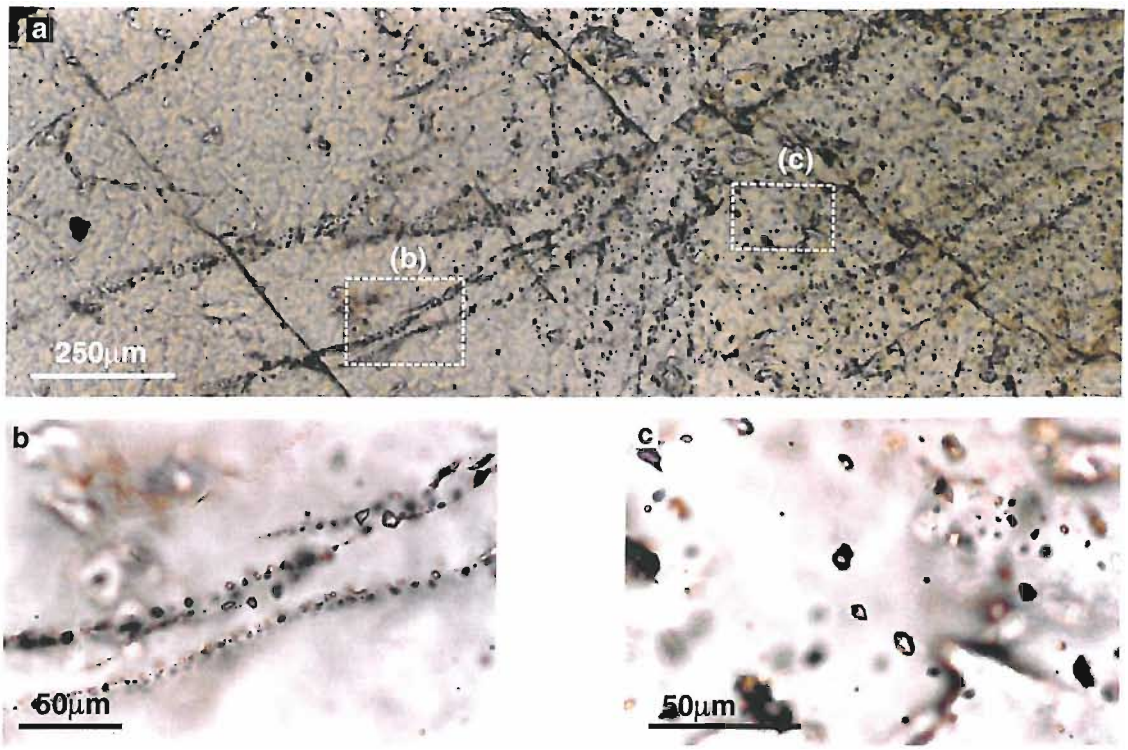

a, b and c. Coarse barite crystal containing abundant primary and secondary inclusions (a) with detailed view of monophase secondary inclusions following sub-parallel fractures (b) and a cluster of primary two phase liquid-vapour inclusions (c). Sample 905, barite lens.

d. Large regular shaped primary inclusion with a fill of 0.9. Sample 906, barite lens (black and white image).

e. Cluster of irregular primary inclusions with a fill of >0.95. Sample 00BT08, barite lens (black and white image).

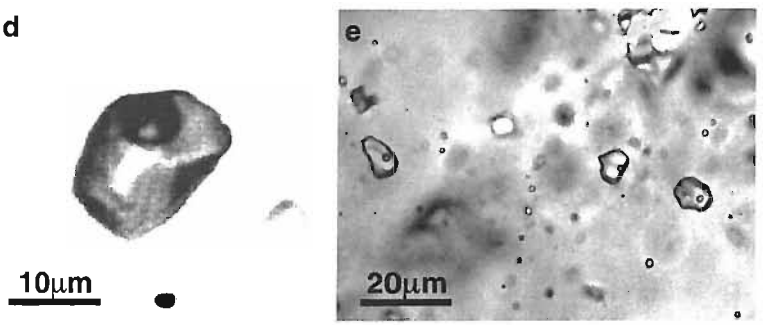

Figure 6.3. Fluid inclusions in barite from Balta Tau.

averaging 0.95, and occur as isolated inclusions, clusters, and trails that do not extend to grain boundaries (Figures 6.1, 6.2, and 6.3). Barite crystals from the barite lens and barite-rich sulphides contain primary populations that vary considerably from predominately L+V inclusions to entirely monophase inclusions. Quartz from massive sulphides, layered sulphides, barite-rich sulphides and the barite lens is fine grained and transparent and primary inclusions were not identified; by contrast, coarsely crystalline quartz in the footwall veins and disseminations contains abundant primary inclusions.

Secondary inclusions (S) in quartz and barite are generally small (<5μm), monophase and irregular to rounded (Figure 6.1d, 6.3b), and in sphalerite are two phase (L+V) as well as monophase,

display a variety of regular morphologies and generally occur in large numbers on fracture planes (Figure 6.2f).

Solid phases were noted in numerous primary inclusions in barite from the barite lens, and include opaque phases (most likely to be one or more of chalcopyrite, galena and tennantite; Figure 6.4a), semi-transparent phases with a deep red colour (possibly tennantite, Figure 6.4b) and pale brown, transparent, globular phases (probably sphalerite, Figure 6.4d, e). Inclusions containing these solid phases are associated with zones of micro-inclusions of sulphide phases (see Chapter 4, Section 4.6.2 and Figure 4.36). Some inclusions in barite also contain euhedral, tabular pale greenish transparent solids which may be small crystals of barite (Figure 6.4c, e, f). In sphalerite, both primary and secondary inclusions sometimes enclose opaque solids in areas of chalcopyrite disease.

a. Liquid+vapour inclusion containing a large opaque solid phase. Sample 00BT08.

b. Liquid+vapour inclusion containing a semi-transparent, dark red solid phase, possibly tennantite. Sample 01BT226.

c. Liquid inclusion containing a pale green, transparent solid phase, possibly barite. Sample 00BT08.

d. Liquid+vapour inclusion containing at least three semi-transparent, brown solids which are probably sphalerite. Sample 01BT226.

e. Liquid inclusion containing two solid phases: brown semi-transparent, ?sphalerite (S1) and euhedral transparent ?barite (S2). Sample 906 (black & white image).

f. Liquid+vapour inclusion with a transparent, tabular solid, possibly barite. Sample 906 (black & white image).

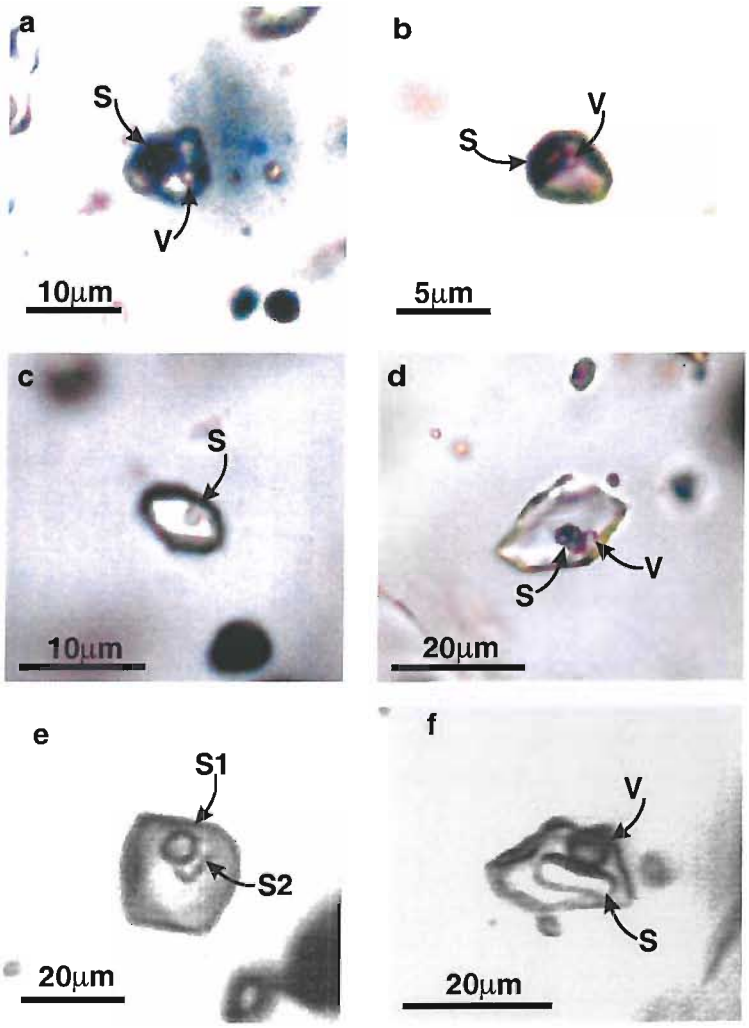

Figure 6.4. Solid phases in primary fluid inclusions in barite from the barite lens at Balta Tau.

Ore facies	Mineral	type	size	description
footwall main-stage	quartz	P	most 1-10μm	isolated, clusters and trails, most regular negative crystal, some irregular morphologies, two phase L+V with fill 0.9-0.95 (Figure 6.1e, f)
		S	<5μm	monophase, irregular morphology (similar to Figure 6.1d)
	sphalerite	P	5-10μm, rarely 10-20μm	isolated inclusions and clusters, regular often negative crystal morphology, L+V with fill 0.9-0.95; rarely enclose opaque solids (Figure 6.2d)
		S	most 1-10μm	regular morphologies including negative crystal, rod-like and tabular, numerous on single fracture planes. Most L+V with fill 0.95-0.98, some monophase (Figure 6.2f)
	barite	P	-	none identified
		S	<10μm	monophase, rounded to irregular (similar to Figure 6.3b)
footwall latestage	quartz	P	5-10μm, rarely 10-20μm	equant, some negative crystal, others irregular, majority are L+V, fill 0.95 (Figure 6.1c), some monophase
		S	most 1-10μm	irregular morphology, mostly monophase (Figure 6.1d), some L+V with variable fill
massive sulphides	sphalerite	P	2-5μm	scarce; isolated, regular morphology, L+V fill 0.95 (Figure 6.2e)
		S	-	none identified
	barite	P	5-10μm	clustered, regular morphology, many negative crystal, mainly L+V fill 0.95 (similar to Figure 6.3d), some monophase
		S	1-10μm	monophase, rounded to irregular (similar to Figure 6.3b)
layered sulphides	sphalerite	P	1-10μm	clustered, negative crystal and elongated morphologies, L+V with fill 0.95; some enclose opaque solid phase
		S	1-10μm	mostly monophase, some L+V, fill 0.9 to 0.95; regular morphologies including negative crystal and rod-like, numerous on single fracture planes (similar to Figure 6.2f), some enclose opaque solid
barite-rich sulphides & barite lens	sphalerite	P	5-20μm, rarely up to40μm	isolated and sometimes clustered, regular negative crystal morphology, L+V with fill 0.9-0.95 (similar to Figure 6.2c, d)
		S	1-10μm	numerous on fractures, regular morphology, include L+V with fill 0.95 or more and monophase (similar to Figure 6.2f)
	barite	P	5-10μm, rarely up to 20μm	densely clustered and isolated, regular often negative crystal morphologies, some irregular; populations variable within and between crystals from L+V dominated with fill 0.90 or more (Figure 6.3c, e, f) to monophase dominated. Contain a variety of solid phases (Figure 6.4a-f) including opaque (sulphides), deep red (?tennantite), pale to dark brown semi-transparent (sphalerite) and pale green transparent, equant to tabular, (barite?)
		S	1-10μm	mostly monophase, irregular (Figure 6.3b), rare L+V with variable 0.2-0.95 fill.

Table 6.1. Petrographical characteristics of fluid inclusions from ore horizons at Balta Tau. Abbreviations: P – primary (including pseudosecondary); S – secondary; L – liquid; V – vapour.

6.2.3 Microthermometric data

Microthermometric analyses were performed on two phase liquid+vapour inclusions and in some cases three phase liquid-vapour-solid inclusions, with temperatures recorded where possible for three phase changes, first ice melt, last ice melt and liquid-vapour homogenisation (see Appendix C1 for a full data listing).

Homogenisation temperatures

Homogenisation temperatures were recorded from 233 inclusions, all of which homogenised into the liquid phase. Reproducibility is generally better than ±2°C, except for dark inclusions in sphalerite where difficulty in observing the vapour bubble reduced this to ±5°C. Relatively few reliable measurements were made from barite due to many inclusions stretching or decrepitating during heating cycles.

The homogenisation temperatures form a unimodal population with a mode of 130°C, a range of 100 to 240°C and a slight positive skew (Figure 6.5a). Subdividing data according to the host mineral (Figure 6.6a) and according to ore facies (Figure 6.7a) indicates that the lower temperatures (100 to 140°C) are predominantly from primary and secondary inclusions in quartz and secondary inclusions in sphalerite. Higher temperatures (140 to 180°C) occur mainly in primary inclusions in sphalerite and barite and some primary inclusions in quartz (Figure 6.5a). The majority of lower temperature inclusions occur in the mainstage and late stage footwall, while the higher temperature inclusions are found in all mainstage ore horizons (Figure 6.6a). High temperature inclusions above 180°C are scarce and restricted to primary inclusions in quartz from the mainstage footwall and barite from massive sulphides.

Salinity

Fluid salinities have been derived using final ice melting temperature (θ, °C) using the following equation for the NaCl-H_2O system (Bodnar, 1993):

$$\text{Salinity (wt\% NaCl)} = 1.78\theta - 0.0442\theta^2 + 0.000557\theta^3$$

Numerous inclusions predominately hosted in quartz were unstable during freezing-heating which precluded measurements of the last melt temperature. In these inclusions the vapour bubble collapsed upon freezing but did not return during subsequent heating until temperatures above 0°C. The presence of a vapour phase is a pre-requisite for obtaining salinity from the final ice melt temperature, and without the vapour bubble the last ice crystal commonly persisted to a few degrees above 0°C and melted instantaneously when the vapour bubble returned. Although salinities could not be obtained from these inclusions, this phenomenon is indicative of very low salinities (Wilkinson, pers. comm.) and the sharp reduction in the frequency of salinity data below

1.5wt% NaCl equivalent suggests that the metastable inclusions probably have salinities below this level. A total of 95 inclusions with this metastable behaviour were recorded, and are referred to as the "NV" ("No Vapour") inclusions in the following discussions.

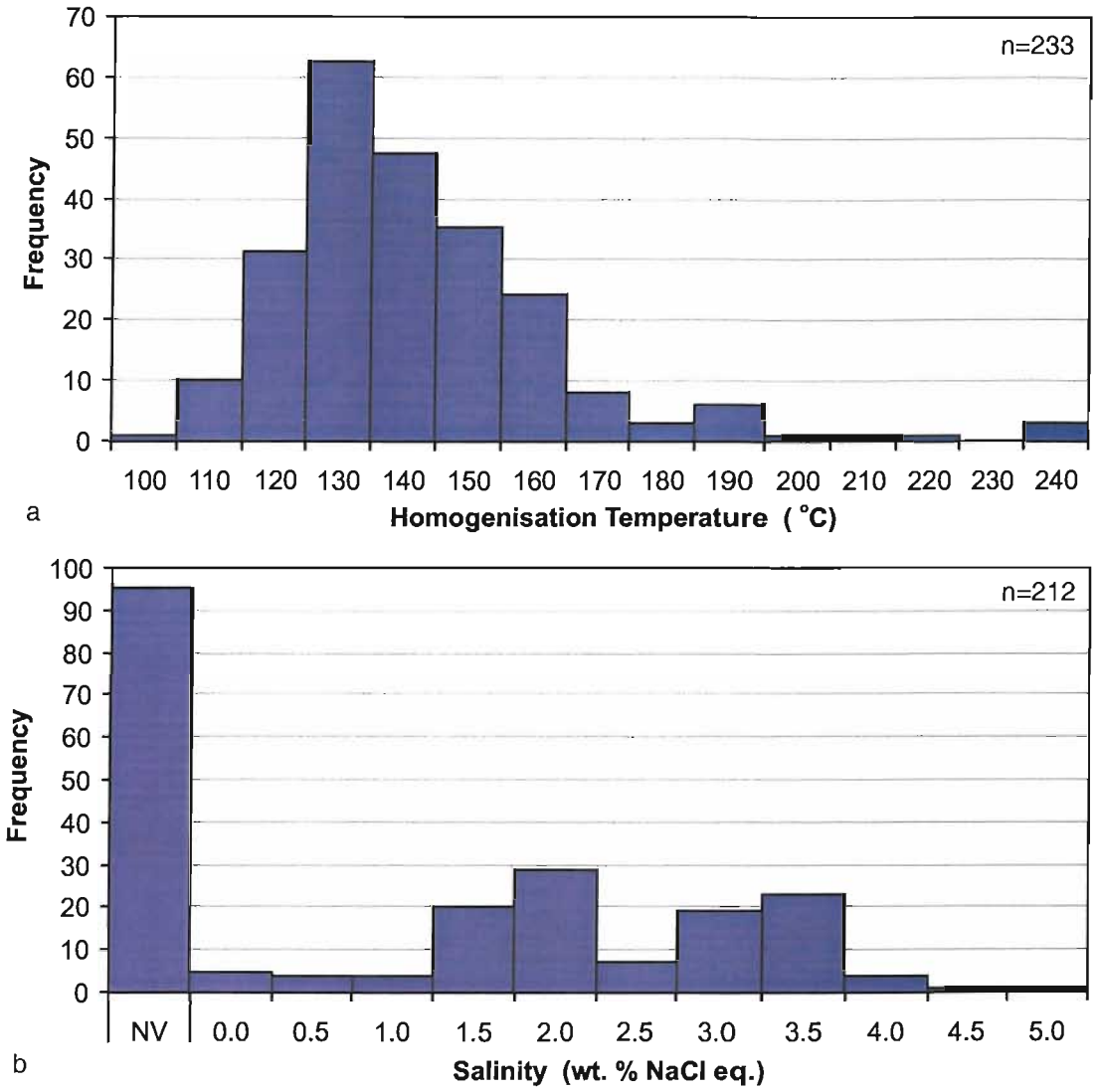

a. Homogenisation temperatures form a unimodal population with a mode of 130°C, a range of 100 to 240°C and a weak positive skew.

b. Salinity data range from 0 to 5 wt% NaCl and display a bimodal distribution with modes at 2.0 and 3.5 wt% NaCl eq. A large proportion of inclusions fall in the "NV" category (see text for explanation).

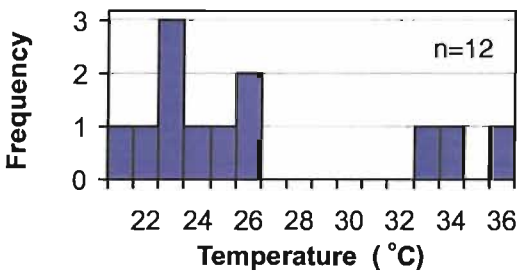

c. Temperatures of first melt were only recorded from inclusions in barite from massive sulphides and the barite lens. The data form two clusters ranging from 20 to 26°C and 33 to 36°C, and do not show a systematic variation with ore facies.

Figure 6.5. Fluid inclusion microthermometric data from Balta Tau mineralization.

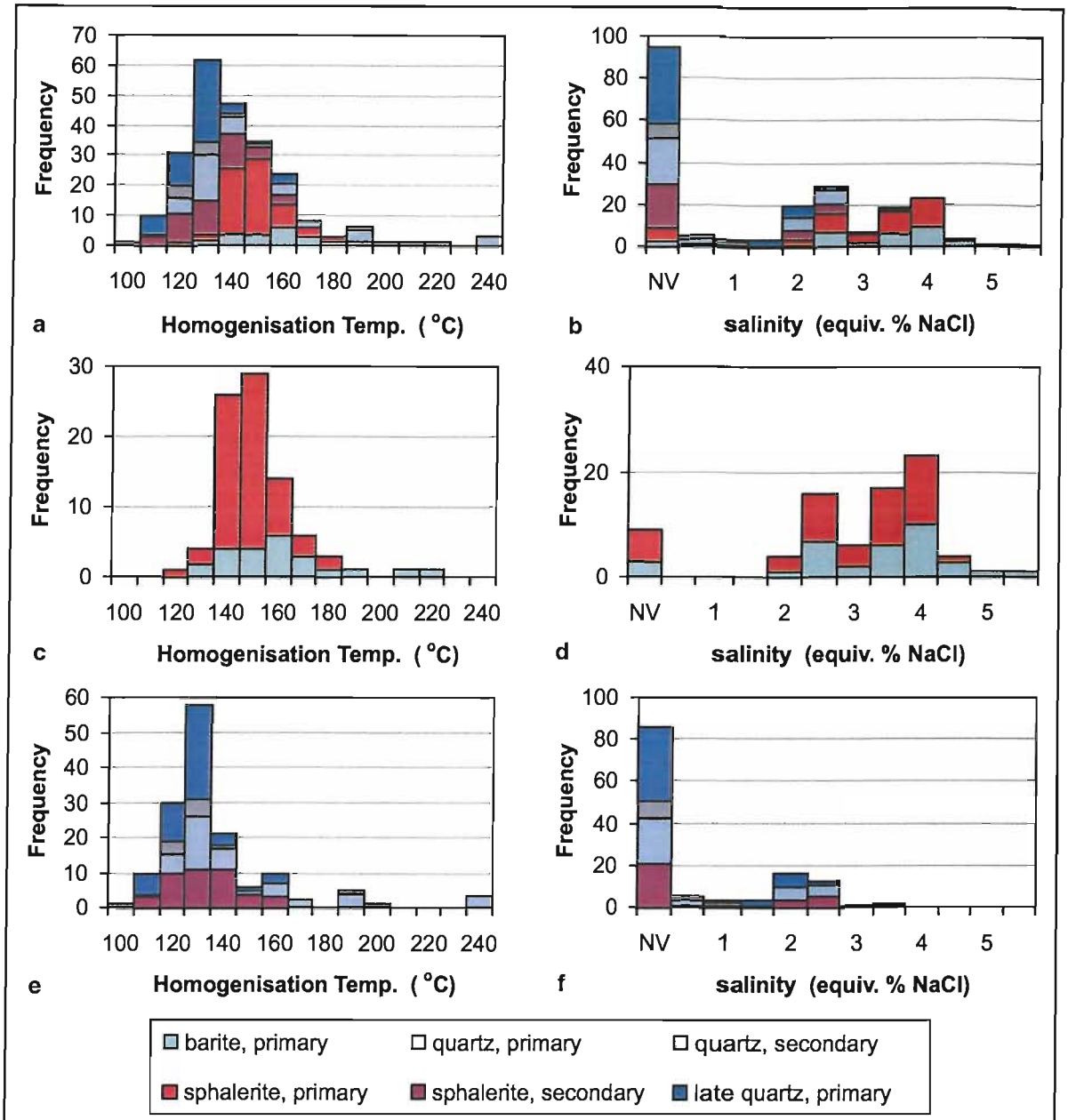

Homogenisation temperatures (Figure a) and salinities (Figure b) subdivided according to the host mineral and inclusion type. Primary inclusions in sphalerite and barite tend to be higher temperature (Figure c) with salinities greater than 2wt% NaCl eq. and very few in the "NV" category (Figure d). Quartz inclusions (primary and secondary) and secondary inclusions in sphalerite tend to be lower temperature (Figure e) and mostly low salinity, less than 3 wt% NaCl eq., with a high proportion in the "NV" category (Figure f).

Figure 6.6. Microthermometric data from Balta Tau subdivided according to host mineral.

Excluding the "NV" category, a total of 117 salinity measurements were obtained with reproducibility within ±0.1°C, corresponding to ±0.18wt% NaCl equivalent. The salinity data range from 0.0 to 5.1 equivalent wt% NaCl and define a bimodal population with modes at 2.0 and 3.5 equivalent wt% NaCl (Figure 6.5b). Subdividing data according to the host mineral phase (Figure 6.6b) and according to ore facies (Figure 6.7b) indicates that the higher salinity population is almost entirely from primary inclusions in barite and sphalerite from the mainstage ore horizons,

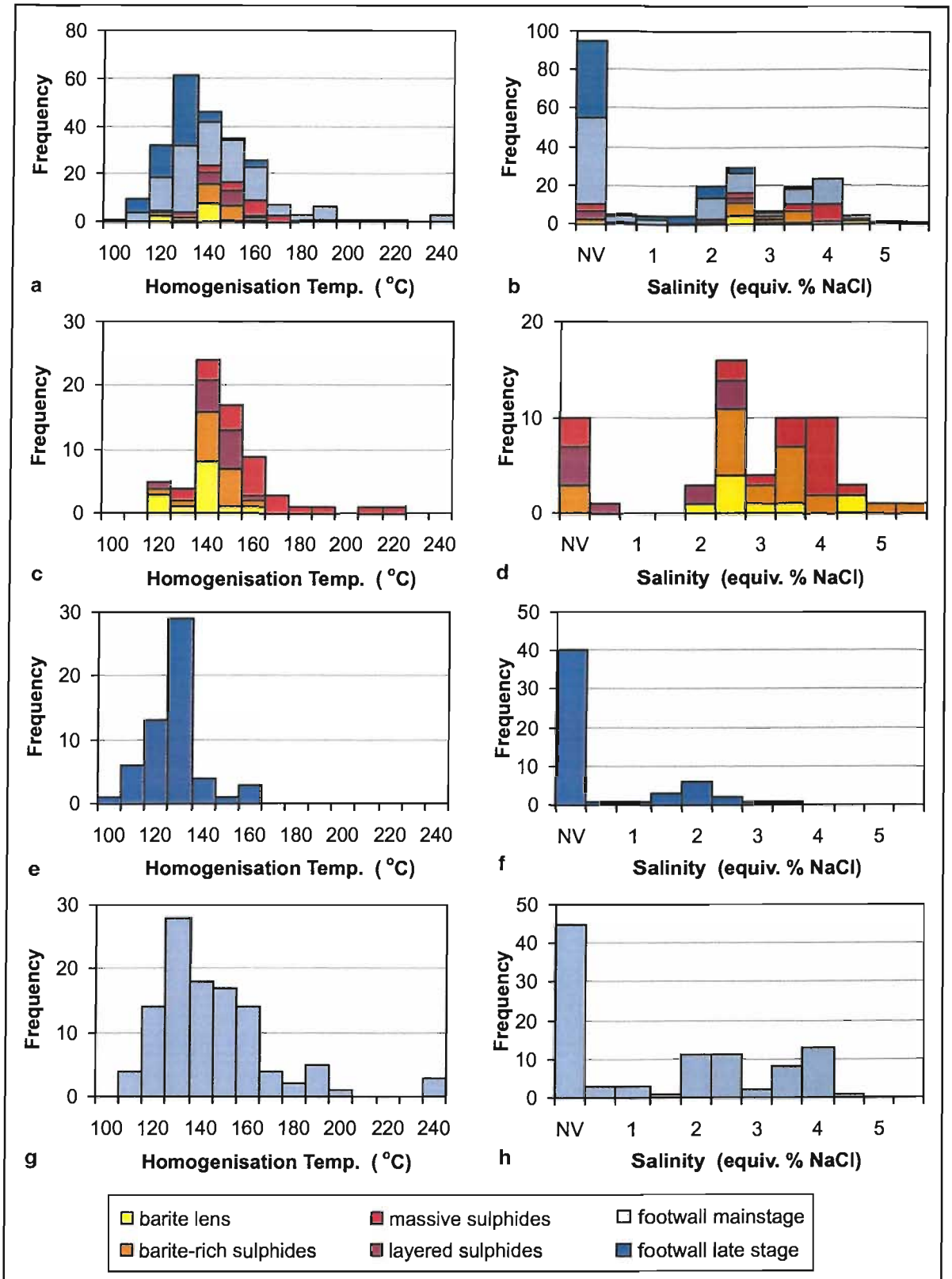

Homogenisation temperatures (Figure a) and salinities (Figure b) subdivided according to host ore facies. The conformable ore horizons contain mainly higher temperature inclusions >140°C (Figure c) with variable salinities and a relatively small proportion in the "NV" category (Figure d). The late stage footwall vains are dominated by low temperature inclusions < 140°C (Figure e) most of which fall into the "NV" catergory (Figure f). The mainstage footwall contains inclusions that span most of the temperature and salinity ranges (Figures g and h) and include numerous in the "NV" category (Figure h).

Figure 6.7. Microthermometric data from Balta Tau subdivided according to ore facies.

while lower salinities are from quartz as well as sphalerite and barite and are from late stage footwall veins as well as mainstage ore horizons. The "NV" category may well define a third population and comprises primary and secondary quartz inclusions from the late stage and mainstage footwall, as well as secondary sphalerite inclusions mainly from the footwall.

Temperature of first melt

The temperature of first melt is representative of the eutectic temperature between solid and liquid phases, which varies according to the composition of the fluid. The temperature of first melt was difficult to identify in the majority of inclusions due to their low salinity. Several measurements were however recorded from the more saline inclusions in barite from the massive sulphides and from the barite lens, summarised in Figure 6.5c, with a reproducibility of ±1°C. The majority of data cluster in the range –21.0 to –26.0°C, with three data points in the range –33.0 to –36.2°C (Figures 6.5c and 6.6c). The first range are suggestive of a simple NaCl-H_2O and NaCl-KCl-H_2O fluids, whereas the second reflects varying proportions of NaCl, $FeCl_2$ and $MgCl_2$ (based on Shepherd et al., 1995; Table 6.2).

salt system	eutectic temperature (°C)	solid phases present
H_2O-NaCl-$CaCl_2$	-55.0	Ice + NaCl.$2H_2O$ + $CaCl_2$.$6H_2O$
H_2O-$MgCl_2$-$CaCl_2$	-52.2	Ice + $MgCl_2$.$12H_2O$ + $CaCl_2$.$6H_2O$
H_2O-KCl-$CaCl_2$	-50.5	Ice + $CaCl_2$.$6H_2O$
H_2O-$CaCl_2$	-49.5	Ice + $CaCl_2$.$6H_2O$
H_2O-Na_2CO_3-K_2CO_3	-37.0	Ice + $(K,Na)_2CO_3$.$6H_2O$ + K_2CO_3.$6H_2O$
H_2O-NaCl-$FeCl_2$	-37.0	Ice + NaCl.$2H_2O$ + $FeCl_2$.$6H_2O$
H_2O-$FeCl_2$	-35.0	Ice + $FeCl_2$.$6H_2O$
H_2O-NaCl-$MgCl_2$	-35.0	Ice + NaCl.$2H_2O$ + $MgCl_2$.$12H_2O$
H_2O-$MgCl_2$	-33.6	Ice + $MgCl_2$.$12H_2O$
H_2O-NaCl-KCl	-23.5	Ice + NaCl.$2H_2O$
H_2O-NaCl	-21.2	Ice + NaCl.$2H_2O$

Table 6.2. Eutectic temperatures (corresponding to the temperature of first melt) for selected salt-water systems. (Shepherd et al., 1985).

Solid phases

None of the solid phases in barite inclusions (Figure 6.4) altered visibly during heating, indicating that they are trapped phases rather than daughter minerals. The transparent green phases are unlikely to be halite crystals given the uniformly low fluid salinities, but may be trapped barite crystals as suggested by their tabular morphology.

6.3 STABLE ISOTOPE STUDY

6.3.1 Introduction and methodology

Analyses of sulphur and oxygen isotopes were carried out at the SUERC (Scottish Universities Environmental Research Centre) laboratories in East Kilbride, Scotland. Sulphide Sulphur analyses were performed on hand picked mineral separates following the method of Robinson and Kusakabe (1975) for sulphides and that of Coleman and Moore (1978) for sulphates. For the sulphate oxygen analyses, hand picked separates were re-precipitated to reduce contamination from other oxygen bearing phases. Silicate analyses were carried out on hand picked monomineralic quartz, chlorite, muscovite and epidote separates, and on whole rock powders of quartz-chlorite rich alteration assemblages, following the laser fluorination method of Fouillac and Girard (1996). Full methodologies and data listings are given in Appendices C3 and C4. The standard delta notation is used to express S and O isotope data, with S quoted as per mil (‰) variations relative to the standard Canyon Diablo Troilite (CDT), and oxygen in per mil variations relative to Vienna Standard Mean Ocean Water (VSMOW).

Analyses of international and internal standards and sample duplicates are summarised in Table 6.3. Data for sulphide $\delta^{34}S$, sulphate $\delta^{18}O$ and silicate $\delta^{18}O$ standards are consistent with accepted values and generally indicate a reproducibility of ±0.2‰ or better. The high variability in data obtained for IAEA-S-3 probably reflects a degree of heterogeneity in the sample, as indicated by the broad range in results from inter-lab comparisons for this standard. $\delta^{34}S$ analyses of the sulphate standard NBS-127 are consistent with the accepted value (Taylor et al., 2001), however the reproducibility of ±0.9‰ is greater than the variability of inter-lab comparisons.

The sample reproducibility is generally better than ±0.5‰ for sulphate $\delta^{34}S$, sulphate $\delta^{18}O$ and silicate $\delta^{18}O$, and within ±0.8‰ for sulphide $\delta^{34}S$. These variations are higher than those for standards reflecting sample heterogeneity.

Also included in this chapter are unpublished oxygen isotope data obtained by Lerouge (2003) for powdered whole rock samples of regional volcanics and Balta Tau mine sequences collected in this study. Analyses were carried out at BRGM laboratories using the laser fluorination method of Fouillac & Girard (1996), with analytical error estimated at ±0.3‰ (Lerouge, pers. comm.). Results from one duplicate sample analysed at both SUERC and BRGM (sample 00BT01, footwall whole rock powder) agree within 0.3‰.

Method	Standards				Sample repeats	
	standard	n	mean (‰)	range (‰)	no. repeats	range (‰)
δ^{34}S sulphide	IAEA-S-2	4	+ 21.8	± 0.2	8	± 0.1 to ± 0.8
	IAEA-S-3	11	- 31.3	± 1.6		
	NBS123	4	+ 17.1	± 0.3		
	CP1*	11	- 4.5	± 0.2		
δ^{34}S sulphate	NBS127	9	+ 21.4	± 0.9	6	± 0.0 to ± 0.5
δ^{18}O sulphate	NBS127	4	+ 9.2	± 0.1	4	± 0.0 to ± 0.4
δ^{18}O silicate	SES	8	+ 10.2	± 0.2	2	± 0.2 to ± 0.3

Table 6.3. Accuracy and precision for stable isotope analytical procedures based on standards and sample repeats. Notes: * SUERC internal standard; all others are international standards.

6.3.2 Sulphide sulphur data

δ^{34}S obtained for 57 mineral separates of pyrite, chalcopyrite, sphalerite, tennantite and galena from Balta Tau mineralised horizons fall in the narrow range -3.3‰ to +2.4‰, with three modes at -1.0, 0.0 and 1.5‰ (Figures 6.8, 6.9a). Dividing data according to mineral phases (Figure 6.8) reveals that chalcopyrite, tennantite and galena have a wide range of δ^{34}S with no distinct mode, while pyrite and sphalerite have modes at 0.0‰ and +1.5‰ respectively.

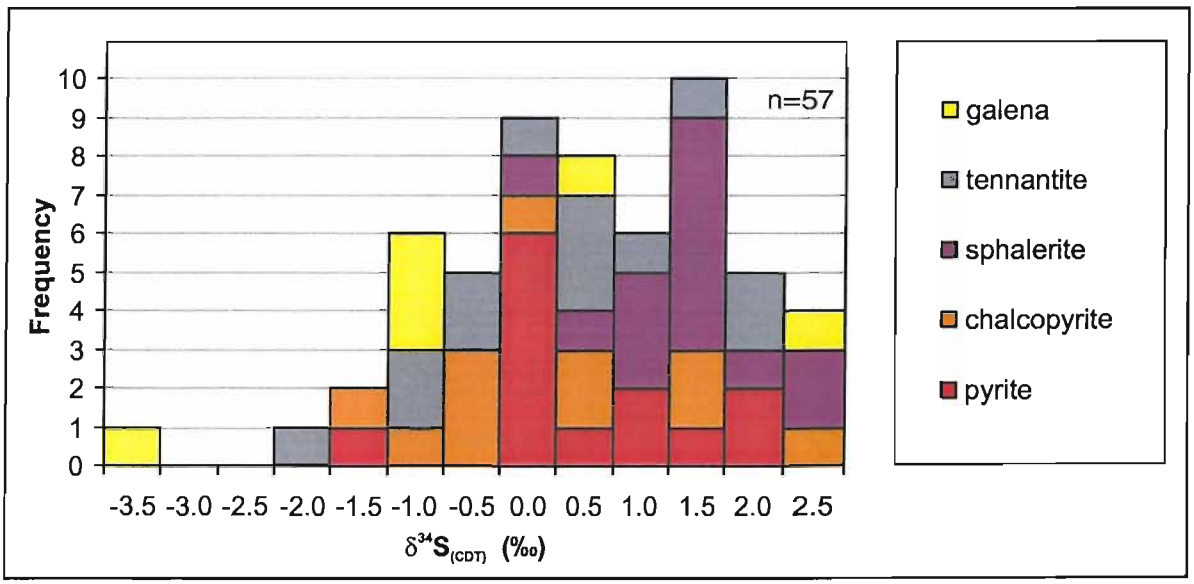

Figure 6.8. Sulphide δ^{34}S from Balta Tau divided according to mineral phases.

Dividing data by ore facies (Figure 6.9a) suggests that the footwall, massive and layered sulphides have similar ranges in sulphide δ^{34}S with the bulk of data falling in the range -1 to +2.5‰. Limited analyses of sulphides in the stratigraphically higher barite rich zones (barite-rich sulphides and barite lens) range from -3.5 to +1.5‰, suggesting a ^{34}S depletion in these sulphides relative to

the other ore horizons (Figure 6.9b). The most ^{34}S enriched analysis from the barite lens of +1.5‰ is from coarse sphalerite, which texturally appears paragenetically earlier than the other sulphide phases in this zone (Section 4.6.2, Chapter 4) and probably formed at the same time as the underlying massive sulphides. Excluding this sphalerite analysis reduces the range in data from the barite lens to -3.5 to -1.0‰, emphasising the ^{34}S depletion of sulphides that co-precipitated with barite in this ore facies.

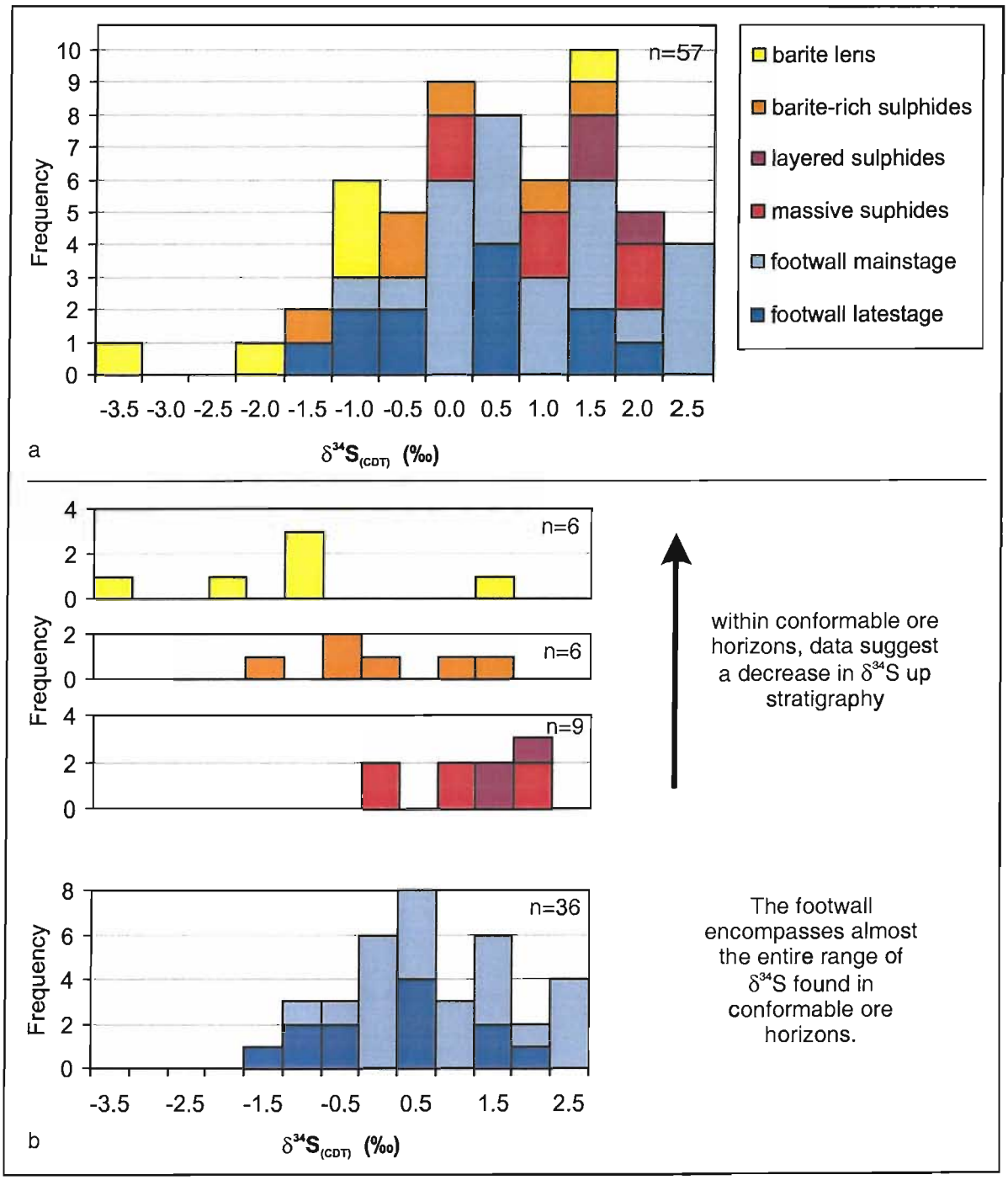

Figure 6.9. Sulphide $\delta^{34}S$ from Balta Tau divided according to host ore facies.

6.3.3 Sulphate sulphur and oxygen data

Analyses of $\delta^{34}S$ from 16 barite samples fall in the range +17.6 to +21.6‰, and define a single population with a mode of +18.5‰ (Figure 6.10a). Barite from the barite lens is generally ^{34}S depleted relative to this mode, while barite from massive sulphides is ^{34}S enriched. However, much of the variation between samples is within the reproducibility indicated by standards (±0.9‰).

$\delta^{18}O$ data obtained for 13 barite samples range from +8.3 to +13.7‰, with a mode of +11 to +11.5‰ (Figure 6.10b). Barite from footwall and massive sulphide ore facies is generally ^{34}S enriched relative to barite from the barite-rich sulphides and the barite lens.

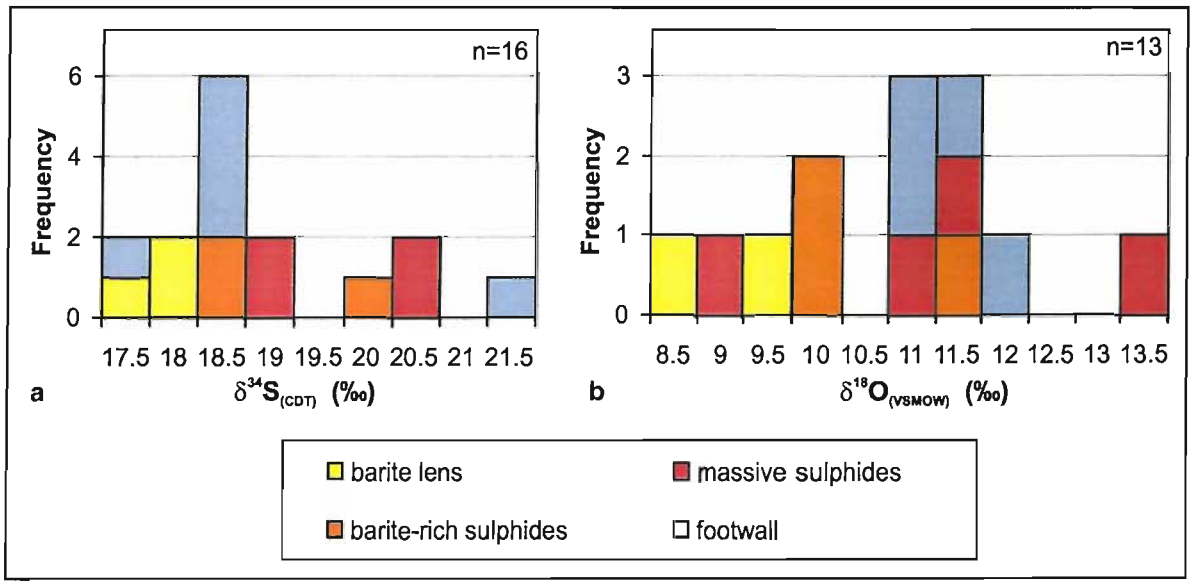

Figure 6.10. Barite $\delta^{34}S$ and $\delta^{18}O$ from Balta Tau subdivided according to host ore facies.

6.3.4 Silicate oxygen data

Balta Tau mineralization and mine sequences

$\delta^{18}O$ analyses of quartz, muscovite, chlorite and epidote vary from +8.4 to +14.2‰ and cluster according to mineralogy (Figure 6.11a). A total of 22 analyses of quartz cluster tightly in the range of +11.6 to +14.2‰ with a mode of +13‰ (Figure 6.11b). Quartz from layered sulphides, barite-rich sulphides and the barite lens is ^{18}O depleted relative to the footwall, and within the footwall the late stage quartz is ^{18}O depleted relative to most of the mainstage quartz.

Three muscovite samples from the footwall and layered sulphides fall in the range +9.9 to +10.5‰, and two footwall chlorite samples have values of +8.6 and +9.2‰. Two epidote samples from the hanging-wall veins have $\delta^{18}O$ values of +8.4 and +8.7‰, and co-exist with quartz of similar isotopic composition to that of the footwall (Figure 6.11a).

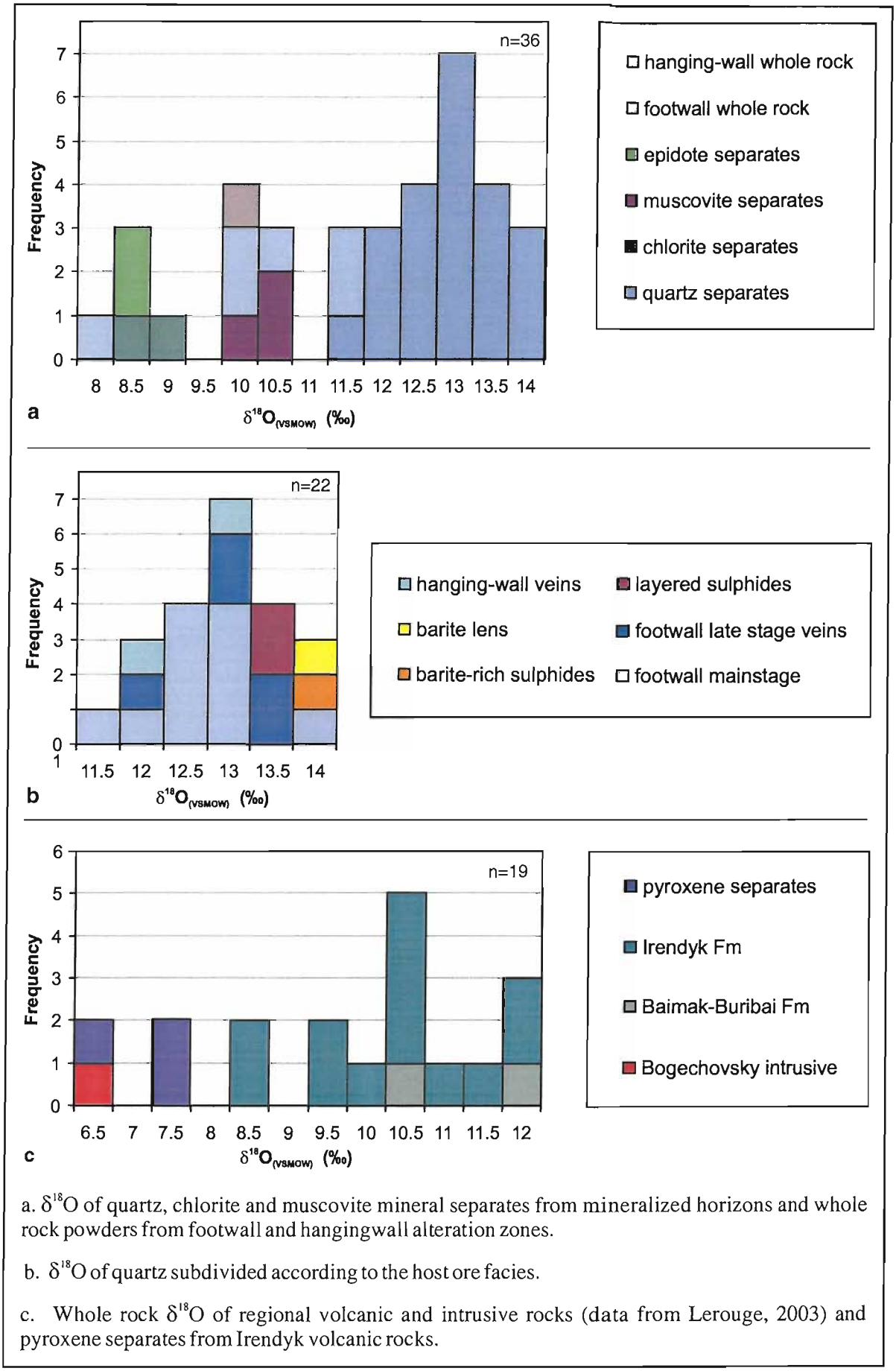

a. $\delta^{18}O$ of quartz, chlorite and muscovite mineral separates from mineralized horizons and whole rock powders from footwall and hangingwall alteration zones.

b. $\delta^{18}O$ of quartz subdivided according to the host ore facies.

c. Whole rock $\delta^{18}O$ of regional volcanic and intrusive rocks (data from Lerouge, 2003) and pyroxene separates from Irendyk volcanic rocks.

Figure 6.11. $\delta^{18}O$ of monomineralic silicates and whole rock powders from Balta Tau.

The $\delta^{18}O$ of altered footwall and hanging-wall whole rock powders range from +8.2 to +11.7‰ (Figure 6.11a, Table 6.4), and are generally consistent with the $\delta^{18}O$ values of the constituent minerals in the proportions estimated from thin sections (Table 6.4). For example, two footwall samples comprising approximately 50% quartz, 50% chlorite have whole rock $\delta^{18}O$ of +9.8 to +10.7‰, intermediate between values for quartz and chlorite separates.

Unit	Approximate composition	Sample No.	$\delta^{18}O_{(VSMOW)}$ ‰
Footwall	50% quartz, 50% chlorite	00BT01	+ 10.7
		01BT085	+ 9.8
		01BT110	+ 10.1
Footwall	90% chlorite, 10% quartz	01BT095	+ 8.2
Footwall	40% quartz, 30% chlorite, 30% sericite	00BT17	+ 11.7
		00BT02	+ 11.3
Hanging-wall	70% sericite, 20% quartz, 5% titanite	01BT075A	+ 10.2

Table 6.4. Composition and $\delta^{18}O$ of altered footwall and hanging-wall sequences.

Whole rock samples

Whole rock samples of regional, hydrothermally altered Irendyk and Baimak-Buribai volcanics have $\delta^{18}O$ in the range +8.4 to +12.2‰ and the Bogochevsky plagiogranite yielded a single value of +6.6‰ (Figure 6.11c). Hand picked separates of unaltered pyroxene phenocrysts from the Irendyk yield three values in the range +6.7 to +7.7‰ (Figure 6.11c).

6.4 STRONTIUM ISOTOPE STUDY

6.4.1 Introduction and methodology

A strontium isotope study of barite and footwall alteration was undertaken to investigate the extent of fluid mixing between hydrothermal fluids and seawater during ore precipitation. $^{87}Sr/^{86}Sr$ analyses were carried out using TIMS (MicromassVG54) based at the Southampton Oceanography Centre, and corresponding Sr, Rb and Ba concentrations were measured by ICP-MS. Silicates were dissolved by HF digest and barite dissolutions were based on the method of Breit et al. (1985), and Sr isolated from solutions using column chemistry. A full methodology is given in Appendix C4. Precision is better than 0.0030 (2SE) for barites and 0.0035 for silicates, and sample repeats are generally within error (Appendix C4). An age correction has been applied to the silicate Sr data (Appendix C4), however this was not necessary for the barites as they did not contain Rb above detection.

6.4.2 Sr isotope data

Sr isotope data are presented in Table 6.5. The pyroxene samples from regional Irendyk volcanics are the least radiogenic with fairly consistent values in the range 0.7040 to 0.7041. Barite has a wide range of $^{87}Sr/^{86}Sr$, with data falling in the range 0.7050 to 0.7069. The least radiogenic signatures are in barite from the footwall and the most radiogenic in barite from the massive sulphides, while the barite-rich ores are in between the two. A chlorite-rich footwall sample yielded a value of 0.7075, significantly more radiogenic than the barite samples.

Description	Sample #	$^{87}Sr/^{86}Sr$	2SE
footwall barite	01BT145	0.70501	0.0014
	01BT106	0.70558	0.0027
	01BT103	0.70637	0.0013
barite in massive sulphides	01BT077a	0.70655	0.0011
	01BT077b	0.70644	0.0017
	903	0.70657	0.0014
	01BT169	0.70690	0.0011
barite in barite-rich sulphides	01BT135	0.70613	0.0013
	01BT138	0.70619	0.0014
	01BT082	0.70627	0.0017
barite from the barite lens	00BT08	0.70624	0.0016
	01BT226#1	0.70621	0.0018
	01BT226#2	0.70618	0.0014
fw chlorite	01BT095	0.70753	0.0013
pyroxene from Irendyk volcanics	010723/12	0.704038	0.0035
	020816/11	0.704085	0.0016
	020816/10	0.704104	0.0011

Table 6.5. Sr isotope data for barite and chlorite from Balta Tau, and pyroxenes from regional volcanics. fw = footwall.

6.5 DISCUSSION

6.5.1 Host volcanics

The isotopic signatures of unaltered host volcanic rocks are useful not only for characterising the volcanic sequences but also for investigation of fluid and metal sources in the Balta Tau hydrothermal system (e.g. Sections 6.5.3, 6.5.4, 6.5.5). All of the regional volcanic samples are affected by alteration, however a few samples from the Irendyk Formation contain unaltered pyroxene phenocrysts. Therefore to avoid the complication of isotopic changes that occur during alteration, $\delta^{18}O$ and $^{87}Sr/^{86}Sr$ analyses were performed on hand picked mineral separates of unaltered pyroxene phenocrysts rather than whole rock powders. The pyroxene $^{87}Sr/^{86}Sr$ vary from 0.7040 to 0.7041 (Table 6.5, Figure 6.22a) which is more radiogenic than MORB and typical of volcanic arc signatures with some Sr derived from the subducting slab (e.g. Woodhead et al., 1987; Gamble et al., 1995). For the purposes of calculations later in this chapter, the regional volcanic signature is taken as the mean of these pyroxene values, 0.7041. The $\delta^{18}O$ range from +6.5 to +7.5‰ with a mean of +7.3‰, which are within the normal range for arc volcanics and

reflect a predominately mantle source (with a signature of +5.8‰) modified by a slab-derived component (Faure, 1986).

None of the volcanic samples collected contain primary sulphides, hence a direct measurement of the volcanic $\delta^{34}S$ was not possible. However, interpretation of the sulphide $\delta^{34}S$ from Balta Tau suggests the regional volcanics may have had a signature of around 0.1‰, close to that of MORB (Section 6.5.6).

6.5.2 Properties of ore forming fluids

Pressure correction for fluid temperatures

In order to estimate the trapping temperatures for fluid inclusions and hence the temperature of ore formation, homogenisation temperatures must be corrected for pressure at the time of trapping. Since Balta Tau is interpreted to have formed at the seafloor, the pressure would have been dependant on water depth. Regional volcanic facies are suggestive of a shallow water environment (Chapter 3, Section 3.2.7), which is also proposed by Herrington et al. (2002). This is supported by the properties of late stage hydrothermal fluids at Balta Tau (see Section 6.5.3) which are best accounted for by fluid evolution in a shallow water system. The water depth is therefore taken as less than 1000m (corresponding to a pressure of 100bars) for the following discussions. Figure 6.12 shows the liquid-vapour curve for a 5wt% NaCl fluid with density isochores constructed at intervals between 110 and 250°C. The isochores for pure water and 5 wt% NaCl are very similar at low pressures (<500 bars; based on the equations of Zhang & Frantz, 1987), therefore the 5 wt% NaCl isochores have been used to calculate pressure corrections for all of the Balta Tau fluid inclusion data.

The correction required for the maximum pressure of 100 bars ranges from +4.5°C at 110°C to +6°C at 190°C. Therefore a pressure correction has not been applied to Balta Tau data, since even the maximum likely correction would have a negligible effect on fluid inclusion temperatures, and the trapping temperatures presented in the following discussions are equal to the measured homogenisation temperatures. The low temperatures of Balta Tau fluid inclusions (mostly <190°C) require a water depth of only 150m to prevent boiling of hydrothermal fluids at the sea-floor (Figure 6.12b). However, Sr isotope studies (Section 6.5.4) indicate that these temperatures are for a hydrothermal fluid that has mixed with up to 50% seawater. The end member hydrothermal fluid may have had temperatures of up to 250°C prior to mixing with cold seawater, which would have required a water depth of 350m to prevent fluid boiling (Figure 6.12b).

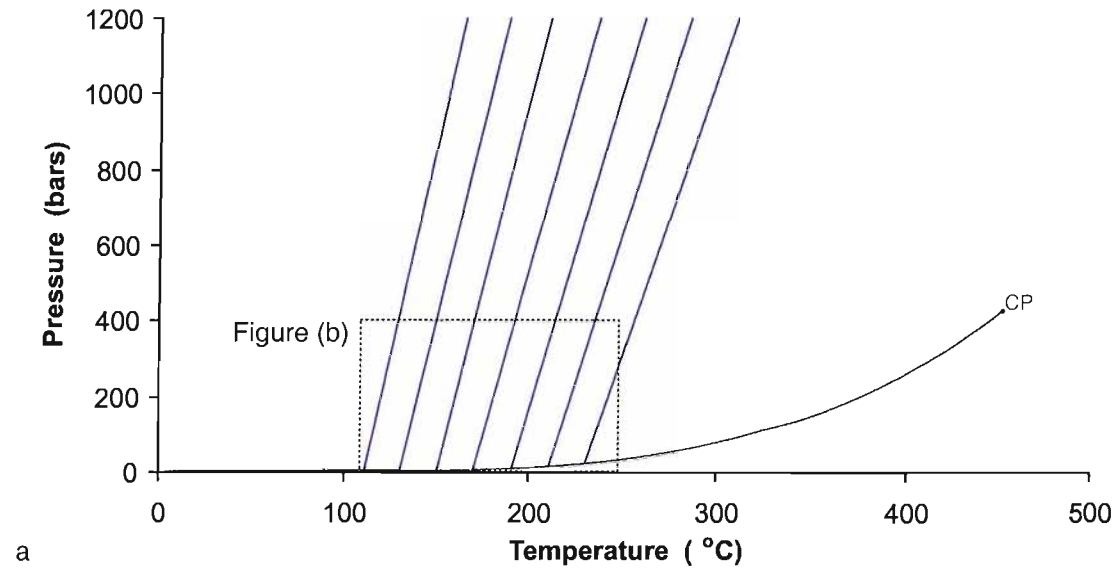

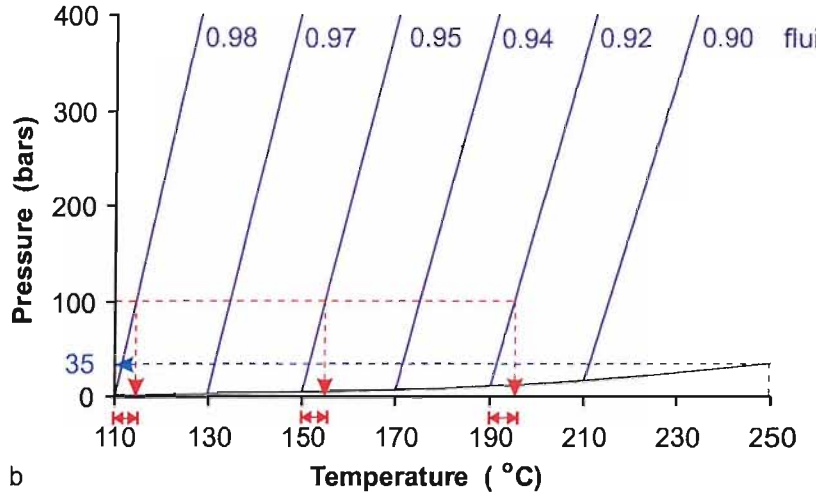

Pressure correction at 100 bars		
Th (°C)	wt% NaCl	correction (°C)
110	5	+4.5
150	5	+5.0
190	5	+6.0

liquid-vapour curve for 5 wt% NaCl eq. — isochores (density, g/cm^3)

pressure corrections are shown in red
minimum pressure required to prevent boiling at 250°C is shown in blue

a. Phase diagram showing the liquid-vapour curve and density isochores for 5wt% NaCl (calculated using equations from Zhang & Frantz, 1987). CP - critical point.

b. Portion of the phase diagram shown in (a) which is relevant for pressure corrections to fluid inclusion data from Balta Tau showing the density for each isochore. Corrections to homogenisation temperatures (Th) of 110°C, 150°C and 190°C for a pressure of 100 bars (corresponding to a water depth of 1000m) are shown graphically and tabulated to the right. A minimum pressure of 35 bars is required to prevent boiling at 250°C.

Figure 6.12. Pressures correction for Balta Tau fluid inclusion homogenisation temperatures.

Temperature and salinity variations

Within the unimodal population of fluid inclusion trapping temperatures there is a correlation between temperature and the host mineral and ore facies (Figures 6.6a, 6.7a). Higher temperatures (130 to 170°C) are found in primary inclusions from sphalerite, barite and quartz in mainstage ores while lower temperatures (110 to 140°C) generally occur in primary and secondary inclusions in footwall late stage and mainstage quartz and secondary inclusions in footwall sphalerite. The range of formational temperatures for each ore facies is summarised in Table 6.6. These temperatures are low compared to the majority of VMS systems, which typically attain temperatures of 250 to 350°C (Figure 6.13). However, some ore facies at Balta Tau are not represented in the fluid inclusion data due to lack of suitable inclusion-bearing phases, which include the pyrite-chalcopyrite rich massive sulphides and footwall veins. The chalcopyrite-rich nature of these ore facies suggests formation at relatively high temperatures of at least 250°C (discussed in Section 7.4.5) which may relate to scarce high temperature inclusions in footwall quartz (180 to 245°C). The scarcity of these inclusions suggests that this was an early stage of ore formation which was subsequently overprinted by lower temperature inclusion bearing phases.

The bimodal distribution of fluid inclusion salinities does not correlate with the host ore facies, but some differences can be identified between the host mineral phases of the two populations. Salinities in the range 2.7 to 5.1 wt% NaCl eq. (mode of 3.5) are restricted to primary inclusions in barite and sphalerite, while those ranging from 1.6 to 2.3 wt% NaCl eq. (mode of 2.0) are more diverse occurring in primary main and late stage quartz inclusions, secondary sphalerite inclusions, and primary sphalerite and barite inclusions (Figure 6.6b). The range in salinity of both populations is comparable with data from numerous ancient and actively forming systems (Figure 6.13). The "NV" inclusions (defined in Section 6.2.3) form a third salinity population with salinities probably less than 1.5wt% NaCl eq.. These very low salinities are generally confined to primary inclusions in main and late stage footwall quartz and secondary inclusions in mainstage footwall quartz and sphalerite, and are not typical of VMS ore forming fluids (Figure 6.13).

The trapping temperatures and salinities together define two populations (Figure 6.14a, b). Statistical analysis using the student's t-test (see Appendix C3) confirms that these two populations have a very highly significant difference between means with respect to salinity data and a highly significant difference between means for the trapping temperatures (with better than 99.9% and 97.5% confidence levels respectively). Population I correspond to the higher salinity group (note that the highest salinities reaching 5.1wt% (Figure 6.6b) are not represented on Figures 6.14a and b because corresponding temperature measurements were unobtainable), while population II are the lower salinity group with a slightly lower temperature range than population I. The "NV" inclusions have the lowest trapping temperatures (Figure 6.14c) and define a distinct third population of low salinity (less than 1.5wt%), low temperature (110 to140°C) inclusions.

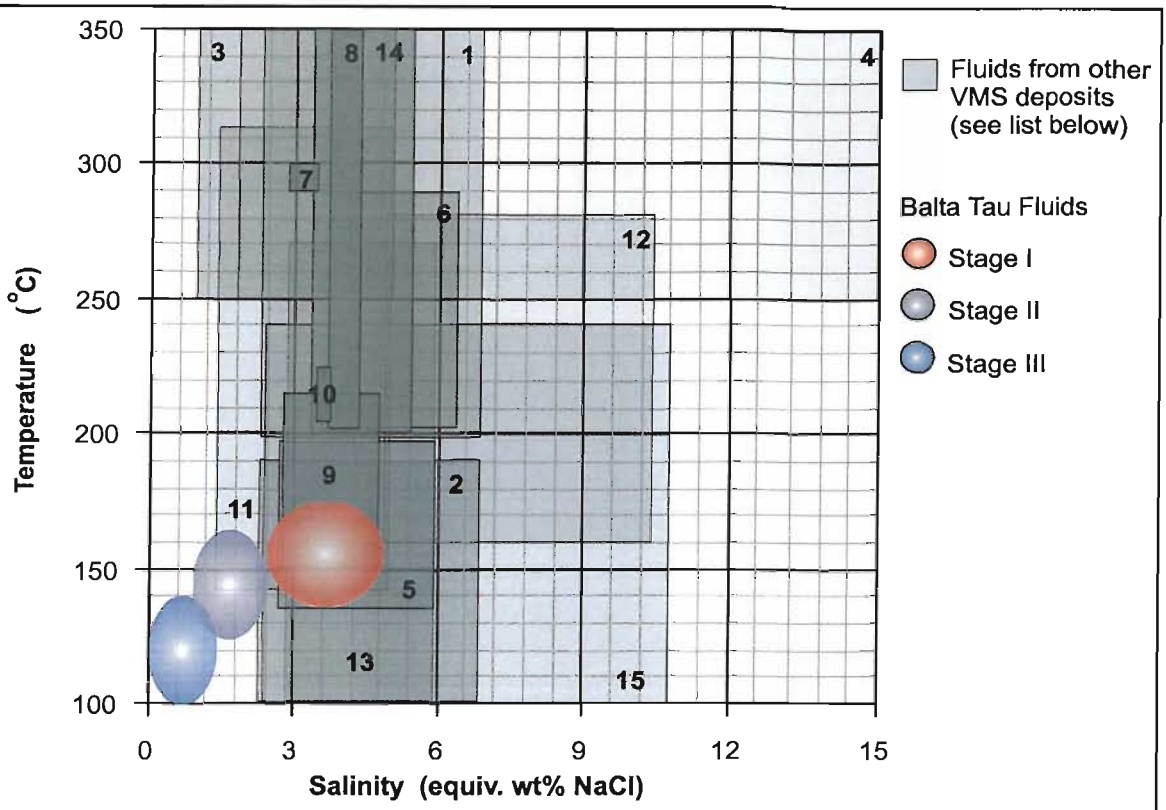

1. High temperature zone (alteration minerals), Middle Valley, JDFR. (Peter et al., 1994).
2. Low temperature zone (carbonates), Middle Valley, JDFR. (Peter et al., 1994)
3. Anhydrite inclusions, TAG, MAR. (Tivey et al., 1998).
4. Sphalerite-enargite inclusions, JADE, Okinawa Trough. (Luders et al., 2001)
5. Barite inclusions, JADE, Okinawa Trough. (Luders et al., 2001)
6. Barite-sphalerite inclusions, Lau Back-Arc Basin. (Herzig et al., 1993)
7. Sphalerite inclusions, 21°N, EPR. (Le Bel & Oudin, 1982).
8. Anhydrite inclusions, 21°N, EPR. (Le Bel & Oudin, 1982)
9. Barite inclusions, Kita-Bayonnaise, Izu-Ogasawara Arc. (Iizasa et al., 1997)
10. Sphalerite inclusions, Kita-Bayonnaise, Izu-Ogasawara Arc. (Iizasa et al., 1997)
11. Barite inclusions, Wetar Island. (Scotney, 2002).
12. Quartz inclusions, Mt. Chalmers, Queensland. (Zaw et al., 2003)
13. Barite inclusions, Furutobe Mine, Kuroko deposits. (Tokunaga & Honma, 1974).
14. Kuroko deposits. (Pisutha-Arnond & Ohmoto, 1983)
15. Quartz and sphalerite inclusions, Eskay Creek. (Sherlock et al., 1999).

Figure 6.13. Temperature-salinity ranges for selected VMS deposits.

Ore facies	Host phases	Trapping temperatures (°C)
mainstage footwall	quartz, sphalerite	130 to 170
late stage footwall	quartz	110 to 140
massive sulphides	sphalerite, barite	140 to 170
layered sulphides	sphalerite	140 to 150
barite-rich sulphides	sphalerite, barite	140 to 150
barite lens	sphalerite, barite	140

Table 6.6. Formational temperatures of Balta Tau ores from fluid inclusion trapping temperatures.

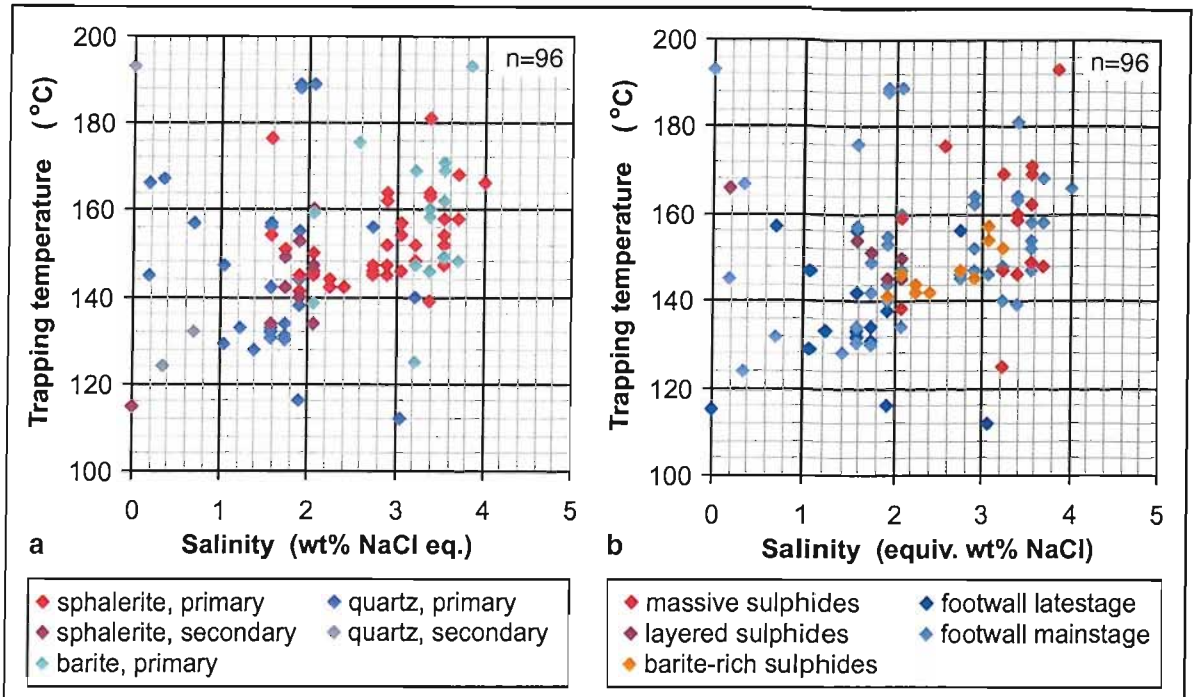

a and b. Trapping temperature-salinity data subdivided according to (a) the host mineral phase and (b) ore facies. The data are positively correlated and form two populations. Population I comprises higher temperature and salinity (140 to 170°C; >2.7 wt% NaCl eq.) primary inclusions in barite, sphalerite and quartz from mainstage ores. Population II contains lower temperature and salinity (130 to 160°C; 1.5 to 2.4wt% NaCl eq.) primary and secondary inclusions in sphalerite and quartz, especially from the mainstage and late stage footwall.

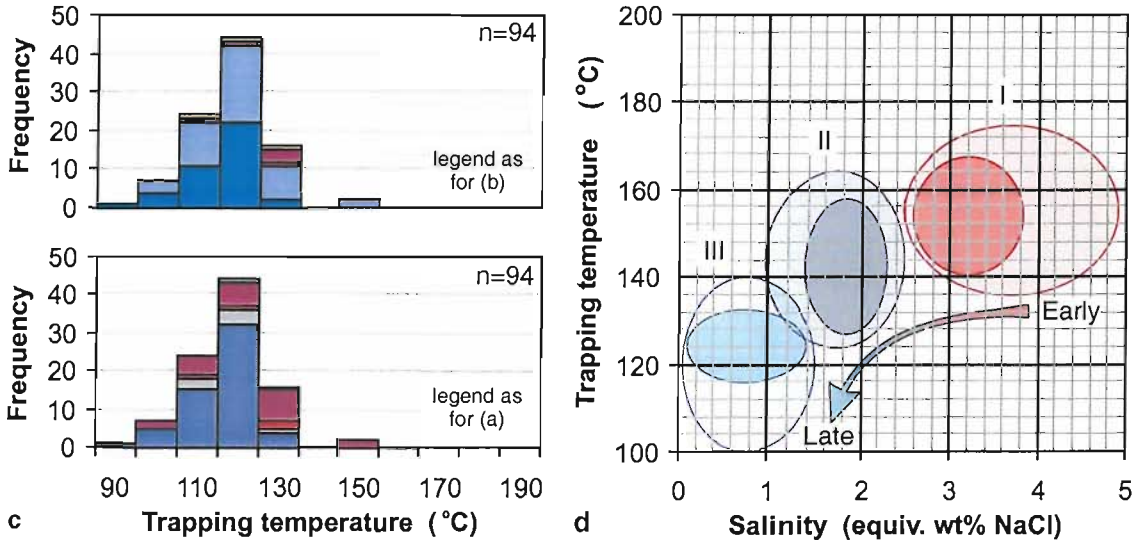

c. Histogram of trapping temperatures for "NV" inclusions (see text) sub-divided according to host mineral (lower) and ore facies (upper), which are low temperature (110 to 140°C) and low salinity (? <1.5 wt% NaCl eq.). They are predominately primary inclusions in main and late stage footwall quartz, and secondary inclusions in footwall quartz and sphalerite.

d. Summary of fluid inclusion data with three populations represented by inner and outer circles that encompass approximately 85 and 60% of data respectively. Populations I and II correspond to those in figures (a) and (b) (population I outer circle includes salinities up to 5wt% from barite inclusions with no T_h data). Population III comprises the "NV" inclusions in figure (c).

Figure 6.14. Summary of temperature-salinity data for Balta Tau fluid inclusions.

These three fluid inclusion populations are summarised in Figure 6.14d. The differences in host mineral phases and ore facies between these populations suggests that they relate to different stages of ore formation, and may represent three distinct fluids or a single fluid with evolving composition.

The dominance of population I in primary inclusions in barite and sphalerite and absence in footwall quartz suggests that these are the earliest fluids recorded and relate to a mainstage of low temperature ore formation. The occurrence of population II in mainstage and some late stage footwall quartz, and as both primary and secondary inclusions in sphalerite, suggests that this fluid post dates population I and relates to the latter part of low temperature mainstage ore formation. In population III, the abundance of primary inclusions in late stage quartz suggests that this is the latest fluid recorded. This is supported by the common occurrence of secondary sphalerite inclusions and absence of primary barite and sphalerite inclusions in this population, indicating that population III post-date mainstage ore formation.

Population III inclusions also occur frequently as primary inclusions in mainstage footwall quartz, suggesting that much of the "mainstage" footwall quartz mineralization occurred at the same time as the late stage veins rather than during mainstage ore formation. Table 6.7 summarises the fluid evolution as recorded by fluid inclusion data.

	earliest fluid recorded → latest fluid recorded		
	population I mainstage ore formation	population II latter part of mainstage ore foprmation	population III latestage fluids post-dating mainstage ore formation
host mineral and ore facies	1° inclusions in barite and sphalerite from all mainstage ore horizons	1° and 2° inclusions in quartz from mainstage ore horizons particularly the footwall; some 1° inclusions in late stage footwall quartz veins	1° inclusions in late stage footwall quartz veins; also 1° inclusions in quartz and 2° inclusions in sphalerite from the mainstage footwall
temperature range (ºC)	140 to 170	130 to 170	110 to 140
salinity (equiv. wt% NaCl)	2.7 to 5.1	1.5 to 2.4	?<1.5

Table 6.7. Summary of fluid properties and evolution based on fluid inclusion analyses. A probable early, high temperature stage of ore formation is not represented in the fluid inclusions studied and is therefore not mentioned here.

Fluid $\delta^{18}O$

The oxygen isotopic composition of minerals may be used in conjunction with independent geothermometers to estimate the $\delta^{18}O$ of mineralising fluids, assuming the minerals and fluid were in isotopic equilibrium during precipitation and the primary isotopic signature of minerals is preserved.

Oxygen isotope analyses of quartz, chlorite, muscovite and barite from Balta Tau may be used to infer the $\delta^{18}O$ of mineralising fluids. Quartz, chlorite and muscovite are likely to be reliable indicators of fluid $\delta^{18}O$-temperature and have been widely used in the study of VMS systems (e.g. Pisutha-Arnond and Ohmoto, 1983; Alt et al., 1998; Huston and Taylor, 1999; Sherlock et al., 1999; Huston, 2000), however at Balta Tau these minerals generally post date mainstage ores and will therefore provide information on later fluids rather than those responsible for the main stages of ore formation. Barite is generally considered less reliable because of the long time required for sulphate minerals to reach oxygen isotope equilibrium with fluids. However at Balta Tau the barite does appear to have been at or close to oxygen isotopic equilibrium with fluids (discussed in Section 6.5.8) and given the intimate association with ore minerals should directly relate to the mainstage ore forming fluid.

Table 6.8 summarises fluid $\delta^{18}O$ values calculated from equilibrium fractionation equations that have been calibrated over low temperature ranges comparable to Balta Tau fluid inclusion data. For quartz, using the modal $\delta^{18}O$ of +13‰ in conjunction with fluid inclusion data (Table 6.6) gives a fluid $\delta^{18}O$ of -1 to -4.5‰ for the mainstage footwall and -3.5 to -6.5‰ for the late stage footwall veins (Figure 6.15a). Taking into account the whole range of $\delta^{18}O$(quartz) values (+11.6 to +14.2‰, Figure 6.15a) expands these fluid ranges by a maximum of ±1.5‰.

For individual samples, there is a negative correlation between the $\delta^{18}O$ and mean of fluid inclusion temperatures (Figure 6.15b; see also Appendix C6), with the mainstage quartz having higher temperatures and lower $\delta^{18}O$ while the late stage quartz has lower temperatures and higher $\delta^{18}O$. The correlation between $\delta^{18}O$(quartz) and temperature narrows the range of corresponding fluid $\delta^{18}O$ to -2.1 to -3.7‰ for mainstage quartz and -5.0 to -5.2‰ for late stage quartz (Table 6.9). One anomalous mainstage quartz sample has temperature - $\delta^{18}O$ comparable with the late stage quartz, suggesting that some of the finer grained quartz associated with sulphides precipitated during formation of the late stage quartz veins. This is consistent with fluid inclusion data which suggest much of the quartz interpreted as mainstage quartz in fact precipitated from the same fluids as the late stage veins (see above).

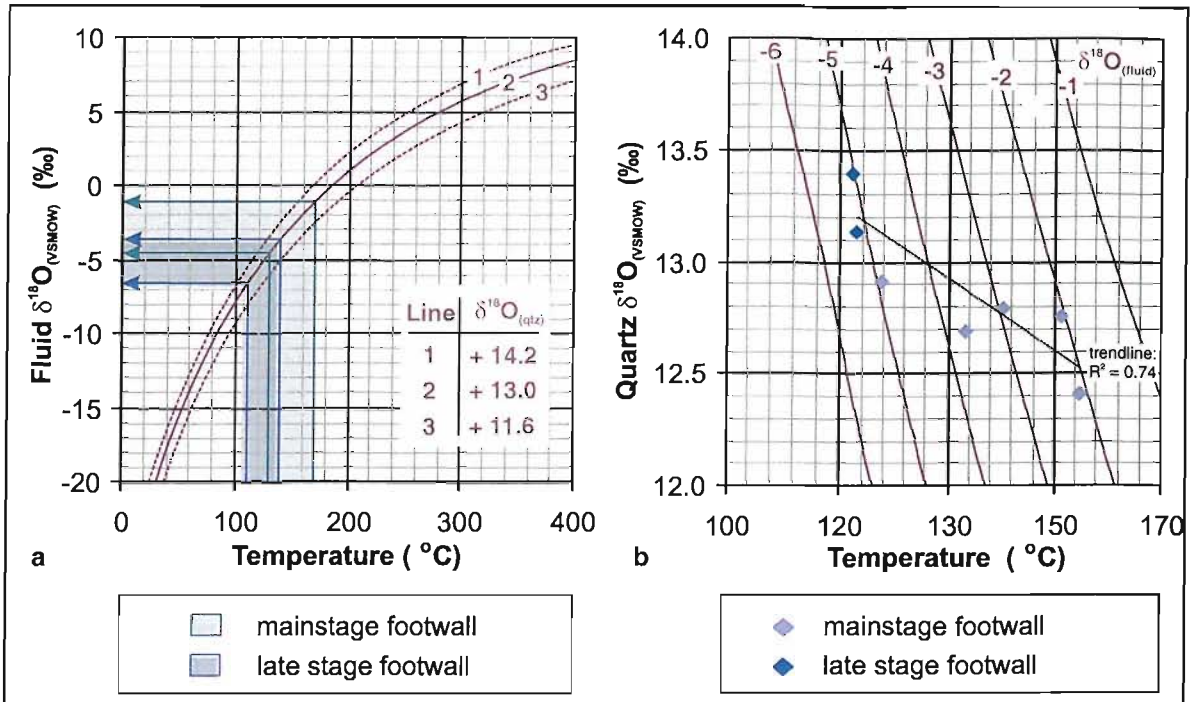

a. Fluid $\delta^{18}O$ - temperature equilibrium fractionation curves for quartz $\delta^{18}O$ compositions of +11.6 to +14.2‰ (equation from Zhang et al., 1989). Using fluid inclusion data and the modal quartz $\delta^{18}O$ (+13.0‰) gives a fluid $\delta^{18}O$ of -4.5 to -1.0‰ for mainstage quartz and -3.5 to -6.5‰ for late stage quartz. Taking into account the full range of quartz $\delta^{18}O$ values (+11.6 to +14.2‰) extends these ranges of fluid $\delta^{18}O$ by +/- 1.5‰.

b. Fluid inclusion temperature and quartz $\delta^{18}O$ plotted for individual samples have a negative correlation (as indicated by the trendline, based on linear regression), which narrows the probable range of fluid $\delta^{18}O$ to -2 to -5‰ for mainstage quartz and around -5‰ for late stage quartz.

Figure 6.15. Fluid $\delta^{18}O$ estimates from quartz $\delta^{18}O$ and fluid inclusion temperatures.

The $\delta^{18}O$ of quartz from layered sulphides, barite-rich sulphides and the barite lens ranges from +13.5 to +14‰ but unfortunately formational temperatures could not be obtained due to a lack of fluid inclusions suitable for microthermometry. Using trapping temperatures of inclusions in associated sphalerite and barite (150 to 160°C) gives a fluid $\delta^{18}O$ of around -1‰. However, quartz in these ore horizons is commonly interstitial to barite and sulphides and is more likely to post date these minerals. The $\delta^{18}O$ of this quartz is comparable with that of the late stage quartz veins, therefore a formational temperature of around 120°C gives a fluid $\delta^{18}O$ of -5‰, comparable with the ^{18}O depleted fluid that formed the late stage footwall veins. The similarity between quartz $\delta^{18}O$ in layered sulphides with that of the barite lens and barite-rich sulphides suggests that the quartz in these horizons may have precipitated from the same fluid, which has important implications for the timing of recrystallization of the layered sulphides, discussed further in Section 7.5.4.

Barite $\delta^{18}O$ ranges from +8.3 to +12.0‰ (excluding one anomalous footwall value of +13.8‰), which in conjunction with fluid inclusion data (Table 6.6) indicates a fluid $\delta^{18}O$ of -2 to +3.5‰ for the massive sulphides and -2 to +2‰ for the barite-rich sulphides and the barite lens (Figure 6.16a). This suggests that the fluid responsible for mainstage massive sulphides and baritic ores was ^{18}O enriched relative to the fluid responsible for mainstage and late stage footwall mineralization. Due to the difficulty in acquiring reliable inclusion temperatures from barite, only three samples have both $\delta^{18}O$ and fluid inclusion data, and for two of these the inclusion data is from cogenetic sphalerite rather than barite. For these three samples the barite $\delta^{18}O$ and mean of fluid inclusion temperatures gives consistent fluid $\delta^{18}O$ estimates of +0.4‰ to -0.3‰ (Figure 6.16b, Table 6.9). The footwall barite has $\delta^{18}O$ in the range +10.9 to +12.0‰ and does not contain fluid inclusions suitable for microthermometry. However if the fluid $\delta^{18}O$ is assumed to be the same as that for massive and barite-rich sulphides, this suggests the footwall barite formed at lower temperatures of 130 to 140°C.

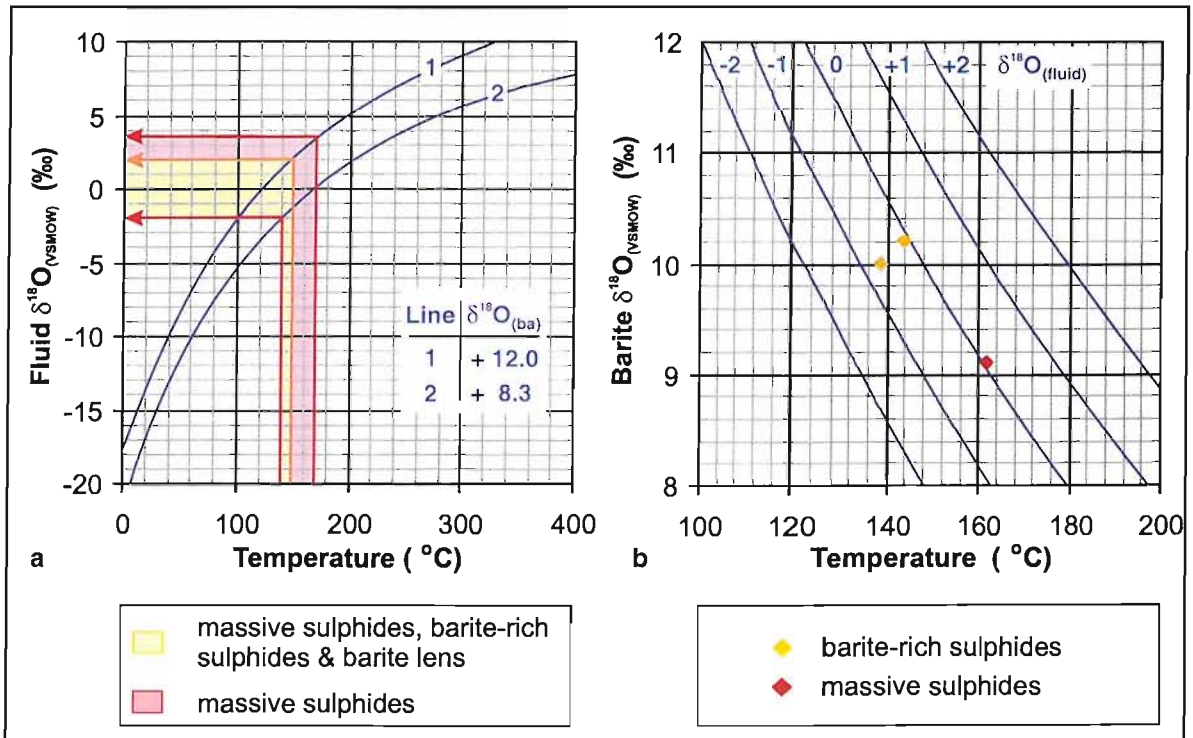

a. Temperature - fluid $\delta^{18}O$ equilibrium fractionation curves for barite $\delta^{18}O$ compositions of +8.3 and +12‰ (fractionation equation from Seal et al., 2001). Using temperatures from fluid inclusions gives a maximum range of fluid $\delta^{18}O$ of -2 to +3.5‰ during formation of massive sulphides, and -2 to +2 ‰ for the barite-rich sulphides and the barite lens.

b. Fluid inclusion temperatures and barite $\delta^{18}O$ plotted for individual samples suggest a fluid $\delta^{18}O$ values of around 0 ‰.

Figure 6.16. Fluid $\delta^{18}O$ estimates from barite $\delta^{18}O$ and fluid inclusion temperatures.

mineral	mineral $\delta^{18}O$ (‰)	temperature (ºC)	fluid $\delta^{18}O$ (‰)	fractionation equation
quartz mainstage	+13.0	130 to 170	-4.5 to -1.0	Zhang et al. (1989), valid 180 to 550ºC
quartz late stage	+13.0	110 to 140	-6.5 to -3.5	Zhang et al. (1989), valid 180 to 550ºC
barite in massive sulphides	+8.3 to +12.0	140 to 170	-2.0 to +3.5	Seal et al. (2001), valid 110 to 350ºC
barite in barite lens & barite-rich sulphides	+8.3 to +12.0	140 to 150	-2.0 to +2.0	Seal et al. (2001), valid 110 to 350ºC

Table 6.8. Fluid $\delta^{18}O$ estimates based on oxygen isotope composition of quartz and barite and fluid inclusion temperatures.

mineral	ore facies	sample no	mineral $\delta^{18}O$ (‰)	temperature (ºC)	fluid $\delta^{18}O$ (‰)
quartz	late stage footwall	01BT002	+13.2	123	-5.2
quartz	late stage footwall	01BT007	+13.4	123	-5.0
quartz	mainstage footwall	01BT003	+12.7	143	-3.7
quartz	mainstage footwall	01BT058	+12.9	128	-5.0
quartz	mainstage footwall	01BT145	+12.8	161	-2.1
quartz	mainstage footwall	01BT157	+12.4	165	-2.1
quartz	mainstage footwall	01BT073	+12.8	151	-2.9
barite	massive sulphides	903	+9.1	162	+0.1
barite	barite-rich sulphides	01BT082	+10.2	144	-0.1
barite	barite-rich sulphides	01BT138	+10.0	138	-0.7

Table 6.9. Fluid $\delta^{18}O$ estimated from individual samples based on a single oxygen isotope analysis and the mean of fluid inclusion trapping temperatures for that sample. (See Appendix C5 for trapping temperatures; fractionation equations used for each mineral are the same as those listed in Table 6.8; note that for samples 01BT157, 01BT073, 01BT082 and 01BT138, inclusion data is from sphalerite which texturally appears to have co-precipitated with the quartz/barite).

Fluid $\delta^{18}O$ have been estimated from chlorite and muscovite which post-date the main stage of ore formation are summarised in Table 6.10. Estimates of formational temperatures based on chlorite compositions are in the range 80 to 160°C (Chapter 5, Table 5.21) which in conjunction with a chlorite $\delta^{18}O$ of +8.9‰ (the mean of two analyses) gives a fluid $\delta^{18}O$ in the range -3.5 to +2.5‰ (Figure 6.17a). An independent estimate of the temperature of formation for muscovite has not been established, however if the muscovite and chlorite precipitated from the same fluids (as proposed from microprobe data, Chapter 5 Section 5.4.7) then the muscovite $\delta^{18}O$ value of +10.2‰ (mean of three analyses) used in conjunction with chlorite geothermometry gives a fluid $\delta^{18}O$ of -3.5 to +3.5‰ (Figure 6.17b), a similar range to that indicated by chlorite.

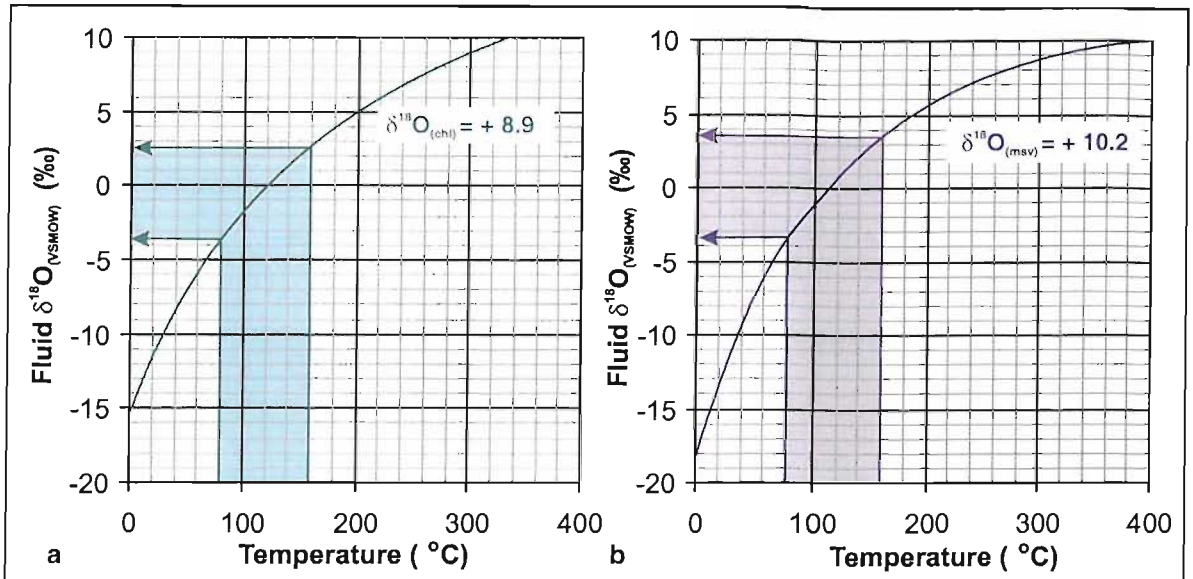

a. Temperature - fluid $\delta^{18}O$ equilibrium fractionation curve for chlorite with a $\delta^{18}O$ of +8.9‰ (fractionation equation from Savin & Lee, 1988). Using temperatures from chlorite geothermometry gives a maximum fluid $\delta^{18}O$ range of -3.5 to +2.5‰.

b. Temperature - fluid $\delta^{18}O$ equilibrium fractionation curve for muscovite with a $\delta^{18}O$ of +10.2‰ (fractionation equation from Zheng et al., 1993). Using temperatures from chlorite geothermometry gives a maximum fluid $\delta^{18}O$ range of -3.5 to +3.5‰.

Figure 6.17. Fluid $\delta^{18}O$ estimates from chlorite and muscovite $\delta^{18}O$ and chlorite composition geothermometry.

mineral	mineral $\delta^{18}O$ (‰)	temperature (ºC)	fluid $\delta^{18}O$ (‰)	fractionation equation
chlorite	+8.9	80 to 160	-3.5 to +2.5	Lee & Savin (1998), valid 66 to 175ºC
muscovite	+10.2	80 to 160	-3.5 to +3.5	Zheng (1993), valid 0 to 1200ºC

Table 6.10. Range of fluid $\delta^{18}O$ estimated from the oxygen isotope composition of chlorite and muscovite and temperature estimates from chlorite compositions.

Summary

Table 6.11 summarises fluid properties based on fluid inclusions and oxygen isotopes for mineralization at Balta Tau.

	early stage →	main stage	→ late stage	
fluid inclusion population	(no representative fluid inclusions)	I	II	III
ore facies	chp-rich footwall & massive sulphides	sph-rich footwall & massive sulphides; barite-rich ores		footwall qtz-ten veins
temperature (ºC)	? 250 to 300	140 to 170	130 to 170	110 to 140
salinity (equiv. wt% NaCl)	?	2.8 to 5.1	1.5 to 2.4	? <1.5
fluid $\delta^{18}O_{(VSMOW)}$ (‰)	?	-0.7 to +0.1	-2.1 to -3.7	-5 to -5.2

Table 6.11. Summary of ore forming fluid characteristics based primarily on fluid inclusion microthermometry and oxygen isotope analyses.

6.5.3 Sources and evolution of hydrothermal fluids

Introduction

The most likely source of hydrothermal fluids in VMS systems is seawater which has been modified by interaction with seafloor volcanic and intrusive rocks (e.g. Franklin et al., 1981). This interaction alters the fluid oxygen isotopic signature by +0.5 to +2‰ based on the $\delta^{18}O$ of hydrothermal fluids from active systems (Shanks, 1995). Early Palaeozoic seawater is predicted to have been ^{18}O depleted relative to present day SMOW (Azmy et al., 1998; Veizer et al., 1999), and in the Devonian probably had a $\delta^{18}O$ signature of -1 to -3‰ (Leuceyer & Allemand, 1999). Therefore by analogy with modern systems, a hydrothermal fluid derived from the interaction of Devonian seawater and oceanic crust would be expected to have a $\delta^{18}O$ signature in the range –2.5 to +1‰. The salinity of oceans through the Palaeozoic has not been established, therefore in the following discussions it is assumed that the Urals palaeo-ocean had a salinity comparable to that of modern oceans, 3.2 wt% NaCl eq.

Additional fluid sources that may be important in the formation or modification of VMS ores include magmatic waters with $\delta^{18}O$ of +5 to +10‰ and variable salinities, metamorphic fluids with $\delta^{18}O$ of 0 to +15‰ and generally low salinity, and meteoric water with zero salinity and significant ^{18}O depletion.

The following discussion investigates possible sources of the Stage I and Stage III fluids at Balta Tau. Stage II fluids are intermediate between Stage I and Stage III both temporally and in terms of fluid properties, suggesting that they may reflect a mixture of these earlier and later fluids. This implies a temporal overlap between the generation of fluids responsible for mainstage ore mineralization and those responsible for the late stage footwall quartz.

Stage I fluids

The stage I fluids responsible for low temperature, mainstage ore formation probably comprised a mixture of hydrothermal fluids and seawater, as indicated by Sr isotope studies of barite (section 6.5.4). The end member Stage I hydrothermal fluid $\delta^{18}O$ is estimated to lie between –0.3 and +1.3‰ (Table 6.12), which by analogy with modern systems is consistent with a fluid derived from the interaction of Devonian seawater and ocean crust. The salinity of end member fluids varies considerably from 75% to 200% of seawater salinity, which is a typical range for VMS fluids (Figure 6.13). The interaction of seawater with oceanic crust may alter the fluid salinity by the precipitation and dissolution of Cl bearing phases and by the precipitation of hydrous alteration minerals, however these do not generally produce salinities in excess of 10% higher or lower than that of seawater (Seyfried et al., 1986; Bowers and Taylor, 1985). Therefore salinity variations in

fluids from modern systems are generally accounted for by phase separation of the hydrothermal fluid followed by variable mixing of the segregated phases (e.g. Kelley and Delaney, 1987; Von Damm, 1988; Butterfield et al., 1990; Butterfield et al., 1994; Edmonds and Edmond, 1995; Dählmann et al., 2001), and this mechanism is also likely to be responsible for salinity variations in Balta Tau fluids.

At Balta Tau, fluid inclusions are not indicative of fluid boiling, suggesting that phase separation probably occurred below the level of mineralization. At significant depths beneath the seafloor and temperatures above the critical point (407°C, Bischoff & Rosenbauer, 1988), seawater may undergo supercritical phase separation resulting in the segregation of a small volume of high salinity brine (30 to 50wt% NaCl eq.) and a fluid with salinity less than seawater. Alternatively, rapid ascent of fluids by adiabatic decompression may result in sub-critical phase separation (boiling) where a low salinity vapour phase segregates from a liquid with moderately elevated salinity.

The salinity range for Stage I fluids may be the result of either supercritical or sub-critical phase separation and subsequent mixing of segregated phases. However, the absence of a high salinity brine is more suggestive of sub-critical separation, although it is possible that a brine produced during supercritical phase separation did not ascend to the seafloor due to high density and is therefore not recorded. Figure 6.18 illustrates a possible scenario for the intersection of Stage I fluids with the sub-critical region of the two phase curve for seawater. A minimum of 50% boiling would have been necessary to produce the maximum salinities estimated for end-member Stage I fluids (Figure 6.19), assuming the vapour phase produced had a salinity of zero. Had the temperature of phase separation been approaching the critical point (above around 380°C), the vapour phase would have been weakly saline (Bischoff and Rosenbauer, 1988) and slightly higher degrees of boiling would have been necessary to produce the Stage I fluid salinities. Although only one stage of boiling is indicated on Figure 6.18 for simplicity, the fluid may have intersected the two phase boundary a number of times during the ascent with multiple episodes of a small degree of boiling. The segregated phases would have continued to react with surrounding rocks during and after phase separation, and the increased salinities of the brine phase may have aided the transportation of metals such as Cu. Phase separation is unlikely to have affected the $\delta^{18}O$ of Stage I fluids, since oxygen isotope fractionation during phase separation at high temperatures (>300°C) is minimal (Figure 6.20) and subsequent fluid:rock interaction would probably mask any changes that did occur.

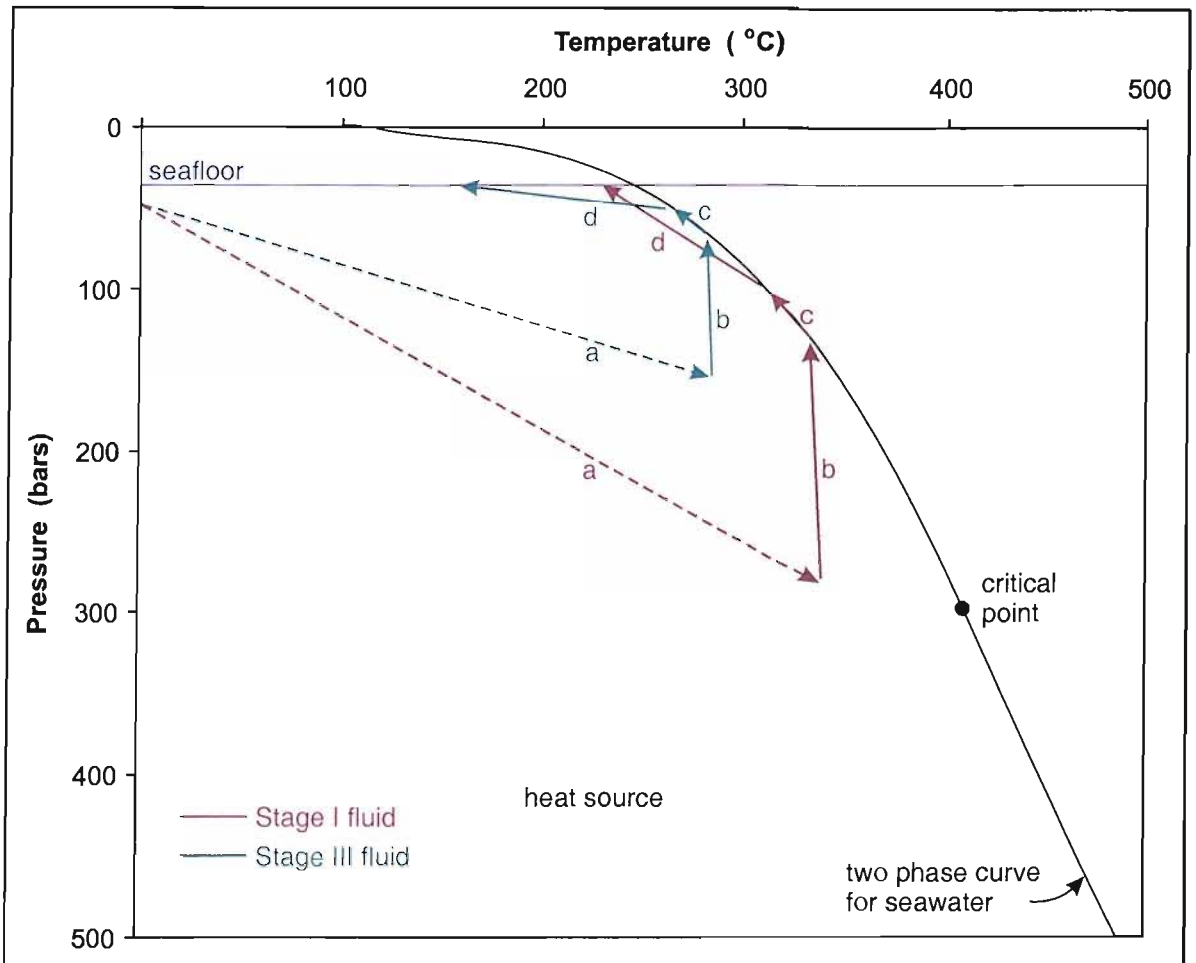

Suggested P-T paths for Stage I and Stage III fluids involving sub-critical phase separation (diagram adapted from Butterfield et al., 1990):
a. Convective heating of seawater by intrusive heat source at depth.
b. Fluid ascent and adiabatic decompression.
c. Fluid intersects the two phase curve for seawater and boils forming a low salinity vapour.
d. Boiling ceases when the fluid departs the two phase curve due to heat loss to surrounding rocks. The recondensed vapour phase and the higher salinity liquid ascend to the seafloor, with continued heat loss to surrounding rocks.

Stage I fluids are produced during temperature phase of mainstage hydrothermal circulation. Phase separation occurs at considerable depth at temperatures of around 300 to 350°C, and subsequently the recondensed vapour phase and more saline liquid recombine to variable degrees producing fluids with salinities varying above and below that of the original fluid (seawater). Rapid and focussed fluid ascent results in fluids of around 250°C reaching the seafloor/immediate sub-seafloor.

Stage III fluids relate to waning, lower temperature stages of the hydrothermal system. Consequently fluids intersect the two phase curve at lower temperatures of around 280°C at shallower levels. When boiling stops, the recondensed vapour phase and higher salinity residual fluid follow separate paths over the relatively short ascent to the seafloor. The rapid cooling may reflect more diffuse flow relative to earlier fluids, and the recondensed vapour reaches the seafloor at temperatures of less than 200°C.

Figure 6.18. Illustration of sub-critical phase separation for Balta Tau mineralising fluids.

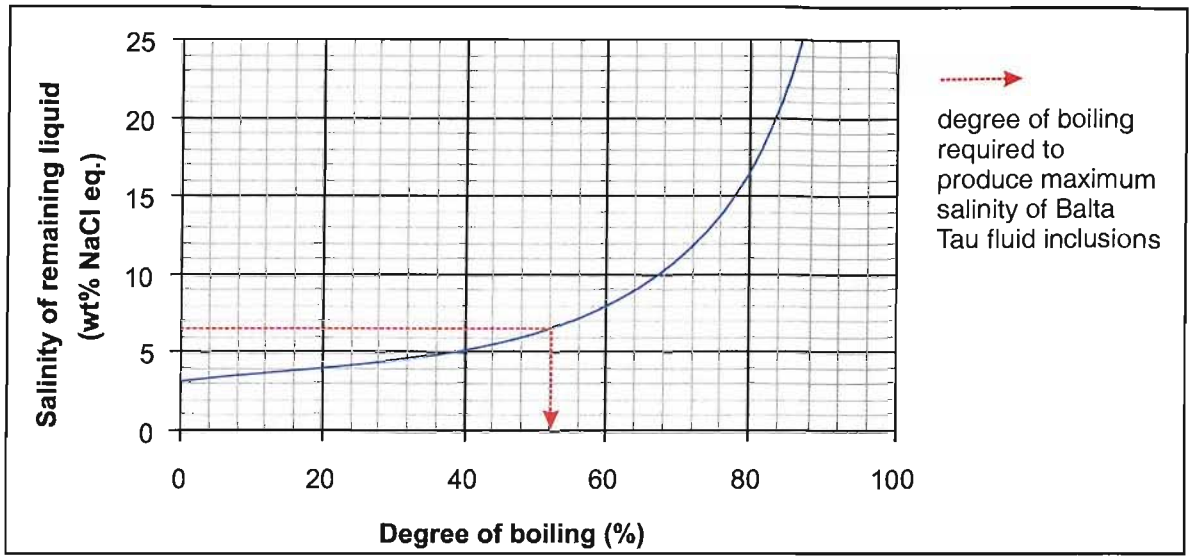

Figure 6.19. Salinity variations in the residual liquid phase during boiling of seawater.

	temperature (ºC)	salinity (wt% NaCl eq.)	$\delta^{18}O$ (‰)
estimated fluid composition during ore formation	140 to 170	2.7 to 5.1	-0.7 to 0.0
end-member hydrothermal fluid (25% mixing)	170 to 225	2.5 to 5.7	-0.3 to +0.7
end-member hydrothermal fluid (40% mixing)	215 to 280	2.4 to 6.4	+0.2 to +1.3

Table 6.12. Stage I end member hydrothermal fluid properties taking into account mixing with ambient seawater during ore formation. Proportion of seawater mixing is estimated in Section 6.5.4 using seawater properties of 3.2wt% NaCl eq. salinity, $\delta^{18}O$ of -2‰, and temperature of 2°C.

Stage III fluids

Stage III fluids are characterised by particularly low $\delta^{18}O$ and low salinities. There are no direct indications of the extent of seawater mixing, since no Sr bearing minerals are known to have precipitated from this fluid. However, both of the proposed origins for Stage III fluids (which are discussed below) would produce a hydrothermal fluid with approximately zero salinity. Therefore salinities of up to 1.5wt% NaCl eq. for Stage III fluids which are suggested from fluid inclusion studies could be produced by mixing up to 45% seawater with end member Stage III fluids of zero salinity. Taking this in to account, the possible range of end member Stage III fluid properties are given in Table 6.13.

	temperature (ºC)	salinity (wt% NaCl eq.)	$\delta^{18}O$ (‰)
end-member hydrothermal fluid (0% mixing)	110 to 140	< 1.5	-4 to -5
end-member hydrothermal fluid (45% mixing)	200 to 250	0	-5.6 to -7.5

Table 6.13. Stage III end member hydrothermal fluid properties taking into account possible mixing with up to 45% ambient seawater. Seawater properties: salinity 3.2wt%; $\delta^{18}O$ -2‰, 2°C.

The low $\delta^{18}O$ of the Stage III fluid rules out a significant contribution from magmatic or metamorphic derived fluids. An ^{18}O depleted fluid could be produced by low temperature (<200°C) regional alteration of volcanic rocks by seawater (discussed in Section 6.5.5), however this would also increase the salinity relative to seawater due to the precipitation of hydrous alteration phases (Pisutha-Arnond & Ohmoto, 1983) and is therefore an unlikely origin of the Stage III fluids. Two sources which can account for both the ^{18}O depletion and low salinity characteristics are:

1. The segregation of a vapour phase resulting from sub-critical phase separation at low temperatures. The degree of oxygen isotope fractionation during boiling and condensation increases with decreasing temperature (Trausdell and Nathenson, 1977), and at temperatures below around 300°C significant fractionation may occur as recorded from epithermal systems (e.g. Faure, 2002). For example, at 280°C a moderate degree of boiling (40%) in an open system produces a vapour phase which is around 1‰ lighter than the initial fluid (assuming Rayleigh fractionation; Figure 6.20a). Subsequent condensation of the vapour results in progressive ^{18}O depletion (assuming an open system with Rayleigh fractionation), with the final 10% vapour condensing to a fluid 3 to 4‰ lighter than the initial vapour phase composition (Figure 6.20b). Therefore the final vapour to condense from low temperature boiling of a hydrothermal fluid would have zero salinity and could be ^{18}O depleted by up to 5‰ relative to the original fluid (seawater), which can account for the properties of Stage III fluids.

The late stage quartz precipitated by Stage III fluids does not show evidence of overprinting by less ^{18}O depleted or more saline fluids suggesting that neither the segregated brine or the liquid produced from initial stages of vapour phase condensation reached the footwall at Balta Tau. This implies that the pathway of ascending fluids altered such that the latest condensed vapours emerged at the Balta Tau site (as Stage III fluids) and subsequent ascending fluids (the initial vapour condensates and segregated brine phase) followed a different pathway and emerged elsewhere at the seafloor. This change in fluid pathway may have occurred as a result of volcanic and tectonic activity, or due to the sealing of fractures and porosity by the extensive silicification caused by Stage III fluids. The venting of a segregated vapour phase without a corresponding brine has been documented from active seafloor systems (e.g. Butterfield et al., 1990; Butterfield and Massoth, 1994; Butterfield et al., 1994; Dählmann et al., 2001), although a significant ^{18}O depletion of the vapour phase has not been recorded suggesting that an analogous system with near-surface, low temperature sub-seafloor phase separation in shallow waters has not been encountered.

The low temperature and late stage nature of Stage III fluids suggests they may reflect waning stages of hydrothermal activity. Low temperature phase separation could only have occurred close

to the seafloor (Figure 6.18), therefore the fluid composition is unlikely to have been significantly modified during fluid:rock interaction subsequent to phase separation. However, the intense silicification caused by Stage III fluids implies considerable leaching of Si did occur, and is consistent with unexpectedly high Si concentrations noted from condensed vapour phases in modern systems (Butterfield et al., 1990).

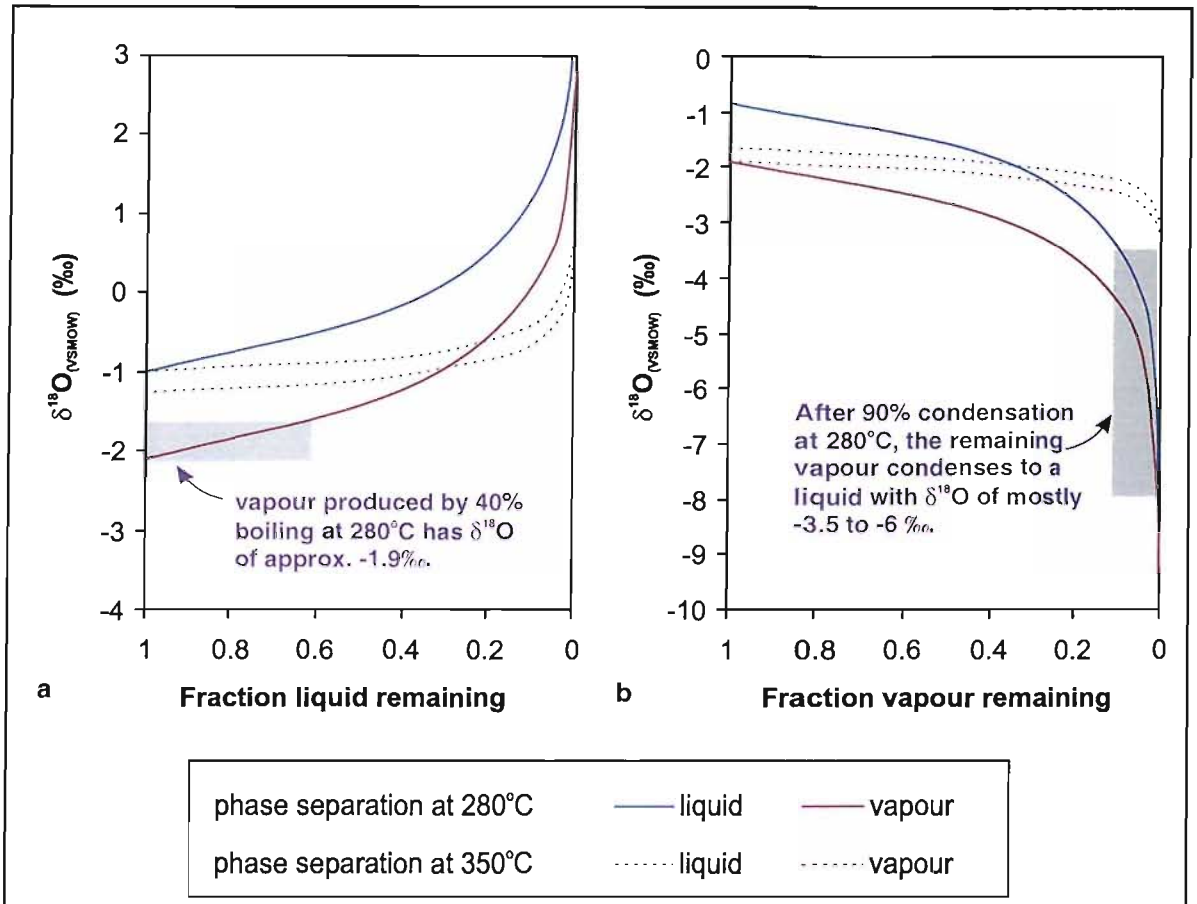

Graphical illustration of oxygen fractionation during low temperature (280°C) sub-critical phase separation which may have produced stage III fluids. Fractionation curves for identical fluids at 350°C have been shown for comparison, to illustrate the significance of temperature on the degree of fractionation produced.

a. Boiling of a fluid with intial $\delta^{18}O$ of -1‰ (a reasonable estimate for Devonian seawater which has undergone relatively low temperature interaction with ocean crust) by open system, rayleigh fractionation. A segregated vapour phase produced by 40% boiling will have a $\delta^{18}O$ of around -1.9‰.

b Condensation of the vapour phase produced in (a) by open system rayleigh fractionation results in the progressive ^{18}O depletion of vapour and liquid phases. After 90% condensation, the vapour will condense to form a liquid with $\delta^{18}O$ of -3.5‰, decreasing to below -7‰ as condensation is completed. Due to the increased buoyancy of vapour relative to liquid, the liquid produced during the final stages of condensation is likely to have the most rapid ascent and reach the seafloor first.

Figure 6.20. Oxygen isotope fractionation during low temperature, sub-critical phase separation.

2. An alternative source of Stage III fluids could be meteoric waters, which would be low salinity and typically have a $\delta^{18}O$ of -5 to -10‰ (Faure, 1986). This would imply that part of the island arc system was subaerial at the time of formation of the Balta Tau deposit. Evidence for subaerial eruptions was not observed in the regional volcanic rocks in this study, and has not been reported elsewhere. However, volcanic facies are suggestive of shallow water depths and it is therefore feasible that part of the arc may have been emergent at this time. Meteoric waters could have been heated by the same source that drove the hydrothermal system, perhaps attaining lower temperatures due to more shallow circulation. At low temperatures and low salinities, leaching of metals from the volcanic rocks may have been minimal, but significant leaching of Si must have occurred which is analogous with the Si enrichment of a low temperature vapour phase reported from modern VMS systems (Butterfield et al., 1990).

6.5.4 Mixing of hydrothermal fluids and seawater during ore formation

Introduction

The mixing of hydrothermal fluids and seawater at or just below the seafloor is known to be an important process in the formation of VMS deposits (e.g. Kusakabe and Chiba, 1983; Tivey, 1995; Teagle et al., 1998) and may trigger rapid precipitation of base and precious metals due to cooling, oxidation, dilution and changes in pH. The extent of seawater mixing during ore precipitation can be investigated using the Sr isotopic signature of minerals such as barite and chlorite. As hydrothermal fluids have a distinctly less radiogenic signature than pristine seawater, the relative proportions of fluid mixing are recorded in the $^{87}Sr/^{86}Sr$ of minerals precipitating from the mixed fluids (e.g. Teagle et al., 1998). The $^{87}Sr/^{86}Sr$ of barite in Balta Tau ore horizons lies between the $^{87}Sr/^{86}Sr$ of Devonian seawater and that of the host volcanic rocks, supporting the idea that fluids responsible for mainstage ores were derived from the interaction of Devonian seawater with volcanic rocks (Section 6.5.3).

Fluid $^{87}Sr/^{86}Sr$

The $^{87}Sr/^{86}Sr$ of hydrothermal fluids at Balta Tau should lie somewhere between that of Devonian seawater, estimated to have a signature of $^{87}Sr/^{86}Sr$ of 0.708 ±0.002 during the Emsian (Denison et al., 1997; Veizer et al., 1999) and the host volcanic rocks with $^{87}Sr/^{86}Sr$ of around 0.7041 (Section 6.5.1). The fluid signature can be further constrained by the $^{87}Sr/^{86}Sr$ of barite, since both Sr and stable isotopes indicate that barite precipitated from a mixture of seawater and the hydrothermal fluid (Sections 6.5.4, 6.5.8). The fluid signature must therefore be less radiogenic than the barite (which has values in the range 0.7050 to 0.7069), constraining the fluid $^{87}Sr/^{86}Sr$ to the range 0.7041 to 0.7050. For the following calculations and discussions, fluid $^{87}Sr/^{86}Sr$ is taken as the approximate mid point of this range, 0.7045.

Sr concentration of fluids

In order to investigate fluid mixing quantitatively, the concentration of Sr (written [Sr]), in the hydrothermal fluids relative to the concentration in seawater is required. This is problematic, since the [Sr] in Balta Tau hydrothermal fluids can not be directly estimated from the data obtained in this study, and by comparison with vent fluids in modern systems may have been considerably greater than or less than that of seawater (Von Damm, 1995). The [Sr] in Devonian seawater is also unknown, as there is no reconstruction for the [Sr] in oceans through the Palaeozoic.

A positive correlation between [Sr] and $[Cl]^2$ has been reported from studies of modern spreading ridge vent fluids, reflecting the transportation of Sr dominantly as $SrCl_{2(aq)}$ (Palmer, 1992). However, when [Sr] and [Cl] data from numerous vent sites including those from island arc environments are plotted, the correlation is poor and there is a wide range of values for the chlorinities predicted for Balta Tau fluids, as detailed in Appendix C8. Vonn Damm (1995) also notes that of the metals transported as chloride complexes in hydrothermal fluids, Sr shows one of the poorest correlations with chlorinity. Chlorinity is not therefore particularly useful for estimating the Sr content of Balta Tau hydrothermal fluids.

A positive correlation between [Sr] and $^{87}Sr/^{86}Sr$ in barite (Figure 6.21) might suggest that the [Sr] in the hydrothermal fluid was less than that of seawater, by around 60% based on extrapolation of this trend to end member fluid values. However, the partitioning of Sr between fluid and barite may be affected by a number of factors other than the [Sr], such as the [Ba] and temperature, which will also vary according to the proportions of fluid mixing. Therefore the trend in Figure 6.21 may not be a direct indication of the relative [Sr] in the hydrothermal fluid and seawater.

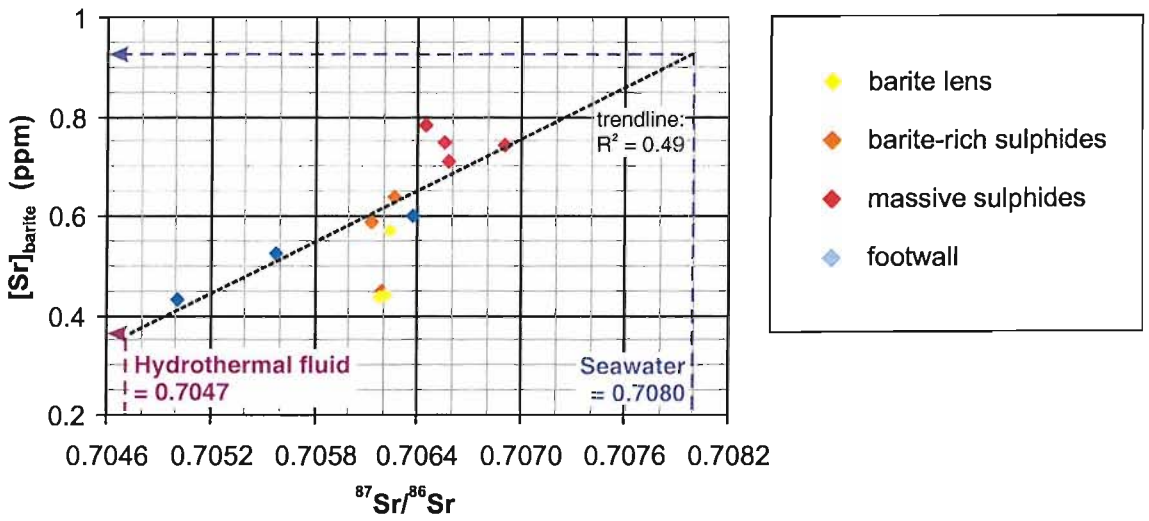

The trend in barite data (trendline defined by linear regression) extrapolated to end member fluid $^{87}Sr/^{86}Sr$ suggests that the ratio of [Sr] in barite precipitated from hydrothermal fluid to [Sr] in barite precipitated from seawater is approximately 0.5.

Figure 6.21. Concentration and isotopic ratio of Sr in barite from Balta Tau.

Modelling of fluid mixing based on both $^{87}Sr/^{86}Sr$ and $\delta^{18}O$ (Section 6.5.8) best fits the barite data if the [Sr] in the hydrothermal fluid was significantly less than that of seawater, with a reduction of around 50% giving the most realistic results. Given that this value is consistent with the trend in Figure 6.21, and in the absence of a more robust estimate, the ratio of [Sr] in hydrothermal fluids to [Sr] in seawater is taken as 0.5 in the following mixing calculations.

Fluid mixing

Qualitative examination of the barite $^{87}Sr/^{86}Sr$ data (Figure 6.22a) indicates that barite from the footwall, interpreted to pre-date mainstage footwall sulphides, contains the smallest seawater contribution indicating relatively minor seawater entrainment in early stages of footwall mineralization. The highest degree of seawater mixing occurred during precipitation of the massive sulphides, with slightly less seawater involved during precipitation of the barite-rich sulphides and the barite lens. The reduction in seawater mixing during precipitation of barite rich ores contradicts some published theories regarding barite precipitation, and is discussed further in Chapter 7, Sections 7.4.3 and 7.4.6. The chlorite-rich footwall sample has a strong seawater signature, which is consistent with the Mg-rich composition of chlorite (Chapter 5, Section 5.4.2) and indicates that significant circulation of seawater occurred in the footwall after the formation of mainstage ores.

Quantitative estimates of seawater mixing based on the estimated fluid $^{87}Sr/^{86}Sr$ and [Sr] are shown in Figure 6.22 and Table 6.14. They suggest that as little as 5% seawater contributed to early barite precipitation in the footwall and up to 50% seawater mixed with hydrothermal fluids during precipitation of massive sulphides, while the majority of samples indicate seawater mixing in the narrower range of 28 to 40%. These estimates are realistic given the probable concentrations of Ba and SO_4^{2-} in respective fluids (discussed in Chapter 7, Section 7.4.3) and are comparable with those estimated for barite in Kuroko deposits (Kusakabe and Chiba, 1983).

ore facies	Sr-bearing phase	seawater mixing (%)
early stage footwall barite	Barite	5 to 34
massive sulphides	Barite	36 to 50
barite-rich sulphides	Barite	28 to 31
barite lens	Barite	30
late stage footwall chlorite	Chlorite	77

Table 6.14. Estimated seawater contributions to various ore facies based on Sr isotopic composition of barite and chlorite (Appendix C7).

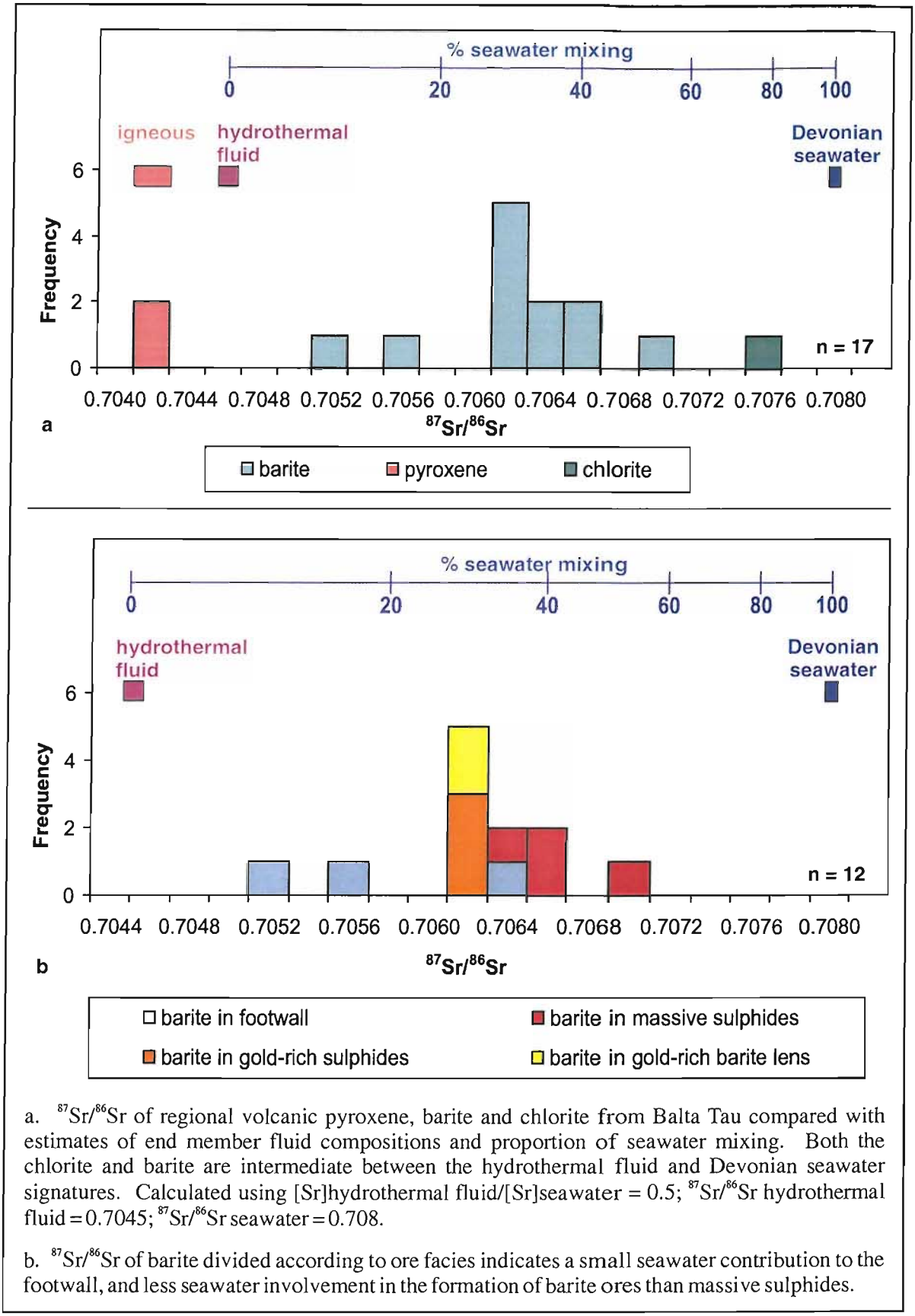

a. $^{87}Sr/^{86}Sr$ of regional volcanic pyroxene, barite and chlorite from Balta Tau compared with estimates of end member fluid compositions and proportion of seawater mixing. Both the chlorite and barite are intermediate between the hydrothermal fluid and Devonian seawater signatures. Calculated using [Sr]hydrothermal fluid/[Sr]seawater = 0.5; $^{87}Sr/^{86}Sr$ hydrothermal fluid = 0.7045; $^{87}Sr/^{86}Sr$ seawater = 0.708.

b. $^{87}Sr/^{86}Sr$ of barite divided according to ore facies indicates a small seawater contribution to the footwall, and less seawater involvement in the formation of barite ores than massive sulphides.

Figure 6.22. Mixing of hydrothermal fluids and seawater as indicated by Sr isotope compositions of gangue phases from Balta Tau.

6.5.5 Footwall, hanging-wall and regional alteration

Introduction

The whole rock oxygen isotope composition of altered rocks is a function of a number of factors, including the original rock $\delta^{18}O$, fluid $\delta^{18}O$, water:rock ratio (W/R), temperature and final mineralogy of the sample. The following sections investigate the fluid:rock ratios and temperature of alteration of footwall and hanging-wall mine sequences and regional volcanics based on whole rock $\delta^{18}O$. In all cases, the initial rock $\delta^{18}O$ is taken as +7.3‰ based on analyses of unaltered pyroxene phenocrysts from regional volcanic samples (Section 6.5.1), and the fluid $\delta^{18}O$ is taketo be -2‰, based on estimates of Devonian seawater. The following equation is used for calculating $\delta^{18}O$ - water:rock ratio curves (Taylor, 1977):

$$\delta^{18}O_{(\text{rock final})} = [\delta^{18}O_{(\text{rock initial})} + (\delta^{18}O_{(\text{fluid})} + \delta^{18}O_{(\text{rock-fluid})}) * W/R] / (1 + W/R)$$

Where $\delta^{18}O_{(\text{rock-fluid})}$ is the fractionation between the rock (based on constituent minerals) and the fluid for a given temperature. This equation is simple and provides a first approximation for estimating water:rock ratios which is useful for the purposes of this study, but is limited in that is can only account for unidimensional processes. More sophisticated two and three dimensional modelling suggests that large isotopic variations may result from a number of additional factors (e.g. Cathles, 1983; Baumgartner and Rumble, 1988), however modelling at this level is beyond the scope of this project.

Mine sequences

The variation in whole rock $\delta^{18}O$ with increasing water:rock ratios has been calculated for a series of temperatures between 100 and 250°C. Separate calculations have been performed for each of three end member rock compositions which approximately represent the footwall and hanging-wall samples (compositions are listed in Table 6.4): 50% chlorite, 50% quartz, Figure 6.23a (for footwall samples comprising quartz-chlorite and quartz-chlorite-muscovite); 100% chlorite, Figure 6.23b (for one footwall sample comprising almost entirely chlorite) and 100% sericite, Figure 6.23c (for the hanging-wall sample). Both footwall and hanging-wall $\delta^{18}O$ can be best explained by low temperature alteration at 125 to 150°C, comparable with temperature estimates from fluid inclusions in footwall quartz and chlorite composition geothermometry. They are indicative of high water:rock ratios greater than 1, consistent with the complete lack of primary mineralogy and partial to complete overprinting of primary igneous textures.

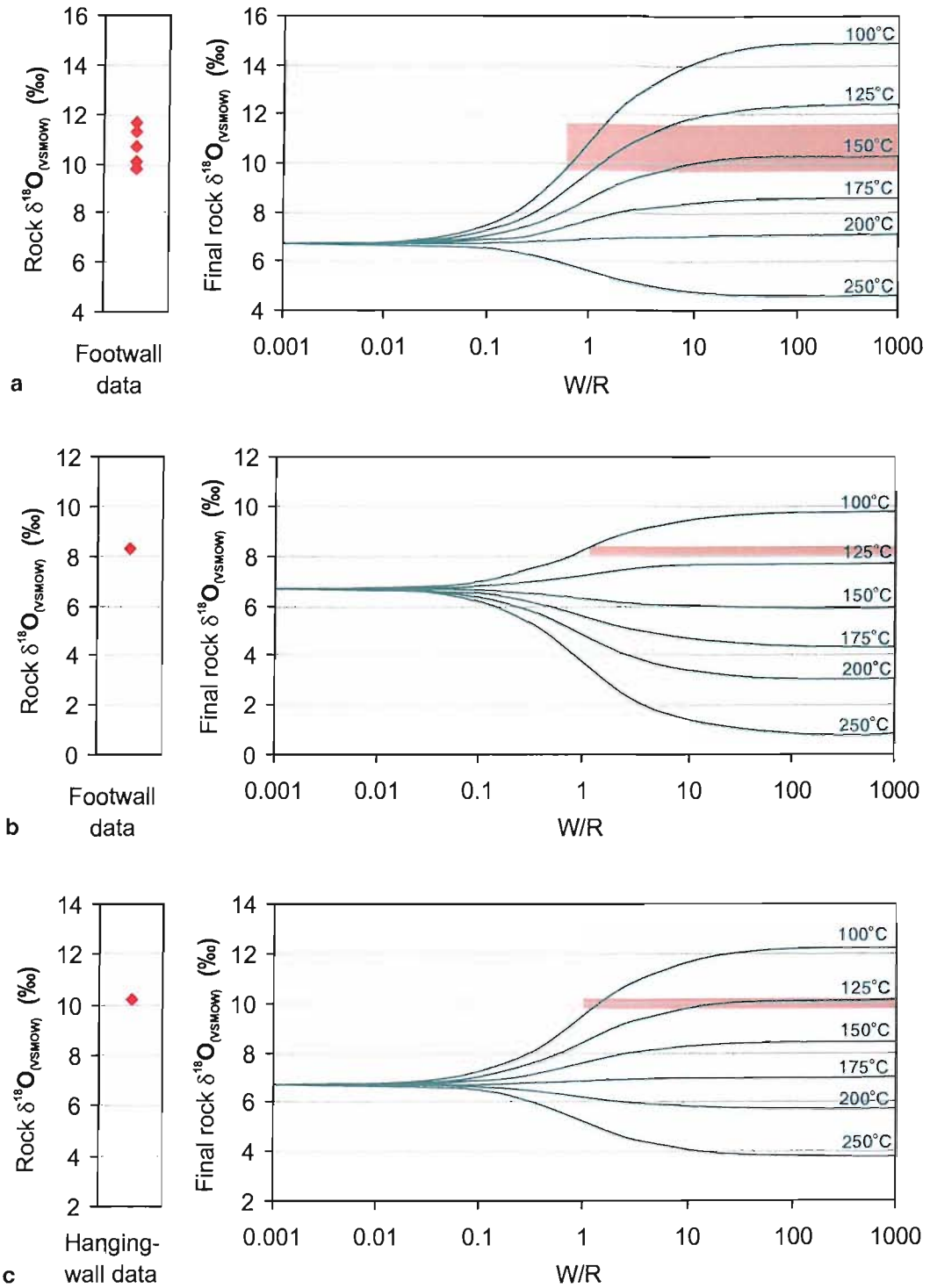

Final whole rock $\delta^{18}O$ as a function of water:rock ratio (W/R) for temperatures between 100 and 250°C (using the equation of Taylor, 1977 with initial rock $\delta^{18}O$ of +7.3‰ and a fluid $\delta^{18}O$ of -2‰), calculated for final rock compositions of (a) 50% quartz, 50% chlorite; (b) 100% chlorite; and (c) 100% muscovite (see Appendix C5 for mineral-water fractionation equations). (a) and (b) are appropriate for footwall compositions and (c) for hanging-wall compositions. Data points to the left are whole rock $\delta^{18}O$ of altered mine sequences. Alteration of both the footwall and the hanging-wall are estimated to have taken place at low temperatures of 125 to 150°C with fluid:rock ratios of at least 1 (indicated by red shaded areas).

Figure 6.23. Alteration of whole rock $\delta^{18}O$ in mine sequences as a function of water:rock ratio and temperature.

Regional volcanics

The whole rock $\delta^{18}O$ of regional volcanics varies from +8.4 to +12.2‰ and does not correlate with the intensity of alteration. Due to the more complicated mineralogy of the regional samples, it is impractical to plot $\delta^{18}O$ - W/R curves for each final whole rock composition. The plagioclase-H_2O fractionation (using the equation of O'Neil & Taylor, 1967) may be used as a good approximation for the fractionation between silicate alteration minerals and H_2O (Green et al., 1981). Figure 6.24a shows curves for $\delta^{18}O$ - W/R based on plagioclase-H_2O fractionation. Curves have also been plotted for a typical alteration assemblage in Irendyk samples (Figure 6.24b) and are very similar over the temperature range of 100 to 250°C, supporting the use of plagioclase as an approximation for the low grade alteration assemblages found in regional samples.

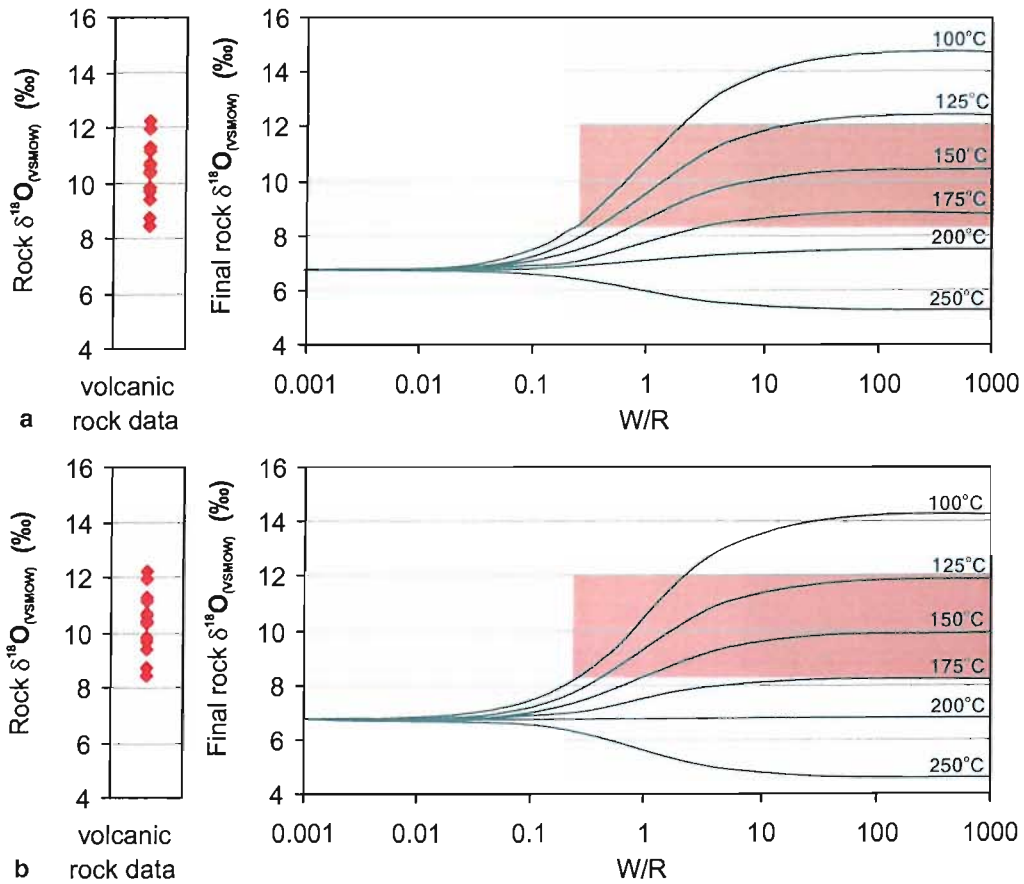

a. Final whole rock $\delta^{18}O$ as a function of water:rock ratio (W/R) for temperatures between 100 and 250°C (using the equation of Taylor (1977) with initial rock $\delta^{18}O$ of +7.3‰ and a fluid $\delta^{18}O$ of -2‰). Plagioclase is used as an approximation of the final rock composition (using the plagioclase-water fractionation equation of O'Neil & Taylor, 1967). Data points to the left are the whole rock $\delta^{18}O$ of regional volcanics, and the red shaded area indicates the estimated range in fluid:rock ratios and temperatures for regional alteration.

b. Recalcuation of the graph in (a) for a final rock composition based on a typical alteration assemblage for Irendyk samples (20% quartz, 20% plagioclase, 20% chlorite, 20% muscovite, 10% epiote and 10% zeolite; see Appendix C5 for fractionation equations). The $\delta^{18}O$ - water:rock ratio curves are very similar to those in (a).

Figure 6.24. Alteration of whole rock $\delta^{18}O$ in regional volcanic rocks as a function of water:rock ratio and temperature.

The low temperature regional alteration produces final whole rock $\delta^{18}O$ which are consistently ^{18}O enriched relative to the unaltered volcanics (7.3‰), and consequently the seawater involved in alteration will become ^{18}O depleted relative to the original seawater composition. This contrasts with many VMS districts where higher temperature regional alteration causes the whole rock $\delta^{18}O$ to become ^{18}O depleted (e.g. in Figure 6.24 it can be seen that at temperatures above 200°C, whole rock $\delta^{18}O$ values decrease with alteration), and interacting fluids will become ^{18}O enriched relative to coeval seawater. A similar low grade regional alteration has been identified in the volcanic rocks hosting Kuroko deposits in Japan, where alteration results in diagenetic/hydrothermal fluids which are significantly ^{18}O depleted relative to seawater (Pisutha-Arnond and Ohmoto, 1983).

6.5.6 Sulphide $\delta^{34}S$ systematics

Introduction

The sulphur isotopic composition of sulphides in VMS deposits is frequently interpreted to directly reflect the $\delta^{34}S$ of sulphur sources. However, processes such as equilibrium or kinetic fractionation between aqueous sulphur species prior to precipitation, and between sulphides and H_2S during precipitation, may alter the sulphide $\delta^{34}S$ from that of the source. This section evaluates the effects of these processes to enable the sources of sulphur to be more reliably determined (Section 6.5.7).

Equilibrium between aqueous sulphur species

The abundance of barite in Balta Tau ores indicates that significant sulphate was present during ore precipitation. If sulphur isotopic equilibrium was achieved between H_2S and aqueous SO_4^{2-}, then the difference in $\delta^{34}S$ of sulphides and sulphates would be a function of temperature. Assuming isotopic equilibrium, the difference in $\delta^{34}S$ (written as $\Delta^{34}S$) between sulphides and barite at Balta Tau indicates a maximum temperature range of 220 to 500°C with an average of 380 to 420°C (Figure 6.25, based on fractionation equations of Ohmoto & Rye, 1979); data from individual samples yields a narrower range of 310 to 490°C (Table 6.15). These temperatures are unrealistically high compared with other geothermometry for Balta Tau (sulphide phase equilibria, chlorite compositions and fluid inclusions), indicating disequilibrium with respect to sulphur isotopes during precipitation of sulphide and sulphate phases. It is possible that these temperatures relate to equilibrium fractionation between H_2S and SO_4^{2-} in deeper, hotter parts of the system, since the slow rate of S exchange between sulphide and sulphate (Ohmoto and Lasaga, 1982) means that hydrothermal fluids cooling rapidly during ascent to the seafloor may not have had time to re-equilibrate before precipitation (Ohmoto and Goldhaber, 1997). This effect is reported from porphyry-epithermal systems where mineralising fluids carry both reduced and oxidized sulphur species, but is less likely to be applicable to VMS deposits because studies of modern

systems suggest that the hydrothermal fluids contain negligible sulphate at depth (e.g. Butterfield and Massoth, 1994; Von Damm, 1995).

Ore facies	Sample number	$\delta^{34}S$ (‰) barite	$\delta^{34}S$ (‰) sulphide	$\Delta\delta^{34}S$ (‰)	temperature (°C)
Footwall mainstage	01BT068	+17.6	chp +2.4	+15.2	490
Footwall mainstage	01BT068	+17.6	sph +2.4	+15.2	475
Footwall mainstage	01BT068	+17.6	ten +1.9	+15.7	470
Massive sulphides	903	+20.4	py +0.2	+20.2	310
Massive sulphides	01BT169	+20.3	sph +1.1	+19.2	350
Barite-rich sulphides	01BT082	+18.6	chp -0.5	+19.1	365
Barite-rich sulphides	01BT082	+18.6	py -1.6	+20.2	310
Barite-rich sulphides	01BT082	+18.6	sph +1.6	+17.0	410
Barite-rich sulphides	01BT082	+18.6	ten -0.3	+18.9	370
Barite lens	01BT226	+18.1	chp -1.5	+19.5	355
Barite lens	01BT226	+18.1	gal -3.3	+21.4	345
Barite lens	01BT226	+18.1	ten -2.0	+20.0	340
Barite lens	00BT08	+18.1	ten -1.2	+19.3	360
Barite lens	905	+17.6	sph +1.6	+16.0	450

Table 6.15. Estimates of formational temperatures assuming sulphur isotopic equilibrium between barite and sulphides. Calculations based on equations from Ohmoto and Rye, 1979 (Appendix C5). Temperatures are unrealistically high indicating isotopic disequilibrium during precipitation.

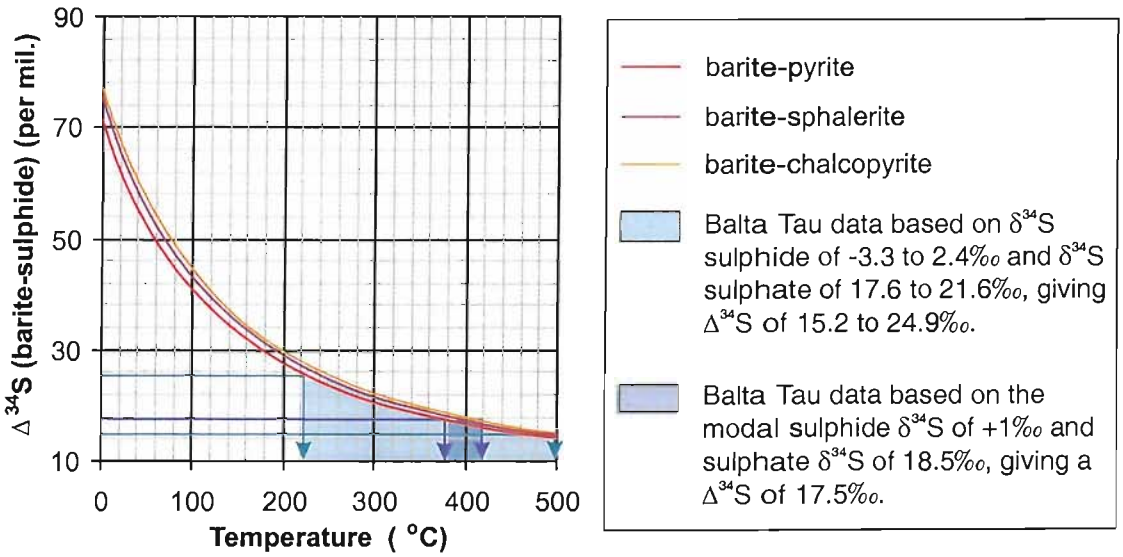

Fractionation of sulphur isotopes between barite and various sulphides as a function of temperature assuming isotopic equilibrium (based on equations from Ohmoto and Rye, 1979). Balta Tau sulphide and sulphate data give formational temperatures in the range 220 to 500°C, with the modal sulphide-sulphate signatures indicating temperatures of 380 to 420°C.

Figure 6.25. Equilibrium sulphur isotope fractionation between barite and sulphide phases.

Equilibrium between sulphide phases

Sulphide phases precipitating in sulphur isotopic equilibrium will follow the trend $\delta^{34}S$(pyrite) > $\delta^{34}S$(sphalerite) > $\delta^{34}S$(chalcopyrite) > $\delta^{34}S$(galena) (based on fractionation equations from Ohmoto & Rye, 1979). The sulphides analysed from Balta Tau do not reflect this trend, but show a systematic variation with $\delta^{34}S$(sphalerite) > $\delta^{34}S$(pyrite) irrespective of ore facies (Figures 6.8a, 6.9a). Assuming equilibrium fractionation, formational temperatures calculated from pairs of co-precipitated sulphides are unrealistic and highly scattered, ranging from <0 to 680°C (Table 6.16), and in a number of cases temperatures can not be calculated. This suggests that sulphide phases did not precipitate in sulphur isotopic equilibrium, which is consistent with the rapid nature of sulphide precipitation observed in modern seafloor systems.

The systematic ^{34}S enrichment in sphalerite relative to pyrite may be explained by temporal differences in fluid $\delta^{34}S$, since it is feasible that the majority of pyrite precipitated earlier than the majority of sphalerite (for example, in the footwall, pyrite is most abundant in central veins which may pre-date peripheral sphalerite dominated zones; pyrite dominates stratigraphically lower massive sulphides whereas sphalerite dominates upper massive and marginal layered ores; in barite-rich ores most of the pyrite is clastic and formed earlier than the other sulphides). Temporal differences in fluid $\delta^{34}S$ were also proposed by Duckworth et al. (1995) to explain systematic, disequilibrium variations between chalcopyrite and pyrite $\delta^{34}S$ from the active Broken Spur site.

Ore facies	Sample number	sulphide $\delta^{34}S$ (‰)		$\Delta\delta^{34}S$ (‰)	temperature (°C)
footwall mainstage	01BT152	py: +0.9	chp: +1.4	-+0.5	n/a
footwall mainstage	01BT003	sph +2.4	chp -0.2	+2.6	< 0
footwall mainstage	00BT01	py -0.2	sph +0.0	-0.2	n/a
footwall mainstage	00BT01	py -0.2	chp -0.7	+0.5	680
footwall mainstage	00BT01	sph 0.0	chp -0.7	+0.7	190
footwall mainstage	01BT058	sph +1.7	chp +0.5	+1.2	80
footwall mainstage	01BT068	sph +2.4	chp +2.4	0.0	n/a
footwall mainstage	01BT130	sph +1.5	chp +0.6	+0.9	135
footwall mainstage	01BT130	sph +1.5	gal -1.2	+2.7	245
footwall mainstage	01BT130	chp +0.6	gal -1.2	+1.8	295
footwall mainstage	01BT127	py +1.5	gal -0.8	+2.3	395
layered sulphides	01BT032	sph +1.9	chp +1.6	+0.3	430
barite-rich sulphides	01BT082	sph +1.6	chp -0.5	+2.1	< 0
barite lens	01BT226	chp -1.5	gal -3.3	+1.8	295
barite lens	01BT226b	chp -1.2	gal -1.2	0.0	n/a

Table 6.16. Temperature estimates based on conventional $\delta^{34}S$ analyses of co-precipitated sulphides. (Calculated using equations of Ohmoto and Rye, 1979 (Appendix C5).

$\delta^{34}S$ of hydrothermal fluid H_2S

The lack of evidence for sulphur isotopic equilibrium between sulphides and sulphate or between sulphide phases indicates that equilibrium fractionation is not an important influence over the $\delta^{34}S$ of sulphides. Kinetic effects during disequilibrium precipitation of sulphides are likely to be small, since these effects are usually less than the equilibrium fractionation and are smaller at fast reaction rates and elevated temperatures (Ohmoto and Goldhaber, 1997). Therefore the sulphide $\delta^{34}S$ are likely to directly reflect the $\delta^{34}S$ of hydrothermal fluid H_2S, with a signature of +1‰ ±1.5.

6.5.7 Sulphide sulphur sources

Sources of reduced sulphur in VMS deposits

The sulphide $\delta^{34}S$ of most VMS deposits varies from 0 to 10‰ in modern systems (Figure 6.26) and 0 to 20‰ in ancient deposits (Figure 6.27).

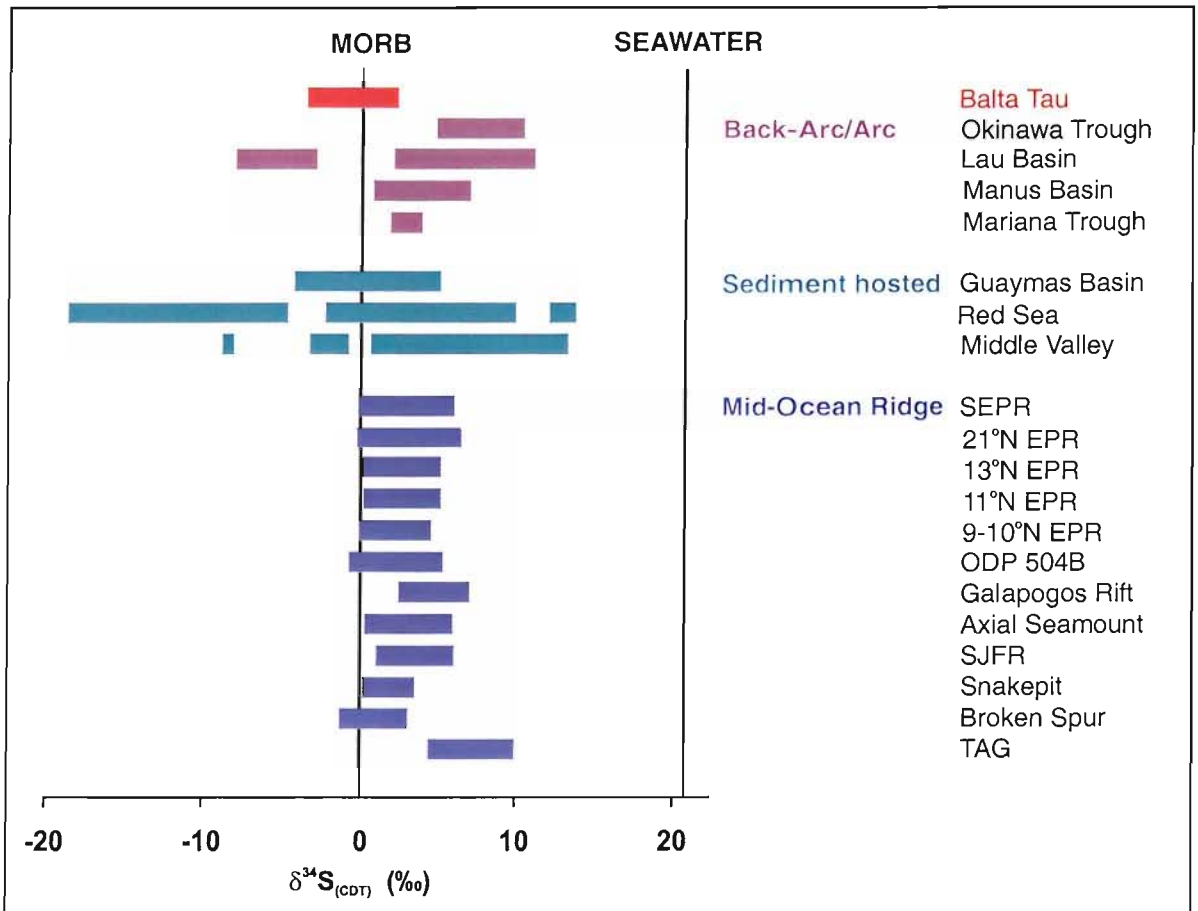

Range of sulphide $\delta^{34}S$ from modern, actively forming VMS deposits. The majority of MOR and arc related systems have compositions intermediate between MORB and seawater sulphate. The ^{34}S depleted sulphides from the Lau Basin reflect a magmatic contribution to sulphur, and the ^{34}S depleted sulphides from sedimented ridges result from baterial reduction of seawater sulphate. Adapted from Shanks et al. (1995; Figure 11).

Figure 6.26. Compilation of sulphide $\delta^{34}S$ from modern VMS systems.

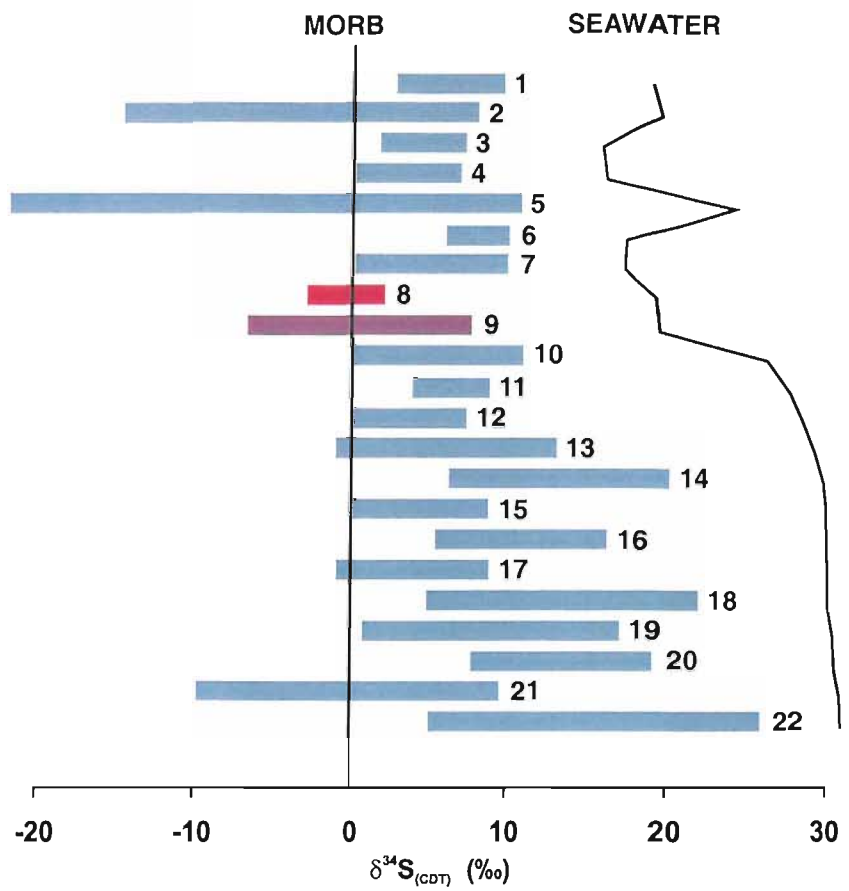

1. Wetar, Indonesia (4)
2. Kuroko, Japan (13)
3. Troodos, Cyprus (80)
4. E. Black Sea, Turkey (95)
5. Iberian Pyrite Belt (343)
6. Trident Glacier District, Alaska (373)
7. Delta District, Alaska (373)
8. Balta Tau, S. Urals, Russia (380)
9. S. Urals, Russia (380)
10. Lachlan, New South Wales (420)
11. Buchans, Newfoundland (434)
12. Notre Dam Bay, Newfoundland (448)
13. Boucher, Bathurst, Newfoundland (465)
14. NFF, Bathurst, Newfoundland (470)
15. Trooper Creek, Mt Windsor, Queensland (468)
16. Thalanga, Mt Windsor, Queensland (471)
17. Lokken, Norway (475)
18. Tilt Cove, Newfoundland (489)
19. Lush's Bight, Newfoundland (495)
20. Central Mt Read, Tasmania (495)
21. S. Meeting Lyell, Tasmania (502)
22. N. Mt Read, Tasmania (503)

Range of sulphide $\delta^{34}S$ for selected Phanerozoic VMS deposits (age in Ma is quoted after each deposit). The majority of sulphides have values intermediate between MORB and seawater sulphate, and there is a correlation between the most ^{34}S enriched sulphides and the $\delta^{34}S$ of contemporaneous seawater sulphate. VMS data are from the compilation of Huston, 1999 (Table 6) except for data from Wetar (Scotney, 2002), the southern Urals (Prokin and Buslaev, 1999) and Balta Tau (this study). Seawater sulphate curve is adapted from Claypool et al. (1980) to correspond with deposit ages.

Figure 6.27. Compilation of $\delta^{34}S$ from ancient VMS systems.

These $\delta^{34}S$ can be explained by variable contributions of sulphur leached from igneous rocks and sulphur derived from the reduction of seawater sulphate. Igneous rocks at mid ocean ridges typically have a $\delta^{34}S$ of 0.1‰ reflecting the mantle composition (Sakai et al., 1984), whereas those

from island arcs may be ^{34}S enriched due to contributions of sulphur from the subducting slab, with typical $\delta^{34}S$ of 5 to 7‰ (Ueda & Sakai, 1984). Seawater sulphate has a present day $\delta^{34}S$ of +21‰ (Rees et al., 1978), which has varied through the Phanerozoic from approximately +12 to +30‰ (Claypool et al., 1980). In ancient deposits a correlation between the most ^{34}S enriched sulphide $\delta^{34}S$ and coeval seawater sulphate $\delta^{34}S$ (Figure 6.27) supports the inference that reduced seawater sulphate provides a significant contribution to sulphides.

Low temperature interaction of seawater with ocean crust in recharge zones (150 to 250°C) removes sulphate from seawater by the precipitation of anhydrite (Bowers, 1989; Alt et al., 1989). In deeper parts of the hydrothermal system (with temperatures of around 350°C and a fluid:rock ratio of around 1) there is complete and rapid reduction of the remaining sulphate with minimal fractionation, producing reduced sulphur with a $\delta^{34}S$ equal to that of the initial seawater sulphate (Alt et al., 1989). Interactions in this high temperature zone also leach igneous sulphur from the ocean crust (Shanks et al., 1981; Bowers, 1989; Alt et al., 1989). Two mechanisms have been proposed to account for the variations in sulphide compositions resulting from contributions of igneous sulphur and reduced seawater sulphate:

1. Variable contributions from leaching of igneous sulphur and reduction of seawater sulphate at depth, producing upwelling hydrothermal fluids with variable $\delta^{34}S$ which are reflected in the sulphide compositions (Bluth & Ohmoto, 1989).

2. Ascending hydrothermal fluids have a consistent $\delta^{34}S$ of +1 to +1.5‰ due to the buffering capacity of basalt during deep hydrothermal fluid circulation (Bowers, 1989), and variations in the $\delta^{34}S$ of venting hydrothermal fluids and sulphide minerals is due to variable contributions of seawater sulphate reduced at or close to the seafloor site of mineralization (Bowers, 1989). An important implication of this model is that the sulphide $\delta^{34}S$ will not necessarily reflect the total component of reduced seawater sulphate, since contributions made early in the fluid's history may be overprinted by continued interaction with basalt. The sulphide $\delta^{34}S$ will however provide an indication of seawater sulphate reduction soon before or during sulphide precipitation (Bowers, 1989). Buffering of fluid $\delta^{34}S$ is suggested to result from simultaneous oxidation of pyrrhotite in basalt and reduction of seawater sulphate by a reaction such as:

$$7FeS + 8H^{+} + SO_4^{2-} = 4FeS_2 + 4H_2O + 3Fe^{2+} \quad (6.1)$$

(Shanks and Seyfried, 1987). This produces pyrite with $\delta^{34}S$ of +2.7‰ (based on igneous sulphur with $\delta^{34}S$ of 0.1‰ and seawater sulphate with $\delta^{34}S$ of +21‰), and fluids in equilibrium with this pyrite at 300°C would have H_2S with $\delta^{34}S$ of +1.5‰ (Alt et al., 1989).

These mechanisms are based on studies of mid ocean ridge systems. Seawater interaction with island arc volcanics may produce different fluid $\delta^{34}S$ since the igneous sulphur tends to be $\delta^{34}S$ enriched relative to MORB, reflected in the more ^{34}S enriched sulphide compositions in modern arc systems compared with MOR systems (Figure 6.26). In addition, intermediate to felsic arc volcanics are more oxidised which may alter the mechanism by which seawater sulphate and igneous sulphur are incorporated into hydrothermal fluid.

In addition to reduced seawater sulphate and leached igneous sulphur, sources of reduced sulphur in VMS systems may include:

1. A direct input from SO_2-rich magmatic fluids. At high temperatures magmatic SO_2 (with a $\delta^{34}S$ of approximately 0‰) directly oxidises to produce H_2S with the same isotopic signature, and this is therefore indistinguishable from sulphur contained within MORB-like igneous rocks. However, at temperatures below 300 to 400°C magmatic SO_2 dissociates into H_2S and HSO_4^-, resulting in a significant fractionation of ^{34}S due to kinetic effects, such that the H_2S is ^{34}S depleted and SO_4^{2-} is ^{34}S enriched (Ohmoto & Rye, 1979). Sulphide-sulphate $\delta^{34}S$ reflecting dissociated magmatic SO_2 is commonly reported from porphyry-epithermal systems, and rarely from VMS systems (e.g. the modern Hine Hina field, Juan de Fuca Ridge, where sulphide $\delta^{34}S$ ranges from -2.8 to -7.7‰; Herzig et al., 1998).

2. Bacterial reduction of seawater sulphate at the seafloor, which produces reduced sulphur that is approximately 40‰ lighter than the coeval seawater sulphate due to kinetic fractionation effects (Ohmoto & Goldhaber, 1997). The influence of baterially derived sulphur is particularly noticeable in deposits located at sediment covered ridges (Figure 6.26).

Sources of reduced sulphur at Balta Tau

The $\delta^{34}S$ of hydrothermal fluids responsible for ore formation at Balta Tau is estimated to be around +1‰ ±1.5 (Section 6.5.6) which is consistent with igneous derived sulphur. The absence of a strong seawater signature indicates little or no reduction of seawater sulphate at the site of mineralization, although there may have been a significant contribution at depth which was overprinted by continued rock interaction (Bowers, 1989).

Following the model of Bowers (1989), the simultaneous reduction of seawater sulphate ($\delta^{34}S$ of +17.5‰ in the Emsian, Devonian, Claypool et al., 1980) and oxidation of basaltic pyrrhotite with 0.1‰ (equation 6.1) would result in pyrite with a $\delta^{34}S$ of around +2.3‰ and a hydrothermal fluid in equilibrium with this pyrite would have a fluid $\delta^{34}S$ of +1.1‰. This is consistent with the estimated $\delta^{34}S$ for Balta Tau hydrothermal fluid, and suggests that the source volcanics had a MORB-like $\delta^{34}S$ signature.

The sulphide $\delta^{34}S$ at Balta Tau are anomalous compared with the majority of ancient and modern VMS systems, which generally display a wider range of $\delta^{34}S$ and a discernable seawater sulphate component (Figures 6.26, 6.27). However, Balta Tau is less anomalous when compared to the regional trend in sulphide $\delta^{34}S$ from VMS deposits of the southern Urals hosted in the same or similar island arc sequences. These deposits span a strike of over a 300km along the arc and are characterised by isotopically light and tightly clustered sulphide $\delta^{34}S$ (Table 6.17), suggesting the unusual sulphide $\delta^{34}S$ of Balta Tau is part of a regional trend rather than specific to Balta Tau deposit.

Deposit	Host volcanics, tectonic setting	n	$\delta^{34}S$ minimum	$\delta^{34}S$ maximum	$\delta^{34}S$ mean
Balta Tau	Baimak-Buribai/Irendyk, island arc	57	-3.3	+2.4	+0.5
Buribai	Baimak-Buribai, fore-arc/arc	10	-1	+4	+1
Sibai	Karamalytash, back arc	130	-2	+7	+3
Molodeznoye	Baimak-Buribai/Irendyk island arc	16	0	+5	+3
Yubileinskoye	Baimak-Buribai/Irendyk island arc	53	-2	+8	+2
Uzelga	Baimak-Buribai/Irendyk island arc	224	-5	+5	+1
Uchaly	Baimak-Buribai/Irendyk island arc	80	-5	+1	+2
Gai	Baimak-Buribai/Irendyk island arc	120	-4	+4	-1
Makan	Baimak-Buribai/Irendyk island arc	68	-4	+5	-2
Podolskoye	Baimak-Buribai/Irendyk island arc	223	-7	+1	-3

Table 6.17. Range in sulphide $\delta^{34}S$ of a number of VMS deposits in the southern Urals. Data from Prokin and Buslaev, 1999 (values are estimated to the nearest 1‰ from a graphical representation of the mean and range); data for Balta Tau from this study.

Although broadly consistent with an igneous source, some sulphides from Balta Tau are ^{34}S depleted with $\delta^{34}S$ values lighter than 0‰ and there is a suggestion that the most significant ^{34}S depletion occurs in upper barite-rich ore horizons (Figure 6.9b) although more data is required to confirm this trend. A stratigraphic influence over sulphide $\delta^{34}S$ is noted from other ancient VMS deposits and is generally attributed to temporal variations in fluid flow regime and the extent of seawater sulphate reduction (e.g. Huston, 1999). However, the isotopically light values at Balta Tau are more ^{34}S depleted than both the seawater sulphate and igneous sources and cannot therefore reflect variations in seawater sulphate contribution. Sulphides with $\delta^{34}S$ lighter than igneous sulphur are also characteristic of the southern Urals VMS deposits (Table 6.17), although deposit scale zoning is not reported with the exception of Uzelga where a decrease in sulphide $\delta^{34}S$ is noted up stratigraphy (Prokin and Buslaev, 1999), consistent with the trend in Balta Tau data. Possible sources of the ^{34}S depleted sulphur at Balta Tau and other deposits in southern Urals could be:

1. A small proportion of bacterially reduced seawater sulphate (with $\delta^{34}S$ of around -20‰) mixing with hydrothermal fluid H_2S to produce sulphides with a slight ^{34}S depletion (e.g. the Yaman Kasy deposit, Herrington et al., 1998). However, an additional source with such a different isotopic composition would have to be thoroughly mixed with the fluid H_2S in order to produce the small ^{34}S depletion observed in the Balta Tau sulphides. This degree of homogenisation is unlikely to occur during rapid precipitation in a seafloor environment, where a contribution of bacterially reduced sulphur would more likely result in a bimodal population with more extreme and variable ^{34}S depletion in sulphides. A consistent contribution is also unlikely to occur on a regional scale, particularly given the scarcity of sediment horizons in the arc volcanic sequences.

2. A direct contribution of ^{34}S depleted reduced sulphur from the low temperature (<300 to 400°C) dissociation of magmatic SO_2 during late stages of ore precipitation. However, a corresponding magmatic signature is not seen in the sulphate $\delta^{34}S$ (Section 6.5.8) and there is no indication of a significant magmatic contribution to ore forming fluids (Section 6.5.3).

6.5.8 Formation of sulphates

Introduction

The majority of sulphate in VMS deposits precipitates either as anhydrite or barite. Anhydrite displays retrograde solubility and will readily dissolve in seawater at temperatures below 150° C, resulting in multiple stages of precipitation and dissolution which complicates the interpretation of isotopic data (Blout and Dickson, 1969; Bischoff and Seyfried, 1978; Teagle et al., 1998). By contrast, barite is relatively insoluble under typical hydrothermal conditions (Blout, 1977) and is therefore likely to remain stable after precipitation in a seafloor hydrothermal environment. Textural evidence of barite dissolution has been reported from the Kita-Bayonnaise Caldera, Izu-Ogasawara Arc, NW Pacific where euhedral barite crystals overgrow corroded barite cores (Iizasa et al., 1997), however this is an unusual occurrence and is not observed in samples from Balta Tau. This, together with textural evidence for barite-sulphide co-precipitation, suggests that the isotopic signatures of barite from Balta Tau may be directly related to fluid properties and processes during ore formation.

The sulphate in VMS deposits may be derived from one or more of the following sources, which can in most cases be distinguished by their $\delta^{34}S$ signature:

1. Directly from coeval seawater (with $\delta^{34}S$ varying from +13 to +30‰ during the Phanerozoic; Claypool et al., 1980).

2. Dissociation of magmatic SO_2 (discussed in Section 6.5.7), producing sulphate $\delta^{34}S$ greater than 0‰ but generally less than seawater sulphate (e.g. values of +16.2 to +16.7 from the modern Hine Hina field, Herzig et al., 1998).
3. Oxidation of H_2S, which causes minimal fractionation of sulphur and produces sulphate with $\delta^{34}S$ equal to that of the H_2S (Ohmoto and Goldhaber, 1997).

Equilibrium fractionation and kinetic effects

It has already been established (Section 6.5.6) that the barite and sulphides, and therefore aqueous SO_4^{2-} and H_2S, were not in sulphur isotopic equilibrium during precipitation. The equilibrium fractionation between aqueous sulphate and barite is probably insignificant, (e.g. +1.65‰ reported for evaporites, Claypool et al., 1980). Kinetic effects relating to precipitation from aqueous sulphate are also likely to be insignificant, since they are typically smaller than the equilibrium fractionation and are reduced at elevated temperatures. The barite $\delta^{34}S$ is therefore likely to reflect the $\delta^{34}S$ signature of the sulphate source.

Equilibration rates for oxygen between aqueous SO_4^{2-} and H_2O are orders of magnitude faster than those for sulphur between SO_4^{2-} and H_2S (Table 6.18), therefore barite $\delta^{18}O$ may reflect an approach to equilibrium with the ore forming fluid rather than the $\delta^{18}O$ of the sulphate source. As with sulphur, the equilibrium and kinetic effects between aqueous sulphate and barite during precipitation are likely to be very small at elevated temperatures.

temperature (ºC)	SO_4^{2-} - H_2S (pH = 4-7), time to reach 90% equilibrium †	SO_4^{2-} - H_2O, time to reach 90% equilibrium *
100	4 x 10^5 yrs	9 yrs (ph = 3); 430 yrs (pH = 4)
150	4 x 10^3 yrs	-
200	90 yrs	38 hrs (ph = 4); 125 days (pH = 5)
250	4.4 yrs	-
300	140 days	38 hrs (ph = 6); 20 days (pH = 7)

Table 6.18. Time taken to reach isotopic equilibrium between aqueous sulphate and H_2S and H_2O. Based on experimental data from †Ohmoto and Lasaga, 1982 and *Chiba and Sakai, 1985.

Sources of sulphate and processes influencing $\delta^{34}S$ and $\delta^{18}O$ for Balta Tau barite

The sulphate $\delta^{34}S$ has a distinct mode at +18‰ (Figure 6.10a), which coincides well with the estimated composition of seawater sulphate in the Emsian epoch of the Devonian of +18 ±2‰ (Figure 6 in Claypool et al. 1980). This suggests that the sulphate component of the barite is likely to have been derived directly from seawater. Three barite samples are significantly ^{34}S enriched relative to the seawater composition, which cannot be explained by the addition of magmatically derived sulphate or by oxidation of H_2S, since both of these result in ^{34}S depletion relative to

seawater sulphate. The ^{34}S enrichment could result from localised partial reduction of seawater sulphate at the seafloor, whereby isotopically light sulphate is preferentially reduced thus enriching the remaining sulphate in ^{34}S. The barite $\delta^{34}S$ of +20.3‰ to 21.6‰ would require around 12 to 16% seawater sulphate reduction in either an open or closed system (Figure 6.28; both yield similar results at low levels of reduction; based on equations in Ohmoto and Goldhaber, 1997 and Ohmoto and Lasaga, 1982). The resultant reduced sulphur would have $\delta^{34}S$ of around 0 to +1.5‰, which is indistinguishable from the hydrothermal fluid H_2S (Section 6.5.6).

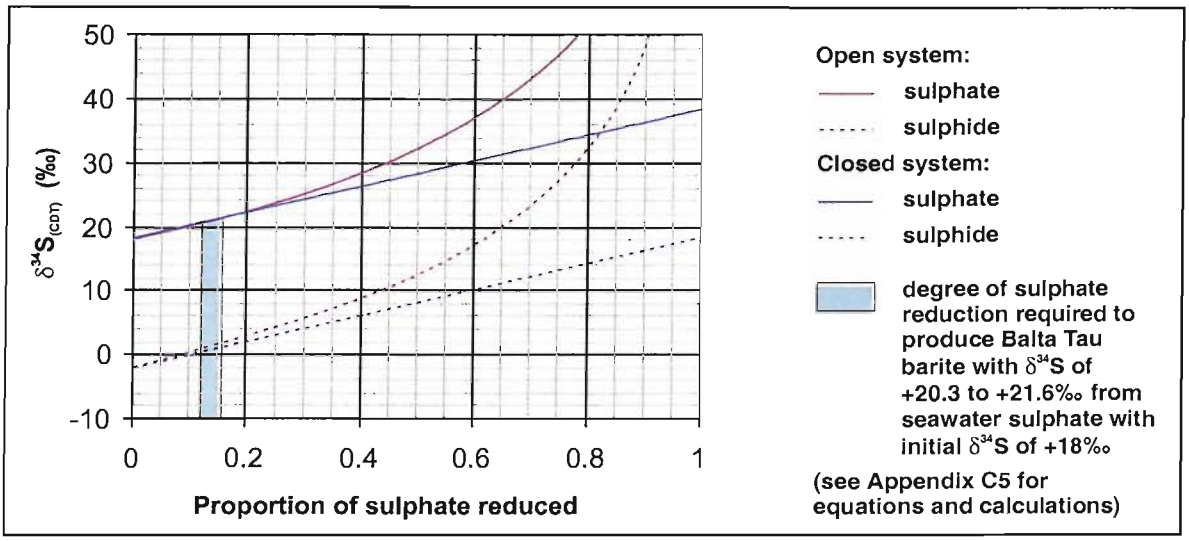

Figure 6.28. Sulphur isotopic fractionation during reduction of seawater sulphate.

The barite $\delta^{18}O$ is significantly ^{18}O depleted relative to the estimated Devonian seawater sulphate signature of +13 ±2‰ (Figure 10 in Claypool et al., 1980). This difference can not be explained by partial seawater sulphate reduction since this would cause ^{18}O enrichment, but is consistent with oxygen exchange between the barite and fluid H_2O towards isotopic equilibrium. Using a fluid $\delta^{18}O$ of 0‰ (consistent with derivation from Devonian seawater interacting with ocean crust) gives temperature estimates based on equilibrium fractionation that are consistent with fluid inclusion temperatures (Figure 6.29). Conversely, combining fluid inclusion data with barite $\delta^{18}O$ yields a fluid $\delta^{18}O$ consistent with derivation from seawater interacting with oceanic crust, as shown in Section 6.5.2. These realistic estimates suggest that oxygen isotopic exchange between sulphate and the hydrothermal fluid was approaching or had reached equilibrium.

The large quantities of Ba required for the barite ores at Balta Tau are probably derived from the hydrothermal fluid, since the Ba concentration of seawater is very low (5 to 20μg/kg, Hanor, 1995). Therefore mixing between seawater (providing the SO_4^{2-}) and hydrothermal fluid (providing the Ba) must have occurred in order for barite to precipitate, which is consistent with the $^{87}Sr/^{86}Sr$ signature of the barite (Section 6.5.4). The equilibrium and disequilibrium of $\delta^{18}O$

and $\delta^{34}S$ respectively suggest that at least hours to days, but less than years, lapsed between fluid mixing and barite precipitation (Table 6.18), discussed further in Chapter 7, Section 7.4.3.

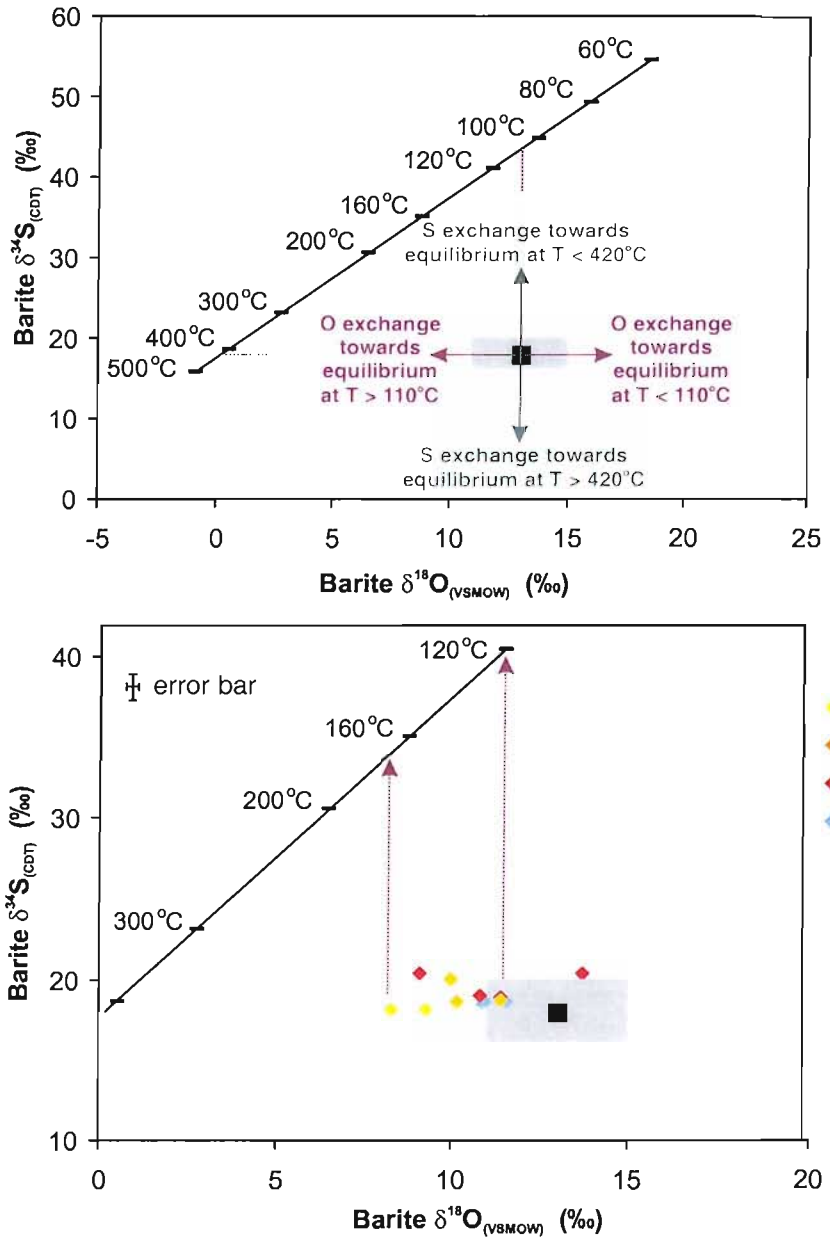

a. Illustration of the effect of S and O exchange with hydrothermal fluid H_2S and H_2O on the isotopic signature of barite precipitated from Devonian seawater sulphate.

b. Barite data from Balta Tau plotted on a portion of the diagram shown in (a). Data is consistent with minimal S exchange between barite and H_2S but significant and variable O exchange between barite and H_2O at temperatures greater than 110°C. The O isotope exchange indicates formational temperatures of 120 to 160°C if the barite had reached isotopic equilibrium with H_2O, or greater than these temperatures if full equilibrium was not attained.

Figure 6.29. Sulphur and oxygen isotopic signatures of barite from Balta Tau compared to values predicted for barite precipitating in equilibrium with H_2O and H_2S.

Ore facies	Number of barite analyses	Estimated temperature (°C)
footwall	3	119 to 133
massive sulphides (py-sph)	4	94 to 149
barite-rich sulphides	3	123 to 140
barite lens	2	149 to 164

Table 6.19. Formational temperatures estimated from barite $\delta^{18}O$. (Calculated using a $\delta^{18}O$ of -2‰ for seawater and 0‰ for the hydrothermal fluid together with mixing proportions calculated from Sr isotopes).

Comparison with sulphate from other VMS deposits

The inference of oxygen isotopic equilibrium between sulphate and fluids at Balta Tau contradicts suggestions that there would be insufficient time for equilibrium to be attained in a seafloor environment (e.g. Chiba and Sakai, 1985; Chiba et al., 1998; Shanks, 2001). However, an alternative explanation has yet to be proposed for the significant difference in $\delta^{18}O$ between seawater sulphate and sulphate minerals which is observed from numerous other deposits (Table 6.20). The barite and anhydrite from deposits listed in Table 6.20 have $\delta^{18}O$ values consistent with O exchange with H_2O towards equilibrium, which may cause ^{18}O enrichment (at temperatures <225°C for anhydrite and <170°C for barite) or ^{18}O depletion (for temperatures >225°C for anhydrite and >170°C for barite) relative to seawater sulphate. The extent to which exchange occurs and degree of equilibrium attained will depend on temperature and rates of cooling/heating, fluid mixing and sulphate precipitation, all of which may vary within and between hydrothermal systems. Therefore temperature estimates from some deposits are close to the formational temperatures (e.g. Wetar), while at others the temperature estimates are considerably lower than those obtained from other geothermometers (e.g. TAG) indicating that equilibrium was not attained. The difference in $\delta^{18}O$ between anhydrite and barite from the Fukazawa deposit is particularly good evidence of shifts in sulphate $\delta^{18}O$ being caused by an approach to isotopic equilibrium, with both minerals indicating similar formational temperatures based on equilibrium oxygen isotope fractionation, while the $\delta^{34}S$ are very similar and reflects a seawater sulphate source.

The $\delta^{34}S$ from anhydrite and barite in Table 6.19 are generally equal to or ^{34}S enriched relative to seawater sulphate, which are best explained by the partial reduction of seawater sulphate at or close to the seafloor, enriching the remaining reservoir in ^{34}S. An exception to this is anhydrite $\delta^{34}S$ from the Manus Basin, where slight ^{34}S depletion may reflect minor oxidation of hydrothermal H_2S; the lack of correlation between $\delta^{34}S$ and $\delta^{18}O$ in these samples suggests that variations in $\delta^{18}O$ are not reflecting this process but may also indicate an approach to oxygen isotopic equilibrium.

deposit	mineral	$\delta^{34}S$ mineral	sw	$\delta^{18}O$ mineral	sw	T from $\delta^{18}O$ (°C)	reference
Wetar Island	barite	22.4 to 28.1	21	5.8 to 11.3	9.3	140 to 240	Scotney, 2002
Mariana BAB	barite	a 21-22	21	6.8 to 9.1	9.3	190 to 210	Kusakabe et al. 1990
Fukazawa Kuroko	barite	19.9 to 23.5	20*	6.4 to 9.4	10.5*	170 to 220	Chiba et al. 1983
Fukazawa Kuroko	anhydrite	20.6 to 23.3	20*	10.8 to 13.6	10.5*	160 to 200	Chiba et al. 1983
TAG-1	anhydrite	21.4 to 23.0	21	6.5 to 9.6	9.3	220 to 290	Chiba et al. 1998
Manus Basin	anhydrite	18.1 to 22.3	21	6.4 to 11.9	9.3	180 to 290	Roberts, 2003 (unpublished)

Table 6.20. Compilation of $\delta^{34}S$ and $\delta^{18}O$ isotope data from barite and anhydrite in other ancient and modern VMS systems. The $\delta^{18}O$ temperature is calculated using the barite-water fractionation equation of Seal et al. (2001) and anhydrite-water equation of Chiba et al. (1981), assuming a fluid $\delta^{18}O$ of +1‰. Notes: *Estimated from reconstructed curves in Claypool et al. (1980); † From Pisutha-Arnond (1983).

Fluid evolution and mixing during the formation of barite

The $^{87}Sr/^{86}Sr$, $\delta^{34}S$ and $\delta^{18}O$ of barite suggest formation during hydrothermal fluid-seawater mixing, and that the barite precipitated at or close to oxygen isotopic equilibrium with the ore forming fluids. Additional information including the extent of conductive heating and cooling of fluids prior to mixing can be attained using barite $^{87}Sr/^{86}Sr$ in conjunction with $\delta^{18}O$ values.

A selection of curves for variable cooling of hydrothermal fluids and heating of seawater (Figure 6.29, equations used in calculations are given in Appendix C8) have been plotted using a $^{87}Sr/^{86}Sr$ of 0.7045 and 0.7080 respectively for hydrothermal fluid and Devonian seawater (Section 6.5.4) and $\delta^{18}O$ of -2‰ for Devonian seawater. The hydrothermal fluid $\delta^{18}O$ has been estimated by analogy with modern systems, where end member hydrothermal fluids are typically +0.5 to +2‰ heavier than coeval seawater (e.g. Shanks et al., 1995); therefore Balta Tau hydrothermal fluids are likely to have had a $\delta^{18}O$ of -1.5 to 0‰. For the graphs in Figure 6.30 a value of -0.5‰ was used, however the curves do not alter significantly for the range -1.5 to 0‰. The concentration of Sr in the hydrothermal fluid and Devonian seawater is not easily estimated, therefore graphs have been plotted for ratios of hydrothermal fluid [Sr]: seawater [Sr] of 0.5, 1 and 2, which cover the range of values generally observed in modern systems (e.g. Von Damm, 1995).

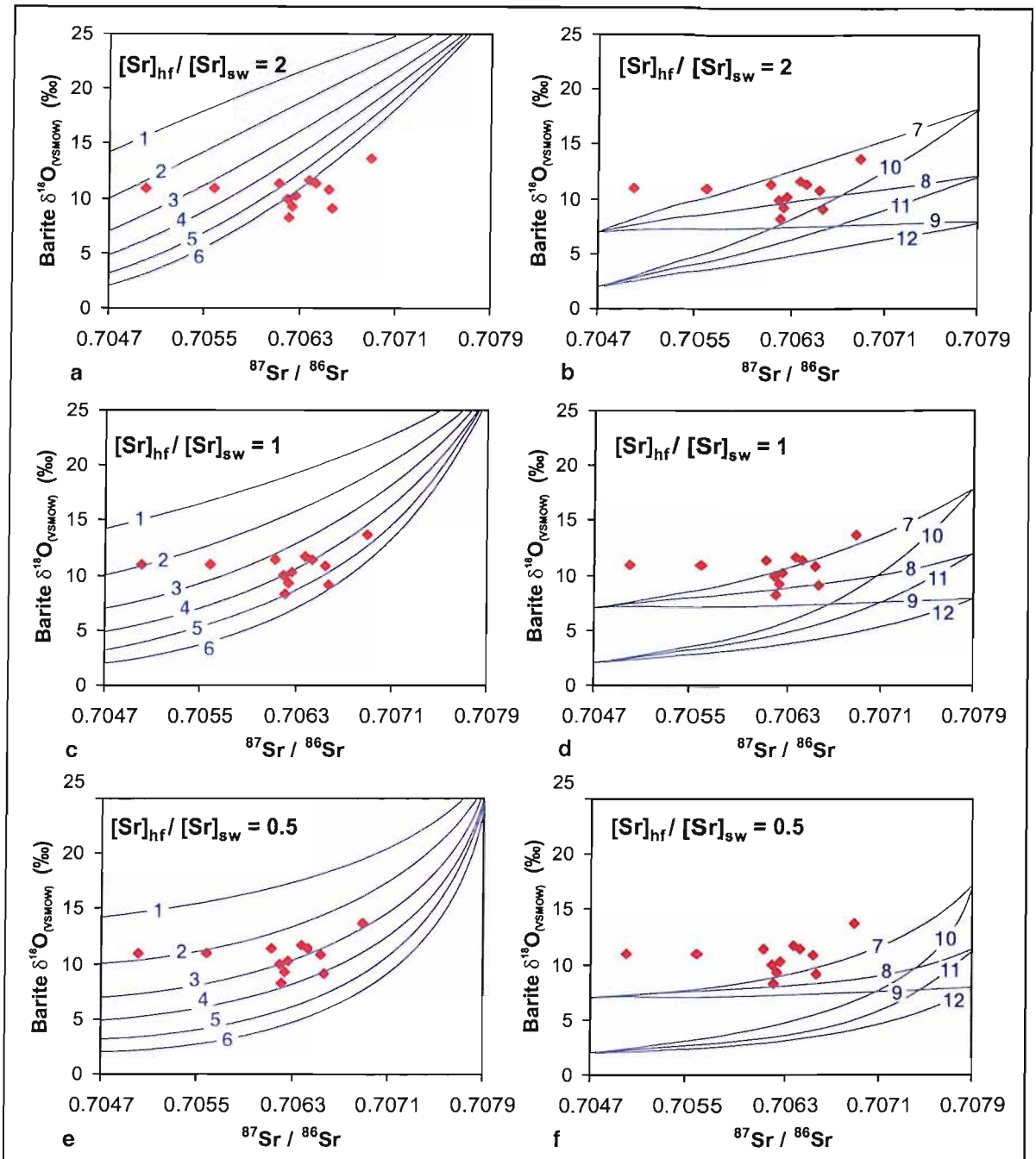

line #	hydrothermal fluid temperature (ºC)	seawater temperature (ºC)
1	100	2
2	150	2
3	200	2
4	250	2
5	300	2
6	350	2

line #	hydrothermal fluid temperature (ºC)	seawater temperature (ºC)
7	200	50
8	200	100
9	200	150
10	350	50
11	350	100
12	350	150

a to f. Calculated curves for barite assuming precipitation in oxygen isotopic equilibrium with hydrothermal fluid ($\delta^{18}O$ of 0 ‰, $^{87}Sr/^{86}Sr$ of 0.7045) mixing with Devonian seawater ($\delta^{18}O$ of -2‰, $^{87}Sr/^{86}Sr$ of 0.7080), for various end member fluid temperatures and Sr concentrations.

Figure 6.30. Modelling of the Sr-O isotopic composition of barite precipitating from a mixture of hydrothermal fluids and seawater.

The Balta Tau barite data can be explained by two general scenarios:

1. Mixing of a hydrothermal fluid conductively cooled to around 200°C with seawater heated to around 50 to 150°C, with [Sr] in seawater lower than the [Sr] in the hydrothermal fluid (Figure 6.30b).
2. Mixing of a hydrothermal fluid conductively cooled to 150 to 250°C with cold seawater, with the [Sr] in seawater approximately twice that of the [Sr] in the hydrothermal fluid (Figure 6.30e). The curves for this scenario with a [Sr] ratio of 1 could also account for the barite data (Figure 6.30c), however this requires highly variable conductive cooling within individual ore facies to produce hydrothermal fluid temperatures spanning the range 350 to 200°C which seems unlikely.

The first option, which accounts for all data except for the footwall barite, requires that the [Sr] be considerably higher in hydrothermal fluid than in seawater (by at least a factor of 1.5 to account for the majority of data). Using this ratio in mixing calculations (Section 6.5.4) dictates that most of the barite formed from a mixture of 50 to 75% seawater, which is unlikely since this amount of seawater is likely to dilute Ba concentrations to below barite saturation (Chapter 7, Section 7.4.3).

The second option can account for all data and since the [Sr] of the hydrothermal fluid is less than that of seawater, provides a more realistic estimate of seawater mixing proportions (5 to 50%, Section 6.5.4). When data are compared to this model in more detail (Figure 6.31), trends within the massive sulphides and the barite rich ores indicate that these mostly precipitated from fluids with relatively constant proportions of seawater-hydrothermal fluid, but with variable degrees of conductive cooling of the hydrothermal fluid prior to mixing.

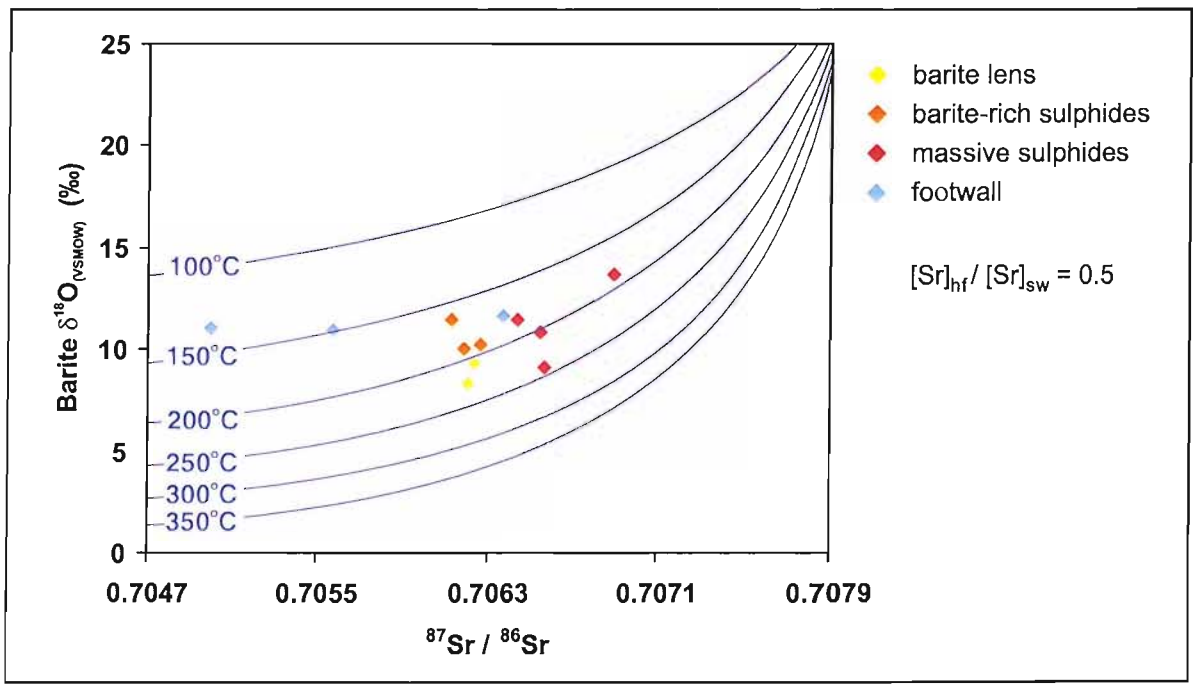

Figure 6.31. Probable scenario for fluid mixing responsible for barite precipitation at Balta Tau.

The formational temperatures can be estimated both from the barite $^{87}Sr/^{86}Sr$ based on mixing of hydrothermal fluid and seawater of given initial temperatures, and from the barite $\delta^{18}O$ assuming equilibrium fractionation with the fluid $\delta^{18}O$. For mixing between hydrothermal fluid at 200°C with $\delta^{18}O$ of -0.5‰, and seawater at 2°C and $\delta^{18}O$ of -2‰, the two estimates give similar temperature ranges (Figure 6.32), which are consistent with fluid inclusion temperatures Deviations may reflect greater or lesser degrees of conductive cooling of the hydrothermal fluid prior to mixing, for example the footwall barite is suggestive of greater degrees of cooling, whereas the barite lens is consistent with less conductive cooling. Alternatively, the footwall barite may have precipitated before reaching full oxygen isotopic equilibrium with the fluid H_2O, so that the oxygen isotope temperature estimates are too low.

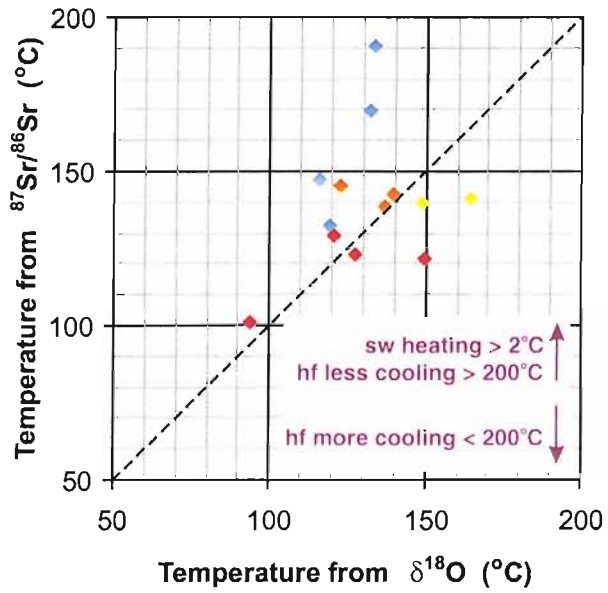

	hydrothermal fluid (hf)	seawater (sw)
temperature (°C)	200	2
$\delta^{18}O$ (‰)	0	-2
$^{87}Sr/^{86}Sr$	0.7045	0.7080
[Sr]*	0.5	1

barite lens
footwall
barite-rich sulphides
massive sulphides

Comparison of temperature estimates based on barite $\delta^{18}O$ assuming equilibrium with the hydrothermal fluid H_2O and on barite $^{87}Sr/^{86}Sr$ as an indication of the degree of seawater mixing. The fluid properties used are given in the adjacent table. * Note that for [Sr] the values were arbitrarily chosen to give a ratio of 0.5 for hydrothermal fluid : seawater (Section 6.5.4).

The temperatures are generally consistent falling mostly in the range 100 to 150°C. The Sr estimates for footwall samples are too high, but would be approximately equal to the $\delta^{18}O$ estimates if the hydrothermal fluid is further cooled to around 150°C. The low Sr temperature estimates from some barite in massive sulphides and the barite lens increase to match those of the $\delta^{18}O$ estimates if the hydrothermal fluid is cooled to a lesser degree, around 240°C, or if the seawater is heated to around 50°C prior to mixing.

Figure 6.32. Comparison of formational temperature estimates for Balta Tau barite based on Sr and O isotopic compositions.

6.6 SUMMARY

The volcanic sequences hosting Balta Tau have a typical island arc Sr signature which is more radiogenic than MORB reflecting a contribution from the subducting slab. The O isotope composition also shows a small deviation from the mantle signature consistent with a contribution from fluids derived from the subducting crust. The predicted isotopic composition of S, however, is consistent with typical MORB suggesting minimal transfer of S from the subducting slab to arc magmas.

Fluid inclusion and stable isotope studies of Balta Tau ores indicate that the mainstage ore forming fluids were derived from the interaction of seawater with volcanic rocks. Reduced sulphur has a dominantly igneous signature reflecting considerable leaching of sulphur from the volcanic rocks, with little evidence of seawater sulphate reduction, although sulphates suggest a small degree of reduction (12 to 16%) may have occurred locally at the site of mineralization. There is no evidence for a significant contribution of magmatic waters, although a small contribution can not be ruled out as the isotopic signature would not be discernable over the dominant seawater signature. Salinity data is suggestive of sub-seafloor, sub-critical phase separation producing fluids with salinities greater than and less than seawater, and the elevated salinities may have aided subsequent leaching and transport of metals as chloride complexes.

Fluid inclusion studies of mainstage ores indicate low formational temperatures of 130 to 170°C, although an earlier, higher temperature stage was probably responsible for more chalcopyrite-rich horizons in the footwall and massive sulphides which is not recorded by fluid inclusions. Sr isotopes indicate that conductive cooling of hydrothermal fluids and mixing of hydrothermal fluids and seawater were important processes prior to and/or during ore formation. Seawater mixing was essential to the formation of barite, indicated by the seawater isotopic signature of the sulphate, although Sr isotopes indicate a smaller contribution of seawater during precipitation of the barite lens compared to the massive sulphides. Isotopic studies also indicate sulphur isotopic disequilibrium between sulphides and sulphates, while the sulphate appears to have approached or reached oxygen isotopic equilibrium with fluid H_2O, suggesting a seawater residence time of hours to a few days prior to barite precipitation.

Late stage quartz precipitated from low temperature, low salinity and ^{18}O depleted fluids which are interpreted to be the product of low temperature sub-critical phase separation during waning stages of the hydrothermal system. The footwall chlorite has a strong seawater signature consistent with its Mg-rich composition and suggests significant seawater infiltration into the footwall after the mainstage ore formation.

7 DISCUSSION OF ORE FORMATION

7.1 INTRODUCTION

This chapter investigates the factors responsible for the mineralogy and metal composition of Balta Tau, and in particular the unusually high gold enrichment of the barite lens, based on the results of preceding chapters and chemical considerations of ore precipitation. The influence of post ore forming processes including late stage hydrothermal activity, diagenesis, metamorphism and deformation are also investigated. In the final section, a model of ore formation is presented.

7.2 INFLUENCE OF TECTONIC SETTING ON BALTA TAU MINERALIZATION

7.2.1 Introduction

The tectonic environment influences a number of factors which are important to ore formation, including the composition of source rocks, host rock lithologies, proximity and abundance of intrusive bodies and water depth. The host units to Balta Tau are tholeiitic to calc-alkaline andesites reflecting early to mainstage island arc formation, and ore formation probably took place during rifting of fore-arc to island arc sequences in shallow water conditions (discussed in Chapter 3; summarised in Figure 7.1). The implications of this setting in relation to ore formation are discussed in the following sections.

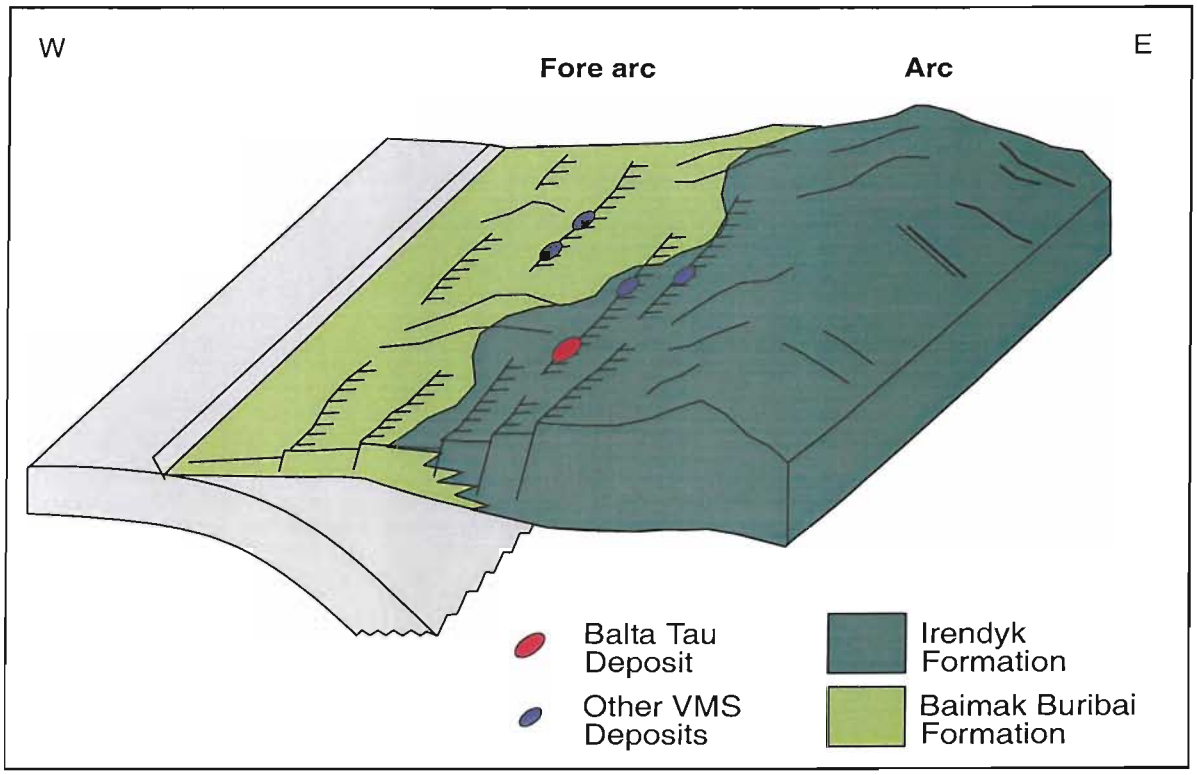

Figure 7.1. Tectonic setting during formation of the Balta Tau deposit.

7.2.2 Source rock composition

The metals and much of the sulphur in the Balta Tau deposit were probably derived from the underlying volcanic rocks (Chapter 6). The geochemistry of volcanic source rocks may influence the composition and mineralogy of VMS deposits in two ways:7

- The base and precious metal content of the source rocks is often reflected in the metal content of overlying VMS deposits. For example, deposits hosted in tholeiitic basalts such as those formed at MOR systems are typically Cu-rich, whereas those in felsic calc-alkaline units such as island arc sequences are enriched in Pb, Ag and Ba (Barrie and Hannington, 1999).
- The degree of oxidation of volcanic rocks controls oxidation state of hydrothermal fluids, which in turn influences the mineralogy of sulphide deposits (e.g. Large, 1992; Hannington et al., 1995). For example, fluid interaction with basalt containing reduced Fe as pyrrhotite results in reduced hydrothermal fluids that are buffered with respect to oxidation by pyrrhotite-pyrite-magnetite, and will precipitate sulphide assemblage that are stable at low oxidation conditions. By contrast, interaction with felsic rocks where Fe predominantly forms magnetite results in more oxidised fluids that are buffered by pyrite-hematite-magnetite and will precipitate more oxidised sulphide assemblages.

The source rocks at depth below Balta Tau are likely to be dominated by andesites of the Irendyk Formation but may also include basaltic to dacitic Baimak-Buribai sequences. The more fractionated nature of these units relative to MORB is consistent with the high Pb-Ba-Ag content of the Balta Tau deposit. The more oxidized nature of sulphides at Balta Tau reflected by the absence of pyrrhotite in sulphide ores, relative to basalt hosted deposits where pyrrhotite is abundant, is also consistent with the more oxidized nature of arc andesites relative to MORB. These factors indicate that the source rock composition was important influence over the metal content and mineralogy of the Balta Tau deposit.

Assessing the influence of host rock composition on Au content of Balta Tau ores is less straightforward, because it is difficult to constrain the probable Au content of unaltered Irendyk/Baimak-Buribai sequences. Limited analyses of volcanic rocks associated with modern subduction zones suggest variable Au enrichment relative to MORB, for example fore-arc to mainstage island arc tholeiitic basalts from Japan are not significantly enriched relative to MORB (Togashi and Terashima, 1997), whereas volcanic sequences from the Manus back-arc basin are significantly enriched (Moss et al., 2001) (Table 7.1). In terms of tectonic setting, the Balta Tau host rocks are more comparable with those from the Japanese arc, however in terms of lithology the Balta Tau sequences are more fractionated and better resemble those from the Manus Basin and may therefore have been significantly Au enriched. In addition, Moss et al. (2001) observe that during fractionation of arc magmas the Au content peaks at andesitic compositions, since Au

tends to be lost in more felsic rocks through degassing and expulsion of volatiles. This also therefore suggests a high potential for the Irendyk to have been Au-rich relative to MORB. Regional considerations also suggest that the Magnitogorsk arc rocks are generally Au enriched, since although the Urals and Baimak type VMS deposits have variable precious metal contents, most are Au-enriched to some degree and a high proportion are significantly Au enriched (e.g. Table 2.1, Chapter 2).

These considerations suggest that the Irendyk source rocks were Au enriched which is reflected in the general Au enrichment of associated VMS deposits, including Balta Tau. However, the variations in content and mode of occurrence of Au between these VMS deposits suggest that other deposit-scale factors are also important in controlling the extent of Au deposition.

	MORB		Japanese forearc and island arc		Manus back arc basin		Irendyk & Baimak-Buribai Formation	
	range	mean	range	mean	range	mean	range	mean
Cu (ppm)	-	75*	27 to 410	184	8 to 406	67	4 to 275	50
Zn (ppm)	-	75*	136 to 59	96	54 to 168	82	22 to 74	56
Pb (ppm)	-	0.7*	nd	nd	<5 to 10	-	1 to 5	3
Ba (ppm)	-	12.0†	67 to 320	174	nd	nd	22 to 749#	169#
Au (ppb)	0.1 to 2.7‡	0.8‡	0.2 to 3.8	1.5	<1 to 15	6	nd	nd

Table 7.1. Selected analyses of base and precious metal contents in oceanic volcanic rocks and summary of data acquired for Balta Tau host units.
Data sources: MORB: *Doe, 1994, †Saunders and Tivey, 1984, ‡Keays and Scott, 1976; Manus Basin: Moss et al. 2001; Japanese arc: Togashi and Terashima, 1997; Balta Tau, this study (Appendix A3). nd – no data. #excludes one anomalously high value.

7.2.3 Porosity of footwall units

The porosity of volcanic rocks in the immediate footwall can strongly influence the style of sub-seafloor and seafloor mineralization, as illustrated by the following "end member" scenarios that have been identified in ancient deposits (e.g. Franklin et al., 1981; Large et al., 1992) and in actively forming systems (Hannington et al., 1995):

- Coherent lavas with low porosity result in focussed, fracture controlled upwelling of fluids with little opportunity for significant conductive cooling or seawater mixing before fluids emerge at the seafloor. This tends to favour the formation of high temperature chimneys above a narrow, discordant feeder zone of sulphide veining and hydrothermal alteration.
- Porous footwall rocks such as volcanic breccias or fine volcaniclastic material allow upwelling fluids to permeate through a large volume of the footwall via small, interconnecting channels. The resultant footwall alteration and mineralization forms a broad,

irregular to stratigraphically controlled zone with a high proportion of disseminated sulphides, and may lack a district feeder zone. There is ample opportunity for significant seawater mixing and conductive cooling prior to fluids reaching the seafloor, so that fluids of variable temperatures may emerge at a number of sites at the seafloor, and are more likely to form complex mounds with multiple chimney structures and variable formational temperatures.

Relict clastic textures in the footwall of Balta Tau suggest that these rocks would initially have had a high porosity, which by analogy with the examples above may account for a number of features of the Balta Tau deposit including:

- The pervasive and extensive nature of footwall mineralization and alteration and high proportion of disseminated sulphides.
- Significant entrainment of seawater in the footwall during and after mainstage ore formation, as suggested by the low formational temperatures in outer zones and the Sr isotopic composition of barite and chlorite.
- A distinct feeder zone has not been identified in the footwall.
- The morphology and textures of the massive sulphide lens are suggestive of a broad seafloor mound, with internal variations in composition reflecting variable fluid temperatures.

7.2.4 Intrusives

Syn-volcanic intrusives are commonplace in island arc systems and as well as providing heat to drive seawater convection, may also supply metal and sulphur rich volatiles to hydrothermal fluids (e.g. de Ronde, 1995; Herzig et al., 1998; Moss et al., 2001). The addition of a magmatic component to hydrothermal fluids may result in "high sulphidation" VMS systems which are typically gold-rich and have an acid-sulphate alteration assemblage such pyrophyllite, kaolinite and alunite, comparable with high sulphidation epithermal deposits (Sillitoe et al., 1996). Although felsic intrusives do occur in the Baimak-Buribai Formation within approximately 10km of Balta Tau and are probably cogenetic with volcanic sequences (Chapter 3), they have not been identified in the Irendyk units which host the Balta Tau deposit. There is also no isotopic evidence for a direct magmatic input to fluids in isotope signatures (based on fluid $\delta^{18}O$ and sulphate-sulphide $\delta^{34}S$; Chapter 6) and ore assemblages do not show high sulphidation characteristics. It can therefore be concluded that magmatic fluids were not a significant component of ore forming fluids, and are not likely to have contributed significant metals or sulphur to the Balta Tau deposit. However, the possibility of a small magmatic contribution to fluids can not be ruled out since the large volume of seawater involved in hydrothermal circulation could easily swamp a small magmatic fluid signature.

7.2.5 Water depth

Water depth is an important influence over the pressure-temperature path of ascending hydrothermal fluids, and perhaps most significantly dictates whether or not fluid boiling will occur at or close to the seafloor in shallow water systems. Phase separation induces dramatic chemical changes which often result in the sudden precipitation of base and precious metals, or at higher temperatures may segregate certain metals such as Au and Cu into the vapour phase. Therefore fluid boiling at the seafloor may precipitate metals that would otherwise be lost to the ocean, and is a particularly effective precipitation mechanism for Au (e.g. Seward, 1989). The Balta Tau deposit is inferred to have formed in shallow waters, however ore textures and fluid inclusion populations do not provide evidence for fluid boiling during sulphide precipitation, and this can not therefore be proposed to account for the selective gold enrichment of Balta Tau ores. There are however indications that phase separation occurred at depth in the hydrothermal system, which may have facilitated the transport of metals due to the high chlorinity of the brine phase. During late stages of hydrothermal activity, a condensed vapour phase derived from low temperature, shallow sub-surface phase separation is inferred to have reached the footwall and precipitated large amounts of quartz (Chapter 6, Section 6.5.3). This silicification probably prevented later diagenetic and metamorphic fluids from significantly permeating the footwall and may therefore have been an important step in the preservation of the Balta Tau ores.

7.2.6 Summary

The source rock composition is an important influence over the composition of Balta Tau ores, in particular Pb and Ag and quite possibly Au contents together with the degree of oxidization of sulphide assemblages. However, deposit scale processes are required to explain the variation in composition and mineralogy between ore facies at Balta Tau, and to account for significant compositional variations between deposits hosted in the Magnitogorsk arc-related volcanics.

7.3 FLUID PROPERTIES AND CONDITIONS OF ORE FORMATION

7.3.1 Introduction

The ore forming conditions, in particular temperature, pH and oxidation-sulphidation, together with the concentration of important ligand forming compounds such as Cl^- and H_2S in ore forming fluids, provide important constraints on the mechanisms and efficiency of sulphide transportation and precipitation. The ore forming conditions and hydrothermal fluid properties during formation of the Balta Tau deposit, as far as can be determined, are summarised in the following sections.

7.3.2 Temperature

Estimates of ore formational temperatures fall in the range of 110 to 200°C for the majority of ore facies (Table 7.2), which are low compared to the typical formational temperatures of 250 to 350°C for ancient and modern VMS systems. However, there are VMS deposits with analogous formational temperatures and comparable polymetallic and precious metal rich ores, including Eskay Creek in British Columbia (Sherlock et al., 1999), the S. Hercules deposit in Australia (Zaw and Large 1992), and baritic ores of the actively forming JADE deposit (Lüders et al., 2001).

The chalcopyrite-rich massive sulphides and central footwall zones probably precipitated at higher temperatures more typical for VMS deposits (discussed in section 7.4), but the general absence of useful geothermometers in these zones precludes reliable temperature estimates for these ore facies.

Ore facies	Temperature estimates (ºC)		
	fluid inclusions	mineral compositions	barite $\delta^{18}O$
early footwall (ba)	-	-	119 to 133
mainstage footwall (sph-rich)	130 to 170	-	-
massive sulphides (py-chp)	-	at least 190*	-
massive sulphides (py-sph)	140 to 170	-	94 to 149
layered sulphides	140 to 150		-
barite-rich sulphides	140 to 150	-	123 to 140
barite lens	140	approx. 200†	149 to 164
late stage footwall chlorite	-	100 to 150*	-
late stage footwall quartz	110 to 140	-	-

Table 7.2. Summary of temperature estimates for the formation of Balta Tau ores.
Notes: *from chlorite geothermometry; †from electrum-sphalerite-fahlore geothermometry.

7.3.3 Oxidation

The degree of oxidation of ore fluids may be constrained by the dominant Fe and Cu phases present in ore assemblages. At Balta Tau, all ore facies contain pyrite but are devoid of pyrrhotite, magnetite and hematite. This indicates that the ore fluids were buffered in the pyrite field throughout precipitation, from high temperature Cu-rich mineralization to low temperature barite-rich ores (Figure 7.2). The abundance of chalcopyrite and absence of bornite further constrains the oxidation by providing an upper limit within the pyrite field (Figure 7.2). Therefore oxidation remained above the pyrite-pyrrhotite boundary and below the bornite-chalcopyrite boundary throughout ore precipitation, and for the purposes of thermodynamic calculations in the following sections, the oxidation is taken as three orders of magnitude higher than the pyrite-pyrrhotite

boundary (Figure 7.2). The buffering of oxidation within the pyrite field is consistent with fluids derived from interaction with intermediate host rocks (Section 7.2).

The presence of barite is often considered to indicate high oxidation conditions (e.g. Huston and Large, 1989). However, at Balta Tau sulphate was derived from seawater during fluid mixing, and sulphur isotopes indicate that isotopic (and therefore chemical) equilibrium was not subsequently attained between aqueous sulphur species (Chapter 6). The presence of barite does not therefore necessarily indicate high oxidation conditions, but rather reflects the slow kinetics of sulphate reduction which enable sulphate to persist for some time in a reducing environment. At Balta Tau this is supported by sulphate sulphur isotopes which do not indicate a significant component of oxidized H_2S. Unlike sulphate reduction, the oxidation of H_2S proceeds rapidly and would therefore have occurred had conditions become significantly oxidized as a result of fluid mixing. This interpretation is also consistent with the modelling of Janecky and Seyfried (1984), who conclude that the oxidation state of hydrothermal fluids doe not deviate significantly even after extensive mixing with seawater due to their strong buffering capacity.

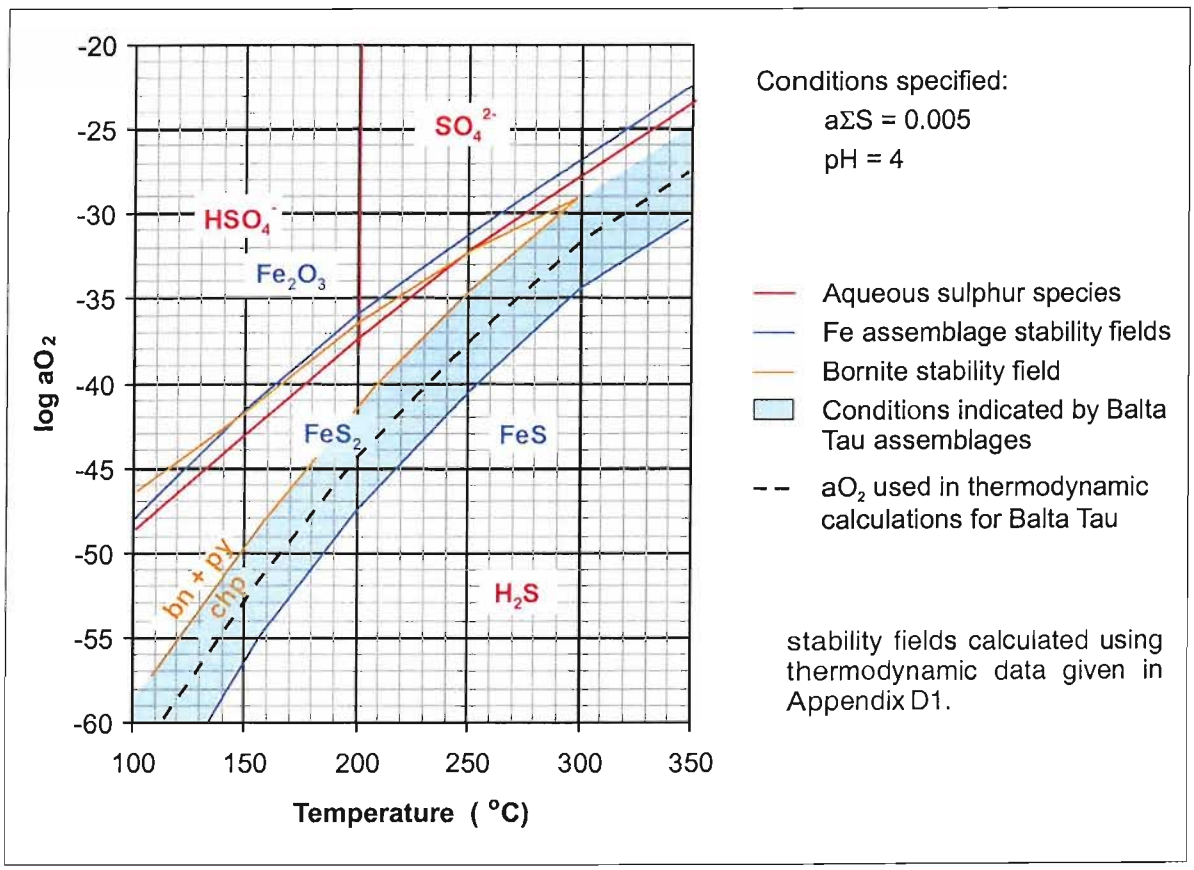

Figure 7.2. Oxidation conditions during ore formation at Balta Tau.

7.3.4 Sulphidation

The sulphide assemblages at Balta Tau are indicative of moderate sulphidation conditions which are higher than typical MOR systems but lower than "high sulphidation" deposits (Chapter 5, Section 5.3.2). This is consistent with the sulphidation being related to oxidation according to equation 7.1:

$$H_2S + ½O_2 \leftrightarrow H_2O + ½S_2 \quad (7.1)$$

Therefore the elevated oxidation of Balta Tau hydrothermal fluids relative to MOR systems results in the precipitation of higher sulphidation assemblages. During mixing with seawater, the degree of oxidation is not inferred to have increased significantly and sulphide assemblages therefore reflect a similar degree of sulphidation throughout precipitation. With reference to Figure 5.19, the progression from chalcopyrite-rich ores to barite-rich sulphides with a decrease in Fe content of sphalerite is likely to reflect a decrease in temperature more than increase in sulphidation, and probably followed closest to path (a).

7.3.5 pH

In ancient VMS systems the pH of ore forming fluids may be inferred from pH-sensitive alteration assemblages that co-precipitated with sulphide minerals (e.g. Hemley and Jones, 1964; Large, 1977; Walshe and Solomon 1981; Schardt et al., 2001). However, this is not possible at Balta Tau because the footwall is overprinted by a late stage Mg-chlorite which did not co-precipitate with sulphide ores, and the pH must therefore be inferred by comparison with other deposits. The pH of vent fluids measured from modern MOR systems generally varies between 2.8 and 5.9 (Table 7.3). Lower pH fluids have also been recorded but generally relate to "high sulphidation" systems such as those in the Lau Basin (Table 7.3). The lack of high sulphidation-high oxidation sulphide assemblages at Balta Tau suggests that fluids are more likely to have been in the "normal" pH range of 3 to 5, and an intermediate pH of 4 has been selected for thermodynamic calculations. Although temperature dependent, the pH will not vary by more than 0.5 units during cooling from 350 to 100°C, therefore the value of 4 has been used over this temperature range. More significant variations in pH may rise during ore formation due to sulphide precipitation which decreases pH, and mixing with seawater which increases the pH.

	pH	H_2S	
		µmol/kg	ppm
MOR systems	2.8 to 5.9	1100 to 12200	37 to 410
Arc systems – Lau Basin	2	-	-
Balta Tau	4	5000	170

Table 7.3. Estimates of pH and H_2S concentration of Balta Tau fluids compared with values measured from venting fluids in modern systems. (Data from compilation in Von Damm, 1995).

7.3.6 H_2S and Cl^- concentration

The majority of metals being considered form aqueous chloride and/or sulphide complexes in hydrothermal solutions, and their transport and precipitation is therefore significantly affected by the Cl^- concentration and the concentration and speciation of aqueous sulphur. For Balta Tau fluids, the salinity estimates from fluid inclusions in mainstage ores are in the range 2 to 5wt%. For the purposes of thermodynamic calculations, chlorides are assumed to be the dominant salts and the Cl^- concentration is taken as 0.6mol/kg (equivalent to 3.5wt%). The Cl^- concentration of Balta Tau fluids would not be affected significantly by mixing with seawater, as both the hydrothermal fluids and seawater have a similar concentration. It will also remain unaffected by precipitation since chlorides are not formed, and unaffected by redox as Cl^- is the dominant species in hydrothermal fluids regardless of oxidation or pH.

The H_2S content of Balta Tau fluids can not be estimated from data obtained in this study. However, analyses of vent fluids from actively forming systems indicate that, unlike metal contents, the H_2S concentrations are relatively consistent and only vary within one order of magnitude. Although fluids may have lost or gained H_2S through precipitation or dissolution of sulphides prior to the venting, metal concentrations are generally orders of magnitude lower than the concentration of H_2S, therefore sulphide precipitation/dissolution is unlikely to affect the H_2S content significantly. For the purposes of thermodynamic calculations in the following sections, an H_2S concentration of 5000μmol/kg (170 ppm) was selected, which is approximately mid-range of the measured values from active vents (Table 7.3). During mineralization, the fluid H_2S may vary considerably due to sulphide precipitation or dissolution, dilution from seawater mixing, or oxidation (where H_2S is converted to HSO_4^- or SO_4^{2-}).

7.4 METAL TRANSPORT AND ORE DEPOSITION

7.4.1 Introduction

The mechanisms of metal transportation and deposition are important factors in controlling the composition of sulphide ores and may account for mineralogical differences between ore facies, in particular the unusual gold enrichment and mineralogy of the barite lens. In this section metal transportation and deposition under conditions inferred for Balta Tau are investigated by calculating metal solubilities as a function of temperature and writing balanced equations for ore precipitation to indicate the effects of pH, oxidation, concentration of H_2S and Cl^-. Combining these with estimates of metal concentrations in hydrothermal fluids enables the probable precipitation mechanisms within individual ore facies to be determined. Calculations are based on the fluid conditions and properties discussed in section 7.3, thermodynamic data and assumptions are given in Appendix D1.

7.4.2 Transport and Deposition of ore forming metals and semi-metals

Introduction

The majority of metals in chloride and sulphur rich hydrothermal fluids are transported as chloride and/or sulphide complexes.

Chloride complexes

Chloride complexes are important for the hydrothermal transportation of Zn, Pb, Ag, Au, Fe and Cu. Metal solubilities have been calculated using equations 7.2 to 7.7 which assume fluids are in equilibrium with sphalerite, galena, native gold, native silver, pyrite and chalcopyrite (Figures 7.3, 7.4 and 7.5). The solubility of all metals considered increases with increasing temperature and will also be favoured by low pH and high concentrations of Cl^-.

$$ZnS_{(s)} + 2H^+ + xCl^- \leftrightarrow ZnCl_x^{2-x} + H_2S \quad (7.2)$$

$$PbS_{(s)} + 2H^+ + xCl^- \leftrightarrow PbCl_x^{2-x} + H_2S \quad (7.3)$$

$$Au_{(s)} + H^+ + xCl^- + \tfrac{1}{4}O_{2(g)} \leftrightarrow AuCl_x^{1-x} + \tfrac{1}{2}H_2O_{(l)} \quad (7.4)$$

$$Ag_{(s)} + H^+ + xCl^- + \tfrac{1}{4}O_{2(g)} \leftrightarrow AgCl_x^{1-x} + \tfrac{1}{2}H_2O_{(l)} \quad (7.5)$$

$$FeS_{2(s)} + 2H^+ + xCl^- + H_2O_{(l)} \leftrightarrow FeCl_x^{2-x} + 2H_2S + \tfrac{1}{2}O_{2(g)} \quad (7.6)$$

$$CuFeS_{2(s)} + H^+ + \tfrac{1}{4}O_{2(g)} + xCl^- \leftrightarrow CuCl_x^{1-x} + FeS_{2(s)} + \tfrac{1}{2}H_2O_{(l)} \quad (7.7)$$

(all species are aqueous unless otherwise stated).

Equations 7.2 to 7.7 are appropriate for describing the precipitation of sulphides and native metals at Balta Tau with the exception of equation 7.7 for chalcopyrite. Equation 7.7 was selected in order to calculate Cu solubility independently of Fe^{2+} concentration in fluids in equilibrium with chalcopyrite. However, precipitation is unlikely to have generally proceeded by equation 7.7 since chalcopyrite is not commonly observed to be replacing pyrite; a more appropriate equation for chalcopyrite would be 7.8:

$$CuFeS_{2(s)} + 3H^+ + \tfrac{1}{2}H_2O_{(l)} + (x+y)Cl^- \leftrightarrow CuCl_x^{1-x} + FeCl_y^{2-y} + 2H_2S + \tfrac{1}{4}O_{2(g)} \quad (7.8)$$

The solubility curves in Figures 7.3 to 7.5 indicate that decreasing temperature from 350 to 100°C causes the solubility of all metal chlorides investigated to decrease by 4 to 10 orders of magnitude. Conductive cooling of hydrothermal fluids or mixing with cool seawater would therefore be effective precipitation mechanisms. As equations 7.2 to 7.6 and 7.8 demonstrate, precipitation may also be triggered by an increase in pH, which could occur due to mixing with seawater although the increase would be small unless at least 70% seawater was involved (Figure 7.6). Changes in oxidation are also important for some metals, with Au and Ag precipitation favoured by a decrease in oxidation (equations 7.4 and 7.5) and pyrite and chalcopyrite favoured by an

increase in oxidation (equations 7.6 and 7.8). Other factors which may trigger precipitation include a decrease in the concentration of Cl^- or increase in the concentration of H_2S, but these are unlikely to have occurred during the precipitation of Balta Tau ores.

Sulphide complexes

All of the metals considered form a variety of stable sulphide complexes, although they are generally less important than chloride complexes. However, in the case of Au, sulphide complexes are dominant over a wide range of conditions (Gammons and Williams-Jones, 1995; Gibert et al., 1998), and in low temperature, sulphide-rich fluids, they may also be important for Ag, Zn and Cu (Bourcier and Barnes, 1987; Gammons and Williams-Jones, 1995; Crerar and Barnes, 1976). The stoichiometry and relative stabilities of metal sulphide complexes are not well known and there is considerable discrepancy in published thermodynamic data. The most likely dominant sulphide complexes and relevant thermodynamic data have been selected based on the review of Wood and Samson (1998), and solubilities have been calculated according to equations 7.9 to 7.14 (Figures 7.3b, 7.4b, 7.5a and b).

$$Au_{(s)} + 2H_2S + \tfrac{1}{4}O_{2(g)} \leftrightarrow Au(HS)_2^- + H^+ + \tfrac{1}{2}H_2O_{(l)} \quad (7.9)$$

$$Au_{(s)} + H_2S + \tfrac{1}{4}O_{2(g)} \leftrightarrow Au(HS)^0 + \tfrac{1}{2}H_2O_{(l)} \quad (7.10)$$

$$Ag_{(s)} + 2H_2S + \tfrac{1}{4}O_{2(g)} \leftrightarrow Ag(HS)_2^- + H^+ + \tfrac{1}{2}H_2O_{(l)} \quad (7.11)$$

$$Ag_{(s)} + H_2S + \tfrac{1}{4}O_{2(g)} \leftrightarrow Ag(HS)^0 + \tfrac{1}{2}H_2O_{(l)} \quad (7.12)$$

$$ZnS_{(s)} + H_2S + \leftrightarrow Zn(HS)_2^0 \quad (7.13)$$

$$CuFeS_{2(s)} + 2H_2S + \tfrac{1}{4}O_{2(g)} \leftrightarrow Cu(HS)_2^- + FeS_2 + H^+ + \tfrac{1}{2}H_2O_{(l)} \quad (7.14)$$

Figures 7.3 to 7.5 indicate that for Au, sulphide complexes dominate at temperatures below around 300°C and are capable of transporting significant Au, whereas for Ag, Cu and Zn, they only predominate at temperatures below 150°C and solubilities are very low. In general the solubilities of metal sulphide complexes do not vary considerably as a function of temperature, therefore cooling of hydrothermal fluids will not necessarily result in precipitation. More effective precipitation mechanisms would be a decrease in oxidation, decrease in concentration of H_2S and for some complexes of Au, Ag and Cu, a decrease in pH.

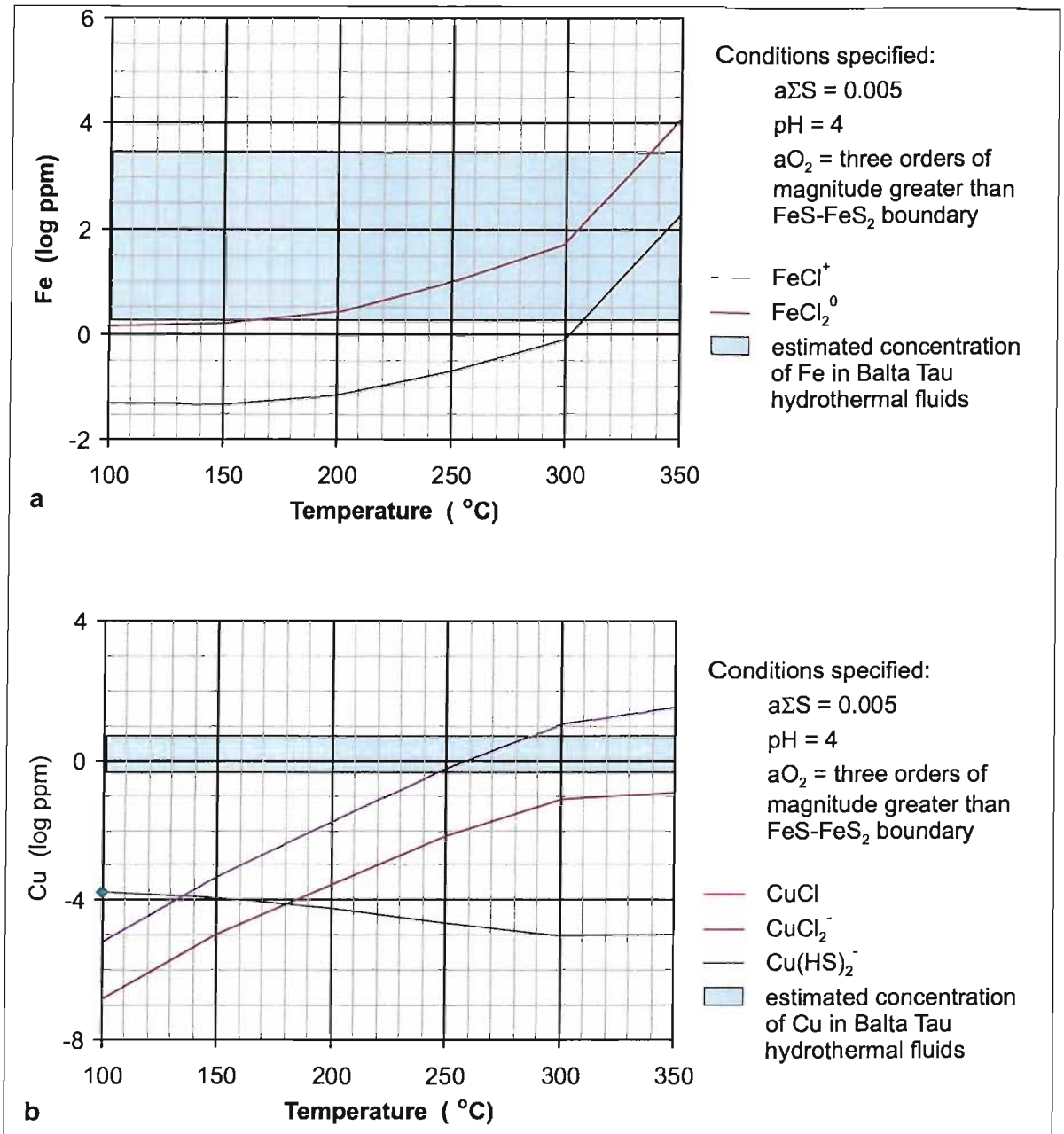

a. The solubility curves for Fe as chloride complexes, which dominate the hydrothermal transport of Fe, indicate that Fe solubility decreases with temperature particularly between 200 and 350°C.

b. Solubility curves for Cu, showing that Cu chloride complexes predominate at temperatures greater than 140°C with solubility decreasing significantly with decreasing temperature. Below 140°C, Cu is transported as bisulphide complexes and solubility does not vary significantly with temperature.

(Solubilities calculated using thermodynamic data given in Appendix D1).

Figure 7.3. Solubility curves for Fe and Cu.

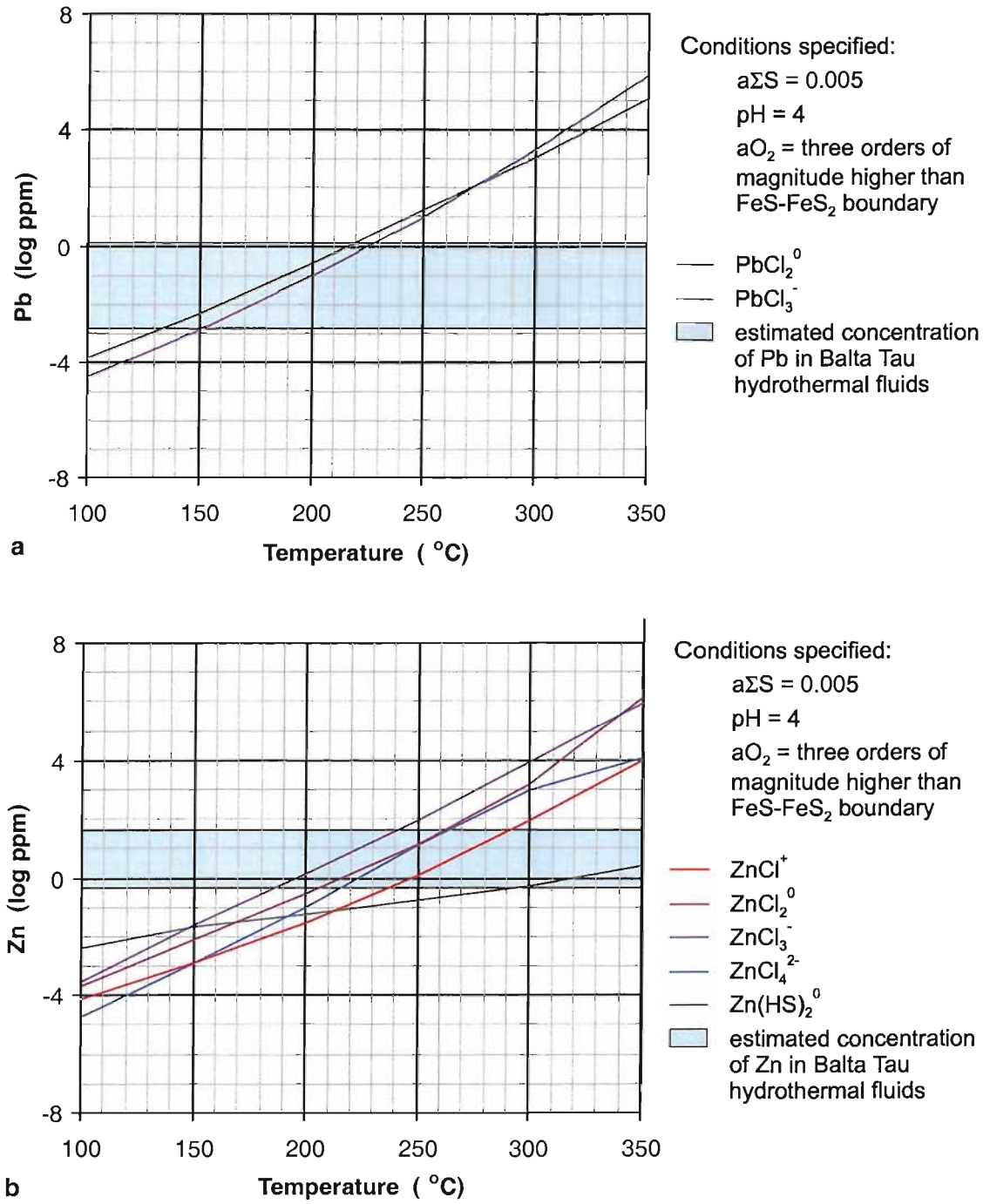

a. Solubility curves for Pb as chloride complexes, which dominate the hydrothermal transport of Pb, indicate that Pb solubility decreases dramatically with temperature.

b. Solubility curves for Zn indicate that chloride complexes predominate at temperatures greater than 150°C and solubility decreases significantly with temperature. Below 150°C, Zn is transported as bisulphide complexes and solubility only decreases slightly with temperature.

(Solubilities calculated using thermodynamic data given in Appendix D1).

Figure 7.4. Solubility curves for Pb and Zn.

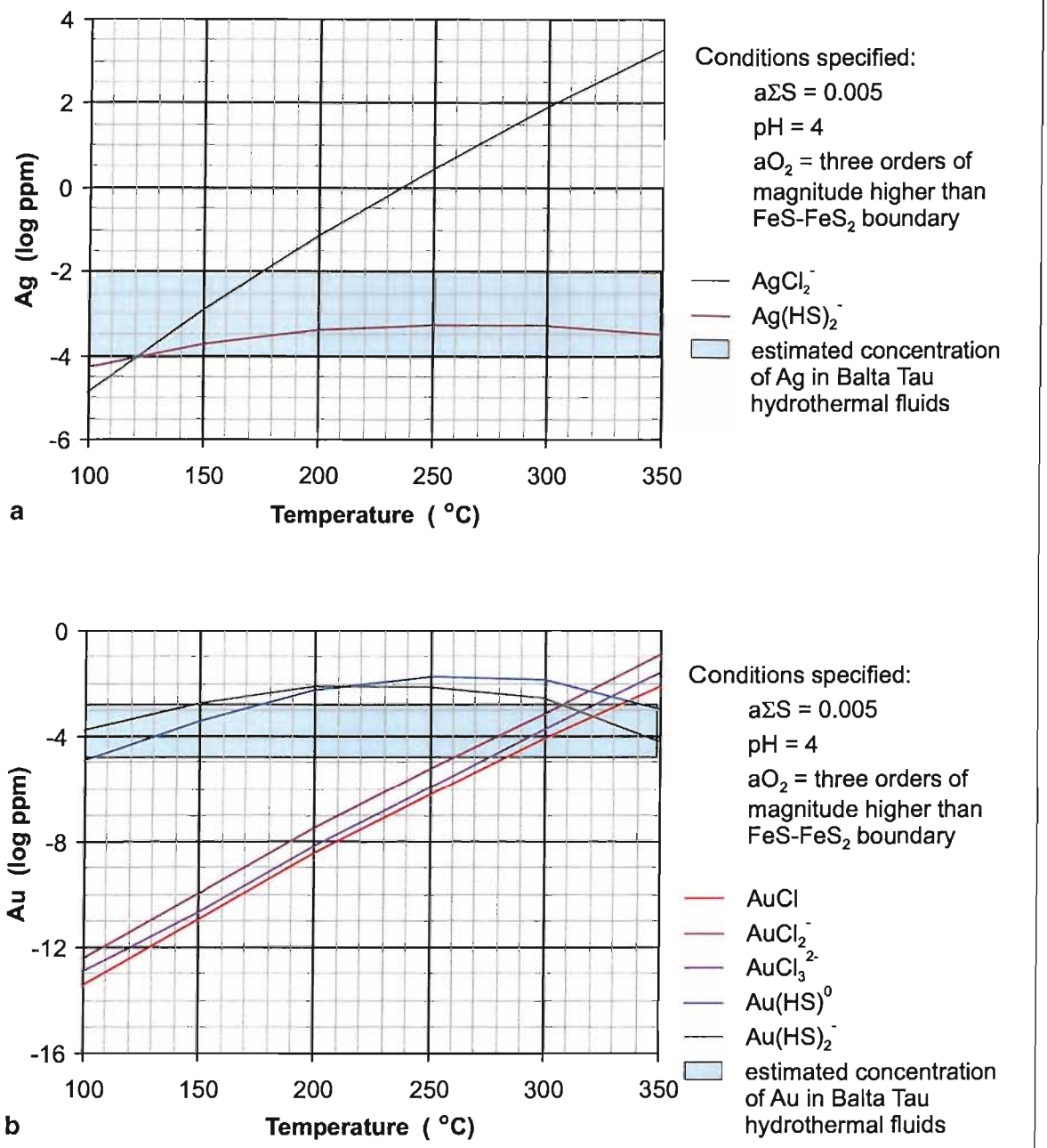

a. Solubility curves for Ag indicate that chloride complexes dominate at temperatures greater than 120°C with the solubility decreasing considerably with temperature. Below 120°C bisulphide complexes predominate and Ag solubility does not vary significantly with temperature.

b. Solubility curves for Au, which indicate that chloride complexes only predominate at temperatures greater than 320°C. Below this temperature, Au preferentially forms bisulphide complexes and solubility does not vary significantly with temperature.

(Solubilities calculated using thermodynamic data in Appendix D1).

Figure 7.5. Solubility curves for Ag and Au.

Au transportation is dominated by $Au(HS)^0$ complexes at temperatures above 220°C (Figure 7.5b), and could precipitate due to an increase in oxidation or decrease in concentration of H_2S (equation 7.10). At temperatures below 220°C, $Au(HS)_2^-$ predominates and in addition to those factors mentioned for $Au(HS)^0$ could be precipitated by decreasing pH (equation 7.9). Mixing with seawater is commonly proposed to be an efficient precipitation mechanism for Au due to destabilization of sulphide complexes by a large increase in oxidation that decreases the concentration of H_2S through oxidation (Hannington et al., 1989a; Herzig et al., 1993) which overrides the increase in Au solubility caused by increased oxidation alone (excluding effects on H_2S). However, at Balta Tau sulphide assemblages and $\delta^{34}S$ studies indicate that significant oxidation of H_2S did not occur during fluid mixing (section 7.3.3) and this is not therefore considered to be applicable. Other effects of seawater mixing are an increase in pH, which would increase Au solubility, and dilution of H_2S which would decrease Au solubility. However, neither of these effects become significant unless extensive seawater mixing occurs in excess of 70% (Figure 7.6a and c), and their effect should counteract one another, therefore seawater mixing is not considered to be an effective precipitation mechanism for Au.

The semimetals Sb and As and are also important constituents of Balta Tau ores, forming abundant tennantite-tetrahedrite. The transportation of these metals is complex and poorly understood. In low temperature, sulphide-rich hydrothermal fluids they are most likely to be transported as polysulphide complexes. However many species may be stable, e.g. $H_2AsS_3^-$, $HAsS_3^{2-}$, $H_2As_3S_6^-$, $HAs_2S_4^-$ and $As_2S_4^{2-}$, and the stoichiometry of dominant species is uncertain with reliable thermodynamic data yet to be determined (Wood and Samson, 1998 and references therein). Similar problems exist with Sb, where thioantimonite complexes are most likely to predominate in sulphur rich fluids but numerous stoichiometries have been proposed, including $HSb_2S_4^-$, $H_2Sb_2S_4^0$, $Sb_2S_4^{2-}$, SbS_2^- and SbS_3^{3-}. Therefore calculations of As and Sb solubility as a function of temperature have not been attempted. The precipitation of tennantite-tetrahedrite would probably have followed equations such as 7.14 to 7.17, which are based on the end member tennantite (7.14 and 7.15) and tetrahedrite (7.16 and 7.17) compositions and examples of As and Sb complexes taken from those listed above.

$$A_{10}B_2As_4S_{13(s)} + 10H^+ + (x+y)Cl^- \leftrightarrow 10ACl_x^{1-x} + 2BCl_y^{2-y} + 4H_2AsS_3^- + H_2S \quad (7.14)$$

$$3A_{10}B_2As_4S_{13(s)} + 38H^+ + (x+y)Cl^- \leftrightarrow 30ACl_x^{1-x} + 6BCl_y^{2-y} + 4H_2As_3S_6^- + 15H_2S \quad (7.15)$$

$$A_{10}B_2Sb_4S_{13(s)} + 12H^+ + (x+y)Cl^- \leftrightarrow 10ACl_x^{1-x} + 2BCl_y^{2-y} + 2HSb_2S_4^- + 5H_2S \quad (7.16)$$

$$A_{10}B_2Sb_4S_{13(s)} + 2H^+ + (x+y)Cl^- \leftrightarrow 10ACl_x^{1-x} + 2BCl_y^{2-y} + 4SbS_3^{3-} + H_2S \quad (7.17)$$

where $A = Cu^+, Ag^+$; $B = Zn^{2+}, Fe^{2+}$

Equations 7.14 to 7.17 illustrate that whatever stoichiometry is selected for the As and Sb sulphide complexes, precipitation of tennantite-tetrahedrite could be triggered either by an increase in pH or by an increase in the concentration of H_2S.

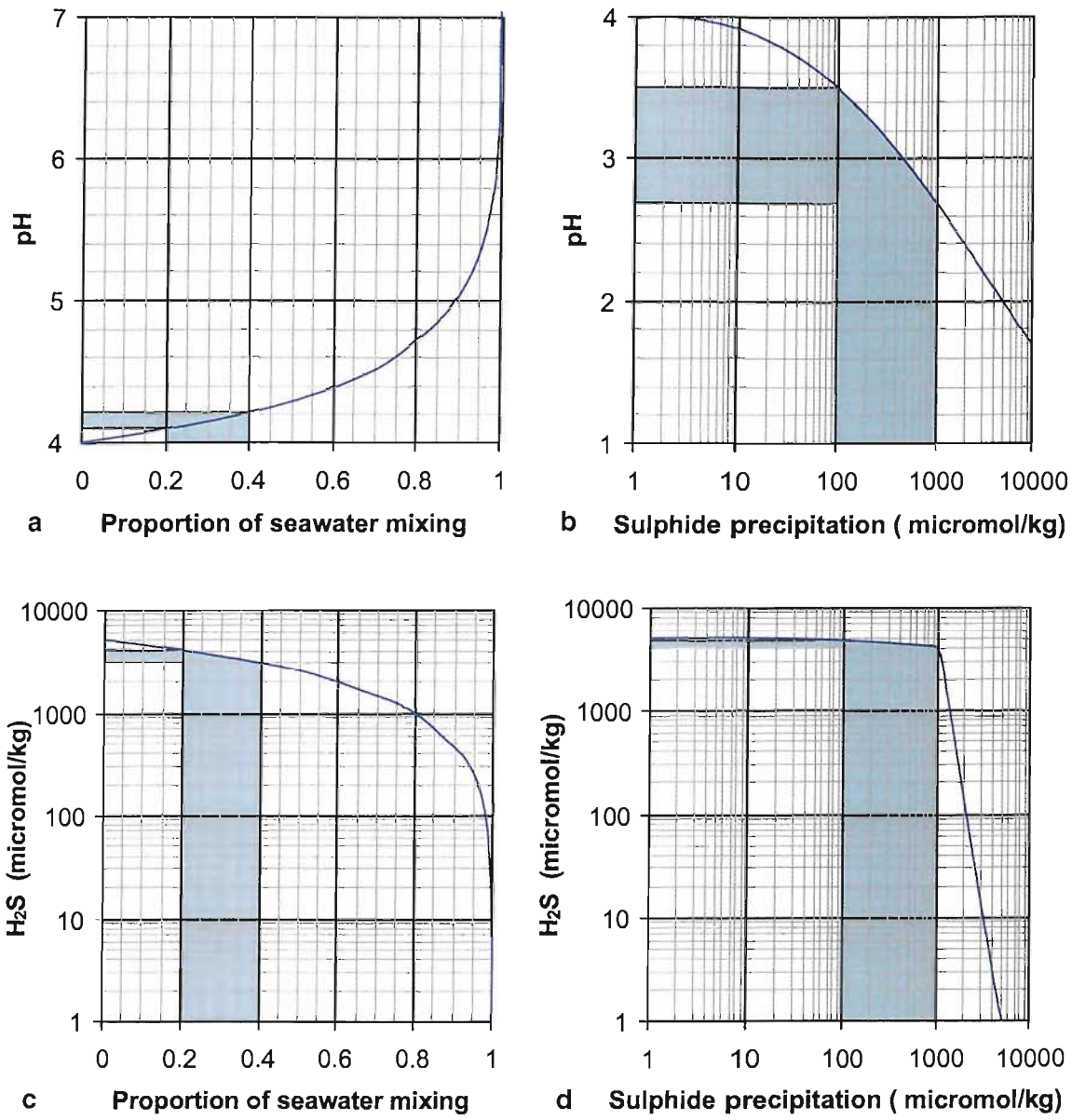

a and b. Graphs to show the effect of seawater mixing (a) and sulphide precipitation (b) on fluid pH. Mixing with approximately 30% seawater does not increase the pH significantly, while precipitation of between 100 and 1000micromol/kg of sulphides may decrease the pH by between 0.5 and 1.5 log units.

c and d. Graphs to show the effect of seawater mixing and sulphide precipitation on fluid concentration of H_2S. Reasonable estimates of seawater mixing and sulphide precipitation do not significantly alter the fluid concentration of H_2S.

(based on calculations detailed in Appendix D2).

Figure 7.6. The effect of seawater mixing and sulphide precipitation on fluid pH and concentration of H_2S.

As-Sb Thiocomplexes

The close association of Au and As has lead to suggestions that Au may be transported as thiocomplexes such as $Au(AsS_3)^{2-}$ or $Au(S,As)^{2-}$ (Seward, 1973; Mao, 1991) in hydrothermal solutions. Since the dominant stoichiometry and thermodynamic quantities for these complexes have not been determined their importance can not be evaluated, however the possibility that such ligands may contribute significantly to the hydrothermal transport of Au should be considered.

7.4.3 Transport and Deposition of Ba

Ba is effectively transported in hydrothermal fluids as a simple Ba^{2+} ion. Precipitation of barite at Balta Tau resulted from the mixing of hydrothermal fluids containing Ba^{2+} and seawater which provided the SO_4^{2-} according to equation 7.15:

$$Ba^{2+} + SO_4^{2-} \leftrightarrow BaSO_{4(s)} \qquad (7.18)$$

The solubility of barite is generally low and is significantly affected by the Cl^- content of fluids (Figure 7.7a). For fluids with salinities close to seawater (equivalent to approximately 0.5mol/kg Cl^-), barite solubility remains fairly constant at around 130μmol/kg over the temperature range 100 to 350°C (Figure 7.7a). This implies that the Balta Tau hydrothermal fluids must have contained at least 130μmol/kg of Ba^{2+} in order for barite precipitation to have occurred. Analyses of Ba^{2+} in hydrothermal fluids from active vents fall in the range of <10 to 100μmol/kg (data compiled in Von Damm, 1995 and Ishibashi and Urabe, 1995) which are all below the concentration required for barite saturation, in spite of the fact that some of these fluids were emitted from barite-bearing vents. These measurements are therefore likely to be underestimates, which is consistent with reported difficulties arising from the precipitation of barite in sample containers occurring between sample collection and analysis (e.g. Von Damm, 1995), as well as probable loss of Ba^{2+} through barite precipitation prior to venting. However, the fact that very high levels of Ba^{2+} have not been recorded from vent fluids does suggest that initial values are not significantly higher than the saturation point, which is consistent with estimates of the maximum probable Ba^{2+} concentration in Kuroko fluids of 300μmol/kg (Ohmoto et al. 1983).

The morphology of barite from Balta Tau also suggests that fluids were not considerably oversaturated with respect to barite, with coarse, euhedral crystals indicative of slow precipitation rates and zones of sulphide inclusions that point to regular pauses in crystal growth. This interpretation is supported by experimental work of Shikazono (1994), who established that at 150°C, barite precipitating from highly oversaturated solutions would form dendritic growths, whereas coarse euhedral crystals formed from weakly to moderately saturated solutions.

Therefore for the purposes of calculations in the following sections, the concentration of Ba^{2+} in Balta Tau fluids is estimated at between 200 and 300μmol/kg, which is sufficient to reach saturation with respect to barite upon mixing with seawater, and also consistent with the generally low concentrations indicated by analyses of modern fluids, estimates of Kuroko fluids and barite morphology.

Isotopic studies of barite from Balta Tau suggest that a period of approximately two days lapsed between fluid mixing and barite precipitation (based on oxygen isotopic equilibrium between barite and H_2O) and indicate that the most barite-rich ores precipitated from fluids containing less seawater than much of the barite from other ore facies (based on Sr isotopic signatures). This contradicts the notion that barite will precipitate immediately and rapidly upon mixing between seawater and hydrothermal fluids. The precipitation of barite may instead reflect the $[Ba^{2+}]$ and $[SO_4^{2-}]$ in hydrothermal fluids and seawater respectively as follows. Assuming the Ba^{2+} contents in Balta Tau hydrothermal fluids were in the order of 200 to 300μmol/kg and that Devonian oceans contained similar sulphate concentrations to modern seawater, 2700μmol/kg SO_4^{2-} (Holland, 1978), only a small fraction of seawater (1 to 5%) is required to give a 1:1 ratio of Ba^{2+} : SO_4^{2-}, therefore the effective precipitation of barite does not require large degrees of seawater mixing. Furthermore, the estimated concentration of Ba^{2+} in hydrothermal fluids is the same order of magnitude as the concentration required for barite saturation. Therefore while a small degree of seawater mixing is necessary to provide the SO_4^{2-} for barite precipitation, prolonged mixing with seawater will dilute the concentration of Ba^{2+} and may result in under-saturation with respect to barite if the proportion of seawater increases above around 50 to 70% (Figure 7.7b). This is consistent with estimated fluid mixing of 5 to 50% seawater for barite in all ore horizons at Balta Tau (Table 6.14, Chapter 6).

Barite in active VMS systems is most commonly observed precipitating at low temperatures, usually below 300°C and often as low as 100 to 200°C. This can not be accounted for by variations in barite solubility, because for the salinity range of most hydrothermal fluids barite solubility does not vary significantly as a function of temperature (Figure 7.7a). A possible explanation is the preferential formation of anhydrite at higher temperatures. Unlike barite, the solubility of anhydrite is high and shows strong retrograde characteristics (Blout and Dickson, 1969), so that in hydrothermal systems anhydrite is generally insoluble above around 150 to 200°C, and is particularly prevalent in high temperature (above 300°C) deposits (e.g. Hannington et al., 1995). Given the high Ca/Ba content of both hydrothermal fluids and seawater, it is reasonable that at high temperatures anhydrite will precipitate preferentially, whereas at low temperatures barite may dominate. The fact that barite precipitation is favoured by low temperatures and by relatively small degrees of seawater mixing (to minimize dilution of Ba^{2+})

supports the inference from isotope studies that conductive cooling of fluids is an important process for barite precipitation (Chapter 6)

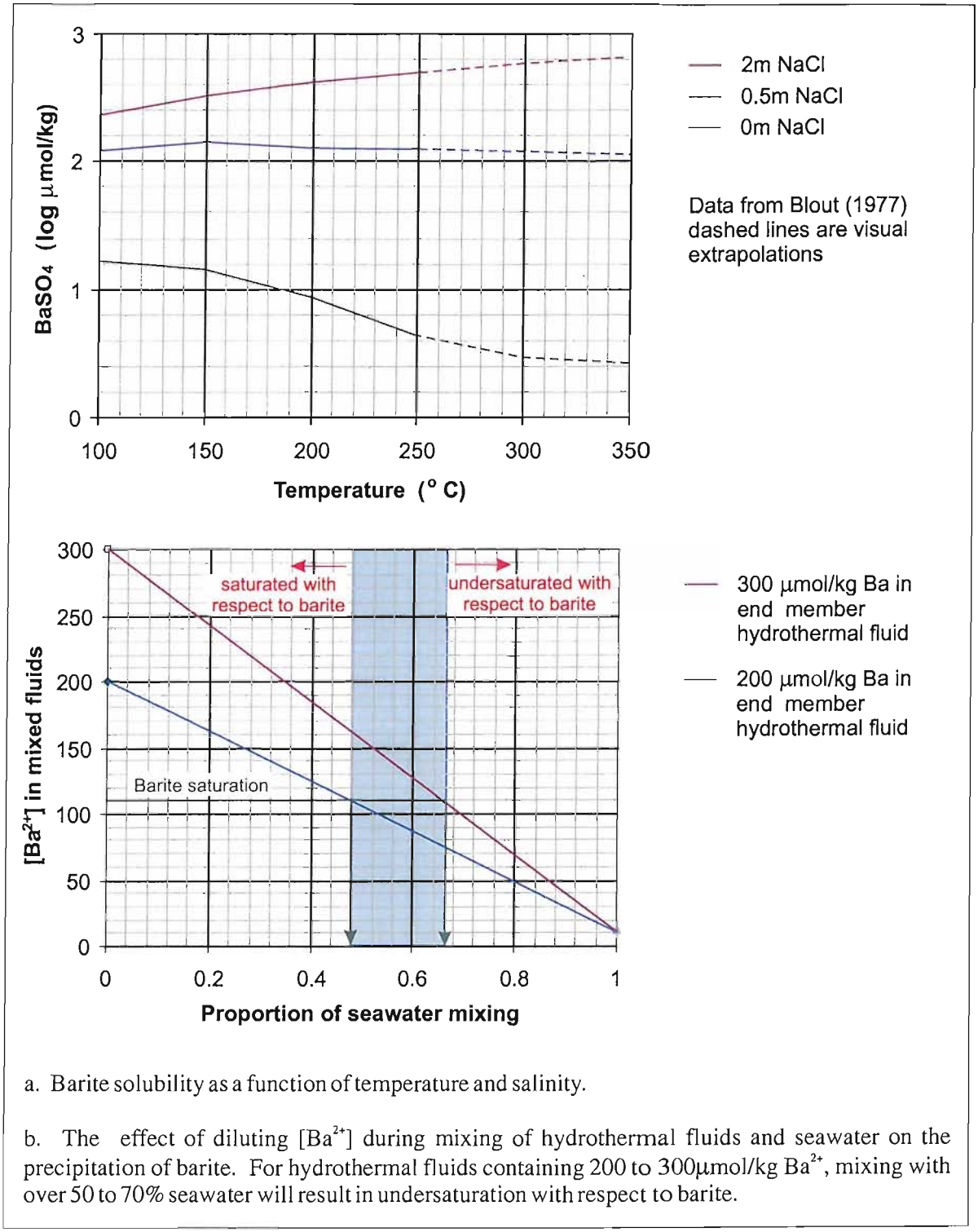

a. Barite solubility as a function of temperature and salinity.

b. The effect of diluting $[Ba^{2+}]$ during mixing of hydrothermal fluids and seawater on the precipitation of barite. For hydrothermal fluids containing 200 to 300µmol/kg Ba^{2+}, mixing with over 50 to 70% seawater will result in undersaturation with respect to barite.

Figure 7.7. Barite solubility in hydrothermal fluids and dilution of Ba^{2+} during seawater mixing.

7.4.4 Metal concentrations in hydrothermal fluids

In order to predict temperatures of sulphide saturation using the solubility curves in Figures 7.3 to 7.5, the concentration of metals in the Balta Tau hydrothermal fluids are required, and estimates (Table 7.2) have been based on the following considerations:

- Metal concentrations analysed in fluids collected from active vents (Table 7.4). These must be treated with caution as fluids may have precipitated or dissolved sulphide minerals in the sub-seafloor, sulphide mound or chimneys, which would increase or decrease metal concentrations. The data available are confined to MOR systems and one high sulphidation back-arc basin deposit in the Lau Basin (Table 7.4), none of which are directly analogous to Balta Tau, but given the anomalous fluid properties of the Lau Basin, the MOR deposits are probably better indications of fluid composition at Balta Tau in spite of the different source rock chemistry.
- The relative concentrations of metals in the source rocks, where Cu and Zn are approximately equal and an order of magnitude greater than Pb and four to five orders of magnitude greater than Au and Ag (Table 7.1).
- Experiments replicating high temperature interaction of seawater with a basalt containing approximately equal concentrations of Cu and Zn show that Zn concentrations are approximately an order of magnitude higher than Cu in the resultant hydrothermal fluid (Seewald and Seyfried, 1990).
- The minimum concentrations that would be reasonably required to form an economic ore deposit with the composition of Balta Tau, i.e. in the region of at least 1ppm for major components (Cu, Fe, Zn) and at least 0.1ppb for trace metals such as Au and Ag (Ohmoto et al., 1983; Large et al., 1989; Huston, 1998).

	MOR systems		Arc systems – Lau Basin		Balta Tau	
	μmol/kg	ppm	μmol/kg	ppm	μmol/kg	ppm
Fe	0 to 1.359×10^6	0.0 to 7590	1200 to 2900	67 to 160	10 to 100000	5.6 to 5600
Cu	0.1 to 21	0.0064 to 1.3	15 to 35	0.95 to 2.2	10 to 100	0.64 to 6.4
Zn	0.7 to 780	0.050 to 51	1200 to 3100	78 to 200	10 to 1000	0.65 to 65
Pb	0.05 to 1.6	0.010 to 0.33 (0.003*)	3.8 to 7.0	0.79 to 1.5	0.01 to 10	0.002 to 2
Ag	0.012 to 0.12	0.0013 to 0.013 0.0027*	-	-	0.001 to 0.1	0.0001 to 0.01
Au	<0.001	<0.0002*	-	-	0.0001 to 0.01	0.00002 to 0.002
Sb	0.007 to 0.018	0.0009 to 0.0022	-	-	1 to 10	0.12 to 1.2
As	0.030 to 1.074	0.0023 to 0.080	6 to 11	0.45 to 0.82	1 to 10	0.07 to 0.7

Table 7.4. End member hydrothermal fluid compositions calculated from direct measurement of fluids actively venting fluids. (Compiled in Von Damm 1995; except for *Hannington and Scott, 1988), and estimates of Balta Tau fluid composition.

7.4.5 Formation of footwall and massive sulphides

Sulphide precipitation and Cu-Zn zoning

The mainstage massive sulphides at Balta Tau comprise chalcopyrite-pyrite rich ores in lower and central zones grading to sphalerite(-galena-tennantite) rich ores in upper and marginal zones, and the footwall shows a similar broad zonation from a central zone of chalcopyrite-pyrite rich sulphides to marginal sphalerite(-galena-tennantite-pyrite). This is typical of sulphide zoning in VMS deposits and is generally interpreted to reflect differences in the temperatures at which Cu, Zn and Pb chloride reach saturation as a hydrothermal fluid cools (e.g. Large, 1977; Eldridge et al., 1983, Fouquet et al., 1993). Combining estimates of metal solubilities and concentrations in Balta Tau hydrothermal fluids suggests that chalcopyrite and pyrite would have precipitated at temperatures of 250 to 300°C (lower than many MOR systems due to the higher oxidation of Balta Tau fluids which increases Cu and Fe solubility), while sphalerite and galena do not become saturated until further cooling to between 190 and 250°C for sphalerite and 140 to 220°C for galena (Figures 7.3 and 7.4). Therefore progressive cooling of Balta Tau fluids could produce the zoning observed in massive sulphides and the footwall as follows (illustrated in Figure 7.8):

Upwelling hydrothermal fluids with initial temperatures of at least 300°C reached the shallow sub-seafloor environment and conductively cooled to between 250 and 300°C, resulting in pyrite and chalcopyrite precipitation in the central footwall and lower massive sulphide ore horizons. The high temperatures and small degree of cooling suggest that little or no seawater mixing was involved. This is consistent with the presence of Fe-chlorite that indicates a strong hydrothermal fluid component, and absence of barite due to high temperatures where anhydrite would preferentially precipitate had sufficient seawater mixing occurred to supply the sulphate.

Stratigraphically higher massive sulphide ores are pyrite-sphalerite dominated with uppermost and marginal ores containing significant tennantite and galena. Marginal footwall zones are also sphalerite dominated, with variable proportions of tennantite, galena, chalcopyrite and pyrite. This is consistent with later, lower temperature fluids reaching the seafloor with temperatures of around 200 to 250°C, and undergoing conductive cooling and a significant degree of seawater mixing as the hydrothermal fluids migrate away from the central zone of upwelling fluids reducing temperatures to less than 200°C. The effect of changes in pH such as an increase due to mixing with seawater or a decrease due to sulphide precipitation (Figure 7.6) on Pb, Zn and Fe solubility would be overshadowed by the effect of decreasing temperature. Lower formational temperatures of these horizons are also reflected by the appearance of barite in massive sulphides, since anhydrite is soluble at these low temperatures and will not therefore inhibit barite precipitation. There is a notable scarcity of barite associated with the low temperature sphalerite-rich footwall sulphides. This could reflect rapid and extensive seawater mixing diluting Ba^{2+} before significant

quantities of barite have time to precipitate, since the rate of barite precipitation is much slower than rates of sulphide precipitation. The temperature range of sphalerite precipitation predicted by solubility curves (250 to 190°C) is higher than the temperatures indicated by fluid inclusions for these sphalerite rich horizons (140 to 170°C). This may be attributed to the slow equilibration rates for Zn, which are significantly slower than Cu and Fe, and result in Zn responding relatively slowly to temperature change (Sewald and Seyfried, 1990). Therefore fluids may have cooled significantly below the saturation point of sphalerite by the time significant sphalerite precipitates.

Zone refining

The enrichment of upper massive sulphide zones in metals soluble at low temperatures (Zn, Pb, As, Sb, Ag, Au, Hg) is often attributed to the process of zone refining, whereby low temperature fluids remobilise these metals from the base of sulphide mounds and redeposit them in lower temperature zones at the top of the mound upon further cooling and mixing with seawater. The zoning in major sulphides in the footwall and massive sulphides at Balta Tau may be explained simply by the progressive cooling of a hydrothermal fluid as described above, however the overall increase in trace element concentration from the footwall to uppermost and marginal sulphide and baritic ore facies (see Figure 5.21) suggests that zone refining did take place during ore formation at Balta Tau.

Au content

Electrum is absent from the footwall and massive sulphides indicating that fluids did not become saturated with respect to Au during precipitation of these ore facies. The solubility curves for Au indicate that Balta Tau fluids should have approached saturation with respect to the dominant species $Au(HS)_2^-$ at temperatures of around 150°C. However, since the solubility of Au as bisulphide complexes only varies slightly with temperature, a further decrease in temperature may not have been an efficient precipitation mechanism and there may have been insufficient time to precipitate Au before the hydrothermal fluids were expelled into the ocean. Increased seawater mixing in the upper sulphide mound (indicated by barite $^{87}Sr/^{86}Sr$) may also discourage Au precipitation due to dilution, a slight increase in oxidation and pH.

Bulk analyses of sphalerite-rich ores in actively forming deposits indicate that although electrum is not visible at a microscopic level, Au is elevated relative to higher temperature Cu-rich ores (e.g. Hannington and Scott, 1988), suggesting that Au does occur as sub-microscopic inclusions or as solid solution in sulphide phases. By analogy, the sphalerite-rich sulphides at Balta Tau may be expected to contain elevated Au, but to a lesser degree than the enrichment in barite-rich ores. This is consistent with the interpretation that Au would have been close to saturation but lacked the efficient precipitation mechanism and time required to form visible native gold/electrum. The rapid entrapment of small quantities of Au by sulphide phases may be facilitated by processes such

as adsorption of Au onto the surfaces of sulphosalts (Renders and Seward, 1989), consistent with the correlation between Au and As-Sb-Pb in some modern systems.

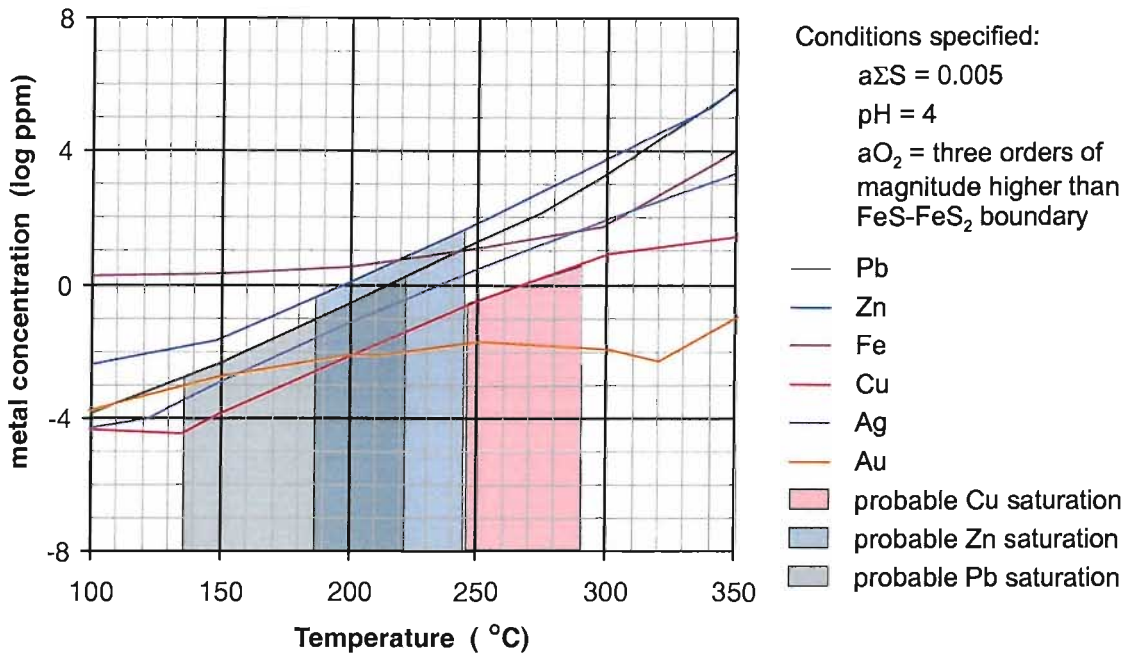

a. Solubility of base and precious metals in Balta Tau hydrothermal fluids showing that predicted temperatures of saturation decrease from Cu to Zn to Pb.

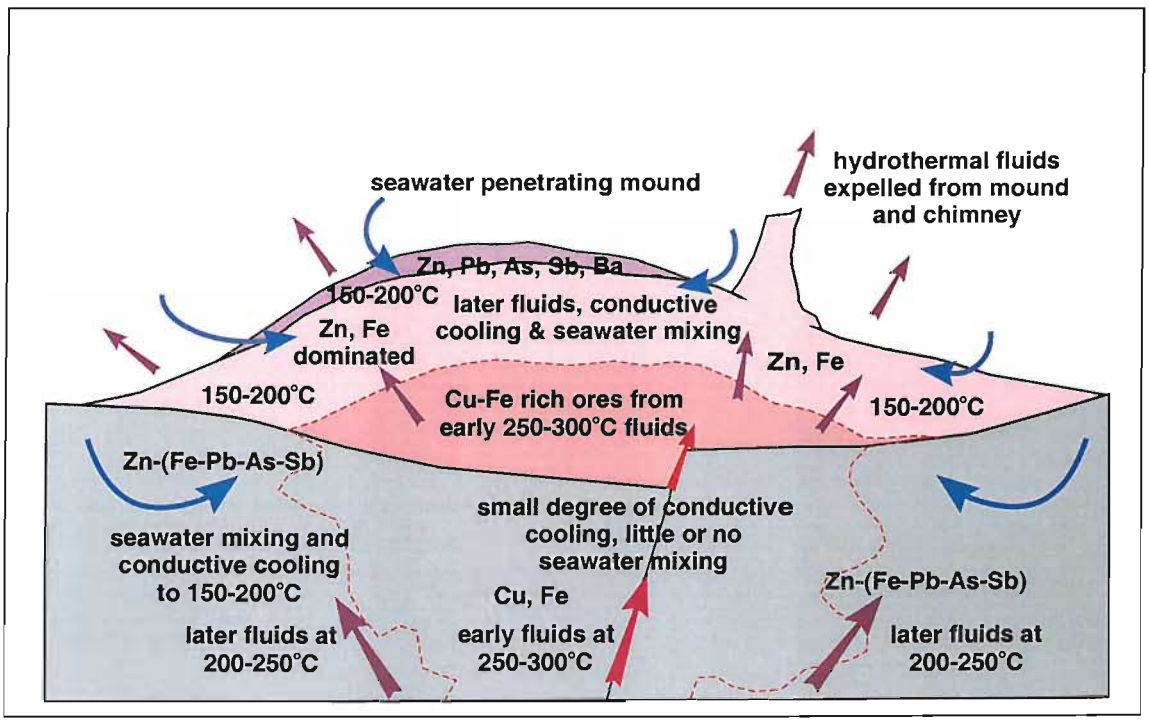

b. Model to show the formation of compositionally zoned footwall and massive sulphides based on the metal solubilties shown in a.

Figure 7.8. Formation of the zoned massive sulphide and footwall ore facies at Balta Tau.

7.4.6 Formation of barite-rich facies

The barite-rich ores at Balta Tau are mineralogically distinct from the sphalerite-rich massive sulphides, in spite of having precipitated from fluids of similar temperature, oxidation, and salinity. The most significant differences include:

- Particularly elevated precious metal contents with an abundance of coarse electrum.
- Low proportion of sphalerite relative to other sulphides.
- High proportion of Cu with chalcopyrite and tennantite the most dominant sulphides.
- High proportion of barite to sulphides.

Barite-rich deposits in ancient and modern systems are characterized by Zn dominated sulphides with depletion in Cu and enrichment in Pb-As-Sb-Ag-Au-Hg and are generally considered the result of low temperature precipitation and zone refining (e.g. Hannington et al., 1995, Huston and Large, 1989). The barite lens and the baritic matrix of barite-rich sulphides at Balta Tau are enriched in the low temperature suite Pb-As-Sb-Ag-Au-Hg, however the unusual characteristics listed above suggest that unlike the sphalerite-rich massive sulphides, barite-rich ores are not typical of low temperature seafloor precipitates or zone refining.

Formation of the barite lens and barite-rich sulphides

Sr isotopes in barite indicate that a smaller degree of seawater mixing was involved in formation of the barite lens compared with pyrite and sphalerite-rich massive sulphides. The coarseness of barite crystals and much of the sulphides (particularly tennantite-chalcopyrite, galena) and electrum are indicative of slow, sustained precipitation, with periods where barite growth ceased enabling micron-sized sulphide blebs to form on barite crystal surfaces, forming zones of sulphide inclusions. This suggests that precipitation occurred in a stable, sustained environment where hydrothermal fluids had a long residence time and seawater mixing was limited, which would enable significant, coarse minerals to precipitate from metals in low concentration over time. The absence of chimney-like structures or chimney fragments suggests that the barite lens at Balta Tau may have been closer to mound or dome-like structure which partially capped the sulphide mound. The barite-rich sulphides, where a barite-sulphide matrix encloses pyrite clasts, probably developed where the barite lens came into contact with mechanically degraded sulphides now forming talus at the top of the sulphide mound. Hydrothermal fluids may have escaped by diffusing through the barite mound, perhaps analogous to the "shimmering waters" emitted at modern sites which contain very little particulate material (e.g. Hannington et al., 1995). Small scale venting may also have occurred through fissures in the barite. The insolubility of barite would enable such a structure to be stable at the seafloor for a considerable length of time. The proposed formation of the barite lens and barite-rich sulphide is illustrated in Figure 7.9.

Comparable barite structures have been reported from active systems. Hannington et al. (1995) describe a feature observed from a number of vent fields where barite structures are not venting but have warm, H_2S-rich water seeping out over much of their surface area, and start to vent again if broken open. This implies that hydrothermal fluid is trapped within the barite structure and diffusing slowly through the chimney walls. Fouquet et al. (1993) describe barite-sphalerite chimneys at Vai Lili, Lau Bain, with an outer zone of barite-sphalerite-galena-tennantite where barite is dendritic reflecting rapid, unstable precipitation, and an inner zone with coarser, more crystalline barite with sulphides reflecting precipitation under more stable conditions. The inner zones of such chimneys may be analogous to the coarse barite-sulphides of the barite lens, supporting the inference of slow, stable, precipitation rates.

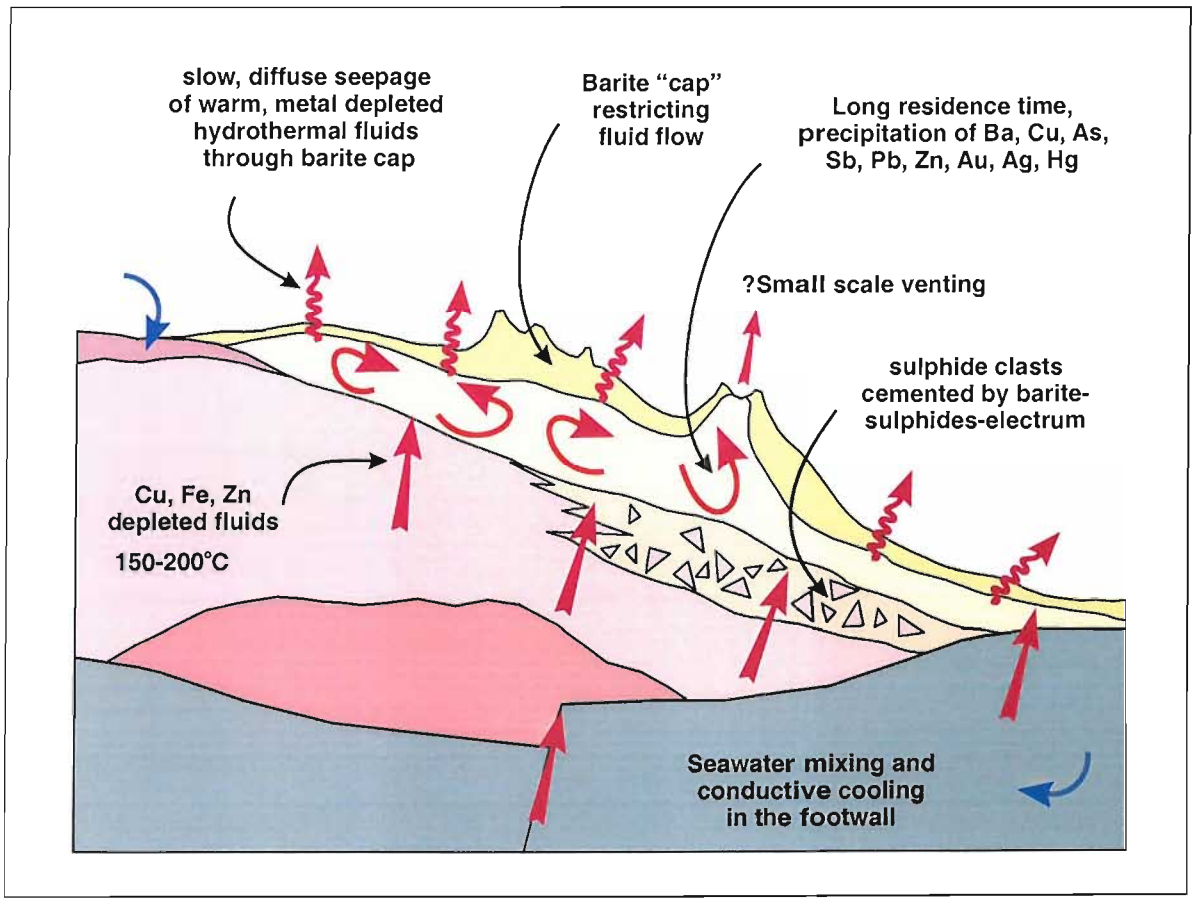

Figure 7.9. Formation of barite-rich ores at Balta Tau.

Precipitation of sulphides, electrum and barite

Hydrothermal fluids reaching the barite mound would have already undergone some degree of conductive cooling and seawater mixing in the footwall and massive sulphide mound, and have precipitated a large proportion of their Cu-Fe-Zn-Pb-As-Sb content as massive sulphides. Therefore the fluids would have had low base metal concentrations, consistent with the relatively low ratios of base to precious metals and base metals to barite.

In contrast to conditions in the upper massive sulphides, the long residence time of hydrothermal fluids in the barite mound would have enabled precipitation of phases even from low concentrations of metals. Therefore slow, sustained precipitation of sulphides forming coarse aggregates of tennantite-chalcopyrite(-galena) which generally lack collomorphic textures could have taken place in spite of the low base metal concentrations. This would have been a favourable environment for the formation of coarse electrum, since at temperatures of around 150°C fluids would probably have been close to saturation with respect to Au as $Au(HS)_2^-$ complexes (Figure 7.5b), and extensive sulphide precipitation in massive sulphide horizons would have resulted in a lowering of fluid pH and a slight depletion in H_2S concentration, which also significantly reduce Au solubility (Figures 7.10 and 7.11). Precipitation of Au would also have been facilitated by the restricted seawater mixing preventing an increase in pH or oxidation (Figures 7.10 and 7.11). The common occurrence of coarse electrum at the margin of sulphide aggregates might reflect a decrease in the pH and concentration of H_2S in the micro-environment surrounding precipitating sulphide grains (as proposed for gold-pyrite associations by Large, 1989). Ag could precipitate in the barite mound due to small degrees of conductive cooling (Figure 7.5a), but would not be favoured by local decreases in pH around sulphide grains (equation 7.5) which could explain the generally higher Au/Ag of electrum grains in sulphides compared to grains in barite (Chapter 5, Section 5.2.8).

The transportation and deposition of Hg has not yet been discussed. The most probable Hg complexes would be bisulphide or sulphide complexes (Wood and Samson, 1998), suggesting that precipitation mechanisms would be comparable to those for Au. However, the positive correlation with Ag and negative correlation with Au in electrum grains suggests that the behaviour of Hg more closely mirrors that of Ag than Au (Section 5.2.8, Chapter 5) which suggests the transport and precipitation of Hg may not be that straightforward.

The close association of electrum with tennantite suggests that adsorption of Au onto colloidal AsS_3 and SbS_3 may also have been an important intermediate stage of precipitation prior to the formation of coarse electrum and tennantite (Renders and Seward, 1989). Had such colloidal particles formed in the upper massive sulphide horizons, they would probably have been lost to the ocean before having a chance to form sulphide grains. The Au-tennantite association may also be enhanced by the transport of additional Au as As-Sb thiocomplexes.

Barite precipitation in this zone is favoured by low temperatures (prohibiting anhydrite formation), reduced seawater mixing that limits the dilution of $[Ba^{2+}]$, and sufficient time for significant quantities to precipitate in a stable environment.

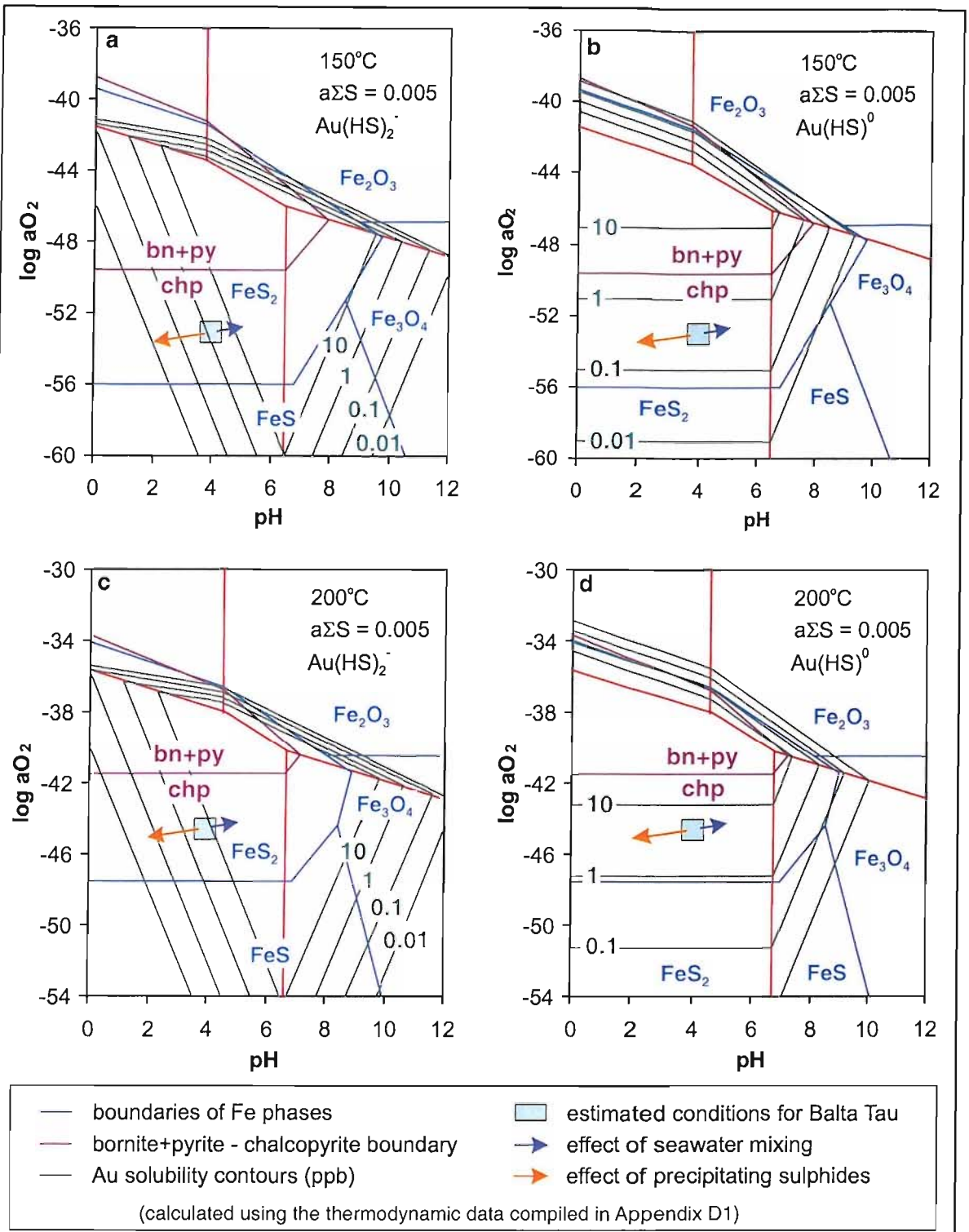

aO_2 - pH diagrams at 150°C (a and b) and 200°C (c and d) showing Au solubility as $Au(HS)^0$ and $Au(HS)_2^-$ complexes. At conditions inferred for Balta Tau, mixing with seawater would cause a slight increase in oxidation and a small increase in pH which would have a negligable effect on the solubility of $Au(HS)_2^-$ or $Au(HS)^0$ complexes. Precipitation of sulphide phases would decrease pH and maybe a slight decrease oxidation, resulting in a decrease in Au solubility as $Au(HS)_2^-$ complexes but having a negligable effect on Au transported as $Au(HS)^0$ complexes.

Figure 7.10. aO_2 – pH diagrams illustrating the relative importance and effect of seawater mixing and sulphide precipitation on gold solubility.

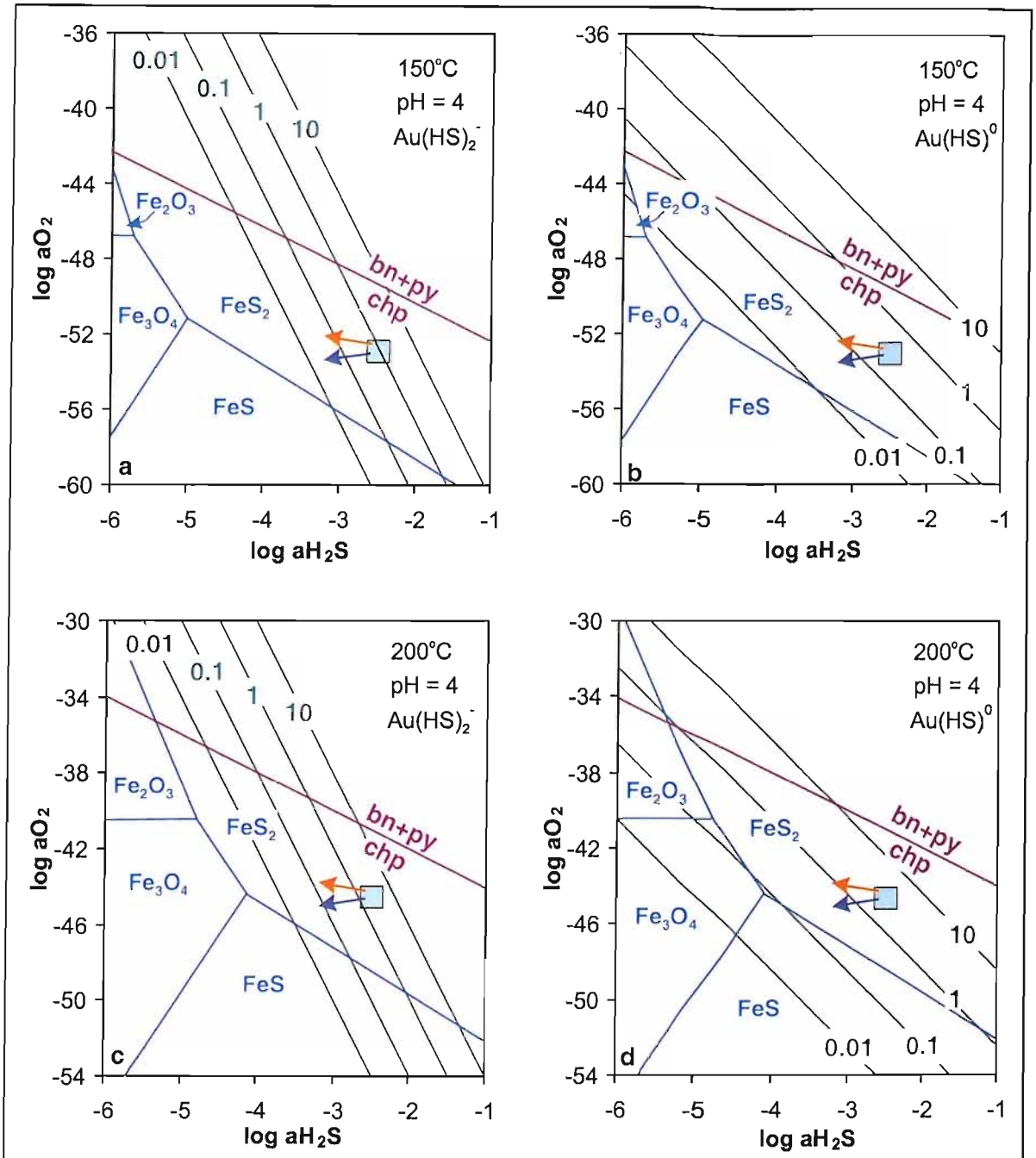

aO_2 - aH_2S diagrams at 150°C (a and b) and 200°C (c and d) showing Au solubility as $Au(HS)^0$ and $Au(HS)_2^-$ complexes. At conditions inferred for Balta Tau, both mixing with seawater and sulphide precipitation would decrease the concentration of H_2S. Therefore both processes would decrease Au solubility whether Au was transported as $Au(HS)_2^-$ or $Au(HS)^0$ complexes.

Figure 7.11. aO_2 - aH_2S diagrams illustrating the effect of seawater mixing and sulphide precipitation on gold solubility.

Anomalous Cu content

Although all of the base metal concentrations were depleted in fluids entering the barite mound, the solubility curves in Figures 7.3b and 7.4b dictate that Zn concentrations should still have been almost two orders of magnitude greater than Cu, particularly in light of the slower equilibration rates of Zn than Cu. The high proportion of chalcopyrite and tennantite relative to sphalerite can not therefore be accounted for by these solubility curves. This may be due to the poor understanding and lack of reliable data for Cu bisulphide complexes at low temperatures, since there is no consensus as to the stoichiometry of dominant complexes and there are considerable discrepancies in thermodynamic data obtained from experimental studies (Wood and Samson, 1998). The solubility of Cu as a bisulphide complex in Figure 7.3b is based on data from Crerar and Barnes (1976), however experiments were not conducted below 200°C and data for 100 and 150°C is extrapolated. Therefore, as noted by Wood and Samson (1998), bisulphide complexes may be more important at low temperatures than the data currently available suggests. In addition, other complexes may be important in the low temperature transport of Cu, such as thioarsenite and thioantimonite complexes, which are suggested to be significant in the transportation of Au.

The barite-rich ores at Balta Tau are not alone in requiring a mechanism for low temperature transportation of Cu. Numerous low temperature (<250°C) seafloor deposits and epithermal systems contain abundant tennantite-tetrahedrite which, unless highly argentiferous, contains around 40wt% Cu, and minor chalcopyrite is also commonly reported. Given that the transport of Cu as chloride complexes is generally considered to be negligible below around 250°C (e.g. Seyfried and Ding, 1995), these occurrences also suggest a more efficient mechanism for transporting Cu at low temperatures than those currently documented is required.

7.5 LATE STAGE PROCESSES

7.5.1 Introduction

Late stages of hydrothermal activity, diagenesis and low grade metamorphism, and local deformation have affected the mainstage ores at Balta Tau to some degree. The most significant modifications occurred during late stages of hydrothermal activity, and include the recrystallization of clastic ores to form layered sulphides and overprinting of footwall alteration to quartz and Mg-chlorite.

7.5.2 Footwall alteration

Alteration assemblages of the footwall are dominated by quartz and Mg-chlorite(-pyrite) which are often intimately associated and appear to have co-precipitated. The Mg-chlorite post-dates ore

formation (Chapter 4, Section 4.2) and precipitated from a seawater dominated fluid at low temperatures of 100 to 150°C (based on chlorite geothermometry, Section 5.4.7), probably replacing alteration minerals that were cogenetic with the sulphides. The quartz also post dates sulphides and is suggested to have formed from a low temperature condensed vapour phase produced during waning stages of hydrothermal activity (Stage III fluids, Chapter 6, Section 6.5.3). Therefore the co-precipitation of quartz and Mg-chlorite points to the mixing of seawater and a condensed vapour phase in the footwall.

The condensed vapour phase most likely segregated from a hydrothermal fluid produced during late, low temperature stage of hydrothermal activity. Temperatures would probably not have been sufficiently high to enable the reduction of seawater sulphate or significant leaching of metals from volcanic rocks. Near neutral pH facilitates Si solubility and the fluid may have leached significant Si from volcanic rocks at low temperatures during final ascent to the seafloor, consistent with extensive precipitation of quartz upon cooling in the footwall. In the footwall, mixing of the vapour phase with seawater would produce an Mg, Si, SO_4^{2-} rich fluid with near neutral pH and low salinity. Since the condensed vapour would have a low Sr concentration, the Sr signature of Mg-chlorite is suggestive of seawater dominance and does not record a condensed vapour phase in spite of fluid mixing in the footwall. Similarly, the low Fe content of the condensed vapour resulted in an Mg-dominated chlorite reflecting the high Mg/Fe composition of seawater. The Mg-chlorite(-pyrite) probably replaced hydrothermal alteration minerals such a more Fe-rich chlorite and/or sericite, by reactions such as:

$$5Mg^{2+} + Fe_5Al(Si_3Al)O_{10}(OH)_8 = Mg_5Al(Si_3Al)O_{10}(OH)_8 + 5Fe^{2+} \quad (7.19)$$

$$5Mg^{2+} + KAl_2(Si_3Al)O_{10}(OH)_2 + 6H_2O = Mg_5Al(Si_3Al)O_{10}(OH)_8 + Al^{3+} + K^+ + 6H^+ \quad (7.20)$$

Excess Al from equation 7.20 was probably incorporated into the chlorite occupying tetrahedral and octahedral sites, as indicated by microprobe data (Chapter 5, Section 5.4.2). Pyrite may have formed from the Fe^{2+} and H^+ produced by sulphate reduction:

$$Fe^{2+} + 2SO_4^{2-} + H^+ = FeS_2 + 8H_2O \quad (7.21)$$

The pyrite associated with chlorite was too fine grained to enable analysis of $\delta^{34}S$, therefore the contribution of reduced seawater sulphate can not be confirmed. The formation of pyrite suggests that although SO_4^{2-} was the dominant aqueous sulphur species, oxidation was still within the pyrite field.

The footwall fluids would not have been capable of significant remobilisation of sulphides, since temperatures were too low for formation of Cl^- complexes and fluids contained insufficient H_2S

for the formation of bisulphide complexes. However, they did remobilise small quantities of tennantite, indicated by the formation of quartz-tennantite veins. Since the fluids did not contain reduced sulphur and the tennantite $\delta^{34}S$ does not support the reduction of seawater sulphate, the sulphur as well as metals must have been remobilised suggesting the formation of thiocomplexes such as AsS_3 and SbS_3. These fluids are also likely to be responsible for the oxidation rims found around some sulphides in the footwall.

Numerous samples from the footwall contain textures suggesting the replacement of sulphides, particularly chalcopyrite and sphalerite, by Mg-chlorite, but this is not likely given the inability of fluids to transport significant metals. The Mg-chlorite is more likely to be pseudomorphing earlier hydrothermal chlorite and/or muscovite which replaced sulphides during mainstage ore formation, when fluids would have been capable of remobilising metals.

7.5.3 Sericite and muscovite formation

The formation of muscovite and sericite in ore horizons and the immediate hanging-wall post-dates ore formation and probably occurred at the same time or slightly later than the footwall Mg-chlorite and quartz (Chapter 4 and Chapter 5, Section 5.4.3). This could reflect the evolving composition of the seawater and condensed vapour phase during footwall interactions, which would have resulted in a progression to lower Mg, higher K and lower Na concentrations and lower pH (equations 7.19 and 7.20), which eventually leads to the precipitation of sericite/muscovite in preference to Mg-chlorite. This is supported by the following observations:

- SEM images from the footwall indicate fine intergrowths of muscovite with Mg-chlorite as well as muscovite replacing Mg-chlorite.
- The abundance of sericite and muscovite increases up stratigraphy, with minor amounts in the footwall and massive sulphides increasing to significant amounts in the layered sulphides, barite rich sulphides and the barite lens, to complete sericitization of the immediate hanging-wall. This is mirrored by an increase in the K/Na ratio of sericite/muscovite up stratigraphy. These trends support the progressive change in fluid chemistry proposed, and the small scale stratigraphic variations suggest the muscovite is not the product of metamorphism (although some may have recrystallized during metamorphism).
- Almost all of the muscovite-sericite is Mg-rich, suggesting precipitation from an Mg-dominated fluid consistent with seawater. Although the replacement of Fe-bearing chlorite with Mg-chlorite would have released Fe during footwall interactions, the overall fluid composition did not evolve to more Fe rich because pyrite co-precipitated with the Mg-chlorite. Therefore the Mg/Fe does not alter appreciably up stratigraphy.
- Where associated with ore assemblages, the muscovite/sericite post dates and replaces sulphides, and also appears to post date barite occurring along grain boundaries. In layered

sulphides and barite-rich sulphides, a thin layer of digenite/covellite has formed at the contact between muscovite and the sulphide grains it is replacing, consistent with the more oxidized nature of seawater mixed with the condensed vapour phase compared to the mainstage hydrothermal fluids.

An important implication of this interpretation is that the immediate hanging-wall must have been deposited before or during the circulation of seawater and the condensed vapour phase. Deposition of this unit may well have reduced the ingress of seawater into the footwall, hence preventing newly entrained seawater from overprinting the sericite with Mg-chlorite. The absence of sulphides other than pyrite in the hanging-wall supports the inference that fluids were not capable of significantly remobilising base and precious metals, although the elevated contents of Zn and As in the sericitized unit indicates that these were mobile in low concentrations. The burial of seafloor sulphides soon after mainstage ore deposition is consistent with the general lack of oxidation of most ores that would result from prolonged exposure to seawater.

7.5.4 Formation of layered sulphides

The layered ores are interpreted to have formed from the recrystallization of fine grained sulphide mud and clasts, which took place during late stages of ore deposition (Chapter 4, Section 4.4.4). The layered ores have a similar mineralogy as the other sulphide horizons confirming that they recrystallized under similar conditions, and the presence of hessite confirms a low temperature and low oxidation (Zhang and Spry, 1994). This suggests that the recrystallization took place during late stages of mainstage hydrothermal activity, probably from low temperature, diffuse flow through the clastic sulphides.

The recrystallized nature of layered ores is consistent with the absence of trace elements held in metastable states such as As in pyrite, since these are likely to be expelled during recrystallization (Chapter 5, Section 5.3.1). Comparable examples of low As recrystallized pyrite are described from metamorphosed ores in other ancient deposits (e.g. Huston et al., 1995; Cook, 1996).

7.5.5 Diagenetic, Metamorphic and Deformational overprinting

Diagenesis and low grade metamorphism do not appear to have had a significant effect on the Balta Tau ore horizons. They have resulted in the minor formation of carbonate infilling porosity in massive sulphide and barite-rich ores, and scarce scolecite (zeolite) and pumpellyite replacing barite and sulphides in all horizons. After deposition of hanging-wall volcaniclastics, there was still a high degree of hydrothermal activity in the vicinity of Balta Tau, as indicated by the intense

quartz-epidote-carbonate veining in these hanging-wall sequences, although they do not penetrate the ore horizons.

Deformation has resulted in the tilting of bedding and formation of a steeply dipping foliation, together with numerous faults with small displacements and the Eastern Fault which truncates ore horizons. Shearing affects units immediately adjacent to massive sulphide horizons particularly at the hanging-wall contact, and in a zone associated with the Eastern Fault. In these sheared zones sericite/muscovite have recrystallized and coarsened, but retained a composition indistinguishable from sericite/muscovite in the rest of the deposit. Local remobilisation of sulphides resulted in the development of an oblique fabric in layered ores, and partial recrystallization of sphalerite-rich sulphides.

7.6 MODEL OF ORE FORMATION

The formation of the Balta Tau interpreted from this study deposit may be summarised as follows (Figures 7.12 and 7.13):

- Figure 7.12a: Initiation of seawater convection following emplacement of a hot intrusive body at depth, with early stages of hydrothermal activity expelling low temperature hydrothermal fluids at the seafloor.
    - Figure 7.13a: These fluids may have precipitated anhydrite and barite, and probably low temperature sulphides. This stage of mineralization has been entirely overprinted by later stages with the exception of early barite veins in the footwall.

- Figure 7.12b: Early phase of mainstage ore formation with the hydrothermal system at its maximum temperature. Seawater derived fluids leached metals and sulphur from the volcanic rocks and seawater sulphate is reduced to sulphide. During fluid ascent, sub-critical phase separation probably occurred at depth in the system followed by remixing of segregated phases, producing fluids with variable salinities. These reached the seafloor at temperatures of at least 300°C, contained high concentrations of metals and reduced sulphur and were moderately reduced.
    - Figure 7.13b(i): In the sub-seafloor environment fluids conductively cooled and possibly mixed with small amounts of seawater reducing temperatures to around 250 to 300°C. This resulted in saturation with respect to Fe and Cu sulphides which precipitated at the seafloor and in a sub-seafloor stockwork zone. Seafloor deposition resulted in mound formation with an outer zone of more sphalerite-rich ores where fluids cooled and mixed with seawater, and may well have included the formation of

black smoker chimneys. Additional phases included Fe-rich chlorite, quartz and probably anhydrite.

- Figure 7.12c. Later phases of mainstage ore formation reflect a cooler period of hydrothermal activity, with temperatures at depth estimated at around 300°C. These correspond to the stage I and stage II fluids identified from fluid inclusion analyses. This lower temperature stage of ore formation is illustrated in two stages as follows.
    - Figure 7.13c(i): Fluids emerged at the seafloor/shallow sub-seafloor at temperatures of around 200 to 250°C, and migrated further from the central zone of upwelling, permeating a large volume of the porous footwall. Shallow entrainment of seawater resulted in extensive fluid mixing in addition to conductive cooling in the footwall resulting in considerable deposition of Zn-rich sulphides at 150 to 200°C in marginal zones. Hydrothermal fluids would also have intensely altered the footwall volcanics, probably to a chlorite-sericite dominated assemblage. At the seafloor, growth of the sulphide mound increased the residence time of fluids in the mound resulting in extensive conductive cooling and some mixing with seawater within the mound. This produced a high proportion of sphalerite-rich sulphides in outer zones together with barite, and may have included white-smoker style venting. Zone refining may also have taken place within the mound. Sphalerite-rich mud and debris accumulated at the margins of the mound from the mechanical degradation of mound (and chimney?) material and particle fall out from venting fluids.
    - Figure 7.13b(iii). Barite-rich precipitates formed a partial cap over the sulphide mound. The relative impermeability and insolubility of barite restricted seawater entrainment and trapped warm, metal poor hydrothermal fluids that had already deposited sulphides within the mound. These fluids slowly precipitated Cu-As-Sb-Pb rich sulphides, electrum and coarse barite at temperatures of around 150°C, facilitated by the long residence time of fluids within the barite structure. Low temperature fluids rising from the marginal footwall permeated clastic sulphide material at the margins of the mound and recrystallized the finer material to form layered sulphides. Fluids emerging from these marginal zones and the barite lens were low temperature and metal poor, forming a diffuse flow that may have been comparable to the shimmering waters described from active systems (e.g. Hannington et al., 1995).

- Figure 7.12c. Late stage hydrothermal activity, which post-dated the mainstage of ore formation, probably involved low temperature, shallow seawater circulation reflecting a reduction in heat supply due to the cooling of intrusive bodies at depth. Fluid temperatures would have been insufficient for the effective leaching and transport of metals or reduction of seawater sulphate. Shallow sub-critical phase separation initially produced a vapour phase

that condensed and reached the footwall at temperatures of less than 200°C with low metal and reduced sulphur contents, near neutral pH, and high contents of leached Si. These correspond to Stage III fluids from inclusion analyses.

- Figure 7.13c. In the footwall, Stage III fluids cooled and mixed extensively with seawater resulting in the rapid deposition of quartz and replacement of original alteration facies with Mg-chlorite, together with remobilisation of tennantite and formation of quartz-tennantite veins.

- Figure 7.12d. Sealing of porosity in the footwall and/or tectonic activity re-routed fluid flow so that no further hydrothermal fluids penetrate the footwall at Balta Tau. Volcanic activity on the Irendyk Arc resulted in deposition of the hanging-wall volcanic breccia.
  - 7.13d. Burial of the deposit reduced the entrainment of seawater into the footwall. Seawater that had already permeated the footwall with fluid chemistry modified by rock interaction precipitated minor sericite/muscovite in ore horizons and migrated into the newly deposited hanging-wall causing in intense sericitization.

- Figure 7.13e. Continued burial, diagenesis and low grade metamorphism with development of minor carbonate, zeolite and pumpellyite in ore horizons. A high degree of hydrothermal activity in the vicinity of the ore deposit long after deposition and burial produced extensive quartz-epidote-carbonate veining in hanging-wall volcaniclastics.

- Finally, deformation relating to arc-continent collision and subsequent continent-continent collision included tilting, development of foliation, shearing, faulting and partial recrystallization of sulphides and muscovite (not illustrated).

Figures presented on the following pages:

Figure 7.12. Model of ore formation illustrating the large scale evolution of hydrothermal fluids.

Figure 7.13. Model of ore formation illustrating deposit scale processes responsible for ore facies.

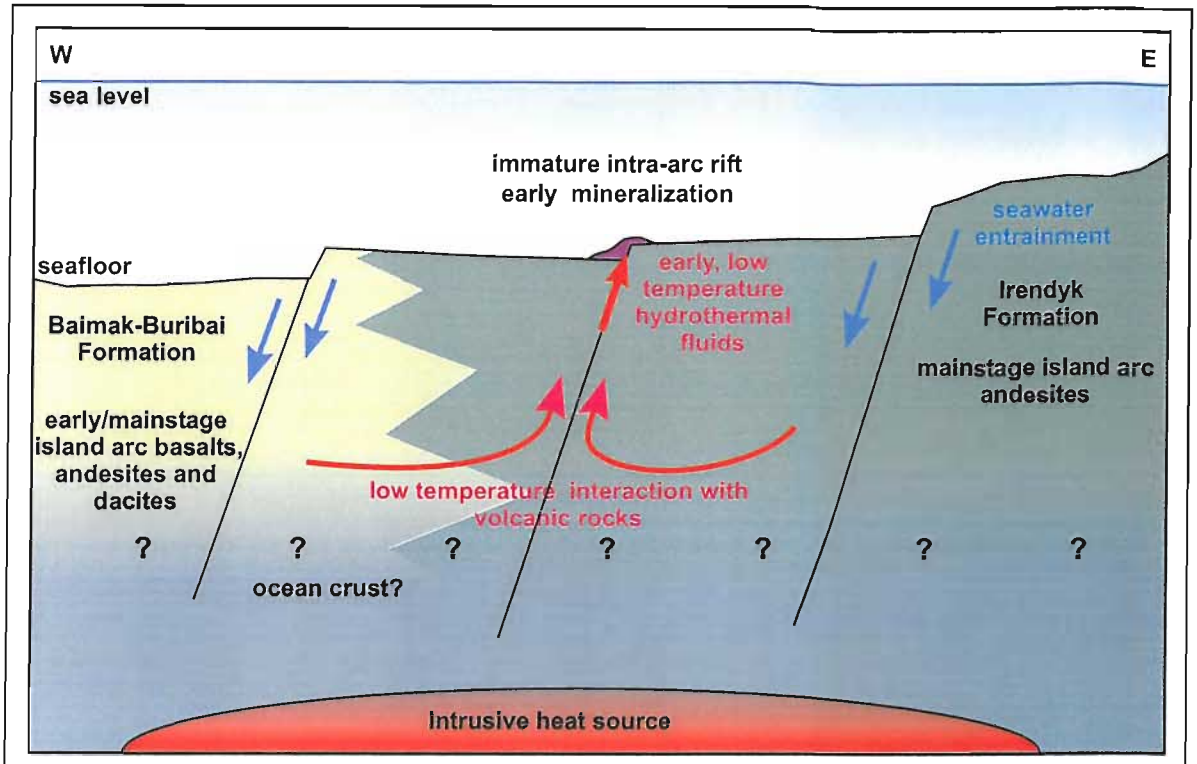

Figure 7.12a

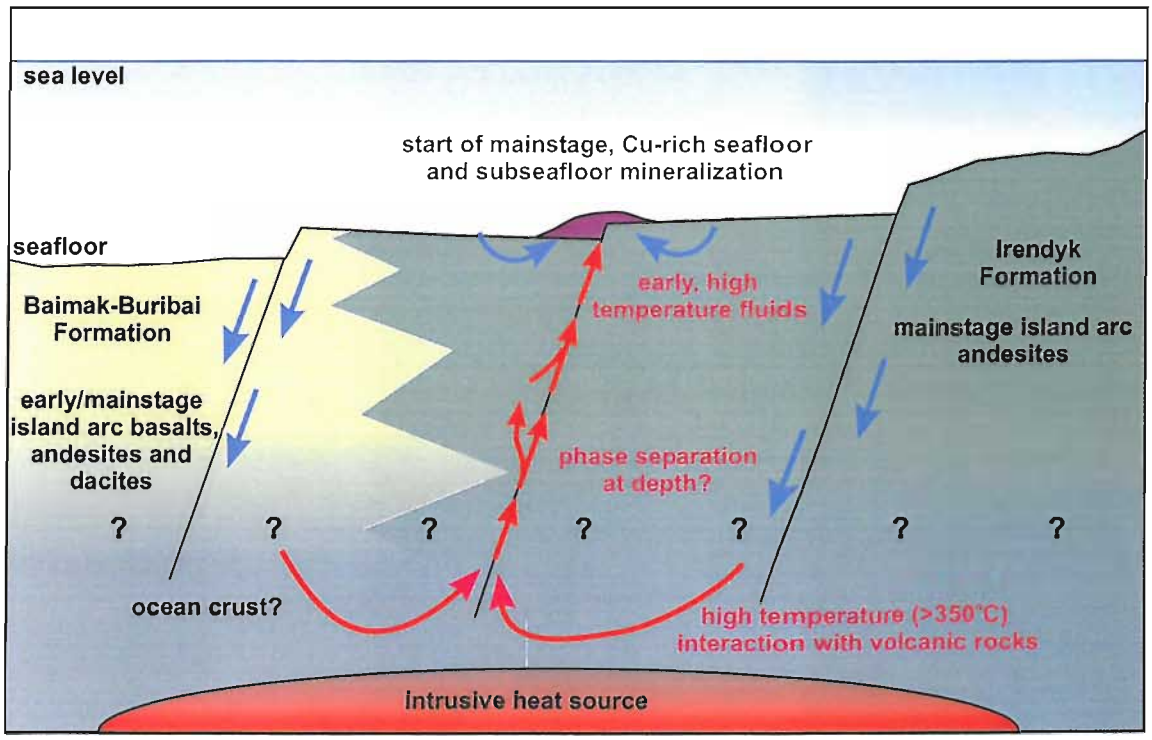

Figure 7.12b

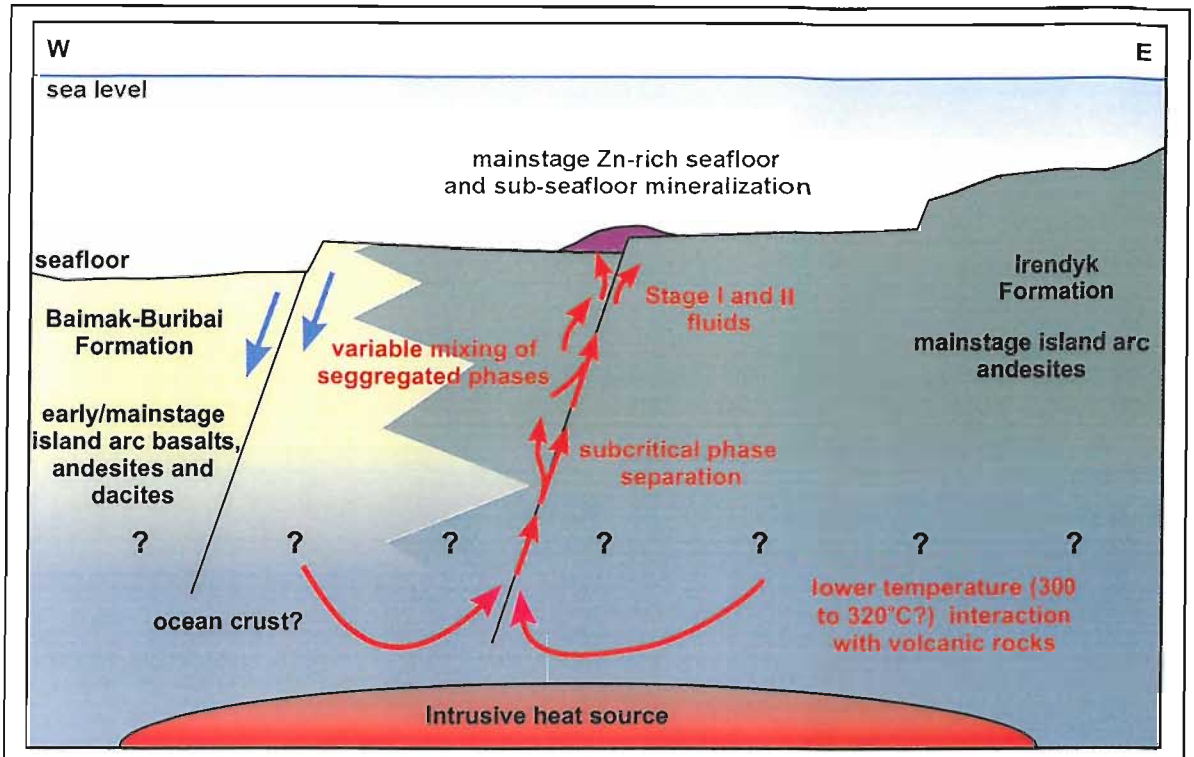

Figure 7.12c

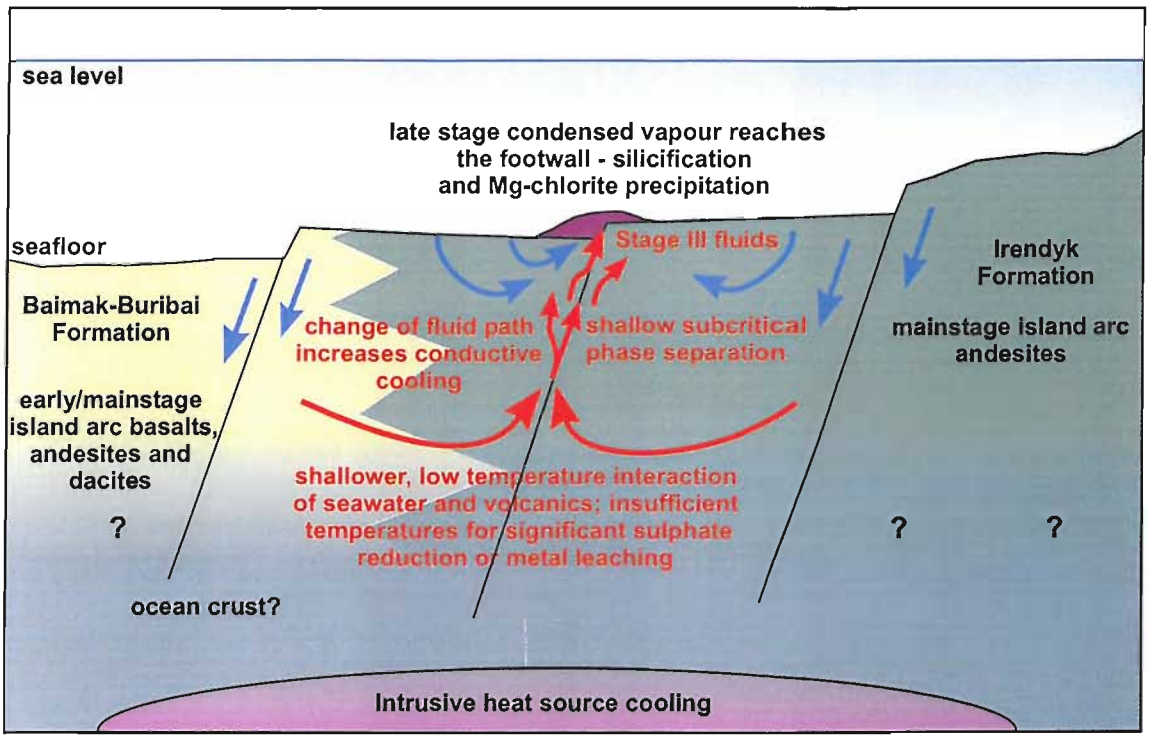

Figure 7.12d

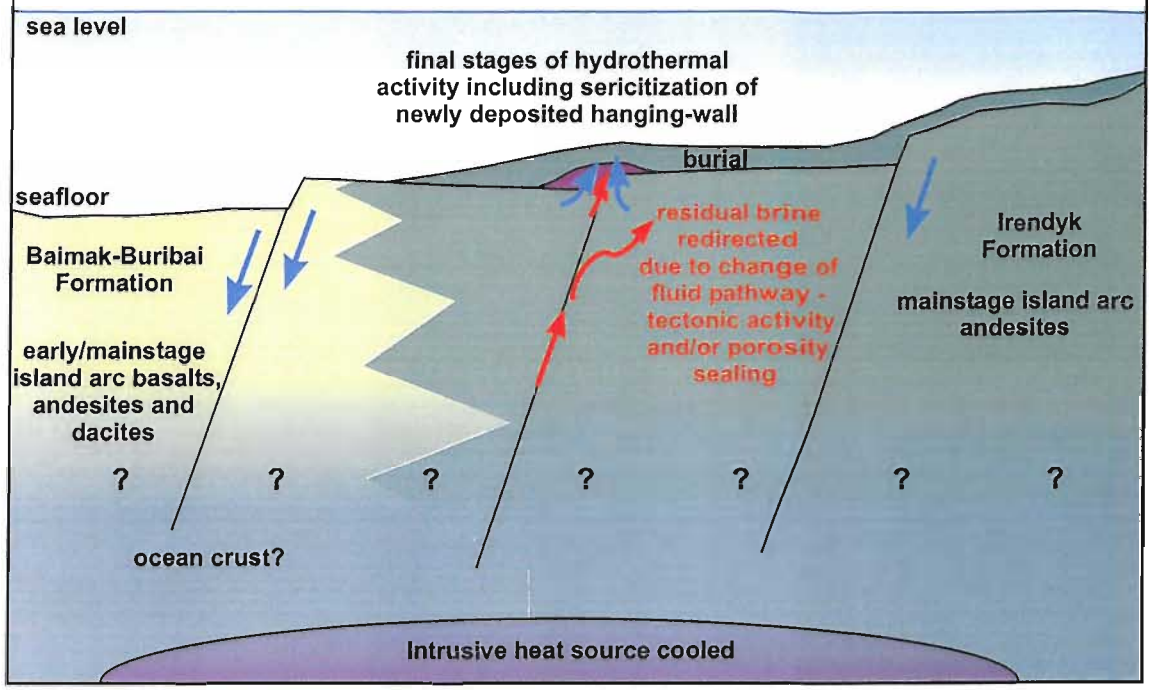
sea level
final stages of hydrothermal activity including sericitization of newly deposited hanging-wall
burial
seafloor
residual brine redirected due to change of fluid pathway - tectonic activity and/or porosity sealing
Irendyk Formation
mainstage island arc andesites
Baimak-Buribai Formation
early/mainstage island arc basalts, andesites and dacites
? ? ? ? ? ? ?
ocean crust?
Intrusive heat source cooled

Figure 7.12e

Key to Figure 7.13

- Fluid flow within sulphide mound
- Hydrothermal fluid flow
- Seawater flow
- Footwall stockwork mineralization
- Unaltered footwall
- Ore related footwall hydrothermal alteration
- Seawater dominated footwall hydrothermal alteration
- Cu-Fe rich massive sulphides
- Zn-Fe rich massive sulphides
- Zn(-Pb-As-Sb) rich massive sulphides
- Layered sulphides
- Barite-rich sulphides
- Barite lens
- Immediate hanging-wall
- Sericitized immediate hanging-wall
- Hanging-wall volcaniclastics

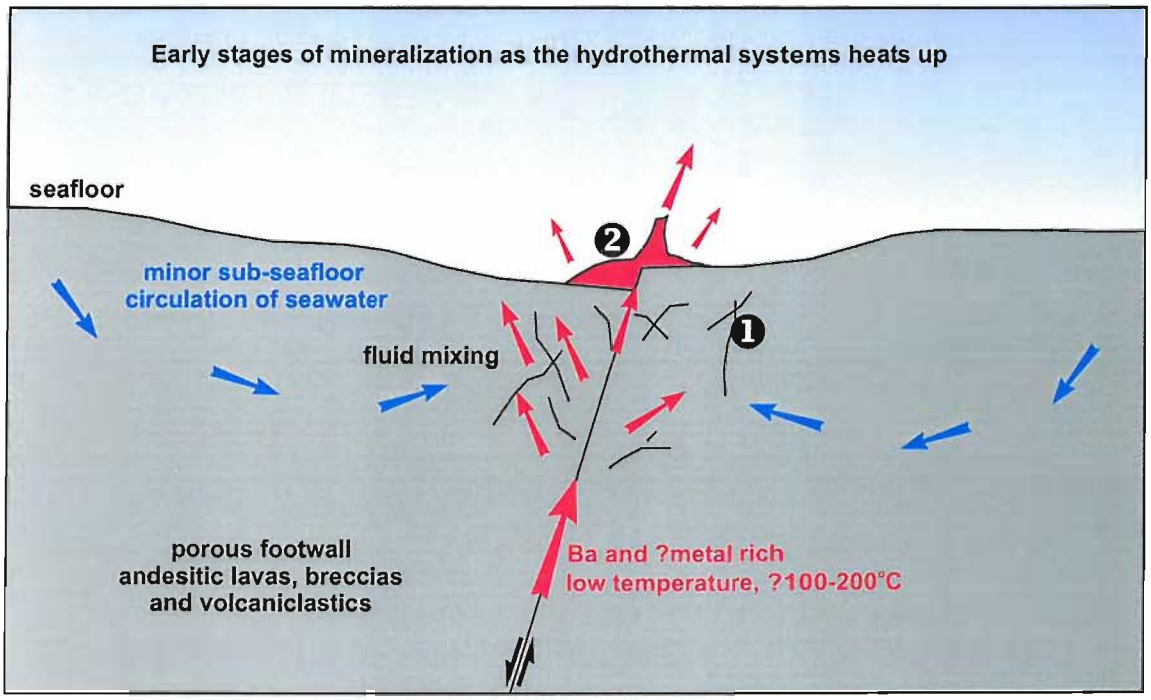

Figure 7.13a

❶ Precipitation of minor barite in the footwall, variable but generlly small contribution of seawater.
❷ Fluids emerge at the seafloor, precipitation of early seafloor mineralization, chimney/mound structures?

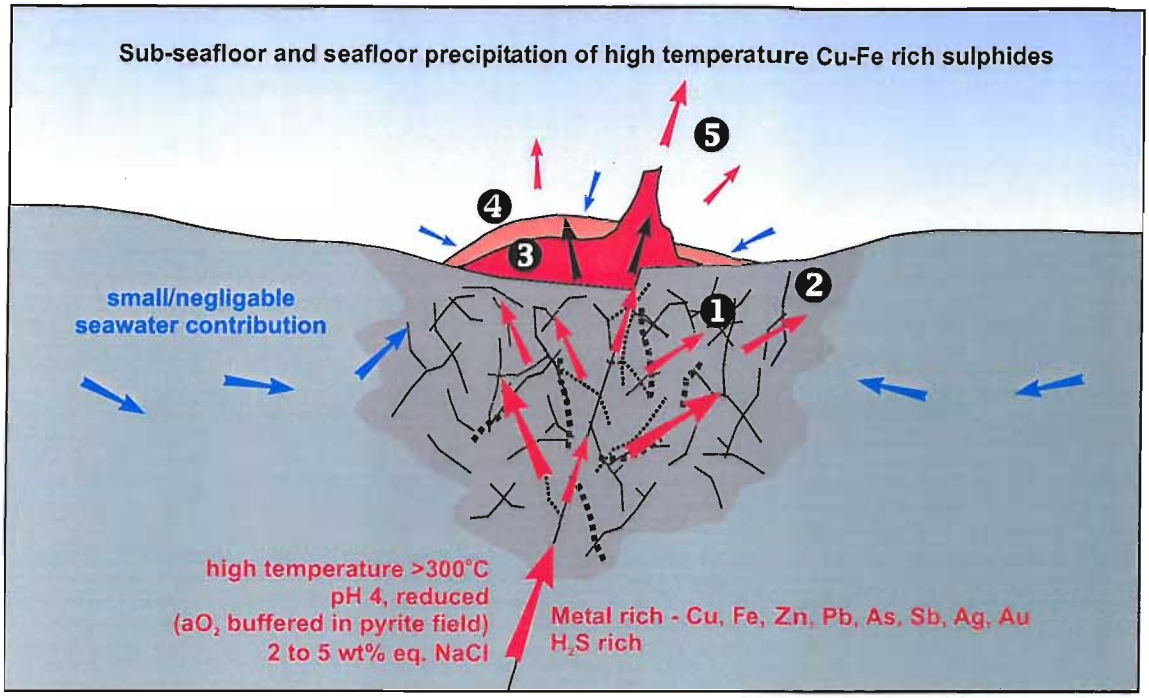

Figure 7.13b

❶ Chp-py rich footwall mineralization formed at 250 to 300°C from conductively cooled hydrothermal fluids with a small to negligable seawater component.
❷ Alteration of footwall volcanics by hydrothermal fluids.
❸ Seafloor mineralization precpitated at 250 to 300°C, comprising chp-py-rich sulphides with Fe-chl-qtz, replacing early stage mineralization. Possibly black smoker chimney formation.
❹ Outer zone of more sphalerite-rich sulphide mineralization precipitated at 150-250°C from conductively cooled hydrothermal fluids mixing with seawater penetrating the margins of the mound.
❺ Fluids rich in metals soluble at low temperatures (Zn, Pb, As, Sb, Ag, Au, Hg) lost to the ocean.

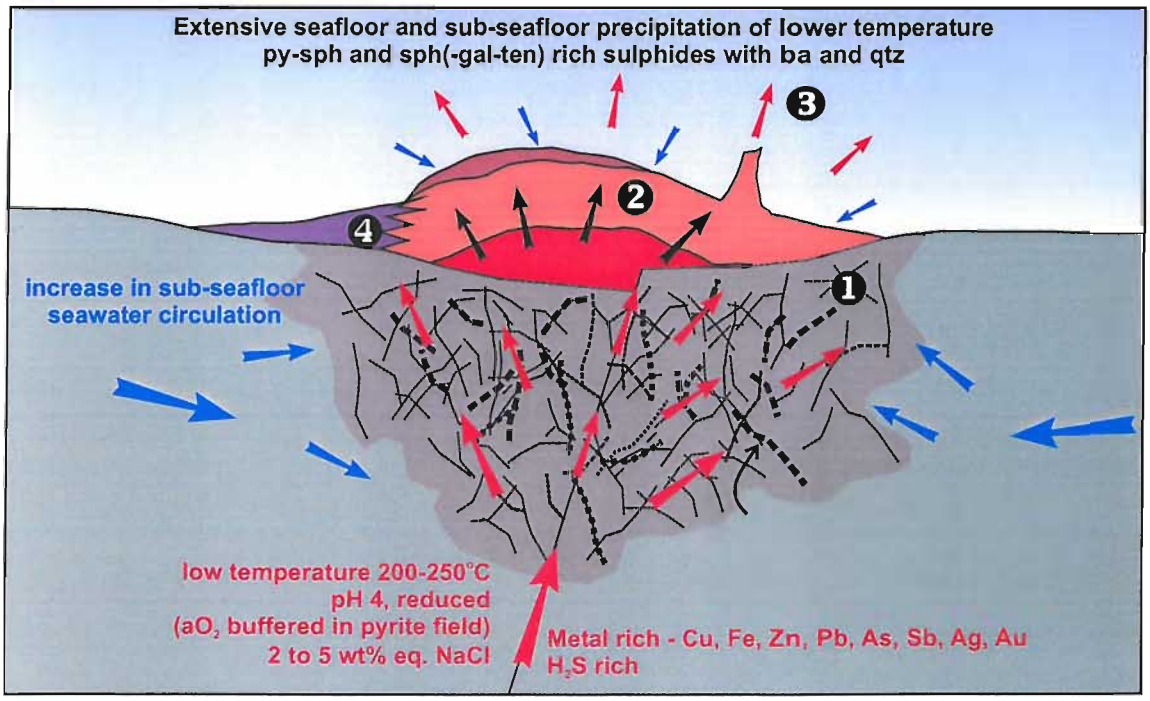

Figure 7.13c

❶ Continued footwall mineralization and alteration from lower temperature fluids initially at 200-250°C, with conductive cooling & seawater miixing resulting in precipitation of sph-(gal-ten)rich sulphides at 150- 200°C.
❷ Continued seafloor mineralization with an increase in sph-py and sph-ten-gal sulphides and ba-qtz precipitated at 150 to 200°C due to the lower initial fluid temperature, cooling of fluids in the footwall/mound and seawater penetration of the mound. Possibly low temperature white smoker chimneys. Zone refining?
❸ Low temperature fluids depleted in Cu-Fe-Zn(-Pb) but still containing Au-Ag-As-Sb-Hg lost to the ocean.
❹ Accumulation of sulphide talus from the mechanical degredation of mound material and particle fall out from venting fluids.

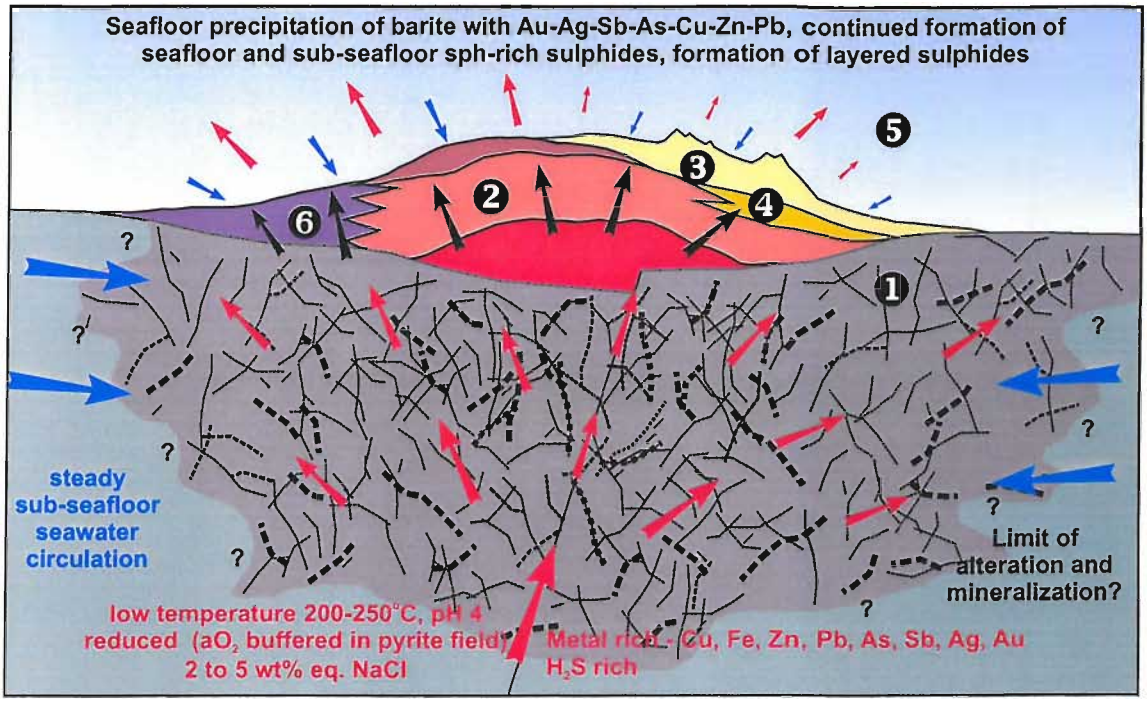

Figure 7.13d

❶ Continued development of footwall mineralization and alteration dominated by sph-rich sulphides precipitated at 130 to 170°C due to low initial fluid temperatures, conductive cooling and seawater mixing.
❷ Continued development of zoned seafloor sulphide mound.
❸ Slow, sustained precipitation of Au-Ag-Hg-Sb-As rich sulphides at around 150°C in a barite dominated mound capping the massive sulphides.
❹ Formation of barite-rich sulphides where the barite-rich precipitates cement sulphide clasts at the top of the massive sulphide mound.
❺ Fluids depleted in base and precious metals escape to the ocean by diffuse flow through barite walls.
❻ Continued accumulation of clastic sulphides, and recrystallization to compositionally layered sulphides.

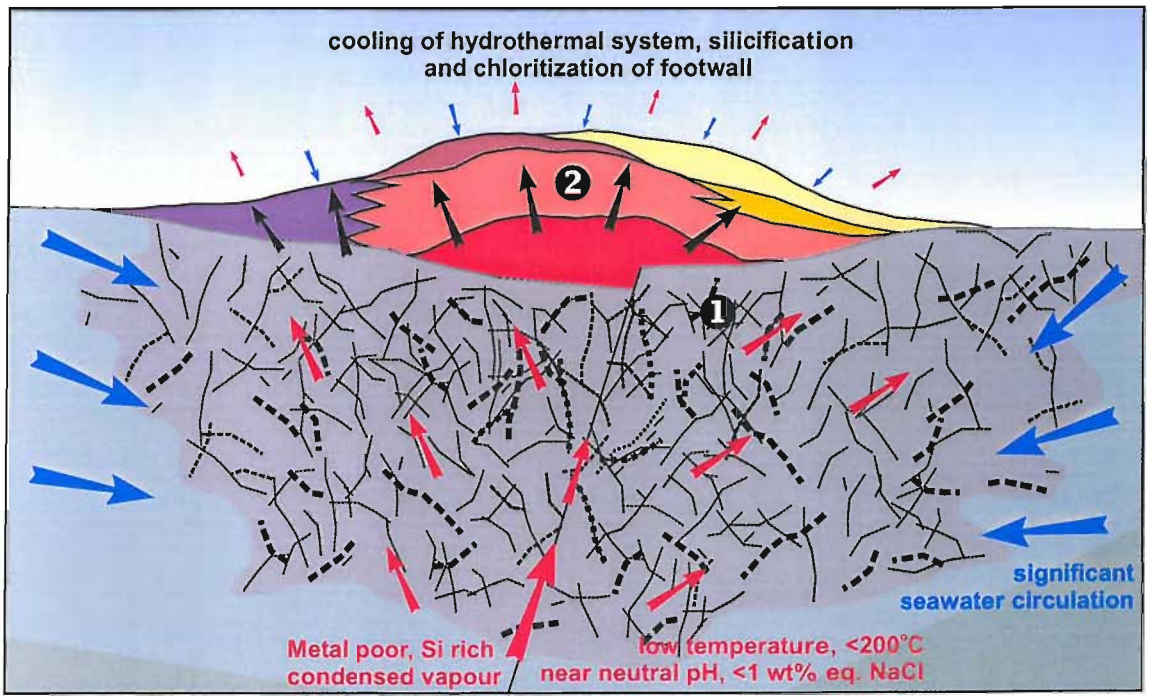

Figure 7.13e

❶ Extensive low temperature (110 to 140°C) sub-seafloor silicification and Mg-chl precipitation overprints ore-related hydrothermal alteration assemblages, with development of sparse quartz veins containing remobilised tennantite.
❷ Low temperature hydrothermal fluids diffuse slowly through mound with minor precipitation of qtz .

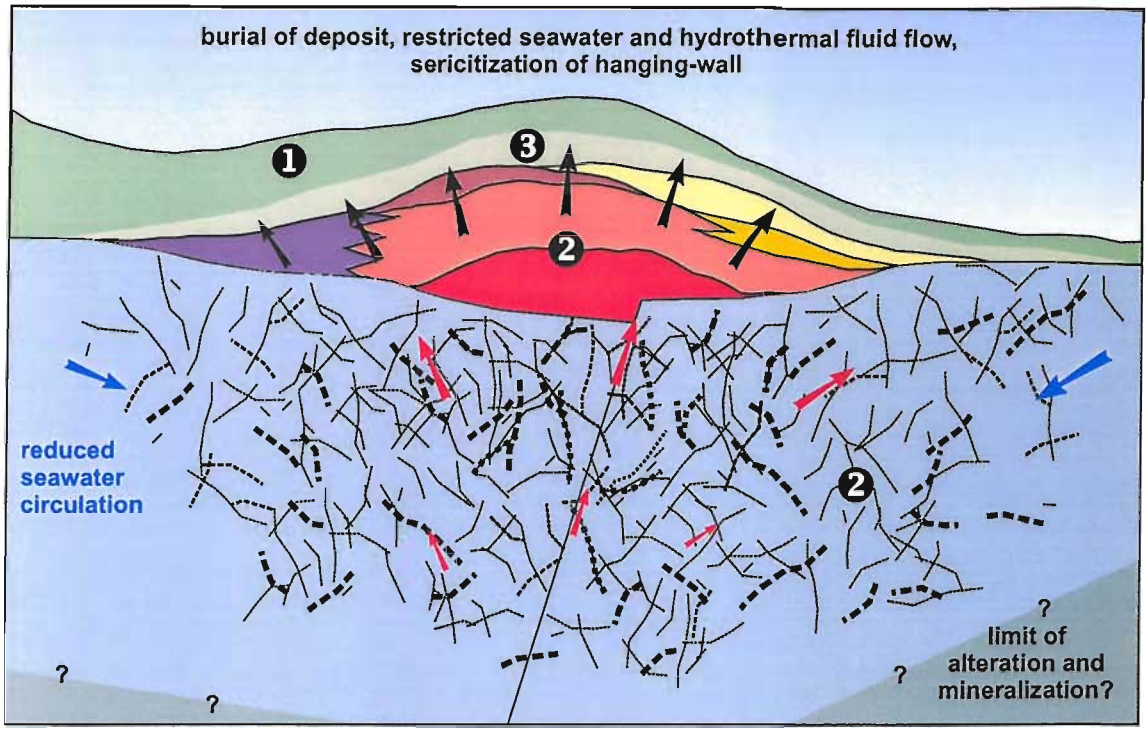

Figure 7.13f

❶ Burial of seafloor mineralization, reducing seawater circulation in the footwall.
❷ Continued qtz and Mg-chl alteration of footwall from seawater and condensed vapour fills porosity.
❸ Alteration of hanging-wall lava by fluids modified during footwall interactions.

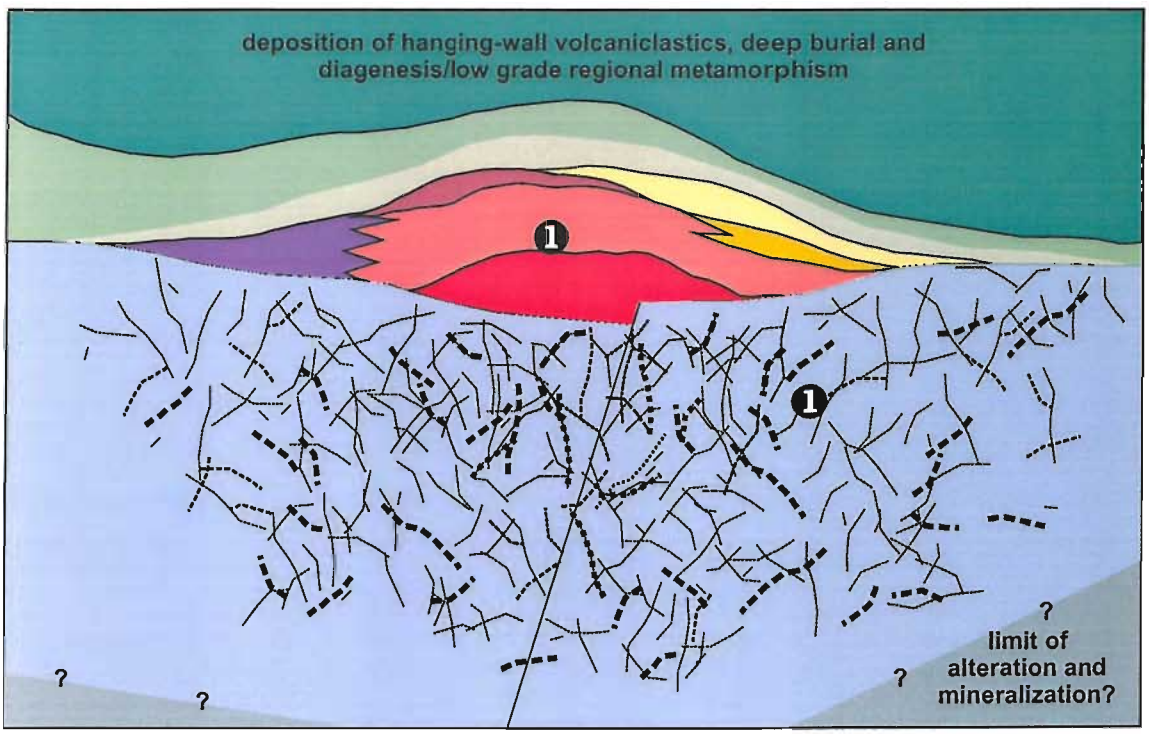

Figure 7.13g

❶ Minor development of carbonates, zeolite and pumpellyite in footwall and massive sulphide ores.

7.7 GOLD ENRICHMENT OF OTHER URALIAN VMS DEPOSITS

Numerous VMS deposits in the southern Urals contain coarse visible gold that appears to be primary and hydrothermal in origin, and the mode of occurrence of this gold (including the stratigraphic position, textures and mineralogy of associated ore facies) is often very different to the gold described from Balta Tau.

Examples include the Tash Tau deposit, where gold occurs in carbonate veins associated with bornite (Figure 7.14a). This suggests that precipitation took place from near-neutral fluids under relatively high oxidation conditions, and the mechanism proposed by Hannington et al. (1989a), whereby oxidation across the H_2S-SO_4^{2-} border destabilises Au bisulphide complexes, may be applicable to gold precipitation in this instance.

At Yaman Kasy, native gold/electrum has been identified in the outer zone of a chalcopyrite dominated chimney associated with native tellurium (Herrington, pers. comm.) (Figure 7.14b). Here, the association with chalcopyrite suggests that the Au precipitated at higher temperatures than at Balta Tau and may have been transported as chloride complexes. The solubility of gold as chloride complexes decreases dramatically with decreasing temperature, therefore precipitation here may have been triggered simply due to a decrease in temperature in the outer chimney wall caused by conductive cooling and/or seawater mixing. A similar mechanism may be responsible for the native gold/electrum observed in zoned sphalerite(-chalcopyrite)-rich chimneys from the Alexandrinka deposit (Tessalina et al., 1999).

These examples illustrate the variety of Au occurrences and associations that have been recorded from the southern Urals deposits. The frequent occurrence of native gold/electrum in primary hydrothermal ores of these deposits supports the conclusion of this study that Au can precipitate directly from hydrothermal fluids, and suggests that this may occur via a number of different mechanisms. These occurrences also highlight the overall Au enrichment of the southern Urals VMS deposits.

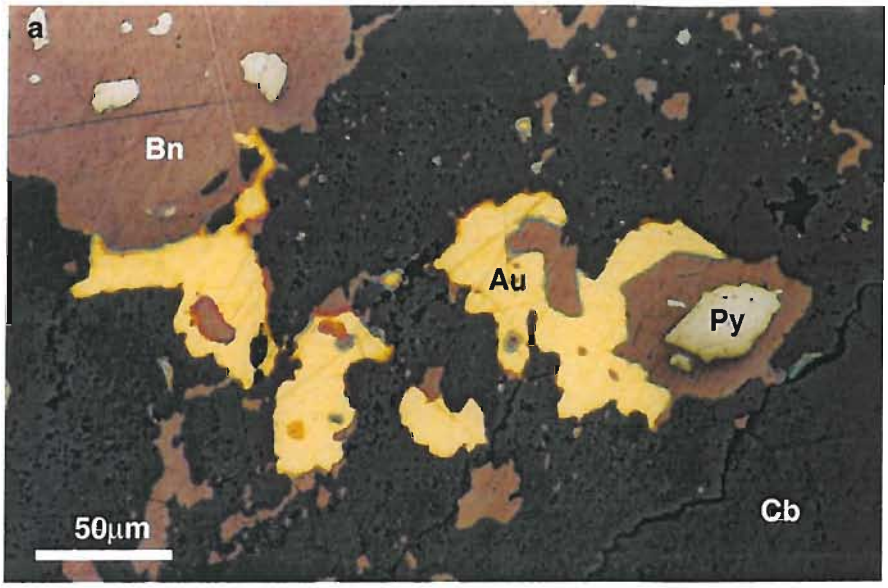

a. Coarse native gold/electrum associated with bornite that is replacing pyrite,enclosed in a carbonate vein. Sample belonging to V. Maslennikov, from the Tash Tau deposit, southern Urals.

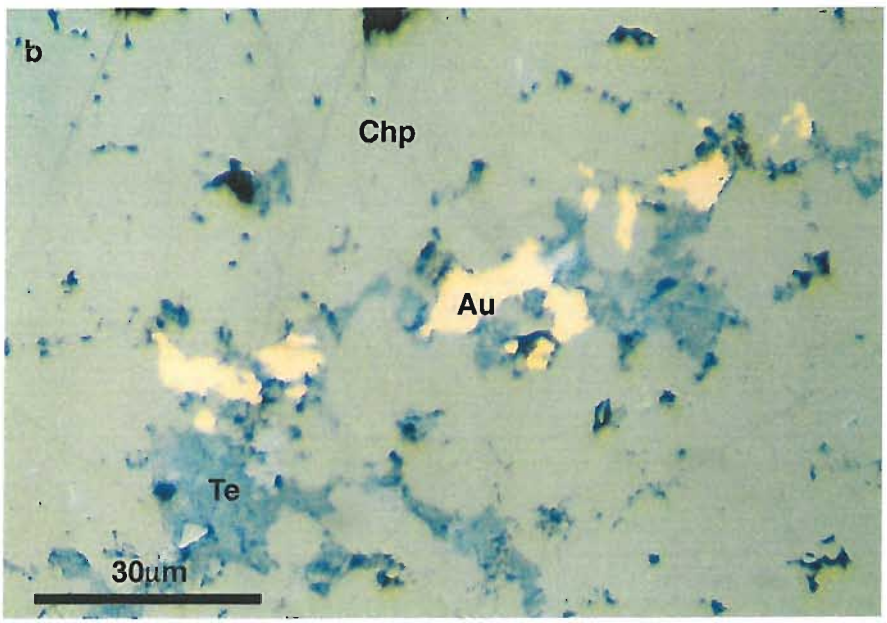

b. Coarse native gold/electrum intimately associated with native tellurium, enclosed in the outer part of a chalcopyrite-rich sulphide chimney. Yaman Kasy deposit, southern Urals (photograph by R. Herrington).

Figure 7.14. Examples of primary, hydrothermal native gold/electrum in sulphide ores from other VMs deposits of the southern Urals.

7.8 IMPLICATIONS OF THE GOLD ENRICHMENT IN SOUTHERN URALS VMS DEPOSITS

The Urals belt provides numerous examples of ancient VMS deposits with primary, syn-VMS gold enrichment including visible gold/electrum. This study of Balta Tau has revealed that considerable gold precipitated as coarse and fine grained electrum directly from low temperature hydrothermal fluids at the seafloor, and the gold occurrences at a number of other deposits (discussed in Section 7.7) are also likely to be of a primary hydrothermal origin. This has important implications for the origin of coarse native gold/electrum in more deformed ancient VMS deposits, such as those hosted in the Mt. Read volcanics in Australia, in the Skellefte region of Sweden and in the Abitibi Belt of Canada, where coarse native gold/electrum is frequently interpreted to result from the concentration of "invisible" gold during metamorphism. However, this study indicates that it is quite feasible for these deposits to have contained primary hydrothermal native gold/electrum.

The VMS deposits of the southern Urals are generally gold enriched, although the extent and nature of gold enrichment is highly variable from one deposit to the next. In spite of this region wide enrichment, there is no indication from this study that an additional source of gold aside from the host volcanic rocks, such as a direct magmatic input to ore forming fluids, was an important factor in the formation of the Urals VMS deposits. This is supported by studies of other deposits in the region where stable isotope data and fluid inclusion studies are suggestive of typical VMS ore forming fluids derived from the interaction of seawater with island arc volcanic rocks (e.g. Maslennikov et al., 2000; Prokin and Buslaev, 1999; Tessalina et al., 1999). It is therefore most probable that the regional trend of gold enrichment reflects the composition of the island arc host rocks. A number of ancient arc-related VMS districts are gold enriched and considerable research has been undertaken to establish the source of this gold; the results of this study suggest that deposits formed in this environment may be gold rich simply as a result of the host rock lithologies, without the requirement of an additional metal source. This is also suggested by recent studies of active hydrothermal systems in arc environments such as the Pacmanus back-arc basin and the Kermadec Arc, which confirm that fluids and precipitates are gold enriched relative to typical MOR systems.

8 CONCLUSIONS

8.1 CONCLUSIONS RELATING TO MINERALIZATION AT BALTA TAU

- The Balta Tau deposit formed at the seafloor with development of mound and probable chimney structures, marginal clastic ores and a broad zone of extensive sub-seafloor mineralization. The majority of sulphide ores are well preserved and retain primary hydrothermal textures.
- The Upper Baimak-Buribai Formation comprises felsic, slightly calc-alkaline arc sequences and the Irendyk is dominated by tholeiitic island arc andesites with local calc-alkaline andesites, which record the progression from late stage fore-arc (upper Baimak-Buribai) to mainstage island arc (Irendyk) environments. A high proportion of fine grained, immature volcaniclastic material within the Irendyk is suggestive of shallow water conditions.
- Sequences hosting the Balta Tau deposit are tholeiitic island arc andesitic lavas, breccias and fine volcaniclastics of the Irendyk Formation. The footwall and immediate hanging-wall units probably may well be part of the same lithological unit, with similar lithologies and geochemistry prior to ore-related alteration.
- The exceptional gold enrichment of barite-rich ores is a primary feature and cogenetic with massive sulphide ores. Textures indicate that both coarse and fine grained electrum co-precipitated with barite and sulphides from mainstage hydrothermal fluids, and are not the result of post-depositional modification of ores. In addition to visible electrum, significant Au may be present locked in pyrite crystals from upper sulphide horizons, where As(-Sb) rich zones are preserved in pyrite indicating that recrystallization has not occurred, and provide a mechanism for the incorporation of Au in pyrite by coupled, metastable substitutions.
- Hydrothermal ore forming fluids were derived from the interaction of seawater with volcanic rocks, the latter providing a source of metals and sulphur, with variable fluid salinities above and below that of seawater indicative of sub-seafloor phase separation.
- Mainstage sulphide and barite-rich ores formed at temperatures ranging from 130 to 300°C, and a high proportion of ores record temperatures at the lower end of this range.
- Footwall porosity was an important factor in determining the style of Balta Tau mineralization, facilitating pervasive footwall mineralization, complex mound development and significant cooling of hydrothermal fluids by conductive cooling and seawater mixing in the footwall.
- Sulphide sulphur is derived predominately from hydrothermal fluid H_2S with little evidence of seawater sulphate reduction at the site of mineralization, and barite precipitated from seawater

sulphate with negligible contribution of oxidized H_2S. The aqueous sulphur species were in isotopic disequilibrium with respect to sulphur, consistent with the slow kinetics of sulphate reduction.

- Sr and O isotopic signatures of barite suggest that hydrothermal fluids were conductively cooled to temperatures of around 200 to 250°C and mixed with 5 to 50% seawater prior to and during ore formation. Evidence of an approach to oxygen isotopic equilibrium between seawater sulphate and hydrothermal fluid H_2O suggests a time lapse in the order of a day or two between seawater mixing and barite precipitation.

- The source rock composition was an important influence over the composition and mineralogy of Balta Tau ores. Source rocks are enriched in Ba-Pb-Ag and probably Au and more oxidized relative to MORB, due to fractionation and subduction zone enrichment of magmas, resulting in the formation of more oxidized, Pb-Ba-Ag-Au rich ores relative to MOR systems.

- Balta Tau does not show "high sulphidation" characteristics and there is no evidence or requirement for a significant contribution of magmatic volatiles to ore forming fluids.

- The variable mineralogy, chemistry and textures of each ore facies may be explained by deposit-scale variations in ore forming conditions and fluid evolution. Temperature changes due to seawater mixing and conductive cooing were important factors governing the deposition of base metals, with a progressive decrease in temperature from central to marginal zones reflected in the progression from chalcopyrite-pyrite- rich to sphalerite-rich ores.

- The mineralogy of the gold-barite rich ores is unusual and can not be explained by temperature variations alone. These ores are interpreted to have formed in a barite structure that trapped metal depleted, low temperature and low pH hydrothermal fluids emerging from the sulphide mound, and limited seawater mixing. These conditions are favourable for the precipitation of Au from bisulphide complexes.

- The distinctive, compositionally layered sulphides contain relict clastic features and most likely formed from the low temperature recrystallization of fine clastic sulphide mud/sand during late stages of hydrothermal activity.

- Shallow, sub-seafloor phase separation during late stage hydrothermal activity produced a condensed vapour phase that mixed with seawater in the footwall. Extensive precipitation of quartz and Mg-chlorite infilled footwall porosity and replaced primary hydrothermal alteration assemblages.

- The immediate hanging-wall unit was deposited before hydrothermal activity ceased resulting in intense sericitic alteration. The Balta Tau area continued to be more hydrothermally active than the surrounding region after ore deposition and burial, as indicated by the intense epidote alteration and veining in hanging-wall volcaniclastic sequences.

8.2 IMPLICATIONS FOR OTHER VMS SYSTEMS AND FURTHER WORK

In relation to Au enrichment of VMS deposits:

- Coarse electrum or native gold in ancient VMS deposits is not necessarily the result of remobilisation and concentration during metamorphism. Balta Tau and other deposits of the southern Urals demonstrate that primary, hydrothermal electrum may precipitate in seafloor sulphides in a variety of mineral associations. In addition, electrum/native gold hosted in pyrite fractures is not necessarily the result of leaching invisible gold from pyrite, but may have been introduced during late stage seafloor mineralization.
- There is the potential to discover coarse electrum in actively forming deposits, and barite structures that trap low temperature hydrothermal fluids (as described by Hannington et al., 1995) may provide an ideal site for the precipitation of Au. Significant Au and other trace metals may accumulate in these structures if they remain stable for a long period of time.
- Au may precipitate in the seafloor environment via a number of precipitation mechanisms. Whilst oxidation due to prolonged seawater mixing may account for a small degree of Au enrichment in low temperature seafloor precipitates (e.g. Hannington and Scott, 1989; Herzig et al., 1993), it can not account for the coarse electrum at Balta Tau and other processes such as lowering of pH due to extensive sulphide precipitation may be more effective for the precipitation of coarse electrum.
- A magmatic component to ore forming fluids is not a prerequisite for the formation of Au-rich VMS deposits. The combination of suitably Au enriched source rocks and an effective precipitation mechanism is sufficient.

In relation to barite formation in VMS ores:

- Barite should not be used to indicate the oxidation state of fluids unless sulphur isotopic equilibrium between reduced and oxidized sulphur species can be established, since slow rates of sulphate reduction enable sulphate to persist in a reducing environment long after seawater mixing.
- The concentration of Ba^{2+} in hydrothermal fluids is not likely to be orders of magnitude greater than the concentration required for barite saturation, therefore although a small degree of seawater mixing is required to provide sulphate for barite precipitation, extensive seawater mixing may inhibit barite formation due to dilution of Ba^{2+}. The proportion of barite in ores is not likely to be a function of the extent of seawater mixing, but may instead reflect evolving Ba^{2+}/base metal ratios in hydrothermal fluids as ore formation proceeds.

- The solubility of barite does not vary significantly as a function of temperature in fluids with salinity close to that of seawater (Blout, 1977). The general increase in abundance of barite in low temperature ores is more likely related to (i) suppression of barite precipitation at high temperatures by anhydrite formation, and (ii) the Ba/base metal content of fluids, which will be higher at low temperatures when hydrothermal fluids have already precipitated a significant proportion of base metals as sulphides.

Additional considerations:

- Compositionally layered or banded sulphide ores are common in ancient VMS deposits and usually attributed to metamorphism. However, they may have originally formed during late stages of fore formation producing compositional layering, that is then later overprinted by metamorphism. This is supported by the common occurrence of layered ores in sphalerite-rich, upper horizons of massive sulphide lenses consistent with the development of clastic ores at mound margins. This could be provide a useful indication of seafloor precipitation in ancient metamorphosed deposits, and the extent of seafloor degradation of mound material. It may be possible to find relict clasts that support a clastic origin of ores, which could otherwise have been interpreted as tectonically derived brecciation of ores.
- The low temperature ores at Balta Tau contain significant chalcopyrite and tennantite, and require a mechanism for the low temperature transportation of Cu that has not yet been established. Many other VMS and epithermal deposits also contain abundant tennantite-tetrahedrite in low temperature assemblages confirming that this is not an isolated occurrence.
- The composition of tennantite and tetrahedrite is an important influence over the Ag distribution in VMS deposits, and systematic variations in tennantite-tetrahedrite chemistry between ore facies at Balta Tau suggests a close link with formational conditions. Better constraints on tennantite-tetrahedrite chemistry from experimental work would enhance our understanding of Ag distribution in VMS ores and enable these minerals to be used as indicators of ore forming conditions.

9 REFERENCES

Aerden D. G. A. M.; 1993. Formation of Massive Sulphide Lenses by Replacement of Folds: The Hercules Pb-Zn Mine, Tasmania. Economic Geology, v. 88, pp. 377-396.

Aerden D. G. A. M.; 1994. Microstructural timing of the Rosebery massive sulphides, Tasmania: evidence for a metamorphic origin through mobilization of disseminated base metals. Journal of Metamorphic Geology, v. 12, pp. 502-522.

Alt J. C., Anderson T. F. and Bonnell L.; 1989. The geochemistry of sulfur in a 1.3 km section of hydrothermally altered oceanic crust, DSDP Hole 504B. Geochimica et Cosmochimica Acta, v. 53, pp. 1011-1023.

Alt J. C. & Teagle D. A. H.; 1998. Probing the TAG hydrothermal mound and stockwork: Oxygen-isotopic profiles from deep ocean drilling. Herzig P. M.; Humphris S. E., Miller D. J. & Zierenberg R. A.(eds), Proceedings of the Ocean Drilling Program, v. 158, pp.285-295.

Alvarez-Marron J., Brown D., Perez-Estaun A., Puchkov V. and Gorozhanina Y.; 2000. Accretionary complex structure and kinematics during Palaeozoic arc-continent collision in the southern Urals. Tectonophysics, v. 325, pp. 175-191.

Azmy K., Veizer J., Bassett M. G. & Cooper P.; 1998. Oxygen and carbon isotopic composition of Silurian brachiopods: Implications for coeval seawater and glaciations. Geological Society of America Bulletin, v. 110, pp. 1499-1512.

Barrie C. T. and Hannington M. D.; 1999. Classification of Volcanic-Associated Massive Sulphide Deposits Based on Host-Rock Composition. Reviews in Economic Geology, v. 8, pp. 1-11.

Bastida F., Aller J., Puchkov V. N., Juhlin Ch. And Oslianski A; 1997. A cross-section through the Zilair Nappe (southern Urals). Tectonophysics, v. 276, pp. 253-263.

Baumgartner L. P. and Rumble D. III; 1988. Transport of stable isotopes: I: Development of a kinetic continuum theory for stable isotope transport. Contributions to Mineralogy and Petrology, v. 98, pp. 417-430.

Benning L. G. and Seward T. G.; 1996. Hydrosulphide complexing of Au(I) in hydrothermal solutions from 150-400°C and 500-1500 bar. Geochimica et Cosmochimica Acta, v. 60, pp. 1849-1871.

Berglund S. and Ekström T. K.; 1980. Arsenopyrite and Sphalerite as T-P Indicators in Sulphide Ores from Northern Sweden. Mineralium Deposita, v. 15, pp. 175-187.

Binns R. A., Parr J. M., Gmmell J. B., Whitford D. J. and Dean J. A.; 1997. Precious metals in barite-silica chimneys from Franklin Seamount, Woodlark Basin, Papua New Guinea. Marine Geology, v. 142, pp. 119-141.

Bischoff J. L. and Rosenbauer R. J.; 1988. Liquid-vapor relations in the critical region of the system NaCl-H_2O from 380 to 415°C: A refined determination of the critical point and two-phase boundary of seawater. Geochimica et Cosmochimica Acta, v. 52, pp. 2121-2126.

Bischoff J. L. and Seyfried W. E.; 1978. Hydrothermal chemistry of seawater from 250°C to 350°C. American Journal of Science, v. 278, pp. 838-860.

Blout C. W.; 1977. Barite solubilities and thermodynamic quantities up to 300°C and 1400 bars. American Mineralogist, v. 62, pp. 942-957.

Blout C. W. and Dickson F. W.; 1969. The solubility of anhydrite ($CaSO_4$) in NaCl-H_2O from 100 to 450°C and 1 to 1000 bars. Geochemica et Cosmochimica Acta, v. 33, pp. 227-245.

Bluth G. J. and Ohmoto H.; 1988. Sulfide-sulfate chimneys on the East Pacific Rise, 11° and 13 °N latitude, Part II: Sulfur isotopes. Canadian Mineralogist, v. 26, pp. 487-505.

Bodnar R. J.; 1993. Revised equation and table for determining the freezing point depression of H_2O-NaCl solutions. Geochimica et Cosmochimica Acta, v. 57, pp. 683-684.

Bourcier W. L. and Barnes H. L.; 1987. Ore Solution Chemistry – VII. Stabilities of Chloride and Bisulphide Complexes of Zinc at 350°C. Economic Geology, v. 82, pp. 1839-1863.

Boynton W. V.; 1984. Cosmochemistry of the rare earth elements; meteorite studies. Elsevier Science Publlications Co., Amsterdam, Netherlands.

Bowers T. S.; 1989. Stable Isotope Signatures of Water-Rock Interaction in Mid-Ocean Ridge Hydrothermal Systems: Sulfur, Oxygen and Hydrogen. Journal of Geophysical Research, v. 94, pp. 5775-5786.

Bowers T. S. and Taylor H. P; 1985. An integrated chemical and stable-isotope model of the origin of midocean ridge hot spring systems. Journal of Geophysical Research, v.90, pp. 12,583-12,606.

Braithwaite R. L.; 1974. The geology and origin of the Rosebery ore deposit, Tasmania. Economic Geology, v. 69, pp. 1086-1101.

Breit G. N., Simmons E. C. and Goldhaber M. B.; 1985. Dissolution of barite for the analysis of strontium isotopes and other chemical and isotopic variations using aqueous sodium carbonate. Chemical Geology, v. 52, pp. 333-336.

Brown D., Alvarez-Marrón J., Pérez-Estaún A., Gorozhanina Y., Baryshev V. and Puchkov V.; 1997. Geometric and kinematic evolution of the foreland thrust and fold belt in the southern Urals. Tectonics, v. 16, pp. 551-562.

Brown D., Hetzel R. and Scarrow J. H.; 2000. Tracking arc-continent collision zone processes from high-pressure rocks in the southern Urals. Journal of the Geological Society, London, v. 157, pp. 901-904.

Brown D., Juhlin C., Alvarez-Marron J., Pérez-Estaún A. and Oslianski A.; 1998. Crustal-scale structure and evolution of an arc-continent collision zone in the southern Urals, Russia. Tectonics, v. 17, pp. 158-171.

Brown D., Juhlin C., Alvarez-Marron J., Pérez-Estaún A., Puchkov V., Gorozhanina Y. and Ayarza P.; 2001. Structure and evolution of the Magnitogorsk forearc basin: Identifying upper crustal processes during arc-continent collision in the southern Urals. Tectonics, v.20, pp. 364-375.

Brown D., Puchkov V., Alvarez-Marron J., Pérez-Estaún A.; 1996. The structural architecture of the footwall to the Main Uralian Fault, southern Urals. Earth-Science Reviews, v. 40, pp. 125-147.

Brown D. and Spadea P.; 1999. Processes of forearc an accretionary complex formation during arc-continent collision in the southern Ural Mountains. Geology, v. 27, pp. 649-652.

Buschmann B., Jonas P., Herzig P. M., Petersen S., Buley C., Zaykov V. V., Maslennikov V. V. and Simonov V.; 2000. Tectonic settings of Middle Palaeozoic VHMS-bearing complexes in the S. Ural. Volcanic Environments and Massive Sulphide Deposits Program and Abstracts, International Field Conference and Field Meeting, Tasmania, Australia, November 2000, pp. 15-16.

Buschmann et al., 2001a. Tectonostratigraphic constraints on VMS formation in the Southern Urals. "Massive sulphide deposits in the Iberian Pyrite Belt: New advances and comparison with equivalent systems", Abstract volume, GEODE workshop Aracena, Spain, October 2001, pp. 11-12.

Buschmann B.l, Jonas P., Maletz J., Maslennikov V. and Zaykov V.; 2001b. The Blyava VMS deposit (Mednogorsk District, Sakmara Zone, South Urals). Part I: Hanging-wall stratigraphy and Evidence of Early Silurian VMS formation; Part II: Petrochemistry of volcanic rocks and implications on the geodynamic setting. In: Zaykov V. V. (ed.), Metallogeny of ancient and modern oceans, 7th Miass Students Summer School 2001, Abstract volume, pp. 247-251.

Butterfield D. A. and Massoth G. J; 1994. Geochemistry of north Cleft segment fluids: Temporal changes in chlorinity and their possible relation to recent volcanism. Journal of Geophysical Research, v. 99, pp. 4951-4968.

Butterfield D. A., Massoth G. J., McDuff R. E., Lupton J. E. and Lilley M. D.; 1990. Geochemistry of Hydrothermal Fluids From Axial Seamount Hydrothermal Emissions Study Vent Field, Juan de Fuca Ridge: Subseafloor Boiling and Subsequent Fluid-Rock Interaction. Journal of Geophysical Research, v. 95, No B8, pp. 12,895-12,921.

Butterfield D. A., McDuff R. E., Mottl M. J., Lilley M. D., Lupton J. E. and Massoth G. J.; 1994. gradients in the composition of hydrothermal fluids from the Endeavour segment vent fluid: Phase separation and brine loss. Journal of Geophysical Research, v. 99, pp. 9561-9583.

Butler I. B., Fallick A. E. and Nesbitt R. W.; 1998. Mineralogy, sulphur isotope geochemistry and the development of sulphide structures at the Broken Spur Hydrothermal vent site, 29°10'N, Mid-Atlantic Ridge. Journal of the Geological Society, London, v. 155, pp.. 773-785.

Çagatay M. N.; 1993. Hydrothermal Alteration Associated with Volcanogenic Massive Sulphide Deposits: Examples from Turkey. Economic Geology, v.88, pp. 606-621.

Cann J. R.; 1970. Rb, Sr, Zr and Nb in some ocean floor basaltic rocks. Earth and Planetary Science Letters, v. 10, pp. 7-11.

Cas R. A. F.; 1992. Submarine Volcanism: Eruption Styles, Products, and Relevance to Understanding the Host-Rock Successions to Volcanic-Hosted Massive Sulphide Deposits. Economic Geology, v. 87, pp. 511-541.

Cathelineau M.; 1988. Cation site occupancy in chlorites and illites as a function of temperature. Clay minerals, v. 23, pp. 471-485.

Cathless, L. M.; 1983. An analysis of the hydrothermal system responsible for massive sulphide deposition in the Hokuroko basin of Japan. Economic Geology Monograph 5, pp. 439-487.

Chemenda A., Matte P. and Sokolov V.; 1997. A model of Paleozoic obduction and exhumation of high-pressure/low-temperature rocks in the southern Urals. Tectonophysics, v. 276, pp. 217-227.

Chiba H., Kusakabe M., Hirano S-I, Matsuo S. and Somiya S.; 1981. Oxygen isotope fractionation factors between anhydrite and water from 100 to 550°C. Earth and Planetary Science Letters, v. 53, pp. 55-62.

Chiba H. and Sakai H., 1985. Oxygen isotope exchange rate between dissolved sulfate and water at hydrothermal temperatures. Geochimica et Cosmochimica Acta, v. 49, pp. 993-1000.

Chiba H., Uchiyama N. and Teagle D. A. H.; 1998. Stable isotope study of anhydrite and sulfide minerals at the TAG hydrothermal mound, Mid-Atlantic Ridge, 26°N[1]. Proceedings of the Ocean Drilling Program, Scientific Results, v. 158, pp. 85-90.

Clark L. A.; 1960. The Fe-As-S system: Phase relations and applications. Economic Geology, v.55, pp. 1345-1381.

Claypool G. E., Holser W. T., Kaplan I. R., Sakai H. and Zak I.; 1980. The age curves of sulphur and oxygen isotopes in marine sulphate and their mutual interpretation. Chemical Geology, v. 28, pp. 199-260.

Coleman M. L. and Moore M. P.; 1978. Direct reduction of sulfates to sulfur dioxide for isotope analysis. Analytical Chemistry, v. 50, pp. 1594-1595.

Constantinou G. and Govett G. J. S.; 1973. Geology, geochemistry and genesis of Cyprus sulfide deposits. Economic Geology, v. 68, pp. 843-858.

Cook, N. J.; 1996. Mineralogy of the sulphide deposits at Sulitjelma, northern Norway. Ore Geology Reviews, v. 11, pp. 303-338.

Cook N. J. and Chryssoulis S. L.; 1990. Concentrations of "invisible" gold in the common sulfides. Canadian Mineralogist, v. 28, pp. 1-16.

Corbett K. D.; 2000. Features of the Mount Leyll alteration zone – a large silica-pyrite rich copper-gold system with an exhalative lead-zinc top. Volcanic Environments and Massive Sulphide Deposits Program and Abstracts, International Field Conference and Field Meeting, Tasmania, Australia, November 2000, pp. 27-28.

Crerar D. A. and Barnes H. L.; 1976. Ore Solution Chemistry V. Solubility of Chalcopyrite and Chalcocite Assemblages in Hydrothermal Solution at 200°C to 350°C. Economic Geology, v. 71, pp. 772-794.

Dählmann A., Wallmann K., Sahling H., Sarthou G., Bohrmann G., Petersen S., Chin C. S. and Klinkhammer G. P.; 2001. Hot vents in an ice-cold ocean: Indications for phase separation at the southernmost area of hydrothermal activity, Bransfield Strait, Antarctica. Earth and Planetary Science Letters, v. 193, pp. 381-394.

De Caritat, P., Hutcheon I. and Walshe J. L.; 1993. Chlorite geothermometry: A review. Clays and Clay Minerals, v. 41, pp. 219-239.

Deer W. A., Howie R. A., and Zussman J.; 1966. An Introduction to the Rock Forming Minerals. Longman, London, 528 p.

Denghong W., Yuchuan C. and Jingwen M.; 1998. The Ashele Deposit; a recently discovered volcanogenic massive sulfide Cu-Zn deposit in Xinjiang, China Resource Geology, v.48, pp. 31-42.

Denison R. E., Koepnick R. B., Burke W. H., Hetherington E.A. and Fletcher A.; 1997. Construction of a Silurian and Devonian seawater $^{87}Sr/^{86}Sr$ curve. Chemical Geology, v. 140, pp. 109-121.

De Ronde C. E. J.; 1995. Fluid chemistry and isotopic characteristics of seafloor hydrothermal systems and associated VMS deposits: Potential for magmatic contributions. Mineralogical Association of Canada Short Course Volume 23, pp. 471-511.

Doe B. R.; 1994. Zinc, copper and lead in mid-ocean ridge basalts and the source rock control on Zn/Pb in ocean-ridge hydrothermal systems. Geochimica et Cosmochimica Acta, v. 58, pp. 2215-2223.

Duckworth R. C., Knott R., Fallick A. E, Rickard D., Murton B. J. & Van Dover C.; 1995. Mineralogy and sulphur isotope geochemistry of the Broken Spur sulphides, 29°N, Mid-Atlantic Ridge. In: Walker L. M. & Dixon D. R. (eds), Hydrothermal Vents and Processes, Geological Society Special Publication No. 87, pp. 175-189.

Ebel D. S. and Sack R. O.; 1989. Ag-Cu and As-Sb exchange energies in tetrahedrite-tennantite fahlores. Geochimica et Cosmochimica Acta, v. 53, pp. 2301-2309.

Ebel D. S. and Sack R. O.; 1991. Arsenic-silver incompatibility in fahlore. Mineralogical Magazine, v. 55, pp. 521-528.

Edmonds H. N. and Edmond J. M.; 1995. A three component mixing model for ridge-crest hydrothermal fluids. Earth and Planetary Science Letters, v. 134, pp. 53-67.

Eldridge C. S., Barton P. B. Jr. and Ohmoto H.; 1983. Mineral Textures and Their Bearing on Formation of the Kuroko Orebodies. Economic Geology Monograph 5, pp. 241-281.

Faure G.; 1986. Principles of Isotope Geology, 2nd Edition, John Wiley & Sons Inc, USA., 589 p.

Faure K., Matsuhisa Y., Metsugi H., Mizota C. and Hayashi S.; 2002. The Hishikari Au-Ag epithermal deposit, Japan: oxygen and hydrogen isotope evidence in determining the source of palaeohydrothermal fluids. Economic Geology, v. 97, pp. 481-498.

Fershtater G. B., Montero P., Borodina N. S., Pushkarev E. V., Smirnov V. N. and Bea F.; 1997. Uralian magmatism: an overview. Tectonophysics, v. 276, 87-102.

Finlow-Bates T. and Stumpfl E. F.; 1981. The Behaviour of So-Called Immobile Elements in Hydrothermally Alteered Rocks Associated with Volcanogenic Submarine-Exhalative Ore Deposits. Mineralium Deposita, v. 16, pp. 319-328.

Fisher R. V. and Schmincke H.-U.; 1984. Pyroclastic Rocks. Springer-Verlag, Berlin, 472 pp.

Fleet M. E., MacLean P. J. and Barrier J.; 1989. Oscillatory-Zoned As-Bearing Pyrite from Strata-Bound and Stratiform Gold Deposits: An Indicator of Ore Fluid Evolution. Economic Geology Monograph 6, pp. 356-362.

Foster M. D.; 1962. Interpretation of the composition and a classification of the chlorites. US Geological Survey Professional Paper 414-A, 33 p.

Fouquet Y., Auclair G., Cambon P. and Etoubleau J.; 1988. Geological Setting and Mineralogical and Geochemical Investigations on Sulfide Deposits Near 13°N on the East Pacific Rise. Marine Geology, v. 84, pp. 145-178.

Fouquet Y., Wafik A., Cambon P., Mevel C., Meyer G. and Gente P.; 1993. Tectonic Setting and Mineralogical and Geochemical Zonation in the Snake Pit Sulphide Deposit (Mid-Atlantic Ridge at 23° N). Economic Geology, v. 88, pp. 2018-2036.

Franklin J. M., Lydon J. W. and Sangster D. F.; 1981. Volcanic-Associated Massive Sulphide Deposits. Economic Geology 75th Anniversary Volume, pp. 485-627.

Gamble J. A., Wright I. C., Woodhead J. D. and McCulloch M. T.; 1995. Arc and back-arc geochemistry in the southern Kermadec arc-Ngatoro Basin and off-shore Taupo Volcanic Zone, SW Pacific. In: Smellie J. L. (ed.), Geological Society Special Publication No. 81, Volcanism Associated with Extension at Consuming Plate Margins, pp. 193-209.

Gammons C. H. and Williams-Jones A. E.; 1995. Hydrothermal Geochemistry of Electrum: Thermodynamic Constraints. Economic Geology, v. 90, pp. 420-432.

Gemmell J. B. & Fulton R.; 2001. Geology, Genesis, and Exploration Implications of the Footwall and Hanging-Wall Alteration Associated with the Hellyer Volcanic-Hosted Massive Sulphide Deposit, Tasmania, Australia. Economic Geology, v. 96, pp. 1003-1035.

Gibert F., Pascal, M.-L. and Pichavant M., 1998. Gold solubility and speciation in hydrothermal solutions: Experimental study of the stability of hydrosulphide complex of gold ($AuHS^o$) at 350 to 450°C and 500 bars. Geochimica et Cosmochimica Acta, v. 62, pp. 2931-2947.

Goodfellow W. D. and Franklin J. M.; 1993. Geology, Mineralogy and Chemistry of Sediment Hosted Clastic Massive Sulphides in Shallow Cores, Middle Valley, Northern Juan De Fuca Ridge. Economic Geology, v. 88, pp. 2037-2068.

Grant J. A.; 1986. The Isocon Diagram – A Simple Solution to Gresens' Equation for Metasomatic Alteration. Economic Geology, v. 81, pp. 1976-1982.

Green G. R., Solomon M. and Walshe J. L.; 1981. The formation of the Volcanic-Hosted Massive Sulfide Ore Deposit at Rosebery, Tasmania. Economic Geology, v. 76, pp. 304-338.

Gresens R. L.; 1967. Composition-Volume Relationships of Metasomatism. Chemical Geology, v. 2, pp. 47-65.

Gribble C. D. and Hall A. J.; 1985. A Practical Introduction to Optical Mineralogy. Chapman & Hall, London, 249 p.

Gusev G. S., Gushchin A. V., Zaykov V. V., Maslennikov V. V., Mezhelovsky N. V., Perevozchikov B. V., Surin T. N., Filatov E. I. and Shirai E. P.; 2000. Geology and Metallogeny of Island Arcs. In: Mezhelovsky et al. (eds.), Geodynamics & Metallogeny: Theory and implications for applied geology, Ministry of Natural Resources & GEOKART, Moscow 2000, pp. 213 – 294.

Hackbarth C. J. and Petersen U.; 1984. A Fractional Crystallization Model for the Deposition of Argentian Tetrahedrite. Economic Geology, v. 79, pp. 448-460.

Haitian, S.; 1992. A general review of volcanogenic massive sulphide deposits in China. Ore Geology Reviews, v. 7, pp. 43-71.

Halbach P., Pracejus B. and Marten A.; 1993. Geology and Mineralogy of Massive Sulphide Ores from the Central Okinawa Trough, Japan. Economic Geology, v. 88, pp. 2210-2225.

Hannington M. D., Peter J. M. and Scott S. D.; 1986. Gold in Sea Floor Polymetallic Sulphide Deposits. Economic Geology Monograph 6, pp. 1867-1883.

Hannington M. D., Jonasson I. R., Herzig P. M. & Petersen S.; 1995. Physical and Chemical Processes of Seafloor Mineralization at Mid-Ocean Ridges. In: Seafloor Hydrothermal Systems: Physical, Chemical, Biological, and Geological Interactions; Geophysical Monograph 91, pp. 115-157.

Hannington M. D., Poulsen K. H., Thompson J. F. H. and Sillitoe R. H.; 1999. Volcanogenic Gold in the Massive Sulphide Environment. Reviews in Economic Geology, v. 8, pp. 325-356.

Hannington M. D. and Scott S. D.; 1989a. Sulphidation Equilibria as Guides to Gold Mineralization in Volcanogenic Massive Sulphides: Evidence from Sulphide Mineralogy and the Composition of Sphalerite. Economic Geology, v. 84, pp. 1978-1995.

Hannington M. D. and Scott S. D.; 1989b. Gold Mineralization in Volcanogenic Massive Sulphides: Implications of Data from Active Hydrothermal Vents on the Modern Sea Floor. Economic Geology Monograph 6, pp. 491-507.

Hannington M. D., Thompson G. Rona P. A. and Scott S. D.; 1988. Gold and native copper in supergene sulphides from the Mid-Atlantic Ridge. Nature, v. 333, pp. 64-66.

Hanor J. S.; 1995. Barite-Celestine Geochemisrty and Environments of Formation. Reviews in Mineralogy & Geochemistry, v. 40, pp. 193-275.

Harris D. C.; 1990. The mineralogy of gold and its relevance to gold recoveries. Mineralium Deposita, v. 25 (suppl), pp. S3-S7.

Healy R. E. and Petruk W.; 1990. Petrology of Au-Ag-Hg alloy and "invisible" gold in the Trout Lake massive sulphide deposit, Manitoba. Canadian Mineralogist, v. 28, pp. 189-206.

Helgeson H. C.; 1969. Thermodynamics of hydrothermal systems at elevated temperatures and pressures. American Journal of Science, v. 267, pp. 729-804.

Hemley J. J. and Jones W. R.; 1964. Chemical Aspects of Hydrothermal Alteration with Emphasis on Hydrogen Metasomatism. Economic Geology, v. 58, pp. 538-569.

Herrington et al.., 2000c. Southern Urals. In: Large R. and Blundell D. (eds), Database on Global VMS Districts, International Field Conference and Field Meeting, Tasmania, Australia, November 2000, pp. 85-104.

Herrington et al, 2003. Tectonics and metallogeny of the Urals Orogen: a reassessment. (Submitted.)

Herrington R., Armstrong R., Zaykov V. and Maslennikov V; 2000b. Volcanic Environments and Massive Sulphide Deposits. Program and Abstracts, International Field Conference and Field Meeting, Tasmania, Australia, November 2000, pp. 81-82.

Herrington R. J., Armstrong R. N., Zaykov V. V., Maslennikov V. V., Tessalina S. G., Orgeval J.-J. and Taylor R. N.; 2002. Massive Sulphide Deposits in the South Urals: Geological Setting Within the Framework of the Uralide Orogen. In: Mountain Building in the Uralides: Pangea to the Present. Geophysical Monograph 132, pp. 155-182.

Herrington R., Zaykov V. V. and Maslennikov V. V.; 2000a. General notes on massive sulphide deposits of the southern Urals. In: Volcanic Hosted Massive Sulphide Deposits of the Southern Urals. Field Excursion Guidebook, SGA 5th Biennial meeting and IAGOG 10th Quadrennial Symposium.

Herrington R. J., Maslennikov V. V., Spiro B., Zaykov V. V. and Little C. T. S.; 1998. Ancient vent chimney structures in the Silurian massive sulphide deposits of the Urals. In: Mills R. A. and Harrison K. (eds), Modern Ocean Floor Processes and the Geological Record, Geological Society of London Special Publication 248, pp. 241-257.

Herzig, P. M., Hannington M. D., Scott S. D., Maliotis G., Rona A. P. and Thompson G; 1991. Gold Rich Sea Floor Gossans in the Troodos Ophiolite and on the Mid-Atlantic Ridge. Economic Geology, v. 86, pp. 1747-1755.

Herzig P. M., Hannington M. D., Fouquet Y., von Stackelberg U. and Petersen S.; 1993. Gold-Rich Polymetallic Sulphides from the Lau Back Arc and Implications for the Geochemistry of Gold in Sea-Floor Hydrothermal Systems of the Southwest Pacific. Economic Geology, v. 88, pp. 2182-2209.

Herzig P. M., Petersen S., Kuhn T., Hannington M. D., Gemmel J. B. and Skinner A. C.; 2003. Shallow drilling of seafloor hydrothermal systems: the missing link. In: Eliopoulos D. G. et al. (eds), Proceedings of the 7th Biennial SGA Meeting, "Mineral Exploration and Sustainable Development", , Athens, Greece, August 2003, pp. 103-106.

Herzig P. M., Von Stackelberg U. and Petersen S.; 1990. Hydrothermal Mineralization from the Valu Fa Ridge, Lau Back-Arc Basin (SW Pacific). Marine Mining, v. 9, pp. 271-301.

Hey M. H.; 1954. A new review of the chlorites. Mineralogical Magazine, v. 30, pp. 277-292.

Holland H. D., 1959. Some Applications of Thermochemical Data to Problems of Ore Deposits I. Stability Relations Among the Oxides, Sulphides, Sulphates and Carbonates of Ore and Gangue Metals. Economic Geology, v. 54, pp. 184-233.

Holland H. D.; 1978. The chemistry of the atmosphere and the oceans. New York, John Wiley and Sons, 351 p.

Horita J. and Wesolowski D. J.; 1994. Liquid-vapour fractionation of oxygen and hydrogen isotopes of water from the freezing to the critical temperature. Geochimica et Cosmochimica Acta, v. 58, pp. 3425-3437.

Humphris S. E., Herzig P. M., Miller D. J., Alt J. C., Becker K., Brown D., Brügmann G., Chiba H., Fouquet Y., Gemmel G. B., Guerin G., Hanningont M. D., Holm N. G, Itturino G. J., Knot R., Ludwig R., Nakamura K., Petersen S., Reysenbach A. L., Rona P. A., Smith S. Sturz A. A., Tivey M. K. and Zhao X.; 1995. The internal structure of an active seafloor massive sulphide deposit. Nature, v. 377, pp. 713-716.

Huston D. L.; 1998. The hydrothermal environment. Journal of Australian Geology and Geophysics, v. 17, pp. 15-30.

Huston D. L.; 1999. Stable Isotopes and Their Significance for Understanding the Genesis of Volcanic-Hosted Massive Sulphide Deposits: A Review. Reviews in Economic Geology, v. 8, pp. 157-179.

Huston D. L.; 2000. Gold in Volcanic-Hosted Massive Sulphide Deposits: Distribution, Genesis and Exploration. Geology, v. 13, pp. 401-426.

Huston D. L., Bottrill R. S., Creelman R. A., Zaw K., Ramsden T. R., Rand S. W., Gemmell J. B., Jablonski W., Sie S. H. and Large R. R.; 1992. Geologic and Geochemical Controls on the Mineralogy and Grain Size of Gold-Bearing Phases, Eastern Australian Volcanic-Hosted Massive Sulphide Deposits. Economic Geology, v. 87, pp. 542-563.

Huston D. L. and Large R. R.; 1988. Distribution, Mineralogy and Geochemistry of Gold and Silver in the North End Orebody, Rosebery, Tasmania. Economic Geology, v. 83, pp. 1181-1192.

Huston D. L. and Large R. R.; 1989. A chemical model for the concentration of gold in volcanogenic massive sulphide deposits. Ore Geology Reviews, v. 4, pp. 171-200.

Huston D. L.; Sie S. H., Suter G. F., Cooke D. R. & Both R. A.; 1995. Trace Elements in Sulfide Minerals from Eastern Australian Volcanic-Hosted Massive Sulfide Deposits: Part I. Proton Microprobe Analyses of Pyrite, Chalcopyrite, and Sphalerite, and Part II. Selenium Levels in Pyrite: Comparison with $\delta^{34}S$ Values and Implications for the Source of Sulfur in Volcanogenic Hydrothermal Systems. Economic Geology, v. 90, pp. 1167-1196.

Huston D. L. and Taylor B. E.; 1999. Genetic Significance of Oxygen and Hydrogen Isotope Variations at the Kidd Creek Volcanic-Hosted Massive Sulfide Deposit, Ontario, Canada. Economic Geology, Monograph 10, pp.. 335-350.

Hutchinson R. W.; 1973. Volcanogenic Sulphide Deposits and Their Metallogenic Significance. Economic Geology, v. 68, No. 8, pp. 1223-1247.

Iishibashi J. and Urabe T.; 1995. Hydrothermal Activity Related to Arc-Backarc Magmatism in the Western Pacific. In: Taylor B. (ed), Backarc Basins: Tectonica and Magmatism, , plenum Press, New York.

Iizasa K., Tereshima S., Sasaki M. and Marumo K.; 1997. Volcanic-Hosted Sulphide-Barite Deposit from the Kit-Bayonnaise Submarine Caldera, Izu-Ogasawara Arc, Northwestern Pacific. Marine Georesources and Geotechnology, v. 15, pp.1-20.

Janecky D. R. and Seyfreid W. E. JR; 1984. Formation of massive sulphide deposits on oceanic ridge crests: Incremental reaction models for mixing between hydrothermal solutions and seawater. Geochimica et Cosmochimica Acta, v. 48, pp. 2723-2738.

Johnson N. E., Craig J. R. and Rimstidt J. D.; 1986. Compositional trends in tetrahedrite. The Canadian Mineralogist, v.24, pp..385-397.

Jowett E. C.; 1991. Fitting iron and magnesium into the hydrothermal chlorite geothermometer. GAC/MAC/SEG Joint Annual Meeting, Toronto May 1991, Program with Abstracts, 16, pp.

Kalogeropoulos S. I. and Scott S. D.; 1983. Mineralogy and geochemistry of tuffaceous exhalites (tetsusekiei) of the Fukazawa Mine, Hokuroku District, Japan. Economic Geology Monograph 5, pp. 412-432.

Karlsson H. R. and Clayton R. N.; 1990. Oxygen isotope fractionation between analcime and water; an experimental study. Geochimica et Cosmochimica Acta, v.54, pp. 1359-1368.

Kelley D. S. and Delaney J. R.; 1987. Two-phase separation and fracturing in mid-ocean ridge gabbros at temperatures greater than 700°C. Earth and Planetary Science Letters, v. 83, pp. 53-66.

Keays R. R. and Scott R. B.; 1976. Precious metals in Ocean-Ridge Basalts: Implications for Basalts as Source Rocks for Gold Mineralization. Economic Geology, v. 71, pp. 705-720.

Kojima S. and Sugaki A.; 1985. Phase Relations in the Cu-Fe-Zn-S System between 500° and 300°C under Hysrothermal Conditions. Economic Geology, v. 80, pp. 158-171.

Koroteev V. A., de Boorder H., Necheukhin V. M. and Sazonov; 1997. Geodynamic setting of the mineral deposits of the Urals. Tectonophysics, v. 276, pp. 291-300.

Kranidiotis P. and MacLean W. H.; 1987. Systematics of chlorite alteration at the Phelps Dodge massive sulfide deposit, Matagami, Quebec. Economic Geology, v. 82, pp. 1898-1911.

Krupp. R. E. and Weiser T.; 1992. On the stability of gold-silver alloys in the weathering environment. Mineralium Deposita, v. 27, pp. 268-275.

Kuleshov Yu. V., Zaykov V. V. and Maslennikov V. V.; 1999. The Tash Tau Massive Sulphide Deposit. In: Volcanic Hosted Massive Sulphide Deposits of the Southern Urals. Field Excursion Guidebook, SGA 5th Biennial meeting and IAGOG 10th Quadrennial Symposium.

Kusakabe M. and Chiba H.; 1983. Oxygen and Sulfur Isotope Composition of Barite and Anhydrite from the Fukazawa Deposit, Japan. Economic Geology Monograph 5, pp. 292-301.

Kusakabe M., Mayeda S. and Nakamura E.; 1990. S, O and Sr isotope systematics of active vent materials from the Mariana backarc basin spreading axis at 18 °N. Earth and Planetary Science Letters, v. 100, pp. 275-282.

Large, R. R.; 1977. Chemical Evolution and Zonation of Massive Sulphide Deposits in Volcanic Terrains. Economic Geology, v. 72, pp. 549-572.

Large R. R.; 1992. Australian Volcanic-Hosted Massive Sulfide Deposits: Features, Styles, and Genetic Models. Economic Geology, v. 87, pp. 471-510.

Large R. R. and Both R. A.; 1980. The Volcanogenic Sulfide Ores at Mount Chalmers, Eastern Queensland. Economic Geology, v. 75, pp. 992-1009.

Large R. R., Huston D. L., McGoldrick P. J., Ruxton P. A. and McArthur G; 1989. Gold Distribution and Genesis in Australian Volcanogenic Massive Sulphide Deposits and Their Significance for Gold Transport Models. Economic Geology Monograph 6, pp. 520-535.

Larocque A. C. L. and Hodgson C. J.; 1993. Gold Distribution in the Mobrun Volcanic-Associated Massive Sulphide Deposit, Noranda, Quebec: A Preliminary Evaluation if the Role of Metamorphic Remobilization. Economic Geology, v. 88, pp. 1443-1459.

Larocque A. C. L. and Hodgson C. J.; 1995. Effects of greenschist-facies metamorphism and related deformation on the Mobrun massive sulfide deposit, Québec, Canada. Mineralium Deposita, v. 30, pp. 439-448.

Leary M. O. and Sack R. O.; 1987. Fe – Zn exchange reaction between tetrahedrite and sphalerite in natural environments. Contributions to Mineralogy and Petrology, v. 96, pp. 415-425.

Le Bel L. and Oudin E.; 1982. Fluid inclusion study of deep-sea hydrothermal sulphide deposits on the East Pacific Rise Near 21° N. Chemical Geology, v. 37, pp. 129-136.

Lécuyer C. & Allemand P.; 1999. Modelling of the oxygen isotope evolution of seawater: Implications for the climate interpretation of the d18) of marine sediments. Geochimica et Cosmochimica Acta, v. 63, pp. 351-361.

Lennykh V. I., Valiser P. M., Beane R., Leech M. and Ernst W. G.; 1995. Petrotectonic evolution of the Makysutov complex, southern Urals Mountains, Russia: Implications for ultrahigh –pressure metamorphism. International Geology Review, v. 37, pp. 584-600.

Lüders V., Pracejus B. and Halbach P.; 2001. Fluid inclusion and sulfur isotope studies in probable modern analogue Kuroko-type ores from the JADE hydrothermal field (Central Okinawa Trough, Japan). Chemical Geology, v. 173, pp. 45-58.

Lydon J. W.; 1984. Volcanogenic massive sulphide deposits Part I: A descriptive model. Geoscience Canada, v. 11, pp. 195-202.

Maclean W. H.; 1990. Mass change calculations in altered rock series. Mineralium Deposita, v. 25, pp. 44-49.

Maclean W. H. & Kranidiotis P., 1987. Immobile Elements as Monitors of Mass Transfer in Hydrothermal Alteration: Phelps Dodge Massive Sulphide Deposit, Matagami, Quebec. Economic Geology, v. 82, pp. 951-962.

Mao S. H.; 1991. Occurrence and distribution of invisible gold in a Carlin-type deposit in China. American Mineralogist, v. 76, pp. 1964-1972.

Marignac C., Diagana B., Cathelineau M., Boiron M.-C., Banks D., Fourcade S. and Vallance J.; 2003. Remobilisation of base metals and gold by Variscan metamorphic fluids in the south Iberian pyrite belt: evidence from the Tharsis VMS deposit. Chemical Geology, v. 194, pp. 143-165.

Marquis P., Hubert C., Brown A. C. & Rigg D. M.; 1990. Overprinting of early, redistributed Fe and Pb-Zn mineralization by late-stage Au-Ag-Cu deposition at the Dumagami mine, Bousquet district, Abitibi, Quebec. Canadian Journal of Earth Sciences, v. 27, pp. 1651-1671.

Maslennikov V. V., Zaykov V. V. Zaykova E. V.; 2000. Paleohydrothermal Fields and Ore Formation Conditions at Massive Sulphide Deposits in the Uralian Paleoocean. In: Geodynamics & Metallogeny: Theory and implications for app.lied geology (Eds. Mezhelovsky et al.). Ministry of Natural Resources & GEOKART, Moscow 2000. pp. 340-357.

Maslov V. A., Cherkasov V. L., Tischchenko V. T., Smirnova I. A., Artyushkova O. V. and Pavlov V. V.; 1993. On the stratigraphy and correlation of the middle Paleozoic complexes of the main copper-pyritic areas of the Southern Urals. Ufa, Russia, Ufimsky Nauchno Tsentr, 217 p.

Matsukuma T., Nitsuma H., Yui S. and Wada F.; 1974. Rare Minerals from Kuroko Ores of the Uwamuki Deposits of the Kosaka Mine, Akita Prefecture, Japan. Mining Geology Special Issue No. 6, pp. 349-361.

Matte P., Maluski H., Caby R., Nicolas A., Kepezhinskas P. and Sobolev S.; 1993. Geodynamic model and 39Ar/40Ar dating for the generation and emplacement of the high pressure (HP) metamorphic rocks in SW Urals. Paris, Academie des Sciences Comptes Rendus, ser. II, v. 317, pp. 1667-1674.

McLeod R. L. and Stanton R. L.; 1984. Phyllosilicates and Associated Minerals in Some Palaeozoic Stratiform Sulfide Deposits of Southeastern Australia. Economic Geology, v. 79, pp. 1-23.

McPhie J., Doyle M, and Allen R,; 1993. Volcanic Textures; A guide to the interpretation of textures in volcanic rocks. University of Tasmania, Hobart, 196 p.

Montero P., Bea F., Gerdes A., Fershtater G., Zin'kova E., Borodina N., Osipova T. and Smirnov V.; 2000. Singe-zircon evapouration ages and Rb-Sr dating of four major Variscan batholiths of the Urals. A perspective on the timing of deformation an granite generation. Tectonophysics, v. 317, 93-108.

Murphy P. J. and Meyer G.; 1998. A gold-copper association in ultramafic-hosted hydrothermal sulfides from the Mid-Atlantic Ridge. Economic Geology, v. 93, pp. 1076-1083.

Ohmoto H., Mizukami M., Drummond S. E., Eldridge C. S., PisuthaArnond V. and Lenagh T. C.; 1983. Chemical Processes of Kuroko Ore Formation. Economic Geology Monograph 5, pp. 570-604.

Ohmoto H. and Goldhaber M. B.; 1997. Sulphur and Carbon Isotopes. In: H. L. Barnes (ed), Geochemistry of Hydrothermal Ore Deposits, 3nd Edition, pp. 517-612.

Ohmoto H. and Lasaga A. C.; 1982. Kinetics of reactions between aqueous sulfates and sulfides in hydrothermal systems. Geochimica et Cosmochimica Acta, v. 63, pp. 1727-1745.

Ohmoto H. and Rye R. O.; 1979. Isotopes of sulphur and carbon. In: Barnes H. L. (ed), Geochemistry of hydrothermal ore deposits, New York, Wiley; pp. 509-567.

O'Neil J. R. & Taylor H. P. Jr.; 1967. The oxygen isotope and cation exchange chemistry of feldspars. American Mineralogist, v. 52, pp. 1414-1437.

Palmer M. R.; 1992. Controls over the chloride concentration of submarine hydrothermal vent fluids: evidence from Sr/Ca and $^{87}Sr/^{86}Sr$ ratios. Earth and Planetary Science Letters, v. 109, p. 37-46.

Pearce J. A.; 1982. Trace element characteristics of lavas from destructive plate boundaries. In: Thorpe R. S. (ed), Andesites, John Wiley & Sons, pp. 525-548.

Pearce J. A.; 1996. A User's Guide to Basalt Discrimination Diagrams. In: Wyman D. A. ed., Trace Element Geochemistry of Volcanic Rocks: Applications for Massive Sulphide Exploration, Geological Association of Canada Short Notes, v. 12, pp. 79-113.

Peter J. M., Goodfellow W. D. and Leybourne M. I.; 1994. Fluid inclusion petrography and microthermometry of the Middle Valley hydrothermal system, northern Juan de Fuca Ridge. Proceedings of the Ocean Drilling Program, Scientific Results, v. 158, pp. 411-425.

Petersen S., Herzig P. M., Hannington M. D. and Gemmel J. B.; 2003. Gold-rich massive sulphides from the interior of the felsic-hosted PACMANUS massive sulfide deposit, Eastern Manus Basin. In: Eliopoulos D. G. et al. (eds), Proceeedings of the 7th Biennial SGA Meeting, "Mineral Exploration and Sustainable Development", Athens, Greece, August 2003, pp. 171-174.

Phillips W. R.; 1964. A numerical system of classification for chlorites and septechlorites. Mineralogical Magazine, v. 34, pp. 1114-1124.

Pisutha-Arnond V. and Ohmoto H.; 1983. Thermal History, and Chemical and Isotopic Compositions of the Ore Forming Fluids for the Kuroko Massive Sulfide Deposits in the Hokuroko District of Japan. Economic Geology Monograph 5, pp. 523-558.

Pouchou J. L. & Pichoir F.; 1984. A new model for quantitative X-ray microanalysis I: Application to in-depth analysis of homogeneous samples: La Recherche Aerospatiale, v. 3, pp.13-38.

Prokin V. A. and Buslaev F. B.; 1999. Massive copper-zinc sulphide deposits in the Urals. Ore Geology Reviews, v. 14, pp. 1-69.

Prokin V. A., Buslaev F. B. and Perepetailo A. P.; 1999. Baimak type sulphide deposits in the Urals : Intermediate between massive sulphide and porphyry copp.er. In: Stanley et al. (eds), Mineral Deposits : Processes to Processing, Balkema, Rotterdam. pp. 567-568.

Puchov, V. N.; 1997. Structure and Geodynamics of the Uralian Orogen. In: Orogeny Through Time, Geological Society Special Publication No. 121, pp. 210-236.

Puchkov V. and Seravkin I.; 2001. Geodynamic aspects of the Magnitogorsk Zone. In : Geodynamic settings of the VMS deposits in the South Urals and comparisons with other belts in Europe; Abstract Volume, GEODE meeting Anglesey, Wales, 14-17 October 2001, pp. 19-20.

Rees C. E., Jenkins W. J. and Monster J.; 1978. The sulphur isotopic composition of ocean water sulphate. Geochimica et Cosmochimica Acta, v.42, pp. 377-382.

Reich, M., Palenik, C. S., Utsonomiya S., Becker U., Sixtrude L., Kesler S. E. and Ewing R.; 2003. Solubility limit of gold in arsenian pyrite from carlin-type and epithermal deposits: EMPA, SIMS, HRTEM and quantum-mechanical constraints. In: Geological Society of America, 2003 annual meeting Abstracts with Programs, v. 35, pp. 358.

Reid D. L., Welke H. J., Erlank A. J., Moyes A.; 1987. The Orange River Group; a major Proterozoic calcalkaline volcanic belt in the western Namaqua Province, Southern Africa Geological Society Special Publications, v. 33, pp.327-346.

Renders P. J. & Seward T. M.; 1989. The adsorption of thio gold(I) complexes by amorphous As_2S_3 and Sb_2S_3 at 25 and 90°C. Geochimica et Cosmochimica Act, v. 53, pp. 255-267.

Riverin G. and Hodgson C. J.; 1980. Wall-rock alteration at the Millenbach Cu-Zn mine, Noranda, Quebec. Economic Geology, v. 75, pp. 424-444.

Roberts M. D., Oliver N. H. S. and Fairclough M. C.; 2003. Geochemcal and Oxygen Isotope Signature of Sea-Floor Alteration Associated with a Polydeformed and Highly Metamorphosed Massive Sulphide Deposit, Ruostesuo, Central Finland. Economic Geology, v. 98, pp. 535-556.

Roberts S., Bach W., Binns R. A., Vanko D. A., Yeats C. J., Teagle D. A. H., Blakclock K., Blusztajn J. S., Boyce A. J., Cooper M. J., Holland N. and McDonald B.; 2003. Contrasting evolution of hydrothermal fluids in the PACMANUS system, Manus Basin; the Sr and S isotope evidence. Geology, v. 31, pp.805-808.

Robinson B. W. and Kusakabe M.; 1975. Quantitative preparation of sulphur dioxide, for 34S/32S analyses, from sulphides by combustion with cuprous oxide. Analytical Geochemistry, v. 47, pp. 1179-1181.

Robinson D. & Bevins R. E.; 1999. Patterns of regional low-grade metamorphism in metabasites. In: Frey M. & Robinson D. (eds), Low-Grade Metamorphism, Blackwell Science Ltd. pp. 143-168.

Rosenbauer R. J. & Bischoff J. L.; 1983. Uptake and transport of heavy metals by heated seawater: A summary of the experimental results. In: Hydrothermal Processes at Sea Floor Spreading Centres, (Eds Rona P. A., Boström K., Laubier L. & Smith Jr. K. L.). NATO Conference Series: Series IV Marine Science. Plenum Press, New York. pp. 177-197.

Saccocia P. & Gillis K. M.; 1995. Hydrothermal upflow zones in the oceanic crust. Earth and Planetary Science Letters, v. 136, pp. 1-16.

Sack R. O. and Loucks R. R.; 1985. Thermodynamic properties of tetrahedrite-tennantites: constraints on the independence of the Ag-Cu, Fe-Zn, Cu-Fe and As-Sb exchange reactions. American Mineralogist, v. 70, pp. 1270-1289.

Sakai H., Des Marais D. J., Ueda A. and Moore J. G.; 1984. Concentrations and isotope ratios of carbon, nitrogen and sulfur in ocean-floor basalts. Geochimica et Cosmochimica Acta, v. 48, pp. 2433-2441.

Santagiuda A. & Hannington M. D.; 1996. Characteristics of gold mineralization in volcanogenic massive sulphide deposits of the Notre Dame Bay area, central Newfoundland. Canadian Journal of Earth Sciences, v. 33, pp. 316-334.

Sato J.; 1974. Ores and Ore Minerals from the Shakanai Mine, Akita Prefecture, Japan. Mining Geology Special Issue No. 6, pp. 323-335.

Saunders A. D. and Tarney J.; 1984. Geochemical characteristics of basaltic volcanism within back-arc basins. In: Kokelaar B. P. and Howells M. F. (eds), Marginal Basin Geology, Geological Society of London Special Publication 16, pp 59-76.

Savelieva G. N., Sharaskin A. Ya., Saveliev A. A., Spadea P and Gaggero L.; 1997. Ophiolites of the southern Uralides adjacent to the East European continental margin. Tectonophysics, v. 276, pp. 117-137.

Savin S. M. and Lee M.; 1988. Isotopic studies of phyllosilicates. Reviews in Mineralogy, v.19, pp. 189-223.

Sawkins, J. F.; 1990. Integrated tectonic-genetic model for volcanic-hosted massive sulphide deposits. Geology, v. 18, pp. 1061-1064.

Scarrow J. H., Spadea P., Savelieva G. N., Glodny J., Montero P., Pertsev A. N., Cortesogno L. and Gaggero L.; 1999. The Mindyak Palaeozoic lherzolite ophiolite, southern Urals. Geochemistry and geochronology. Ofioliti, v. 24, pp. 241-248.

Schardt C., Cooke D. R., Gemmell J. B. and Large R. R., 2001. Geochemical modelling of the Zoned Footwall Alteration Pipe to the Hellyer VHMS Deposit, Western Tasmania, Australia. Economic Geology, v. 96, pp. 1037-1054.

Scotney P.; 2002. The Geology and Genesis of Massive Sulphide, barite-gold deposits on Wetar Island, Indonesia. Unpublished Thesis, Southampton Univerity.

Scott S. D.; 1983. Chemical behaviour of sphalerite and arsenopyrite in hydrothermal and metamorphic environments. Mineralogical Magazine, v. 47, pp. 427-435.

Scott S. D. & Binns R. A.; 1995. Hydrothermal processes and contrasting styles of mineralization in the western Woodlark and eastern Manus basins of the western Pacific. In: Walker L. M. & Dixon D. R. (eds), Hydrothermal Vents and Processes, Geological Society Special Publication No. 87, pp. 175-189.

Seal R. R. II, Alpers C. N. and Rye R. O.; 2000. Stable isotope systematics of sulfate minerals. Reviews in Mineralogy and Geochemistry, v. 40, pp. 541-602.

Seal R. R. II, Essene E. J. and Kelly W. C.; 1990. Tetrahedrite and tennantite: Evaluation of thermodynamic data and phase equilibria. Canadian Mineralogist, v. 28, pp. 725-738.

Seewald J. S. and Seyfreid Jr. W. E.; 1990. The effect of temperature on metal mobility in subseafloor hydrothermal systems: constraints from basalt alteration experiments. Earth and Planetary Science Letters, v. 101, pp. 388-403.

Seward T. M.; 1973. Thio complexes of gold in hydrothermal ore solutions. Geochimica et Cosmochimica Acta, v. 37, pp. 379-399.

Seward, T. M.; 1976. The stability of chloride complexes of silver in hydrothermal solutions up to 350°C. Geochimica et Cosmochimica Acta, v. 40, pp. 1329-1341.

Seward T. M.; 1984. The formation of lead(II) chloride complexes to 300°C: A spectrophotometric study. Geochimica et Cosmochimica Acta, v. 48, pp. 121-134.

Seyfried Jr. W. E. and Ding K.; 1995. Phase Equilibria in Subseafloor Hydrothermal Systems: A Review of the Role of Redox, Temperature, pH and Dissolved Cl on the Chemistry of Hot Spring Fluids at Mid-Ocean Ridges. In: Seafloor Hydrothermal Systems: Physical, Chemical, Biological, and Geological Interactions; Geophysical Monograph 91, pp. 248-272.

Shanks W. C. III, 2001. Vent fluids, hydrothermal deposits, hydrothermal alteration, and microbial processes. Reviews in Mineralogy and Geochemistry, v. 43, pp. 469-525.

Shanks III W. C., Bischoff J. L. and Rosenbauer R. J.; 1981. Seawater sulphate reduction and sulfur isotope fractionation in basaltic systems: Interaction of seawater with fayalite and magnetite at 200-350°C. Geochimica et Cosmochimica Acta, v. 45. pp. 1977-1985.

Shanks III W. C., Böhlke J. K. and Seal II R. R.; 1995. Stable Isotopes in Mid-Ocean Ridge Hydrothermal Systems: Interactions between Fluids, Minerals, and Organisms. In: Seafloor Hydrothermal Systems: Physical, Chemical, Biological, and Geological Interactions; Geophysical Monograph 91, pp. 194-221.

Shanks III W. C. and Seyfried W. E. JR; 1987. Stable Isotope Studies of Vent Fluids and Chimney Minerals, Southern Juan de Fuca Ridge: Sodium Metasomatism and Seawater Sulphate Reduction. Journal of Geophysical Research, v. 92, pp. 11387-11399.

Sharp T. G. and Buseck P. R.; 1993. The distribution of Ag and Sb in galena: Inclusions versus solid solution. American Mineralalogist, v. 78, pp. 85-95.

Shepherd, T. J., Rankin A. H. and Alderton D. H. M.; 1985. A practicle guide to fluid inclusion studies, Blackie, London, 239 p.

Sherlock R. L., Roth T., Spooner E. T. C. and Bray C. J.; 1999. Origin of the Eskay Creek Precious Metal-Rich Volcanogenic Massive Sulphide Deposit: Fluid Inclusion and Stable Isotope Evidence. Economic Geology, v. 94, pp. 803-824.

Shikazono N.; 1994. Precipitation mechanisms of barite in sulfate-sulfide deposits in back-arc basins. Geochimica et Cosmochimica Acta, v. 58, pp. 2203-2213.

Shimazaki Y.; 1974. Ore Minerals of the Kuroko-type Deposits. Mining Geology Special Issue No. 6, pp. 311-322.

Sillitoe, R. H., Hannington M. D. and Thompson J. F. H.; 1996. High sulfidation deposits in the volcanogenic environment. Economic Geology, v. 91, pp. 204-212.

Simon G., Kesler S. E. and Chryssoulis S.; 1999. Geochemistry and Textures of Gold-Bearing Arsenian Pyrite, Twin Creeks, Nevada: Implications for Deposition of Gold in Carlin-Type Deposits. Economic Geology, v. 94, pp. 405-422.

Sinclair B. J., Berry R. F. and Gemmell J. B.; 2000. Mineralogy and textures of the Battle Zone massive sulphide lenses, Myra Falls district, British Columbia, Canada. Program and Abstracts, International Field Conference and Field Meeting, Tasmania, Australia, November 2000, pp. 197-198.

Smellie J. L.; 1995. Volcanism Associated with extension at consuming plate margins. In: Smellie J. L. (ed.), Geological Society Special Publication No. 81, Volcanism Associated with Extension at Consuming Plate Margins, 1995, pp. 1-28.

Solomon M. and Zaw K.; 1997. Formation on the Sea Floor of the Hellyer Volcanogenic Massive Sulphide Deposit. Economic Geology, v. 92, pp. 686-695.

Spadea P., Kabanova L. Y. and Scarrow J. H.; 1998. Petrology, geochemistry and geodynamic significance of the mid-Devonian boninitic rocks from the Baimak-Buribai area. Ofioliti, v. 23, pp. 17-36.

Stanton R. L., 1955. Lower Paleozoic mineralization near Bathurst, New South Wales. Economic Geology, v. 50, pp. 681-714..

Stanton R. L.; 1964. Textures of stratiform ores. Nature, v. 202, pp. 173-174.

Sverjensky D. A., Shock E. L. and Helgeson H. C.; 1997. Prediction of the thermodynamic properties of aqueous metal complexes to 1000°C and 5kb. Geochimica et Cosmochimica Acta, v. 61, pp. 1359-1412.

Teagle, D. A. H., Alt J. C., Chiba H., Humphris S. E. and Halliday A. N.; 1998. Strontium and oxygen isotopic constraints on fluid mixing, alteration and mineralization in the TAG hydrothermal deposit. Chemical Geology, v. 149, pp. 1-24.

Tessalina S., Zaykov V., Masslenikov V., Bailey L. and Orgeval J. J.; 1999. Fluid inclusion data of the Alexandrinka massive sulphide deposit, Urals. In: Stanley et al. (eds), Mineral Deposits: Processes to Processing, pp. 13-16.

Tivey M. K.; 1995. Modelling Chimney Growth and Associated Fluid Flow at Seafloor Hydrothermal Vent Sites. In: Seafloor Hydrothermal Systems: Physical, Chemical, Biological and Geological Interactions, Geophysical Monograph 91, pp. 158-177.

Tivey M. K., Mills R. A. and Teagle D. A. H.; 1998. Temperature and salinity of fluid inclusions in anhydrite as indicators of seawater entrainment and heating in the TAG active mound. Proceedings of the Ocean Drilling Program, Scientific Results, v. 158, pp. 179-190.

Tokunaga M. & Honma H., 1974. Fluid Inclusions in the Minerals from Some Kuroko Deposits. Mining Geology Special Issue No. 6, pp. 385-388.

Truesdell A. H. and Nathenson M.; 1977. The Effects of Subsurface Boiling and Dilution on the Isotopic Compositions of Yellowstone Thermal Waters. Journal of Geophysical Research, v. 82, pp. 3694-3704.

Ueda A. and Sakai H.; 1984. Sulfur isotope study of Quaternary volcanic rocks from the Japanese Island Arc. Geochimica et Cosmochimica Acta, v. 48, pp. 1837-1848.

Urabe T.; 1974. Iron Content of Sphalerite Coexisiting with Pyrite from Some Kuroko Deposits. Mining Geology Special Issue No. 6, pp. 377-384.

Van Hook, H. J.; 1960. The ternary system Ag_2S-Bi_2S_3-PbS. Economic Geology, v. 55, pp. 750-788.

Veizer J., Ala D., Azmy K., Bruckschen P., Buhl D., Bruhn F., Carden G. A. F., Diener A., Ebneth S., Godderis Y., Jasper T., Korte C., Pawellek F., Podlaha O. G. & Strauss H.; 1999. $^{87}Sr/^{86}Sr$, $\delta^{13}C$ and $\delta^{18}O$ evolution of Phanerozoic seawater. Chemical Geology, v. 161, pp. 59-88.

Vokes F. M.; 1969. A review of the metamorphism of sulphide deposits. Earth-Science Reviews, v. 5, pp. 99-143.

Vonn Damm K. L.; 1988. Systematics of and postulated controls on submarine hydrothermal chemistry. Journal of Geophysical Research, v. 93, pp. 4551-4561.

Von Damm K. L.; 1995. Controls on the Chemistry and Temporal Variability of Seafloor Hydrothermal Fluids. In: Seafloor Hydrothermal Systems: Physical, Chemical, Biological and Geological Interactions; Geophysical Monograph 91, pp. 222-247.

Walshe J. L.; 1986. A Six-Component Chlorite Solid Solution Model and the Conditions of Chlorite Formation in Hydrothermal and Geothermal Systems. Economic Geology, v. 81, pp. 681-703.

Walshe J. L. and Solomon M.; 1981. An Investigation into the Environment of Formation of the Volcanic-Hosted Mt. Lyell Copper Deposits Using Geology, Mineralogy, Stable Isotopes, and a Six-Component Chlorite Solid Solution Model. Economic Geology, v. 76, pp. 246-284.

Watson K. D.; 1959. Origin of banded structure in some massive sulphide deposits. Canadian Mining and Metallurgical Bulletin, v. 570, pp. 643-646.

Wiggins L. B. and Craig J. R.; 1980. Reconnaissance of the Cu-Fe-Zn-S system; sphalerite phase relationships. Economic Geology, v. 75, pp. 742-751.

Winchester J. A. and Floyd P. A.; 1977. Geochemical discrimination of different magma series and their differentiation products using immobile elements. Chemical Geology, v. 20, pp. 325-343.

Wood S. A.; 1998. Calculation of Activity-Activity and Logf_{O2}-pH diagrams. Reviews in Economic Ore Geology, v. 10, pp 81-98.

Wood S. A. and Samson I. M.; 1998. Solubility of Ore Minerals and Complexation of Ore Metals in Hydrothermal Solutions. Reviews in Economic Ore Geology, v. 10, pp 33-80.

Woohead J. D., Harmon R. S. and Fraser D. G.; 1987. O, S, Sr and Pb isotope variations in volcanic rocks from the Northern Mariana Islands: implications for crustal recycling in intra-oceanic arcs. Earth and Planetary Science Letters, v. 83, pp. 39-52.

Wu I. and Petersen U.; 1977. Geochemistry of Tetrahedrite and Mineral Zoning at Casapalca, Peru. Economic Geology, v. 72, pp. 993-1016.

Xiao Z., Gammons C. H. and Williams-Jones A. E.; 1998. Experimental study of copper(I) chloride complexing in hydrothermal solutions at 40 to 300oC and saturated water vapor pressure. Geochimica et Cosmochimica Acta, v. 62, pp. 2949-2964.

Yakubchuk A. S.; 2001. New opportunities in deciphering the tectonic zonation of the Urals: A metallogenic implication. In Herrington et al. (eds), Geodynamic settings of the VMS deposits in the south Urals and comparisons with other belts in Europe, Abstract volume, GEODE meeting, Anglesey, Wales, 14-17th October 2001; p 31-32.

Yoder H. S. and Eugster H. P.; 1955. Synthetic and natural muscovites. Geochimica et Cosmochimica Acta, v. 8, pp. 225-280.

Yui S.; 1983. Textures of Some Japanese Besshi-Type Ores and Their Implications for Kuroko Deposits. Economic Geology Monograph 5, pp. 231-240.

Zaw K. and Large R. R.; 1992. The Precious Metal-Rich South Hercules Mineralization, Western Tasmania: A Possible Subsea-Floor Replacement Volcanic-Hosted Massive Sulphide Deposit. Economic Geology, v. 87, pp. 931-952.

Zhang Y-G and Frantz J. D.; 1987. Determination of the homogenisation temperatures and densities of supercritic fluids in the system NaCl-KCl-$CaCl_2$-H_2O using synthetic fluid inclusions. Chemical Geology, v. 64, pp. 335-350.

Zhang L., Liu J., Zhou H. and Chen Z.; 1989. Oxygen isotope fractionation in the quartz-water-salt system. Economic Geology, v. 84, pp. 1643-1650.

Zheng Y.-F.; 1993. Calculation of oxygen isotope fractionation in hydroxyl-bearing silicates. Earth and Planetary Science Letters, v. 120, pp. 247-263.

Zierenberg R. A., Koski R. A, Morton J. L., Bouse R. M. and Shanks III W. C.; 1993. Genesis of Massive Sulphide Deposits on a Sediment-Covered Spreading Center, Escanaba Trough, Southern Gorda Ridge. Economic Geology, v. 88, pp. 2069-2098.

Zonenshain L. P., V. G. Korinevsky, V. G. Kazmin, D. M. Pechersky, V. V. Khain and V. V. Matveenkov; 1984. Plate Tectonic Model of the South Urals Development. Tectonophysics, v. 109, 95-135.

APPENDICES

APPENDIX A

APPENDIX A1 : SAMPLE LISTINGS

Sample listings:

Table A1(i). Balta Tau mine sample list and descriptions.

Table A1(ii). Balta Tau mine samples analytical summary.

Table A1(iii). Regional sample list and descriptions.

Table A1(iv). Regional samples analytical summary.

Sample No	Collected	Material	Hand specimen	Polished slice	Polished block	Polished thin section
JC13062A	1995 RJH	chp-py massive sulphides	-	-	Y	-
JC13062B	1995 RJH	chp-py massive sulphides	-	-	Y	-
JC13062C	1995 RJH	gold-bearing barite lens	-	-	Y	-
901	1999 RJH	fine gr. py-chp rich massive sulphides	small sample	Y	Y	Y
902	1999 RJH	collomorphic py rich massive sulphides	small sample	Y	-	Y
903	1999 RJH	collomorphic py-sph massive sulphides	small sample	Y	-	Y
905	1999 RJH	foliated marginal barite lens	small sample	-	-	Y
906	1999 RJH	foliated marginal barite lens	small sample	-	-	Y
907	1999 RJH	sericitized hanging-wall volcanics	small sample	-	-	Y
908	1999 RJH	sericitized hanging-wall volcanics	small sample	-	-	Y
910	1999 RJH	collomorphic py-sph massive sulphides	small sample	-	Y	Y
BTB01A	1999 RJH	gold-bearing barite lens	-	-	Y	-
BTB01B	1999 RJH	gold-bearing barite lens	-	-	Y	-
BTB01C	1999 RJH	gold-bearing barite lens	-	-	Y	-
BTB01D	1999 RJH	gold-bearing barite lens	-	-	Y	-
BL1	VVM	gold-bearing barite lens	-	-	Y	-
BL1A	VVM	gold-bearing barite lens	-	-	Y	-
BL2	VVM	gold-bearing barite lens	-	-	Y	-
B2	VVM	collomorphic chimney clast	-	-	Y	-
B3	VVM	collomorphic chimney clast	-	-	Y	-
BL10.18A	VVM	layered sulphides	-	-	Y	-
BL10.19B	VVM	layered sulphides	-	-	Y	-
BL10.22B	VVM	layered sulphides	-	-	Y	-
BL711	VVM	layered sulphides	-	-	Y	-
BL711A	VVM	layered sulphides	-	-	Y	-
00BT01	2000 RJH	weakly mineralized footwall	large sample	Y	Y(b)	Y (a)
00BT02	2000 RJH	weakly mineralized footwall	large sample	-	-	Y
00BT08	2000 RJH	gold-bearing barite lens	small sample	-	-	Y
00BT09	2000 RJH	hanging-wall graded volcaniclastics	large sample	-	-	Y
00BT10	2000 RJH	hanging-wall graded volcaniclastics	large sample	-	-	Y
00BT12	2000 RJH	footwall vein mineralization	small sample	-	-	Y
00BT13	2000 RJH	footwall vein mineralization	small sample	-	-	Y
00BT14	2000 RJH	footwall vein mineralization	small sample	-	-	Y
00BT15	2000 RJH	footwall vein mineralization	small sample	-	Y	-
00BT17	2000 RJH	footwall vein mineralization	small sample	-	-	Y
00BT18	2000 RJH	"Eastern" hanging-wall lavas	large sample	-	-	Y
00BT19	2000 RJH	"Eastern" hanging-wall lavas	large sample	-	-	Y
00BT20	2000 RJH	Immediate hanging-wall volcanics	large sample	-	-	Y
00BT21	2000 RJH	hanging-wall volcaniclastics	large sample	-	-	Y (a,b)
01BT001	2001 NGH	weakly mineralized footwall	slice	-	-	Y
01BT002	2001 NGH	quartz-tennantite footwall vein	large sample, ten sep	-	-	Y (a,b)
01BT003	2001 NGH	mineralized footwall	small sample	-	-	-
01BT004	2001 NGH	mineralized footwall	slice	-	-	Y
01BT005	2001 NGH	quartz-tennantite footwall vein	small sample	-	-	-
01BT006	2001 NGH	mineralized footwall	slice	-	-	-
01BT006A	2001 NGH	mineralized footwall	small sample	-	-	-
01BT007	2001 NGH	quartz-tennantite footwall vein	slice, ten-chp sep	-	-	-
01BT008	2001 NGH	mineralized footwall	slice	-	-	-
01BT012	2001 NGH	layered sulphides	slice	-	-	Y
01BT013	2001 NGH	layered sulphides	slices x2	-	-	Y
01BT014	2001 NGH	layered sulphides	slice	-	-	-
01BT017	2001 NGH	quartz-tennantite footwall vein	slice, ten sep	-	-	-
01BT018	2001 NGH	layered sulphides	slice	-	-	Y
01BT019	2001 NGH	sericitized immediate hanging-wall	large sample	Y	-	Y

Table A1(i). Sample list.

Sample No	Collected	Material	Hand specimen	Polished slice	Polished block	Polished thin section
01BT021	2001 NGH	sericitized immediate hanging-wall	large sample	Y	-	Y
01BT022	2001 NGH	altered immediate hanging-wall	large slice	Y	-	Y
01BT024	2001 NGH	altered immediate hanging-wall	large sample	-	-	-
01BT026	2001 NGH	hanging-wall volcaniclastics	slice	-	-	-
01BT029	2001 NGH	layered sulphides	small slice	-	-	-
01BT031	2001 NGH	layered sulphides	large slice	Y	-	-
01BT032	2001 NGH	layered sulphides	slice	-	-	Y
01BT033	2001 NGH	layered sulphides	2x large slices	Y(a)	-	Y(b)
01BT039	2001 NGH	hanging-wall graded volcaniclastics	slice	Y	-	
01BT043	2001 NGH	hanging-wall volcaniclastics	slice	Y	-	-
01BT045	2001 NGH	massive hanging-wall volcaniclastics	large sample	-	-	Y
01BT047	2001 NGH	hanging-wall qtz-cb-ep vein	slice	-	-	-
01BT051	2001 NGH	mineralized footwall	slice	-	-	-
01BT052	2001 NGH	mineralized footwall	slice	-	-	Y
01BT054	2001 NGH	layered sulphides	slice	-	-	Y
01BT056	2001 NGH	mineralized footwall	slice	Y	-	-
01BT058	2001 NGH	mineralized footwall	slice	-	-	Y (b)
01BT061	2001 NGH	mineralized footwall	slice	-	-	Y
01BT062	2001 NGH	sphalerite-rich massive sulphides	slices x2	-	-	Y
01BT064	2001 NGH	sheared weakly mineralized footwall	slice	-	-	Y (a)
01BT065	2001 NGH	sphalerite-rich layered sulphides	small sample	-	-	Y
01BT066	2001 NGH	mineralized footwall	small sample	-	-	-
01BT067	2001 NGH	mineralized footwall	small sample	-	-	Y
01BT068	2001 NGH	mineralized footwall	small sample	-	-	-
01BT069	2001 NGH	mineralized footwall	small slice	-	Y	-
01BT070	2001 NGH	mineralized footwall	small slice	-	-	Y
01BT071	2001 NGH	mineralized footwall	small sample	-	-	-
01BT072	2001 NGH	mineralized footwall	chp sep	-	-	-
01BT073	2001 NGH	mineralized footwall	samples, ten-sph sep	-	-	Y
01BT075	2001 NGH	mineralized footwall	small slice	-	-	-
01BT075A	2001 NGH	sericitized immediate hanging-wall	large sample	Y	-	Y
01BT076	2001 NGH	sphalerite-rich massive sulphides	large slice	Y (a)	-	Y (a)
01BT077	2001 NGH	sphalerite-rich massive sulphides	slices x2	Y (a)	-	-
01BT078	2001 NGH	barite vein in shear zone	small samples	-	-	-
01BT082	2001 NGH	barite-rich massive sulphides	slices x2	-	-	Y (a,b)
01BT085	2001 NGH	altered, unmineralized footwall	large sample	-	-	Y
01BT090	2001 NGH	mineralized footwall	slice	Y	-	-
01BT092	2001 NGH	quartz-tennantite footwall vein	sml sample & slice	-	-	-
01BT094	2001 NGH	mineralized footwall	small sample	-	-	-
01BT095	2001 NGH	altered, unmineralized footwall	small slice	-	-	Y
01BT098	2001 NGH	mineralized footwall	small sample	-	-	Y
01BT099	2001 NGH	mineralized footwall	small sample	-	-	-
01BT103	2001 NGH	mineralized footwall with barite vein	small sample	-	-	-
01BT105	2001 NGH	quartz-tennantite footwall vein	small sample	-	-	-
01BT106	2001 NGH	mineralized footwall with barite vein	slices x2	-	-	-
01BT107	2001 NGH	mineralized footwall	slice	-	-	-
01BT110	2001 NGH	mineralized footwall	slices x2	-	-	Y(a,b)
01BT111	2001 NGH	mineralized footwall	slices x2, chp sep	-	Y (a)	Y (a)
01BT113	2001 NGH	mineralized footwall with barite vein	small sample	-	-	-
01BT118	2001 NGH	footwall coarse chlorite	small sample	-	-	-
01BT119	2001 NGH	"Eastern" hanging-wall volcanics	large sample	-	-	Y
01BT120	2001 NGH	"Eastern" hanging-wall volcanics	large sample	-	-	Y
01BT125	2001 NGH	mineralized, sheared footwall	slice	-	-	Y
01BT127	2001 NGH	mineralized, sheared footwall	slices x2, gal sep	Y	-	-
01BT128	2001 NGH	mineralized, sheared footwall	slices x2	Y	-	Y (a)

Table A1(i). Balta Tau sample list (contd.).

Sample No	Collected	Material	Hand specimen	Polished slice	Polished block	Polished thin section
01BT129	2001 NGH	quartz-tennantite footwall vein	sample, ten sep	-	-	-
01BT130	2001 NGH	quartz-tennantite footwall vein	qtz chips, ten sep	-	-	-
01BT135	2001 NGH	barite-rich massive sulphides	slices x3	-	-	Y(a,b)
01BT136	2001 NGH	barite-rich massive sulphides	slices x2	Y	Y (a)	Y (b)
01BT138	2001 NGH	barite-rich massive sulphides	slice	-	-	Y
01BT142	2001 NGH	mineralization from fw sheared matrix	small samples	-	-	Y
01BT143	2001 NGH	mineralized footwall	slice	Y	-	-
01BT145	2001 NGH	mineralized footwall with barite vein	small sample	-	-	Y
01BT147	2001 NGH	altered, unmineralized footwall	small sample	-	-	-
01BT150	2001 NGH	mineralized footwall	small slices x2	-	-	-
01BT151	2001 NGH	mineralized footwall	small sample		-	Y
01BT152	2001 NGH	mineralized footwall	chp sep	-	-	-
01BT157	2001 NGH	mineralized footwall	sample & slice	-	Y	-
01BT158	2001 NGH	quartz-tennantite footwall vein	sample, ten sep	-	-	-
01BT160	2001 NGH	fine siliceous alteration in footwall	sample & slice	Y	-	-
01BT162	2001 NGH	mineralized footwall	small sample	-	-	Y
01BT166	2001 NGH	footwall chlorite schist from shear zone	small sample	-	-	-
01BT169	2001 NGH	sphalerite-rich massive sulphides	slice	-	-	-
01BT170	2001 NGH	barite-rich massive sulphides	small sample	-	-	Y
01BT171	2001 NGH	mineralization from shear-zone matrix	barite chips	-	-	-
01BT174	2001 NGH	quartz-?zeolite from hanging-wall vein	small sample	-	-	-
01BT175	2001 NGH	"Eastern" hanging-wall volcanics	small slice	-	-	Y
01BT178	2001 NGH	"Eastern" hanging-wall volcanics	small slice	-	-	Y
01BT179	2001 NGH	"Eastern" hanging-wall volcanics	small slice	-	-	Y
01BT180	2001 NGH	"Eastern" hanging-wall volcanics	large sample	-	-	Y
01BT183	2001 NGH	"Eastern" hanging-wall volcanics	small slice	-	-	Y
01BT186	2001 NGH	"Eastern" hanging-wall volcanics	small slice	-	-	Y
01BT187	2001 NGH	"Eastern" hanging-wall volcanics	small slice	-	-	Y
01BT188	2001 NGH	"Eastern" hanging-wall volcanics	large sample	-	-	Y
01BT189	2001 NGH	"Eastern" hanging-wall volcanics	small slice	-	-	Y
01BT190	2001 NGH	"Eastern" hanging-wall volcanics	small slice	-	-	Y
01BT191	2001 NGH	"Eastern" hanging-wall volcanics	large sample	-	-	Y
01BT192	2001 NGH	"Eastern" hanging-wall volcanics	small slice	-	-	Y
01BT194	2001 NGH	"Eastern" hanging-wall volcanics	small slice	-	-	Y
01BT196	2001 NGH	"Eastern" hanging-wall volcanics	small slice	-	-	Y
01BT199	2001 NGH	"Eastern" hanging-wall volcanics	small slice	-	-	Y
01BT200	2001 NGH	"Eastern" hanging-wall volcanics	small slice	-	-	Y
01BT202	2001 NGH	"Eastern" hanging-wall volcanics	small slice	-	-	Y
01BT203	2001 NGH	Hanging-wall volcaniclastics	small slice	-	-	Y
01BT204	2001 NGH	Hanging-wall volcaniclastics	small slice	-	-	Y
01BT207	2001 NGH	Hanging-wall volcaniclastics	large sample	-	-	Y
01BT208	2001 NGH	Hanging-wall volcaniclastics	small slice	-	-	Y
01BT209	2001 NGH	Hanging-wall volcaniclastics	small slice	-	-	Y
01BT210	2001 NGH	Hanging-wall volcaniclastics	small slice	-	-	Y
01BT211	2001 NGH	Hanging-wall volcaniclastics	small slice	-	-	Y
01BT215	2001 NGH	Hanging-wall volcaniclastics	small slice	-	-	Y
01BT216	2001 NGH	quartz-tennantite footwall vein	slice, ten-chp sep	-	-	
01BT217	2001 NGH	mineralized footwall	slice	-	-	Y
01BT218	2001 NGH	mineralized footwall	slice	-	-	-
01BT226	2001 NGH	gold-bearing barite lens	samples, slice	-	-	(a,b,c&d)
02BT02	2002 NGH	immediate hanging-wall volcanic breccia	large sample	Y	-	-
02BT04	2002 NGH	hanging-wall quartz-epidote vein	large sample	-	-	-
02BT09	2002 NGH	altered unmineralized footwall	large sample	Y	-	-
02BT13	2002 NGH	immediate hanging-wall volcanic breccia	large sample	Y	-	-
02BT19	2002 NGH	pyrite from "Eastern" volcanics	large py cubes	-	-	-

Table A1(i). Balta Tau sample list (contd.).

Sample No	Fluid inclusion wafer	Whole rock XRF & ICPMS	Sr isotopes	S isotopes	O isotopes
JC13062A	-	-	-	-	-
JC13062B	-	-	-	-	-
JC13062C	-	-	-	-	-
901	-	-	-	-	-
902	Y (ba)	-	-	Y (py)	-
903	Y (ba,sph)	-	Y (ba)	Y (py,ba)	Y (ba)
905	-	-	-	-	-
906	-	-	-	-	-
907	-	-	-	-	-
908	-	-	-	-	-
910	-	-	-	-	-
BTB01A	-	-	-	-	
BTB01B	-	-	-	-	
BTB01C	-	-	-	-	
BTB01D	-	-	-	-	-
BL1	-	-	-	-	-
BL1A	-	-	-	-	-
BL2	-	-	-	-	-
B2	-	-	-	-	-
B3	-	-	-	-	-
BL10.18A	-	-	-	-	-
BL10.19B	-	-	-	-	-
BL10.22B	-	-	-	-	-
BL711	-	-	-	-	-
BL711A	-	-	-	-	-
00BT01	-	Y	Y (wr)	-	Y (wr,qtz,chl)
00BT02	-	-	-	-	-
00BT08	Y (ba)	-	Y (ba)	-	Y (ba, qtz)
00BT09	-	-	-	-	-
00BT10	-	-	-	-	-
00BT12	Y (qtz)	-	-	-	-
00BT13	-	-	-	Y (gal)	-
00BT14	Y (qtz)	-	-	-	-
00BT15	-	-	-	-	-
00BT17	Y (qtz)	-	-	-	-
00BT18	-	-	-	-	-
00BT19	-	-	-	-	-
00BT20	-	-	-	-	-
00BT21	-	-	-	-	-
01BT001	-	-	-	-	-
01BT002	Y (qtz)	-	-	Y (ten)	Y (qtz)
01BT003	Y (sph, qtz)	-	-	Y (chp,sph)	Y (qtz)
01BT004	-	-	-	-	-
01BT005	-	-	-	Y (ten,sph)	Y (qtz)
01BT006	-	-	-	-	-
01BT006A	-	-	-	-	-
01BT007	Y (qtz)	-	-	Y (ten)	Y (qtz)
01BT008	-	-	-	-	-
01BT012	-	-	-	-	-
01BT013	-	-	-	-	-
01BT014	Y (sph)	-	-	Y (py)	Y (qtz,msc)
01BT017	Y (qtz)	-	-	Y (chp,ten)	Y (qtz)
01BT018	-	-	-	Y (sph)	-
01BT019	-	Y	-	-	Y (ser)

Table A1(ii). Balta Tau samples analytical summary.

Sample No	Fluid inclusion wafer	Whole rock XRF & ICPMS	Sr isotopes	S isotopes (conventional)	O isotopes
01BT021	-	Y	-	-	-
01BT022	-	-	-	-	-
01BT024	-	-	-	-	-
01BT026	-	-	-	-	-
01BT029	-	-	-	-	-
01BT031	-	-	-	-	-
01BT032	Y (sph)	-	-	Y (chp,sph)	Y (qtz)
01BT033	-	-	-	-	-
01BT039	-	-	-	-	-
01BT043	-	-	-	-	-
01BT045	-	Y	-	-	-
01BT047	-	-	-	Y (ba)	Y (qtz)
01BT051	-	-	-	-	-
01BT052	-	-	-	-	-
01BT054	-	-	-	-	-
01BT056	-	-	-	-	Y (qtz)
01BT058	Y (sph,qtz)	-	-	Y (chp,sph)	Y (qtz)
01BT061	-	-	-	-	-
01BT062	-	-	-	-	-
01BT064	-	-	-	-	-
01BT065	Y (sph)	-	-	-	-
01BT066	-	-	-	-	-
01BT067	-	-	Y (ba)	Y (ba)	Y (ba, qtz)
01BT068	-	-	-	Y (chp,ten,sph,ba)	Y (qtz)
01BT069	Y (sph,qtz)	-	-	-	Y (qtz)
01BT070	-	-	-	-	-
01BT071	-	-	-	-	Y (qtz,msc)
01BT072	-	-	-	Y (ten,py)	-
01BT073	Y (sph)	-	-	Y (ten,sph)	Y (qtz)
01BT075	-	-	-	-	-
01BT075A	-	Y	-	-	-
01BT076	Y (sph)	-	-	-	-
01BT077	-	-	Y (ba)	Y (ba)	Y (ba)
01BT078	-	-	-	-	-
01BT082	Y (ba,sph)	-	Y (ba)	Y (chp,ten,sph,py,ba)	Y (ba, qtz)
01BT085	-	Y	-	-	-
01BT090	-	-	-	-	-
01BT092	-	-	-	-	-
01BT094	-	-	-	-	-
01BT095	-	-	Y (wr)	-	Y (wr)
01BT098	-	-	-	-	-
01BT099	-	-	-	-	-
01BT103	-	-	Y (ba)	Y (ba)	Y (ba)
01BT105	Y (qtz)	-	-	-	-
01BT106	-	-	Y (ba)	Y (ba)	Y (ba)
01BT107	-	-	-	-	-
01BT110	-	-	Y (wr)	Y (chp)	Y (wr)
01BT111	-	-	-	-	-
01BT113	-	-	-	-	-
01BT118	-	-	-	-	Y (chl)
01BT119	-	Y	-	-	-
01BT120	-	-	-	-	-
01BT125	-	-	-	-	-
01BT127	-	-	-	Y (gal,py)	Y (qtz)
01BT128	-	-	-	-	-

Table A1(ii). Balta Tau samples analytical summary (contd.).

Sample No	Fluid inclusion wafer	Whole rock XRF & ICPMS	Sr isotopes	S isotopes (conventional)	O isotopes
01BT129	-	-	-	-	-
01BT130	-	-	-	Y (ten,chp,sph,gal)	Y (qtz)
01BT135	Y (sph)	-	Y (ba)	Y (ba)	Y (ba)
01BT136	-	-	-	Y (sph,py)	-
01BT138	-	-	Y (ba)	Y (ba)	Y (ba)
01BT142	-	-	-	Y (gal)	-
01BT143	-	-	-	-	-
01BT145	Y (ba)	-	Y (ba)	Y (ba)	Y (ba, qtz)
01BT147	-	-	-	-	-
01BT150	-	-	-	-	-
01BT151	-	-	-	-	-
01BT152	-	-	-	Y (chp,py)	-
01BT157	Y (sph,qtz)	-	-	Y (ten,sph)	Y (qtz)
01BT158	Y (qtz)	-	-	Y (ten)	Y (qtz)
01BT160	-	-	-	-	-
01BT162	-	-	-	-	-
01BT166	-	-	-	-	-
01BT169	-	-	Y (ba)	Y (sph,ba)	Y (ba)
01BT170	-	-	-	-	-
01BT171	-	-	-	Y (py,ba)	-
01BT174	-	-	-	-	-
01BT175	-	-	-	-	-
01BT178	-	-	-	-	-
01BT179	-	-	-	-	-
01BT180	-	-	-	-	-
01BT183	-	-	-	-	-
01BT186	-	-	-	-	-
01BT187	-	-	-	-	-
01BT188	-	Y	-	-	-
01BT189	-	-	-	-	-
01BT190	-	-	-	-	-
01BT191	-	Y	-	-	-
01BT192	-	-	-	-	-
01BT194	-	-	-	-	-
01BT196	-	-	-	-	-
01BT199	-	-	-	-	-
01BT200	-	-	-	-	-
01BT202	-	-	-	-	-
01BT203	-	-	-	-	-
01BT204	-	-	-	-	-
01BT207	-	-	-	-	-
01BT208	-	-	-	-	-
01BT209	-	-	-	-	-
01BT210	-	-	-	-	-
01BT211	-	-	-	-	-
01BT215	-	-	-	-	-
01BT216	-	-	-	Y (ten)	-
01BT217	-	-	-	-	-
01BT218	-	-	-	-	-
01BT226	Y (ba)	-	Y (ba)	Y (ten,gal,chp,ba)	Y (ba)
02BT02		-	-	-	-
02BT04	-	-	-	-	Y (qtz,ep)
02BT09		-	-	-	-
02BT13		-	-	-	-
02BT19	-	-	-	Y (py)	-

Table A1(ii). Balta Tau samples analytical summary (contd.).

Sample No	Collected	Material	Hand specimen	Polished slice	Polished block	Polished thin section
010813/14	2001 NGH	Barite-sulphides from Ulaly	small slice		-	Y
010819/01	2001 NGH	Irendyk	large sample		-	Y
010819/02	2001 NGH	Irendyk	large sample		-	Y
010819/11	2001 NGH	Irendyk			-	
010819/13	2001 NGH	Irendyk			-	
010819/16	2001 NGH	Irendyk	large sample		-	Y
010820/02	2001 NGH	Irendyk			-	
010820/03	2001 NGH	Irendyk	large sample		-	Y
010820/04	2001 NGH	Irendyk			-	
010820/07	2001 NGH	Irendyk			-	
010820/08	2001 NGH	Irendyk			-	
010820/09	2001 NGH	Irendyk			-	
010820/11	2001 NGH	Ulutau	large sample		-	Y
010820/12	2001 NGH	Ulutau	slice	Y	-	
010820/13	2001 NGH	Irendyk			-	
010824/01	2001 NGH	Irendyk	small slice		-	Y
010824/04	2001 NGH	Irendyk	large sample		-	Y
010824/05	2001 NGH	Ulutau			-	
010824/06	2001 NGH	Ulutau			-	
010824/07	2001 NGH	Baimak-Buribai	slice	Y	-	-
010824/09	2001 NGH	Baimak-Buribai	small slice		-	Y
010824/11	2001 NGH	Baimak-Buribai	large sample		-	Y
010824/12	2001 NGH	Baimak-Buribai	slice	Y	-	-
010824/14	2001 NGH	Baimak-Buribai	large sample	Y	-	Y
010824/15	2001 NGH	Bogachevsky granite			-	
010824/16	2001 NGH	Bogachevsky granite	large sample		-	Y
010824/16A	2001 NGH	Bogachevsky granite			-	
010824/17	2001 NGH	Irendyk			-	
010824/18	2001 NGH	Irendyk			-	
010824/19	2001 NGH	Irendyk			-	
010824/20	2001 NGH	Irendyk			-	
010825/02	2001 NGH	Baimak-Buribai	large sample	Y	-	Y
010825/04	2001 NGH	Baimak-Buribai	large sample		-	Y
010825/05	2001 NGH	Baimak-Buribai	large sample		-	Y
010825/09	2001 NGH	Baimak-Buribai	large sample		-	Y
010825/13	2001 NGH	Baimak-Buribai	slice		-	Y
010825/17	2001 NGH	Irendyk			-	
010825/18	2001 NGH	Irendyk	large sample		-	Y
010825/19	2001 NGH	Irendyk	small slice		-	Y
010826/04	2001 NGH	Irendyk			-	
010826/06	2001 NGH	Baimak-Buribai	large sample		-	Y
010826/07	2001 NGH	Baimak-Buribai	small slice		-	Y
010826/08	2001 NGH	Baimak-Buribai	large sample		-	Y
010826/09	2001 NGH	Irendyk			-	
0/0826/10	2001 NGH	Irendyk	large sample		-	Y
010826/14	2001 NGH	Irendyk	slice	Y	-	-
010826/16	2001 NGH	Ulutau	large sample		-	Y
010826/18	2001 NGH	Irendyk			-	
010826/19	2001 NGH	Irendyk volcaniclastics	slice		-	
010826/19A	2001 NGH	Irendyk volcaniclastics	small sample		-	Y
010826/20	2001 NGH	Irendyk volcaniclastics	small slice		-	Y
010827/01	2001 NGH	Mineralization, local deposit Semnovsky	sample, ten-ba sep	-	-	-
010827/02	2001 NGH	Irendyk			-	
010827/03	2001 NGH	Irendyk			-	
010827/05	2001 NGH	Irendyk			-	

Table A1(iii). Regional sample list.

Sample No	Collected	Material	Hand specimen	Polished slice	Polished block	Polished thin section
010827/08	2001 NGH	Irendyk	small slice		-	Y
010723/09	2001 NGH	Baimak-Buribai - chert, Aktau	large sample		-	Y
010723/10	2001 NGH	Baimak-Buribai	large sample		-	Y
010723/11	2001 NGH	Irendyk	large sample		-	Y
010723/12	2001 NGH	Irendyk	large sample	Y	-	Y
010724/04	2001 NGH	Basal Ulutau	large sample	Y	-	-
020816/10	2002 NGH	Irendyk	large sample	-	-	-
020816/11	2002 NGH	Irendyk	small sample	-	-	-

Table A1(iii). Regional sample list (contd.).

Sample No	Fluid inclusion wafer	Whole rock XRF & ICPMS	Sr isotopes	S isotopes (conventional)	O isotopes
010813/14	Y (ba)	-	Y (ba)	Y (ba)	Y (ba)
010819/01	-	Y	-	-	-
010819/02	-	-	-	-	-
010819/11	-	-	-	-	-
010819/13	-	-	-	-	-
010819/16	-	Y	-	-	-
010820/02	-	-	-	-	-
010820/03	-	Y	-	-	-
010820/04	-	-	-	-	-
010820/07	-	-	-	-	-
010820/08	-	-	-	-	-
010820/09	-	-	-	-	-
010820/11	-	Y	-	-	-
010820/12	-	-	-	-	-
010820/13	-	-	-	-	-
010824/01	-	-	-	-	-
010824/04	-	Y	-	-	-
010824/05	-	-	-	-	-
010824/06	-	-	-	-	-
010824/07	-	-	-	-	-
010824/09	-	-	-	-	-
010824/11	-	Y	-	-	-
010824/12	-	-	-	-	-
010824/14	-	-	-	-	-
010824/15	-	-	-	-	-
010824/16	-	Y	-	-	-
010824/16A	-	-	-	-	-
010824/17	-	-	-	-	-
010824/18	-	-	-	-	-
010824/19	-	-	-	-	-
010824/20	-	-	-	-	-
010825/02	-	Y	-	-	-
010825/04	-	Y	-	-	-
010825/05	-	-	-	-	-
010825/09	-	Y	-	-	-
010825/13	-	-	-	-	-
010825/17	-	-	-	-	-
010825/18	-	Y	-	-	-
010825/19	-	-	-	-	-
010826/04	-	-	-	-	-

Table A1(vi). Regional samples analytical summary.

Sample No	Fluid inclusion wafer	Whole rock XRF & ICPMS	Sr isotopes	S isotopes (conventional)	O isotopes
010826/06	-	Y	-	-	-
010826/07	-	-	-	-	-
010826/08	-	Y	-	-	-
010826/09	-	-	-	-	-
0/0826/10	-	Y	-	-	-
010826/14	-	-	-	-	-
010826/16	-	Y	-	-	-
010826/18	-	-	-	-	-
010826/19	-	-	-	-	-
010826/19A	-	-	-	-	-
010826/20	-	-	-	-	-
010827/01	Y (qtz)	-	Y (ba)	Y (ten,chp,ba)	Y (ba)
010827/02	-	-	-	-	-
010827/03	-	-	-	-	-
010827/05	-	-	-	-	-
010827/08	-	-	-	-	-
010723/09	-	Y	-	-	-
010723/10	-	Y	-	-	-
010723/11	-	Y	-	-	-
010723/12	-	Y	Y (pyx)	-	Y (pyx)
010724/04	-	Y	-	-	-
020816/10	-	-	Y (pyx)	-	Y (pyx)
020816/11	-	-	Y (pyx)	-	Y (pyx)

Table A1(vi). Regional samples analytical summary (contd.).

APPENDIX A2 : LITHOLOGICAL DESCRIPTIONS

Descriptions of key samples (in particular those used for whole rock geochemistry (and those used in illustrations) based on exposures, hand specimens and polished thin sections.

Abbreviations: plag – plagioclase; fspr – feldspar; alkfspr – alkali feldspar; pyx – pyroxene; qtz quartz; ser – sericite; act – actinolite; pmp – pumpellyite; chl – chlorite; ep – epidote; prn – prehnite; zl – zeolite; tn – titanite; ilm – ilmentite; hm – hematite; cb – carbonate; ba – barite; rtl – rutile; mgn – magnetite; Feox – undifferentiated iron oxides; xl – crystal; v. – very; gr – grained; anh – anhedral; subh – subhedral; euh – euhedral; HS – hand specimen; PTS – polished thin section; WRG – sample used for whole rock geochemistry.

Sample	Lithology & Formation	Description	Alteration
010819/01 HS & PTS WRG	Plag- ?pyx-phyric coarse intermediate breccia Irendyk	Exposure: Bright to dark green, porphyritic, angular cm/10's cm sized angular clasts (monomict) enclosed in paler, brighter green matrix. HS taken from a single clast: Phenocrysts: completely altered; 20% plag 0.1-1mm; 5% ?pyx 0.5-3mm. Matrix: v. fine gr., dark brown, semi-opaque.	Intense. Ser/ser-ep replacing plag; qtz-ep-chl replacing ?pyx. Minor act-pmp.
010819/16 HS & PTS WRG	xl-rich massive volcaniclastic Irendyk	Moderate to dark green with a mottled appearance in HS, no bedding visible. Phenocrysts: 25% plag – mostly complete euh xls; partially altered. 2% qtz rounded/irregular/embayed, 0.2-1mm. Lithic clasts – scarce plag-phyric angular mm sized clasts. Matrix: v. fine gr dark brown, semi-opaque, relict fspr lath texture.	Weak to moderate. Ser +/- chl-ep-act-Feox replacing fspr.
010723/12 HS & PTS WRG	Plag-pyx-phyric amygdoidal intermediate lava Irendyk	Pale green massive lava. Phenocrysts: 15% Plag – fresh to weakly altd, lamellae twinning, 0.2-2mm. 5% pyx (CPX) – 0.5-3mm euh twinned xls, concentric zoning; fresh to partial altn; glomeroporphyritic. Amygdales: 5%, spherical, 0.1-1mm. Groundmass: v fine gr, semi-opaque, some relict plag laths <50µm.	Weak. Chl partially replacing pyx; ser partially replacing plag. Qtz+/- pmp amygdales.
010820/03 HS & PTS WRG	Plag-pyx-phyric intermediate lava Irendyk	Dark green massive lava. Phenocrysts: 30% plag, altered but relict lamellae twinning and concentric zoning, 0.2-2mm. 5% pyx – completely altd but euh morphologies preserved, 0.5-1mm. Groundmass: brown, semi-opaque, v fine gr with mottled texture, partially altered.	Intense. Ser replacing feldspar; chl replacing ?fspr; qtz-act replacing pyx; cubic morphologies preserved by Feox. Chl-ser in groundmass
010723/11 HS & PTS WRG	Plag-pyx-qtz-phyric intermediate volcanic breccia Irendyk	Exposure: coarse (10's cm sized) angular porphyritic clasts (monomict?) enclosed in a fine grained matrix. Hs taken from a single greyish green clast: Phenocrysts: 5% plag – euh morphologies preserved, 0.2-1mm. 3% pyx – euh 0.5-2mm, fractured, moderately altered. 2% Qtz – v. rounded, embayed, 0.2-2mm. Groundmass: altd, some relict fspr-lath like texture preserved.	Weak to moderate. Ser altn of plag, chl-Feox altn of pyx (weathering not hydrothermal?), act-ep in groundmass and thin qtz-ep vein.

Sample	Lithology & Formation	Description	Alteration
010825/18 HS & PTS WRG	Plag-pyx-phyric, amygdoidal intermediate lava. Irendyk	Quite pale greyish-green massive lava. Phenocrysts: 20% plag – 0.3-2mm euh, lamellae twinning abundant, mod/intensely altd. 2% pyx – intense altn, euh morphologies preserved 0.5-2mm. Amygdales: 10%, sphaerical to weakly elongated, some irregular, 0.2-2mm. Groundmass: fine laths of fspr define weak trachytic texture within cryptoxlline glassy brown matrix.	Moderate. Ser altn of plag; chl-ep-qtz-act replacement of pyx; ep(qtz-zl) amygdales
010826/10 HS & PTS WRG	Coarse, fspr-phyric, intermediate volcanic breccia Irendyk	Dark green, monomict, porphyritic angular cm sized clasts, slight colour difference due to variable altn distinguishes clasts from matrix of the same composition. Matrix supported. Clasts and matrix on average comprise: Phenocrysts: 25% fspr– 0.2-2mm, partially altd, many simple twins, some lamella twinning, blocky euh morphologies. ?amygdales: 2% irregular shaped voids lined with radiating act and filled with cgr subh qtz. Groundmass: variable between and within clasts; some semi-opaque dk brown cryptopxlline; some has weakly preserved trachytic texture with fspr laths, some completely altd.	Moderate. Ser altn of fspr; scarce chl-(act-ep) replacement of ?fspr. Matrix variably altd to chl-act, act-qtz, with patchy fine gr hm. Some irregular cavities lined with qtz-act, porosity due to altn not vesicles(?).
010824/04 HS & PTS WRG	Plag-(?pyx-) phyric intermediate coarse volcanic breccia Irendyk	Exposure: several large (10's cm sized) porphyritic sub-rounded clasts (monomict) enclosed in fine matrix with foliation wrapping around clasts. Matrix supported. HS taken from a single, large, massive pale green clast: Phenocrysts: completely altd. Total 35%, of which at least 20% plag; 5-15% pyx? Euh morphologies preserved, 0.5-2mm. Groundmass: Highly altd, texture preserved - randomly orientated feldspar laths 200 µm long.	Very intense. Ser-chl-act and chl-pmp altn of fspr; chl-ep, ep-qtz, ep-cb altn of ?pyx (?fspr). Groundmass altd to pmp-chl-ser-tn-Feox.
010723/10 HS & PTS WRG	Fine gr, xl-rich volcaniclastic. Irendyk	Pale greyish green with a weak foliation. Phenocrysts: 8% plag – 0.5-2mm xls, glomeroporphyritic, partially altd, relict lamellae twinning. 4% pyx – most completely altd, scarce relict pyx, euh morphologies preserved, 0.2-1mm. 1% qtz – 0.2-0.5mm, fractured/ fragmented with corroded xl margins. Matrix: v fine gr anh fspr with partial altn and weak foliation. Lens-like texture (mm scale) defined by wisps/bands of Feox, act, ep & chl	Weak to moderate. Ser altn of fspr; chl-ep replacing pyx. Act-chl(-ep-tn) in groundmass; elongated and aligned act defines foliation.
010826/14 HS	xl-rich volcaniclastic Irendyk Formation	Bright green coarse xl -rich volcaniclastic containing sparse dark green angular cm sized porphyritic clasts fragmented with jigsaw fit. Clasts have an outer rim of and fractures filled with epidote. Matrix is euhedral mainly whole mm sized altd feldspar xls.	Intense. Pervasive ep altn in matrix; ser-ep altn of fspr; chl altn if clasts.
010826/19 HS	Graded volcaniclastic Irendyk Formation	Pale to dark green volcaniclastic ranging from fine sandstone to cherty horizons, bedding on a mm to cm scale, some irregular and disrupted. Sparse xls vsible in coarse horizons – angular fragments of white fspr and dk green pyx. No primary qtz.	Moderate. Chl altn of coarser horizons.

Sample	Lithology & Formation	Description	Alteration
010826/20 HS, PTS	xl-rich volcaniclastic Irendyk	Dark green, HS collected from thick medium grained bed in graded bedded volcaniclastics Phenocrysts – 5% pyroxene, euhedral whole and fragmented xls <2mm; <1% feldspar fragments, <1mm. Lithic clasts – scarce <2%, 1-5mm, angular. Clasts v angular, poorly sorted, sparely scattered in v fine gr semi-opaque ashy matrix.	Weak. Chl(-ser) altn of f gr matrix.
010723/09 HS & PTS WRG	Fspr-phyric felsic lava Baimak-Buribai	Dark purple, massive lava. Phenocrysts: 5% fspr – 0.4-1mm, glomeroporphyritic, mainly simple twinning (alkfspr?), stubby morphologies, partial altn. Groundmass: highly altd, relict lath like texture with weak lineation/trachytic texture?	Moderate to intense. Ser-qtz altn of fspr; intense haem-qtz(-tn) altn of groundmass
010825/02 HS & PTS WRG	Massive fspr-phyric felsic/ intermediate lava. Baimak-Buribai	Dark green-grey, massive. Phenocrysts - glomeroporphyritic: 3% fspr; 1% 0.1-0.5 with lamellae twinning – plag?; 2% 0.5-1mm, simple twinning/untwined – alkfspr? Groundmass: v. f gr equant fspr (some qtz?), partially altered.	Weak. Partial altn of fspr to ser, or complete replacement by qtz-cb or ep-Feox-rtl. Weak partial altn of gmass to ser-tn
010826/08 HS & WRG	Massive fspr-phyric lava Baimak-Buribai	Greenish-grey, massive Highly feldspar-phyric – 10% white, blocky xls <2mm. v fine grained groundmass.	Moderate, sericite rich.
010824/11 HS & PTS WRG	Fspr-phyric felsic lava. Baimak-Buribai	Greenish grey, massive with irregular paler grey areas (mm scale) giving blotchy appearance. Phenocrysts: 8% fspr – mostly altd, untwinned, simple & lamellae preserved; 0.4-1mm. 1% - completely replaced euh morphologies 0.2-0.5mm, ?fspr/mafics. Groundmass: fine gr, equigranular, anh fspr ?and qtz, some elongate fspr laths, some altn.	Moderate/intense. Silicification of fspr and groundmass; some chl(-ep-Feox) altn of fspr. Chl-act replacement of ?fspr/mafics. Also act-Feox-tn.
010826/06 HS & PTS WRG	Plag- qtz-phyric felsic lava. Baimak-Buribai Formation	Variable dark purple to paler green blotchy colour, massive. Phenocrysts: 12% fspr – glomeroporphyritic, stubby xls, unusual ?simple twinning, some lamellae, concentric zoning, partially altd, some sub-rounded, 0.4-2mm. 3% qtz – mostly rounded, some euh squarish sections, 0.2-2mm (rounded xls tend to be smaller). 5% ?fspr/mafic – euh morphologies preserved but completely altd, 0.4-2mm. 2% ?ilm/mgn – cubic morphologies 50-200 µm, now altd to f gr oxides. Groundmass: randomly orientated fspr laths 30-50 µm, with interstitial anh fspr (and qtz?).	Weak. Partial ser(-chl) altn of fspr; chl replacing ?fspr/mafic phenos. Groundmass – much v fine gr hm altn and minor chl(-ep) – responsible for variable purple-green colour in HS.
010825/04 HS & PTS WRG	Fspr- qtz-phyric felsic lava. Baimak-Buribai Formation	Massive greenish grey lava. Phenocrysts: 10% fspr – 0.5-2mm, glomeroporphyritic. Mostly untwined, some simple and lamellae, concentric zoning; partial altn. 2%qtz – v rounded and fractured xls 1-3mm; rarer xls. ?mafic phenos completely altd, 3%, euh prismatic morphologies 0.2-0.5mm. Groundmass: fine fspr laths 20-50 µm, weakly trachytic, partially altd.	Moderate. Ser (-ep) partially replacing fspr; act-Feox(-tn) replacing ?pyx-amphb. Act-tn-Feox in groundmass.

Sample	Lithology & Formation	Description	Alteration
010825/05 HS	Fspr-phyric felsic lava Baimak-Buribai Formation	Massive, dark green. Phenocrysts: 5% ?mafic/fspr – small xls <1mm, dk grn. 1% fspr – blocky white xls 0.5-2mm. Groundmass – v f gr, no texture visible in hs.	Weak/moderate. Chl replacing ?mafic/fspr phenos.
010825/09 HS & PTS WRG	Fspr-phyric felsic-intermediate? lava. Baimak-Buribai Formation	Exposures: massive to columnar jointed lavas. HS: dark purple, massive. Phenocrysts: <1% fspr – scarce euh xls 0.2-0.5mm, most untwined, some simple twinning, partially altd, poorly defined corroded xl margins. Groundmass: v fine gr. Anh fspr, some relict cubic opaques.	Weak to moderate. Feox-(pmp) altn of fspr. Feox replacing cubic mafics.
010825/13 HS & PTS	Fspr-phyric, strongly amygdoidal felsic lava	Dark green, massive. Phenocrysts: 10% fspr – moderate altn, relict lamellae twinning visible; 2 size clusters, 0.2-0.4mm and 1-2mm, latter glomeroporphyritic, many xls fractured. <1% ?mafic – completely altd., 0.1-0.4mm euh morphologies preserved. 10% amygdales – spherical, 0.2-3mm. Matrix – moderately preserved fspr laths (50μm long), patchy weakly trachytic.	Moderate. Ser-pmp altn of fspr; chl altn of ?mafics; chl-Feox-tn-ser altn of matrix. Ep-chl-zl-prehnite-qtz amygdales.
010824/12 HS	Felsic volcanic breccia Baimak-Buribai Formation	Coarse angular polymict breccia with few mm to cm sized clasts displaying variable colour (pale grey to dark green), % phenocrysts (<1 to 10% fspr, ±mafics) and altn. One shows banding – relict flow banding? Clast supported, fine grained matrix.	Moderate to intense. Chl or qtz(?-ser) altn of clasts; ep in matrix.
010824/07 HS	Coarse felsic/intermediate volcanic breccia Irendyk	Dark green, angular, monomict, clast-supported breccia. Large cm sized clasts ser in matrix containing small mm sized clasts, some with jig-saw fit texture. Some clasts have well defined margins, others have gradational contact between clast and surrounding matrix. All clasts contain approx 15% fspr phenos, scarce ?mafics. Matrix is bright green, f gr.	Moderate. Chl altn of clasts, ep altn of matix.
010824/16 HS & PTS WRG	Plagioclase-rich granite Intruding Baimak-Buribai Formation	Massive, non-porphyritic but inequigranular. 60% Plag – euh xls -.2-2mm, partially altd, scarce lamellae twinning, most untwinned; weak concentric zoning. 35% Qtz - 0.5-1.5mm subh xls.	Weak. Ser replacing fspr; chl in distinct patches replacing mafic phase (biotite/amphibole? – 3%). Minor tn-ep-Feox.
010826/16 HS & PTS WRG	Fine grained, equigranular, xl-rich volcaniclastic Ulutau Formation	Exposure: fine volcaniclastics with bedding and some graded bedding on mm, cm and m scale. Hs from thick massive bed, no laminations or foliation, mottled greyish green. Phenocrysts: 20% fspr – 0.2-0.5mm angular xl fragments, evenly distributed, partially altd. 2% qtz – angular xl fragments 0.2-0.4mm. 2% porosity – 0.2mm irregular vugs, primary? Matrix – highly altd.	Moderate. Weak ser altn of fspr. Matrix has patchy silicification; fragments of ep xls; also fine gr patchy chl-pmp-Feox, tn, ilm and traces hm.
010820/11 HS & PTS WRG	xl-lithic-rich volcaniclastic Ulutau Formation	HS - Bright dark green, fine clastic texture. Clasts –phenocrysts 25% plag whole and fragmented, 0.2-1mm slight rounding, mostly altd, weak relict twinning; <1% qtz – rounded, 0.2-0.5mm, some fractured/fragmented. 20% Lithic clasts – poorly defined due to alteration. Matrix – v fine gr, completely altd, no primary texture.	Moderate to intense. Ser altn of plag; chl-act-ep altn of ?pyx (clasts?), with minor patchy qtz, hm, cb. Ser (-act-chl-Feox) altn of matrix.

Sample	Lithology & Formation	Description	Alteration
010724/04 HS & WRG	volcanic sandstone Ulutau Formation	Dark green fine to coarse volcanic sandstone with weak graded bedding on mm to cm scale. Angular fspr & qtz xl fragments up to 2mm in coarse horizons, well sorted	Weak to moderate. Chl(-ep).
02BT09 HS	Completely altd qtz- fspr-(?mafic)-phyric felsic volcanic. Balta Tau footwall	Pale greyish green, massive. Phenocrysts: 25% plag ?and mafics – darkish green, completely altd, euh morphologies v well preserved, 0.5-5mm. 1% qtz – squarish sections 1-5mm. Matrix/groundmass – completely altd, v f gr, no primary texture preserved.	Complete altn. Chl(-qtz-py) replacing fspr/?mafic phenocrysts. Qtz-chl(-ser?) altn of matrix/groundmass.
00BT01 HS & PTS WRG	Completely altd qtz-?fspr phyric ?volcaniclastic/ volcanic breccia. Balta Tau Footwall	Irregular dark green cm sized clasts enclosed in pale green/grey-green matrix with irregular white patchy silicification. Phenocrysts: 10%?fspr – completely altd, euhedral morphologies preserved, 0.5-2mm. 2%qtz – v. rounded, some fractured, 0.5-3mm. Matrix: Completely altd. Relict clastic texture? Sulphide mineralization minimal, <1%.	Very intense, complete alteration except for qtz phenocrysts. Predominately chl(50%)-qtz (35%)-py(10%) variably replacing phenocrysts, ?clasts and matrix.
01BT085 HS & PTS WRG	Completely altd qtz-?fspr phyric volcanic. Clastic? Balta Tau Footwall	Pale green, cm sized darker green areas may be relict clasts? Phenocrysts: 10% ?fspr – completely altd to chl, morphologies preserved, mostly 0.2-1mm; also larger morphologies 2-3mm, ?mafic phase, pyx? <1% qtz – squarish sections with slight rounding, fractured, embayed, 1-1.5mm. Matrix: completely altered, no primary texture preserved. No sulphide mineralization.	Very intense, complete alteration except for qtz phenocrysts. Predominately qtz (55%)-chl(40%)-py(4%)-rtl(1%). variably replacing phenocrysts and matrix.
01BT022 HS	Porphyritic, felsic volcanic. Balta Tau hanging-wall	Dark greenish-grey, weakly foliated. Mm sized dark green lenses/streaks parallel to foliation – stretched chloritized ? fspr (and mafic?) phenocrysts.	Intense. Chl replacement of ?phenocrysts; ser altn of groundmass.
01BT021 HS & PTS WRG	Fspr- qtz-phyric felsic volcanic Balta Tau sericitic Hanging-wall	Pale green, strongly foliated with alteration minerals (ser, Cr-mica, py) defining mm-cm lens-like areas. Phenocrysts: 20% fspr – completely altd., morphologies preserved but stretched parallel to foliation, 0.5-2mm xls. 1% qtz – fractured, fragmented and embayed, 0.2-2mm. Matrix: highly altd. Lens-like segregations of ser, v f gr felsic mosaic, Cr-mica and py on a mm to cm scale defines foliation.	Very Intense. Ser replacement of fspr. Ser-Cr mica (dark, bright green), Feox-py altn of groundmass/matrix.
01BT019 HS & PTS WRG	Fspr- qtz-phyric felsic volcanic Balta Tau sericitic hanging-wall	Pale green, strongly foliated, soft. Phenocrysts: 15% fspr – completely altd, preserved morphologies are stretched parallel to foliation, some -wispy/feathery, 0.5-1mm. 2% qtz – 0.5-3mm, squarish sections, fractured or fragmented, some embayed. Matrix: completely altd, irregular bands and lenses of altn minerals defines foliation.	Very intense. Ser altn of fspr. Ser-?ox (semi-opaque v f gr, grey-brown)- py altn of groundmass/ matrix w/ bright green spots of Cr-mica.

Sample	Lithology & Formation	Description	Alteration
01BT075a (and sample 908) HS & PTS WRG	Qtz-phyric ?volcaniclastic Balta Tau Hanging-wall	Pale greenish to yellowish, very strongly foliated, soft soapy feel. Phenocrysts: 2%qtz, some complete, most fractured/fragmented, embayed, 0.2-0.5mm. Matrix: lens-like outlines on a mm scale defined by variable alteration; relict volcaniclastic texture or alteration overprinting primary textures?	Complete alteration. 75% ser, 20% fgr qtz define lens-like shapes parallel to foliation in ser. Tn (5%) forms subh xls/aggs elongated perpendicular to main foliation. Also 2% py. Minor cgr zeolite
01BT039 HS	Graded volcaniclastic Balta Tau hanging-wall	Fine to coarse sandstone with graded bedding on a mm scale. Coarser areas are pale green, highly altered to coarse ep with minor chl. Finer horizons dk grn and chl rich. Scarce angular fspr xl fragments visible, no qtz.	Moderate to intense ep-chl.
01BT045 HS & PTS WRG	Coarse lithic-xl-rich volcaniclastic Balta Tau Hanging-wall	Lithic clasts, 75% – angular, irregular to cuspate, polymict, some fspr-phyric, mostly 1-5mm. Phenocrysts: 10% fspr – 0.2-2mm, highly altd, rarely fragmented. 2% ?pyx – completely altd, euh morphologies preserved 0.5-1mm. 10% ?glass shards – completely altd feathery to cuspate elongate outlines preserved, 0.3-1mm.	Intense. Ser-chl-act replacement of fspr; chl-ep replacement of ?pyx; pure chl replacement of ?glass shards. Act-tn-chl-Feox patchy altn of lithic clasts.
02BT13 HS	Qtz- fspr-phyric felsic lava Balta Tau hanging-wall	Massive, variable dark purple and dark green colour reflecting alteration. Phenocrysts: 25% fspr – 1-2mm xls, altd. 2% qtz – lg squarish sections 2-5mm.	Moderate. ?ser altn of fspr. Patchy f gr hm and chl altn of groundmass.
01BT188 HS & PTS WRG	Qtz- fspr-phyric volcanic breccia Balta Tau Eastern unit	Monomict breccia with angular jigsaw fit cm sized clasts. Clasts: Phenocrysts: 20% fspr – completely altd, 0.5-2mm morphologies well preserved. 3% qtz –some glomeroporphyritic. 0.2-1.5mm; sml xls v. rounded with corroded margins, lger ones squarish and hexagonal sections with slight rounding; many fractured and embayed. Clasts: Groundmass: v f gr felsic mosaic (fspr-qtz). Matrix between clasts: angular fragments of qtz phenocrysts enclosed in felty masses of chl-ser with hm and ep, some f gr felsic material same as clast groundmass.	Moderate to intense. Ser (-hm) and rarely chl-cb(-hm) replacing fspr phenocrysts; chl-ser in groundmass. Matrix between clasts chl-ser-hm(ep).
01BT119 HS & PTS WRG	Fine gr qtz-fspr- bearing volcaniclastic Balta Tau Eastern unit	Phenocrysts: 10% fspr – completely altd, poorly preserved morphologies. 1% qtz – mainly angular and fragmented, some whole xls, embayed, 0.2-1mm. Matrix: highly altd, fspr lath texture poorly preserved.	Intense. Chl-cb-ser altn of fspr. Ser-chl-cb-tn altn of matrix.
01BT191 HS & PTS WRG	Fspr- qtz-?pyx- phyric intermediate lava Balta Tau Eastern unit	Phenocrysts: 15% fspr – completely altd, well preserved blocky morphologies 0.5-2mm, glomeroporphyritic. 3% qtz – squarish euh sections, some rounded with corroded margins, some fractured. 5% ?pyx – completely altd, euh morphologies well preserved, 0.5-3mm. <1% cubic opaques ass w/ ?pyx, 0.2-0.5mm, ?ilm/mg. Groundmass: completely altd.	Intense. Ser±(ep-chl-tn-Feox) altn of fspr; chl-ep-tn altn of ?pyx; fspr-chl-ser-tn-Feox altn of groundmass.

APPENDIX A3 : XRF AND ICP-MS ANALYSES

Sample preparation

Whole Rock Powders

1. Approximately 0.2 - 0.3 kg sized sample selected. Weathered portions removed with diamond saw; then metal coatings from saw, ink and any other marks removed from surface with lapping grit; washed thoroughly and dried.
2. Crushed to <1cm chips inside thick polythene bags using an iron fly-press (cleaned with wire brush between each sample).
3. Approximately 75cm^3 of chips selected at random and ground to a fine (approx. 200 mesh size) powder using an iron TEMA. The TEMA pot was cleaned between samples by grinding clean sand, rinsing with water and drying.

XRF Pellets

1. 12 drops of 8% PVA solution (binding agent) added to 10-12g of rock powder in a plastic pot, and homogenized thoroughly by mixing with a stainless steel spatula.
2. Sample transferred to a clean aluminium container and pressed at 120kN for a few seconds to produce a pressed pellet.
3. Pellets left to dry in an oven at 35°C for 24 hours.

XRF Fusion Bead Preparation

1. Approximately 2g of rock powder weighed into a ceramic crucible and left to dry in an oven for 2 hours at 110°C.
2. Sample plus crucible accurately weighed and placed in a furnace at 1000°C for 4 hours to ignite and drive off volatiles.
3. Sample removed from furnace and left to cool before transferring to a dessicator, then reweighed to calculate Loss On Ignition (L.O.I)
4. 0.8g of ignited powder was added to 4g of Spectroflux 100B (80% lithium metaborate; 20% lithium tetraborate) in a platinum crucible.
5. Crucible placed in a furnace at 1205°C for approximately 10 minutes, stirred twice during that time.
6. The molten sample was poured into a pre-heated platinum casting mould and left to cool assisted by an air jet.
7. Once cool the bead was labelled and removed from the mould.
8. Platinum ware cleaned between samples using hot 20% HCl.

Sample dissolutions for ICP-MS

1. Approximately 50mg of rock powder accurately weighed into Teflon pots.
2. Added 10 drops purified water (milliQ) washing any powder around the edge of the pot into the bottom.
3. Added 20 drops conc. HNO_3 followed by 50 drops conc. HF, and left for 24 hours on a hot at 120°C plate with an air tight lids.
4. Lids removed and solutions dried down on hot plate.
5. Added 1ml 6M HCl, placed on hot plate with the lids on for 1 hour. Minor solid remaining in most samples. Dried down again.
6. Added 2ml conc. HNO_3, left for 12 hours at 120°C. Samples left to cool; now completely transparent with no residue.
7. 1ml sub-sample taken for ICP-MS; dried down and made up in 10ml 2% HNO_3 with a 10ppb Re and In spike for internal drift correction.

ICP-MS calibration and corrections

The following corrections were applied to raw counts per second (CPS) data:

- Drift correction: Internal correction using In-Re spike applied to REE, Hf and Ta (i.e. elements with mass number between In and Re); all other elements corrected using external drift monitor.
- Interference correction for oxide-element overlaps:

oxide	element to be corrected	oxide	element to be corrected
135BaO	151Eu	147SmO	166Er
140CeOH	157Gd	149SmO	165Ho
141PrO	157Gd	151EuO	166Er
143NdO	159Tb	153EuO	169Tm
146NdOH	162Dy	158GdO	172Yb
148NdOH	165Ho	159TbO	175Lu

Table A3(i). Element overlap corrections for ICP-MS data.

- Samples calibrated using linear regression equations (R^2 values >0.990) for calibration curves constructed using three standards.

XRF and ICP-MS Detection Limits

Detection limits are given in Table A3(ii).

- For ICP-MS, these have been calculated using the CPS from blanks analysed in the same run as the samples, using:

  D.L. = Blank(ppb) + 10*SD blank

- For XRF, detection limits are those quoted by Croudace calculated using:

  D. L. = 3m $\sqrt{}$(Rb/Tb)

  where: m = slope factor concentration units/counts per second

  Rb = background count rate

  Tb = background counting time

XRF beads (%)	
SiO_2	0.05
TiO_2	0.05
Al_2O_3	0.05
Fe_2O_3	0.05
MnO	0.05
MgO	0.05
CaO	0.05
K_2O	0.05
Na_2O	0.05
P_2O_5	0.05

XRF pellets (ppm)	
La	5
Nb	2
Ni	2
Pb	2
Rb	2
Sc	7
Sr	2
Y	2
Zn	2
Zr	2
Ba	6
Co	2
V	5
Cr	5
Cu	2

ICP-MS (ppb) (3*STD)	
Rb	0.126
Sr	0.166
Y	0.014
Zr	0.320
Nb	0.008
Cs	0.019
Ba	0.304
La	0.017
Ce	0.006
Pr	0.004
Nd	0.016
Sm	0.014
Eu	0.007
Gd	0.015
Tb	0.003
Dy	0.014
Ho	0.003
Er	0.009
Tm	0.002
Yb	0.019
Lu	0.004
Hf	0.014
Ta	0.013
Pb	0.102
Th	0.010
U	0.018

Table A3(ii). XRF and ICP-MS detection limits

Standards

Data for international andesite and basalt standards that were analysed at the same time as the samples collected in this study are presented in tables A3(iii) and A3(iv) for XRF and ICP-MS respectively. The recommended values for standards, and the difference between measured and recommended values as a percentage of the recommended value are also given.

	JA-1 andesite			BCR1 basalt			BE-N basalt		
	R	M	% diff	R	M	% diff	R	M	% diff
SiO_2	64.06	64.25	0.3						
TiO_2	0.87	0.83	4.9						
Al_2O_3	14.98	15.24	1.7						
Fe_2O_3	6.50	6.89	6.0						
MnO	0.15	0.14	6.1						
MgO	1.61	1.56	3.1						
CaO	5.68	5.69	0.3						
K_2O	0.78	0.79	0.9						
Na_2O	3.86	3.92	1.5						
P_2O_5	0.16	0.16	0.4						
As	3	2	28.1	1	0	38.5	2	1	22.2
Ba	307	280	8.9	681	658	3.4	1025	1015	0.9
Co	12	10	17.8	37	35	5.7	60	62	3.5
Cr	7	8	6.8	16	5	66.9	360	363	0.7
Cu	42	40	4.5	19	23	20.5	72	73	0.6
La	5	5	9.8	25	29	14.9	82	86	4.4
Nb	2	2	0.0	14	12	12.1	105	110	4.7
Ni	2	5	150.0	13	17	33.1	267	273	2.1
Pb	6	8	44.8	14	17	22.1	4	8	100
Rb	12	11	9.3	47	47	0.0	47	49	4.9
Sc	28	29	1.8	33	30	6.7	22	21	3.6
Sr	266	254	4.6	330	328	0.6	1370	1376	0.4
V	105	113	7.2	407	403	1.0	235	228	3.1
Y	31	29	6.5	38	36	4.7	30	28	5.3
Zn	91	86	5.6	129	123	4.6	120	124	3.0
Zr	88	88	0.1	190	186	2.3	260	267	2.5

Table A3(iii). Standards analysed by XRF (major elements on beads, reported as oxide weight%;, trace elements on pellets, reported as ppm). (R – recommended value; M – measured value).

	JB2 andesite			JA2 andesite			JB1A basalt		
	R	M	% diff	R	M	% diff	R	M	% diff
Rb	6.2	6.5	4.4	72.9	73.2	0.5	41.0	39.6	3.4
Sr	178.0	181.1	1.7	248.0	243.0	2.0	443.0	444.6	0.4
Y	26.0	26.9	3.3	18.3	17.2	6.3	25.0	23.7	5.0
Zr	52.0	48.7	6.3	116.0	118.8	2.5	144.0	139.7	3.0
Nb	0.6	0.4	28.8	9.5	8.2	13.5	27.0	26.9	0.4
Cs	0.9	1.0	7.3	4.6	4.7	1.1	1.2	1.5	23.5
La	2.3	2.0	13.7	15.8	14.7	6.8	36.5	36.5	0.1
Ce	6.9	5.8	16.6	32.7	31.4	4.0	65.5	65.2	0.5
Pr	1.1	1.0	7.0	3.8	3.4	11.9	6.7	6.7	1.1
Nd	6.4	6.1	4.0	13.9	13.5	2.8	25.5	25.5	0.0
Sm	2.2	2.2	0.7	3.1	3.0	4.8	4.9	5.0	0.9
Eu	0.8	0.8	0.5	0.9	0.9	6.7	1.4	1.5	1.1
Gd	3.2	3.0	6.2	3.1	2.8	8.5	4.3	4.4	3.0
Tb	0.6	0.5	9.1	0.4	0.4	4.6	0.6	0.6	2.1
Dy	3.9	3.8	2.0	2.8	2.8	0.6	4.0	4.0	1.8
Ho	0.9	0.9	1.2	0.5	0.6	15.6	0.8	0.8	0.3
Er	2.5	2.4	3.6	1.5	1.6	7.7	2.2	2.3	4.9
Tm	0.4	0.4	1.3	0.3	0.2	19.6	0.3	0.3	1.1
Yb	2.5	2.5	0.3	1.6	1.6	4.1	2.0	2.0	1.7
Lu	0.4	0.4	0.2	0.3	0.2	9.7	0.3	0.3	2.7
Hf	1.4	1.6	11.5	2.9	2.9	0.1	3.4	3.5	2.1
Ta	0.1	0.1	60.9	0.8	0.8	5.3	2.0	2.0	1.9
Th	0.3	0.3	15.2	5.0	5.0	0.4	8.8	9.0	2.5
U	0.1	0.2	23.3	2.2	2.2	0.6	1.6	1.6	1.4

Table A3(iv). Standards analysed by ICP-MS (all data in ppm; R – recommended value; M – measured value).

Sample repeats

Repeat analyses of samples from this study are given in tables A3(v) and A3(vi) for XRF beads and XRF pellets respectively.

	010820/11		01BT021	
	#1	#2	#1	#2
SiO_2	66.27	66.22	69.81	70.02
TiO_2	0.36	0.35	0.37	0.37
Al_2O_3	14.87	14.91	17.38	17.59
Fe_2O_3	5.31	5.33	3.37	3.38
MnO	0.05	0.05	0.08	0.08
MgO	2.17	2.19	2.44	2.41
CaO	5.82	5.81	0.76	0.76
K_2O	0.64	0.66	2.98	2.98
Na_2O	3.85	3.85	2.74	2.75
P_2O_5	0.07	0.07	0.05	0.05
Sum	99.41	99.44	99.99	100.39

Table A3(v). Sample repeats for XRF bead analyses (all data in oxide weight%).

	010824/11		010824/16		010825/18	
	#1	#2	#1	#2	#1	#2
Ba	7912.9	7555.1	165.5	144.9	132.6	127.7
Co	5.7	4.7	9.0	7.6	18.0	20.8
Cr	11.2	18.4	17.8	25.3	58.9	57.0
Cu	2.9	4.3	6.0	5.5	284.0	219.1
La	5.6	3.5	5.5	3.0	2.4	1.1
Nb	2.6	2.4	2.2	1.9	0.6	0.5
Ni	-0.6	1.1	-0.6	0.3	13.6	14.1
Pb	0.8	1.9	2.8	4.4	4.4	5.8
Rb	9.6	9.3	4.3	3.8	4.9	3.7
Sc	14.1	15.3	10.4	9.6	35.7	36.5
Sr	189.4	188.5	189.2	192.0	167.7	167.0
V	23.3	25.3	52.2	52.1	257.8	229.5
Y	18.7	17.3	11.1	9.4	8.9	7.5
Zn	48.9	46.0	27.0	21.5	64.3	62.0
Zr	97.7	100.0	84.6	86.6	23.8	25.1

Table A3(vi). Sample repeats for XRF pellet analyses (data in ppm).

Data Listings

Data for XRF beads, XRF pellets and ICP-MS are listed in tables A3(vii), A3(viii) and A3(ix) respectively.

Sample	00BT01	010723/09	010723/10	010723/11	010723/12	010724/04	010819/01	010819/16
SiO_2	68.50	68.12	64.46	51.46	64.61	60.74	61.18	64.26
TiO_2	0.27	0.22	0.30	0.34	0.29	0.57	0.35	0.39
Al_2O_3	13.35	16.75	14.33	18.51	13.02	17.67	16.03	15.32
Fe_2O_3	3.08	2.08	5.44	7.44	5.74	6.77	4.56	5.98
MnO	bd	0.06	0.11	0.13	0.11	0.08	0.06	0.06
MgO	12.84	0.46	4.08	3.78	3.70	2.38	1.82	1.99
CaO	0.05	0.43	3.15	13.76	7.08	2.96	7.27	4.80
K_2O	bd	0.06	0.91	0.12	0.22	0.19	0.23	1.11
Na_2O	0.09	9.92	4.31	1.21	3.15	7.95	4.12	4.21
P_2O_5	0.08	0.06	0.05	0.06	bd	0.08	0.07	0.14
L.O.I.	1.22	0.79	2.28	2.75	1.93	0.14	3.78	1.89
Sum	99.48	98.96	99.41	99.58	99.85	99.52	99.47	100.16

Sample	010820/03	010820/11	010824/04	010824/11	010824/16	010825/02	010825/04	010825/09
SiO_2	57.88	67.71	62.35	70.28	71.43	74.79	68.07	77.07
TiO_2	0.57	0.36	0.35	0.37	0.30	0.29	0.26	0.20
Al_2O_3	16.94	16.86	15.80	12.80	13.85	13.32	12.83	11.40
Fe_2O_3	8.39	3.27	4.57	3.47	3.41	2.64	2.95	2.35
MnO	0.10	0.07	0.07	0.08	bd	bd	bd	bd
MgO	3.24	2.37	2.94	2.52	2.03	0.59	0.89	0.31
CaO	3.37	0.74	5.82	0.50	1.66	1.01	1.80	1.73
K_2O	0.63	2.89	1.06	0.92	0.44	0.51	3.23	0.54
Na_2O	6.24	2.66	3.81	4.86	4.53	6.22	3.93	5.17
P_2O_5	0.16	0.05	0.06	0.12	0.08	0.08	0.08	bd
L.O.I.	2.62	3.00	2.83	3.99	1.77	1.15	4.13	1.04
Sum	100.15	99.99	99.66	99.91	99.50	100.57	98.17	99.81

Sample	010825/18	010826/06	010826/08	010826/10	010826/16	01BT019	01BT021	01BT045
SiO_2	61.49	68.40	63.50	57.46	57.52	50.83	63.49	43.71
TiO_2	0.30	0.31	0.42	0.49	0.44	0.50	0.34	0.39
Al_2O_3	14.54	12.97	14.33	16.17	16.89	23.18	14.29	20.03
Fe_2O_3	7.21	3.26	6.38	7.86	5.87	7.81	5.11	10.21
MnO	0.14	bd	0.08	0.12	0.09	bd	0.05	0.14
MgO	4.00	1.75	3.44	2.83	2.73	3.43	2.10	9.00
CaO	5.49	1.16	3.39	6.02	7.38	0.08	5.57	8.70
K_2O	0.43	0.26	1.44	0.83	1.03	5.30	0.63	0.25
Na_2O	3.70	5.44	2.78	4.56	3.30	0.61	3.69	0.95
P_2O_5	bd	0.07	0.07	0.12	0.10	bd	0.07	bd
L.O.I.	2.46	6.14	3.13	3.28	4.40	7.98	4.13	6.57
Sum	99.77	99.77	98.96	99.74	99.75	99.71	99.47	99.94

Sample	01BT075A	01BT085	01BT119	01BT188	01BT191
SiO_2	61.55	74.02	53.05	61.74	60.18
TiO_2	0.48	0.14	0.35	0.36	0.35
Al_2O_3	21.74	7.79	18.16	16.86	16.68
Fe_2O_3	1.93	5.28	7.53	5.46	5.73
MnO	bd	0.05	0.23	0.09	0.10
MgO	1.53	10.90	7.73	3.62	4.42
CaO	0.73	bd	3.71	2.31	2.99
K_2O	5.67	bd	2.52	2.73	2.30
Na_2O	1.07	bd	0.94	2.06	2.61
P_2O_5	0.13	bd	0.11	0.06	0.05
L.O.I.	4.24	1.32	4.53	4.18	3.10
Sum	99.07	99.51	98.86	99.47	98.51

Table A3(vii). XRF bead data in wt%.

Sample	00BT01	010723/09	010723/10	010723/11	010723/12	010724/04	010819/01	010819/16
SiO_2	65.89	71.67	65.30	54.10	67.59	57.75	63.57	65.28
TiO_2	0.18	0.20	0.31	0.36	0.30	0.52	0.33	0.37
Al_2O_3	12.44	16.68	13.53	15.79	11.91	16.01	15.05	14.97
Fe_2O_3	3.07	1.95	5.66	7.63	5.77	6.98	4.72	5.91
MnO	0.06	0.06	0.13	0.15	0.11	0.10	0.06	0.07
MgO	18.77	0.53	5.74	5.43	5.14	2.80	2.93	2.78
CaO	0.06	0.39	2.94	13.52	6.74	3.88	7.49	4.55
K_2O	bd	bd	0.82	0.10	0.21	0.12	0.17	1.10
Na_2O	0.08	10.33	4.12	1.53	4.00	6.94	4.61	4.91
P_2O_5	bd	bd	0.05	bd	bd	0.06	bd	0.15
Sum	100.55	101.82	98.59	98.60	101.78	95.15	98.94	100.07
Ba	777.8	22.1	107.8	41.5	55.4	79.5	105.9	748.8
Co	7.0	3.4	15.0	19.1	13.1	19.8	10.9	12.4
Cr	73.7	26.5	64.0	157.7	130.6	20.6	73.6	20.4
Cu	1100.1	11.5	35.0	55.4	275.4	71.3	69.4	18.0
La	bd	bd	bd	bd	bd	8.3	bd	15.3
Nb	bd	bd	bd	bd	bd	bd	bd	5.1
Ni	8.5	5.3	11.6	33.3	23.9	2.4	14.4	5.1
Pb	84.4	8.7	5.3	7.5	5.4	7.3	4.7	9.6
Rb	bd	bd	10.3	bd	2.5	bd	2.3	9.4
Sc	20.1	bd	25.7	29.9	31.1	32.1	36.6	14.7
Sr	11.4	95.1	124.7	240.7	103.7	171.5	88.0	140.5
V	111.4	23.7	121.7	236.3	152.6	190.2	213.0	89.3
Y	2.2	8.7	11.7	10.7	8.4	7.7	17.9	19.6
Zn	1023.0	22.8	39.0	63.3	45.6	63.3	40.6	66.1
Zr	27.2	102.7	47.1	43.1	27.0	40.5	29.4	93.1

Sample	010820/03	010820/11	010824/04	010824/11	010824/16	010825/02	010825/04	010825/08
SiO_2	59.84	63.89	62.60	68.80	72.40	76.64	73.32	79.33
TiO_2	0.52	0.35	0.33	0.34	0.26	0.28	0.27	0.20
Al_2O_3	16.89	14.64	15.45	13.81	15.37	13.26	13.53	11.34
Fe_2O_3	8.19	5.40	4.78	3.40	3.37	2.52	3.09	2.30
MnO	0.12	0.06	0.09	0.09	0.05	bd	0.05	bd
MgO	4.37	2.86	4.06	3.47	3.01	0.82	1.12	0.39
CaO	3.41	6.13	5.99	0.50	1.72	1.07	1.86	1.89
K_2O	0.59	0.61	1.07	0.95	0.42	0.50	3.25	0.50
Na_2O	6.29	4.03	3.97	5.16	5.19	7.12	4.17	6.03
P_2O_5	0.15	0.06	bd	0.12	0.09	0.07	0.08	bd
Sum	100.36	98.03	98.34	96.62	101.89	102.28	100.74	101.97
Ba	192.8	214.5	131.6	7555.1	144.9	75.4	317.7	91.1
Co	23.3	11.5	12.9	4.7	7.6	3.1	5.4	3.0
Cr	21.1	43.5	68.5	18.4	25.3	16.4	15.6	13.2
Cu	67.9	10.3	19.3	4.3	5.5	4.2	5.4	6.2
La	17.7	5.5	bd	bd	bd	5.8	10.2	6.3
Nb	5.9	2.6	bd	2.4	bd	2.7	2.6	2.6
Ni	10.7	7.7	17.8	bd	bd	bd	bd	bd
Pb	6.8	5.2	5.0	bd	4.4	5.3	5.1	5.2
Rb	9.1	8.7	19.0	9.3	3.8	6.4	19.1	6.6
Sc	28.3	25.7	34.7	15.3	9.6	10.3	8.8	7.4
Sr	113.5	51.7	172.2	188.5	192.0	119.9	165.7	52.3
V	200.3	140.0	186.4	25.3	52.1	23.9	37.7	14.1
Y	16.7	10.8	10.6	17.3	9.4	16.6	14.3	12.3
Zn	73.9	49.1	49.4	46.0	21.5	44.8	35.2	22.9
Zr	81.7	63.6	28.1	100.0	86.6	98.7	104.3	97.8

Table A3(viii). XRF pellet data; oxides in wt%, trace elements in ppm.

Sample	010825/18	010826/06	010826/08	010826/10	010826/16	01BT019	01BT021	01BT045
SiO_2	61.07	73.05	64.85	59.63	59.00	54.80	65.58	45.00
TiO_2	0.31	0.31	0.40	0.41	0.43	0.54	0.28	0.32
Al_2O_3	13.10	13.73	15.06	15.53	16.33	25.87	19.50	18.86
Fe_2O_3	7.55	3.47	6.63	7.97	6.23	5.38	2.76	10.98
MnO	0.14	bd	0.10	0.14	0.11	bd	0.08	0.15
MgO	5.92	2.62	5.20	3.63	3.45	4.28	3.04	12.34
CaO	5.31	1.10	3.03	6.03	7.95	0.09	0.72	7.72
K_2O	0.30	0.24	1.45	0.76	1.06	5.44	3.12	0.26
Na_2O	3.94	6.17	2.52	4.71	3.25	0.78	2.81	1.36
P_2O_5	bd	0.09	0.07	0.12	0.08	bd	bd	bd
Sum	97.63	100.77	99.30	98.92	97.88	97.17	97.89	96.98
Ba	127.7	50.4	149.2	319.3	386.6	5831.1	4885.7	97.9
Co	20.8	5.6	13.4	17.9	15.9	25.5	11.2	34.7
Cr	57.0	21.4	64.0	11.7	36.2	192.4	111.8	59.4
Cu	219.1	11.4	32.9	55.5	32.7	56.4	9.9	72.1
La	bd	7.4	bd	12.7	bd	8.2	bd	bd
Nb	bd	bd	bd	4.3	bd	bd	bd	bd
Ni	14.1	bd	11.0	7.8	9.2	39.9	18.4	20.1
Pb	5.8	6.2	7.2	9.3	9.1	457.9	6.4	5.6
Rb	3.7	3.6	17.3	10.5	23.7	63.6	32.2	4.0
Sc	36.5	12.5	19.7	26.1	18.7	62.3	40.0	37.7
Sr	167.0	92.6	175.0	61.2	224.2	33.1	68.7	40.1
V	229.5	33.6	109.9	221.5	120.8	313.5	229.7	272.6
Y	7.5	25.0	17.9	16.1	10.9	20.6	12.5	9.4
Zn	62.0	49.1	68.9	65.5	61.9	826.7	3376.1	183.6
Zr	25.1	80.0	60.0	71.6	61.5	52.4	42.6	28.6

Sample	01BT075A	01BT085	01BT119	01BT188	01BT191
SiO_2	56.60	71.22	47.93	58.74	59.82
TiO_2	0.39	0.15	0.31	0.32	0.32
Al_2O_3	25.57	10.32	19.43	18.75	17.96
Fe_2O_3	1.54	3.68	8.04	5.86	5.83
MnO	bd	0.05	0.29	0.11	0.12
MgO	1.82	16.85	8.70	4.74	6.10
CaO	0.68	bd	4.91	2.79	2.53
K_2O	6.12	bd	2.50	3.02	2.51
Na_2O	0.61	0.06	0.92	2.00	2.57
P_2O_5	0.10	bd	0.09	bd	bd
Sum	93.42	102.32	93.11	96.32	97.75
Ba	11062.7	17.2	3344.7	1826.3	361.1
Co	6.7	6.3	23.9	14.6	20.1
Cr	178.0	70.5	26.5	37.1	35.6
Cu	36.8	231.6	39.4	122.5	108.7
La	bd	bd	bd	bd	5.8
Nb	bd	bd	bd	bd	bd
Ni	11.2	9.8	24.2	12.5	16.4
Pb	15.0	189.3	3.1	4.6	5.2
Rb	62.5	bd	22.8	22.9	23.4
Sc	51.1	14.6	32.4	27.4	21.7
Sr	41.8	5.5	32.6	144.7	166.1
V	291.9	72.0	210.0	172.3	144.1
Y	8.6	bd	10.3	7.8	5.5
Zn	194.1	772.8	294.9	126.8	74.5
Zr	51.2	24.5	41.5	46.0	47.7

Table A3(viii). XRF pellet data; oxides in wt%, trace elements in ppm (contd.).

Sample	00BT01	010723/09	010723/10	010723/11	010723/12	010724/04	010819/01	010819/16
Rb	0.23	0.18	10.13	1.02	2.17	1.89	2.10	8.67
Sr	5.93	81.78	115.00	233.05	84.79	146.42	71.26	122.43
Y	2.61	9.01	11.62	10.39	7.88	7.27	16.95	19.45
Zr	13.06	98.48	31.30	24.54	10.12	26.06	15.13	78.72
Nb	0.17	1.24	0.40	0.40	0.20	0.59	0.27	3.95
Cs	0.29	0.04	0.19	bd	0.09	0.11	0.10	0.10
Ba	610.94	26.25	122.60	37.09	45.48	73.88	98.79	832.19
La	1.33	3.64	2.58	2.64	1.19	3.58	1.72	16.69
Ce	3.12	8.15	6.42	6.43	2.89	8.02	4.74	33.13
Pr	0.44	1.03	0.91	0.96	0.48	1.04	0.84	3.76
Nd	1.98	4.78	4.67	4.76	2.54	4.97	4.75	16.34
Sm	0.48	1.25	1.40	1.31	0.83	1.27	1.72	3.58
Eu	0.10	0.35	0.44	0.43	0.33	0.74	0.49	0.92
Gd	0.50	1.22	1.66	1.51	1.09	1.31	2.20	3.23
Tb	0.07	0.22	0.30	0.26	0.18	0.21	0.41	0.51
Dy	0.46	1.47	2.12	1.85	1.38	1.43	2.91	3.47
Ho	0.12	0.31	0.47	0.41	0.31	0.32	0.66	0.73
Er	0.38	0.83	1.42	1.20	0.99	0.89	2.01	2.19
Tm	0.06	0.11	0.21	0.17	0.14	0.12	0.29	0.32
Yb	0.49	0.74	1.45	1.30	1.05	0.88	2.16	2.23
Lu	0.08	0.12	0.24	0.21	0.16	0.14	0.34	0.38
Hf	0.45	2.55	1.07	0.89	0.48	0.98	0.61	2.38
Ta	0.05	0.14	0.05	0.06	0.04	0.08	0.06	0.36
Pb	82.23	4.89	1.38	3.38	1.82	3.41	1.91	6.13
Th	0.17	0.94	0.49	0.51	0.15	0.60	0.18	2.81
U	2.14	0.29	0.30	0.33	0.20	0.27	0.20	0.95

Sample	010820/03	010820/11	010824/04	010824/11	010824/16	010825/02	010825/04	010825/09
Rb	7.81	8.39	19.72	7.97	3.46	6.35	19.18	6.78
Sr	91.88	40.31	164.58	148.74	159.89	103.64	144.78	42.56
Y	15.95	10.76	10.96	15.12	8.15	16.86	13.35	12.00
Zr	68.05	51.00	15.26	75.21	36.24	90.87	92.08	89.60
Nb	4.50	1.84	0.23	1.60	1.04	1.83	1.83	1.78
Cs	0.22	0.20	0.83	0.28	0.09	0.11	0.13	0.09
Ba	194.15	221.83	131.49	5767.29	134.93	69.07	427.14	108.74
La	15.49	5.67	1.51	3.19	5.61	7.03	11.97	8.15
Ce	32.86	12.09	3.73	10.18	12.46	16.80	25.73	18.31
Pr	3.79	1.47	0.61	1.77	1.56	2.22	3.07	2.17
Nd	16.16	6.52	3.36	8.78	6.83	10.22	13.36	9.42
Sm	3.67	1.58	1.09	2.26	1.45	2.47	2.81	2.16
Eu	0.84	0.46	0.40	1.24	0.54	0.65	0.79	0.57
Gd	3.28	1.59	1.34	2.73	1.50	2.44	2.54	2.09
Tb	0.47	0.27	0.22	0.34	0.22	0.39	0.39	0.33
Dy	3.07	1.85	1.64	2.54	1.48	2.80	2.53	2.20
Ho	0.64	0.41	0.38	0.49	0.31	0.60	0.54	0.48
Er	1.79	1.20	1.16	1.50	0.93	1.81	1.61	1.42
Tm	0.25	0.18	0.16	0.24	0.13	0.26	0.22	0.21
Yb	1.74	1.26	1.25	1.64	0.91	1.92	1.58	1.47
Lu	0.28	0.21	0.19	0.26	0.14	0.32	0.26	0.23
Hf	2.06	1.53	0.57	2.23	1.25	2.55	2.62	2.53
Ta	0.48	0.18	0.05	0.17	0.12	0.16	0.19	0.17
Pb	3.37	2.00	1.35	1.53	0.64	1.29	1.78	1.30
Th	2.92	1.16	0.21	0.79	0.55	1.04	1.53	1.22
U	0.94	0.63	0.26	0.38	0.17	0.40	0.51	0.52

Table A3(ix). ICP-MS data (in ppm).

Sample	010825/18	010826/06	010826/08	010826/10	010826/16	01BT019	01BT021	01BT045
Rb	3.73	3.38	17.24	9.49	19.21	66.59	31.54	3.04
Sr	153.34	77.66	160.66	47.19	166.50	24.19	50.39	30.11
Y	7.78	25.24	17.50	14.85	8.09	20.12	12.00	8.47
Zr	10.94	67.69	45.51	56.16	38.71	38.13	27.36	11.75
Nb	0.17	0.99	0.79	3.41	0.65	0.46	0.37	0.25
Cs	0.13	0.10	0.52	0.10	0.74	1.06	1.51	0.21
Ba	117.34	48.21	145.27	343.12	316.04	920.85	971.22	113.15
La	0.91	6.78	4.00	12.81	4.56	4.38	2.18	1.05
Ce	2.26	13.68	9.49	26.12	10.45	8.83	4.78	3.16
Pr	0.39	1.99	1.45	3.06	1.38	1.13	0.74	0.53
Nd	2.11	9.55	7.30	12.79	6.37	5.45	3.98	2.88
Sm	0.73	2.91	2.09	2.88	1.65	1.54	1.23	1.02
Eu	0.22	0.78	0.66	0.69	0.56	1.04	0.81	0.39
Gd	0.98	3.29	2.42	2.50	1.60	2.15	1.73	1.29
Tb	0.17	0.59	0.41	0.39	0.24	0.38	0.27	0.23
Dy	1.31	4.24	2.95	2.60	1.63	2.73	1.85	1.77
Ho	0.30	0.96	0.66	0.57	0.35	0.66	0.45	0.41
Er	0.92	2.93	2.00	1.70	0.96	1.86	1.32	1.27
Tm	0.13	0.44	0.28	0.23	0.14	0.25	0.18	0.19
Yb	1.01	3.41	2.04	1.67	0.92	1.67	1.33	1.43
Lu	0.17	0.53	0.31	0.27	0.15	0.26	0.22	0.21
Hf	0.47	2.17	1.51	1.77	1.30	1.29	0.97	0.54
Ta	0.04	0.10	0.10	0.36	0.09	0.15	0.14	0.05
Pb	1.40	2.61	3.29	5.67	4.00	515.93	3.33	2.25
Th	0.16	0.93	0.66	2.18	1.11	0.54	0.36	0.15
U	0.13	0.42	0.44	0.93	0.44	25.92	0.64	0.14

Sample	01BT075A	01BT085	01BT119	01BT188	01BT191
Rb	66.18	bd	17.90	24.06	23.72
Sr	30.37	1.06	24.37	138.43	160.90
Y	7.69	1.81	9.75	8.45	6.07
Zr	38.47	10.69	27.41	33.51	37.77
Nb	1.07	0.13	0.41	0.42	0.48
Cs	2.09	0.10	0.66	1.40	1.67
Ba	nd	19.49	1258.78	652.77	360.99
La	1.31	0.13	3.12	1.78	1.69
Ce	3.73	0.36	7.91	4.68	4.96
Pr	0.64	0.06	0.95	0.73	0.69
Nd	3.37	0.36	4.80	3.59	3.42
Sm	1.13	0.17	1.31	1.13	1.02
Eu	1.33	0.05	0.79	0.48	0.42
Gd	1.48	0.20	1.76	1.44	1.08
Tb	0.23	0.04	0.25	0.22	0.18
Dy	1.51	0.29	1.78	1.59	1.14
Ho	0.34	0.07	0.40	0.35	0.27
Er	1.11	0.23	1.26	1.04	0.73
Tm	0.18	0.04	0.18	0.16	0.10
Yb	1.46	0.30	1.23	1.12	0.71
Lu	0.26	0.06	0.21	0.17	0.12
Hf	1.04	0.33	1.04	1.12	1.15
Ta	bd	bd	0.09	0.07	0.05
Pb	19.05	255.03	0.78	2.15	1.69
Th	0.48	0.17	0.44	0.67	0.54
U	2.97	1.51	0.37	0.16	0.09

Table A3(ix). ICP-MS data in ppm (contd.).

Assessment of contamination during crushing and grinding

In order to check for possible contamination during crushing and grinding, samples of clean sand were split and half of the sample given the same fly press and TEMA treatment as the whole rock samples, the other half had no preparation. Samples were then dissolved and analysed by ICP-MS following the methods outlined above.

Results are plotted in Figure A3(i), and indicate that with the exception of Pb, the crushing and grinding procedures do not introduce significant trace element contamination to samples.

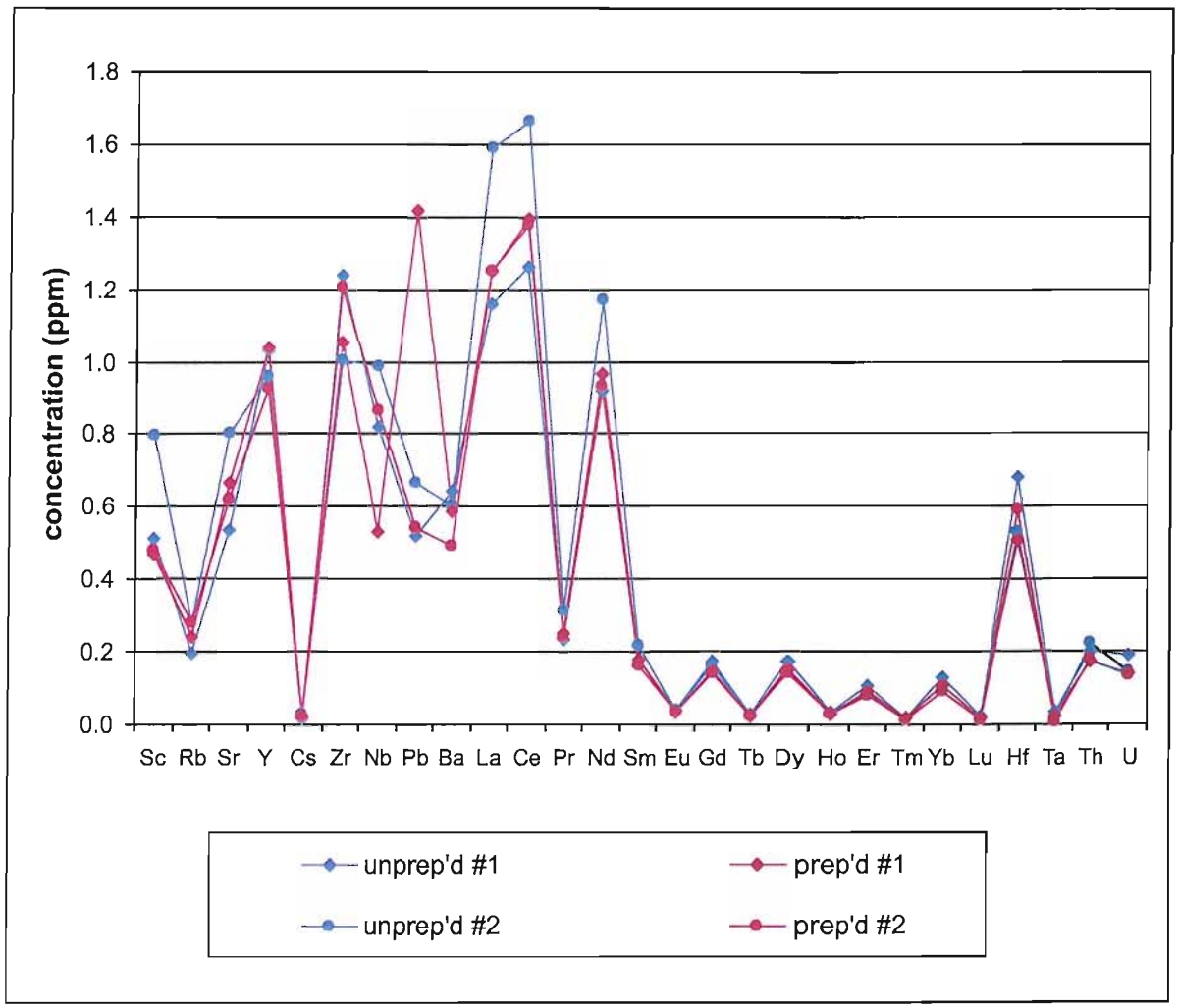

Figure A3(i). ICP-MS analyses of sand samples to investigate crushing and grinding procedures.

Comparison of XRF bead and pellet data

Major element data used in this study have been taken from the bead analyses, which are known to provide better quality major element analyses than pellets due to less problems with matrix affects particularly for the light elements Si, Al, Mg and Na. However, it is useful to compare the bead and pellet data as an additional check on data quality. Comparisons of bead and pellet data from this study (Figure A3(ii)) are generally consistent with the anticipated trends, with a good 1:1 correlation between pellet and bead data for K, Ca, Na, Ti, P and Fe (excluding two anomalous

data points for Fe), while Mg, Si and Al correlate well but deviate significantly from 1:1 ratio, consistent with the lightest elements being the least accurate from pellet analyses. Mn also correlates well but there is a deviation from 1:1 which is less typical for this element.

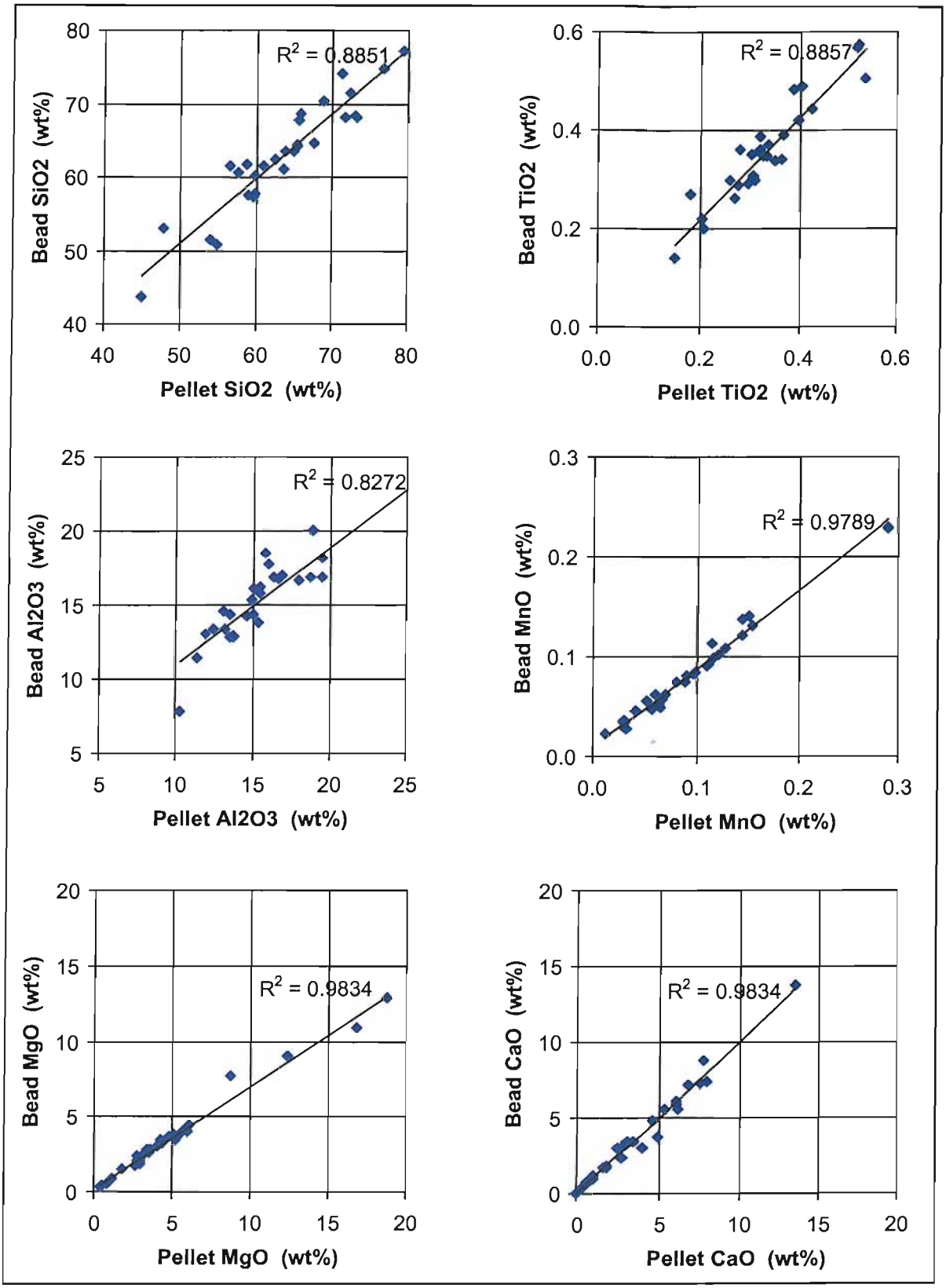

Figure A3(ii). Comparison of major element data from XRF beads and XRF pellets.

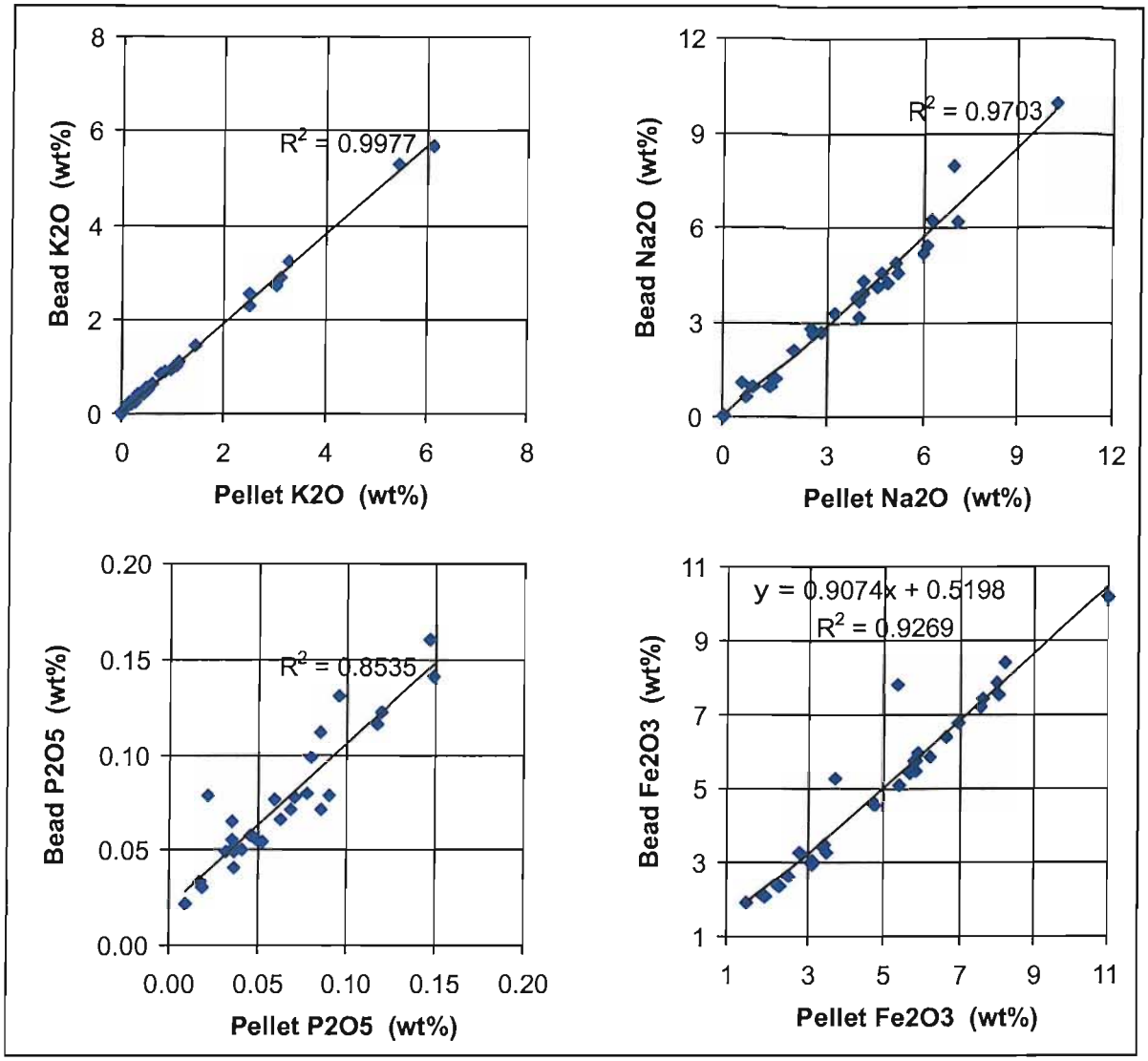

Figure A3(ii). Comparison of major element data from XRF beads and XRF pellets (contd).

Comparison of XRF pellet and ICP-MS trace element data

A number of elements, including Sr, Rb, Zr, Y and La, were determined using both XRF pellets and ICP-MS. Scatter plots comparing the datasets from these two methods are given in Figure A3(iii), and generally show a good correlation. One sample has anomalously low Zr from the ICP-MS analysis and probably reflects the resistance of zircon to dissolution, which is consistent with this being a granite sample. The gradient also deviates slightly from 1:1 for Zr and Nb, suggesting minor discrepencies in the calibration between XRF and ICP-MS. For plots in this study, Zr and Sr were taken from XRF data, and Y, Nb and Rb from ICP-MS.

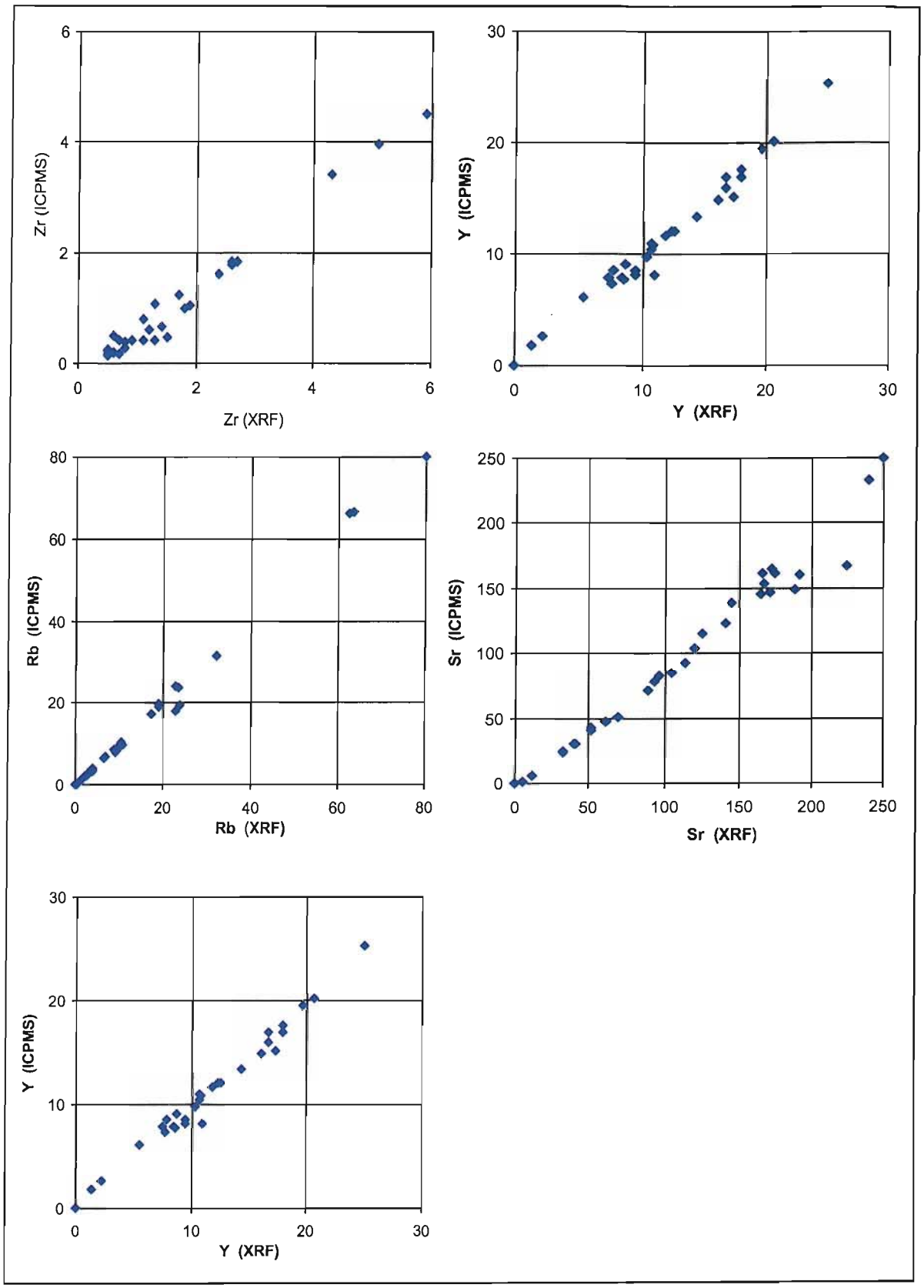

Figure A3(iii). Comparison of major element data from XRF beads and XRF pellets.

APPENDIX A4: ISOCON DIAGRAMS

Following the method of Grant (1986), an isocon diagram is constructed by plotting an altered sample against its unaltered (or least altered) equivalent, where the concentration of a given component in the two samples is defined by:

$C^A = M^o/M^A(C^o+\Delta C)$

where:

C^A and C^o are the concentration of a given component in the altered and unaltered rock respectively.

M^A and M^o are the masses of the altered and unaltered rock respectively.

ΔC is the difference in concentration of a given component between the altered and unaltered sample (caused by actual gain or loss of that component, not due to volume change).

A straight line is constructed that passes through the origin and connects components which have not been lost or gained during alteration (although concentration may have changed due to volume changes), i.e. are immobile. The gradient of this line is M^o/M^A, which represents the reduction (for $M^o/M^A > 1$) or increase (for $M^o/M^A < 1$) in volume during alteration. For components resting on this line, ΔC is zero hence they were immobile during alteration. For all other samples, ΔC indicates the gain ($\Delta C > 0$) or loss ($\Delta C < 0$) of the component during alteration; components with net gain fall above the line, and those with net loss fall below it. For each plot, Zr was chosen as the reference element to construct the line connecting immobile elements, since this is widely reported to be one of the most immobile elements under intense hydrothermal alteration (e.g. Finlow-Bates & Stumpfl, 1991; Maclean & Kranidiotis, 1987), and lines have been constructed to pass through the Zr point and the origin.

Sample pairs were selected to show the maximum variation in alteration for comparable lithologies, the latter estimated mainly by phenocryst mineralogy and abundance. Four isocon diagrams have been constructed using the following pairs of samples:

(i) 010723/12 (least altered) and 010825/18 (altered), plagioclase – pyroxene- phyric lavas of the Irendyk Formation to investigate regional alteration.

(ii) 010825/02 (east altered) and 010824/11 (moderately altered) feldspar-phyric lavas of the Baimak-Buribai Formation to investigate regional alteration.

(iii) 01BT188 (least altered) and 01BT021 (intensely altered) feldspar-quartz-phyric lavas from Balta Tau, to investigate the intense sericitic hanging-wall alteration.

(iv) 01BT188 (least altered) and 00BT01 (intensely altered) feldspar-quartz-phyric lavas from Balta Tau, to investigate the intense quartz-chlorite footwall alteration.

Results of the isocon diagrams (Figures A4(i) and A4(ii)) are summarised in table A4(i).

	Volume change	Immobile (± 5%)	Components lost		Components gained	
			weak (<20%)	large (>20%)	weak (<20%)	large (>20%)
Irendyk	7.5% increase	Na_2O, SiO_2, Zr, Hf, Dy, Er, Tm, Tb, Ho, Gd Yb	CaO Nb, La, Ce, Pr Nd, Sm,	P_2O_5 Ni, Cr, Eu, U	MgO, TiO_2 Al_2O_3 Y, Ta, Pb, Lu, Th	K_2O, MnO, Fe_2O_3 Sr, Ba, Cs, Rb, Sc, V, Co, Zn
Baimak-Buribai	1.3% dec-rease	Al_2O_3, V, Zr, Zn, Ta, U	SiO_2, Nb, Hf. Yb, Er, Y, Dy, Ho, Tm, Lu, Nd, Tb,	CaO, Na_2O, Th, Ce La, Pb,	TiO_2, Rb, Cr, Gd, Co	P_2O_5, MnO, Fe_2O_3, K_2O, MgO Sr, Ba, Cs, Sc, Ni, Eu, Pr
Footwall (intense qtz-chl alteration)	69.1% increase	TiO_2, MnO Zr, Pr	Fe_2O_3, P_2O_5 Nd	Na_2O, K_2O, CaO Sr, Rb, Ba, Cs, Co, Y, Nb, Hf, Sm, Eu, Tb, Dy, Ho, Er, Tm, Yb Th	Al_2O_3 V, Ni, Sc, Ce, Gd,	MgO, SiO_2 Cr, Zn, Ta, Pb, La, Lu, U
Hanging-wall (intense sericitic alteration)	12.0% dec-rease	Zr, Nb, Hf	Fe_2O_3, SiO_2	Na_2O, MgO, P_2O_5, CaO, MnO Sr, Cs, Th	Al_2O_3 Co, Sm	K_2O, TiO_2 Rb, Ba, Sc, V, Cr, Ni, Zn, Y, Ta, Pb, La, Ce, Pr, Nd, Eu, Gd, Tb, Dy, Ho, Er, Tm, Yb, Lu, U

Table A4(i). Mobility of elements suggested by isocon diagrams.

The results of isocon diagrams are clearly unrealistic for most of the sample pairs, for example the Irendyk samples suggest that Si is immobile, while elements such as Nb, Ta, Sc and Cr which are normally considered to be immobile are indicated here to be mobile. There is also variable enrichment and depletion within groups of elements such as HREE and LREE which would be expected to behave in a similar way if they were mobile during alteration.

Since Zr was chosen as the reference element to construct the line connecting immobile elements, the dilution/concentration estimates should be reliable if Zr was immobile during alteration.

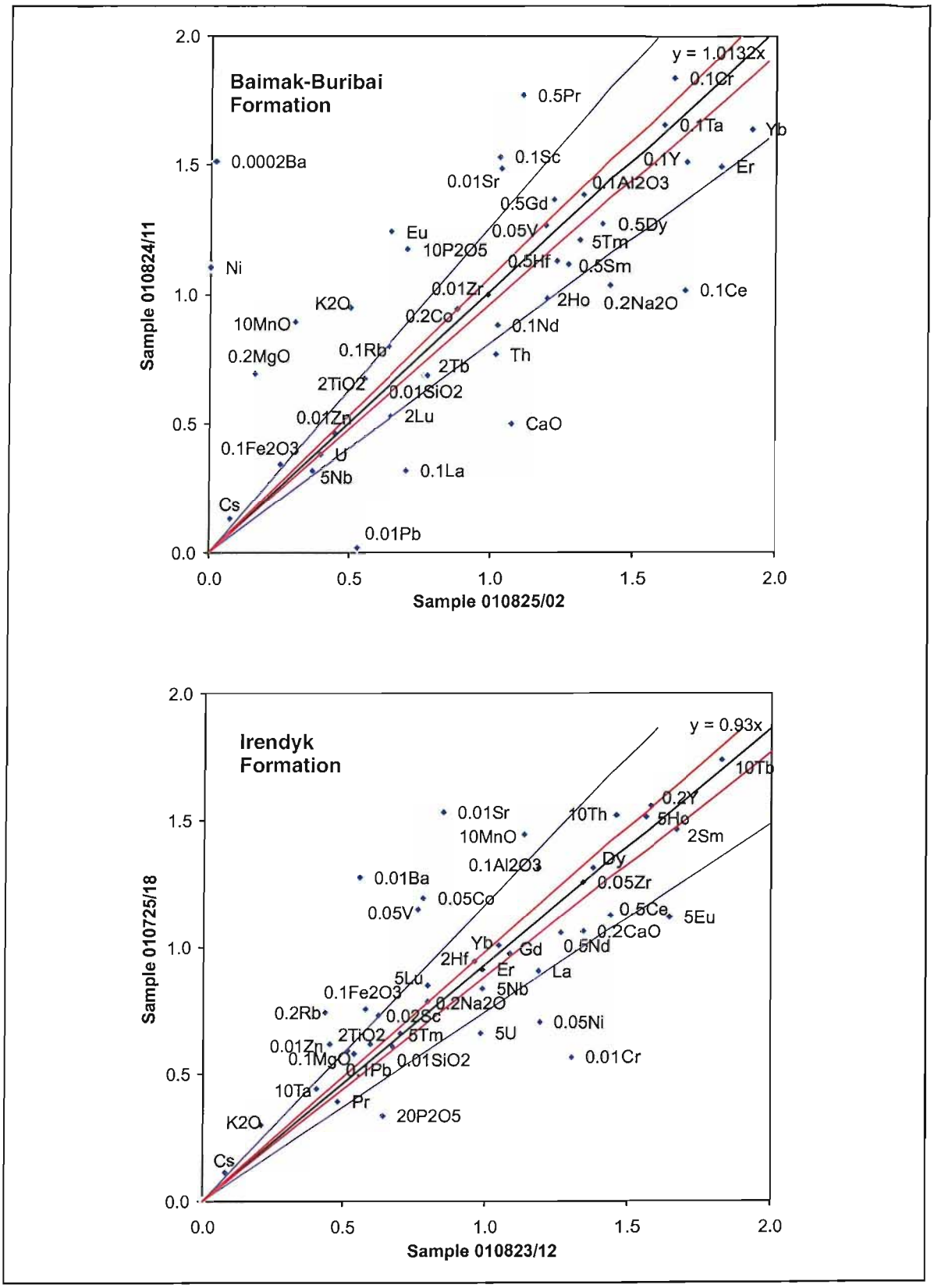

Figure A4(i). Isocon Diagrams for regional samples.

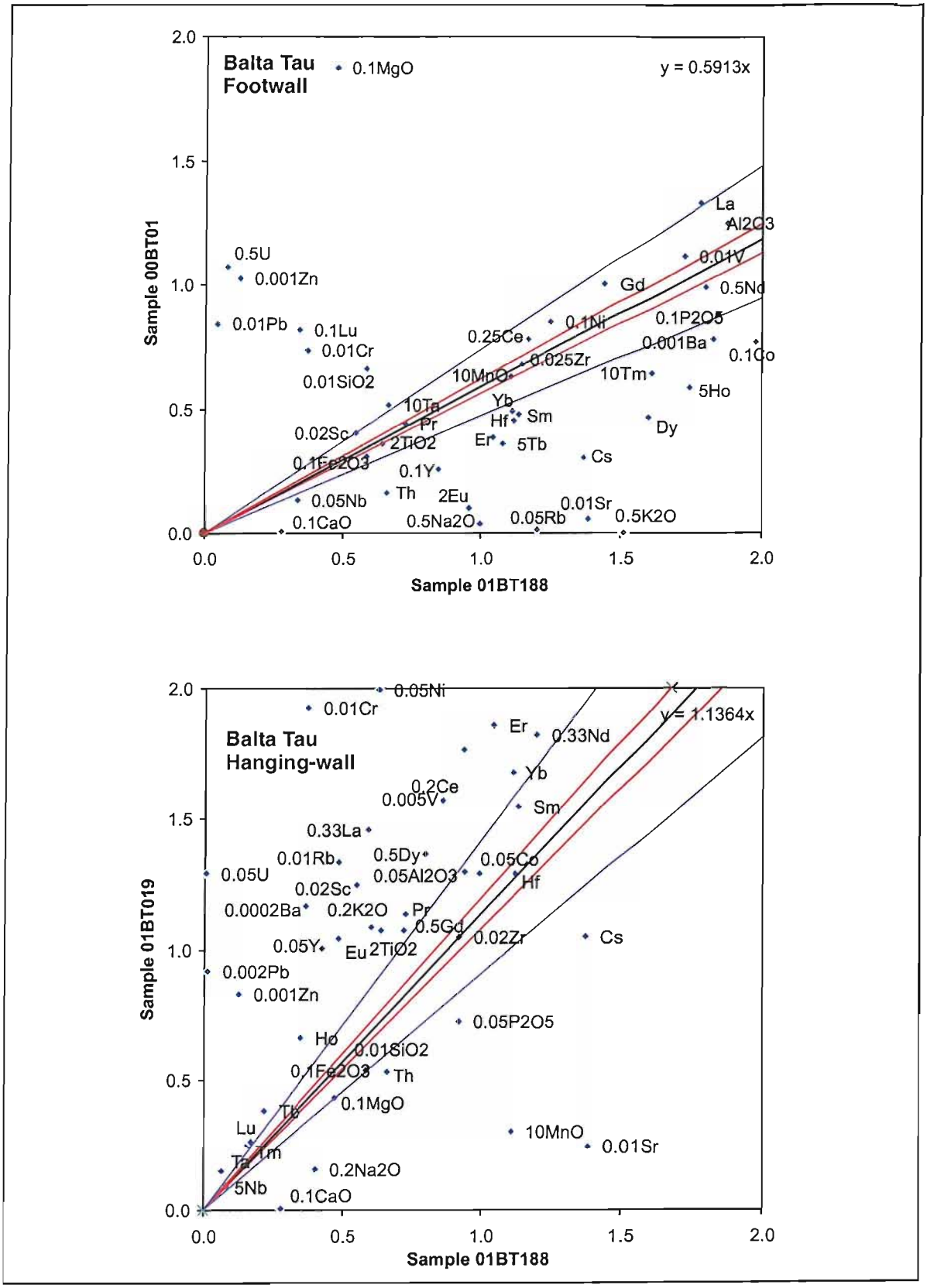

Figure A4(ii). Isocon Diagrams for Balta Tau samples.

APPENDIX A5: NORMALISING VALUES

Table A5(i) gives the chondrite values used to normalise REE elements (from Boynton, 1984) and N-MORB values used for Th, Nb, Ce, Zr, Ti and Y used for multielement diagrams (from Saunders and Tarney, 1984).

Chondrite (ppm)	
La	0.3100
Ce	0.8080
Pr	0.1220
Nd	0.6000
Sm	0.1950
Eu	0.0735
Gd	0.2590
Tb	0.0474
Dy	0.3220
Ho	0.0718
Er	0.2100
Tm	0.0324
Yb	0.2090
Lu	0.0322

N-MORB (ppm)	
Ti	8400
Nb	2.50
Zr	88
Y	35.0
Ce	10.0
Th	0.20

Table A5(i). Normalising values used in REE and multielement plots.

APPENDIX B

APPENDIX B1 : MICROPROBE DATA

Microprobe Detection Limits

Tables B1(i) to B1(iv) specify the conditions employed for microprobe analyses and the calculated detection limits for sulphide, silicate, carbonate and sulphate analyses (based on a spreadsheet template written by J. Spratt, Natural History Museum, London).

Calculations and terms are as follows:

column 1: Bk (c/s) – mean of background counts per second from unknowns

column 2: Pk (c/s/nA) – counts per second per unit current from standard in calibration

column 3: count time – count time used for calibration and unknowns

column 4: % el in std – wt% of element in the standard

column 5: bk (counts) – calculated mean of background counts from unknowns:

bk(counts) = Bk(c/s) * count time

column 5: Pk (counts) – calculated peak counts from standard:

Pk(counts) = Pk(c/s/nA) * count time(s) * nA * (100 / % el in std.)

column 6: 3*std(bk) –calculated from: 3 * Bk(counts)^0.5

column 7: det limit (wt%) – calculated from: det limit = (100 / Pk(counts) * 3*std(bk)

column 8: det limit (ppm) – calculated from: det lmit (ppm) = det limit wt% * 10000

column 9: std used – gives the mineral used for calibration and the peak measured

	Bk (c/s)	Pk (c/s/nA)	count time (s)	nA (pk)	% el. in std.	bk (counts)	Pk (counts)	3*std (bk)	det.limit (wt%)	det.limit (ppm)	std used	
As	30.70	162.69	30	20	51.80	921.00	189365	91.04	0.048	481	La	GaAs
S	17.70	212.22	15	20	36.47	265.50	174836	48.88	0.028	280	Ka	FeS
Se	35.27	199.15	10	20	27.59	352.75	144713	56.34	0.039	389	La	PbSe
Au	6.52	84.36	20	20	100.00	130.47	33872	34.27	0.101	1012	Ma	pure Au
Ag	11.64	160.16	10	20	100.00	116.44	32149	32.37	0.101	1007	La	pure Ag
Pb	74.45	159.14	10	20	72.41	744.49	44699	81.86	0.183	1831	Ma	PbSe
Fe	32.73	520.32	15	20	63.53	490.96	246197	66.47	0.027	270	Ka	FeS
Cu	48.90	474.89	15	20	100.00	733.54	143201	81.25	0.057	567	Ka	pure Cu
Zn	53.08	259.99	15	20	67.10	796.25	117036	84.65	0.072	723	Ka	ZnS
Sb	40.87	510.27	30	20	100.00	1226.12	307388	105.05	0.034	342	La	Pure Sb
Co	33.17	542.42	10	20	100.00	331.75	108815	54.64	0.050	502	Ka	pure Co
Cd	22.89	284.88	20	20	77.81	457.78	146904	64.19	0.044	437	La	CdS
Cr	14.46	396.30	10	20	100.00	144.59	79404	36.07	0.045	454	Ka	pure Cr
Te	34.89	161.77	30	20	37.91	1046.65	257073	97.06	0.038	378	La	BiTe
Hg	9.32	93.32	20	20	61.12	186.35	61260	40.95	0.067	669	Ma	HgTe
Bi	17.10	65.22	20	20	62.09	342.05	42357	55.48	0.131	1310	Ma	BiTe
Ge	39.78	175.29	30	20	100.00	1193.53	106365	103.64	0.097	974	La	pure Ge
Ga	21.20	163.00	30	20	48.20	636.03	203543	75.66	0.037	372	La	GaAs
In	24.15	173.96	30	20	100.00	724.46	105098	80.75	0.077	768	Ka	pure In

Table B1(i). Detection limits for elements in sulphide analyses.

	Bk (c/s)	Pk (c/s/nA)	count time (s)	nA (pk)	% el. in std.	Bk (counts)	Pk (counts)	3*std (bk)	det.limit (wt%)	det.limit (ppm)	std used	
P	1.07	43.17	15	15	18.10	16.11	53677	12.04	0.022	224	Ka	apatite
S	1.72	52.31	20	15	17.45	34.47	89957	17.61	0.020	196	Ka	celestite
Cr	22.24	933.13	25	15	100.00	555.88	350480	70.73	0.020	202	Ka	pure Cr
K	5.64	186.79	10	15	32.86	56.36	85321	22.52	0.026	264	Ka	KBr
Ca	7.89	197.24	15	15	34.17	118.40	129995	32.64	0.025	251	Ka	wollastonite
Ti	15.44	352.83	15	15	59.95	231.56	132655	45.65	0.034	344	Ka	rutile
Mn	2.84	225.08	20	15	100.00	56.83	67581	22.62	0.033	335	Ka	pure Mn
Fe	3.97	239.66	20	15	100.00	79.31	71978	26.72	0.037	371	Ka	pure Fe
Mg	18.75	736.48	10	15	60.32	187.50	183331	41.08	0.022	224	Ka	MgO2
Al	31.43	849.76	10	15	52.92	314.34	241175	53.19	0.022	221	Ka	corundum
Si	37.67	373.77	10	15	24.80	376.72	226448	58.23	0.026	257	Ka	diopside
Na	4.88	66.83	15	15	11.20	73.27	134336	25.68	0.019	191	Ka	jadeite
Sr	30.75	284.52	25	15	47.70	768.67	224444	83.17	0.037	371	La	celestite

Table B1(ii). Detection limits for elements in silicate analyses.

	Bk (c/s)	Pk (c/s/nA)	count time (s)	nA (pk)	% el. in std.	bk (counts)	Pk (counts)	3*std (bk)	det. limit (wt%)	det. limit (ppm)	std used	
Ca	13.18	314.99	5	10	39.97	65.90	39469	24.35	0.062	617	Ka	aragonite
Ba	7.24	130.45	10	10	58.80	72.40	22258	25.53	0.115	1147	La	barite
Fe	2.94	241.13	10	10	100.00	29.40	24142	16.27	0.067	674	Ka	pure Fe
Zn	5.96	298.27	10	10	67.10	59.60	44511	23.16	0.052	520	Ka	ZnS
Mn	2.02	226.20	20	10	100.00	40.30	45279	19.04	0.042	421	Ka	pure Mn
Mg	6.32	734.25	10	10	59.95	63.20	122540	23.85	0.019	195	Ka	MgO2
Sr	13.81	282.00	25	10	47.70	345.25	148144	55.74	0.038	376	La	celestite

Table B1(iii). Detection limits for elements in carbonate analyses.

	Bk (c/s)	Pk (c/s/nA)	count time (s)	nA (pk)	% el. in std.	bk (counts)	Pk (counts)	3*std (bk)	det.limit (wt%)	det.limit (ppm)	std used	
Ca	15.34	197.24	10	15	34.17	153.38	86738	37.15	0.043	428	Ka	wollastonite
Ba	45.20	198.65	10	15	58.80	452.00	51128	63.78	0.125	1247	La	barite
Sr	32.68	282.00	10	15	47.70	326.77	89006	54.23	0.061	609	La	celestite
S	5.74	39.68	10	15	13.00	57.38	45840	22.73	0.050	496	Ka	barite

Table B1(iv). Detection limits for elements in sulphate analyses.

Data corrections

PAP corrections were applied using Cameca software following the method of Pouchou & Pichoir (1984). Corrections for element overlaps have then been applied based on analyses of standards, as summarised in tables B1(v) and B1(vi).

	Pyrite	Pyrite	Galena	Sphalerite	CdS_2	Gold	Silver	Cinnabar	Zinc
S	38.32	38.91	14.27	35.14	22.35	0.07	bd	13.12	0.03
Au	bd	bd	bd	bd	bd	99.61	bd	0.12	bd
Ag	bd	bd	bd	bd	bd	bd	99.45	0.24	bd
Cu	bd	bd	0.12	bd	0.24	0.19	bd	bd	bd
Fe	60.65	59.63	bd	bd	bd	0.71	bd	bd	bd
As	0.10	0.12	bd	bd	bd	bd	bd	bd	bd
Se	bd	0.05	bd	0.04	0.04	0.06	0.05	0.35	bd
Sb	bd	bd	0.07	bd	bd	0.08	bd	bd	bd
Te	bd	bd	0.12	bd	bd	0.09	0.05	bd	0.04
Zn	bd	bd	bd	67.42	bd	bd	bd	bd	98.87
Pb	bd	bd	87.14	bd	bd	bd	bd	bd	bd
Hg	bd	bd	bd	0.09	bd	2.29	bd	87.84	bd
Bi	bd	bd	0.15	0.19	bd	bd	bd	bd	0.21
Co	0.06	bd	bd	bd	bd	bd	bd	NA	NA
Cd	bd	bd	bd	bd	77.66	0.09	0.83	NA	NA
In	bd	bd	bd	bd	0.30	bd	bd	NA	NA
Cr	bd	bd	bd	bd	bd	0.20	bd	NA	NA
Ga	bd	bd	bd	bd	bd	0.29	bd	NA	NA
Ge	bd	bd	bd	bd	bd	bd	bd	NA	NA
Total	99.12	98.70	101.87	102.87	100.58	103.67	100.39	101.69	99.16

Table B1(v). Analyses of standards used to calculate element overlaps (all data in wt%).

correction for 100% of:	element corrections (to be subtracted)				
	Hg	Bi	Cd	Ga	Te
Au	2.30	0.00	0.09	0.29	0.00
Ag	0.00	0.07	0.84	0.00	0.00
Pb	0.00	0.17	0.00	0.00	0.13
Zn	0.00	0.25	0.00	0.00	0.00

Table B1(vi). Corrections for element overlaps applied to sulphide data.

Data Listing

Corrected data is listed in the following tables:

Table B1(vii). Sulphide analyses (wt%).

Table B1(viiii). Sulphide analyses (at%).

Table B1(ix). Silicate analyses (wt% oxide).

Table B1(x). Carbonate analyses (wt% CO_3).

Table B1(xi). Sulphate analyses (wt%).

Note: bd = below detection; NA = not analysed.

Table B1(vii). Sulphide analyses (wt%).

Sample No	Analysis Ref	S	Au	Ag	Cu	Fe	As	Se	Sb	Te	Zn	Pb	Hg	Bi	Ga	Ge	Co	Cd	In	Cr	Total
Pyrite																					
901	04/09/02-037	53.63	bd	bd	bd	48.06	0.12	bd	bd	bd	bd	bd	bd	0.20	0.07	NA	NA	bd	NA	NA	102.07
901	04/09/02-038	53.72	bd	bd	0.14	48.03	0.14	0.04	bd	bd	bd	bd	bd	bd	bd	NA	NA	bd	NA	NA	102.07
901	04/09/02-039	53.64	bd	bd	bd	48.03	0.09	bd	bd	bd	bd	bd	bd	bd	bd	NA	NA	bd	NA	NA	101.76
901	04/09/02-040	53.65	bd	bd	bd	47.92	0.07	0.06	bd	bd	bd	bd	bd	bd	bd	NA	NA	bd	NA	NA	101.70
901	04/09/02-041	53.67	0.10	bd	bd	47.98	0.13	bd	bd	bd	bd	bd	bd	0.18	0.04	NA	NA	bd	NA	NA	102.11
901	04/09/02-042	53.61	bd	bd	bd	48.21	0.10	bd	0.07	bd	bd	bd	bd	bd	bd	NA	NA	bd	NA	NA	101.98
901	04/09/02-043	53.82	bd	bd	bd	48.14	0.07	0.04	bd	bd	bd	bd	bd	bd	bd	NA	NA	bd	NA	NA	102.06
901	04/09/02-044	53.66	bd	bd	bd	48.09	0.22	bd	0.04	bd	bd	bd	bd	0.20	bd	NA	NA	bd	NA	NA	102.21
901	04/09/02-045	53.46	bd	bd	0.17	48.18	0.10	bd	0.05	bd	bd	bd	bd	bd	bd	NA	NA	bd	NA	NA	101.96
901	26/04/01-068	51.47	bd	bd	0.18	45.94	0.23	bd	bd	bd	bd	bd	bd	0.18	bd	bd	0.06	bd	bd	bd	98.05
901	26/04/01-069	50.47	bd	bd	0.07	46.70	0.09	bd	0.06	0.04	bd	bd	bd	0.18	bd	bd	bd	bd	bd	bd	97.61
901	26/04/01-070	51.01	bd	bd	0.21	46.12	0.11	bd	bd	bd	bd	bd	0.10	0.15	bd	bd	bd	0.05	bd	bd	97.76
901	26/04/01-073	51.56	bd	bd	0.09	46.90	0.08	bd	bd	0.04	bd	bd	bd	bd	bd	bd	bd	bd	bd	bd	98.66
901	26/04/01-074	51.84	bd	bd	bd	46.36	0.09	0.05	bd	bd	bd	bd	bd	0.21	0.06	bd	0.05	bd	bd	bd	98.67
901	26/04/01-075	51.26	bd	bd	0.07	46.52	bd	bd	bd	0.06	bd	bd	0.10	bd	bd	bd	0.06	bd	bd	bd	98.06
901	26/04/01-078	48.83	bd	bd	3.47	44.09	0.18	bd	bd	0.05	0.08	bd	bd	0.14	bd	bd	0.07	bd	bd	bd	96.91
901	26/04/01-079	51.70	bd	bd	0.18	46.42	0.19	bd	bd	bd	bd	bd	0.10	bd	bd	bd	0.06	bd	bd	bd	98.65
902	04/09/02-071	53.37	bd	bd	bd	47.66	0.30	bd	bd	0.05	bd	bd	0.11	bd	bd	NA	NA	bd	NA	NA	101.49
902	04/09/02-072	53.26	bd	bd	0.07	47.66	0.33	bd	bd	bd	bd	bd	bd	bd	bd	NA	NA	bd	NA	NA	101.31
902	04/09/02-073	53.48	bd	bd	0.07	47.55	0.19	bd	bd	bd	bd	bd	bd	bd	bd	NA	NA	bd	NA	NA	101.29
902	04/09/02-074	52.99	bd	bd	bd	47.35	0.16	bd	bd	0.04	bd	bd	bd	bd	bd	NA	NA	bd	NA	NA	100.54
902	04/09/02-075	53.01	bd	bd	bd	47.61	0.38	bd	bd	bd	bd	bd	0.07	0.14	bd	NA	NA	bd	NA	NA	101.21
902	04/09/02-076	52.08	bd	bd	2.34	46.33	0.38	0.04	bd	bd	bd	bd	bd	0.15	bd	NA	NA	bd	NA	NA	101.31
902	04/09/02-077	53.05	bd	bd	1.09	47.48	0.14	bd	bd	bd	bd	bd	0.07	0.13	bd	NA	NA	bd	NA	NA	101.96
902	27/04/01-020	52.90	bd	bd	bd	48.04	0.27	bd	bd	bd	bd	bd	0.16	bd	bd	bd	bd	bd	bd	bd	101.36
902	27/04/01-026	52.78	bd	bd	bd	47.62	0.22	bd	bd	bd	bd	bd	0.15	0.18	0.06	bd	bd	bd	bd	bd	101.01
902	27/04/01-032	52.66	bd	bd	bd	47.91	0.38	bd	bd	bd	bd	bd	bd	0.14	0.06	bd	bd	bd	bd	bd	101.14
902	27/04/01-045	53.03	bd	bd	0.15	48.03	0.15	bd	bd	bd	0.20	bd	bd	bd	bd	bd	bd	bd	bd	bd	101.55
902	27/04/01-050	52.60	bd	0.10	bd	47.65	0.56	0.05	bd	bd	0.09	bd	0.12	bd	bd	bd	bd	bd	bd	bd	101.17
906	26/04/01-016	52.87	bd	bd	0.07	47.74	0.10	0.04	bd	0.06	0.10	bd	bd	bd	bd	bd	bd	bd	bd	bd	100.98
910	26/04/01-025	51.47	bd	bd	0.19	46.78	1.67	bd	bd	bd	0.23	bd	bd	bd	bd	bd	bd	bd	bd	bd	100.33
910	26/04/01-030	52.11	bd	bd	bd	47.08	0.79	bd	bd	bd	0.21	bd	bd	0.26	0.04	bd	bd	0.05	bd	bd	100.54
910	26/04/01-033	51.45	bd	bd	bd	46.42	0.21	bd	bd	bd	0.84	bd	bd	bd	bd	bd	bd	bd	bd	bd	98.93
910	26/04/01-034	51.33	bd	bd	0.13	45.63	0.72	bd	0.06	0.04	bd	bd	bd	bd	0.05	bd	0.08	bd	bd	bd	98.03
910	26/04/01-053	52.47	bd	bd	bd	47.11	0.15	bd	bd	0.05	0.37	bd	bd	bd	bd	bd	bd	bd	bd	bd	100.16
910	26/04/01-058	51.85	bd	bd	0.10	47.12	0.13	bd	bd	0.05	bd	bd	bd	0.22	bd	bd	bd	bd	bd	bd	99.46

Table B1(vii). Sulphide analyses (wt%) contd.

Sample No	Analysis Ref	S	Au	Ag	Cu	Fe	As	Se	Sb	Te	Zn	Pb	Hg	Bi	Ga	Ge	Co	Cd	In	Cr	Total
910	26/04/01-059	51.66	bd	bd	bd	46.80	0.22	bd	bd	bd	0.08	bd	bd	0.13	bd	bd	bd	bd	bd	bd	98.90
00-BT-01	27/04/01-105	52.73	bd	bd	0.08	47.72	0.11	bd	bd	bd	0.38	bd	bd	bd	bd	bd	bd	bd	bd	bd	101.02
00-BT-01	27/04/01-109	52.92	bd	bd	0.06	48.16	0.06	bd	bd	bd	bd	bd	0.11	0.13	bd	bd	bd	bd	bd	bd	101.45
00-BT-02	27/04/01-001	52.91	bd	bd	0.14	48.00	0.18	0.04	bd	0.05	bd	bd	bd	bd	bd	bd	bd	bd	bd	bd	101.32
00-BT-02	27/04/01-008	52.81	bd	bd	0.27	47.54	0.36	bd	bd	0.06	bd	bd	bd	0.14	bd	bd	0.12	bd	bd	bd	101.30
00-BT-02	27/04/01-009	53.08	bd	bd	bd	48.45	0.09	bd	bd	bd	bd	bd	bd	bd	bd	bd	bd	bd	bd	bd	101.62
00-BT-02	27/04/01-014	52.56	bd	bd	0.13	48.49	0.24	0.05	bd	0.05	bd	bd	bd	0.19	bd	bd	bd	bd	bd	bd	101.71
00-BT-02	27/04/01-018	53.01	bd	bd	bd	48.00	0.34	bd	0.04	0.05	bd	bd	bd	bd	bd	bd	0.06	bd	bd	bd	101.49
00-BT-13	27/04/01-057	52.78	bd	bd	0.07	48.23	0.09	bd	bd	bd	bd	bd	0.12	0.20	bd	bd	bd	bd	bd	bd	101.49
00-BT-13	27/04/01-060	52.78	bd	bd	bd	48.12	0.14	bd	bd	bd	bd	bd	0.12	bd	bd	bd	bd	bd	bd	bd	101.16
00-BT-13	27/04/01-061	51.27	bd	0.13	0.12	46.13	2.17	bd	0.83	bd	bd	bd	0.22	0.15	bd	bd	bd	bd	bd	bd	101.02
00-BT-13	27/04/01-067	52.99	bd	bd	0.07	47.79	0.07	bd	0.06	bd	bd	bd	bd	bd	bd	bd	bd	0.04	bd	bd	101.02
00-BT-13	27/04/01-070	52.87	bd	bd	bd	47.72	0.11	bd	bd	bd	bd	bd	bd	bd	bd	bd	bd	0.05	bd	bd	100.75
00-BT-13	27/04/01-074	52.74	bd	0.14	bd	47.86	0.07	bd	bd	0.04	bd	bd	0.09	bd	0.04	bd	bd	0.06	bd	bd	101.04
00-BT-15	26/04/01-090	52.90	0.15	bd	0.37	47.70	0.06	bd	bd	bd	bd	bd	bd	bd	bd	bd	bd	bd	bd	bd	101.18
00-BT-15	26/04/01-097	52.80	bd	bd	0.35	47.31	0.13	bd	bd	bd	bd	bd	0.09	0.18	bd	bd	bd	bd	bd	bd	100.86
01BT076a	03/09/02-107	52.37	bd	bd	0.07	45.98	1.93	bd	0.28	bd	0.13	bd	0.09	0.22	bd	NA	NA	bd	NA	NA	101.05
01BT076a	03/09/02-108	52.04	bd	bd	bd	45.80	2.73	0.07	0.41	bd	bd	bd	bd	bd	bd	NA	NA	bd	NA	NA	101.05
01BT076a	03/09/02-109	53.80	bd	bd	bd	47.64	0.10	bd	0.04	bd	0.64	bd	bd	0.18	bd	NA	NA	bd	NA	NA	102.39
01BT076a	03/09/02-110	53.29	bd	bd	bd	46.72	0.65	bd	0.11	0.05	0.12	bd	bd	bd	0.04	NA	NA	bd	NA	NA	100.98
01BT076a	03/09/02-111	53.52	bd	bd	bd	47.32	0.10	bd	bd	0.08	0.29	bd	0.15	bd	bd	NA	NA	0.06	NA	NA	101.51
01BT076a	03/09/02-124	53.34	bd	bd	bd	47.39	0.07	bd	bd	bd	0.27	bd	0.10	bd	bd	NA	NA	bd	NA	NA	101.17
01BT076a	03/09/02-125	53.55	bd	bd	0.08	47.23	0.08	bd	bd	0.04	0.33	bd	bd	bd	bd	NA	NA	bd	NA	NA	101.30
01BT082a	03/09/02-052	52.67	bd	bd	bd	47.10	1.35	bd	0.06	bd	bd	bd	0.08	bd	bd	NA	NA	bd	NA	NA	101.26
01BT082a	03/09/02-053	52.75	bd	bd	0.07	47.02	1.36	bd	0.07	bd	bd	bd	0.07	bd	bd	NA	NA	bd	NA	NA	101.34
01BT082a	03/09/02-054	53.34	bd	bd	0.17	47.52	0.48	bd	bd	bd	bd	bd	bd	bd	0.07	NA	NA	bd	NA	NA	101.58
01BT082a	03/09/02-055	53.21	bd	bd	0.60	46.86	0.76	bd	bd	bd	0.46	bd	bd	0.18	bd	NA	NA	bd	NA	NA	102.07
01BT082a	03/09/02-060	53.57	bd	bd	bd	47.80	0.05	bd	bd	bd	0.12	bd	bd	bd	bd	NA	NA	bd	NA	NA	101.54
01BT082a	03/09/02-061	51.03	bd	bd	bd	46.47	3.78	bd	0.14	bd	bd	bd	bd	bd	bd	NA	NA	bd	NA	NA	101.42
01BT082a	03/09/02-062	51.70	bd	bd	bd	46.62	2.65	0.04	0.28	bd	bd	bd	bd	0.15	bd	NA	NA	bd	NA	NA	101.44
01BT082a	03/09/02-063	51.16	bd	bd	0.06	46.33	4.00	bd	0.10	bd	bd	bd	0.11	bd	bd	NA	NA	bd	NA	NA	101.76
01BT082a	03/09/02-064	53.27	bd	bd	0.36	47.20	0.40	bd	bd	0.05	bd	bd	bd	0.17	bd	NA	NA	bd	NA	NA	101.46
01BT082a	03/09/02-097	53.24	bd	bd	bd	47.43	0.84	bd	0.09	bd	bd	bd	0.10	bd	0.04	NA	NA	bd	NA	NA	101.74
01BT082a	03/09/02-098	53.16	bd	bd	bd	47.32	0.81	bd	0.15	bd	bd	bd	bd	bd	bd	NA	NA	bd	NA	NA	101.45
01BT082a	03/09/02-099	52.01	0.13	bd	0.06	45.56	2.98	bd	0.68	0.04	bd	bd	0.13	0.19	bd	NA	NA	bd	NA	NA	101.78
01BT082a	03/09/02-100	53.33	bd	bd	0.08	46.77	1.03	bd	0.15	bd	bd	bd	0.07	0.18	0.05	NA	NA	bd	NA	NA	101.64
01BT082a	03/09/02-101	53.57	bd	bd	0.09	46.92	0.64	bd	bd	bd	bd	bd	bd	0.15	0.05	NA	NA	bd	NA	NA	101.41
01BT082a	03/09/02-102	52.89	bd	bd	bd	46.98	1.27	bd	0.22	0.05	bd	bd	bd	bd	bd	NA	NA	0.08	NA	NA	101.48

Table B1(vii). Sulphide analyses (wt%) contd.

Sample No	Analysis Ref	S	Au	Ag	Cu	Fe	As	Se	Sb	Te	Zn	Pb	Hg	Bi	Ga	Ge	Co	Cd	In	Cr	Total
01BT082a	03/09/02-103	53.61	bd	bd	0.08	47.68	0.15	bd	0.07	bd	bd	bd	bd	bd	bd	NA	NA	bd	NA	NA	101.58
01BT082a	03/09/02-104	52.38	bd	bd	bd	46.65	2.26	bd	bd	bd	bd	bd	bd	0.16	bd	NA	NA	bd	NA	NA	101.45
01BT082a	03/09/02-105	53.09	bd	bd	0.10	47.34	0.83	bd	0.11	bd	bd	bd	bd	0.14	bd	NA	NA	bd	NA	NA	101.60
01BT082a	03/09/02-106	53.38	bd	bd	bd	47.66	0.64	bd	0.07	0.04	bd	bd	bd	0.19	bd	NA	NA	bd	NA	NA	101.98
01BT136	04/09/02-061	51.81	bd	bd	0.12	46.74	2.53	bd	0.16	bd	0.07	bd	bd	bd	bd	NA	NA	bd	NA	NA	101.43
01BT136	04/09/02-062	50.77	bd	bd	0.17	46.28	3.85	bd	0.41	bd	bd	bd	bd	bd	0.04	NA	NA	bd	NA	NA	101.53
01BT136	04/09/02-063	53.13	bd	bd	bd	48.09	0.43	bd	bd	bd	bd	bd	bd	bd	0.06	NA	NA	bd	NA	NA	101.72
01BT136	04/09/02-064	51.21	bd	bd	1.40	45.54	2.58	bd	0.47	bd	bd	bd	bd	bd	bd	NA	NA	bd	NA	NA	101.20
01BT138	03/09/02-159	52.59	bd	bd	0.11	46.26	1.21	0.05	0.04	bd	0.12	bd	0.07	0.15	bd	NA	NA	bd	NA	NA	100.61
01BT138	03/09/02-160	53.08	bd	bd	0.10	46.50	1.25	0.04	0.05	bd	0.13	bd	bd	bd	bd	NA	NA	bd	NA	NA	101.14
01BT138	03/09/02-164	52.38	0.13	0.21	0.42	45.14	1.47	bd	0.31	bd	bd	bd	bd	0.17	bd	NA	NA	bd	NA	NA	100.23
01BT138	03/09/02-165	53.51	bd	bd	bd	46.26	0.38	bd	0.04	0.04	bd	bd	bd	bd	bd	NA	NA	bd	NA	NA	100.22
01BT138	03/09/02-166	53.09	bd	bd	0.07	44.79	0.71	bd	0.07	bd	bd	bd	bd	0.14	0.08	NA	NA	bd	NA	NA	98.95
01BT162	04/09/02-012	53.53	bd	bd	bd	48.44	0.06	bd	bd	bd	bd	bd	bd	bd	bd	NA	NA	bd	NA	NA	102.03
01BT162	04/09/02-013	53.71	bd	bd	bd	48.08	0.08	bd	bd	bd	bd	bd	bd	0.22	bd	NA	NA	bd	NA	NA	102.08
01BT162	04/09/02-014	53.54	bd	bd	bd	47.98	0.06	bd	bd	bd	bd	bd	0.08	0.14	bd	NA	NA	bd	NA	NA	101.80
01BT162	04/09/02-015	53.59	bd	bd	bd	48.08	0.09	bd	bd	bd	bd	bd	bd	0.17	bd	NA	NA	bd	NA	NA	101.93
01BT162	04/09/02-016	53.56	bd	bd	bd	48.08	0.08	0.04	bd	bd	bd	bd	bd	bd	bd	NA	NA	bd	NA	NA	101.77
01BT162	04/09/02-017	53.51	bd	bd	bd	48.36	0.05	0.06	bd	bd	bd	bd	0.09	0.16	bd	NA	NA	bd	NA	NA	102.24
01BT162	04/09/02-021	53.38	bd	bd	bd	48.04	0.09	bd	bd	0.04	bd	bd	0.11	bd	bd	NA	NA	bd	NA	NA	101.66
01BT162	04/09/02-022	53.46	bd	bd	bd	48.07	bd	bd	bd	bd	bd	bd	0.07	0.23	bd	NA	NA	bd	NA	NA	101.83
01BT162	04/09/02-023	53.23	bd	bd	bd	48.04	0.47	0.04	0.06	bd	bd	bd	0.10	bd	bd	NA	NA	bd	NA	NA	101.93
01BT162	04/09/02-024	52.80	bd	bd	0.06	47.51	1.18	bd	bd	bd	bd	bd	bd	bd	bd	NA	NA	bd	NA	NA	101.54
01BT162	04/09/02-025	53.16	bd	bd	bd	47.55	0.81	bd	0.07	0.04	bd	bd	bd	bd	bd	NA	NA	0.07	NA	NA	101.71
01BT162	04/09/02-026	53.76	bd	bd	bd	48.16	0.16	0.05	bd	bd	bd	bd	bd	bd	0.04	NA	NA	bd	NA	NA	102.17
01BT162	04/09/02-027	53.48	0.11	bd	bd	48.28	0.05	bd	bd	bd	0.10	bd	bd	bd	bd	NA	NA	bd	NA	NA	102.02
BL-19B	27/04/01-090	51.73	bd	bd	0.11	46.62	0.10	bd	bd	bd	0.24	bd	bd	bd	bd	bd	bd	bd	bd	bd	98.80
BL-19B	27/04/01-099	52.98	bd	bd	0.07	48.02	0.10	bd	bd	bd	0.97	bd	bd	0.15	0.05	bd	0.07	bd	bd	bd	102.40
BL22-b	27/04/01-153	52.65	bd	bd	0.06	48.36	0.06	0.04	bd	bd	bd	bd	bd	bd	bd	bd	0.05	bd	bd	bd	101.22
BTB-01(C)	27/04/01-080	51.63	bd	bd	0.22	45.38	1.24	0.05	1.31	bd	bd	bd	0.15	bd	bd	bd	0.07	bd	bd	bd	100.04
BTB-01(C)	27/04/01-083	52.51	bd	bd	0.68	47.15	0.27	bd	0.05	bd	bd	bd	bd	0.17	bd	bd	bd	bd	bd	bd	100.83
BTB-01(C)	27/04/01-085	52.74	bd	bd	0.17	48.21	0.28	0.04	bd	0.06	bd	bd	bd	bd	bd	bd	bd	bd	bd	bd	101.50
Arsenopyrite																					
901	26/04/01-060	19.56	bd	bd	0.11	34.65	44.31	0.20	0.04	0.27	bd	bd	bd	bd	bd	bd	bd	bd	bd	bd	99.14
901	26/04/01-061	19.41	bd	bd	bd	33.29	44.32	0.19	bd	0.04	bd	bd	0.10	bd	bd	bd	bd	bd	bd	bd	97.34
901	26/04/01-062	19.75	bd	bd	0.25	33.49	43.42	0.25	0.05	0.21	bd	bd	0.07	bd	bd	bd	bd	bd	bd	bd	97.49
910	26/04/01-019	20.29	bd	bd	0.24	35.03	45.06	0.14	0.04	0.05	0.57	bd	bd	bd	bd	bd	bd	bd	bd	bd	101.41

Table B1(vii). Sulphide analyses (wt%) contd.

Sample No	Analysis Ref	S	Au	Ag	Cu	Fe	As	Se	Sb	Te	Zn	Pb	Hg	Bi	Ga	Ge	Co	Cd	In	Cr	Total
910	26/04/01-020	19.52	0.15	bd	0.12	34.23	45.92	0.10	bd	0.06	0.28	bd	bd	bd	bd	bd	bd	bd	bd	bd	100.39
910	26/04/01-038	21.00	bd	bd	0.09	34.92	43.73	0.11	bd	0.08	0.34	bd	bd	bd	bd	bd	bd	0.06	bd	bd	100.35
910	26/04/01-039	20.09	0.16	bd	0.06	34.55	44.58	0.15	bd	bd	0.85	bd	0.12	bd	bd	bd	bd	bd	bd	bd	100.55
																					0.00
Chalcopyrite																					0.00
901	26/04/01-066	34.20	0.16	bd	34.43	27.95	0.05	bd	bd	bd	0.33	bd	bd	0.14	bd	bd	bd	bd	bd	bd	97.25
901	26/04/01-071	34.55	bd	bd	34.50	29.31	0.07	bd	bd	bd	0.10	bd	bd	0.15	0.05	bd	bd	0.05	bd	bd	98.78
901	26/04/01-077	34.84	bd	bd	34.67	29.15	0.06	bd	0.04	0.05	bd	bd	bd	bd	bd	bd	bd	bd	bd	bd	98.80
902	27/04/01-022	35.34	bd	bd	34.32	30.07	bd	0.04	bd	bd	bd	bd	bd	bd	bd	bd	bd	bd	bd	bd	99.77
902	27/04/01-024	35.68	bd	bd	34.62	30.15	0.08	0.08	bd	bd	0.10	bd	bd	bd	bd	bd	bd	bd	bd	bd	100.72
902	27/04/01-028	35.72	bd	bd	34.45	30.42	0.09	bd	bd	bd	0.08	bd	0.07	bd	bd	bd	bd	bd	bd	bd	100.84
902	27/04/01-029	35.37	bd	bd	34.12	30.45	0.11	bd	bd	bd	bd	bd	bd	bd	bd	bd	bd	bd	bd	bd	100.04
902	27/04/01-033	34.96	bd	bd	34.47	30.40	0.05	bd	bd	bd	bd	bd	bd	bd	bd	bd	bd	bd	bd	bd	99.89
902	27/04/01-040	35.30	bd	bd	34.56	30.11	0.09	bd	bd	0.06	0.07	bd	0.09	bd	bd	bd	bd	bd	bd	bd	100.29
902	27/04/01-048	35.43	bd	bd	34.71	29.87	0.06	bd	bd	bd	0.20	bd	bd	0.15	0.06	bd	bd	bd	bd	bd	100.48
902	27/04/01-052	37.14	bd	bd	31.83	31.35	0.11	bd	bd	0.05	0.10	bd	0.09	bd	0.11	bd	bd	bd	bd	bd	100.77
906	26/04/01-002	35.65	bd	bd	35.49	30.00	0.10	bd	0.04	bd	bd	bd	bd	bd	0.04	bd	bd	bd	bd	bd	101.32
906	26/04/01-012	34.60	bd	0.87	35.68	26.32	0.78	bd	0.57	bd	1.03	bd	0.07	bd	0.04	bd	bd	bd	bd	bd	99.95
910	26/04/01-027	35.33	bd	bd	33.98	29.37	0.06	bd	bd	bd	0.35	bd	0.07	0.14	bd	bd	bd	0.05	bd	bd	99.35
910	26/04/01-044	34.99	bd	bd	35.02	29.14	bd	bd	bd	0.05	0.28	bd	0.07	0.21	0.05	bd	bd	bd	bd	bd	99.80
910	26/04/01-045	34.88	bd	0.11	33.18	29.10	0.08	bd	0.05	bd	0.18	bd	bd	bd	bd	bd	bd	bd	bd	bd	97.58
00-BT-01	27/04/01-106	35.16	bd	bd	34.88	29.68	bd	bd	bd	0.05	0.71	bd	bd	bd	0.04	bd	bd	bd	bd	bd	100.51
00-BT-02	27/04/01-002	35.63	bd	bd	35.18	30.55	0.07	bd	bd	bd	bd	bd	bd	bd	bd	bd	bd	bd	bd	bd	101.43
00-BT-02	27/04/01-005	35.64	bd	bd	35.32	30.55	0.08	bd	bd	bd	bd	bd	bd	bd	bd	bd	bd	bd	bd	bd	101.59
00-BT-13	27/04/01-056	35.25	bd	bd	35.09	29.94	0.11	bd	bd	0.05	0.09	bd	bd	bd	0.10	bd	bd	bd	bd	bd	100.64
00-BT-13	27/04/01-064	35.46	bd	bd	35.39	29.90	0.06	0.05	bd	bd	bd	bd	bd	bd	bd	bd	bd	bd	bd	bd	100.87
00-BT-13	27/04/01-066	35.21	bd	bd	35.34	30.13	0.08	bd	bd	bd	bd	bd	bd	bd	bd	bd	bd	0.05	bd	bd	100.81
00-BT-13	27/04/01-069	35.19	bd	bd	34.59	30.38	0.11	bd	bd	bd	0.08	bd	0.07	bd	bd	bd	bd	bd	bd	bd	100.42
00-BT-13	27/04/01-073	35.19	bd	bd	35.02	30.00	0.08	bd	bd	0.07	bd	bd	0.08	bd	0.05	bd	bd	bd	bd	bd	100.48
BL1	14/12/00-088	34.66	bd	0.27	34.32	29.98	0.12	bd	bd	0.05	0.23	bd	0.12	bd	NA	NA	NA	NA	NA	NA	99.75
BL-19B	27/04/01-093	35.24	bd	bd	35.44	30.26	0.11	bd	bd	bd	0.17	bd	bd	bd	bd	bd	0.06	bd	bd	bd	101.27
BL-19B	27/04/01-100	35.48	bd	bd	34.89	30.01	0.17	0.06	bd	0.05	0.62	bd	bd	bd	bd	bd	bd	bd	bd	bd	101.26
BL22-b	27/04/01-154	35.12	bd	bd	34.52	30.28	0.06	0.05	bd	bd	0.09	bd	bd	bd	0.05	bd	bd	0.05	bd	bd	100.21
BL22-b	27/04/01-168	35.02	bd	bd	34.72	30.23	0.05	bd	bd	bd	0.22	bd	bd	0.15	0.04	bd	bd	bd	bd	bd	100.43
BTB-01(B)	27/04/01-124	35.25	bd	bd	33.87	30.02	0.09	bd	0.04	bd	0.16	bd	bd	bd	bd	bd	bd	bd	bd	bd	99.42
BTB-01(B)	27/04/01-141	35.27	bd	bd	34.14	29.95	0.08	bd	bd	0.07	bd	bd	bd	bd	bd	bd	bd	bd	bd	bd	99.51
BTB-01(C)	13/12/00-033	34.56	bd	bd	33.42	29.58	0.08	bd	bd	bd	1.46	bd	bd	bd	NA	NA	NA	NA	NA	NA	99.10
BTB-01(C)	13/12/00-034	34.10	bd	0.18	33.38	29.56	0.09	bd	bd	bd	0.96	bd	0.07	bd	NA	NA	NA	NA	NA	NA	98.34

Table B1(vii). Sulphide analyses (wt%) contd.

Sample No	Analysis Ref	S	Au	Ag	Cu	Fe	As	Se	Sb	Te	Zn	Pb	Hg	Bi	Ga	Ge	Co	Cd	In	Cr	Total
BTB-01(C)	13/12/00-047	50.04	bd	bd	24.87	24.87	0.05	bd	bd	bd	0.09	bd	bd	bd	NA	NA	NA	NA	NA	NA	99.92
BTB-01(C)	13/12/00-048	49.78	bd	0.06	24.84	25.12	0.03	bd	bd	bd	0.10	bd	0.02	bd	NA	NA	NA	NA	NA	NA	99.95
BTB-01(C)	13/12/00-049	49.85	bd	0.06	25.04	24.88	0.05	0.04	bd	bd	bd	bd	bd	bd	NA	NA	NA	NA	NA	NA	99.92
BTB-01(C)	27/04/01-079	50.17	bd	bd	24.58	24.11	0.06	0.04	bd	0.02	0.98	bd	bd	bd	bd	bd	bd	bd	bd	bd	99.95
Sphalerite																					
901	04/09/02-033	49.38	bd	bd	0.20	1.60	bd	0.03	bd	0.02	48.67	bd	0.03	bd	bd	NA	NA	0.07	NA	NA	99.99
901	04/09/02-034	49.41	bd	bd	0.32	1.69	bd	0.03	bd	bd	48.47	bd	bd	bd	bd	NA	NA	0.04	NA	NA	99.97
901	04/09/02-035	49.60	bd	bd	0.25	2.09	0.03	0.04	0.04	bd	47.86	bd	bd	bd	bd	NA	NA	0.08	NA	NA	99.99
902	27/04/01-037	50.44	bd	bd	0.26	1.11	bd	bd	bd	bd	48.03	bd	bd	bd	bd	bd	bd	0.11	bd	bd	99.93
902	27/04/01-038	50.60	bd	bd	bd	0.75	bd	bd	0.02	bd	48.35	bd	0.02	bd	bd	bd	bd	0.12	bd	bd	99.86
902	27/04/01-042	50.23	bd	bd	bd	1.12	0.03	bd	bd	bd	48.44	bd	bd	bd	bd	bd	bd	0.08	bd	bd	99.91
902	27/04/01-046	50.09	bd	bd	bd	0.79	bd	bd	bd	bd	48.88	bd	0.03	bd	bd	bd	bd	0.10	bd	bd	99.89
902	27/04/01-049	50.36	bd	bd	0.17	1.54	0.05	bd	bd	bd	47.72	bd	0.03	bd	bd	bd	bd	0.08	bd	bd	99.96
902	27/04/01-053	50.12	bd	bd	0.31	1.57	bd	bd	bd	bd	47.76	bd	bd	bd	bd	bd	bd	0.09	0.03	bd	99.88
910	26/04/01-024	50.39	bd	bd	0.51	1.42	1.86	bd	bd	bd	45.65	bd	bd	bd	bd	bd	bd	0.09	bd	bd	99.93
910	26/04/01-026	50.16	bd	bd	bd	1.13	bd	0.02	bd	bd	48.50	bd	0.02	bd	bd	bd	bd	0.08	bd	bd	99.90
910	26/04/01-031	49.85	bd	bd	bd	0.96	bd	0.03	bd	bd	48.98	bd	bd	bd	bd	bd	bd	0.08	bd	bd	99.89
910	26/04/01-032	50.06	bd	bd	bd	1.29	bd	bd	0.02	bd	48.48	bd	bd	bd	bd	bd	bd	0.08	bd	bd	99.92
910	26/04/01-037	49.94	bd	bd	0.36	0.78	bd	bd	0.02	bd	48.78	bd	bd	bd	bd	bd	bd	0.09	bd	bd	99.96
910	26/04/01-042	49.80	bd	bd	bd	0.77	0.04	bd	bd	bd	49.25	bd	bd	bd	bd	bd	bd	0.07	bd	bd	99.92
910	26/04/01-043	49.83	bd	bd	0.23	0.87	bd	bd	0.02	bd	48.90	bd	0.03	bd	bd	bd	bd	0.05	bd	bd	99.94
910	26/04/01-054	49.86	bd	bd	bd	0.78	0.05	bd	0.02	bd	49.14	bd	bd	bd	bd	bd	bd	0.08	bd	bd	99.93
910	26/04/01-057	50.02	bd	bd	bd	0.82	bd	bd	bd	bd	48.96	bd	bd	bd	bd	bd	bd	0.09	bd	bd	99.88
00-BT-01	27/04/01-104	50.18	bd	0.06	0.10	bd	bd	bd	0.02	bd	49.40	bd	0.02	bd	bd	bd	bd	0.18	bd	bd	99.96
00-BT-15	26/04/01-099	50.19	bd	bd	0.28	0.15	bd	0.03	bd	bd	49.10	bd	0.02	bd	bd	bd	bd	0.16	bd	bd	99.93
00-BT-15	26/04/01-101	49.71	bd	bd	0.42	0.06	0.04	bd	0.02	0.03	49.50	bd	bd	bd	bd	bd	bd	0.15	bd	bd	99.92
00-BT-15	26/04/01-105	50.59	bd	bd	0.44	0.12	0.05	bd	bd	bd	48.56	bd	0.02	bd	bd	bd	bd	0.15	bd	bd	99.93
01BT082a	03/09/02-051	50.07	bd	bd	0.20	0.49	bd	bd	bd	bd	48.87	bd	0.04	bd	bd	NA	NA	0.28	NA	NA	99.96
01BT136	04/09/02-052	49.71	bd	bd	0.51	0.13	0.04	bd	bd	bd	49.50	bd	bd	bd	bd	NA	NA	0.12	NA	NA	100.00
01BT136	04/09/02-053	49.87	bd	bd	0.52	0.10	bd	bd	0.02	bd	49.33	bd	0.02	bd	bd	NA	NA	0.12	NA	NA	99.97
01BT136	04/09/02-056	49.44	bd	bd	0.07	1.74	bd	bd	bd	bd	48.56	bd	bd	bd	bd	NA	NA	0.11	NA	NA	99.92
BL1	14/12/00-085	50.30	bd	bd	0.19	0.19	0.04	bd	bd	bd	49.27	bd	bd	bd	NA	NA	NA	NA	NA	NA	99.99
BL1	14/12/00-086	50.10	bd	0.66	1.52	0.03	bd	0.04	bd	0.02	47.58	bd	0.03	bd	NA	NA	NA	NA	NA	NA	99.98
BL1	14/12/00-091	49.93	bd	bd	0.30	0.43	0.06	0.06	bd	bd	49.16	bd	0.04	bd	NA	NA	NA	0.11	NA	NA	100.08
BL1	14/12/00-092	49.97	bd	bd	0.20	0.11	0.04	0.02	0.02	bd	49.59	bd	bd	bd	NA	NA	NA	0.11	NA	NA	100.07
BL-19B	27/04/01-092	50.33	bd	bd	0.12	0.16	bd	bd	0.02	bd	49.16	bd	0.03	bd	bd	bd	bd	0.14	bd	bd	99.96
BL-19B	27/04/01-095	50.64	bd	bd	0.48	0.44	bd	bd	bd	bd	48.23	bd	bd	bd	bd	bd	bd	0.14	bd	bd	99.93

Table B1(vii). Sulphide analyses (wt%) contd.

Sample No	Analysis Ref	S	Au	Ag	Cu	Fe	As	Se	Sb	Te	Zn	Pb	Hg	Bi	Ga	Ge	Co	Cd	In	Cr	Total
BL22-b	27/04/01-156	33.70	bd	bd	bd	0.17	bd	bd	bd	bd	66.57	bd	0.08	bd	bd	bd	bd	0.37	bd	bd	100.89
BL22-b	27/04/01-169	33.74	bd	bd	0.15	0.31	0.06	bd	bd	bd	66.52	bd	bd	bd	bd	bd	bd	0.37	bd	bd	101.16
BL22-b	27/04/01-172	32.71	bd	bd	0.51	0.95	bd	bd	bd	bd	66.97	bd	bd	bd	bd	bd	bd	0.35	bd	bd	101.49
BL711.A	14/12/00-009	32.92	bd	bd	0.12	0.22	bd	0.06	0.04	bd	66.77	bd	0.11	bd	NA	NA	NA	NA	NA	NA	100.24
BTB-01(C)	13/12/00-036	32.45	bd	bd	0.19	0.17	0.05	0.05	bd	bd	65.30	bd	0.12	bd	NA	NA	NA	NA	NA	NA	98.33
BTB-01(C)	13/12/00-037	32.33	bd	bd	0.28	0.09	bd	bd	0.04	bd	65.48	bd	0.29	bd	NA	NA	NA	NA	NA	NA	98.51
Tennantite-tetrahedrite																					
901	04/09/02-028	26.09	bd	0.12	39.67	5.23	9.32	0.08	17.31	bd	3.04	bd	bd	bd	bd	NA	NA	bd	NA	NA	100.85
901	04/09/02-029	25.84	bd	bd	39.06	4.41	6.49	0.06	21.84	0.06	3.93	bd	bd	bd	bd	NA	NA	bd	NA	NA	101.69
901	04/09/02-030	25.91	bd	bd	39.79	4.78	8.15	0.05	19.46	0.05	3.51	bd	bd	bd	0.10	NA	NA	bd	NA	NA	101.79
901	04/09/02-031	26.03	bd	0.13	39.61	4.83	9.38	0.11	17.33	bd	3.35	bd	bd	0.14	0.05	NA	NA	0.05	NA	NA	101.01
901	04/09/02-032	26.04	bd	0.16	39.46	5.08	8.37	0.09	18.85	bd	3.43	bd	bd	0.16	bd	NA	NA	bd	NA	NA	101.62
901	04/09/02-036	26.19	bd	bd	39.54	5.50	8.01	0.08	18.72	bd	3.32	bd	bd	0.16	bd	NA	NA	0.05	NA	NA	101.56
902	27/04/01-025	28.77	bd	bd	42.22	4.88	16.93	0.07	5.78	0.09	3.92	bd	bd	bd	0.05	bd	bd	0.06	bd	bd	102.77
902	27/04/01-039	28.99	bd	0.33	41.33	4.63	17.66	0.07	5.01	0.06	3.85	bd	bd	bd	0.04	bd	bd	bd	bd	bd	101.97
906	26/04/01-004	28.54	bd	0.87	41.12	1.87	16.79	0.08	5.70	bd	6.30	bd	0.08	bd	bd	bd	bd	bd	bd	bd	101.33
906	26/04/01-005	28.27	bd	5.74	38.61	1.70	15.23	bd	5.16	0.12	5.73	bd	bd	bd	bd	bd	bd	0.07	bd	bd	100.62
906	26/04/01-007	25.33	bd	19.87	31.44	1.30	10.88	bd	4.36	bd	5.31	bd	0.10	bd	bd	bd	bd	0.08	bd	bd	98.66
906	26/04/01-010	25.15	bd	17.62	34.70	1.45	10.74	0.07	4.56	bd	5.91	bd	bd	bd	bd	bd	bd	0.07	bd	bd	100.27
906	26/04/01-013	24.98	bd	18.68	33.16	1.96	10.36	0.08	4.71	bd	5.39	bd	bd	bd	bd	bd	bd	0.08	bd	bd	99.40
906	26/04/01-015	28.41	bd	0.23	42.52	1.65	17.36	bd	5.78	bd	6.64	bd	0.14	bd	bd	bd	bd	0.11	bd	bd	102.84
906	26/04/01-082	25.02	bd	19.82	33.07	1.43	9.80	bd	4.25	bd	5.27	bd	0.08	bd	bd	bd	bd	bd	bd	bd	98.74
910	26/04/01-021	26.64	bd	1.78	38.21	1.81	7.82	bd	20.33	0.04	5.95	bd	0.16	bd	0.07	bd	bd	bd	bd	bd	102.82
910	26/04/01-022	28.55	bd	0.61	41.96	4.50	16.14	0.07	7.19	bd	3.65	bd	bd	bd	bd	bd	bd	bd	bd	bd	102.66
910	26/04/01-036	28.32	bd	0.60	42.56	4.17	16.28	0.12	7.02	bd	3.67	bd	bd	bd	bd	bd	bd	bd	bd	bd	102.73
910	26/04/01-046	28.35	bd	0.47	41.91	4.16	16.43	bd	7.06	0.05	3.99	bd	0.12	bd	bd	bd	bd	0.06	bd	bd	102.59
910	26/04/01-047	27.14	bd	1.01	39.52	3.12	10.43	0.05	15.95	bd	5.12	bd	bd	bd	bd	bd	bd	0.07	bd	bd	102.41
00-BT-02	27/04/01-006	29.27	bd	0.19	42.88	1.39	19.17	0.08	2.18	bd	6.92	bd	0.09	bd	bd	bd	bd	bd	bd	bd	102.18
00-BT-02	27/04/01-007	29.34	bd	0.23	42.14	1.47	18.93	0.08	2.53	0.04	6.89	bd	0.21	bd	0.05	bd	bd	0.07	bd	bd	101.98
00-BT-13	27/04/01-058	29.00	bd	0.21	42.78	1.54	18.70	0.08	3.15	bd	6.96	bd	0.10	bd	bd	bd	bd	bd	bd	bd	102.51
00-BT-13	27/04/01-059	29.31	bd	0.24	42.30	2.00	18.18	0.10	3.25	0.05	6.63	bd	bd	bd	bd	bd	bd	0.11	bd	bd	102.16
00-BT-13	27/04/01-063	28.70	bd	0.17	43.01	1.95	18.73	bd	3.15	bd	6.41	bd	0.10	bd	bd	bd	bd	0.09	bd	bd	102.32
00-BT-13	27/04/01-068	29.01	bd	0.49	43.42	1.30	18.14	0.11	2.84	bd	7.19	bd	bd	bd	bd	bd	bd	0.09	bd	bd	102.59
00-BT-13	27/04/01-072	28.98	bd	0.37	43.03	1.50	18.94	0.09	2.73	0.04	6.92	bd	0.08	bd	bd	bd	bd	0.08	bd	bd	102.74
01BT002a	03/09/02-026	28.45	bd	bd	43.39	1.76	20.23	0.11	0.79	0.04	6.59	bd	bd	0.15	bd	NA	NA	0.07	NA	NA	101.57
01BT002a	03/09/02-027	28.20	bd	0.11	43.20	1.80	20.17	0.05	0.73	bd	6.58	bd	0.11	bd	bd	NA	NA	0.08	NA	NA	101.03
01BT002a	03/09/02-028	28.51	bd	bd	43.47	1.86	20.38	0.13	0.80	bd	6.60	bd	bd	bd	bd	NA	NA	0.08	NA	NA	101.82

Table B1(vii). Sulphide analyses (wt%) contd.

Sample No	Analysis Ref	S	Au	Ag	Cu	Fe	As	Se	Sb	Te	Zn	Pb	Hg	Bi	Ga	Ge	Co	Cd	In	Cr	Total
01BT002a	03/09/02-029	28.11	bd	bd	43.53	1.80	20.78	0.13	0.78	bd	6.56	bd	bd	bd	bd	NA	NA	0.08	NA	NA	101.76
01BT002a	03/09/02-030	28.08	bd	bd	43.45	1.84	20.25	0.08	0.70	0.04	6.57	bd	bd	bd	bd	NA	NA	0.05	NA	NA	101.06
01BT002a	03/09/02-031	28.22	bd	bd	43.12	1.80	20.17	0.07	0.83	bd	6.59	bd	bd	bd	0.04	NA	NA	bd	NA	NA	100.84
01BT002a	03/09/02-032	28.39	bd	bd	43.72	1.84	20.53	0.06	0.77	bd	6.59	bd	0.17	bd	bd	NA	NA	0.10	NA	NA	102.15
01BT002a	03/09/02-033	28.33	bd	bd	42.83	1.65	20.17	0.13	0.68	0.09	6.78	bd	bd	bd	0.06	NA	NA	0.06	NA	NA	100.76
01BT002a	03/09/02-034	28.10	bd	bd	43.18	1.66	20.38	0.10	0.68	0.04	6.78	bd	bd	bd	0.05	NA	NA	0.08	NA	NA	101.05
01BT076a	03/09/02-121	27.17	bd	0.27	40.93	1.93	16.25	0.05	7.04	bd	6.92	bd	0.24	bd	bd	NA	NA	0.11	NA	NA	100.89
01BT076a	03/09/02-122	27.30	bd	0.30	40.91	1.75	16.32	0.07	6.92	bd	7.06	bd	0.43	0.13	bd	NA	NA	0.12	NA	NA	101.29
01BT076a	03/09/02-123	27.25	bd	0.30	41.01	1.78	16.33	0.04	6.91	bd	7.00	bd	0.30	bd	bd	NA	NA	0.15	NA	NA	101.05
01BT082a	03/09/02-078	27.42	bd	1.05	41.02	2.01	16.40	0.07	6.24	0.04	6.20	bd	0.13	bd	bd	NA	NA	0.19	NA	NA	100.78
01BT082a	03/09/02-081	27.03	bd	1.44	40.51	1.73	14.06	0.06	9.87	bd	6.46	bd	0.19	bd	bd	NA	NA	0.21	NA	NA	101.54
01BT082a	03/09/02-082	27.09	bd	1.30	40.71	1.72	14.62	0.06	9.19	bd	6.42	bd	0.22	bd	bd	NA	NA	0.22	NA	NA	101.56
01BT082a	03/09/02-083	26.93	bd	1.15	39.60	1.73	14.86	0.12	8.50	bd	6.24	bd	0.10	bd	0.13	NA	NA	0.18	NA	NA	99.53
01BT082a	03/09/02-084	26.99	bd	1.34	40.72	1.87	15.21	bd	8.37	bd	6.32	bd	0.21	bd	0.07	NA	NA	0.15	NA	NA	101.24
01BT136	04/09/02-050	28.14	bd	0.33	42.68	1.44	19.31	0.07	2.62	0.06	7.50	bd	bd	bd	bd	NA	NA	0.06	NA	NA	102.21
01BT136	04/09/02-051	27.80	bd	0.31	42.93	1.47	19.21	bd	2.45	bd	7.21	bd	bd	bd	0.04	NA	NA	0.11	NA	NA	101.51
01BT136	04/09/02-054	27.78	bd	0.56	41.66	2.42	18.47	0.08	3.51	bd	6.72	bd	0.15	bd	bd	NA	NA	0.10	NA	NA	101.44
01BT136	04/09/02-055	27.87	bd	0.66	41.59	2.44	18.32	bd	3.63	bd	6.71	bd	bd	bd	bd	NA	NA	0.09	NA	NA	101.32
01BT136	04/09/02-057	27.87	bd	0.50	42.39	1.87	18.96	0.05	3.09	bd	6.84	bd	0.08	bd	0.08	NA	NA	0.10	NA	NA	101.82
01BT136	04/09/02-058	27.80	bd	0.52	42.33	1.50	19.04	0.05	2.56	bd	7.06	bd	bd	bd	0.06	NA	NA	0.08	NA	NA	101.01
01BT136	04/09/02-059	27.87	bd	0.46	42.63	1.45	18.91	0.10	2.68	bd	7.16	bd	0.14	bd	bd	NA	NA	0.08	NA	NA	101.48
01BT136	04/09/02-060	27.74	bd	0.39	42.86	1.45	18.95	0.11	2.78	bd	7.10	bd	0.10	bd	bd	NA	NA	0.06	NA	NA	101.53
01BT138	03/09/02-155	27.91	bd	0.45	42.19	2.85	18.53	0.11	3.93	bd	5.49	bd	bd	bd	bd	NA	NA	bd	NA	NA	101.46
01BT138	03/09/02-156	28.02	bd	0.46	42.25	2.95	18.53	0.11	3.83	bd	5.44	bd	bd	bd	bd	NA	NA	bd	NA	NA	101.59
01BT138	03/09/02-157	28.01	bd	0.49	42.21	2.83	18.64	bd	3.81	bd	5.44	bd	bd	bd	bd	NA	NA	0.05	NA	NA	101.48
01BT138	03/09/02-158	28.14	bd	0.31	42.35	2.87	18.69	0.07	3.79	bd	5.57	bd	bd	bd	bd	NA	NA	bd	NA	NA	101.79
01BT162	04/09/02-001	27.41	bd	bd	41.37	1.41	16.95	0.05	5.64	0.07	7.41	bd	bd	bd	bd	NA	NA	0.14	NA	NA	100.45
01BT162	04/09/02-002	27.27	bd	0.12	41.16	1.55	16.91	0.09	5.77	0.09	7.35	bd	0.10	bd	bd	NA	NA	0.10	NA	NA	100.50
01BT162	04/09/02-003	27.21	bd	0.11	41.38	1.56	16.81	0.08	5.66	bd	7.08	bd	0.20	bd	bd	NA	NA	0.14	NA	NA	100.23
01BT162	04/09/02-004	27.37	bd	0.16	41.36	1.45	16.96	0.07	5.76	0.05	7.28	bd	bd	bd	0.06	NA	NA	0.13	NA	NA	100.66
01BT162	04/09/02-005	27.58	bd	0.12	41.71	1.29	17.49	0.05	4.82	0.08	7.12	bd	bd	bd	bd	NA	NA	0.13	NA	NA	100.39
01BT162	04/09/02-006	27.34	bd	0.13	41.52	1.27	17.32	bd	5.16	0.07	7.12	bd	bd	bd	bd	NA	NA	0.08	NA	NA	100.01
01BT162	04/09/02-007	27.20	0.12	0.13	41.54	1.40	17.54	0.09	5.14	0.06	7.01	bd	bd	bd	0.05	NA	NA	0.14	NA	NA	100.41
BL1	14/12/00-032	27.89	bd	0.55	41.51	1.34	17.53	0.09	4.79	bd	6.92	bd	bd	bd	NA	NA	NA	NA	NA	NA	100.62
BL1	14/12/00-045	27.60	bd	0.29	40.73	1.11	16.62	0.04	6.18	0.05	7.41	bd	0.16	bd	NA	NA	NA	NA	NA	NA	100.19
BL1	14/12/00-048	27.70	bd	0.44	42.11	1.32	17.38	0.06	5.13	0.05	6.97	bd	0.12	bd	NA	NA	NA	NA	NA	NA	101.28
BL1	14/12/00-049	27.50	bd	0.49	41.41	2.17	17.38	0.08	4.90	0.05	6.77	bd	0.14	bd	NA	NA	NA	NA	NA	NA	100.89
BL1	14/12/00-050	27.80	0.12	0.15	42.53	1.36	17.10	0.09	5.49	bd	7.09	bd	0.09	bd	NA	NA	NA	NA	NA	NA	101.82

Table B1(vii). Sulphide analyses (wt%) contd.

Sample No	Analysis Ref	S	Au	Ag	Cu	Fe	As	Se	Sb	Te	Zn	Pb	Hg	Bi	Ga	Ge	Co	Cd	In	Cr	Total
BL1	14/12/00-051	28.03	bd	0.56	41.95	1.43	17.46	0.11	5.08	bd	7.07	bd	bd	0.13	NA	NA	NA	NA	NA	NA	101.82
BL1	14/12/00-052	27.73	bd	0.45	42.11	1.38	17.47	0.06	4.81	bd	7.13	bd	0.07	bd	NA	NA	NA	NA	NA	NA	101.21
BL1	14/12/00-053	27.79	bd	0.14	42.22	1.41	17.38	0.07	4.96	bd	6.89	bd	bd	bd	NA	NA	NA	NA	NA	NA	100.86
BL1	14/12/00-054	27.80	bd	0.58	42.59	1.37	17.42	0.09	4.89	bd	7.05	bd	0.08	bd	NA	NA	NA	NA	NA	NA	101.87
BL1	14/12/00-087	27.59	bd	0.42	42.24	1.42	17.55	0.04	4.5	bd	7.47	bd	0.089	bd	NA	NA	NA	NA	NA	NA	101.32
BL1	14/12/00-093	27.7	0.11	0.31	42.42	1.36	17.67	0.11	4.58	bd	7.33	bd	bd	bd	NA	NA	NA	NA	NA	NA	101.59
BL1	14/12/00-106	27.74	bd	bd	42.53	1.48	17.71	0.04	4.49	0.07	6.86	bd	0.068	bd	NA	NA	NA	NA	NA	NA	100.99
BL-19B	27/04/01-102	26.67	bd	2.01	38.51	0.85	8.12	0.11	19.09	0.05	7.04	bd	bd	bd	0.05	bd	bd	0.10	bd	bd	102.60
BL22-b	27/04/01-155	27.92	bd	1.45	40.74	1.96	14.08	0.10	9.85	0.17	6.50	bd	bd	bd	0.05	bd	bd	0.11	bd	bd	102.91
BL22-b	27/04/01-157	28.16	bd	1.46	40.69	2.35	13.71	0.07	9.89	0.13	5.89	bd	bd	bd	bd	bd	bd	0.14	bd	bd	102.47
BL22-b	27/04/01-165	27.69	bd	1.59	40.74	2.88	13.98	0.11	10.10	0.15	5.36	bd	bd	bd	0.04	bd	bd	0.10	bd	bd	102.73
BL22-b	27/04/01-166	27.92	bd	1.47	40.44	2.56	14.01	0.08	10.15	0.13	5.99	bd	bd	bd	bd	bd	bd	0.05	bd	bd	102.80
BTB-01(B)	13/12/00-009	27.76	bd	0.35	41.80	1.45	17.37	0.08	4.06	bd	6.43	bd	0.23	bd	NA	NA	NA	NA	NA	NA	99.53
BTB-01(B)	13/12/00-010	28.03	bd	0.25	41.73	1.45	17.29	0.05	3.94	bd	6.43	bd	0.14	bd	NA	NA	NA	NA	NA	NA	99.31
BTB-01(B)	13/12/00-011	28.07	bd	0.21	40.65	1.37	17.13	0.05	3.91	bd	6.36	bd	0.23	bd	NA	NA	NA	NA	NA	NA	97.98
BTB-01(B)	27/04/01-131	28.78	bd	0.35	42.87	1.41	18.34	0.09	3.75	0.06	6.76	bd	0.08	0.16	bd	bd	bd	0.06	bd	bd	102.68
BTB-01(B)	27/04/01-133	28.47	bd	0.38	42.70	1.46	18.03	0.13	3.74	bd	6.85	bd	0.14	bd	0.06	bd	bd	bd	bd	bd	101.96
BTB-01(B)	27/04/01-140	28.77	bd	0.46	42.07	1.65	17.47	0.09	4.34	bd	6.56	bd	0.16	bd	bd	bd	bd	0.10	bd	bd	101.67
BTB-01(B)	27/04/01-143	28.74	bd	0.25	42.48	1.30	17.26	0.04	4.80	bd	6.95	bd	0.16	bd	bd	bd	bd	0.09	bd	bd	102.05
BTB-01(C)	13/12/00-024	27.54	bd	0.81	41.46	1.63	16.72	0.09	5.27	bd	6.81	bd	0.24	bd	NA	NA	NA	NA	NA	NA	100.57
BTB-01(C)	13/12/00-025	27.38	bd	0.83	40.52	1.42	17.13	0.10	5.75	bd	6.79	bd	0.16	bd	NA	NA	NA	NA	NA	NA	100.08
BTB-01(C)	13/12/00-026	27.14	bd	1.24	40.59	1.48	16.72	0.05	5.53	0.05	6.69	bd	bd	bd	NA	NA	NA	NA	NA	NA	99.49
BTB-01(C)	13/12/00-050	27.31	bd	1.00	41.03	1.56	16.60	0.08	5.84	0.07	7.01	bd	bd	bd	NA	NA	NA	NA	NA	NA	100.50
BTB-01(C)	13/12/00-051	26.96	bd	2.07	40.77	1.38	16.15	0.08	5.78	0.05	6.74	bd	0.11	bd	NA	NA	NA	NA	NA	NA	100.09
BTB-01(C)	13/12/00-052	26.92	bd	3.14	40.04	1.28	15.76	0.06	5.53	bd	6.73	bd	0.11	bd	NA	NA	NA	NA	NA	NA	99.57
BTB-01(C)	27/04/01-087	28.57	bd	bd	40.55	3.15	16.12	0.07	6.93	0.07	6.80	bd	0.08	bd	0.07	bd	bd	0.06	bd	bd	102.47
Galena																					
902	27/04/01-031	13.97	bd	bd	bd	0.75	bd	0.20	bd	bd	bd	85.85	bd	bd	bd	bd	bd	0.08	bd	bd	100.85
902	27/04/01-044	14.09	bd	bd	0.09	0.40	bd	0.24	bd	bd	bd	87.33	bd	bd	bd	bd	bd	bd	bd	bd	102.15
906	26/04/01-018	14.14	bd	bd	bd	bd	bd	0.11	bd	bd	0.64	87.54	bd	bd	bd	bd	bd	bd	bd	bd	102.43
906	26/04/01-081	14.28	bd	bd	0.51	0.28	bd	0.09	0.09	bd	1.06	84.14	bd	bd	bd	bd	bd	bd	bd	bd	100.44
910	26/04/01-035	14.66	bd	bd	bd	1.19	bd	0.06	bd	bd	0.80	85.04	bd	bd	bd	bd	bd	bd	bd	bd	101.74
910	26/04/01-051	14.03	bd	bd	bd	1.68	bd	0.11	bd	bd	0.32	85.46	bd	bd	bd	bd	bd	0.07	bd	bd	101.67
910	26/04/01-055	14.10	bd	bd	bd	0.30	bd	0.09	bd	bd	0.38	85.08	bd	bd	bd	bd	bd	bd	bd	bd	99.95
910	26/04/01-056	14.20	bd	bd	bd	0.15	0.05	0.07	0.11	bd	0.21	87.77	bd	bd	bd	bd	bd	0.05	bd	bd	102.61
00-BT-01	27/04/01-103	14.21	bd	bd	bd	0.04	bd	0.07	0.09	bd	0.18	87.79	bd	bd	bd	bd	bd	0.07	bd	bd	102.43
00-BT-01	27/04/01-111	13.81	bd	bd	0.24	0.03	bd	0.15	bd	bd	bd	85.78	bd	bd	bd	bd	bd	bd	bd	bd	100.00

Table B1(vii). Sulphide analyses (wt%) contd.

Sample No	Analysis Ref	S	Au	Ag	Cu	Fe	As	Se	Sb	Te	Zn	Pb	Hg	Bi	Ga	Ge	Co	Cd	In	Cr	Total
01BT076a	03/09/02-112	13.58	bd	bd	bd	bd	bd	bd	bd	bd	bd	86.01	bd	bd	bd	NA	NA	bd	NA	NA	99.59
01BT076a	03/09/02-113	13.53	bd	bd	bd	bd	bd	bd	0.04	bd	bd	85.96	bd	bd	bd	NA	NA	0.06	NA	NA	99.58
01BT076a	03/09/02-114	13.46	bd	bd	bd	bd	bd	bd	0.05	bd	0.17	86.42	bd	bd	bd	NA	NA	bd	NA	NA	100.09
01BT076a	03/09/02-115	13.65	bd	bd	0.30	0.50	bd	0.05	bd	bd	1.63	84.37	bd	bd	bd	NA	NA	bd	NA	NA	100.49
01BT076a	03/09/02-117	13.51	bd	bd	bd	bd	bd	bd	bd	bd	0.97	86.00	bd	bd	bd	NA	NA	bd	NA	NA	100.48
01BT076a	03/09/02-118	13.49	bd	bd	0.20	0.07	bd	bd	bd	bd	0.50	86.57	bd	bd	bd	NA	NA	bd	NA	NA	100.83
01BT076a	03/09/02-126	13.22	bd	bd	0.08	bd	bd	bd	bd	bd	bd	84.82	bd	bd	bd	NA	NA	bd	NA	NA	98.13
01BT076a	03/09/02-127	13.48	bd	bd	0.07	0.04	bd	bd	bd	bd	bd	86.72	bd	bd	bd	NA	NA	bd	NA	NA	100.31
01BT076a	03/09/02-132	13.48	bd	bd	bd	bd	bd	bd	bd	bd	bd	86.58	bd	bd	bd	NA	NA	bd	NA	NA	100.07
01BT076a	03/09/02-133	13.71	bd	bd	bd	bd	bd	0.07	bd	bd	0.08	86.24	bd	bd	bd	NA	NA	bd	NA	NA	100.09
01BT076a	03/09/02-134	13.49	bd	bd	bd	bd	0.06	0.07	bd	bd	bd	86.52	bd	bd	bd	NA	NA	bd	NA	NA	100.14
01BT076a	03/09/02-135	13.63	bd	bd	bd	0.03	bd	0.05	bd	bd	bd	86.85	bd	bd	bd	NA	NA	bd	NA	NA	100.56
01BT076a	03/09/02-136	13.65	bd	bd	bd	bd	bd	0.04	bd	bd	bd	86.46	bd	bd	bd	NA	NA	0.05	NA	NA	100.20
01BT076a	03/09/02-137	13.47	bd	bd	bd	bd	bd	bd	0.04	bd	bd	86.86	bd	bd	bd	NA	NA	bd	NA	NA	100.37
01BT076a	03/09/02-138	13.35	bd	bd	0.06	bd	bd	bd	bd	bd	bd	87.00	bd	bd	bd	NA	NA	bd	NA	NA	100.40
01BT076a	03/09/02-139	13.49	bd	bd	bd	bd	bd	0.06	0.04	bd	0.08	86.44	bd	bd	0.07	NA	NA	bd	NA	NA	100.18
01BT076a	03/09/02-140	13.62	bd	bd	bd	0.03	bd	bd	bd	bd	0.26	86.45	bd	bd	bd	NA	NA	bd	NA	NA	100.36
01BT082a	03/09/02-044	13.68	bd	bd	0.09	bd	bd	0.04	bd	bd	0.14	86.16	bd	bd	bd	NA	NA	bd	NA	NA	100.11
01BT082a	03/09/02-045	13.44	bd	bd	0.06	bd	bd	0.04	bd	bd	bd	86.44	bd	bd	bd	NA	NA	0.11	NA	NA	100.08
01BT082a	03/09/02-046	13.49	bd	bd	0.07	bd	bd	bd	0.06	bd	bd	85.49	bd	bd	bd	NA	NA	bd	NA	NA	99.10
01BT082a	03/09/02-047	13.50	bd	bd	bd	bd	bd	bd	bd	bd	bd	87.42	bd	bd	bd	NA	NA	bd	NA	NA	100.92
01BT082a	03/09/02-048	13.57	bd	bd	bd	bd	0.06	bd	bd	bd	bd	87.27	bd	bd	bd	NA	NA	0.07	NA	NA	100.96
01BT082a	03/09/02-049	13.53	bd	bd	0.06	bd	bd	0.05	bd	bd	bd	86.80	bd	bd	bd	NA	NA	bd	NA	NA	100.44
01BT082a	03/09/02-050	13.39	bd	bd	0.17	0.14	bd	0.05	bd	bd	1.23	86.04	bd	bd	bd	NA	NA	bd	NA	NA	101.01
01BT082a	03/09/02-056	13.55	bd	bd	0.23	0.13	bd	bd	bd	bd	bd	86.48	bd	bd	bd	NA	NA	bd	NA	NA	100.39
01BT082a	03/09/02-057	13.51	bd	bd	0.29	0.12	0.06	0.04	bd	bd	bd	86.44	bd	bd	bd	NA	NA	bd	NA	NA	100.46
01BT082a	03/09/02-058	13.42	bd	bd	0.16	0.07	bd	0.07	bd	0.04	0.08	85.73	bd	bd	bd	NA	NA	bd	NA	NA	99.56
01BT082a	03/09/02-074	13.53	0.16	bd	0.15	bd	bd	0.05	bd	bd	bd	85.56	bd	bd	bd	NA	NA	bd	NA	NA	99.45
01BT082a	03/09/02-075	13.51	bd	bd	0.06	bd	bd	bd	bd	bd	bd	86.57	bd	bd	bd	NA	NA	bd	NA	NA	100.14
01BT082a	03/09/02-076	13.49	bd	bd	0.29	bd	bd	bd	0.07	bd	0.10	86.37	bd	bd	bd	NA	NA	bd	NA	NA	100.31
01BT082a	03/09/02-077	13.55	bd	bd	0.44	0.06	bd	bd	bd	bd	0.07	85.79	bd	bd	0.05	NA	NA	bd	NA	NA	99.96
01BT082a	03/09/02-085	13.52	bd	bd	0.08	0.03	bd	bd	bd	0.04	bd	86.31	bd	bd	bd	NA	NA	bd	NA	NA	99.98
01BT082a	03/09/02-086	13.49	bd	bd	bd	bd	0.06	0.07	bd	bd	bd	86.32	bd	bd	0.07	NA	NA	0.07	NA	NA	100.08
01BT082a	03/09/02-087	13.45	0.16	bd	bd	bd	bd	0.06	bd	bd	bd	86.46	bd	bd	bd	NA	NA	0.09	NA	NA	100.21
01BT082a	03/09/02-088	13.48	bd	bd	bd	bd	bd	0.06	0.05	bd	0.16	87.04	bd	bd	bd	NA	NA	bd	NA	NA	100.79
01BT082a	03/09/02-089	13.57	bd	bd	bd	bd	bd	0.05	0.05	bd	bd	85.65	bd	bd	0.04	NA	NA	bd	NA	NA	99.36
01BT082a	03/09/02-090	13.45	bd	bd	0.12	0.04	0.06	bd	bd	bd	bd	86.62	bd	bd	bd	NA	NA	bd	NA	NA	100.28
01BT082a	03/09/02-091	13.65	bd	bd	0.06	bd	bd	0.04	0.04	bd	bd	86.84	bd	bd	bd	NA	NA	bd	NA	NA	100.63

Table B1(vii). Sulphide analyses (wt%) contd.

Sample No	Analysis Ref	S	Au	Ag	Cu	Fe	As	Se	Sb	Te	Zn	Pb	Hg	Bi	Ga	Ge	Co	Cd	In	Cr	Total
01BT082a	03/09/02-092	13.65	bd	bd	bd	0.04	bd	0.07	0.05	bd	bd	88.01	bd	bd	bd	NA	NA	bd	NA	NA	101.82
01BT082a	03/09/02-093	13.43	bd	bd	0.10	0.06	0.05	0.05	bd	bd	bd	86.30	bd	bd	0.05	NA	NA	0.08	NA	NA	100.13
01BT082a	03/09/02-094	13.29	bd	bd	bd	0.05	bd	bd	0.06	bd	bd	85.76	bd	bd	bd	NA	NA	bd	NA	NA	99.15
01BT082a	03/09/02-095	13.39	bd	bd	0.10	0.06	bd	bd	0.04	bd	bd	85.63	bd	bd	bd	NA	NA	bd	NA	NA	99.22
01BT082a	03/09/02-096	13.40	bd	bd	0.16	0.03	bd	0.07	bd	bd	bd	85.41	bd	bd	bd	NA	NA	bd	NA	NA	99.06
01BT136	04/09/02-046	13.03	bd	bd	0.33	0.20	bd	0.08	0.07	bd	0.18	83.51	bd	bd	0.05	NA	NA	0.07	NA	NA	97.50
01BT136	04/09/02-047	13.62	bd	bd	1.33	0.08	bd	0.05	bd	bd	0.26	86.45	bd	bd	bd	NA	NA	bd	NA	NA	101.78
01BT136	04/09/02-049	13.15	bd	bd	bd	0.17	bd	0.06	bd	bd	0.17	85.35	bd	bd	bd	NA	NA	bd	NA	NA	98.90
01BT138	03/09/02-151	13.62	bd	bd	0.88	0.52	bd	bd	bd	bd	bd	86.74	bd	bd	bd	NA	NA	bd	NA	NA	101.75
01BT138	03/09/02-152	13.49	bd	bd	0.85	bd	bd	bd	bd	bd	0.26	85.33	bd	bd	bd	NA	NA	bd	NA	NA	99.93
01BT138	03/09/02-153	13.55	bd	bd	0.19	bd	bd	0.07	0.09	bd	0.10	85.88	bd	bd	0.04	NA	NA	bd	NA	NA	99.92
01BT138	03/09/02-154	13.56	bd	bd	bd	bd	bd	0.04	bd	bd	0.16	87.00	bd	bd	bd	NA	NA	bd	NA	NA	100.76
01BT162	04/09/02-008	13.29	bd	bd	0.59	bd	bd	0.23	bd	bd	0.11	85.66	bd	bd	bd	NA	NA	bd	NA	NA	99.89
01BT162	04/09/02-009	13.43	bd	bd	0.18	0.05	bd	0.11	bd	bd	bd	86.06	bd	bd	bd	NA	NA	bd	NA	NA	99.82
01BT162	04/09/02-010	13.18	0.13	bd	0.32	0.19	bd	0.31	bd	bd	0.13	84.71	bd	bd	bd	NA	NA	0.10	NA	NA	99.07
01BT162	04/09/02-011	13.31	bd	bd	0.15	0.12	bd	0.20	bd	0.08	bd	84.99	bd	bd	bd	NA	NA	bd	NA	NA	98.84
01BT162	04/09/02-018	13.25	bd	bd	0.06	0.03	bd	0.22	bd	0.04	0.22	85.56	bd	bd	bd	NA	NA	0.07	NA	NA	99.45
01BT162	04/09/02-019	13.26	bd	bd	bd	bd	0.06	0.24	0.05	bd	0.38	85.60	bd	bd	bd	NA	NA	bd	NA	NA	99.58
01BT162	04/09/02-020	13.24	bd	bd	bd	bd	bd	0.23	bd	bd	0.47	85.17	bd	bd	bd	NA	NA	bd	NA	NA	99.11
01BT226b	03/09/02-013	13.38	bd	0.75	0.17	bd	bd	bd	bd	0.06	bd	84.23	bd	bd	bd	NA	NA	bd	NA	NA	98.59
01BT226b	03/09/02-022	13.31	bd	bd	bd	bd	bd	0.04	0.06	bd	bd	86.81	bd	bd	bd	NA	NA	bd	NA	NA	100.23
01BT226b	03/09/02-023	13.35	bd	bd	bd	bd	bd	0.04	0.04	bd	bd	86.60	bd	bd	0.06	NA	NA	bd	NA	NA	100.08
01BT226b	03/09/02-024	13.30	bd	bd	bd	bd	bd	0.07	bd	bd	bd	86.40	bd	bd	bd	NA	NA	0.08	NA	NA	99.85
01BT226b	03/09/02-025	13.24	bd	bd	bd	bd	bd	bd	0.04	bd	bd	85.70	bd	bd	bd	NA	NA	bd	NA	NA	98.97
01BT226b	03/09/02-037	13.34	bd	bd	0.07	bd	bd	bd	bd	bd	bd	86.20	bd	bd	bd	NA	NA	0.05	NA	NA	99.66
01BT226b	03/09/02-038	13.53	bd	bd	bd	bd	bd	bd	0.10	bd	bd	86.17	bd	bd	bd	NA	NA	0.09	NA	NA	99.89
01BT226b	03/09/02-039	13.42	0.18	bd	0.06	bd	bd	0.05	0.04	bd	bd	86.20	bd	bd	bd	NA	NA	bd	NA	NA	99.94
01BT226b	03/09/02-041	13.47	bd	bd	bd	bd	bd	bd	0.08	bd	bd	85.91	bd	bd	bd	NA	NA	bd	NA	NA	99.46
01BT226b	03/09/02-042	13.48	bd	bd	bd	bd	bd	0.07	bd	bd	bd	86.96	bd	bd	bd	NA	NA	bd	NA	NA	100.52
01BT226b	03/09/02-043	13.42	bd	bd	bd	0.04	bd	bd	bd	bd	bd	86.63	bd	bd	bd	NA	NA	bd	NA	NA	100.09
BL1	14/12/00-079	13.39	bd	0.47	0.28	bd	bd	0.09	bd	bd	bd	85.61	bd	bd	NA	NA	NA	NA	NA	NA	99.84
BL1	14/12/00-082	13.31	bd	0.2	0.39	0.04	bd	0.11	bd	bd	0.16	86.19	bd	bd	NA	NA	NA	NA	NA	NA	100.40
BL1	14/12/00-083	13.4	bd	0.27	0.4	bd	bd	0.14	bd	bd	0.3	86.06	bd	bd	NA	NA	NA	NA	NA	NA	100.57
BL1	14/12/00-105	13.51	bd	0.13	bd	0.03	0.05	0.07	0.08	bd	bd	86.58	bd	bd	NA	NA	NA	NA	NA	NA	100.45
BL-19B	27/04/01-088	14.22	bd	bd	bd	bd	0.05	0.10	0.04	bd	bd	87.84	bd	bd	bd	bd	bd	bd	bd	bd	102.26
BL-19B	27/04/01-101	14.36	bd	bd	bd	bd	bd	0.07	bd	bd	0.15	87.51	bd	bd	bd	bd	bd	bd	bd	bd	102.11
BL22-b	27/04/01-151	13.05	bd	bd	bd	bd	bd	0.39	bd	bd	0.83	83.65	bd	bd	bd	bd	bd	0.06	bd	bd	97.99
BL711.A	14/12/00-007	13.75	bd	bd	0.06	bd	bd	bd	bd	bd	0.58	87.27	bd	bd	NA	NA	NA	NA	NA	NA	101.66

Table B1(vii). Sulphide analyses (wt%) contd.

Sample No	Analysis Ref	S	Au	Ag	Cu	Fe	As	Se	Sb	Te	Zn	Pb	Hg	Bi	Ga	Ge	Co	Cd	In	Cr	Total
BL711.A	14/12/00-008	13.85	bd	bd	0.07	bd	0.05	0.04	bd	bd	0.47	85.88	bd	bd	NA	NA	NA	NA	NA	NA	100.36
BTB-01(B)	13/12/00-006	13.89	0.17	1.79	1.24	bd	bd	0.06	bd	bd	bd	83.01	bd	bd	NA	NA	NA	NA	NA	NA	100.16
BTB-01(B)	13/12/00-007	13.78	bd	1.49	1.04	bd	0.05	0.10	0.04	bd	bd	83.79	bd	bd	NA	NA	NA	NA	NA	NA	100.29
BTB-01(B)	13/12/00-008	13.88	bd	1.76	1.19	bd	bd	0.09	0.06	bd	bd	83.32	bd	bd	NA	NA	NA	NA	NA	NA	100.30
BTB-01(B)	27/04/01-119	14.24	bd	0.41	1.09	bd	bd	0.04	bd	bd	bd	84.83	bd	bd	bd	bd	bd	bd	bd	bd	100.61
BTB-01(B)	27/04/01-120	13.89	bd	0.49	0.11	bd	bd	0.08	bd	0.04	bd	85.79	bd	bd	0.04	bd	bd	bd	bd	bd	100.44
BTB-01(B)	27/04/01-121	14.09	bd	0.27	0.14	bd	bd	0.07	bd	bd	bd	86.86	bd	bd	bd	bd	bd	0.09	bd	bd	101.51
BTB-01(B)	27/04/01-125	13.97	bd	0.36	0.39	bd	bd	0.05	bd	bd	0.08	86.02	bd	bd	bd	bd	bd	0.09	bd	bd	100.96
BTB-01(B)	27/04/01-130	14.19	bd	0.35	0.40	bd	bd	0.09	bd	bd	bd	86.60	bd	bd	bd	bd	bd	bd	bd	bd	101.63
BTB-01(B)	27/04/01-132	14.08	bd	0.23	0.41	bd	bd	bd	bd	bd	bd	85.45	bd	bd	bd	bd	bd	0.07	bd	bd	100.23
BTB-01(B)	27/04/01-135	14.49	bd	0.11	0.72	bd	0.07	0.04	bd	0.06	bd	86.22	bd	bd	bd	bd	bd	bd	bd	bd	101.70
BTB-01(B)	27/04/01-136	14.01	bd	bd	0.51	bd	0.08	0.05	bd	bd	0.15	84.88	bd	bd	bd	bd	bd	bd	bd	bd	99.69
BTB-01(B)	27/04/01-139	14.34	bd	0.39	1.07	0.07	bd	0.07	bd	bd	bd	84.76	bd	bd	bd	bd	bd	bd	bd	bd	100.71
BTB-01(C)	13/12/00-021	13.36	bd	bd	1.13	0.18	0.06	0.12	bd	bd	0.16	85.42	bd	bd	NA	NA	NA	NA	NA	NA	100.43
BTB-01(C)	13/12/00-022	13.46	bd	0.30	1.28	0.45	bd	0.12	0.05	bd	0.17	86.44	bd	bd	NA	NA	NA	NA	NA	NA	102.27
BTB-01(C)	13/12/00-023	13.21	bd	0.26	1.03	0.30	0.05	0.09	0.05	bd	0.12	86.47	bd	bd	NA	NA	NA	NA	NA	NA	101.58
BTB-01(C)	13/12/00-027	13.64	bd	0.46	1.49	bd	bd	0.14	0.08	bd	0.96	84.66	bd	bd	NA	NA	NA	NA	NA	NA	101.43
BTB-01(C)	13/12/00-028	13.39	bd	0.44	1.62	bd	bd	0.17	0.04	bd	0.63	84.41	bd	bd	NA	NA	NA	NA	NA	NA	100.70
BTB-01(C)	13/12/00-031	13.38	bd	0.25	1.50	0.03	bd	0.15	bd	bd	1.23	85.46	bd	bd	NA	NA	NA	NA	NA	NA	102.00
BTB-01(C)	13/12/00-032	13.61	bd	0.34	1.27	bd	bd	0.14	0.05	bd	1.09	85.40	bd	bd	NA	NA	NA	NA	NA	NA	101.90
BTB-01(C)	13/12/00-053	13.42	bd	bd	0.19	bd	0.06	0.10	0.09	bd	0.26	85.11	bd	bd	NA	NA	NA	NA	NA	NA	99.23
BTB-01(C)	13/12/00-054	13.45	0.15	0.15	0.26	bd	bd	0.12	bd	bd	0.19	85.46	bd	bd	NA	NA	NA	NA	NA	NA	99.78
BTB-01(C)	13/12/00-055	13.05	bd	0.13	0.26	bd	bd	0.08	0.08	bd	0.34	84.38	bd	bd	NA	NA	NA	NA	NA	NA	98.32
BTB-01(C)	27/04/01-081	14.27	bd	bd	0.15	0.08	bd	0.15	bd	bd	1.33	86.71	bd	bd	bd	bd	bd	0.10	bd	bd	102.79
BTB-01(C)	27/04/01-115	13.87	bd	0.17	0.18	0.05	bd	0.14	bd	bd	bd	86.57	bd	bd	bd	bd	bd	bd	0.10	bd	101.07
Electrum																					
01BT082a	03/09/02-065	0.08	63.89	32.86	0.12	0.10	bd	0.06	bd	bd	bd	bd	2.36	bd	bd	NA	NA	bd	NA	NA	99.48
01BT082a	03/09/02-066	bd	44.85	45.35	0.09	bd	bd	0.04	bd	bd	bd	bd	10.11	bd	bd	NA	NA	bd	NA	NA	100.44
01BT082a	03/09/02-067	0.11	65.92	32.01	bd	bd	bd	bd	bd	0.06	bd	bd	2.23	bd	bd	NA	NA	bd	NA	NA	100.32
01BT082a	03/09/02-068	0.10	66.26	31.81	bd	bd	bd	bd	bd	0.05	bd	bd	1.96	bd	bd	NA	NA	bd	NA	NA	100.18
01BT082a	03/09/02-069	0.11	64.12	32.99	bd	bd	bd	0.04	bd	bd	bd	bd	2.62	bd	0.05	NA	NA	0.06	NA	NA	99.99
01BT082a	03/09/02-070	0.15	66.34	31.29	0.07	bd	bd	bd	bd	bd	bd	bd	2.05	bd	bd	NA	NA	bd	NA	NA	99.89
01BT082a	03/09/02-071	bd	56.28	37.98	bd	0.03	bd	bd	bd	0.07	bd	bd	5.47	bd	0.07	NA	NA	bd	NA	NA	99.90
01BT082a	03/09/02-073	0.09	62.47	34.76	0.25	0.17	bd	0.08	bd	bd	0.33	bd	3.22	bd	bd	NA	NA	bd	NA	NA	101.36
01BT082a	03/09/02-079	0.09	63.16	33.76	bd	bd	bd	bd	bd	bd	bd	bd	2.74	bd	0.04	NA	NA	bd	NA	NA	99.78
01BT082a	03/09/02-080	0.09	63.61	33.82	0.08	bd	0.08	bd	bd	0.09	bd	bd	2.76	bd	bd	NA	NA	bd	NA	NA	100.52
01BT136	04/09/02-066	bd	50.72	34.62	0.08	0.44	bd	bd	bd	bd	bd	bd	2.89	bd	bd	NA	NA	bd	NA	NA	88.75

Table B1(vii). Sulphide analyses (wt%) contd.

Sample No	Analysis Ref	S	Au	Ag	Cu	Fe	As	Se	Sb	Te	Zn	Pb	Hg	Bi	Ga	Ge	Co	Cd	In	Cr	Total
01BT136	04/09/02-068	14.99	23.21	21.41	14.79	9.52	0.05	bd	bd	0.07	2.60	bd	2.65	bd	0.12	NA	NA	bd	NA	NA	89.40
01BT138	04/09/02-070	22.38	41.65	21.08	13.70	16.55	bd	bd	bd	bd	bd	bd	2.89	bd	bd	NA	NA	bd	NA	NA	118.26
01BT226b	03/09/02-001	0.05	64.36	34.03	0.09	bd	bd	bd	bd	0.09	bd	bd	0.79	bd	bd	NA	NA	bd	NA	NA	99.41
01BT226b	03/09/02-002	0.06	65.94	32.83	0.10	bd	bd	0.07	bd	bd	bd	bd	0.61	bd	bd	NA	NA	bd	NA	NA	99.60
01BT226b	03/09/02-003	0.06	66.22	32.71	0.13	0.05	bd	bd	0.04	bd	bd	bd	0.82	bd	bd	NA	NA	bd	NA	NA	100.02
01BT226b	03/09/02-004	0.03	63.97	34.99	0.10	bd	bd	bd	bd	0.07	bd	bd	0.83	bd	bd	NA	NA	bd	NA	NA	100.00
01BT226b	03/09/02-005	bd	64.46	34.89	0.14	0.04	bd	bd	bd	0.04	bd	bd	0.57	bd	bd	NA	NA	bd	NA	NA	100.14
01BT226b	03/09/02-006	0.09	63.03	35.50	0.13	bd	bd	0.05	bd	0.04	bd	bd	0.63	bd	bd	NA	NA	bd	NA	NA	99.47
01BT226b	03/09/02-011	11.51	3.38	8.85	1.30	bd	0.56	bd	0.21	bd	1.16	bd	bd	0.14	bd	NA	NA	bd	NA	NA	27.13
01BT226b	03/09/02-012	11.44	1.89	10.61	2.12	bd	0.90	bd	0.26	bd	1.34	bd	bd	0.30	bd	NA	NA	bd	NA	NA	28.88
01BT226b	03/09/02-015	0.10	69.35	30.38	0.18	bd	bd	0.05	bd	0.11	bd	bd	0.20	bd	bd	NA	NA	bd	NA	NA	100.38
01BT226b	03/09/02-016	0.04	69.51	29.53	0.08	0.06	0.07	bd	bd	0.07	bd	bd	bd	bd	bd	NA	NA	bd	NA	NA	99.36
01BT226b	03/09/02-017	0.08	69.73	29.72	0.11	bd	bd	bd	bd	0.08	bd	bd	bd	bd	bd	NA	NA	bd	NA	NA	99.71
01BT226b	03/09/02-018	0.09	54.62	42.47	0.37	bd	0.05	bd	bd	0.08	bd	0.21	1.26	bd	bd	NA	NA	bd	NA	NA	99.15
01BT226b	03/09/02-019	0.07	70.18	29.59	0.11	bd	bd	0.04	bd	0.05	bd	bd	0.12	bd	bd	NA	NA	bd	NA	NA	100.16
BL1	14/12/00-074	1.28	70.17	28.32	0.50	bd	bd	bd	bd	0.09	bd	bd	0.77	bd	NA	NA	NA	NA	NA	NA	101.12
BL1	14/12/00-075	1.09	68.71	28.53	0.31	bd	bd	bd	bd	0.06	bd	bd	0.83	0.20	NA	NA	NA	NA	NA	NA	99.73
BL1	14/12/00-076	2.08	68.24	29.59	0.70	0.03	0.06	bd	bd	bd	bd	bd	0.75	bd	NA	NA	NA	NA	NA	NA	101.46
BL1	14/12/00-077	1.62	67.81	30.91	0.35	0.06	0.05	0.05	0.04	0.08	bd	bd	0.82	bd	NA	NA	NA	NA	NA	NA	101.77
BL1	14/12/00-080	0.43	43.39	40.48	0.20	0.08	bd	0.05	bd	bd	bd	0.27	3.52	bd	NA	NA	NA	NA	NA	NA	88.43
BL1	14/12/00-081	0.14	41.60	50.00	0.34	0.05	bd	0.09	bd	0.07	bd	bd	6.28	bd	NA	NA	NA	NA	NA	NA	98.56
BL1	14/12/00-084	8.50	31.20	36.26	13.48	bd	bd	0.06	bd	0.05	bd	3.47	2.82	bd	NA	NA	NA	NA	NA	NA	95.83
BL1	14/12/00-094	0.11	75.03	23.57	bd	bd	bd	bd	bd	bd	bd	bd	0.78	bd	NA	NA	NA	NA	NA	NA	99.48
BL1	14/12/00-095	0.09	74.85	23.59	bd	bd	bd	bd	bd	bd	bd	bd	0.48	0.22	NA	NA	NA	NA	NA	NA	99.22
BL1	14/12/00-103	0.47	72.96	25.75	bd	0.03	0.06	0.04	bd	bd	bd	bd	0.65	bd	NA	NA	NA	NA	NA	NA	99.95
BL1	14/12/00-104	0.08	76.02	22.71	bd	bd	bd	bd	bd	0.09	bd	bd	0.81	0.15	NA	NA	NA	NA	NA	NA	99.87
BL1	14/12/00-107	0.08	74.82	23.02	bd	0.05	bd	0.07	bd	0.05	bd	bd	0.84	bd	NA	NA	NA	NA	NA	NA	98.92
BTB-01(B)	13/12/00-001	0.06	77.34	20.94	0.09	bd	0.07	bd	0.05	0.13	bd	bd	0.34	bd	NA	NA	NA	NA	NA	NA	99.03
BTB-01(B)	13/12/00-002	0.04	77.35	20.93	0.07	0.04	bd	0.05	bd	0.10	bd	bd	0.33	bd	NA	NA	NA	NA	NA	NA	98.91
BTB-01(B)	13/12/00-003	0.04	76.96	20.18	0.08	bd	bd	0.07	bd	0.08	bd	bd	0.53	bd	NA	NA	NA	NA	NA	NA	97.92
BTB-01(B)	13/12/00-004	0.06	76.72	20.50	0.08	0.06	bd	bd	bd	0.16	bd	bd	0.65	bd	NA	NA	NA	NA	NA	NA	98.22
BTB-01(B)	13/12/00-005	bd	76.62	21.27	bd	0.04	bd	bd	bd	bd	bd	bd	0.56	0.22	NA	NA	NA	NA	NA	NA	98.71
BTB-01(C)	13/12/00-029	0.13	72.15	26.83	0.35	0.12	bd	bd	0.05	bd	bd	bd	0.91	bd	NA	NA	NA	NA	NA	NA	100.53
BTB-01(C)	13/12/00-030	0.12	71.88	26.72	0.26	0.06	bd	bd	bd	bd	bd	bd	0.92	bd	NA	NA	NA	NA	NA	NA	99.95
BTB-01(C)	13/12/00-038	0.15	37.51	52.80	0.26	bd	bd	bd	bd	bd	2.54	bd	9.63	bd	NA	NA	NA	NA	NA	NA	102.87
BTB-01(C)	13/12/00-039	0.10	37.70	52.92	0.32	bd	bd	bd	bd	0.08	2.47	bd	9.15	bd	NA	NA	NA	NA	NA	NA	102.75
BTB-01(C)	13/12/00-042	0.07	70.57	26.88	bd	bd	bd	0.04	bd	0.04	bd	bd	1.05	bd	NA	NA	NA	NA	NA	NA	98.65
BTB-01(C)	13/12/00-043	0.11	70.29	28.49	bd	0.03	0.06	bd	bd	bd	bd	bd	1.09	bd	NA	NA	NA	NA	NA	NA	100.06

Table B1(vii). Sulphide analyses (wt%) contd.

Sample No	Analysis Ref	S	Au	Ag	Cu	Fe	As	Se	Sb	Te	Zn	Pb	Hg	Bi	Ga	Ge	Co	Cd	In	Cr	Total
BTB-01(C)	13/12/00-044	0.07	54.53	41.34	bd	0.05	bd	bd	bd	0.10	bd	bd	3.44	bd	NA	NA	NA	NA	NA	NA	99.53
BTB-01(C)	13/12/00-045	0.08	71.26	27.32	0.10	0.04	bd	bd	bd	bd	bd	bd	1.04	0.15	NA	NA	NA	NA	NA	NA	99.99
BTB-01(C)	13/12/00-046	0.05	55.59	40.63	0.18	bd	0.06	bd	bd	0.07	bd	bd	2.85	bd	NA	NA	NA	NA	NA	NA	99.41
BTB-01(C)	14/12/00-002	0.15	37.43	55.18	0.31	bd	0.09	bd	bd	0.14	5.85	bd	7.66	bd	NA	NA	NA	NA	NA	NA	106.81
BTB-01(C)	14/12/00-003	0.15	38.17	51.83	0.24	bd	bd	bd	bd	bd	2.79	bd	6.83	bd	NA	NA	NA	NA	NA	NA	100.01
BTB-01(C)	14/12/00-004	0.07	70.63	29.01	0.34	0.14	0.05	0.04	bd	0.11	2.99	bd	1.13	bd	NA	NA	NA	NA	NA	NA	104.50
BTB-01(C)	27/04/01-116	bd	23.61	64.34	0.33	0.04	bd	0.04	bd	0.08	bd	bd	11.07	bd	0.08	bd	bd	bd	bd	bd	99.59
BTB-01(C)	27/04/01-118	0.06	73.39	26.18	bd	0.06	bd	bd	bd	0.09	bd	bd	0.58	bd	bd	bd	bd	bd	bd	bd	100.35
Pearcite																					
01BT226b	03/09/02-008	16.43	0.16	62.72	10.93	bd	6.84	0.06	bd	0.07	bd	bd	bd	bd	bd	NA	NA	bd	NA	NA	97.20
01BT226b	03/09/02-009	16.31	0.11	65.20	10.23	bd	7.10	bd	bd	0.07	bd	bd	bd	bd	bd	NA	NA	0.06	NA	NA	99.08
01BT226b	03/09/02-010	16.41	bd	65.93	9.94	0.03	6.82	0.04	bd	0.08	bd	bd	0.08	bd	bd	NA	NA	0.06	NA	NA	99.39
BTB-01(C)	27/04/01-082	17.63	bd	60.03	14.68	bd	6.65	0.05	1.05	bd	bd	bd	0.17	bd	bd	bd	bd	bd	bd	bd	100.25
BTB-01(C)	27/04/01-113	17.44	bd	59.99	14.33	bd	7.08	0.05	0.45	0.08	bd	bd	bd	bd	bd	bd	bd	bd	bd	bd	99.41
BTB-01(C)	27/04/01-114	17.45	bd	59.42	15.45	0.04	7.11	bd	0.48	0.05	bd	bd	bd	bd	bd	bd	bd	bd	bd	bd	100.00
Hessite																					
BL711.A	14/12/00-005	0.20	0.30	61.74	0.06	bd	bd	bd	0.21	36.24	0.72	bd	bd	bd	NA	NA	NA	NA	NA	NA	99.47
BL711.A	14/12/00-006	0.30	0.30	61.35	bd	0.06	bd	0.05	0.21	35.96	1.07	0.27	bd	0.14	NA	NA	NA	NA	NA	NA	99.71
Native silver																					
BTB-01(C)	13/12/00-018	0.04	0.16	95.46	0.20	0.06	bd	bd	bd	bd	0.29	bd	0.08	bd	NA	NA	NA	NA	NA	NA	96.29
BTB-01(C)	13/12/00-020	0.08	bd	95.94	0.23	0.06	bd	bd	bd	0.06	0.31	bd	bd	bd	NA	NA	NA	NA	NA	NA	96.68

Table B1(viii). Sulphide analyses (at%).

Sample No	Analysis Ref	S	Au	Ag	Cu	Fe	As	Se	Sb	Te	Zn	Pb	Hg	Bi	Ga	Ge	Co	Cd	In	Cr	Total
Pyrite																					
901	04/09/02-037	65.90	bd	bd	bd	33.91	0.06	bd	bd	bd	bd	bd	bd	0.04	0.04	NA	NA	bd	NA	NA	99.95
901	04/09/02-038	65.93	bd	bd	0.09	33.85	0.07	0.02	bd	bd	bd	bd	bd	bd	bd	NA	NA	bd	NA	NA	99.96
901	04/09/02-039	65.95	bd	bd	bd	33.90	0.05	bd	bd	bd	bd	bd	bd	bd	bd	NA	NA	bd	NA	NA	99.90
901	04/09/02-040	66.02	bd	bd	bd	33.86	0.04	0.03	bd	bd	bd	bd	bd	bd	bd	NA	NA	bd	NA	NA	99.94
901	04/09/02-041	65.95	0.02	bd	bd	33.86	0.07	bd	bd	bd	bd	bd	bd	0.03	0.02	NA	NA	bd	NA	NA	99.96
901	04/09/02-042	65.84	bd	bd	bd	34.00	0.05	bd	0.02	bd	bd	bd	bd	bd	bd	NA	NA	bd	NA	NA	99.91
901	04/09/02-043	65.94	bd	bd	bd	33.87	0.04	0.02	bd	bd	bd	bd	bd	bd	bd	NA	NA	bd	NA	NA	99.87
901	04/09/02-044	65.88	bd	bd	bd	33.90	0.12	bd	0.01	bd	bd	bd	bd	0.04	bd	NA	NA	bd	NA	NA	99.94
901	04/09/02-045	65.75	bd	bd	0.10	34.03	0.05	bd	0.02	bd	bd	bd	bd	bd	bd	NA	NA	bd	NA	NA	99.95
901	26/04/01-068	65.88	bd	bd	0.11	33.77	0.12	bd	bd	bd	bd	bd	bd	0.03	bd	bd	0.04	bd	bd	bd	99.96
901	26/04/01-069	65.15	bd	bd	0.05	34.61	0.05	bd	0.02	0.01	bd	bd	bd	0.04	bd	bd	bd	bd	bd	bd	99.93
901	26/04/01-070	65.61	bd	bd	0.14	34.06	0.06	bd	bd	bd	bd	bd	0.02	0.03	bd	bd	bd	0.02	bd	bd	99.93
901	26/04/01-073	65.57	bd	bd	0.06	34.24	0.04	bd	bd	0.01	bd	bd	bd	bd	bd	bd	bd	bd	bd	bd	99.92
901	26/04/01-074	65.89	bd	bd	bd	33.83	0.05	0.03	bd	bd	bd	bd	bd	0.04	0.04	bd	0.04	bd	bd	bd	99.91
901	26/04/01-075	65.60	bd	bd	0.04	34.19	bd	bd	bd	0.02	bd	bd	0.02	bd	bd	bd	0.04	bd	bd	bd	99.91
901	26/04/01-078	64.12	bd	bd	2.30	33.24	0.10	bd	bd	0.02	0.05	bd	bd	0.03	bd	bd	0.05	bd	bd	bd	99.91
901	26/04/01-079	65.74	bd	bd	0.12	33.89	0.10	bd	bd	bd	bd	bd	0.02	bd	bd	bd	0.04	bd	bd	bd	99.92
902	04/09/02-071	65.92	bd	bd	bd	33.81	0.16	bd	bd	0.01	bd	bd	0.02	bd	bd	NA	NA	bd	NA	NA	99.92
902	04/09/02-072	65.90	bd	bd	0.04	33.86	0.17	bd	bd	bd	bd	bd	bd	bd	bd	NA	NA	bd	NA	NA	99.97
902	04/09/02-073	66.04	bd	bd	0.04	33.72	0.10	bd	bd	bd	bd	bd	bd	bd	bd	NA	NA	bd	NA	NA	99.91
902	04/09/02-074	65.97	bd	bd	bd	33.84	0.08	bd	bd	0.01	bd	bd	bd	bd	bd	NA	NA	bd	NA	NA	99.91
902	04/09/02-075	65.78	bd	bd	bd	33.92	0.20	bd	bd	bd	bd	bd	0.01	0.03	bd	NA	NA	bd	NA	NA	99.94
902	04/09/02-076	65.03	bd	bd	1.47	33.21	0.20	0.02	bd	bd	bd	bd	bd	0.03	bd	NA	NA	bd	NA	NA	99.97
902	04/09/02-077	65.50	bd	bd	0.68	33.66	0.08	bd	bd	bd	bd	bd	0.01	0.02	bd	NA	NA	bd	NA	NA	99.95
902	27/04/01-020	65.55	bd	bd	bd	34.18	0.14	bd	bd	bd	bd	bd	0.03	bd	bd	bd	bd	bd	bd	bd	99.89
902	27/04/01-026	65.67	bd	bd	bd	34.02	0.12	bd	bd	bd	bd	bd	0.03	0.03	0.04	bd	bd	bd	bd	bd	99.91
902	27/04/01-032	65.48	bd	bd	bd	34.21	0.20	bd	bd	bd	bd	bd	bd	0.03	0.03	bd	bd	bd	bd	bd	99.95
902	27/04/01-045	65.54	bd	bd	0.09	34.08	0.08	bd	bd	bd	0.12	bd	bd	bd	bd	bd	bd	bd	bd	bd	99.91
902	27/04/01-050	65.43	bd	0.04	bd	34.03	0.30	0.02	bd	bd	0.05	bd	0.02	bd	bd	bd	bd	bd	bd	bd	99.90
906	26/04/01-016	65.67	bd	bd	0.05	34.05	0.05	0.02	bd	0.02	0.06	bd	bd	bd	bd	bd	bd	bd	bd	bd	99.92
910	26/04/01-025	64.89	bd	bd	0.12	33.87	0.90	bd	bd	bd	0.14	bd	bd	bd	bd	bd	bd	bd	bd	bd	99.92
910	26/04/01-030	65.36	bd	bd	bd	33.90	0.42	bd	bd	bd	0.13	bd	bd	0.05	0.02	bd	bd	0.02	bd	bd	99.90
910	26/04/01-033	65.39	bd	bd	bd	33.87	0.12	bd	bd	bd	0.53	bd	bd	bd	bd	bd	bd	bd	bd	bd	99.90
910	26/04/01-034	65.76	bd	bd	0.08	33.57	0.39	bd	0.02	0.01	bd	bd	bd	bd	0.03	bd	0.05	bd	bd	bd	99.92
910	26/04/01-053	65.70	bd	bd	bd	33.87	0.08	bd	bd	0.02	0.22	bd	bd	bd	bd	bd	bd	bd	bd	bd	99.90
910	26/04/01-058	65.53	bd	bd	0.06	34.19	0.07	bd	bd	0.02	bd	bd	bd	0.04	bd	bd	bd	bd	bd	bd	99.91

Table B1(viii). Sulphide analyses (at%) contd.

Sample No	Analysis Ref	S	Au	Ag	Cu	Fe	As	Se	Sb	Te	Zn	Pb	Hg	Bi	Ga	Ge	Co	Cd	In	Cr	Total
910	26/04/01-059	65.61	bd	bd	bd	34.13	0.12	bd	bd	bd	0.05	bd	bd	0.03	bd	bd	bd	bd	bd	bd	99.93
00-BT-01	27/04/01-105	65.51	bd	bd	0.05	34.04	0.06	bd	bd	bd	0.23	bd	bd	bd	bd	bd	bd	bd	bd	bd	99.89
00-BT-01	27/04/01-109	65.56	bd	bd	0.04	34.25	0.03	bd	bd	bd	bd	bd	0.02	0.03	bd	bd	bd	bd	bd	bd	99.93
00-BT-02	27/04/01-001	65.53	bd	bd	0.08	34.13	0.09	0.02	bd	0.02	bd	bd	bd	bd	bd	bd	bd	bd	bd	bd	99.88
00-BT-02	27/04/01-008	65.56	bd	bd	0.17	33.89	0.19	bd	bd	0.02	bd	bd	bd	0.03	bd	bd	0.08	bd	bd	bd	99.93
00-BT-02	27/04/01-009	65.55	bd	bd	bd	34.35	0.05	bd	bd	bd	bd	bd	bd	bd	bd	bd	bd	bd	bd	bd	99.94
00-BT-02	27/04/01-014	65.14	bd	bd	0.08	34.51	0.13	0.02	bd	0.02	bd	bd	bd	0.04	bd	bd	bd	bd	bd	bd	99.94
00-BT-02	27/04/01-018	65.55	bd	bd	bd	34.08	0.18	bd	0.01	0.02	bd	bd	bd	bd	bd	bd	0.04	bd	bd	bd	99.88
00-BT-13	27/04/01-057	65.43	bd	bd	0.05	34.33	0.05	bd	bd	bd	bd	bd	0.02	0.04	bd	bd	bd	bd	bd	bd	99.92
00-BT-13	27/04/01-060	65.51	bd	bd	bd	34.29	0.08	bd	bd	bd	bd	bd	0.02	bd	bd	bd	bd	bd	bd	bd	99.90
00-BT-13	27/04/01-061	64.80	bd	0.05	0.08	33.47	1.17	bd	0.28	bd	bd	bd	0.05	0.03	bd	bd	bd	bd	bd	bd	99.92
00-BT-13	27/04/01-067	65.73	bd	bd	0.04	34.04	0.04	bd	0.02	bd	bd	bd	bd	bd	bd	bd	bd	0.02	bd	bd	99.89
00-BT-13	27/04/01-070	65.74	bd	bd	bd	34.07	0.06	bd	bd	bd	bd	bd	bd	bd	bd	bd	bd	0.02	bd	bd	99.88
00-BT-13	27/04/01-074	65.58	bd	0.05	bd	34.17	0.04	bd	bd	0.01	bd	bd	0.02	bd	0.03	bd	bd	0.02	bd	bd	99.92
00-BT-15	26/04/01-090	65.64	0.03	bd	0.23	33.98	0.03	bd	bd	bd	bd	bd	bd	bd	bd	bd	bd	bd	bd	bd	99.92
00-BT-15	26/04/01-097	65.73	bd	bd	0.22	33.82	0.07	bd	bd	bd	bd	bd	0.02	0.03	bd	bd	bd	bd	bd	bd	99.89
01BT076a	03/09/02-107	65.61	bd	bd	0.04	33.07	1.03	bd	0.09	bd	0.08	bd	0.02	0.04	bd	NA	NA	bd	NA	NA	99.98
01BT076a	03/09/02-108	65.26	bd	bd	bd	32.97	1.47	0.04	0.14	bd	bd	bd	bd	bd	bd	NA	NA	bd	NA	NA	99.87
01BT076a	03/09/02-109	65.93	bd	bd	bd	33.52	0.05	bd	0.01	bd	0.38	bd	bd	0.03	bd	NA	NA	bd	NA	NA	99.93
01BT076a	03/09/02-110	66.13	bd	bd	bd	33.29	0.34	bd	0.04	0.02	0.08	bd	bd	bd	0.02	NA	NA	bd	NA	NA	99.91
01BT076a	03/09/02-111	66.08	bd	bd	bd	33.55	0.05	bd	bd	0.02	0.17	bd	0.03	bd	bd	NA	NA	0.02	NA	NA	99.93
01BT076a	03/09/02-124	66.01	bd	bd	bd	33.67	0.04	bd	bd	bd	0.16	bd	0.02	bd	bd	NA	NA	bd	NA	NA	99.90
01BT076a	03/09/02-125	66.15	bd	bd	0.05	33.50	0.04	bd	bd	0.01	0.20	bd	bd	bd	bd	NA	NA	bd	NA	NA	99.95
01BT082a	03/09/02-052	65.54	bd	bd	bd	33.65	0.72	bd	0.02	bd	bd	bd	0.02	bd	bd	NA	NA	bd	NA	NA	99.95
01BT082a	03/09/02-053	65.60	bd	bd	0.04	33.57	0.72	bd	0.02	bd	bd	bd	0.01	bd	bd	NA	NA	bd	NA	NA	99.97
01BT082a	03/09/02-054	65.86	bd	bd	0.11	33.69	0.25	bd	bd	bd	bd	bd	bd	bd	0.04	NA	NA	bd	NA	NA	99.95
01BT082a	03/09/02-055	65.67	bd	bd	0.38	33.20	0.40	bd	bd	bd	0.28	bd	bd	0.03	bd	NA	NA	bd	NA	NA	99.96
01BT082a	03/09/02-060	66.02	bd	bd	bd	33.82	0.03	bd	bd	bd	0.07	bd	bd	bd	bd	NA	NA	bd	NA	NA	99.95
01BT082a	03/09/02-061	64.25	bd	bd	bd	33.59	2.03	bd	0.05	bd	bd	bd	bd	bd	bd	NA	NA	bd	NA	NA	99.92
01BT082a	03/09/02-062	64.81	bd	bd	bd	33.56	1.42	0.02	0.09	bd	bd	bd	bd	0.03	bd	NA	NA	bd	NA	NA	99.94
01BT082a	03/09/02-063	64.27	bd	bd	0.04	33.42	2.15	bd	0.03	bd	bd	bd	0.02	bd	bd	NA	NA	bd	NA	NA	99.92
01BT082a	03/09/02-064	65.91	bd	bd	0.23	33.53	0.21	bd	bd	0.02	bd	bd	bd	0.03	bd	NA	NA	bd	NA	NA	99.92
01BT082a	03/09/02-097	65.76	bd	bd	bd	33.64	0.44	bd	0.03	bd	bd	bd	0.02	bd	0.02	NA	NA	bd	NA	NA	99.91
01BT082a	03/09/02-098	65.84	bd	bd	bd	33.65	0.43	bd	0.05	bd	bd	bd	bd	bd	bd	NA	NA	bd	NA	NA	99.97
01BT082a	03/09/02-099	65.22	0.03	bd	0.04	32.80	1.60	bd	0.22	0.01	bd	bd	0.03	0.04	bd	NA	NA	bd	NA	NA	99.99
01BT082a	03/09/02-100	66.02	bd	bd	0.05	33.24	0.54	bd	0.05	bd	bd	bd	0.01	0.03	0.03	NA	NA	bd	NA	NA	99.97
01BT082a	03/09/02-101	66.22	bd	bd	0.05	33.30	0.34	bd	bd	bd	bd	bd	bd	0.03	0.03	NA	NA	bd	NA	NA	99.96
01BT082a	03/09/02-102	65.64	bd	bd	bd	33.47	0.67	bd	0.07	0.02	bd	bd	bd	bd	bd	NA	NA	0.03	NA	NA	99.90

Table B1(viii). Sulphide analyses (at%) contd.

Sample No	Analysis Ref	S	Au	Ag	Cu	Fe	As	Se	Sb	Te	Zn	Pb	Hg	Bi	Ga	Ge	Co	Cd	In	Cr	Total
01BT082a	03/09/02-103	66.02	bd	bd	0.05	33.72	0.08	bd	0.02	bd	bd	bd	bd	bd	bd	NA	NA	bd	NA	NA	99.88
01BT082a	03/09/02-104	65.28	bd	bd	bd	33.39	1.21	bd	bd	bd	bd	bd	bd	0.03	bd	NA	NA	bd	NA	NA	99.91
01BT082a	03/09/02-105	65.73	bd	bd	0.06	33.65	0.44	bd	0.04	bd	bd	bd	bd	0.03	bd	NA	NA	bd	NA	NA	99.95
01BT082a	03/09/02-106	65.82	bd	bd	bd	33.74	0.34	bd	0.02	0.01	bd	bd	bd	0.04	bd	NA	NA	bd	NA	NA	99.98
01BT136	04/09/02-061	64.82	bd	bd	0.08	33.58	1.36	bd	0.05	bd	0.05	bd	bd	bd	bd	NA	NA	bd	NA	NA	99.93
01BT136	04/09/02-062	64.06	bd	bd	0.11	33.53	2.08	bd	0.14	bd	bd	bd	bd	bd	0.02	NA	NA	bd	NA	NA	99.94
01BT136	04/09/02-063	65.58	bd	bd	bd	34.08	0.23	bd	bd	bd	bd	bd	bd	bd	0.04	NA	NA	bd	NA	NA	99.93
01BT136	04/09/02-064	64.51	bd	bd	0.89	32.95	1.39	bd	0.16	bd	bd	bd	bd	bd	bd	NA	NA	bd	NA	NA	99.89
01BT138	03/09/02-159	65.84	bd	bd	0.07	33.26	0.65	0.02	0.01	bd	0.07	bd	0.01	0.03	bd	NA	NA	bd	NA	NA	99.97
01BT138	03/09/02-160	65.94	bd	bd	0.06	33.17	0.66	0.02	0.02	bd	0.08	bd	bd	bd	bd	NA	NA	bd	NA	NA	99.95
01BT138	03/09/02-164	65.99	0.03	0.08	0.27	32.65	0.79	bd	0.10	bd	bd	bd	bd	0.03	bd	NA	NA	bd	NA	NA	99.94
01BT138	03/09/02-165	66.63	bd	bd	bd	33.07	0.20	bd	0.01	0.01	bd	bd	bd	bd	bd	NA	NA	bd	NA	NA	99.92
01BT138	03/09/02-166	66.97	bd	bd	0.05	32.44	0.38	bd	0.02	bd	bd	bd	bd	0.03	0.05	NA	NA	bd	NA	NA	99.94
01BT162	04/09/02-012	65.75	bd	bd	bd	34.17	0.03	bd	bd	bd	bd	bd	bd	bd	bd	NA	NA	bd	NA	NA	99.95
01BT162	04/09/02-013	65.93	bd	bd	bd	33.89	0.04	bd	bd	bd	bd	bd	bd	0.04	bd	NA	NA	bd	NA	NA	99.90
01BT162	04/09/02-014	65.93	bd	bd	bd	33.93	0.03	bd	bd	bd	bd	bd	0.02	0.03	bd	NA	NA	bd	NA	NA	99.94
01BT162	04/09/02-015	65.88	bd	bd	bd	33.94	0.05	bd	bd	bd	bd	bd	bd	0.03	bd	NA	NA	bd	NA	NA	99.90
01BT162	04/09/02-016	65.91	bd	bd	bd	33.97	0.04	0.02	bd	bd	bd	bd	bd	bd	bd	NA	NA	bd	NA	NA	99.94
01BT162	04/09/02-017	65.74	bd	bd	bd	34.11	0.03	0.03	bd	bd	bd	bd	0.02	0.03	bd	NA	NA	bd	NA	NA	99.96
01BT162	04/09/02-021	65.85	bd	bd	bd	34.02	0.05	bd	bd	0.01	bd	bd	0.02	bd	bd	NA	NA	bd	NA	NA	99.96
01BT162	04/09/02-022	65.87	bd	bd	bd	34.01	bd	bd	bd	bd	bd	bd	0.01	0.04	bd	NA	NA	bd	NA	NA	99.93
01BT162	04/09/02-023	65.62	bd	bd	bd	34.01	0.25	0.02	0.02	bd	bd	bd	0.02	bd	bd	NA	NA	bd	NA	NA	99.94
01BT162	04/09/02-024	65.46	bd	bd	0.04	33.82	0.63	bd	bd	bd	bd	bd	bd	bd	bd	NA	NA	bd	NA	NA	99.93
01BT162	04/09/02-025	65.71	bd	bd	bd	33.74	0.43	bd	0.02	0.01	bd	bd	bd	bd	bd	NA	NA	0.02	NA	NA	99.94
01BT162	04/09/02-026	65.91	bd	bd	bd	33.90	0.08	0.03	bd	bd	bd	bd	bd	bd	0.02	NA	NA	bd	NA	NA	99.94
01BT162	04/09/02-027	65.77	0.02	bd	bd	34.09	0.03	bd	bd	bd	0.06	bd	bd	bd	bd	NA	NA	bd	NA	NA	99.97
BL-19B	27/04/01-090	65.66	bd	bd	0.07	33.98	0.05	bd	bd	bd	0.15	bd	bd	bd	bd	bd	bd	bd	bd	bd	99.91
BL-19B	27/04/01-099	65.23	bd	bd	0.04	33.95	0.05	bd	bd	bd	0.59	bd	bd	0.03	0.03	bd	0.04	bd	bd	bd	99.96
BL22-b	27/04/01-153	65.37	bd	bd	0.04	34.47	0.03	0.02	bd	bd	bd	bd	bd	bd	bd	bd	0.04	bd	bd	bd	99.97
BTB-01(C)	27/04/01-080	65.50	bd	bd	0.14	33.06	0.67	0.02	0.44	bd	bd	bd	0.03	bd	bd	bd	0.04	bd	bd	bd	99.91
BTB-01(C)	27/04/01-083	65.50	bd	bd	0.43	33.77	0.15	bd	0.02	bd	bd	bd	bd	0.03	bd	bd	bd	bd	bd	bd	99.89
BTB-01(C)	27/04/01-085	65.34	bd	bd	0.10	34.29	0.15	0.02	bd	0.02	bd	bd	bd	bd	bd	bd	bd	bd	bd	bd	99.92
Arsenopyrite																					
901	26/04/01-060	33.31	bd	bd	0.09	33.89	32.30	0.14	0.02	0.12	bd	bd	bd	bd	bd	bd	bd	bd	bd	bd	99.88
901	26/04/01-061	33.64	bd	bd	bd	33.12	32.87	0.14	bd	0.02	bd	bd	0.03	bd	bd	bd	bd	bd	bd	bd	99.81
901	26/04/01-062	34.11	bd	bd	0.22	33.21	32.09	0.17	0.02	0.09	bd	bd	0.02	bd	bd	bd	bd	bd	bd	bd	99.94
910	26/04/01-019	33.69	bd	bd	0.20	33.40	32.03	0.10	0.02	0.02	0.46	bd	bd	bd	bd	bd	bd	bd	bd	bd	99.92

Table B1(viii). Sulphide analyses (at%) contd.

Sample No	Analysis Ref	S	Au	Ag	Cu	Fe	As	Se	Sb	Te	Zn	Pb	Hg	Bi	Ga	Ge	Co	Cd	In	Cr	Total
910	26/04/01-020	33.00	0.04	bd	0.10	33.23	33.23	0.07	bd	0.03	0.23	bd	bd	bd	bd	bd	bd	bd	bd	bd	99.94
910	26/04/01-038	34.93	bd	bd	0.08	33.36	31.14	0.08	bd	0.03	0.28	bd	bd	bd	bd	bd	bd	0.03	bd	bd	99.93
910	26/04/01-039	33.71	0.04	bd	0.05	33.29	32.02	0.10	bd	bd	0.70	bd	0.03	bd	bd	bd	bd	bd	bd	bd	99.94
Chalcopyrite																					
901	26/04/01-066	50.38	0.04	bd	25.59	23.64	0.03	bd	bd	bd	0.24	bd	bd	0.03	bd	bd	bd	bd	bd	bd	99.96
901	26/04/01-071	50.09	bd	bd	25.23	24.39	0.04	bd	bd	bd	0.07	bd	bd	0.03	0.03	bd	bd	0.02	bd	bd	99.92
901	26/04/01-077	50.33	bd	bd	25.27	24.18	0.03	bd	0.01	0.02	bd	bd	bd	bd	bd	bd	bd	bd	bd	bd	99.85
902	27/04/01-022	50.48	bd	bd	24.74	24.66	bd	0.02	bd	bd	bd	bd	bd	bd	bd	bd	bd	bd	bd	bd	99.90
902	27/04/01-024	50.51	bd	bd	24.73	24.51	0.05	0.04	bd	bd	0.07	bd	bd	bd	bd	bd	bd	bd	bd	bd	99.91
902	27/04/01-028	50.51	bd	bd	24.58	24.70	0.05	bd	bd	bd	0.06	bd	0.02	bd	bd	bd	bd	bd	bd	bd	99.91
902	27/04/01-029	50.41	bd	bd	24.54	24.91	0.06	bd	bd	bd	bd	bd	bd	bd	bd	bd	bd	bd	bd	bd	99.92
902	27/04/01-033	49.99	bd	bd	24.87	24.96	0.03	bd	bd	bd	bd	bd	bd	bd	bd	bd	bd	bd	bd	bd	99.85
902	27/04/01-040	50.29	bd	bd	24.84	24.63	0.05	bd	bd	0.02	0.05	bd	0.02	bd	bd	bd	bd	bd	bd	bd	99.91
902	27/04/01-048	50.36	bd	bd	24.90	24.38	0.04	bd	bd	bd	0.14	bd	bd	0.03	0.04	bd	bd	bd	bd	bd	99.88
902	27/04/01-052	51.97	bd	bd	22.47	25.19	0.06	bd	bd	0.02	0.07	bd	0.02	bd	0.07	bd	bd	bd	bd	bd	99.87
906	26/04/01-002	50.25	bd	bd	25.24	24.28	0.06	bd	0.01	bd	bd	bd	bd	bd	0.03	bd	bd	bd	bd	bd	99.87
906	26/04/01-012	50.11	bd	0.37	26.07	21.89	0.48	bd	0.22	bd	0.73	bd	0.02	bd	0.03	bd	bd	bd	bd	bd	99.92
910	26/04/01-027	50.73	bd	bd	24.62	24.21	0.03	bd	bd	bd	0.25	bd	0.02	0.03	bd	bd	bd	0.02	bd	bd	99.92
910	26/04/01-044	50.22	bd	bd	25.36	24.01	bd	bd	bd	0.02	0.19	bd	0.02	0.05	0.03	bd	bd	bd	bd	bd	99.89
910	26/04/01-045	50.86	bd	0.05	24.41	24.37	0.05	bd	0.02	bd	0.13	bd	bd	bd	bd	bd	bd	bd	bd	bd	99.88
00-BT-01	27/04/01-106	50.06	bd	bd	25.06	24.27	bd	bd	bd	0.02	0.49	bd	bd	bd	0.03	bd	bd	bd	bd	bd	99.92
00-BT-02	27/04/01-002	50.18	bd	bd	25.01	24.70	0.04	bd	bd	bd	bd	bd	bd	bd	bd	bd	bd	bd	bd	bd	99.93
00-BT-02	27/04/01-005	50.08	bd	bd	25.04	24.65	0.05	bd	bd	bd	bd	bd	bd	bd	bd	bd	bd	bd	bd	bd	99.82
00-BT-13	27/04/01-056	50.10	bd	bd	25.17	24.43	0.07	bd	bd	0.02	0.06	bd	bd	bd	0.07	bd	bd	bd	bd	bd	99.91
00-BT-13	27/04/01-064	50.25	bd	bd	25.31	24.33	0.04	0.03	bd	bd	bd	bd	bd	bd	bd	bd	bd	bd	bd	bd	99.95
00-BT-13	27/04/01-066	49.98	bd	bd	25.32	24.56	0.05	bd	bd	bd	bd	bd	bd	bd	bd	bd	bd	0.02	bd	bd	99.92
00-BT-13	27/04/01-069	50.10	bd	bd	24.85	24.83	0.06	bd	bd	bd	0.06	bd	0.02	bd	bd	bd	bd	bd	bd	bd	99.92
00-BT-13	27/04/01-073	50.10	bd	bd	25.16	24.52	0.05	bd	bd	0.03	bd	bd	0.02	bd	0.03	bd	bd	bd	bd	bd	99.90
BL1	14/12/00-088	49.88	bd	0.12	24.92	24.77	0.07	bd	bd	0.02	0.16	bd	0.03	bd	NA	NA	NA	NA	NA	NA	99.97
BL-19B	27/04/01-093	49.83	bd	bd	25.29	24.57	0.07	bd	bd	bd	0.12	bd	bd	bd	bd	bd	0.04	bd	bd	bd	99.92
BL-19B	27/04/01-100	50.15	bd	bd	24.89	24.36	0.10	0.03	bd	0.02	0.43	bd	bd	bd	bd	bd	bd	bd	bd	bd	99.97
BL22-b	27/04/01-154	50.12	bd	bd	24.85	24.81	0.04	0.03	bd	bd	0.06	bd	bd	bd	0.03	bd	bd	0.02	bd	bd	99.96
BL22-b	27/04/01-168	49.94	bd	bd	24.99	24.76	0.03	bd	bd	bd	0.15	bd	bd	0.03	0.03	bd	bd	bd	bd	bd	99.93
BTB-01(B)	27/04/01-124	50.52	bd	bd	24.50	24.71	0.05	bd	0.01	bd	0.11	bd	bd	bd	bd	bd	bd	bd	bd	bd	99.90
BTB-01(B)	27/04/01-141	50.53	bd	bd	24.68	24.63	0.05	bd	bd	0.02	bd	bd	bd	bd	bd	bd	bd	bd	bd	bd	99.91
BTB-01(C)	13/12/00-033	49.94	bd	bd	24.37	24.54	0.05	bd	bd	bd	1.03	bd	bd	bd	NA	NA	NA	NA	NA	NA	99.94
BTB-01(C)	13/12/00-034	49.76	bd	0.08	24.58	24.77	0.06	bd	bd	bd	0.69	bd	0.02	bd	NA	NA	NA	NA	NA	NA	99.95

Table B1(viii). Sulphide analyses (at%) contd.

Sample No	Analysis Ref	S	Au	Ag	Cu	Fe	As	Se	Sb	Te	Zn	Pb	Hg	Bi	Ga	Ge	Co	Cd	In	Cr	Total
BTB-01(C)	13/12/00-047	50.04	bd	bd	24.87	24.87	0.05	bd	bd	bd	0.09	bd	bd	bd	NA	NA	NA	NA	NA	NA	99.92
BTB-01(C)	13/12/00-048	49.78	bd	0.06	24.84	25.12	0.03	bd	bd	bd	0.10	bd	0.02	bd	NA	NA	NA	NA	NA	NA	99.95
BTB-01(C)	13/12/00-049	49.85	bd	0.06	25.04	24.88	0.05	0.04	bd	bd	bd	bd	bd	bd	NA	NA	NA	NA	NA	NA	99.92
BTB-01(C)	27/04/01-079	50.17	bd	bd	24.58	24.11	0.06	0.04	bd	0.02	0.98	bd	bd	bd	bd	bd	bd	bd	bd	bd	99.95
Sphalerite																					
901	04/09/02-033	49.38	bd	bd	0.20	1.60	bd	0.03	bd	0.02	48.67	bd	0.03	bd	bd	NA	NA	0.07	NA	NA	99.99
901	04/09/02-034	49.41	bd	bd	0.32	1.69	bd	0.03	bd	bd	48.47	bd	bd	bd	bd	NA	NA	0.04	NA	NA	99.97
901	04/09/02-035	49.60	bd	bd	0.25	2.09	0.03	0.04	0.04	bd	47.86	bd	bd	bd	bd	NA	NA	0.08	NA	NA	99.99
902	27/04/01-037	50.44	bd	bd	0.26	1.11	bd	bd	bd	bd	48.03	bd	bd	bd	bd	bd	bd	0.11	bd	bd	99.93
902	27/04/01-038	50.60	bd	bd	bd	0.75	bd	bd	0.02	bd	48.35	bd	0.02	bd	bd	bd	bd	0.12	bd	bd	99.86
902	27/04/01-042	50.23	bd	bd	bd	1.12	0.03	bd	bd	bd	48.44	bd	bd	bd	bd	bd	bd	0.08	bd	bd	99.91
902	27/04/01-046	50.09	bd	bd	bd	0.79	bd	bd	bd	bd	48.88	bd	0.03	bd	bd	bd	bd	0.10	bd	bd	99.89
902	27/04/01-049	50.36	bd	bd	0.17	1.54	0.05	bd	bd	bd	47.72	bd	0.03	bd	bd	bd	bd	0.08	bd	bd	99.96
902	27/04/01-053	50.12	bd	bd	0.31	1.57	bd	bd	bd	bd	47.76	bd	bd	bd	bd	bd	bd	0.09	0.03	bd	99.88
910	26/04/01-024	50.39	bd	bd	0.51	1.42	1.86	bd	bd	bd	45.65	bd	bd	bd	bd	bd	bd	0.09	bd	bd	99.93
910	26/04/01-026	50.16	bd	bd	bd	1.13	bd	0.02	bd	bd	48.50	bd	0.02	bd	bd	bd	bd	0.08	bd	bd	99.90
910	26/04/01-031	49.85	bd	bd	bd	0.96	bd	0.03	bd	bd	48.98	bd	bd	bd	bd	bd	bd	0.08	bd	bd	99.89
910	26/04/01-032	50.06	bd	bd	bd	1.29	bd	bd	0.02	bd	48.48	bd	bd	bd	bd	bd	bd	0.08	bd	bd	99.92
910	26/04/01-037	49.94	bd	bd	0.36	0.78	bd	bd	0.02	bd	48.78	bd	bd	bd	bd	bd	bd	0.09	bd	bd	99.96
910	26/04/01-042	49.80	bd	bd	bd	0.77	0.04	bd	bd	bd	49.25	bd	bd	bd	bd	bd	bd	0.07	bd	bd	99.92
910	26/04/01-043	49.83	bd	bd	0.23	0.87	bd	bd	0.02	bd	48.90	bd	0.03	bd	bd	bd	bd	0.05	bd	bd	99.94
910	26/04/01-054	49.86	bd	bd	bd	0.78	0.05	bd	0.02	bd	49.14	bd	bd	bd	bd	bd	bd	0.08	bd	bd	99.93
910	26/04/01-057	50.02	bd	bd	bd	0.82	bd	bd	bd	bd	48.96	bd	bd	bd	bd	bd	bd	0.09	bd	bd	99.88
00-BT-01	27/04/01-104	50.18	bd	0.06	0.10	bd	bd	bd	0.02	bd	49.40	bd	0.02	bd	bd	bd	bd	0.18	bd	bd	99.96
00-BT-15	26/04/01-099	50.19	bd	bd	0.28	0.15	bd	0.03	bd	bd	49.10	bd	0.02	bd	bd	bd	bd	0.16	bd	bd	99.93
00-BT-15	26/04/01-101	49.71	bd	bd	0.42	0.06	0.04	bd	0.02	0.03	49.50	bd	bd	bd	bd	bd	bd	0.15	bd	bd	99.92
00-BT-15	26/04/01-105	50.59	bd	bd	0.44	0.12	0.05	bd	bd	bd	48.56	bd	0.02	bd	bd	bd	bd	0.15	bd	bd	99.93
01BT082a	03/09/02-051	50.07	bd	bd	0.20	0.49	bd	bd	bd	bd	48.87	bd	0.04	bd	bd	NA	NA	0.28	NA	NA	99.96
01BT136	04/09/02-052	49.71	bd	bd	0.51	0.13	0.04	bd	bd	bd	49.50	bd	bd	bd	bd	NA	NA	0.12	NA	NA	100.00
01BT136	04/09/02-053	49.87	bd	bd	0.52	0.10	bd	bd	0.02	bd	49.33	bd	0.02	bd	bd	NA	NA	0.12	NA	NA	99.97
01BT136	04/09/02-056	49.44	bd	bd	0.07	1.74	bd	bd	bd	bd	48.56	bd	bd	bd	bd	NA	NA	0.11	NA	NA	99.92
BL1	14/12/00-085	50.30	bd	bd	0.19	0.19	0.04	bd	bd	bd	49.27	bd	bd	bd	NA	NA	NA	0.11	NA	NA	100.10
BL1	14/12/00-086	48.98	bd	0.03	6.43	0.05	bd	0.05	bd	0.32	43.18	bd	0.01	bd	0.00	0.00	0.00	0.19	0.02	0.00	99.27
BL1	14/12/00-091	49.93	bd	bd	0.30	0.43	0.06	0.06	bd	bd	49.16	bd	0.04	bd	NA	NA	NA	0.11	NA	NA	100.08
BL1	14/12/00-092	49.97	bd	bd	0.20	0.11	0.04	0.02	0.02	bd	49.59	bd	bd	bd	NA	NA	NA	0.11	NA	NA	100.07
BL-19B	27/04/01-092	50.33	bd	bd	0.12	0.16	bd	bd	0.02	bd	49.16	bd	0.03	bd	bd	bd	bd	0.14	bd	bd	99.96
BL-19B	27/04/01-095	50.64	bd	bd	0.48	0.44	bd	bd	bd	bd	48.23	bd	bd	bd	bd	bd	bd	0.14	bd	bd	99.93

Table B1(viii). Sulphide analyses (at%) contd.

Sample No	Analysis Ref	S	Au	Ag	Cu	Fe	As	Se	Sb	Te	Zn	Pb	Hg	Bi	Ga	Ge	Co	Cd	In	Cr	Total
BL22-b	27/04/01-156	50.60	bd	bd	bd	0.14	bd	bd	bd	bd	49.02	bd	0.02	bd	bd	bd	bd	0.16	bd	bd	99.94
BL22-b	27/04/01-169	50.53	bd	bd	0.11	0.27	0.04	bd	bd	bd	48.85	bd	bd	bd	bd	bd	bd	0.16	bd	bd	99.96
BL22-b	27/04/01-172	49.17	bd	bd	0.39	0.82	bd	bd	bd	bd	49.38	bd	bd	bd	bd	bd	bd	0.15	bd	bd	99.91
BL711.A	14/12/00-009	49.93	bd	bd	0.09	0.19	bd	0.04	0.02	bd	49.66	bd	0.03	bd	NA	NA	NA	0.00	NA	NA	99.95
BTB-01(C)	13/12/00-036	50.12	bd	bd	0.15	0.15	0.03	0.03	bd	bd	49.46	bd	0.03	bd	NA	NA	NA	0.00	NA	NA	99.97
BTB-01(C)	13/12/00-037	49.95	bd	bd	0.22	0.08	bd	bd	0.02	bd	49.61	bd	0.07	bd	NA	NA	NA	0.00	NA	NA	99.95
Tennantite-tetrahedrite																					
901	04/09/02-028	44.03	bd	0.06	33.79	5.07	6.73	0.05	7.69	bd	2.52	bd	bd	bd	bd	NA	NA	bd	NA	NA	99.93
901	04/09/02-029	44.08	bd	bd	33.63	4.31	4.74	0.04	9.81	0.02	3.29	bd	bd	bd	bd	NA	NA	bd	NA	NA	99.93
901	04/09/02-030	43.79	bd	bd	33.94	4.64	5.89	0.04	8.66	0.02	2.91	bd	bd	bd	0.07	NA	NA	bd	NA	NA	99.97
901	04/09/02-031	44.00	bd	0.06	33.78	4.69	6.79	0.08	7.71	bd	2.78	bd	bd	0.04	0.04	NA	NA	0.03	NA	NA	99.99
901	04/09/02-032	43.98	bd	0.08	33.63	4.92	6.05	0.06	8.38	bd	2.84	bd	bd	0.04	bd	NA	NA	bd	NA	NA	99.99
901	04/09/02-036	44.10	bd	bd	33.60	5.31	5.77	0.06	8.30	bd	2.74	bd	bd	0.04	bd	NA	NA	0.02	NA	NA	99.95
902	27/04/01-025	45.16	bd	bd	33.44	4.40	11.37	0.05	2.39	0.03	3.02	bd	bd	bd	0.03	bd	bd	0.03	bd	bd	99.92
902	27/04/01-039	45.68	bd	0.16	32.87	4.19	11.91	0.05	2.08	0.03	2.97	bd	bd	bd	0.03	bd	bd	bd	bd	bd	99.96
906	26/04/01-004	45.68	bd	0.41	33.22	1.72	11.50	0.05	2.40	bd	4.95	bd	0.02	bd	bd	bd	bd	bd	bd	bd	99.95
906	26/04/01-005	46.20	bd	2.79	31.84	1.59	10.65	bd	2.22	0.05	4.59	bd	bd	bd	bd	bd	bd	0.03	bd	bd	99.96
906	26/04/01-007	44.97	bd	10.49	28.18	1.32	8.27	bd	2.04	bd	4.63	bd	0.03	bd	bd	bd	bd	0.04	bd	bd	99.96
906	26/04/01-010	43.73	bd	9.11	30.45	1.45	7.99	0.05	2.09	bd	5.04	bd	bd	bd	bd	bd	bd	0.04	bd	bd	99.94
906	26/04/01-013	43.98	bd	9.78	29.47	1.98	7.80	0.06	2.19	bd	4.65	bd	bd	bd	bd	bd	bd	0.04	bd	bd	99.95
906	26/04/01-015	44.98	bd	0.11	33.96	1.50	11.76	bd	2.41	bd	5.15	bd	0.04	bd	bd	bd	bd	0.05	bd	bd	99.95
906	26/04/01-082	44.37	bd	10.45	29.60	1.46	7.44	bd	1.99	bd	4.58	bd	0.02	bd	bd	bd	bd	bd	bd	bd	99.91
910	26/04/01-021	44.99	bd	0.89	32.55	1.76	5.65	bd	9.04	0.02	4.93	bd	0.04	bd	0.06	bd	bd	bd	bd	bd	99.93
910	26/04/01-022	45.22	bd	0.29	33.54	4.09	10.94	0.04	3.00	bd	2.83	bd	bd	bd	bd	bd	bd	bd	bd	bd	99.96
910	26/04/01-036	44.91	bd	0.28	34.05	3.80	11.05	0.08	2.93	bd	2.85	bd	bd	bd	bd	bd	bd	bd	bd	bd	99.95
910	26/04/01-046	45.01	bd	0.22	33.58	3.79	11.17	bd	2.95	0.02	3.11	bd	0.03	bd	bd	bd	bd	0.03	bd	bd	99.90
910	26/04/01-047	44.92	bd	0.49	33.00	2.96	7.39	0.03	6.95	bd	4.16	bd	bd	bd	bd	bd	bd	0.03	bd	bd	99.95
00-BT-02	27/04/01-006	45.71	bd	0.09	33.79	1.25	12.81	0.05	0.90	bd	5.30	bd	0.02	bd	bd	bd	bd	bd	bd	bd	99.92
00-BT-02	27/04/01-007	45.97	bd	0.11	33.32	1.32	12.69	0.05	1.04	0.02	5.30	bd	0.05	bd	0.03	bd	bd	0.03	bd	bd	99.95
00-BT-13	27/04/01-058	45.41	bd	0.10	33.81	1.38	12.53	0.05	1.30	bd	5.35	bd	0.02	bd	bd	bd	bd	bd	bd	bd	99.95
00-BT-13	27/04/01-059	45.88	bd	0.11	33.42	1.80	12.18	0.06	1.34	0.02	5.09	bd	bd	bd	bd	bd	bd	0.05	bd	bd	99.95
00-BT-13	27/04/01-063	45.08	bd	0.08	34.09	1.76	12.59	bd	1.30	bd	4.94	bd	0.03	bd	bd	bd	bd	0.04	bd	bd	99.91
00-BT-13	27/04/01-068	45.35	bd	0.23	34.26	1.16	12.14	0.07	1.17	bd	5.52	bd	bd	bd	bd	bd	bd	0.04	bd	bd	99.94
00-BT-13	27/04/01-072	45.27	bd	0.17	33.92	1.34	12.66	0.06	1.12	0.01	5.30	bd	0.02	bd	bd	bd	bd	0.03	bd	bd	99.92
01BT002a	03/09/02-026	44.76	bd	bd	34.44	1.59	13.62	0.07	0.33	0.02	5.08	bd	bd	0.04	bd	NA	NA	0.03	NA	NA	99.98
01BT002a	03/09/02-027	44.63	bd	0.05	34.50	1.64	13.66	0.03	0.31	bd	5.11	bd	0.03	bd	bd	NA	NA	0.04	NA	NA	99.99
01BT002a	03/09/02-028	44.68	bd	bd	34.39	1.67	13.67	0.08	0.33	bd	5.07	bd	bd	bd	bd	NA	NA	0.04	NA	NA	99.93

Table B1(viii). Sulphide analyses (at%) contd.

Sample No	Analysis Ref	S	Au	Ag	Cu	Fe	As	Se	Sb	Te	Zn	Pb	Hg	Bi	Ga	Ge	Co	Cd	In	Cr	Total
01BT002a	03/09/02-029	44.24	bd	bd	34.57	1.63	14.00	0.08	0.32	bd	5.06	bd	bd	bd	bd	NA	NA	0.03	NA	NA	99.94
01BT002a	03/09/02-030	44.41	bd	bd	34.67	1.67	13.70	0.05	0.29	0.02	5.10	bd	bd	bd	bd	NA	NA	0.02	NA	NA	99.93
01BT002a	03/09/02-031	44.67	bd	bd	34.44	1.64	13.66	0.04	0.35	bd	5.12	bd	bd	bd	0.03	NA	NA	bd	NA	NA	99.94
01BT002a	03/09/02-032	44.48	bd	bd	34.57	1.66	13.77	0.04	0.32	bd	5.06	bd	0.04	bd	bd	NA	NA	0.04	NA	NA	99.97
01BT002a	03/09/02-033	44.84	bd	bd	34.21	1.50	13.67	0.08	0.28	0.03	5.26	bd	bd	bd	0.04	NA	NA	0.03	NA	NA	99.95
01BT002a	03/09/02-034	44.45	bd	bd	34.47	1.50	13.80	0.06	0.28	0.02	5.26	bd	bd	bd	0.03	NA	NA	0.04	NA	NA	99.92
01BT076a	03/09/02-121	44.31	bd	0.13	33.68	1.81	11.34	0.03	3.02	bd	5.53	bd	0.06	bd	bd	NA	NA	0.05	NA	NA	99.97
01BT076a	03/09/02-122	44.43	bd	0.15	33.59	1.63	11.36	0.04	2.96	bd	5.63	bd	0.11	0.03	bd	NA	NA	0.05	NA	NA	99.99
01BT076a	03/09/02-123	44.36	bd	0.14	33.69	1.66	11.38	0.03	2.96	bd	5.59	bd	0.08	bd	bd	NA	NA	0.07	NA	NA	99.96
01BT082a	03/09/02-078	44.66	bd	0.51	33.71	1.88	11.43	0.04	2.68	0.02	4.95	bd	0.03	bd	bd	NA	NA	0.09	NA	NA	100.00
01BT082a	03/09/02-081	44.46	bd	0.70	33.62	1.63	9.90	0.04	4.28	bd	5.21	bd	0.05	bd	bd	NA	NA	0.10	NA	NA	99.99
01BT082a	03/09/02-082	44.43	bd	0.63	33.69	1.62	10.26	0.04	3.97	bd	5.16	bd	0.06	bd	bd	NA	NA	0.10	NA	NA	99.97
01BT082a	03/09/02-083	44.82	bd	0.57	33.25	1.65	10.58	0.08	3.73	bd	5.09	bd	0.03	bd	0.10	NA	NA	0.08	NA	NA	99.98
01BT082a	03/09/02-084	44.27	bd	0.65	33.70	1.76	10.68	bd	3.62	bd	5.08	bd	0.06	bd	0.06	NA	NA	0.07	NA	NA	99.94
01BT136	04/09/02-050	44.44	bd	0.16	34.01	1.30	13.05	0.05	1.09	0.03	5.81	bd	bd	bd	bd	NA	NA	0.03	NA	NA	99.96
01BT136	04/09/02-051	44.22	bd	0.14	34.45	1.34	13.08	bd	1.02	bd	5.62	bd	bd	bd	0.03	NA	NA	0.05	NA	NA	99.96
01BT136	04/09/02-054	44.39	bd	0.27	33.59	2.22	12.63	0.05	1.48	bd	5.27	bd	0.04	bd	bd	NA	NA	0.04	NA	NA	99.98
01BT136	04/09/02-055	44.53	bd	0.31	33.53	2.24	12.53	bd	1.53	bd	5.26	bd	bd	bd	bd	NA	NA	0.04	NA	NA	99.97
01BT136	04/09/02-057	44.32	bd	0.23	34.02	1.71	12.91	0.03	1.29	bd	5.34	bd	0.02	bd	0.06	NA	NA	0.04	NA	NA	99.97
01BT136	04/09/02-058	44.45	bd	0.25	34.15	1.38	13.03	0.03	1.08	bd	5.53	bd	bd	bd	0.05	NA	NA	0.04	NA	NA	99.97
01BT136	04/09/02-059	44.39	bd	0.22	34.27	1.33	12.89	0.07	1.12	bd	5.59	bd	0.03	bd	bd	NA	NA	0.04	NA	NA	99.95
01BT136	04/09/02-060	44.22	bd	0.19	34.49	1.33	12.93	0.07	1.17	bd	5.55	bd	0.02	bd	bd	NA	NA	0.03	NA	NA	99.99
01BT138	03/09/02-155	44.53	bd	0.21	33.97	2.61	12.65	0.07	1.65	bd	4.29	bd	bd	bd	bd	NA	NA	bd	NA	NA	99.99
01BT138	03/09/02-156	44.59	bd	0.22	33.93	2.69	12.62	0.07	1.61	bd	4.25	bd	bd	bd	bd	NA	NA	bd	NA	NA	99.97
01BT138	03/09/02-157	44.63	bd	0.23	33.93	2.59	12.71	bd	1.60	bd	4.25	bd	bd	bd	bd	NA	NA	0.02	NA	NA	99.97
01BT138	03/09/02-158	44.63	bd	0.14	33.90	2.61	12.69	0.05	1.58	bd	4.33	bd	bd	bd	bd	NA	NA	bd	NA	NA	99.94
01BT162	04/09/02-001	44.51	bd	bd	33.90	1.32	11.78	0.04	2.41	0.03	5.90	bd	bd	bd	bd	NA	NA	0.07	NA	NA	99.95
01BT162	04/09/02-002	44.39	bd	0.06	33.81	1.45	11.78	0.06	2.47	0.04	5.86	bd	0.02	bd	bd	NA	NA	0.05	NA	NA	99.99
01BT162	04/09/02-003	44.38	bd	0.05	34.06	1.46	11.73	0.05	2.43	bd	5.66	bd	0.05	bd	bd	NA	NA	0.06	NA	NA	99.95
01BT162	04/09/02-004	44.43	bd	0.08	33.89	1.35	11.78	0.05	2.46	0.02	5.80	bd	bd	bd	0.05	NA	NA	0.06	NA	NA	99.96
01BT162	04/09/02-005	44.68	bd	0.06	34.09	1.20	12.12	0.04	2.05	0.03	5.65	bd	bd	bd	bd	NA	NA	0.06	NA	NA	99.99
01BT162	04/09/02-006	44.52	bd	0.06	34.12	1.19	12.07	bd	2.21	0.03	5.69	bd	bd	bd	bd	NA	NA	0.04	NA	NA	99.94
01BT162	04/09/02-007	44.27	0.03	0.06	34.13	1.30	12.22	0.06	2.20	0.02	5.59	bd	bd	bd	0.04	NA	NA	0.07	NA	NA	100.00
BL1	14/12/00-032	44.99	bd	0.26	33.79	1.24	12.10	0.06	2.04	bd	5.47	bd	bd	bd	NA	NA	NA	NA	NA	NA	99.96
BL1	14/12/00-045	45.01	bd	0.14	33.52	1.04	11.60	0.03	2.65	0.02	5.93	bd	0.04	bd	NA	NA	NA	NA	NA	NA	99.98
BL1	14/12/00-048	44.60	bd	0.21	34.22	1.22	11.98	0.04	2.18	0.02	5.50	bd	0.03	bd	NA	NA	NA	NA	NA	NA	100.00
BL1	14/12/00-049	44.41	bd	0.24	33.75	2.01	12.01	0.05	2.08	0.02	5.36	bd	0.04	bd	NA	NA	NA	NA	NA	NA	99.97
BL1	14/12/00-050	44.55	0.03	0.07	34.39	1.25	11.73	0.06	2.32	bd	5.57	bd	0.02	bd	NA	NA	NA	NA	NA	NA	99.99

Table B1(viii). Sulphide analyses (at%) contd.

Sample No	Analysis Ref	S	Au	Ag	Cu	Fe	As	Se	Sb	Te	Zn	Pb	Hg	Bi	Ga	Ge	Co	Cd	In	Cr	Total
BL1	14/12/00-051	44.82	bd	0.27	33.85	1.31	11.95	0.07	2.14	bd	5.54	bd	bd	0.03	NA	NA	NA	NA	NA	NA	99.99
BL1	14/12/00-052	44.59	bd	0.22	34.17	1.27	12.02	0.04	2.04	bd	5.62	bd	0.02	bd	NA	NA	NA	NA	NA	NA	99.99
BL1	14/12/00-053	44.74	bd	0.07	34.30	1.30	11.97	0.05	2.10	bd	5.44	bd	bd	bd	NA	NA	NA	NA	NA	NA	99.96
BL1	14/12/00-054	44.48	bd	0.28	34.39	1.26	11.93	0.06	2.06	bd	5.53	bd	0.02	bd	NA	NA	NA	NA	NA	NA	100.00
BL1	14/12/00-087	44.32	bd	0.20	34.24	1.31	12.07	0.03	1.90	bd	5.88	bd	0.02	bd	NA	NA	NA	NA	NA	NA	99.97
BL1	14/12/00-093	44.38	0.03	0.15	34.30	1.25	12.12	0.07	1.93	bd	5.76	bd	bd	bd	NA	NA	NA	NA	NA	NA	99.99
BL1	14/12/00-106	44.55	bd	bd	34.47	1.36	12.17	0.03	1.90	0.03	5.40	bd	0.02	bd	NA	NA	NA	NA	NA	NA	99.94
BL-19B	27/04/01-102	44.98	bd	1.01	32.78	0.82	5.86	0.07	8.48	0.02	5.83	bd	bd	bd	0.04	bd	bd	0.05	bd	bd	99.93
BL22-b	27/04/01-155	45.04	bd	0.69	33.17	1.81	9.72	0.07	4.18	0.07	5.14	bd	bd	bd	0.04	bd	bd	0.05	bd	bd	99.98
BL22-b	27/04/01-157	45.45	bd	0.70	33.13	2.18	9.47	0.04	4.20	0.05	4.66	bd	bd	bd	bd	bd	bd	0.06	bd	bd	99.95
BL22-b	27/04/01-165	44.80	bd	0.76	33.27	2.67	9.68	0.07	4.30	0.06	4.25	bd	bd	bd	0.03	bd	bd	0.05	bd	bd	99.96
BL22-b	27/04/01-166	45.08	bd	0.71	32.95	2.37	9.68	0.05	4.31	0.05	4.74	bd	bd	bd	bd	bd	bd	0.03	bd	bd	99.98
BTB-01(B)	13/12/00-009	45.10	bd	0.17	34.27	1.35	12.08	0.05	1.74	bd	5.12	bd	0.06	bd	NA	NA	NA	NA	NA	NA	99.93
BTB-01(B)	13/12/00-010	45.47	bd	0.12	34.16	1.35	12.00	0.03	1.68	bd	5.11	bd	0.04	bd	NA	NA	NA	NA	NA	NA	99.97
BTB-01(B)	13/12/00-011	46.01	bd	0.10	33.62	1.29	12.02	0.03	1.69	bd	5.11	bd	0.06	bd	NA	NA	NA	NA	NA	NA	99.94
BTB-01(B)	27/04/01-131	45.26	bd	0.16	34.01	1.27	12.34	0.06	1.55	0.02	5.21	bd	0.02	0.04	bd	bd	bd	0.02	bd	bd	99.97
BTB-01(B)	27/04/01-133	45.06	bd	0.18	34.10	1.33	12.22	0.08	1.56	bd	5.32	bd	0.04	bd	0.05	bd	bd	bd	bd	bd	99.94
BTB-01(B)	27/04/01-140	45.63	bd	0.22	33.67	1.51	11.86	0.06	1.81	bd	5.10	bd	0.04	bd	bd	bd	bd	0.05	bd	bd	99.95
BTB-01(B)	27/04/01-143	45.49	bd	0.12	33.93	1.18	11.69	0.03	2.00	bd	5.40	bd	0.04	bd	bd	bd	bd	0.04	bd	bd	99.92
BTB-01(C)	13/12/00-024	44.70	bd	0.39	33.96	1.52	11.62	0.06	2.25	bd	5.42	bd	0.06	bd	NA	NA	NA	NA	NA	NA	99.98
BTB-01(C)	13/12/00-025	44.78	bd	0.40	33.44	1.33	11.99	0.07	2.48	bd	5.45	bd	0.04	bd	NA	NA	NA	NA	NA	NA	99.97
BTB-01(C)	13/12/00-026	44.66	bd	0.61	33.71	1.40	11.78	0.03	2.40	0.02	5.40	bd	bd	bd	NA	NA	NA	NA	NA	NA	100.00
BTB-01(C)	13/12/00-050	44.51	bd	0.48	33.75	1.46	11.58	0.05	2.51	0.03	5.60	bd	bd	bd	NA	NA	NA	NA	NA	NA	99.98
BTB-01(C)	13/12/00-051	44.36	bd	1.01	33.85	1.30	11.37	0.05	2.50	0.02	5.44	bd	0.03	bd	NA	NA	NA	NA	NA	NA	99.95
BTB-01(C)	13/12/00-052	44.60	bd	1.55	33.48	1.22	11.18	0.04	2.41	bd	5.47	bd	0.03	bd	NA	NA	NA	NA	NA	NA	99.97
BTB-01(C)	27/04/01-087	45.30	bd	bd	32.44	2.87	10.94	0.04	2.89	0.03	5.29	bd	0.02	bd	0.05	bd	bd	0.03	bd	bd	99.90
Galena																					
902	27/04/01-031	50.16	bd	bd	bd	1.55	bd	0.30	bd	bd	bd	47.70	bd	bd	bd	bd	bd	0.08	bd	bd	99.79
902	27/04/01-044	50.21	bd	bd	0.16	0.82	bd	0.34	bd	bd	bd	48.17	bd	bd	bd	bd	bd	bd	bd	bd	99.70
906	26/04/01-018	50.36	bd	bd	bd	bd	bd	0.16	bd	bd	1.11	48.24	bd	bd	bd	bd	bd	bd	bd	bd	99.87
906	26/04/01-081	50.43	bd	bd	0.90	0.56	bd	0.12	0.09	bd	1.84	45.98	bd	bd	bd	bd	bd	bd	bd	bd	99.91
910	26/04/01-035	50.58	bd	bd	bd	2.35	bd	0.08	bd	bd	1.35	45.42	bd	bd	bd	bd	bd	bd	bd	bd	99.79
910	26/04/01-051	49.24	bd	bd	bd	3.39	bd	0.15	bd	bd	0.56	46.42	bd	bd	bd	bd	bd	0.07	bd	bd	99.82
910	26/04/01-055	50.89	bd	bd	bd	0.62	bd	0.13	bd	bd	0.67	47.53	bd	bd	bd	bd	bd	bd	bd	bd	99.85
910	26/04/01-056	50.48	bd	bd	bd	0.30	0.08	0.11	0.10	bd	0.36	48.30	bd	bd	bd	bd	bd	0.05	bd	bd	99.77
00-BT-01	27/04/01-103	50.72	bd	bd	bd	0.07	bd	0.10	0.08	bd	0.31	48.50	bd	bd	bd	bd	bd	0.07	bd	bd	99.86
00-BT-01	27/04/01-111	50.55	bd	bd	0.43	0.07	bd	0.22	bd	bd	bd	48.61	bd	bd	bd	bd	bd	bd	bd	bd	99.89

Table B1(viii). Sulphide analyses (at%) contd.

Sample No	Analysis Ref	S	Au	Ag	Cu	Fe	As	Se	Sb	Te	Zn	Pb	Hg	Bi	Ga	Ge	Co	Cd	In	Cr	Total
01BT076a	03/09/02-112	50.37	bd	bd	bd	bd	bd	bd	bd	bd	bd	49.36	bd	bd	bd	NA	NA	bd	NA	NA	99.73
01BT076a	03/09/02-113	50.23	bd	bd	bd	bd	bd	bd	0.04	bd	bd	49.38	bd	bd	bd	NA	NA	0.06	NA	NA	99.71
01BT076a	03/09/02-114	49.89	bd	bd	bd	bd	bd	bd	0.04	bd	0.30	49.57	bd	bd	bd	NA	NA	bd	NA	NA	99.81
01BT076a	03/09/02-115	48.78	bd	bd	0.53	1.02	bd	0.07	bd	bd	2.86	46.67	bd	bd	bd	NA	NA	bd	NA	NA	99.94
01BT076a	03/09/02-117	49.35	bd	bd	bd	bd	bd	bd	bd	bd	1.73	48.60	bd	bd	bd	NA	NA	bd	NA	NA	99.67
01BT076a	03/09/02-118	49.44	bd	bd	0.37	0.14	bd	bd	bd	bd	0.90	49.11	bd	bd	bd	NA	NA	bd	NA	NA	99.97
01BT076a	03/09/02-126	50.01	bd	bd	0.16	bd	bd	bd	bd	bd	bd	49.64	bd	bd	bd	NA	NA	bd	NA	NA	99.81
01BT076a	03/09/02-127	49.93	bd	bd	0.12	0.09	bd	bd	bd	bd	bd	49.70	bd	bd	bd	NA	NA	bd	NA	NA	99.84
01BT076a	03/09/02-132	50.08	bd	bd	bd	bd	bd	bd	bd	bd	bd	49.76	bd	bd	bd	NA	NA	bd	NA	NA	99.84
01BT076a	03/09/02-133	50.47	bd	bd	bd	bd	bd	0.10	bd	bd	0.15	49.13	bd	bd	bd	NA	NA	bd	NA	NA	99.84
01BT076a	03/09/02-134	49.97	bd	bd	bd	bd	0.10	0.10	bd	bd	bd	49.58	bd	bd	bd	NA	NA	bd	NA	NA	99.75
01BT076a	03/09/02-135	50.22	bd	bd	bd	0.07	bd	0.07	bd	bd	bd	49.53	bd	bd	bd	NA	NA	bd	NA	NA	99.89
01BT076a	03/09/02-136	50.43	bd	bd	bd	bd	bd	0.06	bd	bd	bd	49.41	bd	bd	bd	NA	NA	0.05	NA	NA	99.95
01BT076a	03/09/02-137	49.90	bd	bd	bd	bd	bd	bd	0.04	bd	bd	49.79	bd	bd	bd	NA	NA	bd	NA	NA	99.73
01BT076a	03/09/02-138	49.57	bd	bd	0.11	bd	bd	bd	bd	bd	bd	50.00	bd	bd	bd	NA	NA	bd	NA	NA	99.69
01BT076a	03/09/02-139	49.93	bd	bd	bd	bd	bd	0.09	0.04	bd	0.14	49.51	bd	bd	0.13	NA	NA	bd	NA	NA	99.83
01BT076a	03/09/02-140	50.11	bd	bd	bd	0.06	bd	bd	bd	bd	0.47	49.20	bd	bd	bd	NA	NA	bd	NA	NA	99.85
01BT082a	03/09/02-044	50.31	bd	bd	0.16	bd	bd	0.06	bd	bd	0.25	49.04	bd	bd	bd	NA	NA	bd	NA	NA	99.83
01BT082a	03/09/02-045	49.82	bd	bd	0.11	bd	bd	0.06	bd	bd	bd	49.60	bd	bd	bd	NA	NA	0.12	NA	NA	99.71
01BT082a	03/09/02-046	50.27	bd	bd	0.13	bd	bd	bd	0.05	bd	bd	49.31	bd	bd	bd	NA	NA	bd	NA	NA	99.76
01BT082a	03/09/02-047	49.82	bd	bd	bd	bd	bd	bd	bd	bd	bd	49.92	bd	bd	bd	NA	NA	bd	NA	NA	99.74
01BT082a	03/09/02-048	49.90	bd	bd	bd	bd	0.09	bd	bd	bd	bd	49.68	bd	bd	bd	NA	NA	0.08	NA	NA	99.75
01BT082a	03/09/02-049	49.99	bd	bd	0.11	bd	bd	0.08	bd	bd	bd	49.64	bd	bd	bd	NA	NA	bd	NA	NA	99.81
01BT082a	03/09/02-050	48.65	bd	bd	0.30	0.29	bd	0.08	bd	bd	2.19	48.37	bd	bd	bd	NA	NA	bd	NA	NA	99.87
01BT082a	03/09/02-056	49.84	bd	bd	0.42	0.28	bd	bd	bd	bd	bd	49.21	bd	bd	bd	NA	NA	bd	NA	NA	99.76
01BT082a	03/09/02-057	49.72	bd	bd	0.53	0.26	0.10	0.06	bd	bd	bd	49.24	bd	bd	bd	NA	NA	bd	NA	NA	99.91
01BT082a	03/09/02-058	49.92	bd	bd	0.30	0.14	bd	0.11	bd	0.04	0.14	49.35	bd	bd	bd	NA	NA	bd	NA	NA	100.00
01BT082a	03/09/02-074	50.22	0.10	bd	0.29	bd	bd	0.08	bd	bd	bd	49.13	bd	bd	bd	NA	NA	bd	NA	NA	99.81
01BT082a	03/09/02-075	50.07	bd	bd	0.11	bd	bd	bd	bd	bd	bd	49.67	bd	bd	bd	NA	NA	bd	NA	NA	99.85
01BT082a	03/09/02-076	49.79	bd	bd	0.53	bd	bd	bd	0.06	bd	0.17	49.33	bd	bd	bd	NA	NA	bd	NA	NA	99.89
01BT082a	03/09/02-077	49.88	bd	bd	0.82	0.12	bd	bd	bd	bd	0.13	48.88	bd	bd	0.08	NA	NA	bd	NA	NA	99.93
01BT082a	03/09/02-085	50.00	bd	bd	0.14	0.07	bd	bd	bd	0.04	bd	49.39	bd	bd	bd	NA	NA	bd	NA	NA	99.63
01BT082a	03/09/02-086	49.94	bd	bd	bd	bd	0.10	0.11	bd	bd	bd	49.46	bd	bd	0.11	NA	NA	0.07	NA	NA	99.79
01BT082a	03/09/02-087	49.92	0.10	bd	bd	bd	bd	0.08	bd	bd	bd	49.67	bd	bd	bd	NA	NA	0.09	NA	NA	99.87
01BT082a	03/09/02-088	49.75	bd	bd	bd	bd	bd	0.09	0.04	bd	0.29	49.71	bd	bd	bd	NA	NA	bd	NA	NA	99.88
01BT082a	03/09/02-089	50.40	bd	bd	bd	bd	bd	0.07	0.05	bd	bd	49.23	bd	bd	0.07	NA	NA	bd	NA	NA	99.82
01BT082a	03/09/02-090	49.78	bd	bd	0.22	0.08	0.10	bd	bd	bd	bd	49.62	bd	bd	bd	NA	NA	bd	NA	NA	99.80
01BT082a	03/09/02-091	50.17	bd	bd	0.11	bd	bd	0.06	0.04	bd	bd	49.39	bd	bd	bd	NA	NA	bd	NA	NA	99.77

Table B1(viii). Sulphide analyses (at%) contd.

Sample No	Analysis Ref	S	Au	Ag	Cu	Fe	As	Se	Sb	Te	Zn	Pb	Hg	Bi	Ga	Ge	Co	Cd	In	Cr	Total
01BT082a	03/09/02-092	49.84	bd	bd	bd	0.09	bd	0.11	0.05	bd	bd	49.75	bd	bd	bd	NA	NA	bd	NA	NA	99.83
01BT082a	03/09/02-093	49.76	bd	bd	0.19	0.13	0.09	0.08	bd	bd	bd	49.48	bd	bd	0.08	NA	NA	0.09	NA	NA	99.88
01BT082a	03/09/02-094	49.81	bd	bd	bd	0.10	bd	bd	0.06	bd	bd	49.75	bd	bd	bd	NA	NA	bd	NA	NA	99.72
01BT082a	03/09/02-095	49.98	bd	bd	0.19	0.12	bd	bd	0.04	bd	bd	49.46	bd	bd	bd	NA	NA	bd	NA	NA	99.78
01BT082a	03/09/02-096	50.05	bd	bd	0.29	0.06	bd	0.11	bd	bd	bd	49.37	bd	bd	bd	NA	NA	bd	NA	NA	99.88
01BT136	04/09/02-046	49.29	bd	bd	0.63	0.44	bd	0.12	0.07	bd	0.33	48.90	bd	bd	0.08	NA	NA	0.07	NA	NA	99.93
01BT136	04/09/02-047	48.79	bd	bd	2.40	0.16	bd	0.07	bd	bd	0.46	47.93	bd	bd	bd	NA	NA	bd	NA	NA	99.80
01BT136	04/09/02-049	49.41	bd	bd	bd	0.36	bd	0.10	bd	bd	0.31	49.65	bd	bd	bd	NA	NA	bd	NA	NA	99.83
01BT138	03/09/02-151	48.92	bd	bd	1.59	1.08	bd	bd	bd	bd	bd	48.23	bd	bd	bd	NA	NA	bd	NA	NA	99.82
01BT138	03/09/02-152	49.34	bd	bd	1.56	bd	bd	bd	bd	bd	0.47	48.30	bd	bd	bd	NA	NA	bd	NA	NA	99.67
01BT138	03/09/02-153	50.01	bd	bd	0.36	bd	bd	0.10	0.09	bd	0.18	49.07	bd	bd	0.08	NA	NA	bd	NA	NA	99.87
01BT138	03/09/02-154	49.95	bd	bd	bd	bd	bd	0.06	bd	bd	0.29	49.59	bd	bd	bd	NA	NA	bd	NA	NA	99.89
01BT162	04/09/02-008	49.18	bd	bd	1.10	bd	bd	0.35	bd	bd	0.20	49.04	bd	bd	bd	NA	NA	bd	NA	NA	99.88
01BT162	04/09/02-009	49.84	bd	bd	0.33	0.10	bd	0.16	bd	bd	bd	49.44	bd	bd	bd	NA	NA	bd	NA	NA	99.87
01BT162	04/09/02-010	49.13	0.08	bd	0.60	0.40	bd	0.46	bd	bd	0.24	48.88	bd	bd	bd	NA	NA	0.11	NA	NA	99.91
01BT162	04/09/02-011	49.71	bd	bd	0.29	0.25	bd	0.31	bd	0.07	bd	49.13	bd	bd	bd	NA	NA	bd	NA	NA	99.76
01BT162	04/09/02-018	49.43	bd	bd	0.11	0.06	bd	0.34	bd	0.04	0.40	49.40	bd	bd	bd	NA	NA	0.07	NA	NA	99.84
01BT162	04/09/02-019	49.35	bd	bd	bd	bd	0.09	0.36	0.05	bd	0.70	49.30	bd	bd	bd	NA	NA	bd	NA	NA	99.84
01BT162	04/09/02-020	49.35	bd	bd	bd	bd	bd	0.35	bd	bd	0.86	49.14	bd	bd	bd	NA	NA	bd	NA	NA	99.72
01BT226b	03/09/02-013	49.93	bd	0.84	0.31	bd	bd	bd	bd	0.06	bd	48.65	bd	bd	bd	NA	NA	bd	NA	NA	99.79
01BT226b	03/09/02-022	49.64	bd	bd	bd	bd	bd	0.06	0.06	bd	bd	50.09	bd	bd	bd	NA	NA	bd	NA	NA	99.85
01BT226b	03/09/02-023	49.72	bd	bd	bd	bd	bd	0.06	0.03	bd	bd	49.92	bd	bd	0.10	NA	NA	bd	NA	NA	99.84
01BT226b	03/09/02-024	49.69	bd	bd	bd	bd	bd	0.11	bd	bd	bd	49.96	bd	bd	bd	NA	NA	0.09	NA	NA	99.85
01BT226b	03/09/02-025	49.83	bd	bd	bd	bd	bd	bd	0.04	bd	bd	49.91	bd	bd	bd	NA	NA	bd	NA	NA	99.78
01BT226b	03/09/02-037	49.80	bd	bd	0.13	bd	bd	bd	bd	bd	bd	49.81	bd	bd	bd	NA	NA	0.06	NA	NA	99.80
01BT226b	03/09/02-038	50.14	bd	bd	bd	bd	bd	bd	0.10	bd	bd	49.42	bd	bd	bd	NA	NA	0.09	NA	NA	99.75
01BT226b	03/09/02-039	49.90	0.11	bd	0.11	bd	bd	0.07	0.04	bd	bd	49.62	bd	bd	bd	NA	NA	bd	NA	NA	99.84
01BT226b	03/09/02-041	50.13	bd	bd	bd	bd	bd	bd	0.08	bd	bd	49.49	bd	bd	bd	NA	NA	bd	NA	NA	99.70
01BT226b	03/09/02-042	49.85	bd	bd	bd	bd	bd	0.11	bd	bd	bd	49.76	bd	bd	bd	NA	NA	bd	NA	NA	99.72
01BT226b	03/09/02-043	49.91	bd	bd	bd	0.08	bd	bd	bd	bd	bd	49.87	bd	bd	bd	NA	NA	bd	NA	NA	99.85
BL1	14/12/00-079	49.56	bd	0.52	0.52	bd	bd	0.14	bd	bd	bd	49.04	bd	bd	NA	NA	NA	NA	NA	NA	99.78
BL1	14/12/00-082	49.18	bd	0.22	0.73	0.08	bd	0.17	bd	bd	0.29	49.29	bd	bd	NA	NA	NA	NA	NA	NA	99.96
BL1	14/12/00-083	49.21	bd	0.29	0.74	bd	bd	0.21	bd	bd	0.54	48.91	bd	bd	NA	NA	NA	NA	NA	NA	99.91
BL1	14/12/00-105	49.89	bd	0.14	bd	0.06	0.08	0.10	0.08	bd	bd	49.48	bd	bd	NA	NA	NA	NA	NA	NA	99.83
BL-19B	27/04/01-088	50.89	bd	bd	bd	bd	0.08	0.14	0.04	bd	bd	48.64	bd	bd	bd	bd	bd	bd	bd	bd	99.78
BL-19B	27/04/01-101	51.19	bd	bd	bd	bd	bd	0.11	bd	bd	0.27	48.27	bd	bd	bd	bd	bd	bd	bd	bd	99.84
BL22-b	27/04/01-151	49.01	bd	bd	bd	bd	bd	0.60	bd	bd	1.53	48.61	bd	bd	bd	bd	bd	0.07	bd	bd	99.81
BL711.A	14/12/00-007	49.80	bd	bd	0.11	bd	bd	bd	bd	bd	1.03	48.91	bd	bd	NA	NA	NA	NA	NA	NA	99.85

Table B1(viii). Sulphide analyses (at%) contd.

Sample No	Analysis Ref	S	Au	Ag	Cu	Fe	As	Se	Sb	Te	Zn	Pb	Hg	Bi	Ga	Ge	Co	Cd	In	Cr	Total
BL711.A	14/12/00-008	50.40	bd	bd	0.13	bd	0.08	0.06	bd	bd	0.84	48.36	bd	bd	NA	NA	NA	NA	NA	NA	99.87
BTB-01(B)	13/12/00-006	49.68	0.10	1.90	2.24	bd	bd	0.09	bd	bd	bd	45.95	bd	bd	NA	NA	NA	NA	NA	NA	99.96
BTB-01(B)	13/12/00-007	49.54	bd	1.59	1.89	bd	0.08	0.15	0.04	bd	bd	46.62	bd	bd	NA	NA	NA	NA	NA	NA	99.90
BTB-01(B)	13/12/00-008	49.59	bd	1.87	2.15	bd	bd	0.13	0.06	bd	bd	46.07	bd	bd	NA	NA	NA	NA	NA	NA	99.85
BTB-01(B)	27/04/01-119	50.63	bd	0.44	1.96	bd	bd	0.06	bd	bd	bd	46.69	bd	bd	bd	bd	bd	bd	bd	bd	99.78
BTB-01(B)	27/04/01-120	50.53	bd	0.53	0.20	bd	bd	0.12	bd	0.04	bd	48.32	bd	bd	0.07	bd	bd	bd	bd	bd	99.80
BTB-01(B)	27/04/01-121	50.70	bd	0.28	0.25	bd	bd	0.11	bd	bd	bd	48.38	bd	bd	bd	bd	bd	0.09	bd	bd	99.81
BTB-01(B)	27/04/01-125	50.37	bd	0.39	0.71	bd	bd	0.08	bd	bd	0.13	48.01	bd	bd	bd	bd	bd	0.09	bd	bd	99.79
BTB-01(B)	27/04/01-130	50.70	bd	0.37	0.72	bd	bd	0.13	bd	bd	bd	47.88	bd	bd	bd	bd	bd	bd	bd	bd	99.80
BTB-01(B)	27/04/01-132	50.90	bd	0.24	0.75	bd	bd	bd	bd	bd	bd	47.82	bd	bd	bd	bd	bd	0.07	bd	bd	99.79
BTB-01(B)	27/04/01-135	51.11	bd	0.11	1.28	bd	0.10	0.06	bd	0.06	bd	47.07	bd	bd	bd	bd	bd	bd	bd	bd	99.78
BTB-01(B)	27/04/01-136	50.79	bd	bd	0.94	bd	0.13	0.08	bd	bd	0.27	47.64	bd	bd	bd	bd	bd	bd	bd	bd	99.85
BTB-01(B)	27/04/01-139	50.82	bd	0.42	1.91	0.14	bd	0.10	bd	bd	bd	46.48	bd	bd	bd	bd	bd	bd	bd	bd	99.87
BTB-01(C)	13/12/00-021	48.68	bd	bd	2.08	0.38	0.09	0.18	bd	bd	0.29	48.17	bd	bd	NA	NA	NA	NA	NA	NA	99.86
BTB-01(C)	13/12/00-022	48.04	bd	0.32	2.31	0.92	bd	0.17	0.05	bd	0.30	47.75	bd	bd	NA	NA	NA	NA	NA	NA	99.86
BTB-01(C)	13/12/00-023	48.03	bd	0.28	1.89	0.63	0.08	0.13	0.05	bd	0.21	48.65	bd	bd	NA	NA	NA	NA	NA	NA	99.95
BTB-01(C)	13/12/00-027	48.37	bd	0.48	2.67	bd	bd	0.20	0.07	bd	1.67	46.47	bd	bd	NA	NA	NA	NA	NA	NA	99.94
BTB-01(C)	13/12/00-028	48.13	bd	0.47	2.94	bd	bd	0.25	0.04	bd	1.11	46.95	bd	bd	NA	NA	NA	NA	NA	NA	99.89
BTB-01(C)	13/12/00-031	47.55	bd	0.26	2.69	0.06	bd	0.22	bd	bd	2.14	47.00	bd	bd	NA	NA	NA	NA	NA	NA	99.93
BTB-01(C)	13/12/00-032	48.28	bd	0.36	2.27	bd	bd	0.20	0.05	bd	1.90	46.88	bd	bd	NA	NA	NA	NA	NA	NA	99.94
BTB-01(C)	13/12/00-053	49.82	bd	bd	0.36	bd	0.10	0.15	0.09	bd	0.47	48.90	bd	bd	NA	NA	NA	NA	NA	NA	99.88
BTB-01(C)	13/12/00-054	49.78	0.09	0.17	0.49	bd	bd	0.18	bd	bd	0.34	48.95	bd	bd	NA	NA	NA	NA	NA	NA	99.99
BTB-01(C)	13/12/00-055	49.21	bd	0.15	0.49	bd	bd	0.12	0.08	bd	0.63	49.24	bd	bd	NA	NA	NA	NA	NA	NA	99.92
BTB-01(C)	27/04/01-081	49.91	bd	bd	0.26	0.16	bd	0.21	bd	bd	2.27	46.92	bd	bd	bd	bd	bd	0.10	bd	bd	99.83
BTB-01(C)	27/04/01-115	50.37	bd	0.19	0.32	0.11	bd	0.21	bd	bd	bd	48.65	bd	bd	bd	bd	bd	bd	0.10	bd	99.94
Electrum																					
01BT082a	03/09/02-065	0.38	50.04	47.00	0.29	0.26	bd	0.12	bd	bd	bd	bd	1.82	bd	bd	NA	NA	bd	NA	NA	99.92
01BT082a	03/09/02-066	bd	32.46	59.92	0.20	bd	bd	0.08	bd	bd	bd	bd	7.18	bd	bd	NA	NA	bd	NA	NA	99.83
01BT082a	03/09/02-067	0.54	51.67	45.82	bd	bd	bd	bd	bd	0.07	bd	bd	1.72	bd	bd	NA	NA	bd	NA	NA	99.82
01BT082a	03/09/02-068	0.49	52.06	45.64	bd	bd	bd	bd	bd	0.06	bd	bd	1.51	bd	bd	NA	NA	bd	NA	NA	99.76
01BT082a	03/09/02-069	0.51	49.99	46.97	bd	bd	bd	0.08	bd	bd	bd	bd	2.01	bd	0.11	NA	NA	0.09	NA	NA	99.76
01BT082a	03/09/02-070	0.70	52.37	45.10	0.16	bd	bd	bd	bd	bd	bd	bd	1.59	bd	bd	NA	NA	bd	NA	NA	99.92
01BT082a	03/09/02-071	bd	42.78	52.71	bd	0.09	bd	bd	bd	0.08	bd	bd	4.08	bd	0.15	NA	NA	bd	NA	NA	99.89
01BT082a	03/09/02-073	0.42	47.23	47.98	0.58	0.46	bd	0.14	bd	bd	0.74	bd	2.39	bd	bd	NA	NA	bd	NA	NA	99.95
01BT082a	03/09/02-079	0.43	49.16	47.97	bd	bd	bd	bd	bd	bd	bd	bd	2.09	bd	0.09	NA	NA	bd	NA	NA	99.74
01BT082a	03/09/02-080	0.40	49.19	47.76	0.20	bd	0.17	bd	bd	0.11	bd	bd	2.09	bd	bd	NA	NA	bd	NA	NA	99.92
01BT136	04/09/02-066	bd	42.70	53.22	0.21	1.32	bd	bd	bd	bd	bd	bd	2.39	bd	bd	NA	NA	bd	NA	NA	99.84

Table B1(viii). Sulphide analyses (at%) contd.

Sample No	Analysis Ref	S	Au	Ag	Cu	Fe	As	Se	Sb	Te	Zn	Pb	Hg	Bi	Ga	Ge	Co	Cd	In	Cr	Total
01BT136	04/09/02-068	37.61	9.48	15.97	18.72	13.70	0.05	bd	bd	0.04	3.20	bd	1.06	bd	0.13	NA	NA	bd	NA	NA	99.96
01BT138	04/09/02-070	42.77	12.96	11.98	13.22	18.17	bd	bd	bd	bd	bd	bd	0.88	bd	bd	NA	NA	bd	NA	NA	99.98
01BT226b	03/09/02-001	0.22	50.20	48.47	0.22	bd	bd	bd	bd	0.11	bd	bd	0.60	bd	bd	NA	NA	bd	NA	NA	99.83
01BT226b	03/09/02-002	0.28	51.76	47.06	0.23	bd	bd	0.14	bd	bd	bd	bd	0.47	bd	bd	NA	NA	bd	NA	NA	99.93
01BT226b	03/09/02-003	0.30	51.77	46.70	0.30	0.13	bd	bd	0.05	bd	bd	bd	0.63	bd	bd	NA	NA	bd	NA	NA	99.89
01BT226b	03/09/02-004	0.15	49.40	49.34	0.24	bd	bd	bd	bd	0.08	bd	bd	0.63	bd	bd	NA	NA	bd	NA	NA	99.85
01BT226b	03/09/02-005	bd	49.77	49.20	0.34	0.10	bd	bd	bd	0.05	bd	bd	0.43	bd	bd	NA	NA	bd	NA	NA	99.90
01BT226b	03/09/02-006	0.44	48.58	49.96	0.31	bd	bd	0.09	bd	0.05	bd	bd	0.48	bd	bd	NA	NA	bd	NA	NA	99.90
01BT226b	03/09/02-011	70.78	3.38	16.18	4.04	bd	1.47	bd	0.35	bd	3.51	bd	bd	0.13	bd	NA	NA	bd	NA	NA	99.84
01BT226b	03/09/02-012	66.71	1.80	18.39	6.24	bd	2.24	bd	0.40	bd	3.83	bd	bd	0.27	bd	NA	NA	bd	NA	NA	99.89
01BT226b	03/09/02-015	0.48	54.79	43.82	0.45	bd	bd	0.10	bd	0.14	bd	bd	0.16	bd	bd	NA	NA	bd	NA	NA	99.93
01BT226b	03/09/02-016	0.22	55.80	43.29	0.20	0.16	0.15	bd	bd	0.08	bd	bd	bd	bd	bd	NA	NA	bd	NA	NA	99.91
01BT226b	03/09/02-017	0.39	55.71	43.35	0.27	bd	bd	bd	bd	0.10	bd	bd	bd	bd	bd	NA	NA	bd	NA	NA	99.82
01BT226b	03/09/02-018	0.40	40.26	57.16	0.85	bd	0.10	bd	bd	0.09	bd	0.15	0.91	bd	bd	NA	NA	bd	NA	NA	99.90
01BT226b	03/09/02-019	0.36	55.99	43.11	0.27	bd	bd	0.08	bd	0.06	bd	bd	0.09	bd	bd	NA	NA	bd	NA	NA	99.97
BL1	14/12/00-074	5.94	53.03	39.08	1.18	bd	bd	bd	bd	0.10	bd	bd	0.57	bd	NA	NA	NA	NA	NA	NA	99.89
BL1	14/12/00-075	5.15	52.96	40.16	0.74	bd	bd	bd	bd	0.07	bd	bd	0.63	0.15	NA	NA	NA	NA	NA	NA	99.86
BL1	14/12/00-076	9.24	49.32	39.05	1.57	0.08	0.12	bd	bd	bd	bd	bd	0.53	bd	NA	NA	NA	NA	NA	NA	99.91
BL1	14/12/00-077	7.27	49.59	41.27	0.79	0.15	0.10	0.09	0.04	0.09	bd	bd	0.59	bd	NA	NA	NA	NA	NA	NA	99.97
BL1	14/12/00-080	2.14	34.78	59.25	0.50	0.22	bd	0.11	bd	bd	bd	0.20	2.77	bd	NA	NA	NA	NA	NA	NA	99.97
BL1	14/12/00-081	0.59	29.41	64.55	0.74	0.11	bd	0.16	bd	0.07	bd	bd	4.36	bd	NA	NA	NA	NA	NA	NA	100.00
BL1	14/12/00-084	26.39	15.77	33.47	21.11	bd	bd	0.08	bd	0.04	bd	1.67	1.40	bd	NA	NA	NA	NA	NA	NA	99.92
BL1	14/12/00-094	0.54	62.55	35.87	bd	bd	bd	bd	bd	bd	bd	bd	0.64	bd	NA	NA	NA	NA	NA	NA	99.61
BL1	14/12/00-095	0.44	62.69	36.08	bd	bd	bd	bd	bd	bd	bd	bd	0.39	0.17	NA	NA	NA	NA	NA	NA	99.77
BL1	14/12/00-103	2.31	58.84	37.92	bd	0.09	0.13	0.08	bd	bd	bd	bd	0.51	bd	NA	NA	NA	NA	NA	NA	99.87
BL1	14/12/00-104	0.42	63.66	34.73	bd	bd	bd	bd	bd	0.11	bd	bd	0.67	0.12	NA	NA	NA	NA	NA	NA	99.72
BL1	14/12/00-107	0.39	63.02	35.40	bd	0.14	bd	0.15	bd	0.07	bd	bd	0.69	bd	NA	NA	NA	NA	NA	NA	99.88
BTB-01(B)	13/12/00-001	0.33	66.02	32.64	0.25	bd	0.15	bd	0.07	0.18	bd	bd	0.28	bd	NA	NA	NA	NA	NA	NA	99.90
BTB-01(B)	13/12/00-002	0.22	66.10	32.66	0.17	0.13	bd	0.10	bd	0.13	bd	bd	0.28	bd	NA	NA	NA	NA	NA	NA	99.80
BTB-01(B)	13/12/00-003	0.19	66.83	31.99	0.21	bd	bd	0.14	bd	0.11	bd	bd	0.45	bd	NA	NA	NA	NA	NA	NA	99.92
BTB-01(B)	13/12/00-004	0.33	66.08	32.24	0.20	0.17	bd	bd	bd	0.22	bd	bd	0.55	bd	NA	NA	NA	NA	NA	NA	99.79
BTB-01(B)	13/12/00-005	bd	65.59	33.25	bd	0.12	bd	bd	bd	bd	bd	bd	0.47	0.18	NA	NA	NA	NA	NA	NA	99.62
BTB-01(C)	13/12/00-029	0.65	57.92	39.33	0.87	0.33	bd	bd	0.06	bd	bd	bd	0.72	bd	NA	NA	NA	NA	NA	NA	99.88
BTB-01(C)	13/12/00-030	0.61	58.26	39.54	0.65	0.16	bd	bd	bd	bd	bd	bd	0.73	bd	NA	NA	NA	NA	NA	NA	99.95
BTB-01(C)	13/12/00-038	0.58	24.55	63.08	0.52	bd	bd	bd	bd	bd	5.00	bd	6.18	bd	NA	NA	NA	NA	NA	NA	99.91
BTB-01(C)	13/12/00-039	0.39	24.71	63.34	0.65	bd	bd	bd	bd	0.08	4.87	bd	5.89	bd	NA	NA	NA	NA	NA	NA	99.94
BTB-01(C)	13/12/00-042	0.33	58.05	40.37	bd	bd	bd	0.08	bd	0.05	bd	bd	0.85	bd	NA	NA	NA	NA	NA	NA	99.74
BTB-01(C)	13/12/00-043	0.53	56.46	41.78	bd	0.08	0.12	bd	bd	bd	bd	bd	0.86	bd	NA	NA	NA	NA	NA	NA	99.82

Table B1(viii). Sulphide analyses (at%) contd.

Sample No	Analysis Ref	S	Au	Ag	Cu	Fe	As	Se	Sb	Te	Zn	Pb	Hg	Bi	Ga	Ge	Co	Cd	In	Cr	Total
BTB-01(C)	13/12/00-044	0.31	40.55	56.14	bd	0.13	bd	bd	bd	0.12	bd	bd	2.51	bd	NA	NA	NA	NA	NA	NA	99.76
BTB-01(C)	13/12/00-045	0.37	57.78	40.44	0.25	0.12	bd	bd	bd	bd	bd	bd	0.83	0.11	NA	NA	NA	NA	NA	NA	99.90
BTB-01(C)	13/12/00-046	0.21	41.54	55.44	0.41	bd	0.11	bd	bd	0.08	bd	bd	2.09	bd	NA	NA	NA	NA	NA	NA	99.87
BTB-01(C)	14/12/00-002	0.55	22.58	60.80	0.58	bd	0.14	bd	bd	0.13	10.63	bd	4.54	bd	NA	NA	NA	NA	NA	NA	99.96
BTB-01(C)	14/12/00-003	0.60	25.47	63.15	0.49	bd	bd	bd	bd	bd	5.60	bd	4.48	bd	NA	NA	NA	NA	NA	NA	99.79
BTB-01(C)	14/12/00-004	0.30	51.88	38.91	0.76	0.36	0.10	0.07	bd	0.13	6.62	bd	0.81	bd	NA	NA	NA	NA	NA	NA	99.93
BTB-01(C)	27/04/01-116	bd	15.37	76.47	0.66	0.08	bd	0.06	bd	0.08	bd	bd	7.07	bd	0.15	bd	bd	bd	bd	bd	99.96
BTB-01(C)	27/04/01-118	0.31	59.79	38.94	bd	0.16	bd	bd	bd	0.11	bd	bd	0.46	bd	bd	bd	bd	bd	bd	bd	99.77
Pearcite																					
01BT226b	03/09/02-008	37.65	0.06	42.73	12.64	bd	6.71	0.05	bd	0.04	bd	bd	bd	bd	bd	NA	NA	bd	NA	NA	99.88
01BT226b	03/09/02-009	37.08	0.04	44.07	11.74	bd	6.90	bd	bd	0.04	bd	bd	bd	bd	bd	NA	NA	0.04	NA	NA	99.91
01BT226b	03/09/02-010	37.25	bd	44.50	11.39	0.04	6.63	0.04	bd	0.05	bd	bd	0.03	bd	bd	NA	NA	0.04	NA	NA	99.96
BTB-01(C)	27/04/01-082	38.25	bd	38.71	16.06	bd	6.18	0.04	0.60	bd	bd	bd	0.06	bd	bd	bd	bd	bd	bd	bd	99.89
BTB-01(C)	27/04/01-113	38.15	bd	39.02	15.82	bd	6.63	0.04	0.26	0.04	bd	bd	bd	bd	bd	bd	bd	bd	bd	bd	99.96
BTB-01(C)	27/04/01-114	37.78	bd	38.25	16.89	0.05	6.59	bd	0.27	0.03	bd	bd	bd	bd	bd	bd	bd	bd	bd	bd	99.86
Hessite																					
BL711.A	14/12/00-005	0.71	0.17	65.06	0.11	bd	bd	bd	0.20	32.29	1.25	bd	bd	bd	NA	NA	NA	NA	NA	NA	99.79
BL711.A	14/12/00-006	1.06	0.17	64.33	bd	0.12	bd	0.07	0.20	31.88	1.85	0.15	bd	0.07	NA	NA	NA	NA	NA	NA	99.90
Native silver																					
BTB-01(C)	13/12/00-018	0.14	0.09	98.63	0.35	0.12	bd	bd	bd	bd	0.49	bd	0.04	bd	NA	NA	NA	NA	NA	NA	99.86
BTB-01(C)	13/12/00-020	0.28	bd	98.53	0.40	0.12	bd	bd	bd	0.05	0.53	bd	bd	bd	NA	NA	NA	NA	NA	NA	99.90

Table B1(ix). Silicate analyses in wt% oxides.

Sample No	Analysis Ref	Al_2O_3	MgO	SiO_2	Na_2O	P_2O_5	SO_3	K_2O	CaO	TiO_2	Cr_2O_3	MnO	FeO	SrO	Total
Chlorite															
00BT12	200802-4#7	24.77	27.30	28.36	0.03	bd	bd	bd	bd	bd	bd	0.19	3.95	bd	84.60
00BT12	200802-4#8	24.70	27.24	28.58	0.04	bd	bd	bd	0.05	bd	bd	0.19	4.02	bd	84.81
00BT12	200802-4#9	25.24	27.85	28.19	bd	0.05	bd	bd	bd	bd	bd	0.18	3.86	bd	85.37
01BT002a	190802-2#1	23.71	29.51	29.43	bd	bd	bd	bd	bd	bd	bd	0.17	1.54	bd	84.37
01BT002a	190802-2#10	25.30	29.40	28.53	0.03	bd	0.14	bd	bd	0.06	0.05	0.20	2.08	bd	85.78
01BT002a	190802-2#11	24.35	28.31	29.66	0.04	bd	0.08	bd	0.07	bd	bd	0.13	1.63	0.05	84.31
01BT002a	190802-2#12	25.06	29.27	29.81	bd	bd	0.08	0.04	bd	bd	bd	0.20	1.68	0.08	86.21
01BT002a	190802-2#13	24.41	29.21	29.08	bd	bd	bd	bd	bd	bd	0.05	0.18	1.85	bd	84.79
01BT002a	190802-2#14	23.66	30.21	29.22	bd	0.07	0.06	bd	0.06	bd	bd	0.16	1.72	bd	85.15
01BT002a	190802-2#15	24.82	29.30	28.97	bd	0.09	bd	bd	bd	bd	bd	0.17	1.72	0.04	85.11
01BT002a	190802-2#2	23.94	30.54	29.12	bd	bd	0.06	bd	0.05	0.06	0.03	0.17	1.57	bd	85.53
01BT002a	190802-2#3	23.47	29.94	29.55	bd	0.10	0.06	bd	0.04	bd	bd	0.12	1.75	bd	85.03
01BT002a	190802-2/#6	24.23	27.80	30.42	0.11	bd	bd	0.75	0.06	bd	bd	0.17	1.41	bd	84.94
01BT061	190802-2#32	23.64	30.85	29.46	bd	bd	0.07	bd	bd	bd	0.05	0.11	1.07	bd	85.26
01BT061	190802-2#33	23.39	30.63	29.42	bd	bd	0.08	0.04	0.07	bd	0.05	0.09	1.06	bd	84.84
01BT061	190802-2#34	22.39	31.21	29.45	bd	0.06	bd	bd	0.05	bd	bd	0.17	1.01	0.08	84.39
901	200802-1#1	20.90	7.75	23.63	bd	bd	0.11	bd	bd	bd	bd	1.42	32.42	bd	86.23
901	200802-1#2	21.81	7.83	23.99	bd	bd	0.20	bd	bd	0.07	0.04	1.42	30.75	bd	86.10
901	200802-1#3	21.66	8.43	24.01	bd	bd	0.13	bd	bd	bd	bd	1.39	31.32	bd	86.93
901	200802-1#4	21.87	7.76	23.40	bd	bd	0.19	bd	0.04	bd	bd	1.32	31.62	bd	86.20
902	200802-5#1	18.60	8.08	24.36	bd	bd	0.44	bd	bd	0.06	bd	bd	35.62	bd	87.15
902	200802-5#2	18.79	7.88	23.74	0.07	bd	0.06	bd	bd	bd	0.07	0.08	35.16	bd	85.85
902	200802-5#3	18.62	7.39	23.46	bd	bd	0.74	bd	bd	0.07	0.06	0.07	36.67	bd	87.08
902	200802-5#4	18.26	6.97	23.27	0.02	bd	0.37	bd	bd	0.06	0.04	0.20	36.64	bd	85.83
010820/03	190802-2#19	18.07	16.96	26.48	bd	0.06	bd	bd	0.06	bd	0.05	0.53	23.45	bd	85.65
010820/03	190802-2#20	18.03	17.22	27.46	0.03	0.07	bd	bd	0.07	bd	0.06	0.45	23.51	bd	86.90
010820/03	190802-2#21	18.10	17.07	27.39	bd	bd	bd	bd	0.10	bd	0.04	0.40	23.10	bd	86.20
010820/03	190802-2#22	18.05	17.08	26.34	bd	bd	0.11	bd	0.04	bd	bd	0.46	23.66	bd	85.73
010820/03	190802-2#23	18.48	17.17	26.53	0.04	bd	bd	bd	0.06	bd	bd	0.55	23.12	bd	85.96
010820/11	200802-7#10	17.46	15.84	27.18	bd	bd	bd	0.04	0.16	bd	bd	0.25	24.83	bd	85.75
010820/11	200802-7#11	17.77	15.46	27.01	0.05	bd	bd	bd	0.12	bd	0.04	0.30	25.27	bd	86.02
010820/11	200802-7#8	17.23	15.41	27.42	0.07	bd	bd	0.05	0.17	bd	0.03	0.20	25.08	bd	85.65
010820/11	200802-7#9	17.65	15.28	27.43	bd	bd	bd	bd	0.16	bd	bd	0.22	24.96	0.05	85.74
01BT004	190802-1#4	23.20	31.23	29.35	bd	bd	bd	bd	bd	bd	bd	0.17	1.21	bd	85.15
01BT004	190802-1#5	24.43	29.45	29.75	bd	bd	0.09	0.04	bd	bd	bd	0.20	1.11	bd	85.06
01BT004	190802-1#6	24.52	29.82	29.71	bd	bd	bd	bd	0.05	bd	bd	0.23	1.05	bd	85.37
01BT052	200802-4#16	25.42	26.22	30.84	0.05	bd	bd	bd	0.09	bd	0.04	0.16	2.20	bd	85.03

Table B1(ix). Silicate analyses in wt% oxides (contd.).

Sample No	Analysis Ref	Al_2O_3	MgO	SiO_2	Na_2O	P_2O_5	SO_3	K_2O	CaO	TiO_2	Cr_2O_3	MnO	FeO	SrO	Total
01BT052	200802-4#17	24.21	28.77	29.55	bd	bd	0.09	bd	bd	bd	0.09	0.27	2.03	0.04	85.05
01BT052	200802-4#18	24.74	28.49	29.26	0.03	bd	0.08	bd	bd	bd	0.09	0.19	1.96	bd	84.83
01BT054	190802-1#13	24.41	29.64	29.00	bd	bd	bd	bd	bd	bd	bd	0.22	2.00	0.07	85.34
01BT054	190802-1#14	24.63	29.49	28.64	bd	bd	bd	bd	bd	bd	0.06	0.21	1.90	0.04	84.97
01BT054	190802-1#15	23.91	29.75	29.40	bd	bd	bd	bd	bd	bd	bd	0.16	1.64	bd	84.85
01BT054	190802-1#20	24.35	28.90	29.80	bd	bd	bd	bd	bd	bd	0.06	0.11	1.55	bd	84.76
01BT058	200802-5/#5	22.89	29.45	31.43	bd	0.06	0.07	bd	0.10	bd	0.03	0.23	1.67	bd	85.92
01BT058	200802-5#6	22.70	29.13	31.49	bd	0.06	0.07	bd	0.14	bd	bd	0.19	1.66	bd	85.43
01BT058	200802-5#7	22.63	29.04	31.10	bd	bd	0.06	bd	0.14	bd	bd	0.26	1.68	bd	84.91
01BT162	200802-7#24	23.80	27.32	28.75	bd	0.10	0.10	bd	bd	bd	0.03	0.09	4.21	bd	84.40
01BT162	200802-7#25	24.21	27.51	29.22	bd	0.10	0.09	bd	0.05	bd	0.03	0.12	4.00	bd	85.32
01BT162	200802-7#26	23.67	27.06	28.41	0.02	0.06	0.08	bd	0.07	bd	0.08	0.17	3.92	bd	83.54
01BT191	200802-5#10	21.37	19.63	26.56	bd	bd	bd	bd	0.04	bd	bd	0.51	18.65	bd	86.75
01BT191	200802-5#8	20.77	20.33	26.83	0.04	0.05	bd	bd	bd	bd	bd	0.45	17.42	bd	85.88
01BT191	200802-5#9	21.25	20.19	26.90	bd	bd	bd	bd	0.04	bd	bd	0.41	18.09	bd	86.87
00BT12	200802-4#4	24.03	24.44	33.48	0.08	bd	0.10	0.29	0.09	bd	0.15	0.14	3.20	bd	86.00
00BT12	200802-4#5	25.38	23.92	33.33	bd	bd	0.10	bd	0.13	bd	0.06	0.09	2.94	bd	85.94
00BT12	200802-4#6	27.11	23.29	33.01	bd	0.14	0.12	0.05	0.07	bd	bd	0.13	2.92	bd	86.84
01BT002a	190802-2#7	24.10	29.79	28.89	bd	bd	0.06	bd	bd	bd	bd	0.20	1.73	bd	84.78
01BT002a	190802-2#8	24.52	29.88	29.33	bd	bd	bd	bd	bd	bd	bd	0.18	1.63	0.05	85.59
01BT002a	190802-2#9	23.64	29.44	29.70	bd	bd	bd	bd	bd	bd	bd	0.15	1.60	bd	84.54
01BT061	190802-2#35	25.47	24.82	34.04	bd	bd	bd	bd	0.16	0.07	0.09	0.20	0.81	bd	85.66
01BT061	190802-2#36	25.26	24.71	33.62	0.03	bd	bd	0.04	0.18	bd	0.07	0.19	0.91	bd	85.01
01BT061	190802-2#37	25.52	24.50	34.51	0.02	0.06	bd	0.04	0.16	bd	0.09	0.10	0.89	bd	85.89
01BT098	200802-4#1	21.12	29.25	30.84	bd	bd	0.12	bd	0.06	bd	bd	0.11	3.38	bd	84.90
01BT098	200802-4#2	21.06	27.65	30.36	0.04	bd	0.19	bd	0.09	bd	bd	0.20	4.69	0.05	84.32
01BT098	200802-4#3	21.63	28.54	31.39	bd	0.07	0.10	bd	0.09	bd	bd	0.16	3.94	bd	85.91
Muscovite															
906	200802-1#5	32.44	1.24	44.10	0.41	bd	bd	9.50	bd	bd	0.03	bd	0.22	bd	87.92
906	200802-1/#6	32.39	1.40	45.28	0.35	bd	bd	9.99	bd	bd	0.08	0.06	0.09	bd	89.64
906	200802-1/#7	32.46	1.26	45.09	0.35	bd	bd	9.50	0.05	bd	bd	bd	0.19	0.06	88.94
906	200802-1#8	32.72	1.19	44.58	0.37	bd	bd	9.62	bd	bd	0.04	bd	0.15	bd	88.65
01BT002a	190802-2#16	35.16	0.74	46.04	1.12	0.08	0.06	8.86	0.08	bd	bd	bd	0.16	0.07	92.37
01BT002a	190802-2#17	35.06	0.70	45.68	1.08	bd	bd	8.97	0.08	0.07	0.04	bd	0.22	0.08	91.98
01BT002a	190802-2#18	34.98	0.71	45.89	1.28	bd	bd	8.70	0.11	bd	0.03	bd	0.05	bd	91.77
01BT052	200802-4#10	34.76	0.72	45.05	0.68	bd	bd	9.79	0.06	bd	0.03	bd	0.27	0.05	91.39
01BT052	200802-4#11	34.88	0.73	45.14	0.84	bd	bd	9.40	bd	bd	0.03	bd	0.24	bd	91.26
01BT052	200802-4#12	35.07	0.64	45.36	1.48	bd	bd	8.21	bd	bd	bd	bd	0.20	0.04	90.99

Table B1(ix). Silicate analyses in wt% oxides (contd.).

Sample No	Analysis Ref	Al_2O_3	MgO	SiO_2	Na_2O	P_2O_5	SO_3	K_2O	CaO	TiO_2	Cr_2O_3	MnO	FeO	SrO	Total
01BT054	190802-1#17	34.64	0.86	45.88	1.20	bd	bd	8.68	bd	bd	0.07	bd	0.17	bd	91.50
01BT054	190802-1#18	34.64	0.72	46.00	1.40	bd	bd	8.55	0.05	bd	0.09	bd	0.14	bd	91.57
01BT054	190802-1#19	35.18	0.77	44.90	1.04	bd	bd	9.11	bd	bd	0.07	bd	0.19	bd	91.25
01BT070	200802-2#6	33.93	0.99	46.60	0.74	0.06	bd	9.55	bd	bd	bd	bd	0.09	0.04	91.99
01BT070	200802-2#7	34.25	0.94	46.40	0.75	bd	bd	9.36	bd	bd	0.04	bd	0.07	bd	91.81
01BT070	200802-2#8	33.93	0.98	47.38	0.89	bd	bd	8.64	0.08	bd	bd	bd	0.12	bd	92.02
01BT138	200802-2#10	32.15	0.36	42.29	0.83	0.06	0.94	8.07	0.18	bd	bd	bd	0.66	0.08	85.60
01BT138	200802-2#11	33.19	0.52	44.12	0.70	0.08	0.22	8.72	0.05	bd	bd	bd	0.59	bd	88.19
01BT138	200802-2#9	33.42	0.45	44.07	0.81	0.05	0.17	8.57	0.06	bd	0.07	bd	0.68	0.09	88.44
01BT162	200802-7#32	34.86	0.64	45.08	0.94	bd	bd	9.11	0.04	bd	bd	bd	0.20	0.07	90.92
01BT162	200802-7#33	34.36	0.70	45.45	0.78	0.09	bd	9.32	0.07	bd	0.04	bd	0.36	bd	91.16
01BT162	200802-7#34	35.05	0.65	45.40	0.89	bd	bd	9.13	0.04	bd	bd	0.04	0.21	bd	91.40
01BT226d	200802-2#17	36.41	0.13	45.31	0.69	bd	bd	10.16	bd	bd	bd	0.05	0.11	bd	92.85
01BT226d	200802-2#18	35.56	0.35	45.30	0.83	bd	bd	9.42	0.11	bd	0.03	bd	0.20	bd	91.80
01BT226d	200802-2#19	36.03	0.26	44.90	0.85	bd	bd	9.73	bd	bd	bd	bd	0.10	0.06	91.93
Sericite															
907	190802-1#21	33.81	1.27	46.02	0.49	bd	bd	9.50	0.11	bd	bd	bd	0.43	bd	91.63
907	190802-1#22	31.68	1.25	44.28	0.44	bd	0.12	8.87	0.54	bd	bd	bd	0.62	bd	87.79
907	190802-1#23	33.53	1.34	45.48	0.47	bd	bd	9.80	0.12	bd	0.04	0.06	0.51	bd	91.34
00BT18	210802-3#2	28.23	4.43	45.60	0.91	bd	bd	9.60	0.04	bd	bd	0.10	5.19	0.05	94.16
00BT18	210802-3#4	27.35	2.25	49.40	0.23	bd	0.06	10.90	0.12	0.10	bd	0.05	4.05	bd	94.49
00BT18	210802-3#5	26.37	2.59	50.43	0.29	bd	bd	10.62	0.08	bd	0.05	bd	3.93	0.05	94.40
00BT18	210802-3#6	26.18	2.59	49.33	0.16	bd	bd	10.69	0.20	bd	0.05	0.07	4.06	0.06	93.40
00BT18	210802-3#7	26.69	3.82	47.46	0.26	bd	bd	9.91	0.24	bd	0.05	0.05	4.81	bd	93.29
00BT18	210802-3#8	26.69	2.44	50.00	0.13	bd	bd	10.70	bd	bd	0.05	bd	4.31	0.05	94.37
01BT070	200802-2#1	33.58	1.03	47.54	0.86	0.06	bd	8.83	0.15	bd	0.07	bd	0.36	0.07	92.53
01BT070	200802-2#2	33.50	1.14	47.88	0.79	bd	bd	9.14	0.09	bd	0.08	bd	0.26	bd	92.88
01BT070	200802-2#5	33.38	1.07	47.24	0.89	bd	0.07	8.88	0.12	bd	0.03	bd	0.28	0.06	92.01
Zeolite & pumpellyite															
907	190802-1#26	23.56	bd	45.57	0.24	bd	bd	0.04	9.96	bd	bd	bd	bd	bd	79.36
907	190802-1#27	23.84	bd	46.21	0.24	0.06	bd	0.07	9.95	bd	bd	bd	bd	bd	80.37
010820/03	190802-2#25	bd	0.24	0.18	0.08	43.06	0.08	bd	54.18	bd	bd	bd	0.97	0.10	98.87
01BT052	200802-4#13	23.74	bd	45.54	0.06	bd	bd	bd	10.11	bd	bd	bd	0.05	bd	79.51
01BT052	200802-4#14	24.02	0.07	45.78	0.13	bd	0.07	0.08	10.05	bd	0.05	bd	0.08	0.05	80.37
01BT052	200802-4#15	23.75	bd	45.76	bd	bd	bd	bd	10.12	bd	bd	bd	bd	bd	79.63
01BT061	190802-2#29	23.94	0.08	45.43	0.15	bd	bd	0.04	10.01	bd	0.05	bd	bd	0.08	79.77
01BT061	190802-2#30	23.85	0.05	45.54	0.20	bd	bd	0.08	9.92	bd	bd	bd	bd	bd	79.63

Table B1(ix). Silicate analyses in wt% oxides (contd.).

Sample No	Analysis Ref	Al_2O_3	MgO	SiO_2	Na_2O	P_2O_5	SO_3	K_2O	CaO	TiO_2	Cr_2O_3	MnO	FeO	SrO	Total
01BT061	190802-2#31	24.38	bd	45.36	0.07	bd	bd	0.04	10.31	bd	0.06	bd	0.07	bd	80.28
01BT061	190802-2#38	22.98	31.34	30.03	0.04	bd	0.09	bd	bd	bd	bd	0.10	0.97	bd	85.56
01BT061	190802-2#39	23.03	31.31	29.64	bd	bd	0.08	bd	bd	bd	bd	0.18	1.06	bd	85.29
01BT061	190802-2#40	23.53	30.92	29.33	bd	bd	0.07	bd	0.04	bd	bd	0.16	1.07	bd	85.11
01BT082a	200802-7#1	25.96	3.34	37.32	0.05	0.06	bd	bd	23.33	0.08	0.05	0.31	1.08	bd	91.57
01BT082a	200802-7#2	25.49	3.84	36.61	0.07	bd	0.35	0.11	23.13	bd	bd	0.43	1.11	bd	91.12
01BT082a	200802-7#3	25.75	3.71	36.93	0.03	bd	bd	bd	23.36	bd	bd	0.38	1.04	bd	91.20
01BT082a	200802-7#4	25.88	3.39	36.96	bd	bd	bd	bd	23.36	bd	0.03	0.32	1.27	bd	91.22
01BT135b	200802-1#10	26.60	3.43	37.38	0.05	bd	bd	bd	23.54	0.08	0.05	0.18	0.70	bd	92.02
01BT135b	200802-1#11	26.07	3.23	37.31	0.05	bd	bd	bd	23.22	bd	0.28	0.25	0.63	bd	91.04
01BT135b	200802-1#12	24.46	3.26	37.45	0.06	bd	bd	bd	23.61	0.09	0.92	0.17	0.77	bd	90.78
01BT135b	200802-1#9	25.41	3.07	37.19	bd	bd	0.27	bd	23.48	0.07	0.32	0.15	0.80	0.05	90.81
01BT138	200802-2#12	23.57	bd	45.04	0.08	bd	bd	bd	9.93	bd	bd	bd	bd	bd	78.61
01BT138	200802-2#13	24.00	bd	46.10	0.05	bd	bd	bd	10.16	bd	bd	bd	0.09	bd	80.40
01BT138	200802-2#14	24.10	bd	46.04	0.04	bd	bd	bd	10.23	bd	bd	bd	bd	bd	80.40
01BT226d	200802-2#15	23.69	bd	46.15	0.04	bd	bd	0.04	10.24	bd	bd	bd	0.10	bd	80.26
01BT226d	200802-2#16	23.83	bd	45.93	0.05	bd	bd	bd	10.24	bd	bd	bd	0.05	bd	80.09

Sample no.	Analysis ref.	$MgCO_3$	$CaCO_3$	$MnCO_3$	$FeCO_3$	$ZnCO_3$	$SrCO_3$	$BaCO_3$	Total
Weight %									
902	210802-1#1	13.79	49.10	3.73	32.24	bd	1.05	bd	99.91
902	210802-1#2	13.05	48.08	2.00	34.67	bd	0.57	bd	98.37
902	210802-1#3	12.68	48.88	2.35	35.45	bd	0.42	bd	99.78
902	210802-2#1	0.17	92.11	2.17	3.59	bd	0.12	bd	98.15
902	210802-2#2	0.22	92.02	2.41	4.07	bd	0.13	bd	98.84
902	210802-2#3	0.39	90.35	2.40	3.50	bd	0.60	bd	97.25
00BT18	210802-4#1	1.44	93.33	3.85	0.18	bd	0.07	bd	98.87
00BT18	210802-4#2	1.49	91.69	4.11	0.15	0.17	0.08	bd	97.69
00BT18	210802-4#5	0.36	93.71	3.26	bd	bd	bd	0.18	97.51
00BT18	210802-4#6	0.07	94.14	3.76	bd	bd	bd	bd	97.97
01BT073	210802-2#4	1.33	2.86	1.03	59.63	34.52	0.07	bd	99.44
01BT073	210802-2#5	1.05	5.19	1.82	68.14	23.13	bd	0.19	99.51
01BT073	210802-2#6	1.19	7.92	2.42	71.54	16.50	bd	bd	99.56
01BT082a	210802-1#11	0.15	97.83	0.77	bd	bd	bd	bd	98.75
01BT082a	210802-1#12	0.08	97.69	0.92	bd	bd	bd	bd	98.69
01BT082a	210802-1#13	0.27	96.85	0.86	bd	bd	0.10	bd	98.07
01BT082a	210802-1#14	bd	97.69	0.64	bd	bd	bd	bd	98.33
01BT082a	210802-1#15	0.14	96.88	0.97	bd	bd	bd	bd	97.98
01BT082a	210802-1#16	bd	96.71	0.84	bd	bd	0.19	bd	97.74
01BT082a	210802-1#17	0.16	95.64	1.18	0.18	bd	0.12	bd	97.27
01BT082a	210802-2#10	0.19	95.95	0.96	0.16	bd	bd	bd	97.26
01BT082a	210802-2#11	0.18	95.30	1.15	0.25	bd	0.12	0.18	97.17
01BT082a	210802-2#12	bd	96.51	1.07	0.36	bd	bd	bd	97.95
01BT082a	210802-2#7	0.24	97.26	0.87	bd	0.22	0.11	bd	98.70
01BT082a	210802-2#8	0.20	98.48	0.82	bd	bd	bd	bd	99.50
01BT082a	210802-2#9	0.15	98.91	0.70	bd	0.12	0.08	bd	99.97
Atomic %									
902	210802-1#1	16.82	50.48	3.34	28.63	bd	0.73	bd	100.00
902	210802-1#2	16.19	50.27	1.82	31.32	bd	0.41	bd	100.00
902	210802-1#3	15.53	50.44	2.11	31.60	bd	0.30	bd	99.97
902	210802-2#1	0.20	94.56	1.94	3.18	bd	0.08	bd	99.97
902	210802-2#2	0.26	93.80	2.14	3.59	bd	0.09	bd	99.88
902	210802-2#3	0.48	93.70	2.17	3.13	bd	0.42	bd	99.91
00BT18	210802-4#1	1.73	94.63	3.40	0.16	bd	0.05	bd	99.97
00BT18	210802-4#2	1.82	94.18	3.68	0.13	0.14	0.05	bd	100.00
00BT18	210802-4#5	0.44	96.49	2.92	bd	bd	bd	0.09	99.94
00BT18	210802-4#6	0.08	96.51	3.35	bd	bd	bd	bd	99.94
01BT073	210802-2#4	1.86	3.39	1.06	60.97	32.62	0.06	bd	99.96
01BT073	210802-2#5	1.46	6.07	1.85	68.89	21.60	bd	0.11	100.00
01BT073	210802-2#6	1.63	9.16	2.43	71.48	15.23	bd	bd	99.94
01BT082a	210802-1#11	0.19	99.02	0.67	bd	bd	bd	bd	99.88
01BT082a	210802-1#12	0.09	98.97	0.81	bd	bd	bd	bd	99.87
01BT082a	210802-1#13	0.32	98.81	0.76	bd	bd	0.07	bd	99.96
01BT082a	210802-1#14	bd	99.36	0.56	bd	bd	bd	bd	99.92
01BT082a	210802-1#15	0.16	98.90	0.86	bd	bd	bd	bd	99.92
01BT082a	210802-1#16	bd	99.07	0.74	bd	bd	0.13	bd	99.95
01BT082a	210802-1#17	0.19	98.46	1.05	0.16	bd	0.08	bd	99.95
01BT082a	210802-2#10	0.23	98.75	0.86	0.14	bd	bd	bd	99.99
01BT082a	210802-2#11	0.22	98.35	1.03	0.22	bd	0.08	0.09	100.00
01BT082a	210802-2#12	bd	98.60	0.95	0.32	bd	bd	bd	99.88
01BT082a	210802-2#7	0.29	98.69	0.77	bd	0.17	0.08	bd	100.00
01BT082a	210802-2#8	0.24	99.00	0.72	bd	bd	bd	bd	99.96
01BT082a	210802-2#9	0.18	99.05	0.61	bd	0.10	0.05	bd	100.00

Table B1(x). Carbonate analyses in wt% and at% carbonate.

Sample no.	Analysis ref.	S	Ba	Sr	O	Total
Weight %						
01BT082a	200802-8#1	13.26	57.49	1.11	26.76	98.65
01BT082a	200802-8#2	13.09	59.04	0.06	26.50	98.74
01BT082a	200802-8#3	12.57	57.68	1.05	25.74	97.07
01BT138	200802-3#1	13.16	58.45	0.63	26.63	98.88
01BT138	200802-3#2	12.97	57.75	0.76	26.28	97.76
01BT138	200802-3#3	12.90	58.85	0.49	26.26	98.51
01BT226d	200802-3#4	12.99	58.98	0.45	26.43	98.92
01BT226d	200802-3#5	13.03	58.38	0.50	26.41	98.35
01BT226d	200802-3#6	13.14	58.83	0.22	26.56	98.76
01BT226d	200802-3#7	12.97	59.23	0.32	26.38	98.91
902	200802-6#1	12.91	58.36	1.13	26.34	98.74
902	200802-6#2	12.61	58.18	1.09	25.85	97.72
902	200802-6#3	12.82	58.03	1.07	26.14	98.05
Atomic %						
01BT082a	200802-8#1	16.43	16.63	0.50	66.44	100.00
01BT082a	200802-8#2	16.36	17.23	0.03	66.38	100.00
01BT082a	200802-8#3	16.12	17.26	0.49	66.13	100.00
01BT138	200802-3#1	16.37	16.98	0.29	66.37	100.00
01BT138	200802-3#2	16.33	16.98	0.35	66.33	100.00
01BT138	200802-3#3	16.24	17.29	0.23	66.24	100.00
01BT226d	200802-3#4	16.27	17.24	0.21	66.29	100.00
01BT226d	200802-3#5	16.33	17.09	0.23	66.35	100.00
01BT226d	200802-3#6	16.39	17.13	0.10	66.39	100.00
01BT226d	200802-3#7	16.26	17.33	0.15	66.26	100.00
902	200802-6#1	16.20	17.09	0.52	66.19	100.00
902	200802-6#2	16.08	17.33	0.51	66.08	100.00
902	200802-6#3	16.20	17.12	0.49	66.19	100.00

Table B1(xi). Sulphate analyses in wt%.

Conversions to atomic%

For sulphide data, at% were calculated from wt% using the following equations, where elements 1 to 19 (E_1 to E_{19}) represent the 19 elements that were analysed:

$$at\%E_1 = \frac{(wt\%E_1/ ME_1)}{\sum_{n=1}^{n=19} (wt\%E/ ME)}, \qquad at\%E_2 = \frac{(wt\%E_2/ ME_2)}{\sum_{n=1}^{n=19} (wt\%E/ ME)} \qquad \text{etc.}$$

where M = atomic mass

Detection limits were also converted to at% for selected elements in order to compare with at% data. When working in at%, the detection limit for a given element will vary according to the atomic mass and abundance of the other elements in the analyses. The at% detection limit for a

given trace element is therefore different for each host sulphide phase. Table B1(x) summarises the at% detection limits that are used in this study. They have been calculated from the wt% detection limit using an adaptation of the above equations as follows:

$$at\%dl(E_s) = \frac{(wt\%dlE_s / ME_s)}{\sum_{n=1}^{n=x} (wt\%E_m / ME_m)}$$

where:

$at\%dl(E_s)$ = the atomic% detection limit for a specific element E_s in a specific mineral m

$wt\%dl(E_s)$ = the weight% detection limit for element E_s

E_m = major elements in the mineral selected (trace elements would have an insignificant effect on calculations and are therefore ignored); wt% E_m is based on the mean value for all analyses of mineral m in this study.

x = the number of major elements in the mineral m.

Mineral (m)	Element (Es)	at% d.l.
chalcopyrite	Ag	0.04
	As	0.03
	Zn	0.05
pyrite	Co	0.03
	Au	0.02
	As	0.03
	Sb	0.01
arsenopyrite	Au	0.03
	Se	0.03
	Zn	0.06
	Cu	0.05
	Te	0.02
sphalerite	Cd	0.02
	Cu	0.04
	Fe	0.03
galena	Se	0.06
	As	0.08
	Ag	0.11
tennantite	Ag	0.05
	Se	0.03
	Te	0.02
	Hg	0.02
	Cd	0.02
Ag-rich electrum	Hg	0.04
Au-rich electrum	Hg	0.05

Table B1(x). Calculated atomic% detection limits for selected elements and minerals.

APPENDIX B2 : ESTIMATION OF ELECTRUM COMPOSITION

With reference to Section 5.28, Chapter 5:

Analyses of very fine grained electrum in barite contain other minerals that may contain Ag; therefore in order to obtain a realistic Au/Ag ratio for these analyses, the amount of Ag that may have been contributed by other phases must be taken into consideration. The phases other than electrum that may have contributed Ag to the analysis are tennantite (Section 5.2.6) or less likely pearcite. The possible contribution of Ag from these minerals is calculated as follows:

Sample No	Analysis Ref	S	Au	Ag	Cu	As	Sb	Zn	Bi	Total
01BT226b	03/09/02-011	70.78	3.38	16.18	4.04	1.47	0.35	3.51	0.13	100.00
01BT226b	03/09/02-012	66.71	1.80	18.39	6.24	2.24	0.40	3.83	0.27	100.00

Table B2(i). Analyses of fine grained electrum. Measured Au/Ag = 0.15.

1. Assuming all As and Sb are from tennantite, and all Cu is from tennantite (as there is no Fe in the analyses):

In the ideal formula for tennantite, (Cu+Ag)/(As+Sb) = 2.5

For each analysis:

(As+Sb) =	1.81	Ag at% in tennantite =	0.488	at% Ag in elec =	15.70	Au/Ag in elec =	0.22
(As+Sb) =	2.64	Ag at% in tennantite =	0.356	at% Ag in elec =	18.04	Au/Ag in elec =	0.10
						AVERAGE	0.16

2. Assuming all As, Sb and Cu are in pearcite:

In the ideal formula for pearcite, (Cu+Ag) : (As+Sb) = 8.0

For each analysis:

(As+Sb) =	1.81	at%Ag in Aspolybasite = 10.46	at% Ag in electrum =	5.73	new Au/Ag =	0.59
(As+Sb) =	2.64	at%Ag in Aspolybasite = 14.87	at% Ag in electrum =	3.52	new Au/Ag =	0.51
					AVERAGE	0.55

The Au/Ag ratio for this electrum can therefore be constrained to the range 0.15 to 0.55.

APPENDIX B3: FORMULAE CALCULATION FOR SILICATE MINERALS

For silicate minerals, formulae proportions of cations and anions have been calculated following the method of Deer et at. (1966) as follows:

1. Divide each oxide wt% by its molecular weight giving molecular proportions of oxides.
2. Multiply each of these by the no of O atoms in the oxide to give a set of numbers proportional to the no of oxygens associated with each element; total these to give T.
3. Set the oxygen atom proportions to equal the ideal total for the formula in question, e.g. for chlorite this is 14. This is done by multiplying each oxygen proportion by the ideal/T, e.g. 14/T.
4. Multiply each oxide proportion by the cation:oxygen ratio in that oxide to give the number of cations associated with each oxygen proportion.
5. The cations can then be grouped according to the formula. For tetrahedral sites, all Si is tetrahedral and any left over is filled with Al; the remaining Al is then assumed to be octahedral.
6. There is no analytical data for H_2O component; therefore this is set to OH = 8 at the end, and the amount of OH back-calculated to give the theoretical oxide H_2O weight percent, which can then be added to the total.

The data required for these calculations is given in table B3(i), and the calculations for chlorite, muscovite, pumpellyite and zeolite are given in tables B3(ii) to B3(v) respectively.

Data for calculation of chlorite formulae

Oxide	Molecular Wt	No O atoms in oxide	Cation:O ratio in oxide
SiO_2	60.09	2	0.50
Al_2O_3	101.94	3	0.67
TiO_2	79.9	2	0.50
FeO	71.85	1	1.00
MnO	70.94	1	1.00
MgO	40.31	1	1.00
CaO	56.08	1	1.00
Na_2O	61.98	1	2.00
K_2O	94.2	1	2.00
H_2O	18.016	1	0.5

Total molecules of OH in chlorite formula = 8

Data for calculation of pumpellyite formulae

Oxide	Molecular Wt	No O atoms in oxide	Cation:O ratio in oxide
SiO_2	60.09	2	0.50
Al_2O_3	101.94	3	0.67
TiO_2	79.9	2	0.50
FeO	71.85	1	1.00
MnO	70.94	1	1.00
MgO	40.31	1	1.00
CaO	56.08	1	1.00
Na_2O	61.98	1	2.00
K_2O	94.2	1	2.00
H_2O	18.016	1	0.5

Total molecules of OH in pumpellyite = 3.5
Total molecules of H2O in pumpellyite = 0.5
Total O atoms in pumpellyite formula = 14

Data for calculation of muscovite formulae

Oxide	Molecular Wt	No O atoms in oxide	Cation:O ratio in oxide
SiO_2	60.09	2	0.50
Al_2O_3	101.94	3	0.67
TiO_2	79.9	2	0.50
FeO	71.85	1	1.00
MnO	70.94	1	1.00
MgO	40.31	1	1.00
CaO	56.08	1	1.00
Na_2O	61.98	1	2.00
K_2O	94.2	1	2.00
H_2O	18.016	1	0.5

Total molecules of OH in muscovite formulae = 4
Total O atoms in muscovite formula = 20

Data for calculation of zeolite formulae

Oxide	Molecular Wt	No O atoms in oxide	Cation:O ratio in oxide
SiO_2	60.09	2	0.50
Al_2O_3	101.94	3	0.67
TiO_2	79.9	2	0.50
FeO	71.85	1	1.00
MnO	70.94	1	1.00
MgO	40.31	1	1.00
CaO	56.08	1	1.00
Na_2O	61.98	1	2.00
K_2O	94.2	1	2.00
H_2O	18.016	1	0.5

Total molecules of H2O in pumpellyite = 6
Total O atoms in pumpellyite formula = 22

Table B3(i). Data used in formulae calculations for silicate minerals

analysis reference		190802-1#4	190802-1#5	190802-1#6	190802-1#13	190802-1#14	190802-1#15	190802-1#20
sample number		01BT004	01BT004	01BT004	01BT054	01BT054	01BT054	01BT054
wt% oxides	SiO_2	29.35	29.75	29.71	29.00	28.64	29.40	29.80
	Al_2O_3	23.20	24.43	24.52	24.41	24.63	23.91	24.35
	TiO_2	bd	bd	bd	bd	bd	bd	bd
	FeO	1.21	1.11	1.05	2.00	1.90	1.64	1.55
	MnO	0.17	0.20	0.23	0.22	0.21	0.16	0.11
	MgO	31.23	29.45	29.82	29.64	29.49	29.75	28.90
	CaO	bd	bd	0.05	bd	bd	bd	bd
	Na_2O	bd	bd	bd	bd	bd	bd	bd
	K_2O	bd	0.04	bd	bd	bd	bd	bd
	H_2O	12.63	12.65	12.71	12.61	12.55	12.59	12.60
Total excl. H_2O		85.15	84.97	85.37	85.27	84.86	84.85	84.70
Total incl. H_2O		97.78	97.63	98.08	97.88	97.42	97.44	97.30
molecular proportions of oxides	SiO_2	0.49	0.50	0.49	0.48	0.48	0.49	0.50
	Al_2O_3	0.23	0.24	0.24	0.24	0.24	0.23	0.24
	TiO_2	0.00	0.00	0.00	0.00	0.00	0.00	0.00
	FeO	0.02	0.02	0.01	0.03	0.03	0.02	0.02
	MnO	0.00	0.00	0.00	0.00	0.00	0.00	0.00
	MgO	0.77	0.73	0.74	0.74	0.73	0.74	0.72
	CaO	0.00	0.00	0.00	0.00	0.00	0.00	0.00
	Na_2O	0.00	0.00	0.00	0.00	0.00	0.00	0.00
	K_2O	0.00	0.00	0.00	0.00	0.00	0.00	0.00
	H_2O	0.70	0.70	0.71	0.70	0.70	0.70	0.70
atomic proportions of oxygen from each molecule	SiO_2	0.98	0.99	0.99	0.97	0.95	0.98	0.99
	Al_2O_3	0.68	0.72	0.72	0.72	0.72	0.70	0.72
	TiO_2	0.00	0.00	0.00	0.00	0.00	0.00	0.00
	FeO	0.02	0.02	0.01	0.03	0.03	0.02	0.02
	MnO	0.00	0.00	0.00	0.00	0.00	0.00	0.00
	MgO	0.77	0.73	0.74	0.74	0.73	0.74	0.72
	CaO	0.00	0.00	0.00	0.00	0.00	0.00	0.00
	Na_2O	0.00	0.00	0.00	0.00	0.00	0.00	0.00
	K_2O	0.00	0.00	0.00	0.00	0.00	0.00	0.00
	H_2O	0.70	0.70	0.71	0.70	0.70	0.70	0.70
	Total	2.45	2.46	2.47	2.45	2.44	2.45	2.45
Multiplying factor		5.71	5.70	5.67	5.71	5.74	5.73	5.72
Number of anions based on 14 oxygen atoms (O, OH)	SiO_2	5.57	5.64	5.61	5.52	5.47	5.60	5.67
	Al_2O_3	3.90	4.09	4.09	4.11	4.16	4.03	4.10
	TiO_2	0.00	0.00	0.00	0.00	0.00	0.00	0.00
	FeO	0.10	0.09	0.08	0.16	0.15	0.13	0.12
	MnO	0.01	0.02	0.02	0.02	0.02	0.01	0.01
	MgO	4.42	4.16	4.20	4.20	4.20	4.23	4.10
	CaO	0.00	0.00	0.00	0.00	0.00	0.00	0.00
	Na_2O	0.00	0.00	0.00	0.00	0.00	0.00	0.00
	K_2O	0.00	0.00	0.00	0.00	0.00	0.00	0.00
H_2O		4.00	4.00	4.00	4.00	4.00	4.00	4.00
Number of cations in the formula (i.e.corres-ponding to 14 O, OH)	Si^{4+}	2.79	2.82	2.80	2.76	2.74	2.80	2.84
	Al^{3+} (total)	2.60	2.73	2.73	2.74	2.77	2.69	2.73
	Ti^{4+}	0.00	0.00	0.00	0.00	0.00	0.00	0.00
	Fe^{2+}	0.10	0.09	0.08	0.16	0.15	0.13	0.12
	Mn^{2+}	0.01	0.02	0.02	0.02	0.02	0.01	0.01
	Mg^{2+}	4.42	4.16	4.20	4.20	4.20	4.23	4.10
	Ca^{2+}	0.00	0.00	0.00	0.00	0.00	0.00	0.00
	Na^{+}	0.00	0.00	0.00	0.00	0.00	0.00	0.00
	K^{+}	0.00	0.01	0.00	0.00	0.00	0.00	0.00
Total oct. 2+	Mg+Fe+Mn	4.53	4.26	4.30	4.38	4.37	4.37	4.23
Al tetrahedral	Al^{3+}	1.21	1.18	1.20	1.24	1.26	1.20	1.16
Al octahedral	Al^{3+}	1.38	1.55	1.53	1.49	1.51	1.49	1.57
Total tet.	Si, Al	4.00	4.00	4.00	4.00	4.00	4.00	4.00
Total oct. 2+	Al,Mg,Fe,Mn	5.90	5.80	5.81	5.86	5.86	5.84	5.79
Octahedral vacancy		0.10	0.20	0.19	0.14	0.14	0.16	0.21
Total OH	OH	8.00	8.00	8.00	8.00	8.00	8.00	8.00
Total O	O	18.00	18.00	18.00	18.00	18.00	18.00	18.00

Table B3(ii). Formulae calculations for chlorite.

analysis reference		190802-2/#1	190802-2/#2	190802-2#3	190802-2/#6	190802-2/#7	190802-2/#8	190802-2#9
sample number		01BT002a	01BT002a	01BT002a	01BT002a	01BT002a	01BT002a	01BT002a
wt% oxides	SiO_2	29.43	29.12	29.55	30.42	28.89	29.33	29.70
	Al_2O_3	23.71	23.94	23.47	24.23	24.10	24.52	23.64
	TiO_2	bd	0.06	bd	bd	bd	bd	bd
	FeO	1.54	1.57	1.75	1.41	1.73	1.63	1.60
	MnO	0.17	0.17	0.12	0.17	0.20	0.18	0.15
	MgO	29.51	30.54	29.94	27.80	29.79	29.88	29.44
	CaO	bd	0.05	0.04	0.06	bd	bd	bd
	Na_2O	bd	bd	bd	0.11	bd	bd	bd
	K_2O	bd	bd	bd	0.75	bd	bd	bd
	H_2O	12.53	12.65	12.58	12.60	12.54	12.68	12.56
Total excl. H_2O		84.37	85.44	84.87	84.94	84.72	85.54	84.54
Total incl. H_2O		96.89	98.09	97.45	97.54	97.26	98.23	97.09
molecular proportions of oxides	SiO_2	0.49	0.48	0.49	0.51	0.48	0.49	0.49
	Al_2O_3	0.23	0.23	0.23	0.24	0.24	0.24	0.23
	TiO_2	0.00	0.00	0.00	0.00	0.00	0.00	0.00
	FeO	0.02	0.02	0.02	0.02	0.02	0.02	0.02
	MnO	0.00	0.00	0.00	0.00	0.00	0.00	0.00
	MgO	0.73	0.76	0.74	0.69	0.74	0.74	0.73
	CaO	0.00	0.00	0.00	0.00	0.00	0.00	0.00
	Na_2O	0.00	0.00	0.00	0.00	0.00	0.00	0.00
	K_2O	0.00	0.00	0.00	0.01	0.00	0.00	0.00
	H_2O	0.70	0.70	0.70	0.70	0.70	0.70	0.70
atomic proportions of oxygen from each molecule	SiO_2	0.98	0.97	0.98	1.01	0.96	0.98	0.99
	Al_2O_3	0.70	0.70	0.69	0.71	0.71	0.72	0.70
	TiO_2	0.00	0.00	0.00	0.00	0.00	0.00	0.00
	FeO	0.02	0.02	0.02	0.02	0.02	0.02	0.02
	MnO	0.00	0.00	0.00	0.00	0.00	0.00	0.00
	MgO	0.73	0.76	0.74	0.69	0.74	0.74	0.73
	CaO	0.00	0.00	0.00	0.00	0.00	0.00	0.00
	Na_2O	0.00	0.00	0.00	0.00	0.00	0.00	0.00
	K_2O	0.00	0.00	0.00	0.01	0.00	0.00	0.00
	H_2O	0.70	0.70	0.70	0.70	0.70	0.70	0.70
	Total	2.43	2.46	2.44	2.45	2.44	2.46	2.44
Multiplying factor		5.75	5.70	5.73	5.72	5.74	5.68	5.74
Number of anions based on 14 oxygen atoms (O, OH)	SiO_2	5.64	5.52	5.63	5.79	5.52	5.55	5.67
	Al_2O_3	4.01	4.01	3.96	4.08	4.07	4.10	3.99
	TiO_2	0.00	0.01	0.00	0.00	0.00	0.00	0.00
	FeO	0.12	0.12	0.14	0.11	0.14	0.13	0.13
	MnO	0.01	0.01	0.01	0.01	0.02	0.01	0.01
	MgO	4.21	4.32	4.26	3.94	4.25	4.21	4.19
	CaO	0.00	0.00	0.00	0.01	0.00	0.00	0.00
	Na_2O	0.00	0.00	0.00	0.01	0.00	0.00	0.00
	K_2O	0.00	0.00	0.00	0.05	0.00	0.00	0.00
H_2O		4.00	4.00	4.00	4.00	4.00	4.00	4.00
Number of cations in the formula (i.e.corres-ponding to 14 O, OH)	Si^{4+}	2.82	2.76	2.82	2.90	2.76	2.77	2.84
	Al^{3+} (total)	2.68	2.67	2.64	2.72	2.72	2.73	2.66
	Ti^{4+}	0.00	0.00	0.00	0.00	0.00	0.00	0.00
	Fe^{2+}	0.12	0.12	0.14	0.11	0.14	0.13	0.13
	Mn^{2+}	0.01	0.01	0.01	0.01	0.02	0.01	0.01
	Mg^{2+}	4.21	4.32	4.26	3.94	4.25	4.21	4.19
	Ca^{2+}	0.00	0.00	0.00	0.01	0.00	0.00	0.00
	Na^{+}	0.00	0.00	0.00	0.02	0.00	0.00	0.00
	K^{+}	0.00	0.00	0.00	0.09	0.00	0.00	0.00
Total oct. 2+	Mg+Fe+Mn	4.35	4.45	4.40	4.07	4.40	4.35	4.33
Al tetrahedral	Al^{3+}	1.18	1.24	1.18	1.10	1.24	1.23	1.16
Al octahedral	Al^{3+}	1.49	1.44	1.46	1.61	1.48	1.51	1.50
Total tet.	Si, Al	4.00	4.00	4.00	4.00	4.00	4.00	4.00
Total oct. 2+	Al,Mg,Fe,Mn	5.83	5.87	5.85	5.67	5.86	5.85	5.82
Octahedral vacancy		0.17	0.13	0.15	0.33	0.14	0.15	0.18
Total OH	OH	8.00	8.00	8.00	8.00	8.00	8.00	8.00
Total O	O	18.00	18.00	18.00	18.00	18.00	18.00	18.00

Table B3(ii). Formulae calculations for chlorite (contd.).

analysis reference		190802-2#10	190802-2#11	190802-2#12	190802-2#13	190802-2/#14	190802-2#15	190802-2#19
sample number		01BT002a	01BT002a	01BT002a	01BT002a	01BT002a	01BT002a	010820/03
wt% oxides	SiO_2	28.53	29.66	29.81	29.08	29.22	28.97	26.48
	Al_2O_3	25.30	24.35	25.06	24.41	23.66	24.82	18.07
	TiO_2	0.06	bd	bd	bd	bd	bd	bd
	FeO	2.08	1.63	1.68	1.85	1.72	1.72	23.45
	MnO	0.20	0.13	0.20	0.18	0.16	0.17	0.53
	MgO	29.40	28.31	29.27	29.21	30.21	29.30	16.96
	CaO	bd	0.07	bd	bd	0.06	bd	
	Na_2O	0.03	0.04	bd	bd	bd	bd	bd
	K_2O	bd	bd	0.04	bd	bd	bd	bd
	H_2O	12.65	12.52	12.78	12.56	12.59	12.60	11.16
Total excl. H_2O		85.60	84.19	86.05	84.74	85.02	84.98	85.55
Total incl. H_2O		98.25	96.71	98.83	97.29	97.61	97.58	96.71
molecular proportions of oxides	SiO_2	0.47	0.49	0.50	0.48	0.49	0.48	0.44
	Al_2O_3	0.25	0.24	0.25	0.24	0.23	0.24	0.18
	TiO_2	0.00	0.00	0.00	0.00	0.00	0.00	0.00
	FeO	0.03	0.02	0.02	0.03	0.02	0.02	0.33
	MnO	0.00	0.00	0.00	0.00	0.00	0.00	0.01
	MgO	0.73	0.70	0.73	0.72	0.75	0.73	0.42
	CaO	0.00	0.00	0.00	0.00	0.00	0.00	0.00
	Na_2O	0.00	0.00	0.00	0.00	0.00	0.00	0.00
	K_2O	0.00	0.00	0.00	0.00	0.00	0.00	0.00
	H_2O	0.70	0.69	0.71	0.70	0.70	0.70	0.62
atomic proportions of oxygen from each molecule	SiO_2	0.95	0.99	0.99	0.97	0.97	0.96	0.88
	Al_2O_3	0.74	0.72	0.74	0.72	0.70	0.73	0.53
	TiO_2	0.00	0.00	0.00	0.00	0.00	0.00	0.00
	FeO	0.03	0.02	0.02	0.03	0.02	0.02	0.33
	MnO	0.00	0.00	0.00	0.00	0.00	0.00	0.01
	MgO	0.73	0.70	0.73	0.72	0.75	0.73	0.42
	CaO	0.00	0.00	0.00	0.00	0.00	0.00	0.00
	Na_2O	0.00	0.00	0.00	0.00	0.00	0.00	0.00
	K_2O	0.00	0.00	0.00	0.00	0.00	0.00	0.00
	H_2O	0.70	0.69	0.71	0.70	0.70	0.70	0.62
	Total	2.46	2.43	2.48	2.44	2.45	2.45	2.17
Multiplying factor		5.70	5.76	5.64	5.74	5.73	5.72	6.45
Number of anions based on 14 oxygen atoms (O, OH)	SiO_2	5.41	5.68	5.60	5.56	5.57	5.52	5.69
	Al_2O_3	4.24	4.12	4.16	4.12	3.99	4.18	3.43
	TiO_2	0.01	0.00	0.00	0.00	0.00	0.00	0.00
	FeO	0.17	0.13	0.13	0.15	0.14	0.14	2.11
	MnO	0.02	0.01	0.02	0.01	0.01	0.01	0.05
	MgO	4.16	4.04	4.09	4.16	4.29	4.16	2.72
	CaO	0.00	0.01	0.00	0.00	0.01	0.00	0.01
	Na_2O	0.00	0.00	0.00	0.00	0.00	0.00	0.00
	K_2O	0.00	0.00	0.00	0.00	0.00	0.00	0.00
H_2O		4.00	4.00	4.00	4.00	4.00	4.00	4.00
Number of cations in the formula (i.e.corres-ponding to 14 O, OH)	Si^{4+}	2.70	2.84	2.80	2.78	2.78	2.76	2.84
	Al^{3+} (total)	2.83	2.75	2.77	2.75	2.66	2.79	2.29
	Ti^{4+}	0.00	0.00	0.00	0.00	0.00	0.00	0.00
	Fe^{2+}	0.17	0.13	0.13	0.15	0.14	0.14	2.11
	Mn^{2+}	0.02	0.01	0.02	0.01	0.01	0.01	0.05
	Mg^{2+}	4.16	4.04	4.09	4.16	4.29	4.16	2.72
	Ca^{2+}	0.00	0.01	0.00	0.00	0.01	0.00	0.01
	Na^{+}	0.00	0.01	0.00	0.00	0.00	0.00	0.00
	K^{+}	0.00	0.00	0.00	0.00	0.00	0.00	0.00
Total oct. 2+	Mg+Fe+Mn	4.34	4.18	4.24	4.32	4.44	4.31	4.87
Al tetrahedral	Al^{3+}	1.30	1.16	1.20	1.22	1.22	1.24	1.16
Al octahedral	Al^{3+}	1.53	1.59	1.57	1.53	1.44	1.54	1.13
Total tet.	Si, Al	4.00	4.00	4.00	4.00	4.00	4.00	4.00
Total oct. 2+	Al,Mg,Fe,Mn	5.85	5.76	5.80	5.83	5.87	5.84	5.96
Octahedral vacancy		0.15	0.24	0.20	0.17	0.13	0.16	0.04
Total OH	OH	8.00	8.00	8.00	8.00	8.00	8.00	8.00
Total O	O	18.00	18.00	18.00	18.00	18.00	18.00	18.00

Table B3(ii). Formulae calculations for chlorite (contd.).

analysis reference		190802-2#20	190802-2#21	190802-2/#22	190802-2/#23	190802-2#32	190802-2/#33	190802-2/#34
sample number		010820/03	010820/03	010820/03	010820/03	01BT061	01BT061	01BT061
wt% oxides	SiO_2	27.46	27.39	26.34	26.53	29.46	29.42	29.45
	Al_2O_3	18.03	18.10	18.05	18.48	23.64	23.39	22.39
	TiO_2	bd	bd	bd	bd	bd	bd	bd
	FeO	23.51	23.10	23.66	23.12	1.07	1.06	1.01
	MnO	0.45	0.40	0.46	0.55	0.11	0.09	0.17
	MgO	17.22	17.07	17.08	17.17	30.85	30.63	31.21
	CaO	0.06	0.07	0.10	0.04	0.06	bd	0.07
	Na_2O	0.03	bd	bd	0.04	bd	bd	bd
	K_2O	bd	bd	bd	bd	bd	0.04	bd
	H_2O	11.36	11.31	11.16	11.24	12.65	12.59	12.51
Total excl. H_2O		86.77	86.16	85.63	85.96	85.13	84.71	84.26
Total incl. H_2O		98.13	97.47	96.78	97.20	97.79	97.29	96.77
molecular proportions of oxides	SiO_2	0.46	0.46	0.44	0.44	0.49	0.49	0.49
	Al_2O_3	0.18	0.18	0.18	0.18	0.23	0.23	0.22
	TiO_2	0.00	0.00	0.00	0.00	0.00	0.00	0.00
	FeO	0.33	0.32	0.33	0.32	0.01	0.01	0.01
	MnO	0.01	0.01	0.01	0.01	0.00	0.00	0.00
	MgO	0.43	0.42	0.42	0.43	0.77	0.76	0.77
	CaO	0.00	0.00	0.00	0.00	0.00	0.00	0.00
	Na_2O	0.00	0.00	0.00	0.00	0.00	0.00	0.00
	K_2O	0.00	0.00	0.00	0.00	0.00	0.00	0.00
	H_2O	0.63	0.63	0.62	0.62	0.70	0.70	0.69
atomic proportions of oxygen from each molecule	SiO_2	0.91	0.91	0.88	0.88	0.98	0.98	0.98
	Al_2O_3	0.53	0.53	0.53	0.54	0.70	0.69	0.66
	TiO_2	0.00	0.00	0.00	0.00	0.00	0.00	0.00
	FeO	0.33	0.32	0.33	0.32	0.01	0.01	0.01
	MnO	0.01	0.01	0.01	0.01	0.00	0.00	0.00
	MgO	0.43	0.42	0.42	0.43	0.77	0.76	0.77
	CaO	0.00	0.00	0.00	0.00	0.00	0.00	0.00
	Na_2O	0.00	0.00	0.00	0.00	0.00	0.00	0.00
	K_2O	0.00	0.00	0.00	0.00	0.00	0.00	0.00
	H_2O	0.63	0.63	0.62	0.62	0.70	0.70	0.69
	Total	2.21	2.20	2.17	2.18	2.46	2.45	2.43
Multiplying factor		6.34	6.37	6.46	6.41	5.70	5.73	5.76
Number of anions based on 14 oxygen atoms (O, OH)	SiO_2	5.80	5.81	5.66	5.66	5.58	5.61	5.65
	Al_2O_3	3.37	3.39	3.43	3.49	3.96	3.94	3.80
	TiO_2	0.00	0.00	0.00	0.00	0.00	0.00	0.00
	FeO	2.08	2.05	2.13	2.06	0.09	0.08	0.08
	MnO	0.04	0.04	0.04	0.05	0.01	0.01	0.01
	MgO	2.71	2.70	2.74	2.73	4.36	4.35	4.46
	CaO	0.01	0.01	0.00	0.01	0.00	0.01	0.00
	Na_2O	0.00	0.00	0.00	0.00	0.00	0.00	0.00
	K_2O	0.00	0.00	0.00	0.00	0.00	0.00	0.00
H_2O		4.00	4.00	4.00	4.00	4.00	4.00	4.00
Number of cations in the formula (i.e.corres-ponding to 14 O, OH)	Si^{4+}	2.90	2.91	2.83	2.83	2.79	2.80	2.82
	Al^{3+} (total)	2.24	2.26	2.29	2.32	2.64	2.63	2.53
	Ti^{4+}	0.00	0.00	0.00	0.00	0.00	0.00	0.00
	Fe^{2+}	2.08	2.05	2.13	2.06	0.09	0.08	0.08
	Mn^{2+}	0.04	0.04	0.04	0.05	0.01	0.01	0.01
	Mg^{2+}	2.71	2.70	2.74	2.73	4.36	4.35	4.46
	Ca^{2+}	0.01	0.01	0.00	0.01	0.00	0.01	0.00
	Na^{+}	0.01	0.00	0.00	0.01	0.00	0.00	0.00
	K^{+}	0.00	0.00	0.00	0.00	0.00	0.01	0.00
Total oct. 2+	Mg+Fe+Mn	4.83	4.78	4.90	4.84	4.45	4.44	4.55
Al tetrahedral	Al^{3+}	1.10	1.09	1.17	1.17	1.21	1.20	1.18
Al octahedral	Al^{3+}	1.14	1.17	1.12	1.15	1.43	1.43	1.35
Total tet.	Si, Al	4.00	4.00	4.00	4.00	4.00	4.00	4.00
Total oct. 2+	Al,Mg,Fe,Mn	5.93	5.92	5.98	5.95	5.88	5.87	5.89
octahedral vacancy		0.07	0.08	0.02	0.05	0.12	0.13	0.11
Total OH	OH	8.00	8.00	8.00	8.00	8.00	8.00	8.00
Total O	O	18.00	18.00	18.00	18.00	18.00	18.00	18.00

Table B3(ii). Formulae calculations for chlorite (contd.).

analysis reference		190802-2#35	190802-2#36	190802-2#37	190802-2#38	190802-2#39	190802-2#40	200802-1#1
sample number		01BT061	01BT061	01BT061	01BT061	01BT061	01BT061	901
wt% oxides	SiO_2	34.04	33.62	34.51	30.03	29.64	29.33	23.63
	Al_2O_3	25.47	25.26	25.52	22.98	23.03	23.53	20.90
	TiO_2	0.07	bd	bd	bd	bd	bd	bd
	FeO	0.81	0.91	0.89	0.97	1.06	1.07	32.42
	MnO	0.20	0.19	0.10	0.10	0.18	0.16	1.42
	MgO	24.82	24.71	24.50	31.34	31.31	30.92	7.75
	CaO	0.05	0.16	0.18	0.16	bd	bd	0.04
	Na_2O	bd	0.03	0.02	0.04	bd	bd	bd
	K_2O	bd	0.04	0.04	bd	bd	bd	bd
	H_2O	12.96	12.84	13.00	12.71	12.65	12.63	10.63
Total excl. H_2O		85.57	84.94	85.74	85.47	85.21	85.05	86.12
Total incl. H_2O		98.52	97.78	98.74	98.17	97.86	97.67	96.75
molecular proportions of oxides	SiO_2	0.57	0.56	0.57	0.50	0.49	0.49	0.39
	Al_2O_3	0.25	0.25	0.25	0.23	0.23	0.23	0.21
	TiO_2	0.00	0.00	0.00	0.00	0.00	0.00	0.00
	FeO	0.01	0.01	0.01	0.01	0.01	0.01	0.45
	MnO	0.00	0.00	0.00	0.00	0.00	0.00	0.02
	MgO	0.62	0.61	0.61	0.78	0.78	0.77	0.19
	CaO	0.00	0.00	0.00	0.00	0.00	0.00	0.00
	Na_2O	0.00	0.00	0.00	0.00	0.00	0.00	0.00
	K_2O	0.00	0.00	0.00	0.00	0.00	0.00	0.00
	H_2O	0.72	0.71	0.72	0.71	0.70	0.70	0.59
ato#mic proportions of oxygen from each molecule	SiO_2	1.13	1.12	1.15	1.00	0.99	0.98	0.79
	Al_2O_3	0.75	0.74	0.75	0.68	0.68	0.69	0.62
	TiO_2	0.00	0.00	0.00	0.00	0.00	0.00	0.00
	FeO	0.01	0.01	0.01	0.01	0.01	0.01	0.45
	MnO	0.00	0.00	0.00	0.00	0.00	0.00	0.02
	MgO	0.62	0.61	0.61	0.78	0.78	0.77	0.19
	CaO	0.00	0.00	0.00	0.00	0.00	0.00	0.00
	Na_2O	0.00	0.00	0.00	0.00	0.00	0.00	0.00
	K_2O	0.00	0.00	0.00	0.00	0.00	0.00	0.00
	H_2O	0.72	0.71	0.72	0.71	0.70	0.70	0.59
	Total	2.52	2.49	2.52	2.47	2.46	2.45	2.07
Multiplying factor		5.56	5.61	5.54	5.67	5.70	5.71	6.78
Number of anions based on 14 oxygen atoms (O, OH)	SiO_2	6.30	6.28	6.37	5.67	5.62	5.57	5.33
	Al_2O_3	4.17	4.17	4.16	3.83	3.86	3.95	4.17
	TiO_2	0.01	0.00	0.00	0.00	0.00	0.00	0.00
	FeO	0.06	0.07	0.07	0.08	0.08	0.08	3.06
	MnO	0.02	0.02	0.01	0.01	0.01	0.01	0.14
	MgO	3.42	3.44	3.37	4.41	4.42	4.38	1.30
	CaO	0.02	0.02	0.02	0.00	0.00	0.00	0.00
	Na_2O	0.00	0.00	0.00	0.00	0.00	0.00	0.00
	K_2O	0.00	0.00	0.00	0.00	0.00	0.00	0.00
H_2O		4.00	4.00	4.00	4.00	4.00	4.00	4.00
Number of cations in the formula (i.e.corres-ponding to 14 O, OH)	Si^{4+}	3.15	3.14	3.18	2.83	2.81	2.79	2.67
	Al^{3+} (total)	2.78	2.78	2.78	2.56	2.57	2.63	2.78
	Ti^{4+}	0.00	0.00	0.00	0.00	0.00	0.00	0.00
	Fe^{2+}	0.06	0.07	0.07	0.08	0.08	0.08	3.06
	Mn^{2+}	0.02	0.02	0.01	0.01	0.01	0.01	0.14
	Mg^{2+}	3.42	3.44	3.37	4.41	4.42	4.38	1.30
	Ca^{2+}	0.02	0.02	0.02	0.00	0.00	0.00	0.00
	Na^{+}	0.00	0.00	0.00	0.01	0.00	0.00	0.00
	K^{+}	0.00	0.00	0.00	0.00	0.00	0.00	0.00
Total oct. 2+	Mg+Fe+Mn	3.50	3.53	3.45	4.49	4.52	4.48	4.50
Al tetrahedral	Al^{3+}	0.85	0.86	0.82	1.17	1.19	1.21	1.33
Al octahedral	Al^{3+}	1.93	1.92	1.96	1.39	1.38	1.42	1.45
Total tet.	Si, Al	4.00	4.00	4.00	4.00	4.00	4.00	4.00
Total oct. 2+	Al,Mg,Fe,Mn	5.42	5.43	5.40	5.88	5.89	5.88	5.81
octahedral vacancy		0.58	0.57	0.60	0.12	0.11	0.12	0.19
Total OH	OH	8.00	8.00	8.00	8.00	8.00	8.00	8.00
Total O	O	18.00	18.00	18.00	18.00	18.00	18.00	18.00

Table B3(ii). Formulae calculations for chlorite (contd.).

analysis reference		200802-1#2	200802-1#3	200802-1/#4	200802-4#1	200802-4#2	200802-4#3	200802-4#4
sample number		901	901	901	01BT098	01BT098	01BT098	00BT12
wt% oxides	SiO_2	23.99	24.01	23.40	30.84	30.36	31.39	33.48
	Al_2O_3	21.81	21.66	21.87	21.12	21.06	21.63	24.03
	TiO_2	0.07	bd	bd	bd	bd	bd	bd
	FeO	30.75	31.32	31.62	3.38	4.69	3.94	3.20
	MnO	1.42	1.39	1.32	0.11	0.20	0.16	0.14
	MgO	7.83	8.43	7.76	29.25	27.65	28.54	24.44
	CaO	bd	bd	bd	0.04	0.06	0.09	0.09
	Na_2O	bd	bd	bd	bd	0.04	bd	0.08
	K_2O	bd	bd	bd	bd	bd	bd	0.29
	H_2O	10.73	10.81	10.68	12.48	12.28	12.60	12.77
Total excl. H_2O		85.86	86.81	86.01	84.78	84.09	85.75	85.75
Total incl. H_2O		96.59	97.62	96.69	97.25	96.37	98.35	98.51
molecular proportions of oxides	SiO_2	0.40	0.40	0.39	0.51	0.51	0.52	0.56
	Al_2O_3	0.21	0.21	0.21	0.21	0.21	0.21	0.24
	TiO_2	0.00	0.00	0.00	0.00	0.00	0.00	0.00
	FeO	0.43	0.44	0.44	0.05	0.07	0.05	0.04
	MnO	0.02	0.02	0.02	0.00	0.00	0.00	0.00
	MgO	0.19	0.21	0.19	0.73	0.69	0.71	0.61
	CaO	0.00	0.00	0.00	0.00	0.00	0.00	0.00
	Na_2O	0.00	0.00	0.00	0.00	0.00	0.00	0.00
	K_2O	0.00	0.00	0.00	0.00	0.00	0.00	0.00
	H_2O	0.60	0.60	0.59	0.69	0.68	0.70	0.71
atomic proportions of oxygen from each molecule	SiO_2	0.80	0.80	0.78	1.03	1.01	1.04	1.11
	Al_2O_3	0.64	0.64	0.64	0.62	0.62	0.64	0.71
	TiO_2	0.00	0.00	0.00	0.00	0.00	0.00	0.00
	FeO	0.43	0.44	0.44	0.05	0.07	0.05	0.04
	MnO	0.02	0.02	0.02	0.00	0.00	0.00	0.00
	MgO	0.19	0.21	0.19	0.73	0.69	0.71	0.61
	CaO	0.00	0.00	0.00	0.00	0.00	0.00	0.00
	Na_2O	0.00	0.00	0.00	0.00	0.00	0.00	0.00
	K_2O	0.00	0.00	0.00	0.00	0.00	0.00	0.00
	H_2O	0.60	0.60	0.59	0.69	0.68	0.70	0.71
	Total	2.08	2.10	2.07	2.42	2.39	2.45	2.48
Multiplying factor		6.72	6.66	6.75	5.78	5.87	5.72	5.64
Number of anions based on 14 oxygen atoms (O, OH)	SiO_2	5.36	5.32	5.26	5.93	5.93	5.98	6.29
	Al_2O_3	4.31	4.25	4.34	3.59	3.64	3.64	3.99
	TiO_2	0.01	0.00	0.00	0.00	0.00	0.00	0.00
	FeO	2.87	2.90	2.97	0.27	0.38	0.31	0.25
	MnO	0.13	0.13	0.13	0.01	0.02	0.01	0.01
	MgO	1.30	1.39	1.30	4.19	4.02	4.05	3.42
	CaO	0.00	0.00	0.00	0.01	0.01	0.01	0.01
	Na_2O	0.00	0.00	0.00	0.00	0.00	0.00	0.01
	K_2O	0.00	0.00	0.00	0.00	0.00	0.00	0.02
H_2O		4.00	4.00	4.00	4.00	4.00	4.00	4.00
Number of cations in the formula (i.e.corres-ponding to 14 O, OH)	Si^{4+}	2.68	2.66	2.63	2.96	2.96	2.99	3.15
	Al^{3+} (total)	2.87	2.83	2.90	2.39	2.42	2.43	2.66
	Ti^{4+}	0.01	0.00	0.00	0.00	0.00	0.00	0.00
	Fe^{2+}	2.87	2.90	2.97	0.27	0.38	0.31	0.25
	Mn^{2+}	0.13	0.13	0.13	0.01	0.02	0.01	0.01
	Mg^{2+}	1.30	1.39	1.30	4.19	4.02	4.05	3.42
	Ca^{2+}	0.00	0.00	0.00	0.01	0.01	0.01	0.01
	Na^{+}	0.00	0.00	0.00	0.00	0.01	0.00	0.01
	K^{+}	0.00	0.00	0.00	0.00	0.00	0.00	0.03
Total oct. 2+	Mg+Fe+Mn	4.31	4.43	4.39	4.47	4.42	4.38	3.69
Al tetrahedral	Al^{3+}	1.32	1.34	1.37	1.04	1.04	1.01	0.85
Al octahedral	Al^{3+}	1.56	1.49	1.52	1.36	1.39	1.41	1.81
Total tet.	Si, Al	4.00	4.00	4.00	4.00	4.00	4.00	4.00
Total oct. 2+	Al,Mg,Fe,Mn	5.74	5.79	5.79	5.82	5.79	5.78	5.48
octahedral vacancy		0.26	0.21	0.21	0.18	0.21	0.22	0.52
Total OH	OH	8.00	8.00	8.00	8.00	8.00	8.00	8.00
Total O	O	18.00	18.00	18.00	18.00	18.00	18.00	18.00

Table B3(ii). Formulae calculations for chlorite (contd.).

analysis reference		200802-4#5	200802-4#6	200802-4#7	200802-4#8	200802-4#9	200802-4#16	200802-4#17
sample number		00BT12	00BT12	00BT12	00BT12	00BT12	01BT052	01BT052
wt% oxides	SiO_2	33.33	33.01	28.36	28.58	28.19	30.84	29.55
	Al_2O_3	25.38	27.11	24.77	24.70	25.24	25.42	24.21
	TiO_2	bd	bd	bd	bd	bd	bd	bd
	FeO	2.94	2.92	3.95	4.02	3.86	2.20	2.03
	MnO	0.09	0.13	0.19	0.19	0.18	0.16	0.27
	MgO	23.92	23.29	27.30	27.24	27.85	26.22	28.77
	CaO	0.09	0.13	0.07	bd	0.05	bd	0.09
	Na_2O	bd	bd	0.03	0.04	bd	0.05	bd
	K_2O	bd	0.05	bd	bd	bd	bd	bd
	H_2O	12.84	12.96	12.40	12.42	12.50	12.67	12.57
Total excl. H_2O		85.79	86.58	84.60	84.81	85.32	84.99	84.83
Total incl. H_2O		98.62	99.54	96.99	97.23	97.81	97.66	97.40
molecular proportions of oxides	SiO_2	0.55	0.55	0.47	0.48	0.47	0.51	0.49
	Al_2O_3	0.25	0.27	0.24	0.24	0.25	0.25	0.24
	TiO_2	0.00	0.00	0.00	0.00	0.00	0.00	0.00
	FeO	0.04	0.04	0.05	0.06	0.05	0.03	0.03
	MnO	0.00	0.00	0.00	0.00	0.00	0.00	0.00
	MgO	0.59	0.58	0.68	0.68	0.69	0.65	0.71
	CaO	0.00	0.00	0.00	0.00	0.00	0.00	0.00
	Na_2O	0.00	0.00	0.00	0.00	0.00	0.00	0.00
	K_2O	0.00	0.00	0.00	0.00	0.00	0.00	0.00
	H_2O	0.71	0.72	0.69	0.69	0.69	0.70	0.70
atomic proportions of oxygen from each molecule	SiO_2	1.11	1.10	0.94	0.95	0.94	1.03	0.98
	Al_2O_3	0.75	0.80	0.73	0.73	0.74	0.75	0.71
	TiO_2	0.00	0.00	0.00	0.00	0.00	0.00	0.00
	FeO	0.04	0.04	0.05	0.06	0.05	0.03	0.03
	MnO	0.00	0.00	0.00	0.00	0.00	0.00	0.00
	MgO	0.59	0.58	0.68	0.68	0.69	0.65	0.71
	CaO	0.00	0.00	0.00	0.00	0.00	0.00	0.00
	Na_2O	0.00	0.00	0.00	0.00	0.00	0.00	0.00
	K_2O	0.00	0.00	0.00	0.00	0.00	0.00	0.00
	H_2O	0.71	0.72	0.69	0.69	0.69	0.70	0.70
	Total	2.49	2.52	2.41	2.41	2.43	2.46	2.44
Multiplying factor		5.61	5.56	5.81	5.80	5.77	5.69	5.73
Number of anions based on 14 oxygen atoms (O, OH)	SiO_2	6.23	6.11	5.49	5.52	5.41	5.84	5.64
	Al_2O_3	4.19	4.43	4.24	4.22	4.28	4.26	4.09
	TiO_2	0.00	0.00	0.00	0.00	0.00	0.00	0.00
	FeO	0.23	0.23	0.32	0.32	0.31	0.17	0.16
	MnO	0.01	0.01	0.02	0.02	0.01	0.01	0.02
	MgO	3.33	3.21	3.94	3.92	3.98	3.70	4.09
	CaO	0.01	0.01	0.00	0.01	0.00	0.01	0.00
	Na_2O	0.00	0.00	0.00	0.00	0.00	0.00	0.00
	K_2O	0.00	0.00	0.00	0.00	0.00	0.00	0.00
H_2O		4.00	4.00	4.00	4.00	4.00	4.00	4.00
Number of cations in the formula (i.e.corres-ponding to 14 O, OH)	Si^{4+}	3.11	3.05	2.74	2.76	2.70	2.92	2.82
	Al^{3+} (total)	2.80	2.96	2.83	2.81	2.86	2.84	2.72
	Ti^{4+}	0.00	0.00	0.00	0.00	0.00	0.00	0.00
	Fe^{2+}	0.23	0.23	0.32	0.32	0.31	0.17	0.16
	Mn^{2+}	0.01	0.01	0.02	0.02	0.01	0.01	0.02
	Mg^{2+}	3.33	3.21	3.94	3.92	3.98	3.70	4.09
	Ca^{2+}	0.01	0.01	0.00	0.01	0.00	0.01	0.00
	Na^{+}	0.00	0.00	0.01	0.01	0.00	0.01	0.00
	K^{+}	0.00	0.01	0.00	0.00	0.00	0.00	0.00
Total oct. 2+	Mg+Fe+Mn	3.57	3.45	4.27	4.26	4.31	3.89	4.28
Al tetrahedral	Al^{3+}	0.89	0.95	1.26	1.24	1.30	1.08	1.18
Al octahedral	Al^{3+}	1.91	2.01	1.57	1.57	1.56	1.76	1.54
Total tet.	Si, Al	4.00	4.00	4.00	4.00	4.00	4.00	4.00
Total oct. 2+	Al,Mg,Fe,Mn	5.47	5.45	5.83	5.81	5.85	5.63	5.80
octahedral vacancy		0.53	0.55	0.17	0.19	0.15	0.37	0.20
Total OH	OH	8.00	8.00	8.00	8.00	8.00	8.00	8.00
Total O	O	18.00	18.00	18.00	18.00	18.00	18.00	18.00

Table B3(ii). Formulae calculations for chlorite (contd.).

analysis reference		200802-4#18	200802-5#1	200802-5#2	200802-5#3	200802-5#4	200802-5#5	200802-5#6
sample number		01BT052	902	902	902	902	01BT058	01BT058
wt% oxides	SiO_2	29.26	24.36	23.74	23.46	23.27	31.43	31.49
	Al_2O_3	24.74	18.60	18.79	18.62	18.26	22.89	22.70
	TiO_2	bd	0.06	bd	0.07	0.06	bd	bd
	FeO	1.96	35.62	35.16	36.67	36.64	1.67	1.66
	MnO	0.19	bd	0.08	0.07	0.20	0.23	0.19
	MgO	28.49	8.08	7.88	7.39	6.97	29.45	29.13
	CaO	bd	bd	bd	bd	bd	bd	0.10
	Na_2O	0.03	bd	0.07	bd	0.02	bd	bd
	K_2O	bd	bd	bd	bd	bd	bd	bd
	H_2O	12.56	10.58	10.45	10.42	10.29	12.76	12.70
Total excl. H_2O		84.67	86.72	85.73	86.27	85.42	85.77	85.30
Total incl. H_2O		97.23	97.30	96.18	96.70	95.71	98.52	98.00
molecular proportions of oxides	SiO_2	0.49	0.41	0.40	0.39	0.39	0.52	0.52
	Al_2O_3	0.24	0.18	0.18	0.18	0.18	0.22	0.22
	TiO_2	0.00	0.00	0.00	0.00	0.00	0.00	0.00
	FeO	0.03	0.50	0.49	0.51	0.51	0.02	0.02
	MnO	0.00	0.00	0.00	0.00	0.00	0.00	0.00
	MgO	0.71	0.20	0.20	0.18	0.17	0.73	0.72
	CaO	0.00	0.00	0.00	0.00	0.00	0.00	0.00
	Na_2O	0.00	0.00	0.00	0.00	0.00	0.00	0.00
	K_2O	0.00	0.00	0.00	0.00	0.00	0.00	0.00
	H_2O	0.70	0.59	0.58	0.58	0.57	0.71	0.70
atomic proportions of oxygen from each molecule	SiO_2	0.97	0.81	0.79	0.78	0.77	1.05	1.05
	Al_2O_3	0.73	0.55	0.55	0.55	0.54	0.67	0.67
	TiO_2	0.00	0.00	0.00	0.00	0.00	0.00	0.00
	FeO	0.03	0.50	0.49	0.51	0.51	0.02	0.02
	MnO	0.00	0.00	0.00	0.00	0.00	0.00	0.00
	MgO	0.71	0.20	0.20	0.18	0.17	0.73	0.72
	CaO	0.00	0.00	0.00	0.00	0.00	0.00	0.00
	Na_2O	0.00	0.00	0.00	0.00	0.00	0.00	0.00
	K_2O	0.00	0.00	0.00	0.00	0.00	0.00	0.00
	H_2O	0.70	0.59	0.58	0.58	0.57	0.71	0.70
	Total	2.44	2.06	2.03	2.03	2.00	2.48	2.47
Multiplying factor		5.74	6.81	6.90	6.91	7.00	5.65	5.67
Number of anions based on 14 oxygen atoms (O, OH)	SiO_2	5.59	5.52	5.45	5.40	5.42	5.91	5.95
	Al_2O_3	4.18	3.73	3.81	3.79	3.76	3.80	3.79
	TiO_2	0.00	0.01	0.00	0.01	0.01	0.00	0.00
	FeO	0.16	3.38	3.37	3.53	3.57	0.13	0.13
	MnO	0.02	0.00	0.01	0.01	0.02	0.02	0.01
	MgO	4.06	1.37	1.35	1.27	1.21	4.13	4.10
	CaO	0.00	0.00	0.00	0.00	0.00	0.01	0.01
	Na_2O	0.00	0.00	0.01	0.00	0.00	0.00	0.00
	K_2O	0.00	0.00	0.00	0.00	0.00	0.00	0.00
H_2O		4.00	4.00	4.00	4.00	4.00	4.00	4.00
Number of cations in the formula (i.e.corres-ponding to 14 O, OH)	Si^{4+}	2.80	2.76	2.72	2.70	2.71	2.95	2.97
	Al^{3+} (total)	2.79	2.48	2.54	2.53	2.51	2.54	2.53
	Ti^{4+}	0.00	0.00	0.00	0.01	0.01	0.00	0.00
	Fe^{2+}	0.16	3.38	3.37	3.53	3.57	0.13	0.13
	Mn^{2+}	0.02	0.00	0.01	0.01	0.02	0.02	0.01
	Mg^{2+}	4.06	1.37	1.35	1.27	1.21	4.13	4.10
	Ca^{2+}	0.00	0.00	0.00	0.00	0.00	0.01	0.01
	Na^{+}	0.01	0.00	0.02	0.00	0.01	0.00	0.00
	K^{+}	0.00	0.00	0.00	0.00	0.00	0.00	0.00
Total oct. 2+	Mg+Fe+Mn	4.23	4.74	4.73	4.80	4.80	4.28	4.25
Al tetrahedral	Al^{3+}	1.20	1.24	1.28	1.30	1.29	1.05	1.03
Al octahedral	Al^{3+}	1.58	1.25	1.27	1.22	1.22	1.49	1.50
Total tet.	Si, Al	4.00	4.00	4.00	4.00	4.00	4.00	4.00
Total oct. 2+	Al,Mg,Fe,Mn	5.79	5.99	5.99	6.02	6.00	5.75	5.73
octahedral vacancy		0.21	0.01	0.01	-0.02	0.00	0.25	0.27
Total OH	OH	8.00	8.00	8.00	8.00	8.00	8.00	8.00
Total O	O	18.00	18.00	18.00	18.00	18.00	18.00	18.00

Table B3(ii). Formulae calculations for chlorite (contd.).

analysis reference		200802-5#7	200802-5#8	200802-5#9	200802-5#10	200802-7#8	200802-7#9	200802-7#10
sample number		01BT058	01BT191	01BT191	01BT191	010820/11	010820/11	010820/11
wt% oxides	SiO_2	31.10	26.83	26.90	26.56	27.42	27.43	27.18
	Al_2O_3	22.63	20.77	21.25	21.37	17.23	17.65	17.46
	TiO_2	bd	bd	bd	bd	bd	bd	bd
	FeO	1.68	17.42	18.09	18.65	25.08	24.96	24.83
	MnO	0.26	0.45	0.41	0.51	0.20	0.22	0.25
	MgO	29.04	20.33	20.19	19.63	15.41	15.28	15.84
	CaO	0.14	0.14	bd	0.04	0.04	0.17	0.16
	Na_2O	bd	0.04	bd	bd	0.07	bd	bd
	K_2O	bd	bd	bd	bd	0.05	bd	0.04
	H_2O	12.62	11.62	11.73	11.67	11.11	11.14	11.14
Total excl. H_2O		84.85	85.83	86.87	86.75	85.63	85.70	85.75
Total incl. H_2O		97.46	97.45	98.61	98.42	96.74	96.84	
molecular proportions of oxides	SiO_2	0.52	0.45	0.45	0.44	0.46	0.46	0.45
	Al_2O_3	0.22	0.20	0.21	0.21	0.17	0.17	0.17
	TiO_2	0.00	0.00	0.00	0.00	0.00	0.00	0.00
	FeO	0.02	0.24	0.25	0.26	0.35	0.35	0.35
	MnO	0.00	0.01	0.01	0.01	0.00	0.00	0.00
	MgO	0.72	0.50	0.50	0.49	0.38	0.38	0.39
	CaO	0.00	0.00	0.00	0.00	0.00	0.00	0.00
	Na_2O	0.00	0.00	0.00	0.00	0.00	0.00	0.00
	K_2O	0.00	0.00	0.00	0.00	0.00	0.00	0.00
	H_2O	0.70	0.65	0.65	0.65	0.62	0.62	0.62
atomic proportions of oxygen from each molecule	SiO_2	1.04	0.89	0.90	0.88	0.91	0.91	0.90
	Al_2O_3	0.67	0.61	0.63	0.63	0.51	0.52	0.51
	TiO_2	0.00	0.00	0.00	0.00	0.00	0.00	0.00
	FeO	0.02	0.24	0.25	0.26	0.35	0.35	0.35
	MnO	0.00	0.01	0.01	0.01	0.00	0.00	0.00
	MgO	0.72	0.50	0.50	0.49	0.38	0.38	0.39
	CaO	0.00	0.00	0.00	0.00	0.00	0.00	0.00
	Na_2O	0.00	0.00	0.00	0.00	0.00	0.00	0.00
	K_2O	0.00	0.00	0.00	0.00	0.00	0.00	0.00
	H_2O	0.70	0.65	0.65	0.65	0.62	0.62	0.62
	Total	2.45	2.26	2.28	2.27	2.16	2.16	2.16
Multiplying factor		5.71	6.20	6.14	6.17	6.49	6.47	
Number of anions based on 14 oxygen atoms (O, OH)	SiO_2	5.91	5.54	5.50	5.46	5.92	5.90	5.85
	Al_2O_3	3.80	3.79	3.84	3.88	3.29	3.36	3.33
	TiO_2	0.00	0.00	0.00	0.00	0.00	0.00	0.00
	FeO	0.13	1.50	1.55	1.60	2.26	2.25	2.24
	MnO	0.02	0.04	0.04	0.04	0.02	0.02	0.02
	MgO	4.12	3.13	3.08	3.01	2.48	2.45	2.54
	CaO	0.01	0.00	0.00	0.00	0.02	0.02	0.02
	Na_2O	0.00	0.00	0.00	0.00	0.01	0.00	0.00
	K_2O	0.00	0.00	0.00	0.00	0.00	0.00	0.00
H_2O		4.00	4.00	4.00	4.00	4.00	4.00	
Number of cations in the formula (i.e.corres-ponding to 14 O, OH)	Si^{4+}	2.96	2.77	2.75	2.73	2.96	2.95	2.93
	Al^{3+} (total)	2.54	2.53	2.56	2.59	2.19	2.24	2.22
	Ti^{4+}	0.00	0.00	0.00	0.00	0.00	0.00	0.00
	Fe^{2+}	0.13	1.50	1.55	1.60	2.26	2.25	2.24
	Mn^{2+}	0.02	0.04	0.04	0.04	0.02	0.02	0.02
	Mg^{2+}	4.12	3.13	3.08	3.01	2.48	2.45	2.54
	Ca^{2+}	0.01	0.00	0.00	0.00	0.02	0.02	0.02
	Na^{+}	0.00	0.01	0.00	0.00	0.01	0.00	0.00
	K^{+}	0.00	0.00	0.00	0.00	0.01	0.00	0.01
Total oct. 2+	Mg+Fe+Mn	4.27	4.67	4.66	4.65	4.76	4.72	4.80
Al tetrahedral	Al^{3+}	1.04	1.23	1.25	1.27	1.04	1.05	1.07
Al octahedral	Al^{3+}	1.49	1.30	1.31	1.32	1.15	1.19	1.14
Total tet.	Si, Al	4.00	4.00	4.00	4.00	4.00	4.00	4.00
Total oct. 2+	Al,Mg,Fe,Mn	5.74	5.93	5.93	5.93	5.90	5.89	5.92
octahedral vacancy		0.26	0.07	0.07	0.07	0.10	0.11	0.08
Total OH	OH	8.00	8.00	8.00	8.00	8.00	8.00	8.00
Total O	O	18.00	18.00	18.00	18.00	18.00	18.00	18.00

Table B3(ii). Formulae calculations for chlorite (contd.).

analysis reference		200802-7#10	200802-7#11	200802-7#24	200802-7#25	200802-7#26
sample number		010820/11	010820/11	01BT162	01BT162	01BT162
wt% oxides	SiO_2	27.18	27.01	28.75	29.22	28.41
	Al_2O_3	17.46	17.77	23.80	24.21	23.67
	TiO_2	bd	bd	bd	bd	bd
	FeO	24.83	25.27	4.21	4.00	3.92
	MnO	0.25	0.30	0.09	0.12	0.17
	MgO	15.84	15.46	27.32	27.51	27.06
	CaO	0.16	0.16	0.12	bd	0.05
	Na_2O	bd	0.05	bd	bd	0.02
	K_2O	0.04	bd	bd	bd	bd
	H_2O	11.14	11.14	12.33	12.49	12.21
Total excl. H_2O		85.75	85.97	84.17	85.10	83.32
Total incl. H_2O		96.88	97.11	96.50	97.59	95.53
molecular proportions of oxides	SiO_2	0.45	0.45	0.48	0.49	0.47
	Al_2O_3	0.17	0.17	0.23	0.24	0.23
	TiO_2	0.00	0.00	0.00	0.00	0.00
	FeO	0.35	0.35	0.06	0.06	0.05
	MnO	0.00	0.00	0.00	0.00	0.00
	MgO	0.39	0.38	0.68	0.68	0.67
	CaO	0.00	0.00	0.00	0.00	0.00
	Na_2O	0.00	0.00	0.00	0.00	0.00
	K_2O	0.00	0.00	0.00	0.00	0.00
	H_2O	0.62	0.62	0.68	0.69	0.68
atomic proportions of oxygen from each molecule	SiO_2	0.90	0.90	0.96	0.97	0.95
	Al_2O_3	0.51	0.52	0.70	0.71	0.70
	TiO_2	0.00	0.00	0.00	0.00	0.00
	FeO	0.35	0.35	0.06	0.06	0.05
	MnO	0.00	0.00	0.00	0.00	0.00
	MgO	0.39	0.38	0.68	0.68	0.67
	CaO	0.00	0.00	0.00	0.00	0.00
	Na_2O	0.00	0.00	0.00	0.00	0.00
	K_2O	0.00	0.00	0.00	0.00	0.00
	H_2O	0.62	0.62	0.68	0.69	0.68
	Total	2.16	2.16	2.39	2.43	2.37
Multiplying factor		6.47	6.47	5.85	5.77	5.90
Number of anions based on 14 oxygen atoms (O, OH)	SiO_2	5.85	5.81	5.59	5.61	5.58
	Al_2O_3	3.33	3.38	4.09	4.11	4.11
	TiO_2	0.00	0.00	0.00	0.00	0.00
	FeO	2.24	2.28	0.34	0.32	0.32
	MnO	0.02	0.03	0.01	0.01	0.01
	MgO	2.54	2.48	3.96	3.94	3.96
	CaO	0.02	0.01	0.00	0.01	0.01
	Na_2O	0.00	0.01	0.00	0.00	0.00
	K_2O	0.00	0.00	0.00	0.00	0.00
H_2O		4.00	4.00	4.00	4.00	4.00
Number of cations in the formula (i.e.corres-ponding to 14 O, OH)	Si^{4+}	2.93	2.91	2.80	2.81	2.79
	Al^{3+} (total)	2.22	2.26	2.73	2.74	2.74
	Ti^{4+}	0.00	0.00	0.00	0.00	0.00
	Fe^{2+}	2.24	2.28	0.34	0.32	0.32
	Mn^{2+}	0.02	0.03	0.01	0.01	0.01
	Mg^{2+}	2.54	2.48	3.96	3.94	3.96
	Ca^{2+}	0.02	0.01	0.00	0.01	0.01
	Na^{+}	0.00	0.01	0.00	0.00	0.00
	K^{+}	0.01	0.00	0.00	0.00	0.00
Total oct. 2+	Mg+Fe+Mn	4.80	4.78	4.31	4.27	4.30
Al tetrahedral	Al^{3+}	1.07	1.09	1.20	1.19	1.21
Al octahedral	Al^{3+}	1.14	1.16	1.53	1.55	1.53
Total tet.	Si, Al	4.00	4.00	4.00	4.00	4.00
Total oct. 2+	Al,Mg,Fe,Mn	5.92	5.92	5.83	5.81	5.82
Octahedral vacancy		0.08	0.08	0.17	0.19	0.18
Total OH	OH	8.00	8.00	8.00	8.00	8.00
Total O	O	18.00	18.00	18.00	18.00	18.00

Table B3(ii). Formulae calculations for chlorite (contd.).

analysis reference		190802-1#17	190802-1#18	190802-1#19	190802-1#21	190802-1#22	190802-1#23	190802-2#16
sample number		01BT054	01BT054	01BT054	907	907	907	01BT002a
wt% oxides	SiO_2	45.88	46.00	44.90	46.02	44.28	45.48	46.04
	Al_2O_3	34.64	34.64	35.18	33.81	31.68	33.53	35.16
	TiO_2	bd	bd	bd	bd	bd	bd	bd
	FeO	0.17	0.14	0.19	0.43	0.62	0.51	0.16
	MnO	bd	bd	bd	bd	bd	0.06	bd
	MgO	0.86	0.72	0.77	1.27	1.25	1.34	0.74
	CaO	bd	0.05	bd	0.11	0.54	0.12	0.08
	Na_2O	1.20	1.40	1.04	0.49	0.44	0.47	1.12
	K_2O	8.68	8.55	9.11	9.50	8.87	9.80	8.86
	H_2O	4.39	4.40	4.36	4.38	4.19	4.35	4.42
Total excl. H_2O		91.42	91.49	91.18	91.63	87.67	91.31	92.16
Total incl. H_2O		95.82	95.88	95.55	96.01	91.86	95.65	96.59
molecular proportions of oxides	SiO_2	0.76	0.77	0.75	0.77	0.74	0.76	0.77
	Al_2O_3	0.34	0.34	0.35	0.33	0.31	0.33	0.34
	TiO_2	0.00	0.00	0.00	0.00	0.00	0.00	0.00
	FeO	0.00	0.00	0.00	0.01	0.01	0.01	0.00
	MnO	0.00	0.00	0.00	0.00	0.00	0.00	0.00
	MgO	0.02	0.02	0.02	0.03	0.03	0.03	0.02
	CaO	0.00	0.00	0.00	0.00	0.01	0.00	0.00
	Na_2O	0.02	0.02	0.02	0.01	0.01	0.01	0.02
	K_2O	0.09	0.09	0.10	0.10	0.09	0.10	0.09
	H_2O	0.24	0.24	0.24	0.24	0.23	0.24	0.25
atomic proportions of oxygen from each molecule	SiO_2	1.53	1.53	1.49	1.53	1.47	1.51	1.53
	Al_2O_3	1.02	1.02	1.04	0.99	0.93	0.99	1.03
	TiO_2	0.00	0.00	0.00	0.00	0.00	0.00	0.00
	FeO	0.00	0.00	0.00	0.01	0.01	0.01	0.00
	MnO	0.00	0.00	0.00	0.00	0.00	0.00	0.00
	MgO	0.02	0.02	0.02	0.03	0.03	0.03	0.02
	CaO	0.00	0.00	0.00	0.00	0.01	0.00	0.00
	Na_2O	0.02	0.02	0.02	0.01	0.01	0.01	0.02
	K_2O	0.09	0.09	0.10	0.10	0.09	0.10	0.09
	H_2O	0.24	0.24	0.24	0.24	0.23	0.24	0.25
	Total	2.68	2.68	2.66	2.67	2.56	2.66	2.70
Multiplying factor		8.20	8.20	8.26	8.22	8.61	8.29	8.14
Number of anions based on 11 oxygen atoms (O, OH)	SiO_2	12.53	12.55	12.34	12.60	12.68	12.54	12.48
	Al_2O_3	8.36	8.36	8.55	8.18	8.02	8.18	8.43
	TiO_2	0.00	0.00	0.00	0.00	0.00	0.00	0.00
	FeO	0.02	0.02	0.02	0.05	0.07	0.06	0.02
	MnO	0.00	0.00	0.00	0.00	0.00	0.01	0.00
	MgO	0.17	0.15	0.16	0.26	0.27	0.28	0.15
	CaO	0.00	0.01	0.00	0.02	0.08	0.02	0.01
	Na_2O	0.16	0.19	0.14	0.07	0.06	0.06	0.15
	K_2O	0.76	0.74	0.80	0.83	0.81	0.86	0.77
H_2O		2.00	2.00	2.00	2.00	2.00	2.00	2.00
Number of cations in the formula (i.e.corres-ponding to 11 O, OH)	Si^{4+}	6.26	6.27	6.17	6.30	6.34	6.27	6.24
	Al total	5.58	5.57	5.70	5.46	5.35	5.45	5.62
	Ti^{4+}	0.00	0.00	0.00	0.00	0.00	0.00	0.00
	Fe^{2+}	0.02	0.02	0.02	0.05	0.07	0.06	0.02
	Mn^{2+}	0.00	0.00	0.00	0.00	0.00	0.01	0.00
	Mg^{2+}	0.17	0.15	0.16	0.26	0.27	0.28	0.15
	Ca^{2+}	0.00	0.01	0.00	0.02	0.08	0.02	0.01
	Na^{+}	0.32	0.37	0.28	0.13	0.12	0.12	0.29
	K^{+}	1.51	1.49	1.60	1.66	1.62	1.72	1.53
Al tetrahedral	Al^{3+}	1.74	1.73	1.83	1.70	1.66	1.73	1.76
Al octahedral	Al^{3+}	3.84	3.84	3.87	3.75	3.69	3.72	3.86
Total tet.	Si, Al	8.00	8.00	8.00	8.00	8.00	8.00	8.00
Total oct.	Al,Mg,Fe,Mn	4.03	4.01	4.05	4.06	4.03	4.06	4.03
Total K	K, Na, Ca	1.83	1.86	1.87	1.81	1.82	1.87	1.84
Total OH		2.00	2.00	2.00	2.00	2.00	2.00	2.00

Table B3(iii). Formulae calculations for muscovite.

analysis reference		190802-2#17	190802-2#18	200802-1#5	200802-1#6	200802-1#7	200802-1#8	200802-2#1
sample number		01BT002a	01BT002a	906	906	906	906	01BT070
wt% oxides	SiO_2	45.68	45.89	44.10	45.28	45.09	44.58	47.54
	Al_2O_3	35.06	34.98	32.44	32.39	32.46	32.72	33.58
	TiO_2	0.07	bd	bd	bd	bd	bd	bd
	FeO	0.22	0.05	0.22	0.09	0.19	0.15	0.36
	MnO	bd	bd	bd	0.06	bd	bd	bd
	MgO	0.70	0.71	1.24	1.40	1.26	1.19	1.03
	CaO	0.08	0.11	bd	bd	0.05	bd	0.15
	Na_2O	1.08	1.28	0.41	0.35	0.35	0.37	0.86
	K_2O	8.97	8.70	9.50	9.99	9.50	9.62	8.83
	H_2O	4.40	4.41	4.20	4.27	4.25	4.24	4.44
Total excl. H_2O		91.87	91.74	87.89	89.56	88.88	88.61	92.34
Total incl. H_2O		96.27	96.14	92.09	93.84	93.14	92.85	96.78
molecular proportions of oxides	SiO_2	0.76	0.76	0.73	0.75	0.75	0.74	0.79
	Al_2O_3	0.34	0.34	0.32	0.32	0.32	0.32	0.33
	TiO_2	0.00	0.00	0.00	0.00	0.00	0.00	0.00
	FeO	0.00	0.00	0.00	0.00	0.00	0.00	0.00
	MnO	0.00	0.00	0.00	0.00	0.00	0.00	0.00
	MgO	0.02	0.02	0.03	0.03	0.03	0.03	0.03
	CaO	0.00	0.00	0.00	0.00	0.00	0.00	0.00
	Na_2O	0.02	002	0.01	0.01	0.01	0.01	0.01
	K_2O	0.10	0.09	0.10	0.11	0.10	0.10	0.09
	H_2O	0.24	0.24	0.23	0.24	0.24	0.24	0.25
atomic proportions of oxygen from each molecule	SiO_2	1.52	1.53	1.47	1.51	1.50	1.48	1.58
	Al_2O_3	1.03	1.03	0.95	0.95	0.96	0.96	0.99
	TiO_2	0.00	0.00	0.00	0.00	0.00	0.00	0.00
	FeO	0.00	0.00	0.00	0.00	0.00	0.00	0.00
	MnO	0.00	0.00	0.00	0.00	0.00	0.00	0.00
	MgO	0.02	0.02	0.03	0.03	0.03	0.03	0.03
	CaO	0.00	0.00	0.00	0.00	0.00	0.00	0.00
	Na_2O	0.02	0.02	0.01	0.01	0.01	0.01	0.01
	K_2O	0.10	0.09	0.10	0.11	0.10	0.10	0.09
	H_2O	0.24	0.24	0.23	0.24	0.24	0.24	0.25
	Total	2.69	2.69	2.56	2.61	2.60	2.59	2.71
Multiplying factor		8.18	8.18	8.58	8.43	8.47	8.51	8.11
Number of anions based on 11 oxygen atoms (O, OH)	SiO_2	12.44	12.49	12.60	12.71	12.71	12.62	12.84
	Al_2O_3	8.44	8.42	8.19	8.04	8.09	8.19	8.02
	TiO_2	0.01	0.00	0.00	0.00	0.00	0.00	0.00
	FeO	0.03	0.01	0.03	0.01	0.02	0.02	0.04
	MnO	0.00	0.00	0.00	0.01	0.00	0.00	0.00
	MgO	0.14	0.14	0.26	0.29	0.26	0.25	0.21
	CaO	0.01	0.02	0.00	0.00	0.01	0.00	0.02
	Na_2O	0.14	0.17	0.06	0.05	0.05	0.05	0.11
	K_2O	0.78	0.76	0.87	0.89	0.85	0.87	0.76
H_2O		2.00	2.00	2.00	2.00	2.00	2.00	2.00
Number of cations in the formula (i.e.corres-ponding to 11 O, OH)	Si^{4+}	6.22	6.25	6.30	6.35	6.36	6.31	6.42
	Al total	5.63	5.61	5.46	5.36	5.39	5.46	5.35
	Ti^{4+}	0.01	0.00	0.00	0.00	0.00	0.00	0.00
	Fe^{2+}	0.03	0.01	0.03	0.01	0.02	0.02	0.04
	Mn^{2+}	0.00	0.00	0.00	0.01	0.00	0.00	0.00
	Mg^{2+}	0.14	0.14	0.26	0.29	0.26	0.25	0.21
	Ca^{2+}	0.01	0.02	0.00	0.00	0.01	0.00	0.02
	Na^{+}	0.29	0.34	0.11	0.09	0.10	0.10	0.22
	K^{+}	1.56	1.51	1.73	1.79	1.71	1.74	1.52
Al tetrahedral	Al^{3+}	1.78	1.75	1.70	1.65	1.64	1.69	1.58
Al octahedral	Al^{3+}	3.85	3.86	3.76	3.71	3.75	3.77	3.77
Total tet.	Si, Al	8.00	8.00	8.00	8.00	8.00	8.00	8.00
Total oct.	Al,Mg,Fe,Mn	4.02	4.01	4.05	4.02	4.04	4.04	4.01
Total K	K, Na, Ca	1.86	1.87	1.84	1.88	1.81	1.84	1.77
Total OH		2.00	2.00	2.00	2.00	2.00	2.00	2.00

Table B3(iii). Formulae calculations muscovite (contd.).

analysis reference		200802-2#2	200802-2#5	200802-2#6	200802-2#7	200802-2#8	200802-2#9	200802-2#10
sample number		01BT070	01BT070	01BT070	01BT070	01BT070	01BT138	01BT138
wt% oxides	SiO_2	47.88	47.24	46.60	46.40	47.38	44.07	42.29
	Al_2O_3	33.50	33.38	33.93	34.25	33.93	33.42	32.15
	TiO_2	bd	bd	bd	bd	bd	bd	bd
	FeO	0.26	0.28	0.09	0.07	0.12	0.68	0.66
	MnO	bd	bd	bd	bd	bd	bd	bd
	MgO	1.14	1.07	0.99	0.94	0.98	0.45	0.36
	CaO	0.09	0.12	bd	bd	0.08	0.06	0.18
	Na_2O	0.79	0.89	0.74	0.75	0.89	0.81	0.83
	K_2O	9.14	8.88	9.55	9.36	8.64	8.57	8.07
	H_2O	4.46	4.41	4.40	4.40	4.44	4.22	4.05
Total excl. H_2O		92.80	91.85	91.89	91.77	92.02	88.06	84.53
Total incl. H_2O		97.26	96.26	96.29	96.17	96.46	92.27	88.58
molecular proportions of oxides	SiO_2	0.80	0.79	0.78	0.77	0.79	0.73	0.70
	Al_2O_3	0.33	0.33	0.33	0.34	0.33	0.33	0.32
	TiO_2	0.00	0.00	0.00	0.00	0.00	0.00	0.00
	FeO	0.00	0.00	0.00	0.00	0.00	0.01	0.01
	MnO	0.00	0.00	0.00	0.00	0.00	0.00	0.00
	MgO	0.03	0.03	0.02	0.02	0.02	0.01	0.01
	CaO	0.00	0.00	0.00	0.00	0.00	0.00	0.00
	Na_2O	0.01	0.01	0.01	0.01	0.01	0.01	0.01
	K_2O	0.10	0.09	0.10	0.10	0.09	0.09	0.09
	H_2O	0.25	0.25	0.24	0.24	0.25	0.23	0.22
atomic proportions of oxygen from each molecule	SiO_2	1.59	1.57	1.55	1.54	1.58	1.47	1.41
	Al_2O_3	0.99	0.98	1.00	1.01	1.00	0.98	0.95
	TiO_2	0.00	0.00	0.00	0.00	0.00	0.00	0.00
	FeO	0.00	0.00	0.00	0.00	0.00	0.01	0.01
	MnO	0.00	0.00	0.00	0.00	0.00	0.00	0.00
	MgO	0.03	0.03	0.02	0.02	0.02	0.01	0.01
	CaO	0.00	0.00	0.00	0.00	0.00	0.00	0.00
	Na_2O	0.01	0.01	0.01	0.01	0.01	0.01	0.01
	K_2O	0.10	0.09	0.10	0.10	0.09	0.09	0.09
	H_2O	0.25	0.25	0.24	0.24	0.25	0.23	0.22
	Total	2.72	2.70	2.69	2.69	2.71	2.58	2.47
Multiplying factor		8.08	8.16	8.18	8.18	8.12	8.54	8.89
Number of anions based on 11 oxygen atoms (O, OH)	SiO_2	12.88	12.83	12.69	12.64	12.81	12.53	12.52
	Al_2O_3	7.97	8.02	8.17	8.25	8.11	8.40	8.41
	TiO_2	0.00	0.00	0.00	0.00	0.00	0.00	0.00
	FeO	0.03	0.03	0.01	0.01	0.01	0.08	0.08
	MnO	0.00	0.00	0.00	0.00	0.00	0.00	0.00
	MgO	0.23	0.22	0.20	0.19	0.20	0.10	0.08
	CaO	0.01	0.02	0.00	0.00	0.01	0.01	0.03
	Na_2O	0.10	0.12	0.10	0.10	0.12	0.11	0.12
	K_2O	0.78	0.77	0.83	0.81	0.75	0.78	0.76
H_2O		2.00	2.00	2.00	2.00	2.00	2.00	2.00
Number of cations in the formula (i.e.corres-ponding to 11 O, OH)	Si^{4+}	6.44	6.42	6.35	6.32	6.40	6.26	6.26
	Al total	5.31	5.34	5.45	5.50	5.41	5.60	5.61
	Ti^{4+}	0.00	0.00	0.00	0.00	0.00	0.00	0.00
	Fe^{2+}	0.03	0.03	0.01	0.01	0.01	0.08	0.08
	Mn^{2+}	0.00	0.00	0.00	0.00	0.00	0.00	0.00
	Mg^{2+}	0.23	0.22	0.20	0.19	0.20	0.10	0.08
	Ca^{2+}	0.01	0.02	0.00	0.00	0.01	0.01	0.03
	Na^{+}	0.21	0.23	0.19	0.20	0.23	0.22	0.24
	K^{+}	1.57	1.54	1.66	1.63	1.49	1.55	1.52
Al tetrahedral	Al^{3+}	1.56	1.58	1.65	1.68	1.60	1.74	1.74
Al octahedral	Al^{3+}	3.75	3.76	3.79	3.82	3.81	3.86	3.87
Total tet.	Si, Al	8.00	8.00	8.00	8.00	8.00	8.00	8.00
Total oct.	Al,Mg,Fe,Mn	4.01	4.01	4.00	4.02	4.02	4.04	4.03
Total K	K, Na, Ca	1.79	1.79	1.85	1.82	1.73	1.79	1.79
Total OH		2.00	2.00	2.00	2.00	2.00	2.00	2.00

Table B3(iii). Formulae calculations muscovite (contd.).

analysis reference		200802-2#11	200802-2#17	200802-2#18	200802-2#19	200802-4#10	200802-4#11	200802-4#12
sample number		01BT138	01BT226d	01BT226d	01BT226d	01BT052	01BT052	01BT052
wt% oxides	SiO_2	44.12	45.31	45.30	44.90	45.05	45.14	45.36
	Al_2O_3	33.19	36.41	35.56	36.03	34.76	34.88	35.07
	TiO_2	bd	bd	bd	bd	bd	bd	bd
	FeO	0.59	0.11	0.20	0.10	0.27	0.24	0.20
	MnO	bd	0.05	bd	bd	bd	bd	bd
	MgO	0.52	0.13	0.35	0.26	0.72	0.73	0.64
	CaO	0.05	bd	0.11	bd	0.06	bd	bd
	Na_2O	0.70	0.69	0.83	0.85	0.68	0.84	1.48
	K_2O	8.72	10.16	9.42	9.73	9.79	9.40	8.21
	H_2O	4.21	4.43	4.39	4.39	4.36	4.36	4.38
Total excl. H_2O		87.90	92.85	91.76	91.86	91.31	91.23	90.95
Total incl. H_2O		92.11	97.28	96.15	96.25	95.67	95.59	95.33
molecular proportions of oxides	SiO_2	0.73	0.75	0.75	0.75	0.75	0.75	0.75
	Al_2O_3	0.33	0.36	0.35	0.35	0.34	0.34	0.34
	TiO_2	0.00	0.00	0.00	0.00	0.00	0.00	0.00
	FeO	0.01	0.00	0.00	0.00	0.00	0.00	0.00
	MnO	0.00	0.00	0.00	0.00	0.00	0.00	0.00
	MgO	0.01	0.00	0.01	0.01	0.02	0.02	0.02
	CaO	0.00	0.00	0.00	0.00	0.00	0.00	0.00
	Na_2O	0.01	0.01	0.01	0.01	0.01	0.01	0.02
	K_2O	0.09	0.11	0.10	0.10	0.10	0.10	0.09
	H_2O	0.23	0.25	0.24	0.24	0.24	0.24	0.24
atomic proportions of oxygen from each molecule	SiO_2	1.47	1.51	1.51	1.49	1.50	1.50	1.51
	Al_2O_3	0.98	1.07	1.05	1.06	1.02	1.03	1.03
	TiO_2	0.00	0.00	0.00	0.00	0.00	0.00	0.00
	FeO	0.01	0.00	0.00	0.00	0.00	0.00	0.00
	MnO	0.00	0.00	0.00	0.00	0.00	0.00	0.00
	MgO	0.01	0.00	0.01	0.01	0.02	0.02	0.02
	CaO	0.00	0.00	0.00	0.00	0.00	0.00	0.00
	Na_2O	0.01	0.01	0.01	0.01	0.01	0.01	0.02
	K_2O	0.09	0.11	0.10	0.10	0.10	0.10	0.09
	H_2O	0.23	0.25	0.24	0.24	0.24	0.24	0.24
	Total	2.57	2.70	2.68	2.68	2.66	2.66	2.67
Multiplying factor		8.56	8.14	8.21	8.21	8.27	8.26	8.24
Number of anions based on 11 oxygen atoms (O, OH)	SiO_2	12.56	12.27	12.37	12.27	12.40	12.41	12.43
	Al_2O_3	8.36	8.72	8.59	8.71	8.46	8.48	8.50
	TiO_2	0.00	0.00	0.00	0.00	0.00	0.00	0.00
	FeO	0.07	0.01	0.02	0.01	0.03	0.03	0.02
	MnO	0.00	0.01	0.00	0.00	0.00	0.00	0.00
	MgO	0.11	0.03	0.07	0.05	0.15	0.15	0.13
	CaO	0.01	0.00	0.02	0.00	0.01	0.00	0.00
	Na_2O	0.10	0.09	0.11	0.11	0.09	0.11	0.20
	K_2O	0.79	0.88	0.82	0.85	0.86	0.82	0.72
H_2O		2.00	2.00	2.00	2.00	2.00	2.00	2.00
Number of cations in the formula (i.e.corres-ponding to 11 O, OH)	Si^{4+}	6.28	6.13	6.19	6.13	6.20	6.20	6.22
	Al total	5.57	5.81	5.72	5.80	5.64	5.65	5.67
	Ti^{4+}	0.00	0.00	0.00	0.00	0.00	0.00	0.00
	Fe^{2+}	0.07	0.01	0.02	0.01	0.03	0.03	0.02
	Mn^{2+}	0.00	0.01	0.00	0.00	0.00	0.00	0.00
	Mg^{2+}	0.11	0.03	0.07	0.05	0.15	0.15	0.13
	Ca^{2+}	0.01	0.00	0.02	0.00	0.01	0.00	0.00
	Na^{+}	0.19	0.18	0.22	0.23	0.18	0.22	0.39
	K^{+}	1.58	1.76	1.64	1.70	1.72	1.65	1.44
Al tetrahedral	Al^{3+}	1.72	1.87	1.81	1.87	1.80	1.80	1.78
Al octahedral	Al^{3+}	3.85	3.95	3.91	3.94	3.84	3.86	3.88
Total tet.	Si, Al	8.00	8.00	8.00	8.00	8.00	8.00	8.00
Total oct.	Al,Mg,Fe,Mn	4.04	3.99	4.01	4.00	4.02	4.03	4.04
Total K	K, Na, Ca	1.79	1.94	1.88	1.92	1.91	1.87	1.83
Total OH		2.00	2.00	2.00	2.00	2.00	2.00	2.00

Table B3(iii). Formulae calculations for muscovite (contd.).

analysis reference		200802-7#32	200802-7#33	200802-7#34	210802-3#2	210802-3#4	210802-3#5	210802-3#6
sample number		01BT162	01BT162	01BT162	00BT18	00BT18	00BT18	00BT18
wt% oxides	SiO_2	45.08	45.45	45.40	45.60	49.40	50.43	49.33
	Al_2O_3	34.86	34.36	35.05	28.23	27.35	26.37	26.18
	TiO_2	bd	bd	bd	bd	0.10	bd	bd
	FeO	0.20	0.36	0.21	5.19	4.05	3.93	4.06
	MnO	bd	bd	0.04	0.10	0.05	bd	0.07
	MgO	0.64	0.70	0.65	4.43	2.25	2.59	2.59
	CaO	0.04	0.07	0.04	0.04	0.12	0.08	0.20
	Na_2O	0.94	0.78	0.89	0.91	0.23	0.29	0.16
	K_2O	9.11	9.32	9.13	9.60	10.90	10.62	10.69
	H_2O	4.35	4.35	4.38	4.34	4.40	4.41	4.35
Total excl. H_2O		90.86	91.04	91.40	94.10	94.43	94.31	93.29
Total incl. H_2O		95.21	95.39	95.78	98.44	98.83	98.72	97.63
molecular proportions of oxides	SiO_2	0.75	0.76	0.76	0.76	0.82	0.84	0.82
	Al_2O_3	0.34	0.34	0.34	0.28	0.27	0.26	0.26
	TiO_2	0.00	0.00	0.00	0.00	0.00	0.00	0.00
	FeO	0.00	0.00	0.00	0.07	0.06	0.05	0.06
	MnO	0.00	0.00	0.00	0.00	0.00	0.00	0.00
	MgO	0.02	0.02	0.02	0.11	0.06	0.06	0.06
	CaO	0.00	0.00	0.00	0.00	0.00	0.00	0.00
	Na_2O	0.02	0.01	0.01	0.01	0.00	0.00	0.00
	K_2O	0.10	0.10	0.10	0.10	0.12	0.11	0.11
	H_2O	0.24	0.24	0.24	0.24	0.24	0.24	0.24
atomic proportions of oxygen from each molecule	SiO_2	1.50	1.51	1.51	1.52	1.64	1.68	1.64
	Al_2O_3	1.03	1.01	1.03	0.83	0.80	0.78	0.77
	TiO_2	0.00	0.00	0.00	0.00	0.00	0.00	0.00
	FeO	0.00	0.00	0.00	0.07	0.06	0.05	0.06
	MnO	0.00	0.00	0.00	0.00	0.00	0.00	0.00
	MgO	0.02	0.02	0.02	0.11	0.06	0.06	0.06
	CaO	0.00	0.00	0.00	0.00	0.00	0.00	0.00
	Na_2O	0.02	0.01	0.01	0.01	0.00	0.00	0.00
	K_2O	0.10	0.10	0.10	0.10	0.12	0.11	0.11
	H_2O	0.24	0.24	0.24	0.24	0.24	0.24	0.24
	Total	2.66	2.66	2.67	2.65	2.69	2.69	2.65
Multiplying factor		8.28	8.27	8.23	8.30	8.19	8.17	8.29
Number of anions based on 11 oxygen atoms (O, OH)	SiO_2	12.42	12.51	12.43	12.60	13.47	13.72	13.61
	Al_2O_3	8.49	8.37	8.49	6.90	6.59	6.34	6.39
	TiO_2	0.00	0.00	0.00	0.00	0.02	0.00	0.00
	FeO	0.02	0.04	0.02	0.60	0.46	0.45	0.47
	MnO	0.00	0.00	0.01	0.01	0.01	0.00	0.01
	MgO	0.13	0.14	0.13	0.91	0.46	0.53	0.53
	CaO	0.01	0.01	0.01	0.01	0.02	0.01	0.03
	Na_2O	0.13	0.10	0.12	0.12	0.03	0.04	0.02
	K_2O	0.80	0.82	0.80	0.85	0.95	0.92	0.94
H_2O		2.00	2.00	2.00	2.00	2.00	2.00	2.00
Number of cations in the formula (i.e.corres-ponding to 11 O, OH)	Si^{4+}	6.21	6.26	6.22	6.30	6.73	6.86	6.81
	Al total	5.66	5.58	5.66	4.60	4.39	4.23	4.26
	Ti^{4+}	0.00	0.00	0.00	0.00	0.01	0.00	0.00
	Fe^{2+}	0.02	0.04	0.02	0.60	0.46	0.45	0.47
	Mn^{2+}	0.00	0.00	0.01	0.01	0.01	0.00	0.01
	Mg^{2+}	0.13	0.14	0.13	0.91	0.46	0.53	0.53
	Ca^{2+}	0.01	0.01	0.01	0.01	0.02	0.01	0.03
	Na^{+}	0.25	0.21	0.24	0.24	0.06	0.08	0.04
	K^{+}	1.60	1.64	1.59	1.69	1.90	1.84	1.88
Al tetrahedral	Al^{3+}	1.79	1.74	1.78	1.70	1.27	1.14	1.19
Al octahedral	Al^{3+}	3.87	3.84	3.87	2.90	3.13	3.09	3.06
Total tet.	Si, Al	8.00	8.00	8.00	8.00	8.00	8.00	8.00
Total oct.	Al,Mg,Fe,Mn	4.03	4.02	4.03	4.42	4.06	4.06	4.07
Total K	K, Na, Ca	1.86	1.86	1.84	1.94	1.97	1.93	1.95
Total OH		2.00	2.00	2.00	2.00	2.00	2.00	2.00

Table B3(iii). Formulae calculations for muscovite (contd.).

analysis reference		210802-3#7	210802-3#8
sample number		00BT18	00BT18
wt% oxides	SiO_2	47.46	50.00
	Al_2O_3	26.69	26.69
	TiO_2	bd	bd
	FeO	4.81	4.31
	MnO	0.05	bd
	MgO	3.82	2.44
	CaO	0.24	bd
	Na_2O	0.26	0.13
	K_2O	9.91	10.70
	H_2O	4.33	4.40
Total excl. H_2O		93.24	94.27
Total incl. H_2O		97.56	98.67
molecular proportions of oxides	SiO_2	0.79	0.83
	Al_2O_3	0.26	0.26
	TiO_2	0.00	0.00
	FeO	0.07	0.06
	MnO	0.00	0.00
	MgO	0.09	0.06
	CaO	0.00	0.00
	Na_2O	0.00	0.00
	K_2O	0.11	0.11
	H_2O	0.24	0.24
atomic proportions of oxygen from each molecule	SiO_2	1.58	1.66
	Al_2O_3	0.79	0.79
	TiO_2	0.00	0.00
	FeO	0.07	0.06
	MnO	0.00	0.00
	MgO	0.09	0.06
	CaO	0.00	0.00
	Na_2O	0.00	0.00
	K_2O	0.11	0.11
	H_2O	0.24	0.24
	Total	2.64	2.69
Multiplying factor		8.33	8.19
Number of anions based on 11 oxygen atoms (O, OH)	SiO_2	13.16	13.63
	Al_2O_3	6.54	6.43
	TiO_2	0.00	0.00
	FeO	0.56	0.49
	MnO	0.01	0.00
	MgO	0.79	0.49
	CaO	0.04	0.00
	Na_2O	0.04	0.02
	K_2O	0.88	0.93
H_2O		2.00	2.00
Number of cations in the formula (i.e.corres-ponding to 11 O, OH)	Si^{4+}	6.58	6.82
	Al total	4.36	4.29
	Ti^{4+}	0.00	0.00
	Fe^{2+}	0.56	0.49
	Mn^{2+}	0.01	0.00
	Mg^{2+}	0.79	0.49
	Ca^{2+}	0.04	0.00
	Na^{+}	0.07	0.03
	K^{+}	1.75	1.86
Al tetrahedral	Al^{3+}	1.42	1.18
Al octahedral	Al^{3+}	2.94	3.11
Total tet.	Si, Al	8.00	8.00
Total oct.	Al,Mg,Fe,Mn	4.29	4.09
Total K	K, Na, Ca	1.86	1.90
Total OH		2.00	2.00

Table B3(iii). Formulae calculations for muscovite (contd.).

analysis reference		200802-7#1	200802-7#2	200802-7#3	200802-7#4	200802-1#10	200802-1#11
sample number		01BT082a	01BT082a	01BT082a	01BT082a	01BT135b	01BT135b
wt% oxides	SiO_2	37.32	36.61	36.93	36.96	37.38	37.31
	Al_2O_3	25.96	25.49	25.75	25.88	26.60	26.07
	TiO_2	bd	bd	bd	bd	bd	bd
	FeO	1.08	1.11	1.04	1.27	0.70	0.63
	MnO	0.31	0.43	0.38	0.32	0.18	0.25
	MgO	3.34	3.84	3.71	3.39	3.43	3.23
	CaO	23.33	23.13	23.36	23.36	23.54	23.22
	Na_2O	bd	bd	bd	bd	bd	bd
	K_2O	bd	0.11	bd	bd	bd	bd
	H_2O	6.32	6.26	6.29	6.31	6.35	6.27
Total excl. H_2O		91.46	90.77	91.20	91.19	91.97	90.76
Total incl. H_2O		97.79	97.03	97.50	97.49	98.31	97.02
molecular proportions of oxides	SiO_2	0.62	0.61	0.61	0.62	0.62	0.62
	Al_2O_3	0.25	0.25	0.25	0.25	0.26	0.26
	TiO_2	0.00	0.00	0.00	0.00	0.00	0.00
	FeO	0.02	0.02	0.01	0.02	0.01	0.01
	MnO	0.00	0.01	0.01	0.00	0.00	0.00
	MgO	0.08	0.10	0.09	0.08	0.09	0.08
	CaO	0.42	0.41	0.42	0.42	0.42	0.41
	Na_2O	0.00	0.00	0.00	0.00	0.00	0.00
	K_2O	0.00	0.00	0.00	0.00	0.00	0.00
	H_2O	0.35	0.35	0.35	0.35	0.35	0.35
atomic proportions of oxygen from each molecule	SiO_2	1.24	1.22	1.23	1.23	1.24	1.24
	Al_2O_3	0.76	0.75	0.76	0.76	0.78	0.77
	TiO_2	0.00	0.00	0.00	0.00	0.00	0.00
	FeO	0.05	0.05	0.04	0.05	0.03	0.03
	MnO	0.00	0.01	0.01	0.00	0.00	0.00
	MgO	0.08	0.10	0.09	0.08	0.09	0.08
	CaO	0.42	0.41	0.42	0.42	0.42	0.41
	Na_2O	0.00	0.00	0.00	0.00	0.00	0.00
	K_2O	0.00	0.00	0.00	0.00	0.00	0.00
	H_2O	0.35	0.35	0.35	0.35	0.35	0.35
	Total	2.56	2.53	2.54	2.55	2.57	2.53
Multiplying factor		4.99	5.04	5.01	5.00	4.97	5.03
Number of anions based on 12.75 oxygen atoms (O, OH)	SiO_2	6.19	6.14	6.16	6.15	6.18	6.25
	Al_2O_3	3.81	3.78	3.80	3.81	3.89	3.86
	TiO_2	0.01	0.00	0.00	0.00	0.01	0.00
	FeO	0.22	0.23	0.22	0.27	0.14	0.13
	MnO	0.02	0.03	0.03	0.02	0.01	0.02
	MgO	0.41	0.48	0.46	0.42	0.42	0.40
	CaO	2.07	2.08	2.09	2.08	2.09	2.08
	Na_2O	0.00	0.01	0.00	0.00	0.00	0.00
	K_2O	0.00	0.01	0.00	0.00	0.00	0.00
H_2O		1.75	1.75	1.75	1.75	1.75	1.75
Number of cations in the formula (corresponding to 12.75 O, OH)	Si^{4+}	3.10	3.07	3.08	3.08	3.09	3.12
	Al total	2.54	2.52	2.53	2.54	2.59	2.57
	Ti^{4+}	bd	bd	bd	bd	bd	bd
	Fe^{2+}	0.15	0.16	0.15	0.18	0.10	0.09
	Mn^{2+}	0.02	0.03	0.03	0.02	0.01	0.02
	Mg^{2+}	0.41	0.48	0.46	0.42	0.42	0.40
	Ca^{2+}	2.07	2.08	2.09	2.08	2.09	2.08
	Na^{+}	bd	bd	bd	bd	bd	bd
	K^{+}	bd	0.01	bd	bd	bd	bd
Total O		14.00	14.00	14.00	14.00	14.00	14.00
total OH		3.50	3.50	3.50	3.50	3.50	3.50
Total H_2O		0.50	0.50	0.50	0.50	0.50	0.50

Table B3(iv). Formulae calculations for pumpellyite.

analysis reference		190802-1/#26	190802-1/#27	190802-2/#29	190802-2/#30	190802-2/#31	200802-2/#13	200802-2/#14
sample number		907	907	01BT061	01BT061	01BT062	01BT138	01BT138
wt% oxides	SiO_2	45.57	46.21	45.43	45.54	45.36	46.10	46.04
	Al_2O_3	23.56	23.84	23.94	23.85	24.38	24.00	24.10
	TiO_2	bd	bd	bd	bd	bd	bd	bd
	FeO	bd	bd	bd	bd	0.07	0.09	bd
	MnO	bd	bd	bd	bd	bd	bd	bd
	MgO	bd	bd	0.08	0.05	bd	bd	bd
	CaO	9.96	9.95	10.01	9.92	10.31	10.16	10.23
	Na_2O	0.24	0.24	0.15	0.20	0.07	0.05	0.04
	K_2O	0.04	0.07	0.04	0.08	0.04	bd	bd
	H_2O	12.93	13.09	12.97	12.97	13.06	13.11	13.10
Total excl. H_2O		79.36	80.31	79.65	79.63	80.22	80.40	80.40
Total incl. H_2O		92.29	93.39	92.62	92.60	93.28	93.51	93.50
molecular proportions of oxides	SiO_2	0.76	0.77	0.76	0.76	0.75	0.77	0.77
	Al_2O_3	0.23	0.23	0.23	0.23	0.24	0.24	0.24
	TiO_2	0.00	0.00	0.00	0.00	0.00	0.00	0.00
	FeO	0.00	0.00	0.00	0.00	0.00	0.00	0.00
	MnO	0.00	0.00	0.00	0.00	0.00	0.00	0.00
	MgO	0.00	0.00	0.00	0.00	0.00	0.00	0.00
	CaO	0.18	0.18	0.18	0.18	0.18	0.18	0.18
	Na_2O	0.00	0.00	0.00	0.00	0.00	0.00	0.00
	K_2O	0.00	0.00	0.00	0.00	0.00	0.00	0.00
	H_2O	0.72	0.73	0.72	0.72	0.72	0.73	0.73
atomic proportions of oxygen from each molecule	SiO_2	1.52	1.54	1.51	1.52	1.51	1.53	1.53
	Al_2O_3	0.69	0.70	0.70	0.70	0.72	0.71	0.71
	TiO_2	0.00	0.00	0.00	0.00	0.00	0.00	0.00
	FeO	0.00	0.00	0.00	0.00	0.00	0.00	0.00
	MnO	0.00	0.00	0.00	0.00	0.00	0.00	0.00
	MgO	0.00	0.00	0.00	0.00	0.00	0.00	0.00
	CaO	0.18	0.18	0.18	0.18	0.18	0.18	0.18
	Na_2O	0.00	0.00	0.00	0.00	0.00	0.00	0.00
	K_2O	0.00	0.00	0.00	0.00	0.00	0.00	0.00
	H_2O	0.72	0.73	0.72	0.72	0.72	0.73	0.73
	Total	2.39	2.42	2.40	2.40	2.42	2.43	2.42
Multiplying factor		4.18	4.13	4.17	4.17	4.14	4.12	4.12
Number of anions based on 10 oxygen atoms (O, OH)	SiO_2	6.34	6.35	6.30	6.32	6.25	6.32	6.32
	Al_2O_3	2.90	2.90	2.94	2.92	2.97	2.91	2.92
	TiO_2	0.00	0.00	0.00	0.00	0.00	0.00	0.00
	FeO	0.00	0.00	0.00	0.00	0.01	0.02	0.00
	MnO	0.00	0.00	0.00	0.00	0.00	0.00	0.00
	MgO	0.00	0.00	0.01	0.00	0.00	0.00	0.00
	CaO	0.74	0.73	0.74	0.74	0.76	0.75	0.75
	Na_2O	0.02	0.02	0.01	0.01	0.00	0.00	0.00
	K_2O	0.00	0.00	0.00	0.00	0.00	0.00	0.00
H_2O		3.00	3.00	3.00	3.00	3.00	3.00	3.00
Number of cations in the formula (corresponding to 10 O, OH)	Si^{4+}	3.17	3.18	3.15	3.16	3.13	3.16	3.16
	Al total	1.93	1.93	1.96	1.95	1.98	1.94	1.95
	Ti^{4+}	bd	bd	bd	bd	bd	bd	bd
	Fe^{2+}	bd	bd	bd	bd	0.01	0.01	bd
	Mn^{2+}	bd	bd	bd	bd	bd	bd	bd
	Mg^{2+}	bd	bd	0.01	0.00	bd	bd	bd
	Ca^{2+}	0.74	0.73	0.74	0.74	0.76	0.75	0.75
	Na^{+}	0.03	0.03	0.02	0.03	0.01	0.01	0.01
	K^{+}	0.00	0.01	0.00	0.01	0.00	bd	bd
Total alkali	(K, Na, Ca)	0.78	0.77	0.77	0.77	0.77	0.75	0.76
Total H_2O		3.00	3.00	3.00	3.00	3.00	3.00	3.00
Total O		13.00	13.00	13.00	13.00	13.00	13.00	13.00

Table B3(v). Formulae calculations for scolecite.

analysis reference		200802-2/#15	200802-2/#16	200802-4/#13	200802-4/#14	200802-4/#15
sample number		01BT226d	01BT226d	01BT052	01BT052	01BT052
wt% oxides	SiO_2	46.15	45.93	45.54	45.78	45.76
	Al_2O_3	23.69	23.83	23.74	24.02	23.75
	TiO_2	bd	bd	bd	bd	bd
	FeO	0.10	0.05	0.05	0.08	bd
	MnO	bd	bd	bd	bd	bd
	MgO	bd	bd	bd	0.07	bd
	CaO	10.24	10.24	10.11	10.05	10.12
	Na_2O	0.04	0.05	0.06	0.13	bd
	K_2O	0.04	bd	bd	0.08	bd
	H_2O	13.09	13.05	12.96	13.07	12.98
Total excl. H_2O		80.26	80.09	79.51	80.21	79.63
Total incl. H_2O		93.35	93.14	92.47	93.28	92.61
molecular proportions of oxides	SiO_2	0.77	0.76	0.76	0.76	0.76
	Al_2O_3	0.23	0.23	0.23	0.24	0.23
	TiO_2	0.00	0.00	0.00	0.00	0.00
	FeO	0.00	0.00	0.00	0.00	0.00
	MnO	0.00	0.00	0.00	0.00	0.00
	MgO	0.00	0.00	0.00	0.00	0.00
	CaO	0.18	0.18	0.18	0.18	0.18
	Na_2O	0.00	0.00	0.00	0.00	0.00
	K_2O	0.00	0.00	0.00	0.00	0.00
	H_2O	0.73	0.72	0.72	0.73	0.72
atomic proportions of oxygen from each molecule	SiO_2	1.54	1.53	1.52	1.52	1.52
	Al_2O_3	0.70	0.70	0.70	0.71	0.70
	TiO_2	0.00	0.00	0.00	0.00	0.00
	FeO	0.00	0.00	0.00	0.00	0.00
	MnO	0.00	0.00	0.00	0.00	0.00
	MgO	0.00	0.00	0.00	0.00	0.00
	CaO	0.18	0.18	0.18	0.18	0.18
	Na_2O	0.00	0.00	0.00	0.00	0.00
	K_2O	0.00	0.00	0.00	0.00	0.00
	H_2O	0.73	0.72	0.72	0.73	0.72
	Total	2.42	2.42	2.40	2.42	2.40
Multiplying factor		4.13	4.14	4.17	4.14	4.16
Number of anions based on 10 oxygen atoms (O, OH)	SiO_2	6.34	6.33	6.32	6.30	6.34
	Al_2O_3	2.88	2.90	2.91	2.92	2.91
	TiO_2	0.00	0.00	0.00	0.00	0.00
	FeO	0.02	0.01	0.01	0.01	0.00
	MnO	0.00	0.00	0.00	0.00	0.00
	MgO	0.00	0.00	0.00	0.01	0.00
	CaO	0.75	0.76	0.75	0.74	0.75
	Na_2O	0.00	0.00	0.00	0.01	0.00
	K_2O	0.00	0.00	0.00	0.00	0.00
H_2O		3.00	3.00	3.00	3.00	3.00
Number of cations in the formula (corresponding to 10 O, OH)	Si^{4+}	3.17	3.16	3.16	3.15	3.17
	Al total	1.92	1.94	1.94	1.95	1.94
	Ti^{4+}	bd	bd	bd	bd	bd
	Fe^{2+}	0.01	0.01	0.01	0.01	bd
	Mn^{2+}	bd	bd	bd	bd	bd
	Mg^{2+}	bd	bd	bd	0.01	bd
	Ca^{2+}	0.75	0.76	0.75	0.74	0.75
	Na^{+}	0.01	0.01	0.01	0.02	bd
	K^{+}	0.00	bd	bd	0.01	bd
Total alkali	(K, Na, Ca)	0.76	0.76	0.76	0.77	0.75
Total H_2O		3.00	3.00	3.00	3.00	3.00
Total O		13.00	13.00	13.00	13.00	13.00

Table B3(v). Formulae calculations for scolecite (contd.).

APPENDIX B4 : CHLORITE GEOTHERMOMETRY CALCULATIONS

Four geothermometers have been used where temperature is calculated from chlorite compositions. Equations used are as follows:

1. Cathelineau (1988): $T = 321.98Al^{VI} - 61.92$

2. Jowett (1991): $T = 319[Al^{VI} + 0.1(Fe/(Fe+Mg))] - 69$

3. Kranidiotis & MacLean 1987: $T = 106[Al^{VI} + 0.7(Fe/(Fe+Mg))] + 18$

4. Walshe (1986):

based on the geothermometer $2Mg_5Al_2Si_3O_{10}(OH)_8 + 14/3SiO_2 + 8/3H_2O_{(l)} \Leftrightarrow Al_4Si_4O_{10}(OH)_8 + 10/6Mg_6Si_4O_{10}(OH)_8$, temperature is calculated based on the six component model from:

$\text{Log } K = 1626/T - 6.542$

where : $K = [(a_1)^{10/6}(a_5)] / [(a_2)^2]$

and: $Mg_5Al_2Si_3O_{10}(OH)_8$ = component 1 with activity a_1

$Al_4Si_4O_{10}(OH)_8$ = component 2 with activity a_2

$Mg_6Si_4O_{10}(OH)_8$ = component 5 with activity a_5

activities are calculated by: $a_1 = (X_{Mg,O})^6(X_{Si,T})^2$

$a_2 = 59.720(X_{Mg,O})^5(X_{Al,O})(X_{Si,T})(X_{Al,T})$

a_5 = mole fraction of component 5 (calculated using the proportion of octahedral vacancies*)

where $X_{y,z}$ = the mole fraction of atom "y" in structural site "z" (O = octahedral; T = tetrahedral)

* where the octahedral vacancy is zero or less than zero, this reaction is not applicable and temperatures have not been obtained. This applies to three analyses from the massive sulphides and three from the regional volcanics.

Calculated temperatures using these four methods are given in table B4(i).

Table B4(i). Calculations for chlorite geothermometry.

analsyis ref	190802-1/#13	190802-1/#14	190802-1/#15	190802-1/#20	190802-1/#4	190802-1/#5	190802-1/#6	190802-2/#1	190802-2/#10	190802-2/#11	190802-2/#12
sample number	01BT054	01BT054	01BT054	01BT054	01BT004	01BT004	01BT004	01BT002a	01BT002a	01BT002a	01BT002a
Si4+	2.76	2.74	2.80	2.84	2.79	2.82	2.80	2.82	2.70	2.84	2.80
Fe2+	0.16	0.15	0.13	0.12	0.10	0.09	0.08	0.12	0.17	0.13	0.13
Mn2+	0.02	0.02	0.01	0.01	0.01	0.02	0.02	0.01	0.02	0.01	0.02
Mg2+	4.20	4.20	4.23	4.10	4.42	4.16	4.20	4.21	4.16	4.04	4.09
Al 3+ tet	1.24	1.26	1.20	1.16	1.21	1.18	1.20	1.18	1.30	1.16	1.20
Al 3+ oct	1.49	1.51	1.49	1.57	1.38	1.55	1.53	1.49	1.53	1.59	1.57
total (Si, Al)	4.00	4.00	4.00	4.00	4.00	4.00	4.00	4.00	4.00	4.00	4.00
total (Al,Mg,Fe, Mn)	5.87	5.88	5.86	5.80	5.91	5.81	5.83	5.84	5.87	5.77	5.81
T (^{o}C) (Cathelineau 1988)	338.08	345.08	324.06	312.89	328.65	318.05	323.17	318.81	355.09	311.40	325.11
T (^{o}C) (Jowett 1991)	328.47	335.34	314.37	303.27	318.64	308.11	313.14	309.12	345.38	301.86	315.44
T (^{o}C) (Kranidiotis & Maclean, 1987)	152.40	154.57	147.29	143.55	148.16	144.62	146.21	145.46	158.12	143.22	147.72
Calculation for Walshe (1986)											
Xmg,o	0.72	0.71	0.72	0.71	0.75	0.72	0.72	0.72	0.71	0.70	0.70
Xsi,t	0.69	0.68	0.70	0.71	0.70	0.70	0.70	0.70	0.68	0.71	0.70
Xal,o	0.25	0.26	0.25	0.27	0.23	0.27	0.26	0.26	0.26	0.28	0.27
Xal,t	0.31	0.32	0.30	0.29	0.30	0.30	0.30	0.30	0.32	0.29	0.30
a1	0.06	0.06	0.07	0.06	0.08	0.07	0.07	0.07	0.06	0.06	0.06
a2	0.61	0.62	0.62	0.59	0.69	0.62	0.64	0.62	0.61	0.57	0.59
a5	0.06	0.06	0.07	0.10	0.04	0.09	0.09	0.08	0.06	0.11	0.09
k	0.00	0.00	0.00	0.00	0.00	0.00	0.00	0.00	0.00	0.00	0.00
T (K)	430.27	434.86	419.29	406.25	438.33	409.86	413.88	414.61	437.03	402.34	413.31
T ^{o}C	157.27	161.86	146.29	133.25	165.33	136.86	140.88	141.61	164.03	129.34	140.31

Table B4(i). Calculations for chlorite geothermometry (contd.).

analsyis ref	190802-2/#13	190802-2/#14	190802-2/#15	190802-2/#19	190802-2/#2	190802-2/#20	190802-2/#21	190802-2/#22	190802-2/#23	190802-2/#3	190802-2/#32
sample number	01BT002a	01BT002a	01BT002a	010820/03	01BT002a	010820/03	010820/03	010820/03	010820/03	01BT002a	01BT061
Si4+	2.78	2.78	2.76	2.84	2.76	2.90	2.91	2.83	2.83	2.82	2.79
Fe2+	0.15	0.14	0.14	2.11	0.12	2.08	2.05	2.13	2.06	0.14	0.09
Mn2+	0.01	0.01	0.01	0.05	0.01	0.04	0.04	0.04	0.05	0.01	0.01
Mg2+	4.16	4.29	4.16	2.72	4.32	2.71	2.70	2.74	2.73	4.26	4.36
Al 3+ tet	1.22	1.22	1.24	1.16	1.24	1.10	1.09	1.17	1.17	1.18	1.21
Al 3+ oct	1.53	1.44	1.54	1.13	1.44	1.14	1.17	1.12	1.15	1.46	1.43
total (Si, Al)	4.00	4.00	4.00	4.00	4.00	4.00	4.00	4.00	4.00	4.00	4.00
total (Al,Mg,Fe, Mn)	5.85	5.88	5.85	6.00	5.89	5.97	5.95	6.02	6.00	5.86	5.89
T (^{o}C) (Cathelineau 1988)	331.59	329.66	338.11	309.99	337.22	292.72	290.63	314.63	314.91	319.03	326.99
T (^{o}C) (Jowett 1991)	321.96	319.94	328.35	313.40	327.34	296.20	294.06	318.01	318.07	309.44	316.92
T (^{o}C) (Kranidiotis & Maclean, 1987)	150.10	149.21	152.07	172.85	151.48	166.93	166.09	174.41	173.99	145.77	147.45
Calculation for Walshe (1986)											
Xmg,o	0.71	0.73	0.71	0.45	0.73	0.45	0.45	0.45	0.46	0.73	0.74
Xsi,t	0.69	0.70	0.69	0.71	0.69	0.72	0.73	0.71	0.71	0.70	0.70
Xal,o	0.26	0.25	0.26	0.19	0.24	0.19	0.20	0.19	0.19	0.25	0.24
Xal,t	0.31	0.30	0.31	0.29	0.31	0.28	0.27	0.29	0.29	0.30	0.30
a1	0.06	0.07	0.06	0.00	0.07	0.00	0.00	0.00	0.00	0.07	0.08
a2	0.60	0.64	0.61	0.04	0.66	0.04	0.04	0.04	0.05	0.62	0.68
a5	0.08	0.06	0.08	0.00	0.06	0.02	0.02	-0.01	0.00	0.07	0.06
k	0.00	0.00	0.00	0.00	0.00	0.00	0.00	0.00	0.00	0.00	0.00
T (K)	421.65	426.81	425.30	NA	432.01	456.83	436.18	NA	NA	416.93	427.84
T ^{o}C	148.65	153.81	152.30	NA	159.01	183.83	163.18	NA	NA	143.93	154.84

Table B4(i). Calculations for chlorite geothermometry (contd.).

analsyis ref	190802-2/#33	190802-2/#34	190802-2/#35	190802-2/#36	190802-2/#37	190802-2/#38	190802-2/#39	190802-2/#40	190802-2/#6	190802-2/#7	190802-2/#8
sample number	01BT061	01BT061	01BT061	01BT061	01BT061	01BT061	01BT061	01BT061	01BT002a	01BT002a	01BT002a
Si4+	2.80	2.82	3.15	3.14	3.18	2.83	2.81	2.79	2.90	2.76	2.77
Fe2+	0.08	0.08	0.06	0.07	0.07	0.08	0.08	0.08	0.11	0.14	0.13
Mn2+	0.01	0.01	0.02	0.02	0.01	0.01	0.01	0.01	0.01	0.02	0.01
Mg2+	4.35	4.46	3.42	3.44	3.37	4.41	4.42	4.38	3.94	4.25	4.21
Al 3+ tet	1.20	1.18	0.85	0.86	0.82	1.17	1.19	1.21	1.10	1.24	1.23
Al 3+ oct	1.43	1.35	1.93	1.92	1.96	1.39	1.38	1.42	1.61	1.48	1.51
total (Si, Al)	4.00	4.00	4.00	4.00	4.00	4.00	4.00	4.00	4.00	4.00	4.00
total (Al,Mg,Fe, Mn)	5.87	5.91	5.43	5.45	5.41	5.88	5.90	5.89	5.68	5.88	5.86
T (^{o}C) (Cathelineau 1988)	323.32	317.08	211.54	215.17	200.63	313.49	321.45	329.21	293.86	336.60	333.05
T (^{o}C) (Jowett 1991)	313.28	307.06	202.50	206.17	191.76	303.48	311.42	319.12	284.37	326.84	323.26
T (^{o}C) (Kranidiotis & Maclean, 1987)	146.24	144.09	109.35	110.73	105.92	142.86	145.59	148.18	137.17	151.54	150.23
Calculation for Walshe (1986)											
Xmg,o	0.74	0.75	0.63	0.63	0.62	0.75	0.75	0.74	0.69	0.72	0.72
Xsi,t	0.70	0.71	0.79	0.78	0.80	0.71	0.70	0.70	0.72	0.69	0.69
Xal,o	0.24	0.23	0.36	0.35	0.36	0.24	0.23	0.24	0.28	0.25	0.26
Xal,t	0.30	0.29	0.21	0.22	0.20	0.29	0.30	0.30	0.28	0.31	0.31
a1	0.08	0.09	0.04	0.04	0.04	0.09	0.09	0.08	0.06	0.07	0.07
a2	0.68	0.70	0.35	0.36	0.33	0.69	0.69	0.69	0.55	0.63	0.63
a5	0.06	0.05	0.28	0.28	0.30	0.06	0.05	0.05	0.16	0.06	0.07
k	0.00	0.00	0.01	0.01	0.01	0.00	0.00	0.00	0.00	0.00	0.00
T (K)	420.96	428.27	357.49	358.85	354.07	419.42	430.22	430.69	386.02	430.91	424.73
T ^{o}C	147.96	155.27	84.49	85.85	81.07	146.42	157.22	157.69	113.02	157.91	151.73

Table B4(i). Calculations for chlorite geothermometry (contd.).

analsyis ref	190802-2/#9	200802-1/#1	200802-1/#2	200802-1/#3	200802-1/#4	200802-4/#1	200802-4/#16	200802-4/#17	200802-4/#18	200802-4/#2	200802-4/#3
sample number	01BT002a	901	901	901	901	01BT098	01BT052	01BT052	01BT052	01BT098	01BT098
Si4+	2.84	2.67	2.68	2.66	2.63	2.96	2.92	2.82	2.80	2.96	2.99
Fe2+	0.13	3.06	2.87	2.90	2.97	0.27	0.17	0.16	0.16	0.38	0.31
Mn2+	0.01	0.14	0.13	0.13	0.13	0.01	0.01	0.02	0.02	0.02	0.01
Mg2+	4.19	1.30	1.30	1.39	1.30	4.19	3.70	4.09	4.06	4.02	4.05
Al 3+ tet	1.16	1.33	1.32	1.34	1.37	1.04	1.08	1.18	1.20	1.04	1.01
Al 3+ oct	1.50	1.45	1.56	1.49	1.52	1.36	1.76	1.54	1.58	1.39	1.41
total (Si, Al)	4.00	4.00	4.00	4.00	4.00	4.00	4.00	4.00	4.00	4.00	4.00
total (Al,Mg,Fe, Mn)	5.83	5.94	5.87	5.92	5.92	5.83	5.65	5.82	5.81	5.81	5.79
T (^{o}C) (Cathelineau 1988)	312.51	367.50	362.57	368.77	379.79	271.33	285.74	318.17	326.06	271.57	264.01
T (^{o}C) (Jowett 1991)	302.92	378.82	373.51	379.27	390.82	263.11	276.87	308.79	316.57	264.18	256.21
T (^{o}C) (Kranidiotis & Maclean, 1987)	143.47	211.41	208.78	209.94	215.05	132.23	135.79	145.96	148.48	134.24	130.64
Calculation for Walshe (1986)											
Xmg,o	0.72	0.22	0.22	0.24	0.22	0.72	0.66	0.70	0.70	0.69	0.70
Xsi,t	0.71	0.67	0.67	0.67	0.66	0.74	0.73	0.70	0.70	0.74	0.75
Xal,o	0.26	0.24	0.27	0.25	0.26	0.23	0.31	0.27	0.27	0.24	0.24
Xal,t	0.29	0.33	0.33	0.33	0.34	0.26	0.27	0.30	0.30	0.26	0.25
a1	0.07	0.00	0.00	0.00	0.00	0.08	0.04	0.06	0.06	0.06	0.07
a2	0.61	0.00	0.00	0.00	0.00	0.51	0.44	0.57	0.57	0.44	0.46
a5	0.08	0.03	0.06	0.04	0.04	0.08	0.18	0.09	0.10	0.09	0.11
k	0.00	0.00	0.00	0.00	0.00	0.00	0.00	0.00	0.00	0.00	0.01
T (K)	409.71	480.33	440.94	465.58	469.52	388.89	386.62	410.87	413.29	386.19	381.74
T ^{o}C	136.71	207.33	167.94	192.58	196.52	115.89	113.62	137.87	140.29	113.19	108.74

Table B4(i). Calculations for chlorite geothermometry (contd.).

analsyis ref	200802-4/#4	200802-4/#5	200802-4/#6	200802-4/#7	200802-4/#8	200802-4/#9	200802-5/#1	200802-5/#10	200802-5/#2	200802-5/#3	200802-5/#4
sample number	00BT12	00BT12	00BT12	00BT12	00BT12	00BT12	902	01BT191	902	902	902
Si4+	3.15	3.11	3.05	2.74	2.76	2.70	2.76	2.73	2.72	2.70	2.71
Fe2+	0.25	0.23	0.23	0.32	0.32	0.31	3.38	1.60	3.37	3.53	3.57
Mn2+	0.01	0.01	0.01	0.02	0.02	0.01	0.00	0.04	0.01	0.01	0.02
Mg2+	3.42	3.33	3.21	3.94	3.92	3.98	1.37	3.01	1.35	1.27	1.21
Al 3+ tet	0.85	0.89	0.95	1.26	1.24	1.30	1.24	1.27	1.28	1.30	1.29
Al 3+ oct	1.81	1.91	2.01	1.57	1.57	1.56	1.25	1.32	1.27	1.22	1.22
total (Si, Al)	4.00	4.00	4.00	4.00	4.00	4.00	4.00	4.00	4.00	4.00	4.00
total (Al,Mg,Fe, Mn)	5.49	5.48	5.46	5.84	5.83	5.87	5.99	5.97	6.00	6.03	6.02
T (°C) (Cathelineau 1988)	213.33	223.63	242.85	342.66	337.82	355.16	337.01	347.08	348.94	356.90	352.84
T (°C) (Jowett 1991)	205.88	215.96	235.04	334.23	329.48	346.52	348.95	347.31	360.85	369.41	365.75
T (°C) (Kranidiotis & Maclean, 1987)	113.69	116.79	123.21	156.76	155.28	160.66	202.17	178.45	206.28	210.47	209.96
Calculation for Walshe (1986)											
Xmg,o	0.62	0.61	0.59	0.67	0.67	0.68	0.23	0.50	0.22	0.21	0.20
Xsi,t	0.79	0.78	0.76	0.69	0.69	0.68	0.69	0.68	0.68	0.67	0.68
Xal,o	0.33	0.35	0.37	0.27	0.27	0.27	0.21	0.22	0.21	0.20	0.20
Xal,t	0.21	0.22	0.24	0.31	0.31	0.32	0.31	0.32	0.32	0.33	0.32
a1	0.04	0.03	0.02	0.04	0.04	0.04	0.00	0.01	0.00	0.00	0.00
a2	0.31	0.30	0.28	0.48	0.47	0.50	0.00	0.09	0.00	0.00	0.00
a5	0.25	0.26	0.27	0.08	0.09	0.07	0.00	0.01	0.00	-0.01	-0.01
k	0.01	0.01	0.01	0.00	0.00	0.00	0.00	0.00	0.00	0.00	0.00
T (K)	356.38	362.42	370.74	425.61	420.55	437.81	NA	503.92	NA	NA	NA
T °C	83.38	89.42	97.74	152.61	147.55	164.81	NA	230.92	NA	NA	NA

Table B4(i). Calculations for chlorite geothermometry (contd.).

analsyis ref	200802-5/#5	200802-5/#6	200802-5/#7	200802-5/#8	200802-5/#9	200802-7/#10	200802-7/#11	200802-7/#24	200802-7/#25	200802-7/#26	200802-7/#8	200802-7/#9
sample number	01BT058	01BT058	01BT058	01BT191	01BT191	010820/11	010820/11	01BT162	01BT162	01BT162	010820/11	010820/11
Si4+	2.95	2.97	2.96	2.77	2.75	2.93	2.91	2.80	2.81	2.79	2.96	2.95
Fe2+	0.13	0.13	0.13	1.50	1.55	2.24	2.28	0.34	0.32	0.32	2.26	2.25
Mn2+	0.02	0.01	0.02	0.04	0.04	0.02	0.03	0.01	0.01	0.01	0.02	0.02
Mg2+	4.13	4.10	4.12	3.13	3.08	2.54	2.48	3.96	3.94	3.96	2.48	2.45
Al 3+ tet	1.05	1.03	1.04	1.23	1.25	1.07	1.09	1.20	1.19	1.21	1.04	1.05
Al 3+ oct	1.49	1.50	1.49	1.30	1.31	1.14	1.16	1.53	1.55	1.53	1.15	1.19
total (Si, Al)	4.00	4.00	4.00	4.00	4.00	4.00	4.00	4.00	4.00	4.00	4.00	4.00
total (Al,Mg,Fe, Mn)	5.77	5.75	5.76	5.96	5.97	5.94	5.95	5.84	5.82	5.83	5.91	5.91
T (^{o}C) (Cathelineau 1988)	274.68	268.57	274.21	334.51	340.89	283.71	289.88	325.37	322.42	327.59	272.92	275.43
T (^{o}C) (Jowett 1991)	265.47	259.42	265.02	334.12	340.75	288.35	294.81	317.24	314.18	319.30	277.97	280.48
T (^{o}C) (Kranidiotis & Maclean, 1987)	131.10	129.10	130.99	172.60	175.43	166.50	169.32	151.41	150.12	151.81	163.65	164.53
Calculation for Walshe (1986)												
Xmg,o	0.72	0.71	0.71	0.52	0.52	0.43	0.42	0.68	0.68	0.68	0.42	0.41
Xsi,t	0.74	0.74	0.74	0.69	0.69	0.73	0.73	0.70	0.70	0.70	0.74	0.74
Xal,o	0.26	0.26	0.26	0.22	0.22	0.19	0.20	0.26	0.27	0.26	0.19	0.20
Xal,t	0.26	0.26	0.26	0.31	0.31	0.27	0.27	0.30	0.30	0.30	0.26	0.26
a1	0.07	0.07	0.07	0.01	0.01	0.00	0.00	0.05	0.05	0.05	0.00	0.00
a2	0.56	0.55	0.55	0.11	0.10	0.03	0.03	0.47	0.47	0.48	0.03	0.03
a5	0.12	0.13	0.12	0.02	0.02	0.03	0.03	0.08	0.09	0.09	0.04	0.05
k	0.00	0.01	0.00	0.00	0.00	0.00	0.00	0.00	0.00	0.00	0.00	0.00
T (K)	385.31	381.25	384.36	481.46	488.93	424.42	429.93	417.00	412.17	415.79	402.35	404.33
T ^{o}C	112.31	108.25	111.36	208.46	215.93	151.42	156.93	144.00	139.17	142.79	129.35	131.33

APPENDIX C

APPENDIX C1 : FLUID INCLUSION DATA

Table C1(i) lists thermometric data for fluid inclusions:

Tfm – temperature of first ice melt (°C)

Tlm – temperature of last ice melt (°C)

Th – homogenisation temperature (°C)

type: P – primary; PS – pseudosecondary; S – secondary

mode: L – homogenises to liquid phase.

nd – not determined.

Date	sample #	inclusion #	mineral	type	Fill	Tfm (°C)	Tlm (°C)	Th (°C)	Mode
2001	906#1	1	Ba	P	0.95	nd	-2.4	stretched	L
2001	906#1	2	Ba	P	0.95	-26.0	-1.3	stretched	L
2001	906#1	3	Ba	P	0.95	-24.8	-0.9	stretched	L
2001	906#1	4	Ba	P	0.95	nd	-1.7	stretched	L
2001	906#1	5	Ba	P	0.95	-36.2	-1.2	stretched	L
2001	906#1	6	Ba	P	0.95	-23.0	-1.1	stretched	L
2001	906#1	7	Ba	P	0.95	-24.0	-1.2	stretched	L
2001	00BT08#4	1	Ba	P	0.95	nd	nd	138.0	L
2001	00BT08#4	2	Ba	P	0.9	nd	-2.5	nd	L
2001	00BT08#4	3	Ba	P	0.85	nd	-1.5	nd	L
2001	905#1	1	Sph	PS	0.95	nd	nd	133.2	L
2001	905#1	2	Sph	PS	0.95	nd	nd	139.1	L
2001	905#1	3	Sph	PS	0.95	nd	nd	151.8	L
2001	905#1	4	Sph	PS	0.95	nd	nd	162.8	L
2001	905#1	5	Sph	PS	0.95	nd	nd	137.0	L
2001	905#1	6	Sph	PS	0.95	nd	nd	141.6	L
2001	905#1	7	Sph	PS	0.95	nd	nd	140.3	L
2001	905#1	8	Sph	PS	0.95	nd	nd	137.5	L
2001	905#1	9	Sph	PS	0.95	nd	nd	143.4	L
2001	905#1	10	Sph	S	0.95	nd	nd	139.1	L
2001	905#1	11	Sph	S	0.95	nd	nd	121.4	L
2001	905#1	12	Sph	S	0.95	nd	nd	124.8	L
2001	905#1	13	Sph	S	0.95	nd	nd	122.5	L
2002	01BT082#1	1	ba	P	0.95	nd	-1.8	nd	L
2002	01BT082#1	2	ba	P	0.95	nd	-2.6	nd	L
2002	01BT082#1	3	ba	P	0.95	nd	-1.9	nd	L
2002	01BT082#1	4	ba	P	0.95	nd	-2	nd	L
2002	01BT082#1	5	ba	P	0.95	nd	-3.1	nd	L
2002	01BT082#1	6	ba	P	0.95	nd	-2.2	nd	L
2002	01BT082#1	7	ba	P	0.95	nd	-1.1	nd	L
2002	01BT082#2	1	Sph	P	0.95	nd	-1.1	141.0	L
2002	01BT082#2	2	Sph	P	0.95	nd	-1.3	nd	L
2002	01BT082#2	3	Sph	P	0.95	nd	-1.2	146.0	L
2002	01BT082#2	4	Sph	P	0.95	nd	-1.8	154.0	L
2002	01BT082#2	5	Sph	P	0.95	nd	nd	142.0	L
2002	01BT082#2	6	Sph	P	0.95	nd	-1.8	157.0	L
2002	01BT082#2	7	Sph	P	0.95	nd	nd	139.0	L
2002	01BT082#2	8	Sph	P	0.95	nd	-1.9	152.0	L
2002	01BT082#2	9	Sph	P	0.95	nd	-1.3	144.0	L
2002	01BT082#2	10	Sph	P	0.95	nd	-1.4	142.0	L
2002	01BT082#1	8	Sph	P	0.95	nd	-1.3	nd	L
2002	01BT082#1	9	Sph	P	0.95	nd	NV	118.0	L
2002	01BT082#1	10	Sph	P	0.95	nd	nd	144.0	L
2002	01BT082#1	11	Sph	P	0.95	nd	-1.3	142.0	L
2002	01BT082#1	12	Sph	P	0.95	nd	nd	145.0	L
2002	01BT082#1	13	Sph	P	0.95	nd	-1.6	147.0	L
2002	01BT138#1	1	Sph	P	0.95	nd	NV	128.0	L
2002	01BT138#1	3	Sph	P	0.95	nd	NV	142.0	L
2002	01BT138#1	4	Sph	P	0.95	nd	-1.7	145.0	L
2002	01BT157#1	10	Qtz	P	0.95	nd	NV	118.0	L
2002	01BT157#1	11	Qtz	P	0.95	nd	nd	138.0	L
2002	01BT157#1	12	Qtz	P	0.95	nd	-1.9	140.0	L
2002	01BT157#1	13	Qtz	P	0.95	nd	nd	192.0	L
2002	01BT157#1	14	Qtz	P	0.9	nd	-1.2	189.0	L

Table C1(i). Fluid inclusion thermometric data.

Date	sample #	inclusion #	mineral	type	Fill	Tfm (°C)	Tlm (°C)	Th (°C)	Mode
2002	01BT157#1	15	Qtz	P	0.95	nd	-1.1	188.0	L
2002	01BT157#1	16	Qtz	P	0.9	nd	-1.1	189.0	L
2002	01BT145a#2	3	Qtz	P	0.95	nd	NV	113.0	L
2002	01BT145a#2	5	Qtz	P	0.95	nd	-0.8	nd	L
2002	01BT145a#2	6	Qtz	P	0.95	nd	-0.8	nd	L
2002	01BT145a#2	7	Qtz	P	0.95	nd	-0.5	nd	L
2002	01BT145a#2	8	Qtz	P	0.95	nd	NV	124.0	L
2002	01BT145a#2	9	Qtz	P	0.95	nd	NV	117.0	L
2002	01BT145a#2	10	Qtz	P	0.95	nd	NV	128.0	L
2002	01BT145a#2	11	Qtz	P	0.95	nd	NV	130.0	L
2002	01BT145a#2	12	Qtz	P	0.95	nd	-1.1	155.0	L
2002	01BT145a#2	13	Qtz	P	0.95	nd	nd	158.0	L
2002	01BT145a#2	14	Qtz	P	0.95	nd	-0.9	157.0	L
2002	01BT145a#2	15	Qtz	P	0.95	nd	NV	138.0	L
2002	01BT145a#2	16	Qtz	P	0.8	nd	nd	242.0	L
2002	01BT145a#2	17	Qtz	P	0.7	nd	nd	238.0	L
2002	01BT145a#2	18	Qtz	P	0.8	nd	-1.1	235.0	L
2002	01BT157#1	7	Qtz	S	0.9	nd	-0.1	>180	L
2002	01BT157#1	8	Qtz	S	0.9	nd	0.3	>180	L
2002	01BT069#1	1	Qtz	S	0.95	nd	NV	126.0	L
2002	01BT069#1	2	Qtz	S	0.95	nd	NV	130.0	L
2002	01BT069#1	3	Qtz	S	0.95	nd	NV	136.0	L
2002	01BT157#1	1	Sph	P	0.95	nd	-2.1	158.0	L
2002	01BT157#1	2	Sph	P	0.95	nd	-2.1	147.0	L
2002	01BT157#1	3	Sph	P	0.95	nd	-2.1	149.0	L
2002	01BT157#1	4	Sph	P	0.95	nd	-2.1	152.0	L
2002	01BT157#1	5	Sph	P	0.95	nd	-1.9	148.0	L
2002	01BT157#1	6	Sph	P	0.95	nd	-2.1	154.0	L
2002	01BT073#1	1	Sph	P	0.95	nd	-1.7	162.0	L
2002	01BT073#1	5	Sph	P	0.95	nd	NV	140.0	L
2002	01BT073#1	9	Sph	P	0.95	nd	-1.6	145.0	L
2002	01BT014#1	1	Sph	P	0.95	nd	-2.0	139.0	L
2002	01BT014#1	2	Sph	P	0.95	nd	-2.1	147.0	L
2002	01BT014#1	3	Sph	P	0.95	nd	-2.2	158.0	L
2002	01BT014#1	4	Sph	P	0.95	nd	-2.4	166.0	L
2002	01BT014#1	5	Sph	P	0.95	nd	-2.0	181.0	L
2002	01BT014#1	6	Sph	P	0.95	nd	-2.0	164.0	L
2002	01BT014#1	7	Sph	P	0.95	nd	-2.2	168.0	L
2002	01BT014#1	8	Sph	P	0.95	nd	-2.0	163.0	L
2002	01BT014#1	9	Sph	P	0.95	nd	-2.0	139.0	L
2002	01BT073#1	2	Sph	PS	0.95	nd	-1.7	147.0	L
2002	01BT073#1	3	Sph	PS	0.95	nd	-1.8	146.0	L
2002	01BT073#1	4	Sph	PS	0.95	nd	-1.8	154.0	L
2002	01BT073#1	6	Sph	PS	0.95	nd	-1.7	164.0	L
2002	01BT073#1	7	Sph	PS	0.95	nd	-1.7	152.0	L
2002	01BT073#1	8	Sph	PS	0.95	nd	-1.6	146.0	L
2002	01BT157#1	9	Sph	S	0.95	nd	-1.1	140.0	L
2002	01BT017#1	1	Qtz	P	0.9	nd	-0.9	142.0	L
2002	01BT017#1	2	Qtz	P	0.9	nd	-1.6	156.0	L
2002	01BT017#1	3	Qtz	P	0.95	nd	NV	127.0	L
2002	01BT017#1	4	Qtz	P	0.9	nd	-0.7	133.0	L
2002	01BT017#1	5	Qtz	P	0.95	nd	NV	118.0	L
2002	01BT017#1	6	Qtz	P	0.95	nd	NV	128.0	L
2002	01BT017#1	7	Qtz	P	0.95	nd	NV	129.0	L

Table C1(i). Fluid inclusion thermometric data (contd.).

Date	sample #	inclusion #	mineral	type	Fill	Tfm (°C)	Tlm (°C)	Th (°C)	Mode
2002	01BT017#1	8	Qtz	P	0.95	nd	NV	130.0	L
2002	01BT017#1	9	Qtz	P	0.95	nd	-0.6	129.0	L
2002	01BT017#1	10	Qtz	P	0.95	nd	-0.9	132.0	L
2002	01BT017#1	11	Qtz	P	0.95	nd	-0.4	157.0	L
2002	01BT017#1	12	Qtz	P	0.95	nd	NV	127.0	L
2002	01BT017#1	13	Qtz	P	0.95	nd	NV	134.0	L
2002	01BT017#1	14	Qtz	P	0.95	nd	NV	128.0	L
2002	01BT017#1	15	Qtz	P	0.95	nd	NV	133.0	L
2002	01BT017#1	16	Qtz	P	0.95	nd	NV	135.0	L
2002	01BT007#1	1	Qtz	P	0.9	nd	-1.0	134.0	L
2002	01BT007#1	2	Qtz	P	0.95	nd	NV	122.0	L
2002	01BT007#1	3	Qtz	P	0.95	nd	NV	127.0	L
2002	01BT007#1	4	Qtz	P	0.95	nd	-1.0	131.0	L
2002	01BT007#1	5	Qtz	P	0.95	nd	-0.6	147.0	L
2002	01BT007#1	6	Qtz	P	0.95	nd	NV	133.0	L
2002	01BT007#1	7	Qtz	P	0.95	nd	NV	128.0	L
2002	01BT007#1	8	Qtz	P	0.95	nd	NV	127.0	L
2002	01BT007#1	9	Qtz	P	0.95	nd	NV	130.0	L
2002	01BT007#1	10	Qtz	P	0.95	nd	NV	128.0	L
2002	01BT007#1	11	Qtz	P	0.95	nd	NV	128.0	L
2002	01BT007#1	12	Qtz	P	0.95	nd	NV	132.0	L
2002	01BT007#1	13	Qtz	P	0.95	nd	-0.9	133.0	L
2002	01BT007#1	17	Qtz	P	0.95	nd	NV	124.0	L
2002	01BT002#1	5	Qtz	P	0.95	nd	NV	133.0	L
2002	01BT002#2	1	Qtz	P	0.95	nd	NV	118.0	L
2002	01BT002#2	3	Qtz	P	0.95	nd	NV	118.0	L
2002	01BT002#2	4	Qtz	P	0.95	nd	NV	121.0	L
2002	01BT002#2	5	Qtz	P	0.95	nd	NV	113.0	L
2002	01BT002#2	6	Qtz	P	0.95	nd	NV	131.0	L
2002	01BT002#2	7	Qtz	P	0.95	nd	NV	126.0	L
2002	01BT002#2	8	Qtz	P	0.95	nd	NV	116.0	L
2002	01BT002#2	9	Qtz	P	0.95	nd	nd	132.0	L
2002	01BT105#2	1	Qtz	P	0.95	nd	-1.1	116.0	L
2002	01BT105#2	2	Qtz	P	0.95	nd	-0.9	156.0	L
2002	01BT105#2	3	Qtz	P	0.95	nd	-1.8	112.0	L
2002	01BT105#2	4	Qtz	P	0.95	nd	NV	105.0	L
2002	01BT105#2	5	Qtz	P	0.95	nd	NV	113.0	L
2002	01BT105#2	6	Qtz	P	0.95	nd	NV	NV	L
2002	01BT105#2	7	Qtz	P	0.95	nd	NV	98.0	L
2002	01BT105#2	8	Qtz	P	0.95	nd	NV	112.0	L
2002	01BT105#2	9	Qtz	P	0.95	nd	nd	110.0	L
2002	01BT105#2	10	Qtz	P	0.95	nd	NV	118.0	L
2002	01BT007#1	14	Qtz	PS	0.95	nd	NV	123.0	L
2002	01BT007#1	15	Qtz	PS	0.95	nd	-1.1	138.0	L
2002	01BT007#1	16	Qtz	PS	0.95	nd	NV	122.0	L
2002	01BT002#2	2	Qtz	PS	0.95	nd	NV	125.0	L
2002	01BT002#1	1	Sph	S	0.95	nd	0.0	115.0	L
2002	01BT002#1	2	Sph	S	0.95	nd	NV	130.0	L
2002	01BT002#1	3	Sph	S	0.95	nd	NV	122.0	L
2002	01BT002#1	4	Sph	S	0.95	nd	NV	139.0	L
2002	01BT002#1	6	Sph	S	0.95	nd	NV	133.0	L
2002	01BT065#1	12	Qtz	P	0.95	nd	-0.1	166.0	L
2002	01BT065#1	13	Qtz	P	0.95	nd	NV	122.0	L
2002	01BT065#1	2	Sph	PS	0.95	nd	nd	143.0	L

Table C1(i). Fluid inclusion thermometric data (contd.).

Date	sample #	inclusion #	mineral	type	Fill	Tfm (°C)	Tlm (°C)	Th (°C)	Mode
2002	01BT065#1	3	Sph	PS	0.95	nd	NV	135.0	L
2002	01BT065#1	4	Sph	PS	0.95	nd	nd	137.0	L
2002	01BT065#1	5	Sph	PS	0.95	nd	-1.2	145.0	L
2002	01BT065#1	6	Sph	PS	0.95	nd	-1.0	151.0	L
2002	01BT065#1	7	Sph	PS	0.95	nd	-0.9	154.0	L
2002	01BT065#1	8	Sph	PS	0.95	nd	nd	152.0	L
2002	01BT065#1	9	Sph	PS	0.95	nd	NV	141.0	L
2002	01BT065#1	10	Sph	PS	0.95	nd	-1.1	145.0	L
2002	01BT065#1	11	Sph	PS	0.95	nd	-1.2	150.0	L
2002	01BT065#1	1	Sph	S	0.95	nd	NV	137.0	L
2001	BTFL03#3	1	Qtz	P	0.9	nd	-1.0	130.0	L
2001	BTFL03#3	2	Qtz	P	0.9	nd	-1.1	143.8	L
2001	BTFL03#3	3	Qtz	P	0.9	nd	NV	129.0	L
2001	BTFL03#3	4	Qtz	P	0.9	nd	NV	130.1	L
2001	BTFL03#3	5	Qtz	P	0.9	nd	NV	122.9	L
2001	BTFL03#3	6	Qtz	P	0.9	nd	NV	126.4	L
2001	BTFL03#3	7	Qtz	P	0.95	nd	NV	128.0	L
2001	BTFL03#3	8	Qtz	P	0.95	nd	-0.9	130.5	L
2001	BTFL03#4	1	Qtz	P	0.95	nd	NV	127.0	L
2001	BTFL03#4	2	Qtz	P	0.95	nd	NV	126.0	L
2001	BTFL03#4	3	Qtz	P	0.95 + S (tspt)	nd	-0.8	128.0	L
2001	BTFL01#1	7	Qtz	P	0.95	nd	0.0	158.5	L
2001	BTFL01#1	11	Qtz	P	0.95	nd	nd	203.0	L
2001	BTFL01#1	12	Qtz	P	0.95	nd	nd	160.2	L
2001	00BT12#1	1	Qtz	P	0.95	nd	NV	126.2	L
2001	00BT12#1	2	Qtz	P	0.95	nd	NV	129.4	L
2001	00BT12#1	3	Qtz	P	0.95	nd	NV	143.2	L
2002	01BT003b#2	1	Qtz	P	0.95	nd	NV	129.0	L
2002	01BT003b#2	2	Qtz	P	0.95	nd	NV	132.0	L
2002	01BT003b#2	3	Qtz	P	0.95	nd	NV	144.0	L
2002	01BT003b#2	13	Qtz	P	0.95	nd	-0.2	167.0	L
2002	01BT003b#2	14	Qtz	P	0.95	nd	-0.1	145.0	L
2002	01BT003b#2	4	Qtz	S	0.95	nd	NV	124.0	L
2002	01BT003b#2	5	Qtz	S	0.95	nd	-0.4	132.0	L
2002	01BT003b#2	6	Qtz	S	0.95	nd	NV	129.0	L
2002	01BT003b#2	7	Qtz	S	0.95	nd	NV	115.0	L
2002	01BT003b#2	8	Qtz	S	0.95	nd	NV	122.0	L
2002	01BT003b#2	10	Qtz	S	0.95	nd	-0.2	124.0	L
2002	01BT003b#2	11	Qtz	S	0.95	nd	0.0	193.0	L
2002	01BT003b#2	12	Qtz	S	0.95	nd	NV	131.0	L
2001	BTFL01#2	1	Sph	P	0.95	nd	-0.9	176.2	L
2001	BTFL01#2	2	Sph	P	0.95	nd	nd	173.0	L
2001	BTFL01#1	1	Sph	S	0.95	nd	nd	112.0	L
2001	BTFL01#1	2	Sph	S	0.95 + S (op)	nd	NV	159.0	L
2001	BTFL01#1	3	Sph	S	0.95 + S (op)	nd	NV	128.0	L
2001	BTFL01#1	4	Sph	S	0.95	nd	NV	122.0	L
2001	BTFL01#1	5	Sph	S	0.95	nd	NV	155.5	L
2001	BTFL01#1	6	Sph	S	0.95 + S (op)	nd	NV	115.0	L
2001	BTFL01#3	1	Sph	S	0.95	nd	leaked	121.4	L
2001	BTFL01#1	13	Sph	S	0.95	nd	nd	118.5	L
2001	BTFL01#1	14	Sph	S	0.95 + S (op)	nd	NV	131.2	L
2001	BTFL01#1	15	Sph	S	0.95 + S (op)	nd	nd	128.5	L
2002	01BT003b#1	1	Sph	S	0.95	nd	NV	131.0	L
2002	01BT003b#1	2	Sph	S	0.95	nd	NV	144.0	L

Table C1(i). Fluid inclusion thermometric data (contd.).

Date	sample #	inclusion #	mineral	type	Fill	Tfm (°C)	Tlm (°C)	Th (°C)	Mode
2002	01BT003b#1	3	Sph	S	0.95	nd	NV	140.0	L
2002	01BT003b#1	5	Sph	S	0.95	nd	-1.0	142.0	L
2002	01BT003b#1	6	Sph	S	0.95	nd	-1.2	147.0	L
2002	01BT003b#1	7	Sph	S	0.95	nd	-1.0	149.0	L
2002	01BT003b#1	8	Sph	S	0.95	nd	-0.9	134.0	L
2002	01BT003b#1	9	Sph	S	0.95	nd	-1.1	153.0	L
2002	01BT003b#1	10	Sph	S	0.9	nd	-1.2	160.0	L
2002	01BT003b#1	11	Sph	S	0.95	nd	NV	129.0	L
2002	01BT003b#1	12	Sph	S	0.95	nd	-1.2	134.0	L
2002	01BT003b#1	13	Sph	S	0.95	nd	NV	108.0	L
2002	01BT003b#1	14	Sph	S	0.95	nd	NV	139.0	L
2002	01BT003b#1	15	Sph	S	0.95	nd	-1.0	149.0	L
2002	01BT003b#1	16	Sph	S	0.95	nd	NV	141.0	L
2002	01BT058a#2	2	Sph	S	0.95	nd	nd	134.0	L
2002	01BT058a#2	3	Sph	S	0.95	nd	NV	114.0	L
2002	01BT058a#2	4	Sph	S	0.95	nd	NV	121.0	L
2002	01BT058a#2	5	Sph	S	0.95	nd	NV	118.0	L
2002	01BT058a#2	6	Sph	S	0.95	nd	nd	138.0	L
2002	01BT058a#2	7	Sph	S	0.95	nd	nd	142.0	L
2001	902#1	3	Ba	P	0.95	-21.0	-2.1	162.2	L
2001	902#1	4	Ba	P	0.95	-23.0	-2.1	171.0	L
2001	902#1	5	Ba	P	0.95	-26.0	-1.9	169.1	L
2001	902#1	6	Ba	P	0.95	nd	-2.0	158.3	L
2001	902#1	7	Ba	P	0.95	-21.5	-1.5	175.5	L
2001	902#1	8	Ba	P	0.95	34.0	-1.2	159.1	L
2001	902#1	9	Ba	P	0.9	-23.0	-2.1	148.9	L
2001	902#1	10	Ba	P	0.95	nd	-1.9	147.1	L
2001	902#1	11	Ba	P	0.95	-33.0	-1.2	138.4	L
2001	902#1	12	Ba	P	0.95	nd	NV	134.0	L
2001	902#1	13	Ba	P	0.95	nd	NV	144.1	L
2001	903#2	3	Ba	P	0.95	nd	NV	220.2	L
2001	903#3	3	Ba	P	0.95	nd	nd	159.5	L
2002	902#4	1	ba	P	0.95	nd	-2.0	146.0	L
2002	902#4	2	ba	P	0.95	nd	-2.2	148.0	L
2002	902#4	3	ba	P	0.95	nd	-2.0	160.0	L
2002	902#4	4	ba	P	0.95	nd	-1.9	125.0	L
2002	902#4	5	ba	P	0.95	nd	-2.3	193.0	L
2002	902#4	6	ba	P	0.95	nd	nd	210.0	L
2002	902#4	7	ba	P	0.95	nd	nd	159.0	L
2002	902#4	8	ba	P	0.95	nd	-2.1	169.0	L
2001	903#3	1	Sph	P	0.95	nd	nd	137.8	L

Table C1(i). Fluid inclusion thermometric data (contd.).

Statistical distinction of Population I and Population II fluid inclusion data

Using the student's two-tailed t-test, where t is calculated from:

$t = (x_2-x_1)/\sqrt{((s_1^2/n_1)+(s_2^2/n_2))}$

Salinity data in Population I (wt% eq. NaCl)					Salinity data in Population II (wt% eq. NaCl)			
0.00	1.22	1.74	1.90	2.07	2.73	3.06	3.38	3.54
0.00	1.40	1.74	1.90	2.07	2.73	3.06	3.38	3.54
0.00	1.57	1.74	1.90	2.07	2.73	3.06	3.38	3.54
0.18	1.57	1.74	1.90	2.07	2.73	3.22	3.38	3.54
0.18	1.57	1.74	1.90	2.07	2.90	3.22	3.38	3.54
0.35	1.57	1.74	1.90	2.07	2.90	3.22	3.38	3.70
0.35	1.57	1.74	1.90	2.24	2.90	3.22	3.54	3.70
0.70	1.57	1.90	2.07	2.24	2.90	3.22	3.54	3.70
0.70	1.57	1.90	2.07	2.40	2.90	3.22	3.54	3.85
1.05	1.57	1.90	2.07	2.57	3.06	3.38	3.54	4.01
1.05	1.57	1.90			3.06	3.38	3.54	
mean x_1			1.56		mean x_2			3.29
n_1			53		n_2			43
standard deviation s_1			0.66		standard deviation s_2			0.32
s_1^2			0.43		s_2^2			0.10
degrees of freedom ($n_1 - 1$)			52		degrees of freedom ($n_2 - 1$)			42

Table C1(ii). data and statistics for Population I and Population II fluid inclusion salinity data.

salinity data statistics	
total degrees of freedom	92
t value	3.10

Table C1(iii). Student's t-test for Population I and Population II fluid inclusion salinity data.

Temperature data in Population I (°C)					Temperature data in Population II (°C)			
115.0	133.0	134.0	189.0	150.0	147.0	146.0	164.0	154.0
193.0	128.0	131.0	140.0	147.0	145.0	154.0	163.0	162.2
158.5	157.0	151.0	138.0	160.0	146.0	112.0	139.0	171.0
166.0	133.0	142.0	116.0	134.0	156.0	152.0	158.3	148.9
145.0	142.0	149.0	145.0	159.1	145.0	140.0	146.0	169.0
167.0	132.0	149.0	153.0	138.4	162.0	148.0	160.0	158.0
124.0	156.0	130.0	143.8	142.0	147.0	169.1	147.0	168.0
157.0	154.0	141.0	146.0	144.0	164.0	147.1	158.0	148.0
132.0	134.0	155.0	189.0	142.0	152.0	125.0	147.0	193.0
147.0	176.2	235.0	145.0	175.5	154.0	139.0	149.0	166.0
129.0	130.5	188.0			157.0	181.0	152.0	
mean x_1			149.3		mean x_2			153.7
n_1			53		n_2			43
standard deviation s_1			21.4		standard deviation s_2			13.7
s_1^2			459.1		s_2^2			186.3
degrees of freedom ($n_1 - 1$)			52		degrees of freedom ($n_2 - 1$)			42

Table C1(4). Data and statistics for Population I and Population II fluid inclusion temperature data.

temperature data statistics	
total degrees of freedom	92
t value	2.15

Table C1(5). Student's t-test for Population I and Population II fluid inclusion temperature data.

P	0.2	0.1	0.05	0.01	0.005	0.001	0.0005	0.0001
t	1.29	1.66	1.99	2.63	2.87	3.40	3.60	4.06

Table C1(6). Tabulated t values for a range of probabilities (P) for 94 degrees of freedom.

Comparing the calculated t values with those tabulated in table C1(6): For salinity data, the calculated t value of 3.10 lies between the tabulated values of 2.87 and 3.40, indicating that the probability of the means of population I and population II data being different lies between 99.5 and 99.9%. For trapping temeprature data, the calculated t value of 2.15 lies between the tabulated values of 1.99 and 2.63, indicating that the probability of the means of population I and population II data being different lies between 95 and 99%.

APPENDIC C2 : SULPHUR ISOTOPE ANALYSES

Sample preparation

Sulphide samples:

1. 10mg of monomineralic sulphide minerals hand picked using a binocular microscope.
2. Cleaned in purified water to remove lose fine grains of other phases where necessary.

Sulphate samples - dissolved and re-precipitated based on the method of Breit et al. (1985):

1. 20-50mg of barite hand picked with a binocular microscope and ground to a fine powder using an agate pestle and mortar (mass depending on sample availability).
2. 20-25mg of each sample weighed accurately into cleaned 2ml plastic centrifuge tubes, and 0.4ml saturated Na2CO3 solution (prepared by dissolving 15g of Aristar anhydrous solid Na2CO3 in 100ml purified water) added to each, which gives the recommended 1:10 ratio for BaSO4:Na2CO3.
3. Left for 12 hours in an oven at 95°C, shaken periodically. Components react by Na-Ba exchange to form solid $BaCO_3$ and SO_4^{2-} in solution.
4. Removed from oven, left to cool. Centrifuged and excess Na_2CO_3 solution containing SO_4^{2-} removed by pipette and transferred to a clean 2ml plastic centrifuge tubes, and the solid $BaCO_3$ residue is left in the original tubes. (Note the solid residue was used for Sr isotope analyses – see Appendix C4).
5. Acidified SO_4^{2-} bearing solution by adding 6M HCl dropwise until effervescence ceased. This prevents precipitation of $BaCO_3$ in the following stage.
6. Added 0.6ml of near-saturated $BaCl_2$ solution (prepared by dissolving 4.5g Aristar $BaCl_2$ solid in 15ml purified water), sufficient to fully precipitate the SO_4^{2-} in solution as $BaSO_4$, which precipitates as a fine white solid immediately upon adding the $BaCl_2$.
7. Centrifuged, removed and discarded overlying solution.
8. Washed residue with 2M HCl to remove any $BaCO_3$ which may have precipitated, and a further 2 washes with purified water to remove any excess $BaCl_2$.
9. Sample dried in oven.
10. Reprecipitated $BaSO_4$ subdivided into two samples each approximately 10mg, one for $\delta^{34}S$ and one for $\delta^{18}O$. Where insufficient amount was recovered, steps 1-9 repeated.

Analytical procedure

Sulphides - conventional method of Robinson and Kusakabe (1975):

1. 5 to15g sulphide sample accurately weighed and added to 150-200mg Cu_2O in a 5mm quartz tube plugged at each end with glass wool.
2. Sample degassed and combusted in a quartz tube in a furnace at 1075°C for 20mins, to produce SO_2 (SO_3 also produced but is reduced to SO_2 by Cu_2O).
3. Gas collected by freezing into cold finger with liquid nitrogen (-196°C), uncondensibles pumped off at the end of combustion.
4. Gas then passed through a slush trap (acetone + $CO_{2(s)}$, -78°C) to remove H_2O vapour; pentane trap used to remove $CO_{2(g)}$ by fractional sublimation/evapouration using an n-pentane trap (total gas frozen in to finger cooled by solid n-pentane (cooled by liquid nitrogen) at −130°C, upon removing the liquid nitrogen from the pentane trap and allowing to warm, CO_2 comes off first after 1-2mins and frozen into cold finger and isolated, then the pentane trap warmed to release SO_2)
5. SO_2 is transferred to the baratron by freezing into the baratron finger and residual uncondensibles pumped off.
6. Baratron isolated, finger warmed to room temperature (25°C) releasing SO_2 and a reading taken to calculate the yield.
7. SO_2 is transferred to a gas bottle ready for analysis.
8. Sample analysed using VG Sira II mass spectrometer; calibrated using a range of international and internal standards with the $\delta^{34}S_{(CDT)}$ values calculated directly from the $\delta^{66}SO_2$ ratio that is measured.

Sulphates – method of Coleman and Moore (1978), follows the above method with the following modifications:

- to step 1: added 600mg clean sand (acts as a catalyst) to sample + Cu_2O for combustion.
- to step 2: combusted at 1120°C for 40minutes, and gasses passed over a spiral of Cu wire placed in the quartz tube to assist reduction of SO_3 to SO_2.
- additional between steps 2 and 3: Throughout combustion gasses passed through a second furnace maintained at 400°C to further assist reduction of SO_3.

Data Listing

line number	standard	mineral	measured $\delta^{34}S_{(CDT)}$ (‰)	n	mean	range
SA8855	IAEA-S-2	Ag_2S	21.8			
SA8861	IAEA-S-2	Ag_2S	21.7	4	21.8	+/- 0.2
SA8873	IAEA-S-2	Ag_2S	22.0			
SA8900	IAEA-S-2	Ag_2S	21.6			
SA8801	IAEA-S-3	Ag_2S	-31.1			
SA8815	IAEA-S-3	Ag_2S	-31.0			
SA8832	IAEA-S-3	Ag_2S	-32.1			
SA8867	IAEA-S-3	Ag_2S	-31.1			
SA8898	IAEA-S-3	Ag_2S	-30.9			
SA8906	IAEA-S-3	Ag_2S	-31.5	11	-31.3	+/- 1.6
SA9270	IAEA-S-3	Ag_2S	-29.6			
SA9275	IAEA-S-3	Ag_2S	-31.9			
SA9405	IAEA-S-3	Ag2S	-31.4			
SA9279	IAEA-S-3	Ag_2S	-32.2			
SA8135	IAEA-S-3	Ag_2S	-31.0			
SA8136	NBS123	sph	17.1			
SA9411	NBS123	sph	17.2	4	17.1	+/- 0.3
SA9272	NBS123	sph	17.4			
SA9276	NBS123	sph	16.8			
SA8800	CP1	chp	-4.4			
SA8818	CP1	chp	-4.3			
SA8837	CP1	chp	-4.7			
SA8849	CP1	chp	-4.5			
SA8907	CP1	chp	-4.5			
SA9271	CP1	chp	-4.5	11	-4.5	+/- 0.2
SA9274	CP1	chp	-4.5			
SA9281	CP1	chp	-4.3			
SA9401	CP1	chp	-4.5			
SA8133	CP1	chp	-4.6			
SA8134	CP1	chp	-4.4			

Table C2(i). Standards for sulphide sulphur isotope analsyes. All are international standards except for CP1, which is an internal standard used at SUERC.

sample no	mineral	measured $\delta^{34}S_{(CDT)}$ (‰)		mean	range
		#1	#2		
01BT003	sph	2.7	2.0	2.4	+/- 0.4
01BT007	ten	-0.5	1.0	0.3	+/- 0.8
01BT003	chp	-0.8	0.5	-0.2	+/- 0.7
901	py	1.8	1.8	1.8	+/- 0.0
01BT003	sph	2.0	2.7	2.4	+/- 0.4
01BT032	sph	1.5	2.2	1.9	+/- 0.4

Table C2(ii). Sample repeats for sulphide sulphur isotope analyses.

line no	sample no	mineral	sample wt (mg)	baratron reading	yield	mass spec #	$\delta^{66}SO_2$	$\delta^{34}S_{(CDT)}$ (‰)
standards								
SA8855	IAEA-S-2	Ag_2S	9.8	23.13	93	23049	12.066	21.8
SA8861	IAEA-S-2	Ag_2S	9.8	23.42	94	23055	11.965	21.7
SA8873	IAEA-S-2	Ag_2S	10.8	26.94	98	23081	12.263	22.0
SA8900	IAEA-S-2	Ag_2S	11.1	27.71	98	23109	11.958	21.6
SA8801	IAEA-S-3	Ag_2S	12.1	30.73	100	22966	-33.204	-31.1
SA8815	IAEA-S-3	Ag_2S	11.4	29.60	102	22988	-34.076	-31.0
SA8832	IAEA-S-3	Ag_2S	11.8	30.01	100	23034	-35.304	-32.1
SA8867	IAEA-S-3	Ag2S	10.8	25.26	92	23073	-34.375	-31.1
SA8898	IAEA-S-3	Ag_2S	9.3	22.80	97	23122	-33.833	-30.9
SA8906	IAEA-S-3	Ag_2S	10.5	27.03	101	23121	-34.396	-31.5
SA9270	IAEA-S-3	Ag_2S	9.4	23.40	98	23903	-33.509	-29.6
SA9275	IAEA-S-3	Ag_2S	9.4	23.30	98	23920	-35.607	-31.9
SA9405	IAEA-S-3	Ag2S	9.3	23.70	100	24191	-35.083	-31.4
SA9279	IAEA-S-3	Ag_2S	8.3	21.30	101	23929	-35.835	-32.2
SA8135	IAEA-S-3	Ag_2S			83			-31.0
SA8800	CP1	chp	8.5	51.69	88	22957	-9.693	-4.4
SA8818	CP1	chp	9.6	64.33	97	23006	-10.584	-4.3
SA8837	CP1	chp	13.6	91.10	97	23030	-11.211	-4.7
SA8849	CP1	chp	10.5	71.40	99	23040	-11.046	-4.5
SA8907	CP1	chp	9.9	64.45	95	23112	-10.765	-4.5
SA9271	CP1	chp	11.6	77.50	97	23904	-11.315	-4.5
SA9274	CP1	chp	12.5	84.60	98	23919	-11.327	-4.5
SA9281	CP1	chp	9.7	64.60	97	23931	-11.100	-4.3
SA9401	CP1	chp	9.7	64.9	97	24187	-11.313	-4.5
SA8133	CP1	chp			87			-4.6
SA8134	CP1	chp			89			-4.4
SA8136	NBS123	sph			100			17.1
SA9272	NBS123	sph	9.1	58.90	100	23905	8.030	17.4
SA9276	NBS123	sph	9.9	63.10	98	23921	7.567	16.8
SA9411	NBS123	sph	8.6	56.50	101	24205	7.895	17.2
samples								
SA8807	01BT003	chp	11.2	77.80	101	22972	-5.358	0.5
SA8828	01BT003	chp	6.4	46.04	105	23029	-6.366	-0.8
SA8805	01BT017	chp	16.6	88.89	78	22970	-7.220	-0.5
SA8819	01BT032	chp	9.2	75.68	119	23025	-5.653	1.6
SA8874	01BT068	chp	9.0	60.17	97	23082	-4.963	2.4
SA8824	01BT082	chp	5.9	41.21	102	23009	-7.207	-0.5
SA8851	01BT130	chp	12.6	110.46	127	23061	-6.538	0.6
SA8840	01BT152	chp	7.6	52.18	100	23053	-5.891	1.4
SA8838	01BT226	chp	7.3	47.41	94	23039	-8.373	-1.5
SA9413	01BT058	chp	8.8	34.50	57	24207	-6.903	0.5
SA8912	01BT226b	chp	8.1	48.28	87	23126	-7.905	-1.2
SA8145	00BT01	chp			75			-0.7
SA8139	BTFL01	chp			69			0.9
SA8142	901	chp			69			1.8
SA8878	01BT013	gal	13.8	42.55	117	23085	-5.043	2.3
SA8843	01BT127	gal	7.4	19.26	99	23033	-7.760	-0.8
SA8852	01BT130	gal	11.4	23.72	79	23060	-8.115	-1.2
SA8913	01BT142	gal	7.6	23.52	118	23127	-6.453	0.5
SA8836	01BT226	gal	9.5	28.74	115	23038	-9.962	-3.3

Table C2(iii). Sulphide sulphur isotope analyses.

line no	sample no	mineral	sample wt (mg)	baratron reading	yield	mass spec #	$\delta^{66}SO_2$	$\delta^{34}S_{(CDT)}$ (‰)
SA8911	01BT226b	gal	6.1	20.48	128	23111	-7.873	-1.2
SA8141	901	py			62			1.8
SA8148	00BT01	py			54			-0.2
SA8137	00BT12	py			73			-0.1
SA8816	01BT014	py	11.3	81.90	69	22991	-6.932	-0.2
SA8841	01BT072	py	11.4	70.61	59	23037	-6.572	0.6
SA8831	01BT082	py	11.9	53.90	43	23035	-8.505	-1.6
SA8846	01BT127	py	7.2	55.64	73	23046	-5.734	1.5
SA8834	01BT136	py	14.7	109.12	70	23051	-7.016	0.1
SA8842	01BT152	py	11.4	97.46	81	23044	-6.324	0.9
SA8904	902b	py	3.6	36.70	97	23114	-5.183	1.9
SA8905	903b	py	5.8	40.86	67	23113	-6.658	0.2
SA8149	903	py			78			0.2
SA8143	902	py			71			1.0
SA8138	905	sph			93			1.6
SA8146	00BT01	sph			93			0.0
SA8809	01BT003	sph	14.0	88.80	98	22989	-5.049	2.0
SA8901	01BT003	sph	9.0	59.88	103	23119	-4.478	2.7
SA8808	01BT005	sph	15.5	99.89	99	22990	-6.497	0.4
SA8813	01BT018	sph	15.0	95.11	98	22986	-5.455	1.5
SA8821	01BT032	sph	11.3	71.75	98	23008	-5.497	1.5
SA8822	01BT032	sph	10.1	63.28	97	23022	-5.114	2.2
SA8876	01BT068	sph	13.7	87.20	98	23092	4.768	2.4
SA8848	01BT073	sph	14.1	79.82	87	23041	-6.241	1.0
SA8827	01BT082	sph	9.8	61.24	96	23011	-5.421	1.6
SA8854	01BT130	sph	5.5	35.19	99	23070	-5.769	1.5
SA9412	01BT169	sph	10.2	64.10	97	24206	-6.344	1.1
SA9414	01BT058	sph	6.5	39.60	94	24208	-5.873	1.7
SA8833	01BT136	sph	12.4	36.90	46	23036	-6.120	1.1
SA8850	01BT157	sph	10.7	69.14	100	23042	-5.886	1.4
SA8140	BTFL01	sph			84			1.8
SA8802	01BT002	ten	10.0	55.86	90	22967	-6.510	-0.8
SA8803	01BT005	ten	11.6	64.51	90	22968	-6.213	-0.5
SA8804	01BT007	ten	16.2	86.15	86	22969	-6.232	-0.5
SA8902	01BT007	ten	10.9	60.40	89	23110	-5.954	1.0
SA8875	01BT068	ten	11.0	64.02	94	23091	-5.380	1.9
SA8847	01BT073	ten	10.1	43.48	69	23043	-6.186	1.0
SA8826	01BT082	ten	9.8	34.86	57	23028	-7.357	-0.3
SA8853	01BT130	ten	11.2	59.09	85	23059	-5.110	2.2
SA8844	01BT157	ten	10.6	15.30	23	23054	-7.180	-0.1
SA8820	01BT158	ten	9.4	50.05	86	23026	-5.994	1.3
SA8810	01BT216	ten	14.2	77.60	88	22987	-6.561	0.3
SA8835	01BT226	ten	8.4	35.73	69	23045	-8.809	-2.0
SA8147	00BT01	ten			98			0.4
SA8144	00BT08	ten			104			-1.2

Table C2(iii). Sulphide sulphur isotope analyses (contd.).

line number	standard	mineral	measured $\delta^{34}S_{(CDT)}$ (‰)	mean	range
SA9258	NBS127	ba	20.5	21.4	+/- 0.9
SA9262	NBS127	ba	22.2		
SA9265	NBS127	ba	20.8		
SA9268	NBS127	ba	22.3		
SA9269	NBS127	ba	21.6		
SA9280	NBS127	ba	20.7		
SA9282	NBS127	ba	21.0		
SA9297	NBS127	ba	22.1		

Table C2(iv). International standards for sulphate sulphur isotope analyses.

sample no	mineral	measured $\delta^{34}S_{(CDT)}$ (‰)		mean	range
		#1	#2		
903	ba	20.4	20.4	20.4	+/- 0.0
00BT08	ba	18.4	17.7	18.1	+/- 0.4
01BT068	ba	17.7	17.4	17.6	+/- 0.2
01BT077b	ba	18.9	18.7	18.8	+/- 0.1
01BT082	ba	19.0	18.1	18.6	+/- 0.5

Table C2(iv). Sample repeats for sulphate sulphur isotope analyses.

line no	sample no	mineral	sample wt (mg)	baratron reading	yield	mass spec no	$\delta^{66}SO_2$	$\delta^{34}S_{(CDT)}$ (‰)
standards								
SA9258	NBS127	ba	10.0	14.5	54	23875	10.841	20.5
SA9262	NBS127	ba	10.6	19.3	68	23886	12.347	22.2
SA9265	NBS127	ba	11.1	16.7	56	23889	11.109	20.8
SA9268	NBS127	ba	9.7	17.9	69	23897	12.397	22.3
SA9269	NBS127	ba	9.6	20.3	78	23898	11.819	21.6
SA9280	NBS127	ba	8.5	17.2	75	23930	10.975	20.7
SA9282	NBS127	ba	8.5	18.2	80	23936	11.272	21.0
SA9293	NBS127	ba	7.1	16.5	86	23962	12.628	22.6
SA9297	NBS127	ba	8.8	21	89	23977	12.234	22.1
samples								
SA9285	903	ba	6.5	9.6	55	SA23955	10.687	20.4
SA9296	903	ba	4.9	11.4	87	SA23976	10.695	20.4
SA9259	00BT08	ba	9.9	25.7	96	SA23876	8.371	17.7
SA9301	00BT08	ba	6.1	6.8	42	SA23990	8.946	18.4
SA9286	01BT067	ba	5.0	11.6	87	SA23956	11.807	21.6
SA9264	01BT077a	ba	7.6	12.8	63	SA23888	9.407	18.9
SA9267	01BT077b	ba	7.0	7.4	38	SA23890	9.368	18.9
SA9291	01BT077b	ba	5.7	12.1	79	SA23960	9.232	18.7
SA9278	01BT082	ba	7.6	18.1	88	SA23938	8.684	18.1
SA9294	01BT082	ba	5.0	10.6	79	SA23978	9.487	19.0
SA9284	01BT103	ba	6.4	9.5	56	SA23940	9.169	18.6
SA9283	01BT106	ba	5.8	10.9	70	SA23937	9.026	18.5
SA9263	01BT135	ba	7.1	9.1	48	SA23887	9.251	18.7
SA9287	01BT138	ba	5.8	9.0	58	SA23957	10.274	19.9
SA9288	01BT145	ba	7.1	9.7	51	SA23958	9.159	18.6
SA9289	01BT169	ba	5.1	8.1	60	SA23959	10.626	20.3
SA9277	01BT226	ba	7.4	18.6	93	SA23939	8.659	18.1
SA8155	905	ba			41			17.6
SA8877	01BT068	ba	13.2	14.67	41	23087	8.202	17.4
SA8908	01BT068	ba	9.1	13.53	55	23128	8.954	17.7
SA8860	01BT171	ba	14.7	35.32	89	23064	9.158	18.5

Table C2(iv). Sulphate sulphur isotope analyses.

APPENDIX C3 : OXYGEN ISOTOPE ANALYSES

Sample preparation

Sulphates:

- Sulphate samples were hand picked, dissolved and reprecipitated using the method given in Appendix C2.

Silicates:

- For monomineralic samples (quartz, epidote, pyroxene, muscovite, chlorite), 5mg was handpicked using a binocular microscope and washed in distilled water.
- For whole rock samples, powders prepared for whole rock geochemistry were used (Appendix A3), together with additional powders prepared by the same method (given in Appendix A3).

Analytical procedures

Sulphates:

1. Approximately 10mg accurately weighed and thoroughly mixed with an equal or slightly greater mass of carbon, then placed in a clean platinum crucible.
2. Sample degassed by warming for 2hrs at 120°C in a continuously pumped vacuum.
3. Sample heated incrementally in a vacuum using an electromagnet until the crucible glowed bright orange/yellow; corresponding to a temperature of approximately 1200-1300°C, and kept at this temperature for at least 20mins until no more gas was released; SO_2 produced during combustion of sulphate is converted to CO and CO_2 by the carbon.
4. During combustion, gasses were passed though an electrode which converted any CO to CO_2. Gasses then frozen into spiral trap using liquid nitrogen (-196°C).
5. At the end of combustion, uncondensibles pumped away.
6. Spiral trap isolated and warmed to release CO_2, which was then passed through a slush trap (acetone + $CO_{2(s)}$ at -78°C) to remove H_2O vapour.
7. CO_2 frozen into a baratron finger, residual uncondensibles pumped away.
8. Baratron isolated and finger warmed to room temperature (25°C); reading taken and used to calculate yield.
9. CO_2 transferred to a gas bottle.
1. CO_2 analysed on a VG Sira 10 mass spectrometer measuring $\delta^{45}CO_2$ and $\delta^{46}CO_2$. $\delta^{45}CO_2$ gives the $^{12}C/^{13}C$ ratio which gives a qualitative indication of data quality (since this value deviates if there are problems during CO_2 preparation). The $\delta^{46}CO_2$ relates to $^{18}O/^{16}O$ and is directly converted $\delta^{18}O_{(SMOW)}$ using a set of international standards for calibration.
10. where $\delta^{44}CO_2$ and $\delta^{46}CO_2$ are measured and directly converted $\delta^{18}O_{(SMOW)}$ using a set of international standards for calibration.

Silicates: analysed using the laser fluorination method of Fouillac and Girard (1996):

2. 1-2mg of each sample weighed into individual holed holes in a steel turret (18 holes in total).
3. Turret placed in the laser chamber and degassed overnight.
4. Small volume of ClF_3 introduced into the laser chamber, and sample fluorinated using the laser until no solid residue is visible in the turret hole (turret viewed using a camera mounted at the top of the laser chamber); this produces SiF_4 and O_2 from the silicate.
5. Gasses drawn out of laser chamber under vacuum and SiF_4 and unused ClF_3 frozen into finder using liquid nitrogen (-196°C) and isolated.
6. O_2 passed through slush trap (acetone + $CO_{2(s)}$ at -78°C) to remove H_2O vapour.
7. O_2 transferred to a chamber containing a carbon rod heated until glowing red, to convert O_2 to CO_2; CO_2 frozen into bottom of chamber using liquid nitrogen. When all O_2 has been converted (monitored using pressure gauge), uncondensables pumped away.
8. Chamber thawed to release CO_2 and gas transferred to baratron, reading taken at 25°C and to calculate yield.
9. CO_2 transferred directly into VG Sira 10 mass spectrometer and $\delta^{45}CO_2$ and $\delta^{46}CO_2$ are measured as for sulphate oxygen (above). The $\delta^{46}CO_2$ relates to $^{18}O/^{16}O$ and is directly converted to $\delta^{18}O_{(SMOW)}$ using a set of international standards for calibration.

line no	standard	mineral	measured $\delta^{18}O_{(VSMOW)}$ (‰)	mean	range
SO1666	NBS127	barite	9.1	9.2	+/- 0.1
SO1672	NBS127	barite	9.1		
SO1678	NBS127	barite	9.3		
SO1684	NBS127	barite	9.2		

Table C3(i). International standards for sulphate oxygen isotope analyses.

sample no	mineral	measured $\delta^{18}O_{(VSMOW)}$ (‰)		mean	range
		#1	#2		
00BT08	barite	9.4	9.1	9.3	+/- 0.2
01BT106	barite	11.2	10.5	10.9	+/- 0.4
01BT169	barite	13.7	13.7	13.7	+/- 0.0
01BT226	barite	8.6	8	8.3	+/- 0.3

Table C3(ii). Sample repeats for sulphate oxygen isotope analyses.

line no	sample number	mineral	sample wt (mg)	C wt (mg)	baratron reading	$\delta^{45}CO_2$ (‰)	$\delta^{46}CO_2$ (‰)	$\delta^{18}O_{(VSMOW)}$ (‰)
standards								
SO1666	NBS127	barite	8.8	10.6	51.0	15.208	8.906	9.1
SO1672	NBS127	barite	7.5	11.5	43.6	15.084	8.854	9.1
SO1678	NBS127	barite	6.7	13.7	39.2	15.141	9.036	9.3
SO1684	NBS127	barite	7.2	12.9	42.3	15.234	8.920	9.2
samples								
SO1670	01BT226	barite	8.1	17.0	46.3	15.526	8.416	8.6
SO1682	01BT226	barite	8.9	13.7	50.0	14.818	7.766	8.0
SO1676	01BT169	barite	6.3	10.4	33.0	14.884	13.461	13.7
SO1683	01BT169	barite	4.2	8.3	23.8	14.615	13.442	13.7
SO1677	01BT145	barite	8.3	11.7	46.6	15.001	10.761	11.0
SO1679	01BT138	barite	6.4	9.5	34.1	14.830	9.816	10.0
SO1667	01BT135	barite	9.8	11.4	46.7	15.522	11.122	11.4
SO1668	01BT106	barite	9.5	12.2	52.2	15.713	10.923	11.2
SO1685	01BT106	barite	6.8	9.3	40.4	14.591	10.250	10.5
SO1673	01BT103	barite	9.4	15.2	51.5	16.020	11.387	11.6
SO1669	01BT082	barite	7.0	13.0	38.1	14.907	9.966	10.2
SO1681	01BT077b	barite	6.0	10.8	33.5	15.531	11.185	11.4
SO1671	01BT077a	barite	8.2	9.5	43.1	15.420	10.595	10.8
SO1680	01BT067	barite	6.4	8.8	34.8	15.452	11.747	12.0
SO1675	00BT08	barite	6.3	8.2	28.4	14.571	8.904	9.1
SO1687	00BT08	barite	7.9	14.8	45.7	15.284	9.216	9.4
SO1674	903	barite	6.2	12.8	34.2	15.236	8.830	9.1

Table C3(iiii). Sulphate oxygen isotope analyses.

date	standard	mineral	$\delta^{18}O_{(VSMOW)}$ (‰)	mean	range
22/05/02	SES	qtz	10.2	10.2	+/- 0.2
22/05/02	SES	qtz	10.4		
23/05/02	SES	qtz	10.2		
26/02/03	SES	qtz	10.2		
26/02/03	SES	qtz	10.3		
26/02/03	SES	qtz	10.2		
26/02/03	SES	qtz	10.1		
26/02/03	SES	qtz	10.3		

Table C3(iv). Standards for silicate oxygen isotope analyses.

sample no	mineral	$\delta^{18}O_{(VSMOW)}$ (‰)		mean	range
		#1	#2		
01BT073	qtz	12.9	12.6	12.8	+/- 0.2
01BT007	qtz	13.7	13.1	13.4	+/- 0.3

Table C3(v). Sample repeats for silicate oxygen isotope analyses.

date	turret #	sample number	mineral	sample wt (mg)	baratron reading	$\delta^{45}CO_2$ (‰)	$\delta^{46}CO_2$ (‰)	$\delta^{18}O_{(VSMOW)}$ (‰)
standards								
22/05/02	2	SES	qtz	1.7	OFF	-25.564	-23.925	10.2
22/05/02	3	SES	qtz	2.0	OFF	-25.448	-23.740	10.4
23/05/02	2	SES	qtz	1.2	15.70	-25.524	-23.864	10.2
26/02/03	3	SES	qtz	1.8	OFF	10.438	1.598	10.2
26/02/03	4	SES	qtz	1.8	OFF	10.319	1.760	10.3
26/02/03	5	SES	qtz	1.7	OFF	10.272	1.633	10.2
26/02/03	6	SES	qtz	1.5	15.90	10.254	1.713	10.3
26/02/03	7	SES	qtz	1.4	15.30	10.543	1.501	10.1
samples								
22/05/02	11	00BT01	qtz	1.8	OFF	-25.453	-22.382	11.8
26/02/03	16	00BT08	qtz	1.7	12.90	10.268	5.543	14.2
22/05/02	5	01BT002	qtz	1.6	OFF	-25.493	-21.045	13.1
22/05/02	10	01BT003	qtz	1.8	OFF	-25.361	-21.458	12.7
23/05/02	11	01BT005	qtz	1.7	OFF	-25.443	-21.429	12.8
22/05/02	6	01BT007	qtz	1.8	OFF	-25.481	-21.067	13.1
22/05/02	7	01BT007	qtz	1.3	OFF	-25.415	-20.501	13.7
22/05/02	17	01BT014	qtz	1.0	OFF	-25.371	-20.658	13.6
22/05/02	18	01BT032	qtz	1.1	OFF	-25.331	-20.738	13.5
23/05/02	12	01BT056#1	qtz	1.6	OFF	-25.454	-20.968	13.2
24/05/02	13	01BT056#2	qtz	2.0	9.60	-25.342	-22.570	11.6
22/05/02	14	01BT058	qtz	0.9	15.30	-25.483	-21.264	12.9
23/05/02	10	01BT068	qtz	1.3	12.20	-25.213	-20.429	13.8
23/05/02	8	01BT069	qtz	1.5	OFF	-25.549	-21.803	12.4
23/05/02	6	01BT073	qtz	1.1	11.40	-25.537	-21.271	12.9
23/05/02	9	01BT073	qtz	1.4	14.20	-25.492	-21.530	12.6
26/02/03	15	01BT082	qtz	1.7	11.60	10.392	5.258	13.9
23/05/02	5	01BT127	qtz	1.3	14.50	-25.526	-21.841	12.3
22/05/02	8	01BT130	qtz	1.5	OFF	-25.436	-20.531	13.7
22/05/02	9	01BT145	qtz	1.5	15.60	-25.353	-21.422	12.8
22/05/02	13	01BT157	qtz	2.0	OFF	-25.471	-21.749	12.4
23/05/02	3	01BT158	qtz	1.5	OFF	-25.597	-22.192	12.0
26/02/03	8	02BT04#1	qtz	2.2	OFF	10.247	4.493	13.1
26/02/03	9	02BT04#2	qtz	2.0	OFF	10.110	3.351	12.0
26/02/03	12	pyx#1	pyx	2.3	OFF	10.179	-1.883	6.7
26/02/03	13	pyx#2	pyx	1.6	14.00	10.140	-0.825	7.7
26/02/03	14	pyx#3	pyx	1.9	OFF	10.339	-1.215	7.4
27/05/02	16	01BT014	musc	1.6	OFF	-25.497	-24.199	9.9
26/05/02	15	01BT019	musc	1.5	15.60	-25.590	-23.625	10.5
28/05/02	17	01BT071	musc	1.6	14.60	-25.421	-23.762	10.3
26/02/03	10	02BT04#1	ep	2.9	OFF	10.318	-0.143	8.4
26/02/03	11	02BT04#2	ep	2.2	OFF	9.706	0.144	8.7
29/05/02	18	00BT01	chl	1.9	OFF	-25.531	-24.886	9.2
30/05/02	19	01BT118	chl	2.0	OFF	-25.582	-25.479	8.6
26/02/03	17	00BT01	wr	1.8	13.00	10.184	2.228	10.8
26/02/03	18	01BT095	wr	2.0	13.70	10.176	-0.425	8.2
26/02/03	19	01BT110	wr	2.2	8.30	10.154	1.491	10.1

Table C3(vi). Silicate oxygen isotope analyses.

Additional d18O data for whole rock samples analysed at BRGM

Analyses of whole rock samples collected in this study were carried out by C. Lerouge at BRGM using the laser fluorinaiton method of Fouillac and Girard (1996). Precision is ±0.2‰ (Lerouge, pers. comm.). Data is listed in table C3(vii).

sample number	whole rock description	$\delta^{18}O_{(VSMOW)}$ (‰)
00BT01	footwall	10.5
01BT085	footwall	9.8
00BT02	footwall	11.3
00BT17	footwall	11.7
01BT019	hanging-wall	10.2
010819/01	irendyk	11.3
010819/11	irendyk	11.1
010819/16	irendyk	11.9
010820/03	irendyk	10.4
010824/01	irendyk	8.7
010824/20	irendyk	10.6
010825/02	baimak-buribai	10.3
010826/14	irendyk	12.2
010826/20	irendyk	10.7
010825/09	baimak-buribai	12.2
010825/18	irendyk	10.4
010723/11	irendyk	8.4
010723/12	irendyk	9.8
010827/05	irendyk	9.7
010827/08	irendyk	9.4
010824/16	bogechovsky plagiogranite	6.6

Table C3(vii). Oxygen isotopic analyses of whole rock samples from Lerouge, BRGM.

APPENDIX C4 : STRONTIUM ISOTOPE ANALYSES

Sample preparation

Sulphates:

1. Sulphates were dissolved and the Ba precipitated as $BaCO_{3(s)}$ following steps 1 to 4 in the sulphate preparation method in Appendix C2. After obtaining $BaCO_{3(s)}$, which will also contain Sr from the barite, the following steps were taken:

1. $BaCO_{3(s)}$ washed three times in Elga purified water, then dried in an oven at 95°C for 3 hours.
2. $BaCO_{3(s)}$ transferred into a pre-weighed, clean plastic 2ml centrifuge tubes and weighed.
3. Added 0.5ml Elga H_2O, then 6M Aristar HNO_3 dropwise until $BaCO_3$ dissolved. Made solution up to 1.5ml volume with Elga H_2O. (Note: if too much HNO_3 is added, solid $Ba(NO_3)_2$ precipitates; this can be redissolved by further dilution with Elga H_2O).
4. Sub-sample of solutions analysed for Ba, Sr and Rb by ICP-MS calibrated using standards made up with a range of Ba, Sr and Rb concentrations; internal In-Re spike used for drift correction; data processed as described in Appendix A3.
5. Solutions sub-sampled with the volume calculated to give 2μg Sr (calculated using ICP-MS data) for column chemistry (see below).

Silicates

- For pyroxene, 100-200mg mono-mineralic samples hand-picked using a binocular microscope and cleaned in warm Aristar 2M HCl for 1 hour.
- For whole rock samples, powders prepared for whole rock geochemistry were used (Appendix A3), together with additional powders prepared by the same method (given in Appendix A3). 400mg of powder was selected.

1. Pyroxene samples and whole rock powders were dissolved with HF digest following the method for whole rock ICP-MS (Appendices A3), with volumes of acids used in digest multiplied as appropriate for sample sizes.
2. Sub-sample of solutions analysed for Sr and Rb by ICP-MS, calibrated using basalt/andesite international standards; internal In-Re spike used for drift correction; data processed as described in Appendix A3.
3. Solutions sub-sampled with the volume calculated to give 2μg Sr (calculated using ICP-MS data) for column chemistry (see below).

Sr separation using column chemistry

1. The sulphate an silicate sub-samples (containing an estimated 2μg of Sr) were dried down and redissolved in 2ml 6M Aristar HNO_3.
2. Columns prepared with a 6mm deep bed of Sr spec resin (*tert*-butyl dicyclohexano18-crown-6) overlain by 3mm anion exchange resin in a CHECK 6mm diameter column.
3. The columns were washed through with 10ml Elga H_2O followed by 10ml 6M Aristar HNO_3 twice over, and each wash collected and discarded.
4. Clean scintillation vials placed under each column and the samples (in 2ml 6M HNO3) were loaded on to the columns.
5. Samples were washed through with 6ml 6M HNO_3 followed by 9ml 6M HNO_3, collected and stored.
6. Clean Teflon pots were placed under each column, and the samples washed through with 10ml Elga H_2O. This washes out the Sr fraction which was collected in the Teflon pots.
7. The Sr fractions were dried down and loaded on to clean, degassed single Ta ribbon filaments using a Ta activator.
8. Filaments loaded into turret.

$^{87}Sr/^{86}Sr$ analysis using TIMS

Samples were analysed at 1.5 to 2V with the ion beam typically between 2.8 and 3.6A. Up to 15 blocks of data were recorded, each block containing 10 measurements. The final output is the mean of data (measurements >10% different to the rest of the data in that block are rejected).

Errors are quoted in % Standard Error (SE), which have been converted to 2SE using:
$2SE = \%SE * {}^{87}Sr/^{86}Sr * 2$

Sr isotope data

$^{87}Sr/^{86}Sr$ data is presented in Table C4(i).

sample no	type	Analysis #1				Analysis #2			
		$^{87}Sr/^{86}Sr$ as measured	$^{87}Sr/^{86}Sr$ age corrected	%SE	2SE	$^{87}Sr/^{86}Sr$ as measured	$^{87}Sr/^{86}Sr$ age corrected	%SE	2SE
010723/12	pyroxene	0.704260	0.704038	0.0025	0.0035				
020816/11	pyroxene	0.704169	0.704085	0.0011	0.0016				
020816/10	pyroxene	0.704219	0.704104	0.0008	0.0011				
01BT095	chl-rich footwall	0.708606	0.707557	0.0009	0.0013	0.708554	0.707474	0.0024	0.0034
903	barite	0.706597	0.706597	0.0011	0.0016	0.706572	0.706572	0.0010	0.0014
01BT169	barite	0.706900	0.706900	0.0008	0.0011	0.706917	0.706917	0.0011	0.0016
01BT226a	barite	0.706209	0.706209	0.0013	0.0018				
01BT226b	barite	0.706175	0.706175	0.001	0.0014				
01BT138	barite	0.706190	0.706190	0.001	0.0014				
01BT082	barite	0.706267	0.706267	0.0012	0.0017				
01BT145	barite	0.705005	0.705005	0.001	0.0014				
01BT106	barite	0.705576	0.705576	0.0019	0.0027				
01BT103	barite	0.706382	0.706382	0.0013	0.0018	0.706373	0.706373	0.0009	0.0013
01BT077a	barite	0.706546	0.706546	0.0008	0.0011				
01BT077b	barite	0.706439	0.706439	0.0012	0.0017				
00BT08	barite	0.706238	0.706238	0.0011	0.0016				
01BT135	barite	0.706129	0.706129	0.0009	0.0013				

Table C4(i). $^{87}Sr/^{86}Sr$ analyses for silicates and barite.

Age correction

For silicates, an age correction has been applied using the equation:

$$^{87}Sr/^{86}Sr(t=0) = {}^{87}Sr/^{86}Sr \text{ (measured)} - [^{87}Rb] / [^{86}Sr] * e^{(\lambda t - 1)}$$

where: $^{87}Sr/^{86}Sr(t=0)$ is the initial $^{87}Sr/^{86}Sr$ ratio at the time of barite formation (i.e. time = 0)

λ = decay constant for the reaction:

$$^{87}_{37}Rb \rightarrow {}^{87}_{38}Sr + {}^{0}_{-1}e$$

t = age of the sample, estimate at 380Ma

and:

$$[^{87}Rb] / [^{86}Sr] = ([Rb]/[Sr]) * (A^{87}Rb * RAM^{86}Sr)/(A^{86}Sr * RAM^{87}Rb)$$

where

[Rb] = concentration of Rb in ppm (as measured using ICP-MS)

[Sr] = concentration of Sr in ppm (as measured using ICP-MS)

$A^{87}Rb$ = isotopic abundance of ^{87}Rb = 27.835%

$A^{86}Sr$ = isotopic abundance of ^{86}Sr = 9.86%

$RAM^{87}Rb$ = relative atomic mass of ^{87}Rb = 86.9091

$RAM^{86}Sr$ = relative atomic mass of ^{86}Sr = 85.909265

Age correction calculations are given in table C4(ii). No age correction has been applied to barites since they contain Rb below detection.

Sample No	measured $^{87}Sr/^{86}Sr$	[Sr] ppm	[Rb] ppm	Rb/Sr	$^{87}Rb/^{86}Sr$	(λ)	age (yrs)	$e^{(\lambda t - 1)}$	$^{87}Sr/^{86}Sr$ at t=0
01BT095	0.7085543	13.42	0.96	0.072	0.200	1.42E-11	3.8E+08	0.0054106	0.7074742
01BT095(rpt)	0.7086061	13.09	0.91	0.070	0.194	1.42E-11	3.8E+08	0.0054106	0.7075565
010723/12	0.7042600	26.47	0.39	0.015	0.041	1.42E-11	3.8E+08	0.0054106	0.7040375
020816/11	0.7041690	21.96	0.12	0.006	0.015	1.42E-11	3.8E+08	0.0054106	0.7040853
020816/10	0.7042190	10.46	0.08	0.008	0.021	1.42E-11	3.8E+08	0.0054106	0.7041035

Table C4(ii). Age correction for silicate $^{87}Sr/^{86}Sr$ data.

Calculations for barite dissolutions

The extent of barite dissolution has been estimated using the Ba concentration from ICP-MS data by assuming that the initial samples was 100% pure barite, as follows:

% dissolution = $[Ba]_{(measured)} / [Ba]_{(total)} * 100$

where:

$[Ba]_{(measured)}$ = measured [Ba] in mother solution (ppm)

$[Ba]_{(total)}$ = theoretical [Ba] in mother solution had 100% dissolution been achieved

and: $[Ba]_{(total)}$ = (initial sample weight * 0.5884) / weight of mother solution

where 0.5844 = proportion by mass of Ba in barite

The Sr concentration in barite samples have the been calculated from the [Sr] in mother solutions taking into consideration the %dissolution as well as the dilution factor from sample to mother solution. These results are given in table C4(iii).

This assumes that the initial samples was 100% pure barite.

sample no	% dissolution	Sr (%)
903	60.7	0.71
00BT08	64.8	0.57
01BT077a	56.3	0.75
01BT077b	68.3	0.78
01BT082	64.5	0.64
01BT103	66.3	0.60
01BT106	63.9	0.52
01BT135	58.5	0.59
01BT138	63.2	0.49
01BT145	60.9	0.43
01BT169	52.8	0.74
01BT226a	71.8	0.44
01BT226b	64.5	0.44

Table C4(iii). Calculated barite dissolutions and Sr concentrations in barite.

APPENDIX C5 : FRACTIONATION EQUATIONS

Stable isotope equilibrium fractionation equations

The following tables list the temperature dependent O and S fractionation equations based on:

$\delta^{18}Ox\text{-}y = \delta^{18}Ox - \delta^{18}Oy \approx 1000 \ln\alpha$

and

$1000 \ln\alpha = A(10^{12}/T^4)+B(10^9/T^3)+C(10^6/T^2)+D(10^3/T)+E$

where α = fractionation factor; T = temperature in Kelvin

together with the temperature range that they are valid for, and the figure/table numbers in Chapter 6 where the equations are utilised.

x - y	reference	T (°C)	A	B	C	D	E
chlorite - H_2O	Savin & Lee (1988)	66-175	0.028	-0.312	2.50	3.72	-12.62
quartz - H_2O	Zhang et al. (1989)	180-550	-	-	3.306	-	-2.71
muscovite - H_2O	Zheng et al. (1993)	0-1200	-	-	2.380	-	-3.89
barite - H_2O	Seal et al., 2001	110-350	-	-	2.65	-	-4.97
plagioclase - H_2O	O'Neil & Taylor (1967)	350-800	-	-	2.68	-	-3.53
analcime - H_2O	Karrison & Clayton (1990)	25-400	-	-	2.78	-	-2.89
epidote - H_2O	Zheng (1993)	?	-	-	4.05	-7.81	2.29

Table C5(i). Fractionation equations for oxygen isotopes.

x - y	reference	T (°C)	A	B	C	D	E
chalcopyrite - H_2S	Ohmoto & Rye (1979)	200-600	-	-	-0.05	-	-
pyrite - H_2S	Ohmoto & Rye (1979)	200-700	-	-	0.40	-	-
sphalerite - H_2S	Ohmoto & Rye (1979)	50-705	-	-	0.10	-	-
galena - H_2S	Ohmoto & Rye (1979)	50-700	-	-	-0.63	-	-
SO_4^{2-} - H_2S	Ohmoto & Lasaga (1982)	200-350	-	-	6.46	-	0.57

Table C5(i). Fractionation equations for sulphur isotopes.

Calculation of salinity increase in liquid phase during fluid boiling

Assuming vapour phase has zero salinity, and initial fluid has seawater salinity (3.2 wt% NaCl eq.):

Salinity of residual liquid = 3.2*(1/X)

where X = fraction of fluid that has boiled

Calculation of $\delta^{18}O$ Rayleigh fractionation between liquid and vapour during boiling and condensation

To calculate the $\delta^{18}O$ fractionation factor for liquid-vapour, α(l-v): Equilibrium oygen isotope fractionation between liquid and vapour (Horita & Wesolowski, 1994):

$1000\ \ln\alpha(l\text{-}v) \approx \delta^{18}O(l) - \delta^{18}O(v) = 0.35041(10^9/T^3) - 1.6664(10^6/T^2) + 6.7123(10^3/T) - 7.685$

where T = temperature at which phase separation occurs (Kelvin)

Boiling with Rayleigh fractionation

To calculate $\delta^{18}O$ of the residual liquid (R):

$\delta^{18}O(l) = \delta^{18}O(i) * f^{(\alpha-1)}$

where: f = fraction of liquid remaining; $\delta^{18}O(i) = \delta^{18}O$ of initial fluid; $\alpha = \alpha(v\text{-}l) = 1/\alpha(l\text{-}v)$

To calculate $\delta^{18}O$ of the vapour phase produced:

$\delta^{18}O(v) = [(\delta^{18}O(l)+1000)/\alpha]-1000$

where $\alpha = \alpha(l\text{-}v)$

Condensation with Rayleigh fractionation

To calculate $\delta^{18}O$ of the residual vapour:

$\delta^{18}O(v) = \delta^{18}O(i) * f^{(\alpha-1)}$

where: f = fraction of vapour remaining; $\delta^{18}O(i) = \delta^{18}O$ of initial vapour; $\alpha = \alpha(l\text{-}v)$

To calculate $\delta^{18}O$ of the liquid phase produced:

$\delta^{18}O(v) = \alpha(\delta^{18}O(v)+1000)]-1000$

where $\alpha = \alpha(l\text{-}v)$

Calculation of $\delta^{34}S$ fractionation during the inorganic reduction of seawater sulphate

To calculate the $\delta^{34}S$ fractionation factor between SO_4^{2-} and H_2S (Ohmoto and Lasaga, 1982):

$1000 \ln\alpha \approx \delta^{34}S(SO_4^{2-}) - \delta^{34}S(H_2S) = 6.46(10^6/T^2)+0.57$

where T = temperature at which sulphate reduction occurs (Kelvin)

Assuming a closed system

$\delta^{34}S$ of the reduced sulphur produced is calculated from:

$\delta^{34}S(H_2S) = \delta^{34}S(i) + f*\alpha$

where: $\delta^{34}S(i) = \delta^{34}S$ of initial sulphate; f = fraction of sulphate reduced; α = fractionation factor

$\delta^{34}S$ of the residual sulphate is calculated from:

$\delta^{34}S(SO_4^{2-}) = \delta^{34}S(i) - [(\delta^{34}S(H_2S)*(1-f)]/f$

Assuming open system Rayleigh fractionation

$\delta^{34}S$ of the remaining sulphate produced is calculated from:

$\delta^{34}S(SO_4^{2-}) = (\delta^{34}S(i) + 1000)*f^{[(\alpha-1)\,-1000]}$

where: $\delta^{34}S(i) = \delta^{34}S$ of initial sulphate; f = fraction of sulphate reduced; α = fractionation factor

$\delta^{34}S$ of the reduced sulphur produced is calculated from:

$\delta^{34}S(H_2S) = \delta^{34}S(SO_4^{2-}) + 1000(\alpha-1)$

APPENDIX C6 : FLUID $\delta^{18}O$ CALCULATIONS

For individual samples, fluid d18O were calculated from mineral d18O and fluid inclusion data for that specific sample, using fractionation equations given in Appendix C5. Results are tabulated in table C6(i).

sample	mineral	homogenisation temperatures (°C)	mean trapping temperature (°C)	quartz $\delta^{18}O_{(VSMOW)}$ (‰)	comments
late stage footwall vein 01BT002	quartz	133 118 118 121 113 131 126 116 132 125	123	13.1	
footwall latestage vein 01BT007	quartz	134 122 127 131 147 133 128 127 130 128 128 132 133 124 123 138 122	123	13.4	$\delta^{18}O$ is mean of two values (sample repeats)
footwall mainstage 01BT003	quartz	129 132 144 167 145	143	12.7	temperatures are from fluid inclusions in cogenetic sphalerite
footwall mainstage 01BT058	quartz	134 138 142 114 121 118	128	12.9	
Footwall mainstage 01BT145	quartz	113 124 117 128 130 155 158 157 138 242 238 235	161	12.8	
footwall mainstage 01BT157	quartz	118 138 140 192 189 188 189	165	12.4	

Table C6(i). Fluid $\delta^{18}O$ calculations for individual samples.

sample	mineral	homogenisation temperatures (°C)	mean trapping temperature (°C)	quartz $\delta^{18}O_{(VSMOW)}$ (‰)	comments
footwall mainstage 01BT073	quartz	145 146 162 147 164 152 146 154 140	151	12.8	temperatures from fluid inclusions in cogenetic sphalerite. $\delta^{18}O$ is mean of two values (sample repeats)
903	barite	159 138 176 169 147 158 162 171 149 134 144 125 146 160 169 148 193 210 159 220 160	162	9.1	temperatures are from fluid inclusions in barite in sample 902 as well as 903; these two samples are very similar
01BT082	barite	141 146 144 142 142 147 154 157 152 142 139 144 145 118	144	10.2	temperatures are from fluid inclusions in cogenetic sphalerite
01BT138	barite	138 133 139 152 163 137 142 140 138 143 139 121 125 123	138	9.3	temperatures are from fluid inclusions in cogenetic sphalerite

Table C6(i). Fluid $\delta^{18}O$ calculations for individual samples (contd.).

APPENDIX C7 : [Sr] - $^{87}Sr/^{86}Sr$ - $\delta^{18}O$ FLUID MIXING CALCULATIONS

Calculation of $^{87}Sr/^{86}Sr$ during fluid mixing

The proportion of seawater (X) mixed with hydrothermal fluid for the formation of barites are calculated using:

$$X = [Sr]_{HF}*((^{87}Sr/^{86}Sr)_{BA} - (^{87}Sr/^{86}Sr)_{SW}) / [Sr]_{SW}*((^{87}Sr/^{86}Sr)_{SW} - (^{87}Sr/^{86}Sr)_{MIN}) + [Sr]_{HF}*((^{87}Sr/^{86}Sr)_{MIN} - (^{87}Sr/^{86}Sr)_{HF})$$

Where:

$[Sr]_{HF}$ = Sr concentration of hydrothermal fluid

$[Sr]_{SW}$ = Sr concentration of seawater

$(^{87}Sr/^{86}Sr)_{BA}$ = Sr isotope signature of barite

$(^{87}Sr/^{86}Sr)_{HF}$ = Sr isotope signature of hydrothermal fluid

$(^{87}Sr/^{86}Sr)_{SW}$ = Sr isotope signature of seawater

$^{87}Sr/^{86}Sr$ - $\delta^{18}O$ curves for modelling barite formation

The $^{87}Sr/^{86}Sr$ of barite during fluid mixing is calculated using:

$$(^{87}Sr/^{86}Sr)_{BA} = (^{87}Sr/^{86}Sr)_{MIX}$$

where the fluid $(^{87}Sr/^{86}Sr)_{MIX}$ produced by the mixing of hydrothermal fluid and seawater is calculated using:

$$(^{87}Sr/^{86}Sr)_{MIX} = X*[Sr]_{SW}*(^{87}Sr/^{86}Sr)_{SW} + (1-X)*[Sr]_{HF}*(^{87}Sr/^{86}Sr)_{HF} / X*[Sr]_{SW} + (1-X)*[Sr]_{HF}$$

Barite $\delta^{18}O$ is calculated assuming isotopic equilibrium with fluid H_2O, where the temperature and fluid $\delta^{18}O$ are a function of mixing of end member hydrothermal fluid and seawater, calculated as follows:

$$\delta^{18}O_{(BA)} = (2.65 * (10^6 / T_{(MIX)}^2) - 4.97) + \delta^{18}O_{(MIX)}$$

and: $$T_{(MIX)} = X * T_{(SW)} + (1-X) * T_{(HF)}$$

$$\delta^{18}O_{(MIX)} = X * \delta^{18}O_{(SW)} + (1-X) * \delta^{18}O_{(HF)}$$

Temperature estimates from barite $^{87}Sr/^{86}Sr$ and $\delta^{18}O$

Formational temperature estimates were calculated from barite $^{87}Sr/^{86}Sr$ using the following (abbreviations as in previous section):

$$T = (T_{(SW)} * X) + (T_{(HF)} * (1-X))$$

where:

$$X = ([Sr]_{HF} * (((^{87}Sr/^{86}Sr)_{BA} - (^{87}Sr/^{86}Sr)_{HF})) / (([Sr]_{SW} * ((^{87}Sr/^{86}Sr)_{SW} - (^{87}Sr/^{86}Sr)_{BA}) + ([Sr]_{HF} * ((^{87}Sr/^{86}Sr)_{BA} - (^{87}Sr/^{86}Sr)_{HF}))$$

Formational temperature estimates were calculated from barite $\delta^{18}O$ using:

$$T = \sqrt{((2.65 * 10^6) / (\delta^{18}O_{(BA)} - \delta^{18}O_{(MIX)} + 4.97))}$$

where:

$$\delta^{18}O_{(MIX)} = X * \delta^{18}O_{(SW)} + (1-X) * \delta^{18}O_{(HF)}$$

using the equation above to calculate X.

APPENDIX C8 : SR AND CL CONCENTRATIONS FROM MODERN VENT FLUIDS

Table C8(i) lists Sr and Cl concentrations of end member hydrothermal fluids. A scatter plot of Sr concentration versus the square of Cl concentration (Figure C8(i)) indicates a poor correlation, and a wide range of Sr concentrations for the salinities of Balta Tau mainstage hydrothermal fluids (which are estimated at 2.4 to 6.4wt% equiv. NaCl, equivalent to approximately 400 to 1,100 mmol/kg Cl, or 170,000 to 1,200,000 $(mmol/kg)^2$).

Hydrothermal Site	[Sr] μmol/kg	[Cl] mmol/kg	$[Cl]^2$	Reference
Escanaba Trough, Gorddon Ridge	209	668	446224	Von Damm (1995)
Plume, South Cleft, JDFR	312	1087	1181569	Von Damm (1995)
Vent 1, South Cleft, JDFR	230	896	802816	Von Damm (1995)
Vent 3, South Cleft, JDFR	267	951	904401	Von Damm (1995)
Pipe Organ, North Cleft, JDFR	348	1245	1550025	Von Damm (1995)
Monolith, North Cleft, JDFR	236	908	824464	Von Damm (1995)
Monolith, North Cleft, JDFR	224	875	765625	Von Damm (1995)
TableBrigadoon, North Cleft, JDFR	226	852	725904	Von Damm (1995)
Fountain, North Cleft, JDFR	221	880	774400	Von Damm (1995)
Diffuse Composite, North Cleft, JDFR	335	784	614656	Von Damm (1995)
Hulk, Endeavour Segment, JDFR	153	505	255025	Von Damm (1995)
Crypto, Endeavour Segment, JDFR	139	479	229441	Von Damm (1995)
TP, Endeavour Segment, JDFR	129	448	200704	Von Damm (1995)
Dante, Endeavour Segment, JDFR	134	457	208849	Von Damm (1995)
Grotto, Endeavour Segment, JDFR	134	425	180625	Von Damm (1995)
LOBO, Endeavour Segment, JDFR	135	428	183184	Von Damm (1995)
Dudley, Endeavour Segment, JDFR	97	349	121801	Von Damm (1995)
S&M, Endeavour Segment, JDFR	87	334	111556	Von Damm (1995)
Peanut, Endeavour Segment, JDFR	60	253	64009	Von Damm (1995)
North, Endeavour Segment, JDFR	149	477	227529	Von Damm (1995)
TAG, MAR	99	659	434281	Von Damm (1995)
NGS, 21 EPR	90.8	573	328329	Von Damm (1990)
OBS, 21 N EPR	77	494	244036	Von Damm (1990)
SW, 21 N EPR	78	500	250000	Von Damm (1990)
HG, 21 N EPR	65	496	246016	Von Damm (1990)
HG, 21 N EPR	62	496	246016	Von Damm (1990)
Vent 1, 13 EPR	171	718	515524	Von Damm (1990)
Vent 2, 13 EPR	182	712	506944	Von Damm (1990)
Vent 3, 13 EPR	168	760	577600	Von Damm (1990)
Vent 4, 11 EPR	80	563	316969	Von Damm (1990)
Vent 5, 11 EPR	135	686	470596	Von Damm (1990)
Vent 6, 11 EPR	38	338	114244	Von Damm (1990)
TAG	103	636	404496	Edmond & Edmonds (1995)
MARK, MAR	50	559	312481	Edmond & Edmonds (1995)
MARK, MAR	51	559	312481	Edmond & Edmonds (1995)

Table C8(i). Compilation of vent fluid data for Cl and Sr concentrations.

Hydrothermal Site	[Sr] µmol/kg	[Cl] mmol/kg	$[Cl]^2$	Reference
MARK, MAR	48	563	316969	Edmond & Edmonds (1995)
Inferno, Ashes	192	624	389376	Butterfield et al. (1990)
Hillock, Ashes	145	482	232324	Butterfield et al. (1990)
Crack, Ashes	81	258	66564	Butterfield et al. (1990)
Virgin Mound, Ashes	46	176	30976	Butterfield et al. (1990)
Lau Basin, Vai Lili	20	790	624100	Fouquet et al. (1993)
Okinawa Minami-Ensei	227	527	277729	Ishibashi et al.,
Okinawa Izena	110	550	302500	Ishibashi et al.,
Izu-Bonin Suiyo	300	658	432964	Ishibashi et al.,
21 N EPR NGS	97	579	335241	Von Damm et al. (1985)
21 N EPR OBS	81	489	239121	Von Damm et al. (1985)
21 N SW	83	496	246016	Von Damm et al. (1985)
21 N HG	85	496	246016	Von Damm et al. (1985)
white lady 17 S N Fiji Ridge Basin	25	255	65025	Grimaud et al. (1991)
Kaiyo LHOS, N Fiji Basin	43	267	71289	Ishibashi et al.
Guaymas	253	637	405769	Palmer & Edmond (1989)
Guaymas	226	599	358801	Palmer & Edmond (1989)
Guaymas	172	582	338724	Palmer & Edmond (1989)
Guaymas	160	581	337561	Palmer & Edmond (1989)
Marianas	78	544	295936	Palmer & Edmond (1989)
Marianas	67	544	295936	Palmer & Edmond (1989)
Marianas	74	544	295936	Palmer & Edmond (1989)

Table C8(i). Compilation of vent fluid data for Cl and Sr concentrations (contd.).

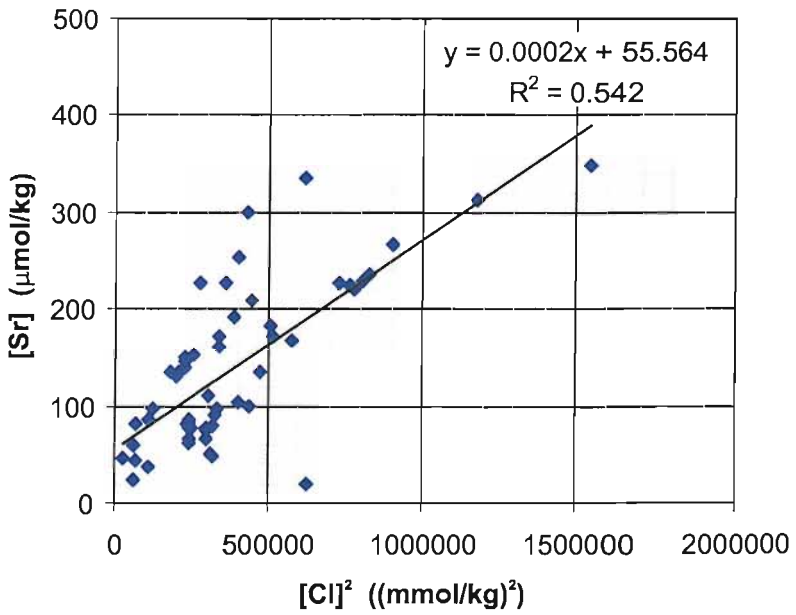

Figure C8(i). Correlation of [Sr] and $[Cl]^2$ from end member hydrothermal vent fluids.

APPENDIX D

APPENDIX D1 : THERMODYNAMIC DATA

Oxidation estimation

Table D1(i) lists the values for aO2 from 100 to 350oC used in thermodynamic calculations (taken as 3 log unit higher than the FeS – FeS_2 boundary at pH = 4, aH_2S = 0.005).

temperature (ºC)	log K*	$logaO_2$ for FeS- FeS_2 boundary	$logaO_2$ inferred for Balta Tau
100	35.73	-66.86	-63.86
150	30.34	-56.07	-53.07
200	26.05	-47.49	-44.49
250	22.56	-40.51	-37.51
300	19.57	-34.53	-31.53
350	17.51	-30.42	-27.42

Table D1(i). Oxidation conditions inferred for Balta Tau. Calculations based on logK for the reaction $FeS + 0.5O_2 + H_2S = FeS_2 + H_2O$, which rearranges to give $logaO_2 = 2*(-logK - logaH_2S)$.

Thermodynamic Data

Table D1(ii) lists the thermodynamic data used for solubility calculations, and aO_2 – temperature, aO_2-pH and aO_2-aH_2S diagrams. The aO_2-pH and aO_2-aH_2S diagrams were calculated following the method outlined in Wood (1998).

In table D1(ii), equations 1 to 17 are used for calculation of oxidation diagrams, while equations 18 to 60 relate to solubility calculations. Reaction constant (K) values marked * have been extrapolated using polynomial regression.

Table D1(ii). Thermodynamic data used.

#	Reaction	log K						reference
		100 (°C)	150 (°C)	200 (°C)	250 (°C)	300 (°C)	350 (°C)	
E1	$H_2S = HS^- + H^+$	-6.50*	-6.50	-6.68	-7.02	-7.56	-8.50	SUPCRT92 (in Gilbert et al. 1998)
E2	$HSO_4^- = SO_4^{2-} + H_+$	-3.22*	-3.72	-4.47	-5.26	-6.18	-7.40	SUPCRT92 (in Gilbert et al. 1998)
E3	$H_2S + 2O_2 = HSO_4^- + H_+$	95.35	82.93	71.44	61.97	53.93	46.69	calculated from: E3 = E4 - E2
E4	$H_2S + 2O_2 = SO_4^{2-} + 2H^+$	92.13*	79.21	66.97	56.71	47.75	39.29	SUPCRT92 (in Gilbert et al. 1998)
E5	$H_2S + 2O_2 = HSO_4^- + H^+$	98.63	85.71	73.65	63.73	55.31	47.79	E5 = E4 - E1
E6	$FeS + + 1/2O_2 + H_2S = FeS_2 + H_2O$	35.73	30.34	26.05	22.56	19.57	17.51	Huston & Large 1989
E7	$3FeS_2 + 6H_2O = Fe_3O_4 + 6H_2S + O_2$	-94.62	-79.44	-67.43	-57.66	-49.00	-44.48	Huston & Large 1990
E8	$1/3Fe_3O_4 + 1/12O_2 = 1/2Fe_2O_3$	4.59	3.91	3.38	2.94	2.59	2.29	Huston & Large 1991
E9	$2FeS_2 + 4H_2O + 15/2O_2 = Fe_2O_3 + 4SO_4^{2-} + 8H^+$	323.22	271.42	229.24	193.65	161.79	128.12	Huston & Large 1992
E10	$2FeS_2 + 4H_2O + 15/2O_2 = Fe_2O_3 + 4HSO_4^- + 4H^+$	335.18	286.30	247.16	214.73	186.11	155.72	Huston & Large 1993
E11	$3FeS + 1/2O_2 + 3H_2O = Fe_3O_4 + 3H_2S$	12.57	11.57	10.71	10.01	9.70	8.05	Huston & Large 1994
E12	$5CuFeS_2 + S_2 = Cu_5FeS_4 + 4FeS_2$	18.2*	14.20	11.10	8.50	6.40	4.30	Helgeson 1969
E13	$H_2S + 1/2O_2 = H_2O + 1/2S_2$	22.79*	20.02	17.49	15.41	13.65	12.12	SUPCRT92 (in Gilbert et al. 1998)
E14	$5CuFeS_2 + 2H_2S + O_2 = CuFeS_4 + 4FeS_2 + 2H_2O$	63.78	54.24	46.08	39.32	33.7	28.54	calculated from: E14 = E12 + 2*E13
E15	$5CuFeS_2 + 2SO_4^{2-} + 4H^+ = CuFeS_4 + 4FeS_2 + 2H_2O + 3O_2$	-120.48	-104.18	-87.86	-74.1	-61.8	-50.04	calculated from: E15 = E12 + 2*(-E4)
E16	$5CuFeS_2 + 2HSO_4^- + 2H^+ = CuFeS_4 + 4FeS_2 + 2H_2O + 3O_2$	-126.92	-111.62	-96.8	-84.62	-74.16	-64.84	E16 = E15 + 2*E2
E17	$PbS + 2H^+ = Pb^{2+} + H_2S$	-5.69	-4.68	-3.79	-2.98	-2.37	-1.84*	Bourcier & Barnes 1987
E18	$Pb^{2+} + Cl^- = PbCl^+$	1.67	2.09	2.55	3.18	3.89	4.71*	Seward 1984
E19	$Pb^{2+} + 2Cl^- = PbCl_2$	2.62	3.18	4.00	4.98	6.26	7.73*	Seward 1984
E20	$Pb^{2+} + 3Cl^- = PbCl_3^-$	2.21	2.84	3.81	5.03	6.76	8.74*	Seward 1984
E21	$Pb^{2+} + 4Cl^- = PbCl_4^{2-}$	1.93	2.36	-	-	-	-	Seward 1984
E22	$ZnS + 2H^+ = Zn^{2+} + H_2S$	-4.17	-3.80	-3.46	-3.09	-2.60	-1.72	Bourcier & Barnes 1987
E23	$Zn^{2+} + Cl^- = ZnCl^+$	1.20	2.10	3.10	4.40	5.70	7.00	Bourcier & Barnes 1987
E24	$Zn^{2+} + 2Cl^- = ZnCl_2$	1.90	3.00	4.30	5.60	7.20	9.30	Bourcier & Barnes 1987
E25	$Zn^{2+} + 3Cl^- = ZnCl_3^-$	2.30	3.80	5.20	6.70	8.10	9.30	Bourcier & Barnes 1987
E26	$Zn^{2+} + 4Cl^- = ZnCl_4^{2-}$	1.40	2.70	4.40	6.00	7.40	7.70	Bourcier & Barnes 1987
E27	$ZnS + 2H^+ = Zn^{2+} + H_2S$	-4.17	-3.80	-3.46	-3.09	-2.60	-1.72	Bourcier & Barnes 1987
E28	$Zn^{2+} + 2HS^- = Zn(HS)_2^0$	12.30	12.30	12.90	13.80	15.00	16.30	Bourcier & Barnes 1987
E29	$Zn^{2+} + 2H_2S = Zn(HS)_2^0 + 2H^+$	-0.66	-0.30	-0.20	-0.10	-0.05	-0.30	E29 = E28 + 2*E1
E30	$Zn^{2+} + 3HS^- = Zn(HS)_3^-$	14.20	14.20	14.60	15.30	16.20	17.10	Bourcier & Barnes 1987
E31	$Zn^{2+} + 3H_2S = Zn(HS)_3^- + 3H^+$	-5.24	-2.30	-2.36	-2.50	-2.81	-3.65	E31 = E30 + 3*E1
E32	$Zn^{2+} + 4HS^- = Zn(HS)_4^{2-}$	13.00	13.30	14.00	15.00	16.00	17.10	Bourcier & Barnes 1987

Table D1(ii). Thermodynamic data used (contd.).

#	Reaction	log K						reference
		100 (°C)	150 (°C)	200 (°C)	250 (°C)	300 (°C)	350 (°C)	
E33	$Zn^{2+} + 4H_2S = Zn(HS)_4^{2-} + 4H^+$	-12.92	-5.52	-5.52	-5.68	-6.18	-7.34	E33 = E32 + 4*E1
E34	$Au + H^+ = Au^+ + 1/2H^2$	-21.19	-18.29	-15.68	-13.57	-11.83	-10.37	Benning & Seward 1996
E35	$H_2O = H_2 + 1/2O_2$	-32.18	-26.85	-23.18	-20.22	-17.8	-15.78	SUPCRT92 quoted in gibert et al. 1998
E36	$Au + H^+ + 1/4O_2 = Au^+ + 1/2H_2O$	-5.1	-4.865	-4.09	-3.46	-2.93	-2.48	E36 = E34 + 0.5*(-E35)
E37	$Au^+ + Cl^- = AuCl$	6.57	6.03	5.69	5.54	5.62	6.13	Sverjensky et al. 1997
E38	$Au^+ + 2Cl^- = AuCl_2^-$	7.88	7.24	6.88	6.75	6.92	7.6	Sverjensky et al. 1997
E39	$Au^+ + 3Cl- = AuCl_3^{2-}$	7.46	6.79	6.41	6.29	6.45	7.09	Sverjensky et al. 1997
E40	$Au^+ + HS^- = Au(HS)^0$	19.62	18.17	16.58	15.08	13.53	11.83	Benning & Seward 1996
E41	$Au^+ + H_2S = Au(HS)^0 + H^+$	13.12	11.67	9.9	8.06	5.97	3.33	E41 = E40 + E1
E42	$Au^+ + 2HS^- = Au(HS)_2^-$	25.69	23.64	21.7	20.12	18.76	17.49	Benning & Seward 1996
E43	$Au^+ + 2H_2S = Au(HS)_2^- + 2H_+$	12.69	10.64	8.34	6.08	3.64	0.49	E43 = E42 +2*E1
E44	$Ag + H^+ + 2Cl^- + 1/4O_2 = AgCl_2^- + 1/2H_2O$	10.49	9.76	9.37	9.21	9.22	9.54*	Gammons & Williams-Jones 1995
E45	$Ag + 2H_2S + 1/4O_2 = Ag(HS)_2^- + 1/2H_2O + H^+$	7.2	5.09	3.26	1.63	0.13	-1.1*	Gammons & Williams-Jones 1995
E46	$FeS_2 + H_2O = Fe^{2+} + 7/4S_2^- + 1/4SO_4^{2-} + 2H^+$	-42.97	-39.74	-37.29	-35.37	-34.01	-33.32*	Helgeson 1969
E47	$H_2S + 2O_2 = 2H^+ + SO_4^{2-}$	94.31	79.31	67.13	57.10	48.55	41.00*	Helgeson 1969
E48	$HS^- = H^+ + S^{2-}$	-11.77	-10.62	-9.57	-8.61	-7.72	-6.90*	Helgeson 1969
E49	$FeS_2 + H_2O + 2H^+ = Fe^{2+} + 2H_2S + 1/2O_2$	-34.58	-29.61	-25.64	-22.30	-19.41	-16.62	E49 = E46 + 0.25*(-E47) + 1.75*(-E48) + 1.75*(-E1)
E50	$Fe^{2+} + Cl^- = FeCl^+$	0.21	0.61	1.09	1.69	2.45	3.52	Sverjensky et al. 1997
E51	$Fe^{2+} + 2Cl^- = FeCl_2$	1.92	2.39	2.95	3.63	4.47	5.57	Sverjensky et al. 1997
E52	$CuFeS_2 = Cu^{2+} + Fe^{2+} + 2S^{2-}$	-53.10	-49.20	-46.20	-43.70	-41.90	-40.98*	Helgeson 1969
E53	$Cu^{2+} + 1/2H_2O = Cu^+ + 1/4O_2 + H^+$	-12.83	-10.34	-8.35	-6.64	-5.33	-4.49*	Helgeson 1969
E54	$CuFeS_2 + H^+ + 1/4O_2 = FeS_2 + Cu^+ + 1/2H_2O$	5.19	4.31	3.59	3.22	2.74	1.95	E54 = E52 + E53 + 2*(-E48) + 2*(-E49)
E55	$Cu^+ + Cl^- = CuCl$	3.35	3.37	3.39	3.40	3.41	3.43	Xiao et al 1998
E56	$Cu^+ + 2Cl^- = CuCl^{2-}$	5.01	5.03	5.18	5.37	5.59	5.81	Xiao et al 1998
E57	$Cu^+ + 3Cl^- = CuCl_3^{2-}$	2.23	1.70	1.59	1.71	1.94	2.24	Xiao et al 1998
E58	$1/4Cu_5FeS_4 + 3/2H_2S = 1/4CuFeS_2 + H^+ + Cu(HS)_2^-$	-7.81*	-8.25*	-8.70	-9.10	-9.60	-10.00	Crerar & Barnes 1976
E59	$5CuFeS_2 + S_2 = Cu_5FeS_4 + 4FeS_2$	18.20	14.20	11.10	8.50	6.40	5.00*	Helgeson 1969
E60	$2H_2S + CuFeS_2 + 1/4O_2 = H^+ + Cu(HS)_2^- + FeS_2 + 1/2H_2O$	8.14	5.31	2.82	0.73	-1.20	-2.69	E60 = E58 + 0.25*E59 + 0.5*E13

Assumptions made in thermodynamic calculations

- Activity coefficients are assumed to be unity, i.e. activity = concentration
- The effect of other cations complexing with chloride and sulphide anions has not been taken into consideration, i.e. the concentration of the total free anion is taken to be equal to the total concentration of that anion.

The effect of these factors is likely to alter results by less than one order of magnitude (e.g. Wood and Samson, 1998), and are not therefore considered important for the general estimations used in this study as they are less than other uncertainties such as metal concentrations in fluids and aO_2-pH conditions.

APPENDIX D2: CALCULATIONS FOR pH AND H_2S VARIATIONS

Variations in pH

1. The increase in fluid pH change during seawater mixing ($pH_{(MIX)}$) was calculated from:

$$pH_{(MIX)} = X * 10^{-pH(sw)} + (1-X) * 10^{-pH(hf)}$$

where:

X = proportion of seawater

pH(sw) = pH of seawater (taken as 8)

pH(hf) = pH of hydrothermal fluid (taken as 4)

2. The decrease in pH due to sulphide precipitation ($pH_{(new)}$) was calculated using:

$$pH_{(new)} = -\log((2*S/10^6) + 10^{-pH(hf)})$$

where:

S = amount of sulphide precipitation in μmol/kg

pH(hf) = pH of hydrothermal fluid prior to sulphide precipitation (taken as 4)

Note: S is multiplied by 2 because precipitation of Fe, Cu, Zn and Pb sulphides releases 2 moles H^+ for every 1 mole of sulphide produced.

Variations in concentration of H_2S

1. The decrease in fluid H_2S concentration change during seawater mixing ($H_2S_{(MIX)}$) was calculated from:

$$H_2S_{(MIX)} = X * H_2S_{(sw)} + (1-X) * H_2S_{(hf)}$$

where:

X = proportion of seawater

$H_2S_{(sw)}$ = concentration of H_2S in seawater approximated to zero mol/kg)

$H_2S_{(hf)}$ = concentration of H_2S in hydrothermal fluid (taken as 0.005 mol/kg)

2. The decrease in H_2S due to sulphide precipitation ($H_2S_{(new)}$) was calculated using:

$$H_2S_{(new)} = H_2S_{(hf)} - (S/10^6)$$

where:

$H_2S_{(hf)}$ = concentration of H_2S in hydrothermal fluid prior to sulphide precipitation (taken as 0.005 mol/kg)

S = amount of sulphide precipitation in μmol/kg.